THE NEW FRONTIERS OF EARTHQUAKE EARLYWARNING SYSTEMS

EDITED BY: Simona Colombelli, Maren Böse, Angela Isobel Chung, Huseyin Serdar Kuyuk, Mitsuyuki Hoshiba and Masumi Yamada

PUBLISHED IN: Frontiers in Earth Science

frontiers Research Topics

ISSN 1664-8714
ISBN 978-2-88974-446-6
DOI 10.3389/978-2-88974-446-6

About Frontiers

Frontiers is more than just an open-access publisher of scholarly articles: it is a pioneering approach to the world of academia, radically improving the way scholarly research is managed. The grand vision of Frontiers is a world where all people have an equal opportunity to seek, share and generate knowledge. Frontiers provides immediate and permanent online open access to all its publications, but this alone is not enough to realize our grand goals.

Frontiers Journal Series

The Frontiers Journal Series is a multi-tier and interdisciplinary set of open-access, online journals, promising a paradigm shift from the current review, selection and dissemination processes in academic publishing. All Frontiers journals are driven by researchers for researchers; therefore, they constitute a service to the scholarly community. At the same time, the Frontiers Journal Series operates on a revolutionary invention, the tiered publishing system, initially addressing specific communities of scholars, and gradually climbing up to broader public understanding, thus serving the interests of the lay society, too.

Dedication to Quality

Each Frontiers article is a landmark of the highest quality, thanks to genuinely collaborative interactions between authors and review editors, who include some of the world's best academicians. Research must be certified by peers before entering a stream of knowledge that may eventually reach the public - and shape society; therefore, Frontiers only applies the most rigorous and unbiased reviews.
Frontiers revolutionizes research publishing by freely delivering the most outstanding research, evaluated with no bias from both the academic and social point of view. By applying the most advanced information technologies, Frontiers is catapulting scholarly publishing into a new generation.

What are Frontiers Research Topics?

Frontiers Research Topics are very popular trademarks of the Frontiers Journals Series: they are collections of at least ten articles, all centered on a particular subject. With their unique mix of varied contributions from Original Research to Review Articles, Frontiers Research Topics unify the most influential researchers, the latest key findings and historical advances in a hot research area! Find out more on how to host your own Frontiers Research Topic or contribute to one as an author by contacting the Frontiers Editorial Office: frontiersin.org/about/contact

THE NEW FRONTIERS OF EARTHQUAKE EARLY WARNING SYSTEMS

Topic Editors:
Simona Colombelli, University of Naples Federico II, Italy
Maren Böse, ETH Zurich, Switzerland
Angela Isobel Chung, University of California, Berkeley, United States
Huseyin Serdar Kuyuk, Harvard University, United States
Mitsuyuki Hoshiba, Japan Meteorological Agency, Japan
Masumi Yamada, Kyoto University, Japan

Citation: Colombelli, S., Böse, M., Chung, A. I., Kuyuk, H. S., Hoshiba, M., Yamada, M., eds. (2022). The New Frontiers of Earthquake Early Warning Systems. Lausanne: Frontiers Media SA. doi: 10.3389/978-2-88974-446-6

Table of Contents

05 ***Source Parameters of Moderate-To-Large Chinese Earthquakes From the Time Evolution of P-Wave Peak Displacement on Strong Motion Recordings***
Yuan Wang, Simona Colombelli, Aldo Zollo, Jindong Song and Shanyou Li

19 ***Magnitude Estimation for Earthquake Early Warning Using a Deep Convolutional Neural Network***
Jingbao Zhu, Shanyou Li, Jindong Song and Yuan Wang

30 ***A Framework for Evaluating Earthquake Early Warning for an Infrastructure Network: An Idealized Case Study of a Northern California Rail System***
Sarah E. Minson, Elizabeth S. Cochran, Stephen Wu and Shunta Noda

44 ***Onsite Early Prediction of PGA Using CNN With Multi-Scale and Multi-Domain P-Waves as Input***
Ting-Yu Hsu and Chao-Wen Huang

57 ***Earthquake Early Warning System in Israel—Towards an Operational Stage***
Ran N. Nof, Itzhak Lior and Ittai Kurzon

69 ***Comparing the Performance of Regional Earthquake Early Warning Algorithms in Europe***
Elisa Zuccolo, Gemma Cremen and Carmine Galasso

83 ***Performance Evaluation of an Earthquake Early Warning System in the 2019–2020 M6.0 Changning, Sichuan, China, Seismic Sequence***
Chaoyong Peng, Peng Jiang, Qiang Ma, Peng Wu, Jingrong Su, Yu Zheng and Jiansi Yang

96 ***Earthquake Early Warning System for Structural Drift Prediction Using Machine Learning and Linear Regressors***
Antonio Giovanni Iaccarino, Philippe Gueguen, Matteo Picozzi and Subash Ghimire

111 ***Real-Time Characterization of Finite Rupture and Its Implication for Earthquake Early Warning: Application of FinDer to Existing and Planned Stations in Southwest China***
Jiawei Li, Maren Böse, Yu Feng and Chen Yang

131 ***An Earthquake Early Warning System for Southwestern British Columbia***
Angela Schlesinger, Jacob Kukovica, Andreas Rosenberger, Martin Heesemann, Benoît Pirenne, Jessica Robinson and Michael Morley

145 ***FinDerS(+): Real-Time Earthquake Slip Profiles and Magnitudes Estimated from Backprojected Displacement with Consideration of Fault Source Maturity Gradient***
Maren Böse, Allie A. Hutchison, Isabelle Manighetti, Jiawei Li, Frédérick Massin and John Francis Clinton

166 ***Between Necessity and Legal Responsibility: The Development of EEWS in Italy and its International Framework***
Cecilia Valbonesi

182 ***Application of the Modified PLUM Method to a Dense Seismic Intensity Network of a Local Government in Japan: A Case Study on Tottori Prefecture***
Takao Kagawa

192 ***Feasibility Study of an Earthquake Early Warning System in Eastern Central Italy***
Chiara Ladina, Simone Marzorati, Alessandro Amato and Marco Cattaneo

206 ***Four Years of Earthquake Early Warning in Southern Iberia: 2016–2019***
Marta Carranza, Maurizio Mattesini, Elisa Buforn, Aldo Zollo and Irene Torrego

218 ***Status of Earthquake Early Warning in Switzerland***
Frédérick Massin, John Clinton and Maren Böse

238 ***Applicability of Accurate Ground Motion Estimation Using Initial P Wave for Earthquake Early Warning***
Zijun Wang and Boming Zhao

249 ***Real-Time Prediction of Impending Ground Shaking: Review of Wavefield-Based (Ground-Motion-Based) Method for Earthquake Early Warning***
Mitsuyuki Hoshiba

264 ***Preliminary Results of an Earthquake Early Warning System in Costa Rica***
Juan Porras, Frédérick Massin, Mario Arroyo-Solórzano, Ivonne Arroyo, Lepolt Linkimer, Maren Böse and John Clinton

277 ***Design, Implementation and Testing of a Network-Based Earthquake Early Warning System in Greece***
M. Bracale, S. Colombelli, L. Elia, V. Karakostas and A. Zollo

290 ***Developments of the Nationwide Earthquake Early Warning System in Japan After the 2011 M_w9.0 Tohoku-Oki Earthquake***
Yuki Kodera, Naoki Hayashimoto, Koji Tamaribuchi, Keishi Noguchi, Ken Moriwaki, Ryo Takahashi, Masahiko Morimoto, Kuninori Okamoto and Mitsuyuki Hoshiba

303 ***Applicability of On-Site P-Wave Earthquake Early Warning to Seismic Data Observed During the 2011 Off the Pacific Coast of Tohoku Earthquake, Japan***
Seiji Tsuno

frontiers in Earth Science

ORIGINAL RESEARCH
published: 18 March 2021
doi: 10.3389/feart.2021.616229

Source Parameters of Moderate-To-Large Chinese Earthquakes From the Time Evolution of P-Wave Peak Displacement on Strong Motion Recordings

Yuan Wang[1], Simona Colombelli[2], Aldo Zollo[2], Jindong Song[1] and Shanyou Li[1]**

[1]Key Laboratory of Earthquake Engineering and Engineering Vibration of China Earthquake Administration, Institute of Engineering Mechanics, China Earthquake Administration, Harbin, China, [2]Department of Physics, University of Naples Federico II, Naples, Italy

In this work we propose and apply a straightforward methodology for the automatic characterization of the extended earthquake source, based on the progressive measurement of the P-wave displacement amplitude at the available stations deployed around the source. Specifically, we averaged the P-wave peak displacement measurements among all the available stations and corrected the observed amplitude for distance attenuation effect to build the logarithm of amplitude vs. time function, named LPDT curve. The curves have an exponential growth shape, with an initial increase and a final plateau level. By analyzing and modelling the LPDT curves, the information about earthquake rupture process and earthquake magnitude can be obtained. We applied this method to the Chinese strong motion data from 2007 to 2015 with Ms ranging between 4 and 8. We used a refined model to reproduce the shape of the curves and different source models based on magnitude to infer the source-related parameters for the study dataset. Our study shows that the plateau level of LPDT curves has a clear scaling with magnitude, with no saturation effect for large events. By assuming a rupture velocity of 0.9 Vs, we found a consistent self-similar, constant stress drop scaling law for earthquakes in China with stress drop mainly distributed at a lower level (0.2 MPa) and a higher level (3.7 MPa). The derived relation between the magnitude and rupture length may be feasible for real-time applications of Earthquake Early Warning systems.

Keywords: P-wave amplitude parameter, magnitude, rupture length, stress drop, earthquake early warning

OPEN ACCESS

Edited by:
Carmine Galasso,
University College London,
United Kingdom

Reviewed by:
Gemma Cremen,
University College London,
United Kingdom
Alon Ziv,
Tel Aviv University, Israel

****Correspondence:***
Yuan Wang
wangyuanseis@gmail.com
Shanyou Li
shanyou@iem.ac.cn

Specialty section:
This article was submitted to Geohazards and Georisks, a section of the journal Frontiers in Earth Science

Received: *11 October 2020*
Accepted: *10 February 2021*
Published: *18 March 2021*

Citation:
Wang Y, Colombelli S, Zollo A, Song J and Li S (2021) Source Parameters of Moderate-To-Large Chinese Earthquakes From the Time Evolution of P-Wave Peak Displacement on Strong Motion Recordings. Front. Earth Sci. 9:616229. doi: 10.3389/feart.2021.616229

INTRODUCTION

The characterization of the seismic source in terms of earthquake magnitude and source radius (or length of the rupture) is now a routinely operation in any standard seismological laboratory. However, both parameters are generally computed off-line, through fairly complex procedures, mainly performed in the frequency domain. The seismic moment, for example, is estimated from the low frequency amplitude of displacement spectra. The source radius is typically obtained from the spectral corner frequency (Brune, 1970; Madariaga, 1976) or from time-domain, source duration measurements, generally available several minutes after the earthquake occurrence (Boatwright,

1980; Duputel et al., 2012). Although the fitting of spectral shapes is a straightforward operation, a major issue is the adequate correction of the observed spectra for path attenuation and site response effects.

In the context of Earthquake Early Warning (EEW), the point source characterization is usually based on the measurement of a few parameters (typically peak amplitude and/or characteristic period) in the early portion of the recorded P waves (3–4 s). These parameters are related to the earthquake size or to the peak ground shaking through empirical relationships (Allen and Kanamori, 2003; Kanamori, 2005; Wu and Zhao, 2006; Zollo et al., 2006; Böse et al., 2007; Wu and Kanamori, 2008; Zollo et al., 2010).

More recently, new strategies have been proposed to improve the accuracy of source parameter estimation for EEW applications and provide an estimate of the rupture area extent and the slip distribution on the fault. Among these strategies, some of them are based on the rapid inversion of geodetic and/or accelerometer data or fitting the spectrum in real-time (Allen and Ziv, 2011; Ohta et al., 2011; Colombelli et al., 2013; Caprio et al., 2011; Ziv and Lior, 2016). However, the rapid inversion of geodetic and/or accelerometer data need a catalog of the active faults for the construction of a rupture model plane in real-time (Colombelli et al., 2013). The azimuth dependency and the simplifying assumptions (e.g., directivity and segmentation) may introduce large discrepancies between modeled and observed spectra, leading to large variability in corner frequency estimates during the real-time spectrum inversion method (Ziv and Lior, 2016).

A second class of algorithms is based on the real-time spatial assessment of ground motion values. The FinDer algorithm (Böse et al., 2012), indeed, provides an estimate of the fault rupture extent and strike by continuously monitoring the spatial distribution of ground motions in real time. The results of this approach can be affected by the accuracy of near/far source classification and by the shortcomings in the GMPE used for the template generation (Böse et al., 2012, 2015).

More innovative approaches to EEW bypass the real-time source parameter estimation (location and magnitude) and use physics-based data assimilation techniques to directly predict the incoming evolution of ground shaking (PLUM) algorithm (Hoshiba and Aoki, 2015).

Recently, Colombelli and Zollo (2015) looked at the time evolution of the early P-wave information and used it as a proxy for the rupture process of earthquakes to extract the seismic moment and rupture extent of moderate-to-large Japanese earthquake records., Nazeri et al. (2019) explored a similar approach using strong-motion data of the 2016–2017 Central Italy sequence and estimated moment magnitude, fault length and average stress drop for each single event. The proposed method accounts for the effects of azimuth and distances by averaging the distance-corrected peak displacement among many stations, distributed over azimuth and distance, to approximate the moment rate function (MRF) and can be applied to general geometries with no need of prior knowledge of fault information. The proposed method is a remarkably simple and straightforward approach that does not require any complex calculation for automatically estimating two main source parameters (the earthquake magnitude and the expected length of the rupture) before the rupture has finished.

Since 2005, the National Strong Motion Observation Network System of China was established. Stations in the network were mainly equipped with force balance accelerometers with a broadband frequency range of 0–80 Hz, which ensures that the network is reliable to record large quantities of high-quality strong-motion data for research purposes (Li et al., 2008).

Following the idea of Colombelli and Zollo (2015) and Nazeri et al. (2019), in this study we use a database of moderate-to-large Chinese earthquake records and explore a similar approach to estimate the earthquake magnitude and rupture length, and to provide an approximate estimate of the average stress drop to be used for Earthquake Early Warning and rapid response purposes. The aim is twofold: 1) establish source scaling relationships for moderate to large earthquakes in China and 2) build the foundation for further studying the feasibility of a network-based EEW method based on the time evolution of the early P-wave peak displacement amplitude.

DATA AND METHODOLOGY

Data Selection and Construction of LPDT Curves

For the present analysis, we selected the earthquakes occurred in China in the period 2007–2015. The magnitude of all the events (surface wave magnitude, Ms) varies between 4.0 and 8.0. To avoid the inclusion of bad quality data in our analysis, we selected seismic records with an epicentral distance smaller than 120 km, but for the M8 event we expanded the limit to 200 km and required that each event had at least three records. A total of 1293, 3-component accelerometric waveforms, relative to 88 earthquakes and 540 stations were used for the regression of P-wave peak displacement amplitude attenuation relationship, among which we selected 31 earthquakes (for a total of 617 records) with at least ten recording stations for the computation of the LPDT curve. **Figure 1A** shows the epicentral position of the selected earthquakes and the location of stations, in which two main seismic regions (Sichuan-Yunnan and Xinjiang regions) in China have been enlarged for clarity. **Figure 1B** shows the histogram distribution of the analysed records as a function of the epicentral distance and magnitude.

We identified the onset of the P wave on the vertical component of acceleration records, using a standard short-term/long-term average method for automatic picking (Allen, 1978). Then, we visually inspected all the available waveforms and made manual picks where necessary, to adjust potential mistakes from the automatic picking algorithm. After removing the mean value and the linear trend, the acceleration waveforms are integrated once to velocity and twice to get displacement. Finally, we applied a 0.075 Hz high-pass Butterworth filter to remove the low frequency drift on displacement records. We impose the zero-crossing of the signal amplitude at the onset of the P-wave, to eliminate any potential residual noise contaminations resulting from the double integration operation.

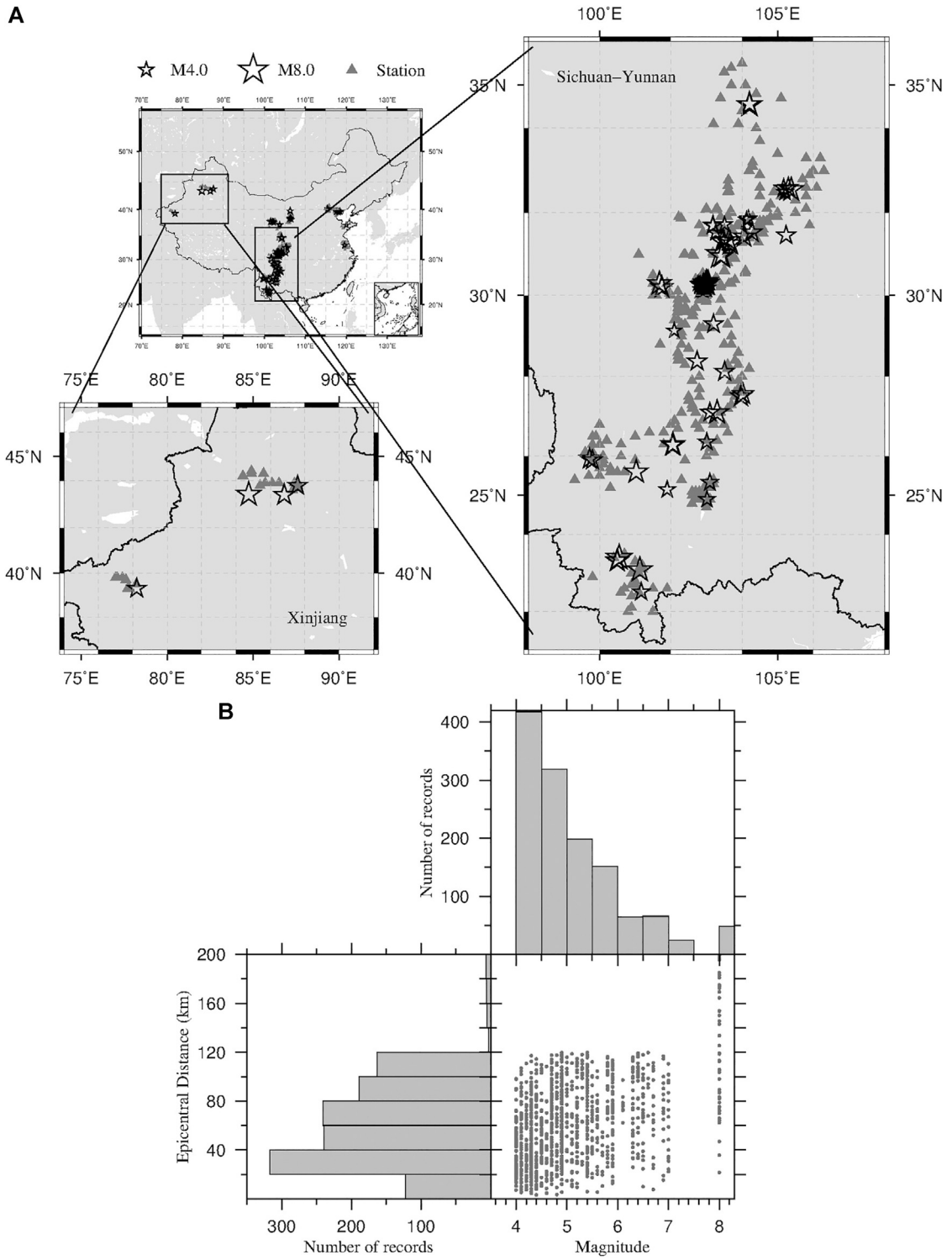

FIGURE 1 | Data distribution. Plot of **(A)** the epicentral position of the selected earthquakes and the location of stations and **(B)** the distribution of the analysed records as a function of the epicentral distance and magnitude.

We then measure the absolute maximum of the initial P-wave amplitude on the vertical component of displacement (named Pd) using an expanding time window, starting at the arrival of the P-wave and moving forward with a time step of 0.01 s. The peak amplitude is related to the earthquake magnitude (M) and to the source-to-receiver distance (R) through an attenuation

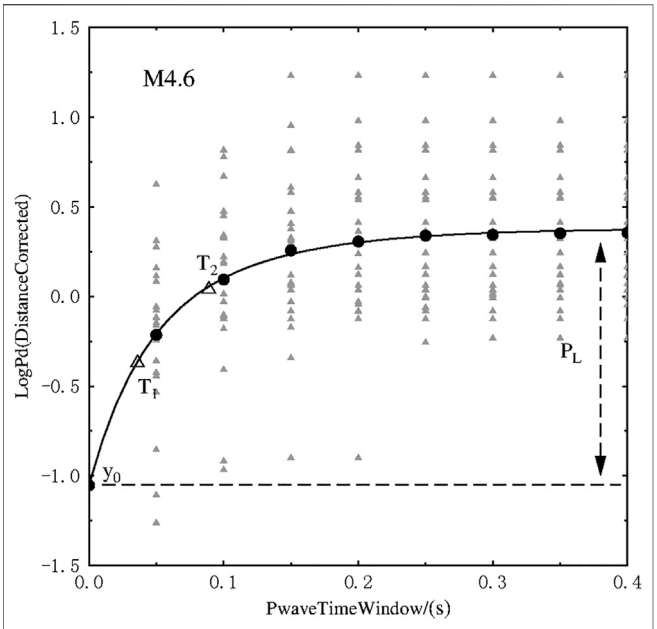

FIGURE 2 | The LPDT curve of M4.6 event and the model parameters. The grey triangles stand for the corrected amplitude Pd^C for the available stations at each P-wave time window, then the circle represents the average Pd^C value of all these stations. Our exponential fit model is shown in black line. The time parameters T_1 and T_2 are shown in the empty triangles.

relationship of the general form (Wu and Zhao, 2006; Zollo et al., 2006):

$$\boldsymbol{log}_{10}(\boldsymbol{Pd}) = \boldsymbol{A} + \boldsymbol{BM} + \boldsymbol{Clog}_{10}(\boldsymbol{R}) \quad (1)$$

where Pd is the P-wave peak measurements and A, B and C are coefficients empirically determined from select dataset using 2 or 3 s after the P-wave arrival. Unlike the previous study, here we calibrated the coefficients by performing a specific least-squares multiple regression analysis, in which we fixed the distance attenuation coefficient (C) and chose a fixed length of the P-wave time window for the parameter measurements, which was set at 3 s for $M \leq 7$ and 9 s for $5.5 < M \leq 7$, respectively. Further details about the estimation of the coefficients of **Eq. 1** are provided in **Supplementary Material**.

For the computation of the LPDT curve of each event, the peak amplitudes Pd of all records are measured at every P-wave time window and the distance-corrected amplitudes ($logP^cd$) are obtained as $logP^cd = logPd - ClogR$. In order to avoid the contamination by the S-waves on the selected portion of the P-wave, we picked out four stations with clear seismic phase randomly from the dataset in each distance bin (every 20 km). A total number of 40 records were used, and their S-wave arrival time were manually picked to estimate the coefficients of the following equation:

$$\boldsymbol{T_S} - \boldsymbol{T_P} = \boldsymbol{bR} \quad (2)$$

where *Tp* is the P-wave onset time, *Ts* is the arrival time of the S-wave, *R* is the hypocentral distance in km, $b = 0.13$ is the coefficient derived from a linear regression analysis. To minimize any potential S-wave contamination, we regarded *Tp+0.8bR* as the expected S-wave arrival. As the time window increases, the stations with the expected S-wave arrivals were automatically excluded to make sure only P-wave part involved in the computation. Finally, the LPDT curve is obtained by averaging the distance-corrected amplitude of all the valid stations at each time window. The computation of the curves stops when the number of stations is less than a minimum of data (Five stations).

Observation and Modelling of LPDT Curve

Figure 2 shows an example of the generated LPDT curve for the M4.6 event. The LPDT curve has an exponential growth shape with an initial increase, a gradual intermediate curvature and a final plateau level. Generally, the LPDT curve of larger event needs more time to reach the plateau and the plateau level of the curves scale with the final magnitude (**Figure 3A**).

The shape of the LPDT curve, as obtained from the average of many stations distributed over azimuth and distance, can be interpreted as a proxy of the Moment Rate Function (MRF), from the initial time up to its maximum peak value. Therefore, two essential features of the MRF, i.e., peak value and peak time, which are both related to the source properties, should be embodied in the LPDT curves. Following the idea of Colombelli and Zollo (2015), for near-triangular source time functions, the peak value of the MRF (related to the magnitude) will correspond to the plateau level of the LPDT curve, and the peak time of the MRF (related to rupture half-duration) is a proxy for the time at which the LPDT curve reaches its plateau level (Plateau Time). With this in mind, the magnitude and rupture duration can be estimated from the plateau level and the plateau time of the curves.

To model the LPDT curves, we fit data using the following function (Colombelli et al., 2020):

$$\boldsymbol{log}_{10}\boldsymbol{Pd}(\boldsymbol{t}) = \boldsymbol{P_L}\left\{1 - \left[\boldsymbol{ae}^{-\frac{t}{T_1}} + (1-\boldsymbol{a})\left(\boldsymbol{e}^{-\frac{t}{T_2}}\right)\right]\right\} + \boldsymbol{y_0} \quad (3)$$

where y_0 is fixed as the first point of the curve, P_L is the interval between y_0 and the plateau level, a is the weighting factor which is set to 0.5, T_1, and T_2 are the time parameters (here we define the larger value as T_2). T_1 controls the very initial part which usually has a faster increasing speed and T_2 represents the second part, whose increasing speed gradually becomes slower. This double corner time, exponential model accounts finely for the two different behaviors of LPDT curve-that is to say, a sharp increase to the plateau (ramp-like) for small events and a more gentle and smooth increase (exponential) for large events. The model parameters are shown in **Figure 2**.

We used a non-linear, weighted-fitting approach to model our curves, accounting for the standard error on each point of LPDT curves. Specifically, at each time step, the weight is obtained as:

$$\boldsymbol{Weight} = 1/\left(N \cdot SE^2\right) \quad (4)$$

where *SE* is the standard error in each P-wave time window, *N* is the number of stations used for that time window. **Figure 3B** shows that the LPDT curves of all the events are quite well

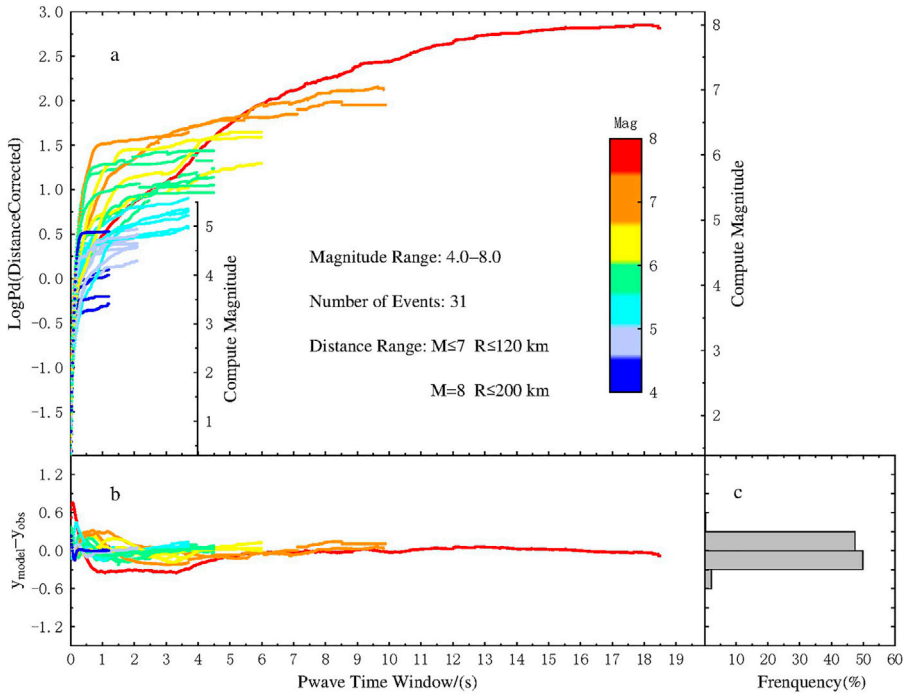

FIGURE 3 | The LPDT curve and the misfit. **(A)** The average peak amplitude with distance corrected at each P-wave time window for different magnitude with color scale. **(B)** The difference between the observed value and the value from the fit model. **(C)** The normalized histograms of the misfit value.

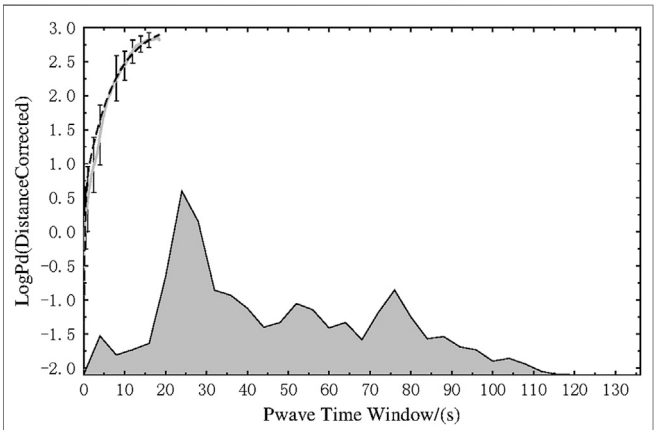

FIGURE 4 | The LPDT curve of the M 8.0 Wenchuan earthquake and its fit model. The grey and the dashed line represent the observed data and the best fit model, respectively. The standard error of the corrected amplitude Pd^C for the available stations at each P-wave time window is shown by the vertical error bars. The moment rate function of this event provided by the USGS was shown in the bottom with grey area.

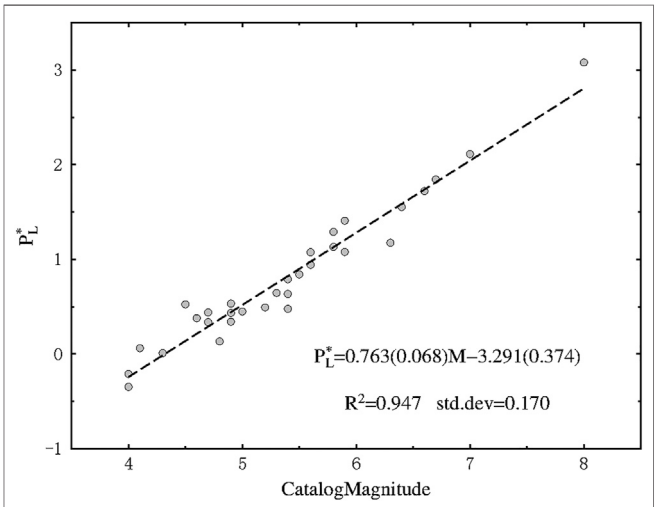

FIGURE 5 | Scaling relationship between P_L* and magnitude. The circles present the P_L* value of each event. The dashed line indicates the best-fit relation between P_L* and magnitude.

reproduced by the fitting model, with an average residual of 0.3. Generally, at the beginning of the curve computation, several stations from a broad range of distances and azimuths are involved in the calculation, so that the scatter of data is large and the fitting procedure gives a smaller weight to this part, as compared to the plateau of the curves, which is instead, well reproduced. A slightly larger (about 0.7) difference between the real data and the model is observed for the initial part of the curve of the M 8.0 Wenchuan earthquake, which could be related to the complexity of the source process of this peculiar event. Indeed, when looking at the seismic moment release of this event (**Figure 4**), a small peak value is observed at 4–5 s, before the

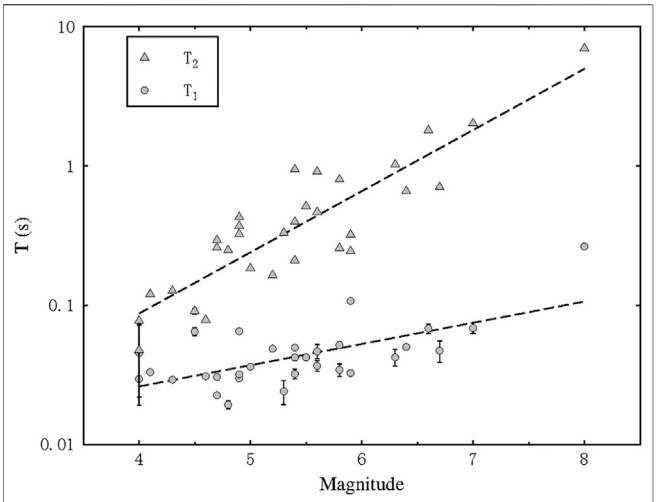

FIGURE 6 | Scaling relationship between T_1 and T_2 as a function of magnitude. Triangles and circles represent T_2 and T_1 for LPDT curves, respectively. The error bars which represent the standard deviation of the parameters fitted by our exponential model are shown as black lines (where visible). The best fitting line for each parameter is shown as dashed line.

arrival of the absolute main peak value (at about 25 s), and this leads to a sag of the LPDT curve around 4 s.

RESULTS

We fit the LPDT curves with our exponential model and obtain the three relevant parameters mentioned above (T_1, T_2, P_L) while y_0 has been fixed to the first point amplitude. For simplicity, we defined a new variable called $P_L^* = P_L + y_0$ to represent the true plateau level of the LPDT curves. Both the amplitude parameter (P_L^*) and the two characteristic times (T_1 and T_2) scale with earthquake magnitude. **Figure 5** shows the plateau level P_L^* as a function of magnitude. A good correlation between P_L^* and magnitude (the correlation coefficient reaches 0.95) can be found. The parameters T_1 and T_2 extracted from our fitting model are shown in **Figure 6** as a function of magnitude. As the best fitting line indicates, both parameters linearly increase with magnitude (in logarithmic scale). Due to the very rapid initial increase of the curves, T_1 and T_2 are close to each other for small events, while they gradually separate when the magnitude becomes larger and the initial part of the curves increases gently.

Magnitude Estimation

Once the observed amplitude has been corrected for the distance effect, the LPDT value at each P-wave time window can be associated to a corresponding magnitude using the coefficients of **Eq. 1** (**Supplementary Table S1**). **Figure 3** shows the dynamic process of estimating magnitude for the LPDT curve. The y axis on the left stands for the distance corrected Pd, and the corresponding magnitude or estimated magnitude scale is shown on the right. The magnitude then can be estimated accurately based on the true plateau level of the LPDT curves and the coefficients of **Eq. 1** listed in **Supplementary Table S1**. As shown in **Figure 3**, the occurrence of the plateau for large events (M > 6–7) needs more than 9 s after the P-wave arrival, suggesting that the typical approaches for the magnitude estimate using fixed 3–4 s P-wave time windows (PTWs) would provide underestimated magnitudes for such large events. Moreover, the B coefficient (calibrated using a 3 s PTW) could not be suitable to compute the corresponding magnitude based on the P_L^* obtained in a longer time window. We therefore choose two magnitude ranges, with two different PTW lengths, to calibrate and use the optimal coefficients (**Supplementary Table S1**) for magnitude estimation. In this way, when an event reached its plateau within 4 s, we use the relation coefficients A and B for fixed 3 s PTW, while we used the coefficients A and B established with a fixed 9 s PTW when its LPDT curve keeps increasing after 4 s.

The estimated final magnitude based on the P_L^* for the LPDT curve and obtained with the two sets of coefficients for small and large events respectively, is plotted in **Figure 7** as a function of the catalog magnitude. As it can be seen in **Figure 7**, most of the points are distributed around the dashed line representing the 1:1 relationship between the estimated magnitude and the catalog magnitude. The scatter of data is rather small, with an average estimated error of 0.23 magnitude units.

Prediction of Rupture Length and Estimation of Stress Drop $\Delta\sigma$

The rupture duration is the total duration of a seismic event, given by the whole-time length of the moment rate function (Vallée,

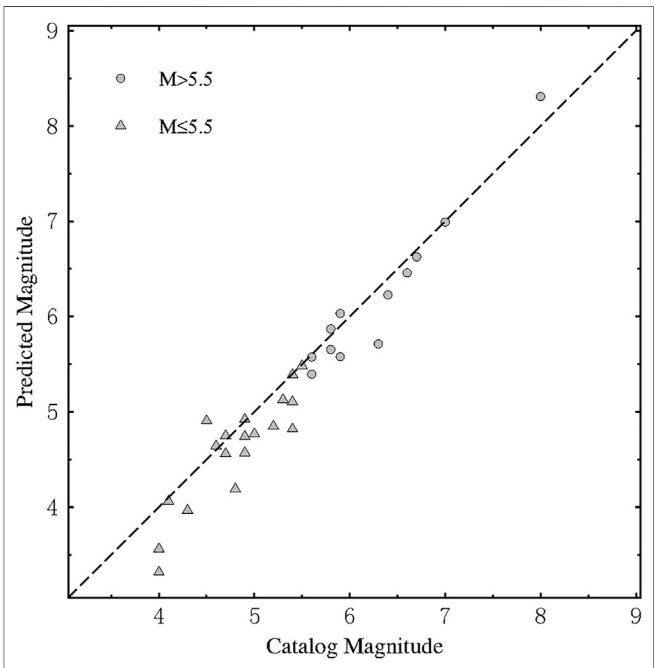

FIGURE 7 | The estimation of the magnitude and catalog magnitude. The dashed line corresponds to the 1:1 scaling. The triangles and circles indicate the estimated magnitude with P_L^* using the relation coefficients A and B for a fixed 3 s PTW and a fixed 9 s PTW, respectively.

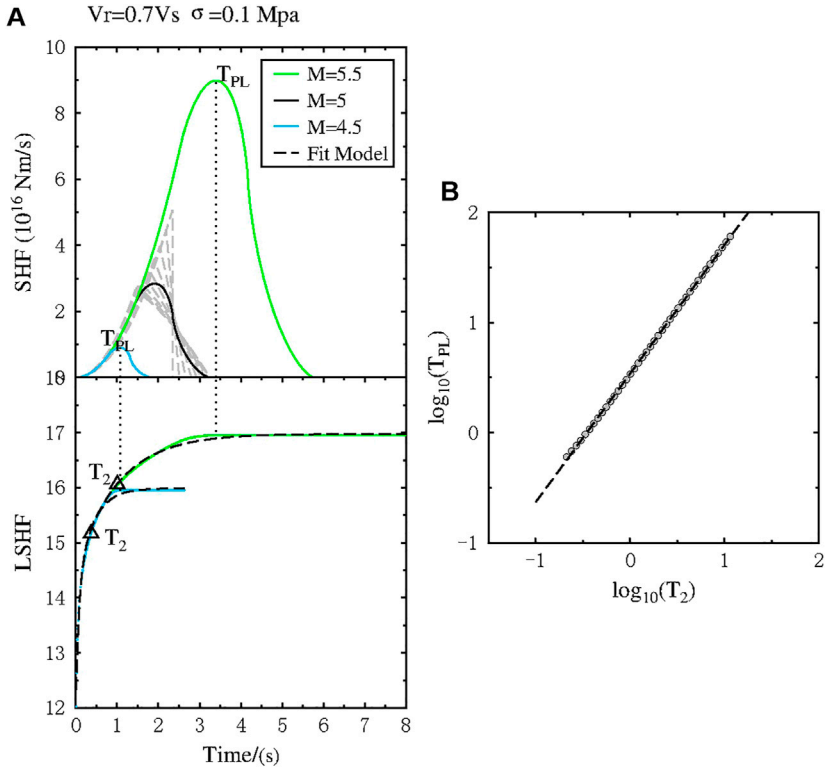

FIGURE 8 | The exploratory simulations for $\Delta\sigma = 0.1$ MPa. **(A)** Fitting of the Sato & Hirasawa function with exponential model. The SHF and LSHF stand for the Sato & Hirasawa moment rate Function (SHF) and the log of the SHF (LSHF), respectively. The grey hatched curves display different SHFs, obtained by changing the polar angle of the observation point from 0° to 90°. The black solid line shows the average SHF for $M = 5$ event. The blue and green line represent the averaged SHF for $M = 4.5$ and $M = 5.5$ event, respectively. The dashed line represents the fitted model. **(B)** Relationship between T_2 and T_{PL} for magnitude from 4 to 8 with an interval of 0.1 magnitude units. The dashed line shows the fitting relationship between T_2 and T_{PL}.

2013). It is generally observed that the rupture duration scales with magnitude and is related to the rupture length, assuming a value for the rupture velocity (Wells and Coppersmith, 1994). As the moment rate function can be simplified as a symmetric triangle (Bilek et al., 2004), the peak time of the MRF, corresponding to the plateau time (T_{PL}) of the LPDT curve, is a measure of the Half-duration of each event (Colombelli and Zollo, 2015; Nazeri et al., 2019). Having in mind the Sato & Hirasawa model (Sato and Hirasawa, 1973) here we investigate the relation between parameter T_2 of LPDT curves and T_{PL}, the time at which occurs the peak of the MRF. In the Sato & Hirasawa model, the rupture spreads radially outwards at a constant velocity with a circular fault, and stress drop ($\Delta\sigma$) and rupture velocity (Vr) are two relevant parameters controlling the earthquake rupture process. Since $\Delta\sigma$ and Vr of earthquakes can vary significantly for each event (Allmann and Shearer, 2009), we performed a set of dedicated simulations to explore stress drop values between 0.05 and 20 MPa with rupture velocities between 0.5 Vs (S-wave velocity) and 0.9 Vs, for a total of 55 combinations of the two parameters.

For each given magnitude, we fixe $\Delta\sigma$ and Vr, and generate the corresponding Sato & Hirasawa moment rate Function (SHF) by changing the polar angle of the observation point from 0° to 90° and computing the average SHF (an example of $M = 5$ event shown in the **Figure 8A**). We then compute the log of the SHF and keep unchanged after the SHF reaches its peak to get a curve (hereinafter LSHF) with a similar shape of our LPDT curve. Since most of the selected earthquakes in our database occurred at an average depth of about 10 km, we set the Vp = 6.2 km/s, Vs = 3.4 km/s based on the velocity model for this region (Wang et al., 2014). Examples of the average SHF with fixed Vr = 0.7 Vs and $\Delta\sigma$ = 0.1 MPa is shown in **Figure 8**, while examples with other $\Delta\sigma$ values are shown in the **Supplementary Material**. For each available couple of stress drop and rupture velocity, we used the exponential model (**Eq. 3**) to fit the LSHF curve and extract the T_2 parameter for different magnitudes. As expected, we found that T_2 has linear relationship with T_{PL} obtained directly from the peak time of the generated SHF (in logarithmic scale) for the entire magnitude range with a small deviation when exploring the $\Delta\sigma$ and Vr, suggesting that the T_2 parameter extracted from the observed curves can be used to predict T_{PL}:

$$\boldsymbol{log}_{10}(\boldsymbol{T_{PL}}) = 1.111\,(0.051)\boldsymbol{log}_{10}(\boldsymbol{T_2}) + 0.542\,(0.030) \quad (5)$$

For the circular model with a symmetric triangular shaped MRF, the obtained T_{PL} can be regard as the Half-Duration (HD) of the source function. Considering all azimuthal coverage around the fault, the relation between averaged half-duration

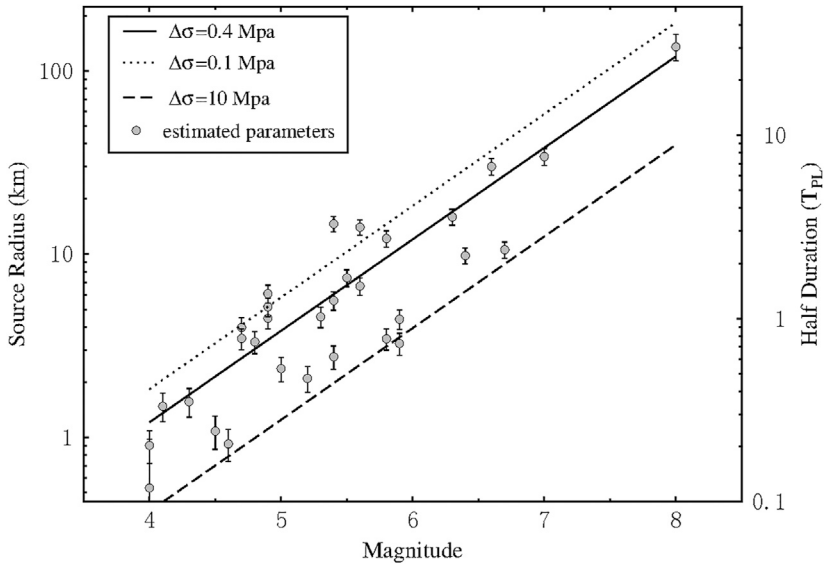

FIGURE 9 | The scaling relation between source radius and magnitude with a fixed rupture velocity of 0.9 Vs. The right y-axis represents the corresponding Half-duration. The circles stand for the T_{PL} parameter extracted from LPDT curve. The estimated errors computed through the error propagation theory are shown by the vertical error bars. The dotted line and dashed line represent the theoretical scaling with constant $\Delta\sigma$ = 0.1 and 10 MPa, respectively. The averaged constant $\Delta\sigma$ of the analysed dataset are shown in the solid line.

and the source radius was given as follows (Aki and Richards, 2002):

$$T_{PL} = \langle HD \rangle = \frac{\int_0^{\frac{\pi}{2}} \frac{a}{V_r}\left(1 - \frac{V_r sin\theta}{V_P}\right) d\theta}{\frac{\pi}{2}} = \frac{a}{V_r}\left(1 - \frac{2}{\pi}\frac{V_r}{V_P}\right) \quad (6)$$

where a is the source radius, Vr is rupture velocity, θ is the polar angle of the observation point and Vp is the P-wave velocity. Given the half-duration of the source, the source radius of the analysed events can be estimated.

Figure 9 shows the predicted source radius as a function of magnitude and its corresponding half-duration with a fixed rupture velocity of 0.9 Vs. Based on the computation of stress drop ($\Delta\sigma$) for the circular model using the source radius (a) and the seismic moment (M_0) (Keilis-Borok, 1959), $\Delta\sigma = \frac{7}{16}\frac{M_0}{a^3}$, the theoretical scaling lines of the source radius as a function of M with a constant $\Delta\sigma$ = 0.1 and 10 MPa were given in the same figure as a comparison. The predicted source radius shows a similar increasing trend with the theoretical lines, indicating that the source radius of the analysed events has a consistent self-similar, constant stress drop scaling with magnitude. We fit the source radius with a weight-based fitting approach (same as **Eq. 4**, here, the *SE* is the standard error of the source radius computed from the predicted T_{PL} and its error obtained by the error propagation theory) to obtain the best-fit constant stress drop of 0.4 MPa. In addition, we repeated the process by setting Vr = 0.7 Vs and Vr = 0.8 Vs, and found that the mean value of $\Delta\sigma$ are 1.0 and 0.6 MPa, respectively.

The definition of rupture length changes in case of a circular fault (rupture length = rupture radius) and long-rectangular fault (rupture length = larger rectangular fault dimension). For a circular fault, the rupture lengths (source radius) predicted from LPDT curve were shown in **Figure 10**. As the figure indicates, most of our predicted rupture lengths as a function of magnitude agrees with the magnitude-rupture scaling relation studied by Cheng et al. (2019)

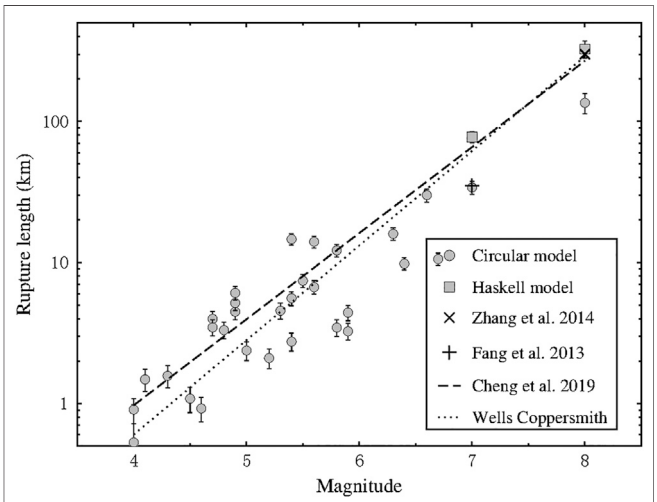

FIGURE 10 | The scaling relationship between the predicted rupture length and *M*. The circles and the squares are the predicted rupture length from circular model and Haskell model, respectively. The dashed line is the linear regression relationship in mainland China calibrated by Cheng et al. (2019). The dotted line represents the relationship proposed by Wells and Coppersmith (1994). The diagonal cross and cross are the results of M 8.0 Wenchuan earthquake by Zhang et al. (2014) and M 7.0 Lushan earthquake by Fang et al. (2013), respectively. The estimated errors computed through the error propagation theory are shown by the vertical error bars.

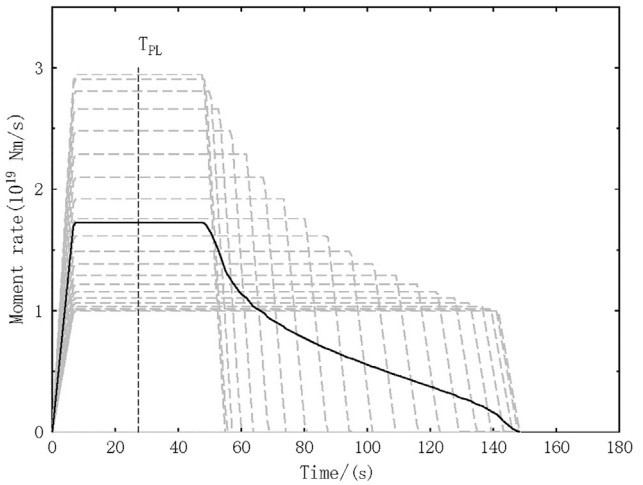

FIGURE 11 | The trapezoid-like moment rate function (MRF) and the averaged MRF with azimuth from 0° to 180°. The dashed black line represents that the T_{PL} of the LPDT curves (Plateau time) occurs at the middle point of the average trapezoid plateau.

using 91 earthquakes in Mainland China and the empirical scaling relation for strike-slip earthquakes with M 4.8 to M 8.1 proposed by Wells and Coppersmith (1994). However, our predicted results were smaller than the rupture length of two models in the moderate-large magnitude range (M 7.0 Lushan earthquake and M 8.0 Wenchuan earthquake). To better assess the performances of our LPDT scheme in predicting rupture length, we collect the rupture lengths of these two largest events derived from other methodologies. Our approach provides a rupture length of 34 km for the M 7.0 Lushan earthquake, which is consistent with the results of relocated aftershocks by Fang et al. (2013) (L~35 km) and the inversion results by Liu et al. (2013) (L~28 km). For the M 8.0 Wenchuan earthquake, our predicted rupture length of 135 km is obviously underestimated as compared to the inversion results of Zhang et al. (2014) (L~300 km) and the observed aftershock distribution over a length of 330 km (Huang et al., 2008).

The circular model is well suitable for small-to-moderate magnitudes (i.e., M < 6). Here, we also investigated the results of large magnitudes when applying the rectangular source model of Haskell. The far-field displacement radiated by a Haskell type fault model is equivalent to the convolution of two box-car functions of different amplitude and durations: rise time (τ) and rupture time (T_R). The resulting function has a trapezoidal shape with total duration given by the sum of τ + T_R. The rupture time T_R depends on the finite length of the fault (L) and the azimuth (θ) between source and receiver (Haskell, 1964):

$$\boldsymbol{T_R} = \frac{\boldsymbol{L}}{\boldsymbol{V_r}}\left(1 - \frac{\boldsymbol{V_r}}{\boldsymbol{V_P}}\boldsymbol{cos\theta}\right) \tag{7}$$

The rise time τ is independent of azimuth (Hwang et al., 2011) and can be obtained using the following relationship derived by Melgar and Hayes (2017) from a database of finite faults:

$$\boldsymbol{log}_{10}(\boldsymbol{\tau}) = -5.323 + 0.293\boldsymbol{log}_{10}(\boldsymbol{M_0}) \tag{8}$$

Figure 11 shows an example of the average total duration of Haskell model with azimuth (θ) changed from 0° to 180°. Assuming that T_{PL} is the middle point of the average trapezoid plateau, the following relationship between L and T_{PL} can be obtained and be used for estimating rupture length of large events when assuming the Haskell model:

$$\boldsymbol{T_{PL}} = \frac{1}{2}\left(\boldsymbol{\tau} + \frac{\boldsymbol{L}}{\boldsymbol{V_r}}\left(1 - \frac{\boldsymbol{V_r}}{\boldsymbol{V_P}}\right)\right) \tag{9}$$

We computed the predicted rupture length for the two largest events using the Haskell model. As shown in **Figure 10**, with the same T_{PL}, applying the Haskell model appears to predict larger rupture lengths than the results using circular model. Specifically, we obtain an estimate of rupture length of 326 km without underestimation for Wenchuan earthquake, whereas the rupture length of Lushan earthquake has been overestimated (L = 77.3 km). The circular model produced a triangle-like MRF, as the Sato & Hirasawa moment rate Function of M = 5 event shown in the **Figure 8A** indicates, the peak time (T_{PL}) is almost half-duration. However, as the MRF of M 8.0 Wenchuan earthquake (download from USGS, shown in **Figure 4**) indicates, the MRF of some large events usually have the major peak occurring at the beginning of the rupture and followed by a long-time duration coda (Vallée, 2013). In this case, the circular model with a triangle-shape MRF may be not able to correctly reproduce this kind of source time function, and considering the peak time as the half-duration of the large events may result into underestimated rupture lengths. The averaged MRF from Haskell model shown in **Figure 11** reaches its peak (T_{PL}) around 1/5 of the total duration, which is more like the characteristic of MRF of the large magnitude earthquakes stated above. Moreover, for large earthquakes, the width (W) of the fault is already saturated, i.e., equal to the thickness of the brittle fracturing zone in the lithosphere. Accordingly, the growth of the fault area with increasing seismic moment (M_0) is in the length direction only (Bormann et al., 2009; Cheng et al., 2019). Therefore, in the situation of L >> W for large events, the Haskell model is more appropriate. Since the rupture surface of Lushan earthquake presents the focal characteristics of small-moderate earthquakes (L ≈ W) (Chen et al., 2013; Hao et al., 2013), the Haskell model is not suitable for this event leading to an overestimated rupture length.

According to the derived rupture length of the analysed events, the stress drop can be computed based on different geometrical faults. Madariaga (1977) proposed that the general form $\Delta\sigma = \frac{M_o}{CSW} \cong \frac{M_o}{CS^{3/2}}$ (S is the rupture surface), where $C = \frac{16}{7\pi}$ for a circular fault, same as Keilis-Borok (1959)'s formula $\Delta\sigma = \frac{7}{16}\frac{M_0}{a^3}$ and $C = \frac{\pi}{2}$ for a long rectangular fault (L >> W) as follows:

$$\Delta\boldsymbol{\sigma} = \frac{2}{\boldsymbol{\pi}}\frac{\boldsymbol{M_0}}{\boldsymbol{W^2 L}} \tag{10}$$

where W is the rupture width. Referring to the observation of Cheng et al. (2019) that large events with M > 6.7 have a nearly constant rupture width of ~20 km, here, we set W to 20 km.

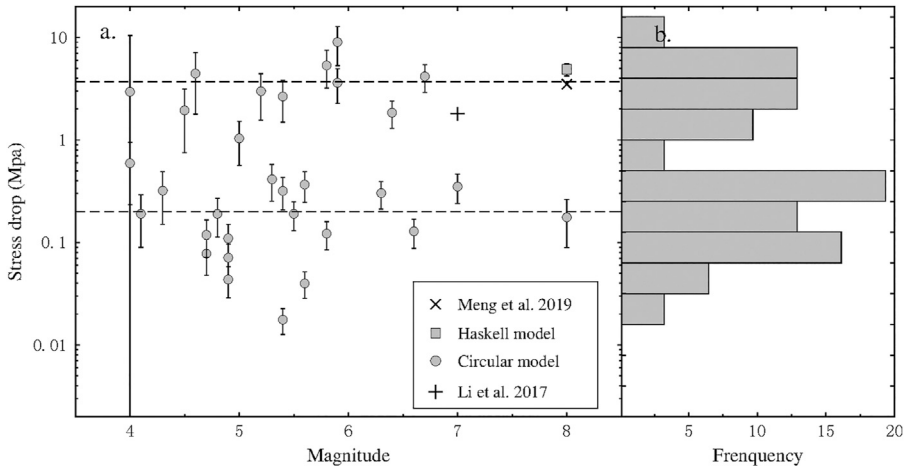

FIGURE 12 | The estimated stress drop of the analyzed earthquakes. **(A)** The distribution of the estimated stress drop. The circles and the squares are the predicted stress drop from circular model and Haskell model, respectively. The estimated errors computed through the error propagation theory are shown by the vertical error bars. Events have been divided into two groups based on $\Delta\sigma = 0.6$ MPa. The average stress drops of these two groups are shown as the dashed lines. The diagonal cross and cross are the results of M 8.0 Wenchuan earthquake by Meng et al. (2019) and M 7.0 Lushan earthquake by Li et al. (2017), respectively. **(B)** The normalized histograms of the predicted stress drop.

We therefore suggest to use the circular model for small-moderate-strong events ($M \leq 7$) and the Haskell model (rectangle model) for large events ($M > 7$) in the estimation of rupture length and stress drop. The computed stress drop of each event is shown in **Figure 12**. After applying the rectangle source model for M 8.0 Wenchuan earthquake, the derived stress drop = 4.9 MPa is comparable with the results of Meng et al. (2019) (3.5 MPa). However, the circular model in this study provides an underestimated stress drop of 0.4 MPa for M 7.0 Lushan earthquake when comparing with the results (1.8 MPa) obtained by Li et al. (2017). As **Figure 12B** shows, the stress drops vary from 0.01 to 10 MPa. We divide the events into two groups based on $\Delta\sigma = 0.6$ MPa and calculate the averaged stress drop for these two groups. The higher stress drop group ($\Delta\sigma > 0.6$ MPa) has an averaged stress drop of 3.7 MPa, which is close to the world-wide measured median value of 4 MPa (Allmann and Shearer, 2009). The lower stress drop group with an averaged stress drop of 0.2 MPa consists of 19 events, in which half of the events are the aftershocks of the M 8.0 Wenchuan earthquake and the M 7.0 Lushan earthquake. Consistent with Wang et al. (2018), the lower stress drop of aftershocks may result from the remaining locked parts on the fault plane of the mainshock. All these source parameters of the analyzed events ($M \geq 5.5$) are summarized in **Table 1**.

DISCUSSION AND CONCLUSION

In this study, we generalized the approach proposed by Colombelli and Zollo (2015) to estimate the source parameters of a set of Chinese earthquakes with magnitude ranging from 4 to 8. The methodology is based on the use of the time evolution of the P wave (LPDT curve) as a proxy for the source time function to extract earthquake magnitude and rupture duration.

Comparing with the previous works by Colombelli and Zollo (2015) and Nazeri et al. (2019), we used the double corner time, exponential model proposed by Colombelli et al. (2020) for better modeling the behavior of LPDT curves. We improved the magnitude estimation based on the plateau level of LPDT curve, by using two different scaling coefficients with fixed C, which have been properly calibrated. Based on the analysis of 31 events in the magnitude range between 4 and 8, we found that the plateau level of LPDT curves has a strong correlation with magnitude (the coefficient of correlation is up to 0.95). Comparing with the catalog magnitude of the analyzed events, our predicted magnitude from the displacement data shows an average deviation of 0.23 magnitude units. The time at which these estimates are available implicitly depends on the event itself. Small events have a rapid initial increase and reach the plateau quickly, and for these events, the magnitude estimates would be available within a short time from the first P-wave detection. For the large events, like Wenchuan earthquake (M 8.0), the time needed to reach the plateau is longer. The near-source stations with a short fraction portion of the P-wave time-series cannot provide robust magnitude estimates for these large events, which is consistent with our observation that the LPDT curve at this stage is still growing and the plateau has not yet been reached. However, the expansion of hypocentral distance allows to capture longer P-wave signal portion of large events, and thus we provide a magnitude estimation of 8.3 for the Wenchuan earthquake after the LPDT curve reaches its plateau. By capturing the curve that reaches its plateau or looking at larger distances, our approach can estimate the magnitude of large events accurately, without saturation effects, typically observed when using shorter P-wave time windows (Lomax and Michelini, 2009; Bormann and Saul, 2009; Colombelli et al., 2012).

Together with the plateau level, the plateau time (T_{PL}) of the LPDT curve has also a clear scaling with magnitude, being

TABLE 1 | List of source parameters including catalog magnitude (Ms), predicted magnitude (Ms^{PRED}), half duration, Rupture length (RL) and stress drop ($\Delta\sigma$) determined in this study for moderate-larger events ($M \geq 5.5$).

No	Location	Date	Epicenter		Magnitude			Half duration		Rupture parameters			References
			Lat.	Long.	M_S	M_S^{PRED}	M_W (source)	LPDT	GCMT	*RL (km)*	*RL (WC94)*	*SSD (MPa)*	
1	Wenchuan	2008/05/12	31.00	103.40	8.0	8.3	7.9 (GCMT)	30.4	21.8	135.5 (circular) 326 (Haskell) 300 330	290	0.2 4.9 3.5	This study Zhang, wang, zschau, et al. (2014) Huang et al., 2008 Meng et al., (2019)
2	Wenchuan (aftershock)	2008/05/13	31.43	104.06	5.8	5.9	5.6 (GCMT)	0.8	1.6	3.4 (circular) 4.3	9.7	5.3 0.7	This study Wang et al., (2018)
3	Wenchuan (aftershock)	2008/05/14	31.34	103.63	5.8	5.7	5.4 (GCMT)	2.7	1.3	12.2 (circular) 7.5	9.7	0.1 0.2	This study Wang et al., (2018)
4	Yaoan	2009/07/09	25.60	101.03	6.3	5.7	5.7 (GCMT)	3.6	1.8	16 (circular)	21.0	0.3	This study
5	Yiliang	2012/09/07	27.56	104.03	5.6	5.6	5.3 (GCMT)	3.1	1.1	14 (circular)	7.1	0.04	This study
6	Eryuan	2013/03/03	25.93	99.72	5.5	5.3	5.4 (GCMT)	1.7	1.2	7.4 (circular)	6.1	0.2	This study
7	Changji	2013/03/29	43.40	86.80	5.6	5.4	5.4 (GCMT)	1.5	1.3	6.7 (circular)	7.1	0.4	This study
8	Lushan	2013/04/20	30.30	103.00	7	7.0	6.6 (GCMT)	7.6	4.9	34 (circular) 77.3 (Haskell) 35 28	61.9	0.4 0.7 1.8	This study Fang et al., (2013) Liu et al., (2013) Li et al., (2017)
9	Minxian	2013/07/22	34.54	104.21	6.7	6.6	6.0 (GCMT)	2.4	2.4	10.6 (circular)	38.9	4.2	This study
10	Ludian	2014/08/03	27.11	103.33	6.6	6.5	6.2 (GCMT)	6.7	2.9	30.0 (circular) 12	33.4	0.1	This study Cheng et al., (2015)
11	Kangding	2014/11/22	30.29	101.68	6.4	6.2	6.1 (GCMT)	2.2	2.8	9.8 (circular) 20 16	24.5	1.9	This study Fang et al., (2015) Jiang et al., (2015)
12	Kangding	2014/11/25	30.20	101.75	5.9	5.6	5.7 (GCMT)	0.7	1.8	3.2 (circular)	11.3	9.0	This study
13	Jinggu	2014/12/06	23.32	100.50	5.9	6.0	5.5 (GCMT)	1.0	1.5	4.4 (circular)	11.3	3.6	This study

M_S^{PRED} = predicted ms, RL = rupture length = source radius (circular model), WC94 = Wells and Coppersmith (1994), SSD = statics stress drop, GCMT data are available at www.globalcmt.org (last accessed May. 6, 2020).

approximately related to the half-duration of the source. In order to estimate the plateau time, we performed a series of simulations based on the Sato and Hirasawa (1973) circular rupture model and on the assumption that T_{PL} corresponds to the peak time of the MRF. We generated a set of MRFs exploring $\Delta\sigma$ and Vr values and studied the relation between T_{PL} and the time characteristic parameter T_2. Finally, we established a linear scaling relationship between the two parameters for predicting the T_{PL}.

Considering the circular model with a symmetric triangular-shaped MRF, the obtained T_{PL} can be regarded as the Half-Duration (HD) of the events to predict the source radius. The obtained source radius in this study shows a consistent self-similar, constant stress drop scaling with magnitude. We obtained the best-fit stress drop (0.4 MPa) for the 31 analysed events, with fixing rupture velocity to 0.9 Vs. This value is lower than world-wide measured median value of 4 MPa (Allmann and Shearer, 2009), but it is comparable with the mean value of 0.5 MPa by studying the strong-motion recordings of the Wenchuan aftershocks (2008–2013) (Wang et al., 2018).

One major result of this paper concerns the determination of the scaling law of earthquakes in China. We obtained the rupture length of the analysed events using circular model and found the M 8.0 Wenchuan earthquake has a shorter predicted rupture length with comparing to other results. We realize that for the largest events in the sequence, the circular fault model may underestimate the total rupture length. Thus, we suggested to estimate the rupture length of the large events ($M > 7$) assuming the Haskell, rectangular fault model. Our predicted rupture length of different source models as a function of M is close to the rupture scaling relationship proposed by Cheng et al. (2019) and Wells and Coppersmith (1994).

The most critical issue of the proposed methodology is to assume a triangular shape to represent the source function. The assumption of a circular fault model can be inadequate to describe the complexity of the source for large events, for which multiple

peaks of moment release can occur. Moreover, the rupture process of an earthquake is a chaotic process, and the simple exponential LPDT curve may hardly represent the complex nature of this process, especially at the very beginning. However, the now massive and well documented observation of LPDT empirical curves analysed in many worldwide seismic regions and in a wide magnitude and distance range confirm that the general ramp-like behavior of the curves is a universal evidence (Colombelli et al., 2012; Colombelli et al., 2015; Colombelli et al., 2020; Melgar et al., 2015; Trugman et al., 2019) which is well matched by the chosen exponential model (Colombelli et al., 2020). When the curve has reached its peak, the schematic representation with two parameters (plateau time and amplitude), may properly catch the essential features of the process we are interested in.

Concerning the anelastic attenuation effect on LPDT curves, the overall features of the curves are essentially dominated by the event magnitude, which mainly controls the plateau level and the time to reach this plateau, for each curve. Using similar LPDT curves, Colombelli et al., (2020) recently investigated the effect of anelastic attenuation on the shape of the curves. This was done both theoretically and through a careful and detailed analysis of real earthquake data. They found that the chosen anelastic attenuation parametrization (**Eq. 1**) is appropriate to correct the distance attenuation effect on LPDT curves and this does not produce a systematic effect on plateau and T_{PL} parameter determination in all the observed curves in the same distance range.

The source parameters of the larger events are a major focus of - and motivation for - the proposed methodology. Although the selected dataset has a relatively wide magnitude range from 4.0 to 8.0, there is an obvious lack of large-magnitude data for events with magnitudes between 7 and 8. The proposed methodology would be better verified through the application to other seismic areas, once that the proper calibration of scaling coefficients has been done. It is worth to mention that the findings (e.g., rupture scaling relation and stress drop distribution) obtained through applying the methodology to the selected events (31 earthquakes) are mainly based on the data from Sichuan-Yunnan region, and may not be applicable to other areas as they are.

We notice that in the presence of a jump in the increasing shape of the LPDT curve, our approach likely fits the curve with a longer T_2 thus resulting in a lower stress drop value. **Supplementary Figure S2** shows the LPDT curve for the M 6.6 Ludian earthquake: a jump in the curve is clearly visible around 3.5 s. A similar magnitude event (M 6.4) which has a normal LPDT curve shape without jumps is selected for comparison. Our double corner time, exponential model (**Eq. 3**) fits the LPDT curve of this M 6.4 event with a T_2 = 0.66 s. However, due to the presence of jump, our exponential model tends to find a parameter (T_1 and T_2) with slower growth to fit the middle part (2 ~ 4 s) of the LPDT curve for M 6.6 Ludian earthquake. This resulted in our model fitting the LPDT curve with a longer T_2 = 1.8 s. We further justify the effect of LPDT curve shape on the exponential fitting model in **Supplementary Figure S3**. The virtual LPDT curve with normal LPDT curve shape was generated as follow: the initial increasing part (0 ~ 1.85 s) and the approach plateau part (4.26 ~ 6 s) are the same as the observed LPDT curve, and only the middle part, we add points with exponential growth. After using our exponential model to fit the curves separately, we obtained a T_2 = 1.46 s for the virtual LPDT curve with a normal shape and a slightly longer T_2 (1.8 s) for the observed LPDT curve with a jump in the middle. Thus, based on the relationship between T_2 and T_{PL}, the predicted T_{PL} (plateau time) of LPDT curve with normal shape then will be 5.3 s, whereas the T_{PL} of the LPDT curve with jump will be 6.7 s. The jumps on the curve can be given by different effects, both related to the source process itself, such as multiple peaks on the Moment Rate Function, and/or to propagation effects, such as the arrival of intermediate phases (preceding the S-wave arrival), arriving at a receiver within the coda of P-wave phase. However, the presence of jumps on the LPDT curves is not frequently observed in our catalogue, only happens in two events. Meanwhile, the jump in the LPDT curve does not have a serious impact on the derived parameters. Thus, we believe that, on average, this is a negligible effect on the overall estimation of rupture length and stress drop.

The shape of the curves may change in real-time, when we do not have all the available stations. As a perspective of the work, we could evaluate the feasibility of application in real-time, that can be relevant for EEW applications. The accurate estimation of the rupture extent and magnitude at the early stage of the process can be a useful piece of information to add to the early shake-map computation, and the estimation of ground shaking can be strongly improved by considering the effect of the finite fault (Colombelli et al., 2013). While in this off-line study we used the post-earthquake location instead of the real-time estimation, a reliable estimation of the earthquake location is needed for the real-time application. Having in mind that the far-field stations must wait enough time to reach the plateau of the curve for large events, we need more time to get the plateau information. Hence, the real-time application performance and the timeliness based on the network distribution for this approach will be further studied. A possible method could be that we can estimate the final curve at each time step with a given probability and study the real-time curve reached how many percent of the final curve (maybe after T_2) can give a reliable probability for estimating final curve.

DATA AVAILABILITY STATEMENT

The original contributions presented in the study are included in the article/**Supplementary Material**, further inquiries can be directed to the corresponding authors.

AUTHOR CONTRIBUTIONS

YW applied the methodology and drafted the manuscript; SC and AZ critically revised the paper and supervised the study; JS and SL provided suggestions on the results. All authors contributed to the article and approved the submitted version.

FUNDING

This research was financially supported by the National Key Research and Development Program of China (2018YFC1504003) and its provincial funding, the Italian Ministry of Research and the University of Naples Federico II (Project Number AIM1834927-3; E66C19000090001), and the Scientific Research Fund of Institute of Engineering Mechanics, China Earthquake Administration (2016A03).

ACKNOWLEDGMENTS

We thank the China Strong Motion Network Centre (CSMNC) at the Institute of Engineering Mechanics, China Earthquake Administration, for providing the ground motion recording data. We would like to thank the University of Naples Federico II where the work has been carried out during the visiting period. We would also like to thank Jia Cheng (Institute of Crustal Dynamics, China Earthquake Administration) for the discussion about the calculation of stress drop. The moment rate function of the M 8.0 Wenchuan earthquake has been provided by the USGS: https://earthquake.usgs.gov/earthquakes/eventpage/usp000g650/finite-fault (last accessed May 2020). This manuscript has been posted on Earth and Space Science Open Archive (ESSOAr) with a preprint service (https://www.essoar.org/doi/abs/10.1002/essoar.10503831.1).

SUPPLEMENTARY MATERIAL

The Supplementary Material for this article can be found online at: https://www.frontiersin.org/articles/10.3389/feart.2021.616229/full#supplementary-material.

REFERENCES

Aki, K., and Richards, P. G. (2002). *Quantitative seismology*. Sausalito, CA: University Science Books.

Allen, R. M., and Kanamori, H. (2003). The potential for earthquake early warning in southern California. *Science* 300 (5620), 786–789. doi:10.1126/science.1080912

Allen, R. M., and Ziv, A. (2011). Application of real-time GPS to earthquake early warning. *Geophys. Res. Lett.* 38 (16) doi:10.1029/2011gl047947

Allen, R. V. (1978). Automatic earthquake recognition and timing from single traces. *Bull. Seismological Soc. America* 68 (5), 1521–1532.

Allmann, B. P., and Shearer, P. M. (2009). Global variations of stress drop for moderate to large earthquakes. *J. Geophys. Res.* 114 (B1). doi:10.1029/2008jb005821

Bilek, S. L., Lay, T., and Ruff, L. J. (2004). Radiated seismic energy and earthquake source duration variations from teleseismic source time functions for shallow subduction zone thrust earthquakes. *J. Geophys. Res.* 109 (B9), a. doi:10.1029/2004jb003039

Brune, J. N. (1970). Tectonic stress and the spectra of seismic shear waves from earthquakes. *J. Geophys. Res.* 75 (26), 4997–5009. doi:10.1029/JB075i026p04997

Boatwright, J. (1980). A spectral theory for circular seismic sources; simple estimates of source dimension, dynamic stress drop, and radiated seismic energy. *Bull. Seismological Soc. America* 70 (1), 1–27.

Bormann, P., Baumbach, M., Bock, G., Grosser, H., Choy, G. L., and Boatwright, J. (2009). "Seismic sources and source parameters," in *New manual of seismological observatory practice (NMSOP)*. Editor P. Bormann (Potsdam: Deutsches GeoForschungsZentrum GFZ), 1–94.

Bormann, P., and Saul, J. (2009). "Earthquake magnitude," in *Encyclopedia of complexity and systems science*. Editor R. Meyers (New York, N Y: Springer). doi:10.1007/978-0-387-30440-3_151

Keilis-Borok, V. (1959). On estimation of the displacement in an earthquake source and of source dimensions. Ann. Geofis. *(Rome)* 12, 205–214. doi:10.4401/ag-5718

Böse, M., Felizardo, C., and Heaton, T. H. (2015). Finite-fault rupture detector (FinDer): going real-time in CalifornianShakeAlertWarning system. *Seismological Res. Lett.* 86 (6), 1692–1704. doi:10.1785/0220150154

Böse, M., Heaton, T. H., and Hauksson, E. (2012). Real-time finite fault rupture detector (FinDer) for large earthquakes. *Geophys. J. Int.* 191 (2), 803–812. doi:10.1111/j.1365-246X.2012.05657.x

Böse, M., Ionescu, C., and Wenzel, F. (2007). Earthquake early warning for Bucharest, Romania: novel and revised scaling relations. *Geophys. Res. Lett.* 34 (7). doi:10.1029/2007gl029396

Caprio, M., Lancieri, M., Cua, G. B., Zollo, A., and Wiemer, S. (2011). An evolutionary approach to real-time moment magnitude estimation via inversion of displacement spectra. *Geophys. Res. Lett.* 38 (2), a. doi:10.1029/2010gl045403

Chen, Y., Yang, Z., Zhang, Y., and Liu, C. (2013). From 2008 Wenchuan earthquake to 2013 Lushan earthquake (in Chinese). *Sci. China Ser. D: Earth Sci.* 43, 1064–1072.

Cheng, J., Rong, Y., Magistrale, H., Chen, G., and Xu, X. (2019). Earthquake rupture scaling relations for mainland China. *Seismological Res. Lett.* 91 (1), 248–261. doi:10.1785/0220190129

Cheng, J., Wu, Z., Liu, J., Jiang, C., Xu, X., Fang, L., et al. (2015). Preliminary report on the 3 august 2014, mw 6.2/ms 6.5 ludian, yunnan-sichuan border, southwest China, earthquake. *Seismological Res. Lett.* 86 (3), 750–763. doi:10.1785/0220140208

Colombelli, S., Allen, R. M., and Zollo, A. (2013). Application of real-time GPS to earthquake early warning in subduction and strike-slip environments. *J. Geophys. Res. Solid Earth* 118 (7), 3448–3461. doi:10.1002/jgrb.50242

Colombelli, S., Festa, G., and Zollo, A. (2020). Early rupture signals predict the final earthquake size. *Geophys. J. Int.* 223 (1), 692–706. doi:10.1093/gji/ggaa343

Colombelli, S., and Zollo, A. (2015). Fast determination of earthquake magnitude and fault extent from real-timeP-wave recordings. *Geophys. J. Int.* 202 (2), 1158–1163. doi:10.1093/gji/ggv217

Colombelli, S., Zollo, A., Festa, G., and Kanamori, H. (2012). Early magnitude and potential damage zone estimates for the great Mw 9 Tohoku-Oki earthquake. *Geophys. Res. Lett.* 39 (22), a. doi:10.1029/2012gl053923

Duputel, Z., Rivera, L., Kanamori, H., and Hayes, G. (2012). W phase source inversion for moderate to large earthquakes (1990-2010). *Geophys. J. Int.* 189 (2), 1125–1147. doi:10.1111/j.1365-246X.2012.05419.x

Fang, L., Wu, J., Liu, J., Cheng, J., Jiang, C., Han, L., et al. (2015). Preliminary report on the 22 november 2014Mw 6.1/ms 6.3 kangding earthquake, western sichuan, China. *Seismological Res. Lett.* 86 (6), 1603–1613. doi:10.1785/0220150006

Fang, L., Wu, J., Wang, W., Lü, Z., Wang, C., Yang, T., et al. (2013). Relocation of the mainshock and aftershock sequences of M S7.0 Sichuan Lushan earthquake. *Chin. Sci. Bull.* 58 (28-29), 3451–3459. doi:10.1007/s11434-013-6000-2

Hao, J., Ji, C., Wang, W., and Yao, Z. (2013). Rupture history of the 2013Mw6.6 Lushan earthquake constrained with local strong motion and teleseismic body and surface waves. *Geophys. Res. Lett.* 40 (20), 5371–5376. doi:10.1002/2013gl056876

Haskell, N. A. (1964). Total energy and energy spectral density of elastic wave radiation from propagating faults. *Bull. Seismological Soc. America* 54 (6A), 1811–1841.

Heaton, T. H. (1990). Evidence for and implications of self-healing pulses of slip in earthquake rupture. *Phys. Earth Planet. Interiors* 64 (1), 1–20. doi:10.1016/0031-9201(90)90002-f

Hoshiba, M., and Aoki, S. (2015). Numerical shake prediction for earthquake early warning: data assimilation, real-time shake mapping, and simulation of wave propagation. *Bull. Seismological Soc. America* 105 (3), 1324–1338. doi:10.1785/0120140280

Huang, Y., Wu, J., Zhang, T., and Zhang, D. (2008). Relocation of the M8.0 Wenchuan earthquake and its aftershock sequence. *Sci. China Ser. D-earth Sci.* 51 (12), 1703–1711. doi:10.1007/s11430-008-0135-z

Hwang, R.-D., Chang, J.-P., Wang, C.-Y., Wu, J.-J., Kuo, C.-H., Tsai, Y.-W., et al. (2011). Rise time and source duration of the 2008 M W 7.9 Wenchuan (China) earthquake as revealed by Rayleigh waves. *Earth Planet. Sp* 63 (5), 427–434. doi:10.5047/eps.2011.01.002

Jiang, G., Wen, Y., Liu, Y., Xu, X., Fang, L., Chen, G., et al. (2015). Joint analysis of the 2014 Kangding, southwest China, earthquake sequence with seismicity relocation and InSAR inversion. *Geophys. Res. Lett.* 42 (9), 3273–3281. doi:10.1002/2015gl063750

Kanamori, H. (2005). Real-time seismology and earthquake damage mitigation. *Annu. Rev. Earth Planet. Sci.* 33 (1), 195–214. doi:10.1146/annurev.earth.33.092203.122626

Li, J., Liu, C., Zheng, Y., and Xiong, X. (2017). Rupture process of the M s 7.0 Lushan earthquake determined by joint inversion of local static GPS records, strong motion data, and teleseismograms. *J. Earth Sci.* 28 (2), 404–410. doi:10.1007/s12583-017-0757-1

Li, X., Zhou, Z., Yu, H., Wen, R., Lu, D., Huang, M., et al. (2008). Strong motion observations and recordings from the great Wenchuan Earthquake. *Earthq. Eng. Eng. Vib.* 7 (3), 235–246. doi:10.1007/s11803-008-0892-x

Liu, C., Zheng, Y., Ge, C., Xiong, X., and Hsu, H. (2013). Rupture process of the M s7.0 Lushan earthquake, 2013. *Sci. China Earth Sci.* 56 (7), 1187–1192. doi:10.1007/s11430-013-4639-9

Lomax, A., and Michelini, A. (2009). Mwpd: a duration-amplitude procedure for rapid determination of earthquake magnitude and tsunamigenic potential fromPwaveforms. *Geophys. J. Int.* 176 (1), 200–214. doi:10.1111/j.1365-246X.2008.03974.x

Madariaga, R. (1976). Dynamics of an expanding circular fault. *Bull. Seismological Soc. America* 66 (3), 639–666.

Madariaga, R. (1977). Implications of stress-drop models of earthquakes for the inversion of stress drop from seismic observations. *Pageoph* 115, 301–316. doi:10.1007/bf01637111

Melgar, D., Crowell, B. W., Geng, J., Allen, R. M., Bock, Y., Riquelme, S., et al. (2015). Earthquake magnitude calculation without saturation from the scaling of peak ground displacement. *Geophys. Res. Lett.* 42 (13), 5197–5205. doi:10.1002/2015gl064278

Melgar, D., and Hayes, G. P. (2017). Systematic observations of the slip pulse properties of large earthquake ruptures. *Geophys. Res. Lett.* 44 (19), 9691–9698. doi:10.1002/2017gl074916

Meng, L., Zang, Y., McGarr, A., and Zhou, L. (2019). High-frequency ground motion and source characteristics of the 2008 wenchuan and 2013 lushan, China, earthquakes. *Pure Appl. Geophys.* 177 (1), 81–93. doi:10.1007/s00024-019-02291-4

Nazeri, S., Colombelli, S., and Zollo, A. (2019). Fast and accurate determination of earthquake moment, rupture length and stress release for the 2016-2017 Central Italy seismic sequence. *Geophys. J. Int.* 217 (2), 1425–1432. doi:10.1093/gji/ggz097

Ohta, Y., Miura, S., Ohzono, M., Kita, S., Iinuma, T., Demachi, T., et al. (2011). Large intraslab earthquake (2011 April 7, M 7.1) after the 2011 off the Pacific coast of Tohoku Earthquake (M 9.0): coseismic fault model based on the dense GPS network data. *Earth Planet. Sp* 63 (12), 1207–1211. doi:10.5047/eps.2011.07.016

Sato, T., and Hirasawa, T. (1973). Body wave spectra from propagating shear cracks. *J,Phys,Earth* 21 (4), 415–431. doi:10.4294/jpe1952.21.415

Trugman, D. T., Page, M. T., Minson, S. E., and Cochran, E. S. (2019). Peak ground displacement saturates Exactly when expected: implications for earthquake early warning. *J. Geophys. Res. Solid Earth* 124 (5), 4642–4653. doi:10.1029/2018jb017093

Vallée, M. (2013). Source time function properties indicate a strain drop independent of earthquake depth and magnitude. *Nat. Commun.* 4 (1), 2606. doi:10.1038/ncomms3606

Wang, H., Ren, Y., and Wen, R. (2018). Source parameters, path attenuation and site effects from strong-motion recordings of the Wenchuan aftershocks (2008-2013) using a non-parametric generalized inversion technique. *Geophys. J. Int.* 212 (2), 872–890. doi:10.1093/gji/ggx447

Wang, W., Wu, J., Fang, L., Lai, G., Yang, T., and Cai, Y. (2014). Swave velocity structure in southwest China from surface wave tomography and receiver functions. *J. Geophys. Res. Solid Earth* 119 (2), 1061–1078. doi:10.1002/2013jb010317

Wells, D. L., and Coppersmith, K. J. (1994). New empirical relationships among magnitude, rupture length, rupture width, rupture area, and surface displacement. *Bull. Seismological Soc. America* 84 (4), 974–1002.

Wu, Y.-M., and Kanamori, H. (2008). Exploring the feasibility of on-site earthquake early warning using close-in records of the 2007 Noto Hanto earthquake. *Earth Planet. Sp* 60 (2), 155–160. doi:10.1186/BF03352778

Wu, Y.-M., and Zhao, L. (2006). Magnitude estimation using the first three seconds P-wave amplitude in earthquake early warning. *Geophys. Res. Lett.* 33 (16). doi:10.1029/2006gl026871

Zhang, Y., Wang, R., Zschau, J., Chen, Y.-t., Parolai, S., and Dahm, T. (2014). Automatic imaging of earthquake rupture processes by iterative deconvolution and stacking of high-rate GPS and strong motion seismograms. *J. Geophys. Res. Solid Earth* 119 (7), 5633–5650. doi:10.1002/2013jb010469

Ziv, A., and Lior, I. (2016). Real-time moment magnitude and stress drop with implications for real-time shaking prediction. *Bull. Seismological Soc. America* 106 (6), 2459–2468. doi:10.1785/0120160091

Zollo, A., Amoroso, O., Lancieri, M., Wu, Y.-M., and Kanamori, H. (2010). A threshold-based earthquake early warning using dense accelerometer networks. *Geophys. J. Int.* 183 (2), 963–974. doi:10.1111/j.1365-246X.2010.04765.x

Zollo, A., Lancieri, M., and Nielsen, S. (2006). Earthquake magnitude estimation from peak amplitudes of very early seismic signals on strong motion records. *Geophys. Res. Lett.* 33 (23). doi:10.1029/2006gl027795

Conflict of Interest: The authors declare that the research was conducted in the absence of any commercial or financial relationships that could be construed as a potential conflict of interest.

frontiers in Earth Science

ORIGINAL RESEARCH
published: 13 May 2021
doi: 10.3389/feart.2021.653226

Magnitude Estimation for Earthquake Early Warning Using a Deep Convolutional Neural Network

Jingbao Zhu[1,2], Shanyou Li[1,2], Jindong Song[1,2] and Yuan Wang[1,2]*

[1] Institute of Engineering Mechanics, China Earthquake Administration, Harbin, China, [2] Key Laboratory of Earthquake Engineering and Engineering Vibration, China Earthquake Administration, Harbin, China

Magnitude estimation is a vital task within earthquake early warning (EEW) systems (EEWSs). To improve the magnitude determination accuracy after P-wave arrival, we introduce an advanced magnitude prediction model that uses a deep convolutional neural network for earthquake magnitude estimation (DCNN-M). In this paper, we use the inland strong-motion data obtained from the Japan Kyoshin Network (K-NET) to calculate the input parameters of the DCNN-M model. The DCNN-M model uses 12 parameters extracted from 3 s of seismic data recorded after P-wave arrival as the input, four convolutional layers, four pooling layers, four batch normalization layers, three fully connected layers, the Adam optimizer, and an output. Our results show that the standard deviation of the magnitude estimation error of the DCNN-M model is 0.31, which is significantly less than the values of 1.56 and 0.42 for the τ_c method and P_d method, respectively. In addition, the magnitude prediction error of the DCNN-M model is not affected by variations in the epicentral distance. The DCNN-M model has considerable potential application in EEWSs in Japan.

Keywords: earthquake early warning, magnitude, estimation, P-wave, deep convolutional neural network

OPEN ACCESS

Edited by:
Maren Böse,
ETH Zürich, Switzerland

Reviewed by:
Kiran Kumar Singh Thingbaijam,
GNS Science, New Zealand
Dong-Hoon Sheen,
Chonnam National University,
South Korea

****Correspondence:***
Jindong Song
jdsong@iem.ac.cn

Specialty section:
This article was submitted to Geohazards and Georisks, a section of the journal Frontiers in Earth Science

Received: *14 January 2021*
Accepted: *20 April 2021*
Published: *13 May 2021*

Citation:
Zhu J, Li S, Song J and Wang Y (2021) Magnitude Estimation for Earthquake Early Warning Using a Deep Convolutional Neural Network. Front. Earth Sci. 9:653226. doi: 10.3389/feart.2021.653226

INTRODUCTION

Earthquake early warning (EEW) systems (EEWSs) depend on stations located near the earthquake source area to monitor earthquakes and obtain location, ground shaking, and magnitude information using data from the first few seconds after P-wave arrival. They then send EEW information to the target sites before destructive seismic waves arrive (Allen and Kanamori, 2003). Over the past few decades, EEWSs have been shown to be an effective earthquake hazard mitigation approach and have been applied in many regions around the world, such as Japan (Hoshiba et al., 2008), Mexico (Aranda et al., 1995), Taiwan (Wu and Teng, 2002; Chen et al., 2015), California (Allen et al., 2009a), southern Italy (Zollo et al., 2009; Colombelli et al., 2020), and Iran (Heidari et al., 2012).

Magnitude estimation is an essential EEW task. Reliable EEW information and estimates of damage areas both rely on accurate magnitude determination. EEWSs estimate earthquake magnitudes based on the initial few seconds after P-wave arrival (Allen et al., 2009b). The final earthquake magnitude may be determined by the initial rupture rather than the overall earthquake rupture process (Olson and Allen, 2005; Wu and Zhao, 2006). The existing magnitude estimation methodologies mainly establish the regression functions between the parameter extracted from the initial several seconds after P-wave arrival and the catalog magnitudes (CMs) to predict the

earthquake magnitudes. The τ_c method, which establishes the empirical relationship between the average period (τ_c) and the CMs, was proposed by Kanamori (2005) and has been demonstrated to have a relationship with the magnitude that is acceptable for EEWSs (Wu and Kanamori, 2008; Yamada and Mori, 2009). Wu and Zhao (2006) proposed the P_d method, which establishes an empirical correlation between the peak amplitude of displacement during the first 3 s after P-wave arrival and the CMs and was applied to predict magnitudes in southern California. The P_d method provides robust magnitude estimation, and it is feasible to use the peak amplitude of displacement during the first several seconds after P-wave arrival to predict magnitudes for EEWSs (Zollo et al., 2006; Tsang et al., 2007; Lin et al., 2011). The squared velocity integral (IV2), which was proposed by Festa et al. (2008), is related to the early radiated energy and can be used to determine earthquake magnitudes.

However, since a single parameter might provide little magnitude information regardless of whether it is governed by the frequency, amplitude, or energy, the accuracy of EEW magnitude estimation still needs to be improved. More accurate magnitude estimation will lead to more effective hazard mitigation. With the development of artificial intelligence, some researchers have combined magnitude estimation and support vector machines (SVMs) and indicated that artificial intelligence has excellent potential for use in EEW magnitude estimation applications (Reddy and Nair, 2013; Ochoa et al., 2017). In this study, we developed an advanced magnitude prediction model by using a deep convolutional neural network for magnitude estimation (DCNN-M). Following the analyses by Kanamori (2005), Wu and Kanamori (2005), and Wu and Zhao (2006), we also used the 3-s time window after P-wave arrival for DCNN-M model estimation. We used 12 magnitude estimation parameters from P-wave arrival for EEW related to the frequency, amplitude, and energy as input, which make the DCNN-M model interpretable, and trained the DCNN-M model using the training dataset. Then, the test dataset was used to test the DCNN-M model performance, and DCNN-M model magnitude estimates were compared to the τ_c method and P_d method results. Furthermore, as a test, we used the DCNN-M model to predict 31 additional earthquake events and obtained reliable magnitude estimates. We show that the DCNN-M model is robust enough to predict magnitudes in Japan and that it has considerable potential for application to EEWSs.

DATA AND PROCESSING

In this study, we used strong-motion data from October 2007 through October 2017, which were obtained from the Kyoshin Network (K-NET) stations of the National Research Institute for Earth Science and Disaster Prevention (NIED) in Japan[1] (Aoi et al., 2011). The sampling rate of the strong-motion data was 100 Hz. We selected inland earthquakes from the K-NET catalog with magnitudes within the $3 \leq M_{JMA} \leq 8$ range and focal depths shallower than 10 km. We had no epicentral distance requirements for the strong-motion data.

There were 1,836 inland earthquakes (**Figure 1A**) characterized by 19,263 three-component seismograms recorded by the K-NET stations (**Figure 1B**). The data were composed mainly of events within $3 \leq M_{JMA} \leq 6.9$ but included three $M_{JMA}7$ and $M_{JMA}7.4$ events (see **Supplementary Table 1**). The P-wave arrival was determined automatically using the short-term averaging/long-term averaging algorithm (Allen, 1978). Acceleration records were integrated once and twice to obtain velocity and displacement seismograms, respectively. Then, the displacement seismograms were processed by using a Butterworth filter with a high-pass frequency of 0.075 Hz to remove low-frequency drift (Wu and Zhao, 2006). Moreover, selected seismic records were randomly divided into two datasets: a training dataset (15,410 three-component seismic records), which accounted for 80% of the strong-motion data, was used to train the DCNN-M model, and a test dataset (3,853 three-component seismic records), which accounted for 20% of the strong-motion data, was used to assess the DCNN-M model performance after training (**Figure 2**).

THE INPUT PARAMETERS

The P-wave parameters used to predict magnitude mainly include three categories for EEW: parameters related to amplitude, frequency and energy. Since a single parameter provides little earthquake magnitude information, multiple parameters might provide more information useful in magnitude prediction; thus, for EEW, 12 magnitude estimation parameters of the P-wave arrival related to the frequency, amplitude, and energy are selected as inputs to the DCNN-M model to make the DCNN-M model interpretable. It is important that these 12 P-wave parameters are correlated with magnitude in this paper. In this study, these P-wave parameters are introduced in the following paragraphs. Following the analysis of Kanamori (2005), Wu and Kanamori (2005), Wu and Zhao (2006), we also used the 3-s time window after P-wave arrival for DCNN-M model magnitude estimation. Furthermore, we corrected the parameters related to amplitude, energy and derivative parameters for the distance effect by normalizing them to a reference distance of 10 km (Zollo et al., 2006).

First, P-wave parameters related to amplitude include peak displacement (P_d), peak velocity (P_v), and peak acceleration (P_a), which provide information on the earthquake size and these amplitude-related parameters have relationships with the magnitude (Wu and Kanamori, 2005; Wu and Zhao, 2006). The single data points for the P-wave parameters related to amplitude as a function of magnitude are shown in **Supplementary Figure 1**. In addition, these parameters are defined as:

$$P_d = \max_{0 \leq t \leq T} \left| d_{ud}(t) \right| \quad (1)$$

$$P_v = \max_{0 \leq t \leq T} \left| v_{ud}(t) \right| \quad (2)$$

$$P_a = \max_{0 \leq t \leq T} \left| a_{ud}(t) \right| \quad (3)$$

[1] http://www.kyoshin.bosai.go.jp/

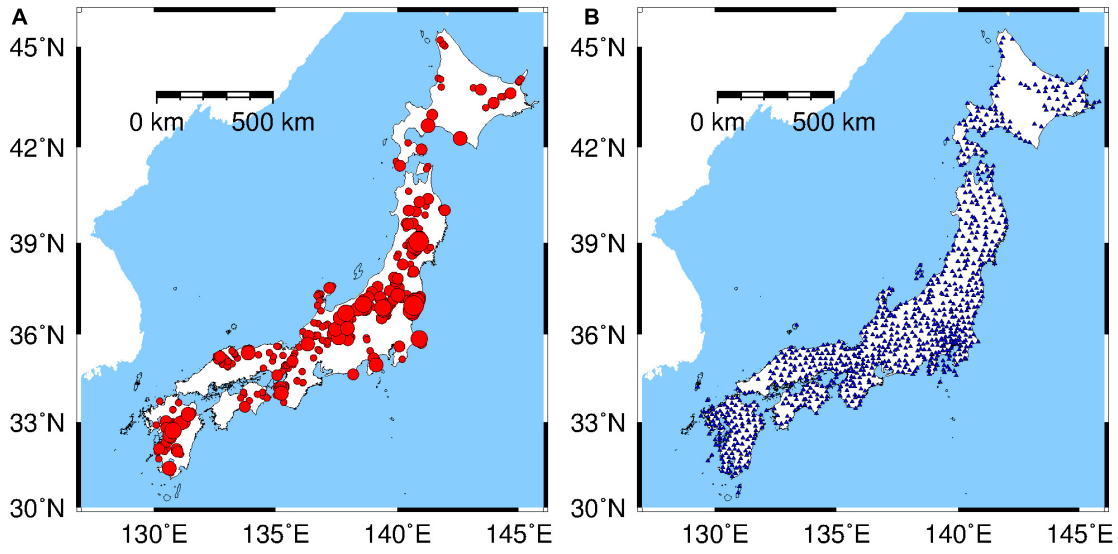

FIGURE 1 | (A) The epicenter locations of the 1,836 inland earthquakes used in this paper. Solid red circles of different sizes indicate magnitudes within the range of $3 \leq M_{JMA} \leq 7.4$. **(B)** The distribution of the stations (solid blue triangles) that recorded the strong-motion data used in this paper.

where $d_{ud}(t)$, $v_{ud}(t)$, and $a_{ud}(t)$ are the vertical components of the displacement, velocity, and acceleration time histories of the strong-motion data, respectively. Zero is the P-wave arrival time, and T is the length of the P-wave time window. In this paper, the linear relationship between the amplitude parameters, the magnitude and the hypocentral distance is shown in **Supplementary Table 3**, and the linear relationship between the amplitude parameters after normalization to a reference distance of 10 km and magnitude is shown in **Supplementary Table 4**.

Next, the P-wave parameters related to frequency include the average period (τ_c), product parameter (TP), and peak ratio (T_{va}). The average period has been proven to have an acceptable relationship with the magnitude (Kanamori, 2005) and it can be calculated as:

$$r = \frac{\int_0^T v_{ud}^2(t)\,dt}{\int_0^T d_{ud}^2(t)\,dt} \tag{4}$$

$$\tau_c = \frac{2\pi}{\sqrt{r}} \tag{5}$$

The correlation of TP and magnitude was proposed by Huang et al. (2015), which has correlations with τ_c and P_d, and TP is defined as:

$$TP = \tau_c \times P_d \tag{6}$$

where τ_c is the average period and P_d is the peak displacement. The peak ratio reflects the frequency components of the ground motion and has a correlation with magnitude (Böse, 2006; Ma, 2008), which has correlations with P_v and P_a, and it can be calculated as:

$$T_{va} = 2\pi\,(P_v/P_a) \tag{7}$$

where P_v and P_a are the peak velocity and peak acceleration, respectively. The single data points for the P-wave parameters related to frequency as a function of magnitude are shown in **Supplementary Figure 2**. In this paper, the linear relationship between the frequency parameters and the magnitude is shown in **Supplementary Table 5**.

Finally, P-wave parameters related to the power of earthquakes include the P-wave index value (PI_v) (Nakamura, 2003), velocity squared integral ($IV2$) (Festa et al., 2008) and cumulative absolute velocity (CAV) (Reed and Kassawara, 1988; Böse, 2006). The single data points for the P-wave parameters related to energy as a function of magnitude are shown in **Supplementary Figure 3**. In addition, these parameters are calculated as:

$$PI_v = \max_{0\leq t\leq T} \log\left|a_{ud}(t)\cdot v_{ud}(t)\right| \tag{8}$$

$$IV2 = \int_0^T v_{ud}^2(t)\,dt \tag{9}$$

$$CAV = \int_0^T |a_3(t)|\,dt \tag{10}$$

$$a_3(t) = \sqrt{a_{ud}^2(t) + a_{ew}^2(t) + a_{ns}^2(t)} \tag{11}$$

where $a_3(t)$ is the total acceleration of the three components. In this paper, the linear relationship between the energy parameters, the magnitude and the hypocentral distance is shown in **Supplementary Table 6**, and the linear relationship between the energy parameters after normalization to a reference distance of 10 km and magnitude is shown in **Supplementary Table 7**. Because, CAV considers the influence of both the amplitude and the duration of motion, we proposed three derivative parameters according to the CAV. They are cumulative vertical absolute displacement($cvad$), cumulative vertical absolute velocity($cvav$) and cumulative vertical absolute acceleration($cvaa$). The single data points for the derivative parameters as a function of

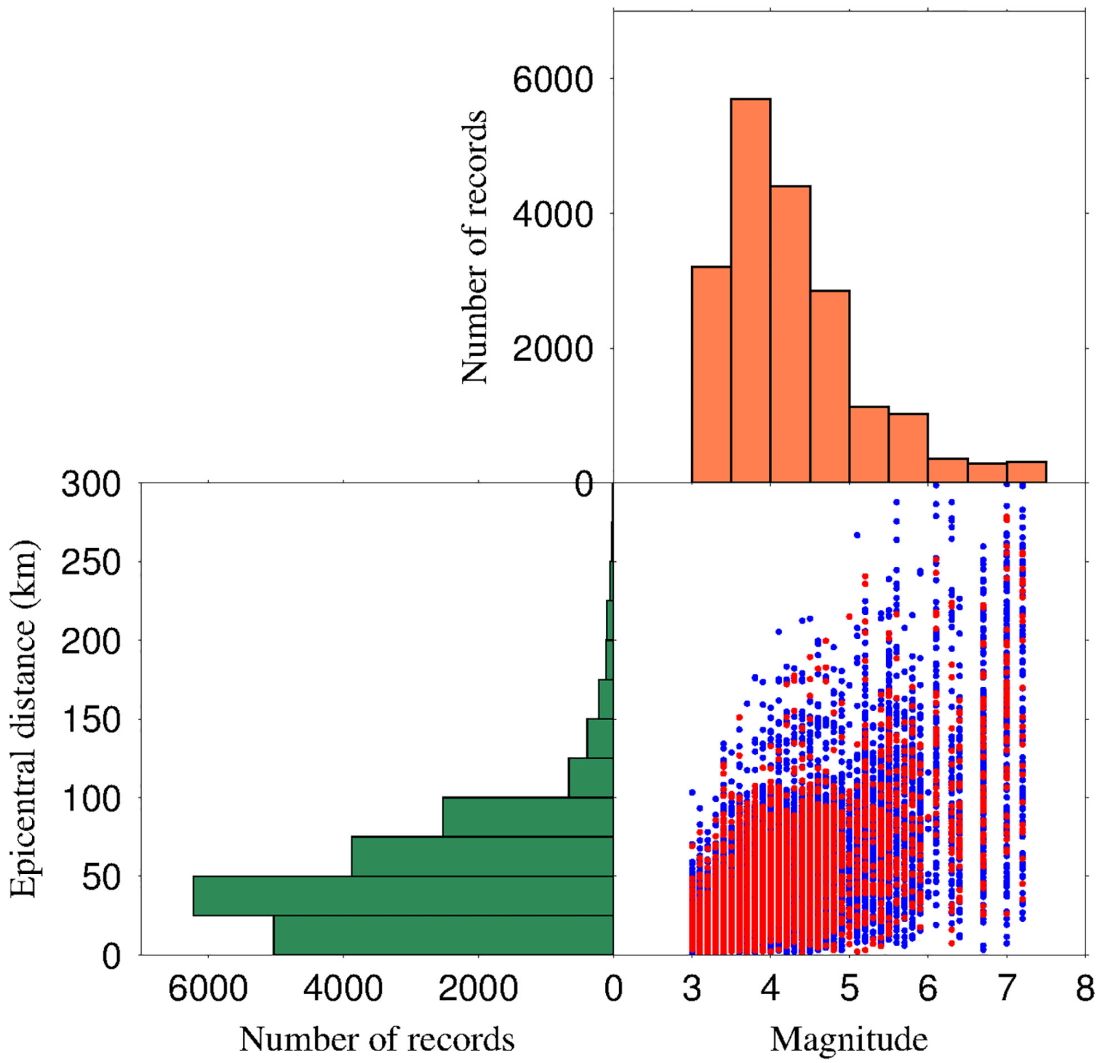

FIGURE 2 | The distribution of the epicentral distance and magnitude records. A histogram for the number of selected seismic records with the magnitude is shown at the top. An interval of 0.5 is used for each magnitude bin. A histogram of the number of selected seismic records with the epicentral distance is shown at the bottom left. An interval of 25 km is used for each epicentral distance bin. The distribution between the magnitude and epicentral distance is shown at the bottom right. Solid blue circles indicate the training dataset used to train the DCNN-M model. Solid red circles indicate the test dataset used to test the DCNN-M model performance.

magnitude are shown in **Supplementary Figure 4**. These parameters are calculated as:

$$cvad = \underset{0\le t\le T}{sum}\left(\left|d_{ud}\left(t\right)\right|\right) \tag{12}$$

$$cvav = \underset{0\le t\le T}{sum}\left(\left|v_{ud}\left(t\right)\right|\right) \tag{13}$$

$$cvaa = \underset{0\le t\le T}{sum}\left(\left|a_{ud}\left(t\right)\right|\right) \tag{14}$$

In this paper, the linear relationship between the derivative parameters, the magnitude and the hypocentral distance is shown in **Supplementary Table 8**, and the linear relationship between the derivative parameters after normalization to a reference distance of 10 km and magnitude is shown in **Supplementary Table 9**.

To prevent numerical problems caused by large variations between the ranges of the parameters and to improve the training efficiency of the model, these parameters are linearly scaled to [−1, 1] as the input of the deep convolutional neural network (Tezcan and Cheng, 2012). When scaled to [−1, 1], every parameter becomes:

$$x_{\text{norm}} = \frac{2x - (x_{\max} + x_{\min})}{x_{\max} - x_{\min}} \tag{15}$$

where x_{norm} is the original P-wave parameter and x_{max} and x_{min} are the maximum and minimum values of every P-wave parameter extracted from the strong-motion data in this study, respectively.

THE DCNN-M MODEL

Earthquake early warning magnitudes are usually predicted via the empirical relationship between a single parameter extracted from the seismic data collected during the first few seconds after P-wave arrival and CMs. Since a single parameter provides little earthquake magnitude information, multiple parameters might provide more information useful in magnitude prediction. In addition, to make the model interpretable, for EEW, we used 12 magnitude estimation parameters related to the amplitude, frequency, and energy following the P-wave arrival (see **Supplementary Text 1**) as the inputs of the DCNN-M model.

The DCNN-M model was constructed based on a deep convolutional neural network and was used to predict magnitudes for EEW. The architecture of the DCNN-M model comprised 12 parameters extracted from the 3 s period after P-wave arrival as inputs, four convolutional layers, four batch normalization layers, four pooling layers, three fully connected layers, and an output (**Figure 3**). The output was the predicted magnitude (PM). The four convolutional layers had 124, 150, 190, and 250 filters. In each convolutional layer, the kernel size of the filter was 4, the stride was 2, the padding type was "same," and the initialization was "TruncatedNormal." A batch normalization layer followed each convolutional layer. The batch normalization layers made the setting of the hyperparameters freer, the network convergence speed faster, and the performance better (Ioffe and Szegedy, 2015). A pooling layer followed each batch normalization layer; we used max pooling, each max pooling size was 2, each stride was 2, and each padding type was "same." The final pooling layer was flattened and then fed to the first fully connected layer. The three fully connected layers had 250, 125, and 60 neurons.

To prevent overfitting and ensure better generalizability, we applied L2 regularization with a regularization rate of 10^{-4} to the convolutional layers and dropout with a dropout rate of 0.5 following the last fully connected layer (Srivastava et al., 2014; Jozinović et al., 2020). Moreover, the rectified linear unit (ReLU) activation function (Nair and Hinton, 2010) followed each pooling layer and fully connected layer. Because larger batch sizes lead to worse generalization performance (Keskar et al., 2016), we used 76 batch sizes and 48 epochs based on a tradeoff between efficiency and generalizability. We used a training dataset to train the DCNN-M model based on the Adam optimizer with a learning rate of 0.001 by optimizing a loss function defined as the mean squared error of the output (Kingma and Ba, 2014). In this study, the DCNN-M model was programmed using TensorFlow GPU 2.3 and trained using the training dataset, requiring approximately 1.5 min on an Nvidia Quadro T1000 GPU with 12 GB memory.

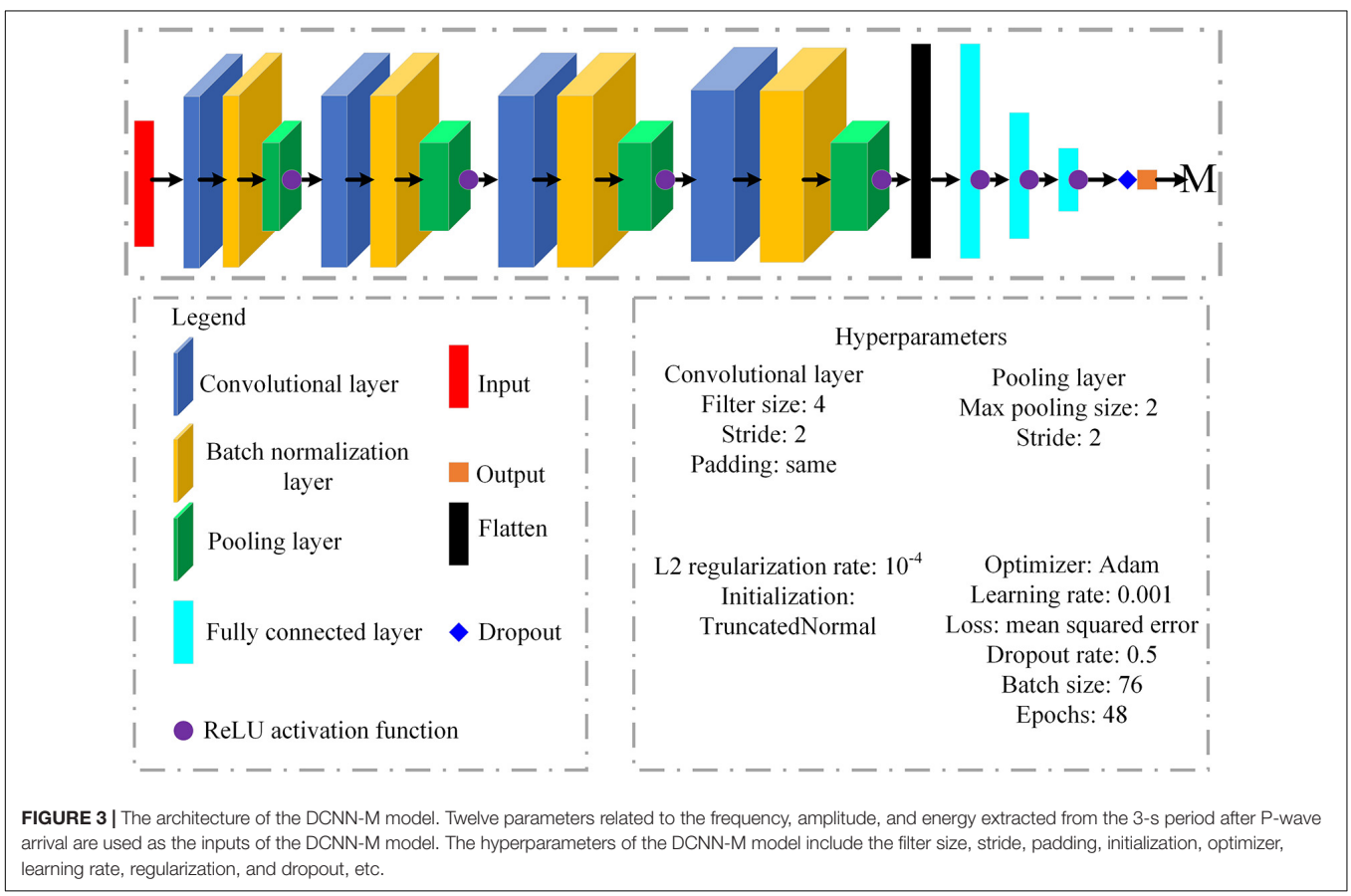

FIGURE 3 | The architecture of the DCNN-M model. Twelve parameters related to the frequency, amplitude, and energy extracted from the 3-s period after P-wave arrival are used as the inputs of the DCNN-M model. The hyperparameters of the DCNN-M model include the filter size, stride, padding, initialization, optimizer, learning rate, regularization, and dropout, etc.

RESULTS

In this study, the difference between the PM and CM is defined as the error (ω). The error (ω) and the standard deviation (σ) of the errors are expressed as:

$$\omega = \mathrm{PM} - \mathrm{CM} \tag{16}$$

$$\sigma = \sqrt{\frac{1}{N}\sum_{i=1}^{N}(\omega_i - \varpi)^2} \tag{17}$$

where N is the number of records and ϖ is the mean of the errors.

Figure 4 depicts magnitude estimation for the training dataset (**Figure 4A**) and the test dataset (**Figure 4B**) based on the DCNN-M model. The PMs approximate the CMs in the training and test datasets. The standard deviations of the magnitude estimation errors are 0.31 for both the training and test datasets. This finding indicates excellent generalization performance and an absence of overfitting within the DCNN-M model.

The τ_c method and P_d method are widely used in the study of EEWS magnitude prediction (Kanamori, 2005; Wu and Kanamori, 2005; Wu and Zhao, 2006; Zollo et al., 2006; Colombelli et al., 2014). To evaluate the performance of the DCNN-M model, the τ_c method and P_d method were used to predict the magnitudes, and the results were compared.

For the same test dataset and the 3-s time window after P-wave arrival, **Figures 5A–C** show the τ_c method, P_d method, and DCNN-M model estimation results, respectively. The magnitude estimates of the τ_c method and P_d method are obtained based on **Supplementary Tables 4, 5**, respectively. The relationships used for magnitude estimation by the τ_c method and P_d method are given by:

$$\log(\tau_c) = -1.07\,(\pm 0.02) + 0.19(\pm 0.01)M \tag{18}$$

$$\log\left(P_d^{10\mathrm{km}}\right) = -4.84\,(\pm 0.02) + 0.78(\pm 0.01)M \tag{19}$$

Compared to the DCNN-M model results, the magnitude estimation results from the τ_c method and P_d method exhibit considerable scatter. The standard deviations of the magnitude estimation error are 1.56, 0.42, and 0.31 for the τ_c method, P_d method, and DCNN-M model, respectively. There is obvious magnitude overestimation ($M_{JMA} \leq 5$) from the τ_c method and P_d method, but this issue is improved considerably in the DCNN-M model results. The magnitudes predicted by the DCNN-M model are closer to the vs. than those from the τ_c method and P_d method.

Furthermore, the variation in the magnitude estimation error with the epicentral distance is presented in **Figure 5** for the τ_c method (**Figure 5D**), P_d method (**Figure 5E**), and DCNN-M model (**Figure 5F**). It can be observed from the distribution of circles that the τ_c method and P_d method exhibit larger errors than the DCNN-M model. In addition, the magnitude estimation errors from the τ_c method and P_d method have larger discreteness (black bars) than those from the DCNN-M model, and the means (red squares) of the magnitude estimation errors from the τ_c method and P_d method clearly vary with increasing epicentral distance. This phenomenon is especially true for the τ_c method. The mean (red square) of the DCNN-M model magnitude estimation errors is nearly zero, and the DCNN-M model magnitude estimation errors are not affected by the epicentral distance.

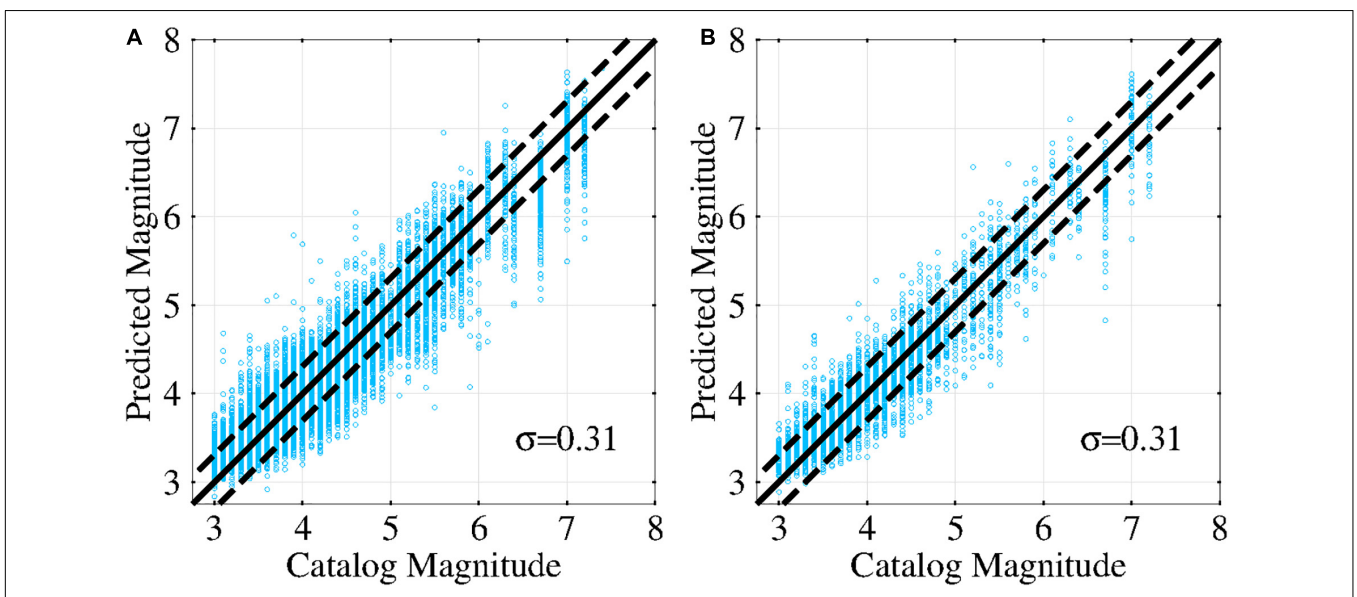

FIGURE 4 | Correlations between the predicted and catalog magnitudes. **(A)** Magnitude estimation for the training dataset used to train the DCNN-M model. **(B)** The magnitude estimation of the test dataset used to test the DCNN-M model performance. When a data point is on the solid black 45° line, the predicted magnitude is equal to the catalog magnitude. The two black dashed lines indicate the range of one standard deviation of error.

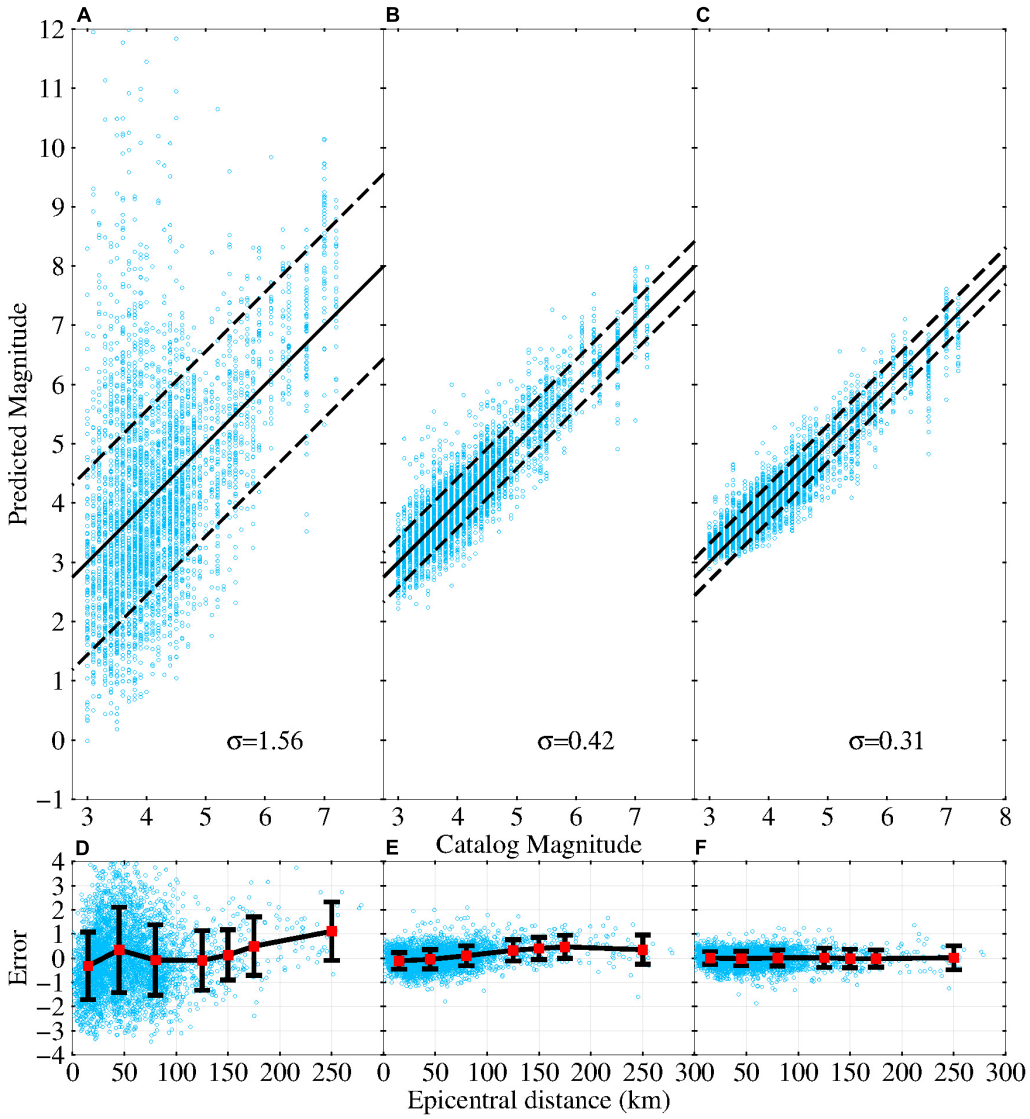

FIGURE 5 | Catalog magnitudes versus predicted magnitudes produced using the test dataset by **(A)** the τ_c method, **(B)** the P_d method, and **(C)** the DCNN-M model. On the solid black 45° line, the predicted magnitude is equal to the catalog magnitude. The two black dashed lines indicate the locations of one standard deviation of error. The relationship between the epicentral distance and the error in the predicted magnitude for **(D)** the τ_c method, **(E)** the P_d method, and **(F)** the DCNN-M model. The epicentral distance is divided into seven sections: (0 km, 30 km), (30 km, 60 km), (60 km, 100 km), (100 km, 150 km), (125 km, 175 km), (150 km, 200 km), and (200 km, 200+ km). The position of the solid red square represents the mean of the errors within an epicentral distance. The length of the black bar shows the standard deviation of the magnitude estimation errors within an epicentral distance, which reflects the discreteness of the errors.

For a given test dataset, **Table 1** compares the distribution of the magnitude estimation absolute errors for the τ_c method, P_d method, and DCNN-M model. As shown in **Table 1**, the absolute magnitude estimation errors of the DCNN-M model are concentrated mainly in the range of 0.6 magnitude units of approximately 2σ, and the results for the DCNN-M model are nearly 60 and 10% greater than those of the τ_c method and P_d method, respectively, in the range of 0.6 magnitude units. Moreover, for the absolute magnitude estimation errors greater than 1.2 magnitude units, the percentage of DCNN-M model results is nearly zero and is much less than those from the τ_c method and P_d method. These analyses also indicate that the DCNN-M model is more accurate than the τ_c method and P_d method and has considerable EEW application potential.

OFFLINE APPLICATION OF THE DCNN-M MODEL

To test the robustness of the DCNN-M model in analyzing new earthquake events, we tested the magnitude prediction of 31 additional events. These events were not included in the training and test datasets. These events (see **Supplementary Table 2**) occurred mainly between April 2018 and December 2019. Due

TABLE 1 | The distribution of the magnitude estimation errors for the τ_c method, P_d method, and DCNN-M model.

Absolute error range	Percentage of records		
	τ_c method (%)	P_d method (%)	DCNN-M model (%)
$0 \leq \lvert \text{error} \rvert \leq 0.6$	34.13	86.71	94.78
$0.6 < \lvert \text{error} \rvert \leq 1.2$	27.82	12.30	4.98
$1.2 < \lvert \text{error} \rvert$	38.05	0.99	0.24

to the small number of large earthquakes with $M_{JMA} \geq 6$ in this time period, we also selected seven earthquakes with $M_{JMA} \geq 6$ that occurred before October 2007. The distribution of stations and epicenters for the 31 events and the magnitude prediction for these events are shown in **Figures 6A,B**, respectively. The solid red circle shows the mean estimated magnitude of the DCNN-M model for an earthquake event. The PMs of these events are quite similar to the CMs, and nearly all of the PMs are within the standard deviation (0.31) of the errors for the DCNN-M model. In addition, the standard deviation of the errors for these events is 0.21. Moreover, reliable results without obvious magnitude overestimation and underestimation are obtained for events with $M_{JMA} \leq 7.2$.

DISCUSSION AND CONCLUSION

For the past several decades, EEW magnitudes have been determined by establishing regression functions between a single P-wave parameter and the CMs. The τ_c method and P_d method have been widely used in the study of EEW magnitude estimation (Kanamori, 2005; Wu and Kanamori, 2005; Wu and Zhao, 2006; Zollo et al., 2006; Colombelli et al., 2014). Since a single parameter might provide little magnitude information, we introduce an advanced magnitude prediction model named DCNN-M in this paper. DCNN-M uses a deep convolutional neural network to perform magnitude estimation. We used a training dataset to train the DCNN-M model and 12 parameters extracted from the initial 3 s of the P-wave record as inputs to the DCNN-M model. These parameters are related to the frequency, amplitude, and energy, which make the DCNN-M model interpretable. Additionally, although many of these input parameters might not be independent of each other, they are not completely the same, and more parameters might provide more information about the magnitude. In addition, a test dataset was used to test the DCNN-M model performance. The results were compared to those from the τ_c method and P_d method. As a further test, we used the DCNN-M model to predict 31 additional events.

In this study, we used 1,836 inland earthquakes from the K-NET catalog with magnitudes in the $3 \leq M_{JMA} \leq 7.2$ range and focal depths shallower than 10 km. To use more accurate P-wave arrival information, first, we use the short-term averaging/long-term averaging algorithm (Allen, 1978) to determine the P-wave arrival automatically. Then compared with the P-wave arrival determined manually, the records that have a larger difference between the P-wave arrival determined automatically and the P-wave arrival determined manually are discarded. For the test dataset, DCNN-M magnitude estimation provided smaller errors and no obvious overall magnitude underestimation or overestimation relative to the τ_c method and P_d method. In principle, the DCNN-M model can be extended to earthquakes in other regions. We plan to test it with strong-motion data from China because most earthquakes in China are inland earthquakes

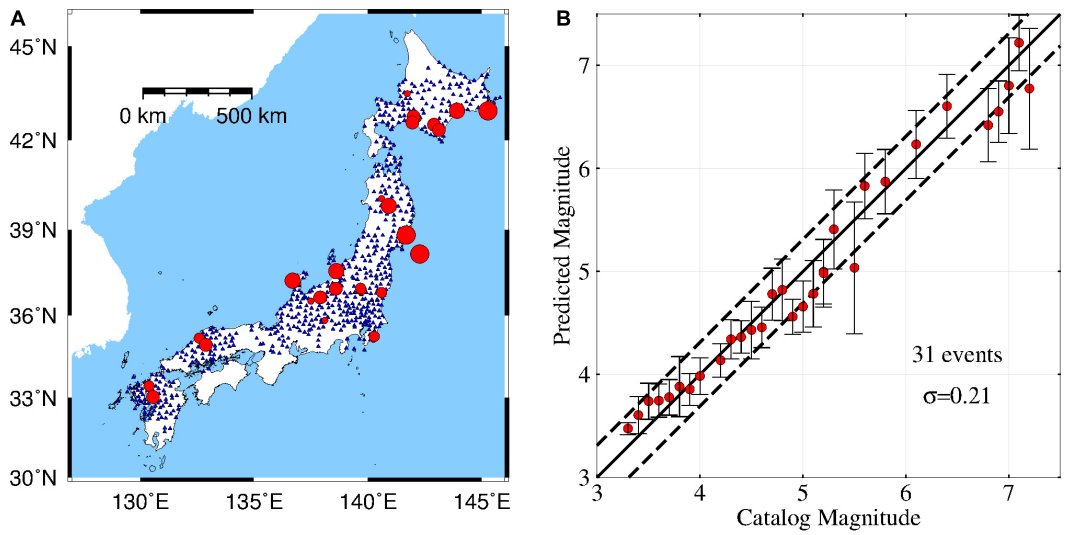

FIGURE 6 | (A) The distribution of the epicenter locations and stations for 31 additional earthquakes. The solid red circles of different sizes represent magnitudes of $3 \leq M_{JMA} \leq 7.2$. The solid blue triangles represent stations that recorded the 31 events. **(B)** Magnitudes determined using the DCNN-M model versus the catalog magnitudes for the 31 additional events. On the solid black 45° line, the predicted magnitude is equal to the catalog magnitude. The two black dashed lines indicate the locations (0.31) of the one standard deviation of errors for the DCNN-M model. The solid red circles show the mean of the estimated magnitudes of the DCNN-M model for the earthquake events. The length of the black bar shows the standard deviation of the magnitude estimation errors for each event.

with focal depths shallower than 10 km (Song et al., 2018). In this study, the problem of the possible underestimation of large earthquakes did not appear in the dataset of earthquakes with magnitudes in the $3 \leq M_{JMA} \leq 7.2$ range. The problem of underestimation of large earthquakes ($M_{JMA} \geq 7.5$) remains to be studied. Extending the training dataset magnitude range or the time window after P-wave arrival may solve problems related to larger ($M_{JMA} \geq 7.5$) earthquakes (Colombelli et al., 2012; Chen et al., 2017).

The DCNN-M model trained using the training dataset could provide ideal test dataset magnitude estimation results. The standard deviations of the magnitude estimation errors of the training and test datasets were both 0.31. This finding indicates that the DCNN-M model provided good generalizability with no overfitting. Our results show that the magnitudes predicted by the DCNN-M model, which provided a standard deviation of 0.31 based on the 3-s time window after P-wave arrival, exhibited better agreement with the CMs than the magnitudes predicted using the τ_c method and P_d method, which provided standard deviations of 1.56 and 0.42, respectively. In addition, the magnitude estimates from the τ_c method provided considerable scatter and overestimation at $M_{JMA} \leq 5$. These phenomena are consistent with the results of Carranza et al. (2015). In contrast, the PMs from the DCNN-M model significantly approximate the CMs. The τ_c parameter is used as an input to the DCNN-M model, but there is no significant overestimation at $M_{JMA} \leq 5$. The reason may be that the DCNN-M model training reduces the influence of τ_c on the model magnitude, and the correlation between the frequency content of the τ_c parameter and magnitude is learned. The magnitude estimates from the DCNN-M model were not affected by the epicentral distance, unlike those of the τ_c method and P_d method. For the same test dataset, the absolute magnitude estimation errors of the DCNN-M model are mainly concentrated in the range of 0.6 magnitude units at approximately 2σ, and the percentage of the magnitude estimation error is 94.78% greater than those of the τ_c method and P_d method. This finding means that the DCNN-M model has better magnitude determination performance than the τ_c method and P_d method, and the probability that the magnitude estimation error is in the range of 0.6 magnitude units is 94.78%. Furthermore, we obtained reliable magnitude estimates without obvious magnitude overestimation and underestimation for 31 additional events using the DCNN-M model. These results indicate that the DCNN-M model has considerable EEW magnitude estimation application potential in Japan.

In Japan, magnitude is measured with the magnitude scale M_{JMA}; hence, the magnitude scale M_{JMA} is used as the target predicted by the DCNN-M model for the area of Japan in this paper. For different magnitude scales and user requirement, we could use the conversion relationship between different magnitude scales or use a different magnitude scale (likely M_w) as the target predicted by the DCNN-M model. Different magnitude scales might influence our results. We mainly propose a new magnitude model (DCNN-M) for magnitude determination in this paper for EEW. In the next step we will deeply study the influence of different magnitude scales on the DCNN-M model.

Importantly in this study, we corrected the parameters related to amplitude, energy and derivative parameters for the distance effect by normalizing them to a reference distance of 10 km (Zollo et al., 2006). In our application, based on real-time earthquake locations provided by an EEWS, the magnitude estimation of the DCNN-M model is determined. The method used to determine real-time earthquake locations is similar to that of Zollo et al. (2010), which was developed by Satriano et al. (2008). Moreover, it also provides the possibility to detect earthquake locations based on the deep learning method (Perol et al., 2018; Zhang et al., 2019, 2020) and has potential for future application in EEW.

However, the DCNN-M model hyperparameters, the size of the training dataset and the input parameters are also important in magnitude estimation. The hyperparameters include the number of layers, number of filters, dropout rate, optimizer, learning rate, batch size, and stride. In this paper, we tried several times to debug each hyperparameter of the DCNN-M model manually to identify those hyperparameters that might not be optimal. However, the comparison of the DCNN-M model magnitude estimates with those produced via the τ_c method and P_d method indicated that the DCNN-M model has considerable potential for EEW applications and provides robust magnitude estimation. In this study, we use 12 parameters extracted from the initial 3 s of the P-wave record as inputs to the DCNN-M model, and we may find that more parameters with magnitude information could be used as the input of the DCNN-M model in the future. To improve the performance of the DCNN-M model with regard to the magnitude estimation accuracy, the DCNN-M model hyperparameters and the input parameters need to be optimized, and the amount of strong-motion data still needs to be expanded (Perol et al., 2018). The DCNN-M model will be more effective at avoiding false EEW alarms than the τ_c method and P_d method.

DATA AVAILABILITY STATEMENT

The original contributions presented in the study are included in the article/**Supplementary Material**, further inquiries can be directed to the corresponding author.

AUTHOR CONTRIBUTIONS

JZ implemented and applied the method and wrote the related text. JS contributed to designing the methodology and revised the manuscript. SL and YW provided important suggestions for the interpretation of the results. All authors contributed to the redaction and final revision of the manuscript.

FUNDING

This research was financially supported by the National Key Research and Development Program of China (2018YFC1504003) and its provincial funding, the National

Natural Science Foundation of China (51408564 and U1534202), and the Scientific Research Fund of Institute of Engineering Mechanics, China Earthquake Administration (2016A03).

ACKNOWLEDGMENTS

We thank the National Research Institute for Earth Science and Disaster Prevention (NIED), Japan, for providing the K-NET station strong-motion data. We are also grateful for the GMT software used by Wessel and Smith (1988).

SUPPLEMENTARY MATERIAL

The Supplementary Material for this article can be found online at: https://www.frontiersin.org/articles/10.3389/feart.2021.653226/full#supplementary-material

REFERENCES

Allen, R. M., Brown, H., Hellweg, M., Khainovski, O., Lombard, P., and Neuhauser, D. (2009a). Real–time earthquake detection and hazard assessment by ElarmS across California. *Geophys. Res. Lett* 36:L00B08. doi: 10.1029/2008gl036766

Allen, R. M., Gasparini, P., Kamigaichi, O., and Böse, M. (2009b). The status of earthquake early warning around the world: an introductory overview. *Seismol. Res. Lett.* 80, 682–693. doi: 10.1785/gssrl.80.5.682

Allen, R. M., and Kanamori, H. (2003). The potential for earthquake early warning in Southern California. *Science* 300, 786–789. doi: 10.1126/science.1080912

Allen, R. V. (1978). Automatic earthquake recognition and timing from single traces. *Bull. Seismol. Soc. Am.* 68, 1521–1532. doi: 10.1007/BF02247958

Aoi, S., Kunugi, T., Nakamura, H., and Fujiwara, H. (2011). *Deployment of New Strong Motion Seismographs of K–NET and KiK–net*. Berlin: Springer Netherlands Press.

Aranda, J. M. E., Jiménez, A., Ibarrola, G., Alcantar, F., Aguilar, A., Inostroza, M., et al. (1995). Mexico city seismic alert system. *Seismol. Res. Lett.* 66, 42–53. doi: 10.1785/gssrl.66.6.42

Böse, M. (2006). *Earthquake Early Warning for Istanbul Using Artificial Neural Networks* [Ph.D. thesis]. Karlsruhe: University of Karlsruhe.

Carranza, M., Buforn, E., and Zollo, A. (2015). Testing the earthquake early–warning parameter correlations in the Southern Iberian Peninsula. *Pure Appl. Geophys.* 172, 2435–2448. doi: 10.1007/s00024-015-1061-6

Chen, D. Y., Hsiao, N. C., and Wu, Y. M. (2015). The earthworm based earthquake alarm reporting system in Taiwan. *Bull. Seismol. Soc. Am.* 105, 568–579. doi: 10.1785/0120140147

Chen, D. Y., Wu, Y. M., and Chin, T. L. (2017). An empirical evolutionary magnitude estimation for early warning of earthquakes. *J. Asian. Earth Sci.* 135, 190–197. doi: 10.1016/j.jseaes.2016.12.028

Colombelli, S., Carotenuto, F., Elia, L., and Zollo, A. (2020). Design and implementation of a mobile device app for network–based earthquake early warning systems (EEWSs): application to the PRESTo EEWS in southern Italy. *Nat. Hazards Earth Syst. Sci.* 20, 921–931. doi: 10.5194/nhess-20-921-2020

Colombelli, S., Zollo, A., Festa, G., and Kanamori, H. (2012). Early magnitude and potential damage zone estimates for the great Mw 9 Tohoku–Oki earthquake. *Geophys. Res. Lett.* 39:L22306. doi: 10.1029/2012gl053923

Colombelli, S., Zollo, A., Festa, G., and Picozzi, M. (2014). Evidence for a difference in rupture initiation between small and large earthquakes. *Nat. Comm.* 5:3958. doi: 10.1038/ncomms4958

Festa, G., Zollo, A., and Lancieri, M. (2008). Earthquake magnitude estimation from early radiated energy. *Geophys. Res. Lett.* 35:L22307. doi: 10.1029/2008gl035576

Heidari, R., Shomali, Z. H., and Ghayamghamian, M. R. (2012). Magnitude–scaling relations using period parameters τc and τpmax, for Tehran region. *Iran. Geophys. J. Int.* 192, 275–284. doi: 10.1093/gji/ggs012

Hoshiba, M., Kamigaichi, O., Saito, M., Tsukada, S., and Hamada, N. (2008). Earthquake early warning starts nationwide in Japan. *Eos. Trans. Am. Geophys. Union* 89, 73–74. doi: 10.1029/2008EO080001

Huang, P. L., Lin, T. L., and Wu, Y. M. (2015). Application of τc*Pd in earthquake early warning. *Geophys. Res. Lett.* 42, 1403–1410. doi: 10.1002/2014gl063020

Ioffe, S., and Szegedy, C. (2015). *Batch normalization: Accelerating Deep Network Training by Reducing Internal Covariate Shift* arXiv [Preprint]. Available online at http://arxiv.org/abs/1502.03167 (accessed September 2020).

Jozinović, D., Lomax, A., Štajduhar, I., and Michelini, A. (2020). Rapid prediction of earthquake ground shaking intensity using raw waveform data and a convolutional neural network. *Geophys. J. Int.* 222, 1379–1389. doi: 10.1093/gji/ggaa233

Kanamori, H. (2005). Real–time seismology and earthquake damage mitigation. *Annu. Rev. Earth Planet Sci.* 33, 195–214. doi: 10.1146/annurev.earth.33.092203.122626

Keskar, N. S., Mudigere, D., Nocedal, J., Smelyanskiy, M., and Tang, P. T. P. (2016). *On Large–Batch Training for Deep Learning: Generalization Gap and Sharp Minima* arXiv [Preprint]. Available online at: http://arxiv.org/abs/1609.04836 (accessed September 2020).

Kingma, D. P., and Ba, J. (2014). *Adam: A Method for Stochastic Optimization* arXiv [Preprint]. available online at: http://arxiv.org/abs/1412.6980 (accessed November 2020).

Lin, T. L., Wu, Y. M., and Chen, D. Y. (2011). Magnitude estimation using initial P–wave amplitude and its spatial distribution in earthquake early warning in Taiwan. *Geophys. Res. Lett.* 38:L09303. doi: 10.1029/2011gl047461

Ma, Q. (2008). *Study and Application on Earthquake Early Warning* [Ph.D. thesis]. Harbin: Institute of engineering mechanics.

Nair, V., and Hinton, G. E. (2010). "Rectified linear units improve restricted boltzmann machines," in *Proceedings of the 27th International Conference on International Conference on Machine Learning (ICML-10)* (Haifa: Omnipress).

Nakamura, Y. (2003). "A new concept for the earthquake vulnerability estimation and its application to the early warning system," in *Early Warning Systems for Natural Disaster Reduction*, eds J. Zschau and A. Küppers (Berlin: Springer-Verlag).

Ochoa, L. H., Niño, L. F., and Vargas, C. A. (2017). Fast magnitude determination using a single seismological station record implementing machine learning techniques. *Geod. Geodyn.* 9, 34–41. doi: 10.1016/j.geog.2017.03.010

Olson, E. L., and Allen, R. M. (2005). The deterministic nature of earthquake rupture. *Nature* 438, 212–215. doi: 10.1038/nature04214

Perol, T., Gharbi, M., and Denolle, M. (2018). Convolutional neural network for earthquake detection and location. *Sci. Adv.* 4, 1–8. doi: 10.1126/sciadv.1700578

Reddy, R., and Nair, R. R. (2013). The efficacy of support vector machines (SVM) in robust determination of earthquake early warning magnitudes in central Japan. *J. Earth Syst. Sci.* 122, 1423–1434. doi: 10.1007/s12040-013-0346-3

Reed, J. W., and Kassawara, R. P. (1988). A criterion for determining exceedance of the operating basis earthquake. *Nucl. Eng. Des.* 123, 387–396. doi: 10.1016/0029-5493(90)90259-z

Satriano, C., Lomax, A., and Zollo, A. (2008). Real-time evolutionary earthquake location for seismic early warning. *Bull. seism. Soc. Am.* 98, 1482–1494. doi: 10.1785/0120060159

Song, J. D., Jiao, C. C., Li, S. Y., and Hou, B. R. (2018). Prediction method of first–level earthquake warning for high speed railway based on two–parameter threshold of seismic P–wave. *China Railw. Sci.* 39, 138–144. (in Chinese),

Srivastava, N., Hinton, G., Krizhevsky, A., Sutskever, I., and Salakhutdinov, R. (2014). Dropout: a simple way to prevent neural networks from overfitting. *J. Mach. Learn. Res.* 15, 1929–1958.

Tezcan, J., and Cheng, Q. (2012). Support vector regression for estimating earthquake response spectra. *B Earthq. Eng.* 10, 1205–1219. doi: 10.1007/s10518-012-9350-2

Tsang, L. L. H., Allen, R. M., and Wurman, G. (2007). Magnitude scaling relations from P–waves in southern California. *Geophys. Res. Lett.* 34:L19304. doi: 10.1029/2007gl031077

Wu, Y. M., and Kanamori, H. (2005). Rapid assessment of damage potential of earthquakes in Taiwan from the beginning of P waves. *Bull. Seismol. Soc. Am.* 95, 1181–1185. doi: 10.1785/0120040193

Wu, Y. M., and Kanamori, H. (2008). Development of an earthquake early warning system using real–time strong motion signals. *Sensors Basel* 8, 1–9. doi: 10.3390/s8010001

Wu, Y. M., and Teng, T. L. (2002). A virtual subnetwork approach to earthquake early warning. *Bull. Seismol. Soc. Am.* 92, 2008–2018. doi: 10.1785/0120010217

Wu, Y. M., and Zhao, L. (2006). Magnitude estimation using the first three seconds P–wave amplitude in earthquake early warning. *Geophys. Res. Lett.* 33:L16312. doi: 10.1029/2006gl026871

Yamada, M., and Mori, J. (2009). Using τc to estimate magnitude for earthquake early warning and effects of near–field terms. *J. Geophys. Res.* 114:B05301. doi: 10.1029/2008jb006080

Zhang, M., Ellsworth, W. L., and Beroza, G. C. (2019). Rapid earthquake association and location. *Seismol. Res. Lett.* 90, 2276–2284. doi: 10.1785/0220190052

Zhang, X., Zhang, J., Yuan, C., Liu, S., Chen, Z., and Li, W. (2020). Locating induced earthquakes with a network of seismic stations in Oklahoma via a deep learning method. *Sci. Rep.* 10:1941. doi: 10.1038/s41598-020-58908-5

Zollo, A., Iannaccone, G., Lancieri, M., Cantore, L., Convertito, V., Emolo, A., et al. (2009). Earthquake early warning system in southern Italy: Methodologies and performance evaluation. *Geophys. Res. Lett.* 36:L00B07. doi: 10.1029/2008GL036689

Zollo, A., Lancieri, M., and Nielsen, S. (2006). Earthquake magnitude estimation from peak amplitudes of very early seismic signals on strong motion records. *Geophys. Res. Lett.* 33:L23312. doi: 10.1029/2006gl027795

Zollo, A., Ortensia, A., Maria, L., Wu, Y. M., and Kanamori, H. (2010). A threshold-based earthquake early warning using dense accelerometer networks. *Geophys J Int* 183, 963–974. doi: 10.1111/j.1365-246X.2010.04765.x

Conflict of Interest: The authors declare that the research was conducted in the absence of any commercial or financial relationships that could be construed as a potential conflict of interest.

frontiers in Earth Science

ORIGINAL RESEARCH
published: 02 June 2021
doi: 10.3389/feart.2021.620467

A Framework for Evaluating Earthquake Early Warning for an Infrastructure Network: An Idealized Case Study of a Northern California Rail System

Sarah E. Minson[1]*, *Elizabeth S. Cochran*[2], *Stephen Wu*[3,4] and *Shunta Noda*[5]

[1]United States Geological Survey, Earthquake Science Center, Moffett Field, CA, United States, [2]United States Geological Survey, Earthquake Science Center, Pasadena, CA, United States, [3]The Institute of Statistical Mathematics, Research Organization of Information and Systems, Tachikawa, Tokyo, Japan, [4]The Graduate University for Advanced Studies, Tachikawa, Japan, [5]Center for Railway Earthquake Engineering Research, Railway Technical Research Institute, Kokubunji, Japan

Earthquake early warning (EEW) systems provide a few to tens of seconds of warning before shaking hits a site. Despite the recent rapid developments of EEW systems around the world, the optimal alert response strategy and the practical benefit of using EEW are still open-ended questions, especially in areas where EEW systems are new or have not yet been deployed. Here, we use a case study of a rail system in California's San Francisco Bay Area to explore potential uses of EEW for rail systems. Rail systems are of particular interest not only because they are important lifeline infrastructure and a common application for EEW around the world, but also because their geographically broad yet networked infrastructure makes them almost uniquely well suited for utilizing EEW. While the most obvious potential benefit of EEW to the railway is to prevent derailments by stopping trains before the arrival of shaking, the lead time for warnings is usually not long enough to significantly reduce a train's speed. In reality, EEW's greatest impact is preventing derailment by alerting trains to slow down or stop before they encounter damaged track. We perform cost-benefit analyses of different decision-making strategies for several EEW system designs to find an optimal alerting strategy. On-site EEW provides better outcomes than source-parameter-based EEW when warning at a threshold of 120 gal (the level of shaking at which damage might occur) regardless of false alarm tolerance. A source-parameter-based EEW system with a lower alerting threshold (e.g., 40 gal) can reduce the exposure to potentially damaged track compared to an on-site system alerting at 120 gal, but a lower alerting threshold comes at the cost of additional precautionary system stops. The optimal EEW approach for rail systems depends strongly on the ratio of the cost of stopping the system unnecessarily to the potential loss from traversing damaged tracks.

Keywords: earthquake early warning, cost-benefit analysis, rail systems, San Francisco Bay area, natural hazards warning

OPEN ACCESS

Edited by:
Huseyin Serdar Kuyuk, Harvard University, United States

Reviewed by:
Matteo Picozzi, University of Naples Federico II, Italy
Masumi Yamada, Kyoto University, Japan

***Correspondence:**
Sarah E. Minson
sminson@usgs.gov

Specialty section:
This article was submitted to Geohazards and Georisks, a section of the journal Frontiers in Earth Science

Received: *22 October 2020*
Accepted: *21 May 2021*
Published: *02 June 2021*

Citation:
Minson SE, Cochran ES, Wu S and Noda S (2021) A Framework for Evaluating Earthquake Early Warning for an Infrastructure Network: An Idealized Case Study of a Northern California Rail System. Front. Earth Sci. 9:620467. doi: 10.3389/feart.2021.620467

INTRODUCTION

The original idea for EEW is generally credited to a piece by Dr J. D. Cooper in the November 3, 1868, San Francisco Daily Evening Bulletin (Nakamura, 1996; Saita and Nakamura, 2003). The idea as first proposed was to send an electrical signal from a network of earthquake sensors to trigger an alarm in the city. The first practical implementation of an EEW system began nearly a hundred years later, in 1965, when a M6.1 earthquake led what is now the Japan Railways Group (JR) to install seismometers every 20–25 km along the Shinkansen bullet train tracks to issue an alert to slow trains if horizontal accelerations exceeding 40 gal were observed (Saita and Nakamura, 2003). In 1984, this EEW system was supplemented by JR's Coastline Detection System based on seismometers placed along the coast to detect offshore earthquakes. A P-wave scaling relationship was then used to estimate source magnitude and thus decide whether a warning should be issued to the inland Shinkansen system. The Coastline Detection System was later upgraded and replaced with the Urgent Earthquake Detection and Alarm System (UrEDAS) (Saita and Nakamura, 2003). In 2004, JR replaced the UrEDAS with another new EEW system that also estimates source parameters, while continuing its ground-motion-based system of stopping trains if acceleration, bandpass filtered between 0.5 and 5 Hz, exceeds a given threshold (Yamamoto and Tomori, 2013).

In the past three decades, EEW systems designed to notify the general public have been developed all around the world. Some, such as Mexico's Seismic Alert System (SAS) that began operating August 1991 (Aranda et al., 1995), used similar approaches to JR's coastline system with near-coast seismometers detecting offshore earthquakes and transmitting warnings to inland population centers. Other systems, such as the Japan Meteorological Agency (JMA) EEW system for Japan (Hoshiba et al., 2008; Doi, 2011), the Central Weather Bureau (CWB) system for Taiwan (Hsiao et al., 2009), and the United States' ShakeAlert system, which provides warning to the States of California, Oregon, and Washington, take a fundamentally different approach: they all use a network of stations (both onshore and offshore) to detect earthquakes within, and provide warning to, a broad region. In contrast, the JR and original SAS systems were designed only to protect a localized area. Despite this fundamental difference with the JR and original SAS systems, these regional EEW systems typically use methods similar to UrEDAS: seismic data are used to infer the source parameters of the earthquake (i.e., location and magnitude), and this information is then input to a ground motion prediction equation (GMPE) in order to forecast whether the expected shaking will exceed some critical threshold for triggering a warning.

In recent years, different EEW approaches have proliferated, such as algorithms that utilize geodetic data (Murray et al., 2018) or store seismogram filter banks (Meier et al., 2015). JMA has updated their source parameter algorithm using the Integrated Particle Filter (IPF) method and complemented that approach with the ground-motion-based Propagation of Local Undamped Motion (PLUM) method. The IPF method uses a particle filter technique to combine, in a Bayesian estimation framework, ground motion observations and information about where shaking has not been observed (Tamaribuchi et al., 2014). The PLUM method is noteworthy for using ground motion to directly forecast ground motion without first estimating earthquake source parameters (Kodera et al., 2018). But with a few exceptions such as the PLUM method, EEW systems are still largely divided into two camps: source-parameter-based methods (which infer earthquake location and magnitude, and then input that information into a GMPE to identify which regions should be alerted) and on-site methods (which trigger alerts to specific assets when strategically placed seismometers observe shaking above some critical threshold). The ShakeAlert and UrEDAS systems are typical examples of the former, whereas the original JR EEW system exemplifies the latter.

Despite the rapid advancement of EEW in recent years, studies on effective applications of EEW are few, often focusing on creating a cost-benefit analysis framework for rapid decision-making under uncertain EEW information (Iervolino, 2011; Wu et al., 2013). Those studies that have been done on specific EEW engineering applications have tended to explore rather simple scenarios, such as elevator control (Wu et al., 2016), although Cauzzi et al., 2016 focused on the complexities of utilizing EEW for nuclear power plants. Even fewer are the studies that look at specific EEW engineering examples for complex systems and attempt to optimize the EEW system's performance for that application, with Veneziano and Papadimitriou (2003) being a notable exception. In that study, the authors compared different approaches for determining which sections of the Shinkansen rail system the JR early warning system should close for inspection while minimizing both the total system delay and expected number of derailments.

One of the major challenges of studying EEW applications comes from the complexity of the uncertainty of the EEW system itself interacting with the uncertainty of human decision-makers, especially because EEW-related decisions often involve the potential for human casualties. Another major challenge comes from the physical limitations of EEW. For example, the on-site approach has obvious limitations on the amount of warning it can provide because an alert cannot be issued until shaking is already impinging somewhere along the rail system. On the other hand, previous studies have demonstrated the difficulty in providing timely source-parameter-based EEW especially for the very strong levels of shaking that pose a hazard to heavy infrastructure (e.g., Meier, 2017; Minson et al., 2018; Trugman et al., 2019).

While understanding the role of EEW in a real application is extremely difficult, knowing the true value of EEW and finding an optimal EEW-based emergency response strategy for mitigating seismic risk is essential. In this study, we considered a rail system based on the Northern California Bay Area Rapid Transit (BART) system as an example of a special type of infrastructure network where it is critical not just to forecast shaking at the user's (i.e., train's) current location but also at distant parts of the track that the train will later encounter in its route. This presents an almost unique opportunity for EEW since long warning times are possible when an earthquake damages track far from any

train's current location. However, this usefulness is tempered by the fact that trains require a significant amount of time, and thus track length, to stop. By going through an end-to-end case study (from event catalog to cost-benefit analysis of the decision to stop trains), we examine the performance of several different EEW alerting strategies for a rail network located in California. Furthermore, our approach demonstrates a general framework to design decision-making strategies for large-scale EEW applications.

While our goal is to present a framework that can be employed by the relevant decision-makers to guide EEW application to rail systems, it would not be appropriate here to make specific recommendations for rail system operations. Rather than focusing on a specific application, we instead present an example of our framework in which we evaluate the utility of different EEW system designs assuming the theoretical performance of an ideal system with zero noise, data latency, or computational delays, thus quantifying the maximum possible risk reduction from EEW. In so doing, we quantify the maximum theoretical potential benefit of EEW for rail systems, that is, the amount of risk reduction that can be accomplished with EEW given physical limitations such as the closeness between the faults and the track system, and the relative speeds of seismic waves and trains.

EXAMPLE EARTHQUAKE EARLY WARNING SCENARIO

Distributed infrastructure networks such as rail systems can utilize EEW uniquely well because there is value to be had from protecting the network as a whole even if timely warning is not possible in the near field where shaking is strongest. An example cartoon of EEW applied to a rail system is shown in **Figure 1**. Useful EEW for a train directly threatened by the earthquake is actually quite difficult because it takes significant time to bring a train to a complete stop (In the examples that follow, a commuter train in the United States takes ~17 s to stop while a Shinkansen bullet train can take more than a minute (Arai et al., 2008).) Thus, it would be nearly impossible to halt a train before shaking arrives at its location, especially for trains in the near field of the rupture where shaking is strongest. However, the goal of using EEW to slow and stop trains is generally not to prevent the train from being directly derailed by ground shaking; in fact, being stopped does not necessarily prevent a train from being toppled (e.g., Veeraraghavan et al., 2019). Instead, the goal is to slow or stop the train before it encounters damaged track that might itself trigger a derailment (Veneziano and Papadimitriou, 2003). This means that, except in the unfortunate case where the train's current location is hit with damaging ground shaking, the train has additional time to stop or take other protective action before it encounters damaged track.

OVERVIEW OF THE RAIL SYSTEM CASE STUDY

For this study, we use the track geometry of the BART system, the light rail serving California's San Francisco Bay Area (**Figure 2**). To assess seismic hazard, we use a 1,000-year-duration catalog of earthquake rupture scenarios generated from the earthquake probabilities of the Third Uniform California Earthquake Rupture Forecast with spatiotemporal clustering (UCERF3-ETAS) (Field et al., 2017) (**Figure 2A**). For each scenario rupture, we calculate the expected horizontal peak ground acceleration (PGA) at all track locations using the Chiou and Youngs (2014) GMPE with the Vs_{30} model of Allen and Wald (2009) (**Figure 2B**). Our analysis is done on the rail system as a whole: when potentially damaging shaking is expected at any location along the tracks, all trains are signaled to start braking and potentially halted to allow track inspection. We assume that an alert is issued when the expected shaking exceeds a low level of non-damaging shaking (40 gal) with the goal of slowing or stopping trains before they encounter potentially damaged track (**Figure 2C**) (40 gal is ~4% g, equivalent to Modified Mercalli Intensity, MMI, IV-V.) We further assume that track damage occurs at accelerations greater than 120 gal (~12% g, equivalent to about MMI VI) (**Figure 2D**). These shaking levels (including the use of units of gal) are taken directly from the original design of the JR EEW system for Japan's Shinkansen bullet train. In the original system, trains were halted when seismometers detected shaking along the tracks that exceeded 40 gal (Nakamura and Tucker, 1988; Nakamura and Saita, 2007). Shaking corresponding to 40 gal, or MMI ~ IV, is also a good comparison point for EEW performance in California; when ShakeAlert went live in December 2018, the initial public alerting threshold was set to MMI IV, although that level has since been lowered (Cochran and Husker, 2019). A study of Japan earthquakes that caused track damage found that damage was concentrated at shaking levels exceeding 120 gal (Nakamura, 1996), which is also the level used for triggering stops based on shaking at coastal seismometers (Ogura, 2006; Japan Transport Safety Board, 2013; Strauss and Allen, 2016). More recently, 120 gal has been adopted as a general shaking threshold for safe operation of high-speed rail (Hu et al., 2014).

If those criteria were applied to BART track locations using UCERF3-ETAS seismic hazard probabilities, we would expect the rail system to be alerted to PGA>40 gal shaking approximately once per year (**Figure 2C**), but most of those system alerts would be precautionary. No individual site is expected to be impacted by damaging shaking (PGA>120 gal) more than once per decade (**Figure 2D**), but damage anywhere could impact system operations everywhere. The rate of earthquakes with hazardous expected ground motions impinging anywhere on the track system is ~2/decade. These numbers are average shaking rates based on median ground motions, neglecting hazard from small magnitude earthquakes with anomalously strong shaking and temporal clustering of earthquakes. Earthquakes are often clustered in time with, for example, periods of little to no seismicity separating productive mainshock-aftershock sequences. In our 1,000-year chronology, location 13 (city of Fremont) goes as long as 126 years between earthquakes that are expected to produce potentially damaging shaking (PGA>120 gal), but also experiences 12 such events within a one-year period.

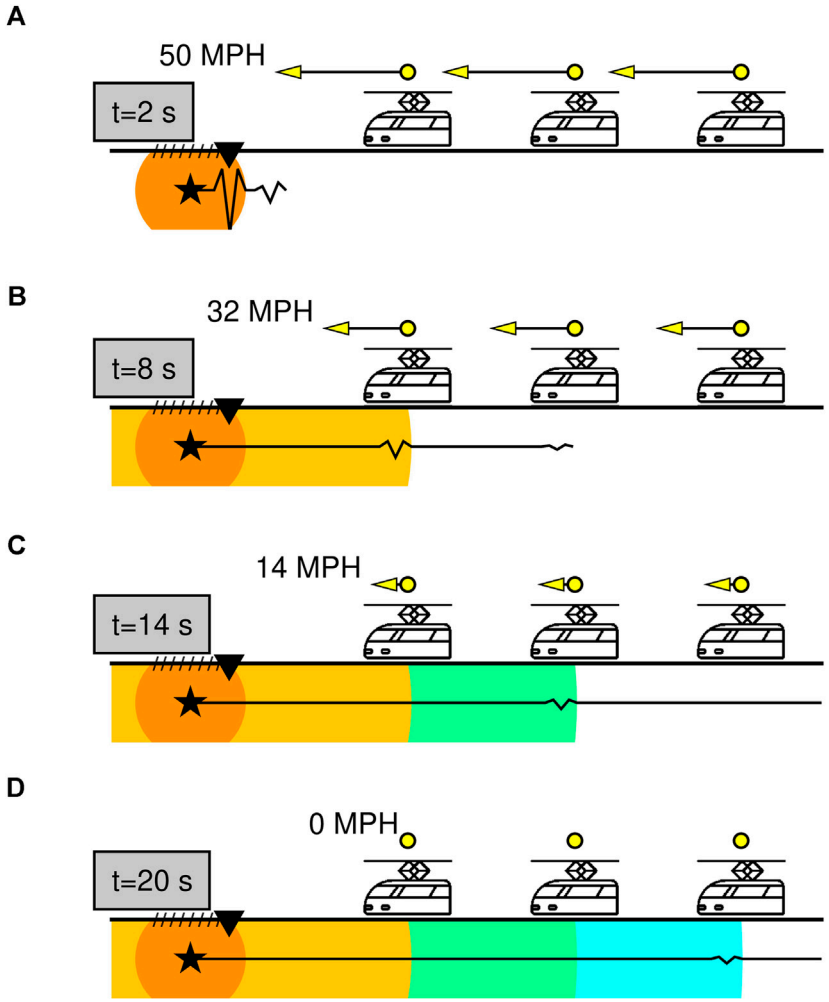

FIGURE 1 | Cartoon example of EEW for a rail system. **(A)** An earthquake nucleates (star) and when shaking reaches a seismometer (black inverted triangle), all trains are signaled to start braking. As time increases (**B–D**), decreasing amplitudes of shaking reach the locations of more distant trains, which will have been able to further slow. The trains will still be traveling at 32 MPH when the shaking reaches the closest train **(B)**, they will have slowed to 14 MPH by the time shaking reaches the middle train **(C)**, and the trains will be completely stopped just as shaking reaches the most distant train **(D)**. While all but the most distant train will still be traveling at significant speed when the shaking arrives at their locations, they can all be successfully slowed and stopped before traveling to a region where they might encounter damaged track (denoted by hatches). Black wiggles show move-out of P-wave and S-wave, and how shaking amplitude decays with distance. Seismic wave arrival times and amplitudes are calculated assuming a Poisson medium with S-wave velocity of 3.5 km/s and shear modulus of 30 GPa.

All trains in the rail system will be alerted to slow down (and potentially stop) if an alert is triggered for any track location. 78% of system alerts will be precautionary, that is the peak shaking somewhere along the track is forecast to exceed 40 gal (triggering an alert) but potentially damaging shaking (PGA>120 gal) is not experienced anywhere along the tracks. However, this is calculated for median expected ground motions. In reality, ground motion variability can result in a greater number of smaller magnitude earthquakes producing greater than expected shaking (e.g., Minson et al., 2021) making some of these precautionary alerts, in fact, necessary (Minson et al., 2019).

Shaking hazard is not the same everywhere. Among the 22% of alerts that are necessary for the rail system because potentially damaging (PGA>120 gal) shaking occurred somewhere along the tracks (assuming median expected shaking), some track locations are more likely to be directly threatened by shaking and some are more likely to be alerted to stop for shaking in some other part of the rail system. In **Figure 3**, we plot the breakdown between how often each of 15 sample locations along the tracks will itself be threatened vs. be alerted for potentially damaging shaking elsewhere in the system. Strong shaking is more probable along the southern Hayward Fault and Santa Clara Valley (**Figure 2D**), and thus sites such as location 12 and location 13 (city of Fremont) are more likely to be directly threatened. However, other locations, such as location 2 (southern San Francisco) and location 9 (eastern exurbs) have low shaking hazard because they are farther from high hazard faults. These locations are mostly alerted to stop when some other part of the system is expected to be in danger due to shaking, their local track is less likely to be damaged, and they are more likely to have

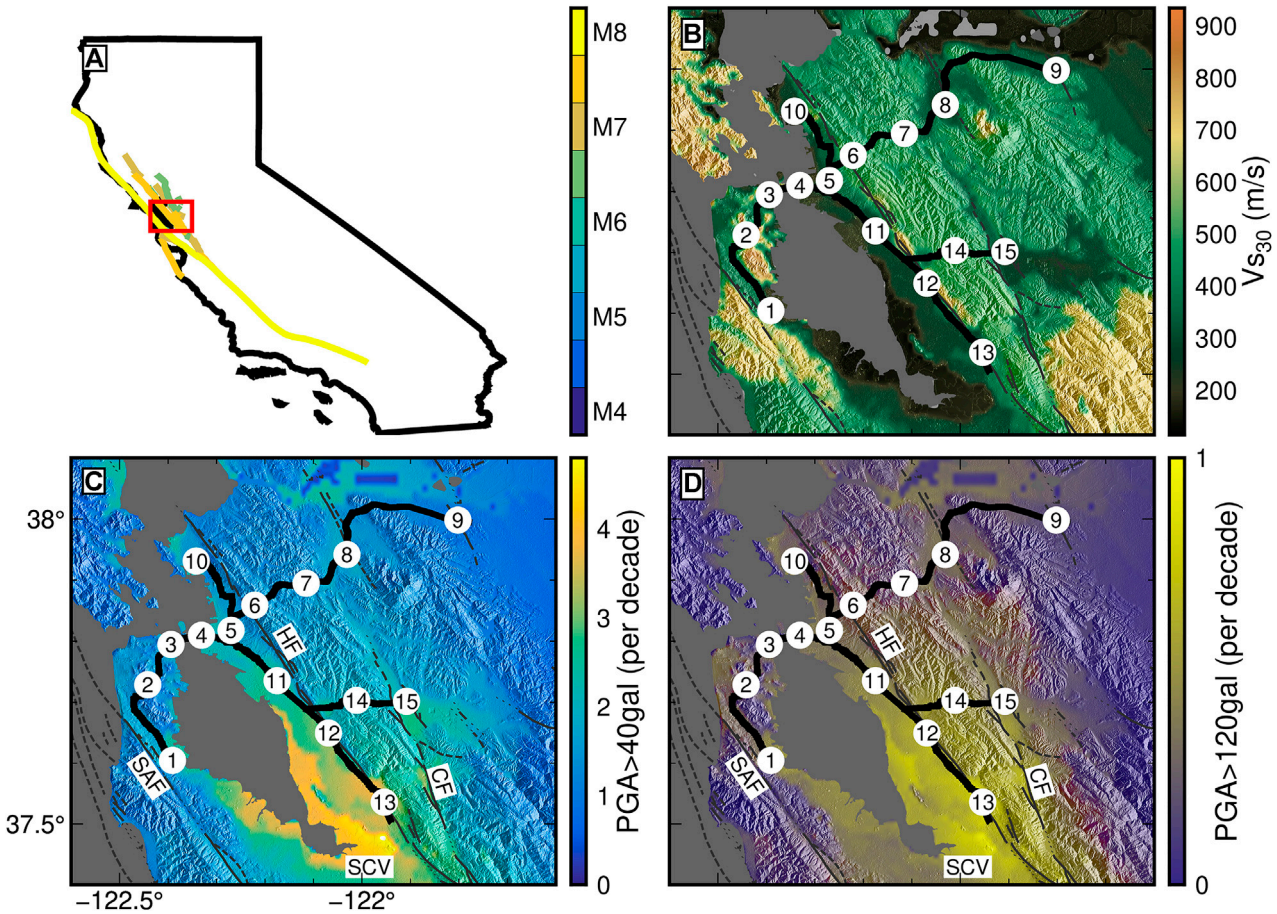

FIGURE 2 | (A) Plot of 1,000 years of ruptures generated with UCERF3-ETAS probabilities. Red box is area shown in plots b-d. **(B)** Vs_{30} from topographic proxy. Black lines show train tracks. Numbers in circles show sample locations along tracks for which detailed results will be shown. **(C)** Frequency of ground motion exceeding 40 gal, i.e., how often alerts to stop trains would be generated. While no location is expected to trigger an alert more than five times per decade, when shaking is expected anywhere, the entire system is alerted. The total number of times the train system would be stopped for this catalog is ~10 times per decade or once per year. **(D)** The frequency of potentially damaging ground motions exceeding 120 gal. Text labels denote San Andreas Fault (SAF), Hayward Fault (HF), Calaveras Fault (CF), and the Santa Clara Valley (SCV).

plenty of time to slow or stop before encountering damaged track elsewhere. For example, of the 22% of alerts where >120 gal is expected somewhere in the track system, location 13 (Fremont), situated near the Hayward Fault in the flatlands of the East Bay, experiences >120 gal in 36% of those events, while location 2 (south San Francisco) experiences >120 gal in just 10% of those events. Again, note that these percentages are calculated for median expected ground motions.

CONVENTIONAL EARTHQUAKE EARLY WARNING VIEW: HOW MUCH WARNING DOES EACH LOCATION RECEIVE?

To date, most EEW analyses focus on how much warning time a particular location receives, defined as the time difference between when a location is alerted until when hazardous shaking arrives at that location (e.g., Meier, 2017; Minson et al., 2018). With trains, the main goal is to give the train enough warning to stop not before the shaking gets to the train's current location, but before the train traverses damaged tracks. For completeness and comparison to existing studies, we first analyze how much warning time a train gets before it experiences shaking. But then, in the next section, we instead explore how the distributed nature of track systems makes them ideal for EEW because there is potentially significant time to take protective action before a train encounters damaged track.

The amount of warning time at any location will be the elapsed time from when the rail system is alerted until shaking arrives at that location. But when is the rail system alerted? The answer depends on the type of EEW system deployed.

In Japan, the first EEW system installed by JR was what might be termed an on-site ground-motion-based EEW system: seismometers were deployed along the tracks and if shaking above 40 gal was detected anywhere, the local tracks were de-energized (Nakamura and Tucker, 1988). More recently, this system has been augmented with a network source-parameter-based EEW system that uses seismic waveforms to estimate the

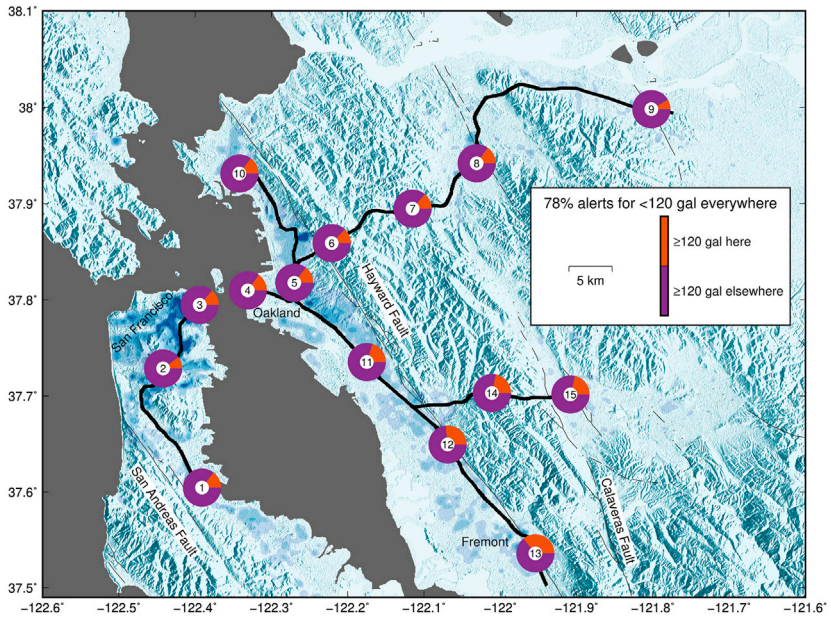

FIGURE 3 | In this example, we consider only median expected ground motions and the system is alerted to stop all trains when 40 gal is observed (for on-site systems) or forecast (for source-parameter-based systems) somewhere on the tracks. Based on the 1,000-year catalog of ruptures, 78% of these alerts will be unnecessary because, although shaking exceeds 40 gal, it does not exceed 120 gal anywhere on the tracks, and thus is not damaging. Of the 22% of cases where stops were required because 120 gal was exceeded somewhere along the tracks, we categorize the alerts into an alert required because >120 gal shaking was recorded at the marked location vs. those required to accommodate stopping the whole system and inspecting for damage because 120 gal was recorded somewhere along the tracks. Shaking of 120 gal is most frequently observed on sites along the southern Hayward Fault (e.g., locations 12 and 13). Locations far from high rupture probability faults (e.g., location 9) most frequently stop due not to local strong shaking but instead strong shaking elsewhere in the train network. Background color shows population density, with darker blues indicating more population.

location and magnitude of an earthquake, inputs that information into a GMPE to forecast shaking, and, if the predicted shaking exceeds the alerting threshold, issues an alert. This latter system design is the same as the ShakeAlert EEW system being operated in California, Oregon, and Washington States (Given et al., 2018).

At each second as the rupture expands, we compute the peak shaking at every point along the tracks to determine when an on-site ground motion system could issue an alert (i.e., when shaking exceeds 40 gal) and when dangerous shaking arrives (i.e., shaking exceeds 120 gal). Because we assume ideal noise-free EEW system performance, one station exceeding 40 gal is sufficient to trigger an alert. Real-world system operators might prefer to use data from multiple seismometers (co-located or not) to confirm an event before issuing an alert, but not necessarily. The original on-site JR system de-energized track and warned controllers when any seismometer exceeded 40 gal (Nakamura and Tucker, 1988).

We also input the current accumulated magnitude and rupture extent at each second of the evolving rupture into a GMPE (Chiou and Youngs, 2014) to forecast shaking at every point along the tracks to determine when a source-parameter-based system could issue an alert. Note that this is an ideal limit to how fast EEW could operate. We have ignored all system latencies including data telemetry, analysis, and alert distribution, and have implicitly assumed an infinitely dense seismic network. We have further assumed that all EEW shaking forecasts are perfect when, in reality, ground motion is highly variable and will cause source-parameter-based EEW to have many missed alerts and some false alerts even if the source parameters of the earthquake rupture are known perfectly (Minson et al., 2019; Saunders et al., 2020).

Several points are worth noting about how ground motion variability affects EEW performance and how we treat shaking variability in this study. While ground motion models (i.e., GMPEs) constrain the variability of shaking at any location due to an earthquake rupture, unfortunately little is known about the spatial covariance of shaking. Thus, for much of the analyses that follow, all ground motions by necessity are fixed to the median expected value predicted by the GMPE. We compute the hazard exposure of the rail system, and potential gains and losses, as long-term expected values so that the specific spatial variation of shaking in any particular earthquake averages out. But two important caveats about our analysis remain. First, we will be missing additional exposure from earthquakes that produce unusually strong shaking for their magnitude. Second, as discussed earlier, because ground motion varies from median expected values, real source-parameter-based EEW shaking forecasts will be uncertain, leading to missed and false alerts when shaking turns out be stronger or weaker than expected, respectively. On-site ground-motion-based EEW systems, barring some sort of instrumental malfunction, never produce these types of missed and false alerts because they are triggering warnings based on the actual observed shaking. (These missed and false alerts are separate and in addition to unnecessary stops

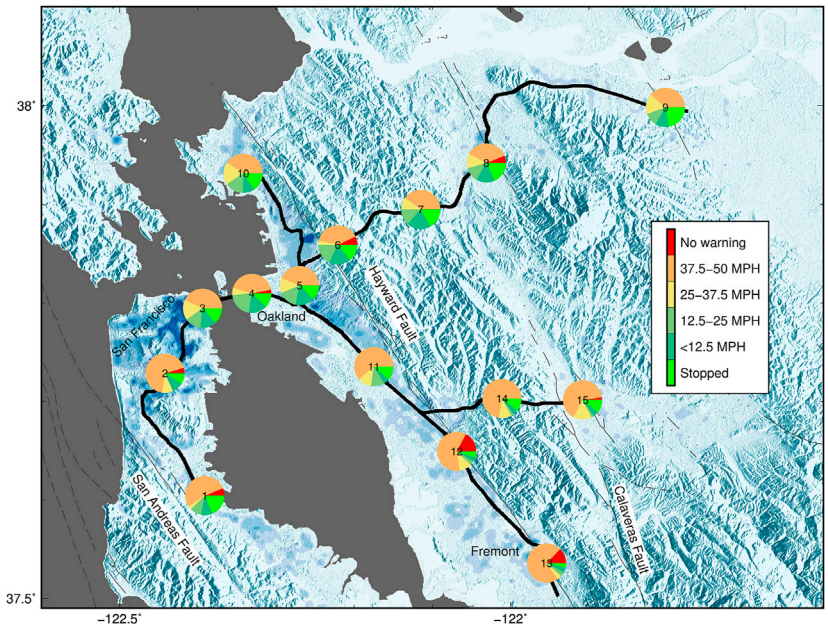

FIGURE 4 | Based on the 1,000-year UCERF3-ETAS rupture catalog, we plot the percentage of earthquakes for which trains traveling at 50 MPH have sufficient warning time to stop, to slow to less than 12.5 MPH, to slow to 12.5–25 MPH, 25–37.5 MPH, 37.5–50 MPH, or have no warning at all. In general, the no warning outcome only occurs for locations very close to major faults, such as locations 12–13 on the southern Hayward Fault. But locations that are far from major faults, e.g., location 3 in downtown San Francisco, always receive at least some warning. However, at every location, warning is usually not sufficient to decrease velocity by even half. Background color shows population density, with darker blues indicating more population. Warning times are calculated for a source-parameter-based EEW system that alerts all trains to stop when 40-gal shaking is forecast anywhere in the track system.

resulting from the alerting threshold being lower than the shaking threshold at which damage is expected, as in our example where we alert at 40 gal but damage is expected at PGA>120 gal.) By ignoring forecasting errors from source-parameter-based EEW systems, our analysis inflates the potential usefulness of source-parameter-based approaches relative to both their real-world performance and the performance of on-site ground-motion-based approaches.

It is worth noting that ground motion variability is not addressed explicitly in most EEW systems. Instead, the most common way that EEW systems incorporate ground motion variability is by setting an alerting threshold that is significantly less than the target level of ground motion for which the user would actually like to take action, thus helping ensure that the user is alerted to take action in cases that an earthquake produces stronger shaking than expected. For example, the original on-site JR EEW system used an alerting threshold of 40 gal even though damage is not expected for shaking that is less than 120 gal (Nakamura and Tucker, 1988; Nakamura, 1996; Nakamura and Saita, 2007; Hu et al., 2014). Another example would be the ShakeAlert EEW system in the United States. When the system went live in December 2018, the alerting threshold was MMI IV for a target level of MMI VI. Since then, the target level has been decreased to felt shaking (MMI IV) and the alerting level has been correspondingly lowered (Cochran and Husker, 2019).

Most trains in the BART system have a maximum speed of 70 MPH and make 20-s stops at each station [http://bart.gov/about/history/facts]. We assume that a train in motion has an average speed of 50 MPH. When braking, BART trains can decrease their speed by 3 MPH every second requiring just under 17 s to come to a complete stop over a distance of 0.1 mi (186 m) (https://www.bart.gov/guide/safety/earthquake).

In **Figures 4**, **5**, we present an example of the performance, in the conventional EEW view, of a source-parameter-based EEW system that alerts when forecast shaking exceeds 40 gal (although damage is not expected unless shaking exceeds 120 gal). (Up to now our analysis has held equally for on-site and source-parameter-based systems.) For each earthquake in the full 1,000-year-duration UCERF3-ETAS catalog, we compute the final velocity to which a train at each of the 15 example locations in **Figure 1** could decelerate before peak shaking arrives. (For simplicity, we assume that peak shaking is carried by the direct S-wave.) These example locations were chosen to explore the variety of experiences a train could encounter from being close to a high hazard fault to far from any fault, from being in a place with high local ground motion amplification to being on a hard rock site.

The average amount of warning is 8.4 s, averaged over all track locations for all earthquakes in the scenario catalog. This is about half the time necessary to completely stop a train traveling at 50 MPH, and it is rare for any location to receive enough warning to completely halt a train before peak shaking arrives (**Figure 4**). However, not all trains are traveling at full speed, and 8 s is sufficient to decrease train velocity by more than 20 MPH.

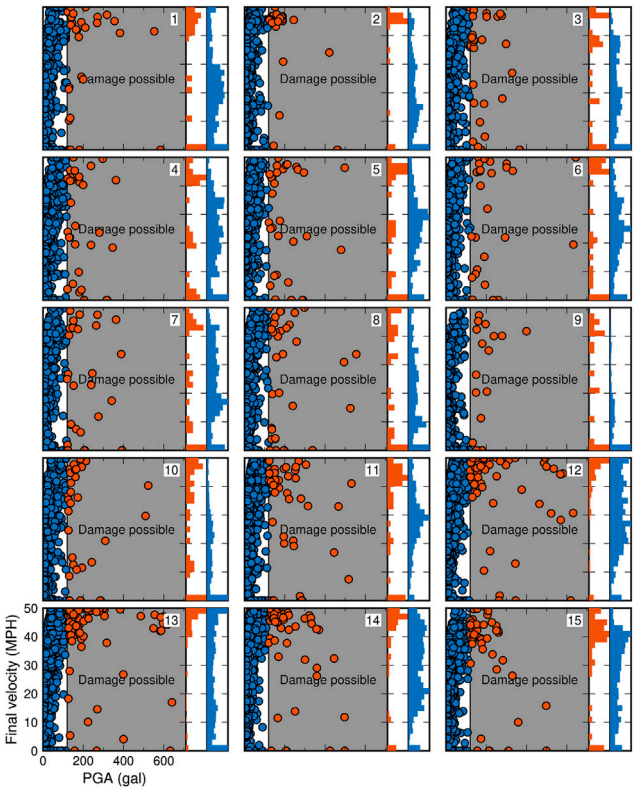

FIGURE 5 | Final train velocity at all locations due to all earthquakes in the 1,000-year UCERF3-ETAS catalog. Each circle represents the final velocity to which a train at that location could decelerate for a single earthquake. Circles are colored red if the median expected ground motion is at least 120 gal at that location and thus could cause damage at the train's current location, blue otherwise. Marginal histograms show total frequency of occurrence. While trains can often be slowed to low velocities, most damaging shaking (red circles) arrive with little warning time, generally allowing trains to only slow by 10 MPH or so. EEW system design is same as **Figure 4**.

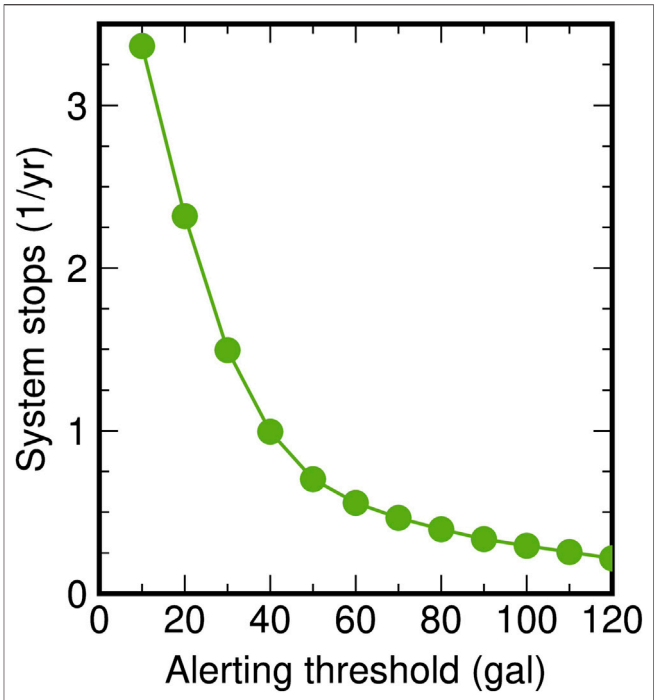

FIGURE 6 | Number of system stops for different choices of the forecast ground motion level that triggers an alert. This represents both the number of stops for a source-parameter-based system that perfectly forecasts observed shaking or an on-site system neglecting ground motion variability.

The above statistics are for all earthquakes in the 1,000-year catalog, including the events that did not cause hazardous shaking at the example location. In **Figure 5**, we separate outcomes based on whether hazardous shaking (defined as PGA>120 gal or ~12% g) is experienced at that specific location (assuming median ground motions). Locations that experience hazardous shaking typically have short warning times such that only minimal braking can occur. For example, at location 13 (Fremont), of the 78 events with hazardous median expected shaking (>120 gal or ~12% g), 63 events (81%) result in such little warning that a train could only decelerate <10 MPH before dangerous shaking arrived.

Neglecting any false alarms due to technical or forecasting errors, an EEW system (either on-site or source-parameter-based) that alerts at 120 gal would have zero unnecessary stops (**Figure 6**). However, raising the alert threshold to 120 gal would decrease potential warning times since the EEW system would have to wait for the waveforms to increase in amplitude (for on-site EEW systems) or wait for more moment to be released by the evolving rupture (for source-parameter-based EEW systems) before it could issue an alert. If an on-site system is triggered by the S-wave arrival, the average warning time across the track system would be 7.3 s for an on-site system and 7.1 s for a source-parameter-based system. The source-parameter-based system lags slightly behind the on-site system despite benefiting from observations near the earthquake source because it takes substantial time for the earthquake source process to release sufficient magnitude that the source-parameter-based system can forecast at least 120 gal shaking anywhere along the tracks (Minson et al., 2018), while the on-site system can issue an alert as soon as strong shaking impinges anywhere on the track system. If we consider only sites along the track that experience damaging shaking (PGA>120 gal), the average warning time decreases to just 3.6 and 3.3 s for on-site and source-parameter-based EEW, respectively.

Conversely, warning times could be increased by lowering the alerting threshold. However, lower alerting thresholds also increase the frequency with which the train system would be halted unnecessarily. It is worth noting that seismicity rates are so low in the San Francisco Bay Area that choosing an alert threshold of just 10 gal (~1%*g*) would cause ~3.5 system stops per year, but allow for an average of 11.7 s warning at all sites and 7.5 s at sites exceeding 120 gal for a source-parameter-based EEW system.

THE SPECIAL UTILITY OF EARTHQUAKE EARLY WARNING FOR RAIL SYSTEMS: AVOIDING DAMAGED TRACK

The preceding analysis looks at the ability to stop a train at any location before dangerous shaking arrives at that location. But

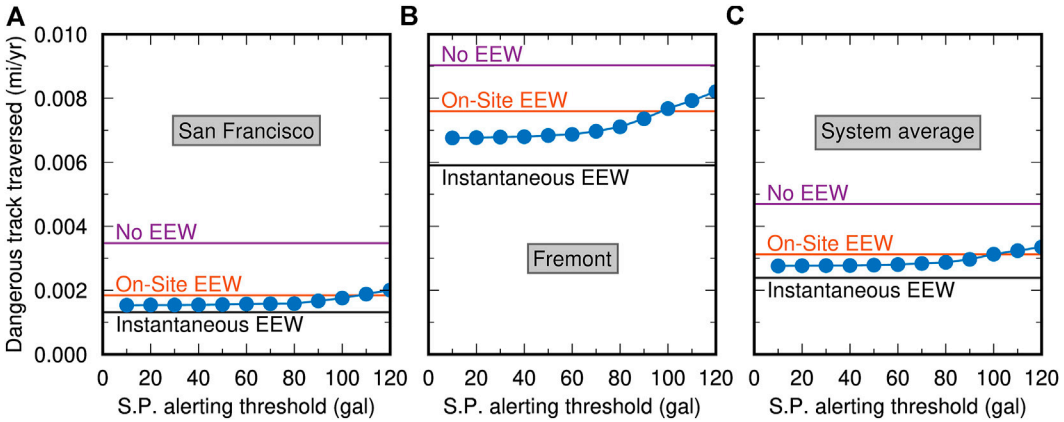

FIGURE 7 | Exposure to potentially damaged track, that is, track that is expected to experience at least 120 gal shaking, in miles per year. Blue lines and symbols show expected performance for a source-parameter-based EEW system as a function of the threshold expected shaking that triggers an alert. Performance is shown for track locations in **(A)** San Francisco and **(B)** Fremont, and **(C)** averaged over the entire track system. For comparison, we also show the expected dangerous track traversed for an on-site EEW system (that alerts when 120 gal is observed anywhere in the train system), an instantaneous EEW system that alerts at the instant the earthquake nucleates, and the situation of no EEW system in which case the train began braking once shaking arrived. The lower the alerting threshold, the earlier an alert is triggered, and the less stopping distance occurs after shaking has arrived and potentially damaged the track.

when it comes to protecting rail systems, EEW does not need to stop (or slow) the train before the shaking arrives at the train's location. It primarily needs to stop the train before it arrives at a location where the tracks are damaged. In this section, we consider how EEW can best accomplish this (much more achievable) goal.

We again assume that the entire rail system is halted if observed (for on-site EEW systems) or forecast (for source-parameter-based EEW systems) shaking exceeds the alerting threshold anywhere along the tracks. If the train's current location is not itself subject to damaging shaking, it is assumed that the train can be safely slowed or stopped without danger of encountering damaged track. If the PGA at the current location does end up being so large as to potentially cause damage, the train is assumed to be able to begin safely slowing. However, once the S-wave arrives, the tracks might be damaged, and the train faces the hazard of traversing potentially damaged track for the distance of track it travels from that time until it comes to a complete stop. If braked at 3 MPH/second, it takes about 186 m to come to a stop from an initial speed of 50 MPH. The longer the advance warning the train receives from the EEW system, the more braking will occur before the S-wave arrives, and the stopping distance from that reduced velocity (that is, the amount of potentially damaged track traversed) will be proportionately lowered.

Exposure to Potentially Damaged Track for On-Site and Source-Parameter-Based Earthquake Early Warning Systems

We compute the distance of potentially damaged track that a train at two sample locations (3-San Francisco and 13-Fremont) is expected to traverse based on the 1,000-year-duration UCERF3-ETAS catalog given alerts from ideal on-site and source-parameter-based EEW systems (**Figures 7A,B**). The distance of potentially damaged track crossed in each earthquake is simply the fraction of the stopping distance that is traveled after the arrival of potentially damaging (>120 gal) shaking. (Peak shaking at each point along the track is calculated as described in the Methodology section.)

We also plot the average exposure to potentially damaged track across the whole system (**Figure 7C**). San Francisco and Fremont represent end-members: San Francisco is farther from hazardous faults, and thus less often directly impacted by dangerous shaking (**Figure 3**), so trains located there more often can completely avoid encountering damaged track. Fremont is close to the hazardous Hayward Fault, more often directly impacted, and thus trains there will more often encounter damaged track. The expected exposure averaged over all locations in the track system is, as expected, in between these two end-members.

In addition to considering an alerting threshold of 40 gal, we examine how different alerting thresholds change the outcomes. Lower alerting thresholds allow alerts to be issued earlier because less of the rupture has to be observed to forecast that shaking will exceed a lower threshold than a higher threshold (Minson et al., 2018), and earlier alerting means braking initiates sooner after the earthquake begins and reduces stopping distance over potentially damaged track (**Figure 7**). However, the cost of lowering the alerting threshold is that the EEW system will issue more precautionary alerts, resulting in possibly many stops for smaller earthquakes that never go on to produce potentially damaging shaking (**Figure 6**). For the source-parameter-based EEW system, we consider expected outcomes for alert thresholds ranging from 10 gal (~1% g) to the damage threshold (120 gal, or ~12% g).

Ideally, we would repeat this comparison of different alerting thresholds for on-site EEW as well. Indeed, we should note that the original threshold for triggering a warning based on observations at along-track seismometers (as opposed to

coastal seismometers) is not the damage threshold of 120 gal but rather 40 gal (Nakamura and Tucker, 1988; Nakamura and Saita, 2007), which presumably yields additional warning time from when the 40 gal threshold is crossed until shaking reaches 120 gal at the cost of causing unnecessary system stops when an event that causes 40 gal shaking does not go on to produce 120 gal shaking. However, given limited knowledge of the ratio of S-wave amplitudes to P-wave amplitudes, or the evolution of shaking amplitudes throughout an earthquake rupture, we cannot reliably model when specific thresholds of shaking will be exceeded in a waveform. So we can only consider the performance of a reference on-site ground-motion-based EEW system that is triggered when the S-wave impinges somewhere on the track system and, for simplicity, we assume that the threshold that triggers alerts is set to 120 gal and thus there are zero unnecessary system stops.

We also consider the reference case of a rail system that does not have the benefit of EEW. For this case, we assume that the train operator begins braking as soon as they feel shaking, specifically the arrival of the S-wave (This assumption is based on author S.N.'s interview with JR drivers, 2008.) If the S-wave amplitude is > 120 gal, then the train is exposed to potentially damaged track for the full stopping distance.

The final case we explore is that of a system that receives an EEW alert the instant that an earthquake nucleates that will eventually grow to produce damaging shaking and which never triggers unnecessary system stops. This is not a realistic scenario. The purpose of this scenario is not to explore any actual potential EEW system performance but rather to quantify how much damaged track is simply impossible to avoid given the geometry between earthquake ruptures and track locations, as well as the stopping distance of trains. The performance of any other EEW system design should then not be evaluated based on whether it eliminates the possibility of traversing any damaged track but rather on how close the amount of potentially damaged track traversed is to this theoretical floor.

We find that on-site warning systems provide more protection (as measured by the amount of potentially damaged track traversed) than source-parameter-based EEW systems when the alerting threshold is set to the level of potentially damaging shaking (120 gal, or ~12% g). However, a source-parameter-based EEW system that utilizes an alerting threshold less than 120 gal could potentially provide trains with additional braking time before the S-wave arrives, decreasing the amount of potentially damaged track traversed. Lowering the ground motion level that triggers an on-site alert would presumably also increase warning time and decrease the amount of hazardous track traversed. Unfortunately, we cannot quantify whether it adds more or less warning time than lowering the source-parameter-based EEW alerting threshold. Regardless of the type of EEW system, alerting at lower thresholds comes at the cost of more systemwide stops (**Figure 6**); but, for on-site systems, the number of stops may be further increased by ground motion variability triggering an alert due to outlier motions from small earthquakes.

Cost-Benefit Analysis

We can perform a rudimentary cost-benefit analysis by assuming that there is some expected loss for running a train over a unit distance of potentially damaged track (track that has been exposed to 120 gal or higher) and that there is also some loss associated with stopping the system be it necessarily (to inspect potentially damaged tracks) or unnecessarily (when an alert was issued for an earthquake too small to cause damage). Following the approach in Minson et al., 2019, Minson et al., 2020, and Saunders et al., 2020, we non-dimensionalize the costs by defining a ratio, r, the false alarm tolerance of the system. That is, r is the expected loss per unit distance of potentially damaged track traveled to the cost for stopping the train system (either necessarily or unnecessarily). If this ratio is large, then the system is very false-alarm tolerant and it is advantageous to alert for little earthquakes just in case they grow into damaging earthquakes even though that will result in unnecessary system stops. If r is small (a relatively false-alarm-intolerant system), then the optimal strategy is to stop the system only when it is very likely that damage could occur so as to minimize the number of relatively costly system stops (**Figure 8**).

Each rail system must determine its own false alarm tolerance, r, in order to identify the optimal EEW alerting strategy for that rail system. The value may vary from system to system depending on factors such as infrastructure fragility, train speeds and braking ability, seismicity rates, shaking hazard, and public expectations about earthquake safety and public transit reliability. The considerations surrounding EEW for Shinkansen trains are not the same as California commuter rail systems in almost every aspect from operations (e.g., speed), to seismic hazard (the most significant earthquakes in Japan are offshore while onshore continental faults dominate in California), to the expectations of its ridership. But what we can say is that, if r is large, then a source-parameter-based approach with a low alerting threshold (such as has been adopted by both JR and the new ShakeAlert EEW system) may be the best approach. But if r is smaller, then the winning approach is to use on-site ground-motion-based alerting (similar to the original JR system). Further, on-site EEW provides better outcomes than source-parameter-based EEW when warning at the damage threshold of 120 gal regardless of false alarm tolerance.

For the systemwide analysis (**Figure 8C**), the minimum r value for which source-parameter-based EEW could outperform on-site EEW is just less than $r = 800$ (for an alerting threshold of 80 gal or ~8% g). So, for example, if running over 1 mi of track exposed to >120 gal shaking has a 50% chance of causing a derailment costing $1.6 million in loss (so that the expected loss is $800,000) and the loss to the rail operator and its passengers for stopping the entire system unnecessarily is just $1,000, then $r = 800$. If the cost of halting all trains unnecessarily is relatively higher than this example ratio, then on-site EEW is the winning strategy; if the expected loss for running a train over a unit length of dangerous track is relatively higher, then source-parameter-based EEW with a low alerting threshold is the optimal choice.

However, that conclusion comes with two enormous caveats. First, we were unable to quantify the effects of lowering the alerting threshold for on-site EEW, and thus we cannot

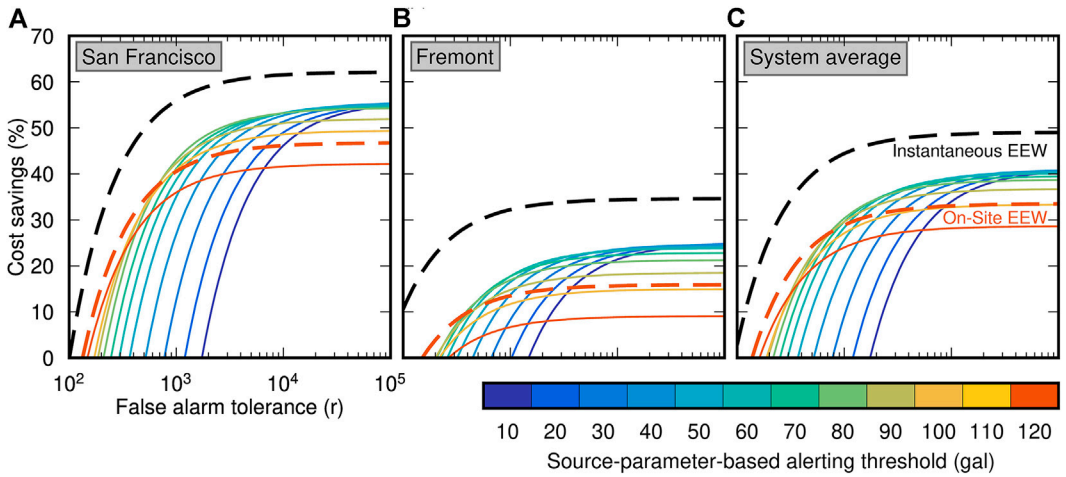

FIGURE 8 | Cost savings for different alerting strategies as a function of false alarm tolerance. Each colored line is the cost savings that could be realized if a source-parameter-based EEW system alerted when the forecast shaking exceeded a specified threshold (ranging from 10 to 120 gal). The black dashed line shows the cost savings for a perfect instantaneous EEW system that alerted at the moment the earthquake nucleated. This is the maximum possible cost savings that could be realized but is less than 100% due to the physical limitations that trains require a finite distance to stop and the fact that even necessary stops due to hazardous shaking incur some cost. Finally, the red dashed line shows the expected cost savings from an on-site EEW system that triggers an alert when 120 gal is observed anywhere along the tracks (The two red lines present cost savings for EEW systems with alerting thresholds of 120 gal. The dashed red line is an on-site EEW system and the solid red line is a source-parameter-based EEW system.) Cost savings is computed for locations in **(A)** San Francisco and **(B)** Fremont, and averaged over the entire track system **(C)**.

determine how an on-site EEW system with low alerting threshold compares to a source-parameter-based system with low alerting threshold. Second, this cost-benefit analysis assumed that the source-parameter-based EEW system could perfectly forecast shaking without error or uncertainty. But ground motion is in reality highly variable; observed ground motions are log-normally distributed with typically a factor of 2 scatter (e.g., Gregor et al., 2014). Minson et al., 2019 demonstrated that the effects of this variability are so large that, even if a source-parameter-based EEW system always perfectly forecast the median expected shaking, the choice to alert or not alert for an earthquake would turn out to be incorrect the majority of the time when an earthquake expected to be dangerous ended up producing weaker-than-expected shaking or a small earthquake thought inconsequential ended up producing hazardous shaking. Because of this, source-parameter-based EEW systems must be tuned to alert for smaller earthquakes than those expected to cause damaging shaking so as to avoid missing an alert when an earthquake produces shaking stronger than the median expected shaking that is forecast when its magnitude and location are input to a GMPE. In contrast, on-site ground-motion-based EEW is in a sense a perfect shaking forecast: either shaking was seen at the tracks and an alert was required, or there was no shaking and no alert was needed. This contrast between the large uncertainty in source-parameter-based EEW systems and relative lack of uncertainty in on-site ground motion systems, combined with neglecting increased warning times for on-site systems with low alerting thresholds, might mean that the on-site approach is favorable for all values of r. Further, we have not considered system latencies, such as telemetry latencies to send networked data back to a processing center, or latencies to transmit messages to slow trains or trigger de-energization. If these latencies are significant, on-site systems may have additional advantages in that they do not need to send data to a center for processing and may even be able to directly trigger automated actions.

Alternatively, perhaps the effects of the uncertainty in the shaking forecast would be absorbed into the desire to alert for low levels of shaking so as to potentially give trains additional warning time. (This is especially likely for systems where r is large.) Or perhaps JR's approach of combining source-parameter-based and on-site EEW systems provides optimal protection. Untangling these factors would require a much larger study and knowing the value of r for real-world rail systems.

DISCUSSION

While EEW has been utilized for rail systems in Japan since 1966 (Nakamura and Tucker, 1988), public EEW in California did not begin until the end of 2018. There are several important differences between United States rail systems and JR's Shinkansen line. On one hand, United States trains travel much slower than bullet trains and can be stopped sooner; a Shinkansen train traveling at full speed has similar braking speed but takes an order of magnitude longer to stop: 4,000 m or 2.5 miles (Arai et al., 2008) compared to 186 m or 0.1 miles for BART. On the other hand, seismic hazard in California is dominated by continental faults such that hazardous earthquakes rupture much closer to railways than the subduction zone events that contribute significantly to seismic hazard in Japan, and thus warning times will tend to be shorter in California. In fact, the only derailment of an in-service passenger train due to

earthquake shaking suffered in the 40-year history of the Shinkansen line was caused by the 2004 M_w6.6 Niigata-Chuetsu earthquake, an onshore earthquake that occurred too close to the tracks (Horioka, 2013). Additionally, a test train derailed during the 2011 M_w9.0 Tohoku-oki earthquake (Horioka, 2013; Japan Transport Safety Board, 2013), an in-service train derailed in 2013 in poor weather (Straits Times, 2013), and an out-of-service train derailed during the 2016 Kumamoto sequence (Goda et al., 2016).

By analyzing a 1,000-year chronology of scenario earthquake ruptures from UCERF3-ETAS, we have explored how effective EEW might be for California rail systems and how it can best be utilized. Despite the slower speed of the trains, the warning is generally only enough to slow but not completely stop trains before dangerous shaking arrives. However, rail systems are uniquely good candidates for utilizing EEW, because it is just as important to stop trains before they reach some other part of the track system that may have been damaged. In this second, unique framework, there is significant potential for EEW to limit trains' exposure to damaged tracks. Although, it is worth noting that even so, one of EEW's greatest benefits may be psychological (in terms of reassuring the ridership) (Nakayachi et al., 2019) or as a training opportunity for rail systems to practice earthquake response. In fact, of the 100 times that the Shinkansen system was stopped due to EEW alerts in the first 20 years that its EEW system was operating, only twice were tracks deformed and, in both cases, the deformation was so minor that it did not pose a derailment hazard (Nakamura and Tucker, 1988).

Rail systems can additionally benefit from EEW because warnings have value even if the warning time is too short to complete protective actions. Many potential EEW protective actions are all or nothing or, worse, may lead to increased harm if shaking arrives mid-action. For example, some piece of infrastructure that is in the process of being moved into a protected state may be more vulnerable to shaking than if it had been left in its normal operational state. But even if a train does not receive sufficient warning to completely stop before encountering damaged track, it can still utilize whatever warning it does receive to slow as much as possible before reaching the damaged area.

These observations indicate that EEW should be seen less as a standalone system and more as part of a continuum of real-time and near-real-time earthquake information. Here, too, rail systems have been forerunners. Long before ShakeAlert development began in the United States, the United States Geological Survey provided freight and passenger trains with normal (non-EEW) locations of M5+ earthquakes as soon as they were available so that the railroads could slow and stop trains and inspect tracks (Hasenberg, 2019). This is not EEW in its strict definition as the alert came after the earthquake rupture had finished and shaking had ceased. But it functioned exactly as EEW should; it provided users with warning so that their trains could take protective action before they encountered dangers caused by earthquake shaking.

In this paper, we have explored the many ways that rail systems can especially benefit from EEW or even real-time earthquake information that is too slow to be considered early warning in other applications. Other types of networked infrastructure could similarly derive these extra benefits. Besides passenger and freight rail, any type of transportation system that involves moving discrete items, such as road networks, should be able to receive similar benefits. While systems that involve continuous flow, such as power and gas lines, may not be able to achieve all the benefits of discrete systems like rail (where there is always some chance that the shaking will impact an unoccupied section of the network), our analysis illustrates how warnings can be used to mitigate loss across the system even if the warning does not come early enough to prevent exposure and loss everywhere in the system.

CONCLUSION

Our analysis indicates that on-site EEW provides better outcomes than source-parameter-based EEW when warning at the damage threshold of 120 gal regardless of false alarm tolerance. This is because it takes too long for an earthquake rupture to evolve to a large enough magnitude that a source-parameter-based system can forecast that shaking will exceed 120 gal (See *Conventional Earthquake Early Warning View: How Much Warning Does Each Location Receive?* for warning time comparison and Minson et al., 2018 for background discussion.). A source-parameter-based EEW system with a lower alerting threshold (e.g., 40 gal) can further reduce the exposure to potentially damaged track compared to an on-site system alerting at 120 gal, increasing the average warning time to 8.4 s compared to 7.9 s for on-site warning. However, this comes at the cost of more frequent halting of the rail system unnecessarily. An alerting threshold of 40 gal would result in one stop/yr on average, which is about 4.5 times the rate of earthquakes whose median expected ground motion is potentially damaging (>120 gal) anywhere in the system. The optimal EEW approach for rail systems depends strongly on the ratio of the cost of traversing damaged tracks to the cost of halting the system, with a higher potential benefit if that ratio is large.

We demonstrated a framework with which to examine the application of EEW to distributed systems. Our framework uses earthquake rupture probabilities and ground motion models to forecast both hazard and potential warning times across a geographically distributed infrastructure network. It then uses a cost-benefit analysis that considers expected gains and losses across the entire network as well as potential marginal increases in gain with changes in warning time (also varying across the network) to guide selection of the optimal EEW system design. Real-world use of this framework to make actionable decisions on the appropriate alerting threshold will be highly dependent on what amplitude of ground motion is damaging, r values, and other considerations of the specific application. In this paper, we have developed the framework for application to rail systems, but each rail system must consider and assign values (including monetary and societal consideration) to the costs associated with precautionary stops and the benefit from slowing trains when damaging shaking occurs.

Lack of knowledge limits our analysis in two areas. First, we lack models for the spatial covariance of ground motions,

limiting our ability to calculate shaking hazard across the entire rail system. Second, the lack of models for S to P ratios and for how shaking amplitudes evolve with time during a rupture prevents us from considering how lowering the alerting threshold for on-site ground-motion-based EEW systems could increase warning time. If the seismological community were to develop models for shaking covariance and evolution, it could potentially have significant impacts on the EEW community including improved performance assessments of ground-motion-based EEW methods such as PLUM, quantifying the potential utility of EEW methods that aim to predict peak shaking from P-wave amplitudes (Kodera, 2018), and improving real-time shaking forecasts.

DATA AVAILABILITY STATEMENT

The raw data supporting the conclusions of this article will be made available by the authors, without undue reservation.

AUTHOR CONTRIBUTIONS

SM, EC, and SW jointly designed the analysis. SM conducted the analysis. SN provided technical data on EEW and rail systems. SM, EC, SW, and SN jointly prepared the manuscript.

ACKNOWLEDGMENTS

The authors would like to thank a host of people at BART for helpful background discussions on EEW for rail systems. These kind people include Kevin Copley, Chung-Soo Doo, Kristyl Horton, and Charles Weiland. Morgan Page and Kevin Milner generously provided a chronology of scenario earthquakes drawn from the UCEF3-ETAS model (Field et al., 2017). The authors would also like to thank Bob deGroot for facilitating this collaboration; and Annemarie Baltay, Andy Michael, and Evelyn Roeloffs for reviewing the manuscript.

REFERENCES

Allen, T. I., and Wald, D. J. (2009). On the Use of High-Resolution Topographic Data as a Proxy for Seismic Site Conditions (VS30). *Bull. Seismological Soc. America* 99, 935–943. doi:10.1785/0120080255

Arai, H., Kanno, S., and Yanase, N. (2008). Brake System for Shinkansen Speed Increase. *JR East Tech. Rev.* 12, 12–15.

Aranda, J. M. E., Jimenez, A., Ibarrola, G., Alcantar, F., Aguilar, A., Inostroza, M., et al. (1995). Mexico City Seismic Alert System. *Seismological Res. Lett.* 66 (6), 42–53. doi:10.1785/gssrl.66.6.42

Cauzzi, C., Behr, Y., Le Guenan, T., Douglas, J., Auclair, S., Woessner, J., et al. (2016). Earthquake Early Warning and Operational Earthquake Forecasting as Real-Time hazard Information to Mitigate Seismic Risk at Nuclear Facilities. *Bull. Earthquake Eng.* 14 (9), 2495–2512. doi:10.1007/s10518-016-9864-0

Chiou, B. S.-J., and Youngs, R. R. (2014). Update of the Chiou and Youngs NGA Model for the Average Horizontal Component of Peak Ground Motion and Response Spectra. *Earthquake Spectra* 30 (3), 1117–1153. doi:10.1193/072813EQS219M

City of Los Angeles *Emergency Management Department's 2019 Report, "Earthquake Alerts: City of LA Announces New Earthquake Early Warning App"*. (last accessed December 18, 2019).

Cochran, E. S., and Husker, A. L. (2019). How Low Should We Go when Warning for Earthquakes? *Science* 366, 957–958. doi:10.1126/science.aaz6601

Doi, K. (2011). The Operation and Performance of Earthquake Early Warnings by the Japan Meteorological Agency. *Soil Dyn. Earthquake Eng.* 31, 119–126. doi:10.1016/j.soildyn.2010.06.009

Field, E. H., Milner, K. R., Hardebeck, J. L., Page, M. T., van der Elst, N., Jordan, T. H., et al. (2017). A Spatiotemporal Clustering Model for the Third Uniform California Earthquake Rupture Forecast (UCERF3-ETAS): Toward an Operational Earthquake Forecast. *Bull. Seismological Soc. America* 107 (3), 1049–1081. doi:10.1785/0120160173

Given, D. D., Allen, R. M., Baltay, A. S., Bodin, P., Cochran, E. S., Creager, K., et al. (2018). Revised Technical Implementation Plan for the ShakeAlert System-An Earthquake Early Warning System for the West Coast of the United States. *Geol. Surv. Open-File Rep. 2018–1155*, 42. doi:10.3133/ofr20181155

Goda, K., Campbell, G., Hulme, L., Ismael, B., Ke, L., Marsh, R., et al. (2016). The 2016 Kumamoto Earthquakes: Cascading Geological Hazards and Compounding Risks. *Front. Built Environ.* 2, 2–17. doi:10.3389/fbuil.2016.00019

Gregor, N., Abrahamson, N. A., Atkinson, G. M., Boore, D. M., Bozorgnia, Y., Campbell, K. W., et al. (2014). Comparison of NGA-West2 GMPEs. *Earthquake Spectra* 30, 1179–1197. doi:10.1193/070113eqs186m

Hasenberg, C. (2019). *Development of Earthquake Early Warning Systems*. Geological Society of the Oregon Country. Available at:

Horioka, K. (2013). Clarification of Mechanism of Shinkansen Derailment in the 2011 Great East Japan Earthquake and Countermeasures against Earthquakes. *JR East Tech. Rev.* (27), 13–16.

Hoshiba, M., Kamigaichi, O., Saito, M., Tsukada, S. Y., and Hamada, N. (2008). Earthquake Early Warning Starts Nationwide in Japan. *Eos Trans. AGU* 89 (8), 73–74. doi:10.1029/2008eo080001

Hoshiba, M. (2013). Real-time Prediction of Ground Motion by Kirchhoff-Fresnel Boundary Integral Equation Method: Extended Front Detection Method for Earthquake Early Warning. *J. Geophys. Res. Solid Earth* 118, 1038–1050. doi:10.1002/jgrb.50119

Hsiao, N. C., Wu, Y. M., Shin, T. C., Zhao, L., and Teng, T. L. (2009). Development of Earthquake Early Warning System in Taiwan. *Geophys. Res. Lett.* 36 (5), L00B02. doi:10.1029/2008gl036596

Hu, Q., Gao, N., and Zhang, B. (2014). High Speed Railway Environment Safety Evaluation Based on Measurement Attribute Recognition Model. *Comput. Intell. Neurosci.* 2014, 1–10. doi:10.1155/2014/470758

Iervolino, I. (2011). Performance-based Earthquake Early Warning. *Soil Dyn. Earthquake Eng.* 31 (2), 209–222. doi:10.1016/j.soildyn.2010.07.010

Japan Transport Safety Board (2013). "Train Derailment Accident in the Premises of Sendai Station of the Tohoku Shinkansen of the East Japan Railway Company," in *Railway Accident Investigation Report*. Available at: (Accessed February 22, 2013).

Kodera, Y., Yamada, Y., Hirano, K., Tamaribuchi, K., Adachi, S., Hayashimoto, N., et al. (2018). The Propagation of Local Undamped Motion (PLUM) Method: a Simple and Robust Seismic Wavefield Estimation Approach for Earthquake Early Warning. *Bull. Seismol. Soc. America* 108, 983–1003. doi:10.1785/0120170085

Kodera, Y. (2018). Real-time Detection of Rupture Development: Earthquake Early Warning Using P Waves from Growing Ruptures. *Geophys. Res. Lett.* 45, 156–165. doi:10.1002/2017GL076118

Meier, M. A., Heaton, T., and Clinton, J. (2015). The Gutenberg Algorithm: Evolutionary Bayesian Magnitude Estimates for Earthquake Early Warning with a Filter Bank. *Bull. Seismol. Soc. America* 105 (5), 2774–2786. doi:10.1785/0120150098

Meier, M.-A. (2017). How "good" Are Real-Time Ground Motion Predictions from Earthquake Early Warning Systems? *J. Geophys. Res. Solid Earth* 122, 5561–5577. doi:10.1002/2017JB014025

Minson, S. E., Meier, M.-A., Baltay, A. S., Hanks, T. C., and Cochran, E. S. (2018). The Limits of Earthquake Early Warning: Timeliness of Ground Motion Estimates. *Sci. Adv.* 4, eaaq0504. doi:10.1126/sciadv.aaq0504

Minson, S. E., Baltay, A. S., Cochran, E. S., Hanks, T. C., Page, M. T., McBride, S. K., et al. (2018). The Limits of Earthquake Early Warning: Accuracy and Best Alerting Strategy. *Scientific Rep.* 9 (1), 2478. doi:10.1038/s41598-019-39384-y

Minson, S. E., Saunders, J. K., Bunn, J. J., Cochran, E. S., Baltay, A. S., Kilb, D. L., et al. (2020). Real-Time Performance of the PLUM Earthquake Early Warning Method during the 2019 M 6.4 and 7.1 Ridgecrest, California, Earthquakes. *Bull. Seismol. Soc. Am.* 110, 1887–1903. doi:10.1785/0120200021

Minson, S. E., Baltay, A. S., Cochran, E. S., McBride, S. K., and Milner, K. R. (2021). Shaking Is Almost Always a surprise: the Earthquakes that Produce Significant Ground Motion. *Seismol. Res. Lett.* 92, 460–468. doi:10.1785/0220200165

Murray, J. R., Crowell, B. W., Grapenthin, R., Hodgkinson, K., Langbein, J. O., Melbourne, T., et al. (2018). Development of a Geodetic Component for the U.S. West Coast Earthquake Early Warning System. *Seismol. Res. Lett.* 89 (6), 2322–2336. doi:10.1785/0220180162

Nakamura, Y., and Saita, J. (2007). "UrEDAS, the Earthquake Warning System: Today and Tomorrow," in *Earthquake Early Warning Systems*. Berlin, Heidelberg: Springer, 249–281.

Nakamura, Y., and Tucker, B. E. (1988). Japan's Earthquake Warning System: Should it Be Imported to California? *Calif. Geology.*, 33–40.

Nakamura, Y. (1996). "Real-time Information Systems for Hazards Mitigation," in Proceedings of the 11th World Conference on Earthquake Engineering. Mexico: . Acapulco. doi:10.2514/6.1996-2078

Nakayachi, K., Becker, J. S., Potter, S. H., and Dixon, M. (2019). Residents' Reactions to Earthquake Early Warnings in Japan. *Risk Anal.* 39 (8), 1723–1740. doi:10.1111/risa.13306

Ogura, M. (2006). The Niigata Chuetsu Earthquake-Railway Response and Reconstruction. *Jpn. Railway Transport Rev.* 43 (44), 46–63.

Saita, J., and Nakamura, Y. (2003). *Early Warning Systems for Natural Disaster Reduction*. Berlin, Heidelberg: Springer, 453–460. doi:10.1007/978-3-642-55903-7_58

Saunders, J. K., Aagaard, B. T., Baltay, A. S., and Minson, S. E. (2020). Optimizing Earthquake Early Warning Alert Distance Strategies Using the July 2019 Mw 6.4 and Mw 7.1 Ridgecrest, California, Earthquakes. *Bull. Seismol. Soc. America* 110 (4), 1872–1886. doi:10.1785/0120200022

Straits Times (2013). *High-speed Bullet Train Derails in Japan: Media*. Available at: (Accessed March 2, 2013).

Strauss, J. A., and Allen, R. M. (2016). Benefits and Costs of Earthquake Early Warning. *Seismological Res. Lett.* 87 (3), 765–772. doi:10.1785/0220150149

Tamaribuchi, K., Yamada, M., and Wu, S. (2014). A New Approach to Identify Multiple Concurrent Events for Improvement of Earthquake Early Warning. *Jssj* 67 (67), 41–55. (in Japanese with English abstract and figure captions). doi:10.4294/zisin.67.41

Trugman, D. T., Page, M. T., Minson, S. E., and Cochran, E. S. (2019). Peak Ground Displacement Saturates Exactly when Expected: Implications for Earthquake Early Warning. *J. Geophys. Res. Solid Earth* 124, 4642–4653. doi:10.1029/2018jb017093

Veeraraghavan, S., Heaton, T. H., and Krishnan, S. (2019). Lower Bounds on Ground Motion at Point Reyes during the 1906 San Francisco Earthquake from Train Toppling Analysis. *Seismological Res. Lett.* 90 (2A), 683–691. doi:10.1785/0220180327

Veneziano, D., and Papadimitriou, A. G. (2003). "Optimizing the Seismic Early Warning System for the Tohoku Shinkansen," in *Early Warning Systems for Natural Disaster Reduction*. Berlin, Heidelberg: Springer, 727–734. doi:10.1007/978-3-642-55903-7_97

Wu, S., Beck, J. L., and Heaton, T. H. (2013). ePAD: Earthquake Probability-based Automated Decision-making Framework for Earthquake Early Warning. *Computer-Aided Civ. Infrastruct. Eng.* 28 (10), 737–752. doi:10.1111/mice.12048

Wu, S., Cheng, M. H., Beck, J. L., and Heaton, T. H. (2016). An Engineering Application of Earthquake Early Warning: ePAD-Based Decision Framework for Elevator Control. *J. Struct. Eng.* 142 (1), 04015092. doi:10.1061/(asce)st.1943-541x.0001356

Yamamoto, S., and Tomori, M. (2013). Earthquake Early Warning System for Railways and its Performance. *J. JSCE* 1, 322–328. doi:10.2208/journalofjsce.1.1_322

Disclaimer: Any use of trade, firm, or product names is for descriptive purposes only and does not imply endorsement by the United States Government.

Conflict of Interest: The authors declare that the research was conducted in the absence of any commercial or financial relationships that could be construed as a potential conflict of interest.

frontiers in Earth Science

ORIGINAL RESEARCH
published: 10 June 2021
doi: 10.3389/feart.2021.626908

Onsite Early Prediction of PGA Using CNN With Multi-Scale and Multi-Domain P-Waves as Input

Ting-Yu Hsu and Chao-Wen Huang*

National Taiwan University of Science and Technology, Taipei, Taiwan

Although convolutional neural networks (CNN) have been applied successfully to many fields, the onsite earthquake early warning by CNN remains unexplored. This study aims to predict the peak ground acceleration (PGA) of the incoming seismic waves using CNN, which is achieved by analyzing the first 3 s of P-wave data collected from a single site. Because the amplitude of P-wave data of large and small earthquakes can differ, the multi-scale input of P-wave data is proposed in this study in order to let the CNN observe the input data in different scales. Both the time and frequency domains of the P-wave data are combined into multi-domain input, and therefore the CNN can observe the data from different aspects. Since only the maximum absolute acceleration value of the time history of seismic waves is the target output of the CNN, the absolute value of the P-wave time history data is used instead of the raw value. The proposed arrangement of the input data shows its superiority to the one directly inputting the raw P-wave data into the CNN. Moreover, the predicted PGA accuracy using the proposed CNN approach is higher than the one using the support vector regression approach that employed the extracted P-wave features as its input. The proposed CNN approach also shows that the accuracy of the predicted PGA and the alert performances are acceptable based on data from two independent and damaging earthquakes.

Keywords: PGA, CNN, on-site earthquake early warning, multi-scale, single station

OPEN ACCESS

Edited by:
Angela Isobel Chung, University of California, Berkeley, United States

Reviewed by:
Sarah Minson, United States Geological Survey, United States
Masumi Yamada, Independent Researcher, Kyoto, Japan

****Correspondence:***
Ting-Yu Hsu
tyhsu@ntust.edu.tw

Specialty section:
This article was submitted to Solid Earth Geophysics, a section of the journal Frontiers in Earth Science

Received: *07 November 2020*
Accepted: *25 March 2021*
Published: *10 June 2021*

Citation:
Hsu T-Y and Huang C-W (2021) Onsite Early Prediction of PGA Using CNN With Multi-Scale and Multi-Domain P-Waves as Input. Front. Earth Sci. 9:626908. doi: 10.3389/feart.2021.626908

INTRODUCTION

Earthquake early warning (EEW) approach aims to issue alerts for impending intense ground shaking events. The alerts will be issued when faster and smaller P-waves are detected after an earthquake has occurred. Public earthquake early alerts during several recent large earthquakes have been provided successfully (Fujinawa and Noda, 2013; Cuéllar et al., 2014; Yamada et al., 2014; Hsu et al., 2016, 2018, 2021; Kodera et al., 2016; Allen and Melgar, 2019; Wu et al., 2019). The algorithms of EEW techniques can be classified into regional and onsite warning ones based on their concept required to estimate an earthquake's parameters. Compared to regions that are located farther away, the regions surrounding the epicenter suffer much higher seismic intensity. However, existing regional warning techniques involve the collection of data from several seismic stations and some computational time is needed to acquire source parameters, such that there is sometimes little to no lead time before a destructive wave hits. On the other hand, an onsite warning system may provide a longer lead time for regions surrounding an epicenter because it only requires the data of the target site for predicting the intensity of the impending seismic waves.

Most of the onsite EEW techniques issue alerts based on simple parameters extracted from the initial P waves observed at a seismic station. For instance, Kanamori (2005) estimated the magnitude using a predominant frequency of P wave. Odaka et al. (2003) proposed using fitting parameter of the waveform envelope and the P-wave amplitude to estimate the magnitude and epicentral distance. Wu and Kanamori (2005) obtained for a relationship between the peak displacement amplitude of the P wave (Pd) and the peak ground velocity (PGV). They proposed issuing an alert based on the value of Pd. Zollo et al. (2010) proposed using the thresholds of both the Pd and the predominant period of seismic waves to issue alerts. Nakamura et al. (2011) used the inner product of acceleration and velocity to predict the PGV. All these algorithms tried to establish simple empirical functions between the extracted P-wave parameters and interested source parameters and seismic intensity.

Because only one to two P-wave parameters could be dealt with when establishing the empirical functions and only simple empirical functions could be established based on observation, artificial intelligence became a powerful alternative approach for establishing the complex relationship between more P-wave parameters and the source parameters or seismic intensity. Böse et al. (2012) proposed using fully connected artificial neural networks to estimate the PGA, epicenter distance, and magnitude using the acceleration, velocity, and displacement of the three-component waveforms. Hsu et al. (2013) proposed to estimate the peak ground acceleration (PGA) of an incoming earthquake by relying on a support vector regression (SVR) approach. Six P-wave features—the peak displacement, peak velocity, peak acceleration, cumulative absolute velocity, effective predominant period, and the integral of the squared velocity—extracted from of the first few seconds after trigger of the vertical acceleration component were used to predict the PGA of the target site. The regression model to predict the PGA according to these P-wave features was established based on the SVR approach. The algorithm they developed has been implemented successfully to issue alerts during several large earthquakes (Hsu et al., 2016, 2018, 2021). Furthermore, site effects on the PGA have been accommodated by including the horizontal-to-vertical spectral ratio into the input of an artificial neural network prediction model (Hsu et al., 2020). These approaches, however, require the extraction of the P-wave parameters in advance before being input into the neural networks or support vector regression models. In these approaches, only some important P-wave parameters (instead of the original and complex acceleration time history) are used so other important P-wave-related information may be ignored.

Deep convolutional neural networks (CNN) are capable of extracting features from raw data (LeCun et al., 2015). Recently, CNN has been applied successfully to many fields, including face identification (Sajjad et al., 2018), speech recognition (Abdel-Hamid et al., 2014), playing "Go" (Silver et al., 2016), and crack detection (Xu et al., 2019). In other research, Wu and Jahanshahi (2019), Wu et al. (2019) showed the ability of CNN to estimate structural dynamic responses accurately and identify the structurally dominant frequency of the acceleration signal. Yu et al. (2018) showed the proposed CNN method had outstanding identification accuracy for structural damage of a benchmark building than other commonly used machine learning methods. Shrestha and Dang (2020) customized a CNN framework for real-time auto classification of bridge vibration data. As for earthquakes, Mousavi et al. (2019) applied the CNN and recurrent units to earthquake signal detection. Perol et al. (2018) tried to detect the earthquakes' occurrences and classify the locations of the epicenters within seven predefined regions using three-component seismic waveforms recorded on a seismic station using CNN. Jozinovic et al. (2020) tried to estimate the intensity measurements of ground-shaking earthquake events within Central Italy by simultaneously using the seismic waveform data of 39 stations located close to epicenters with the input of the CNN.

In this study, we propose to implement CNN for onsite EEW. The original measured P-wave data at a single station were inputted into the CNN for predicting the PGA of the coming earthquake without a loss of any information in the seismic waveforms. To the authors' best knowledge, our attempt is the first in the literature to perform onsite EEW using CNN, i.e., to predict the coming seismic intensity at one site using the measured data at the same site. However, because the amplitude of the P-wave data of large earthquakes and small earthquakes can be very different, the multi-scale inputs of the P-wave data are proposed in this study in order to let the CNN observe the input data in different scales. Note that the multi-scale input proposed in this study is different from the down-sampling approach that reduces the dimension along the time-series direction (Cui et al., 2016). The multi-scale proposed in this study scales the input along the amplitude direction. Moreover, both the time and frequency domains of the P-wave data are combined into multi-domain input, hence the CNN can observe the data in different aspects.

In the Methodology section of this paper, a brief description of the CNN is summarized because it has been applied to many fields and the basic details have been well-documented in many studies in the literature. Instead, we focused on describing how we designed both the input data and the architecture of the CNN. The earthquake data and the process of training and validation are also described in this section. Next, in Results and Discussions, the effect of input is studied first, followed by a discussion of the performance of the earthquake data using the proposed CNN. Finally, the Concluding Remarks summarizes this study's results and implications for the future.

MATERIALS AND METHODS

Brief Description of CNN

Convolutional neural networks has a great capability to extract features from raw data and has been successfully employed to solve many real-world problems. A typical CNN usually consists of convolution, pooling, activation, and fully connected layers. The convolution layer extracts features from the input data using different kernels, thus enabling a large number of features to be

obtained. During the convolution, users can design specific stride sizes to scan through the input data and then obtain feature maps with different weights.

The pooling layer subsamples the feature maps and extracts the dominant information in these maps, and by doing this reduces the dimensionality of the feature maps and keeps their essential information at the same time. As the CNN can be deeper, multiple convolution and pooling layers can be stacked together to solve more complex problems. Finally, fully connected layers with activation functions are used to classify or do regressions using the flattened feature maps.

Input Data of the CNN

In order to perform onsite EEW, the initial ground motion observed at a site was used to predict the peak value of the incoming ground motion. In this study, after the first 3 s post-triggering, the observed acceleration time history was used for predicting the PGA, the maximum absolute value of the entire acceleration time history in three components. Note that the differences between the amplitudes of the P-wave data of large and small earthquakes can be very large. The amplitude of input data with relatively small values may have fewer effects on the loss function when training the CNN compared to the one with larger values. In order to obtain better regression results for data with different amplitudes, for example, predicting the PGA more accurately for earthquakes with different intensities, we had tried to use logarithm values of the acceleration time history as the input of the CNN, but because the time history does not follow the lognormal distribution, the prediction results were quite bad. As a result, we propose to use the multi-scale inputs of P-wave data for observing the data in different scales when performing feature extraction using the CNN.

For the first 3 s of the P-wave data in this study, the maximum amplitude of most of the data (99.9%) was below 250 gal (cm/s^2). This indicates that one of the scales of time history data could be chosen as $\pm$ 250 gal. That is, the original time history data with values larger than 250 gal and smaller than -250 gal were truncated and set to 250 and -250 gal, respectively (Truncation Step). Then the truncated data were rescaled to have values between -1 and 1 (Normalization Step). Four more scales with ranges of ± 2.5, ± 8, ± 25, and ± 80 gal were also considered to extract the features of time history data with different amplitudes. These range of scales is referred to the seismic intensity scale of the Central Weather Bureau (CWB), Taiwan. The discussion of determining the scales of time history data are provided in section 3.1 Effect of Input.

It is well-known in the geoscience research community that the seismic ground motions caused by a longer fault-rupture process may contain signals with longer periods (Satriano et al., 2011). This identifies the frequency content of the P-wave as very important. However, because it is not easy to identify the frequency content clearly by observing the complex and chaotic ground acceleration time history directly, the frequency domain of the P-wave data was also included in the input into the CNN. As a result, both the time and frequency domains of the P-wave data are combined as multi-domain input so that the CNN can observe the data in different aspects.

Similar to the time history of the P-wave data, three different scales of the Fourier spectrogram, i.e., 1, 20, and 40 gal/Hz, were also considered in order to observe the frequency content more clearly in different scales using the CNN. The Fourier spectrogram is the amplitude obtained by using fast Fourier transformation of the first 3 s of P-wave data. Take the scale 20 gal/Hz as an example, the original Fourier spectrogram with values larger than 20 gal/Hz was truncated and set to 20 gal/Hz (Truncation Step). Then the truncated data were rescaled to have values between -1 and 1 (Normalization Step). For 3 s of three components' time history with a 200 Hz sampling rate, the size of each scale of P-wave time history data was 600×3. However, because most of the energy of the P-wave data is located within a frequency range between 0 and 50 Hz, only the spectrogram of this range was used (150 points in length). In order to have the same dimensions for both the time and frequency domain data, 600 points, the spectrogram was linearly interpolated. Finally, there were five multi-scale and multi-domain P-wave data as the input of the CNN, as shown in **Figure 1**, and the dimensions of the input data were $600 \times 3 \times 5$.

Architecture of the CNN

It is well known that intensive periodicity may exist in the time-domain vibration signals and the signals at different time points could be deeply related to each other in a large range. Hence, it may be difficult to find valuable information about periodic data and the relationship behind the time history signals by using kernels with short lengths along the time dimension. As for the data in the frequency domain, the relationship between higher and lower frequencies can be extracted using kernels with longer lengths along the frequency dimension. For instance, Yu et al. (2018) successfully identified structural damage using a $1{,}000 \times 1$ kernel size for extracting features from frequency spectra along the frequency dimension. In this study, 16 1-D kernels 150×1 in size in the first layer were implemented to extract the features of the data for both the time and frequency domains. Then a max pooling layer with 1-D kernels with a size of 3×1 and a stride of 3×1 was used to extract the maximum value of the features along the time-series direction. **Figure 1** shows the architecture of the proposed CNN. The max pooling could greatly improve the statistical efficiency and computational speed of the neural network. The schematic diagrams of the operation of convolution and pooling, as well as the resulting sizes of the feature maps, are shown in **Figure 2**.

After the feature maps were extracted from the time history data and frequency spectra, we treated these feature maps more like 2-D images. Therefore, the second convolution layer with 32 2-D kernels that were 5×3 in size and a pooling layer with kernels of 3×1 in size were employed to extract more condensed features. And the third convolution layer with 32 kernels 1×3 in size and a pooling layer with kernels 3×1 in size were employed again to further extract more condensed features.

Finally, after the features were flattened, two fully connected layers of 128 neurons that served as feature-selection layers were utilized to transform the feature maps into the output PGA value, so as most unnecessary or redundant features will be cast aside in the fully connected layers. The details of

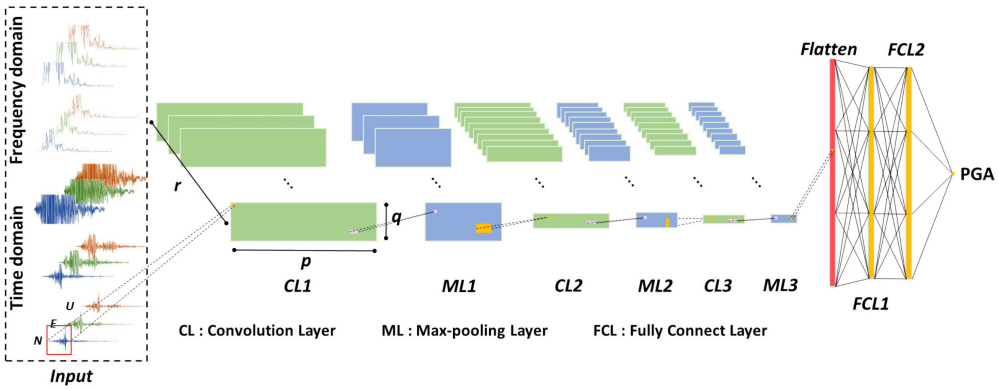

FIGURE 1 | The proposed CNN architecture in this study.

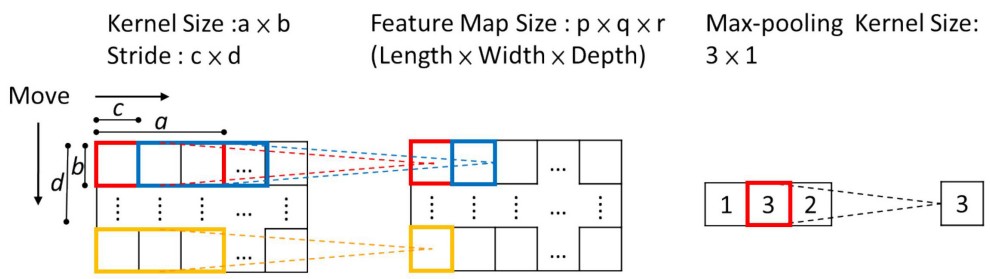

FIGURE 2 | The schematic diagram of the operation of convolution and pooling, as well as the resulted size of the feature maps.

the sizes of the convolution and pooling operations, as well as the resulted sizes of the feature maps, are summarized in **Table 1**. The rectified linear unit (ReLU) activation function was employed in this study (Nair and Hinton, 2010), and the dropout operation was applied to avoid over-diffing problems (Srivastava et al., 2014).

Earthquake Data

The earthquake data provided by the Taiwan Strong Motion Instrument Program (TSMIP) were employed in this study.

TABLE 1 | The detail of the size of the convolution and pooling operations, as well as the resulting sizes of the feature maps of the proposed CNN.

Layer	Kernel Size (*a*, *b*)	Output feature size (*p*, *q*, *r*)
Input	N/A	(600, 3, 5)
CL 1	(150, 1)	(451, 15, 16)
ML 1	(3, 1)	(150, 15, 16)
CL 2	(5, 3)	(146, 5, 32)
ML 2	(3, 1)	(48, 5, 32)
CL 3	(1, 3)	(48, 3, 32)
ML 3	(3, 1)	(16, 3, 32)
Flatten	N/A	1,536
FCL 1	N/A	128
FCL 2	N/A	128
Output	N/A	1

High-quality strong ground motions caused by earthquakes around Taiwan were collected by the TSMIP network, which is operated by the CWB. In total, data on 10,000 earthquakes (denoted as T-data) were selected from the TSMIP data covering the period from July 29, 1992, to December 31, 2006. All the earthquake data with PGAs larger than 250 cm/s^2 (gal) and less than 2.5 gal in the TSMIP data were selected because they are quite rare. As for the earthquake data with PGAs between 2.5 and 250 gal, data on more than 2,000 earthquakes were selected. The number of T-data within different ranges of PGA when performing training, validating and testing for the CNN is summarized in **Table 2**. For instance, the number of all the data with PGAs larger than 400 gal in the TSMIP data was only 78, and 50, 12, and 16 of these data were used for training, validation, and testing, respectively. The number of events within different ranges of PGA is also summarized in the same table. There were 2,279 earthquake events in the T-data, and the magnitude (Mw) range is 1.66∼7.6. Besides the Chi-Chi earthquake event with a magnitude 7.6, there were also some large earthquake events in the T-data and the number of earthquake events with a magnitude not smaller than 6.5 was 17. The frequency of the magnitude for training, validation, and testing datasets is illustrated in **Supplementary Figure 1**. The magnitude vs. hypocentral distance of the T-data is shown in **Supplementary Figure 2**. The Short-Term-Average through Long-Term-Average algorithm was employed herein to pick the arrival time of

TABLE 2 | The 10,000 TSMIP earthquake data used for training, validating, and testing for the CNN.

Dataset		PGA (cm/s^2)						
		0.8∼ 2.5	2.5∼ 8	8∼ 25	25∼ 80	80∼ 250	250∼ 400	400∼
Number of events	Total	99	694	729	721	697	80	37
Number of data	Training	75	1,443	1,443	1,443	1,821	127	50
	Validation	19	361	361	361	455	32	12
	Test	23	450	450	450	569	39	16
	Total	117	2,254	2,254	2,254	2,845	1,98	78

P-wave automatically, and the T-data were used to train, validate, and test the CNN.

In addition, two earthquake datasets recorded during the 2016 Meinong earthquake event (Mw = 6.53) and 2018 Hualien Earthquake event (Mw = 6.2) in Taiwan were adopted herein to understand the capability of the proposed CNN approach for PGA prediction. The Meinong earthquake event resulted in 117 deaths and damaged to 253 buildings (six totally collapsed). The Hualien earthquake event caused 17 fatalities and caused serious damage to 179 buildings (four totally collapsed). Another typical earthquake dataset recorded during a relatively small earthquake event with magnitude 5.3 Mw occurred in 2016 (denoted as M5.3 earthquake) was also adopted to see how the performance of the proposed CNN approach varies with magnitude. The M5.3 earthquake was selected because of its number of the recorded earthquake data were relatively large among the earthquake events with a magnitude between 5.0 and 5.5.

Training and Validation

The goal of the CNN was to predict the PGAs as accurately as possible for small and large earthquakes. However, the differences between these PGAs were quite enormous. To be more specific, the PGAs of large earthquakes could be almost 1,000 times those of the small ones. When the root mean squared errors was used to estimate the loss of the CNN, only the PGAs of larger earthquakes were predicted with high accuracy because the error of these earthquakes contributed to the root mean squared errors much more than did the small earthquakes. In this study, the root mean squared logarithmic errors (RMSLE) was employed to estimate the loss of the CNN, denoted as E, as defined in Equation (1).

$$E = \sqrt{\frac{1}{N}\sum_{j=1}^{N}\left(log(y_j^p + 1) - log(y_j^r + 1)\right)^2} \quad (1)$$

where y_j^r and y_j^p were the real and predicted PGA of the jth earthquake, respectively. N is the total number of earthquakes.

The T-data of each PGA range in **Table 2** was randomly split into training (64%), validation (16%), and test (20%) sets. We trained the network on one NVIDIA RTX 2080 GPU. We updated the CNN parameters using the Adam optimizer with $\beta_1 = 0.9$, $\beta_2 = 0.999$, and decay = 0, and learning rate = 0.001 (Kingma and Ba, 2015). During the train process, the CNN was updated by evaluating and reducing the loss on a batch-by-batch basis with batch size = 32. When the loss of the validation dataset was larger than the one of the training dataset for five epochs successively, the training process was stopped. **Supplementary Figure 3** illustrates the typical training process of the CNN.

RESULTS

Effect of Input

In this section, we studied the effects of the input on the PGA predictions using CNN. First, the effects of adding one more scale of P-wave time history data or spectrogram were studied as an initial study to understand if adding one different measure of the input help the PGA prediction or not. The means of the RMSLE of 15 repeated trials of the 2,000 test data of these cases are summarized in **Supplementary Table 1**. The results of using only a single scale of the P-wave time history, i.e., scale of 250 gal, are also listed in the same table for comparison. The results show that adding one more scale of P-wave time history data or spectrogram reduced the RMSLE values quite a lot, especially when one scale of the spectrogram was included.

Next, the effects of combinations of three different scales of P-wave time history data were studied. These results were also compared to the ones using only a single scale of the P-wave time history data (Case TH1). These are the five scales of P-wave time history data that were considered: 2.5, 8, 25, 80, and 250 gal. In total, one single-scale (Case TH1) and 10 different combinations of these five scales (Case TH2 to TH11) were studied, as listed in **Table 3**. The box plots of the RMSLE of 15 repeated trials of the 2,000 test data are plotted in **Figure 3**. Apparently, all the combinations of three different scales of P-wave time history data outperformed the single-scale one. Among the combinations of the three different scales of P-wave time history data, the RMSLE of Case TH5 to TH8 is relatively smaller than the others, as can also be observed from the mean of the RMSLE as listed in **Table 3**. Nevertheless, these results indicate that combining different scales of P-wave time history data helped the CNN extract more informative features and achieve a better PGA prediction.

Since only the maximum absolute acceleration value of the entire time history of seismic waves is the target output of the CNN, it is possible the signs of the P-wave time history are not so informative, but the amplitude may already provide the necessary information. Therefore, for the input data of CNN, we tried to replace the raw P-wave time history data of the studied combinations with the absolute ones. The box plots of the RMSLE of 15 repeated trials of the 2,000 test data of these combinations

using absolute values are plotted in **Figure 4**. Again, all of the combinations of the three different scales of P-wave time history data outperformed the single-scale one. Based on these results, taking the absolute value of P-wave time history data seems to help the CNN predict the PGA more accurately because the errors are lower in general, and the mean of the RMSLE of all the 11 cases using absolute values are 0.02∼0.03 smaller than the ones using raw values, as listed in **Table 3**. Besides, the mean of the RMSLE of Case TH6 (the combinations of 2.5++25+250 scales) was the smallest one. Since both the mean and the box plot of the RMSLE of Case TH6 outperforms the others, the combination of 2.5 + 25 + 250 scales using absolute values was selected.

TABLE 3 | The details of the combinations and the RMSLE of cases TH1 to TH11.

Case	Combination of scales*	RMSLE	
		Raw	Absolute
TH1	E	0.6439	0.6169
TH2	A + B + C	0.6174	0.5878
TH3	A + B + D	0.6089	0.5859
TH4	A + B + E	0.6084	0.582
TH5	A + C + D	0.6084	0.5856
TH6	A + C + E	0.6043	0.5740
TH7	A + D + E	0.6044	0.5827
TH8	B + C + D	0.6051	0.5827
TH9	B + C + E	0.6057	0.5829
TH10	B + D + E	0.6111	0.5866
TH11	C + D + E	0.6171	0.5967

**Scale A: 0∼2.5 cm/s^2; Scale B: 0∼8 cm/s^2; Scale C: 0∼25 cm/s^2; Scale D: 0∼80 cm/s^2; Scale E: 0∼250 cm/s^2.*

Next, the effects of including a spectrogram on the PGA prediction using CNN were studied. Because the range of the spectrogram amplitude of small and large earthquakes was not as large as the range of the time histories' amplitudes, only three scales of the spectrogram were considered herein: 0∼1, 0∼20, and 0∼40 gal/Hz. In total, five combinations of the best studied combinations of three different scales of P-wave time history data (Case TH6), and the three scales of the spectrogram were studied as listed in **Table 4**: cases TH6+F3, TH6+F12, TH6+F13, TH6+F23, and TH6+F123. The box plots of the RMSLE of 15 repeated trials of the 2,000 test data are plotted in **Figure 5**. It is evident that including the spectrogram can achieve much smaller RMSLE values than the one without any spectrogram. These results indicate that combining the frequency domain with the time domain P-wave data helped the CNN understand more deeply the P-wave data for PGA prediction. Among the five cases, case TH6+F12, which includes the smallest two scales of the spectrogram, has the smallest RMSLE value, as can also be observed in **Table 4**, hence it should be employed in future studies. Finally, the procedures to obtain the multi-domain and multi-scale input for the CNN as described previously are summarized in **Figure 6**.

Results of the T-Data

Based on the results of the input study, we took case TH6+F12, which has three scales of the absolute value of the P-wave time history data and two scales of the Fourier spectrograms of the original value of the P-wave data, as the final input of

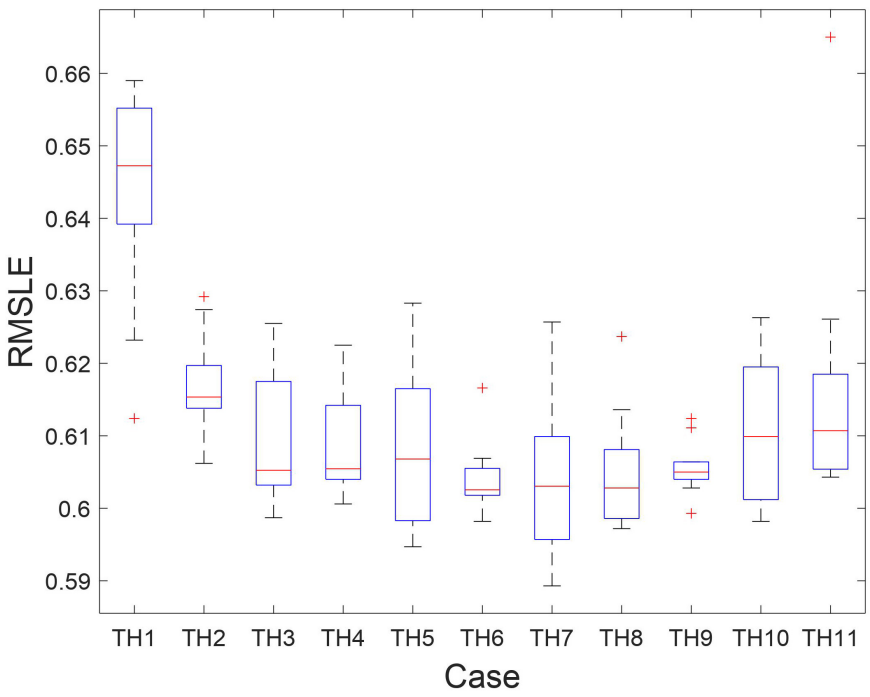

FIGURE 3 | The box plots of the RMSLE of the Cases TH1 to TH11 (using raw values of time history data).

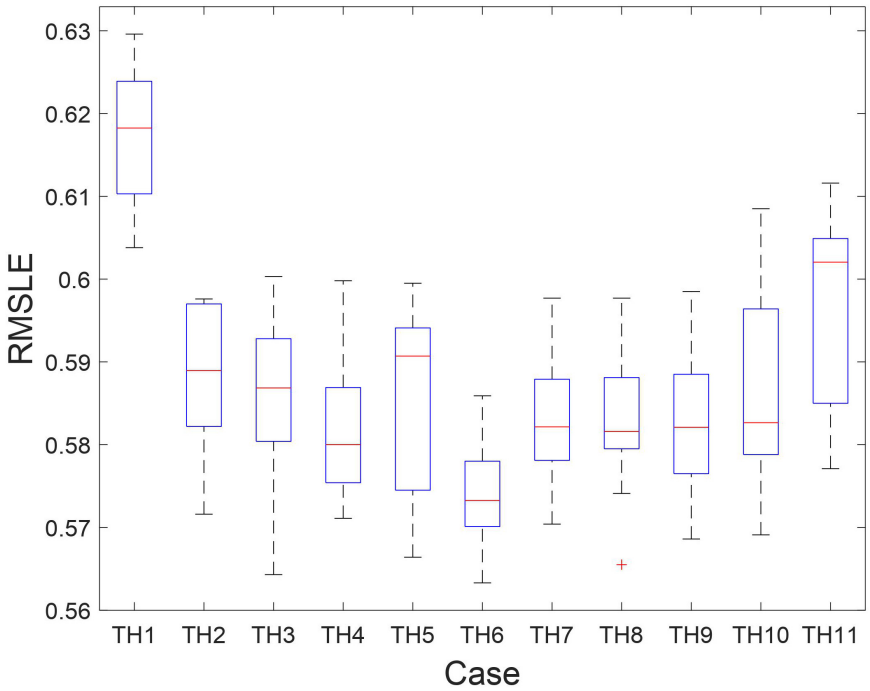

FIGURE 4 | The box plots of the RMSLE of the Cases TH1 to TH11 (using absolute values of time history data).

the CNN used in this study. The predicted PGA distribution of the 2,000 test data is illustrated in **Figure 7A**. Besides, the predicted PGA distribution of all 10,000 T-data is illustrated in **Figure 7B**. Apparently, the PGA distributions of the test data and all the T-data are quite similar. The RMSLE of all the T-data was still quite small at 0.454, which indicates that overfitting had not occurred. For easier comparison to other approaches, the standard variation (σ) of the errors between the predicted and real PGAs in natural logarithmic scale of all the T-data was also calculated, and its value was 0.512.

The PGA distribution using the best combination, case TH6+F12, can be found in **Figure 7**. Despite most of the predicted PGAs being quite close to the real PGAs, there are still some earthquakes with larger real PGAs that are apparently underestimated (e.g., a PGA greater than 80 gal). These earthquakes actually belong to the Chi-Chi earthquake event on September 21, 1999, as marked in **Figure 7** and separately illustrated in **Figure 8A**. This is mainly because only the first few seconds of P-wave data is employed to predict PGA, but the Chi-Chi earthquake event had at least two asperities, which makes the slip propagation process quite long and complex (Ma et al., 2001). More specifically, the Chi-Chi earthquake intensity was predominantly contributed by the major asperity rupture 13 s after another minor one, making the PGA prediction based on the first few seconds of the P-wave harder. Hsu et al. (2013) has illustrated the PGA can be predicted much closer to the real PGA if the information of the longer P-wave data is used. More details about the discussion the PGA prediction of the Chi-Chi earthquake event using the SVR approach are in Hsu et al. (2013). Herein, the PGA prediction results using the SVR approach with the same first 3 s of time history after the triggering of the Chi-Chi earthquake are illustrated in **Figure 8B** for comparison. The RMSLE of the Chi-Chi earthquake using the proposed CNN and the SVR approaches was 1.419 and 1.867, respectively. Evidently, the proposed CNN approach can predict the PGAs of these earthquakes more accurately than the SVR approach.

TABLE 4 | The details and RMSLE of the combinations of cases TH6+F3 to TH6+F123.

Case	Combination of scales	RMSLE
TH6+F3	A + C + E + C′*	0.5287
TH6+F12	A + C + E + A′ + B′	0.4911
TH6+F13	A + C + E + A′ + C′	0.5067
TH6+F23	A + C + E + B′ + C′	0.5197
TH6+F123	A + C + E + A′ + B′ + C′	0.5043

** Scale A′: 0∼1 gal/Hz; Scale B′: 0∼20 gal/Hz; Scale C′: 0∼40 gal/Hz.*

Results of the Test Earthquakes

In addition to the T-data, we tested the performance of the proposed CNN approach using the independent 2016 Meinong earthquake event and the 2018 Hualien earthquake event. The predicted PGA distribution of these two earthquake events are illustrated in **Figures 8C,D**. The RMSLE of the Meinong and Hualien earthquake events are 0.561 and 0.476, respectively. It seems the proposed CNN can, in general, predict the PGAs of separate damaging earthquake events with anticipated accuracy.

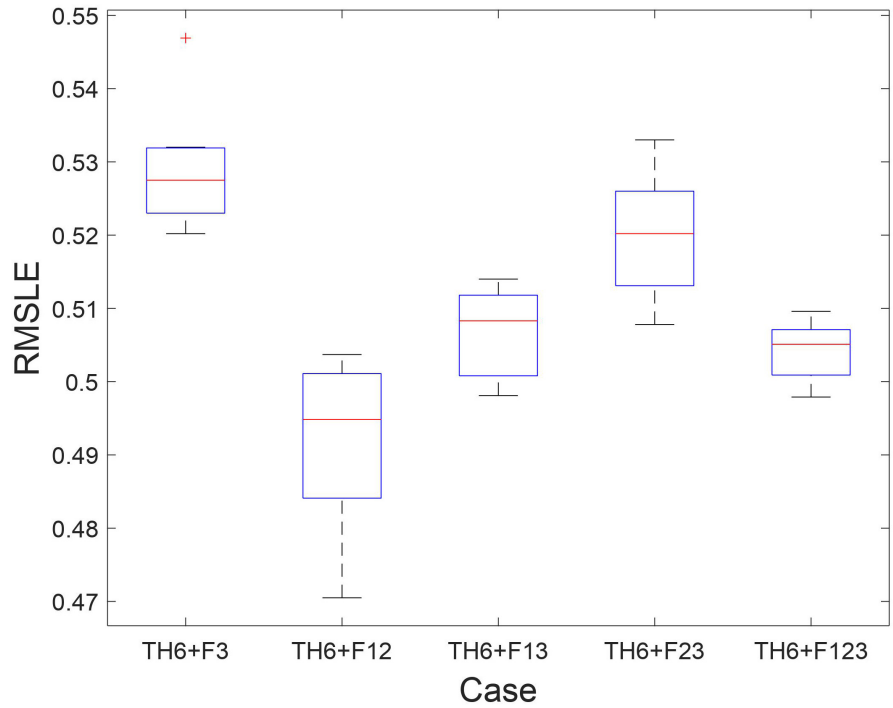

FIGURE 5 | The box plots of the RMSLE of the Cases TH6+F3 to TH6+F123.

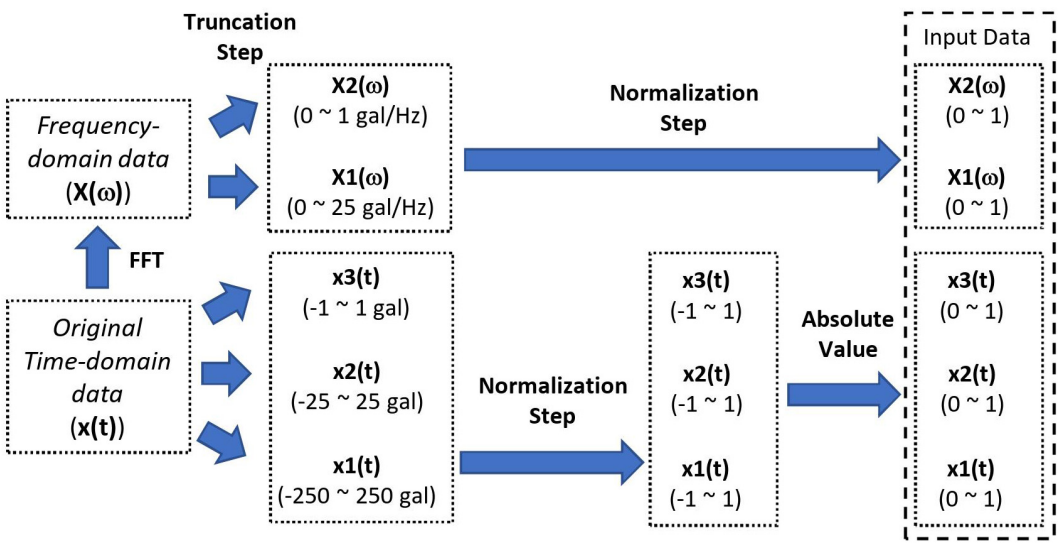

FIGURE 6 | The summarized procedures to obtain the multi-domain and multi-scale input for the CNN.

Besides, in order to understand the performance of PGA prediction using the CNN approach during a typical earthquake event with a smaller magnitude (between 5 and 5.5), the predicted PGA distribution during the M5.3 earthquake is illustrated in **Figure 8E**. The RMSLE of the PGA prediction results of the M5.3 event is only 0.378. It seems the proposed CNN approach can predict the PGAs of the typical earthquake event with a smaller magnitude quite well. For easier comparison to other approaches, the standard variation (σ) of the errors between the predicted and real PGAs in natural logarithmic scale of these three test earthquake events and the Chi-Chi earthquake event was also listed in **Table 5**.

To further understand the potential alert performance using the proposed CNN of these two earthquake events, the confusion matrix was employed herein. The threshold was set to 25 gal, which is identical to the one used in the onsite EEW algorithm

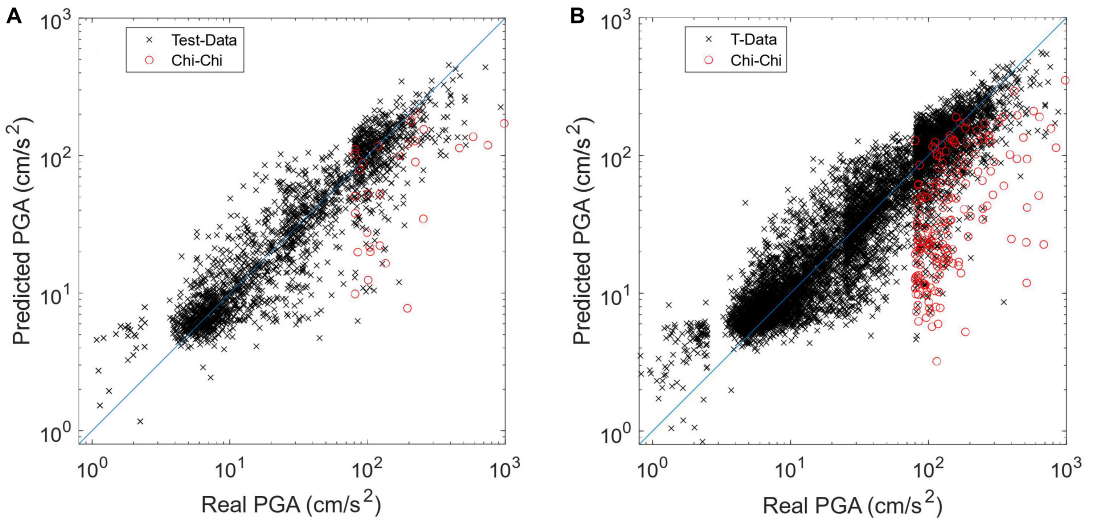

FIGURE 7 | The predicted PGA distribution of **(A)** the 2,000 test data and **(B)** all the 10,000 T-data.

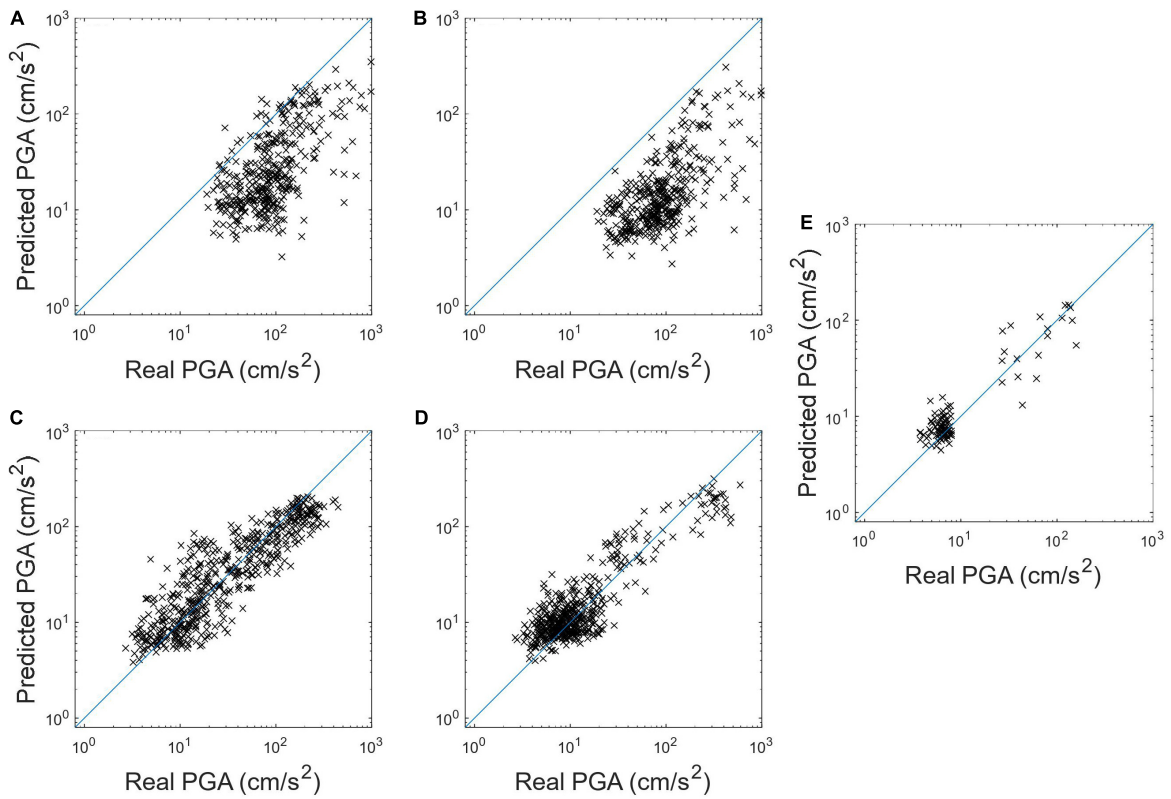

FIGURE 8 | The predicted PGA distribution of the Chi-Chi earthquake event using **(A)** the proposed CNN approach and **(B)** the SVR approach in Hsu et al. (2013). The predicted PGA distribution of **(C)** the Meinong earthquakes, **(D)** the Hualien earthquakes, and **(E)** the M5.3 earthquake using the proposed CNN approach.

of the EEW System of the National Center for Research on Earthquake Engineering, Taiwan (NEEWS) during these two earthquake events (Hsu et al., 2016, 2018). In order to focus on the discussion of the accuracy of the predicted PGAs, the lead-time of all the earthquakes was assumed as valid. As a result, as summarized in the confusion matrix of **Figure 9A**, if both the predicted PGA and the real PGA are ≥25 gal, we considered this result a true positive ("TP"). Conversely, if the predicted PGA is ≥25 gal, but the real PGA never reached the threshold, we considered this result a false positive ("FP"). If both the

TABLE 5 | The summary of the metrics of the proposed CNN.

Metrics	T-data		Chi-Chi earthquake		Meinong earthquake		Hualien earthquake		M5.3 earthquake	
	w/o tolerance	w/tolerance	w/o tolerance	w/tolerance	w/o tolerance	w/tolerance	w/o tolerance	w/tolerance	w/o tolerance	w/tolerance
RMSLE	0.454		1.419		0.561		0.476		0.378	
Standard deviation	0.512		0.770		0.596		0.498		0.383	
Precision (%)	97.18	99.78	100.00	100.00	81.79	99.29	82.27	97.70	100.00	100.00
Recall (%)	88.31	97.61	42.82	64.49	90.51	100.00	92.31	100.00	84.21	100.00
F1-Score (%)	91.11	98.69	59.96	78.41	85.93	99.64	87.27	98.84	91.43	100.00

predicted PGA and the real PGA are <25 gal, we considered this result a true negative ("TN"). If the final ground motion amplitude reached the threshold, but the predicted PGA did not, then we considered this result a false negative ("FN"). The performance metrics based on the confusion matrix, such as F1-score, precision, and recall are shown in **Table 5**.

As proposed by Meier (2017), to evaluate the classification performance of the EEW system, a tolerance range can be used. We use the same tolerance as the NEEWS (Hsu et al., 2018) during these three earthquake events, i.e., a ± 1 level of CWB intensity scale, to evaluate the performance of the proposed CNN herein, as shown in **Figure 9B**. The performance metrics based on the confusion matrix with a tolerance are also summarized in **Table 5**. The values of the precision, recall, and F1-score when no tolerance is allowed are approximately between 81% and 100%, while the ones when the tolerance is allowed increased to approximately at least 97%. Hence in general, the overall potential alert performance using the proposed CNN during these three test earthquake events seems quite promising.

In Comparison With the SVR and GMPE-Based Approaches

As described in the Introduction section, the SVR approach developed previously has been employed in the NEEWS in Taiwan and has successfully demonstrated its ability during several damaging earthquakes. Six P-wave features are extracted from the first 3 s of the vertical acceleration and then used as the input to the SVR prediction model for PGA prediction. The same T-data were used herein to know if the predicted PGA of the proposed CNN is more accurate than the one using the SVR or not. The PGA distributions of the T-data earthquakes using the SVR prediction model of the NEEWS are illustrated in **Figure 10A**, with the RMSLE and σ value equal to 0.748 and 0.664, respectively. These values are much larger than the ones using the proposed CNN approach. These results indicate the superiority of the CNN for PGA prediction.

Many EEW systems around the world use a ground motion prediction equation (GMPE) to forecast shaking based on estimates of the source parameters (location and magnitude). For comparison, under the assumption that the location and magnitude could be accurately estimated, the PGA could be predicted based on the GMPE. The GMPE accommodating site effects developed by Jean et al. (2006) was employed herein and the same T-data were used to compare the proposed CNN with the typical GMPE-based approach. The PGA distributions of the T-data earthquakes using the GMPE-based approach are illustrated in **Figure 10B**, with the RMSLE and σ value equal to 0.870 and 0.896, respectively. Again, these values are much larger than the ones using the proposed CNN approach, which indicates the accuracy of the CNN for PGA prediction is quite promising.

DISCUSSION

In this study, the CNN is proposed as having successfully predicted the PGA of the incoming seismic wave at the same site based on the information of the first 3 s of P-wave data

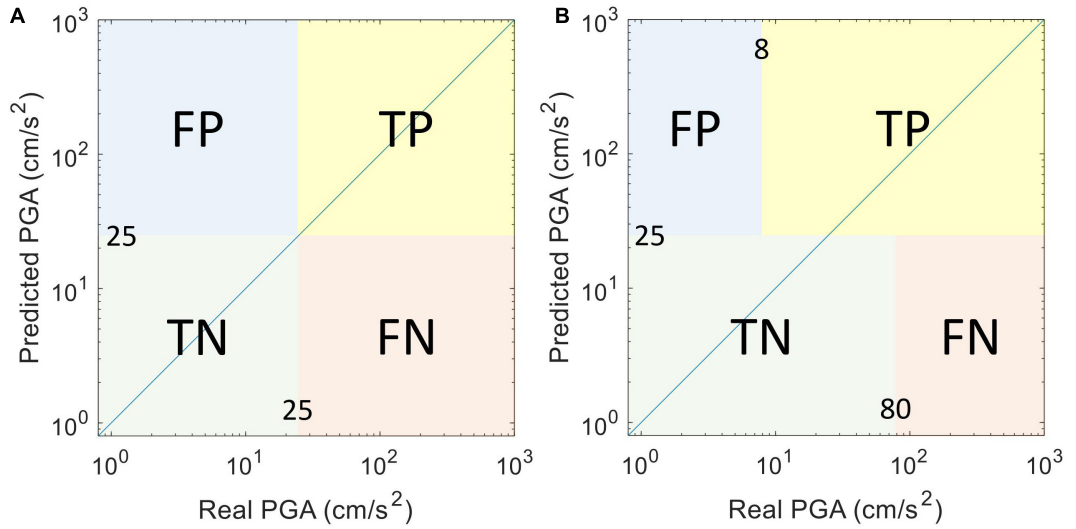

FIGURE 9 | The confusion matrix **(A)** without a classification tolerance and **(B)** with a classification tolerance range of ± 1 level of CWB intensity scale.

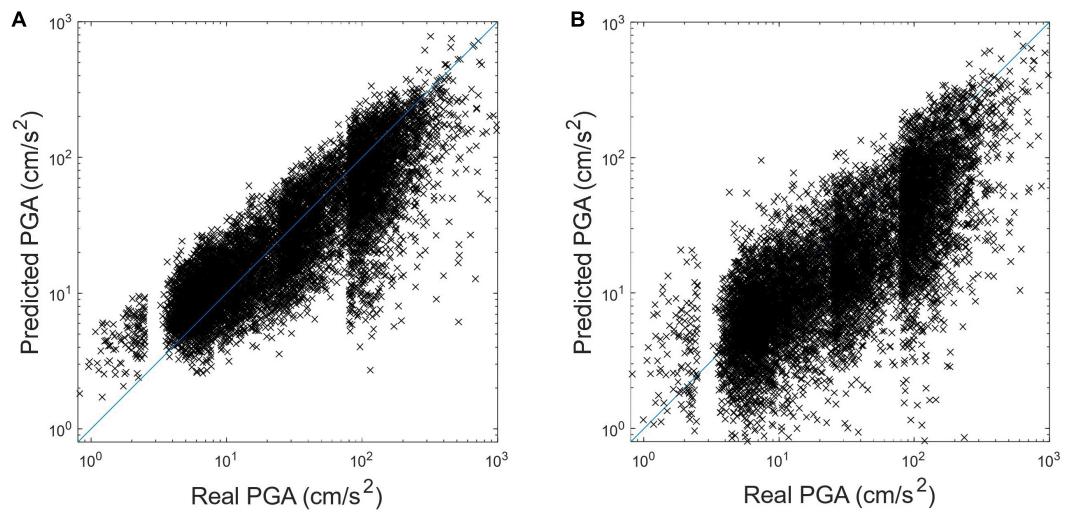

FIGURE 10 | The predicted PGA distribution of the 10,000 T-data earthquakes using **(A)** the SVR approach in Hsu et al. (2013), and **(B)** the GMPE-based approach.

after an event is triggered. Due to this specific application to EEW, the proposed CNN is specially designed. The novel multi-scale input of the CNN is proposed to deal with the enormous differences of the amplitudes of the input data. The multi-domain information of the P-wave data (both the time history and Fourier spectrogram) is also proposed as helping to achieve better PGA prediction accuracy for the CNN. The multi-scale and multi-domain input data are treated as different aspects of the P-wave data. Moreover, the absolute value of the time history data is employed when input to the CNN, instead of the raw one, since only the maximum absolute acceleration value of the coming seismic wave is needed to be predicted for the CNN. Note that we aim to propose using the combination of different scales of both the P-wave time history data and spectrogram, but not to propose the best combination of that. Therefore, not all the possible combinations were considered in this study.

The proposed arrangement of the input data shows its superiority to the one directly inputting the raw P-wave data into the CNN. In addition, the proposed CNN approach also shows its superiority for PGA prediction without extracting any P-wave features in advance to the SVR approach employed by the NEEWS where P-wave features must be extracted in advance.

Two independent damaging earthquake events that occurred recently in Taiwan were employed to understand the capability of the proposed CNN. The results show the accuracy of the predicted PGAs of these earthquakes are quite acceptable. The potential alert performance using the proposed CNN under the assumption that the lead-time of all the earthquakes were valid was also studied. The F1-score of the proposed CNN during these

two damaging earthquake events was approximately 93.4% and increased to approximately 98.8% if the tolerance of ± 1 level of CWB intensity scale was acceptable. Besides, the proposed CNN also shows its performance during a typical smaller earthquake event (Mw = 5.3) could be also quite promising.

Based on the results of the T-data and the three test earthquake events, the proposed CNN approach seems quite promising for PGA prediction. However, for the Chi-Chi earthquake event with a long and complex slip propagation process, using only the first few seconds of P-wave data for PGA prediction is still very difficult. This limitation of the proposed CNN approach has been pointed out, and further studies are still required to develop a PGA prediction model for such an earthquake event. One of the possible approaches is to train multiple CNNs for longer durations and change to different ones as the earthquake progresses for better PGA prediction; however, the response time will be sacrificed, as discussed in Hsu et al. (2013) using the SVR approach.

The SVR approach and the proposed CNN approach use seismic wave measured at one seismic station and predict the coming peak ground shaking of the same station. On the other hand, the GMPE-based approach forecast shaking based on estimates of the source parameters. Based on the experience of two real earthquake events, the accuracy of the predicted PGAs of SVR and GMPE-based approaches was quite similar, but the SVR approach could provide a longer lead time for near-epicentral sites (Hsu et al., 2018, 2021). We believe the CNN approach would show similar performance to the SVR approach because their computation time is similar. There are other approaches that use shaking to directly predict shaking, such as the propagation of local undamped motion (PLUM) and the approximation by local pseudo-hypocenter attenuation (ALPHA) approaches developed by the JMA (Kodera et al., 2018; Kodera, 2019). Based on the results of the first-year performance of the PLUM approach, this kind of approach seems to have great potential to provide a more accurate prediction of ground motion intensity and a longer lead time than the GMPE-based approach, especially for destructive earthquakes. However, it is still difficult to provide timely ground motion predictions for near-epicentral sites. Nevertheless, more researches on the performance, comparison, and combination of different EEW approaches are necessary in the future in order to provide better EEW for the public.

DATA AVAILABILITY STATEMENT

The original contributions presented in the study are included in the article/**Supplementary Material**, further inquiries can be directed to the corresponding author/s.

AUTHOR CONTRIBUTIONS

T-YH designed the research study and wrote sections of the manuscript. C-WH constructed the CNN and ran the analysis. Both authors contributed to the article and approved the submitted version.

FUNDING

This research is partially supported by the Taiwan Building Technology Center from The Featured Areas Research Center Program within the framework of the Higher Education Sprout Project by the Ministry of Education in Taiwan.

ACKNOWLEDGMENTS

The authors would like to thank the Taiwan Strong Motion Instrument Program operated by Central Weather Bureau (CWB) in Taiwan for providing high-quality strong ground motions caused by earthquakes around Taiwan.

SUPPLEMENTARY MATERIAL

The Supplementary Material for this article can be found online at: https://www.frontiersin.org/articles/10.3389/feart.2021.626908/full#supplementary-material

REFERENCES

Abdel-Hamid, O., Mohamed, A., Jiang, H., Deng, L., Penn, G., and Yu, D. (2014). Convolutional neural networks for speech recognition. *IEEE/ACM Trans. Audio Speech Lang. Process.* 22, 1533–1545.

Allen, R. M., and Melgar, D. (2019). Earthquake early warning: advances, scientific challenges, and societal needs. *Annu. Rev. Earth Planet. Sci.* 47, 361–388. doi: 10.1146/annurev-earth-053018-060457

Böse, M., Heaton, T., and Hauksson, E. (2012). Rapid *Estimation* of earthquake source and ground-motion parameters for earthquake early warning using data from a single three-component broadband or strong-motion sensor. *Bull. Seismol. Soc. Am.* 102, 738–750. doi: 10.1785/0120110152

Cuéllar, A., Espinosa-Aranda, J. M., Suarez, R., Ibarrola, G., and Uribe, A. (2014). "The Mexican seismic alert system (SASMEX): its alert signals, broadcast results and performance during the M 7.4 Punta Maldonado earthquake of March 20th, 2012," in *Early Warning for Geological Disasters*, eds F. Wenzel and Z. Zschau (Berlin: Springer-Verlag), 71–87. doi: 10.1007/978-3-642-12233-0_4

Cui, Z., Chen, W., and Chen, Y. (2016). Multi-scale convolutional neural networks for time series classification. *arXiv* [Preprint] arXiv: 1603.06995,

Fujinawa, Y., and Noda, Y. (2013). Japan's earthquake early warning system on 11 March 2011: performance, shortcomings, and changes. *Earthq. Spectra* 29, S341–S368.

Hsu, T. Y., Huang, S. K., Chang, Y. W., Kuo, C. H., Lin, C. M., Chang, T. M., et al. (2013). Rapid on-site peak ground acceleration estimation based on support vector regression and P-wave features in Taiwan. *Soil Dyn. Earthq. Eng.* 49, 210–217. doi: 10.1016/j.soildyn.2013.03.001

Hsu, T. Y., Kuo, C. H., Wang, H. H., Chang, Y. W., Lin, P. Y., and Wen, K. L. (2021). The realization of an earthquake early warning system for schools and its performance during the 2019 ML 6.3 Hualien (Taiwan) earthquake. *Seismol. Res. Lett.* 92, 342–351. doi: 10.1785/0220190329

Hsu, T. Y., Lin, P. Y., Wang, H. H., Chiang, H. W., Chang, Y. W., and Kuo, C. H. (2018). Comparing the performance of the NEEWS earthquake early warning system against the CWB system during the 6 February 2018 Mw 6.2 Hualien earthquake. *Geophys. Res. Lett.* 45, 6001–6007.

Hsu, T. Y., Wang, H. H., Lin, P. Y., Lin, C. M., Kuo, C. H., and Wen, K. L. (2016). Performance of the NCREE's on-site warning system during the 5 February 2016 Mw 6.53 Meinong earthquake. *Geophys. Res. Lett.* 43, 8954–8959. doi: 10.1002/2016gl069372

Hsu, T. Y., Wu, R. T., Liang, C. W., Kuo, C. H., and Lin, C. M. (2020). Peak ground acceleration estimation using P-wave parameters and horizontal-to-vertical spectral ratios. *Terr. Atmos. Ocean. Sci.* 31, 1–8. doi: 10.3319/tao.2019.07.04.01

Jean, W. Y., Chang, Y. W., Wen, K. L., and Loh, C. H. (2006). Early estimation of seismic hazard for strong earthquakes in Taiwan. *Nat. Hazards* 37, 39–53. doi: 10.1007/s11069-005-4655-y

Jozinovic, D., Lomax, A., Stajduhar, I., and Michelini, A. (2020). Rapid prediction of earthquake ground shaking intensity using raw waveform data and a convolutional neural network. *Geophys. J. Int.* 222, 1379–1389. doi: 10.1093/gji/ggaa233

Kanamori, H. (2005). Real-time seismology and earthquake damage mitigation. *Annu. Rev. Earth Planet. Sci.* 33, 195–214. doi: 10.1146/annurev.earth.33.092203.122626

Kingma, D. P., and Ba, J. (2015). "Adam: a method for stochastic optimization," in *Proceedings of the 3rd International Conference on Learning Representations (ICLR), Conference Track Proceedings*, San Diego, CA.

Kodera, Y. (2019). An earthquake early warning method based on Huygens principle: Robust ground motion prediction using various localized distance-attenuation models. *J. Geophys. Res.* 124, 12981–12996. doi: 10.1029/2019jb017862

Kodera, Y., Saitou, J., Hayashimoto, N., Adachi, S., Morimoto, M., Nishimae, Y., et al. (2016). Earthquake early warning for the 2016 Kumamoto earthquake: performance evaluation of the current system and the next-generation methods of the Japan meteorological agency. *Earth Planets Space* 68:202.

Kodera, Y., Yamada, Y., Hirano, K., Tamaribuchi, K., Adachi, S., Hayashimoto, N., et al. (2018). The propagation of local undamped motion (PLUM) method: a simple and robust seismic wavefield estimation approach for earthquake early warning. *Bull. Seismol. Soc. Am.* 108, 983–1003. doi: 10.1785/0120170085

LeCun, Y., Bengio, Y., and Hinton, G. (2015). Deep learning. *Nature* 521, 436–444.

Ma, K. F., Mori, J., Lee, S. J., and Yu, S. B. (2001). Spatial and temporal distribution of slip for the 1999 Chi-Chi, Taiwan, earthquake. *Bull. Seismol. Soc. Am.* 91, 1069–1087. doi: 10.1785/0120000728

Meier, M. A. (2017). How "good" are real-time ground motion predictions from earthquake early warning systems? *J. Geophys. Res. Solid Earth* 122, 5561–5577. doi: 10.1002/2017jb014025

Mousavi, S. M., Zhu, W., Sheng, Y., and Beroza, G. C. (2019). CRED: a deep residual network of convolutional and recurrent units for earthquake signal detection. *Sci. Rep.* 9:10267.

Nair, V., and Hinton, G. E. (2010). "Rectifed linear units improve restricted boltzmann machines," in *Proceedings of the 27th International Conference on International Conference on Machine Learning, ICML'10*, (Madison, WI: Omnipress), 807–814.

Nakamura, Y., Saita, J., and Sato, T. (2011). On an earthquake early warning system (EEW) and its applications. *Soil Dyn. Earthq. Eng.* 31, 127–136. doi: 10.1016/j.soildyn.2010.04.012

Odaka, T., Ashiya, K., Tsukada, S., Sato, S., Ohtake, K., and Nozaka, D. (2003). A new method of quickly estimating epicentral distance and magnitude from a single seismic record. *Bull. Seismol. Soc. Am.* 93, 526–532. doi: 10.1785/0120020008

Perol, T., Gharbi, M., and Denolle, M. (2018). Convolutional neural network for earthquake detection and location. *Sci. Adv.* 4:e1700578. doi: 10.1126/sciadv.1700578

Sajjad, M., Khan, S., Hussain, T., Muhammad, K., Sangaiah, A. K., and Castiglione, A. (2018). CNN-based anti-spoofing two-tier multi-factor authentication system. *Pattern Recognit. Lett.* 126, 123–131. doi: 10.1016/j.patrec.2018.02.015

Satriano, C., Wu, Y. M., Zollo, A., and Kanamori, H. (2011). Earthquake early warning: concepts, methods and physical grounds. *Soil Dyn. Earthq. Eng.* 31, 106–118. doi: 10.1016/j.soildyn.2010.07.007

Shrestha, A., and Dang, J. (2020). Deep learning-based real-time auto classification of smartphone measured bridge vibration data. *Sensors* 20:2710. doi: 10.3390/s20092710

Silver, D., Huang, A., Maddison, C., Guez, A., Sifre, L., van den Driessche, G., et al. (2016). Mastering the game of Go with deep neural networks and tree search. *Nature* 529, 484–489. doi: 10.1038/nature16961

Srivastava, N., Hinton, G., Krizhevsky, A., Sutskever, I., and Salakhutdinov, R. (2014). Dropout: a simple way to prevent neural networks from overfitting. *J. Mach. Learn. Res.* 15, 1929–1958.

Wu, R. T., and Jahanshahi, M. R. (2019). Deep convolutional neural network for structural dynamic response estimation and system identification. *J. Eng. Mech.* 145:04018125. doi: 10.1061/(asce)em.1943-7889.0001556

Wu, Y. M., and Kanamori, H. (2005). Rapid assessment of damaging potential of earthquakes in Taiwan from the beginning of P waves. *Bull. Seismical Soc. Am.* 95, 1181–1185. doi: 10.1785/0120040193

Wu, Y. M., Mittal, H., Huang, T. C., Yang, B. M., Jan, J. C., and Chen, S. K. (2019). Performance of a low-cost earthquake early warning system (P-Alert) and Shake Map production during the 2018 Mw 6.4 Hualien, Taiwan, earthquake. *Seismol. Res. Lett.* 90, 19–29. doi: 10.1785/0220180170

Xu, Y., Wei, S., Bao, Y., and Li, H. (2019). Automatic seismic damage identification of reinforced concrete columns from images by a region-based deep convolutional neural network. *Struct. Control Health Monit.* 26:e2313. doi: 10.1002/stc.2313

Yamada, M., Tamaribuchi, K., and Wu, S. (2014). Faster and more accurate earthquake early warning system–combination of velocity and acceleration-type seismometers. *J. Japan Assoc. Earthq. Eng.* 14-4, 21–34. 2014.8. (in Japanese), doi: 10.1007/978-3-540-72241-0_3

Yu, Y., Wang, C., Gu, X., and Li, J. (2018). A novel deep learning-based method for damage identification of smart building structures. *Struct. Health Monit.* 18, 1–21.

Zollo, A., Amoroso, O., Lancieri, M., Wu, Y. M., and Kanamori, H. (2010). A threshold-based earthquake early warning using dense accelerometer networks. *Geophys. J. Int.* 183, 963–974. doi: 10.1111/j.1365-246x.2010.04765.x

Conflict of Interest: The authors declare that the research was conducted in the absence of any commercial or financial relationships that could be construed as a potential conflict of interest.

frontiers in Earth Science

ORIGINAL RESEARCH
published: 11 June 2021
doi: 10.3389/feart.2021.684421

Earthquake Early Warning System in Israel—Towards an Operational Stage

Ran N. Nof[1]*, *Itzhak Lior*[2,3] *and Ittai Kurzon*[1]

[1]The Geological Survey of Israel, Jerusalem, Israel, [2]Université Côte d'Azur, CNRS, Observatoire de la Côte d'Azur, IRD, Géoazur, Valbonne, France, [3]The Institute of Earth Sciences, The Hebrew University, Jerusalem, Israel

The Geological Survey of Israel has upgraded and expanded the national Israeli Seismic Network (ISN), with more than 110 stations country-wide, as part of the implementation of a governmental decision to build a national Earthquake Early Warning (EEW) system named TRUAA. This upgraded seismic network exhibits a high station density and fast telemetry. The stations are distributed mainly along the main fault systems, the Dead Sea Transform, and the Carmel-Zfira Fault, which may potentially produce M_w 7.5 earthquakes. The system has recently entered a limited operational phase, allowing for initial performance estimation. Real-time performance during eight months of operation (41 earthquakes) matches expectations. Alert delays (interval between origin-time and Earthquake Early Warning alert time) are reduced to as low as 3 s, and source parameter errorstatistics are within expected values found in previous works using historical data playbacks. An evolutionary alert policy is implemented based on a magnitude threshold of Mw 4.2 and peak ground accelerations exceeding 2 cm/s^2. A comparison between different ground motion prediction equations (GMPE) is presented for earthquakes from Israel and California using median ground motion prediction equations values. This analysis shows that a theoretical GMPE produced the best agreement with observed ground motions, with less bias and lower uncertainties. The performance of this GMPE was found to improve when an earthquake specific stress drop is implemented.

Keywords: TRUAA, earthquake early warning, epic, Israel, ground motion prediction

OPEN ACCESS

Edited by:
Masumi Yamada,
Kyoto University, Japan

Reviewed by:
Gemma Cremen,
University College London,
United Kingdom
Rosemary Fayjaloun,
Bureau de Recherches Géologiques et Minières, France

***Correspondence:**
Ran N. Nof
ran.nof@gmail.com

Specialty section:
This article was submitted to Geohazards and Georisks, a section of the journal Frontiers in Earth Science

Received: *23 March 2021*
Accepted: *21 May 2021*
Published: *11 June 2021*

Citation:
Nof RN, Lior I and Kurzon I (2021) Earthquake Early Warning System in Israel—Towards an Operational Stage. Front. Earth Sci. 9:684421. doi: 10.3389/feart.2021.684421

INTRODUCTION

Earthquake Early Warning Systems (EEWS) are a tool to reduce earthquake risk. Their basic approach is to issue an alert as soon as possible following the occurrence of an earthquake, before damaging seismic waves arrive at a target. Some EEWS are based on identifying P-wave onsets or a preset acceleration threshold crossing, and to raise an alert that can be used to mitigate the effects of the expected ground shaking. Earthquake detection, by either single or multiple seismic or geodetic stations, can be done "on-site" close to the target or "regional" close to the source (Nakamura, 1988). Various algorithms are currently available—operational or under development around the world based on point-source, finite fault, and ground motion models (Allen and Melgar, 2019 and references therein).

Israel's main seismic risk is attributed to the tectonically-active plate boundary fault system of the Dead Sea Transform (DST) and its branches (**Figure 1**) (e.g., Garfunkel et al., 1981), with earthquake magnitude potential of up to M_w7.5 (Hamiel et al., 2009). The increase in population density and in industrial and commercial infrastructures have amplified the

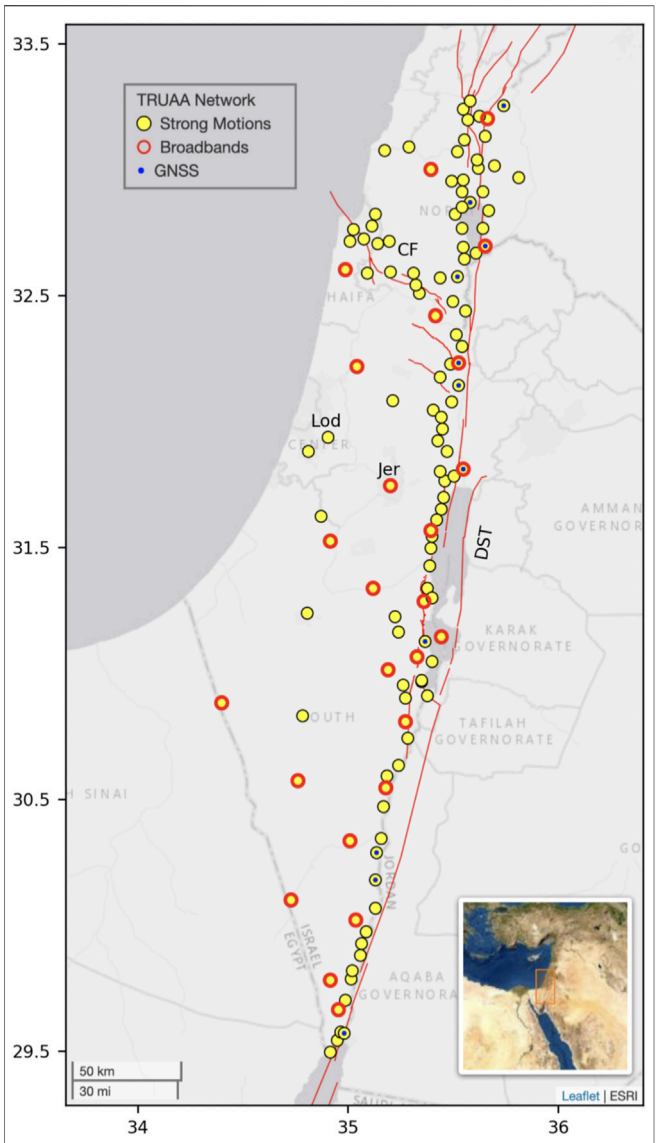

FIGURE 1 | Location map of TRUAA seismic stations network. Strong motion sensors are marked as yellow circles. Co-located broadbands are marked as red circles and GNSS receivers are marked as blue dots. Active faults (red lines) are after Sharon et al., 2020. DST—Dead Sea Transform, CF—Carmel Fault, Lod—Lod data center, Jer—Jerusalem data center.

seismic risk for Israel and led the Israeli government to appoint the Geological Survey of Israel (GSI) as responsible for establishing an EEWS, named TRUAA; TRUAA refers to the Hebrew word for the sounds of trumpet and of the traditional Jewish horn (Shofar), used for both, religious ceremonies and alerting (e.g. Joshua 6:20, Holy Bible: KJV).

The Israeli EEWS consists of three main components: 1) Seismic data acquisition system (Kurzon et al., 2020; 2) EEW Algorithm (Nof and Kurzon, 2021; 3) Dissemination system. While the former two are under the responsibility of the GSI, the latter is under the responsibility of the Home Front Command (HFC), of the Israeli Defense Force.

In Israel, several geographical and seismological considerations pose unique challenges for EEW. Since the country's shape is narrow and sub-parallel to the main hazardous fault system (DST is oriented north-south), most of the population lives in proximity to potential earthquakes. Thus, the main challenge is the expected short response times, defined as the interval between earthquake alert issuing time and S-wave arrival time at a certain location. In addition, the DST coincides with the international border and the seismic network is deployed only on its western side. Therefore, the performance of the system suffers from limited azimuthal coverage, which results in reduced accuracy and increased uncertainties for automatic earthquake locations (Nof and Allen, 2016; Nof et al., 2019). Finally, EEW optimization and calibration using real time or historical playbacks, as commonly used elsewhere (Nof and Allen, 2016; Cochran et al., 2017; Meier et al., 2020), is challenged by the low seismicity rate (e.g., ~ten times lower than California) and limited historical data.

TRUAA INFRASTRUCTURE AND ACQUISITION SYSTEM

Until 2017, the Israeli Seismic Network (ISN) consisted of 23 broadbands and short period sensors, collecting data in real-time at the Seismological Division data center formerly of the Geophysical Institute of Israel, located at the city of Lod (central Israel). Data acquisition and network geometry were not optimized for EEW, with high latencies (~3 s) and large data packets (~6 s), leading to poor performance in real-time (Nof and Allen, 2016).

TRUAA infrastructure follows one of the main principals set by the EEW international committee (Allen et al., 2012), requiring a state-of-the-art real-time seismic network, as the underlying foundation for efficient and reliable EEWS. Therefore, the ISN has gone through significant upgrades and modifications, since September 2017. In order to overcome the main challenge of short response times (see previous section), the network was designed to minimize alert delays, by densifying the station distribution (Kuyuk and Allen, 2013b) along the main seismic sources [DST and the Carmel-Zfira Fault System (CF)], and significantly reducing telemetry latencies. The resulting seismic network currently has 110 working stations, out of 121 planned stations, with below 1s data packets, and station-intervals of 5–10 km along the major faults (**Figure 1**). All stations are equipped with strong motion Titan accelerometers, and Centaur dataloggers, sampling in 200 samples per second; some (25 stations) have collocated broadband Trillium 120 s seismometers; seismic instrumentation is provided by Nanometrics. A full overview on TRUAA infrastructure is given by Kurzon et al. (2020). In order to increase reliability and robustness of the EEWS, several layers of redundancy were implemented at all network scales: 1) each station has two telemetry routes, the main and fast route, by ethernet or cellular, with latencies of 600–900 ms, and the backup route, by cellular or satellite, with latencies of 700–1500 ms; 2) there are two

data centers synchronized and working in parallel using an active-active cluster configuration, the main one in Jerusalem and the backup in Lod; 3) Each data center hosts two parallel acquisition and processing chains (hence, a total of four independent chains).

The acquisition system is based on Nanometrics' Apollo Servers which forward the data for both routine seismic monitoring procedures and the EEWS at each data center. Each data packet is multi-casted separately via the two routes and reaches each of the four separate acquisition systems. Since Jerusalem main data center is located ~20 km from the DST, this redundant configuration of four independent EEWS is expected to provide high robustness in case of a catastrophic event.

TRUAA EARTHQUAKE EARLY WARNING ALGORITHM

The collected seismic data is processed using the United States. West Coast ShakeAlert's Earthquake Point-source Integrated Code (EPIC) EEW algorithm (Given et al., 2018; Kohler et al., 2020), providing rapid alerts for potentially damaging earthquakes. The EPIC algorithm, formerly under the codename ElarmS (e.g. Chung et al., 2019), is a regional (network based) point source algorithm. In order to issue an alert, the algorithm requires P-wave detections by a minimum of four different stations and at least 40% of active stations in the P-phase wave-front area. The earthquake location is obtained by a 200 × 200 km grid search, in which the residuals of the calculated and observed arrival-times are minimized based on a one-dimensional layered global velocity model, AK135 (Kennett et al., 1995). Then, event magnitude is estimated from the hypocenteral distances combined with the peak displacement (Pd) values, calculated from accelerations or velocities measured at the different stations (Kuyuk and Allen, 2013a; Sadeh et al., 2014). The event's magnitude estimate used is the average of the estimates at all near-source stations and an uncertainty on this value is also computed but not used for alerting purposes. As time progress and additional data become available, the origin-time, location, Pd values and magnitude are all updated with higher accuracy (e.g. Kohler et al., 2020). Modifications and developments of ShakeAlert are carefully examined and implemented after adjustments to the local seismic network and conditions (Nof and Allen, 2016; Nof and Kurzon, 2021). The TRUAA EEWS consists of TRUAA's acquisition system, EPIC's Waveform Processor (WP), and Event Associator (EA) that identifies events and sends alerts to a Decision Module (DM) that forwards alerts based on a predefined magnitude and geographic location. ActiveMQ messaging system (Kohler et al., 2018; Chung et al., 2019) is used for communication between the modules. In our implementation, EPIC EA alert messages, limited to M > 2.5, are shared between all four DM instances and each DM finally converges the EA alerts to produce a single EEW alert with updating intervals of 1 s. The HFC listens to the DM alerts and is responsible for disseminating proper alerts to the public. Although the HFC alert dissemination system is actively working for various threats, currently, earthquake alerts are distributed only to a limited test group via a cellular application. In addition to the HFC alerting channels, a test group receives alerts *via* a dedicated GSI Telegram bot.

TRUAA EARTHQUAKE EARLY WARNING ALGORITHM PERFORMANCE

The deployment phase of TRUAA, ongoing since September 2017, provided the opportunity to test the EEW algorithm in real-time. As data centers were being configured and additional stations deployed, telemetry and stations have shown variability in performance and availability, with occasional data outage in all or in parts of the network, and variable latencies or completeness levels. Nevertheless, the available data was sufficient to examine the performance of ElarmS, and carefully upgrade the EEW into EPIC (Nof and Kurzon, 2021). In this work, we attempt to assess the expected performance of the EEWS in terms of alert-delays and source parameter accuracy (location, origin-time and magnitude) by analyzing statistics of the available data between May 2020 and January 2021. Although most of the stations were already deployed during this period, we note that not all stations were available to the system at all times and occasional outages occurred. We use data from a real-time testing system utilizing a single processing chain (e.g. WP and EA) which has the most complete real-time data record and its performances are similar for the four operational processing chains.

Expected Alert Delays in Israel

The expected performance, in terms of alert delays, were estimated as the minimal alert delay for earthquakes occurring in and around Israel, i.e., estimating the theoretical time for EPIC to provide EEW to the HFC dissemination system, given an earthquake location and seismic network geometry (Nof and Kurzon, 2021). This analysis presented by Nof and Kurzon (2021; their Figure 3) shows that the minimal delay time is 4.7 s, where the seismic network is most dense. This estimation assumes an earthquake depth of 10 km and processing and telemetry times of 1 s, each. Typically, latency and processing times are less than 1 s. Longer telemetry delays as well as deeper hypocenters would result in longer alert delays. Alert delays are expected to be ~5 s for events occurring along the main hazardous fault lines. Assuming a very conservative S-wave velocity of 3.5 km/s and depth 10 km this delay would translate into a ~15 km blind-zone (~22 km with added 2 s for alert dissemination), wherein S-wave would precede alert issuance. This is a significant improvement relative to previous blind-zone estimation of over 30 km (Pinsky, 2015). Slower S-wave velocity would yield smaller blind zone while shallower events might yield larger blind zone.

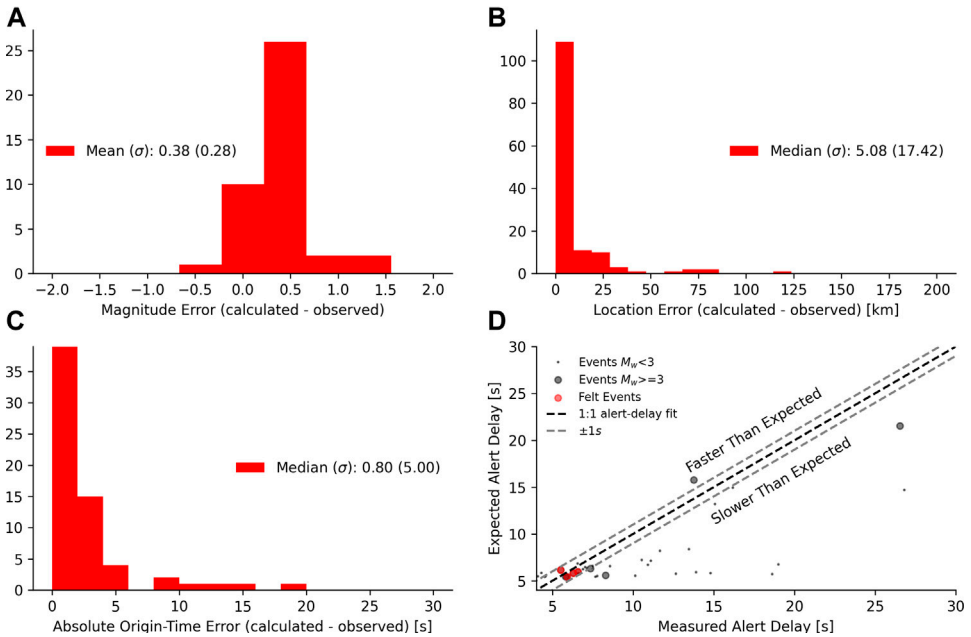

FIGURE 2 | EPIC real-time performance evaluation. **(A)** magnitude errors; **(B)** location errors; **(C)** origin time errors; **(D)** measured alert delays vs. expected alert delays (*Nof and Kurzon, 2021; See their **Figure 3** for expected alert delays spatial distribution*). Dots denote events with catalog magnitude of Mw < 3, gray circles denote events with catalog magnitude Mw > 3, red circles represent felt events, dark dashed line represents a 1:1 fit between expected and measured alert delay, gray dashed lines represent ±1 s from the 1:1 fit line; All errors are referenced to the ISN catalog.

Real Time Performance

Since it's installation on May 5th' 2020, EPIC version 3.2.1-2020-04-17 was running in real-time. Until January 1st' 2021, EPIC EA has identified and alerted on 154 events of M > 2.5 (EPIC magnitude estimation). In order to assess the EEW algorithm performance, the GSI catalog (earthquake.co.il last access 2021-03-01) is considered as a reference and a careful association is required between the two datasets. We first use large area catalog events to associate EPIC events and then process only those associated with catalog events located in a more local area that corresponds to the TRUAA coverage.

For this period, the GSI catalog includes a total of 2,674 events (525 with Mw > 3) located between 27–36 latitudes and 32–38 longitudes with maximal magnitude of Mw 6.7 (the 2020-10-30 11:51 Aegean Sea earthquake). While the catalog's geographic coverage is larger than the expected EEW coverage (limited to ~200 km from the seismic network stations) distant events may trigger an alert with large location errors and therefore should be considered. We associate the GSI catalog records with EPIC's EA alerts based on a time window of 130 s to allow association of distant events. For the 2674 GSI catalog events only six are categorized as "Felt" (e.g. were reported by the public to be felt) and 1,610 events are categorized as quarry blasts or explosions (all with Mw < 3, some without recorded catalog magnitude).

Out of the 154 EPIC alerts, two were not associated with any catalog event (False alerts) and one was associated with an un-cataloged teleseismic event (2020-10-06 Mw 5.9 Fiji). The EPIC first magnitude estimation for these three events was in the range of 2.6—3.1. For the six felt events that occurred during this period, five were identified and alerted by EPIC and one missed - the Mw 5.3 2020-12-05 Near Antalya, Turkey. This missed felt event was a distant event (>450 km from ISN) and as such should not be considered, though it was widely felt in Israel (21 reports at the USGS "did you feel it" with MMI III).

As previously mentioned, TRUAA is yet to be fully operational and data acquisition in real-time suffer from different challenges. We use the EPIC alerts database to investigate the system performance in terms of alert delay times, magnitude errors and locations errors. These parameters are of high importance for decision makers in establishing the appropriate public alerting approach in Israel. Previous analysis of historical playbacks have found median and standard deviation (σ) of 3.7 km (σ 32.26 km) and 0.8 s (σ 4.33 s) for the location errors and time errors, respectively, and mean magnitude error of 0.41 (σ 0.43) for the population of all 49 felt events (2.8 < Mw < 4.8) during January 2012 to March 2020 (Nof and Kurzon, 2021). In order to compare these findings with current real-time performance we use all 41 catalog events (2.1 < Mw < 3.7) that occurred at the same spatial reference of 29°–35° Latitudes and 32.5°–36.5° Longitudes and their first EPIC EA alerts. **Figure 2** summarizes these statistics with a mean magnitude error of 0.38 (σ 0.28), median location error of 5.08 km (σ 17.42 km) and median time errors of 0.8 s (σ 5 s). These obtained statistical values are similar to those previously found using historical events playbacks (Nof

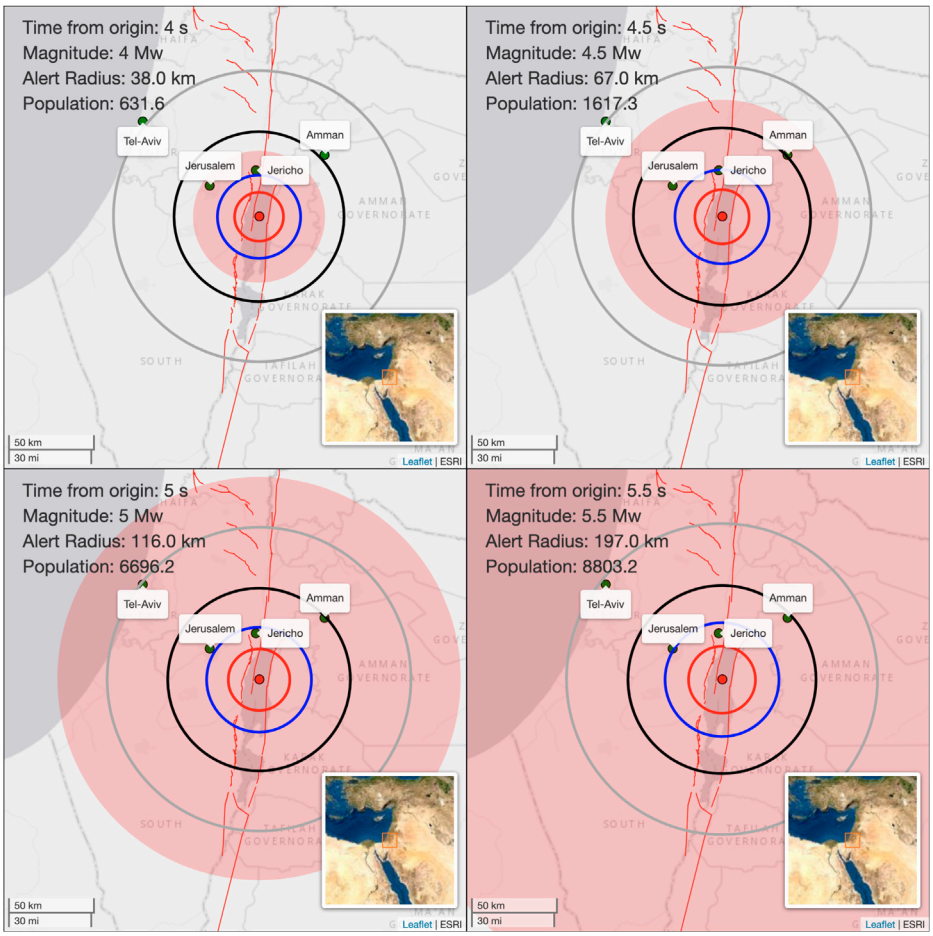

FIGURE 3 | "Evolutionary" EEW alert. With time, magnitude estimation is updated and the alerted area (pink) increases. Population numbers represent units of 1,000 per alert area. In a different scenario, where magnitude estimation would not increase (e.g. magnitude is stable at M_w 4), the alerted area is minimal and other areas are not disturbed. Alert area limit is calculated as 2 cm/s^2 using Lior and Ziv (2018) GMPE around the epicenter (red mark). Blue and red circles indicate the front of the P- and S- waves, respectively. Black and gray circles are 10 s intervals for S-wave front e.g. the expected S-wave front within 10 and 20 s, respectively.

and Kurzon, 2021). The alert-delays (**Figure 2D**) show good fit with the expected alert delays, detailed in Expected Alert Delays in Israel section, especially for the stronger events with catalog magnitude of Mw ≥ 3. All four felt events in the analyzed subset are within ±1 s of the expected alert-delays. Significant deviations, with larger than the expected alert-delays can be explained by small events (Mw < 3) that require additional time to fulfill the required magnitude threshold of M ≥ 2.5 in order to trigger an alert by the algorithm or by distant location from the seismic network. Although the datasets are limited in numbers and magnitude range, the EEWS performance within reported felt events is in accordance with expectations in terms of alert delays (see Expected Alert Delays in Israe Section) and in terms of location and magnitude errors based on historical data estimations (Nof and Kurzon, 2021). The results show that the EEW algorithm performance in real-time is as expected and that decision makers may rely on these findings to determine the alert approach for Israel.

ALERT APPROACH FOR ISRAEL

The initial earthquake alert approach for Israel was to alert educational institutions country-wide in case of a Mw ≥ 5.5 earthquake. Nof and Kurzon (2021) discussed the potential limitations of TRUAA and proposed an alternative approach for Israel. This alternative approach adopted herein. The main challenge is the potential earthquake magnitude under or over-estimation, which may respectively lead to damage (structural, personal physical or psychological) when alert should have been issued or unnecessary disturbance when alert was not required.

Given the inherent EPIC point source algorithm limitations and the need to balance between the short time for disseminating useful alerts and reducing needless alerts (e.g., alerting when damage is not expected), the proposed alerting approach is now approved by the decision makers and will allow for an "evolutionary" alert to both educational institutions and the general public. Currently, it is not scheduled to deliver EEW

to sensitive infrastructures due to the current high uncertainty of the solutions and the sensitivity of infrastructures to unrequired alerts. In the following, we present the current EEW policy in Israel and the considerations for this approach.

TRUAA Alerting Policy

Following the recommendations of Nof and Kurzon (2021) for an "evolutionary" alert (**Figure 3**), similar to the USGS ShakeAlert's approach (Given et al., 2018), alerts for magnitudes in the range of $4.2 \leq Mw < 6.0$ will be limited to areas where the ground shaking is expected to be above 2 cm/s^2 (pink zone in **Figure 3**), which is well felt (MMI II-III), but should not cause any significant structural damage (Worden et al., 2012). For events with magnitude $Mw \geq 6$—A country-wide alert will be assigned.

The described approach is aimed to balance the need to alert as soon as possible for potentially damaging events and the need to avoid alerting for regions where no action is required (Cochran and Husker, 2019; Le Guenan et al., 2016; Minson et al., 2018). While public demand and expectations in some places are to receive alerts even when no physical damage is expected (MMI > III), such as following the 2019 Ridgecrest earthquake in California (Cochran and Husker, 2019), in other places alerts are expected only for more damaging events, such as in New Zealand (Becker et al., 2020). Common public alert approaches are aimed at higher intensities such as the JMA L5 in Japan (Hoshiba et al., 2008) and the initial alert threshold of MMI IV in California (Given et al., 2018). The relatively low threshold of 2 cm/s^2, balanced with a low magnitude threshold of Mw 4.2, allows to account for local amplifications and the uncertainties in magnitude, location and ground motion prediction equations (GMPEs) (Minson et al., 2019). The apparent public acceptance and tolerance for receiving alerts even where no damage occurred (Allen, 2017; Allen et al., 2018) allows the use of such a low threshold to ensure alerts are sent only to areas that are expected to feel shaking (Worden et al., 2012) and reduce disturbance to the public where no action is required. The Mw 4.2 threshold mitigates the risk of delaying alerts for initially underestimated large earthquakes (Böse et al., 2012; Meier, 2017; Melgar and Hayes, 2017; Minson et al., 2018; Meier et al., 2020) while avoiding unrequired alerts to non-damaging lower magnitude events. Since for large magnitude earthquakes additional time might be required in order to converge to its maximal peak displacement (Trugman et al., 2019), hence, as additional information is gathered and becomes available for the EEWS, magnitude estimation is expected to be more accurate and corresponding alert area would increase. Initiating the alert to a limited area at an early stage reduces the "blind zone" where alerts are received after S-wave arrivals. In addition to the lower-bound magnitude threshold, a second threshold was selected at Mw six to spread an alert country-wide. Since most of the country is likely to be included in the 2 cm/s^2 zone, extending the alert to the whole country mitigates the point-source algorithm potential saturation at magnitudes larger than Mw six (e.g. Brown et al., 2009).

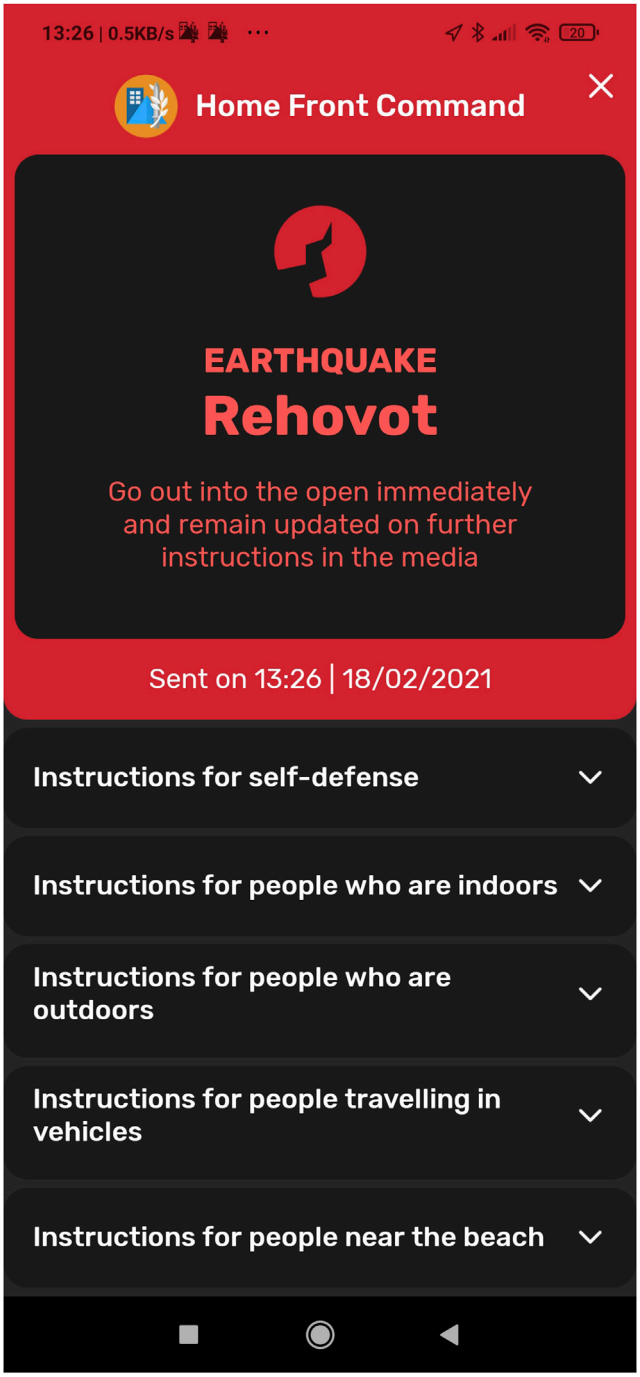

FIGURE 4 | Alert panel screenshot taken from the HCF app. Red frame surrounding dedicated earthquake icon with the name of user place, action instructions, date, time and type of threat (earthquake in this case). A unique alerting sound and additional instructions are also available. Instructions include information on how to react at different places (indoors, outdoors, cars, coastline).

TRUAA Alert Dissemination to the Public

Currently, disseminating alerts is the responsibility of the HFC. EPIC's DM point source solutions are acquired from the ActiveMQ messaging system as XML format by a dedicated new module and translated into Common Alerting Protocol (CAP) format (Jones et al., 2010). A pre-calculated magnitude-distance table is used to set the alert radius around the epicenter, based on the selected thresholds and GMPEs. The EPIC alert is forwarded to the HFC disseminating system in less than 0.5 s (~400 milliseconds). HFC can forward the alerts to the public using various methods (cellular application, emergency sirens, TV, radio etc.) which adds an additional 1–10 s depending on the alert medium. Currently, a test group of subscribers to the HFC alert applications can receive alerts. The subscriber can register to any location (city/settlement) and receive simple informative push messages in case of an alert to these locations. In addition, a full alert panel will appear in case of an alert to the device's current location. The alert panel (**Figure 4**) includes red colors, earthquake icon, user location name, date, time and type of threat (earthquake in this case). A unique alerting sound and additional instructions are also available in Hebrew, English, Arabic and Russian. Instructions include information on how to react at different places (indoors, outdoors, cars, coastlines). Emergency sirens are currently designed to sound verbally the word "Earthquake" in Hebrew to distinguish from other threats. The system is yet to be operational on a national level.

SELECTION OF THE APPROPRIATE GROUND MOTION PREDICTION EQUATIONS FOR EARTHQUAKE EARLY WARNING IN ISRAEL

Following real-time magnitude and location determination—alert issuance and alert region are determined based on GMPEs. GMPE development requires large earthquake dataset with a wide magnitude range. The low seismicity rate in the region limits the development of rigorous local GMPEs, thus, several global GMPEs are tested to determine the optimal one for TRUAA. The appropriate GMPEs should meet the following criteria: 1) regionally adjustable; 2) Based and validated on a large global dataset with $3 \leq M_w \leq 7$; and 3) Yields low standard deviations between observed and predicted median values of ground motions, in particular when tested against regionally recorded earthquakes. The latter is crucial for EEW, due to the limited information available in real-time (Magnitude and epicentral distance). In this section, the performance of three different GMPEs is compared: the model-based GMPE of Lior and Ziv (2018, LZ18), the empirical GMPE of Abrahamson, Silva and Kamai (2014, ASK14) and the empirical GMPE of Cua et al., 2009, CH09. The LZ18 GMPE is formulated as follows (Eq. 20c in Lior and Ziv, 2018):

$$PGA = \frac{3.3 M_0^{\frac{1}{3}} \Delta\tau^{\frac{2}{3}} \beta_A}{R\sqrt{\kappa\left[\frac{1}{\kappa C_S}\left(\frac{7M_0}{16\Delta\tau}\right)^{\frac{1}{3}} + R/C_S\right]}\left[1 + 1.5^{-\frac{1}{4}}\pi\kappa k C_S\left(\frac{16\Delta\tau}{7M_0}\right)^{\frac{1}{3}}\right]^2} \quad (1)$$

where PGA is peak ground accelerations, M_0 is the seismic moment, $\Delta\tau$ is the stress drop, β_A is a constant, R is the source-to-site distance, κ is the high-frequency attenuation parameter, k is a source model dependent constant (e.g., Brune, 1970; Madariaga, 1976), and C_S is the S-wave velocity. Parameter values are set to those used by Lior and Ziv (2020): $\beta_A = 2.05 \cdot 10^{-8} \frac{m^2 s}{kg}, \kappa = 0.025\, s$, (Lior and Ziv, 2018), $k = 0.21$, (Madariaga, 1976) and $C_S = 3.2$ km/s (Lior and Ziv, 2020). The CH09 GMPE is presented in **Eq. 4** of Cua and Heaton (2009):

$$log_{10}(PGA) = aM + b(R_1 + C(M)) + d \cdot log_{10}(R_1 + C(M)) + e \quad (2)$$

where PGA is measured in cm, M is magnitude, $R_1 = \sqrt{R^2 + 9}$, R is the epicentral distance (in km), $C(M) = c_1 e^{c_2 (M-5)} \times \left(\arctan(M-5) + \frac{\pi}{2}\right)$ and e is a constant. The coefficients for hard rock sites were used (Table three of Cua and Heaton, 2009): a = 0.73, b = -7.2×10^{-4}, $c_1 = 1.16$, $c_2 = 0.96$, d = −1.48 and e = −0.42. We tested the fit between observed PGA and the CH09 GMPE using both the "hard rock" and "soft soil" coefficients and found a better agreement using the "hard rock" coefficients. This is not surprising given that the vast majority of ground motion records used in this study were recorded at hard rock sites.

For ASK14, we use the basic form of the GMPE since many coefficients are unknown for Israel. This formulation is presented in **Eqs 2–4** of Abrahamson, Silva and Kamai (2014):

$$\log(PGA) = \begin{cases} a_1 + a_5(M - M_1) + a_8(8.5 - M)^2 + [a_2 + a_3(M - M_1)]\log(R) + a_{17}R_{RUP} & M > M_1 \\ a_1 + a_4(M - M_1) + a_8(8.5 - M)^2 + [a_2 + a_3(M - M_1)]\log(R) + a_{17}R_{RUP} & M_2 \leq M < M_1 \\ a_1 + a_4(M_2 - M_1) + a_8(8.5 - M_2)^2 + a_6(M - M_2) + a_7(M - M_2)^2 + [a_2 + a_3(M - M_1)]\log(R) + a_{17}R_{RUP} & M < M_2 \end{cases} \quad (3)$$

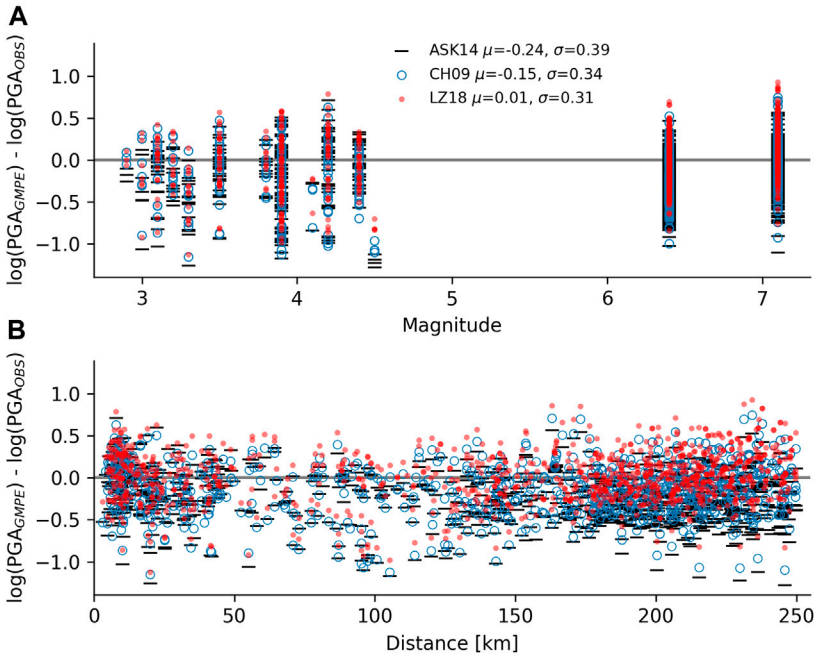

FIGURE 5 | The logarithm of predicted PGA (PGA_{GMPE}) minus the logarithm of observed PGA (PGA_{OBS}) as functions of **(A)** catalog moment magnitude and **(B)** source-to-site distance. Discrepancies calculated using CH09, ASK14 and LZ18 are indicated by blue circle, black line and red dots, respectively. Average discrepancies (μ) and standard deviations to the residuals (σ) between predicted and observed PGAs are indicated in the legend.

Where $R = \sqrt{R_{RUP}^2 + c_{4M}^2}$ and

$$c_{4M} = \begin{cases} c_4 & M > 5 \\ c_4 - (c_4 - 1)(5 - M) & 4 < M \leq 5 \\ 1 & M \leq 4 \end{cases} \quad (4)$$

R_{RUP} is the closest distance to the rupture plane, equivalent to the epicentral distance for small earthquakes. The following coefficient values were used: $c_4 = 4.5$, $M_1 = 6.75$, $M_2 = 5$, $a_1 = 0.587$, $a_2 = -0.79$, $a_3 = 0.275$, $a_4 = -0.1$, $a_5 = -0.41$, $a_6 = 2.154$, $a_7 = 0.0$, $a_8 = -0.015$ and $a_{17} = -0.0072$ (Abrahamson et al., 2014). Both CH09 and ASK14 describe the median PGA while LZ18 describes a theoretical PGA, based on commonly used seismological models (Brune, 1970; Anderson and Hough, 1984). The validation of LZ18 to a diverse data set of earthquakes, mainly from Japan and California, revealed low uncertainties of 0.7 in natural log units (0.3 is 10 base log units) (Lior and Ziv, 2018), comparable to 0.31 determined for CH09 (10 base log units) (Cua and Heaton, 2009). For ASK14, standard deviation are not reported specifically for the base form of the GMPE used here.

All GMPEs meet criteria 2) so they will be appraised based on criteria 1) and 3). The tested GMPEs are compared using locally recorded earthquakes, as well as the 2019 M_w 6.4 and M_w 7.1 Ridgecrest earthquakes to compensate for the lack of large magnitude events in our local seismic record. In contrast to the empirical GMPEs (ASK14 and CH09), which are a function of magnitude and epicentral distance (under the EEW algorithm point source assumption), the LZ18 GMPEs also depend on stress drop. Since stress drop is currently not resolved in real-time, it will be estimated using the magnitude—stress drop relation established for California earthquakes by Lior and Ziv (2018; their Eq. 18a):

$$log_{10}\Delta\tau = 4.57 + 0.14 log_{10} M_0 \quad (5)$$

This relation, determined for earthquakes of similar mechanism (mostly strike-slip), provides a good fit to observed ground motions, as further shown.

To examine the performance of the different GMPEs, they are compared to recorded ground motions. Predicted PGA are calculated using the different GMPEs and catalog magnitudes and source-to-site distances. We focus on the median predictions of the GMPEs, neglecting their uncertainties, since the EEW alerts are binary—either alert or not and these GMPEs uncertainties cannot be considered in real-time. Thus, we do not perform a complete evaluation of each GMPE. **Figure 5** shows the discrepancies between observed and predicted PGA (using different GMPEs) as functions of magnitude and distance, and **Figure 6** shows observed PGA as a function of distance, along with a fit to the different GMPEs, for four different earthquakes in Israel and California. In **Figure 5**, only PGA >1 cm/s^2 are considered, since lower values are of little interest for EEW. **Figure 5** reveals that the residuals are invariant to magnitude and distance for all GMPEs. The average discrepancies and the standard deviations of the residuals (μ and σ, respectively, in the legends of **Figure 5A** and **Figure 6**) indicate that LZ18 produces a better fit to the observations compared with the two empirical GMPEs,

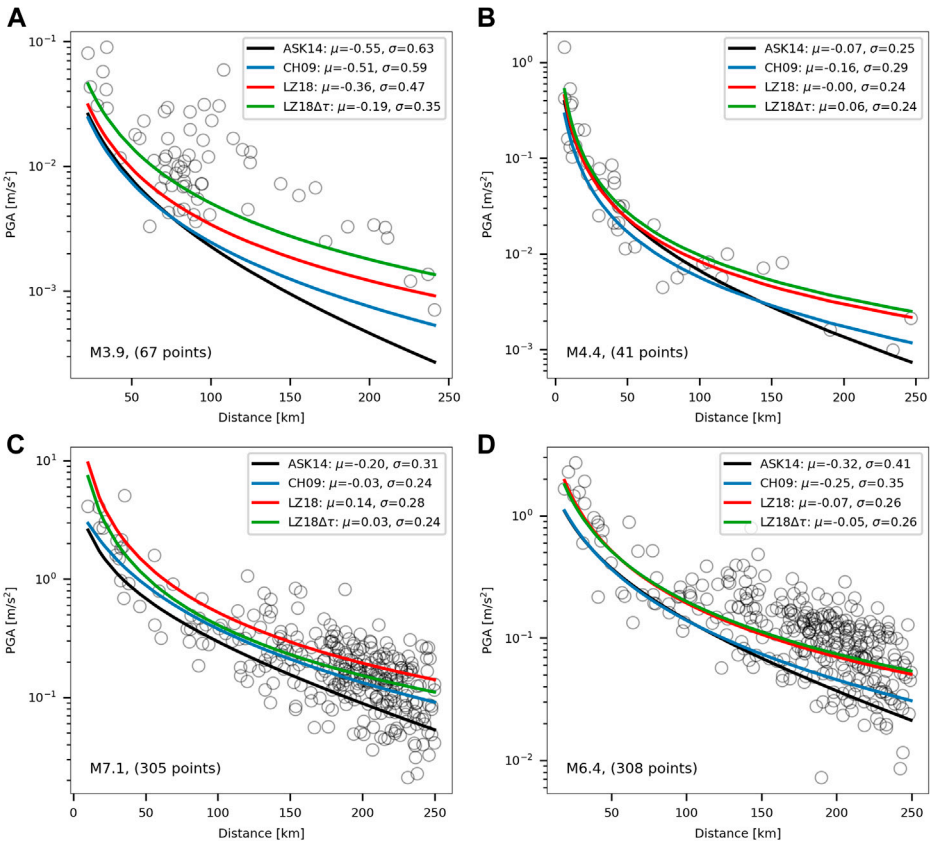

FIGURE 6 | PGA as a function of distance for **(A)** MW 3.9 in the eastern Mediterranean Sea, **(B)** MW 4.4 in north Israel, and **(C)** MW7.1 and **(D)** MW6.4 near Ridgecrest California. Magnitudes and the number of data points are indicated at the bottom left corner of each panel. The GMPEs of LZ18, ASK14, CH09, and LZ18 with earthquake specific stress drop (LZ18Δτ) are indicated by red, black, blue and green curves, respectively. Average discrepancies (μ) and standard deviations to the residuals (σ) are indicated in the legends.

showing a lower standard deviation, and a more symmetric residual distribution (μ closer to 0). The negative average discrepancies, typically observed for CH09 and ASK14, indicate a general ground motions underestimation. Such underestimation has been previously reported by Nof and Allen (2016) who implemented a simple globally derived GMPE for real-time magnitude estimation of Israeli earthquakes. Thus, we conclude that LZ18 is the more suitable GMPE, producing lower ground motion uncertainties, as required by criteria 3) defined earlier.

Since LZ18 explicitly includes the stress drop, we test whether implementing an earthquake specific Δτ improves PGA predictions. Unlike the stress drops given by **eq. 5**, which describes stress drop averaged for many investigated earthquakes in California, an earthquake specific Δτ is determined for each individual earthquake separately. Average earthquake stress drops are calculated for each event using the single-step source parameter inversion of Lior and Ziv (2018). To obtain reliable stress drop estimates, only stations at hypocentral distances of less than 50 km are used. Predicted LZ18 PGA calculated using earthquake specific stress drops, provide a better fit to observed data, as indicated by the blue curves in **Figure 6**. These results demonstrate the ability to locally adjust the LZ18 GMPE (criteria one), and confirms that shaking intensities may be better predicted by incorporating real-time stress drop determination (e.g. Lior and Ziv, 2020). In contrast to the large additional dataset required to locally adjust CH09 or ASK14, the real-time stress drop calculation may be implemented in the EEW algorithm without additional seismic data.

The underestimation of PGA using CH09 and ASK14 (**Figures 5**, **6**) typically results in smaller alert areas compared to those imposed by LZ18. To demonstrate this effect, **Figure 7** shows magnitude as a function of the predicted alert area radius for the different GMPEs. Here, alert radius corresponds to the predefined threshold of peak ground accelerations >2 cm/s^2. Similar alert radii are predicted for small magnitudes (M<~4), while at larger magnitudes, the LZ18 GMPE is the most conservative, producing the largest alert areas. The latter characteristic is particularly appealing for the early stages of TRUAA's operation, where public expectation and long-term performance are still unclear. We conclude that LZ18 will produce the most reliable and

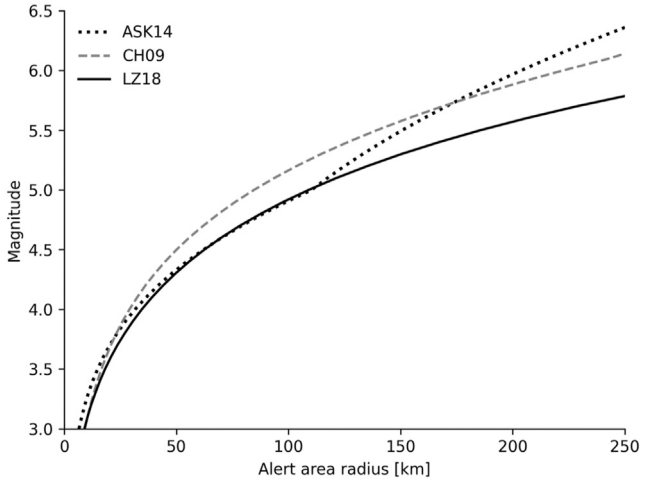

FIGURE 7 | Magnitude as a function of alert radius for a PGA threshold of 2 cm/s^2 (MMI II-III) using LZ18 (black solid line), ASK14 (black dotted line) and CH09 (gray dashed line).

robust ground shaking predictions, which may be improved if a real-time stress drop estimate is available.

CONCLUSION

The State of Israel's TRUAA EEWS, along with its new real-time seismic network, achieve state-of-the-art real-time capabilities owing to the: 1) fast telemetry, 2) high station density along the main fault systems, and 3) local implementation of the EPIC algorithm. In this manuscript we demonstrated that the real-time performance of the EPIC EEW algorithm is in-line with the expected alert-delays and source parameters error uncertainty. We evaluated the real-time performance of TRUAA between May 5th, 2020 and January 1st, 2021 using 41 events with catalog magnitude range of ($2.1 < Mw < 3.7$) and found that all felt events within the seismic network coverage led to accurate and timely alerts. We found mean magnitude error of 0.38 (σ 0.28), median location error of 5.08 km (σ 17.42 km) and median time errors of 0.8 s (σ 5 s). These statistics are robust and similar to previously reported values (Kurzon et al., 2020; Nof and Kurzon, 2021). The suggested "evolutionary" alert has been approved and alerts to limited areas will be provided for $4.2 \geq M_w < 6$. For $M_w \geq 6$ a country-wide alert will be issued. We note that the dataset used in this research lacks large magnitude events and the seismic network is yet to be fully completed. Thus, the performance statistics may change in the future and further assessments would be required.

This alerting approach is expected to balance the need for rapid alerts in the presence of high uncertainties, on the one hand, and the desire to reduce alerts for areas with low ground motions, on the other hand. This balance is achieved by setting a lower alert magnitude threshold, and alerting to a radial distance from the epicenter, where ground accelerations are predicted to be higher than 2 cm/s^2. This threshold may be adjusted in the future, considering TRUAA's performance and public expectations, to provide more accurate and targeted alerts. A comparison between three different GMPEs concluded that the model-based GMPE of Lior and Ziv (2018) produces the better agreements between predicted median values and observed PGA. In addition, this GMPE has the potential to be further adjusted by implementing real-time stress-drop, a parameter that can be reliably determined in real-time. Thus, the limited alert area is determined using this GMPE.

A complementary essential component to EEWS is public outreach, education and exercise of earthquake response (Allen et al., 2009 and references therein; Santos-Reyes, 2019; Wald, 2020). These are critical for a successful EEWS, especially in areas with low seismic activity, where public awareness is low, such as in Israel, and should be addressed in the near future, as TRUAA becomes fully operational.

DATA AVAILABILITY STATEMENT

The raw data supporting the conclusion of this article will be made available by the authors, without undue reservation.

AUTHOR CONTRIBUTIONS

RN and IK contributed to conception and design of the study. IK performed the seismic network analysis. RN performed the EPIC performance analysis. IL performed the GMPEs analysis. RN wrote the first draft of the manuscript. IK and IL wrote sections of the manuscript. All authors contributed to manuscript revision, read, and approved the submitted version.

ACKNOWLEDGMENTS

We thank the GSI EEW workgroup and the National Steering Committee for Earthquake Preparedness for fruitful discussions on alerting strategy for Israel. We thank the U.C Berkeley Seismology Lab for making EPIC updates available for us. Figures were generated using *Python*'s modules Matplotlib (https://matplotlib.org/, last accessed Mar 1, 2021) and map using *Python*'s module Folium (https://python-visualization.github.io/folium/, last accessed Mar 1, 2021). Background map in **Figure 2** obtained from ESRI (http://server.arcgisonline.com/ArcGIS/rest/services, last accessed Mar 1, 2021). Coastlines in **Figure 1** obtained from Global Self-consistent Hierarchical High-resolution Geography (https://www.soest.hawaii.edu/pwessel/gshhg/, last update June 14, 2017, last accessed Mar 1, 2021). Population density data obtained from WorldPop (http://www.worldpop.org, last accessed June 25, 2020). Finally, We thank the editor and two anonymous reviewers who helped make this manuscript clearer and more accurate.

REFERENCES

Abrahamson, N. A., Silva, W. J., and Kamai, R. (2014). Summary of the ASK14 Ground Motion Relation for Active Crustal Regions. *Earthquake Spectra* 30, 1025–1055. doi:10.1193/070913EQS198M

Allen, R., Cochran, E., Huggins, T., Miles, S., and Otegui, D. (2018). Lessons from Mexico's Earthquake Early Warning System. *Lessons from Mexico's Earthquake Early Warning System*, 99. Washington. DC: Eos. doi:10.1029/2018eo105095

Allen, R. M., Baer, G., Clinton, J., Hamiel, Y., Hofstetter, R., Pinsky, V., et al. (2012). Earthquake Early Warning for Israel: Recommended Implementation Strategy. Jerusalem, Israel: Geological Survey of Israel.

Allen, R. M., and Melgar, D. (2019). Earthquake Early Warning: Advances, Scientific Challenges, and Societal Needs. *Annu. Rev. Earth Planet. Sci.* 47, 361–388. doi:10.1146/annurev-earth-053018-060457

Allen, R. M. (2017). Quake Warnings, Seismic Culture. *Science* 358, 1111. doi:10.1126/science.aar4640

Anderson, J. G., and Hough, S. E. (1984). A Model for the Shape of the Fourier Amplitude Spectrum of Acceleration at High Frequencies. *Bull. Seismol. Soc. Am.* 74, 1969–1993.

Becker, J. S., Potter, S. H., Vinnell, L. J., Nakayachi, K., McBride, S. K., and Johnston, D. M. (2020). Earthquake Early Warning in Aotearoa New Zealand: a Survey of Public Perspectives to Guide Warning System Development. *Humanit. Soc. Sci. Commun.* 7, 138. doi:10.1057/s41599-020-00613-9

Böse, M., Heaton, T. H., and Hauksson, E. (2012). Real-time Finite Fault Rupture Detector (FinDer) for Large Earthquakes. *Geophys. J. Int.* 191, 803–812. doi:10.1111/j.1365-246X.2012.05657.x

Brown, H. M., Allen, R. M., and Grasso, V. F. (2009). Testing ElarmS in Japan. *Seismological Res. Lett.* 80, 727–739. doi:10.1785/gssrl.80.5.727

Brune, J. N. (1970). Tectonic Stress and the Spectra of Seismic Shear Waves from Earthquakes. *J. Geophys. Res.* 75, 4997–5009. doi:10.1029/JB075i026p04997

Chung, A. I., Henson, I., and Allen, R. M. (2019). Optimizing Earthquake Early Warning Performance: ElarmS-3. *Seismol. Res. Lett.* 90, 727–743. doi:10.1785/0220180192

Cochran, E. S., and Husker, A. L. (2019). How Low Should We Go when Warning for Earthquakes? *Science* 366, 957–958. doi:10.1126/science.aaz6601

Cochran, E. S., Kohler, M. D., Given, D. D., Guiwits, S., Andrews, J., Meier, M. A., et al. (2017). Earthquake Early Warning ShakeAlert System: Testing and Certification Platform. *Seismol. Res. Lett.* 89, 108–117. doi:10.1785/0220170138

Cua, G., Fischer, M., Heaton, T., and Wiemer, S. (2009). Real-time Performance of the Virtual Seismologist Earthquake Early Warning Algorithm in Southern California. *Seismological Res. Lett.* 80, 740–747. doi:10.1785/gssrl.80.5.740

Cua, G., and Heaton, T. H. (2009). Characterizing Average Properties of Southern California Ground Motion Amplitudes and Envelopes. Available at: https://resolver.caltech.edu/CaltechEERL:EERL-2009-05.

Garfunkel, Z., Zak, I., and Freund, R. (1981). Active Faulting in the Dead Sea Rift. *Tectonophysics* 80, 1–26. doi:10.1016/0040-1951(81)90139-6

Given, D. D., Allen, R. M., Baltay, A. S., Bodin, P., Cochran, E. S., Creager, K., et al. (2018). Revised Technical Implementation Plan for the ShakeAlert System-An Earthquake Early Warning System for the West Coast of the United States. *Revised Technical Implementation Plan for the ShakeAlert System—An Earthquake Early Warning System for the West Coast of the United States*. Reston, VA: USGS. doi:10.3133/ofr20181155

Hamiel, Y., Amit, R., Begin, Z. B., Marco, S., Katz, O., Salamon, A., et al. (2009). The Seismicity along the Dead Sea Fault during the Last 60,000 Years. *Bull. Seismological Soc. America* 99, 2020–2026. doi:10.1785/0120080218

Hoshiba, M., Kamigaichi, O., Saito, M., Tsukada, S. y., and Hamada, N. (2008). Earthquake Early Warning Starts Nationwide in Japan. *Eos Trans. AGU* 89, 73–74. doi:10.1029/2008EO080001

Jones, E., Systems, W., and Westfall, J. (2010). Common Alerting Protocol Version 1.2. 1–47. Available at: http://docs.oasis-open.org/emergency/cap/v1.2/CAP-v1.2.pdf.

Kennett, B. L. N., Engdahl, E. R., and Buland, R. (1995). Constraints on Seismic Velocities in the Earth from Traveltimes. *Geophys. J. Int.* 122, 108–124. doi:10.1111/j.1365-246X.1995.tb03540.x

Kohler, M. D., Cochran, E. S., Given, D., Guiwits, S., Neuhauser, D., Henson, I., et al. (2018). Earthquake Early Warning ShakeAlert System: West Coast Wide Production Prototype. *Seismol. Res. Lett.* 89, 99–107. doi:10.1785/0220170140

Kohler, M. D., Smith, D. E., Andrews, J., Chung, A. I., Hartog, R., Henson, I., et al. (2020). Earthquake Early Warning ShakeAlert 2.0: Public Rollout. *Seismol. Res. Lett.* 91, 1763–1775. doi:10.1785/0220190245

Kurzon, I., Nof, R. N., Laporte, M., Lutzky, H., Polozov, A., Zakosky, D., et al. (2020). The "TRUAA" Seismic Network: Upgrading the Israel Seismic Network-Toward National Earthquake Early Warning System. *Seismol. Res. Lett.* 91, 3236–3255. doi:10.1785/0220200169

Kuyuk, H. S., and Allen, R. M. (2013a). A Global Approach to Provide Magnitude Estimates for Earthquake Early Warning Alerts. *Geophys. Res. Lett.* 40, 6329–6333. doi:10.1002/2013GL058580

Kuyuk, H. S., and Allen, R. M. (2013b). Optimal Seismic Network Density for Earthquake Early Warning: A Case Study from California. *Seismological Res. Lett.* 84, 946–954. doi:10.1785/0220130043

Le Guenan, T., Smai, F., Loschetter, A., Auclair, S., Monfort, D., Taillefer, N., et al. (2016). Accounting for End-User Preferences in Earthquake Early Warning Systems. *Bull. Earthquake Eng.* 14, 297–319. doi:10.1007/s10518-015-9802-6

Lior, I., and Ziv, A. (2020). Generic Source Parameter Determination and Ground-Motion Prediction for Earthquake Early Warning. 110, 345–356. doi:10.1785/0120190140

Lior, I., and Ziv, A. (2018). The Relation between Ground Motion, Earthquake Source Parameters, and Attenuation: Implications for Source Parameter Inversion and Ground Motion Prediction Equations. *J. Geophys. Res. Solid Earth* 123, 5886–5901. doi:10.1029/2018JB015504

Madariaga, R. (1976). Dynamics of an Expanding Circular Fault. *Bull. Seismol. Soc. Am.* 66, 639–666. Available at: http://bssa.geoscienceworld.org/content/66/3/639.abstract.

Meier, M.-A. (2017). How "good" Are Real-Time Ground Motion Predictions from Earthquake Early Warning Systems? *J. Geophys. Res. Solid Earth* 122, 5561–5577. doi:10.1002/2017JB014025

Meier, M. A., Kodera, Y., Böse, M., Chung, A., Hoshiba, M., Cochran, E., et al. (2020). How Often Can Earthquake Early Warning Systems Alert Sites with High-Intensity Ground Motion? *J. Geophys. Res. Solid Earth* 125, 2019JB017718. doi:10.1029/2019JB017718

Melgar, D., and Hayes, G. P. (2017). Systematic Observations of the Slip Pulse Properties of Large Earthquake Ruptures. *Geophys. Res. Lett.* 44, 9691–9698. doi:10.1002/2017GL074916

Minson, S. E., Baltay, A. S., Cochran, E. S., Hanks, T. C., Page, M. T., McBride, S. K., et al. (2019). The Limits of Earthquake Early Warning Accuracy and Best Alerting Strategy. *Sci. Rep.* 9, 1–13. doi:10.1038/s41598-019-39384-y

Minson, S. E., Meier, M.-A., Baltay, A. S., Hanks, T. C., and Cochran, E. S. (2018). The Limits of Earthquake Early Warning: Timeliness of Ground Motion Estimates. *Sci. Adv.* 4, eaaq0504. doi:10.1126/sciadv.aaq0504

Nof, R. N., and Allen, R. M. (2016). Implementing the ElarmS Earthquake Early Warning Algorithm on the Israeli Seismic Network. *Bull. Seismological Soc. America* 106, 2332–2344. doi:10.1785/0120160010

Nof, R. N., Chung, A. I., Rademacher, H., Dengler, L., and Allen, R. M. (2019). MEMS Accelerometer Mini-Array (MAMA): A Low-Cost Implementation for Earthquake Early Warning Enhancement. *Earthquake Spectra* 35, 21–38. doi:10.1193/021218EQS036M

Nof, R. N., and Kurzon, I. (2021). TRUAA-earthquake Early Warning System for Israel: Implementation and Current Status. *Seismol. Res. Lett.* 92, 325–341. doi:10.1785/0220200176

Pinsky, V. (2015). Modeling Warning Times for the Israel's Earthquake Early Warning System. *J. Seismol.* 19, 121–139. doi:10.1007/s10950-014-9454-z

Sadeh, M., Ziv, A., and Wust-Bloch, H. (2014). Real-time Magnitude Proxies for Earthquake Early Warning in Israel. *Geophys. J. Int.* 196, 939–950. doi:10.1093/gji/ggt407

Sharon, M., Sagy, A., Kurzon, I., Marco, S., and Rosensaft, M. (2020). Assessment of seismic sources and capable faults through hierarchic tectonic criteria: implications for seismic hazard in the Levant. *Nat. Hazards Earth Syst. Sci.*, 20, 125–148. doi:10.5194/nhess-20-125-2020

Trugman, D. T., Page, M. T., Minson, S. E., and Cochran, E. S. (2019). Peak Ground Displacement Saturates Exactly when Expected: Implications for Earthquake Early Warning. *J. Geophys. Res. Solid Earth* 124, 4642–4653. doi:10.1029/2018JB017093

Worden, C. B., Gerstenberger, M. C., Rhoades, D. a., and Wald, D. J. (2012). Probabilistic Relationships between Ground-Motion Parameters and Modified Mercalli Intensity in California. *Bull. Seismological Soc. America* 102, 204–221. doi:10.1785/0120110156

Conflict of Interest: The authors declare that the research was conducted in the absence of any commercial or financial relationships that could be construed as a potential conflict of interest.

frontiers in Earth Science

ORIGINAL RESEARCH
published: 01 July 2021
doi: 10.3389/feart.2021.686272

Comparing the Performance of Regional Earthquake Early Warning Algorithms in Europe

Elisa Zuccolo[1], *Gemma Cremen*[2] *and Carmine Galasso*[2,3]*

[1]European Centre for Training and Research in Earthquake Engineering (EUCENTRE), Pavia, Italy, [2]Department of Civil, Environmental and Geomatic Engineering, University College London, London, United Kingdom, [3]Scuola Universitaria Superiore (IUSS) Pavia, Pavia, Italy

Several earthquake early warning (EEW) algorithms have been developed worldwide for rapidly estimating real-time information (i.e., location, magnitude, ground shaking, and/or potential consequences) about ongoing seismic events. This study quantitatively compares the operational performance of two popular regional EEW algorithms for European conditions of seismicity and network configurations. We specifically test PRobabilistic and Evolutionary early warning SysTem (PRESTo) and the implementation of the Virtual Seismologist magnitude component within SeisComP, VS(SC), which we use jointly with the SeisComP *scanloc* module for locating events. We first evaluate the timeliness and accuracy of the location and magnitude estimates computed by both algorithms in real-time simulation mode, accounting for the continuous streaming of data and effective processing times. Then, we focus on the alert-triggering (decision-making) phase of EEW and investigate both algorithms' ability to yield accurate ground-motion predictions at the various temporal instances that provide a range of warning times at target sites. We find that the two algorithms show comparable performances in terms of source parameters. In addition, PRESTo produces better rapid estimates of ground motion (i.e., those that facilitate the largest lead times); therefore, we conclude that PRESTo may have a greater risk-mitigation potential than VS(SC) in general. However, VS(SC) is the optimal choice of EEW algorithm if shorter warning times are permissible. The findings of this study can be used to inform current and future implementations of EEW systems in Europe.

Keywords: earthquake early warning, PRESTo, Virtual Seismologist, SeisComp, scanloc, warning time, timeliness, accuracy

OPEN ACCESS

Edited by:
Simona Colombelli,
University of Naples Federico II, Italy

Reviewed by:
Matteo Picozzi,
University of Naples Federico II, Italy
Elisa Buforn,
Universidad Complutense de Madrid, Spain

***Correspondence:**
Carmine Galasso
c.galasso@ucl.ac.uk

Specialty section:
This article was submitted to Geohazards and Georisks, a section of the journal Frontiers in Earth Science

Received: *26 March 2021*
Accepted: *12 May 2021*
Published: *01 July 2021*

Citation:
Zuccolo E, Cremen G and Galasso C (2021) Comparing the Performance of Regional Earthquake Early Warning Algorithms in Europe. Front. Earth Sci. 9:686272. doi: 10.3389/feart.2021.686272

INTRODUCTION

The goal of an earthquake early warning (EEW) system is to deliver a rapid alert about impending strong shaking that provides sufficient time for protective, loss-mitigating actions to be taken by targeted end users. The process of EEW generally consists of the following steps: 1) detection of an event in the early stages of fault rupture; 2) prompt prediction of the relevant source parameters (e.g., location and magnitude) and/or the intensity of the consequent ground motion; and 3) warning issuance to end users before they experience the strong shaking that might cause damage and losses.

EEW systems may be broadly classified as "regional," "on-site," or "hybrid." We specifically focus on regional systems, which are based on a dense sensor network covering a geographical area of high

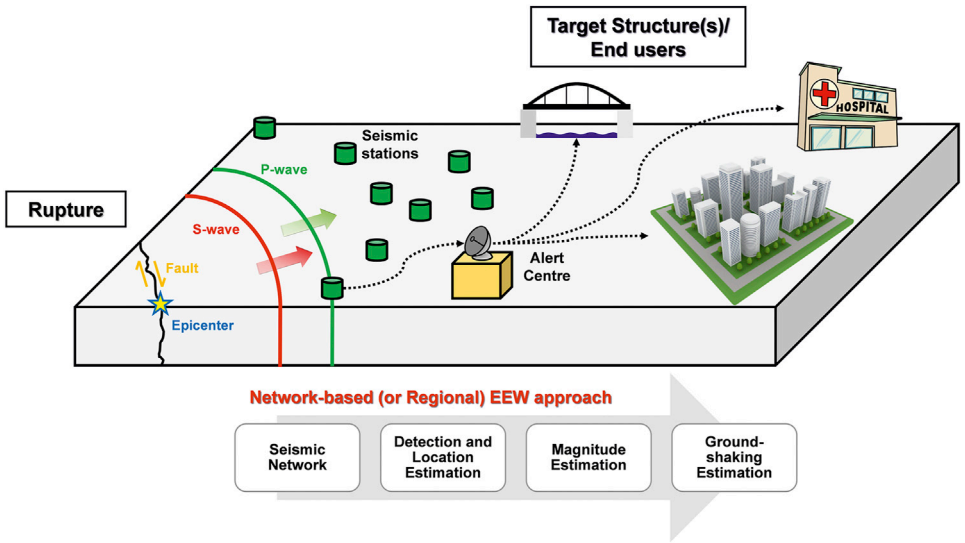

FIGURE 1 | The principles of a standard regional EEW system and conceptual outline of the corresponding EEW process. Information from an EEW system sensor network is input to an EEW algorithm to detect events and compute estimates of earthquake location, magnitude, and ground-motion amplitude. An alert may then be issued to warn end users of impending shaking.

seismicity. When an earthquake occurs, these systems typically estimate source parameters from the early portion of signals recorded at sensors close to the rupture. Location (and resulting source-to-site distance, R) is generally computed by accounting for geometrical constraints associated with both triggered and not-yet-triggered stations; earthquake magnitude (M) is typically calculated based on empirical relationships relating the earthquake size to parameters obtained in the first 3–4 s of P- and (sometimes) S-wave signals. **Figure 1** illustrates the principles of a conventional regional EEW system. For a more detailed review of various approaches to estimate location and magnitude in regional EEW systems, interested readers are referred to Cremen and Galasso (2020).

R and M estimates can be continuously updated (through Bayesian approaches or otherwise) by adding new station data as the P-wave front propagates through the regional EEW network. The real-time values are then used to predict, with quantified uncertainty, ground-motion intensity measures (IMs) at sites far away from the source (where target structures/infrastructure of interest and end users are located), by using, for example, ground-motion models (GMMs). If probabilistic distributions of M and R are available, the prediction of different IMs (e.g., Iervolino et al., 2006; Convertito et al., 2008) may be performed by analogy to the well-known Probabilistic Seismic Hazard Analysis (PSHA) framework but in real-time, as discussed in detail in Iervolino et al. (2009). Regional EEW systems typically require the arrival of P-wave signals at a number of stations to provide stable early estimates of R, M, and IM. Thus, event detection is a fundamental task for EEW. Erroneously detected or inaccurate phases, along with poor event associations, lead to inaccurate location and magnitude estimates and, ultimately, possible false or missed alerts. It is worth noting that most regional EEW algorithms assume a point-source model of the earthquake source and isotropic wave amplitude attenuation, which neglects the finite geometry of earthquake ruptures. These assumptions are generally suitable for estimating the final magnitude of events with M 6.5 7.0 (Meier et al., 2020), which are consistent with the largest seismicity that is typically observed in Europe (i.e.,the focus of our study) and the range of magnitudes we consider (5.5–6.9). We acknowledge that M > 7.0 events can occur in Europe, like the 1755 moment magnitude (M_W) 8.5 Lisbon earthquake, which is the largest listed in the SHEEC catalog (the "SHARE European Earthquake Catalog," Grünthal et al., 2013; Stucchi et al., 2013). However, these types of events were not accounted for in this study given their very low occurrence rate.

European approaches to regional EEW have been promoted and progressed through recent EU-funded research projects (Clinton et al., 2016), such as SAFER ("*Seismic early warning for Europe*") and REAKT ("*Strategies and tools for real-time earthquake risk reduction*"). These two projects have facilitated the development and testing of the PRESTo (Probabilistic and Evolutionary Early Warning System) and VS(SC) (Virtual Seismologist in SeisComP) regional EEW algorithms, which are the most widely applied regional EEW algorithms in Europe to date (Cremen and Galasso, 2020) and are therefore the focus of our investigations in this paper. PRESTo is currently operating in Southern Italy (Irpinia region), Turkey, Romania, and Southern Iberia (Carranza et al., 2017). It has also been tested for application at the border of Italy, Austria, and Slovenia (Picozzi et al., 2015). Instead, VS(SC) is currently operational in Switzerland and has been tested for use in Greece, Turkey, Romania, and Iceland (Behr et al., 2016).

Efforts to compare the performance of PRESTo and VS(SC) are currently underway within the Early Warning Test Center of the EPOS ("*European Plate Observing System*") EU project. However, they have so far been limited to the Irpinia region of Italy. We build on the attempts of the Early Warning Test Center in this study by comparing the performance of the PRESTo and VS(SC) algorithms for multiple European conditions of seismicity and existing seismic network configurations (i.e., geometries and densities). We specifically consider five European geographic areas - Southern Italy, Pyrenees, Southwest Iceland, Western Greece, and the Vrancea region in Romania - that represent a range of hazard levels and various seismotectonic settings: collisional/subduction complex with a complicated back-arc/fore-arc/trench system (Southern Italy), continent-continent collision with the evolution of an orogenic belt (Pyrenees), oceanic crust interplate transform faulting (Southwest Iceland), interplate subduction zones (Western Greece), and intermediate-depth subcrustal seismicity (Romania).

We quantitatively assess the operational performance of the PRESTo and VS(SC) algorithms in real-time simulation mode by using playbacks of recorded seismic waveforms or those simulated through a physics-based method. EEW alerts need to be both timely and sufficiently accurate to be useful (Meier, 2017), especially in Europe, where most earthquake-prone target sites are associated with short available lead times, significant exposure, and earthquake-related vulnerability (e.g., Picozzi et al., 2015). Therefore, our performance assessment focuses on the algorithms' capability to both quickly and correctly characterize the earthquake source (location and magnitude). We also use GMMs to investigate the impact of the source-parameter predictions on the temporal trend and quality of the resulting ground-motion amplitude estimations. Note that a further performance assessment of the two algorithms is carried out in our companion paper (Cremen et al., 2021), which focuses on the accuracy and uncertainty of the underlying methods from a theoretical perspective using similar event data.

The purpose of our comparison is to identify the best-performing regional EEW algorithms to be implemented in the TURNkey FWCR (Forecasting–Early Warning–Consequence Prediction–Response) platform, a comprehensive information system for facilitating operational earthquake forecasting, EEW, and post-earthquake rapid response actions across the continent. This platform is being developed as part of the TURNkey ("*Towards more Earthquake-resilient Urban Societies through a Multi-Sensor-based Information System enabling Earthquake Forecasting, Early Warning and Rapid Response Actions*") EU Project and will rely on SeisComP (version 3-Jakarta release) for waveform acquisition. SeisComP (Helmholtz-Centre Potsdam - GFZ German Research Centre for Geosciences and gempa GmbH, 2008) is a freely available and widely distributed standard real-time earthquake monitoring platform developed by the GEOFON Program at Helmholtz Center Potsdam, GFZ German Research Centre for Geosciences and gempa GmbH (Hanka et al., 2010). It is based on a comprehensive software framework, which includes waveform acquisition (SeedLink), automated earthquake detection, source location and characterization, manual event relocation, event alerting, waveform archiving and dissemination. SeisComP follows a modular approach in which standalone programs communicate through a messaging system connected to a shared database that contains events and station metadata. This modular structure also facilitates the incorporation of seismological and EEW algorithms, which can be individually used for estimating different parameters. TURNkey will ultimately be tested for adoption across six regions with varying characteristics of seismicity in Italy, France, Iceland, Greece, Romania, and the Netherlands.

The paper is organized as follows. We first introduce the considered algorithms and the relevant input data required. We then describe the methodologies used for evaluating the performance of the algorithms. We next assess and compare the algorithms. The paper ends with a discussion of the results, which includes recommendations on the most appropriate algorithms for the TURNkey platform.

TABLE 1 | Coefficients (A, B, C) and SE of the *RTMag* regression law used in this study for PRESTo (Festa, not published, implemented in the available release of the PRESTo platform).

phase	Time window (s)	A	B	C	SE
P	2	−7.69 ± 0.06	1.00 ± 0.00	−1.89 ± 0.03	±0.2
P	4	−7.69 ± 0.06	1.00 ± 0.00	−1.89 ± 0.03	±0.2
S	2	−7.30 ± 0.06	1.00 ± 0.00	−1.80 ± 0.03	±0.2

This law has the form: $M = (\log_{10}(Pd) - A - C \cdot \log_{10}(R/10))/B$, where Pd is the peak displacement (m) in different time windows and R is the hypocentral distance in km. See Lancieri and Zollo (2008) for more details about the functional form of the regression law.

ALGORITHMS

We specifically focus on the performance of PRESTo and VS(SC) in this study. PRESTo (Lancieri and Zollo, 2008; Satriano et al., 2008; Satriano et al., 2011) is a free and open-source software platform specifically developed for EEW, which was designed by the Ricerca in Sismologia Sperimentale e Computazionale research group (RISSC-Lab) at the University of Naples Federico II, Italy. It processes real-time waveforms that are streamed from stations using a SeisComP server via the SeedLink protocol and produces hypocentral location estimates in the form of a multivariate normal probability density function (PDF), using the *RTLoc* method developed by Satriano et al. (2008). According to the *RTMag* procedure proposed by Lancieri and Zollo (2008), a Bayesian framework is used for predicting magnitude. The *RTMag* regression-law coefficients that we adopt in this study are listed in **Table 1**.

PRESTo uses the picker algorithm *FilterPicker* initially proposed by Vassallo et al. (2012) to detect an event, which operates on continuous data-streams by applying a multiband signal processing procedure (i.e., the signal is analyzed in different predetermined frequency bandwidths). The event declaration is constrained to a predefined number of picks within a given time window. Full details of the PRESTo

platform can be found in its technical manual (http://www.prestoews.org/documentation.php).

VS(SC) (Virtual Seismologist in SeisComP) (Behr et al., 2016) is the magnitude likelihood component of the Virtual Seismologist EEW algorithm (Cua, 2005; Cua and Heaton, 2007; Cua et al., 2009) that is implemented in SeisComP. It incorporates phase picks and location estimates provided by other SeisComP modules. The coefficients for magnitude estimation are hard-coded in SeisComP (*scvsmag* module) and provided in Cua (2005).

SeisComP allows a free configuration of recursive filters and filter chains before picking, which is performed by the *scautopick* module. Several types of filter can be applied, but we use the default option in this study that involves subtraction of the running mean for a given time window, a single application of a one-sided cosine taper at the beginning of new data streams, a Butterworth bandpass filter, and a Short Time Average over Long Time Average (*STA/LTA*) filter, i.e., the ratio of a short-time average signal amplitude to a long-time average calculated continuously in two partially overlapping time windows of different length. The *STA/LTA* approach is used as the basis for many triggering algorithms (Allen, 1982). A trigger is declared when the *STA/LTA* exceeds a certain threshold. A second-stage picker can refine the final pick of the phase. We use the Akaike Information Criterion picker for this purpose, which implements the non-*AR* algorithm (Maeda 1985; Zhang et al. 2003). The picker is re-initialized after a data gap.

SeisComP location estimates are typically performed using the *scautoloc* module, which is optimized for teleseismic phase association and requires at least 6 P-wave detections to determine a location estimate. However, we instead pair VS(SC) with the *scanloc* location module of SeisComP (Roessler et al., 2016; Grigoli et al., 2018) in this study, which is more appropriate for EEW purposes. *scanloc* can produce fast location estimates with very few P- and S- wave detections from nearby stations (i.e., 2 to define the general epicentral area and 3 to obtain a unique epicenter). It makes use of an advanced cluster search algorithm (*DBSCAN*) to automatically associate phase detections to potential earthquakes; when a cluster of at least a prescribed minimum number of P-wave picks is identified, all picks within configured time windows and maximum epicentral distance ranges are provisionally associated with it. It should be noted that the cluster search itself is based on P phases only; however, in a second step, more P and S phases are associated and used for locating the earthquake.

For the sake of simplicity, the suite of modules used to produce EEW estimates from SeisComP (which include *scanloc* and VS(SC)) are referred to as the "VS(SC) algorithm" throughout the rest of the paper. To maintain consistency in our terminology, we herein refer to the PRESTo platform as the "PRESTo algorithm."

INPUT DATA

Seismic Waveforms

We use observed recordings from past events and physics-based synthetic seismograms to test the two algorithms' performance. Specifically, we consider observed recordings from Southwest Iceland, Western Greece, and Romania, while synthetic seismograms are computed for Southern Italy and the Pyrenees to compensate for the lack of empirical data from moderate-to-large events in these regions. The use of seismograms from different regions enables the performance of the considered EEW algorithms to be evaluated across a wide range of focal mechanisms, magnitudes, hypocentral depths, and seismic network densities/configurations.

We select observed seismograms from earthquakes with M_w greater than 5.5 that occurred in the last 20 years and were recorded by at least eight of the seismic stations we examined in this study, which were constrained by the availability of recordings in the consulted databases. Recordings for Greece and Romania are retrieved from the European Integrated Data Archive (EIDA, see *Data Availability Statement*). We consider only strong-motion and broadband sensors. We use one sensor per station, which is always the strong-motion instrument (where present); in all other cases, the broadband seismograms are clipped to prevent the use of saturated velocigrams. Strong-motion recordings from Iceland are obtained from the Internet Site for European Strong-motion Data (ISESD, see *Data Availability Statement*).

The synthetic seismograms for Southern Italy and the Pyrenees are computed from physics-based numerical simulations, using the broadband ground-motion simulation code described in Crempien and Archuleta (2015), which can simulate the high-frequency content of seismic waves and has already proved to be suitable for EEW feasibility studies (Zuccolo et al., 2016). We specifically generate seismograms for one scenario earthquake on each active fault in both regions. Faults parameters are retrieved from the European Database of Seismogenic Faults (ESDF; Basili et al., 2013). The magnitude of each scenario earthquake is randomly determined by assuming a uniform distribution between 5.5 and the maximum magnitude associated with the fault. The hypocentre is assumed to be located in the center of the fault plane's horizontal projection, at the minimum fault depth plus 2/3 of the fault's vertical width (i.e., the difference between the maximum and minimum fault depths). The focal mechanism is defined based on the average strike, dip, and rake values. Rupture fault dimensions are estimated from the Wells and Coppersmith (1994) relationships, and the position of the hypocentre on the fault plane (i.e., along the width and along the length of the fault) is established using the distributions by Causse et al. (2008). The average rupture velocity is determined by assuming a uniform distribution between 65 and 85% of the shear wave velocity on the fault plane. The corner frequency is estimated from the stress drop (Allmann and Shearer, 2009), which is assumed to be equal to 3 MPa (Caporali et al., 2011) for both regions. The seismograms are computed at the location of currently operating permanent stations according to the Incorporated Research Institutions for Seismology (IRIS) database (see *Data Availability Statement*), up to a maximum epicentral distance of 100 km. Finally, white noise is added to the computed seismograms to facilitate the *STA/LTA* algorithm's operation. A detailed engineering validation of these physics-based simulated ground motions (e.g., Galasso et al., 2012; Galasso et al., 2013) is outside the scope of this study.

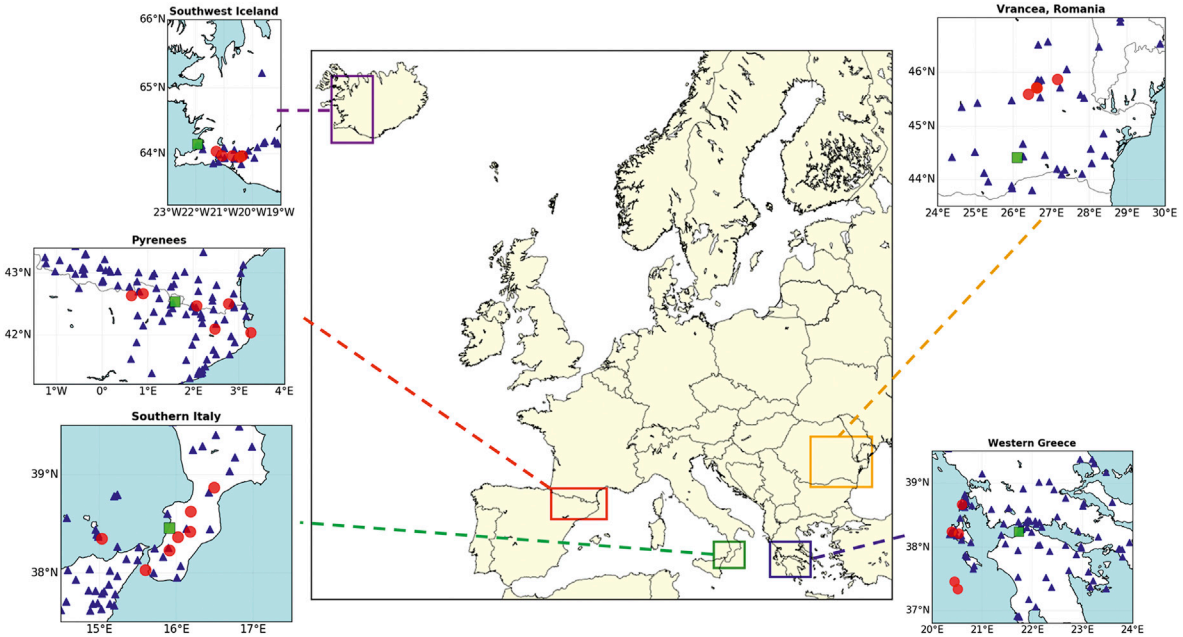

FIGURE 2 | Locations of the earthquakes (red circles) and target sites (green squares) considered in this study. Blue triangles represent the considered seismic stations. The target sites are the Port of Gioia Tauro for Southern Italy, Andorra for the Pyrenees, Reykjavík for Southwest Iceland, Patras for Western Greece and Bucharest for Romania.

We consider 27 events in total; their locations are highlighted in **Figure 2**, and their main features are listed in **Table 2**, along with the considered seismic networks. Throughout the rest of the paper, we refer to all magnitude, longitude, latitude, and depth values listed in **Table 2** as "bulletin" values (for both observed and simulated events).

Velocity Models

We use rocky regional velocity models from the literature (see **Table 3**) for both location estimation and the computation of synthetic seismograms. Where not explicitly defined, P-wave velocities are converted into S-wave velocities (and vice-versa), using the Poisson solid's approximation. Densities are converted from P-wave velocities using the Nafe-Drake relationship (Ludwig et al., 1970). The quality factors (Q_S and Q_P), necessary for the computation of synthetic seismograms, are set as follows: $Q_S = 100 \times V_S$, where V_S is the shear wave velocity (km/s), and $Q_P = 9/4 \times Q_S$ (Lay and Wallace, 1995).

To run PRESTo, we compute 3D travel-time grids for both P- and S-waves at all stations (introduced in *Seismic Waveforms*), using the *NonLinLoc* software (Lomax et al., 2000). Grid dimensions adopted for the *NonLinLoc* software are defined according to the size of the considered regions ($1 \times 1 \times 1$ km for Iceland, $2 \times 2 \times 2$ km for the remaining regions). For SeisComP, the locator is user-defined; we apply *LocSAT* (Bratt and Nagy, 1991) with travel-time tables prepared by replacing the shallow layers of the *IASP91* model (Kennett and Engdahl, 1991) with the local velocity models of **Table 3**.

Ground-Motion Models

The most appropriate IM to characterize ground motion for earthquake engineering applications of EEW systems is application-specific. Since we compute ground-motion estimates only for comparison purposes in this study, we use Peak Ground Acceleration (PGA) as the selected IM in all cases, given its widespread use in the literature. The choice of GMM also has a significant impact on the estimated IM. Despite the availability of region-specific GMMs for various European regions (e.g., Zuccolo et al., 2017; Huang and Galasso 2019), we use European and global GMMs to estimate PGA, since identifying optimal GMMs for each target site is outside the scope of this paper. We specifically use the hypocentral distance version of the GMM by Akkar et al. (2014) for all earthquakes with hypocentral depth <30 km and the model of Youngs et al. (1997) for the intermediate-depth Vrancea earthquakes (Vacareanu et al., 2013). Note that we approximate the rupture distance metric of the Youngs et al. (1997) GMM using hypocentral distance, which is a valid assumption for the magnitude range of the deep events considered in this study (Cauzzi et al., 2015).

We estimate PGA values at the following target sites (**Figure 2**): port of Gioia Tauro (15.91 E, 38.46 N) for Southern Italy, Andorra (1.60 E, 42.54 N) for the Pyrenees, Reykjavík (21.94 W, 64.15 N) for Southwest Iceland, Patras (21.73 E, 38.25 N) for Western Greece and Bucharest (26.10 E, 44.43 N) for Romania. We assume representative rock ground conditions for all target locations, given that site class is not relevant for the comparative analyses performed in this paper.

TABLE 2 | Magnitude, longitude, latitude, and depth of the events considered in this study (retrieved from the seismological agencies provided in the table footnote), along with the seismic networks used in each region.

Region	Fault ID	Origin time	M_w	Lon (°)	Lat (°)	Depth (km)	Seismic networks
Southern Italy[a]	ITCS042		5.6	15.03	38.35	17.0	IV, AM, MN
	ITCS016		6.9	15.60	38.03	9.3	
	ITCS053		6.2	16.19	38.63	8.3	
	ITCS055		5.9	15.91	38.23	9.0	
	ITCS068		6.4	16.49	38.87	11.0	
	ITCS080		5.6	16.18	38.42	9.0	
	ITCS082		6.3	16.02	38.37	8.3	
Pyrenees[a]	ESCS071		5.6	2.47	42.10	6.8	AM, CA, ES, FR
	ESCS112		6.0	3.26	42.04	6.8	
	FRCS007		6.2	2.07	42.48	10.3	
	ESCS126		5.7	0.64	42.64	6.3	
	FRCS002		6.0	2.77	42.51	10.3	
	ESCS125		6.5	0.89	42.67	6.7	
Southwest Iceland[b]		1998-06-04T21:36:53	5.5	−21.29	64.04	5.9	SM
		2000-06-17T15:40:41	6.4	−20.37	63.97	6.4	
		2000-06-17T15:42:50	5.7	−20.45	63.95	5.4	
		2000-06-21T00:51:47	6.5	−20.71	63.97	5.0	
		2008-05-29T15:45:58	6.3	−21.07	63.97	5.1	
Western Greece[c]		2014-01-26T13:55:43.0	6.0	20.53	38.22	16.4	AC, CL
		2014-02-03T03:08:44	5.9	20.40	38.25	11.3	HA, HC
		2015-11-17T07:10:07	6.4	20.60	38.67	10.7	HI, HL
		2018-10-25T22:54:49	6.7	20.51	37.34	9.9	HP, HT
		2018-10-30T15:12:02	5.8	20.45	37.46	5.5	MN
Vrancea, Romania[d]		2014-11-22T19:14:17.2	5.6	27.16	45.87	39.0	BS, GE
		2016-09-23T23:11:20.2	5.7	26.62	45.71	92.0	MD, RO
		2016-12-27T23:20:56.3	5.6	26.61	45.72	91.0	
		2018-10-28T00:38:10.8	5.5	26.40	45.60	151.0	

Details on the seismic networks can be retrieved from The International Federation of Digital Seismograph Networks (FDSN; see Data Availability Statement*). European Database of Seismogenic Faults (EDSF) fault IDs and origin times are also provided for simulated and observed earthquakes, respectively.*

[a]*Event parameters of simulated earthquakes.*

[b]*Event parameters retrieved from a catalog assembled and revised by Panzera et al. (2016).*

[c]*Event parameters retrieved from the National Observatory of Athens (NOA) earthquake catalog.*

[d]*Event parameters retrieved from the European Mediterranean Seismological Center (EMSC) earthquake catalog.*

METHODOLOGY FOR COMPARISON

We run playbacks of the seismic waveforms associated with the 27 considered events (**Figure 2**) through the PRESTo and VS(SC) algorithms. We evaluate and compare the performance of both algorithms in terms of their source-parameter estimates and the corresponding ground-shaking predictions at the selected target sites.

Performance in Terms of Source Parameters

The comparison of the algorithms' performance is first assessed in terms of both the timeliness and accuracy of location and magnitude estimates. We specifically examine the most probable hypocentral estimates and the maximum likelihood magnitude estimates of each algorithm at two specific temporal instances:

a) time of the first estimate, which is the time, with respect to the actual origin time, required to produce the first joint estimate of location and magnitude;
b) time of stable estimate, which is the time at which the EEW estimates stop changing significantly, i.e., the time from which the difference between the estimated and final values is consistently less than a prefixed difference threshold. Different stable estimate times are defined with respect to the epicenter, depth, and magnitude estimates. For epicentral distance, the difference thresholds are fixed at 5 km if the final estimated depth is less than 30 km and are fixed at 10 km for larger depths. For depth and magnitude, the thresholds are fixed at 5 km and 0.2 units, respectively.

Figure 3 demonstrates the temporal evolution of the algorithms' source-parameter performance for two sample earthquakes (i.e., the 2000-06-17 South Iceland event in the left column and the 2016-09-23 Vrancea event in the right

TABLE 3 | Regional velocity models used in this study.

Region	Velocity model
Southern Italy	Barberi et al. (2004)
Pyrenees	Theunissen et al. (2017)
Southwest Iceland	Tryggvason et al. (2002)
Western Greece	Rigo et al. (1996)
Vrancea region, Romania	Raykova and Panza (2006)–Vrancea cell

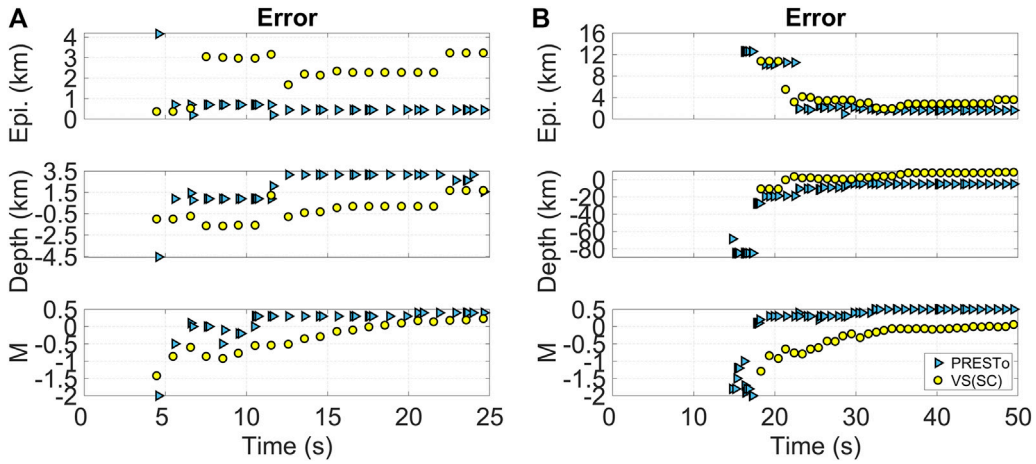

FIGURE 3 | Temporal evolution (starting from the origin time) of the estimates by the PRESTo and VS(SC) algorithms for two example earthquakes: **(A)** the 2000-06-17 observed event in South Iceland; and **(B)** the 2016-09-23 observed event in Vrancea. Top: epicentral error timeline; middle: depth error timeline; and bottom: magnitude (M) error timeline. All error values are computed by subtracting the bulletin values from the corresponding estimates of the algorithms. Different symbols distinguish the two algorithms.

column) that capture the range of magnitudes and depths considered in this study. These plots demonstrate the full temporal evolution of the epicentral error, the depth error, and the magnitude error. Bulletin values are assumed to be correct, such that magnitude and depth errors are computed by subtracting these values from the corresponding estimates of the algorithms, while epicentral errors are estimated as the distance between the bulletin and estimated epicenter locations. The timeline plots enable us to assess the timeliness of EEW (i.e., how quickly each algorithm can produce the first joint location-magnitude estimate and the time necessary to achieve stable source estimates, as defined above), and the accuracy of the source parameters (i.e., how much these parameter estimates deviate with respect to the bulletin values listed in **Table 2**).

Performance in Terms of Ground Motion

We also explore the effect of location and magnitude estimates on the corresponding PGA predictions at the selected target sites. We compute the ground shaking for both algorithms by applying a GMM to the algorithms' location and magnitude estimates, as described in *Ground-Motion Models*. We perform two analyses in terms of ground motion. The first analysis examines the temporal evolution of PGA estimates, and the second analysis investigates their accuracy.

Because of the temporal evolution of the location and magnitude estimates (**Figure 3**), the resulting computation of PGA also changes in time. This is an important consideration, as some EEW systems trigger an alert based on a prefixed threshold associated with the predicted ground shaking (Cremen and Galasso, 2020). For example, a warning may be issued if there is an unacceptable probability of a critical PGA value (PGA_c) being exceeded, according to Iervolino (2011):

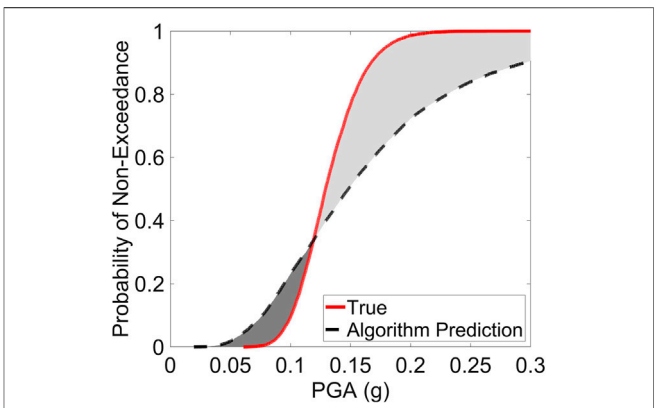

FIGURE 4 | Demonstration of the GMM evaluation procedure, which measures the difference between the true and estimated GMM CDF for a given set of location and magnitude predictions. The light gray shading indicates PGA exceedance thresholds for which the predicted ground shaking is greater than the true value, which may lead to a false alert. The dark gray shading indicates exceedance thresholds for which the predicted shaking is less than the true value, which may lead to a missed alert.

$$\Pr[PGA > PGA_c] = 1 - \int_{-\infty}^{IM_c} f(PGA)dPGA \geq Pr_c \qquad 1$$

where Pr_c is a critical risk threshold related to potential damage associated with the incoming event (Cremen and Galasso, 2020), and $f(PGA)$ is the PDF of PGA, which is dependent on real-time estimates of location and magnitude at a given temporal instant.

Since location and magnitude estimates can evolve in time in a non-monotonic way, the predefined ground-motion-related threshold can be exceeded at a certain instant, but not exceeded at a subsequent instant, then exceeded again

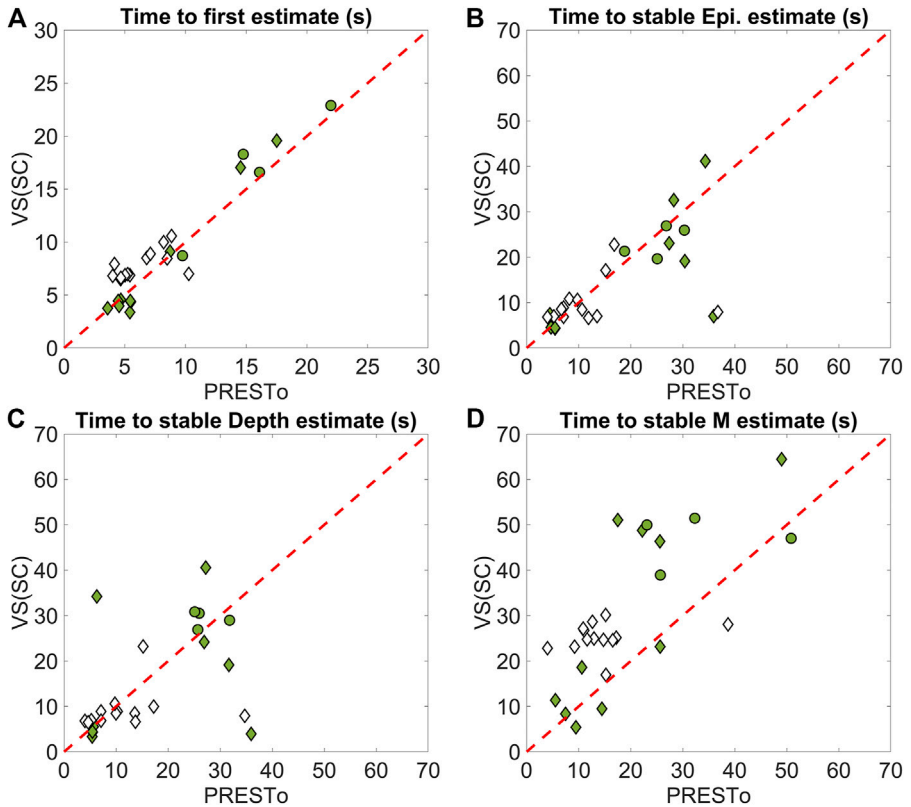

FIGURE 5 | Comparison between the PRESTo and VS(SC) algorithms in terms of timeliness. The average ratio between the times of PRESTo and VS(SC) estimates is: **(A)** 0.94; **(B)** 1.3; **(C)** 1.5; and **(D)** 0.7. Note that times shown are relative to actual event times. Filled and empty markers indicate observed and simulated events, respectively. Diamond and circle markers indicate shallow and deep events, respectively.

later in time, and so on (Wu et al., 2013; Wu et al., 2016). This behavior can raise questions about the integrity of an issued alarm and should be addressed when designing a decision-support system for EEW. Therefore, we perform a comparison by evaluating the number of trend inversions in the temporal evolution of the predicted PGA at the selected target sites provided in *Ground-Motion Models*.

In line with our companion paper (Cremen et al., 2021), ground-shaking prediction accuracy is quantified using the *MD* metric for sensitivity analyses (Chun et al., 2000), which has already been leveraged to examine the performance of GMMs (Cremen et al., 2020). *MD* measures the difference between the cumulative distribution function (CDF) of PGA produced when the bulletin source parameters are used in the GMM and the CDF obtained for a given algorithm's source-parameter estimates at a prescribed temporal instant (considering the total standard deviation of the GMM in both cases); see **Figure 4**. Since the GMMs used in this study provide lognormal distributions of PGA, we calculate *MD* according to the following equation:

$$MD = \frac{\sqrt{\tilde{y}_i^2 \exp\left(2\beta_i^2\right) + \tilde{y}_o^2 \exp\left(2\beta_o^2\right) - 2\tilde{y}_i\tilde{y}_o exp\left(\frac{\left(\beta_i+\beta_o\right)^2}{2}\right)}}{\tilde{y}_o exp\left(\frac{\beta_o^2}{2}\right)} \quad 2$$

The *i* and *o* subscripts respectively refer to the GMM CDF computed using the algorithmic source-parameter estimates and the GMM CDF produced by the bulletin source parameters. $\tilde{y}$ is the median predicted PGA and β is the total logarithmic standard deviation of the PGA prediction. A lower *MD* value indicates a higher similarity between the GMM distributions based on estimated and bulletin source parameters. This type of comparison is useful, as discrepancies in the CDFs indicate the potential for erroneous decisions by an end user, if EEW alerts are issued based on a given probability of exceeding a prescribed value of PGA, as discussed above.

PERFORMANCE ASSESSMENT: RESULTS AND DISCUSSION

Timeliness of Location and Magnitude Estimates

The timeliness comparison of both algorithms is provided in **Figure 5**. Our analysis reveals that the first EEW estimates are provided slightly faster by PRESTo, with an average time-to-first-estimate ratio between PRESTo and VS(SC) of 0.94. This is partially related to the fact that VS(SC) requires 3 s of P-wave information at a single station to estimate magnitude, while

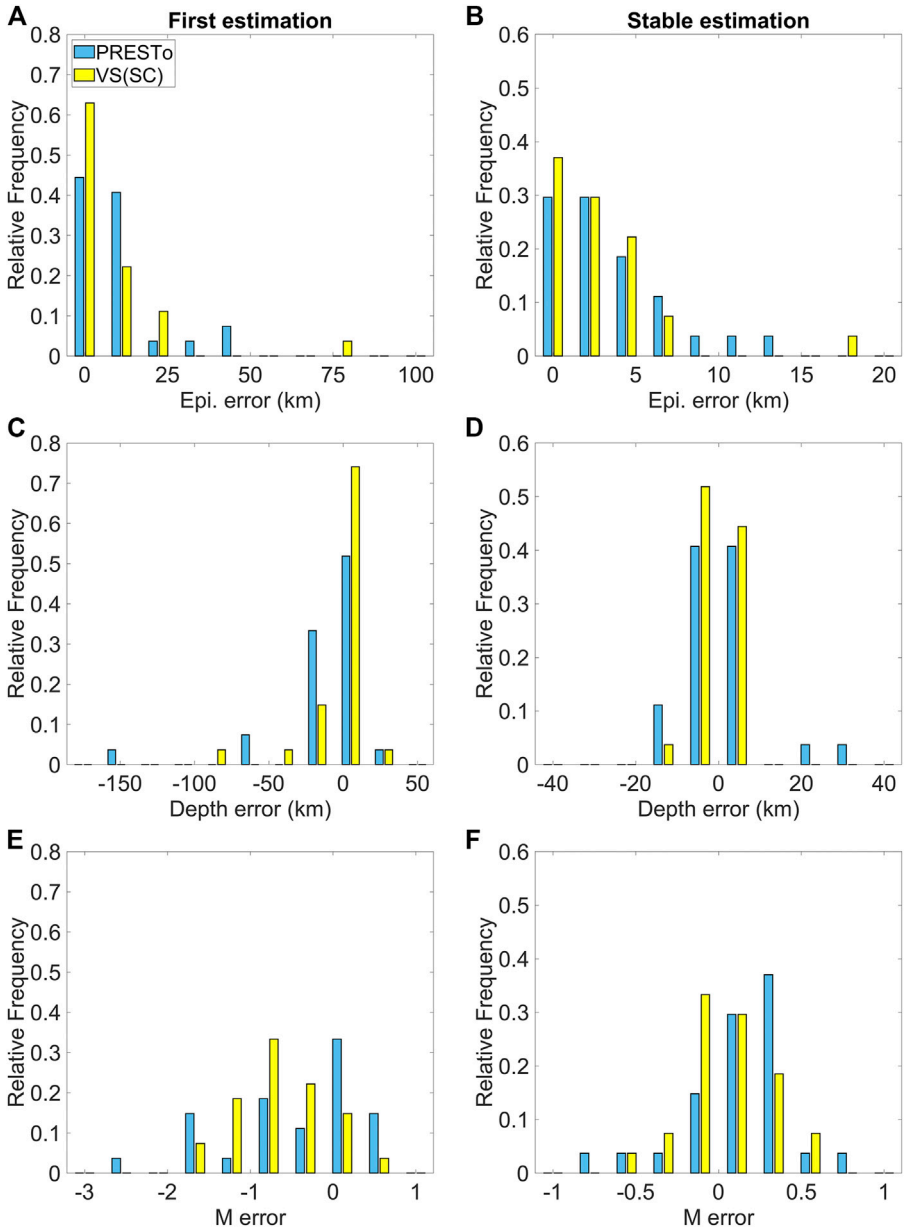

FIGURE 6 | Comparison between the PRESTo and VS(SC) algorithms in terms of **(A,B)** epicentre; **(C,D)** depth; and **(E,F)** magnitude (M) accuracy. Each histogram contains results for all 27 considered events. The left column provides errors associated with first estimates. The right column provides errors associated with stable estimates. Magnitude and depth errors are computed by subtracting the bulletin values from the corresponding estimates of the algorithms, while epicentral errors represent the distance between the bulletin and estimated epicentre locations.

RTMag uses only 2 s of P-wave signal to deliver a first magnitude estimate. VS(SC) location estimates retrieved from *scanloc* converge to stable values faster than those of PRESTo (the average time-to-stable-estimate ratio between PRESTo and VS(SC) is 1.3 for the epicenter and 1.5 for the depth); in contrast, VS(SC) magnitude estimates require a longer time to become stable (the average time-to-stable-estimate ratio between PRESTo and VS(SC) is 0.7), which confirms a similar observation by Chung and Allen (2019).

Accuracy of Location and Magnitude Estimates

The comparison in terms of accuracy is given in **Figure 6** and **Table 4** for the temporal instances associated with the first and stable estimates.

The first estimates of epicentral distance and depth by VS(SC) are more accurate than those provided by PRESTo (by approximately 5 km for the epicenter and 3 km for the depth). The location performance of both algorithms is fairly similar at the

TABLE 4 | Median (η), mean (μ), and standard deviation (σ) of the error distributions shown in **Figure 6**.

Component/time	Algorithm	
	PRESTo	VS(SC)
a) Epicentre: First estimate (km)	η = 7.97	η = 2.48
	μ = 11.00	μ = 8.68
	σ = 12.14	σ = 15.27
b) Epicentre: Stable estimate (km)	η = 2.05	η = 1.75
	μ = 3.51	μ = 3.02
	σ = 3.14	σ = 3.61
c) Depth: First estimate (km)	η = −5.54	η = −1.72
	μ = −13.10	μ = −6.29
	σ = 32.46	σ = 16.85
d) Depth: Stable estimate (km)	η = −0.59	η = −0.83
	μ = 0.01	μ = −0.23
	σ = 9.28	σ = 3.82
e) Magnitude: First estimate	η = −0.32	η = −0.49
	μ = −0.46	μ = −0.55
	σ = 0.84	σ = 0.59
f) Magnitude: Stable estimate	η = 0.20	η = 0.01
	μ = 0.13	μ = 0.03
	σ = 0.30	σ = 0.19

stable instant, although the dispersion of the stable depth estimate error for PRESTo (9.28) is almost 2.5 times that for VS(SC) (3.82).

The first magnitude estimate is generally underestimated with respect to the bulletin value for both algorithms due to a sparsity of recorded data. The corresponding error distributions for PRESTo and VS(SC) have respective medians of −0.32 and −0.49 and respective means of −0.46 and −0.55, which imply that the underestimation of VS(SC) is larger than that of PRESTo. However, PRESTo magnitude estimate errors are associated with a larger standard deviation (0.84) than those of VS(SC) (0.59). In contrast, the stable magnitude estimates computed by VS(SC) are more accurate than those computed by PRESTo; the corresponding error distributions for VS(SC) and PRESTo have respective medians of 0.01 and 0.20, and respective means of 0.03 and 0.13. However, accurate magnitude estimations from VS(SC) require a significantly longer time (**Figure 5**), which may not justify the greater amount of accuracy achieved.

It should be highlighted that the accuracy of the computed location and magnitude estimations is directly affected by the performance of each algorithm's event-detection capability (i.e., phase picking and the seismic phase association methodology). Phase detection and association are difficult and error-prone tasks, especially during intense aftershock sequences (Meier et al., 2020). The event-detection algorithms (for both PRESTo and VS(SC)) are optimized consistently for each region of interest through an ad-hoc tuning of the relevant parameters that considers overall seismicity and the network geometry. However, discrepancies in phase picking and event association can still remain due to differences in the parameters and related procedures used in both algorithms. It should also be noted that the most appropriate tuning for a certain area could be different from that used in this study, which was calibrated using only the small sample of events analyzed.

Moreover, it should be mentioned that we do not consider an optional Bayesian prior distribution for PRESTo, to be consistent with the format of the VS(SC) magnitude calculation. Inclusion of this prior may improve PRESTo's magnitude estimates. Finally, it should be highlighted that the empirical scaling relationships used for magnitude computation in *RTMag* and VS(SC) may not be appropriate/optimal for the regions considered in this study, especially for the deep events of the Vrancea region (for example, the VS(SC) relationships were calibrated for Californian events by assuming a depth of 3 km). The need for conducting region-specific recalibration of the relationship coefficients should always be investigated when implementing an EEW system in a new region (see, for example, Carranza et al., 2013). Otherwise, it may be most practical to simply evaluate and add empirically derived offsets (if any) to the magnitudes estimated for particular regions.

Trend of PGA Estimates

Figure 7 shows the number of trend inversions that occur over time for the median PGA predictions computed using the locations and magnitudes estimated by both algorithms. To eliminate insignificant changes in trend, we only consider inversions that result in at least a 20% change with respect to the previous PGA estimate. Our analysis shows that the number of inversions for VS(SC) is lower on average (1.52, compared to 3.37 for PRESTo) and has a smaller standard deviation (1.69, compared to 4.45 for PRESTo). VS(SC) has also a slightly greater number of cases with zero inversions, which correspond to situations in which there is no significant variation of the computed PGA in time (ideal case, in which the maximum possible lead time is achieved if the alert threshold is exceeded and the PGA is predicted correctly), or there is a near monotonic increase of its estimated value. Conversely, PRESTo has some cases with more than ten trend inversions, corresponding to two Greek offshore events and one event located in the central Pyrenees. They are related to erroneous PRESTo location predictions due to particular geometric network conditions that have a significantly negative effect on ground-motion estimation, thus contributing to the multiple inversion cases observed. Therefore, we conclude that the integrity of the

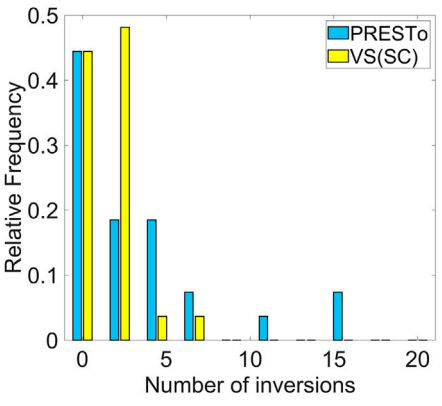

FIGURE 7 | Number of trend inversions in the evolution of PGA estimates for both considered algorithms. The median (η), mean (μ) and standard deviation (σ) of the distributions are: η = 2.00, μ = 3.37, σ = 4.45 for PRESTo, and η = 1.00, μ = 1.52, σ = 1.69 for VS(SC).

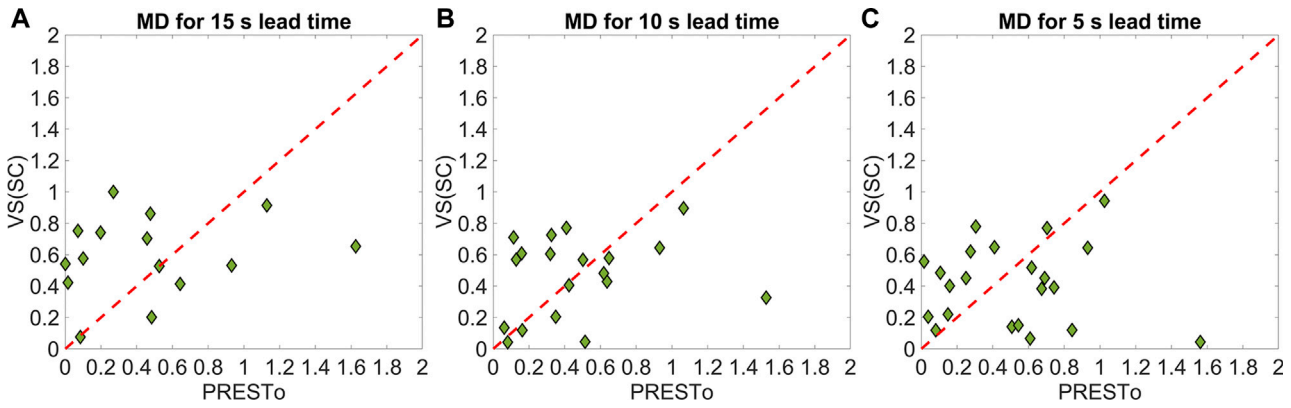

FIGURE 8 | Comparing the ground-shaking prediction accuracy of both considered algorithms for three lead times: **(A)** 15 s, **(B)** 10 s, and **(C)** 5 s. The average MD ($\overline{MD}$) estimate is: **(A)** $\overline{MD}$ = 0.45 for PRESTo and $\overline{MD}$ = 0.86 for VS(SC), **(B)** $\overline{MD}$ = 0.47 for PRESTo and $\overline{MD}$ = 0.47 for VS(SC), **(C)** $\overline{MD}$ = 0.82 for PRESTo and $\overline{MD}$ = 0.42 for VS(SC).

EEW alarm issued by the VS(SC) algorithm is higher than that for PRESTo.

Ground-Shaking Prediction Accuracy

We specifically investigate *MD* values for the algorithms' source-parameter estimates at temporal instances that correspond with three different lead times at target sites: 15, 10, and 5 s. The lead time at a given target site is defined as the time difference between the S-wave arrival and the first EEW estimate; a 1 s transmission delay is also accounted for. For each lead-time analysis, only the scenario events capable of providing that lead-time at the target site of interest are considered. This means that 16 events are examined for the 15 s lead time, 19 events are examined for the 10 s lead time, and 23 events are examined for the 5 s lead time. The results of the ground-shaking prediction assessments are presented in **Figure 8**. It can be observed that PRESTo provides more accurate ground-motion estimates at the largest lead times considered; PRESTo average *MD* ($\overline{MD}$) value for 15 s lead time is 0.45, whereas the corresponding VS(SC) $\overline{MD}$ value is 0.86. However, VS(SC) produces more accurate ground-shaking predictions than PRESTo for the smallest considered lead time (5 s); in this case, the PRESTo $\overline{MD}$ value is 0.82 and the VS(SC) $\overline{MD}$ value is 0.42. The average $\overline{MD}$ values are similar for the intermediate considered lead time (10 s). Note that the temporal variations in the optimal algorithm for ground-motion accuracy reflect those observed for magnitude accuracy in *Accuracy of Location and Magnitude Estimates*.

CONCLUDING REMARKS

This study used scenario earthquakes across five European regions to quantitatively compare the performance of the PRESTo and VS(SC) (using *scanloc* for location) regional EEW algorithms. Our overall aim was to identify the best options for EEW location and magnitude estimation in the TURNkey platform, a multi-sensor-based information system to be implemented in Europe for earthquake forecasting, EEW, and post-earthquake rapid response actions.

We first assessed the ability of PRESTo and VS(SC) to produce rapid and accurate source (i.e., location and magnitude) estimates of events. We then evaluated the accuracy of the algorithms' corresponding ground-shaking predictions for various lead times at prescribed target sites. We found that PRESTo may have a greater risk-mitigation potential than VS(SC) in general. This is because PRESTo produces faster and more accurate early magnitude estimates, which result in better ground-motion estimates for long lead times (15 s) that potentially enable significant earthquake preparation actions to take place, such as shutting down industrial equipment, evacuating the ground floors of buildings, and stopping surgical procedures (Goltz, 2002). Predictions by VS(SC) are eventually more accurate than those of PRESTo; however, the length of time this requires results in smaller warning windows that may only allow stakeholders to take simple automatic risk-mitigation actions like stopping traffic (i.e., turning lights red) or switching on semi-active control systems for structures (Goltz, 2002; Iervolino et al., 2008). It is also important to note that we did not use an optional Bayesian prior distribution for the *RTMag* magnitude algorithm of PRESTo. Its inclusion may have resulted in an even better performance of the PRESTo magnitude estimates and the associated ground-motion predictions.

We, therefore, ultimately recommend that, out of the two considered regional EEW algorithms, PRESTo is used for EEW in the TURNkey platform, which is consistent with the conclusions of our companion paper (Cremen et al., 2021). Alternatively, the PRESTo *RTMag* algorithm could be independently implemented within SeisComP (and, therefore, the TURNkey platform) as an additional module for EEW magnitude evaluation. This configuration would also enable *scanloc* to be used within the TURNkey platform, which we found to be the best algorithm for location estimation.

Therefore, the combination *RTMag* plus *scanloc* may facilitate more accurate EEW ground-motion estimates than those provided by the full PRESTo algorithm.

This study's results were obtained through playbacks of the seismic waveforms and EEW parameters associated with 27 historic/simulated earthquakes representative of different tectonic environments and regional European variation in station distributions and densities. We used actual network configurations for testbeds where synthetic seismograms were used (i.e., Southern Italy and the Pyrenees). The availability of recordings constrained the number of considered stations for all other regions examined (i.e., Greece, Romania, and Iceland). Therefore, the study's outcome should be interpreted as an average performance of the examined algorithms across different seismicity and network geometries in Europe. A more detailed feasibility study is recommended for target- or region-specific applications of the algorithms.

DATA AVAILABILITY STATEMENT

The raw data supporting the conclusions of this article will be made available by the authors, upon reasonable request. SeisComP is available at https://www.seiscomp.de, with professional software support from gempa GmbH (http://www.gempa.de). VS(SC) is available as part of the SeisComP software suite, while *scanloc* is a commercial software by gempa. PRESTo is available at http://www.prestoews.org/about.php. The European Integrated waveform Data Archive (EIDA, https://www.orfeus-eu.org/data/eida/) was consulted through the ORFEUS Data Center WebDC3 Web Interface (http://orfeus-eu.org/webdc3/) (doi: 10.5880/GFZ.2.4/2016.001; last accessed January 2021). The Internet Site for European Strong-motion Data (ISESD, http://www.isesd.hi.is/) was also used (last accessed January 2021). Stations metadata were retrieved from The International Federation of Digital Seismograph Networks (FDSN), accessible through http://www.fdsn.org/ (last accessed January 2021). IRIS (Incorporated Research Institutions for Seismology) station database is accessible through https://ds.iris.edu/gmap (last accessed January 2021). The European Mediterranean Seismological Center (EMSC) earthquake catalog is available at https://www.emsc-csem.org/(last accessed January 2021), while the National Observatory of Athens (NOA) earthquake catalog can be retrieved from https://bbnet.gein.noa.gr/HL (doi: https://doi.org/10.7914/SN/HL; last accessed January 2021). The European Database of Seismogenic Faults (ESDF) is available at http://diss.rm.ingv.it/share-edsf/ (doi: 10.6092/INGV.IT-SHARE-EDSF; last accessed January 2021).

AUTHOR CONTRIBUTIONS

EZ computed synthetic seismograms, ran playbacks of the seismic waveforms, and analyzed the results. GC evaluated the ground-shaking prediction accuracy. CG and EZ prepared the figures. All authors contributed to the methodological development, the interpretation of the results and the manuscript preparation.

FUNDING

This paper is supported by the European Union's Horizon 2020 research and innovation programme under grant agreement No 821046, project TURNkey (Towards more Earthquake-resilient Urban Societies through a Multi-sensor-based Information System enabling Earthquake Forecasting, Early Warning and Rapid Response actions; https://earthquake-turnkey.eu).

ACKNOWLEDGMENTS

We would like to thank Dirk Roessler (gempa GmbH, Germany) for his generous assistance with running SeisComP and his very valuable advice and feedback on this study. We would also like to express our gratitude to Nikos Melis and Stratos Liadopoulos (National Observatory of Athens, Greece), Benedikt Halldorsson and Atefe Darzi (Haskoli Islands - University of Iceland, Iceland), Stefan Balan and Alexandru Marmureanu (Institutul National de Cercetare si Dezvoltare pentru Fizica Pamantului, Romania), and Pierre Gehl (Bureau de Recherches Géologiques et Minières, France) for providing input data for the regions considered in this study. We are grateful to Bernd Weber (gempa GmbH, Germany) and the gempa team for providing the *scanloc* module and assistance with SeisComP. The study has also benefited from the support on PRESTo provided by Luca Elia (RISSC-Lab, University of Naples Federico II, Italy). We are additionally grateful to Alireza Azarbakht and John Douglas (University of Strathclyde, United Kingdom) for helpful feedback on parts of this study. The authors also acknowledge the insightful comments from Matteo Picozzi (RISSC-Lab University of Naples Federico II, Italy) and Elisa Buforn (Universidad Complutense de Madrid, Spain) that improved the quality of this study. Figures for this manuscript were produced using the Matplotlib Python library (Hunter, 2007) and MATLAB®.

REFERENCES

Akkar, S., Sandıkkaya, M. A., and Bommer, J. J. (2014). Empirical Ground-Motion Models for point- and Extended-Source Crustal Earthquake Scenarios in Europe and the Middle East. *Bull. Earthquake Eng.* 12 (1), 359–387. doi:10.1007/s10518-013-9461-4

Allen, R. (1982). Automatic Phase Pickers: Their Present Use and Future Prospects. *Bull. Seismological Soc. America* 72 (6B), S225–S242.

Allmann, B. P., and Shearer, P. M. (2009). Global Variations of Stress Drop for Moderate to Large Earthquakes. *J. Geophys. Res. Solid Earth* 114 (1), 1–22. doi:10.1029/2008JB005821

Barberi, G., Cosentino, M. T., Gervasi, A., Guerra, I., Neri, G., and Orecchio, B. (2004). Crustal Seismic Tomography in the Calabrian Arc Region, South Italy. *Phys. Earth Planet. Interiors* 147 (4), 297–314. doi:10.1016/j.pepi.2004.04.005

Basili, R., Kastelic, V., Demircioglu, M. B., Garcia Moreno, D., Nemser, E. S., Petricca, P., et al. (2013). *The European Database of Seismogenic Faults (EDSF) Compiled in the Framework of the Project SHARE*.

Behr, Y., Clinton, J. F., Cauzzi, C., Hauksson, E., Jónsdóttir, K., Marius, C. G., et al. (2016). The Virtual Seismologist in SeisComP3: A New Implementation Strategy for Earthquake Early Warning Algorithms. *Seismological Res. Lett.* 87 (2A), 363–373. doi:10.1785/0220150235

Bratt, S., and Nagy, W. (1991). *The LocSAT Program*. San Diego: Science Applications International Corporation.

Caporali, A., Barba, S., Carafa, M. M. C., Devoti, R., Pietrantonio, G., and Riguzzi, F. (2011). Static Stress Drop as Determined from Geodetic Strain Rates and Statistical Seismicity. *J. Geophys. Res. Solid Earth* 116 (2), 1–15. doi:10.1029/2010JB007671

Carranza, M., Buforn, E., Colombelli, S., and Zollo, A. (2013). Earthquake Early Warning for Southern Iberia: A P Wave Threshold-Based Approach. *Geophys. Res. Lett.* 40 (17), 4588–4593. doi:10.1002/grl.50903

Carranza, M., Buforn, E., and Zollo, A. (2017). Performance of a Network-Based Earthquake Early Warning System in the Ibero-Maghrebian Region. *Seismological Res. Lett.* 88 (6), 1499–1507. doi:10.1785/0220170081

Causse, M., Cotton, F., Cornou, C., and Bard, P. Y. (2008). Calibrating Median and Uncertainty Estimates for a Practical Use of Empirical Green's Functions Technique. *Bull. Seismological Soc. America* 98 (1), 344–353. doi:10.1785/0120070075

Cauzzi, C., Faccioli, E., Vanini, M., and Bianchini, A. (2015). Updated Predictive Equations for Broadband (0.01–10 S) Horizontal Response Spectra and Peak Ground Motions, Based on a Global Dataset of Digital Acceleration Records. *Bull. Earthquake Eng.* 13 (6), 1587–1612. doi:10.1007/s10518-014-9685-y

Chun, M. H., Han, S. J., and Tak, N. Il. (2000). An Uncertainty Importance Measure Using a Distance Metric for the Change in a Cumulative Distribution Function. *Reliability Eng. Syst. Saf.* 70 (3), 313–321. doi:10.1016/S0951-8320(00)00068-5

Chung, A. I., and Allen, R. M. (2019). Optimizing Earthquake Early Warning Performance: ElarmS-3 ElarmS View Project Building Response Using Ambient Noise View Project. *Seismological Res. Lett.* 90 (2A). doi:10.1785/0220180192

Clinton, J., Zollo, A., Marmureanu, A., Zulfikar, C., and Parolai, S. (2016). State-of-the Art and Future of Earthquake Early Warning in the European Region. *Bull. Earthquake Eng.* 14 (9), 2441–2458. doi:10.1007/s10518-016-9922-7

Convertito, V., Iervolino, I., Zollo, A., and Manfredi, G. (2008). Prediction of Response Spectra via Real-Time Earthquake Measurements. *Soil Dyn. Earthquake Eng.* doi:10.1016/j.soildyn.2007.07.006

Cremen, G., and Galasso, C. (2020). Earthquake Early Warning: Recent Advances and Perspectives. *Earth-Science Rev.* 205 (February), 103184. doi:10.1016/j.earscirev.2020.103184

Cremen, G., Werner, M. J., and Baptie, B. (2020). A New Procedure for Evaluating Ground-Motion Models, with Application to Hydraulic-Fracture-Induced Seismicity in the United Kingdom. *Bull. Seismol. Soc. Am.* 110 (5), 2380–2397. doi:10.1785/0120190238

Cremen, G., Zuccolo, E., and Galasso, C. (2021). Accuracy and Uncertainty Analysis of Selected Methodological Approaches to Earthquake Early Warning in Europe. *Seismol. Res. Lett.* doi:10.1785/0220200414

Crempien, J. G. F., and Archuleta, R. J. (2015). UCSB Method for Simulation of Broadband Ground Motion from Kinematic Earthquake Sources. *Seismological Res. Lett.* 86 (1), 61–67.

Cua, G. B. (2005). *Creating the Virtual Seismologist: Developments in Ground Motion Characterization and Seismic Early Warning*. California. California Institute of Technology.

Cua, G., Fischer, M., Heaton, T., and Wiemer, S. (2009). Real-time Performance of the Virtual Seismologist Earthquake Early Warning Algorithm in Southern California. *Seismological Res. Lett.* 80 (5), 740–747. doi:10.1785/gssrl.80.5.740

Cua, G., and Heaton, T. (2007). The Virtual Seismologist (VS) Method: a Bayesian Approach to Earthquake Early Warning by. *Earthquake Early Warning Syst.*, 97–132.

Galasso, Carmine., Zhong, Peng., Zareian, Farzin., Iervolino, Iunio., and Graves, R. W. (2013). Validation of Ground-Motion Simulations for Historical Events Using MDoF Systems. *Earthquake Eng. Struct. Dyn.* 42, 1395–1412. doi:10.1002/eqe

Galasso, C., Zareian, F., Iervolino, I., and Graves, R. W. (2012). Validation of Ground-Motion Simulations for Historical Events Using SDoF Systems. *Bull. Seismological Soc. America* 102 (6), 2727–2740. doi:10.1785/0120120018

Goltz, James. D. (2002). *Introducing Earthquake Early Warning in California - A Summary of Social Science and Public Policy Issues*. California: Pasadena.

Grigoli, F., Scarabello, L., Böse, M., Weber, B., Wiemer, S., and Clinton, J. F. (2018). Pick- and Waveform-Based Techniques for Real-Time Detection of Induced Seismicity. *Geophys. J. Int.* 213 (2), 868–884. doi:10.1093/gji/ggy019

Grünthal, G., Wahlström, R., and Stromeyer, D. (2013). The SHARE European Earthquake Catalogue (SHEEC) for the Time Period 1900-2006 and its Comparison to the European-Mediterranean Earthquake Catalogue (EMEC). *J. Seismology* 17 (4), 1339–1344. doi:10.1007/s10950-013-9379-y

Hanka, W., Saul, J., Weber, B., Becker, J., and Harjadi, P. (2010). Real-time Earthquake Monitoring for Tsunami Warning in the Indian Ocean and beyond. *Nat. Hazards Earth Syst. Sci.* 10 (12), 2611–2622. doi:10.5194/nhess-10-2611-2010

Helmholtz-Centre Potsdam - GFZ German Research Centre for Geosciences and gempa GmbH (2008). *The SeisComP Seismological Software Package*. GFZ Data Services. doi:10.5880/GFZ.2.4.2020.003

Huang, C., and Galasso, C. (2019). Ground-motion Intensity Measure Correlations Observed in Italian strong-motion Records. *Earthquake Eng. Struct. Dyn.* 48 (15), 1634–1660. doi:10.1002/eqe.3216

Hunter, J. D. (2007). Matplotlib: A 2D Graphics Environment. *Comput. Sci. Eng.* 9 (3), 90–95. doi:10.1109/MCSE.2007.55

Iervolino, I., Galasso, C., and Manfredi, G. (2008). Information-Dependent Lead-Time Maps for Earthquake Early Warning in the Campania Region, 14th World Conference on Earthquake Engineering, Beijing, China, October 17, 2008, 12. Available at: http://www.rissclab.unina.it.

Iervolino, Iunio., Convertito, V., Giorgio, M., Manfredi, G., and Zollo, A. (2006). Real-time Risk Analysis for Hybrid Earthquake Early Warning Systems. *J. Earthquake Eng.* 10 (6), 867–885. doi:10.1142/S1363246906002955

Iervolino, Iunio., Giorgio, M., Galasso, C., and Manfredi, G. (2009). Uncertainty in Early Warning Predictions of Engineering Ground Motion Parameters: What Really Matters?. *Geophys. Res. Lett.* 36 (4), L00B06. doi:10.1029/2008GL036644

Iervolino, Iunio. (2011). Performance-based Earthquake Early Warning. *Soil Dyn. Earthquake Eng.* 31 (2), 209–222. doi:10.1016/j.soildyn.2010.07.010

Kennett, B. L. N., and Engdahl, E. R. (1991). Traveltimes for Global Earthquake Location and Phase Identification. *Geophys. J. Int.* 105 (2), 429–465. doi:10.1111/j.1365-246X.1991.tb06724.x

Lancieri, M., and Zollo, A. (2008). A Bayesian Approach to the Real-Time Estimation of Magnitude from the Early P and S Wave Displacement Peaks. *J. Geophys. Res. Solid Earth* 113 (12). doi:10.1029/2007JB005386

Lay, T., and Wallace, T. (1995). *Modern Global Seimology*, Vol. 58.

Lomax, A., Virieux, J., Volant, P, and Thierry, C. B. (2000). *Probabilistic Earthquake Location in 3D and Layered Models: Introduction of a Metropolis-Gibbs Method and Comparison with Linear Locations*, Madison, WI: USA, 101–134.

Ludwig, W., Nafe, J., and Drake, C. (1970). Seismic Refraction. *The Sea* 4, 53–84.

Maeda, N. (1985). A Method for Reading and Checking Phase Time in Auto-Processing System of Seismic Wave Data. *Zisin (Journal of the Seismological Society of Japan. 2nd Ser.)* 38 (3), 365–379. doi:10.4294/zisin1948.38.3_365

Meier, M. A. (2017). How "Good" Are Real-Time Ground Motion Predictions from Earthquake Early Warning Systems?. *J. Geophys. Res. Solid Earth* 122 (7), 5561–5577. doi:10.1002/2017JB014025

Meier, M., Kodera, Y., Chung, A., Hoshiba, M., Minson, S., Hauksson, E., et al. (2020). How Often Can Earthquake Early Warning Systems Alert Sites with High-Intensity Ground Motion?. *J. Geophys. Res. Solid Earth*. doi:10.1029/2019JB017718

Panzera, F., Zechar, J. D., Vogfjörd, K. S., and Eberhard, D. A. J. (2016). A Revised Earthquake Catalogue for South Iceland. *Pure Appl. Geophys.* 173 (1), 97–116. doi:10.1007/s00024-015-1115-9

Picozzi, M., Elia, L., Pesaresi, D., Zollo, A., Mucciarelli, M., Gosar, A., et al. (2015). Trans-national Earthquake Early Warning (EEW) in north-eastern Italy, Slovenia and Austria: First Experience with PRESTo at the CE3RN Network. *Adv. Geosciences* 40, 51–61. doi:10.5194/adgeo-40-51-2015

Picozzi, M., Zollo, A., Brondi, P., Colombelli, S., Elia, L., and Martino, C. (2015). Exploring the Feasibility of a Nationwide Earthquake Early Warning System in Italy. *J. Geophys. Res. Solid Earth* 120 (4), 2446–2465. doi:10.1002/2014JB011669

Raykova, R. B., and Panza, G. F. (2006). Surface Waves Tomography and Non-linear Inversion in the Southeast Carpathians. *Phys. Earth Planet. Interiors* 157 (3–4), 164–180. doi:10.1016/j.pepi.2006.03.019

Rigo, A., Lyon-Caen, H., Armijo, R., Deschamps, A., Hatzfeld, D., Makropoulos, K., et al. (1996). A Microseismic Study in the Western Part of the Gulf of Corinth (Greece): Implications for Large-Scale normal Faulting Mechanisms. *Geophys. J. Int.* 126 (3), 663–688. doi:10.1111/j.1365-246X.1996.tb04697.x

Roessler, D., Becker, J., Ellguth, E., Herrnkind, S., Weber, B., Henneberger, R., et al. (2016). "Cluser-search Based Monitoring of Local Earthquakes in SeisComp3," in Fall Meeting American Geophysical Union, San Francisco, December 12–16, 2016.

Satriano, C., Elia, L., Martino, C., Lancieri, M., Zollo, A., and Iannaccone, G. (2011). PRESTo, the Earthquake Early Warning System for Southern Italy: Concepts, Capabilities and Future Perspectives. *Soil Dyn. Earthquake Eng.* 31 (2), 137–153. doi:10.1016/j.soildyn.2010.06.008

Satriano, C., Lomax, A., and Zollo, A. (2008). Real-Time Evolutionary Earthquake Location for Seismic Early Warning. *Bull. Seismological Soc. America* 98 (3), 1482–1494. doi:10.1785/0120060159

Stucchi, M., Rovida, A., Gomez Capera, A. A., Alexandre, P., Camelbeeck, T., Demircioglu, M. B., et al. (2013). The SHARE European Earthquake Catalogue (SHEEC) 1000-1899. *J. Seismology* 17 (2), 523–544. doi:10.1007/s10950-012-9335-2

Theunissen, T., Chevrot, S., Sylvander, M., Monteiller, V., Calvet, M., Villaseñor, A., et al. (2017). Absolute Earthquake Locations Using 3-D versus 1-D Velocity Models below a Local Seismic Network: Example from the Pyrenees. *Geophys. J. Int.* 212 (3), 1806–1828. doi:10.1093/gji/ggx472

Tryggvason, A., Rögnvaldsson, S. T., and Flóvenz, Ó. G. (2002). Three-dimensional Imaging of the P- and S-Wave Velocity Structure and Earthquake Locations beneath Southwest Iceland. *Geophys. J. Int.* 151 (3), 848–866. doi:10.1046/j.1365-246X.2002.01812.x

Vacareanu, R., Pavel, F., and Aldea, A. (2013). On the Selection of GMPEs for Vrancea Subcrustal Seismic Source. *Bull. Earthquake Eng.* 11 (6), 1867–1884. doi:10.1007/s10518-013-9515-7

Vassallo, M., Satriano, C., and Lomax, A. (2012). Automatic Picker Developments and Optimization: A Strategy for Improving the Performances of Automatic Phase Pickers. *Seismological Res. Lett.* 83 (3), 541–554. doi:10.1785/gssrl.83.3.541

Wells, D. L., and Coppersmith, K. J. (1994). New Empirical Relationships Among Magnitude, Rupture Length, Rupture Width, Rupture Area, and Surface Displacement. *Bull. Seismological Soc. America* 84 (4), 974–1002. Available at: https://pubs.geoscienceworld.org/ssa/bssa/article-pdf/84/4/974/2707918/BSSA0840040974.pdf.

Wu, S., Beck, J. L., and Heaton, T. H. (2013). ePAD: Earthquake Probability-Based Automated Decision-Making Framework for Earthquake Early Warning. *Computer-Aided Civil Infrastructure Eng.* 28 (10), 737–752. doi:10.1111/mice.12048

Wu, S., Cheng, M. H., Beck, J. L., and Heaton, T. H. (2016). An Engineering Application of Earthquake Early Warning: EPAD-Based Decision Framework for Elevator Control. *J. Struct. Eng. (United States)* 142 (1). doi:10.1061/(ASCE)ST.1943-541X.0001356

Youngs, R. R., Chiou, S.-J., Silva, W. J., and Humphrey, J. R. (1997). Strong Ground Motion Attenuation Relationships for Subduction Zone Earthquakes. *Seismological Res. Lett.* 68 (1), 58–73. doi:10.1785/gssrl.68.1.58

Zhang, H., Thurber, C., and Rowe, C. (2003). Automatic P-Wave Arrival Detection and Picking with Multiscale Wavelet Analysis for Single-Component Recordings. *Bull. Seismological Soc. America* 93 (5), 1904–1912. doi:10.1785/0120020241

Zuccolo, E., Bozzoni, F., and Lai, C. G. (2017). Regional Low-Magnitude GMPE to Estimate Spectral Accelerations for Earthquake Early Warning Applications in Southern Italy. *Seismological Res. Lett.* 88 (1), 61–71. doi:10.1785/0220160038

Zuccolo, E., Gibbs, T., Lai, C. G., Latchman, J. L., Salazar, W., Di Sarno, L., et al. (2016). Earthquake Early Warning Scenarios at Critical Facilities in the Eastern Caribbean. *Bull. Earthquake Eng.* 14 (9), 2579–2605. doi:10.1007/s10518-016-9878-7

Conflict of Interest: The authors declare that the research was conducted in the absence of any commercial or financial relationships that could be construed as a potential conflict of interest.

frontiers in Earth Science

ORIGINAL RESEARCH
published: 06 July 2021
doi: 10.3389/feart.2021.699941

Performance Evaluation of an Earthquake Early Warning System in the 2019–2020 *M*6.0 Changning, Sichuan, China, Seismic Sequence

Chaoyong Peng[1,2]*, *Peng Jiang*[3], *Qiang Ma*[4], *Peng Wu*[3], *Jingrong Su*[3], *Yu Zheng*[1] and *Jiansi Yang*[1]

[1]Institute of Geophysics, China Earthquake Administration, Beijing, China, [2]Key Laboratory of Earthquake Source Physics, China Earthquake Administration, Beijing, China, [3]Sichuan Earthquake Administration, Chengdu, China, [4]Institute of Engineering Mechanics, China Earthquake Administration, Harbin, China

China is currently building a nationwide earthquake early warning system (EEWS) which will be completed in June 2023. Several regions have been selected as pilot areas for instrumentation, software system and dissemination verification. For these regions, their construction tasks will be completed in advance with trial runs being carried out in June 2021. Before the trial operation, we need to understand the actual processing capabilities of different EEWSs. In this work, we focus on the system deployed in Sichuan province and evaluate its real-time performance during the 2019–2020 *M*6.0 Changning seismic sequence. This period was divided into two stages. The first stage was the time from the occurrence of the *M*6.0 (M_w5.7) mainshock (June 17, 2019) to the end of October 2019 with no MEMS-based stations around the Changning seismic sequence deployed and most of the broadband and short period seismic stations not upgraded to low latency streaming, and the second one was from the beginning of November 2019 to March 2021 with deployments of more than 700 MEMS-based stations and low latency upgrades of ~30 seismic stations. Median errors for the epicentral locations, depths and magnitude estimations were almost the same for both stages, 1.5 ± 6.0 km, 0.0 ± 3.6 km and –0.1 ± 0.46 for the first stage and 2.3 ± 3.0 km, –3.0 ± 3.6 km and –0.2 ± 0.32 for the second one. However, an obvious underestimation of the magnitude for earthquakes with *M* 5.0 + occurring in the first stage was observed, which would be caused by the clipped waveforms, sensors deployed in short period seismic stations and MEMS-based stations, the adopted magnitude estimation method, and the method used to computer the network magnitude. The median reporting time was significantly improved from 10.5 ± 3.0 s after origin time for the first stage to 6.3 ± 3.5 s for the second stage because of introduction of newly deployed MEMS-based stations. The results obtained from the second stage indicate that the system has entered a stable operating stage and we can officially launch the trial operation in the pilot areas for public early warning services.

Keywords: earthquake early warning, hybrid seismic network, magnitude estimation, location accuracy, reporting time, data latency, changning earthquake

OPEN ACCESS

Edited by:
Maren Böse,
ETH Zurich, Switzerland

Reviewed by:
Frédérick Massin,
ETH Zürich, Switzerland
Jennifer Andrews,
California Institute of Technology, United States

***Correspondence:**
Chaoyong Peng
pengchaoyong@cea-igp.ac.cn

Specialty section:
This article was submitted to Geohazards and Georisks, a section of the journal Frontiers in Earth Science

Received: *24 April 2021*
Accepted: *22 June 2021*
Published: *06 July 2021*

Citation:
Peng C, Jiang P, Ma Q, Wu P, Su J, Zheng Y and Yang J (2021) Performance Evaluation of an Earthquake Early Warning System in the 2019–2020 M6.0 *Changning, Sichuan, China, Seismic Sequence. Front. Earth Sci. 9:699941. doi: 10.3389/feart.2021.699941*

INTRODUCTION

As an effective way to mitigate seismic hazards, earthquake early warning (EEW) systems (EEWSs) have shown their great potential by providing alarms immediately after a destructive earthquake occurs and before damaging seismic waves reach the target areas. They can enable people and automated systems to take action for preventing the potential damage, such as "drop, cover and hold on," slowing high-speed trains, shutting down gas pipelines, and stopping elevators at the nearest floor (Allen and Melgar, 2019; Cremen and Galasso, 2020). Nowadays, EEWSs are under testing or operational in many earthquake-prone countries and regions, like Japan (Hoshiba et al., 2008), Mexico (Cuéllar et al., 2017), the West Coast of the United States (Chung et al., 2020), China (Peng et al., 2011; Zhang et al., 2016; Peng et al., 2019; Peng et al., 2020), Turkey (Alick et al., 2009), Taiwan (Wu, 2014; Wu et al., 2016; Hsu et al., 2018), South Korea (Sheen et al., 2017), Italy (Zollo et al., 2009; Satriano et al., 2011), and India (Mittal et al., 2019).

In June 2018, China started to build a nationwide EEWS. This project, namely the National System for Fast Seismic Intensity Report and Earthquake Early Warning project (hereafter called the National System project), was led by the China Earthquake Administration (CEA) and its implementation cycle is five years. Detailed information can be found in Peng et al. (2020). To make the project effective as soon as possible, several regions have been selected as pilot areas for instrumentation, software system and dissemination verification, including Sichuan province, Yunnan province, and the Beijing-Tianjin-Hebei region. For these pilot areas, all construction tasks will be completed in June 2021, and the trial run will then be carried out in advance for providing the second-level EEW information service to the public.

Before the trial operation, we need to understand the actual processing capabilities of different EEWSs. We have evaluated the real-time performance of the demonstration EEWS deployed in the Sichuan-Yunnan border region during the test period (2017–2018). Although the results showed excellent magnitude estimation and epicentral location, the average report time for the first alert was relatively long, approximately 13.4 ± 5.1 s and 26.3 ± 13.5 s after the origin time respectively for the earthquakes occurring inside and outside the seismic network (Peng et al., 2020). This means that the average radius of blind zone was more than 45 km considering an *S*-wave velocity of 3.5 km/s and a shallow seismicity depth of 10 km, and it was unable to meet the key time goal of the National System project (4–6 s after the first trigger in the four key seismic zones). Here using the time after the first trigger as one of the system goal is that it would not be influenced by the varied focal depth (from several kilometers to more than 30 km) and whether an earthquake occurs inside or outside the seismic network.

Within the past 2 years (2019–2020), the EEWS has been upgraded by introducing more newly constructed stations and optimizing EEW algorithms. And for improving the 3G/4G network environment, all the micro-electro-mechanical system (MEMS) accelerometer based stations belong to the National System project were directly built in the houses of the cellular towers maintained by the China Tower company (https://ir.china-tower.com/en/business/macro.php), and about 50 MEMS-based stations deployed in the Sichuan-Yunnan border region (Peng et al., 2020) were moved to the same environment. In addition, an *M*6.0 (M_w5.7) Changning earthquake with many aftershocks of *M*3.0 + occurred in this period, which was the largest event occurring in the four key seismic zones since the build-out of the first prototype EEWS in 2009 (Peng et al., 2011). This seismic sequence provides us an outstanding opportunity to reevaluate the EEWS performance in the current situation.

In this study, we focus on the system deployed in Sichuan province and evaluate its real-time processing capabilities during the 2019–2020 *M*6.0 Changning, Sichuan, China, seismic sequence. We start by briefly summarizing the Changning seismic sequence. In the *Sichuan Seismic Network*, we introduce the Sichuan seismic network and present the network latency for different types of seismic stations. Then, we discuss the EEWS performances for the *M*6.0 Changning mainshock and all the selected aftershocks. The performance analysis is based on comparing the location, origin time, and magnitude estimated by the EEWS with the reference catalogs. In addition, we also analyze the report time of the first alert for the selected aftershocks.

CHANGNING SEISMIC SEQUENCE

The Changning area is located on the southern margin of Sichuan Basin and the western margin of the Yangtze Plate (**Figure 1**). It is one of the main salt (well and rock) and shale-gas production regions, with fluid injection wells drilled to ~3 km depths, and was considered as one of the sites of induced seismic events (Lei et al., 2019; Meng et al., 2019; Hu et al., 2021). The enhanced seismicity has been observed in the last ~10 years and the occurrence of earthquakes has recently increased significantly. According to the China Earthquake Networks Center (CENC), there were no earthquakes of *M* 5 or higher in this area before December 2018. However, since the occurrence of December 16, 2018 Xingwen *M*5.7 earthquake, a devastating and long-lasting earthquake sequence with many *M* 5 + events started to shake this region, resulting in 13 people dead, more than 200 injured and thousands of buildings damaged (Yi et al., 2019; Li et al., 2020). Here, the generic symbol *M* denotes either local magnitude M_L or the surface-wave magnitude transferred from an empirical estimating equation $M_S = 1.13M_L—1.08$, for earthquakes below or above M_L5, respectively (Chen et al., 2014).

Until now, the seismic sequence generated more than 100 events with *M* larger than 3.0 (**Figure 1**). The largest magnitude event (*M*6.0 Changning earthquake) occurred on June 17, 2019, at 22:55 Beijing Time (14:55 UTC), locating in the southwestern margin of Sichuan Basin with a very shallow focal depth of ~5 km (**Table 1**). It was a doublet with two faulting styles (Liu and Zahradník, 2020). The initial thrust faulting could be associated with previously known reverse faults, which were favorably oriented to the regional stress field, while the following strike-slip faulting was probably facilitated by increased pore pressure because of previous injections. The event caused Modified

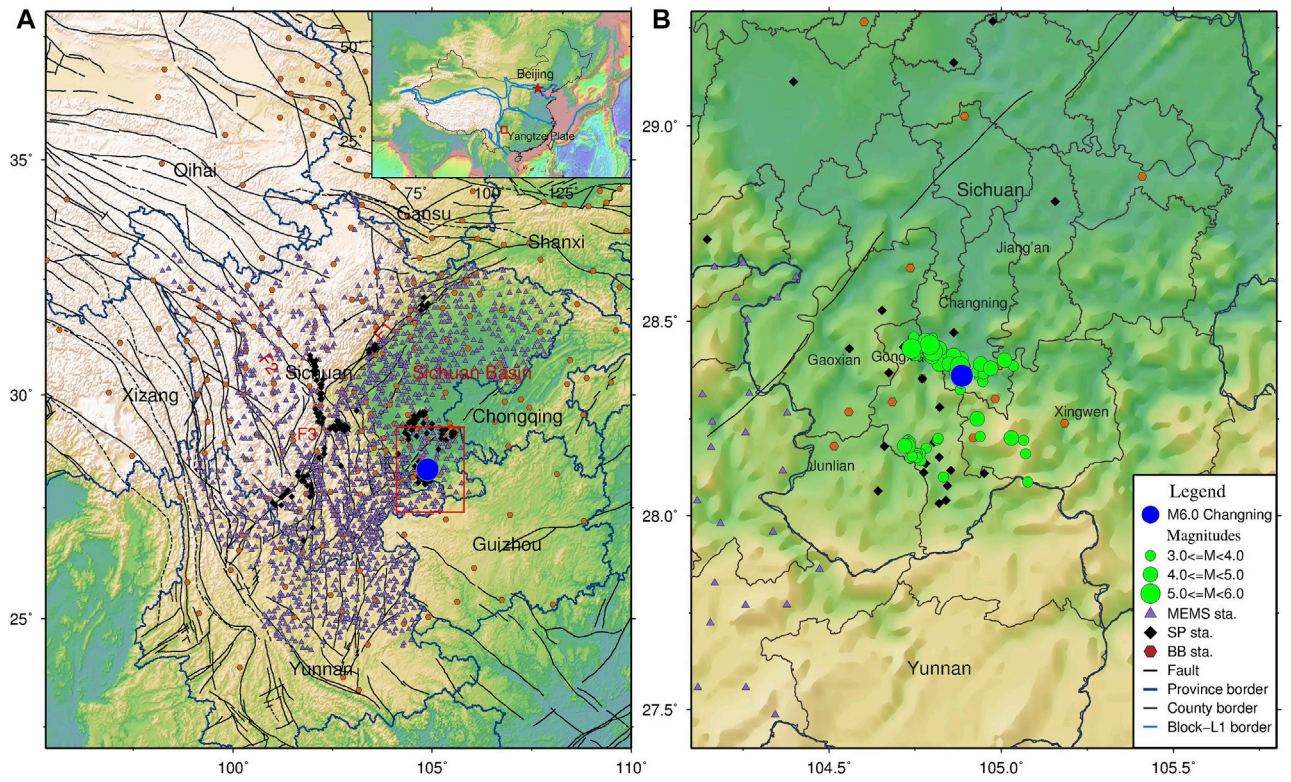

FIGURE 1 | (A) Station distribution of the currently used Sichuan Seismic Network (March 31, 2021). F1, F2, and F3 are the Longmenshan, Xishuihe, and Xiaojiang fault zones, respectively. **(B)** Station distribution in the area around the Changning seismic sequence for the first stage. Purple triangles, black diamonds and brown hexagons represent MEMS-based stations, short period seismic stations and broadband seismic stations, respectively. The blue circle shows the epicenter of the June 17, 2019 *M* 6.0 Changning earthquake. A large map with the marked studied area is shown in the inset. Green circles indicate the earthquakes with *M* 3.0 or more in the Changning seismic sequence, and their sizes are proportional to their magnitudes. Black lines are faults presented by Deng et al. (2003).

TABLE 1 | Earthquake catalogs for five *M*5.0 + events occurring during the 2019–2020 Changning seismic sequence.

Event number	Name	Origin time (yyyy/mm/dd hh:mm:ss)	Longitude (°N)	Latitude (°E)	Depth (km)	*M*
1	Changning *M*6.0	2019/06/17 22:55:44	104.886	28.361	5.1	6.0
2	Gongxian *M*5.3	2019/06/17 23:36:04	104.802	28.423	8.5	5.3
3	Changning *M*5.1	2019/06/18 07:34:33	104.880	28.385	3.3	5.1
4	Changning *M*5.6	2019/06/22 22:29:56	104.793	28.440	3.9	5.6
5	Gongxian *M*5.5	2019/07/04 10:17:58	104.740	28.430	7.0	5.5

Mercalli Intensity VIII near the epicenter, with the affected area larger than VI being about 2,538 km^2. The shock was widely felt in many places of Sichuan, Yunnan, Chongqing, and Guizhou provinces, including Chengdu city approximately 260 km from the epicenter.

SICHUAN SEISMIC NETWORK

The Sichuan seismic network is operated by the Sichuan Earthquake Administration. It was constructed by several projects, including the National System project, the Sichuan-Yunnan Demonstration project (Peng et al., 2019; Peng et al., 2020), the Western Sichuan Earthquake Monitoring Capability Improvement project, the Jiuzhaigou Earthquake Recovery and Reconstruction project, and the Kangding Earthquake Recovery and Reconstruction project. The stations are classified into three types: seismic stations, strong-motion stations, and low-cost MEMS-based stations. A seismic station is equipped with a three-component broadband seismometer and a force-balanced accelerometer, and a strong-motion station is only equipped with a force-balanced accelerometer. Detailed information is shown in **Table 2**. In addition, some stations built by other agencies are also included into the seismic network, such as reservoir stations

TABLE 2 | Number of stations under construction in different projects.

Project name	Construction time	Station number		
		Seismic station	Strong-motion station	MEMS-based station
The national system project	2018–2021	210	261	727
The Sichuan-Yunnan demonstration project	2015–2017			150
The western Sichuan earthquake monitoring capability improvement project	2018			70
The Jiuzhaigou earthquake recovery and reconstruction project	2018–2021	29	56	136
The Kangding earthquake recovery and reconstruction project	2015–2016	30		

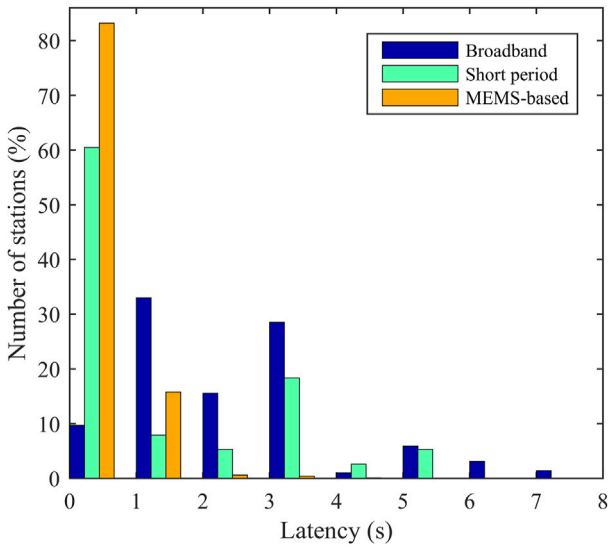

FIGURE 2 | Normalized data latency distribution (%) for the Sichuan Seismic Network. Here distribution in each class of instrument is normalized to its total number of sample. All MEMS-based stations sent 0.5 or 1.0 s data packets; for the upgraded broadband and short period seismic stations, they used the same low-latency data packetizing function as the MEMS-based stations and acquired data with data packetizing of 0.5 or 1.0 s; for the broadband and short period seismic stations not upgraded, they sent data after the data packet is full and compressed.

(equipped with short period seismometers) and other provincial stations in the border regions. For a newly constructed station, to ensure its stable operation, we need it to go through a trial run of 3 months before being included into the EEWS. Until now, although construction of ~80% of the seismic stations and strong-motion stations belong to the National System project and the Jiuzhaigou Earthquake Recovery and Reconstruction project was completed, these stations are at the stage of data quality verification and have not been included into the EEWS. The total number of stations currently used in the EEWS is approximately 2000, containing 363 seismic stations and 1631 MEMS-based stations (**Figure 1A**).

All stations are operated at a sampling rate of 100 Hz and the real-time continuous data are transferred to the Sichuan Earthquake Data Processing and Alert Issuing Center and processed by the Java-based EEWS (JEEWS; Peng et al., 2020). Most MEMS-based stations were installed in the houses of the cellular towers and used their field supervision unit (FSU) for data transmission, which could significantly improve the network environment and lower maintenance costs. Except for some not upgraded broadband and short period seismic stations, most of the data loggers at the stations integrate a low-latency data packetizing function which is designed specifically to support the EEWS (Peng et al., 2015; 2017a). Theoretically, the data packetizing length can be reduced to 0.1 s. Here, for reducing network load, we chose either an interval of 0.5 or 1.0 s to packetize the real-time data depending on the telemetry type. For those not upgraded seismic stations, they still used the high-latency data transmission protocol with 512 bytes packet.

In JEEWS, the P_d scaling from Kuyuk and Allen (2013) is adopted for EEW magnitude estimation. When the system detects *S*-wave for stations close to an earthquake epicenter (<10 km), the local M_L scaling is directly used to calculate the magnitude for avoiding *S*-wave contamination (Colombelli et al., 2012). The reason is that the peak ground motion will reach these stations soon after the *S*-wave arrival, generally in 1 or 2 s (Peng et al., 2020). If we still use *S*-wave data to estimate the P_d magnitude, a larger deviation will be introduced. Immediately after the magnitude estimated, a point-source algorithm based on the traditional ground motion prediction equation (GMPE) is used to compute seismic intensities at different target sites.

Using the method similar to Stubailo et al., 2021, we measured data latencies for all stations in March 2021 (**Figure 2**). Here data latency is defined as the time difference between the time when the last sample of the data packet was recorded and the time when the same packet is received by the data processing center. Because data processing by the station and waveform-receiving server at the center are very rapid, the measured latency can be interpreted as the delay of data transmission in the telemetry system. Therefore, we ignored the delay awaited between subsequent packets, approximately the packet length. The median values for broadband seismic stations, short period seismic stations, MEMS-based stations and all stations were 2.9 ± 1.61 s, 0.87 ± 1.54 s, 0.5 ± 0.42 s and 0.59 ± 1.1 s, respectively. The relative large standard deviations for broadband and short period seismic stations were due to the high data latencies introduced by those not upgraded stations.

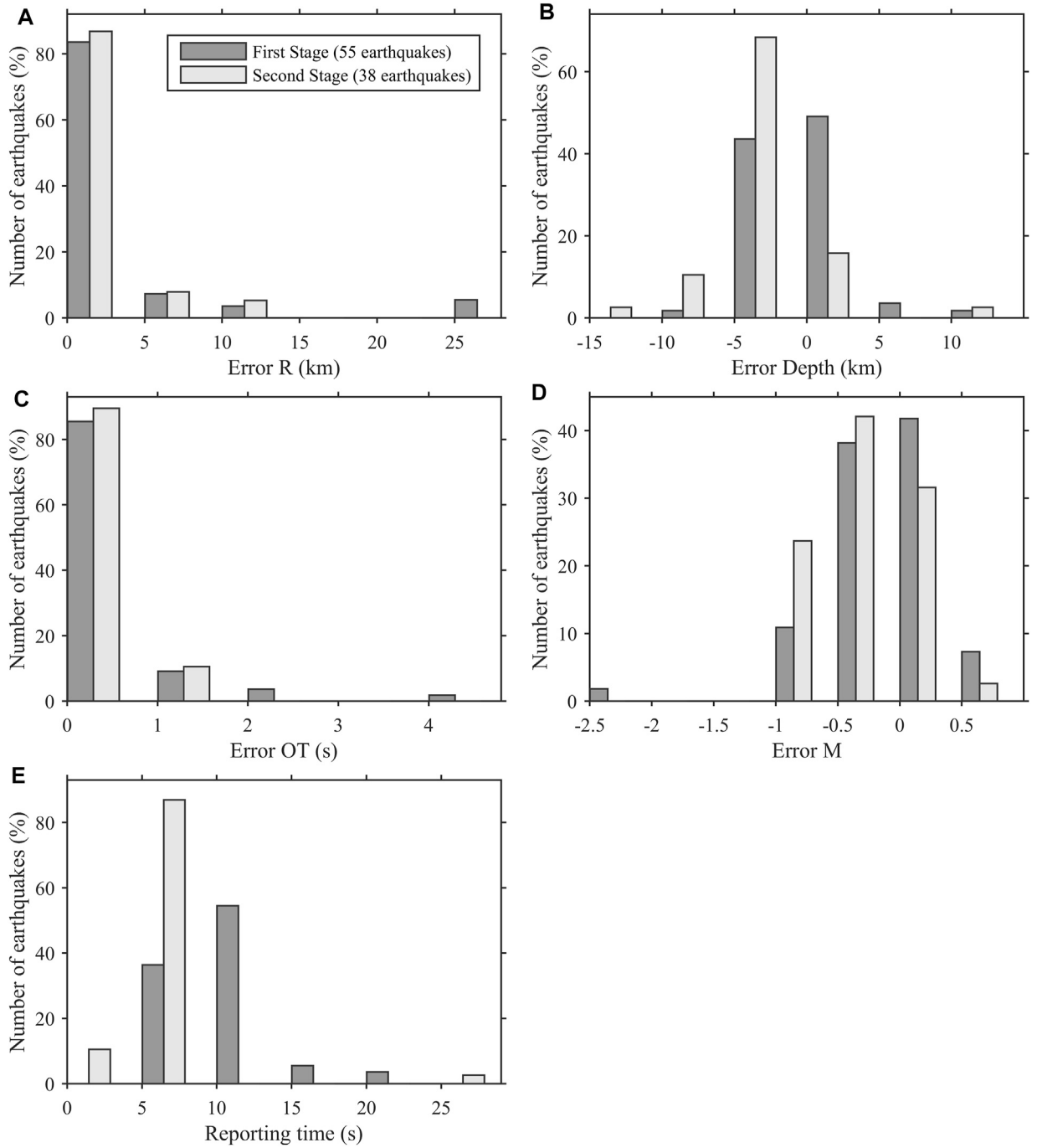

FIGURE 3 | Normalized number of earthquakes (%) vs. deviations between the first alert estimates for the 93 successful alerts output by JEEWS and the China Earthquake Network Center (CENC) catalogs for **(A)** epicenter, **(B)** depth, **(C)** origin time, and **(D)** magnitude. **(E)** Normalized number of earthquakes (%) vs. reporting time. This is a comparison of CENC and JEEWS earthquake parameter estimates for all Changning events studied, 55 from the first stage and 38 from the second stage.

PERFORMANCE OF JEEWS

System Performance for the Changning Seismic Sequence

To evaluate the system performance for the Changning seismic sequence, we investigated the real-time results of 101 earthquakes of M 3.0 or more from the occurrence of the M6.0 mainshock to March 2021, including 17 light aftershocks ($4.0 \leq M \leq 4.9$) and four moderate aftershocks ($5.0 \leq M \leq 5.9$). This period could be divided into two stages. The first stage was the time between the occurrence of the M6.0 mainshock (June 17, 2019) to the end of October 2019, and the second one was from the beginning of

November 2019 to March 2021. In the first stage, the MEMS-based stations around the Changning seismic sequence were not deployed, and most of the broadband and short period seismic stations were not upgraded (**Figure 1B**). The nearest MEMS-based station belong to the Sichuan-Yunnan Demonstration project (Peng et al., 2019; Peng et al., 2020) was 50 km away from the sequence. Additionally, most of the short period seismic stations were temporary stations and transferred real-time data with the old high-latency protocol. Therefore the report time for earthquakes occurring in this stage would be significantly influenced and we needed to evaluate the performance of the two stages separately.

For the 101 earthquakes, 62 occurred in the first stage and 39 happened during the second one. All earthquakes with M 5.0 + occurred in the first stage. Here the first alert was selected to derive all statistics because of its importance for EEW. Although other EEW projects have moved towards more ground motion based metrics and warning time calculations (Cochran et al., 2018; Chung et al., 2020; Meier et al., 2020), at this stage of the National System project, we are mainly concerned about the correctness of results of the first alert. The result of each earthquake identified by the EEWS was compared with those in the China Earthquake Network Center (CENC) catalogs. In addition, three alert levels were defined according to the catalog magnitude of an earthquake. They are successful alert (SA), false alert and missed alert. Based on these definitions, as for the M 3.0 + earthquakes, JEEWS issued 55 SA events and missed seven events for the first stage and 38 SA events and missed one event for the second stage. No false alert was issued during the both periods. Detailed results for the SA events are shown in **Figure 3**.

Figure 3A represents the epicentral error of SA events. The median deviations in epicenter location for the first and second stages were 1.5 ± 6.0 and 2.3 ± 3.0 km respectively. About 84% of the SA events had an error of less than 5 km. Among the earthquakes with epicentral errors of more than 10 km, there were 5 (9.1%) in the first stage and 2 (5.3%) in the second stage.

For an EEWS, depth is usually difficult to be determined correctly, especially for earthquakes occurred outside the seismic network (Carranza et al., 2017). Many studies have ignored this parameter and not analyzed it (Zhang et al., 2016; Sheen et al., 2017; Peng et al., 2020). From **Figure 3B**, one can observe that depth errors for most earthquakes lie between −5 and 5 km, with median errors of 0.0 ± 3.6 and −3.0 ± 3.6 km for the first and second stages, respectively. This means that the depth value of the first alert is excellent, although the depth error for the second stage is relatively large, which was caused by the MEMS-based stations and the events themselves being of a relatively smaller magnitude. In the second stage, most of the triggered stations contributing to the events were the newly constructed MEMS-based stations. Because of their high noise levels relative to the seismic stations, it is difficult to accurately identify P-wave arrivals from their recorded data for small earthquakes with magnitude less than 4.0, leading to a relatively large depth error.

Generally events with a large deviation in epicenter estimate also had a large deviation in the OT (**Figures 3A,C**). For the first and second stages, the median differences in OT were 0.4 ± 0.7 s and 0.3 ± 0.4 s, respectively. And ~69 and ~89% of the events in both stages had errors of less than 0.5 and 1.0 s. There were eight events (14.5%) with an OT error larger than 1.0 s for the first stage and 4 events (10.5%) for the second stage.

Figure 3D shows the deviation in M. About 83% of the events had an error of no more than 0.5 and 61% of the events had a deviation of less than 0.4. The median magnitude differences for the first and second stages were −0.1 ± 0.46 and −0.2 ± 0.32 respectively. For the larger events with $M \geq 4.0$ and $M \geq 5.0$, the deviations were −0.5 ± 0.55 and −0.9 ± 0.71 respectively, indicating that JEEWS significantly underestimated the magnitude.

We further compared the magnitudes obtained from events in both stages according to JEEWS with those in the CENC catalogs (**Figure 4**). The magnitudes estimated at broadband seismic stations, short period seismic stations, and MEMS-based stations are indicated by empty circles, crosses, and triangles, respectively, while the network magnitudes, the average value of all station magnitudes, are presented as blue circles. Here, both P_d magnitude and M_L based station contributions are shown in the graph. The same trend of magnitude underestimation for larger events could also be found in **Figure 4**. It is alarming that an extrapolation of **Figures 4A,C,E** suggests that a M7.0 earthquake would get a M_{EEW} 5.5. However, the broadband seismic station magnitudes are better correlated with the CENC magnitudes relative to the short period station and MEMS-based station magnitudes, especially for the larger earthquakes. In addition, we also considered each type of station's performance in magnitude bins [3, 4), [4, 5) and [5, 6], shown in **Table 3**. From **Figure 4** and **Table 3**, one can observe that:

- Measurements for the broadband seismic stations in general slightly overestimate M3-4 events and slightly underestimate earthquakes with higher magnitude. Scatter is generally lower for this station type.
- Measurements for the short period seismic stations in general more strongly overestimate M3-4 events, are good for M4-5 and slightly underestimate earthquakes with higher magnitude. However, scatter is very large (up to two magnitude units) for this station type. This may be a result of the deployment sites for this sensor type. Most of the short period seismic stations were temporary stations directly deployed on the hard soil layer. This would lead to amplification effects on the recorded ground motion.
- For the MEMS-based stations, measurements in general slightly overestimate M3-4 events, are good for M4-5 and more strongly underestimate earthquakes with higher magnitude. Scatter is similar to the broadband seismic stations, except for the magnitude bin [5, 6].

Reporting time, as another important feature, directly influences the effectiveness of an EEWS. From **Figure 3E** we can find that there was a huge difference in the reporting time for earthquakes occurring between the first and second stages. The median reporting times for the first and second stages were 10.5 ± 3.0 s and 6.3 ± 3.5 s, respectively.

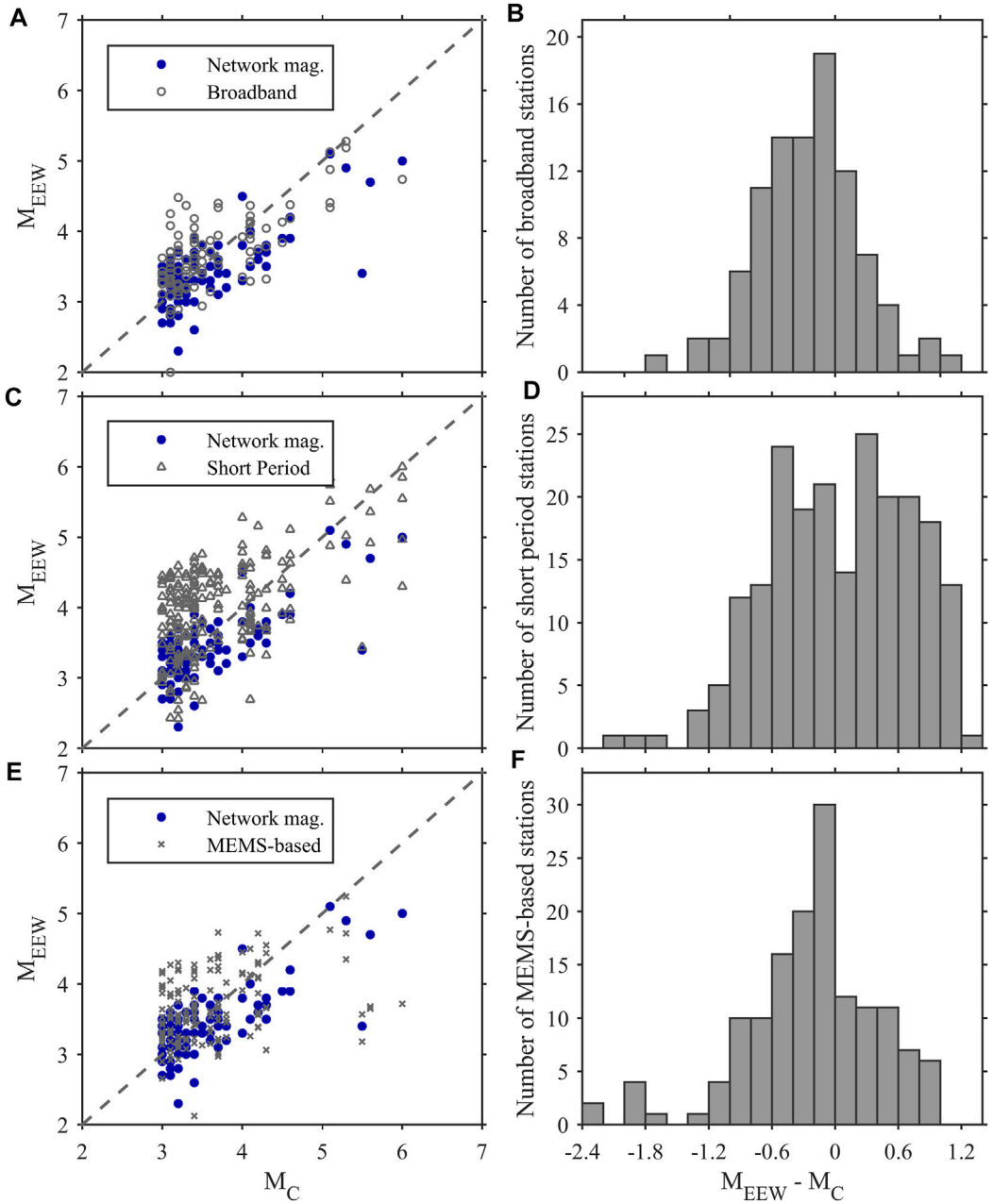

FIGURE 4 | Comparison of the JEEWS magnitudes of the Changning seismic sequence for both stages. **(A, C, E)** JEEWS vs. the China Earthquake Network Center (CENC) catalogs for different station types. Empty circles, broadband seismic station magnitude; crosses, short period seismic station magnitude; triangles, MEMS-based station magnitude; blue circle, network magnitude. **(B, D, F)** Histograms of the magnitude differences for different station types.

TABLE 3 | Median and standard deviation of the uncertainty on magnitude estimation for each type of station, computed in different magnitude bins.

Station type	Magnitude bin		
	[3, 4)	[4, 5)	[5, 6]
Broadband seismic stations	0.24 ± 0.40	−0.38 ± 0.30	−0.22 ± 0.45
Short period seismic stations	0.63 ± 0.55	−0.16 ± 0.52	−0.24 ± 0.76
MEMS-based seismic stations	0.26 ± 0.46	−0.11 ± 0.47	−1.92 ± 0.84

Real-Time Results for the *M* 5 + Earthquakes

From the occurrence of the *M*6.0 mainshock, five earthquakes with magnitudes larger than 5.0 struck the Changning area. The list of events is presented in **Table 1**. All these earthquakes occurred in the first stage with no MEMS-based stations introduced and no broadband and short period seismic

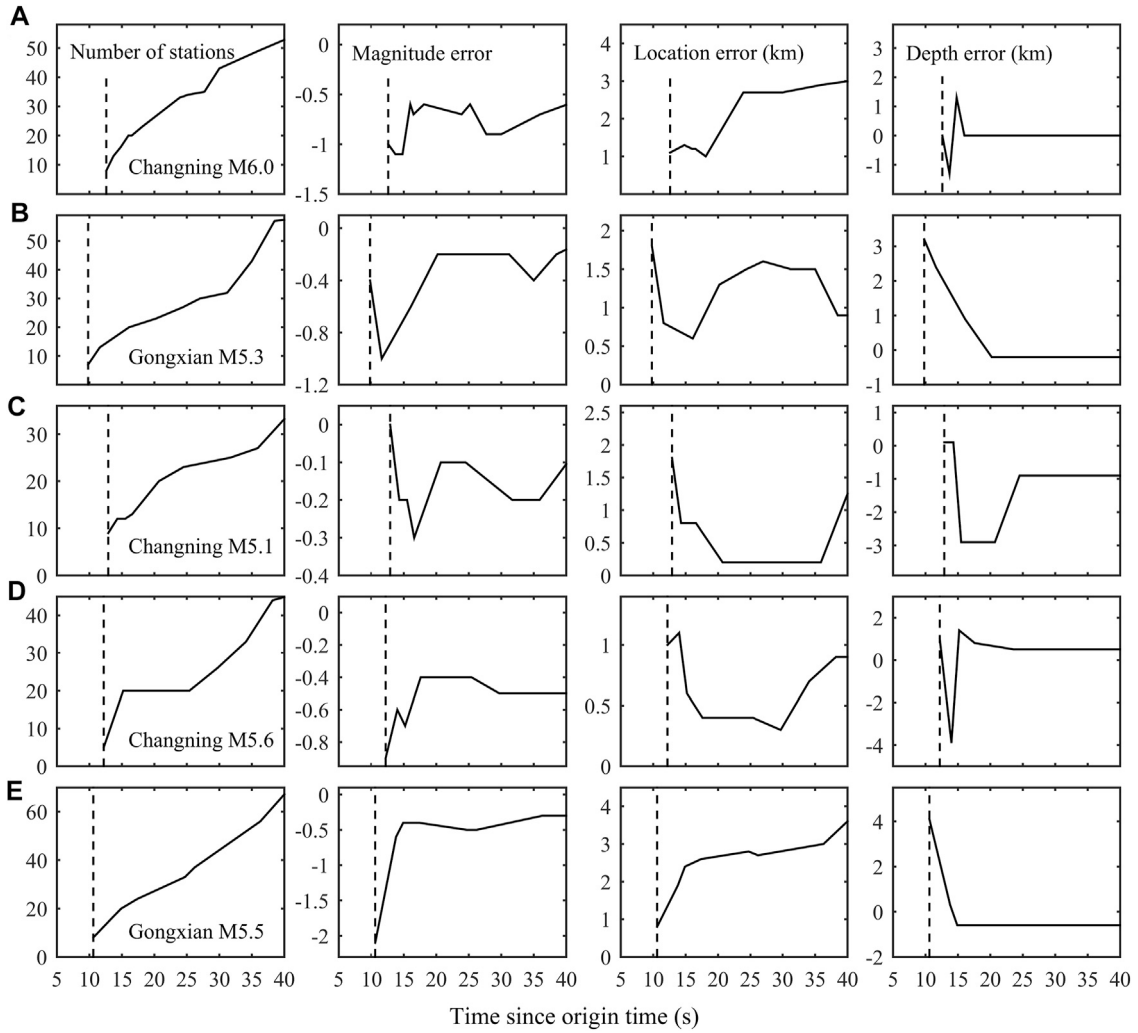

FIGURE 5 | Real-time processing results of JEEWS for five M5.0 + earthquakes occurring in the Changning seismic sequence. **(A)** Changning M6.0 (2019/06/17 22:55:44); **(B)** Gongxian M5.3 (2019/06/17 23:36:04); **(C)** Changning M5.1 (2019/06/18 07:34:33); **(D)** Changning M5.6 (2019/06/22 22:29:56); **(E)** Gongxian M5.5 (2019/07/04 10:17:58). From left to right, each panel is the number of triggered stations, the magnitude error, the location error, and the depth error as a function of time, respectively. Vertical lines indicate the first alert time.

stations upgraded (**Figure 1B**). Therefore the first reporting time for these earthquakes was long (**Figure 5**), with an average of 11.6 ± 1.2 s after origin time. For the two Gongxian events, they are faster due to closer to the non-MEMS sub-networks. Additionally, although the location and depth errors were small with slight variations, the magnitudes for these earthquakes were significantly underestimated with large fluctuations and did not seem to converge toward the catalog values, except the Changning *M*5.1 event. Considering an *S*-wave velocity of 3.5 km/s, these earthquakes had a blind zone with radius of more than 30 km.

DISCUSSION AND CONCLUSION

After several years of construction, the number of stations of the Sichuan seismic network had reached ~2000, and the average distance between stations was about 12 km, which is comparable to the Italian Strong Motion Network used for PRESTo (Festa et al., 2018) and the California Integrated Seismic Network used for ShakeAlert (Chung et al., 2020). In some regions, such as the Xianshuihe, Longmenshan and Xiaojiang fault zones (**Figure 1A**), the average interstation distance was less than 10 km. In addition, most stations integrated a low-latency data packetizing function for real-time continuous data transmission (Peng et al., 2015; 2017a). These factors have greatly improved the EEW capabilities, which could be observed from the EEW results of all earthquakes with *M*3.0 or more in the Changning seismic sequence.

However, during the first stage, the MEMS-based stations around the Changning seismic sequence were still under construction and most data loggers installed in the broadband and short period seismic stations were not changed to those specially designed for EEW purposes, such as EDAS-24GN (http://www.geolight.com.cn/p.aspx?id=49&&type=2) and HG-D (http://www.szadpr.cn/a/yewufangxiang/xianjindizhenyiqishebei/

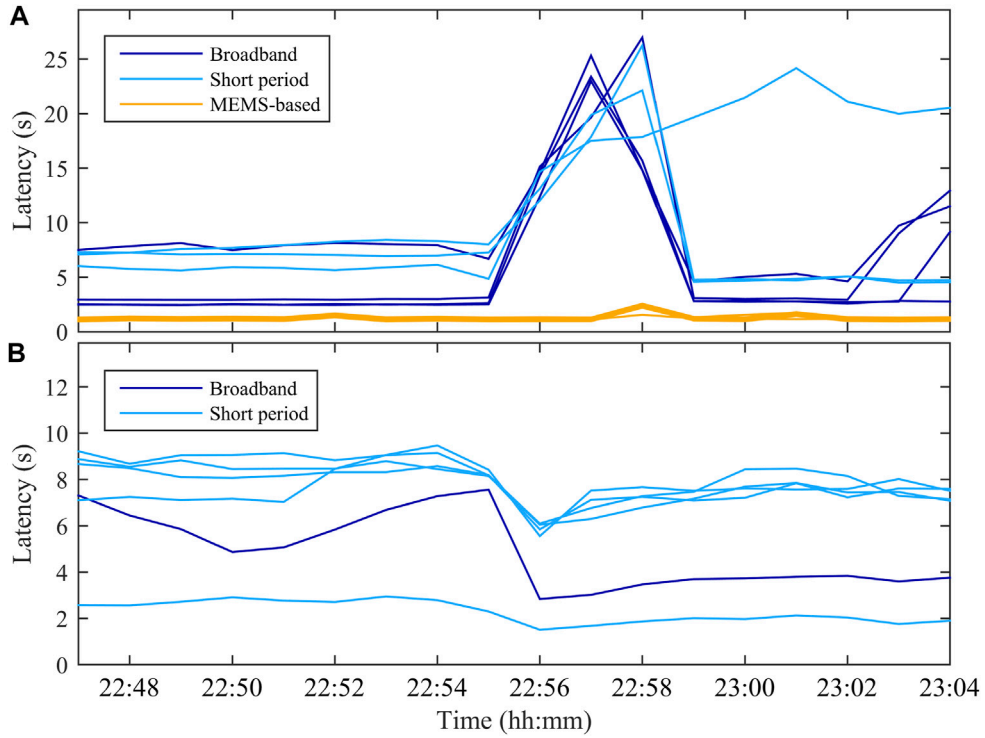

FIGURE 6 | Data latency responses of different stations types with real-time data being transmitted by **(A)** cellular modem links and **(B)** fiber lines to the June 17, 2019 *M* 6.0 Changning earthquake.

20200716/442.html), leading to reporting time more than 10 s for the first alerts of most earthquakes. In the second stage, with the introduction of more than 1,000 MEMS-based stations, the reporting time has been significantly improved to 6.3 s, meaning that radii of the blind zones for most events have been reduced to ~20 km under an *S*-wave velocity of 3.5 km/s and a shallow seismicity depth of 7 km. This is an impressive result and is comparable to those obtained by other excellent EEWSs, such as ShakeAlert (Chung et al., 2020), NEEWS (Hsu et al., 2018), on-site P-Alert system (Wu et al., 2019), and PRESTo in Italy (Festa et al., 2018). In addition, this result can meet the key time goal requirement of the National System project.

As to the seismic stations not upgraded, they adopted a fixed-size packet of 512 bytes for data transmission. Generally, during an earthquake, fixed-size data packet will be filled out quicker with large amplitudes, leading to shorter duration. However, the delay for transmitting and receiving the packet might become problematic during a large earthquake as stations sending high data rates will be a significantly additional stress for the telemetry infrastructure (Stubailo et al., 2021). One example is shown in **Figure 6**. For those not upgraded seismic stations transferring data with cellular modems (**Figure 6A**), huge latency could be observed after shaking onset. However, for the seismic stations delivering data over fiber lines (**Figure 6B**), a clear downward trend was presented because the packet was filled out quicker during the earthquake. Only a slight fluctuation was observed for the MEMS-based stations because of their low resolution (14–15 bits). The sensitivity of all MEMS-based accelerometers has been corrected to 500 counts/cm/s^2. This means that 1 count is equal to 0.002 cm/s^2. Usually, in the quiet time, the recorded data for an MEMS-based station vary between ±0.1 gals (±50 counts). During a large event, if the PGA value recorded can reach ±100 cm/s^2, the counts will fluctuate between ±50,000, significantly lower than the seismic stations with waveforms clipped and approximately ±8,000,000 counts (23 bits resolution). Therefore, to lower the large latency introduced by the seismic stations, we can upgrade the data loggers by integrating a low-latency data packetizing function and increase the telemetry bandwidth by substituting the cellular modem links with fiber lines.

In terms of earthquake location and magnitude estimation, most of the deviations were within 5 km and 0.5 magnitude units, a significant improvement compared to the results reported in Peng et al. (2020). In addition, most of the depth errors lied in ±5 km. The reason is mainly related to the increase in station density and the improvement of the network environment. However, eight earthquakes with *M*3.0 or more were missed by JEEWS, all of which occurred within a short time after earthquakes at the same location. Currently, a time threshold of 49 s, an empirical value, is used for an event detection to avoid declaring a secondary trigger at the same station as a new earthquake. This is an inherent limitation of JEEWS, especially in case of a foreshock and the mainshock occurring in a short time, which cannot be avoided because reducing the time threshold for new event detection would be controversial and could lead to many false alerts (Carranza et al., 2017; Peng et al., 2020). To reduce the impacts of this limitation on JEEWS, some effective methods like the integrated particle filter (IPF; Tamaribuchi et al., 2014), propagation of local undamped motion (PLUM; Kodera et al., 2016) algorithms or using an

TABLE 4 | Result comparison of the same earthquakes with the first alert triggered by two stations and the second alert triggered by more stations.

Catalog						Errors of JEEWS		
OT (UTC+8) (yyyy/mm/dd hh:mm:ss)	Lat. (°N)	Lon. (°E)	*M*	Depth (km)	Nsta	OT_err (s)	Loc_err (km)	M_err
2019/06/18 04:11:08	28.43	104.75	3.4	8	2	−6.9	51.9	−2.9
					4	−0.2	1.6	0.3
2019/06/18 05:49:15	28.41	104.80	3.7	7	2	−7.7	7.9	−4.6
					8	−0.2	0.7	−0.3
2019/06/19 03:25:30	28.41	104.82	3.0	6	2	−0.4	5.4	0.3
					3	−0.4	0.8	0.4
2019/06/20 10:55:52	28.40	104.83	3.0	5	2	0.1	5.5	−0.2
					5	−0.6	0.4	0.1
2019/06/21 06:56:49	28.44	104.78	3.3	5	2	−1.3	5.0	0.7
					4	−0.6	1.1	−0.1
2019/06/22 22:29:56	28.44	104.79	5.6	4	2	−2.6	24.4	−1.6
					5	−0.7	14.1	−1.4
2019/06/23 05:08:24	28.44	104.78	3.4	6	2	0.1	3.1	−0.2
					5	−0.1	1.0	0.1
2019/07/03 12:26:54	28.39	104.85	4.6	9	2	0.0	1.5	−0.3
					5	−0.1	0.8	−0.4
2019/07/04 06:45:19	28.40	104.85	3.4	8	2	0.0	2.2	0.5
					4	−0.2	1.1	0.1
2019/07/04 07:34:06	28.41	104.84	3.0	2	2	−0.7	1.4	1.1
					4	−0.6	1.4	0.4
2019/07/08 00:37:40	28.40	104.85	3.0	8	2	−0.7	3.8	1.2
					4	−0.2	0.8	0.3
2019/07/19 01:21:29	28.19	104.74	3.4	9	2	−4.8	34.5	0.6
					4	−−0.3	1.1	0.5
2019/07/22 16:26:38	28.39	104.94	4.0	8	2	−1.6	7.2	−4.9
					7	−1.8	7.8	−0.7
2019/08/13 06:31:54	28.37	104.87	4.3	10	2	−1.3	1.9	0.1
					4	−0.9	1.0	−0.5
2019/09/06 15:25:34	28.45	104.78	4.1	7	2	0.2	6.1	−1.0
					3	−0.3	1.5	−0.1
2019/09/12 20:17:55	28.41	104.80	4.0	10	2	−2.4	14.0	0.2
					8	−0.8	3.7	−0.2
2019/11/10 21:28:07	28.44	104.74	3.3	7	2	0.1	5.6	0.0
					3	−0.3	1.5	0.3
2019/12/29 08:47:13	28.38	104.97	4.2	13	2	0.2	4.1	−1.1
					3	0.0	4.4	−0.6
2020/01/08 01:09:39	28.25	104.93	4.2	10	2	−1.9	8.3	−0.7
					5	−1.6	4.2	−0.5
2020/02/03 23:55:51	28.46	104.75	3.7	8	2	0.2	4.8	−0.5
					3	0.3	1.5	−0.6
2020/04/09 09:14:24	28.10	104.83	3.2	8	2	0.1	9.3	−0.2
					4	0.5	12.0	0.0
2020/04/27 09:37:12	28.17	104.78	3.2	7	2	0.5	7.8	−0.5
					4	0.0	1.4	0.0
2020/05/10 15:42:28	28.14	104.77	3.4	6	2	0.3	6.0	−0.2
					4	−0.1	2.0	0.1
2020/05/22 03:12:50	28.16	104.77	3.7	8	2	0.1	2.6	−0.7
					4	0.1	1.9	−0.2
2020/06/28 05:37:41	28.35	104.95	3.0	4	2	−0.2	4.6	0.1
					3	0.2	2.9	−0.3
2020/07/02 20:44:17	28.34	104.89	3.3	5	2	−0.2	3.4	−0.1
					7	−0.1	1.8	−0.1
2020/07/27 16:07:00	28.39	104.95	3.4	7	2	0.5	2.8	−0.6
					7	−0.1	1.5	0.1
2020/08/17 12:43:33	28.15	104.74	3.0	8	2	−0.4	9.0	−0.1
					4	0.4	2.1	0.0
2020/09/16 15:03:08	28.45	104.80	3.4	6	2	−0.4	4.8	−0.5
					4	−0.6	2.3	−0.4
2020/09/26 04:34:09	28.09	105.08	3.8	13	2	1.3	12.0	−1.0
					3	1.0	6.6	−0.4
2020/11/13 03:18:12	28.18	104.72	4.3	7	2	−0.4	2.0	−0.4
					4	−0.4	2.3	−0.6

OT, origin time; Lat., latitude; Lon., longitude; Nsta., number of used stations; OT_err, origin time error; Loc_err, location error; M_err, magnitude error.

intensity threshold can be introduced to process multiple simultaneous events within a short time and distance.

In JEEWS, one of the alert filters was the event being triggered by at least two stations. It can be seen from the results in **Table 4** that this alert filter would lead to larger location and magnitude errors. For earthquakes occurring in the second stage, with seismic network density increased and seismic stations upgraded, most of the first alerts were triggered by three or more stations and the reporting time was not significantly influenced. Therefore, when in the trial operation, the alerting strategy should be adjusted for the pilot areas, requiring at least three stations to take part in the EEW processing for declaring an earthquake. However, for other regions with different station densities, the number of stations would probably varies from place to place.

From the results of earthquakes with magnitude larger than 5.0, there was an obvious underestimation of the magnitude, which persisted even as time increased with more triggered stations. This may be caused by the following four reasons:

One is the seismic stations with clipped waveforms. Due to these larger earthquakes occurring in the first stage, except for some MEMS-based stations 50 km away from the epicenter, most stations used to estimate magnitude were seismic stations. Waveforms from the seismic stations close to the epicenter clipped, and some even clipped in the first second immediately after the *P*-wave arrival. These clipped data were not excluded and still used for EEW processing. To avoid this problem, we need to introduce a strategy to eliminate the clipped seismic stations, such as with a threshold on the number of counts.

The second reason comes from the sensors deployed in short period seismic stations and MEMS-based stations. It is well-known that the short period sensors have saturation problems when using to estimate the magnitude of a large earthquake (Xu et al., 2008), because they will miss the long period vibration of large events. However, the magnitude contributions are surprisingly good for these stations (**Figure 4C**). The reason may be related to the energy release of the large earthquakes themselves, which is out of the scope of this paper. As to the MEMS-based stations, except for the GL-P2B device (Peng et al., 2017a, 2019, 2020), most of the deployed sensors, including Palert (Wu, 2014; Wu et al., 2019; Peng et al., 2020), with a low signal resolution (14–15 bits) and dynamic range (less than 90 dB), had a relative high noise level, making them difficult to clearly record *p* wave arrivals of small earthquakes and more suitable for earthquakes with *M*4.0+ (**Figure 4E**).

The third one is the adopted magnitude estimation method itself (Kuyuk and Allen, 2013). The data selected to deriving the P_d magnitude relationship were records from broadband seismic stations and strong motion stations. In JEEWS, we also used short period seismic stations and MEMS-based stations. For the sensors deployed in these stations, they had different frequency bands and noise levels. From **Figures 4C–F**, we could find that this magnitude estimation method was not working well for these two types of stations. Therefore we need to calibrate new relationships with data directly recorded by the stations.

The final one lies in the method used to compute the network magnitude. In the current system, the network magnitude outputted is directly obtained by averaging the magnitude of each triggered station. This would lead to magnitude underestimation because of the magnitudes calculated from the newly triggered stations (Melgar and Hayes, 2019; Trugman et al., 2019; Chung et al., 2020) using a short *P*-wave time window (less than 2 s), especially for the MEMS-based stations ~50 km away from the epicenter (**Table 3**). Usually, for a large earthquake with rupture duration longer than 4 s, the magnitude calculated from such a short window will be significantly underestimated (Meier et al., 2016, 2021; Trugman et al., 2019). To avoid this risk, we can use the time window length of each triggered station as a weight for computing the network magnitude. The effectiveness has been proved in Colombelli et al. (2012) and Peng et al. (2017b).

For the *M* 3.0 + earthquakes that occurred in the second stage, JEEWS obtained excellent results, indicating that the system has entered a stable operating state. However there is a high risk that is lack of *M* 7.0 + earthquake verification. So far, the largest intra-network event handled by JEEWS was the 2019 Changning *M*6.0 earthquake. In JEEWS we adopted a simple point-source algorithm to calculate seismic intensities at different target areas. This would lead to significant ground-motion underprediction for devastating (*M* 7.0+) earthquakes because fault finiteness was not considered (Chung et al., 2020). This limitation can be efficiently solved by introducing FinDer (Böse et al., 2012, 2018) or other algorithms (Yamada et al., 2007; Crowell et al., 2016) into JEEWS.

Recently we are developing a decision module which is used for combining results from different EEW algorithms. In this module, some rules are currently adopted, such as 1) the first alert is the fastest received result; 2) if multiple results are received in a time window of less than 1 s, the origin time, epicenter and depth from the one with the largest number of triggered stations are selected as the source parameters, and the magnitude is set as the largest one. Based on the results after decision, peak ground motion estimates at different target sites are calculated by using GMPEs. As the system runs, more suitable rules will be integrated into this module for further improving accuracy of the system.

Besides, in the near future we need to consider providing customized services from the perspectives of an end user, such as triggering interpretable alerts according to probabilistic risk-based estimation optimized for the preferences of a given stakeholder (Cremen and Galasso, 2020), or providing an open public (event or ground motion-based) service to users for building their own customized applications. This will further improve the efficiency of an EEWS and transform it into a more useful tool.

DATA AVAILABILITY STATEMENT

The datasets for this study, including seismic waveforms recorded by broadband and short period seismic stations, the micro-electromechanical system (MEMS) based recordings, processing results of the earthquake early warning system (EEWS) and data latency for each station, can be obtained from the Sichuan Earthquake Administration (http://www.scdzj.gov.cn). Please contact jiang_0057@163.com for information about how to access the data for research purposes. The earthquake catalogs used for compared with results of the EEWS are acquired from the China Earthquake

Network Center (CENC; http://news.ceic.ac.cn). All websites were last accessed in March 2021.

AUTHOR CONTRIBUTIONS

CP analyzed the data and drafted the manuscript; PJ and PW carried out the experiment and test; QM, JS, and JY contributed to the design and helped to write the paper; YZ provided suggestions on the results and figure production. All authors contributed to the article and approved the submission.

FUNDING

This research was financially co-funded by the National Key Research and Development Program of China (2018YFC1504001), the Special Fund of the Institute of Geophysics, China Earthquake Administration (DQJB20R14, DQJB20B17), and the Beijing Natural Science Foundation (8202051).

ACKNOWLEDGMENTS

The authors are grateful to Editor MB, and two reviewers for their constructive advices that have significantly improved the manuscript. The authors also thank Sichuan Earthquake Administration for providing the seismic and ground motion recording data, the processing results of the earthquake early warning system and logging files for all stations' data latency. The Generic Mapping Tools (GMT) software from Wessel and Smith (1998) and the MATLAB software with version R2015a were used in plotting part of the figures and are gratefully acknowledged.

REFERENCES

Alick, H., Ozel, O., Apaydin, N., and Erdik, M. (2009). A Study on Warning Algorithms for Istanbul Earthquake Early Warning System. *Geophys. Res. Lett.* 36, L00B05. doi:10.1029/2008GL036659

Allen, R. M., and Melgar, D. (2019). Earthquake Early Warning: Advances, Scientific Challenges, and Societal Needs. *Annu. Rev. Earth Planet. Sci.* 47, 361–388. doi:10.1146/annurev-earth-053018-060457

Böse, M., Heaton, T. H., and Hauksson, E. (2012). Real-time Finite Fault Rupture Detector (FinDer) for Large Earthquakes. *Geophys. J. Int.* 191, 803–812. doi:10.1111/j.1365-246x.2012.05657.x

Böse, M., Smith, D. E., Felizardo, C., Meier, M. A., Heaton, T. H., and Clinton, J. F. (2018). FinDer v.2: Improved Real-Time Ground-Motion Predictions for M2-M9 with Seismic Finite-Source Characterization. *Geophys. J. Int.* 212, 725–742. doi:10.1093/gji/ggx430

Carranza, M., Buforn, E., and Zollo, A. (2017). Performance of a Network-Based Earthquake Early Warning System in the Ibero-Maghrebian Region. *Seismological Res. Lett.* 88 (6), 1499–1507. doi:10.1785/0220170081

Chen, Z., Chen, H., Zhao, C., Wang, Q., Hua, W., and Zhou, L. (2014). Measurement of Earthquake Size. *Earthquake Res. China* 28 (3), 285–298.

Chung, A. I., Meier, M. A., Andrews, J., Böse, M., Crowell, B. W., McGuire, J. J., et al. (2020). ShakeAlert Earthquake Early Warning System Performance during the 2019 Ridgecrest Earthquake Sequence. *Bull. Seismol. Soc. Am.* 110 (4), 1904–1923. doi:10.1785/0120200032

Cochran, E., Aagaard, B., Allen, R., Andrews, J., Baltay, A., Barbour, A., et al. (2018). Research to Improve ShakeAlert Earthquake Early Warning Products and Their Utitlity. *U.S. Geol. Surv. Open-file Rept.* 2018-1131, 1–24. doi:10.3133/ofr20181131Reston, Virginia

Colombelli, S., Zollo, A., Festa, G., and Kanamori, H. (2012). Early Magnitude and Potential Damage Zone Estimates for the Great Mw 9 Tohoku-Oki Earthquake. *Geophys. Res. Lett.* 39, a–n. doi:10.1029/2012gl053923

Cremen, G., and Galasso, C. (2020). Earthquake Early Warning: Recent Advances and Perspectives. *Earth-Science Rev.* 205, 103184. doi:10.1016/j.earscirev.2020.103184

Crowell, B. W., Schmidt, D. A., Bodin, P., Vidale, J. E., Gomberg, J., Renate Hartog, J., et al. (2016). Demonstration of the Cascadia G-FAST Geodetic Earthquake Early Warning System for the Nisqually, Washington, Earthquake. *Seismological Res. Lett.* 87 (4), 930–943. doi:10.1785/0220150255

Cuéllar, A., Suárez, G., and Espinosa-Aranda, J. M. (2017). Performance Evaluation of the Earthquake Detection and Classification Algorithm 2(tS-tP) of the Seismic Alert System of Mexico (SASMEX). *Bull. Seismological Soc. America.* 107 (3), 1451–1463. doi:10.1785/0120150330

Deng, Q., Zhang, P., Ran, Y., Yang, X., Min, W., and Chu, Q. (2003). Basic Characteristics of Active Tectonics of China. *Sci. China Earth Sci.* 46 (4), 356–372. doi:10.1360/03ys9030

Festa, G., Picozzi, M., Caruso, A., Colombelli, S., Cattaneo, M., Chiaraluce, L., et al. (2018). Performance of Earthquake Early Warning Systems during the 2016-2017 Mw 5-6.5 Central Italy Sequence. *Seismol. Res. Lett.* 89 (1), 1–12. doi:10.1785/0220170150

Hoshiba, M., Kamigaichi, O., Saito, M., Tsukada, S. y., and Hamada, N. (2008). Earthquake Early Warning Starts Nationwide in Japan. *Eos Trans. AGU.* 89 (8), 73–80. doi:10.1029/2008eo080001

Hsu, T., Lin, P., Wang, H., Chiang, H., Chang, Y., Kuo, C., et al. (2018). Comparing the Performance of the NEEWS Earthquake Early Warning System against the CWB System during the 6 February 2018 M_W 6.2 Hualien Earthquake. *Geophys. Res. Lett.* 45, 6001–6007. doi:10.1029/2018GL078079

Hu, X., Cui, X., Zhang, G., Wang, G., Zang, A., Shi, B., et al. (2021). Analysis on the Mechanical Causes of the Complex Seismicity in Changning Area, China. *Chin. J. Geophys.* 64 (1), 1–17. doi:10.6038/cjg2021O0232 (in Chinese)

Kodera, Y., Saitou, J., Hayashimoto, N., Adachi, S., Morimoto, M., Nishimae, Y., et al. (2016). Earthquake Early Warning for the 2016 Kumamoto Earthquake: Performance Evaluation of the Current System and the Next-Generation Methods of the Japan Meteorological Agency. *Earth Planets Space*. 68 (202). doi:10.1186/s40623-016-0567-1

Kuyuk, H. S., and Allen, R. M. (2013). A Global Approach to Provide Magnitude Estimates for Earthquake Early Warning Alerts. *Geophys. Res. Lett.* 40, 6329–6333. doi:10.1002/2013gl058580

Lei, X., Wang, Z., and Su, J. (2019). The December 2018 ML 5.7 and January 2019 ML 5.3 Earthquakes in South Sichuan Basin Induced by Shale Gas Hydraulic Fracturing. *Seismol. Res. Lett.* 86 (3), 750–763. doi:10.1785/0220190029

Li, J., Zhou, B., Rong, M., Chen, S., and Zhou, Y. (2020). Estimation of Source Spectra, Attenuation, and Site Responses from strong-motion Data Recorded in the 2019 Changning Earthquake Sequence. *Bull. Seismol Soc. Am.* 110, 410–426. doi:10.1785/0120190207

Liu, J., and Zahradník, J. (2020). The 2019 M_W 5.7 Changning Earthquake, Sichuan Basin, China: A Shallow Doublet with Different Faulting Styles. *Geophys. Res. Lett.* 47, e2019GL085408. doi:10.1029/2019gl085408

Meier, M.-A., Ampuero, J.-P., Cochran, E., and Page, M. (2021). Apparent Earthquake Rupture Predictability. *Geophys. J. Int.* 225, 657–663. doi:10.1093/gji/ggaa610

Meier, M.-A., Heaton, T., and Clinton, J. (2016). Evidence for Universal Earthquake Rupture Initiation Behavior. *Geophys. Res. Lett.* 43, 7991–7996. doi:10.1002/2016gl070081

Meier, M., Kodera, Y., Böse, M., Chung, A., Hoshiba, M., Cochran, E., et al. (2020). How Often Can Earthquake Early Warning Systems Alert Sites with High Intensity Ground Motion?. *J. Geophys. Res.* 125 (2), e2019JB017718. doi:10.1029/2019jb017718

Melgar, D., and Hayes, G. (2019). Characterizing Large Earthquakes before Rupture Is Complete. *Sci. Adv.* 5, eaav2032. doi:10.1126/sciadv.aav2032

Meng, L., Mcgarr, A., Zhou, L., and Zang, Y. (2019). An Investigation of Seismicity Induced by Hydraulic Fracturing in the Sichuan Basin of China Based on Data from a Temporary Seismic Network. *Bull. Seismol Soc. Am.* 109, 348–357. doi:10.1785/0120180310

Mittal, H., Wu, Y.-M., Sharma, M. L., Yang, B. M., and Gupta, S. (2019). Testing the Performance of Earthquake Early Warning System in Northern India. *Acta Geophys.* 67, 59–75. doi:10.1007/s11600-018-0210-6

Peng, C., Chen, Y., Chen, Q., Yang, J., Wang, H., Zhu, X., et al. (2017a). A New Type of Tri-axial Accelerometers with High Dynamic Range MEMS for Earthquake Early Warning. *Comput. Geosciences*. 100, 179–187. doi:10.1016/j.cageo.2017.01.001

Peng, C., Yang, J., Zheng, Y., Zhu, X., Xu, Z., and Chen, Y. (2017b). New τ_c Regression Relationship Derived from All P Wave Time Windows for Rapid Magnitude Estimation. *Geophys. Res. Lett.* 44, 1724–1731. doi:10.1002/2016GL071672

Peng, C., Jiang, P., Chen, Q., Ma, Q., and Yang, J. (2019). Performance Evaluation of a Dense MEMS-Based Seismic Sensor Array Deployed in the Sichuan-Yunnan Border Region for Earthquake Early Warning. *Micromachines*. 10, 735. doi:10.3390/mi10110735

Peng, C., Ma, Q., Jiang, P., Huang, W., Yang, D., Peng, H., et al. (2020). Performance of a Hybrid Demonstration Earthquake Early Warning System in the Sichuan-Yunnan Border Region. *Seismol. Res. Lett.* 91, 835–846. doi:10.1785/0220190101

Peng, C., Xue, B., Yang, J., Chen, Y., Li, J., Liu, M., et al. (2015). "A Low-Latency Seismic Recorder for Earthquake Early Warning," in *5th International Conference on Information Engineering for Mechanics and Materials (ICIMM 2015)* (Atlantis: Press). doi:10.2991/icimm-15.2015.167

Peng, H., Wu, Z., Wu, Y.-M., Yu, S., Zhang, D., and Huang, W. (2011). Developing a Prototype Earthquake Early Warning System in the Beijing Capital Region. *Seismological Res. Lett.* 82 (3), 394–403. doi:10.1785/gssrl.82.3.394

Satriano, C., Elia, L., Martino, C., Lancieri, M., Zollo, A., and Iannaccone, G. (2011). PRESTo, the Earthquake Early Warning System for Southern Italy: Concepts, Capabilities and Future Perspectives. *Soil Dyn. Earthquake Eng.* 31, 137–153. doi:10.1016/j.soildyn.2010.06.008

Sheen, D. H., Park, J. H., Chi, H. C., Hwang, E. H., Lim, I. S., Seong, Y. J., et al. (2017). The First Stage of an Earthquake Early Warning System in South Korea. *Seismological Res. Lett.* 88 (6), 1491–1498. doi:10.1785/0220170062

Stubailo, I., Alvarez, M., Biasi, G., Bhadha, R., and Hauksson, E. (2021). Latency of Waveform Data Delivery from the Southern California Seismic Network during the 2019 Ridgecrest Earthquake Sequence and its Effect on ShakeAlert. *Seismol. Res. Lett.* 92 (1), 170–186. doi:10.1785/0220200211

Tamaribuchi, K., Yamada, M., and Wu, S. (2014). A New Approach to Identify Multiple Concurrent Events for Improvement of Earthquake Early Warning (In Japanese). *Zisin*. 2 (67), 41–55. doi:10.4294/zisin.67.41

Trugman, D. T., Page, M. T., Minson, S. E., and Cochran, E. S. (2019). Peak Ground Displacement Saturates Exactly when Expected: Implications for Earthquake Early Warning. *J. Geophys. Res. Solid Earth*. 124 (5), 4642–4653. doi:10.1029/2018jb017093

Wessel, P., and Smith, W. H. F. (1998). New, Improved Version of Generic Mapping Tools Released. *Eos Trans. AGU* 79 (47), 579. doi:10.1029/98EO00426

Wu, Y.-M. (2014). Progress on Development of an Earthquake Early Warning System Using Low-Cost Sensors. *Pure Appl. Geophys.* 172 (9), 2343–2351. doi:10.1007/s00024-014-0933-5

Wu, Y. M., Liang, W. T., Mittal, H., Chao, W. A., Lin, C. H., Huang, B. S., et al. (2016). Performance of a Low-Cost Earthquake Early Warning System (P-Alert) during the 2016ML 6.4 Meinong (Taiwan) Earthquake. *Seismological Res. Lett.* 87 (5), 1050–1059. doi:10.1785/0220160058

Wu, Y. M., Mittal, H., Huang, T. C., Yang, B. M., Jan, J. C., and Chen, S. K. (2019). Performance of a Low-Cost Earthquake Early Warning System (P-Alert) and Shake Map Production during the 2018 Mw 6.4 Hualien, Taiwan, Earthquake. *Seismol. Res. Lett.* 90 (1), 19–29. doi:10.1785/0220180170

Xu, Y., Wu, Z., Jiang, C., Yu, Y., and Yang, J. (2008). Estimating the Size of an Earthquake Using Short-Period Seismograms of the First Three Seconds: A Simulated experiment Using the 1999 Jiji (Chi-Chi) Earthquake Sequence. *Acta Seismologica Sinica*. 30 (2), 135–143

Yamada, M., Heaton, T., and Beck, J. (2007). Real-time Estimation of Fault Rupture Extent Using Near-Source versus Far-Source Classification. *Bull. Seismological Soc. America*. 97 (6), 1890–1910. doi:10.1785/0120060243

Yi, G., Long, F., Liang, M., Zhao, M., Wang, S., Gong, Y., et al. (2019). Focal Mechanism Solutions and Seismogenic Structure of the 17 June 2019 M_S 6.0 Sichuan Changning Earthquake Sequence. *Chin. J. Geophys.* 62 (9), 3432–3447. (in Chinese). doi:10.6038/cjg2019N0297

Zhang, H., Jin, X., Wei, Y., Li, J., Kang, L., Wang, S., et al. (2016). An Earthquake Early Warning System in Fujian, China. *Bull. Seismological Soc. America*. 106 (2), 755–765. doi:10.1785/0120150143

Zollo, A., Iannaccone, G., Lancieri, M., Cantore, L., Convertito, V., Emolo, A., et al. (2009). Earthquake Early Warning System in Southern Italy: Methodologies and Performance Evaluation. *Geophys. Res. Lett.* 36, L00B07. doi:10.1029/2008gl036689

Conflict of Interest: The authors declare that the research was conducted in the absence of any commercial or financial relationships that could be construed as a potential conflict of interest.

frontiers in Earth Science

ORIGINAL RESEARCH
published: 08 July 2021
doi: 10.3389/feart.2021.666444

Earthquake Early Warning System for Structural Drift Prediction Using Machine Learning and Linear Regressors

Antonio Giovanni Iaccarino[1]*, *Philippe Gueguen*[2], *Matteo Picozzi*[1] and *Subash Ghimire*[2]

[1]Dipartimento di Fisica "Ettore Pancini", Università Degli Studi di Napoli, Federico II, Napoli, Italy, [2]ISTerre, Université Grenoble Alpes, CNRS/IRD/Univ Savoie Mont-Blanc/Univ Gustave Eiffel, Grenoble, France

In this work, we explored the feasibility of predicting the structural drift from the first seconds of P-wave signals for On-site Earthquake Early Warning (EEW) applications. To this purpose, we investigated the performance of both linear least square regression (LSR) and four non-linear machine learning (ML) models: Random Forest, Gradient Boosting, Support Vector Machines and K-Nearest Neighbors. Furthermore, we also explore the applicability of the models calibrated for a region to another one. The LSR and ML models are calibrated and validated using a dataset of ~6,000 waveforms recorded within 34 Japanese structures with three different type of construction (steel, reinforced concrete, and steel-reinforced concrete), and a smaller one of data recorded at US buildings (69 buildings, 240 waveforms). As EEW information, we considered three P-wave parameters (the peak displacement, Pd, the integral of squared velocity, IV^2, and displacement, ID^2) using three time-windows (i.e., 1, 2, and 3 s), for a total of nine features to predict the drift ratio as structural response. The Japanese dataset is used to calibrate the LSR and ML models and to study their capability to predict the structural drift. We explored different subsets of the Japanese dataset (i.e., one building, one single type of construction, the entire dataset. We found that the variability of both ground motion and buildings response can affect the drift predictions robustness. In particular, the predictions accuracy worsens with the complexity of the dataset in terms of building and event variability. Our results show that ML techniques perform always better than LSR models, likely due to the complex connections between features and the natural non-linearity of the data. Furthermore, we show that by implementing a residuals analysis, the main sources of drift variability can be identified. Finally, the models trained on the Japanese dataset are applied the US dataset. In our application, we found that the exporting EEW models worsen the prediction variability, but also that by including correction terms as function of the magnitude can strongly mitigate such problem. In other words, our results show that the drift for US buildings can be predicted by minor tweaks to models.

Keywords: earthquake early warning, onsite EEW, structural drift, machine learning regressors, building monitoring

OPEN ACCESS

Edited by:
Maren Böse,
ETH Zurich, Switzerland

Reviewed by:
Stephen Wu,
Institute of Statistical Mathematics (ISM), Japan
Enrico Tubaldi,
University of Strathclyde, United Kingdom

***Correspondence:**
Antonio Giovanni Iaccarino
antoniogiovanni.iaccarino@unina.it

Specialty section:
This article was submitted to Geohazards and Georisks, a section of the journal Frontiers in Earth Science

Received: *10 February 2021*
Accepted: *21 June 2021*
Published: *08 July 2021*

Citation:
Iaccarino AG, Gueguen P, Picozzi M and Ghimire S (2021) Earthquake Early Warning System for Structural Drift Prediction Using Machine Learning and Linear Regressors. Front. Earth Sci. 9:666444. doi: 10.3389/feart.2021.666444

INTRODUCTION

Seismic risk is one of the main concerns for public authorities in seismic prone regions. Earthquake Early Warning Systems (EEWSs) are complex infrastructures that can mitigate the seismic risk of citizens and losses by the rapid analysis of seismic waves (Gasparini et al., 2011). Typically, EEWS analyzes seismic data in real-time for automatically detects and predict the earthquake size using the first seconds of P-wave signals. Generally, by these pieces of information, EEWSs attempt predicting the ground motion (e.g., Peak Ground Acceleration, PGA) at specified targets. Hence, EEWSs disseminate alerts to targets where the shaking intensity is expected to overcome a damage threshold.

There are two main families of EEWS: on-site and regional systems (Satriano et al., 2011). The on-site approaches use a single station, or a small seismic network, installed near the target. On the other hand, in regional systems, a seismic network is placed near the seismogenic zone, which normally is placed sufficiently far from the target area to protect. Furthermore, on-site systems use P-waves information to directly predict ground motion through empirical scaling laws, while regional ones exploit primarily P-waves, but also S-waves information, from stations close to the epicenter for estimating the source location and magnitude, which in turn are feeding GMPEs (Ground Motion Prediction Equation) for predicting the ground motion at targets.

A fundamental EEWS parameter is the time available to mitigate the seismic risk at a target before damaging ground motion related to S-waves or surface waves reach it (hereinafter called "lead-time"). Depending on the hypocentral distance between seismic source and target, the lead-time of the EEWS approaches is different: at higher distances, the lead-time is greater for regional systems; at shorter distances, on-site EEWSs are faster and can provide useful alerts when the regional systems fail (Satriano et al., 2011).

In the last 2 decades, several works have proposed the use of P-wave features in on-site EEW framework. Wu and Kanamori (2005) proposed the inverse of the predominant period, τ_c, measured on the first 3s of P-wave waveforms to predict the magnitude. The same authors have also proposed the Peak of Displacement, Pd, on 3s window to predict the Peak Ground Velocity, PGV (Wu and Kanamori, 2008). Brondi et al. (2015) used the Pd and the Integral of squared Velocity, IV^2 to predict the PGV and the Housner Intensity, I_H. Spallarossa et al. (2019) and Iaccarino et al. (2020) explored the use of Pd and the IV^2 and for predicting PGV and the Response Spectra of Acceleration, RSA, amplitudes at nine periods, respectively, using a mixed-effect regression approach aiming to account for site-effects.

Besides the ground motion in free field, recently, efforts to predict the structural response in EEWS applications have also been proposed (i.e., applications where the Structural Health Monitoring, SHM, meets the EEWS goal to disseminate real-time alerts). The outputs of these methods can, for instance, trigger automatic isolation systems (Chan et al., 2019; Lin et al., 2020) based on damage level predictions through Engineering Demand Parameters (EDP). For example, Picozzi (2012) proposed to combine P-wave features with the structural building response retrieved by interferometry and a multi-sensors system (Fleming et al., 2009) to predict both the earthquake parameters and the structural response. Kubo et al. (2011) proposed a built-in EEWS for buildings that is able to automatically stop the elevator, start an acoustic alert at each floor, and predict displacement intensity and story drift angle at each floor. In perspective, the use of new advanced technologies, such as Internet of Things and 5G, will significantly facilitate for the easy and huge implementation of such systems (D'Errico et al., 2019).

This work aims to explore the use of P-wave parameters (i.e., Pd, IV^2 and the integral of squared displacement, ID^2) to predict the structural response in on-site EEWS applications. In particular, following Astorga et al. (2020), we considered the drift ratio (Dr.) as a robust and reliable parameter to link in the building response. The parameter Dr. is computed as the relative displacement between two sensors in the building (one placed at the top floor and the other at the bottom floor of the building) divided by the height difference between the sensors.

To this purpose, we investigated the performance of different algorithms to develop robust empirical model between our EEWS parameters and Dr Specifically, we explored both Least Square Regression (LSR) and Machine Learning (ML) techniques. Since Mignan and Broccardo (2019) have demonstrated that complex ML models are often overused, one of our goal is to verify whether MLs, considering their complexity and the difficulties in a suitable training, provide advantages or not with respect to simpler linear models in EEW applications.

We investigated four different machine learning regressors: Random Forest (RF, Breiman, 2001), Gradient Boosting (GB, Friedman, 2001), Support Vector Machine (SVM, Cortes and Vapnik, 1995) and K-Nearest Neighbors (KNN, Altman, 1992). These MLs are used to parameterize models aiming to predicting $\log_{10}Dr$ from the three P-wave proxies and three time-windows (i.e., 1, 2, and 3 s). For each regressor, we tune two hyper-parameters by comparing the results of K-fold cross-validation (with K = 5) using the training set (Stone, 1974). Then, the best hyper-parameters set is used to train the ML algorithms with the entire training set (i.e., 80% of the data), and finally, we test their performance with a testing set (i.e., 20% of the data). This procedure allows us to assess in a robust way the regression performance. In parallel, we calibrated models also using linear least square regressors (LSR). To this aim, we used two strategies: we calibrated LSR models for single P-wave features (i.e., three P-wave proxies times three time-window lengths); we used all the features together for calibrating LSR models, mimicking what is done for ML. Therefore, we compare the ML performance with the LSR models.

The calibration and performance analysis are carried out by progressive steps, where the complexity of the dataset is increased at each step. In the first analysis, we focused on the Shiodome Annex (ANX) building, a Japanese Steel-Reinforce-Concrete (SRC) building. With its 20 years-long history of earthquakes recording, ANX represents the perfect starting case study to understand the capabilities of the methods.

In the second step, we considered all the Japanese SRC buildings. The rationale in this choice is that, even if they are

TABLE 1 | Dataset summary.

	Japanese dataset		US dataset	
	Low-rize	High-rize	Low-rize	High-rize
RC	10	3	13	9
SRC	5	7	0	0
ST	1	8	28	19

of the same typology of ANX, we expect that the combination of the buildings response with different site conditions can contribute to inflate the drift variability.

Finally, in the third step we used the complete Japanese dataset, and we performed a residuals analysis de-aggregating them for building and earthquake characteristics. The aim of this last analysis is to explore the possibility of retrieving correction factors that in future EEW applications can be used for improving the drift predictions.

Finally, we verified the validity of the ergodic assumption for the EEWS calibrated models, a typical problem in seismology when models calibrated for a region are applied to data in other areas. To this aim, we applied the models calibrated using the Japanese dataset to the waveforms recorded in U.S. buildings.

DATASETS AND METHODS

Datasets

We consider 3-components waveforms recorded at Japanese and U.S. buildings (Astorga et al., 2020). The considered buildings belong to three different types of construction (**Table 1**): steel (ST), reinforced concrete (RC) and steel-reinforced concrete (SRC, only Japanese buildings). All buildings have one sensor at the ground floor and one at the top floor. We measure P-waves EEW parameters (Pd, IV^2, ID^2; hereinafter we refer to them in general way as XP parameters) for different signal lengths (i.e., 1, 2 and 3 s) from the station at the ground level, while Dr. is measured using both sensors.

The Japanese dataset (**Figure 1A**) is made up by 5,942 waveforms collected from 2,930 earthquake recorded at 34 buildings. The magnitude of the events, from the Japan Meteorological Agency (JMA), ranges from M_{JMA} 2.6 to M_{JMA} 9, and the epicentral distances vary between 2.2 and 2,514 km.

The US dataset (**Figure 1B**) is formed by 240 waveforms from 90 events recorded at 69 buildings. The magnitude of these events ranges from Mw 3.5 to Mw 7.3, while the epicentral distance ranges from 2.7 to 391 km.

Table 1 presents the buildings classification according to construction material and height. The largest set of data is available for ANX (**Figure 1A**), an SRC building in Japan that includes 1,616 waveforms recordings. Since the height is considered important in determining the buildings response, we used the number of floors to divide the dataset into two categories: 1) low-rize buildings when the number of floors is less than eight; 2) high-rize buildings for the others. This classification is similar to the one done in Astorga et al., 2020, but, here, low-rize and mid-rize categories are merged in the low-rize category.

P-Wave Features

Waveforms are filtered using a narrow bandpass Butterworth filter between the frequencies 0.5 and 2 Hz. This choice was made following Astorga et al. (2019) and is motivated by the aim of selecting signals that are strongly related to the structural response. Indeed, for the building as those considered in this study the co-seismic fundamental frequency is usually within this range (Astorga et al., 2020).

Since our objective is to calibrate models for on-site EEW application, we considered as proxy of drift parameters estimated from P-wave signal windows of limited lengths (i.e., 1, 2 and 3 s after the P-waves first arrival). The rationale behind this choice is that the three time windows can allow to capture the temporal evolution of the drift, and also to assess the consistence/robustness of the estimates in time. Furthermore, selecting a fixed time window length in EEW systems is not a trivial task. Indeed, two contrasting effects play a role in taking this decision.

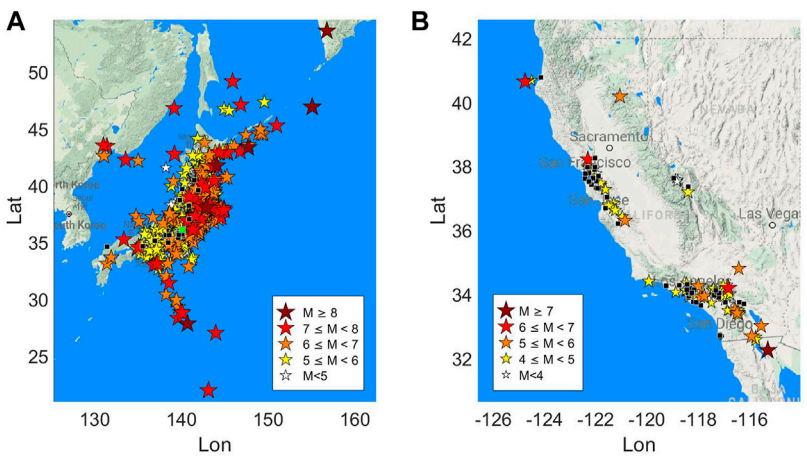

FIGURE 1 | Map of the dataset used in the study. The stars indicate the events, the color and the size refer to the magnitude following the legends in the figure. The black squares indicate the buildings, the green one in figure a) is the ANX building.

From one hand, the signal windows should be as shorter as possible to increase the lead-time. On the other hand, since the rupture duration increases with magnitude, selecting too short time-windows lead to the saturation of the prediction, which results in wrong prediction for large earthquakes (i.e., in analogy with the typical magnitude saturation problem in seismology). In this study, using time windows with maximum length equal to 3 s, we expect our P-wave proxies to saturate around magnitude Mw 7 (e.g., Yamada and Mori, 2009).

To assess the structural response, we consider the dimensionless structural drift, Dr., defined as (Astorga et al., 2020)

$$Dr = (PTD - PGD)/h \tag{1}$$

where *PTD* is the Peak of Displacement in the top of the building, *PGD* is the Peak of Displacement at the ground level of the building and *h* is the distance between the two sensors.

Concerning the P-waves features, we rely on the peak of displacement (*Pd*), the integral of the squared velocity (IV^2) and the integral of the squared displacement (ID^2).

These features are computed on the vertical component following Iaccarino et al. (2020).

$$ID^2 = \int_{t_p}^{t_p+\tau} d^2(t)\, dt \tag{2}$$

$$IV^2 = \int_{t_p}^{t_p+\tau} v^2(t)\, dt \tag{3}$$

$$Pd = \max_{t_p \le t \le t_p+\tau} |d(t)| \tag{4}$$

where t_p is the first arrival time, *t* is the window length, *d(t)* is the displacement, and *v(t)* is the velocity. *Pd* is measured in cm, IV^2 in cm^2/s and ID^2 in $cm^2 \cdot s$. Since we measure these three XPs on three different windows, we have a total of nine different features: ID^2_{1s}, ID^2_{2s}, ID^2_{3s}, IV^2_{1s}, IV^2_{2s}, IV^2_{3s}, Pd_{1s}, Pd_{2s}, Pd_{3s}.

Case Studies

The availability of two rich datasets, relevant to two countries with different building typology and tectonic contexts, motivated us to explore the effect of the dataset complexity in the robustness of EEW model predictions. It is quite common in seismology, and especially in EEW applications, to use an ergodic approach in the use of EEW models. In other words, models calibrated combining datasets from different regions are exported to further areas assuming that regional effects do not play role in the model uncertainty (Stafford, 2014). However, results of recent EEW studies (e.g., among others Spallarossa et al., 2019; Iaccarino et al., 2020) have shown the opposite; that is to say, regional characteristics can play an important role in the robustness and accuracy of the EEW predictions, leading to increase the epistemic uncertainty (Al Atik et al., 2010). For this reason, we proceeded setting four different case studies using datasets of increasing order of heterogeneity. We started calibrating EEW models from a specific building (i.e., ANX in Japan); then, we moved forwards including more buildings from the same typology and region (i.e., SRC from Japan); and then, the same region but with different construction typology. Finally, we applied the models calibrated with Japanese data to those recorded at U.S. buildings. Our strategy of assessing the performance of LSR and ML models in progressively harder conditions (i.e., varying dataset size and composition) aims to unveil eventual drawbacks and limitations in their use.

To set a robust assessment of the models calibrated by different approaches (i.e., ML and linearized algorithms) and datasets (i.e., #1 ANX, #2 SRC-JAPAN, #3 all JAPAN buildings, #4 U.S. buildings), we define a training set (80% of the data) and a testing set (20% of the data) for each of the case studies. In all cases, the data for training and testing are selected by randomly splitting the dataset. The training set is used to tune the model parameters. Then, the trained model is used to predict the drift of the testing set. This will provide a trustworthy way to compare LSR and ML models. This procedure will avoid any bias in the evaluation of the models.

Case 1. The ANX building is considered for a building specific analysis (i.e., the same site conditions and building features characterize all the data). Therefore, the variability of data in terms of amplitude and duration length is, in this case, due to only the within-event and aleatory variability (Al Atik et al., 2010).
Case 2. In the second step of our analysis, we considered the dataset formed by all the data from SRC buildings in Japan. This second dataset is made up by 3,086 waveforms from 2,034 events and 12 buildings (of course including also ANX). This analysis, thus, allows us to study the variability related to different site conditions and building responses.
Case 3. We considered the complete Japanese dataset. With respect to the previous one, this dataset also includes the complexity due to differences in the seismic response between different types of construction.
Case 4. We studied the implications of exporting the retrieved model for Japan to another region. To do this, we apply the models trained on the Japanese dataset to the U.S. dataset. Clearly, this application is expected to be the more difficult since different aspects can play a role in degrading the model prediction capability. First of all, there are well-known tectonic and geological differences between Japan and California. The main difference is that the former is a subduction zone with a prevalence of thrust earthquakes, while, in the latter, most of the earthquakes are associated to strike-slip faults. Another important aspect to account for is that differences may exist within the building type of construction, due to different building design codes between Japan and United States.

Linear Least Square Regression

The selected nine XP_w (see *P-Wave Features*) are strongly covariant, since they are relevant to the same P-wave signals observed in different domains (i.e., displacement, and velocity) and time (i.e., 1, 2 and 3 s). While ML techniques can address this issue, the LSR approaches are prone to problems in cases where the dependent variables are correlated each other. For this reason, we applied the LSR in two different ways.

In the first approach, we used the features separately. This leads us to have nine different linear models that, for the sake of simplicity, have the same functional form, as:

$$\log_{10} Dr = a + b*\log_{10} XP_w \quad (5)$$

where XP_w can be any of the P-wave parameters (**Eqs 2–4**) at a specific window-length w (i.e., 1, 2 or 3 s). We will refer to these models as "LSR XP_w".

For all these techniques, we calibrated ML models by adopting an approach that mimics increase of information with time typical of EEW applications (i.e., the temporal evolution of time-windows in 1, 2, and 3°s). In particular, for the first time-window (1 s), we use only the 3 P-wave parameters available at that time. For the second time-window (2 s), we consider the information available at this moment (i.e., the features at 1 and 2 s, for a total of 6 features). Finally, for the 3 s window, we use all nine features.

In the second approach we mimic the increasing of information with time typical of EEW applications (i.e., the temporal evolution of time-windows in 1, 2, and 3 s). In particular, for the first time-window (1 s), we use only the 3 P-wave parameters available at that time. For the second time-window (2 s), we consider the information available at this moment (i.e., the features at 1 and 2 s, for a total of 6 features). Finally, for the 3s window, we use all nine features. We will refer to three combined models as "LSR_w".

In total, we will compare 12 linear models.

Machine Learning Regressors

As previously said, we use four different ML techniques: Random Forest (RF, Breiman, 2001), Gradient Boosting (GB, Friedman, 2001), Support Vector Machine (SVM, Cortes and Vapnik, 1995) and K-Nearest Neighbors (KNN, Altman, 1992). In this section, we shortly present them focusing on hyper-parameters tuned by a K-fold cross validation. Of course, we refer to the referenced works for their deeper understanding.

RF Regressor

RF regressor (Breiman, 2001) is an ensemble of a specified number of decision tree regressors (N_{tr}). A decision tree regressor works as a flow-chart in which, for each node, a feature is selected randomly to subdivide the data in two further nodes through a threshold. This latter is chosen to minimize the node impurity, as follows:

$$I = \frac{1}{N}\sum_{i=1}^{N}\left(y_i - \hat{y}\right)^2 \quad (6)$$

where N is the number of the training data in the node, y_i is the real value of the target for the ith datum and $\hat{y}$ is the predicted value of the end node in which the ith point is assigned. The predicted value of the end node is simply the mean value of the data in the end node itself. The depth of the trees is controlled by a tolerance factor that stops the subdivision procedure if the gain in impurity is not enough, or by reaching a maximum depth value M_{dep}. The final regression is given by the average prediction of all the trees. We select N_{tr} and M_{dep} as the hyper-parameters to tune.

GB Regressor

In a similar way to RF, the GB regressor is an ensemble of N_{tr} decision tree regressors (Friedman, 2001). The main difference between the two is that in GB the steepest descent technique is applied to minimize a least square loss function. In this algorithm, each decision tree plays the role of a new iteration, while the procedure is controlled by the hyper-parameter learning rate (L_r). From preliminary studies, we decide to fix $N_{tr} = 300$ and we tune M_{dep} and L_r.

SVM Regressor

The SVM regressor searches the best hyperplane to predict the target value also minimizing the number of predictions that lies outside an ε-margin from the hyperplane (Cortes and Vapnik, 1995). The result is achieved solving the problem:

$$\min_{\omega,b,\xi}\left[\frac{1}{2}\omega^T\omega + C\sum_i\left(\xi_i + \xi_i^*\right)\right] \quad (7)$$

where $\omega \in \mathbb{R}^p$ and $b \in \mathbb{R}$ are the linear regression parameters for p features, C is a penalty factor, and ξ_i, ξ_i^* are positive slack variables representing the distance from the lower or the upper margins. It is worth to note that the slack variables (ξ_i and ξ_i^*) are both non-zero only if the datum lies inside the margins. Furthermore, to include any nonlinear trends, we used a Gaussian kernel with σ_{SVM} as variance. In summary, the main hyper-parameters for this technique are ε, C and σ_{SVM}. Looking at preliminary testing results, we fixed $\varepsilon = 0.1$ and we tuned C and σ_{SVM}.

KNN Regressor

Finally, the KNN regressor predicts the target of a certain datum as the weighted average of the K_N nearest data target, where the weights are the opposite of the distance (Altman, 1992). This technique is a lazy learner because the training step consists only in the memorization of a training set. We use the Minkowski distance of order p (van de Geer, 1995). We use K_N and p as hyper-parameters to tune.

For all these techniques, we calibrated ML models by adopting an approach similar to the one adopted for combined LSR models. That is to say, we will use all the available features at each second (i.e., 3 features at 1s, 6 at 2s and, finally, nine features at 3s) to calibrate the ML models. In this way, we have three configurations for each ML regressor with a total of 12 ML models. Hereinafter, we will refer to these models as ML_w, where ML can be RF, GB, SVM or KNN, and w is the time window used.

Validation Process

For all ML methods, we apply the logarithm base 10 to all the features and then we standardize them to have a unit variance. For each ML algorithm, we apply a K-fold cross-validation (Stone, 1974) on the training set with K = 5 for each set of hyper-parameters. We use the coefficient of determination R^2 as comparative score, so as to find the optimal configuration for each model. This effort is done to avoid two critical issues that are well-known with ML techniques: underfitting and overfitting (Dietterich, 1995; Hawkins, 2004; Raschka and Mirjalili, 2017). A model is underfitted when it is too simple and is not able to retrieve good predictions even on the training set (e.g., this can

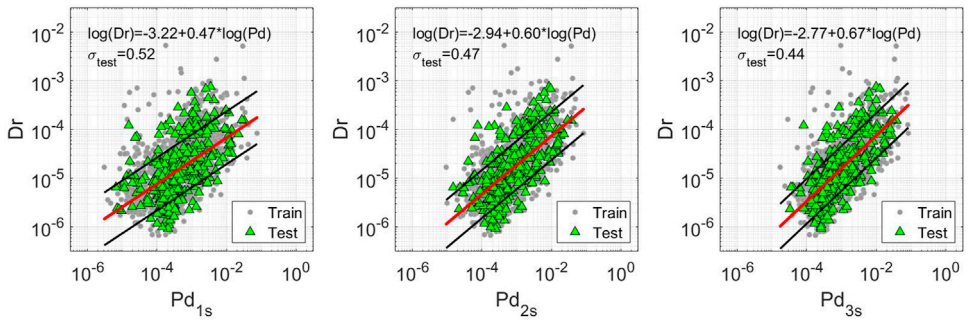

FIGURE 2 | Dr. vs. Pd (cm) of the ANX dataset for three different windows. Gray dots refer to train set data. Green dots refer to test set data. The red lines are the least square regression performed for the train set. The black lines, instead, represent the ±σtrain confidence level. The equation of this line is written in the upper part of each figure with its own test residual variability, σ_{test}.

TABLE 2 | Least square regression results, ANX dataset.

XP_w	a	b	σ_{train}	σ_{test}	R^2_{train}	R^2_{test}
ID^2_{1s}	−3.41	0.21	0.56	0.54	0.22	0.25
ID^2_{2s}	−3.13	0.27	0.51	0.49	0.35	0.39
ID^2_{3s}	−3.01	0.31	0.48	0.46	0.43	0.46
IV^2_{1s}	−3.56	0.22	0.54	0.52	0.27	0.31
IV^2_{2s}	−3.42	0.27	0.49	0.47	0.40	0.43
IV^2_{3s}	−3.34	0.30	0.46	0.44	0.46	0.49
Pd_{1s}	−3.22	0.47	0.54	0.52	0.26	0.29
Pd_{2s}	−2.94	0.60	0.49	0.47	0.39	0.43
Pd_{3s}	−2.77	0.67	0.46	0.44	0.47	0.50
LSR_{1s}			0.53	0.51	0.30	0.34
LSR_{2s}			0.44	0.43	0.51	0.53
LSR_{3s}			0.41	**0.39**	0.57	**0.60**

TABLE 3 | Least square regression results, SRC dataset.

XP_w	a	b	σ_{train}	σ_{test}	R^2_{train}	R^2_{test}
ID^2_{1s}	−3.25	0.22	0.53	0.54	0.32	0.33
ID^2_{2s}	−3.17	0.26	0.50	0.51	0.41	0.40
ID^2_{3s}	−3.14	0.28	0.47	0.48	0.47	0.46
IV^2_{1s}	−3.49	0.22	0.53	0.54	0.34	0.33
IV^2_{2s}	−3.47	0.25	0.49	0.51	0.42	0.41
IV^2_{3s}	−3.47	0.27	0.47	0.48	0.47	0.47
Pd_{1s}	−3.18	0.47	0.52	0.54	0.35	0.33
Pd_{2s}	−3.08	0.54	0.49	0.51	0.43	0.39
Pd_{3s}	−3.03	0.58	0.46	0.49	0.49	0.45
LSR_{1s}			0.52	0.54	0.36	0.33
LSR_{2s}			0.46	0.49	0.49	0.45
LSR_{3s}			0.44	**0.46**	0.54	**0.51**

happen also when LSR is performed on strongly non-linear databases). On the other hand, a model is overfitted when it performs very well on the training set but presents a lack of accuracy on the testing set. This problem arises when a model is so complex that it results too linked with the training data variability.

ANX AND SRC ANALYSIS

In this section, we analyze the EEW models calibrated considering the ANX and SRC buildings subsets.

Least Square Regression Models

As said above, we develop 12 linear models (i.e., derived combining three P-wave proxies and three different windows, and the combined LSR models) for the two datasets. As example, we show in **Figure 2** the results of the regression performed for *Pd* considering the three windows on the ANX (similar figures are shown for IV^2 and ID^2 as supplementary information, **Supplementary Figures S1, S2**). **Figure 2** shows that both the training set (gray circles) and testing set (green triangles) have the same variability around the fit. We report the results of all the linear regressions, for ANX in **Table 2**, and for SRC in **Table 3**, whereas the first two columns report the regression parameters as in **Eq. 5** (for LSR_w models, we reported the regression coefficients in **Supplementary Table S1**). Moreover, the third column, σ_{train}, contains the standard deviation of the residuals for the training set, while the fourth column, σ_{test}, contains the same but for the testing set. Finally, in the last two columns, we report the R^2 value for training and testing sets.

Looking at the results shown in **Table 2** (i.e., ANX), the models perform slightly better on the testing set both in terms of σ and R^2. This difference is probably due to the different amount of data within the two sets. It is worth to note that the prediction improves with the increasing of the window length for all the models, i.e., looking at Pd, σ_{test} is 0.52 at 1 s, 0.47 at 2 s and 0.44 at 3 s. In the end, comparing XPs, we note that IV^2 and Pd have similar performances, while ID^2 is the worst. The combined models perform always better than the single-feature models looking window-by-window. LSR_{3s} provides the best performances with σ_{test} = 0.39 and R^2_{test} = 0.60 (these values are bolded in **Table 2**).

From **Table 3**, we can note that the performance of the LSR models for the Japanese SRC buildings is always slightly worse than that for ANX. This result is probably due to the increase in the between-buildings variability of the observations, that can also be affected by different site conditions (we will focus on this important aspect in the following section). An improvement of predictions with the time window lengths

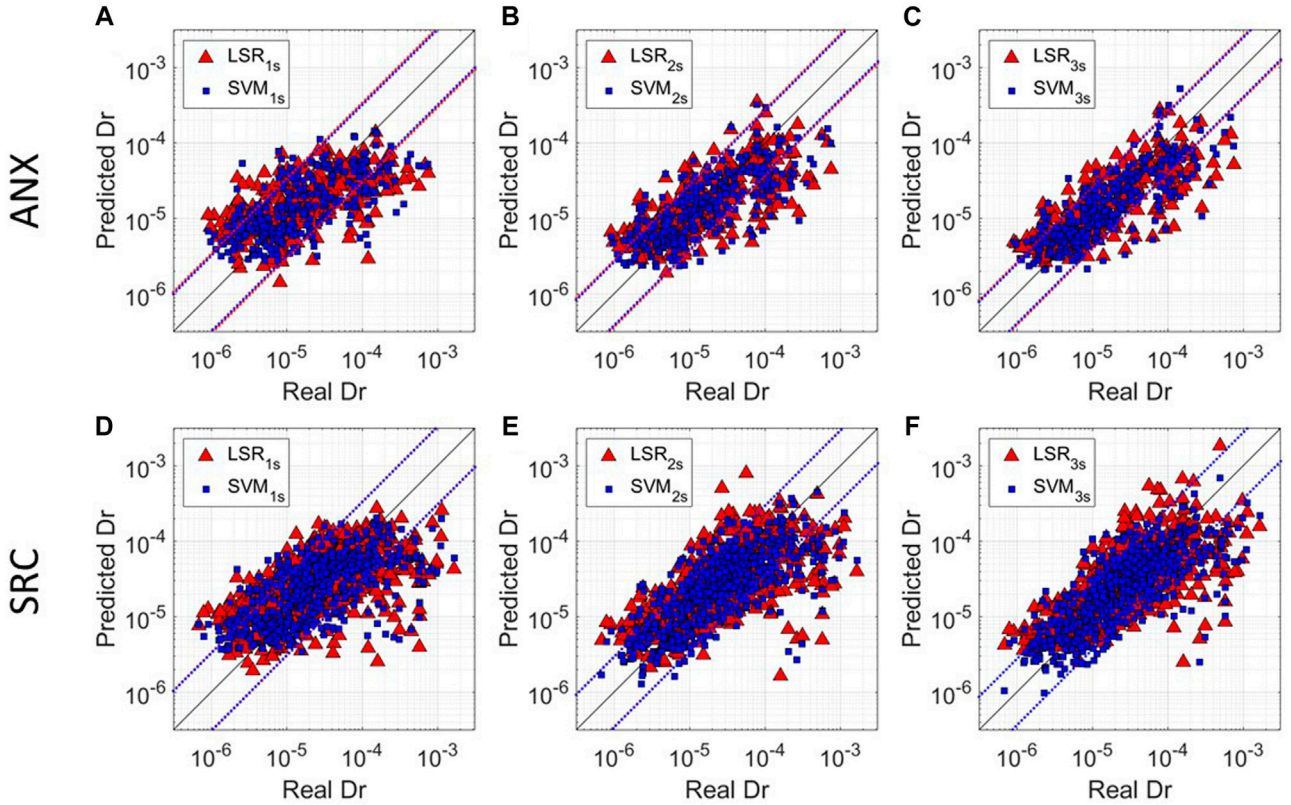

FIGURE 3 | Predicted Dr. vs. Real Dr. for three different windows for ANX dataset **(A–C)** and for SRC dataset **(D–F)**. Red triangles refer to the prediction made least square regression using combined LSR for both datasets measured at the reference window. Blue squares refer to the predictions of the SVM regressor at the reference window. The black line Real Dr. = Predicted Dr. reference line. The dotted lines represent $\pm\sigma_{train}$ confidence level for LSR (red) and ML (blue) models.

TABLE 4 | ML regression results, ANX dataset.

ML_w	σ_{train}	σ_{test}	R^2_{train}	R^2_{test}
RF_{1s}	0.49	0.49	0.38	0.38
RF_{2s}	0.44	0.42	0.51	0.53
RF_{3s}	0.42	0.39	0.55	0.60
GB_{1s}	0.50	0.49	0.36	0.38
GB_{2s}	0.44	0.42	0.50	0.53
GB_{3s}	0.43	0.39	0.53	0.59
SVM_{1s}	0.49	0.47	0.39	0.43
SVM_{2s}	0.42	0.40	0.54	0.57
SVM_{3s}	0.40	**0.37**	0.58	**0.64**
KNN_{1s}	0.49	0.50	0.37	0.35
KNN_{2s}	0.44	0.42	0.51	0.54
KNN_{3s}	0.42	0.39	0.56	0.59

TABLE 5 | ML regression results, SRC dataset.

ML_w	σ_{train}	σ_{test}	R^2_{train}	R^2_{test}
RF_{1s}	0.50	0.51	0.41	0.40
RF_{2s}	0.46	0.46	0.50	0.51
RF_{3s}	0.44	0.43	0.54	0.57
GB_{1s}	0.50	0.51	0.40	0.40
GB_{2s}	0.46	0.46	0.50	0.51
GB_{3s}	0.44	0.44	0.54	0.55
SVM_{1s}	0.49	0.50	0.42	0.41
SVM_{2s}	0.45	0.45	0.52	0.53
SVM_{3s}	0.42	**0.42**	0.57	**0.58**
KNN_{1s}	0.50	0.51	0.39	0.39
KNN_{2s}	0.46	0.47	0.49	0.49
KNN_{3s}	0.43	0.44	0.55	0.55

is again observed. In this case, the combined models improve the predictions only for 2 s, and 3 s windows. Finally, we obtain again the best results for LSR_{3s} with $\sigma_{test} = 0.46$ and $R^2_{test} = 0.51$ (bolded in **Table 3**).

We show, in **Figure 3**, the predicted Dr. vs. the real Dr. using the LSR model calibrated using the combined model LSR_w for the three windows on the ANX (**Figures 3A–C**) and SRC (**Figures 3D–F**) testing datasets as red triangles. We also plot the standard deviation references as red dashed lines. From these results, we can see the improving of the performances due to the increasing of the window length.

Machine Learning Regression

Tables 4, **5** report the results for 12 ML regression models (see *Linear Least Square Regression*) for the ANX and SRC datasets, respectively. In these tables, each row refers to a different ML_w. The parameters σ_{train} and R^2_{train} are the mean of the same parameters obtained by the K-fold cross-validation on the

TABLE 6 | Least square regression results, Japanese dataset.

XP_w	a	b	σ_{train}	σ_{test}	R^2_{train}	R^2_{test}
ID^2_{1s}	–3.52	0.18	0.54	0.54	0.23	0.24
ID^2_{2s}	–3.46	0.21	0.52	0.52	0.29	0.30
ID^2_{3s}	–3.41	0.23	0.50	0.50	0.33	0.34
IV^2_{1s}	–3.75	0.17	0.54	0.54	0.22	0.24
IV^2_{2s}	–3.72	0.20	0.52	0.52	0.28	0.29
IV^2_{3s}	–3.71	0.22	0.51	0.50	0.32	0.34
Pd_{1s}	–3.48	0.37	0.54	0.54	0.23	0.24
Pd_{2s}	–3.38	0.43	0.52	0.52	0.30	0.29
Pd_{3s}	–3.32	0.48	0.50	0.50	0.35	0.34
LSR_{1s}			0.54	0.54	0.23	0.25
LSR_{2s}			0.50	0.50	0.35	0.34
LSR_{3s}			0.47	**0,48**	0.41	**0,41**

TABLE 7 | ML regression results, Japanese dataset.

ML_w	σ_{train}	σ_{test}	R^2_{train}	R^2_{test}
RF_{1s}	0.52	0.52	0.28	0.29
RF_{2s}	0.48	0.48	0.39	0.39
RF_{3s}	0.46	0.46	0.43	0.46
GB_{1s}	0.52	0.52	0.28	0.29
GB_{2s}	0.49	0.49	0.38	0.38
GB_{3s}	0.47	0.46	0.43	0.44
SVM_{1s}	0.52	0.52	0.27	0.31
SVM_{2s}	0.49	0.48	0.38	0.40
SVM_{3s}	0.46	**0,45**	0.43	**0,47**
KNN_{1s}	0.53	0.53	0.26	0.28
KNN_{2s}	0.48	0.48	0.38	0.40
KNN_{3s}	0.46	0.45	0.43	0.46

training set. After the training, we apply the calibrated models to the testing dataset.

Looking at **Table 4**, σ_{test} and R^2_{test} are in general equal or slightly better than the values for the training set. A similar result has been observed also in the least square regression analysis (**Table 2**). Since our predictions do not worsen on the testing set, we are confident that we are avoiding overfitting. Furthermore, applying ML analyses, the prediction performance is improved by using the longest time window available. Lastly, SVM_{3s} is the best ML among the tested ones, with σ_{test} = 0.37 and R^2_{test} = 0.64 (bolded in **Table 4**).

As for the least square regression analysis results, also in this case we observe that drift prediction worsens increasing the building numbers (i.e., going from ANX to SRC buildings). This result shows us that despite buildings are of the same construction typology, the varying site conditions can play a significant role in increasing the drift estimates variability. As for the ANX analysis, the SVM technique provides the best Dr. predictions; in particular, SVM_{3s} provides the best model with σ_{test} = 0.42 and R^2_{test} = 0.58.

Figure 3 shows the comparison between the best LSR model (i.e., combined LSR for both datasets, red triangles) and the best ML technique (i.e., SVM for both datasets, blue squares). As expected, we observe for both datasets that the model prediction improves with the time window length (i.e., predictions and observations get closer to the 1:1 reference line; black line), especially for higher Dr. values.

Our results highlight also that the SVM technique provides slightly better predictions than LSR models for both ANX and SRC datasets. Indeed, the variability of prediction for SVM is smaller than that from the linear regression models. This effect is even more evident looking at low and high Dr. values (**Figure 3**), for which the linear regression models lead to higher variability in the prediction (i.e., especially for SRC buildings, panels d–f).

Such underestimation increases with drift amplitude, which is clearly function also of the events magnitude. For this reason, we hypothesize that the drift underestimation is due to two main effects: 1, for larger magnitude earthquakes (i.e., Mw > 7.5) the moment rate function is longer than 3 s, leading the maximum time-window (3s) to saturate, which in turns makes it difficult to predict Dr.; 2, differently from most of the datasets, the waveforms of large magnitude events are recorded at very large hypocentral distances and can be dominated by high amplitude surface waves. The dominance of surface waves in such signals can pose a problem to our analyses, because our dataset is mostly dominated by moderate to large magnitude events (the 90% of the Japanese data is between Mw 3.6 and 7.0) and the larger ground motion is related to the S-waves. Therefore, models calibrated for estimating the drift associated to S-waves are not efficient in predicting Dr. associated to very large magnitude earthquakes at large hypocentral distances generating high amplitude surface waves.

The analysis on the ANX and SRC datasets suggest us that it is possible to predict in real-time Dr. using P-wave parameters. The best predictions are obtained using the 3stime-windows and using ML models (i.e., the model SVM_{3s}).

JAPANESE DATASET ANALYSIS

In this section, we discuss the development and testing of prediction models considering the entire Japanese dataset.

Least Square Regression Laws

Table 6 reports the results for LSR models calibrated on the Japanese dataset. In this case, we observe that the performances on training and testing set are very similar. Again, we notice an overall worsening of both the scores with respect to the ANX (**Table 2**) and SRC buildings (**Table 3**). Clearly, this outcome was expected, given that the Japanese dataset includes more variability than the other two datasets.

In this case, all the P-wave proxies (XPs) show basically the same results in terms of σ_{test} and R^2_{test} for the same windows. On the other hand, combined LSR models perform slightly better at 2 and 3s. We have the best results for LSR_{3s}, as in the other cases, σ_{test} = 0.48 and R^2_{test} = 0.41. Despite such low fitting score can generate skepticism about these LSR models utility, in the following *Residual Analysis*, we will show that by a residual analysis we can identify some of the component generating the large variability of predictions.

Machine Learning Regression

Table 7 is the analogue of **Tables 4**, **5** for the Japanese dataset. As for the previous cases, MLs perform better than LSR for the same

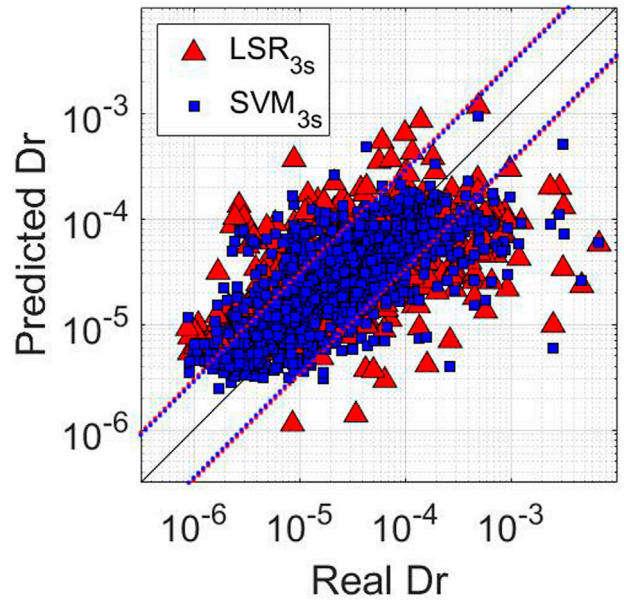

FIGURE 4 | Predicted Dr. vs. Real Dr. of the test set for the Japanese dataset for 3s windows. Red triangles refer to the predictions with LSR_{3s}. Blue squares refer to the predictions of the SVM_{3s} model. The black line Real Dr. = Predicted Dr. reference line. The dotted lines represent ±σtrain confidence level for LSR (red) and ML (blue) models.

time window. In this case also, the best model is SVM_{3s}, with $\sigma_{test} = 0.45$ and $R^2_{test} = 0.47$. In **Figure 4**, we compare the predictions of LSR_{3s} for one of the best LSR models (**Table 5**) with that of SVM_{3s}. This comparison clearly shows us that the cloud of SVM_{3s} estimates is thinner than that for LSR. Despite that, both models seem to saturate above Dr. equal to $4^{*}10^{-4}$.

The performances of the calibrated models seem to be worse than those proposed by on-site EEW studies (among others, (Olivieri et al., 2008; Wu and Kanamori, 2008; Zollo et al., 2010; Brondi et al., 2015; Caruso et al., 2017). A direct comparison among different approaches is however unfair. Indeed, despite the appearance, we must consider that generally on-site EEW studies focus on the prediction of ground motion parameters (e.g., peak ground acceleration, PGA) using data collected in free field. On the contrary, in this study, we predict an engineering demand parameter (Dr.) using data from in-building sensors. Our approach is certainly challenging because building responses inflate the variability of our predictions. Furthermore, we must also consider that recent studies (Astorga et al., 2020; Ghimire et al., 2021) explored the prediction of drift from PGA measures using the same dataset considered here and found a prediction variability similar to that of our models. Moreover, other studies, such as Tubaldi et al., 2021, pointed out that event-to-event variability contributes significatively to the uncertainties in the damage prediction, even for single structure models.

Residual Analysis

As we saw in **Tables 6**, **7**, the fitting scores for all the methods are generally rather low. This can be due to numerous factors. One reason can be the lack of information of the EEW input features that, as said, are extracted from *p* waves, while the final building drift is related to S and surface waves. Anyway, this effect is unavoidable in onsite EEW and also difficult to quantify. Instead, we can try to assess which other factors influence the variability of our methods. So, to better understand the strengths and weaknesses of the calibrated models, we performed a residual analysis (Al Atik et al., 2010). To this purpose, we disaggregate the residuals (predicted minus real Dr. values) by site and event characteristics. In **Figure 5**, we compare the testing set residuals for the LSR model considering Pd_{3s} (red error-bars) and the equivalent for SVM_{3s} (blue error-bars). For each group, we show the mean and the standard deviation of residuals. In all sub-plots of **Figure 5**, we also show the $\pm\sigma_{train}$ references for both methods (i.e., 0.50 for Pd_{3s} represented as red lines, and 0.46 for SVM_{3s} represented as blue lines).

Figure 5A presents the residuals grouped by buildings, which are ordered by the mean of the residuals for the two methods. We colored the labels of the buildings by type of construction (pink for RC, light green for SRC, blue for ST) and the edge of the label by the height (brown for low-rize, green for high-rise). At first glance, we observe that the two methods show similar performance in terms of mean of the residuals for all the buildings. Looking at residual variability, however, we observe that in most of the cases ML performs better than LSR, especially for two buildings "YKH1" and "SKS".

A more detailed examination to residuals variation for different buildings suggests conclusions similar to those of Al Atik et al. (2010) for ground motion prediction equations (GMPEs). These authors, indeed, explored the epistemic uncertainty by splitting it into source, path, and site contributions. If we consider one or many of these factors in our model, we are relaxing the ergodic assumption which states that the variability of the dataset is completely aleatory. The variability of the residuals in **Figure 5A** is the result of the site-effect, which in our particular case is a term used to describe the response of the soil-structure system that can lead to a very complex behavior. Nevertheless, the full investigation and explanation of the causes of these site conditions is beyond the aim of this paper. In our opinion, the significant variation in residuals shown in **Figure 5A** is not surprising, being in agreement with other studies (Spallarossa et al., 2019; Iaccarino et al., 2020); which have recently discussed how to reduce the prediction variability considering site-effect terms in EEW model using the mixed-effect regression approach (Pinheiro and Bates, 2000).

As second step, we analyze the residuals grouping them for building characteristics and height (see **Table 1** and **Figure 5B**). Our results show that the mean of residuals for all building groups are close to zero, except for low-rize ST buildings. This latter class, however, includes only the building KWS, that also in the previous analysis showed a peculiar response (**Figure 5A**). Being the average of residuals consistent with zero, the predictions seem independent from the type of construction and the height of the buildings.

In **Figures 5C,D**, we show the residuals vs. the event parameters magnitude and distance. It is worth noting that

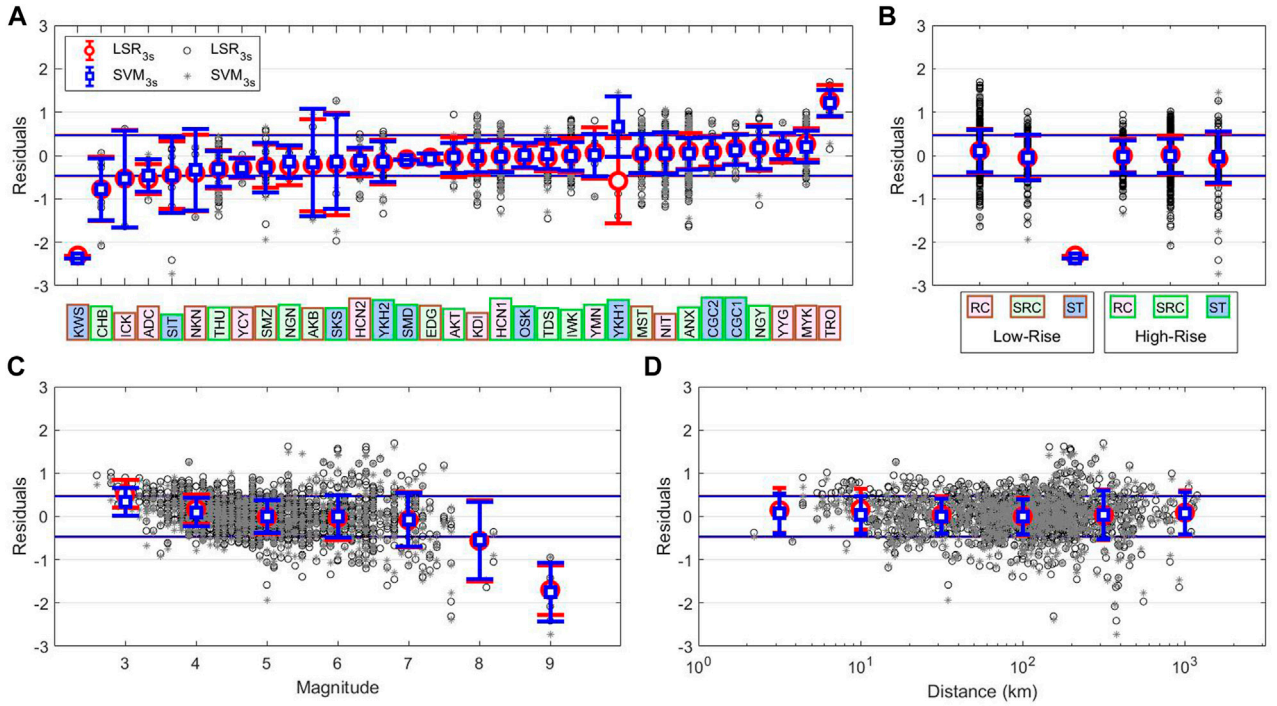

FIGURE 5 | Decomposition of the residuals of Dr. prediction for Japanese test set. The residuals are computed as real Dr. - predicted Dr., so positive values mean overestimation, and negative residuals mean underestimation. In each panel we show the residuals for two different models: LSR_{3s} with circles representing the single prediction and red errorbars representing the mean prediction of the group; SVM_{3s} with stars for the single prediction and blue errorbars for the group mean. Red and blue lines represent the $\pm\sigma$train for LSR_{3s} and SVM_{3s}, respectively. The labels in panels **(A)** and **(B)** are colored by construction type and height: pink for RC; light green for SRC; blue for ST; brown edges for low-rize; green edges for high-rize. In panel **(A)** we decompose the residuals by buildings. In **(B)** we group them by building type of construction and height. In panel **(C)** we use the magnitude to decompose residuals, the groups are evenly spaced and the errorbars are placed in the center of the bin. In panel **(D)** the residuals are grouped by distance in km, the groups are evenly spaced and the errorbars are placed in the center of the bin.

these are not "sufficiency analysis" as intended by Luco (2002). Indeed, in the sufficiency analysis a cinematic parameter is defined as sufficient for predicting an engineering demand parameter (e.g., Dr.) if the predictions are independent from magnitude and distance. To confirm this property, a probabilistic analysis would be needed (Ghimire et al., 2021), but that is beyond the aim of this study.

Figure 5C shows the error bars, the residual mean and standard deviation in bins of 1 unit centered on the magnitude value. From these results, we can clearly see that the magnitude has a great effect on the prediction. In particular, we see that the predictions are good between magnitude 4 and 7, while we overestimate Dr. at lower magnitudes and underestimate Dr. at higher magnitudes. The overestimation at magnitudes lower than 3.5 is probably due to the fact that the predominant frequencies of such events are too high to stimulate an effective response of the building (i.e., we consider a frequencies range between 0.5 and 2 Hz). On the other hand, as previously discussed, the underestimation for magnitude greater than 7.5 is likely due to: 1) the window length of 3 s, which is too small compared to the rupture duration and lead to saturation problems of the prediction; 2) the measured Dr. can be affected by the presence of surface waves associated to large magnitude events. Measures of Dr. form signals dominated by surface waves, indeed, might add non-linear terms to the equation between our XP and Dr. itself. The underestimation at high magnitudes can be also caused by the lower number of recordings in the dataset with respect to those for the smaller magnitudes, i.e. a typical problem for all the EEWS (Hoshiba et al., 2011; Chung et al., 2020). Moreover, another possible bias that big events can introduce are the non-linear responses of site and buildings, especially during long sequence of earthquakes (Guéguen et al., 2016; Astorga et al., 2018). The saturation of Dr. predictions for earthquakes with M > 7.5 is certainly a big issue for the application of the calibrated models in operational EEW systems in areas where very large earthquakes are expected, and further studies are necessary to deal with it. Nevertheless, our results indicate that the calibrated models can be useful in countries characterized by moderate to large seismic hazard (e.g., Italy, Greece, Turkey; where the seismic risk is high due to high vulnerability and exposure). A more in-depth analysis of the performances for EEW systems using the models calibrated is beyond the aim of this study, because it would require target dependent economic cost-benefit analyses (Strauss and Allen, 2016; Minson et al., 2019).

Interestingly, SVM_{3s} seems providing better results than LSR for both for lowest and highest magnitude events. In our opinion, this result suggests a higher performance of non-linear models.

TABLE 8 | Least square regression results, complete dataset.

XP_w	a	b	σ_{train}	σ_{test}	R^2_{train}	R^2_{test}
ID^2_{1s}	–3.52	0.18	0.54	0.48	0.23	–0.45
ID^2_{2s}	–3.46	0.21	0.52	0.46	0.29	–0.37
ID^2_{3s}	–3.42	0.23	0.50	0.46	0.34	–0.25
IV^2_{1s}	–3.75	0.17	0.54	0.47	0.23	–0.48
IV^2_{2s}	–3.73	0.20	0.52	0.45	0.28	–0.39
IV^2_{3s}	–3.72	0.22	0.51	0.46	0.33	–0.25
Pd_{1s}	–3.49	0.37	0.54	0.48	0.24	–0.44
Pd_{2s}	–3.39	0.43	0.52	0.46	0.30	–0.36
Pd_{3s}	–3.33	0.47	0.50	0.46	0.35	–0.25
LSR_{1s}			0.54	0.47	0.24	–0.44
LSR_{2s}			0.50	0.46	0.35	–0.35
LSR_{3s}			0.48	0.54	0.41	–0.32

Finally, **Figure 5D** shows the residuals grouped by the distance, using 6 bins evenly spaced in logarithmic scale from $10^{0.5}$ to 10^3 km. The mean of residuals and the associated standard deviation are plotted at the center of each corresponding bin. We observe that all the residuals are close to zero. Nevertheless, we observe a small overestimation of the prediction at distances lower than 20 km. This effect is partially connected to the overestimation seen for low magnitudes (**Figure 5C**), because in this range of distances the magnitude is limited between 2.6 and 5.2. In this case too, the machine learning seems able to learn how to solve the bias.

The results of the residual analysis suggest: 1) SVM_{3s} is confirmed as the best model; 2) decomposing the residuals with respect to buildings, construction type, magnitude, and distance, we found a broad variation of the mean residuals with the buildings typology. This result suggests that site-correction terms should be included in future EEW application to buildings. 3) The residuals are correlated to the magnitude, while they seem be much less dependent from the distance.

US DATASET APPLICATION

In the last part of this work, we apply the models calibrated using the Japanese dataset to the U.S. dataset. Our aim is to verify if the usual ergodic assumption often used in EEW application is valid or not, and eventually to look for strategies that could allow to successfully export the models from one region to another.

Least Square Regression Laws

Table 8 reports the results for the linear regression performed on the complete dataset. The most noticeable aspect here is the R^2_{test} column that presents all negative value. This is due to a quite important bias in the prediction of Dr. for U.S. building. In **Figure 6**, we show the mean residual for U.S. dataset, which are plotted as orange error bars with the length equal to $\sigma_{test}/\sigma_{train}$. Since the residuals are computed as differences between predicted and observed Dr., the linear regression of the Japanese dataset underestimates the Dr. of the U.S. buildings of about 1σ. We find a similar bias also for ML techniques. These observations confirm that exporting EEW models among different regions, independently from the algorithm used for their calibration, is not a straightforward operation.

In the next section, we analyze the causes of this bias, and we propose a solution.

Bias Analysis

We present here the results of the residual analysis carried out on the U.S. buildings predictions. **Figure 6** shows the results as orange error-bars for LSR with IV^2_{2s}. We selected this particular model because, as we will show also later, after the application of a correction term it becomes the best predictive model for drift on U.S. buildings.

To correctly evaluate the effectiveness of the method, we divided the U.S. dataset in two subsets (60 and 40%): whereas the first subset is used to compute the correction terms and the second one is used to test the models. The residuals for the corrected model are plotted as green error-bars for the U.S. train set and as light blue for the U.S. test set. We report as reference level the $\pm\sigma_{train}$ as black lines (see also **Table 8**).

First, we consider only the uncorrected residuals (i.e., orange error-bars). In **Figure 6A**, we plot only the results for U.S. buildings with at least 3 records, grouping the remaining ones as "Others". The buildings are ordered for increasing mean value of residuals. We observe a general smaller variability of the residuals with the buildings than for Japanese buildings (**Figure 5A**), but at the same time we notice that the majority of the buildings have predictions underestimated and non-zero residuals. These results indicate that there is a bias in the global trend of predictions with respect to the buildings.

Looking at **Figure 6B**, we can note that, while a small bias is still present for high-rize buildings, the majority of the bias is due to low-rize buildings. However, this difference between building classes is not significant since all the bars are consistent with each other.

In **Figure 6C**, as for **Figure 5C**, we notice a strong correlation between residuals and magnitude. We can see, indeed, that the predictions worsen with the increasing of the magnitude.

Finally, in **Figure 6D**, the residuals for U.S. dataset seem to be not significantly affected by the distance. Indeed, the residuals remain equally underestimated but in the second range that goes from about 6 to 18 km. The anomaly in this range of distances is probably connected to data distribution. In fact, here we find events with magnitude between 3.5–4.5 and we can relate this result with what we observe for low magnitude in **Figure 6C**.

Bias Correction

In this section, we propose a methodology to account for the bias observed from the residual analysis applied to U.S. buildings drift predictions. To this aim, we borrowed the strategy adopted in seismic hazard studies where the decomposition of the variability in the ground motion predictions can be used to improve the estimates (Al Atik et al., 2010).

We consider, as correction terms, the residuals for magnitude classes, ΔDr_M, computed for the U.S. training set (**Figure 5C**, orange error-bars). Estimating the magnitude in EEW applications is a well-established task, with a large number of operational, reliable algorithms and a wide literature, at least for

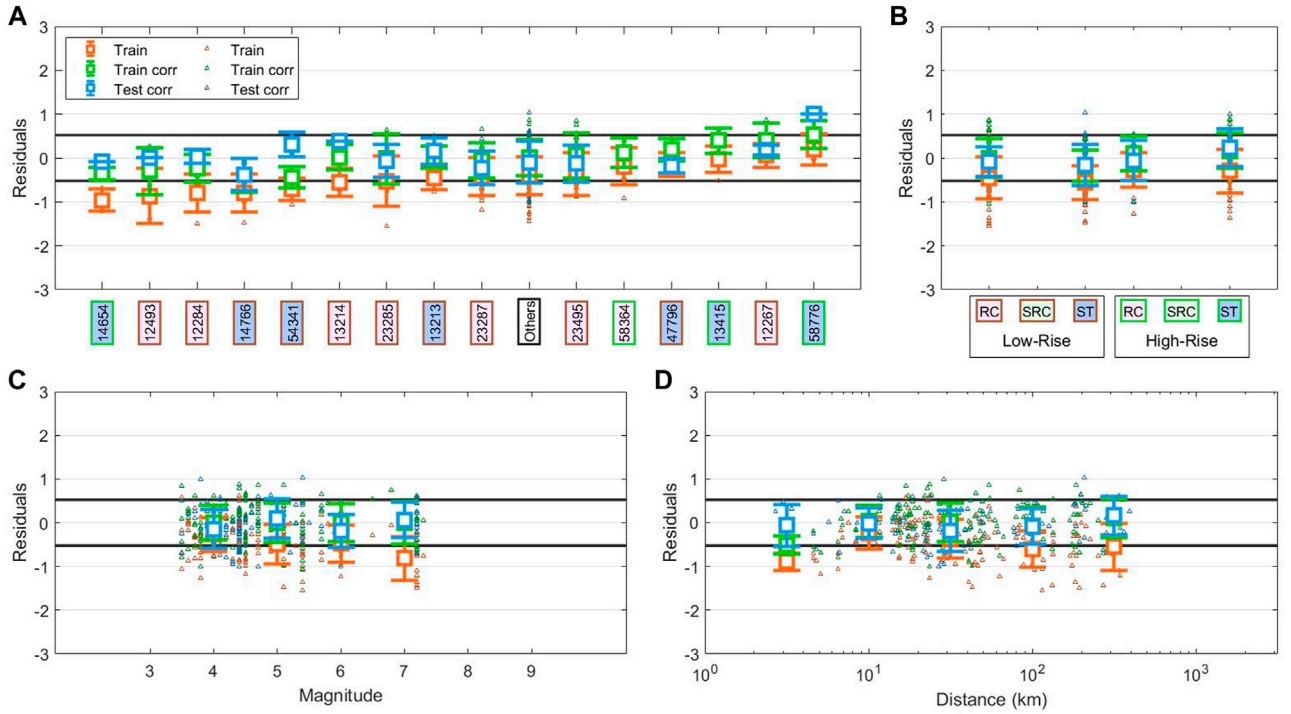

FIGURE 6 | Decomposition of the residuals of Dr. prediction for US dataset using Japanese model. The residuals are computed as real Dr. - predicted Dr., so positive values mean overestimation, and negative residuals mean underestimation. In each panel we show the residuals for LSR IV^2_{2s} model in three cases: for the training set without corrections, with orange tringles representing the single prediction and orange errorbars representing the mean prediction of the group; for the training set with magnitude dependent correction with green triangles for the single prediction and green errorbars for the group mean; for the testing set with magnitude dependent correction with light blue triangles for the single prediction and light blue errorbars for the group mean. Black lines represent the $\pm\sigma_{train}$ for LSR IV^2_{2s}. The labels in panels **(A)** and **(B)** are colored by construction type and height: pink for RC; light green for SRC; blue for ST; brown edges for low-rize; green edges for high-rize. The "Others" label is white. In panel **(A)** we decompose the residuals by buildings. In **(B)** we group them by building type of construction and height. In panel **(C)** we use the magnitude to decompose residuals, the groups are evenly spaced and the errorbars are placed in the center of the bin. In panel **(D)** the residuals are grouped by distance in km, the groups are evenly spaced and the errorbars are placed in the center of the bin.

earthquakes with magnitude smaller than Mw 7.5. For example, Mousavi and Beroza (2020) showed that by ML approaches reliable estimation of earthquake magnitude from raw waveforms recorded at single stations can be obtained (standard deviation ~0.2). We thus foresee similar achievements in EEW in the next future. Here, we considered suitable to set corrections for our models be magnitude dependent. Therefore, for the sake of simplicity, we assume that magnitude estimates are provided in real-time by other EEW systems and are available as input for our Dr. predictions.

It is worth noting that for very large earthquakes (Mw > 7.5) the 3-s P-wave windows considered in our study do not include enough information to estimate the magnitude (Hoshiba et al., 2011; Chung et al., 2020). Therefore, the proposed magnitude dependent correction is considered valid only for events smaller than Mw 7.5.

The ΔDr_M terms computed using the EEW magnitude estimates as input can thus be subtracted to the predicted Dr. in order to set at zero the mean residual in each magnitude range: $\log_{10} Dr^{corr} = \log_{10} Dr - Dr_M$.

Table 9 shows the R^2 scores for all the models and time windows after that we have applied the Dr_M corrections on the testing dataset. We observe that, in this case, the 2s predicting models performs better than the 3s ones. Moreover, LSR_{3s} has still negative R^2 and so the correction in this case is ineffective. It is difficult to understand if this effect is due to the correction or to the window that can include more S-wave content at 3s for these events. The most interesting aspect is that the LSR methods with single feature perform now better than combined LSR, and ML models. This result is probably connected to the characteristics of ML techniques. In fact, ML algorithms are typically less able than LSR ones to extrapolate the predictions outside the features'

TABLE 9 | R^2 scores for US dataset corrected drift prediction.

Model	1s	2s	3s
LSR-ID^2	0.21	0.26	0.25
LSR-IV^2	0.27	**0,30**	0.27
LSR-Pd	0.20	0.24	0.20
Combined LSR	0.22	0.21	–0.03
RF	0.21	0.19	0.09
GB	0.23	0.21	0.08
SVM	0.16	0.21	0.18
KNN	0.10	0.15	0.16

domain of the training set. In addition, some of them, like RF or KNN, cannot predict target values outside the target domain for the training set by construction. Probably, combined LSR models also suffer of the same problems of ML techniques because of their complexity.

The best model after the Dr_M correction is the LSR with IV^2_{2s}. As anticipated, this is the reason why we plotted the result for this model in **Figure 6**.

By construction, after the magnitude correction, the error-bars (green) have all zero-mean, but we can see that also the residuals for the test set are consistent with zero (**Figure 6C**). **Figure 6A** now shows that residuals for the training set have the same number of buildings with underestimated and overestimated predictions. Moreover, the residuals for the testing set are consistent the training one, but for three buildings (i.e., "14,654", "54,341", and "58,776"). This variability well agrees with **Figure 5A** and as discussed, it depends on site and buildings effects. In **Figure 6B**, for both training and testing set, we find again the difference in mean residuals for low-rize and high-rize buildings, but this effect is present especially for ST buildings. Moreover, the drift for high-rize ST buildings is now meanly overestimated. In the end, in **Figure 6D**, we see that, despite some oscillation, the residuals have not any more dependence with distance, as seen for Japanese buildings in **Figure 5D**.

As conclusion of this analysis, we can state that when the models retrieved considering the Japanese dataset are applied to the U.S. dataset, the Dr. predictions present a severe bias. However, by including a magnitude dependent correction term seems a relatively simple and practice solution to solve the problem. We have also found that the LSR models, after the correction, perform better than ML models. The best model, in this case, is the LSR with IV^2_{2s}.

CONCLUSION

In this work, we tested the performance of several predicting models for building drift using three different EEW P-wave parameters computed considering three time-window lengths, for a total of nine features. We used a dataset of almost 6,000 waveforms from in-building sensors recorded in Japan and California. We compared linear least square and non-linear machine learning regressions for a total of 21 different models. We set up four different case-studies to understand how the data variability affects the predictions.

Our results can be summarized as follow:

Analyzing a single building ("ANX") with a very long history of records, then all the data for the steel-reinforced concrete buildings (which contains "ANX"), and finally the entire Japanese dataset, we show that the training and the testing set have the same kind of variability and ML models perform always better than least square regression. In particular, ML models result more efficient in dealing with the non-linearity of the problem, likely because they are able to get more information from features combining them together. Moreover, the results prove that the increasing of the time window always improves the predictions. The results showed us that it is possible to retrieve building specific EEW models for Dr. prediction. This result is probably also related to the large size and good quality of the ANX dataset.

The results for the steel-reinforced concrete buildings dataset show that we can retrieve reliable models also grouping data from similar buildings. Having a lot of data from more buildings can help to overcome the problems of a few data from a single building, but at the price of a decrease in the accuracy of the predictions. Indeed, we observed a further reduction in accuracy when we used the entire Japanese dataset. So, increasing in variability of the dataset lead to models prone to precision of the predictions problems that should be considered accurately.

To better understand this issue, we used models retrieved on the entire dataset to explore the residuals correlation with buildings, types of construction, magnitude, and distance. This analysis has shown that the prediction residuals are strongly dependent from buildings and magnitude. In particular, we have found that some buildings are not well described by the models. This effect can be considered as a site-effects, which is in this application due to effects of many combined factors (e.g., 1D-to-3D soil amplification, soil-structure interaction, building resonance). Instead, looking at the magnitude, we observed a drift overestimation at lower magnitude ($M < 4$) and an underestimation at higher magnitude ($M > 7.5$). Such latter effect is the more worrying for EEW applications and it is likely due to both the lack of data in this range of larger magnitude, and to the time window length of 3s that does not contain enough information about the source size.

We have applied the Japanese models to predict the Dr. in U.S. buildings, and we have found that in this case the predictions are biased leading Dr. being underestimated. An important warning from our study is that EEW models for drift prediction are not directly exportable. This bias may be mainly due to geological and seismological differences between Japan and California. An analysis of residuals decomposed for different factors has shown a strong dependency from site-effects and magnitude.

We proposed a method to correct the prediction bias resulting from exporting EEW model to other regions from those of calibration. We showed that by applying a magnitude dependent correction terms to the predictions the biases can be removed. Hence, we showed that by the suggested method, the predictions become reliable again.

Finally, an interesting result is that, in the particular case of exporting models to another region, the linear models perform better than machine learning. This result, despite is not very surprising since it is well-known that the non-linear models are less able to extrapolate predictions outside the features' domain of the training set, can be a useful warning for the EEWS community approaching to ML regressors.

Future studies will explore the application of the proposed methodology considering dataset from different regions. For those areas characterized by very large earthquakes, as Japan or Chile, we will explore the use of larger P-wave time-windows. We believe that this study can stimulate applications of non-linear ML models in the on-site EEW framework. Indeed, future studies can use similar approaches for the computation of ground

motion parameters (i.e., PGV, PGA, etc.), as well as of other engineering demand parameters.

A final key point coming out from our analysis is the importance to better understand how the inner variability of a dataset affects the predictions. Our results suggest in fact that by increasing the datasets, we can improve the characterization of the prediction variability ascribed to site effects (e.g. soil-conditions, building response, soil to structure interaction, etc.).

DATA AVAILABILITY STATEMENT

The pre-processed data supporting the conclusion of this article will be made available by the authors, without undue reservation.

AUTHOR CONTRIBUTIONS

AI made most of the analysis and wrote the first draft. PG provided the dataset. SG organized the database. All authors contributed to conception and design of the study. All authors contributed to manuscript revision, read, and approved the submitted version.

FUNDING

AI was funded by the "Programma Operativo Nazionale FSE-FESR Ricerca e Innovazione" (PON FSE-FESR RI) 2014-2020. PG and SG were funded by the URBASIS-EU project (H2020-MSCA-ITN-2018, grant number 813137). Part of this work (PG) was supported by the Real-time earthquake rIsk reduction for a reSilient Europe (RISE) project, funded by the EU Horizon 2020 program under Grant Agreement Number 821115.

SUPPLEMENTARY MATERIAL

The Supplementary Material for this article can be found online at: https://www.frontiersin.org/articles/10.3389/feart.2021.666444/full#supplementary-material

REFERENCES

Altman, N. S. (1992). An Introduction to Kernel and Nearest-Neighbor Nonparametric Regression. *The Am. Statistician* 46, 175–185. doi:10.1080/00031305.1992.10475879

Astorga, A., Guéguen, P., Ghimire, S., and Kashima, T. (2020). NDE1.0: a New Database of Earthquake Data Recordings from Buildings for Engineering Applications. *Bull. Earthquake Eng.* 18, 1321–1344. doi:10.1007/s10518-019-00746-6

Astorga, A., Guéguen, P., and Kashima, T. (2018). Nonlinear Elasticity Observed in Buildings during a Long Sequence of Earthquakes. *Bull. Seismol. Soc. Am.* 108, 1185–1198. doi:10.1785/0120170289

Astorga, A. L., Guéguen, P., Rivière, J., Kashima, T., and Johnson, P. A. (2019). Recovery of the Resonance Frequency of Buildings Following strong Seismic Deformation as a Proxy for Structural Health. *Struct. Health Monit.* 18, 1966–1981. doi:10.1177/1475921718820770

Atik, L. A., Abrahamson, N., Bommer, J. J., Scherbaum, F., Cotton, F., and Kuehn, N. (2010). The Variability of Ground-Motion Prediction Models and its Components. *Seismological Res. Lett.* 81 (5), 794–801. doi:10.1785/gssrl.81.5.794

Breiman, L. (2001). Random Forests. *Mach. Learn.* 45, 5–32. doi:10.1023/A:1010933404324

Brondi, P., Picozzi, M., Emolo, A., Zollo, A., and Mucciarelli, M. (2015). Predicting the Macroseismic Intensity from Early Radiated P Wave Energy for On-Site Earthquake Early Warning in Italy. *J. Geophys. Res. Solid Earth* 120, 7174–7189. doi:10.1002/2015JB012367

Caruso, A., Colombelli, S., Elia, L., Picozzi, M., and Zollo, A. (2017). An On-Site Alert Level Early Warning System for Italy. *J. Geophys. Res. Solid Earth* 122, 2106–2118. doi:10.1002/2016JB013403

Chan, R. W. K., Lin, Y.-S., and Tagawa, H. (2019). A Smart Mechatronic Base Isolation System Using Earthquake Early Warning. *Soil Dyn. Earthquake Eng.* 119, 299–307. doi:10.1016/j.soildyn.2019.01.019

Chung, A. I., Meier, M.-A., Andrews, J., Böse, M., Crowell, B. W., McGuire, J. J., et al. (2020). Shakealert Earthquake Early Warning System Performance during the 2019 ridgecrest Earthquake Sequence. *Bull. Seismol. Soc. Am.* 110, 1904–1923. doi:10.1785/0120200032

Cortes, C., and Vapnik, V. (1995). Support-vector Networks. *Mach. Learn.* 20, 273–297. doi:10.1007/bf00994018

D'Errico, L., Franchi, F., Graziosi, F., Marotta, A., Rinaldi, C., Boschi, M., et al. 2019, Structural Health Monitoring and Earthquake Early Warning on 5g Urllc Network, in IEEE 5th World Forum on Internet of Things, WF-IoT 2019 - Conference Proceedings.

Dietterich, T. (1995). Overfitting and Undercomputing in Machine Learning. *ACM Comput. Surv.* 27, 326–327. doi:10.1145/212094.212114

Fleming, K., Picozzi, M., Milkereit, C., Kuhnlenz, F., Lichtblau, B., Fischer, J., et al. (2009). The Self-Organizing Seismic Early Warning Information Network (SOSEWIN). *Seismological Res. Lett.* 80, 755–771. doi:10.1785/gssrl.80.5.755

Friedman, J. H. (2001). Greedy Function Approximation: A Gradient Boosting Machine. *Ann. Statist.* 29. doi:10.1214/aos/1013203451

Gasparini, P., Manfredi, G., and Zschau, J. (2011). Earthquake Early Warning as a Tool for Improving Society's Resilience and Crisis Response. *Soil Dyn. Earthquake Eng.* 31, 267–270. doi:10.1016/j.soildyn.2010.09.004

Ghimire, S., Guéguen, P., and Astorga, A. (2021). Analysis of the Efficiency of Intensity Measures from Real Earthquake Data Recorded in Buildings. *Soil Dyn. Earthquake Eng.* 147, 106751. doi:10.1016/j.soildyn.2021.106751

Guéguen, P., Johnson, P., and Roux, P. (2016). Nonlinear Dynamics Induced in a Structure by Seismic and Environmental Loading. *The J. Acoust. Soc. America* 140, 582–590. doi:10.1121/1.4958990

Hawkins, D. M. (2004). *The Problem of Overfitting.* doi:10.1002/0471667196.ess1896

Hoshiba, M., Iwakiri, K., Hayashimoto, N., Shimoyama, T., Hirano, K., Yamada, Y., et al. (2011). Outline of the 2011 off the Pacific Coast of Tohoku Earthquake (M W 9.0) -Earthquake Early Warning and Observed Seismic Intensity-. *Earth Planet. Sp* 63 (7), 547–551. doi:10.5047/eps.2011.05.031

Iaccarino, A. G., Picozzi, M., Bindi, D., and Spallarossa, D. (2020). Onsite Earthquake Early Warning: Predictive Models for Acceleration Response Spectra Considering Site Effects. *Bull. Seismol. Soc. Am.* 110 (3), 1289–1304. doi:10.1785/0120190272

Kubo, T., Hisada, Y., Murakami, M., Kosuge, F., and Hamano, K. (2011). Application of an Earthquake Early Warning System and a Real-Time strong Motion Monitoring System in Emergency Response in a High-Rise Building. *Soil Dyn. Earthquake Eng.* 31, 231–239. doi:10.1016/j.soildyn.2010.07.009

Lin, Y.-S., Chan, R. W. K., and Tagawa, H. (2020). Earthquake Early Warning-Enabled Smart Base Isolation System. *Automation in Construction* 115, 103203. doi:10.1016/j.autcon.2020.103203

Luco, N. (2002). *Probabilistic Seismic Demand Analysis, SMRF Connection Fractures, and Near-Source Effects.* Stanford University.

Mignan, A., and Broccardo, M. (2019). One Neuron versus Deep Learning in Aftershock Prediction. *Nature* 574, E1–E3. doi:10.1038/s41586-018-0438-y

Minson, S. E., Baltay, A. S., Cochran, E. S., Hanks, T. C., Page, M. T., McBride, S. K., et al. (2019). The Limits of Earthquake Early Warning Accuracy and Best Alerting Strategy. *Sci. Rep.* 9–1. doi:10.1038/s41598-019-39384-y

Mousavi, S. M., and Beroza, G. C. (2020). A Machine-Learning Approach for Earthquake Magnitude Estimation. *Geophys. Res. Lett.* 47. doi:10.1029/2019GL085976

Olivieri, M., Allen, R. M., and Wurman, G. (2008). The Potential for Earthquake Early Warning in Italy Using ElarmS. *Bull. Seismological Soc. America* 98 (1), 495–503. doi:10.1785/0120070054

Picozzi, M. (2012). An Attempt of Real-Time Structural Response Assessment by an Interferometric Approach: A Tailor-Made Earthquake Early Warning for Buildings. *Soil Dyn. Earthquake Eng.* 38, 109–118. doi:10.1016/j.soildyn.2012.02.003

Pinheiro, J. C., and Bates, D. M. (2000). *Mixed-Effects Models in S and S-Plus: Statistics and Computing*. Switzerland: Springer Nature. doi:10.1007/978-1-4419-0318-1

Raschka, S., and Mirjalili, V. (2017). *Python Machine Learning: Machine Learning and Deep Learning with Python, Scikit-Learn, and TensorFlow*. 2nd Edition Packt Publishing

Satriano, C., Wu, Y.-M., Zollo, A., and Kanamori, H. (2011). Earthquake Early Warning: Concepts, Methods and Physical Grounds. *Soil Dyn. Earthquake Eng.* 31, 106–118. doi:10.1016/j.soildyn.2010.07.007

Spallarossa, D., Kotha, S. R., Picozzi, M., Barani, S., and Bindi, D. (2019). On-site Earthquake Early Warning: A Partially Non-ergodic Perspective from the Site Effects point of View. *Geophys. J. Int.* 216 (2), 919–934. doi:10.1093/gji/ggy470

Stafford, P. J. (2014). Crossed and Nested Mixed-Effects Approaches for Enhanced Model Development and Removal of the Ergodic assumption in Empirical Ground-Motion Models. *Bull. Seismological Soc. America* 104, 702–719. doi:10.1785/0120130145

Stone, M. (1974). Cross-validation and Multinomial Prediction. *Biometrika* 61, 509–515. doi:10.1093/biomet/61.3.509

Strauss, J. A., and Allen, R. M. (2016). Benefits and Costs of Earthquake Early Warning. *Seismological Res. Lett.* 87, 765–772. doi:10.1785/0220150149

Tubaldi, E., Ozer, E., Douglas, J., and Gehl, P. (2021). Examining the Contribution of Near Real-Time Data for Rapid Seismic Loss Assessment of Structures. *Struct. Health Monit.*, 147592172199621. doi:10.1177/1475921721996218

van de Geer, J. P. (1995). *Some Aspects of Minkowski Distance*. Leiden, Netherlands: Leiden University, Department of Data Theory, Esearch report.

Wu, Y.-M., and Kanamori, H. (2008). Development of an Earthquake Early Warning System Using Real-Time strong Motion Signals. *Sensors* 8, 1–9. doi:10.3390/s8010001

Wu, Y.-M., and Kanamori, H. (2005). Experiment on an Onsite Early Warning Method for the Taiwan Early Warning System. *Bull. Seismological Soc. America* 95, 347–353. doi:10.1785/0120040097

Yamada, M., and Mori, J. (2009). Using τC to Estimate Magnitude for Earthquake Early Warning and Effects of Near-Field Terms. *J. Geophys. Res.* 114, B05301–353. doi:10.1029/2008JB006080

Zollo, A., Amoroso, O., Lancieri, M., Wu, Y.-M., and Kanamori, H. (2010). A Threshold-Based Earthquake Early Warning Using Dense Accelerometer Networks. *Geophys. J. Int.* 183 (2), 963–974. doi:10.1111/j.1365-246X.2010.04765.x

Conflict of Interest: The authors declare that the research was conducted in the absence of any commercial or financial relationships that could be construed as a potential conflict of interest.

frontiers in Earth Science

ORIGINAL RESEARCH
published: 15 July 2021
doi: 10.3389/feart.2021.699560

Real-Time Characterization of Finite Rupture and Its Implication for Earthquake Early Warning: Application of FinDer to Existing and Planned Stations in Southwest China

Jiawei Li[1], *Maren Böse*[2]*, *Yu Feng*[1,3] *and Chen Yang*[4]

[1]Institute of Risk Analysis, Prediction and Management (Risks-X), Academy for Advanced Interdisciplinary Studies, Southern University of Science and Technology (SUSTech), Shenzhen, China, [2]Swiss Seismological Service (SED), Swiss Federal Institute of Technology Zürich (ETH Zürich), Zürich, Switzerland, [3]Department of Civil and Mineral Engineering, University of Toronto, Toronto, ON, Canada, [4]China Earthquake Networks Center (CENC), China Earthquake Administration (CEA), Beijing, China

OPEN ACCESS

Edited by:
Carmine Galasso, University College London, United Kingdom

Reviewed by:
Hongcai Zhang, Earthquake Administration of Fujian Province, China
Dongwang Tao, China Earthquake Administration, China

***Correspondence:**
Maren Böse
mboese@sed.ethz.ch

Specialty section:
This article was submitted to Geohazards and Georisks, a section of the journal Frontiers in Earth Science

Received: *23 April 2021*
Accepted: *29 June 2021*
Published: *15 July 2021*

Citation:
Li J, Böse M, Feng Y and Yang C (2021) Real-Time Characterization of Finite Rupture and Its Implication for Earthquake Early Warning: Application of FinDer to Existing and Planned Stations in Southwest China. Front. Earth Sci. 9:699560. doi: 10.3389/feart.2021.699560

Earthquake early warning (EEW) not only improves resilience against the risk of earthquake disasters, but also provides new insights into seismological processes. The Finite-Fault Rupture Detector (FinDer) is an efficient algorithm to retrieve line-source models of an ongoing earthquake from seismic real-time data. In this study, we test the performance of FinDer in the Sichuan-Yunnan region (98.5°E–106.0°E, 22.0°N–34.0°N) of China for two datasets: the first consists of seismic broadband and strong-motion records of 58 earthquakes with $5.0 \leq M_S \leq 8.0$; the second comprises additional waveform simulations at sites where new stations will be deployed in the near future. We utilize observed waveforms to optimize the simulation approach to generate ground-motion time series. For both datasets the resulting FinDer line-source models agree well with the reported epicenters, focal mechanisms, and finite-source models, while they are computed faster compared to what traditional methods can achieve. Based on these outputs, we determine a theoretical relation that can predict for which magnitudes and station densities FinDer is expected to trigger, assuming that at least three neighboring stations must have recorded accelerations of 4.6 cm/s^2 or more. We find that FinDer likely triggers and sends out a report, if the average distance between the epicenter and the three closest stations, D_{epi}, is equal or smaller than $\log_{10}(M^a + b) + c$, where $a = 1.91$, $b = 5.93$, and $c = 2.34$ for $M = M_W \geq 4.8$, and $c = 2.49$ for $M = M_S \geq 5.0$, respectively. If the data used in this study had been available in real-time, 40–70% of sites experiencing seismic intensities of V-VIII (on both Chinese and MMI scales) and 20% experiencing IX-X could have been issued a warning 5–10 s before the *S*-wave arrives. Our offline tests provide a useful reference for the planned installation of FinDer in the nationwide EEW system of Chinese mainland.

Keywords: earthquake early warning, fault rupture, ground-motion prediction equation, Sichuan-Yunnan region, national system for fast report of intensities and earthquake early warning

INTRODUCTION

Earthquake early warning (EEW) systems quickly detect earthquakes (possibly while still evolving) and alert users (e.g. the public, automated response applications, situational awareness users) prior to the onset of strong ground shaking at a given location (Allen et al., 2009; Satriano et al., 2011; Allen and Melgar, 2019). In the last few decades, EEW systems have been used successfully and are generally regarded as a promising tool for earthquake risk reduction (Strauss and Allen, 2016).

Many countries around the world have operational EEW systems; among them the systems in Japan, Mexico and Taiwan are probably best known and advanced (Espinosa-Aranda et al., 1995; Nakamura and Saita, 2007; Wu et al., 2007). Other countries and regions, such as Romania, Turkey, South Korea, Israel and the West Coast of the United States, have installed EEW systems, and these systems have provided valuable warnings to the public and automated emergency systems of key infrastructures (Clinton et al., 2016; Sheen et al., 2017; Suárez et al., 2018; Kohler et al., 2020; Kurzon et al., 2020). Some regions (e.g. Italy, Chinese mainland, Switzerland, Chile, Nicaragua, Costa Rica and El Salvador) are currently testing EEW systems within their seismic monitoring networks (Clinton et al., 2016; Leyton et al., 2018; Massin et al., 2019; and see next section for details of Chinese mainland), while others are only at the stage of discussing the need and feasibility of developing EEW systems (Bird et al., 2008; Stankiewicz et al., 2015; Romeu Petit et al., 2016; Sokos et al., 2016; Zuccolo et al., 2016; Ogweno et al., 2019). Recently, crowdsourcing (Hammon and Hippner, 2012) has been applied as a promising new technique to EEW, allowing the general public to record seismic data/records with micro-electro-mechanical systems (MEMS) in smart devices and to receive earthquake alerts in real-time on a global or regional scale (Minson et al., 2015). Some well-known examples are the Earthquake Network (Finazzi, 2016), MyShake (Kong et al., 2016), Quake Catcher Network (Cochran et al., 2009), Home Seismometer (Horiuchi et al., 2009), and Google's EEW effort based on Android phones (Stogaitis et al., 2020).

EEW algorithms, such as the Virtual Seismologist (VS; Cua and Heaton, 2007), ElarmS (Chung et al., 2019) or OnSite (Wu and Kanamori, 2005), have demonstrated their usefulness for providing earthquake source parameters in near real-time. Although these algorithms are fast, they assume that seismic sources are a point in time and space, which is unsuitable for large magnitude earthquakes. Since ignoring the finiteness of earthquake ruptures, the point-source model fails to capture the true temporal-spatial variance of the radiation of high-frequency seismic energy in earthquakes with $M > 6$, and tends to saturate in earthquake magnitude estimation (Allen and Melgar, 2019). Furthermore, point-source model-based algorithms typically rely on early information from *P*-wave and/or rupture nucleation to predict the final size of the (evolving) fault rupture, even though earthquake rupture predictability remains controversial (Ide, 2019; Hutchison et al., 2020; Meier et al., 2020). Hence, a multi-dimensional characterization of the source model to represent the complexities of a large earthquake is necessary to improve EEW.

Several geodetic and seismic algorithms have been developed to estimate the extended size of fault ruptures in (near) real-time. For example, the G-larmS (Grapenthin et al., 2014a; 2014b), G-FAST (Crowell et al., 2016, 2018), BEFORES (Minson et al., 2014) and REGARD (Kawamoto et al., 2016, 2017) algorithms use high-rate GPS/GNSS (Global Positioning System/Global Navigation Satellite System) observations for real-time source inversion. Although usually providing an accurate characterization of seismic sources, these algorithms require dense network observations and tend to be computationally time-consuming. Moreover, GPS/GNSS-based algorithms are usually unable to provide earthquake alerts to sites that are close to the epicenter due to the sparsity of the existing monitoring networks (McGuire et al., 2021). A promising alternative is to adopt the seismic Finite-Fault Rupture Detector (FinDer) algorithm (Böse et al., 2012, 2015, 2018), which uses the spatial distribution of seismic high-frequency ground-motions to estimate the centroid, length (L) and strike (Θ) of an assumed line-source.

In this study, we explore the feasibility of operating FinDer in Chinese mainland, where a nationwide EEW projects are currently underway, including the installation of several thousands of low-cost MEMS sensors. We will begin this article with a review of Chinese EEW efforts. Then, using waveform playbacks of both real and simulated waveform data of recent seismicity, we will test FinDer for existing and planned stations, and discuss its performance with a view to possible future operation of FinDer in Chinese mainland.

DEVELOPMENT OF EEW IN CHINESE MAINLAND

In 1994, the first EEW system in Chinese mainland was deployed at the Daya Bay nuclear power plant; since then, Chinese mainland has been continuously developing and evolving EEW systems in order to improve their performance for earthquake risk mitigation (Li et al., 2004).

Top-Level Design

Around the turn of the 21st century, a series of scientific projects related to EEW and fast earthquake intensity reports, organized by the China Earthquake Administration (CEA), were launched (Li, 2014). Mainly due to constructions between 2001 and 2008, the density of broadband seismic and strong-motion networks in Chinese mainland has been greatly increased (**Figure 1A**), and all stations have been digitized (Zhou, 2006; Liu et al., 2008).

City/Infrastructure Scale

In 1994, a small earthquake alert system with 12 strong-motion stations was deployed on-site around Daya Bay nuclear power plant. This system issued a warning when a trigger threshold of 0.01 *g* was exceeded. Following this, similar alert systems were installed at more than 10 additional nuclear power plants. In 2001, PetroChina Dalian Branch developed an alert system for petrochemical enterprises. In 2007, an earthquake monitoring and alarm system was developed for the Hebei-Nanjing gas

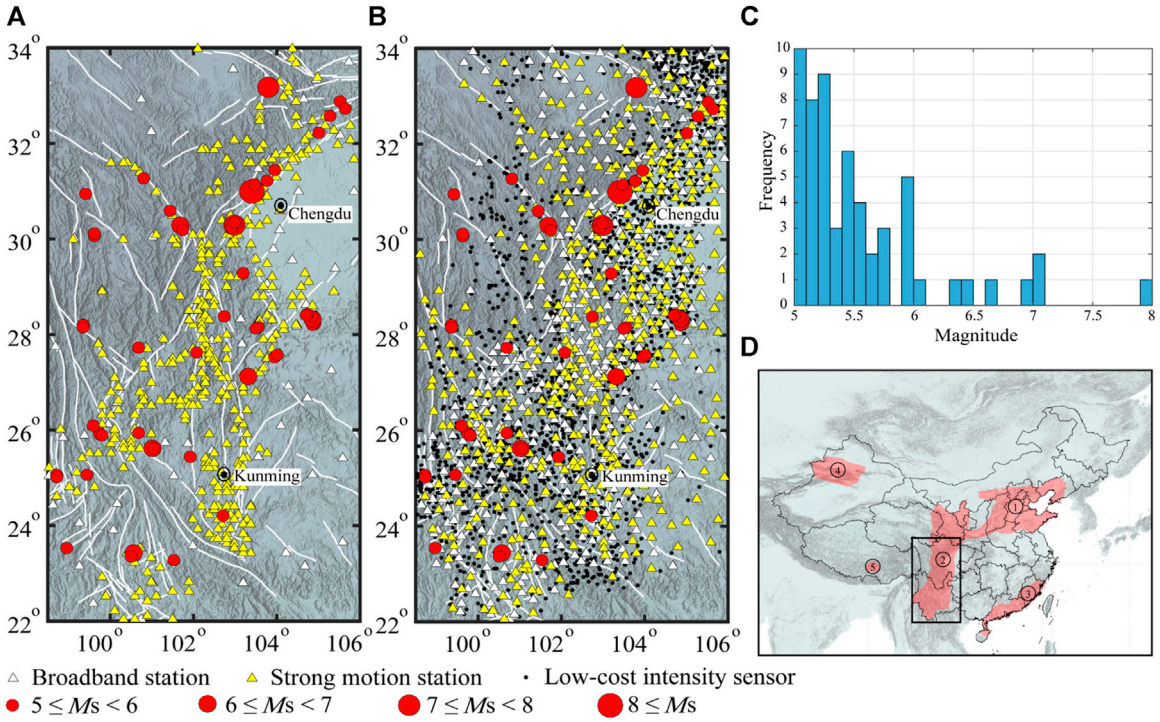

FIGURE 1 | (A) Existing (as of 2018) and **(B)** planned (as of 2022) stations, deployed or upgraded as part of the National System for Fast Report of Intensities and Earthquake Early Warning of Chinese mainland. Red dots show the epicenters (from China Earthquake Networks Center, CENC) of the 2008 M_S 8.0 Wenchuan and 57 5.0 ≤ M_S < 7.0 earthquakes studied in this paper. White lines show the fault locations. **(C)** Magnitude distribution of earthquakes shown in **(A)** and **(B)**. **(D)** The larger tectonic setting with the five key EEW regions: 1) north China, 2) central China north-south seismic belt, 3) southeast coast, 4) middle section of Tianshan Mountains of Xinjiang, and 5) Lhasa of Tibet.

pipeline. In the same year, as part of China's digital strong-motion network, a fast earthquake intensity report system was deployed in some Chinese cities, including Beijing, Tianjin, Lanzhou, Urumqi and Kunming (Zhou, 2006). For the Three Gorges water conservancy project, 15 seismic and 16 mobile stations were deployed to provide EEW and earthquake information service. In addition, the EEW system is functioning for more than 20 lines of high-speed railways such as the Beijing-Tianjin, the Beijing-Shanghai, the Chengdu-Chongqing, the Beijing-Shijiazhuang-Wuhan lines (Li, 2014).

Provincial Scale

To demonstrate the feasibility of EEW on provincial scale, China has implemented prototype test systems in three areas (Sichuan Earthquake Administration, 2015). In 2007, the Institute of Geophysics at CEA and the Department of Geosciences at National Taiwan University built an EEW prototype system for the Beijing Capital Region (Peng et al., 2011). This system was based on the Capital Circle Seismograph Network of China and included 94 broadband and 68 short-period stations, with an average interstation spacing of roughly 50 km. In 2014, six years after the Wenchuan M_S 8.0 earthquake, new system in the region was expanded to 130 broadband seismic and 80 strong-motion stations with an average interstation spacing of around 40 km for whole covered land, and around 15 km in urban area. The seismic network allows data to be transmitted to the data center in real-time. In March 2015, an earthquake fast report system was deployed in this region, which integrated additional data from 100 intensity sensors in the Tangshan region. The second provincial EEW demonstration system deployed in Fujian province was completed in September 2013 and consists of 128 stations with an average interstation spacing of around 30 km. The system accesses data from 16 stations of Taiwan in real-time and provides warning for the earthquakes in Taiwan (Zhang et al., 2016). The Lanzhou EEW demonstration system was completed in October 2014, and connected to 83 broadband seismic and 80 strong-motion stations from the provincial networks of Gansu, Qinghai and Ningxia. Additional EEW demonstration systems were built in the Sichuan-Yunnan region and the east part of Guangdong successively over the last years.

National Scale

In order to improve the capability of EEW, earthquake parameter and fast intensity reports, and earthquake seismological research on a nationwide scale, the National System for Fast Report of Intensities and Earthquake Early Warning project of Chinese mainland, led by the CEA, was launched and implemented in 2015 and 2018, respectively. A nationwide EEW system covering five key EEW zones (north China, central China north-south seismic belt, southeast coast, middle section of Tianshan Mountains of Xinjiang, and Lhasa of Tibet; **Figure 1D**) is

currently being built, with an average interstation spacing of around 10–15 km. It is expected that by 2022, close to around 2,000 broadband stations (equipped with three-component broadband or very broadband seismometers and all with accelerometers), around 3,200 strong-motion stations (equipped with three-component accelerometers), and around 10,200 low-cost intensity sensors (equipped with MEMS; Peng et al., 2017) will be deployed or upgraded throughout Chinese mainland. The EEW system will build on the Jopens seismic monitoring platform developed by CEA. Some areas (e.g. Sichuan-Yunnan and Beijing-Tianjin-Hebei regions) that have completed most of the station deployment have taken the lead in testing EEW algorithms (China Earthquake Administration, 2020; Peng et al., 2020). The system successfully provided early warning services for the 2018 Yongqing M_S 4.3 earthquake of Hebei, the 2019 Hualian M_S 6.7 earthquake of Taiwan, and 2019 M_S 6.0 earthquake of Sichuan. At present, the project is actively supporting and guiding social entities to participate (Song et al., 2021), e.g. the Institute of Care-life at Chengdu.

THE FINITE-FAULT RUPTURE DETECTOR

The Finite-Fault Rupture Detector (FinDer) is an efficient algorithm to compute a line-source model of an ongoing earthquake fault rupture from real-time high-frequency seismic data using template matching (Böse et al., 2012, 2015, 2018). The resulting model has four independent parameters that characterize the seismic source: length, strike, centroid, and rupture directivity. In recent years, FinDer has been adopted in various EEW systems, including the U.S. West Coast ShakeAlert warning system (Given et al., 2018; Chung et al., 2019; Kohler et al., 2020). FinDer is also undergoing real-time testing in Central America (Nicaragua, Costa Rica, and El Salvador), Chile, and Switzerland (Böse et al., 2018). Integration of FinDer into the nationwide EEW system of Chinese mainland is underway. Furthermore, Böse et al. (2021) recently applied FinDer to calculate line-source models for large (M > 6) global earthquakes using felt reports.

FinDer Algorithm

FinDer determines earthquake line-source models by matching the spatial distribution of the recorded high-frequency strong ground-motion (usually acceleration) amplitudes with theoretical template maps, which are computed for different line-source lengths and magnitudes. The strike of the fault rupture, Θ, is determined by rotating the templates around various trial angles and calculating the respective misfit with the spatial distribution of recorded PGA. Combined with the optimum spatial position and orientation, the template with the smallest misfit and highest correlation with the recorded amplitudes is found from a combined grid-search and divide-and-conquer approach (Böse et al., 2018). FinDer is computationally highly efficient and allows updating outputs every second until peak shaking across the seismic network is reached.

Ground-Motion Prediction Equations

Ground-motion prediction equations (GMPEs) are an essential element of FinDer. They are used to generate templates that FinDer matches with spatial distributions of observed peak ground acceleration (PGA) amplitudes. In most installations, FinDer adopts the GMPEs developed by Cua and Heaton (2009) that were derived from strong-motion records in California (M 2–M 7.3) and the Next Generation Attenuation (NGA) strong-motion dataset (M 2–M 8). Real-time and offline tests of FinDer in the U.S. West Coast, Switzerland, Italy, Japan, and China (Böse et al., 2012, 2015, 2018, 2021; Li et al., 2020a) have confirmed that the templates are globally applicable to crustal earthquakes. In previous work (Li et al., 2020a), we compared the GMPE of Cua and Heaton (2009) with the regional relationship used in the fifth-generation hazard zoning map in southwestern China, as well as with PGA values, that were observed during the 2008 M_S 8.0 Wenchuan, 2013 M_S 7.0 Lushan and 2017 M_S 7.0 Jiuzhaigou earthquakes. We found that the GMPEs and PGA values are in good agreement, so we use the same templates based on Cua and Heaton (2009) here in this study.

FinDer Magnitude

For small earthquakes (M < 5.5) and at the early stage of rupture in larger events, the FinDer magnitude, M_{FD}, is determined from the regression of P- and S-wave acceleration amplitudes using relations of Cua and Heaton (2009). For larger events ($M \geq 5.5$) M_{FD} is computed from empirical rupture length-magnitude relationships (typically Wells and Coppersmith, 1994) using the length of the FinDer determined line-source. FinDer line-source models were introduced to characterize the temporal-spatial distribution of high-frequency ground-motions (PGA) rather than to provide an accurate source characterization (Li et al., 2020a). These high-frequency ground-motions are of primary concern in practice and therefore are critically important to real-time seismology. Because of its high-frequency physical background, M_{FD} is more consistent with the energy magnitude (Picozzi et al., 2017) rather than the long-period M_W. In general, M_{FD} can be thought of as a scaling factor that quantifies the level and temporal-spatial distribution of high-frequency ground-motions (Böse et al., 2018; Li et al., 2020b). M_{FD} does not necessarily show great agreement with other magnitude scales, especially with those that are sensitive to longer periods such as M_W. Compared to the magnitude scales that are based on seismic displacement amplitudes, M_{FD} has the strong advantage that it does not saturate in large earthquakes. This is because FinDer does not use absolute amplitudes, but spatial patterns of ground-motions in order to derive source dimensions which scale with magnitude.

STUDY REGION AND AVAILABLE DATASETS

The Sichuan-Yunnan Region

We select the Chinese Sichuan and Yunnan provinces (98.5°E–106.0°E, 22.0°N–34.0°N) as our study area (**Figure 1**). This region is exposed to a very high earthquake risk and has been hit by a number of large and damaging earthquakes in the past, including the 1833 Songming M 8 earthquake with about 6,700

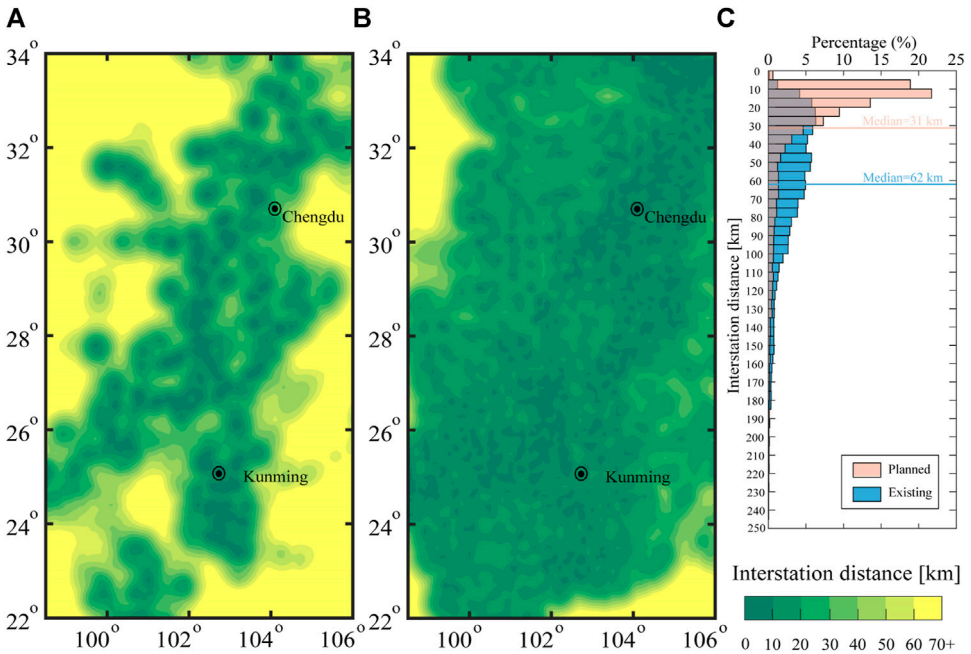

FIGURE 2 | Maps showing the interstation distances for the **(A)** existing, and **(B)** planned network shown in **Figure 1**. Areas colored in dark green have the densest station coverage. For any given site (computed on a grid of 0.1 × 0.1 resolution), the interstation distance is calculated as the average distance to the three closest seismic stations. In order to compare with networks in Japan, California and Beijing Capital Region, we apply the same color scale range as in Kuyuk and Allen (2013) and Li et al. (2016). The histogram in **(C)** shows the variability in the interstation distances across the Sichuan-Yunnan region. The interstation distance is currently around 60 km for half of the study region and will be reduced to around 30 km for three quarters of the whole region by 2022.

fatalities, the 1879 Wudu M 8 earthquake with about 22,000 fatalities, and the 2008 Wenchuan M_S 8.0 earthquake with about 90,000 fatalities (Department of Earthquake Disaster Prevention of the State Seismological Bureau, 1995; Department of Earthquake Disaster Prevention of the China Earthquake administration, 1999). Since January 1, 2009, roughly 530,000 earthquakes have been recorded in this region and their waveforms have been archived by the China Strong Motion Networks Center (CSMNC) and the China Earthquake Networks Center (CENC; Zheng et al., 2010) at CEA.

Before 2008, 105 broadband seismic and 383 strong-motion stations were deployed in the study region (**Figure 1A**). These stations had interstation distances of around 30 km along the line from Chengdu to Kunming and of 15–20 km in some key areas (**Figure 2A**). The median interstation distance in the current networks is around 60 km; in 30% of the study area the interstation distance is less than 35 km (**Figure 2C**). We computed these values from the average distance of a given site to its closest three broadband and/or strong-motion stations (Kuyuk and Allen, 2013) using a mesh of 0.1 × 0.1 resolution.

By 2022, 434 broadband seismic stations (equipped with three-component seismometers and accelerometers), 488 strong-motion stations (equipped with three-component accelerometers) and 1,609 low-cost intensity sensors (equipped with MEMS) will be added or upgraded throughout the study region through the construction of the National System for Fast Report of Intensities and Earthquake Early Warning (**Figure 1B**). With these installations, three quarters of Sichuan and Yunnan region is expected to reach a mean interstation distance of about 30 km; 70 and 40% of the area will have interstation distances of less than 30 and 15 km, respectively. In large parts of Chengdu and Kunming urban areas, the interstation distance will be even 10–15 km only (**Figure 2C**).

Waveform Data

In this study, we use seismic waveform records of the 2008 Wenchuan M_S 8.0 earthquake and of 57 earthquakes with 5.0 ≤ M_S ≤ 7.0 and depth of H ≤ 35 km that occurred in the study region between January 1, 2009 and August 4, 2019 (**Figure 1** and **Table 1**). Based on their moment magnitude, M_W, we divide these 58 earthquakes into two groups: for earthquakes in the first group (with M_W < 6) we use both broadband and strong-motion records; for the second group, consisting of six earthquakes with M_W ≥ 6, we use strong-motion records only. Throughout this paper, we will treat the earthquakes in the first group as point-source events, and those in the second group as finite-source events (with rupture lengths of 10–300 km).

Observed Waveforms

For each of the earthquakes in our dataset, we exclude the recordings of obviously malfunctioning broadband/strong-motion sensors and those with PGA smaller than 3 cm/s^2. For baseline correction we subtract from each trace the mean noise amplitude taken over a time window of several seconds before the P-wave onset.

TABLE 1 | Source parameters of the 2008 Wenchuan M_S 8.0 and 57 $M_S \geq 5.0$ earthquakes (2009-01-01–2019-08-04) in the study region (98.5°E–106.0°E, 22.0°N–34.0°N) from China Earthquake Networks Center (CENC) and the Global Centroid-Moment-Tensor (GCMT).

No	Yyyy-mm-dd hh:mm:ss[1]	Lat[1] [°]	Lon[1] [°]	H[1] [km]	M_S[1]/M_W[2]	Strike1/dip1/rake1[2] Strike2/dip2/rake2 [°]
1	2008-05-12 14:28:04	31.01	103.42	16	8.0/7.9	231/35/138 357/68/63
2	2009-06-30 02:03:51	31.46	103.96	24	5.5/5.3	212/29/54 71/67/108
3	2009-06-30 15:22:20	31.46	103.98	24	5.0/4.9	206/41/83 34/49/96
4	2009-07-09 19:19:14	25.60	101.03	6	6.3/5.7	204/84/-3 294/87/-174
5	2009-07-10 17:02:01	25.60	101.05	10	5.4/5.2	21/83/4 291/86/173
6	2009-09-19 16:54:13	32.90	105.56	8	5.2/4.9	350/40/82 180/50/96
7	2009-11-02 05:07:16	25.94	100.69	10	5.0/4.9	286/84/180 16/90/6
8	2009-11-28 00:04:04	31.23	103.80	15	5.0/4.9	43/44/80 236/47/99
9	2010-02-25 12:56:51	25.42	101.94	20	5.2/5.2	14/76/-9 106/81/-166
10	2010-04-28 04:22:27	30.60	101.45	8	5.0/5.1	236/79/176 327/86/11
11	2010-05-25 14:11:53	31.17	103.49	20	5.0/5.0	14/44/59 233/53/116
12	2011-04-10 17:02:42	31.28	100.80	10	5.4/5.4	313/75/-7 45/83/-165
13	2011-06-20 18:16:49	25.05	98.69	10	5.3/5.0	271/44/82 103/46/98
14	2011-08-09 19:50:17	25.00	98.70	11	5.2/5.1	251/86/1 161/89/176
15	2011-11-01 05:58:15	32.60	105.30	6	5.2/5.0	232/44/70 79/50/108
16	2012-06-24 15:59:33	27.71	100.69	11	5.7/5.6	313/46/-126 179/55/-59
17	2012-09-07 11:19:41	27.51	103.97	14	5.7/5.6	350/51/35 236/63/136
18	2012-09-07 12:16:30	27.56	104.03	14	5.6/5.3	234/58/155 338/69/34
19	2013-01-18 20:42:50	30.95	99.40	15	5.5/5.6	208/86/179 298/89/4
20	2013-03-03 13:41:15	25.93	99.72	9	5.5/5.4	337/42/-113 187/52/-71
21	2013-04-17 09:45:55	25.90	99.75	10	5.1/5.3	332/52/-131 206/54/-50
22	2013-04-20 08:02:47	30.30	102.99	17	7.0/6.6	212/42/100 19/49/81
23	2013-04-20 08:07:30	30.32	102.92	10	5.0/-	–/–/-/ –/–/-
24	2013-04-20 11:34:16	30.24	102.94	15	5.4/5.4	215/45/100 21/46/80
25	2013-04-21 04:53:44	30.36	103.05	27	5.0/4.8	177/42/74 17/50/103
26	2013-04-21 17:05:23	30.34	103.00	17	5.4/5.2	35/45/86 221/45/94
27	2013-08-28 04:44:52	28.20	99.33	9	5.2/5.2	66/50/-125 294/51/-55
28	2013-08-31 08:04:16	28.15	99.35	10	5.9/5.7	97/42/-95 284/48/-85
29	2014-04-05 06:40:33	28.14	103.57	13	5.1/4.9	360/45/45 235/60/125
30	2014-08-03 16:30:12	27.11	103.33	10	6.6/6.2	71/81/-175 340/86/-9
31	2014-08-17 06:07:59	28.12	103.51	7	5.2/5.1	317/78/5 226/86/168
32	2014-10-01	28.38	102.74	10	5.2/5.2	254/66/169

(Continued on following page)

TABLE 1 | (*Continued*) Source parameters of the 2008 Wenchuan M_S 8.0 and 57$M_S \geq 5.0$ earthquakes (2009-01-01–2019-08-04) in the study region (98.5°E–106.0°E, 22.0°N–34.0°N) from China Earthquake Networks Center (CENC) and the Global Centroid-Moment-Tensor (GCMT).

	09:23:29					349/80/25
33	2014-10-07	23.40	100.55	10	6.9/6.1	329/81/174
	21:49:39					60/84/9
34	2014-11-22	30.29	101.68	20	6.4/6.1	143/85/-1
	16:55:28					233/89/-175
35	2014-11-25	30.20	101.75	16	5.9/5.7	238/89/179
	23:19:09					328/89/1
36	2014-12-06	23.32	100.49	10	5.9/5.6	79/72/9
	02:43:45					346/81/162
37	2014-12-06	23.33	100.50	10	5.9/5.5	339/71/173
	18:20:00					71/84/19
38	2015-01-14	29.30	103.20	20	5.0/4.9	158/44/89
	13:21:40					340/46/91
39	2015-03-01	23.50	98.94	11	5.5/5.3	69/66/9
	18:24:39					336/82/156
40	2015-10-30	25.04	99.44	10	5.0/4.9	177/45/-118
	19:26:39					35/51/-64
41	2016-05-18	26.08	99.58	17	5.1/5.0	293/86/177
	00:48:48					23/87/4
42	2016-09-23	30.08	99.60	19	5.2/5.2	281/47/-55
	00:47:13					56/53/-122
43	2016-09-23	30.11	99.61	16	5.2/5.2	288/47/-61
	01:23:16					69/51/-117
44	2017-03-27	25.89	99.80	12	5.1/5.1	318/85/179
	07:55:01					48/89/5
45	2017-08-08	33.20	103.82	10	7.0/6.5	151/79/-8
	21:19:48					243/82/-168
46	2017-09-30	32.25	105.05	10	5.4/5.1	21/54/42
	14:14:37					263/57/135
47	2018-08-13	24.18	102.72	14	5.1/5.1	201/61/3
	01:44:24					110/88/151
48	2018-08-14	24.19	102.73	6	5.0/4.9	206/77/9
	03:50:36					113/81/167
49	2018-09-08	23.26	101.53	17	5.9/5.7	126/80/-178
	10:31:29					36/88/-10
50	2018-09-12	32.75	105.67	11	5.3/5.1	75/83/-176
	19:06:34					344/86/-7
51	2018-10-31	27.62	102.09	20	5.1/5.0	183/84/2
	16:29:56					92/88/174
52	2018-12-16	28.24	104.95	12	5.7/5.3	79/81/-174
	12:46:07					348/84/-9
53	2019-01-03	28.19	104.88	15	5.1/5.0	349/41/43
	08:48:08					223/63/122
54	2019-06-17	28.34	104.90	16	6.0/5.7	184/40/123
	22:55:43					323/57/65
55	2019-06-17	28.43	104.77	16	5.1/5.1	178/43/115
	23:36:01					326/52/69
56	2019-06-18	28.37	104.89	17	5.3/4.8	155/33/116
	07:34:33					305/61/74
57	2019-06-22	28.43	104.77	10	5.4/5.2	343/45/71
	22:29:56					190/48/108
58	2019-07-04	28.41	104.74	8	5.6/5.5	11/39/75
	10:17:58					210/52/102

[1]*Data sources: CENC;*
[2]*Data sources: GCMT.*

The broadband seismic records provided by the Data Management Centre of China National Seismic Network at Institute of Geophysics of CEA start from the origin time (OT) of the earthquakes, so there is no need for time corrections. We only correct for the sensor gain and differentiate the time series to obtain acceleration. A large number of high-gain broadband seismic waveforms recorded during the large earthquakes, however, are clipped. Therefore, we only use broadband data for earthquakes in the first group with $M_W < 6$. In real-time operation, FinDer uses both strong-motion and broadband station data, but discards sensors with clipped amplitudes. In smaller and distant earthquakes,

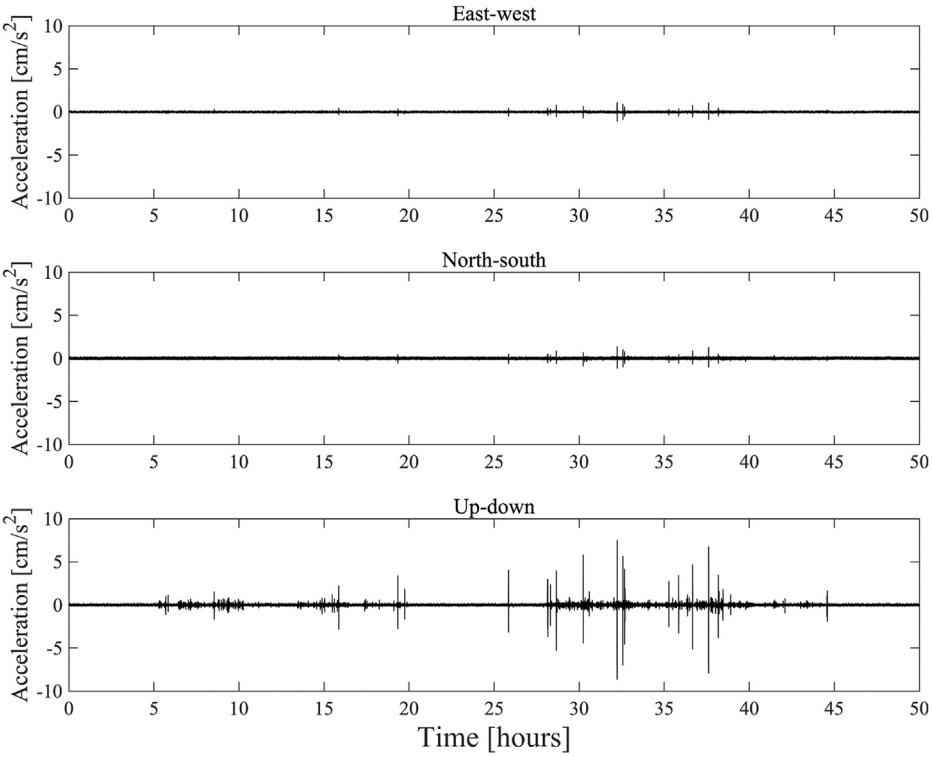

FIGURE 3 | Three-component noise time series recorded at a low-cost intensity sensor (23.67°N, 116.64°E). The records start on February 19, 2019, and are 50 h long. The noise is largest on the vertical component, likely due to human activities. See **Supplementary Figure S1** for frequency domain plot.

(unclipped) broadband records can serve as an important supplement to strong-motion records if station density is sparse. The broadband seismic three-component traces for each event in the first group are provided in the **Supplementary Material**.

The strong-motion records are obtained from CSMNC. These records start at a certain time (usually 20 s) before the *P*-wave arrival. To recover the absolute time, we take the source parameters in **Table 1** and align the theoretical *P*-wave arrival (assuming V_P = 6.0 km/s) with the *P*-arrival in each record. FinDer uses the temporal-spatial distribution of PGA, including the information that certain stations have not yet recorded strong shaking at a given time. Therefore, we fill pre-event data gaps with random noise amplitudes that we determine from the recorded noise before the *P*-wave. As this is only for testing FinDer, we are not concerned about the details of this noise, but are primarily interested in simulating realistic amplitudes and a representative temporal evolution of PGA. The simulated noise before *P*-wave arrivals does not impact the FinDer results. All strong-motion three-component traces for the studied earthquakes are shown in the **Supplementary Material**.

Seismic waveform data recorded by low-cost intensity sensors have not yet been systematically archived. As described in the next section, we simulate these records from an empirical waveform envelope approach. In order to make these simulations as realistic as possible, we add observed background noise. The typical noise level of a low-cost intensity sensor is shown in **Figure 3** in the time domain and in **Supplementary Figure 1** in the frequency domain. The waveforms were originally in velocity. To convert them to acceleration we applied the same differentiation method as used for the broadband records. The maximum pulse acceleration of the horizontal (north-south and east-west) and the vertical components in **Figure 3** is ±1 cm/s^2 and ±8 cm/s^2, respectively. The background noise level for all three-component traces is ±0.5 cm/s^2. The background noise level is obviously higher than that recorded by broadband seismic (usually about ±0.01 cm/s^2) and strong-motion (usually about ±0.05 cm/s^2) stations.

Simulated Waveforms

To simulate the acceleration time series and the temporal evolution of PGA at sites where broadband, strong-motion and low-cost intensity sensor stations are expected to be deployed in the future (**Figure 1B**), we compute waveform envelopes developed by Cua and Heaton (2009) for the first group of earthquakes (M_W < 6), and combine stacked waveform envelopes (Yamada and Heaton, 2008) with stochastic simulations (Böse et al., 2012) for the second group (M_W ≥ 6). For the second group, the fault rupture is divided into a number of smaller sub-faults, each radiating *P*- and *S*-waves once the rupture front arrives. The radiated waves from each sub-fault are computed from a stochastic time series assuming a simple Brune

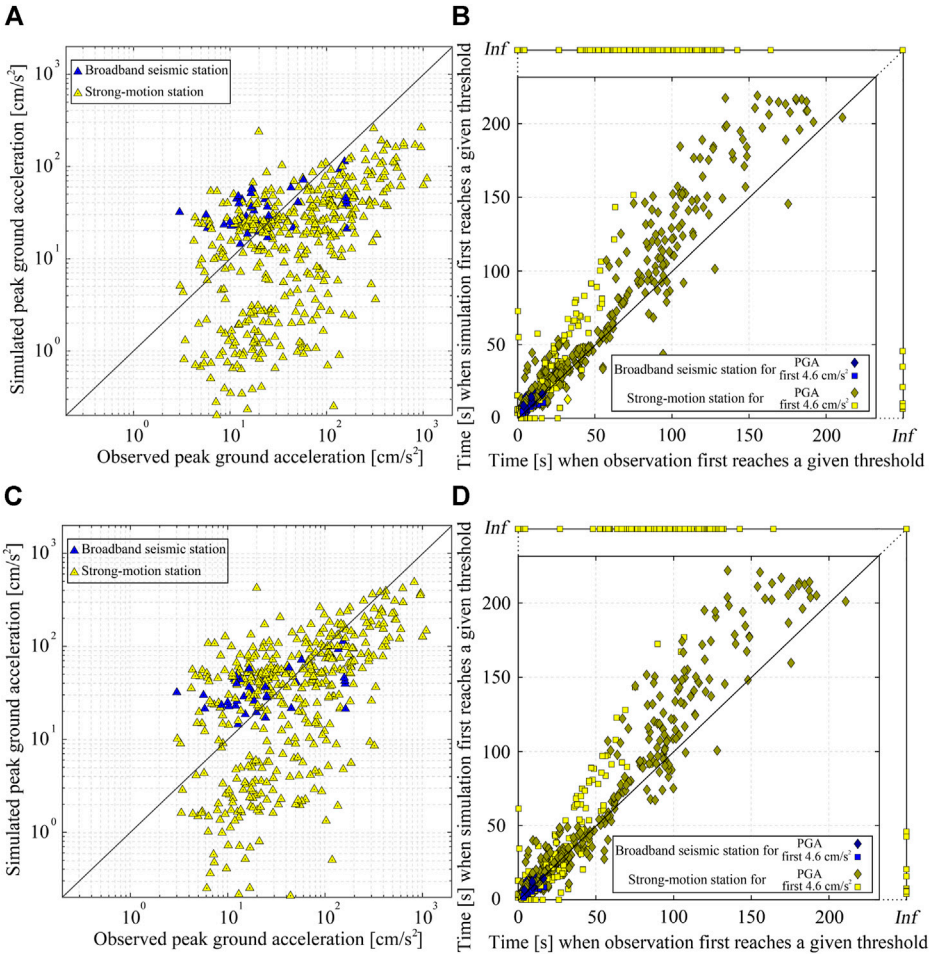

FIGURE 4 | Comparison of observed and simulated waveforms for the 58 studied earthquakes in terms of **(A)** peak ground acceleration (PGA) amplitudes and, **(B)** the time when they first reach PGA and 4.6 cm/s^2 (which we will later use as a trigger threshold for FinDer), respectively, before correction. Inf means that the three-component records of the corresponding station never reach this threshold. **(C)** and **(D)** show the same comparison after amplitude and time correction.

source model (Brune, 1970), random phase, and a characteristic waveform envelope (Cua and Heaton, 2009). Based on the reference line-source model in **Supplementary Table 1** (which is derived from the 1 day-long aftershock distribution), we model the Wenchuan earthquake with 25 sub-faults of 10 km length (around *M* 6); for the other five earthquakes we use sub-fault of 5 km length (around *M* 5.5). We assume a constant rupture speed of 2.8 km/s and use the crustal velocity model of Wang et al. (2003) (**Supplementary Table 2**) for the Sichuan-Yunnan region to model the onsets of the *P*- and *S*-wave envelopes.

In order to make our simulated waveforms as realistic as possible (in terms of both the envelope shape and peak amplitudes), we compare them to the observed broadband seismic and strong-motion data at the same station (see Supplementary Material) and conduct the following corrections: first, we use the observed broadband records (that have reliable time measurements) to calibrate the phase arrivals in the simulations. Second, we use both strong-motion and (unclipped) broadband records to calibrate peak amplitudes (PGA).

Figure 4 shows the peak values (PGA) and temporal evolution of amplitudes for both the observed and simulated series at each station before and after the calibration. This figure compares the times of when the series reach PGA (diamonds) and first reach 4.6 cm/s^2 (rectangles), respectively. We select 4.6 cm/s^2, because this is the FinDer trigger threshold that we will use later (see *FinDer Thresholds*). Results for other thresholds are shown in **Supplementary Figure 2**. We determine the following corrections: 1) using the *P*-wave arrivals of observed broadband records as benchmarks for our calibration, we move the phase arrivals in the simulations forward by 2 s (that is the onsets of the original simulations tend to be 2 s late); we apply the same time correction also to the simulated data at strong-motion stations, and 2) using the peak amplitudes of the observed strong-motion and broadband records as a reference, we amplify the amplitudes in the synthetics by a factor of 2 for the

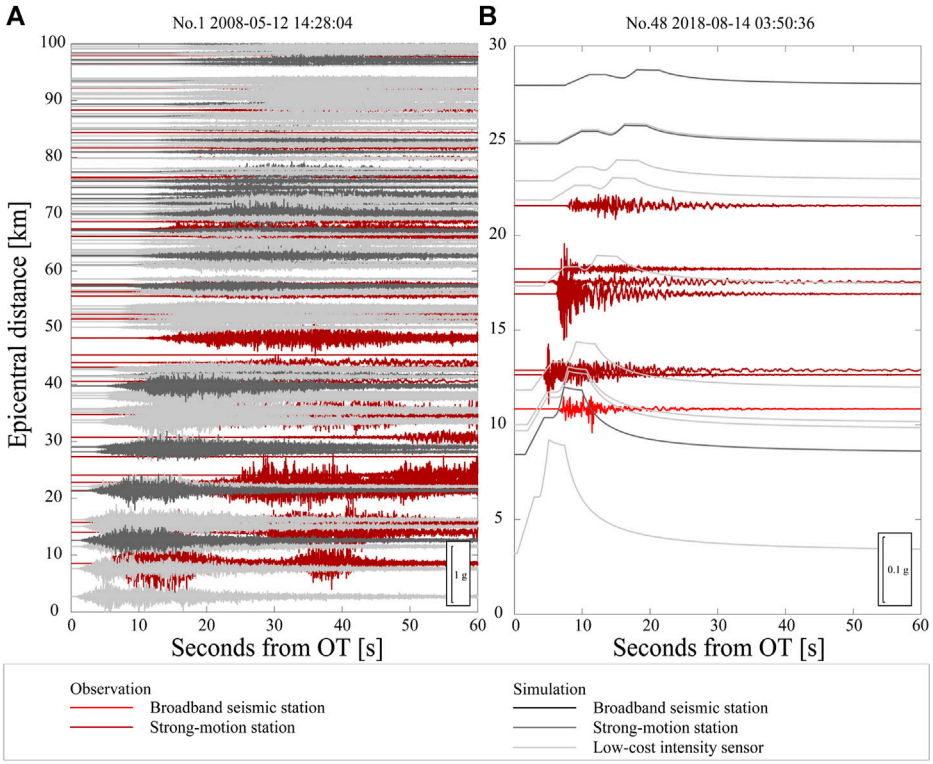

FIGURE 5 | Observed and simulated waveforms (vertical component) for the **(A)** 2008 Wenchuan M_W 7.9 earthquake and **(B)** a smaller M_W 4.9 earthquake, corresponding to events no.1 and 48 in **Table 1**. The Wenchuan earthquake is modelled from multiple stacked envelopes and a stochastic time series; the smaller event from a single waveform envelope. See main text for further details.

strong-motion stations; amplitude corrections for simulations of broadband records are not required.

Adopting these corrections, we simulate the time series at sites where new stations are expected to be deployed in the future (**Figure 1B**). We add Gaussian white noise with power spectral density (PSD) of $-120\,cm^2/(s^4{\cdot}Hz)$ and $-100\,cm^2/(s^4{\cdot}Hz)$ to broadband seismic and strong-motion stations, respectively. Additionally, we use a series of random time windows to intercept the observed MEMS data in **Figure 3** and add them as background noise to the simulated data in low-cost intensity sensors. In this process, we do not remove the large background ground-motion spikes, in order to make our simulations as realistic as possible. As an example, **Figure 5** shows the observed and simulated vertical envelopes/waveforms for two events with $M_W \geq 6$ and $M_W < 6$, respectively. The simulated envelopes/waveforms for the other events are shown in the Supplementary Material.

RESULTS

With the processing described above, we obtain two datasets: dataset 1 contains the observed data recorded at the existing stations (**Figure 1A**); dataset 2 contains both the data from dataset 1 plus the simulations at future stations (**Figure 1B**). In this section, we use these two datasets to simulate and analyze the off-line performance of FinDer in Chinese mainland. In order to mimic the temporal evolution of the FinDer estimated line-source models, we determine in this retrospective study the peak absolute ground-motion amplitudes (taken over all three waveform/envelope components) in time windows of 1 s and feed the logarithmic value of these amplitudes into FinDer (Böse et al., 2018). However, before running the waveform playbacks, we first need to configure the FinDer trigger thresholds, which depend on station density.

FinDer Trigger Thresholds

As described in Böse et al. (2018), FinDer uses a cascade of increasing PGA thresholds for its binary template matching. The smallest PGA threshold (and the minimum number of stations at which this threshold needs to be exceeded) controls the triggering of the algorithm. Typically, these parameters are set as 2 cm/s^2 and 3, respectively (Böse et al., 2018). However, it is necessary to tune these values in order to account for the respective station density and noise characteristics of the network in which FinDer is applied. In this study, we use the 2008 Wenchuan earthquake to define the trigger parameters.

We are testing in **Figure 6** four PGA trigger thresholds for the Wenchuan earthquake (2.0, 4.6, 10.5, and 23.2 [cm/s^2]), corresponding to the average peak acceleration caused by an earthquake of M = 2.5, 3.0, 3.5, and 4.0 at 5 km distance will produce (Cua and Heaton, 2009). In parallel, we vary the

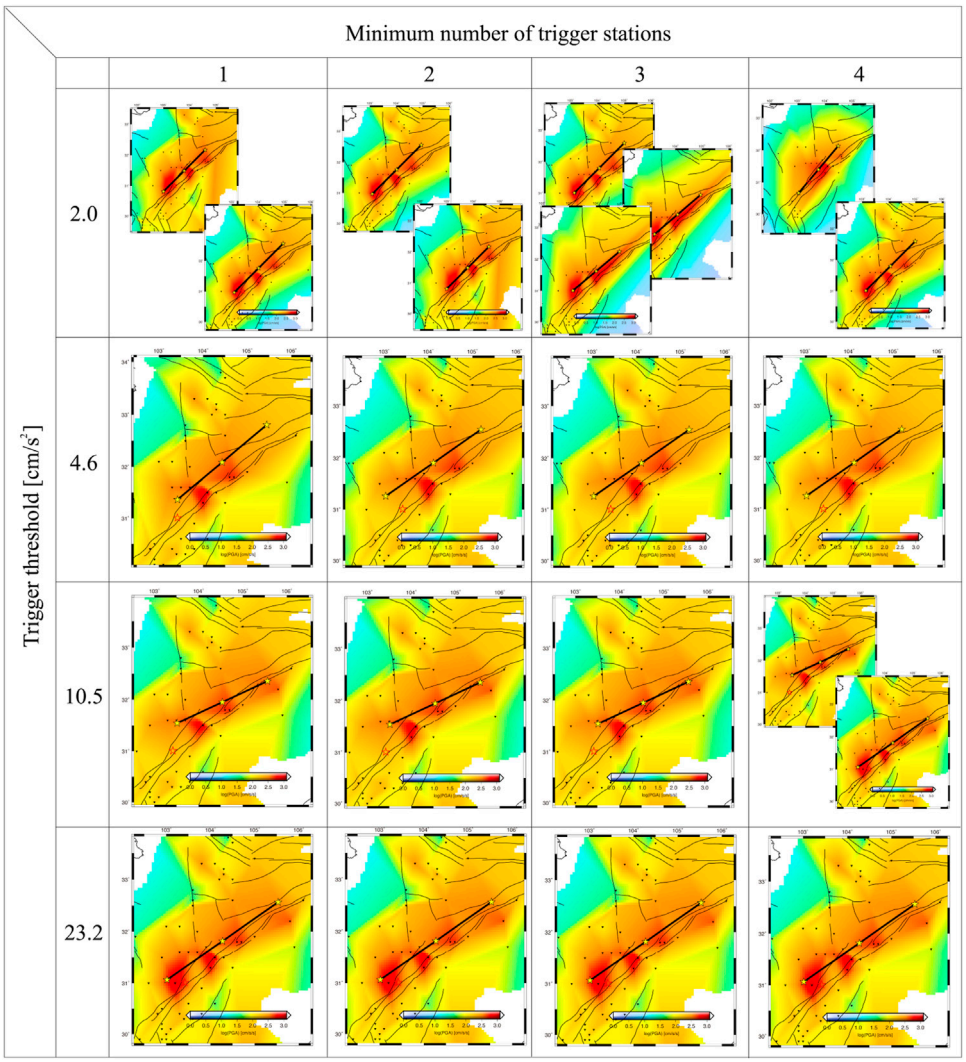

FIGURE 6 | Testing FinDer trigger parameters for different PGA thresholds (top to bottom: 2.0, 4.6, 10.5, and 23.2 cm/s^2) and minimum numbers of stations (left to right: 1–4), at which this threshold needs to be exceeded, using the 2008 M_S 8.0 Wenchuan earthquake. The maps show the final FinDer line-source models (black lines) for the respective trigger configuration. In general, the trigger parameters depend on the density and noise conditions of the network in which FinDer is applied. For some configurations, e.g. for a trigger threshold of 2 cm/s^2, FinDer creates multiple solutions (split events). As a compromise between accuracy and timeliness of the line-source models, we chose in this study a trigger threshold of 4.6 cm/s^2 and a minimum number of three stations.

minimum number of triggered stations from 1 to 4. Details are given in **Supplementary Table 3**. For some configurations, e.g. for a trigger threshold of 2 cm/s^2, FinDer creates multiple solutions (split events), which is not desired.

As a compromise between the accuracy and timeliness (the lower the threshold and the fewer stations are required, and the faster the first FinDer model is calculated) we chose for this study a trigger threshold of 4.6 cm/s^2 and a minimum number of three stations at which this threshold needs to be exceeded. With this setting, FinDer triggers 12 s after the OT of the Wenchuan earthquake (neglecting data latencies). The final FinDer line-source model is estimated as L = 249 km long (corresponding M_{FD} 7.9) and with the strike of 55°. These values are in good agreement with the results of field surveys following the Wenchuan earthquake that identified two separate parallel surface ruptures of L = 240 km and L = 90 km at a strike of N45°E (Xu et al., 2008). The FinDer line-source model characterizes the entire fault rupture including those segments with no surface exposure. Compared with the results of Li et al. (2020a), who tested FinDer with a larger trigger threshold (20 cm/s^2), the length of the line-source model is underestimated by about 50 km (corresponding to 0.1 magnitude units). This difference is caused by sparse station density around the Wenchuan earthquake as discussed in Li et al. (2020b).

To determine the FinDer trigger parameters for this study (**Figure 6**), we used the Wenchuan records in Dataset 1, which contains only observed data, i.e. no simulations at future stations. In

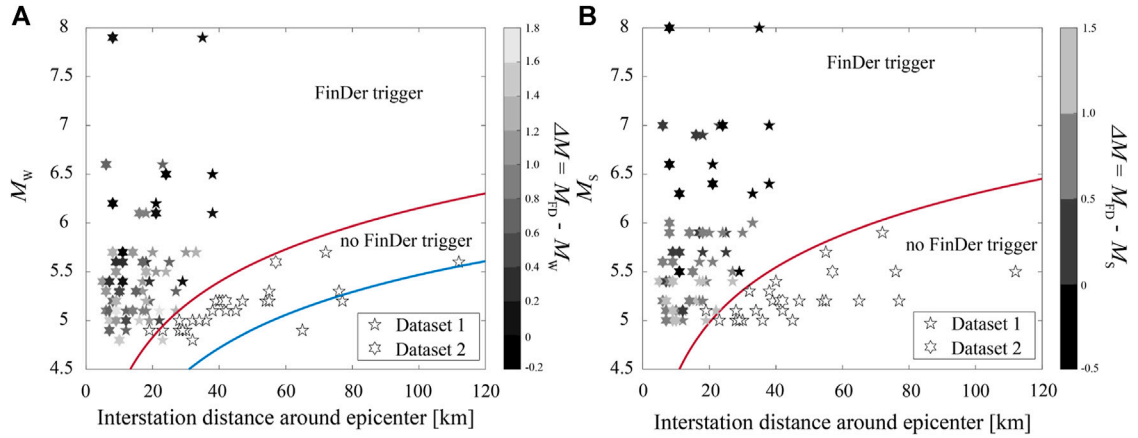

FIGURE 7 | Testing FinDer trigger settings (4.6 cm/s^2 at neighboring three stations) for all 58 earthquakes as a function of interstation distance, D_{epi}, and **(A)** moment magnitude, M_W (here of GCMT) and **(B)** surface-wave magnitude, M_S (here of CENC), respectively. D_{epi} is defined as the average distance between the epicenter to the three closest stations. The blue line shows the GMPE of Cua and Heaton (2009) for PGA = 4.6 cm/s^2. The two red lines illustrate the boundary condition: FinDer is expected to trigger, if $D_{epi} \leq \log_{10}(M^a + b)$+c, where $a = 1.91$, $b = 5.93$, and $c = 2.34$ for $M = M_W \geq 4.8$, and $c = 2.49$ for $M = M_S \geq 5.0$, respectively. The datasets used here, however, cannot fully constrain these relationships, and our boundary conditions provide a rough estimate only.

general, we expect that the trigger threshold can be chosen to be lower, the denser the network. The choice of the threshold, however, should be discussed in the context of the whole system: higher thresholds come at the cost of the system being triggered later, which means less available warning time. In practice, one can only trade-off the threshold (i.e. the system trigger time) and the accuracy. There is currently no strict empirical relationship between threshold and station density. For a better comparison of the performance of FinDer in a sparse and dense sensor network, we will adopt for this study the same trigger parameters for both datasets.

Relationship Between FinDer Trigger Thresholds and Station Density

In this section, we investigate the relationship between the FinDer trigger thresholds and station density. Using the trigger configuration optimized for the Wenchuan earthquake (4.6 cm/s^2 at three or more stations) we plot in **Figure 7** all earthquakes that trigger FinDer and those that do not. A first-order function to separate triggered and non-triggered events can be determined from a representative GMPE. This is illustrated by the blue line in **Figure 7A**, which is determined by transforming the GMPE of Cua and Heaton (2009) into an explicit function of the epicentral distance, R_{epi}, and M_W, $R_{epi} = \log_{10}(M^a + b) + c$. For our trigger threshold of 4.6 cm/s^2 and $0 \leq R_{epi} \leq 120$ km, we find $a = 1.91$, $b = 5.93$, and $c = 1.64$. As shown in **Figure 7A** (blue line), this relation, however, does not provide a satisfying boundary between triggered and non-triggered events. This is expected, because our data is plotted as of function of D_{epi}, that is the average distance between the epicenter to the closest three broadband seismic and/or strong-motion stations, and not of R_{epi}. Keeping the same functional form and coefficients a and b, we find that FinDer has a high probability to trigger, if $D_{epi} \leq \log_{10}(M^a + b)+c$, where $a = 1.91$, $b = 5.93$, and $c = 2.34$ for $M = M_W \geq 4.8$, and $c = 2.49$ for $M = M_S \geq 5.0$, respectively (red lines in **Figures 7A,B**). Note, however, that these functions provide a first-order approximation only, because there is in general considerable variability in the seismic ground-motions and the two datasets (observed data *v.s.* observed + simulated data) cannot fully constrain these relations as we will discuss later.

When calculating D_{epi} in **Figure 7**, we also included stations that did not work properly. This means that our results consider the possible failure of stations. This likely explains the two data outliers in **Figure 7**: a M_W 4.8 for which FinDer triggers even though station density is sparse (**Figure 7A**), and a M_S 5.1 event that FinDer misses (**Figure 7B**). Of course, in general there is also a significant level of variability in the radiation of high-frequency motions.

Based on the results in **Figure 7**, we can roughly determine a magnitude completeness, M_{FDc}, which defines the lowest magnitude at which FinDer is likely to trigger, given a certain interstation distance, D_{epi}. For one-third of the Sichuan-Yunnan region, where the current interstation distance is around 30 km, the smallest detectable events are $M_{FDc} \approx M_S$ 5.3. With the planned network densification with interstation distances of around 20 km in half of Sichuan-Yunnan after 2020, we expect $M_{FDc} \approx M_S$ 5.0 and $M_{FDc} \approx M_S$ 4.4 in some urban areas.

Playback Results

Figures 8–11 and **Supplementary Table 4** illustrate and summarize the FinDer playback results for all 58 earthquakes. Additional information is given in the Supplementary Material. **Figure 8A** shows the magnitude difference between the FinDer estimated final magnitude, M_{FD}, and the reported M_W from GCMT and M_S from CENC, respectively. The average difference is 0.73 for M_W and 0.53 for M_S in dataset 1, and 0.64 for M_W and 0.47 for M_S in dataset 2. Overall, M_{FD} tends to be more consistent with M_S, which is in line with the high-frequency physical background of M_{FD} as discussed in *FinDer Magnitude*. The comparison of the two datasets suggests that the future

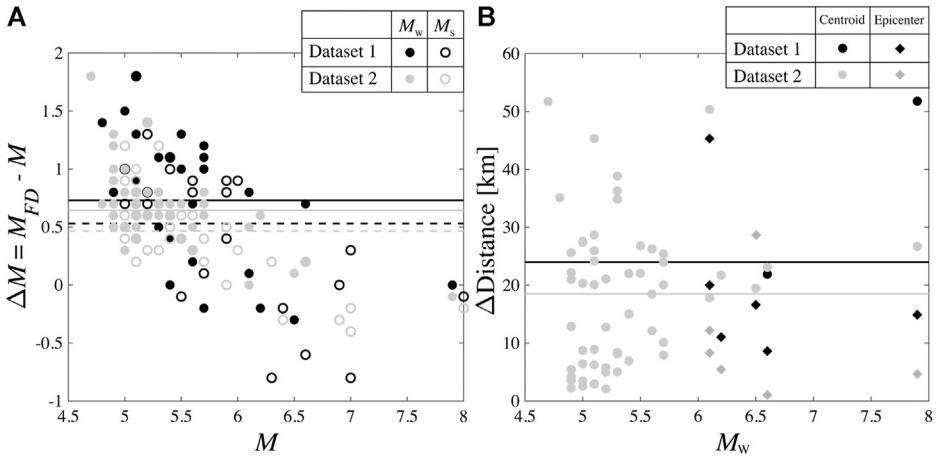

FIGURE 8 | (A) Difference between the final FinDer estimated magnitude, M_{FD}, and the reported M_W/M_S. **(B)** Distance between the estimated final epicenter (for $M_W \geq 6$ only)/centroid (for all events) and the reported epicenter/centroid. The solid and dashed lines show the average values for M_W and M_S for dataset 1 (black) and dataset 2 (gray), respectively.

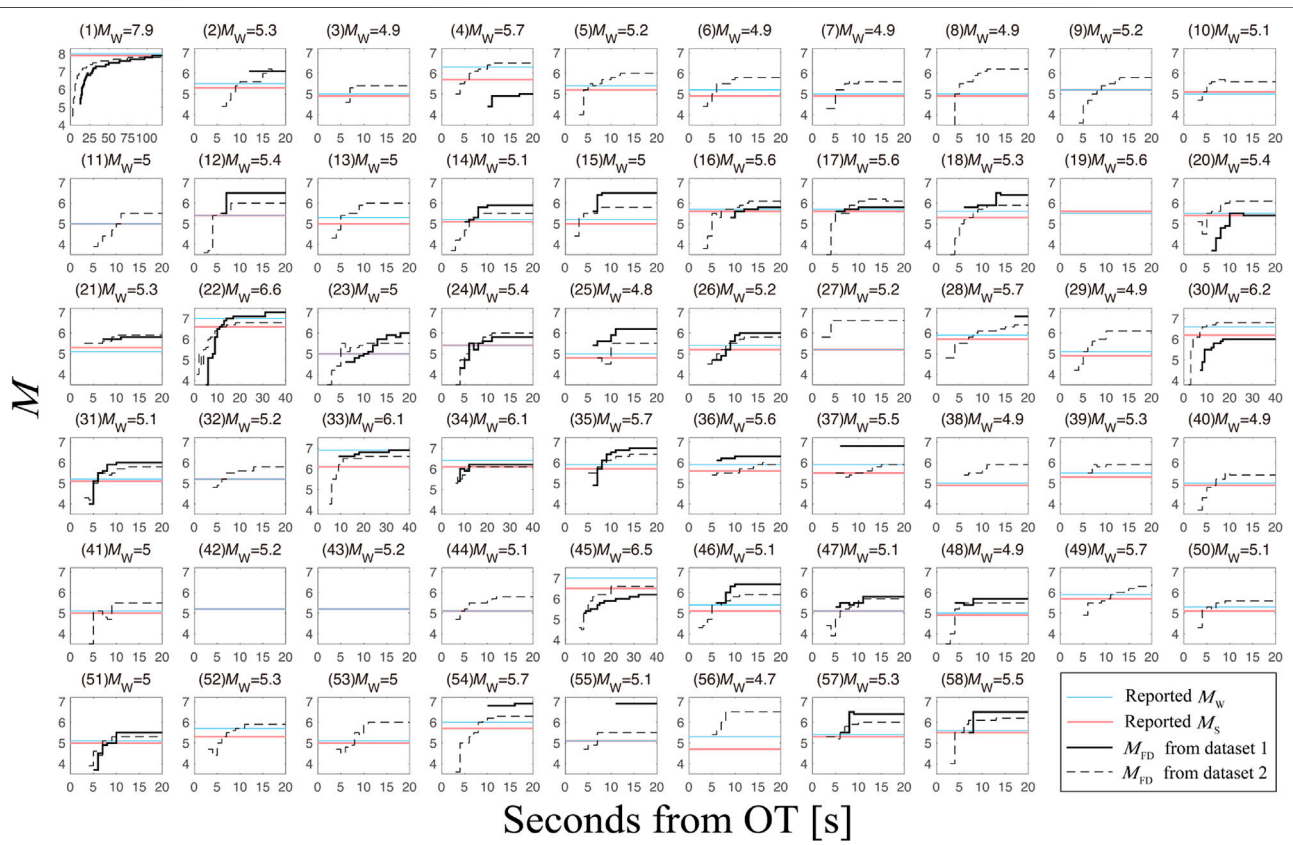

FIGURE 9 | Temporal evolution of FinDer magnitude, M_{FD}, from event origin time (OT) for all 58 earthquakes (neglecting data latencies).

networks will be able to better constrain earthquake magnitudes once more stations are deployed.

Figure 8B illustrates the distance between the estimated final centroid as the midpoint of the line-source and the reported epicenter (for $M_W < 6$)/centroid (for $M_W \geq 6$). The FinDer centroid defines the mid-point of the FinDer line-source. Therefore, **Figure 8B** also shows the distance between the estimated and reported epicenters of the six larger earthquakes. It should be noted that 22 out of 25 earthquakes that do not generate FinDer triggers in dataset 1, produce triggers

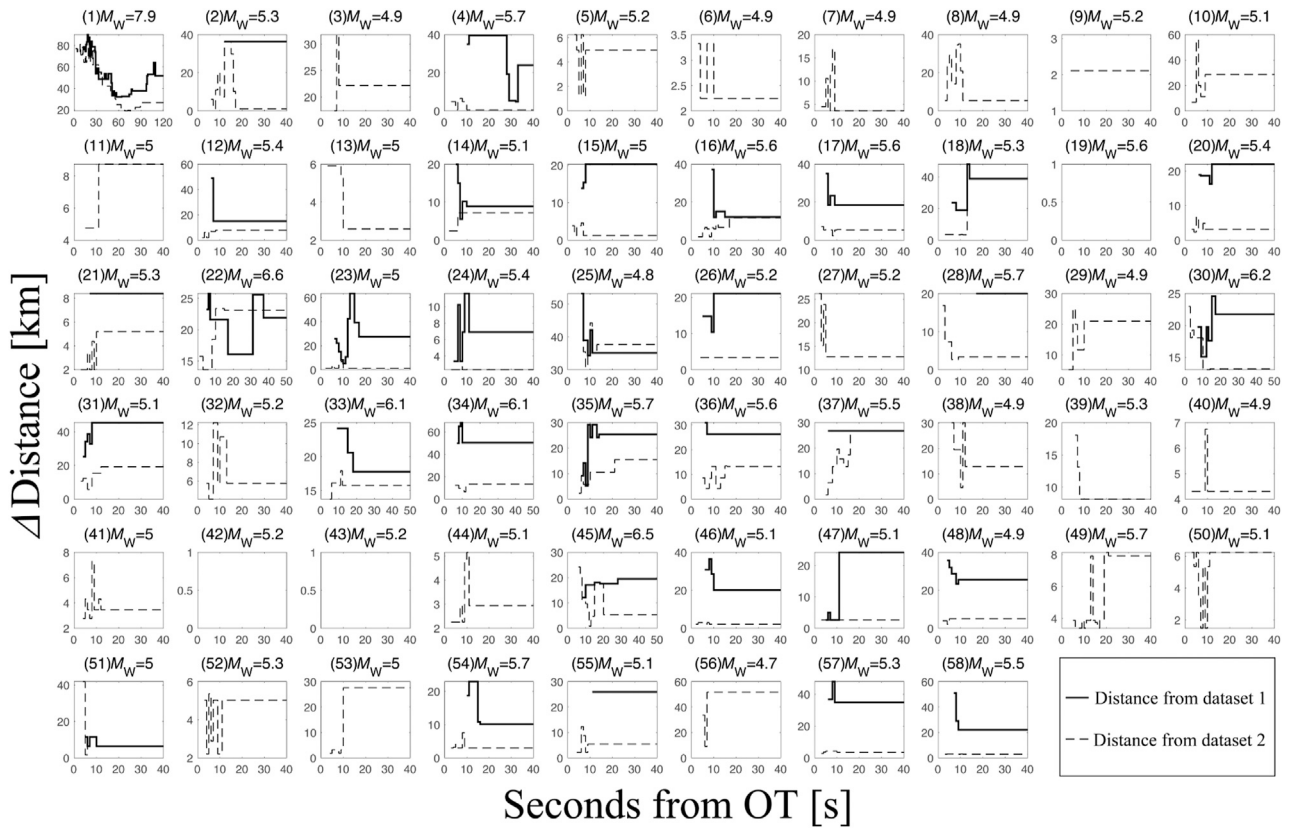

FIGURE 10 | Temporal evolution of the distance between the FinDer centroid and the reported epicenter (for M_W < 6)/centroid (for M_W ≥ 6) from event origin time (OT) for all 58 earthquakes (neglecting data latencies).

for the extended dataset 2, which includes additional simulations at future stations. Except for the significant difference between the two datasets for the two major earthquakes, the results for the other events are similar (**Figure 8B**). This can be explained by the fact that for the 33 earthquakes that triggered FinDer in dataset 1, the additional stations in dataset 2 have little impact on the epicenter constraints. This implies that the FinDer estimated epicenter/centroid is stable even when the network is quite sparse (provided that the azimuthal gap is not too large; see Böse et al. (2021)). In **Figure 8B**, the average value of the epicenter/centroid difference (18 km) obtained from dataset 2 is smaller compared with that from dataset 1 (24 km). This means that the 25 earthquakes that triggered FinDer only for the denser network in dataset 2 all have smaller epicenter errors.

Figures 9–10 show the temporal evolution of M_{FD} for all 58 earthquakes, as well as the distance between the FinDer epicenter/centroid and reported ones from OT, respectively. For the Wenchuan earthquake, FinDer yields its final line-source around 120 s after OT. For the other five large earthquakes (M 6.0–6.9), the final results are obtained within 30–40 s after OT. For the smaller earthquakes (M < 6), the final values are usually reached within 10–20 s. In general, FinDer provides 5–10 s faster and more accurate estimates of the final rupture for the earthquakes in dataset 2, which simulates a denser network. **Figure 11** shows the final FinDer strike from dataset 1 with the background of the focal mechanism from GCMT. The line-source model calculated by FinDer immediately after the earthquake can help to quickly determine the underlying seismogenic fault if prior local tectonic/geological information is available, and that is of great significance in the likelihood of strong aftershocks, time-dependent seismic hazard assessment, and even operational earthquake forecasting (OEF). Note, however, that FinDer does not require any prior information on fault locations.

Implications for EEW

The goal of EEW is to estimate the earthquake's damage potential and to issue an alarm of expected ground-motions to areas before the strong shaking starts. The primary concern of EEW is the time delay between triggering and OT as this time is directly related to the EEW blind-zone (or no-warning zone). **Figure 12** illustrates the relationship between D_{epi} and the time when FinDer triggers relative to OT, T_{tri}. Based on a series of evenly distributed modelled point-sources and stations, Kuyuk and Allen (2013) determined a semi-quantitative empirical curve that describes the relationship between the minimum number of triggered stations, the average interstation distance and the radius of the blind-zone. In **Figure 12** we regress a similar curve for T_{tri} as the function of D_{epi} and find that

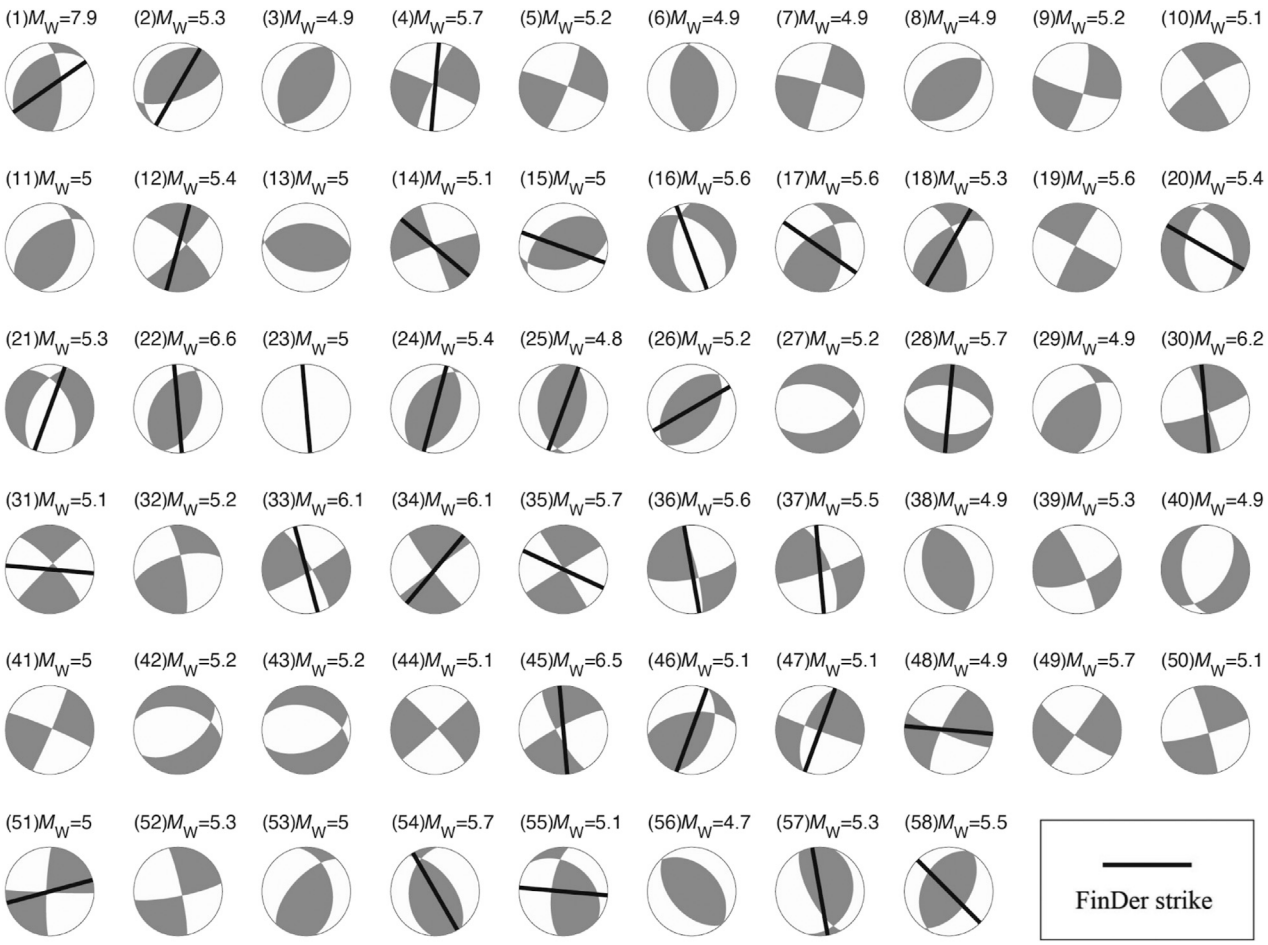

FIGURE 11 | Comparison of the strike of the final FinDer line-source and the GCMT focal mechanism for all 58 earthquakes. The absence of FinDer strike means that FinDer has not been triggered.

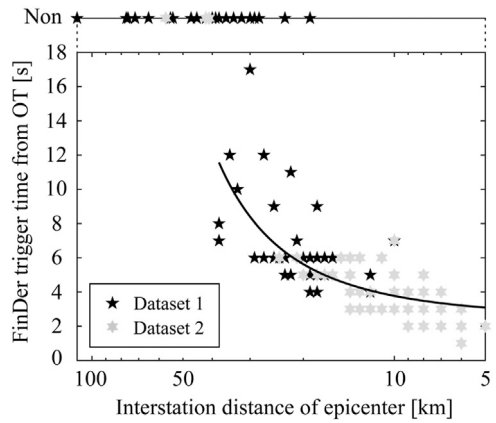

FIGURE 12 | Relationship between the interstation distance, D_{epi}, defined as the average distance between the epicenter to the three closest stations, and FinDer trigger time from OT, T_{trig}.

$$T_{tri} = 2.5exp\left(0.04D_{epi}\right) \quad (1)$$

T_{tri} can be converted into the radius of the no-warning zone by simply multiplying the *S*-wave velocity (e.g. V_S = 3.5 km/s).

The regression curve in **Figure 12** has two characteristics: 1) for $D_{\mathrm{epi}} > 15$ km, T_{tri} (and thus the radius of the no-warning zone) grows exponentially with D_{epi}, which means that network densification has a very strong impact on reducing T_{tri}; 2) for $D_{\mathrm{epi}} < 15$ km, T_{tri} saturates and further network densification has little impact on T_{tri}. However, it should be noted that this does not imply that a densification beyond 15 km is useless. Given the actual operation of a seismic network, it is common for a subset of stations to malfunction. In a threshold triggered system (e.g. based on FinDer), stations near the epicenter that are not functioning properly have the same effect as an increase in D_{epi}. Densifying networks thus effectively controls the growth of no-warning areas (Li et al., 2016).

The on-going network densification in Sichuan-Yunnan from the current mean value of D_{epi} = 60 km (**Figure 2A**) to D_{epi} =

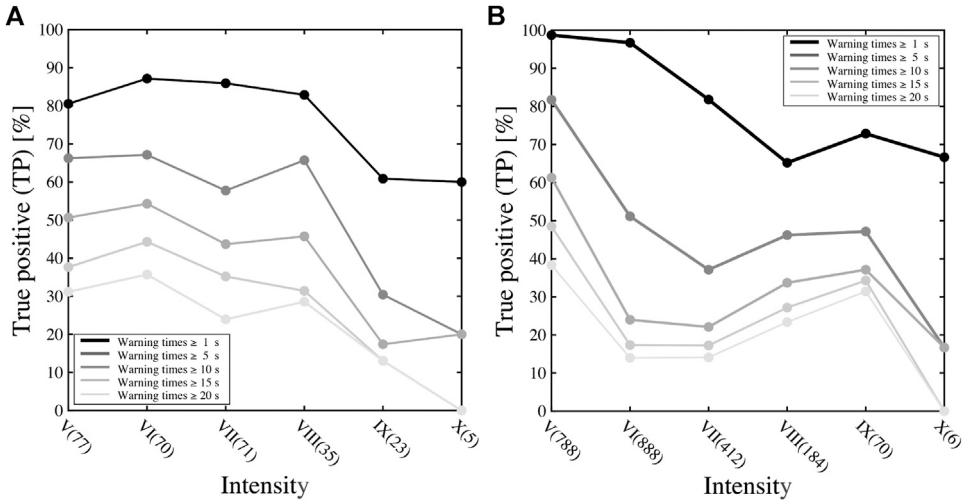

FIGURE 13 | Percentage of true positives (TP) for different levels of intensity (both Chinese and MMI scale) and different ranges of warning time using FinDer models for the **(A)** current network (dataset 1) and **(B)** future network (dataset 2). Numbers in brackets on *x*-axis give station counts for each intensity bin.

30 km (**Figure 2B**) will significantly reduce T_{tri} (and thus no-warning areas) across the whole region after 2020: based on **Eq. 1** we expect T_{tri} to decrease from currently around 8–9 s for one-third of the region to around 4–5 s for half, and even 3–4 s in the key urban areas. These estimates do not include data latencies. Preliminary tests for newly-built and upgraded stations suggest that data latencies of 1 s are a realistic expectation (Peng et al., 2020; Wenhui Huang, written communication, 2021).

Finally, we investigate how much warning time FinDer could provide for different levels of ground-shaking (again neglecting data latencies). We doing this by analyzing the potential performance on a per-station basis. We define the warning time (at each station) as the time interval between the first prediction (which is not necessarily in the first report) that ground-motions will exceed 10 cm/s^2 using the GMPEs developed by Cua and Heaton (2009) and the actual first exceedance of this level. If the observed and predicted PGA values both exceed that threshold, the station is considered to have hit the warning (i.e. true positive, TP). The occurrence of peak shaking usually occurs later, so the true warning times might actually be a bit longer.

Figure 13 shows the TP ratios of stations with successful alerting to the total number of stations for different intensity bins and for different ranges of warning time (≥1 s, ≥ 5 s, ≥ 10 s, ≥ 15 s, and ≥ 20 s). The results are calculated for the Chinese intensity scale, but the difference to the MMI scale is small (Hu, 2009). If the set of broadband seismic and strong-motion data used in this study had been available in real-time and without (or with short) delay, 40–70% of sites experiencing intensities of V–VIII and 20% experiencing IX-X could have been issued a warning with 5–10 s for the current station network (**Figure 13A**). Once the full network is deployed, these warning times are expected to increase: as shown in **Figure 13B** the TP ratios are expected to increase by 5–20% for 5–20 s of warning for V and VIII, and by almost 20% for IX for all warning time intervals. Adapting the FinDer trigger setting to account for the denser network, will probably lead to additional improvements in the new network.

DISCUSSION

The triggering of an EEW algorithm obviously depends on the earthquake magnitude and the network density near the epicenter. We found that FinDer has a high probability to trigger if the network density around the epicenter, D_{epi}, is less than $\log_{10}(M^a + b) + c$, where $a = 1.91$, $b = 5.93$, and $c = 2.34$ for $M = M_W \geq 4.8$, and $c = 2.49$ for $M = M_S \geq 5.0$, respectively. The relationship is unlikely linear. Otherwise, it would suggest that FinDer will not trigger for any earthquake below magnitude 4.5, regardless of station density. Real-time and offline tests of FinDer in other parts of the world, however, have shown that earthquakes as small as M 2.5 can be detected (Böse et al., 2018). Our dataset is probably insufficient to fully constrain the boundary condition for FinDer triggering.

Peng et al. (2020) recently analysed the alert performance of a hybrid demonstration EEW system installed in the same region as studied here. This system is equipped with MEMS-based sensors and broadband seismic stations with low-latency data transmission of 0.5–1.5 s, and determines the magnitude by the P_d scaling algorithm. For nearly half of the 130 M_L 3.0–5.1 earthquakes that occurred in this region between 2017 and 2018 the demonstration system triggered and sent first alerts within 15 s from OT. Using a different dataset and a larger magnitude range (M 5.0–8.0), our results in **Figure 12** suggest that FinDer could detect nearly two-thirds of the events within 12 s from OT (neglecting latencies).

FinDer determines seismic line-source models assuming that the dislocations are evenly distributed along this model. Such a model can be understood as the integral of the Haskell model (Haskell, 1964, 1966, 1969) in time and the width of the rupture surface. This assumption is theoretically reasonable. Using a list of candidate source models (homogeneous slip model, triangular slip model, *k*-square model, slip tip taper model, and restricted stochastic source model), Li et al. (2020b) applied the Akaike information

criterion (AIC) to identify the model that is most consistent with inverted slip distributions for the 2011 Van (Turkey) M_W 7.1 earthquake. The authors found that the homogeneous slip model with the smallest degree-of-freedom is only inferior to the *k*-square model and the triangular slip model. This suggests that the homogeneous slip model performs reasonably well.

The recently proposed extension of FinDer, FinDerS (+), assumes an elliptical slip model described by two independent parameters: the maximum slip and a skewness factor that controls the asymmetry of the slip profile (Hutchison et al., 2020; Böse et al., 2021). This model has similar features and the same degree-of-freedom like the triangular slip model, so this could be an important improvement, even though a systematic evaluation of source models for a representative set of earthquakes is needed, such as provided through the Source Inversion Validation (SIV) project and US Geological Survey finite-source earthquake database.

Combing different (point-source/finite-fault) algorithms allows EEW systems to deliver fast and accurate alerts for a large range of magnitudes. However, this combination in an actual EEW system is challenging. In the US ShakeAlert system, for instance, the Solution Aggregator (SA) module associates the source parameters from the EPIC and the FinDer algorithms if locations are within 100 km and OTs within 30 s, respectively. The combined source parameters are then determined as the average of the estimated parameters weighted by the normalized uncertainties of each algorithm (Kohler et al., 2020). In the future, both the event association and solution combination will likely move to the ground-motion space (Minson et al., 2017).

CONCLUSION

Rapid finite-rupture information, such as provided by FinDer, is important for EEW (and rapid response), in particular in large earthquakes (Böse et al., 2012; Li et al., 2020b; Böse et al., 2021). In this study, we tested the performance of the FinDer algorithm (Böse et al., 2018) for 58 $5.0 \leq M_S \leq 8.0$ earthquakes in the Sichuan-Yunnan region of China. We used playbacks of waveforms recorded by the high-gain seismic network stations and simulated waveforms/envelopes for planned future station installations. Based on the 2008 Wenchuan earthquake, we determined the optimum FinDer trigger setting as 4.6 cm/s^2 at neighboring three stations as a compromise between speed and accuracy of alerts. Overall, the FinDer estimated line-source models agree well with the catalog source parameters and focal mechanisms, but they can be computed faster compared to traditional approaches. The planned densification of seismic networks in Chinese mainland in the near future is expected to further reduce magnitude uncertainties and allow to better constrain epicenter and centroid. In another study (Böse et al., 2021) we recently developed an empirical equation that relates FinDer performance (in terms of length, strike, and location of the line-source) to the azimuthal gap between observing stations. While calibrated for the moment magnitude M_W, we compared FinDer magnitudes in this study also to the surface wave magnitude M_S, which is more commonly used in China. We found that the overall difference between M_{FD} and M_S is smaller than between M_{FD} and M_W, which is consistent with the high-frequency physical background of M_{FD}.

We estimated the magnitude of completeness for FinDer, M_{FDc}, as 5.3 for one-third of the Sichuan-Yunnan region with interstation distance of around 30 km, and as 4.4 in some urban areas after 2022. The FinDer trigger time, T_{tri}, may be reduced from currently around 8–9 s for one-third of the Sichuan-Yunnan region with D_{epi} = 30 km to around 4–5 s for half, and to 3–4 s in the key urban areas (plus data latencies). If the waveform data used in this study had been available in real-time, 40–70% of sites experiencing intensities of V–VIII and 20% experiencing IX-X could have been issued a warning with 5–10 s, before the arrival of the *S*-wave.

This study provides a useful reference for the planned future installation of FinDer in the nationwide EEW system of Chinese mainland. With the increasing number of broadband seismic, strong-motion and low-cost intensity stations with low latency being deployed in the near-future, FinDer has the potential to quickly report finite-source parameters (e.g. length, strike, rupture direction, rupture velocity etc.), and is expected to significantly improve both EEW and rapid loss estimates in China (Li et al., 2020a).

DATA AVAILABILITY STATEMENT

Strong-motion waveforms used in this study were provided by the China Strong Motion Network Center (CSMNC) at the Institute of Engineering Mechanics (China Earthquake Administration). Broadband seismic records were obtained from the Data Management Centre of China National Seismic Network at Institute of Geophysics (IGP, SEISDMC, doi: 10.11998/SeisDmc/SN) at China Earthquake Administration. The earthquake catalog was downloaded from China Earthquake Networks Center (CENC; http://10.5.160.18/console/exit.action, last accessed: December 2020). The moment magnitude and focal mechanism were extracted from Global Centroid-Moment-Tensor (GCMT; https://www.globalcmt.org/, last accessed: January 2021). The fault data is taken from GMT Chinese community (https://gmt-china.org/data/, last accessed: January 2021).

AUTHOR CONTRIBUTIONS

JL: computed FinDer models, conducted analysis, wrote manuscript; MB: gave idea and guided research, wrote manuscript; YF: helped with discussions and writing manuscript; CY: provided the planned station information, helped with discussing the Chinese mainland's EEW project.

FUNDING

This project is supported by the Guangdong Basic and Applied Basic Research Foundation (Grant No. 2020A1515110844). JL's visit at ETH Zürich is funded by the China Scholarship Council (201804190032) and the Swiss Seismological Service (SED).

ACKNOWLEDGMENTS

The authors would like to thank Liangqiong Lou (China Strong Motion Networks Center), Xiaoxiao Song (Hubei Earthquake Agency), Xiaojing Ma (Guangdong Earthquake Agency), Tianyang Gao and Yan Zhang (Institute of Geophysics, China Earthquake Administration) for helping us to apply for and download the earthquake data. The authors would also like to thank Wenhui Huang (Shenzhen Academy of Disaster Prevention and Reduction), Chaoyong Peng (Institute of Geophysics, China Earthquake Administration), John F. Clinton (Swiss Federal Institute of Technology Zürich), Frédérick Massin (Swiss Federal Institute of Technology Zürich) for related scientific discussions, as well as the topic editor Masumi Yamada and two reviewers for their feedback and suggestions.

SUPPLEMENTARY MATERIAL

The Supplementary Material for this article can be found online at: https://www.frontiersin.org/articles/10.3389/feart.2021.699560/full#supplementary-material

REFERENCES

Allen, R. M., and Melgar, D. (2019). Earthquake Early Warning: Advances, Scientific Challenges, and Societal Needs. *Annu. Rev. Earth Planet. Sci.* 47, 361–388. doi:10.1146/annurev-earth-053018-060457

Allen, R. M., Gasparini, P., Kamigaichi, O., and Böse, M. (2009). The Status of Earthquake Early Warning Around the World: An Introductory Overview. *Seismol. Res. Lett.* 80, 682–693. doi:10.1785/gssrl.80.5.682

Bird, D., Roberts, M. J., and Dominey-Howes, D. (2008). Usage of an Early Warning and Information System Web-Site for Real-Time Seismicity in Iceland. *Nat. Hazards* 47, 75–94. doi:10.1007/s11069-007-9198-y

Böse, M., Heaton, T. H., and Hauksson, E. (2012). Real-time Finite Fault Rupture Detector (FinDer) for Large Earthquakes. *Geophys. J. Int.* 191, 803–812. doi:10.1111/j.1365-246x.2012.05657.x

Böse, M., Felizardo, C., and Heaton, T. H. (2015). Finite-Fault Rupture Detector (FinDer): Going Real-Time in CalifornianShakeAlertWarning System. *Seismol. Res. Lett.* 86, 1692–1704. doi:10.1785/0220150154

Böse, M., Hutchison, A. A., Manighetti, I., Li, J. W., Massin, F., and Clinton, J. F. (2021). FinDerS(+): Real-Time Earthquake Slip Profiles and Magnitudes Estimated from Backprojected Slip with Consideration of Fault Source Maturity Gradient. *Front. Earth Sci.* (Accepted).

Böse, M., Smith, D. E., Felizardo, C., Meier, M.-A., Heaton, T. H., and Clinton, J. F. (2018). FinDer v.2: Improved Real-Time Ground-Motion Predictions for *M*2-*M*9 with Seismic Finite-Source Characterization. *Geophys. J. Int.* 212, 725–742. doi:10.1093/gji/ggx430

Böse, M., Julien-Laferrière, S., Bossu, R., and Massin, F. (2021). Near Real-Time Earthquake Line-Source Models Derived from Felt Reports. *Seismol. Res. Lett.* 92, 1961–1978. doi:10.1785/0220200244

Brune, J. N. (1970). Tectonic Stress and the Spectra of Seismic Shear Waves from Earthquakes. *J. Geophys. Res.* 75, 4997–5009. doi:10.1029/jb075i026p04997

China Earthquake Administration (2020). From Research to Application: Development of Earthquake Early Warning Technology in China, Available at: https://www.cea.gov.cn/cea/xwzx/fzjzyw/5556114/index.html (Accessed January 7, 2021). in Chinese

Chung, A. I., Henson, I., and Allen, R. M. (2019). Optimizing Earthquake Early Warning Performance: ElarmS-3. *Seismol. Res. Lett.* 90, 727–743. doi:10.1785/0220180192

Clinton, J., Zollo, A., Marmureanu, A., Zulfikar, C., and Parolai, S. (2016). State-of-the Art and Future of Earthquake Early Warning in the European Region. *Bull. Earthquake Eng.* 14, 2441–2458. doi:10.1007/s10518-016-9922-7

Cochran, E. S., Lawrence, J. F., Christensen, C., and Jakka, R. S. (2009). The Quake-Catcher Network: Citizen Science Expanding Seismic Horizons. *Seismological Res. Lett.* 80, 26–30. doi:10.1785/gssrl.80.1.26

Crowell, B. W., Schmidt, D. A., Bodin, P., Vidale, J. E., Gomberg, J., Renate Hartog, J., et al. (2016). Demonstration of the Cascadia G-FAST Geodetic Earthquake Early Warning System for the Nisqually, Washington, Earthquake. *Seismological Res. Lett.* 87, 930–943. doi:10.1785/0220150255

Crowell, B. W., Schmidt, D. A., Bodin, P., Vidale, J. E., Baker, B., Barrientos, S., et al. (2018). G-FAST Earthquake Early Warning Potential for Great Earthquakes in Chile. *Seismol. Res. Lett.* 89, 542–556. doi:10.1785/0220170180

Cua, G., and Heaton, T. (2007). "The Virtual Seismologist (VS) Method: A Bayesian Approach to Earthquake Early Warning," in *In Earthquake Early Warning Systems*. Editors P. Gasparini, G. Manfredi, and J. Zschau (Berlin and New York: Springer), 97–132.

Cua, G. B., and Heaton, T. H. (2009). *Characterizing Average Properties of Southern California Ground-Motion Amplitudes and Envelopes*, Earthquake Engineering Research Laboratory [EERL report 2009-05]. Available at: http://resolver.caltech.edu/CaltechEERL:EERL-2009-05 (Accessed January 16, 2021).

Department of Earthquake Disaster Prevention of the China Earthquake administration (1999). *The Catalogue of Chinese Modern Earthquakes*. (Chinese with English Abstract) (Beijing: China Science and Technology Press).

Department of Earthquake Disaster Prevention of the State Seismological Bureau (1995). *The Catalogue of Chinese Historical strong Earthquakes* (in Chinese with English Abstract) (Beijing: Seismological Press).

Aranda, J. M. E., Jimenez, A., Ibarrola, G., Alcantar, F., Aguilar, A., Inostroza, M., et al. (1995). Mexico City Seismic Alert System. *Seismological Res. Lett.* 66, 42–53. doi:10.1785/gssrl.66.6.42

Finazzi, F. (2016). The Earthquake Network Project: Toward a Crowdsourced Smartphone-Based Earthquake Early Warning System. *Bull. Seismological Soc. America* 106, 1088–1099. doi:10.1785/0120150354

Given, D., Allen, R. M., Baltay, A. S., Bodin, P., Cochran, E. S., Creager, K., de Groot, R. M., Gee, L. S., Hauksson, E., Heaton, T. H., Hellweg, M., Murray, J. R., Thomas, V. I., Toomey, D., and Yelin, T. S. (2018). *Implementation Plan for the ShakeAlert System-An Earthquake Early Warning System for the West Coast of the United States*. U.S. Geol. Surv. [open-file report 2018-1155]. Available at: . https://pubs.usgs.gov/of/2018/1155/ofr20181155.pdf (Accessed January 16, 2021) doi:10.3133/ofr20181155

Grapenthin, R., Johanson, I. A., and Allen, R. M. (2014a). Operational Real-Time GPS-Enhanced Earthquake Early Warning. *J. Geophys. Res. Solid Earth* 119, 7944–7965. doi:10.1002/2014jb011400

Grapenthin, R., Johanson, I., and Allen, R. M. (2014b). The 2014 M W 6.0 Napa Earthquake, California: Observations from Real-time GPS-enhanced Earthquake Early Warning. *Geophys. Res. Lett.* 41, 8269–8276. doi:10.1002/2014gl061923

Hammon, L., and Hippner, H. (2012). Crowdsourcing. *Wirtschaftsinf* 54, 165–168. doi:10.1007/s11576-012-0321-7

Haskell, N. A. (1964). Total Energy and Energy Spectral Density of Elastic Wave Radiation from Propagating Faults. *Bull. Seismol. Soc. Am.* 54, 1811–1841.

Haskell, N. A. (1966). Total Energy and Energy Spectral Density of Elastic Wave Radiation from Propagating Faults. Part II. A Statistical Source Model. *Bull. Seismol. Soc. Am.* 56, 125–140.

Haskell, N. A. (1969). Elastic Displacements in the Near-Field of a Propagating Fault. *Bull. Seismol. Soc. Am.* 59, 865–908.

Horiuchi, S., Horiuchi, Y., Yamamoto, S., Nakamura, H., Wu, C., Rydelek, P. A., et al. (2009). Home Seismometer for Earthquake Early Warning. *Geophys. Res. Lett.* 36, L00B04. doi:10.1029/2008gl036572

Hu, Y. X. (2009). *Earthquake Engineering* (In Chinese). Beijing: Seismological Press.

Hutchison, A. A., Böse, M., and Manighetti, I. (2020). Improving Early Estimates of Large Earthquake's Final Fault Lengths and Magnitudes Leveraging Source Fault Structural Maturity Information. *Geophys. Res. Lett.* 47, e2020GL087539. doi:10.1029/2020gl087539

Ide, S. (2019). Frequent Observations of Identical Onsets of Large and Small Earthquakes. *Nature* 573, 112–116. doi:10.1038/s41586-019-1508-5

Kawamoto, S., Hiyama, Y., Ohta, Y., and Nishimura, T. (2016). First Result from the GEONET Real-Time Analysis System (REGARD): The Case of the 2016 Kumamoto Earthquakes. *Earth Planets Space* 68, no190. doi:10.1186/s40623-016-0564-4

Kawamoto, S., Ohta, Y., Hiyama, Y., Todoriki, M., Nishimura, T., Furuya, T., et al. (2017). REGARD: A New GNSS-Based Real-Time Finite Fault Modeling System for GEONET. *J. Geophys. Res. Solid Earth* 122, 1324–1349. doi:10.1002/2016jb013485

Kohler, M. D., Smith, D. E., Andrews, J., Chung, A. I., Hartog, R., Henson, I., et al. (2020). Earthquake Early Warning ShakeAlert 2.0: Public Rollout. *Seismol. Res. Lett.* 91, 1763–1775. doi:10.1785/0220190245

Kong, Q. K., Allen, R. M., Schreier, L., and Kwon, Y. W. (2016). MyShake: A Smartphone Seismic Network for Earthquake Early Warning and beyond. *Sci. Adv.* 2, 1–8. doi:10.1126/sciadv.1501055

Kurzon, I., Nof, R. N., Laporte, M., Lutzky, H., Polozov, A., Zakosky, D., et al. (2020). The "TRUAA" Seismic Network: Upgrading the Israel Seismic Network-Toward National Earthquake Early Warning System. *Seismol. Res. Lett.* 91, 3236–3255. doi:10.1785/0220200169

Kuyuk, H. S., and Allen, R. M. (2013). Optimal Seismic Network Density for Earthquake Early Warning: A Case Study from California. *Seismological Res. Lett.* 84, 946–954. doi:10.1785/0220130043

Leyton, F., Ruiz, S., Baez, J. C., Meneses, G., and Madariaga, R. (2018). How Fast Can We Reliably Estimate the Magnitude of Subduction Earthquakes?. *Geophys. Res. Lett.* 45, 9633–9641. doi:10.1029/2018gl078991

Li, J. W., and Wu, Z. L. (2016). Controlling the 'blind Zone'of an Earthquake Early Warning System (EEWS): A Case Study of the Beijing Capital Circle Prototype EEWS. *Earthq. Res. China* 32, 584–594. (In Chinese with English Abstract).

Li, S. Y., Jin, X., Ma, Q., and Song, J. D. (2004). Study on Earthquake Early Warning System and Intelligent Emergency Controlling System. *World Earthquake Eng.* 20, 21–26. (In Chinese with English Abstract).

Li, J., Böse, M., Wyss, M., Wald, D. J., Hutchison, A., Clinton, J. F., et al. (2020a). Estimating Rupture Dimensions of Three Major Earthquakes in Sichuan, China, for Early Warning and Rapid Loss Estimates. *Bull. Seismol. Soc. Am.* 110, 920–936. doi:10.1785/0120190117

Li, J., Wu, Z., Jiang, C., Zhou, S., and Zhang, Y. (2020b). Simple Models of Complex Slip Distribution? A Case Study of the 2011 Mw 7.1 Van (Eastern Turkey) Earthquake. *Pure Appl. Geophys.* 177, 387–395. doi:10.1007/s00024-019-02167-7

Li, X. (2014). *Study on Earthquake Intensity Rapid Report System in Wuhan City circle*. (Beijing: Institute of Geophysics, China Earthquake Administration). (in Chinese with English abstract) [dissertation/doctoral thesis].

Liu, R. F., Gao, J. C., Chen, Y. T., Wu, Z. L., Huang, Z. B., Xu, Z. G., et al. (2008). Construction and Development of Digital Seismograph Networks in China. *Acta Seismol. Sinica* 30, 533–539. (In Chinese with English Abstract).

Massin, F., Clinton, J., Porras, J., Marroquin, G., Strauch, W., and Böse, M. (2019). "Evaluating and Improving Earthquake Early Warning in Central America," in Abstract retrieved from Abstracts in 2019 SSA Annual Meeting (Seattle, Washington) April 23–26.

McGuire, J. J., Smith, D. E., Frankel, A. D., Wirth, E. A., McBride, S. K., and de Groot, R. M. (2021). "Expected Warning Times from the ShakeAlert Earthquake Early Warning System for Earthquakes in the Pacific Northwest,". U.S. Geol. Surv. [open-file report 2021-1026]. Available at: https://pubs.usgs.gov/of/2021/1026/ofr20211026_v1.1.pdf (Accessed April 5, 2021) doi:10.3133/ofr20211026

Meier, M.-A., Ampuero, J.-P., Cochran, E., and Page, M. (2020). Apparent Earthquake Rupture Predictability. *Geophys. J. Int. Ggaa610.* 225, 657–663. doi:10.1093/gji/ggaa610

Minson, S. E., Murray, J. R., Langbein, J. O., and Gomberg, J. S. (2014). Real-time Inversions for Finite Fault Slip Models and Rupture Geometry Based on High-Rate GPS Data. *J. Geophys. Res. Solid Earth* 119, 3201–3231. doi:10.1002/2013jb010622

Minson, S. E., Brooks, B. A., Glennie, C. L., Murray, J. R., Langbein, J. O., Owen, S. E., et al. (2015). Crowdsourced Earthquake Early Warning. *Sci. Adv.* 1, 1–7. doi:10.1126/sciadv.1500036

Minson, S. E., Wu, S., Beck, J. L., and Heaton, T. H. (2017). Combining Multiple Earthquake Models in Real Time for Earthquake Early Warning. *Bull. Seismol. Soc. Am.* 107, 1868–1882. doi:10.1785/0120160331

Nakamura, Y., and Saita, J. (2007). "UrEDAS, the Earthquake Warning System: Today and Tomorrow," in *Earthquake Early Warning Systems*. Editors P. Gasparini, G. Manfredi, and J. Zschau (Berlin and New York: Springer), 249–282.

Ogweno, L. P., Withers, M. M., and Cramer, C. H. (2019). Earthquake Early Warning Feasibility Study for the New Madrid Seismic Zone. *Seismol. Res. Lett.* 90, 1377–1392. doi:10.1785/0220180163

Peng, H., Wu, Z., Wu, Y.-M., Yu, S., Zhang, D., and Huang, W. (2011). Developing a Prototype Earthquake Early Warning System in the Beijing Capital Region. *Seismological Res. Lett.* 82, 394–403. doi:10.1785/gssrl.82.3.394

Peng, C., Chen, Y., Chen, Q., Yang, J., Wang, H., Zhu, X., et al. (2017). A New Type of Tri-axial Accelerometers with High Dynamic Range MEMS for Earthquake Early Warning. *Comput. Geosci.* 100, 179–187. doi:10.1016/j.cageo.2017.01.001

Peng, C., Ma, Q., Jiang, P., Huang, W., Yang, D., Peng, H., et al. (2020). Performance of a Hybrid Demonstration Earthquake Early Warning System in the Sichuan-Yunnan Border Region. *Seismol. Res. Lett.* 91, 835–846. doi:10.1785/0220190101

Picozzi, M., Bindi, D., Brondi, P., Di Giacomo, D., Parolai, S., and Zollo, A. (2017). Rapid Determination of *P* Wave-Based Energy Magnitude: Insights on Source Parameter Scaling of the 2016 Central Italy Earthquake Sequence. *Geophys. Res. Lett.* 44, 4036–4045. doi:10.1002/2017gl073228

Romeu Petit, N., Colom Puyané, Y., Jara Salvador, J. A., Goula Suriñach, X., and Susagna Vidal, T. (2016). Development of an Earthquake Early Warning System Based on Earthworm: Application to Southwest Iberia. *Bull. Seismol. Soc. America* 106, 1–12. doi:10.1785/0120150192

Satriano, C., Wu, Y.-M., Zollo, A., and Kanamori, H. (2011). Earthquake Early Warning: Concepts, Methods and Physical Grounds. *Soil Dyn. Earthquake Eng.* 31, 106–118. doi:10.1016/j.soildyn.2010.07.007

Sheen, D. H., Park, J. H., Chi, H. C., Hwang, E. H., Lim, I. S., Seong, Y. J., et al. (2017). The First Stage of an Earthquake Early Warning System in South Korea. *Seismol. Res. Lett.* 88, 1491–1498. doi:10.1785/0220170062

Sichuan Earthquake Administration (2015). Construction and Operation of Earthquake Early Warning Demonstration System, Available at: http://www.scdzj.gov.cn/xwzx/xydt/201511/t20151130_31224.html (Accessed January 7, 2021). in Chinese

Sokos, E., Tselentis, G.-A., Paraskevopoulos, P., Serpetsidaki, A., Stathopoulos-Vlamis, A., and Panagis, A. (2016). Towards Earthquake Early Warning for the Rion-Antirion Bridge, Greece. *Bull. Earthquake Eng.* 14, 2531–2542. doi:10.1007/s10518-016-9893-8

Song, Y. Y., Peng, H. S., and Ma, Q. (2021). Carrying Out the New Development Concept and Promoting the Modernization of Earthquake Early Warning in China. *Seismol. Geomagnetic Obs. Res.* 42, 155–161. (In Chinese with English Abstract).

Stankiewicz, J., Bindi, D., Oth, A., Pittore, M., and Parolai, S. (2015). The Use of Spectral Content to Improve Earthquake Early Warning Systems in central Asia: Case Study of Bishkek, Kyrgyzstan. *Bull. Seismological Soc. America* 105, 2764–2773. doi:10.1785/0120150036

Stogaitis, M., Barski, A., Spooner, B., Wimpey, G., Robertson, P., Kong, Q. K., Allen, R., Bosch, R., Malkos, S., Jiang, S., Gadh, T., Chen, Y. W., and Cho, Y. M. (2020). "Earthquakes at Google," in Abstract retrieved from Abstracts in 2020 AGU Fall Meeting. Online 14 December S044-08 .

Strauss, J. A., and Allen, R. M. (2016). Benefits and Costs of Earthquake Early Warning. *Seismological Res. Lett.* 87, 765–772. doi:10.1785/0220150149

Suárez, G., Espinosa-Aranda, J. M., Cuéllar, A., Ibarrola, G., García, A., Zavala, M., et al. (2018). A Dedicated Seismic Early Warning Network: The Mexican Seismic Alert System (SASMEX). *Seismol. Res. Lett.* 89, 382–391. doi:10.1785/0220170184

Wang, C.-Y., Chan, W. W., and Mooney, W. D. (2003). Three-dimensional Velocity Structure of Crust and Upper Mantle in Southwestern China and its Tectonic Implications. *J. Geophys. Res.* 108, B92442. doi:10.1029/2002jb001973

Wells, D. L., and Coppersmith, K. J. (1994). New Empirical Relationships Among Magnitude, Rupture Length, Rupture Width, Rupture Area, and Surface Displacement. *Bull. Seismol. Soc. Am.* 84, 974–1002.

Wu, Y.-M., and Kanamori, H. (2005). Experiment on an Onsite Early Warning Method for the Taiwan Early Warning System. *Bull. Seismological Soc. America* 95, 347–353. doi:10.1785/0120040097

Wu, Y. M., Hsiao, N. C., Lee, W. H. K., Teng, T. L., and Shin, T. C. (2007). "State of the Art and Progress in the Earthquake Early Warning System in Taiwan," in *In Earthquake Early Warning Systems*. Editors P. Gasparini, G. Manfredi, and J. Zschau (Berlin and New York: Springer), 283–306.

Xu, X. W., Wen, X. Z., Ye, J. Q., Ma, B. Q., Chen, J., Zhou, R. J., et al. (2008). The M_S 8.0 Wenchuan Earthquake Surface Ruptures and its Seismogenic Structure (In Chinese with English Abstract). *Seismology Geology*. 30, 597–629.

Yamada, M., and Heaton, T. (2008). Real-time Estimation of Fault Rupture Extent Using Envelopes of Acceleration. *Bull. Seismol. Soc. America* 98, 607–619. doi:10.1785/0120060218

Zhang, H., Jin, X., Wei, Y., Li, J., Kang, L., Wang, S., et al. (2016). An Earthquake Early Warning System in Fujian, China. *Bull. Seismol. Soc. America* 106, 755–765. doi:10.1785/0120150143

Zheng, X.-F., Yao, Z.-X., Liang, J.-H., and Zheng, J. (2010). The Role Played and Opportunities provided by IGP DMC of China National Seismic Network in Wenchuan Earthquake Disaster Relief and Researches. *Bull. Seismol. Soc. America* 100, 2866–2872. doi:10.1785/0120090257

Zhou, Y. N. (2006). Strong Motion Observation in Chinese Continent. *Recent Dev. World Seismol.* 11, 1–6. (In Chinese with English Abstract).

Zuccolo, E., Gibbs, T., Lai, C. G., Latchman, J. L., Salazar, W., Di Sarno, L., et al. (2016). Earthquake Early Warning Scenarios at Critical Facilities in the Eastern Caribbean. *Bull. Earthquake Eng.* 14, 2579–2605. doi:10.1007/s10518-016-9878-7

Conflict of Interest: The authors declare that the research was conducted in the absence of any commercial or financial relationships that could be construed as a potential conflict of interest.

frontiers in Earth Science

ORIGINAL RESEARCH
published: 04 August 2021
doi: 10.3389/feart.2021.684084

An Earthquake Early Warning System for Southwestern British Columbia

Angela Schlesinger[1], Jacob Kukovica[1], Andreas Rosenberger[1], Martin Heesemann[1], Benoît Pirenne[1], Jessica Robinson[1] and Michael Morley[2]*

[1]Ocean Networks Canada, University of Victoria, Victoria, BC, Canada, [2]Fisheries and Oceans Canada Pacific Region, Sidney, BC, Canada

Southwestern British Columbia (BC) is exposed to the highest seismic hazard in Canada. Ocean Networks Canada (ONC) has developed an Earthquake Early Warning (EEW) system for the region. The system successfully utilizes offshore cabled seismic instruments in addition to land-based seismic sensors and integrates displacement data from Global Navigation Satellite Systems (GNSS). The seismic and geodetic data are processed in real-time onsite at 40 different stations along the coast of BC. The processing utilizes P-wave and S-wave detection algorithms for epicentre calculations as well as incorporation of geodetic and seismic displacement data into a Kalman filter to provide magnitude estimates. The system is currently in its commissioning phase and has successfully detected over 60 earthquakes since being deployed in October 2018. To increase the coverage of the EEW system, we are in the process of incorporating detection parameters from neighbouring networks (e.g., the Pacific Northwest Seismic Network (PNSN)) to provide additional information for future event notifications.

Keywords: earthquake early warning, Cascadia subduction zone, subsea instrumentation, global navigation satellite system, onsite processing, British Columbia, Canada, earthquake hazard

OPEN ACCESS

Edited by:
Angela Isobel Chung, University of California, Berkeley, United States

Reviewed by:
Garry Rogers, Geological Survey of Canada, Canada
Jessie Saunders, United States Geological Survey, United States

****Correspondence:***
Angela Schlesinger
schlesin@uvic.ca

Specialty section:
This article was submitted to Geohazards and Georisks, a section of the journal Frontiers in Earth Science

Received: *22 March 2021*
Accepted: *20 July 2021*
Published: *04 August 2021*

Citation:
Schlesinger A, Kukovica J, Rosenberger A, Heesemann M, Pirenne B, Robinson J and Morley M(2021) An Earthquake Early Warning System for Southwestern British Columbia. Front. Earth Sci. 9:684084. doi: 10.3389/feart.2021.684084

INTRODUCTION

Earthquake Early Warning (EEW) systems rapidly detect and characterize earthquakes to generate alerts so that protective action can be taken before strong ground shaking occurs. Currently, EEW systems operated in Mexico, Japan, South Korea, Taiwan and the United States provide public alerts for some areas with acute seismic hazard. Allen and Melgar (2019) provide a review of currently operational systems and the rapid development that took place over the last 10 years. In comparison to traditional observation-based seismology, the problem setting for an EEW system is different because of the limited time available to make an accurate earthquake detection. The time needed to analyze the full-waveform seismic data over the total duration of an earthquake cannot be afforded; hence algorithms to estimate the location and magnitude of an earthquake are based on the initial P-wave arrival times. In Canada, the southwestern coast of British Columbia (BC) and Vancouver Island are situated tens of kilometres east of the locked portion of the Cascadia Subduction Zone (CSZ) where the Juan de Fuca plate is subducting beneath the North American plate; exposing the region to the highest seismic hazard in the country (Adams et al., 2019). This imposes a great demand for an EEW system that could provide timely notifications for damaging earthquakes, including tsunamigenic megathrust events.

In 2015 Ocean Networks Canada (ONC), in collaboration with Natural Resources Canada (NRCan) (1975), started developing an EEW system for southwestern BC that currently consists of 32 land-based stations and eight seafloor stations (**Figure 1**). The EEW system combines land-based

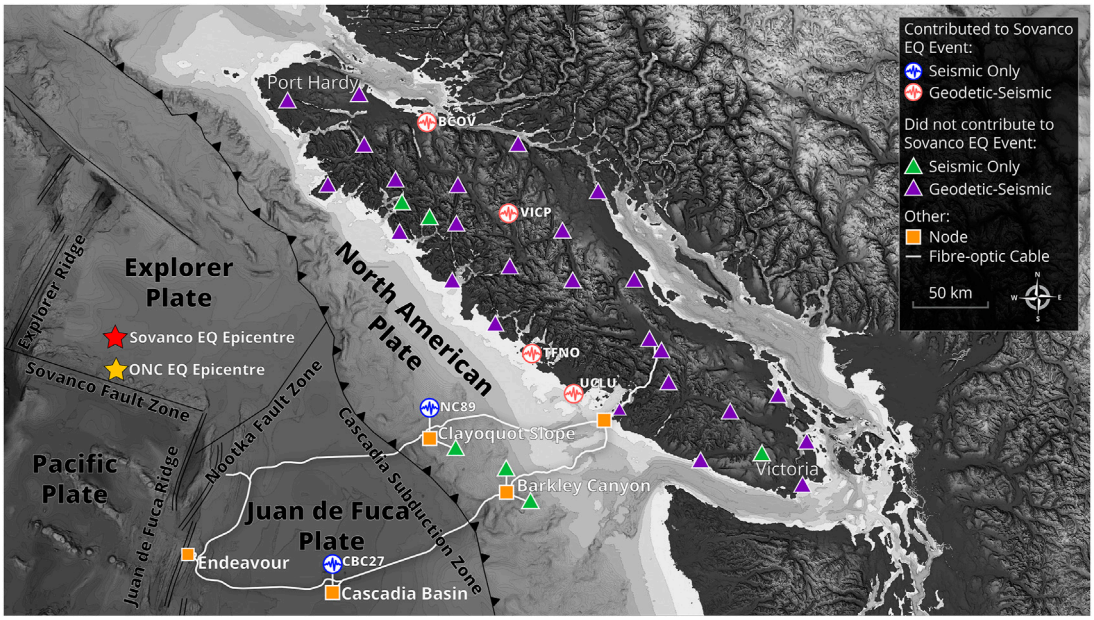

FIGURE 1 | Overview map of EEW sites. Purple triangles display sites that have both GNSS and seismic instruments. Green triangles represent sites that only have seismic instruments deployed. The red star marks the location of the M6.6 Sovanco earthquake from October 22, 2018 as identified in the NRCan earthquake catalog. The yellow star displays the location calculated by our EEW system for the same event (see ***Preliminary Results***). Circles with waveform symbols display the geographic locations of sites that contributed to the first notification of this event as described in ***Preliminary Results***. Triangles are stations that did not contribute to detection of the Sovanco earthquake. Data sources: Plate margin boundaries are obtained from Hyndman and Wang, 1995. Digital Elevation model derived from Ryan et al., 2009 NRCAN topography, and Canadian Hydrographic Service bathymetry.

seismic sensors with seafloor-installed seismic instruments that are connected to ONC's subsea cabled network (NEPTUNE: North-East Pacific Time-series Undersea Networked Experiments). NEPTUNE is the world's first multi-node cabled ocean observatory consisting of an 800 km cable loop that drapes across the CSZ (Barnes and Tunnicliffe, 2008). Seismic sensors located at nodal points along the cabled network on top and seaward of the inter-seismically locked portion of the CSZ aim to contribute to more accurate results of offshore earthquake locations and may also lead to more rapid detection times for some events.

The addition of seafloor seismic instrumentation into a real-time warning system has only been successfully implemented in Japan. The Dense Oceanfloor Network System for Earthquakes and Tsunamis (DONET[1]) was first installed in 2006 with a series of cabled seafloor nodes that connect various seismic instruments and pressure sensors to monitor the hypocentral region of the Nankai Through, Japan. The Seafloor Observation Network for Earthquakes and Tsunamis (S-net) was installed following the damaging Mw 9.0 Tohoku earthquake and tsunami in 2011. This additional network consists of 150 pressure gauges deployed along the Japan Trench linked by fiber-optic cables (Yamamoto et al., 2016; Wang and Satake, 2021).

By incorporating 3-axial accelerometers to co-located Global Navigation Satellite System (GNSS) stations onshore, the accuracy of calculated magnitudes from P-wave displacements can be significantly improved (Crowell et al., 2009; Bock et al., 2011; Melgar et al., 2013; Niu and Xu, 2014; Li 2015). In collaboration with the Federal Government's (Natural Resources Canada (NRCan), 1975), its Canadian Hazard Information Service (CHIS), and the Canadian Geodetic Survey, land-based seismic stations have been added and upgraded with geodetic instruments to acquire accurate geospatial displacement information on-site.

Precise point positioning (PPP) algorithms use corrections from the Canadian Spatial Reference System to allow for centimeter-level precision of ground displacements (Rosenberger et al., 2018; Hembroff et al., 2019). Data are then analyzed by applying a Kalman filter (Kalman, 1960; Smyth and Wu, 2007; Bock et al., 2011; Rosenberger et al., 2018) that combines the geodetic and seismic displacement values. The computational complexities involved in reliably combining real-time acceleration and geodetic data streams make ONC's implementation unique as it takes advantage of the co-location of the two instrument types, the on-site processing of the raw data streams, and the minimal data latency of all sensors. Ongoing research into the viability and contribution of geodetic information in an EEW system is under development by various groups such as Geng et al. (2013),

[1]https://www.jamstec.go.jp/donet/e/.

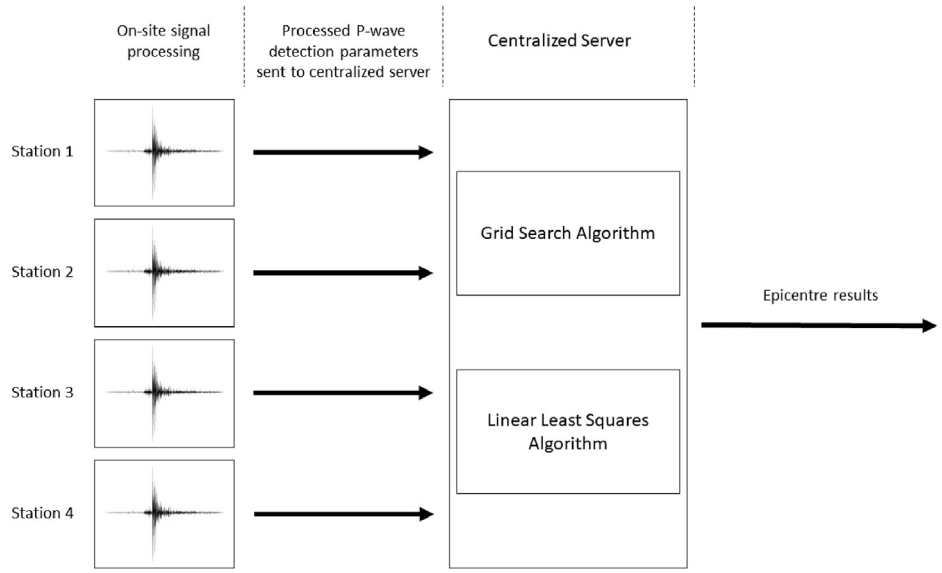

FIGURE 2 | Schematic representation of the EEW detection process. The waveform data are processed on site and the detection parameter are sent to a centralized server. There the two algorithms, Direct Grid Search (DGS) and Linearized Least Squares (LLS) method are independently calculating an epicentre location. A more detailed schematic for the EEW system is shown in **Figure 4**.

Murray et al. (2018), Goldberg et al. (2019), Ruhl et al. (2019), and Hodgkinson et al. (2020).

In addition to the presence of offshore seismic and pressure sensors located across the locked portion of the subduction zone, the most significant aspect of the EEW system is the capability to process real-time waveform acceleration data and GNSS observations on-site at each onshore station, after which the relevant detection information is sent to a central server to associate detections and issue notifications. This is not common practice in other EEW systems where the full-waveform seismic data from each station are sent *via* network to a central processing location (e.g., ShakeAlert; Wurman et al., 2007; Hartog et al., 2016; Kohler et al., 2018; Kohler et al., 2020). The specific topographical, geological, and environmental challenges of Vancouver Island increase the difficulty and cost to ensure a reliable, high-bandwidth network coverage to all deployed locations. With on-site processing of seismic and geodetic data, and by transmitting only parametric information to a central server (associator), bandwidth efficiency is greatly improved and operational costs are reduced, alleviating the need for an extensive communication infrastructure.

The EEW system is now successfully operating in testing mode with over 60 successful detections to date. Within this paper we only focus on the detected events between October 2018 and October 2020.

THE EARTHQUAKE DETECTION ALGORITHMS

Several algorithms which determine the epicentre of an event from just the first arrival times of a wave (in the case of earthquakes, the P-wave) have initially been developed in acoustical engineering rather than in seismology (Friedlander, 1987; Schau and Robinson, 1987; Huang and Benesty, 2000; Pirinen et al., 2003; Pirinen, 2006; Gillette and Silverman, 2008).

With the arrival of a P-wave at an individual seismic station, the earthquake detection processing is initiated. The seismic signal is processed onsite with a polarization filter and detection algorithms utilizing short time average, long time average ratios (STA/LTA). P-wave detection parameters from at least four seismic stations within a given time window are processed using two independent algorithms to calculate the earthquake epicentre; Direct Grid Search (DGS) and Linearized Least Squares (LLS) (see **Figure 2** and ***Magnitude Estimates***).

We describe the implemented methods for epicentre and magnitude calculations in the following sections.

P- and S-Wave Detection

EEW systems are dependent on the rapid identification of P-waves and S-waves that arrive at a seismic station. P-wave particle motions exhibit small incidence angles and approximately linear polarization in the direction of propagation (Aki and Richards, 2002; Rosenberger, 2010; Rosenberger, 2019). Hence, P-waves can be distinguished from background noise, or other seismic waves such as S-waves, through polarization filtering. The mathematical approach is discussed in more detail in Rosenberger (2010).

Transient signals within the background noise are detected at each station using STA/LTA ratios (Allen, 1982; Küpperkoch et al., 2012; Rosenberger, 2019). An STA/LTA detector works by computing the ratio of two moving-averages with different sizable time window lengths ΔT such that

$$S(t) = \frac{\underline{y}(t)_{\Delta T_{short}}}{\underline{y}(t)_{\Delta T_{long}}} \quad (2.1)$$

where $\underline{y}(t)$ is the moving average for the signal $y(t)$ at time t for varying window lengths. When a detection ratio $S(t)$ exceeds a programmable threshold, a detection is recorded. Ideally, STA time windows are selected for a given station to be longer than a few periods of a typically measured seismic signal (Trnkoczy, 2012). If the STA time window is too short, the detector will be highly sensitive to spike-like events in the signal. The overall sensitivity of the detector decreases with an increasing time window. For the LTA, a longer time window makes the detection more sensitive to P-wave signals (Trnkoczy, 2012). The initial STA and LTA window sizes for P-wave detections from all land-based and subsea sites were 1 –10 s, respectively. For S-wave detections the window sizes were 3 –30 s, respectively. Fine-tuning of these parameters on a site-by-site basis will be followed up in the EEW system commissioning phase.

The Direct Grid Search and Linear Least Squares Algorithms

When four or more stations within the network detect a P-wave within a given time window of 120 s, two independent algorithms calculate the earthquake epicentre. Within the DGS algorithm, the region of interest is overlain by a grid of geographical coordinates of appropriate resolution (0.15° × 0.15°; ~15 km) (Moni and Rickard, 2009; Rosenberger et al., 2019a). The current grid limits are set to be within 46°N and 52.2°N, and 131.75°W and 123°W. The hypocentre depth is fixed at 25 km, which is approximately the depth of the down-dip limit of partial locking of the CSZ (as discussed in McCrory et al., 2004; Wang and Trehu, 2016; Bilek and Lay, 2018). The potential epicentre of an earthquake can be determined with a grid-search based on the time differences of P-wave arrivals (TDOAs) at seismic stations (N). For each grid point, the hyperbolic intersection forward problem is computed and the possible source location based on two stations at a time is computed (i.e., the TDOA between stations 1 and 2, the TDOA between stations 2 and 3, etc . . .). The sum of these values at each grid point indicates the maximum likelihood estimate of the source location. The DGS algorithm, from our experience during the commissioning phase, has proven to be very robust in the presence of errors. Additionally, a staggered grid approach, which is described in more detail by Rosenberger et al. (2019a), is used to improve the results and decrease computation times by starting with the larger cell size (0.15°; ~15 km) and gradually decreasing the overlain grid size (0.05°; ~5 km). To account for the quality (further referred to as quality factor) of the solution the root-mean-square (RMS) value from all TDOA combinations is calculated as

$$\Delta TRMS = \sqrt{\frac{2}{N(N-1)} \sum_{m=1}^{N-1} \sum_{n=m+1}^{N} \left(\|\delta t_{m,n}\| - \|\sigma_{m,n}\| \right)^2} \quad (2.2)$$

where δt are the measured and σ the theoretical TDOAs derived from the current epicentre.

The LLS algorithm follows a method suggested by Gillette and Silverman (2008) as a "one step" source location calculation based on TDOA. The basic algorithm provides two source station coordinates from initially four seismic stations which have detected the signal. By expressing the location problem as a set of linear equations, the epicentre can be resolved by calculating the obtained inverse matrix. As described in Gillette and Silverman (2008) using a singular value decomposition (SVD) to compute the inverse matrix is justified by the fact that for arbitrary source-receiver geometries the matrix may have a high condition number (γ)

$$\gamma = \frac{\sigma_0}{\sigma_N} \quad (2.3)$$

The problem is ill-conditioned, meaning small errors in the data may cause large errors in the solution.

The quality of the best solution for the LLS method depends on the choice of the reference sensor r, as the one yielding the smallest product of condition number and TDOA residual:

$$C = \gamma(r) * \Delta TRMS \quad (2.4)$$

Further details on ONC's implementation of the DGS and LLS algorithms can be found in Rosenberger et al. (2019a).

When epicentre results from both methods converge within less than 80 km, an earthquake event is reported with the epicentre location being the mean of both results. A constant initial P-wave velocity of 7,000 m/s is used for the DGS and LLS epicentre calculations (Rosenberger et al., 2019a). The results are refined by testing if smaller or larger velocities would produce a more accurate epicentre based on the quality indicators within these two algorithms. The most accurate epicentre result is determined based on P-wave velocities between 6,000 m/s and 8,000 m/s with an incremental step-size of 500 m/s.

Magnitude Estimates

In the last 10 years several research publications have discussed methods that incorporate the information contained in the first few seconds of a P-wave record to estimate reliable event magnitudes quickly (e.g. Kuyuk and Allen, 2013). This is an area of active research and in consequence there is no single, generally accepted set of methods. Additionally, seismologists engaged in EEW research propose a variety of empirical scaling relationships to address different tectonic settings.

For earthquakes with smaller moment magnitudes (M; <M5) two independent algorithms are applied in the EEW system to estimate the magnitude; one based on the frequency content of the early seismic signal (Lockman and Allen, 2007; Wurman et al., 2007), the other based on initial displacement amplitudes (Kuyuk and Allen, 2013). The first algorithm based on Wurman et al. (2007) uses empirically derived scaling relationships incorporating the maximum predominant period ($\tau_p^{\max}$) of the waveform signal from the first 4 s after the initial P-wave detection. The latter contains the frequency content of the P-wave signal and therefore acts as an indicator of the size of

an event (Allen and Kanamori, 2003; Wurman et al., 2007). Wurman et al. (2007) describe the estimated magnitude based on the scaling relationship valid for Northern California as,

$$M = 5.22 + 6.66 * \log_{10}\left(\tau_p^{\max}\right) \quad (2.5)$$

The second method relies on the peak amplitude information of the P-wave displacement (P_D), which is derived from the vertical component waveform data. Again the first 4 s of the P-waveform are utilized to retrieve the absolute maximum value (Kuyuk and Allen, 2013). The empiric relationship between the peak displacement (P_D) and the epicentral distance (R) to an individual station (i) gives the magnitude estimate,

$$M_i = 1.23\left(\log_{10} P_{Di}\right) + 1.38\left(\log_{10} R_i\right) + 5.39 \quad (2.6)$$

Kuyuk and Allen (2013) state that this relationship is valid globally and not restricted to one particular tectonic setting. $\tau_p^{\max}$ and P_D are further referred to as the seismic Berkeley (Rosenberger et al., 2019a; Rosenberger, 2019). The mean of these two magnitude estimates determines the final magnitude used by the EEW system. If either of the two magnitudes is smaller than M1 the other would be chosen. In the case of both magnitude estimates being smaller than M1 or both differing by more than two magnitudes, the event association process does not declare an event.

For larger earthquakes (≥M6), the magnitude estimates will be continuously updated using data from the unbiased displacements over the total duration of the earthquake (Crowell et al., 2013). Assuming the magnitude can be determined from the GNSS data (see next sections), it will be selected as the estimated event magnitude value, otherwise the magnitude will be solely computed from the seismic data.

Incorporation of GNSS Data

More recent research shows that incorporating real-time displacement data from GNSS will provide more robust magnitude estimates and updates during a large earthquake (Crowell et al., 2009; Crowell et al., 2013; Hodgkinson et al., 2020; Melgar et al., 2020). The technique to integrate a GNSS component into a seismic station is relatively new and currently only a small number of sites with collocated instruments exist world-wide. The algorithms for the joint processing of seismic and GNSS data to-date have been verified with recorded data in offline experiments (Bock et al., 2011; Melgar et al., 2013; Niu and Xu, 2014; Li, 2015). During large earthquakes greater than M5, these data will provide more reliable magnitude estimates in the early stages of a developing earthquake, especially a megathrust event. The initial algorithms developed within ONC for an EEW system using only acceleration data have been extended to incorporate GNSS data to produce an unbiased displacement time series (Rosenberger, 2019).

Magnitude Estimates From Utilizing GNSS Data

In general, accelerometer data provide the high frequency information while applying a high-pass filter to remove any bias. The low frequency content of the derived displacement data is reconstructed when incorporating the GNSS data. Adding these data provide the system with two magnitude parameters – peak displacement (P_D) and peak ground displacement (P_{GD}) (Crowell et al., 2013) - that are derived from processing the GNSS data using three separate instances of PPP functions (Zumberge et al., 1997; Collins et al., 2009; Geng et al., 2013; Melgar et al., 2020; Hodgkinson, et al., 2020). The three PPP instances produce independent data streams referred to as the Orbit, Floating-point, and Integer ambiguity solutions based on their increase in accuracy, respectively.

Unbiased displacement values are computed by combining the individual displacement values retrieved from each separate PPP stream with the incoming acceleration values from the seismic instrument, applying a Kalman filter. The two horizontal displacement values are used to calculate the P_D, whereas the horizontal and vertical displacement values provide the P_{GD}.

Although the incorporation of GNSS data presents challenges, the solution yields reliable results with added redundancy. Crowell et al. (2013) described empirical relationships for geodetic derived P_D and P_{GD} values as,

$$M_{PD} = \frac{\log_{10} P_D + 0.893 + 1.73 \log_{10} R}{0.562} \quad (2.7)$$

$$M_{PGD} = \frac{\log_{10} P_{GD} + 5.013}{1.219 - 0.178 \log_{10} R} \quad (2.8)$$

where R is the hypocentral distance in units of kilometres. P_D and P_{GD} displacements are in units of centimetres. For larger events (>M6) the final magnitude estimate from the P_{GD} scaling relationship (**Eq. (2.8)**) will be prioritized over all other magnitude estimates in the EEW system (Rosenberger et al., 2019c).

Experiment-Based Validation of the GNSS Data Incorporation

ONC in collaboration with NRCan experimentally proved the viability of combining GNSS measurements with acceleration data by using the test system consisting of a Nanometrics Titan SMA accelerometer and GNSS antenna both attached to a rotating base with a radius of 50 cm (**Figure 3**) (Rosenberger, 2018). The mechanical system, designed by engineers at NRCan, keeps the orientation of the accelerometer fixed in one directionwhile the platform rotates. The unbiased displacement time-series from real-time PPP and acceleration data were obtained with the system conducting six experiments with varying rotational periods between 2.0 and 12.5 s (Rosenberger, 2018). Acceleration data was subjected to a 0.075–5 Hz band-pass filter before processing to replicate real-time conditions in the online processing. Positional results from the Kalman filter matched well with an average standard deviation (STD) of 0.83 cm.

The Event Association

Each land-based station hosts an accelerometer and a fitlet[2] computer; a small fanless high-performance mini PC.

[2]https://fit-iot.com/web/products/fitlet2/.

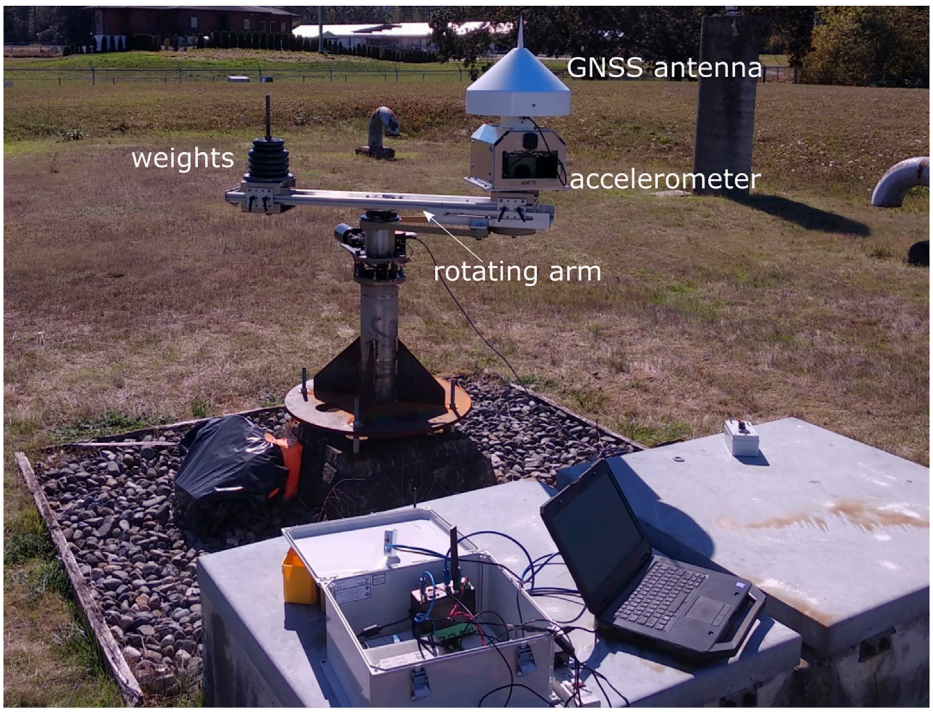

FIGURE 3 | The rotating system of an accelerometer and GNSS antenna used for testing the EEW detection algorithms. The base holding the antenna and accelerometer does not change relative orientation while testing. The plan and design was developed by Natural Resources Canada (NRCan) (1975) and the Geodetic Survey of Canada (GSC).

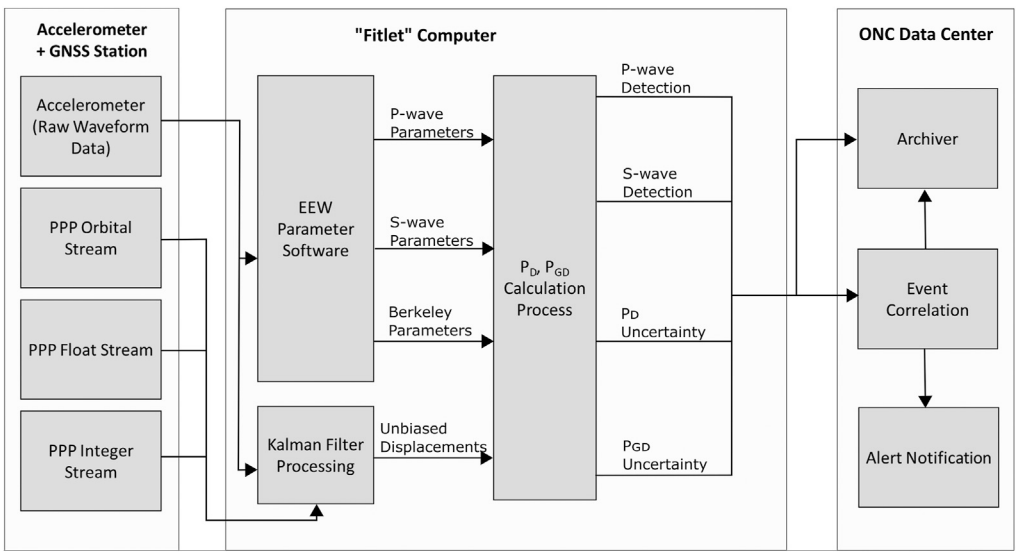

FIGURE 4 | Schematic overview of data flow from one land-based site to the event association in ONC's data centre. The raw acceleration data are processed to obtain the detection times of P-wave and S-wave onsets and the seismically derived Berkeley parameters. The raw acceleration data and the data from the three PPP streams are combined in the Kalman Filter algorithm to obtain unbiased displacement values. These unbiased displacements are correlated with the Berkeley parameter values and the P-wave and S-wave detection times to compute an epicenter and magnitude estimate for the detected event. Parameter data from all sites that detected an event are sent to ONC's data center where the event is associated, archived, and event notifications are sent out.

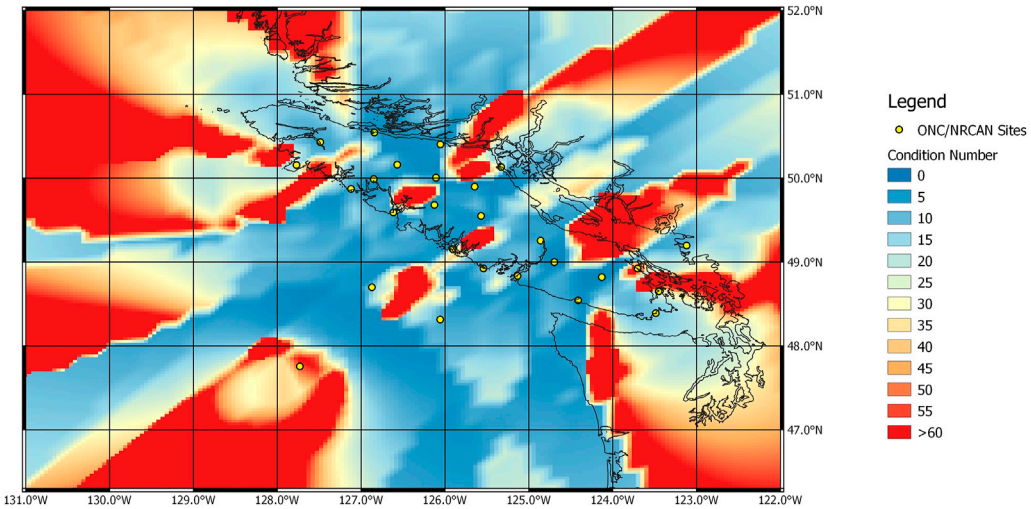

FIGURE 5 | Results from the LLS algorithm for the first four stations that detected an event located anywhere in the geographic region. Condition numbers greater than 30 are connected predominately to regions where the relative base-line of the respective four station array is short. Yellow circles mark the location of the seismic stations that were included in the modelling approach.

Additionally, most land-based sites are equipped with GNSS antennas and receivers to obtain the GNSS data. The three-component raw acceleration waveform data are recorded continuously with a 100 Hz sample rate and sent to the fitlet computer, where the detection algorithms (see ***P- and S-wave Detection***) are deployed to compute P-wave and S-wave detection times as well as the seismic Berkeley parameters: τ_p^{max} and P_D (see ***The Direct Grid Search and Linear Least Squares Algorithms***). The 100 Hz raw waveform data are also sent to the Kalman algorithm deployed on the fitlet computer to be co-processed with the three incoming PPP data streams sampled at 1 Hz. The resulting unbiased displacement values, seismically derived Berkeley parameters, and detection times of P-wave and S-wave onsets, are then processed to calculate the final P_D and P_{GD} values that contribute to the magnitude calculation. For subsea based accelerometers, raw waveform data are sent to the network server located at the shore station in Port Alberni, BC, where the seismic Berkeley parameters and the P-wave and S-wave detection times are computed.

All data are sent from each site (fitlet computer on land-based stations; Port Alberni shore station server for subsea instruments) to the ONC data centre located at the University of Victoria, BC (UVic) and to a redundant data centre in Kamloops, BC. Data are then evaluated (associated), archived, and event notifications are sent out (**Figure 4**).

Algorithm Testing

The robustness and accuracy of the algorithms applied in the EEW system were tested by simulating a large number (>2000) of magnitude M7 earthquakes (Rosenberger et al., 2019b). However, only the epicentre algorithms were tested at this stage. Simulations of GNSS displacement data were not available at the time of testing. The simulated earthquakes were placed at a hypocentral depth of 20 km on individual points of a regular geographical grid (UTM Zone 10N projection) with a grid cell size of 15 km by 15 km. The grid encompasses the locked zone of the CSZ as outlined in Gao et al. (2018). For a limited number of stations in the EEW system, an epicentral distance was calculated for each simulated event. The theoretical arrival times of P-wave and S-wave were computed based on a spherical Earth model travel-time algorithm using the TauP-toolkit hosted at IRIS (see Acknowledgements and Data Resources). The seismic Berkeley parameters, P_D and τ_p^{max}, were derived based on the empirical relationship of magnitude and epicentral distance (**Eqs 2.5** and **2.6**; ***Incorporation of GNSS Data***).

In this testing approach the first arrivals of four and then ten stations were used in the event association to simulate the progression of time as more stations detected the event. The condition number γ for the matrix inversion of the LLS algorithm serves as a first proxy for the quality of a solution. **Figure 5** shows results of the first four stations that detected an event from anywhere in the geographic region. Higher condition numbers (>30) represent areas where an epicentre was more difficult to calculate from P-waves arriving at these few stations. The geographical locations of these poorly constrained regions (yellow to red) are in alignment with the seismic sensor distribution of the network (**Figure 5**; yellow circles; Note: The testing was performed prior to all EEW stations being deployed hence the sparse distribution.).

Waiting for ten stations to detect the same event shows a rapid improvement in quality of the solution (**Figure 6**). However, the condition numbers for events occurring underneath most of Vancouver Island and less than 200 km offshore from central Vancouver Island only showed slight improvements when including more stations in the detection algorithms.

High condition numbers amplify errors in the real-time data and affect epicentre relocations as well as magnitude estimates. **Figure 7** represents spatial errors between true (simulated) and calculated epicentre locations obtained from the averaged

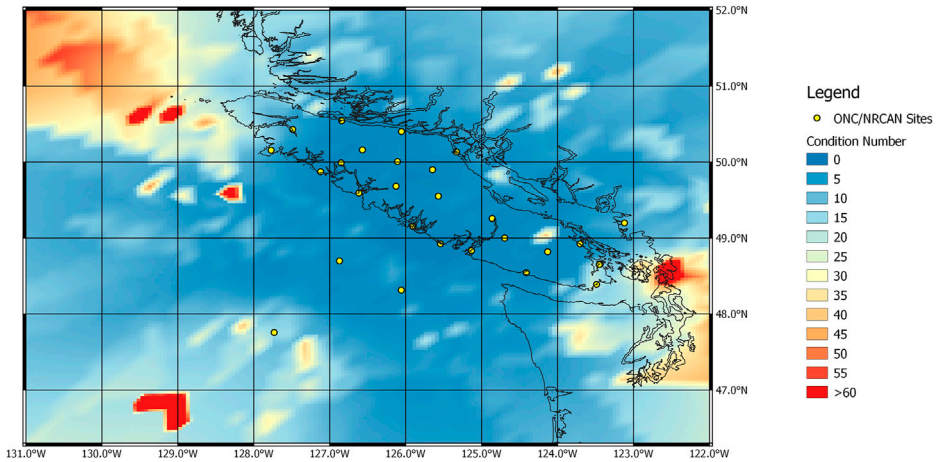

FIGURE 6 | Results from the LLS algorithm for the first ten stations that detected an event located anywhere in the geographic region. Condition numbers greater than 30 are connected predominately to regions where the relative base-line of the respective 10 station array is short. Yellow circles mark the location of the seismic stations that were included in the modelling approach.

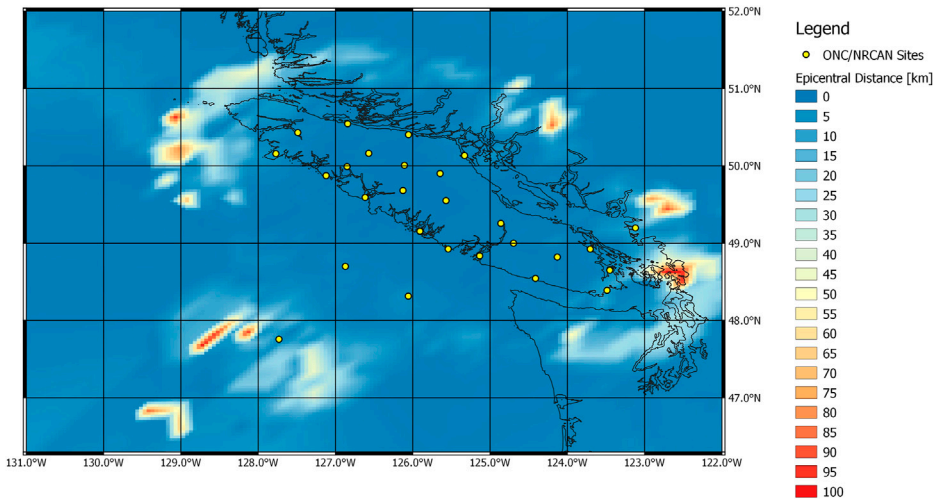

FIGURE 7 | The distribution of errors in epicentral distances from the combined algorithms after the first ten stations have detected the P-wave arrival. Yellow circles mark the location of the seismic stations that were included in the modelling approach.

solution of the DGS and the LLS algorithms. The results represent the event association from P-wave arrival detections at the first ten stations. Areas with greater distance errors (>30 km) are related to the station array consisting of the first ten stations having increased uncertainty within the Gaussian function utilized by the DGS algorithm as the distances between sources and stations increases (Rosenberger et al., 2019a).

PRELIMINARY RESULTS

While the EEW system was only partially installed and algorithms were still under development, the first successful event detection occurred in late 2018, when a series of seismic events along the Sovanco Fracture Zone (red star; **Figure 1**) was detected. According to the NRCan earthquake catalog the first earthquake (M6.1) occurred at 05:39:35 (UTC) on October 22, 2018. The hypocentre was located 218 km SW off the northern tip of Vancouver Island at a depth of 11 km. The first EEW event notification was sent after the P-wave was detected on six stations within the network (see **Figure 1**; contributing sites are indicated with round symbols). The detections were made within 45 s after the origin time (**Figure 8**). The notification was issued 4 s later (49 s after the origin time). The initial magnitude reported by the EEW system was M6.6 and later updated to M6.75. The calculated epicentre from the EEW system (yellow star, **Figure 1**) was within 30 km of the epicentre reported in the NRCan catalog (red star, **Figure 1**). This event is so far the only

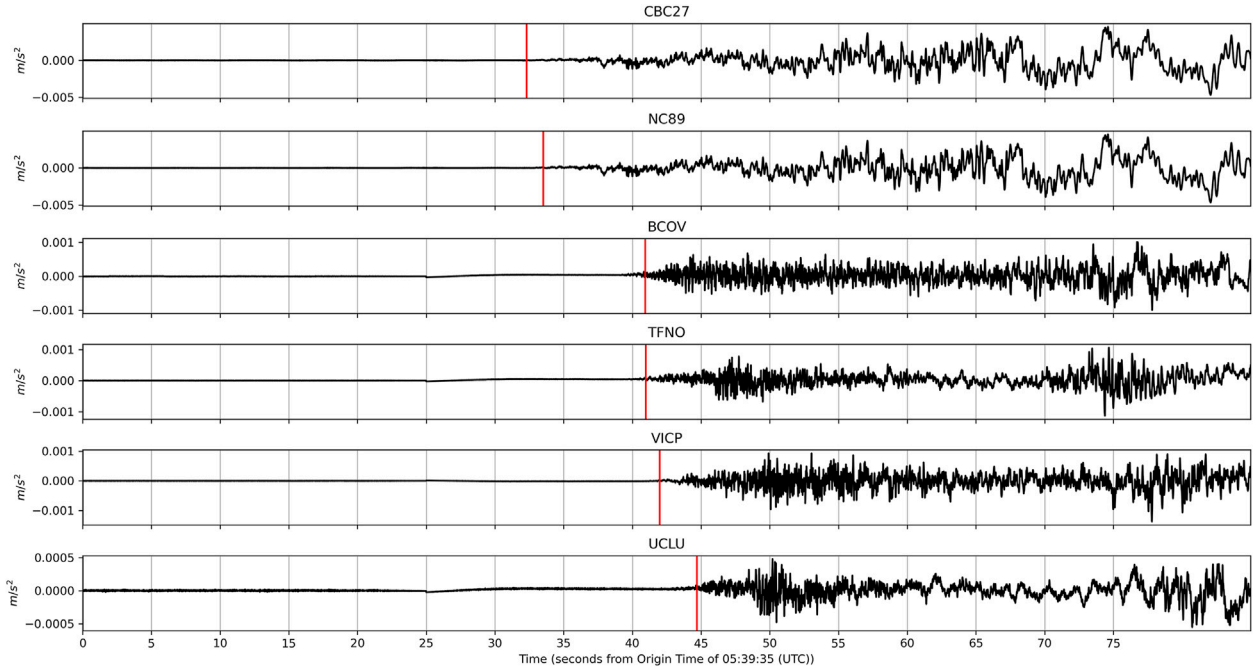

FIGURE 8 | Waveforms that contributed to the first notification for the Sovanco earthquake that happened on October 22, 2018. Time is given in seconds after the origin time (5:39:35 UTC) as identified in the NRCan catalog. The first two waveforms were recorded at offshore stations (CBC27: Cascadia Basin: ODP Site 1027, NC89: Clayoquot Slope—ODP Site 889) while the following four traces were recorded onshore (BCOV: Beaver Cove, TFNO: Tofino, UCLU: Ucluelet, VICP: Victoria Peak). Site locations are shown in **Figure 1**. The parametric data from these sites can be obtained from Ocean Networks Canada Society (2021). Raw waveform data from the subsea instruments can be obtained from Ocean Networks Canada, (2009).

earthquake detected within the EEW system that used the unbiased displacements from GNSS for magnitude calculations, due to all other detected events being of magnitudes less than M6. It is important to note the first P-wave from this event was detected on two subsea stations, Clayoquot Slope Bullseye (NC89) and Cascadia Basin (CBC27); 8 s prior to the first land-based station detecting the same event (**Figure 8**). This allowed for the EEW system to begin classifying the earthquake earlier than if the system relied solely on detections from land based stations. Three aftershocks within the geographical range of the first detection were also recorded by the EEW system and confirmed as successful detections based on results from the NRCan and USGS catalogs.

EVENT NOTIFICATION

This EEW system does not deliver warnings to the general public but rather notifications of a detected event that occurred within the current grid boundaries of the EEW system. The notification is a small data package that conforms to the Common Alerting Protocol (CAP) format. It details the earthquake epicentre coordinates, the magnitude estimate, the estimated event origin time, and the number of stations that contributed to the detection.

The notification is sent to each subscriber, assumed to be an operator of critical infrastructure or responsible authority in charge of important assets. The distributed software architecture implemented by ONC allows each subscriber to run codes, triggered by the arrival of the notification package, to calculate the time left before shaking starts and the expected Modified Mercalli Intensity (MMI) for their specific locations of concern. Subscribers have the ability to utilize the newly calculated information to trigger their own automated event response workflow based on safety protocols they have designed. For example, a mass transit operator could calculate the MMI for the different locations of their trains across their network and determine the best course of action to maximize the safety of their passengers. ONC aims to reliably provide messages for earthquakes of M4 and greater that are relevant for the region.

DISCUSSION

Observations made in empirical tests and associated real-time detections show good initial performance of the system. The first successful event detection for the Sovanco earthquake series shows the EEW system can detect earthquake events occurring further offshore from Vancouver Island with a magnitude of >M6. The calculated magnitude values and epicentre locations aligned with those reported by the NRCan and USGS catalogs. Following this first successful event detection, improvements on the algorithms and the overall EEW system were implemented with many subsequent earthquake events successfully detected between October 22, 2018 and October 20, 2020 with magnitudes ranging from M1.7 to M6.5 as confirmed with the NRCan and USGS catalogs.

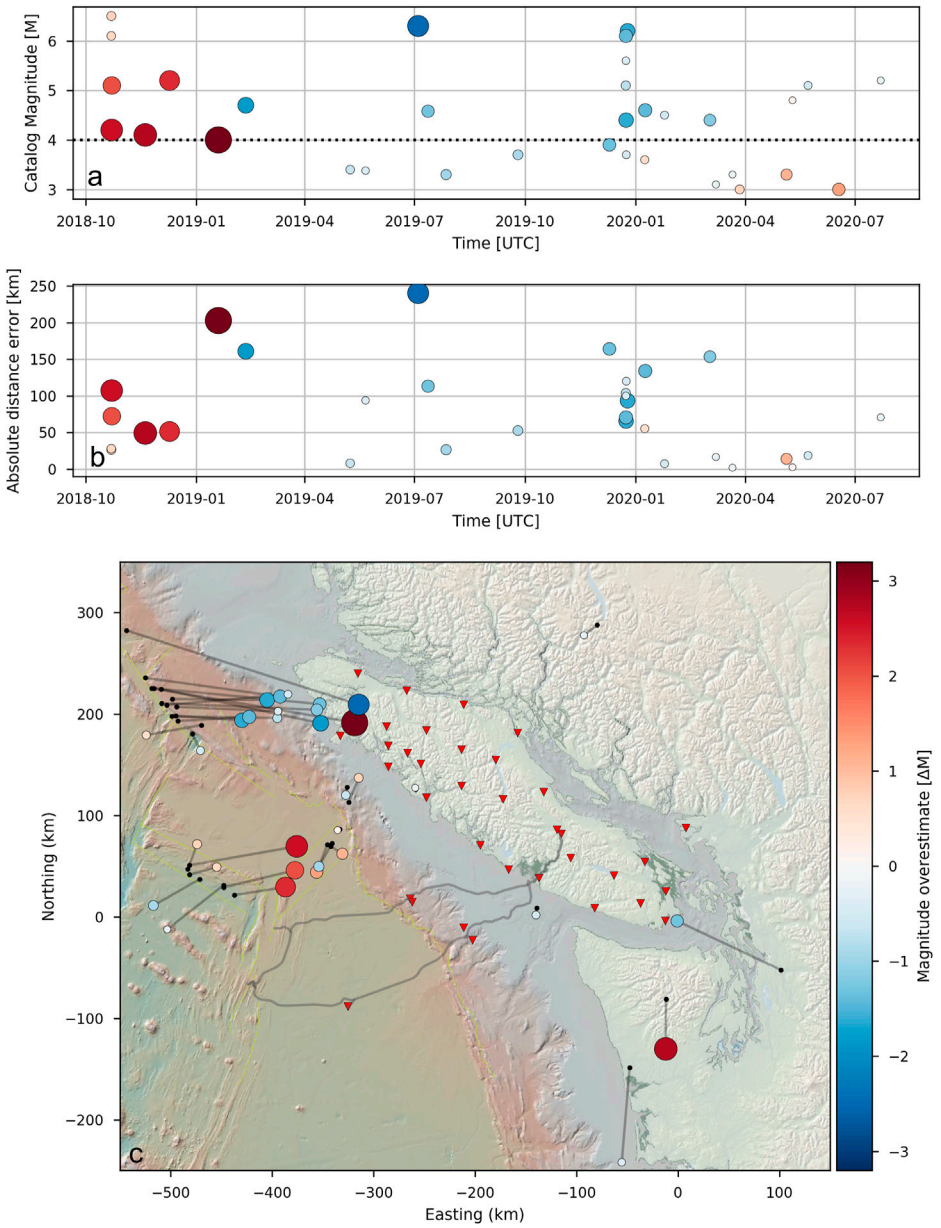

FIGURE 9 | (A) Time series of magnitude errors of the final EEW system event notification in relation to the same events detected and cataloged by NRCan or USGS (priority was given to NRCan cataloged events). The magnitude error is represented by the colour and the size of the circles. The black dotted line highlights our goal of generating reliable notifications for relevant events of ≥M4. **(B)** Time-series of epicentral distance errors for the same events and represented by the same symbols as in **(A)**. **(C)** Map view of the events shown in **(A)** and **(B)**. We only show events recorded by the EEW system between October-2018 and October-2020 with magnitudes ≥ M3. The EEW system generated epicentres (colored circles) and the reference epicenter locations retrieved from NRCan or USGS (black dots) are connected by lines.

It should be noted that the system currently is not designed to report for events outside of the grid boundaries or for magnitudes smaller than M4. Even though smaller events might get detected with the sensors distributed within the ONC network and an event association could have been declared, these results will not be considered validated.

Figure 9A shows the distribution of magnitude errors over time (magnitude errors are represented by color and circle size). Magnitudes prior to April 2019 were mostly over-estimated with the EEW system, whereas more recent event notifications tend to slightly underestimate the earthquake magnitude. The black dotted line in **Figure 9A** indicates the current magnitude threshold for which ONC intents to send out reliable notifications. Further improvement to the station network and synthetic system testing will hopefully improve the magnitude calculations. Events detected with the EEW system that were identified in the NRCan catalog were given priority over the events identified in the USGS catalog. **Figure 9B** shows errors in

final epicentre location compared to catalog epicentres from NRCan and USGS for the same events as shown in the panel above. Smaller errors in magnitude (smaller circles) tend to correlate with more accurate epicenter locations. **Figure 9C** shows the spatial distribution using the same events and symbols as above. Black lines connect the EEW epicentres (shown as colored circles) to the epicentre locations from the NRCan and USGS catalogs (shown as black points with priority given to events catalogued by NRCan).

The spatial distribution of location errors aligns with the findings of our test results described in ***Algorithm Testing***. The epicentre locations of events especially to the north-west and south-east of the network are not well constrained. This is well demonstrated by a series of events that took place on the southern section of the Queen Charlotte Fault Zone. The locations that our EEW system estimates for these events are systematically too close to the network, resulting in underestimated magnitudes. All earthquakes that occurred close to the shoreline or underneath Vancouver Island were successfully detected with significantly smaller epicentre differences and closer magnitude estimates. The NRCan and USGS catalogs contain no events ≥ M3.5 with epicenters on Vancouver Island or the CSZ offshore Vancouver Island that were missed by our EEW system during the studied time range.

Over the next couple of years, the EEW system will undergo a more thorough system testing which will incorporate simulated events that represent megathrust rupture earthquakes using the approach detailed in Melgar et al., 2016. Additionally, improvements to the EEW network are underway, mostly to reduce overall system latency. On average, there is a 2.5 s latency that comprises the computation time on the fitlet computers at the various sites and the data transfer from each site to the two servers in operation within the system. The ~400 km distance between these servers is intentional in case of catastrophic damage occurring in one of the cities. The latency of the processed PPP streams arriving at the server locations is slightly larger, hence their data incorporation into the magnitude computation increases the latency of the magnitude parameters on average to 5 s after a P-wave detection occurred at any individual station. However, if the PPP streams are not utilized in the magnitude computation, only the seismic derived Berkeley parameters are applied and the latency decreases.

Latency issues pose integral challenges to achieve high efficiency and accuracy of a system; however, there are approaches used to overcome latency. Firstly, added network densification increases the number of stations that can contribute to detection. Station failures affect latency, and so by adding more stations, system-wide internal redundancy can be improved. Additionally, volatile weather conditions cannot be ignored. Weather varies greatly across Vancouver Island, where most of the land-based stations are located. The winter months are especially harsh, adding difficulty and challenges to maintaining instrument uptime. Consequently, station outages and data latencies can be mitigated by densifying the station network and increasing local station reliability with resilient power supply systems and multiple data paths.

Lastly, it is beneficial to identify site-specific characteristics that impact the instrument response to a seismic signal. As seismic waves travel through the subsurface, changes in ground velocity greatly affect the ground shaking observed by accelerometers, or the travel time for a P-wave to reach a station. Applying constant parameters across the entire system could skew the calculated magnitudes or epicentres if a station does not account for amplification factors that affect the recording. We intend to test the detection algorithms with simulated earthquake events overlain by measured noise floor values for urban sites to identify limits in our detection approach.

To increase its coverage, the modular EEW system architecture has allowed us to incorporate detection parameters from neighbouring networks. Through the Pacific Northwest Seismic Network (PNSN), additional P-wave and S-wave detection times and seismic Berkeley parameters are streamed to the ONC server and contribute to earthquake event associations, and conversely the parameters extracted from our sensors are made available to PNSN. Validation of these station contributions to limit erroneous detections is currently underway.

CONCLUSION

The EEW system developed by ONC in collaboration with NRCan has been successfully operating in test mode since September 2018. It's ability to incorporate offshore seismic stations thanks to ONC's NEPTUNE cabled observatory, to correlate geospatial GNSS data with collocated acceleration data, and to calculate real-time onsite earthquake detection parameters makes this EEW system one of the more advanced systems in the world. The addition of underwater seismic stations contributes to a potential decrease in warning time for offshore events when compared to purely land-based seismic networks as shown for the Sovanco earthquake event detection. The combination of seismic and geodetic data is leading-edge technology that was experimentally validated using a controlled test setup (**section 2.5.2**) and the first successful M6 earthquake detections on October 22, 2018. Lastly, on-site computations of P-wave detections and displacement values greatly reduce the overall bandwidth usage for an EEW system and allow for efficient and immediate implementation of the Kalman filter to combine accelerometer and GNSS-based ground displacement data. Algorithm testing has shown the station distribution within the area of interest is adequate for detecting earthquake events that occur ~120 km offshore and underneath Vancouver Island. In addition, tests have shown that four stations are sufficient for reliably calculating an earthquake epicentre when using the LLS and DGS algorithms. The EEW system still needs to be further tested and improved to enhance its reliability and detection accuracy. Upgrades to the systems infrastructure (e.g. improved power supplies and communication links) will increase the system reliability. Performing site-specific characterizations will improve the overall accuracy and further densifying the EEW network would increase the number of contributing sites available for an event detection. This could reduce the detection time, as well as add more redundancy to the overall network.

OUTLOOK

Currently ONC, and its partners at Natural Resources Canada, are performing the commissioning of the system. At this time, reviews on

the current status of the system are on-going and concerns mentioned in the Discussion and Conclusions sections are being addressed. To increase the coverage of the EEW system, work on incorporating detection parameters from neighbouring networks such as the Pacific Northwest Seismic Network (PNSN) is under way with the objective of providing additional information for events close to the southern border of the detection grid.

DATA AVAILABILITY STATEMENT

Real-time and historical earthquake parameter data from the accelerometer and PPP streams in the context of this project can be obtained by visiting http://data.oceannetworks.ca/PlottingUtilitydata.oceannetworks.ca. Parameter data from instruments that contributed to the Sovanco earthquake event detection can be obtained from Ocean Networks Canada Society (2021). The raw acceleration waveform data from instruments that contributed to the Sovanco event shown in this article can be obtained from IRIS (Ocean Networks Canada, 2009). The raw acceleration waveform data from shared NRCan sites can be obtained from Natural Resources Canada (NRCAN Canada, 1975). Both the ONC and IRIS data archives are World Data System (https://www.worlddatasystem.org/) certified science data repositories. The TauP calculation toolkit can be accessed from IRIS (http://services.iris.edu/irisws/traveltime/docs/1/builder/).

AUTHOR CONTRIBUTIONS

AS, JK, AR, and MH contributed to conception and design of the study. AR provided the initial concept and methods. AS wrote the first draft of the manuscript. MH provided the scientific oversight. BP and JR are the projects managers and contributed to reviewing the finalized manuscript. MM contributed to reviewing the final manuscript. All authors contributed to manuscript revision, read, and approved the submitted version.

ACKNOWLEDGMENTS

We would like to thank Emergency Management BC, part of the Government of the Province of British Columbia and the Federal Government of Canada for funding the project through the Canada Safety and Security Program. This work is the result of collaborations between ONC and the Canadian Hazard Information Service (CHIS), the Canadian Geodetic Service (CGS) and the Geological Survey of Canada (GSC with staff located at the Pacific Geoscience Centre), all within the Canadian Federal Government's (Natural Resources Canada (NRCan), 1975). Additional institutions key to the success of this project include the Canadian and United States Navies; the Canadian Coast Guard; the Pacific Northwest Seismic Network (PNSN); Ocean Exploration Trust; Shared Services Canada; ProTrans; BC Hydro; the Pacheedaht First Nation; Mosaic Forest Management; various provincial and municipal authorities; Public Safety Canada; and the Defence Research and Development Department. The authors would also like to acknowledge key people inside ONC and NRCan including Paul Collins (CGS), Joe Henton (CGS), Eli Ferguson (ONC), Bob Crosby (ONC), Ryan Key (ONC), Teron Moore (ONC), and Deg Hembroff (ONC). Lastly, thank you to the numerous staff members within ONC and NRCan that were involved in installing equipment, implementing software, troubleshooting issues, and managing this large undertaking. Finally, we would like to thank the two anonymous reviewers, who provided thoughtful comments and recommendations that significantly improved the quality of this manuscript.

REFERENCES

Adams, J., Allen, T., Halchuk, S., and Kolaj, M. (2019). "Canada's 6th Generation Seismic hazard Model, as Prepared for the 2020 National Building Code of Canada," in Proceedings in: 12th Canadian Conference on Earthquake Engineering, Quebec City, June 17–20, 2019.

Aki, K., and Richards, P. G. (2002). *Quantitative Seismology*. second edition. Sausalito CA: University Science Books.

Allen, R. (1982). Automatic Phase Pickers: Their Present Use and Future Prospects. *Bull. Seismol. Soc. America* 72 (6), 225–242. doi:10.1785/bssa07206b0225

Allen, R. M., and Kanamori, H. (2003). The Potential for Earthquake Early Warning in Southern California. *Science* 300, 786–789. doi:10.1126/science.1080912

Allen, R. M., and Melgar, D. (2019). Earthquake Early Warning: Advances, Scientific Challenges, and Societal Needs. *Annu. Rev. Earth Planet. Sci.* 47, 361–388. doi:10.1146/annurev-earth-053018-060457

Barnes, C. R., and Tunnicliffe, V. (2008). "Building the World's First Multi-Node Cabled Ocean Observatories (NEPTUNE Canada and VENUS, Canada): Science, Realities, Challenges and Opportunities," in Conference proceedings in: OCEANS 2008 MTS/IEEE Kobe-Techno-Ocean, Kobe, Japan, April 8–11, 2008. doi:10.1109/OCEANSKOBE.2008.4531076

Bilek, S. L., and Lay, T. (2018). Subduction Zone Megathrust Earthquakes. *Geosphere* 14 (4), 1468–1500. doi:10.1130/GES01608.1

Bock, Y., Melgar, D., and Crowell, B. W. (2011). Real-time strong-motion Broadband Displacements from Collocated GPS and Accelerometers. *Bull. Seismol. Soc. America* 101 (6), 2904–2925. doi:10.1785/0120110007

Collins, P., Henton, J., Mireault, Y., Héroux, P., Schmidt, M., Dragert, H., and Bisnath, S. (2009). "Precise point Positioning for Real-Time Determination of Co-seismic Crustal Motion," in 22nd International Technical Meeting of the Satellite Division of the Institute of Navigation 2009, 1876–1885. ION GNSS 2009.

Crowell, B. W., Bock, Y., and Squibb, M. B. (2009). Demonstration of Earthquake Early Warning Using Total Displacement Waveforms from Real-Time GPS Networks. *Seismol. Res. Lett.* 80 (5), 772–782. doi:10.1785/gssrl.80.5.772

Crowell, B. W., Melgar, D., Bock, Y., Haase, J. S., and Geng, J. (2013). Earthquake Magnitude Scaling Using Seismogeodetic Data. *Geophys. Res. Lett.* 40 (23), 6089–6094. doi:10.1002/2013GL058391

Friedlander, B. (1987). A Passive Localization Algorithm and its Accuracy Analysis. *IEEE J. Oceanic Eng.* 12 (1), 234–245. doi:10.1109/joe.1987.1145216

Gao, D., Wang, K., Insua, T. L., Sypus, M., Riedel, M., and Sun, T. (2018). Defining Megathrust Tsunami Source Scenarios for Northernmost Cascadia. *Nat. Hazards* 94, 445–469. doi:10.1007/s11069-018-3397-6

Geng, J., Bock, Y., Melgar, D., Crowell, B. W., and Haase, J. S. (2013). A New Seismogeodetic Approach Applied to GPS and Accelerometer Observations of the 2012 Brawley Seismic Swarm: Implications for Earthquake Early Warning. *Geochem. Geophys. Geosyst.* 14 (7), 2124–2142. doi:10.1002/ggge.20144

Gillette, M. D., and Silverman, H. F. (2008). A Linear Closed-Form Algorithm for Source Localization From Time-Differences of Arrival. *IEEE Signal. Process. Lett.* 15, 1–4. doi:10.1109/LSP.2007.910324

Goldberg, D. E., Melgar, D., and Bock, Y. (2019). Seismogeodetic P-wave Amplitude: No Evidence for Strong Determinism. *Geophys. Res. Lett.* 46 (20), 11118–11126. doi:10.1029/2019GL083624

Hartog, J. R., Kress, V. C., Malone, S. D., Bodin, P., Vidale, J. E., and Crowell, B. W. (2016). Earthquake Early Warning: ShakeAlert in the Pacific Northwest. *Bull. Seismol Soc. America* 106 (4), 1875–1886. doi:10.1785/0120150261

Hembroff, D., Farrugia, J. J., Schlesinger, A., Kreimer, N., and Kulin, I. (2019). "Initial Implementation and Performance of a Cascadia Subduction Zone Earthquake Early Warning System for British Columbia," in Poster in: AGU Fall Meeting, San Francisco, California, December 9–13, 2019.

Hodgkinson, K. M., Mencin, D. J., Feaux, K., Sievers, C., and Mattioli, G. S. (2020). Evaluation of Earthquake Magnitude Estimation and Event Detection Thresholds for Real-Time GNSS Networks: Examples from Recent Events Captured by the Network of the Americas. *Seismol. Res. Lett.* 91, 1628–1645. doi:10.1785/0220190269

Huang, Y., and Benesty, J. (2000). "Passive Acoustic Source Location for Video Camera Steering," in Conference Proceedings in: Acoustics, Speech, Signal Processing International Conference, Istanbul, Turkey, June 5–7, 2000.

Hyndman, R. D., and Wang, K. (1995). The Rupture of Cascadia Great Earthquakes from Current Deformation and the Thermal Regime. *J. Geophys. Res. Solid Earth* 100 (B11). doi:10.1029/95JB01970

Kalman, R. E. (1960). A New Approach to Linear Filtering and Prediction Problems. *J. Basic Eng.* 82, 35–45. doi:10.1115/1.3662552

Küpperkoch, L., Meier, T., and Diehl, T. (2012). "New Manual of Seismological Observatory Practice (NMSOP-2) (Chapter 16)," in *Potsdam: Deutsches GeoForschungszentrum GFZ; IASPEI*. Editor P. Borman Potsdam, Germany: GFZ German Research Center for Geosciences. doi:10.2312/GFZ.NMSOP-2

Kohler, M. D., Cochran, E. S., Given, D. D., Guiwits, S., Neuhauser, D., Hensen, I., et al. (2017). Earthquake Early Warning ShakeAlert System: West Coast Wide Production Prototype. *Seismol. Res. Lett.* 89 (1). doi:10.1785/0220170140

Kohler, M. D., Smith, D. E., Andrews, J., Chung, A. I., Hartog, R., Henson, I., et al. (2020). Earthquake Early Warning ShakeAlert 2.0: Public Rollout. *Seismol. Res. Lett.* 91 (3). doi:10.1785/0220190245

Kuyuk, H. S., and Allen, R. M. (2013). A Global Approach to Provide Magnitude Estimates for Earthquake Early Warning Alerts. *Geophys. Res. Lett.* 40 (24), 6329–6333. doi:10.1002/2013GL058580

Li, X. (2015). *Real-time High-Rate GNSS Techniques for Earthquake Monitoring and Early Warning, (Doctoral Dissertation)*. Berlin, Germany: Technische Universität.

Lockman, A. B., and Allen, R. M. (2007). Magnitude-Period Scaling Relations for Japan and the Pacific Northwest: Implications for Earthquake Early Warning. *Bull. Seismological Soc. America* 97 (1B), 140–150. doi:10.1785/0120040091

McCrory, P. A., Blair, L., Oppenheimer, D. H., and Walter, S. R. (2004). *Depth to the Juan de Fuca Slab Beneath the Cascadia Subduction Margin: A 3-D Model for Sorting Earthquakes*, 91. Reston, VA: U.S. Geological Survey, 22.

Melgar, D., Bock, Y., Sanchez, D., and Crowell, B. W. (2013). On Robust and Reliable Automated Baseline Corrections for strong Motion Seismology. *J. Geophys. Res. Solid Earth* 118 (3), 1177–1187. doi:10.1002/jgrb.50135

Melgar, D., LeVeque, R. J., Dreger, D. S., and Allen, R. M. (2016). Kinematic Rupture Scenarios and Synthetic Displacement Data: An Example Application to the Cascadia Subduction Zone. *J. Geophys. Res. Solid Earth* 121, 6658–6674. doi:10.1002/2016JB013314

Melgar, D., Melbourne, T. I., Crowell, B. W., Geng, J., Szeliga, W., ScrivnerSantillan, C. M., et al. (2020). Real-Time High-Rate GNSS Displacements: Performance Demonstration during the 2019 Ridgecrest, California, Earthquakes. *Seismol. Res. Lett.* 91 (4), 1943–1951. doi:10.1785/0220190223

Moni, A., and Rickard, S. (2009). "Comparison of Localization Algorithms Using Attenuation Estimates," in Digital Signal Processing Workshop and 5th IEEE Signal Processing Education Workshop, Marco Island, Florida, January 4–7, 2009 (IEEE), 42–47. DSP/SPE 2009.

Murray, J. R., Crowell, B. W., Grapenthin, R., Hodgkinson, K., Langbein, J. O., Melbourne, T., et al. (2018). Development of a Geodetic Component for the U.S. West Coast Earthquake Early Warning System. *Seismol. Res. Lett.* 89 (6), 2322–2336. doi:10.1785/0220180162

Natural Resources Canada (NRCAN Canada). (1975). Canadian National Seismograph Network [Data set]. International Federation of Digital Seismograph Networks.

Niu, J., and Xu, C. (2014). Real-time Assessment of the Broadband Coseismic Deformation of the 2011 Tohoku-Oki Earthquake Using an Adaptive Kalman Filter. *Seismol. Res. Lett.* 85 (4), 836–843. doi:10.1785/0220130178

Ocean Networks Canada. (2009). *NEPTUNE Seismic Stations* [Data set]. International Federation of Digital Seismograph Networks.

Ocean Networks Canada Society. (2021). Collection: An Earthquake Early Warning System for Southwestern British Columbia Enables Detection of Sovanco Fracture Zone Seismic Events in 2018 (Version 1.0). Ocean Networks Canada Society.

Pirinen, T., Pertilä, P., and Visa, A. (2003). "Toward Intelligent Sensors - Reliability for Time Delay Based Direction of Arrival Estimates," in Conference Proceedings in: Acoustics, Speech, Signal Processing International Conference, Hong Kong, April 6–10, 2003, 197–200. doi:10.1109/ICASSP.2003.1199902

Pirinen, T. W. (2006). "A Lattice Viewpoint for Direction of Arrival Estimation Using Quantized Time Differences of Arrival," in Conference Proceedings in: Acoustics, Speech, Signal Processing International Conference, Toulouse, France, May 14–19, 2006.

Rosenberger, A. (2018). Observations from the September 19, 2018 Test with Titan Accelerometer and GNSS Antenna on the HERB Device. Technical Report. Victoria, BC: ONC, University of Victoria. Version 0.1. doi:10.5281/zenodo.4774346

Rosenberger, A., Banville, S., Collins, P., Henton, J., and Ferguson, E. (2018). Kalman Filter Algorithm for the Joint Processing of GNSS PPP and Accelerometer Data, EEW Parameters from the Unbiased Displacement Time-Series. Technical Report. ONC, University of Victoria. Version 0.9. doi:10.5281/zenodo.4774348

Rosenberger, A., Collins, P., Henton, J., Ferguson, E., Pirenne, B., and Schlesinger, A. (2019c). *Extensions to the WARN Associator, Integrating Magnitude Estimates Based on Parameters from Unbiased Displacements*. Version 0.4. Technical report ONC, University of Victoria. doi:10.5281/zenodo.4774315Rosenberger

Rosenberger, A., Crosby, B., Ferguson, E., Leech, B., MacArthur, M., Schlesinger, A., et al. (2019a). Epicenter Location and Association of Events from P-Wave On-Set Times, Magnitude Estimation. Technical Report. ONC, University of Victoria. Version 2.1. doi:10.5281/zenodo.4774330

Rosenberger, A., Ferguson, E., and Schlesinger, A. (2019b). Testing the Associator: Simulating Seismic Events. Technical Report. ONC, University of Victoria. Version 0.3. doi:10.5281/zenodo.4815165

Rosenberger, A. (2010). Real-time Ground-Motion Analysis: Distinguishing P and S Arrivals in a Noisy Environment. *Bull. Seismol. Soc. America* 100 (3), 1252–1262. doi:10.1785/0120090265

Rosenberger, A. (2019). Three Component Accelerometer Signal Processing for WARN. Technical Report. ONC, University of Victoria. Version 0.6. doi:10.5281/zenodo.4774354

Ruhl, C. J., Melgar, D., Chung, A. I., Grapenthin, R., and Allen, R. M. (2019). Quantifying the Value of Real-Time Geodetic Constraints for Earthquake Early Warning Using a Global Seismic and Geodetic Data Set. *J. Geophys. Res. Solid Earth* 124 (4), 3819–3837. doi:10.1029/2018JB016935

Ryan, W. B. F., Carbotte, S. M., Coplan, J., O'Hara, S., Melkonian, A., Arko, R., et al. (2009). Global Multi-Resolution Topography (GMRT) Synthesis Data Set, Geochem. *Geophys. Geosyst.* 10, Q03014. doi:10.1029/2008GC002332

Schau, H., and Robinson, A. (1987). Passive Source Localization Employing Intersecting Spherical Surfaces from Time-Of-Arrival Differences. *IEEE Trans. Acoust. Speech, Signal. Process.* 35 (8), 1223–1225. doi:10.1109/tassp.1987.1165266

Smyth, A., and Wu, M. (2007). Multi-rate Kalman Filtering for the Data Fusion of Displacement and Acceleration Response Measurements in Dynamic System Monitoring. *Mech. Syst. Signal Process.* 21, 706–723. doi:10.1016/j.ymssp.2006.03.005

Trnkoczy, A. (2012). "Understanding and Parameter Setting of STA/LTA Trigger Algorithm," in *New Manual of Seismological Observatory Practice (NMSOP-2). Potsdam: Deutsches GeoForschungszentrum GFZ; IASPEI*. Editor P. Borman. Potsdam, Germany: GFZ German Research Center for Geosciences. doi:10.2312/GFZ.NMSOP-2

Wang, K., and Tréhu, A. M. (2016). Invited Review Paper: Some Outstanding Issues in the Study of Great Megathrust Earthquakes-The Cascadia Example. *J. Geodynamics* 98, 1–18. doi:10.1016/j.jog.2016.03.010

Wang, Y., and Satake, K. (2021). Real-Time Tsunami Data Assimilation of S-Net Pressure Gauge Records during the 2016 Fukushima Earthquake. *Seismol. Res. Lett.* 92, 2145–2155. doi:10.1785/0220200447

Wurman, G., Allen, R. M., and Lombard, P. (2007). Toward Earthquake Early Warning in Northern California. *J. Geophys. Res.* 112, B08311. doi:10.1029/2006JB004830

Yamamoto, N., Hirata, K., Aoi, S., Suzuki, W., Nakamura, H., and Kunugi, T. (2016). Rapid Estimation of Tsunami Source Centroid Location Using a Dense Offshore Observation Network. *Geophys. Res. Lett.* 43 (9), 4263–4269. doi:10.1002/2016GL068169

Zumberge, J. F., Heflin, M. B., Jefferson, D. C., Watkins, M. M., and Webb, F. H. (1997). Precise point Positioning for the Efficient and Robust Analysis of GPS Data from Large Networks. *J. Geophys. Res.* 102 (B3), 5005–5017. doi:10.1029/96jb03860

Conflict of Interest: The authors declare that the research was conducted in the absence of any commercial or financial relationships that could be construed as a potential conflict of interest.

frontiers in Earth Science

ORIGINAL RESEARCH
published: 04 August 2021
doi: 10.3389/feart.2021.685879

FinDerS(+): Real-Time Earthquake Slip Profiles and Magnitudes Estimated from Backprojected Displacement with Consideration of Fault Source Maturity Gradient

Maren Böse[1]*, *Allie A. Hutchison*[1,2], *Isabelle Manighetti*[2], *Jiawei Li*[3], *Frédérick Massin*[1] and *John Francis Clinton*[1]

[1]Eidgenössische Technische Hochschule (ETH), Swiss Seismological Service (SED), Zurich, Switzerland, [2]Université Côte d'Azur, Observatoire de la Côte d'Azur, IRD, CNRS, Géoazur, Sophia Antipolis, Nice, France, [3]Southern University of Science and Technology (SUSTech), Institute of Risk Analysis, Prediction and Management (Risks-X), Shenzhen, China

OPEN ACCESS

Edited by:
Joanna Faure Walker,
University College London,
United Kingdom

Reviewed by:
Yuki Kodera,
Japan Meteorological Agency, Japan
Francesco Iezzi,
University of Studies G. d'Annunzio
Chieti and Pescara, Italy

***Correspondence:**
Maren Böse
mboese@sed.ethz.ch

Specialty section:
This article was submitted to Geohazards and Georisks, a section of the journal Frontiers in Earth Science

Received: 26 March 2021
Accepted: 02 July 2021
Published: 04 August 2021

Citation:
Böse M, Hutchison AA, Manighetti I, Li J, Massin Fé and Clinton JF (2021) FinDerS(+): Real-Time Earthquake Slip Profiles and Magnitudes Estimated from Backprojected Displacement with Consideration of Fault Source Maturity Gradient. Front. Earth Sci. 9:685879. doi: 10.3389/feart.2021.685879

The Finite-Fault Rupture Detector (FinDer) algorithm computes rapid line-source rupture models from high-frequency seismic acceleration amplitudes (PGA). In this paper, we propose two extensions to FinDer, called FinDerS and FinDerS+, which have the advantage of taking into account a geological property of the source fault, its structural maturity, as well as its relation to the earthquake slip distribution. These two new algorithms calculate real-time earthquake slip profiles by backprojecting seismic and/or geodetic displacement amplitudes onto the FinDer line-source. This backprojection is based on a general empirical equation established in previous work that relates dynamic peak ground displacement (PGD) at the stations to on-fault coseismic slip. While FinDerS projects PGD onto the current FinDer line-source, FinDerS+ allows the rupture to grow beyond the current model extent to predict future rupture evolution. For an informed interpolation and smoothing of the estimated slip values, FinDerS and FinDerS+ both employ a generic empirical function that has been shown to relate the along-strike gradient of structural maturity of the ruptured fault, the earthquake slip distribution, and the rupture length. Therefore, while FinDer derives magnitudes from a relatively uncertain and general empirical rupture length-magnitude relations, FinDerS and FinDerS+ provide alternate and better informed magnitude estimates using the mean slip of the profiles derived from the integration of fault source maturity. The two new algorithms can incorporate both seismic strong-motion and geodetic displacement data. In order to recover PGD from strong-motion instruments, we double-integrate and high-pass filter ($>$ 0.075 Hz) the seismic acceleration records. Together, the three algorithms exploit the full spectrum of ground-motions, including high frequencies to derive a source fault model (FinDer) and low frequencies to determine the static offsets along this model (FinDerS and FinDerS+). We test the three algorithms for the 2019 M_W 7.1 Ridgecrest (California), 2016 M_W 7.0 Kumamoto (Japan), and 2008 M_W 7.9 Wenchuan (China) earthquakes. Conclusively, low-frequency PGD data and integration of the fault maturity gradient do not speed-up calculations for these events, but provide additional information on slip distribution and

final rupture length, as well as alternative estimates of magnitudes that can be useful to check for consistency across the algorithm suite. The FinDer algorithms systematically outperform previously established real-time PGD-based magnitude estimates in terms of speed and accuracy. The resulting slip distributions can be useful for improved ground-motion prediction given the observed relationship between seismic radiation and fault maturity.

Keywords: earthquake early warning, seismology, earthquake, natural Hazard, earthquake magnitude, fault properties, fault maturity, rupture determinism

1 INTRODUCTION

Earthquake early warning (EEW) uses real-time data from an ongoing earthquake to provide seconds of warning to people and users prior to the arrival of strong ground motions (e.g. Allen et al., 2009; Clinton et al., 2016; Allen and Melgar, 2019). Using the earliest radiated energy, EEW systems attempt to rapidly characterize the final size of an earthquake and to predict seismic ground motions in potentially affected areas. The timing of EEW depends on multiple factors, including the speed of the earthquake fault source location and size characterization, the distance from the earthquake's source to the alert recipient, as well as delays for data transmission and processing. Different approaches exist to constrain the location and size of the ongoing earthquake, including for instance the Earthquake Point-Source Integrated Code (EPIC; Chung et al. (2019), Virtual Seismologist [VS; Cua et al. (2009)], PRobabilistic and Evolutionary early warning SysTem [PRESTo; Satriano et al. (2011)], Propagation of Local Undamped Motion [PLUM; Kodera et al. (2018)], and Finite-Fault Rupture Detector [FinDer; Böse et al. (2018)] algorithms. In addition to these regional, network-based EEW approaches, a number of faster, though less accurate, single-station onsite algorithms have been proposed (e.g. Wu et al., 2006; Böse et al., 2012a). Regional EEW algorithms differ in how they utilize the energy radiated from a growing earthquake to derive information about the source fault. EPIC, for instance, uses trilateration and a grid search to determine the earthquake location, while the magnitude is estimated from empirical scaling relations (Chung et al., 2019). FinDer generates line-source models (i.e., location, strike, and length of the fault source) from the spatial distribution of high-frequency ground motions (Böse et al., 2012b). PLUM, by contrast, does not determine the earthquake fault source properties, but simply extrapolates observed motions to larger distances (Kodera et al., 2018).

Large earthquakes provide the best opportunity to implement EEW: they are associated with long fault ruptures of tens to hundreds of kilometers in length. Since earthquake ruptures typically propagate at fairly low speed (about 2.8 km/s), warning times to affected areas can thus exceed several tens of seconds, allowing efficient EEW. In small and moderate-sized ($M < 6.0$) earthquakes, by contrast, the rupture length is short, such that the strongest shaking typically occurs in small areas around the epicenter only; to be effective, warnings would need to be issued within a few seconds or less, which is challenging and in many cases impossible. In large earthquakes, however, EEW requires rapid determination of finite-source fault dimensions (in particular of rupture length) in order to predict ground motions and warning areas as those mainly depend on the distance to the fault rupture (Böse et al., 2012b). This is even more challenging, as it is unclear how large the rupture will eventually grow. For example, Meier et al. (2017) showed that the source time functions - the rates at which energy is released from the earthquake fault source - of subduction-zone earthquakes do not deviate until they are halfway over; this implies that the earthquake's final size is not implicit until the event is 50% over. Alternatively, other studies suggest that information is contained within the first seconds to tens of seconds following the earthquake origin time, suggesting some determinism in the rupture behavior (e.g., Colombelli et al. (2014); Goldberg et al. (2018); Denolle (2019); Melgar and Hayes (2019); Hutchison et al. (2020)).

A recent study by Hutchison et al. (2020) showed that the final rupture length of an earthquake can be predicted from 20%, and its magnitude from 15% of the way through the rupture length, if the earthquake slip is known accurately and some intrinsic long-term properties of the source fault, namely its structural maturity, were considered. Structural maturity relates to the longevity of fault slip over geological time; the longer the slip history, the more mature the fault is overall (Manighetti et al., 2007). Additionally, a fault extends laterally (i.e., propagates) as it grows over the long-term (commonly, millions of years), generating a gradient in structural maturity along its length: the more mature part of the fault is where it originally initiated, while the fault becomes increasingly more immature towards its propagating tip(s) (Manighetti et al., 2001). Interestingly, as a fault or fault section becomes more mature, some of its geometrical (i.e., segment connections) and mechanical (damage compliance and possibly friction) properties evolve, and these changes impact an earthquake's behavior (Wesnousky, 1988; Manighetti et al., 2007; Perrin et al., 2016a). In particular, coseismic earthquake slip is greatest on the most mature section of the ruptured fault, generating an asymmetry in the earthquake slip-length distribution (Manighetti et al., 2005; Perrin et al., 2016a). Hutchison et al. (2020) formalized this generic relation between the along-strike fault maturity gradient and the earthquake slip asymmetry, and demonstrated that this empirical equation can be used to anticipate the final earthquake rupture length from several slip values measured in the first stages of the rupture growth, provided these slip values are accurately determined.

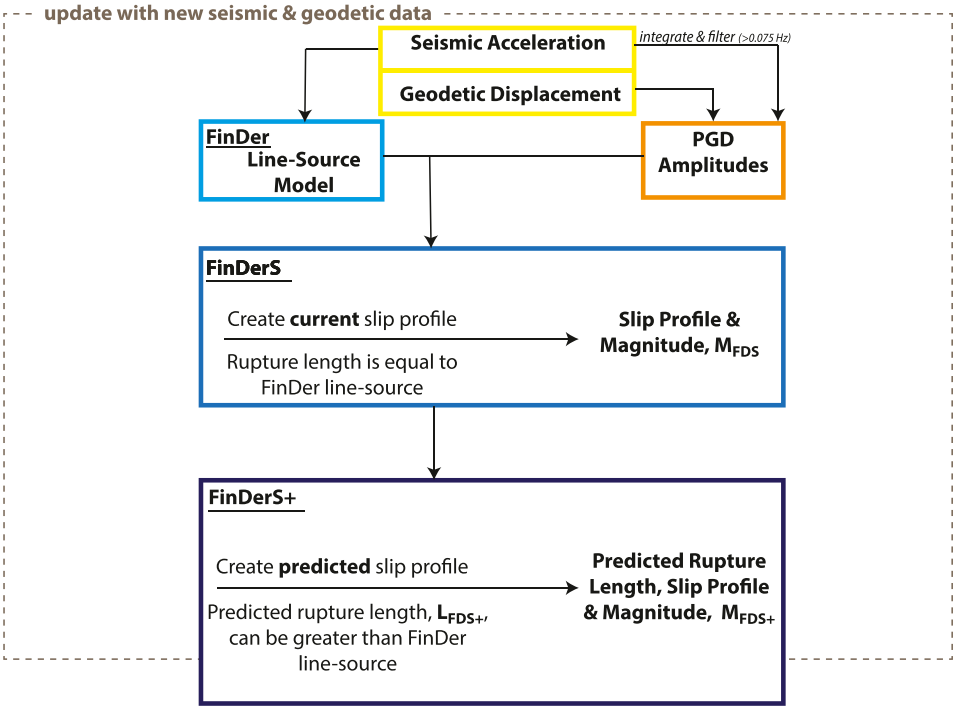

FIGURE 1 | Schematic illustration of FinDer algorithms, including the original FinDer main algorithm that computes line-source models from seismic acceleration data, and the new FinDerS and FinDerS+ algorithms (from **top** to **bottom**). FinDerS determines slip profiles by backprojecting peak ground displacement (PGD) amplitudes onto the FinDer line-source. FinDerS+ does the same, but allows the line-source to grow beyond the current FinDer model. This enables FinDerS+ to predict future rupture growth, while FinDer and FinDerS both characterize the (close to) current rupture state. PGD amplitudes are derived from integrated and high-pass (> 0.075 Hz) filtered seismic strong-motion and/or geodetic displacement records. We use a generic empirical equation derived in Hutchison et al. (2020) for an informed interpolation and smoothing of slip values. The two new algorithms provide alternate magnitude estimates that are based on seismic slip, while FinDer magnitudes are computed from the length of the line-source estimate. Together, the three algorithms exploit the full spectrum of ground-motions, including high frequencies to derive a source model (FinDer) and low frequencies to determine the static offsets along this source (FinDerS and FinDerS+).

However, the study of Hutchison et al. (2020) was done on final static earthquake slip profiles, that is, the time required to reach and to calculate final displacements is neglected. Furthermore, the slip profiles are accurate as they were measured in the field or remote data right after the earthquakes. Here, we explore the application of the algorithm in a retrospective study by simulating the real-time streams of seismic and geodetic data in a regional network recording a growing earthquake. In order for this to operate, it is necessary that we can generate an earthquake slip profile in real-time. This requires two pieces of information: 1) a finite-source model that characterizes the spatial dimensions (i.e., location, length) and orientation (i.e., strike) of the fault source and that updates in real-time based on the growing available data, and 2) a real-time estimated slip distribution along this source model. For the first element, we utilize in this study the line-source models computed from the Finite-Fault Rupture Detector (FinDer) algorithm (Böse et al., 2012b, 2015, 2018). For the second element, we utilize an empirically-based algorithm (Aagaard et al., 2004; Yamada, 2007) that backprojects dynamic peak ground displacement (PGD) amplitudes from individual stations onto this source model to determine slip (FinDerS, FinDerS+).

We test the FinDer algorithms here on three earthquakes for which available data are dense enough: the 2019 M_W 7.1 Ridgecrest, California, the 2016 M_W 7.0 Kumamoto, Japan, and the 2008 M_W 7.9 Wenchuan, China, earthquakes.

2 METHODS

The three FinDer algorithms presented in this paper exploit the full spectrum of seismic ground-motions (**Figure 1**): FinDer (Böse et al., 2012b; Böse et al., 2015; Böse et al., 2018) derives a line-source model from high-frequency amplitudes; FinDerS and FinDerS+ determine the static offsets along this model from low-frequency displacement. FinDerS and FinDerS+ both estimate slip profiles along the source fault by backprojecting dynamic displacement (PGD) amplitudes onto the FinDer source model. However, while FinDerS projects PGD onto the current line-source, FinDerS+ allows the rupture to grow beyond the current model to predict future rupture evolution. For an informed interpolation and smoothing of the estimated slip values, FinDerS and FinDerS+ both employ the generic empirical relationship developed by Hutchison et al. (2020) that relates the along-strike gradient of long-term structural maturity of the ruptured fault to the coseismic slip distribution along the rupture. With both PGA and PGD changing over time,

estimates from FinDer, FinDerS, and FinDerS+ are continuously updated. Each of these processes is described in more detail in the following.

2.1 FinDer: Current Rupture Line-Source Model and Magnitude, M_{FD}

The Finite-Fault Rupture Detector (FinDer) algorithm (Böse et al. (2012b), Böse et al. (2015), Böse et al. (2018)) provides rapid earthquake line-source models, that describe the position, length (LFD) and strike of a fault rupture. These parameters are computed from the spatial distribution of high-frequency PGA amplitudes recorded across a dense seismic network. Using template matching, FinDer compares these motions with theoretical spatial PGA templates, which are calculated from an empirical ground-motion model (here: Cua and Heaton (2009)) derived from worldwide earthquake data with different magnitudes, rupture lengths, and source mechanisms. The best template and resulting FinDer line-source model is found from a combined grid-search and divide-and-conquer approach (Böse et al., 2018). The FinDer magnitude, MFD, is estimated from a selected empirical rupture length-magnitude relation [typically Wells and Coppersmith (1994)]. Comparing different relationships (Wells and Coppersmith, 1994; Blaser et al., 2010; Leonard, 2014) suggest that the resulting magnitude estimates have an uncertainty of about +/−0.3 magnitude units.

2.2 FinDerS: Slip Profile and Magnitude, M_{FDS}

FinDerS ("S" stands for slip) determines 1D slip profiles from the backprojection of PGD amplitudes onto the FinDer line-source. The backprojection is done by employing a general empirical equation developed by Yamada (2007) and Aagaard et al. (2004) from worldwide earthquake data and simulations. This equation relates the seismic slip (or static offset), D, to the dynamic PGD amplitudes measured at closest distance, R, of the surface projected rupture

$$D = \frac{PGD\sqrt{1 + 0.125R^{1.55}}}{0.7} \tag{1}$$

where D and PGD are in cm and R in km. According to **Eq. 1** the dynamic PGD is approximately 2/3 of the static slip along the ruptured fault. As originally proposed by Böse et al. (2013), we apply **Eq. 1** here to dynamically backproject PGD observations (i.e. backproject the time-dependent data) onto the FinDer line-source, which will also evolve and grow over time. Here, the FinDerS slip profile has, at each time step, the length of the FinDer line-source model. We only backproject PGD from stations within a certain distance to the fault (here: R < 30 km, R < 60 km, and R < 90 km, respectively).

Then, to interpolate and smooth the estimated backprojected slip values, FinDerS employs the empirical relationship developed in Hutchison et al. (2020) that relates the along-strike gradient of long-term structural maturity of the ruptured fault to the coseismic slip distribution along the rupture. This equation solves for D at any given point along the rupture, l, up to length L using a least squares fitting technique:

$$D(l) = \frac{3D_{peak}l^q}{L^{2q}}\left(L^{2q} - l^{2q}\right)^{3/4} \tag{2}$$

where D_{peak} and q represent amplitude and skewedness of the slip profile, respectively. These are interdependent variables that change with each other. See Hutchison et al. (2020) for details.

Finally, as described in Hutchison et al. (2020), we estimate the (moment) magnitude from the profile average slip value, D_{mean}, and the rupture length, L, at each time step:

$$M \approx \frac{2}{3}\log_{10}\left(2LD_{mean} * 10^7\right) + 1 \tag{3}$$

Since FinDerS is based upon the FinDer line-source, L corresponds in **Eqs. 2**, **3** to L_{FD}. The resulting magnitude is named M = M_{FDS}. Since both the FinDer line-source and PGD evolve over time, **Eqs. 1**–**3**) are dynamically recomputed.

2.3 FinDerS+: Predicted Final Rupture Length, Slip Profile and Magnitude, M_{FDS+}

As opposed to FinDerS, which fits the slip profile to the current FinDer line-source, FinDerS+ does not restrict the final rupture length and allows the FinDer-determined fault rupture to continue growing towards both directions up to a maximum reasonable rupture length, which we here set to 500 km (Manighetti et al., 2007). The slip values are determined as in FinDerS, by backprojection of PGD amplitudes. Then, as for FinDerS, FinDerS+ interpolates the slip values by using **Eq. 2**, where L = L_{FDS+} (same in **Eq. 3**). Again, FinDerS+ estimates are updated over time. From the slip profiles derived at each step, FinDerS+ predicts the final rupture length, the final slip distribution, and the final magnitude, M = M_{FDS+}.

2.4 PGD-Based Magnitude, M_{PGD}

Throughout this paper, we will compare the magnitude results of the three FinDer algorithms to estimates obtained from more simple, previously established PGD-magnitude scaling relationships of the form

$$M_{PGD} = \left(\log(PGD) - A\right)/\left(B + C\log(R)\right) \tag{4}$$

where R is the distance in km between the earthquake hypocenter and the station at which the PGD is observed. We are testing here three sets of coefficients published by various authors: 1) A = −5.919, B = 1.009, C = −0.145 (Ruhl et al., 2019); 2) A = −4.434, B = 1.047, C = −0.138 (Melgar et al., 2015), and 3) A = −6.687, B = 1.5, C = −0.214 (Crowell et al., 2016), respectively. PGD, here defined as $PGD = max\sqrt{E(t)^2 + N(t)^2 + Z(t)^2}$ (with E, N, and Z the East, North and vertical displacement components), is in cm for Melgar et al. (2015) and Crowell et al. (2016) and in m for Ruhl et al. (2019). The regression for the three coefficients A, B, and C was done with different global GNSS datasets of continental and subduction-zone earthquakes (Ruhl et al., 2019). We name the three resulting PGD-based magnitudes M_{PGD}^{Melgar}, $M_{PGD}^{Crowell}$, and M_{PGD}^{Ruhl}, respectively.

TABLE 1 | Source parameters and final FinDer line-source parameters for the M_W 7.1 Ridgecrest (California), M_W 7.0 Kumamoto (Japan), and M_W 7.9 Wenchuan (China) earthquakes.

Name	Origin time [UTC]	Latitude [degrees]	Longitude [degrees]	Depth [km]	MW	Approx. rupture length and duration [km] [s]	Source mechanism	Final FinDer linesource parameters • Time from origin [s] • Length [km] • Strike [degrees] • lat1/lon1 • lat2/lon2
Ridgecrest	2019-07-06 03:19:53	35.770	−117.599	8	7.1	50 20	Strike-slip	• 26 • 53 • 145 • 35.92/−117.73 • 35.53/−117.40
Kumamoto*	2016-04-15 16:25:06	32.791	130.754	10	7.0	40 (65) 15	Strike-slip and normal	• 36 • 85 • 30 • 32.61/130.81 • 33.27/131.26
Yufuin*	2016–04–15 16:25:39	33.266	131.340	5	5.7–6.5		Normal and strike-slip	
Wenchuan	2008–05–12 06:28:01	31.002	103.322	19	7.9	300 100	Thrust and strike-slip	• 124 • 290 • 50 • 31.24/103.33 • 32.92/105.69

**Secondary (triggered) event.*

2.5 Magnitude from Seismic Moment-Rate Function, M_{mr}

Finally, we will compare all magnitude estimates to the moment-rate function-derived magnitude, M_{mr}. To determine M_{mr} at time t relative to the rupture nucleation time, we use the moment magnitude definition of Hanks and Kanamori (1979), $M_{\mathrm{mr}}(t) = \frac{2}{3}(\log_{10}(m_0(t)) - 9.1)$, where the seismic moment at time t is $m_0(t) = \int_0^t \dot{M}_0(t)dt$ and $\dot{M}_0$ is the moment-rate function, which we here take from the US Geological Survey (USGS) finite-fault database.

3 DATA AND PREPROCESSING

3.1 Earthquakes

We will demonstrate our suite of FinDer algorithms for three continental earthquakes: the 2019 M_W 7.1 Ridgecrest earthquake with a right-lateral slip, the 2016 M_W 7.0 Kumamoto earthquake with a dominant right-lateral and additional normal slip, and finally the 2008 M_W 7.9 Wenchuan earthquake that had a right lateral and reverse slip (**Table 1**). We select these earthquakes mainly because of their availability of seismic (and in the cases of Ridgecrest and Kumamoto of geodetic) data, and their large rupture sizes (M_W 7.0+). As will be shown later, the slip distributions of the three earthquakes show the generic asymmetry encapsulated in the empirical equation from Hutchison et al. (2020) (**Eq. 2**), even though the surface slip data for the Kumamoto earthquake are few. This means that the gradient of maturity along the three ruptured faults can be derived from the empirical **Eq. 2**. Furthermore, the performance of the FinDer algorithm, although for older code versions, has been demonstrated and documented for these three events in previous studies (Böse et al., 2018; Chung et al., 2020; Li et al., 2020). Finally, the empirical equation from Hutchison et al. (2020) has been previously applied to the static slip distribution of the Wenchuan earthquake. It demonstrated a very good performance on the magnitude prediction (from the rupture start), and modest results on the length prediction (from ~ 50% throughout the rupture), due to large displacements over the first 100 km of the rupture.

The July 5, 2019 M_W 7.1 Ridgecrest earthquake ruptured a major NW-trending right-lateral fault in the eastern California shear zone, along with many secondary subparallel faults, and others of sub-perpendicular orientation (Milliner and Donnellan, 2020). The earthquake produced strong shaking with up to Modified Mercalli Intensity (MMI) IX in the epicentral area, and was felt in large parts of southern California and Nevada (e.g. Barnhart et al., 2019). The earthquake mainly produced a NW-SE surface rupture of ~ 50 km (Hudnut et al., 2020; Milliner and Donnellan, 2020) and a maximum coseismic slip of ~ 4.5 m at surface, located in the northernmost part of the fault, close to the epicenter (Wang and Bürgmann, 2020). Most slip occurred at shallow depths of less than 10 km (Barnhart et al., 2019). The slip-length profile revealed to be asymmetric, with greatest slip to the north (Milliner and Donnellan, 2020). While the overall maturity of the fault ruptured in the Ridgecrest earthquake has not been described in prior works, neighboring, similar faults in the

eastern California shear zone have been shown to be immature (Perrin et al., 2016a). Furthermore, according to (Perrin et al., 2016b), the structure of the Ridgecrest fault zone, with a dense network of diverging splays at its southern tip, suggests that the fault is more mature to the north, in keeping with the asymmetry of the Ridgecrest earthquake slip profile.

The M_W 7.0 Kumamoto earthquake of April 16, 2016, ruptured at least ~40 km (at surface) of the NE-trending Futugawa fault, including its southern Hinagu splay (Shirahama et al., 2016; Scott et al., 2018; Milliner et al., 2020). The rupture length at depth is likely longer, up to ~65 km (Uchide et al., 2016). The earthquake accommodated mainly right-lateral slip, yet with an additional small normal component (Shirahama et al., 2016). A maximum dextral slip of about 3.2 m was measured at the ground surface (Shirahama et al., 2016; Milliner et al., 2020), while the rupture also produced ~1.5 m of vertical slip (Milliner et al., 2020). The total largest slip at surface might thus be about 3.5 m. The largest slip occurred in the northeastern part of the ruptured fault (Shirahama et al., 2016; Milliner et al., 2020), reaching about 6–7 m at 4–5 km depth (Uchide et al., 2016; Milliner et al., 2020). The strong directivity of the Kumamoto event is thought to have dynamically triggered a second event close to Yufuin, approximately 80 km to the NE relative to the mainshock epicenter (Uchide et al., 2016; Yoshida, 2016). This event might have ruptured about 20 km of fault length, north of its epicenter, in the same overall fault zone as the mainshock (Uchide et al., 2016). Because of the difficulty to isolate its waveforms from those of the mainshock, the magnitude of this secondary event has various estimates: M5.7 (Japanese Meteorological Agency, JMA), M6.0 (Yoshida, 2016), and M6.5 (Uchide et al., 2016). Like the Kumamoto mainshock, the Yufuin event has a dominant right-lateral slip, and is thought to have occurred ~30 s after the onset of the Kumamoto event (Uchide et al., 2016; Yoshida, 2016). We include the location of this event in our analysis (**Table 1**), since the wave trains for the two events are nearly indistinguishable and affect our results. The overall structural maturity of the Futugawa fault is unknown, but its architecture with fan-splays at its western tip suggests that it might be more mature to the northeast (Perrin et al., 2016b), in keeping with the earthquake slip asymmetry.

The M_W 7.9 Wenchuan earthquake on May 12, 2008 produced seismic intensities of up to XI on the MMI scale (Chen and Booth, 2011). The event primarily ruptured the NE-trending Beichuan fault with a dextral and reverse slip, along with the adjacent Pengguan reverse fault, both within the Longmenshen fault zone. The total rupture length was about 280 km, while the earthquake produced 12–13 m of slip at the ground surface. The largest slip occurred in the southwest, close to the epicenter (Shen et al., 2009; Perrin et al., 2016a). The earthquake slip profile is markedly asymmetric with slip tapering from the SW to the NE (Shen et al. (2009); Perrin et al. (2016a)). The fault has been described as of intermediate maturity, with a gradient of maturity decreasing towards NE (Perrin et al., 2016a).

3.2 Data Preprocessing

For the Ridgecrest earthquake, we use strong-motion data from the Southern California Seismic Network (SCSN), as well as preprocessed 1-Hz displacement time series from 10 GNSS stations from the Geodetic Facility for the Advancement of Geoscience (GAGE) Network of the Americas (NOTA) that were obtained through UNAVCO (Mattioli et al., 2020). For the Kumamoto earthquake, we use strong-motion records from both KiK-net and K-NET stations, as well as preprocessed GEONET Global Positioning System time series downloaded from Ruhl et al. (2019). For the Wenchuan earthquake, we use strong-motion records obtained through the China Strong Motion Networks Center (CSMNC) at the Institute of Engineering Mechanics, China Earthquake Administration. These records start 20 s before the P-wave arrival. As described in Li et al. (2020) we reconstruct absolute times from the event location and origin time (**Table 1**) and align in each record the theoretical and observed P-wave arrivals assuming vp = 6.1 km/s. **Figure 2** shows the distributions of seismic and geodetic sensors used in this study along with the final FinDer line-source models (**Table 1**) for the Ridgecrest, Kumamoto, and Wenchuan earthquakes at 26 s, 36 s, and 124 s from origin times, respectively.

While the FinDer line-source models are recovered directly from the high-frequency strong-motion data (Böse et al., 2018), the slip values are computed from the backprojected dynamic displacement amplitudes using **Eq. 1**. Following Yamada (2007; page 45), we determine the maximum peak ground displacement at each seismic/geodetic station as $PGD = max(PGD_Z, \sqrt{PGD_E^2 + PGD_N^2})$, where PGD_Z, PGD_N, and PGD_E are the peak ground displacement amplitudes along the vertical, north and east components, respectively.

Recovering displacement from strong-motion recordings is generally challenging and will be discussed further in later sections. We are doing the following: first, we cut all strong-motion waveforms so that they begin at the origin time, t_0. Then we calculate and remove the background median noise of each waveform by determining the median amplitude between the start time of the waveform and the arrival of the P-wave and subtracting this median value from the entire waveform. At this stage, we also detrend the data, removing the change in the mean as it changes over time. We do not apply a taper, which would artificially decrease the amplitudes at the edges of the time window. Next, we double-integrate the waveforms to obtain displacements and apply a 4th order high-pass causal butterworth filter with a cutoff-frequency of 0.075 Hz (Yamada, 2007). This filter is made to reduce long period noise artifacts that are typically induced when integrating accelerograms due to the lack of sensitivity of an accelerometer to longer periods. High-pass filtered PGDs are typically smaller than true PGDs (Yamada, 2007). We only use PGD data from seismic stations at perpendicular fault rupture distances of up to a certain distance (here 30 km, 60 km, and 90 km relative to the FinDer line-source). We remove stations that backproject off the line-source. This means the list of stations used is updated with every new solution, as the line-source geometry is constantly changing over time.

The GNSS data for Ridgecrest and Kumamoto is already preprocessed with a precise-point-positioning (PPP) algorithm

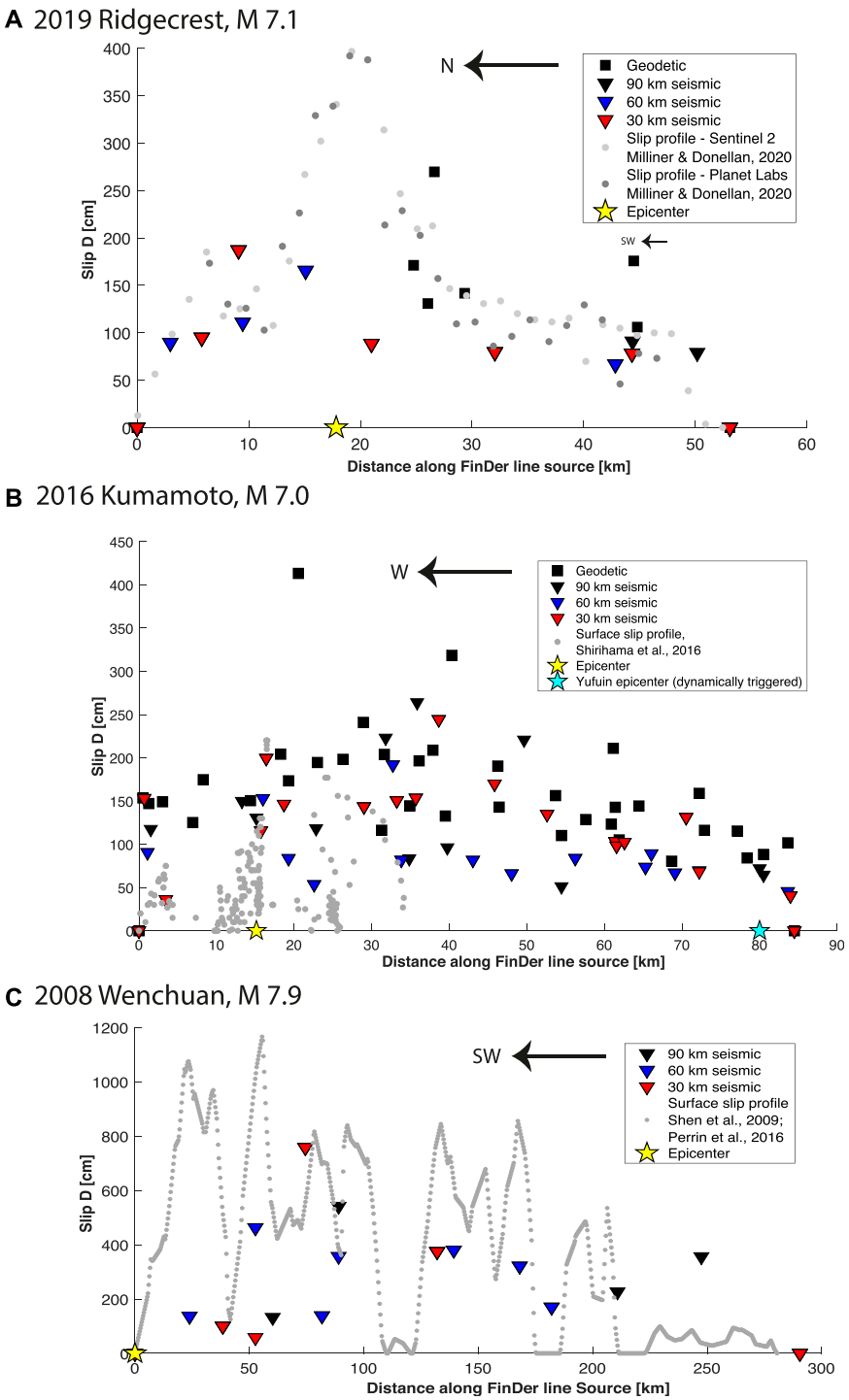

FIGURE 2 | Maps showing earthquake epicenters (stars), seismic strong-motion and geodetic GNSS stations (triangles and squares, respectively), and FinDer line-source models (black lines) for the a) M_W 7.1 Ridgecrest, California, b) M_W 7.0 Kumamoto (and Yufuin), Japan, and c) M_W 7.9 Wenchuan, China, earthquakes. The line-source models were calculated from seismic waveform playback and correspond to the final FinDer solutions at 26, 36, and 124 s, respectively (**Table 1**). Color of station markers shows their respective distance range relative to the FinDer line-source.

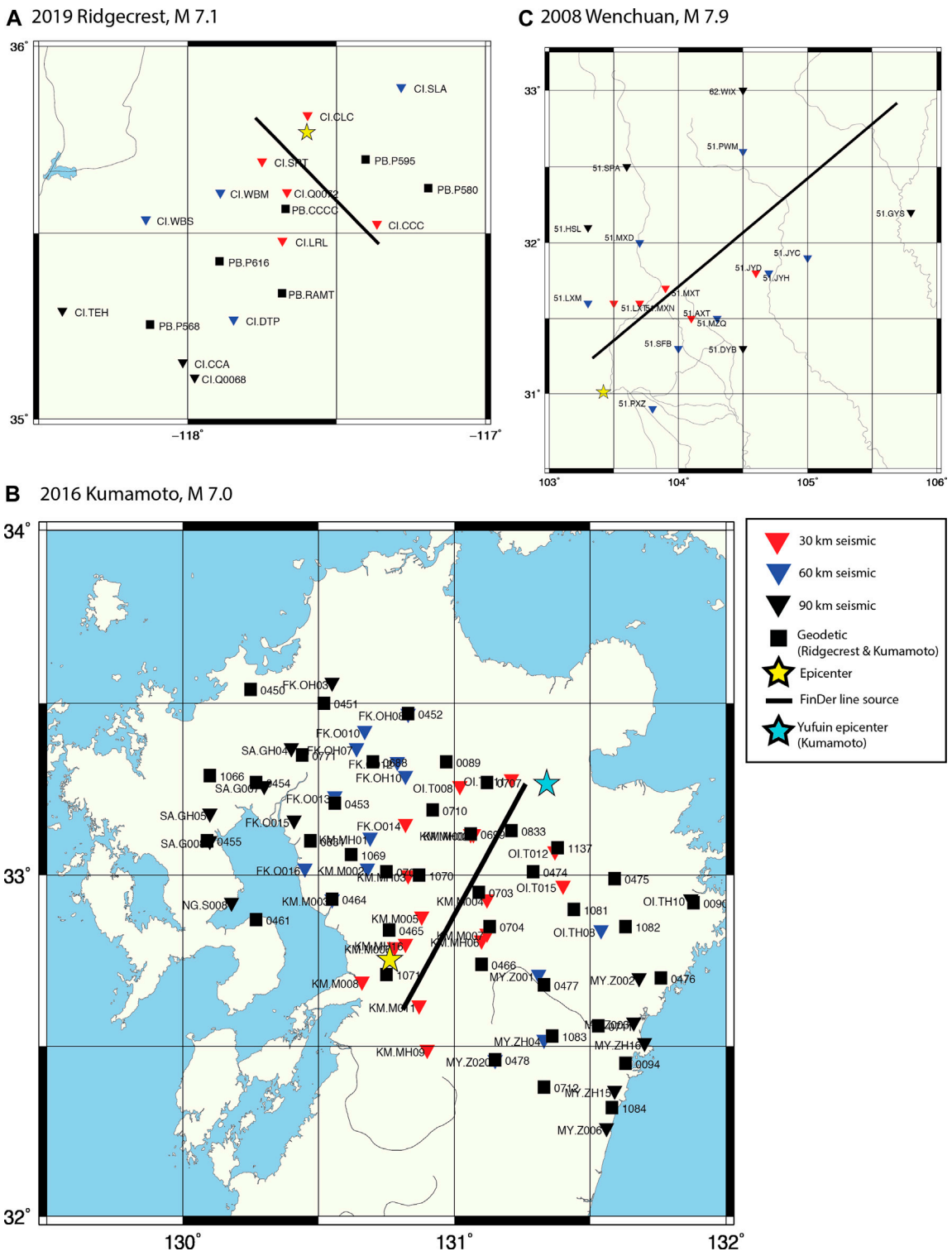

FIGURE 3 | Peak ground displacement (PGD) amplitudes recovered from high-pass filtered seismic and geodetic recordings of the Ridgecrest, Kumamoto, and Wenchuan earthquakes, sorted as a function of the closest distance to the final FinDer line-source. Values are listed in **Supplementary Table 1** (**Supplementary Material**). Seismic (triangles) and geodetic (squares) PGD values generally agree well. In the new FinDerS and FinDerS+ algorithms we backproject the time-varying PGD amplitudes onto the evolving FinDer line-source to estimate seismic slip profiles at any given time through the rupture.

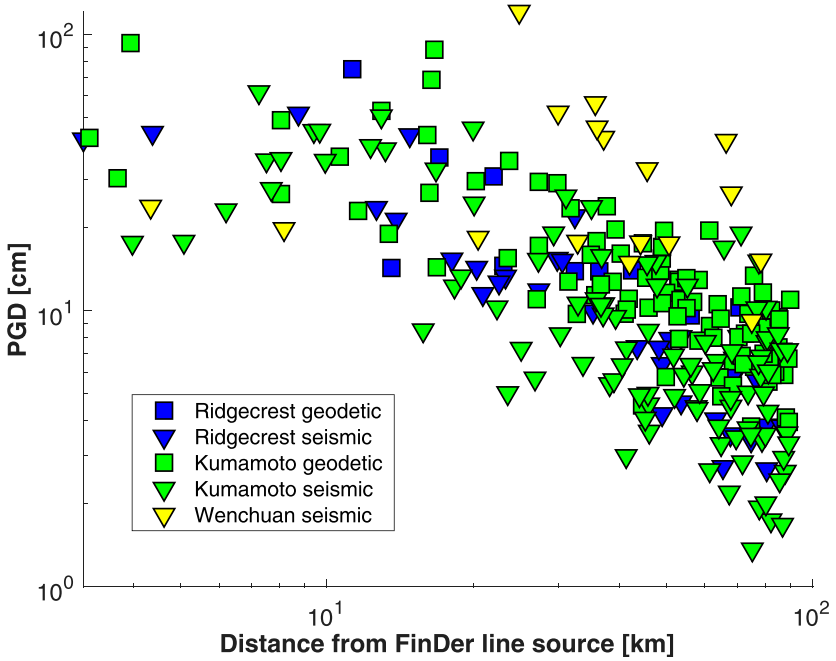

FIGURE 4 | Fault slip, D, estimated from the backprojection of final PGD amplitudes onto the final FinDer line-source (**Figure 2**) for the a) Ridgecrest, b) Kumamoto, and c) Wenchuan earthquakes. Gray dots show surface slip profiles published by various authors as given in the legends. For Ridgecrest and Kumamoto, the published values show lateral slip, while for Wenchuan, they show net slip. Note that the backprojected slip values and epicenters are relative to the respective FinDer line-source model, oriented as indicated on the plots.

and in displacement (Ruhl et al., 2019; Mattioli et al., 2020), so we do not apply any filters. We simply detrend the data and, like the seismic data, we remove the pre-event median of the data by calculating the median amplitude between the start time of the waveform and the arrival of the P-wave, assuming vp = 6.1 km/s, and subtracting this value from the entire waveform. We use all geodetic stations within 100 km from the FinDer line-source regardless of the seismic threshold we are testing (30 km, 60 km, 90 km). We remove again stations that backproject onto the tips of the FinDer line-source.

The resulting displacement waveforms are shown in the Supplementary Material of this paper (**Supplementary Figures 2A–4**). The extracted final PGD amplitudes from the preprocessed seismic and geodetic waveforms are summarized in **Supplementary Table 1** (**Supplementary Material**) and plotted in **Figure 3**. As expected the amplitudes decay as a function of distance from the (final) FinDer line-source with values of about 1 m close to the rupture and of a few cm at about 100 km distance. PGD amplitudes extracted from seismic and GNSS recordings generally agree well.

4 RESULTS

4.1 Static Application: Final Rupture Lengths and Slips

Figure 4 shows the backprojection results of final dynamic PGD amplitudes onto the final FinDer line-source models (**Table 1**) compared to measured surface slip profiles available in the literature. Even though **Eq. 1** has been calibrated with the slip at depth, for a steep-dipping fault (as examined here) the results should provide a first-order approximation of surface slip. As shown in (Manighetti et al., 2005), the general (oblique-triangular) pattern of the slip profiles, which we take advantage of in **Eq. 2**, persists at depth.

For Ridgecrest (**Figure 4A**), we compare backprojected values with surface slip values derived from subpixel correlation of high-resolution optical imagery from two different satellites (Milliner and Donnellan, 2020). The backprojected seismic and geodetic slip values follow the overall distribution of surface slip along strike, though, the maximum slip value identified by Milliner and Donnellan (2020) of ~ 400 cm, is not matched neither by the backprojected geodetic nor seismic data, where the maximum slip value is ~ 270 cm. Consistent with the inference of Milliner and Donnellan (2020), the closest stations which best constrain the slip suggest that largest displacements occurred in the northern part of the rupture.

For Kumamoto (**Figure 4B**), the rupture trace observed at the ground surface was only ~ 40 km long (Shirahama et al., 2016; Scott et al., 2018; Milliner et al., 2020), while the rupture at depth was likely longer, ~ 65 km (Uchide et al., 2016). The final FinDer line-source is estimated as ~ 84 km long, that is 20 km longer than the likely rupture length. This is because the model integrates both the mainshock and the subsequent triggered Yufuin event towards the NE, and also because it slightly overshoots the rupture towards the SW relative to the

epicenter, possibly because of FinDer's simplified line-source approximation. We can thus only compare backprojected slip values with the first ~ 40 km of the FinDer line-source. Here, we compare our values with horizontal surface slip values measured at the surface by Shirahama et al. (2016). Like for the Ridgecrest earthquake, the slip values compare quite well, particularly for stations closer than 60 km to the rupture. Overall, as observed in the field, they suggest a slip increase towards the NE over the considered 40 km length.

For Wenchuan (**Figure 4C**) backprojected slip values also compare quite well with the surface slip profile measured in the field. Like in the other events, however, the maximum backprojected slip values (~ 8 m) never reach the surface slip values reported in the literature (~ 12 m). At the beginning of the slip profile, that is near the hypocenter, the backprojected slip values are notably lower than the measured surface slip. This may in part be due to limited station coverage, as there are only two stations within the first 50 km of the rupture. However, overall, the largest slip is well located to the SW of the rupture, as observed in the field.

In all three earthquakes, we note that the backprojected slip tends to under-estimate the actual surface slip. In general, there is no clear distance range of stations (here: 30 km, 60 km and 90 km from the line-source model) that works best for the backprojection, but stations less than 60 km from the line-source provide slip values in closer agreement with those in the literature. Therefore, in the subsequent analyses we will select the 60 km station cutoff for further demonstration of our approach. Results for the other two cutoffs are shown in the **Supplementary Material** (**Supplementary Figures 5, 6**).

4.2 Dynamic Application: Evolving Ruptures and Slips

For the dynamic application of the three FinDer algorithms (**Figure 1**) we run playbacks for the three earthquakes using the preprocessed seismic and geodetic waveform records (see **Section 3.2**) to emulate the evolution of possible output of FinDer, FinDerS, and FinDerS+ over time using the respectively available information (even if final peak values have not yet been reached). **Table 2** summarizes the results (here with parameters being updated every 5 s even though a higher resolution is possible), while **Figures 5–7** illustrate the results at some selected time steps. **Figure 8** compares the evolution of estimated magnitudes for the various approaches.

For simplicity we neglect data latencies, which typically are on the order of 1–2 s for a fast seismic network (e.g. Behr et al., 2015).

Details on the FinDer results for the three earthquakes are given in Böse et al. (2018), Chung et al. (2020), and Li et al. (2020). Due to the FinDer trigger settings applied in this study, which requires the P-wave to have reached at least 4 neighbouring stations, FinDer triggers in this retrospective study 8 s after t_0 for Ridgecrest, 4 s for Kumamoto, and 13 s for Wenchuan. FinDerS and FinDerS+ require PGD data from at least three stations (and the FinDer line-source model), and results from these two algorithms are typically given a bit later (**Table 2**).

4.2.1 Playback Results for M_W 7.1 Ridgecrest

For the M_W 7.1 Ridgecrest earthquake (**Figure 5** and **Table 2**) FinDer triggers 8 s after t_0 (Chung et al., 2020) and gives a rupture length of 29 km at 15 s, and of 45 km at 20 s. The final rupture length and magnitude at 30 s are estimated as L_{FD} ~ 53 km and M_{FD} 6.9, respectively. These values are in excellent agreement in terms of both length and orientation with the 54 km-long rupture determined through high-resolution optical imagery (Milliner and Donnellan, 2020). The performance of FinDerS closely follows that of FinDer, but provides an independent and more informed estimate of the magnitude as the latter is derived from the average slip resulting from backprojection and interpolation with the maturity gradient-based empirical relation (**Eq. 2**). We note, however, that the backprojected slip is significantly under-estimated. Furthermore, the slip profile fit of FinDerS is somewhat symmetric (**Figure 5**), likely due to the rupture length being fixed to the FinDer line-source determination. As a matter of fact, FinDerS+ best reproduces the asymmetry of the slip profile and produces higher performance in terms of magnitude. However, FinDerS+ over-estimates the rupture length, probably as a result of the under-estimated slip.

4.2.2 Playback Results for M_W 7.0 Kumamoto

For the M_W 7.0 Kumamoto earthquake (**Figure 6** and **Table 2**) FinDer triggers 4 s after t_0 (Böse et al., 2018). We show in **Figure 6** only the results until 25 s, because just after 30 s the dynamically triggered M ~ 6 Yufuin earthquake at ~ 80 km distance starts and may contaminate the results from FinDer, FinDerS, and FinDerS+. However, in **Table 2** we show results of all the algorithms until they stabilize at ~ 40 s.

FinDerS+ performs very similarly to FinDerS, which indicates a well-formed slip profile resulting from a good station coverage, which does not leave much room for fitting a longer rupture in FinDerS+. Notably, despite the over-estimated rupture length, the maximum slip values are fairly consistent with observed surface slip values (Shirahama et al., 2016), particularly in the earliest time windows.

4.2.3 Playback Results for M_W 7.9 Wenchuan

FinDer triggers 13 s after t_0 for the MW 7.9 Wenchuan earthquake (Li et al., 2020). FinDer performs quite well (**Figure 7** and **Table 2**), nearly predicting the magnitude (M_{FD} 7.8) correctly 50% of the way through the event duration (**Figure 7C**). The final magnitude prediction (M_{FD} 8.0) is only slightly larger than the true magnitude.

The backprojected slip values are significantly under-estimated, by a factor of 3–6. With such poor slip estimates, we cannot expect that FinDerS and FinDerS+ perfom well. FinDerS, using the FinDer rupture length, performs less well than FinDer for magnitude, never arriving at the cataloged final value, M_W 7.9. FinDerS+, however, performs somewhat better in terms of magnitude, at least in the middle time steps, with M_{FDS+} 7.7 at 45 s, compared to M_{FDS} 7.3 (**Figure 7B**). This, however, results from an over-prediction of the final rupture length, where at 45–85 s, the predicted final rupture length for FinDerS+ is 500 km (our theoretically allowed maximum value), showing that

TABLE 2 | Results from FinDer (rupture length, L_{FD}, and magnitude, M_{FD}), FinDerS (mean slip, Dmean, and magnitude, M_{FDS}, both from fitted slip profile) and FinDerS+ (predicted final rupture length, L_{FDS+}, predicted final mean slip, mean, and predicted final magnitude, M_{FDS+}) for the a) Ridgecrest, b) Kumamoto, and c) Wenchuan earthquake as a function of time from origin for a 60 km station distance cutoff. Magnitudes Mmr and M_{PGD} are estimated from the USGS moment rate function and empirical PGD-distance relationships (Melgar et al., 2015; Crowell et al., 2016; Ruhl et al., 2019), respectively. Table shows updates in increments of 5 s.

Time from origin [s]

	Moment Rate	FinDer (current line-source)		FinDerS (current slip profile)		FinDerS+ (predicted slip profile)			PGD scaling (M_{PGD})					
	M_{mr}	L_{FD} [km]	M_{FD}	D_{mean} [m]	M_{FDS}	L_{FDS+} [km]	D_{mean} [m]	M_{FDS+}	$M_{PGD}^{Crowell}$	$M_{PGD}^{Crowell\ GNSS}$	M_{PGD}^{Melgar}	$M_{PGD}^{Melgar\ GNSS}$	M_{PGD}^{Ruhl}	$M_{PGD}^{Ruhl\ GNSS}$
a) Ridgecrest earthquake														
5	6.1	(first solution at 8s)	(first solution at 8s)	—	—	—	—	—	5.4	—	5.4	—	5.0	—
10	6.8	7	5.6	—	—	—	—	—	6.0	6.2	5.9	6.1	5.7	5.8
15	6.9	29	6.5	0.5	6.6	30	0.4	6.6	6.5	6.7	6.5	6.7	6.3	6.5
20	7.0	45	6.8	0.7	6.8	75	0.6	6.9	6.6	6.8	6.6	6.8	6.4	6.6
25	7.0	45	6.8	0.8	6.9	91	0.6	7.0	6.7	6.8	6.6	6.8	6.4	6.6
30	7.0	53	6.9	0.8	6.9	239	0.5	7.3	6.8	6.9	6.7	6.9	6.4	6.7

b) Kumamoto earthquake

	M_{mr}	L_{FD} [km]	M_{FD}	D_{mean} [m]	M_{FDS}	L_{FDS+} [km]	D_{mean} [m]	M_{FDS+}	$M_{PGD}^{Crowell}$	$M_{PGD}^{Crowell\ GNSS}$	M_{PGD}^{Melgar}	$M_{PGD}^{Melgar\ GNSS}$	M_{PGD}^{Ruhl}	$M_{PGD}^{Ruhl\ GNSS}$
5	6.6	5	5.4	0.1	5.4	—	—	—	5.4	4.9	5.4	4.5	5.0	4.2
10	6.9	39	6.7	0.1	6.2	40	0.1	6.3	6.0	6.0	5.9	5.8	5.7	5.5
15	7.0	62	7.0	0.3	6.7	63	0.3	6.7	6.5	6.6	6.5	6.6	6.3	6.4
20	7.0	72	7.1	0.5	6.9	81	0.5	6.9	6.6	6.8	6.6	6.7	6.4	6.5
25	7.1	84	7.2	0.6	7.0	87	0.6	7.0	6.7	6.8	6.6	6.8	6.4	6.5
30	7.1	84	7.2	0.7	7.0	94	0.7	7.1	6.8	6.9	6.7	6.8	6.4	6.6
35	7.1	84	7.2	0.8	7.1	92	0.7	7.1	6.8	6.9	6.7	6.8	6.5	6.6
40	7.1	84	7.2	0.8	7.1	101	0.7	7.1	6.8	6.9	6.7	6.8	6.5	6.6

(c) Wenchuan earthquake

	M_{mr}	L_{FD} [km]	M_{FD}	D_{mean} [m]	M_{FDS}	L_{FDS+} [km]	D_{mean} [m]	M_{FDS+}	$M_{PGD}^{Crowell}$	M_{PGD}^{Melgar}	M_{PGD}^{Ruhl}
5	6.8	(first solution at 13s)	(first solution at 13s)	—	—	—	—	—	5.9	5.9	5.6
10	6.9	(first solution at 13s)	(first solution at 13s)	—	—	—	—	—	6.1	6.2	5.9
15	7.1	39	6.7	—	—	—	—	—	6.3	6.4	6.1
20	7.3	62	7.0	0.4	7.0	90	0.3	6.8	6.7	6.6	6.3
25	7.5	99	7.3	0.5	6.9	100	0.4	6.9	6.8	6.7	6.4
30	7.6	134	7.5	0.7	7.2	145	0.7	7.2	6.9	6.7	6.5
35	7.7	134	7.5	0.8	7.2	150	0.8	7.2	6.9	6.8	6.6
40	7.7	157	7.6	1.0	7.3	195	1.0	7.4	7.0	6.8	6.6
45	7.7	157	7.6	1.1	7.3	500	1.0	7.7	7.0	6.9	6.7
50	7.7	183	7.7	1.3	7.4	500	1.0	7.7	7.2	7.0	6.8
55	7.8	183	7.7	1.3	7.4	500	1.1	7.7	7.2	7.1	6.9
60	7.8	183	7.7	1.4	7.4	500	1.0	7.7	7.2	7.1	6.9
65	7.8	213	7.8	1.4	7.5	500	1.2	7.7	7.2	7.1	6.9
70	7.8	213	7.8	1.4	7.5	500	1.1	7.7	7.2	7.1	6.9
75	7.8	213	7.8	1.4	7.5	500	1.1	7.7	7.2	7.1	6.9
80	7.9	213	7.8	1.4	7.5	500	1.2	7.7	7.2	7.1	6.9
85	7.9	213	7.8	1.5	7.5	500	1.3	7.7	7.2	7.1	6.9

(Continued on following page)

TABLE 2 | (*Continued*) Results from FinDer (rupture length, L_{FD}, and magnitude, M_{FD}), FinDerS (mean slip, Dmean, and magnitude, M_{FDS}, both from fitted slip profile) and FinDerS+ (predicted final rupture length, L_{FDS+}, predicted final mean slip, mean, and predicted final magnitude, M_{FDS+}) for the a) Ridgecrest, b) Kumamoto, and c) Wenchuan earthquake as a function of time from origin for a 60 km station distance cutoff. Magnitudes Mmr and M_{PGD} are estimated from the USGS moment rate function and empirical PGD-distance relationships (Melgar et al., 2015; Crowell et al., 2016; Ruhl et al., 2019), respectively. Table shows updates in increments of 5 s.

(c) Wenchuan earthquake

	M_{mr}	L_{FD} [km]	M_{FD}	D_{mean} [m]	M_{FDS}	L_{FDS+} [km]	D_{mean} [m]	M_{FDS+}	$M_{PGD}^{Crowell}$	M_{PGD}^{Melgar}	M_{PGD}^{Ruhl}
90	7.9	249	7.9	1.4	7.5	263	1.3	7.6	7.3	7.1	6.9
95	7.9	249	7.9	1.3	7.5	276	1.2	7.6	7.3	7.1	6.9
100	7.9	290	8.0	1.3	7.6	423	1.1	7.6	7.3	7.2	7.0
105	7.9	290	8.0	1.4	7.6	446	1.1	7.7	7.3	7.2	7.0
110	7.9	290	8.0	1.5	7.6	323	1.3	7.6	7.3	7.2	7.0
115	7.9	290	8.0	1.5	7.6	323	1.3	7.6	7.3	7.2	7.0
120	7.9	290	8.0	1.5	7.6	323	1.3	7.6	7.3	7.2	7.0

the fitting does not converge. The fitting resumes converging in the later stages, predicting the final rupture length fairly well.

4.2.4 Magnitudes

Figure 8 and **Table 2** compare the magnitude estimates from the FinDer algorithms with magnitudes derived from the USGS moment rate function, M_{mr}, as well as from simple PGD-magnitude scaling relationships (**Eq. 4**). While these PGD-magnitude relations (Melgar et al., 2015; Crowell et al., 2016; Ruhl et al., 2019) were regressed originally from GNSS displacement data, we are applying them here to both seismic+GNSS and GNSS-only amplitudes. We compute M_{PGD} for each of the three earthquakes by taking the median magnitude estimate taken over all stations at which the seismic waves should have arrived at a given time assuming a moveout velocity of 3 km/s.

For the M_W 7.1 Ridgecrest earthquake (**Figure 8A** and **Table 2**), M_{PGD} for both GNSS data and the combined seismic and GNSS datasets are the same for each of the three empirical scaling relationships, so we discuss them together. On the whole, M_{PGD} under-estimates the magnitude of the Ridgecrest earthquake, and is similar to what is predicted by the FinDer family of algorithms. At the earliest time step when each FinDer algorithm is giving magnitudes, 15 s after t_0, the FinDer algorithms give magnitudes between M_{FD} 6.5 and M_{FDS+} 6.6, whereas the PGD-based magnitudes range between M_{PGD} 6.3 (seismic+GNSS) and M_{PGD} 6.7 (GNSS-only). The final estimate for magnitudes based on PGD ranges from M_{PGD} 6.4 (seismic+GNSS) to M_{PGD} 6.9 (GNSS-only), whereas the FinDer algorithms give magnitudes between M_{FD} 6.9 to M_{FDS+} 7.3. The range of FinDer algorithms give magnitudes closer to the moment rates, M_{mr}, cataloged by the USGS (**Table 2**).

PGD-based magnitude estimates for the M_W 7.0 Kumamoto earthquake (**Figure 8B** and **Table 2**) continuously under-estimate the true magnitude. For the first calculation of magnitude at 5 s, using **Eq. 4**, the values range from M_{PGD} 4.2 (GNSS-only) to M_{PGD} 5.4 (seismic+GNSS). For the same time step, the FinDer family of algorithms give M_{FD} 5.4. At 10 s, the PGD based magnitudes range from M_{PGD} 5.5 (GNSS-only) to M_{PGD} 6.0 (seismic+GNSS), and FinDer magnitudes range from MF_{DS} 6.2 to M_{FD} 6.7. At 20 s, halfway through the time period, we calculate M_{PGD} 6.4 (seismic+GNSS) to MP_{GD} 6.8 (GNSS-ony), however, the FinDer algorithms give larger values that are closer to the cataloged magnitude of M_W 7.0, M_{FDS} 6.9 to M_{FD} 7.1. Finally, at 40 s, the PGD based magnitudes give a range of M_{PGD} 6.5 (seismic+GNSS) to M_{PGD} 6.9 (GNSS-only), and the FinDer algorithms give a range of M_{FDS} 7.1 to M_{FD} 7.2. It is notable that at first the combined geodetic and seismic PGD-based magnitude estimates are higher, and thus closer to the cataloged values. However, in the final time step, the geodetic (only) dataset gives higher PGD-based magnitudes.

For the M_W 7.9 Wenchuan earthquake (**Figure 8C** and **Table 2**), we have only seismic records, so our PGD-based magnitude estimates are solely based on seismic data. Throughout the duration of the event, there is a relatively large discrepancy between M_{PGD} and the true magnitude; the FinDer algorithms arrive at magnitude estimates much closer to

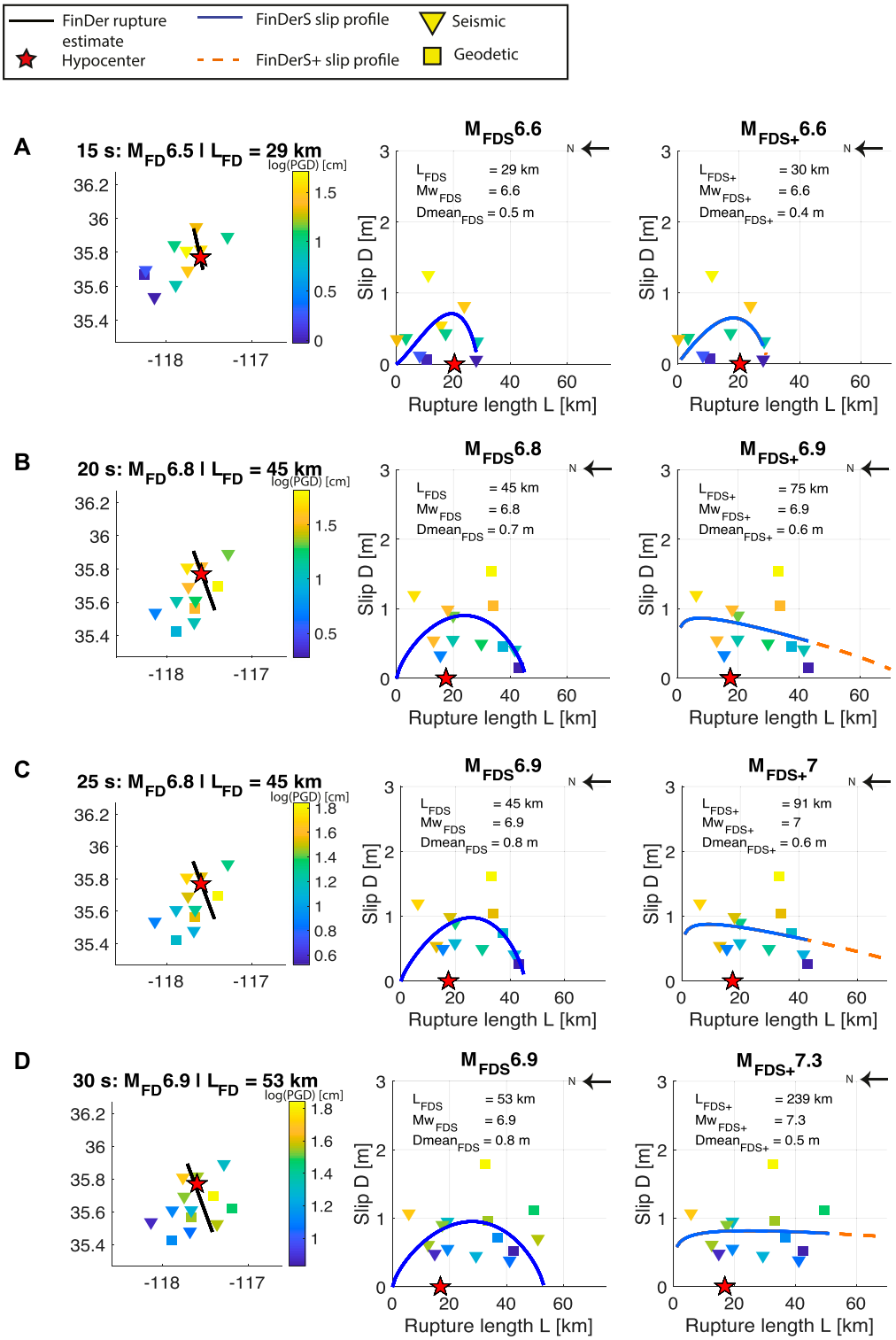

FIGURE 5 | Playback results for the M_W 7.1 Ridgecrest earthquake (L ~ 50 km, ~ 20 s rupture duration) at a) 15 s, b) 20 s, c) 25 s, and d) 30 s from event origin. Plots on the left show FinDer line-source (black line) and PGD measurements at seismic (triangles) and geodetic (squares) sensors. Plots in the middle show interpolated slip profiles from FinDerS. Plots on the right show predicted slip profiles from FinDerS+. Epicenters are relative to the respective FinDer line-source model, oriented as indicated on the plots. See **Table 2** for details.

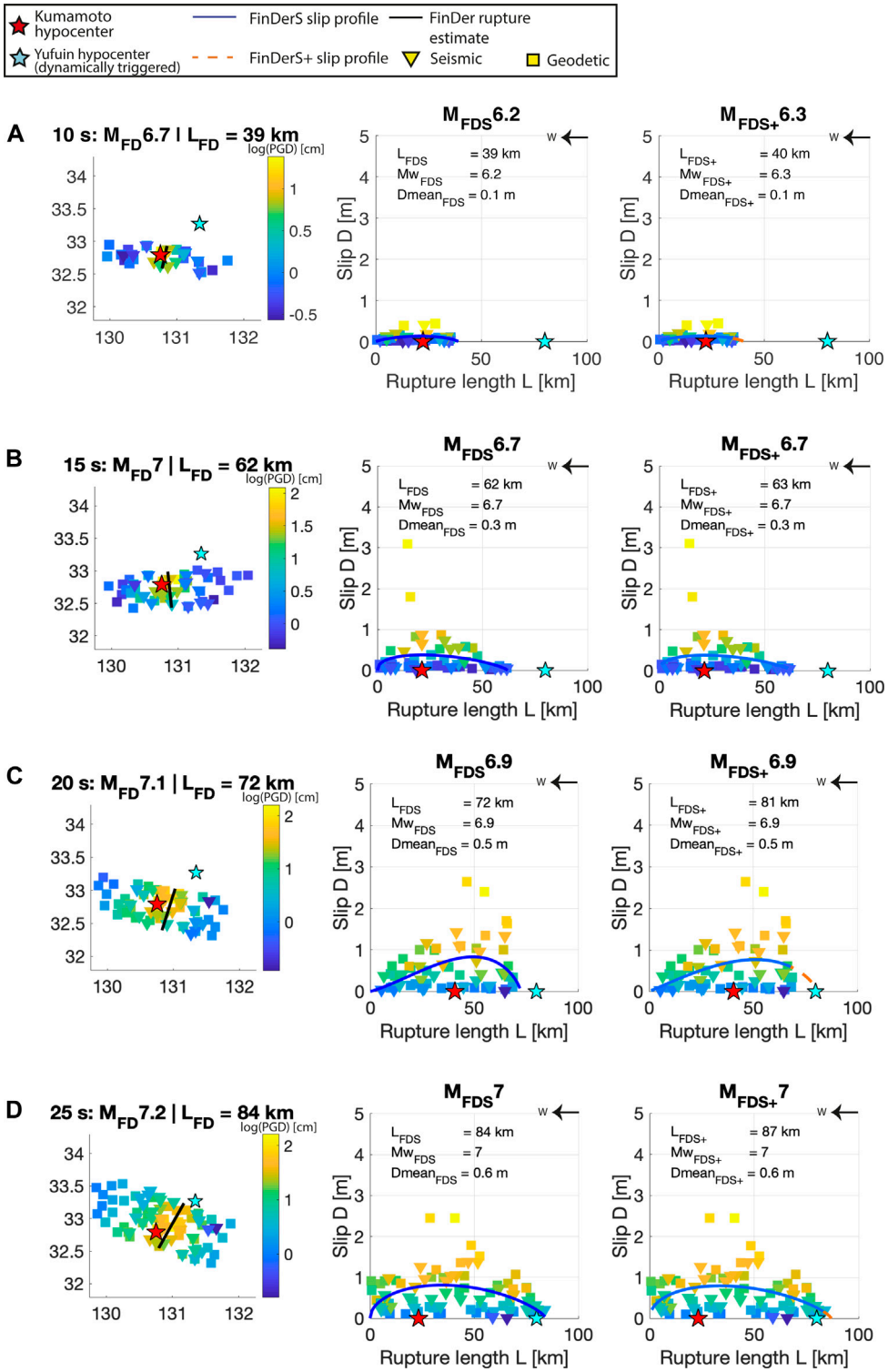

FIGURE 6 | Playback results for the M_W 7.0 Kumamoto earthquake (L ~ 40 km, ~ 15 s rupture duration) at a) 10 s, b) 15 s, c) 20 s, and d) 25 s from event origin. Follows **Figure 5**. See **Table 2** for details.

that of the event. To begin with, at 20 s, once more than three stations can be used to calculate the entire FinDer suite of algorithms, the PGD based magnitude estimates range from MP_{GD} 6.3 to M_{PGD} 6.7. Meanwhile, the FinDer algorithms give a range of M_{FDS+} 6.8 to M_{FD} 7.0. At 60 s, the FinDer suite of algorithms gives a range of M_{FDS} 7.4 to M_{FD} 7.7,

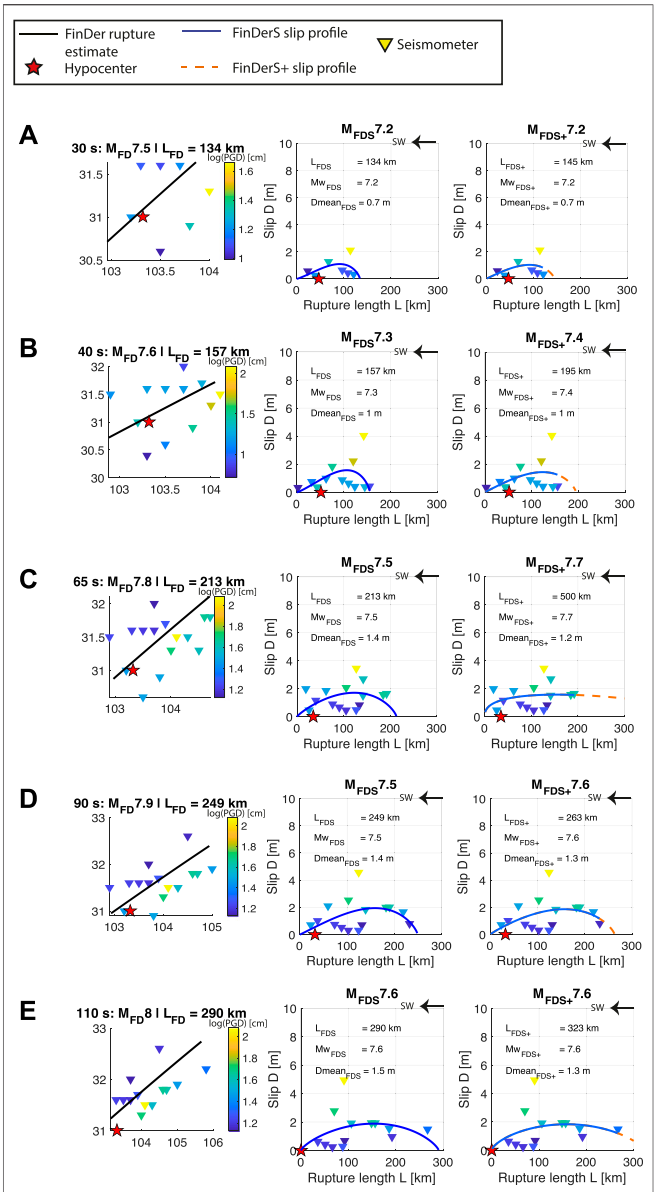

FIGURE 7 | Playback results for the M_W 7.9 Wenchuan earthquake (L ~ 300 km, ~ 100 s rupture duration) at a) 30 s, b) 40 s, c) 65 s, d) 90 s and e) 110 s from event origin. Follows **Figure 5**. See **Table 2** for details.

while the PGD based magnitudes give a range between M_{PGD} 6.9 and M_{PGD} 7.2. The final spread of magnitude estimates at 120 s from PGD based estimates is M_{PGD} 7.0 to M_{PGD} 7.3, while the FinDer family of algorithms gives magnitude estimates much closer to the cataloged final magnitude M_W 7.9, $M_{FDS(+)}$ 7.6 to M_{FD} 8.0.

Generally, in terms of magnitude, the FinDer suite of algorithms performs quite well with respect to Mmr. FinDer continues to perform consistently for all three events, matching the M_{mr} values for all three events, though for Kumamoto and Ridgecrest, FinDerS and FinDerS+ perform similarly well. The FinDerS+ magnitude estimates are slightly better aside from the Wenchuan earthquake, where FinDer has the best results. This is mainly due to FinDerS+ under-estimating the Wenchuan slip significantly. The algorithms consistently outperform the PGD-based magnitude estimates.

5 DISCUSSION

Ideally, FinDerS+ is expected to provide the best performance because, on the one hand, it builds on the FinDer results which determine the fault location and strike, and on the other hand, it takes into account an important property of the source fault, its structural maturity gradient, in the form of the empirical equation **Eq. 2**. The latter allows integration of the location and strike of the fault delivered by FinDer with the slip estimates independently obtained from PGD amplitudes, and derives the best-fitting slip-length profile at every stage of the growing rupture. FinDerS provides a more basic approach as, at each stage of the rupture growth, it adopts the rupture length delivered by FinDer.

5.1 Performance for M_W 7.1 Ridgecrest

Since March 2018, the U.S. West Coast ShakeAlert system (Given et al., 2018) is comprised of two independent algorithms - FinDer and the EPIC point-source algorithm (Chung et al., 2019). Both algorithms detected the 2019 M_W 7.1 Ridgecrest shortly after its nucleation and sent an alert within 6.9 s from t_0, even though they both under-estimated the magnitude of the mainshock by 0.8 units (Chung et al., 2020). In the case of FinDer this magnitude under-estimation was caused mostly by strongly increasing data latencies (> 20–30 s) of seismic data telemetered from the stations to the main data center in Pasadena due to inefficient data compression and limited bandwidth (Stubailo et al., 2021). After the Ridgecrest earthquake, the FinDer code was updated to better handle latent data, as well to allow for a faster magnitude convergence (Böse et al., in prep.). We are presenting results from this new FinDer code here.

In our playback, FinDer determines the final rupture length of the M_W 7.1 Ridgecrest earthquake within 25–30 s after t_0 as 53 km, with a close prediction of 45 km at 15–20 s (**Table 2**). FinDerS+, however, mildly over-estimates the final rupture length at 20–25 s (**Figures 5B,C**; **Table 2**), and grossly over-estimates the final rupture length at a value of 239 km at 30 s, when FinDer (and thus also FinDerS) has an accurate grip on the final rupture length. This length over-estimation with FinDerS+ is due to its inability to recover the earthquake slip asymmetry at 30 s.

While, for the most part, the slip profiles predicted through FinDerS and especially FinDerS+ match the overall pattern of the observed slip profile (Milliner and Donnellan, 2020), the backprojected slip values are under-estimated, with a maximum slip that is about half as large as measured at surface shortly after the earthquake (thus, these measures are not expected to include significant post-seismic slip, Barnhart et al., 2019; Wang and Bürgmann, 2020) (**Figures 4A**, **5A–D**). This under-estimation may be a product of our approach using a very simple equation to estimate slip (**Eq. 1**), combined with

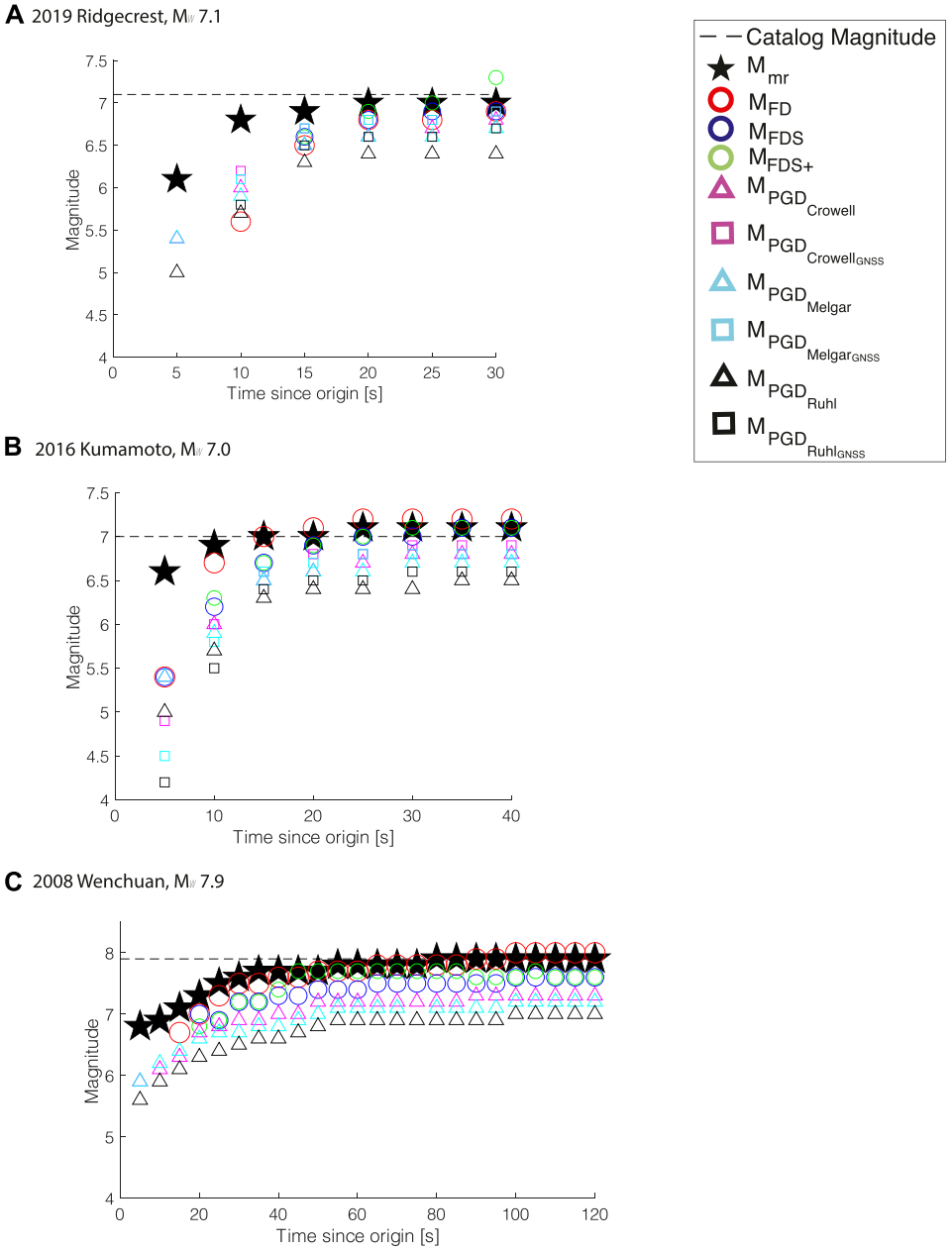

FIGURE 8 | Comparison of magnitudes from FinDer, FinDerS, FinDerS+, and PGD-based magnitude estimates as function of time from event origin for a) M_W 7.1 Ridgecrest, b) M_W 7.0 Kumamoto, and c) M_W 7.9 Wenchuan. Triangles mark estimates derived from seismic and geodetic data, squares mark estimates from geodetic data only. M_{mr} is determined from the seismic moment rate and shown for reference. See **Table 2** for details.

using filtered PGD data, which is known to artificially reduce PGD amplitudes (Yamada, 2007). We come back to this point further below. The under-estimated slip values are likely the source of low magnitude predictions in FinDerS, and of the difficulty of FinDerS+ to recover the asymmetry of the final slip profile and hence, its actual (shorter) final length.

The main output of the FinDer algorithm is a line-source model, not a magnitude estimate (Böse et al., 2018). As a matter of fact, while the FinDer rupture length estimate of 53 km is excellent, the final FinDer magnitude M_{FD} 6.9 under-estimates the cataloged magnitude by 0.2 units. This is mainly due to the use of a simple empirical rupture length-magnitude relation (Wells and Coppersmith, 1994) in FinDer; although valuable, this relation has significant uncertainties. Using the slip information in addition to rupture length is expected to compensate for limitations in the empirical error-prone

relation used in FinDer. In the Ridgecrest earthquake, FinDerS, however, also never arrives at the cataloged magnitude, M_W 7.1 (**Figures 5A–D**). FinDerS+, while over-predicting the final rupture length, does provide a better magnitude prediction. This, however, comes at the cost of a largely over-estimated rupture length, in turn likely related to slip under-estimation. This raises a fundamental question about trade-offs in algorithms, where accuracy in one area (magnitude) may mean a sacrifice in other metrics (final rupture length). In the future, it may be useful to combine the family of FinDer algorithms to find a magnitude and a length prediction that considers all three values.

5.2 Performance for M_W 7.0 Kumamoto

The Japanese EEW system operated by Japan Meteorological Agency (JMA) issued a first alert 8 s after t_0 of the M_W 7.0 Kumamoto earthquake with an initial magnitude estimate of M_{JMA} 5.9. About 5 s later, the magnitude was updated to M_{JMA} 6.9 (Kodera et al., 2016). In comparison, 5 s after t_0 (neglecting data latencies, which typically are on the order of 1–2 s), FinDer gives M_{FD} 5.4. Then, 5 s later, FinDer updates its estimate to M_{FD} 6.7, and to M_{FD} 7.0 after 15 s from t_0.

For the Kumamoto earthquake, the family of FinDer algorithms predicts the final rupture length at surface from 10 s after t_0 (**Table 2**), and the final rupture length at depth at 15 s. Subsequently, FinDer, as well as FinDerS and FinDerS+ (due to their reliance on FinDer for the rupture length), over-estimate and over-predict the rupture length of the Kumamoto earthquake by ~20 km. However, the final rupture length of the event determined by FinDer(S) is 84 km, which is approximately the distance from the hypocenter to the triggered event at Yufuin. Since this secondary event did not occur until > 30 s after t_0 of the original Kumamoto earthquake, the results do not reflect the combined energy from both events until after ~35 s. While we do not have an explanation, we suggest it is possible that this finding (which was already observed in (Böse et al., 2018)) is not simply fortuitous; the mainshock originally had enough energy to rupture, in one way or another (i.e., in one or two earthquakes), the total fault length of 84 km. This is supported by the anomalously strong ground motions towards NE direction, which might have been a product of strong directivity, the simultaneous slipping of two oblique faults with strong pulse like ruptures, and high slip rates (Kobayashi et al., 2017; Somei et al., 2019). These motions may have been strong enough to break the fault entirely, although in two parts somewhat delayed (dynamic triggering of the Yufuin event Uchide et al., 2016; Yoshida, 2016).

Looking at slip distributions up to ~40 km along strike (the final rupture length at the ground surface), the maximum slip values calculated through backprojection at 25 s are consistent with the largest surface slip measures. However, overall, the backprojected slips are about half that measured at surface (Shirahama et al., 2016) (**Figure 4B**), while the asymmetry of the slip profile is recovered at 20 s only.

5.3 Performance for M_W 7.9 Wenchuan

At the time of the M_W 7.9 Wenchuan earthquake, which is by far the largest event in this study and hence has the longest rupture duration, China had no operational EEW system. Thus, we cannot compare the performance of the FinDer suite of algorithms to another early warning system. However, in a previous study using the FinDer algorithm and the same dataset, Li et al. (2020) reported a slightly slower magnitude convergence for the Wenchuan earthquake, which can be attributed to their use of an older version of the FinDer code.

The FinDer algorithms all anticipate from the very start (25–30 s after t_0) that the rupture will be long, at least 100–150 km, and the magnitude large, at least 7.2 (**Table 2**). FinDer and FinDerS then predict an increasing length, up to the accurate estimate of the final rupture length by 95–100 s after t_0 (**Table 2**). While FinDerS+ over-predicts the length between about 45 and 85 s, it predicts it well from 90 s on, even though its final estimate is slightly greater than the actual rupture length. As for the Ridgecrest and the Kumamoto earthquakes, the backprojected slip values are under-estimated, in this case significantly with the maximum slip about three times lower than the largest displacements measured at surface, and the mean backprojected slip about 5–6 times smaller than what was observed. The actual asymmetry of the slip profile is not well recovered either, even though FinDerS+ anticipates a westward asymmetry from 45 s.

In terms of magnitude, FinDer predicts a MFD 7.8 by 60–65 s after t_0, which is approximately 50% of the rupture duration. At 100 s, FinDer reaches a final magnitude of M_{FD} 8.0, which is a reasonable estimate. Compared to Ridgecrest and Kumamoto, seismic recordings of the Wenchuan earthquake are sparse, which partially explains the longer duration needed for source characterization, along with the generally expected longer duration of such a large earthquake (**Table 1**).

5.4 Seismic/Geodetic Displacement Versus Fault Slip

Long-period PGD amplitudes provide information about fault slip and magnitudes (e.g. Melgar et al., 2015; Crowell et al., 2016; Ruhl et al., 2019). As demonstrated in this study, both GNSS and seismic data can produce PGD datasets that can help to quickly constrain the metrics of an ongoing earthquake. Although more reliable at long periods and in particular at the static offset, GNSS data is generally more noisy compared to strong-motion data. The GNSS noise level is typically 1–2 cm and data is thus useful only for moderate and large earthquakes at local to regional distances (Ruhl et al., 2019).

It is well known that recovering seismic displacement from double-integrated strong-motion data can present issues in the presence of strong nonphysical drifts and saturation of the sensor (Bock et al., 2011). These drifts typically emerge from small baseline offsets in the acceleration data that are accentuated when double-integrated to displacement (Emore et al., 2007). Since this issue mainly affects long-period motions (and we are mainly interested in dynamic rather than static displacement), we apply in this study a high-pass filter with a cutoff-frequency at 0.075 Hz. A drawback of this approach, however, is that PGD amplitudes are reduced (Yamada, 2007), which will be reflected in smaller slip values resulting from the backprojection of PGD

using **Eq. 1**. Nonetheless, first-order differences between seismic and geodetic dynamic PGD amplitudes are small (**Figure 3**) and the utility of the filtered amplitudes is clearly demonstrated in this paper.

Contrary to the results of the same algorithm using accurate static slip profiles, where final rupture lengths and magnitudes could be determined within 10–20% of the way through the signal's duration (Hutchison et al., 2020), the results from the dynamic application of FinDerS+ in this paper suggest that the true convergence might actually take longer. Instead, as shown by the examples of the earthquakes presented here, FinDerS and FinDerS+ rarely reach the cataloged magnitude until 40–50% of the rupture duration. For Wenchuan, the actual magnitude is never reached, though both algorithms do converge at a reasonable solution (within 0.2–0.5 magnitude units) about 30% of the way through the event. This slower ability to predict the final length and magnitude of the earthquake arises from two issues: first, it takes some time until final slip values in an earthquake are reached. Second, the (final) slip tends to be significantly under-estimated in our backprojection algorithm. This difficulty to reproduce the slip values accurately leads in some cases to over-predict the rupture length (see **Figures 5D**, **7C**). While this over-prediction might not be too much an issue in large earthquakes as those analyzed here, it would become more critical for smaller magnitude earthquakes. The approach developed here is thus best suited for earthquakes with M_W greater than 7. However, more systematic studies (and adjustments of the algorithms) are required to determine the best range of applicability.

The systematic under-estimation of slip from the backprojected PGD amplitudes largely relates to the function **Eq. 1** we are applying. This function, taken from Yamada (2007), was derived from near-source ground motion simulations by Aagaard et al. (2004), made to relate dynamic ground displacements at some distance from the fault rupture to on-rupture slip. These simulations were done using reference rupture source models, having variable dips and slip modes, but similar length of 100 km and similar largest slips of about 6 m. Would these ruptures be real, available earthquake slip-length scaling relations (Manighetti et al., 2007) would suggest that these reference earthquakes occurred on fairly mature faults. In contrast, the three earthquakes we analyzed here ruptured fairly immature faults, as described in **Section 3.1**. Their slip-to-length ratios actually confirm this inference (compare their slip-length values to **Figure 5A** in (Manighetti et al., 2007)). Earthquakes on immature faults have been shown to produce larger displacements and stronger ground accelerations than earthquakes on more mature faults (Radiguet et al., 2009). As the function from Aagaard et al. (2004) does not take these source differences into account, it likely smooths them out, in effect under-estimating the slips produced by earthquakes on fairly immature faults, as those analyzed here.

To address the problem of slip under-estimation in the future, we might consider an updated backprojection function that takes the overall maturity of the ruptured fault into account, provided that the latter can be known in real-time (Böse and Heaton, 2010). Alternatively, if the ruptured fault is not identified or if its overall maturity is unknown, in future we might be able to derive from analysis of the increasing number of well instrumented earthquakes, a "generic" coefficient of correction that would compensate for the systematic slip under-estimation for immature faults. As a first estimate, for the three earthquakes analyzed here, a factor of two is suggested. By using simultaneously the "raw" and the corrected slip data, the FinDer algorithms might be able to bracket more efficiently, i.e., faster, the actual final rupture length and magnitude.

5.5 FinDer-Versus PGD-Based Magnitudes

For the three earthquakes studied here, the FinDer family of algorithms systematically outperforms the simple PGD-based magnitude estimates, both using exclusively GNSS data or combined GNSS and seismic datasets. While the PGD-hypocentral distance scaling relationship is simple, the fact that the coefficients in **Eq. 4** change repeatedly based on the introduction of new earthquakes (Melgar et al., 2015; Crowell et al., 2016; Ruhl et al., 2019), and that station selectivity can have a significant impact on the accuracy of the magnitude estimate (e.g. Dahmen et al., 2020), make this scaling relationship imprecise. Furthermore, these PGD-based magnitude relations ignore the earthquake fault source dimensions and properties, while those have been shown to impact both the ground accelerations (Radiguet et al., 2009) and displacements (Manighetti et al., 2007). The FinDer group of algorithms consistently does a better job of calculating magnitude accurately, without the introduction of complex station selection parameters or subsequently extending empirical datasets. FinDerS and FinDerS+, which take some of the earthquake fault source properties into account, are generally more efficient at predicting the final magnitudes (**Figures 8A,B**).

Our PGD-based magnitudes for the Kumamoto earthquake (**Figure 8**) differ from the results of a previous GNSS data-based study (Dahmen et al., 2020), in which magnitude predictions are much closer to the cataloged magnitude. For example, Dahmen et al. (2020) estimate M_{PGD} 6.3 14 s after the event detection, M_{PGD} 6.8 after 20 s, and finally M_{PGD} 7.0 after 100 s. However, there are a couple of differences compared to our study. First, at least five stations that were included in the Dahmen et al. (2020) study, were not included in the GNSS dataset available through Ruhl et al. (2019) that we used here. Second, Dahmen et al. (2020) utilized a noise-based threshold criteria to select stations. Because of this, Dahmen et al. (2020) used only 27 of the 39 available GNSS stations that we used (Ruhl et al., 2019). Without applying this selection criteria, the PGD-based magnitude estimate of Dahmen et al. (2020) 14 s after the event detection is M_{PGD} 6.7, which is similar to our estimates. It is notable that - despite not applying station selection criteria - the FinDer algorithm suite magnitude estimates are consistent with the PGD-based magnitude estimates from Dahmen et al. (2020) and the true magnitude evolution reflected in M_{mr} (**Table 2**). The same applies for the M_W 7.1 Ridgecrest earthquake, where the M_{PGD} values of Hodgkinson et al. (2020) differ slightly from our results.

5.6 Implications and Benefits for EEW

The main output of the FinDer algorithm is a line-source model, which is determined from the spatial distribution of

high-frequency PGA amplitudes. FinDer magnitudes, M_{FD}, are a secondary product only, that are estimated from the application of general empirical rupture length-magnitudes relationships. These relations are known to have significant uncertainties. Our two new algorithms, FinDerS and FinDerS+, can help to improve magnitude estimates by incorporating the additional information on the earthquake slip-fault maturity relation and on long-period motions, which are closely related to the static fault offset and seismic moment (Hanks and Kanamori, 1979).

Furthermore, the new addition of a fault slip profile estimated by FinDerS and FinDerS+ can improve the spatial prediction of the ground motions, the ultimate goal of EEW. Slip distributions with large and smooth slip patches affect mainly long-period ground motions along the fault rupture and thus matter most for high-rise buildings at close distance as well as tsunami generation (e.g. Scholz, 2019). Furthermore, by associating the greatest coseismic slip with the most mature parts of the rupture, we can extrapolate the locations of the strongest radiation of high-frequency ground motions. It has indeed been shown that the amplitude of the ground motions is partly controlled by the structural maturity of the source fault, with immature faults or fault sections producing the largest ground motions (Radiguet et al., 2009), furthermore, likely, of highest frequencies. This implies that the output of FinDerS and FinDerS+ does not help only with magnitude estimates (at least for redundancy checks), but potentially improves the seismic ground-motion predictions for EEW.

As proposed by Hutchison et al. (2020), we could even go further by deriving and using two extreme slip-length-maturity empirical functions (**Eq. 1** in Hutchison et al. (2020)), one describing the slip behavior of earthquakes on mature faults, and one that of earthquakes on immature faults (see Manighetti et al., 2007). By using simultaneously these two extreme equations, the FinDer algorithms would better bracket the actual range of lengths and magnitudes and hence probably converge faster towards the actual final length and magnitude of the earthquake.

6 CONCLUSION

We recover earthquake line-source models from high-frequency seismic acceleration data using FinDer (Böse et al., 2012b, 2015, 2018) and give 1D slip profile estimates from the backprojection of long-period displacement amplitudes onto these models using two new algorithms, FinDerS and FinDerS+. While FinDerS backprojects displacement onto the current FinDer line-source, FinDerS+ allows for additional rupture growth along this model. Both FinDerS and FinDerS+ make use of a general relationship that we established in an earlier study (Hutchison et al., 2020) that relates the along-strike gradient of long-term structural maturity of the ruptured fault to the coseismic slip distribution along the rupture. As such, FinDerS and FinDerS+ incorporate a part of the earthquake physics described through this empirical relation, which we use to produce an informed interpolation and smoothing of the backprojected slip values. The two new algorithms provide independent magnitude estimates from FinDer based on slip which could be useful to speed-up magnitude convergence and for redundancy checks with FinDer estimated magnitudes.

FinDerS+ can over-predict the rupture length in two cases: 1) when the slip data are not well determined, as is the case here, in particular showing sparse measures with abrupt fluctuations as in Ridgecrest; 2) when the ongoing slip is gradually increasing away from the hypocenter [see Hutchison et al. (2020)]. This is because the empirical relation between earthquake slip, rupture length, and gradient in fault structural maturity relies on the envelope shape of the along-fault slip distribution and the generic asymmetry of the earthquake slip profiles [see Manighetti et al. (2005)]. Therefore, in the cases where slip fluctuations are too large, or the major slip drop occurs at the end of the rupture growth, the model is unable to recover the envelope shape of the slip distribution. To overcome the problem of slip fluctuations (in the presence of multiple large asperities), dense and accurate slip data are needed. To overcome the problem of the few earthquake cases where slip gradually increasing away from the hypocenter (those cases are fairly rare), in future work, we may incorporate the overall maturity of the source faults: the earthquake slip-length curves have indeed an amplitude that decreases with the overall maturity of the ruptured fault (Manighetti et al., 2007). These amplitude relations will provide slip maximums and force tighter constraints on upper slip bounds of the evolving slip curves, especially for these very asymmetric earthquake profiles. Even though our approach over-predicts the final length of the Ridgecrest and Wenchuan earthquakes at specific stages of their growth, it does predict their magnitude well, from fairly early stages of the rupture growth. In playback, these early large magnitudes indicate that these earthquakes will end up being large, even during the initial stages of the rupture.

For the earthquakes shown here (Kumamoto, Ridgecrest, Wenchuan) the magnitudes computed by the FinDer algorithms converge faster and reach values closer to the cataloged magnitudes than compared to those computed directly from PGD. FinDerS and FinDerS+ benefit from real-time GNSS data streams, but could also use seismic data only. This study has been a preliminary work to understand the basic utility of two new FinDer-based algorithms, but further tests are needed to better constrain the capabilities and limitations of these new EEW algorithms. Further work is also needed to improve our capacity to estimate ongoing slip in real-time. The accuracy of slip estimation is critical to make FinDerS and FinDerS+ efficient. Furthermore, larger sets of earthquakes need to be analyzed, including subduction earthquakes for which information about slip is especially critical in a tsunami context, and rupture length of vital importance to warn the populations along the coastline.

DATA AVAILABILITY STATEMENT

The original contributions presented in the study are included in the article/**Supplementary Material**, further inquiries can be directed to the corresponding author.

AUTHOR CONTRIBUTIONS

MB: gave idea and guided research, computed FinDer models, wrote manuscript; AH: conducted analysis, co-developed FinDerS(+) algorithm, wrote manuscript; IM: provided fault background/interpretation, wrote manuscript, leads the project in which this work was done; FM: helped with discussions and writing manuscript; JL: provided the strong ground motion records of the Wenchuan earthquake, assisted in analysis of Wenchuan earthquake; JC: helped with discussions and writing manuscript.

FUNDING

This project is funded by the ANR Grant FAULTS_R_GEMS #ANR-17-CE31-0008.

ACKNOWLEDGMENTS

This material is based on services provided by UNAVCO, Inc., the National Research Institute for Earth Science and Disaster Resilience (NIED), the GEONET Global Positioning System, the China Strong MotionNetworks Center (CSMNC), and the Southern California Earthquake Data Center (SCEDC) and Southern California Seismic Network (SCSN). The SCEDC and SCSN are funded through U.S. Geological Survey Grant G10AP00091.

SUPPLEMENTARY MATERIAL

The Supplementary Material for this article can be found online at: https://www.frontiersin.org/articles/10.3389/feart.2021.685879/full#supplementary-material

REFERENCES

Aagaard, B. T., Hall, J. F., and Heaton, T. H. (2004). Effects of Fault Dip and Slip Rake Angles on Near-Source Ground Motions: Why Rupture Directivity Was Minimal in the 1999 Chi-Chi, Taiwan, Earthquake. *Bull. Seismological Soc. America* 94, 155–170. doi:10.1785/0120030053

Allen, R. M., Gasparini, P., Kamigaichi, O., and Bose, M. (2009). The Status of Earthquake Early Warning Around the World: An Introductory Overview. *Seismological Res. Lett.* 80, 682–693. doi:10.1785/gssrl.80.5.682

Allen, R. M., and Melgar, D. (2019). Earthquake Early Warning: Advances, Scientific Challenges, and Societal Needs. *Annu. Rev. Earth Planet. Sci.* 47, 361–388. doi:10.1146/annurev-earth-053018-060457

Barnhart, W. D., Hayes, G. P., and Gold, R. D. (2019). The July 2019 Ridgecrest, California, Earthquake Sequence: Kinematics of Slip and Stressing in Cross-Fault Ruptures. *Geophys. Res. Lett.* 46, 11859–11867. doi:10.1029/2019gl084741

Behr, Y., Clinton, J., Kästli, P., Cauzzi, C., Racine, R., and Meier, M.-A. (2015). Anatomy of an Earthquake Early Warning (EEW) Alert: Predicting Time Delays for an End-To-End EEW System. *Seismological Res. Lett.* 86, 830–840. doi:10.1785/0220140179

Blaser, L., Krüger, F., Ohrnberger, M., and Scherbaum, F. (2010). Scaling Relations of Earthquake Source Parameter Estimates with Special Focus on Subduction Environment. *Bull. Seismological Soc. America* 100, 2914–2926. doi:10.1785/0120100111

Bock, Y., Melgar, D., and Crowell, B. W. (2011). Real-time strong-motion Broadband Displacements from Collocated GPS and Accelerometers. *Bull. Seismological Soc. America* 101, 2904–2925. doi:10.1785/0120110007

Böse, M., Felizardo, C., and Heaton, T. H. (2015). Finite-Fault Rupture Detector (FinDer): Going Real-Time in CalifornianShakeAlertWarning System. *Seismological Res. Lett.* 86, 1692–1704. doi:10.1785/0220150154

Böse, M., Heaton, T., and Hauksson, E. (2012a). Rapid Estimation of Earthquake Source and Ground-Motion Parameters for Earthquake Early Warning Using Data from a Single Three-Component Broadband or strong-motion Sensor. *Bull. Seismological Soc. America* 102, 738–750. doi:10.1785/0120110152

Böse, M., Heaton, T. H., and Hauksson, E. (2012b). Real-time Finite Fault Rupture Detector (FinDer) for Large Earthquakes. *Geophys. J. Int.* 191, 803–812. doi:10.1111/j.1365-246x.2012.05657.x

Böse, M., and Heaton, T. H. (2010). Probabilistic Prediction of Rupture Length, Slip and Seismic Ground Motions for an Ongoing Rupture: Implications for Early Warning for Large Earthquakes. *Geophys. J. Int.* 183, 1014–1030. doi:10.1111/j.1365-246x.2010.04774.x

Böse, M., Heaton, T., and Hudnut, K. (2013). Combining Real-Time Seismic and GPS Data for Earthquake Early Warning. *AGU Fall Meet. Abstr.* 2013, G51B–G05.

Böse, M., Smith, D. E., Felizardo, C., Meier, M.-A., Heaton, T. H., and Clinton, J. F. (2018). FinDer v.2: Improved Real-Time Ground-Motion Predictions for M2-M9 with Seismic Finite-Source Characterization. *Geophys. J. Int.* 212, 725–742. doi:10.1093/gji/ggx430

Chen, Y., and Booth, D. C. (2011). *The Wenchuan Earthquake of 2008: Anatomy of a Disaster*. Springer Science & Business Media.

Chung, A. I., Henson, I., and Allen, R. M. (2019). Optimizing Earthquake Early Warning Performance: ElarmS-3. *Seismological Res. Lett.* 90, 727–743. doi:10.1785/0220180192

Chung, A. I., Meier, M.-A., Andrews, J., Böse, M., Crowell, B. W., McGuire, J. J., et al. (2020). Shakealert Earthquake Early Warning System Performance during the 2019 Ridgecrest Earthquake Sequence. *Bull. Seismological Soc. America* 110, 1904–1923. doi:10.1785/0120200032

Clinton, J., Zollo, A., Marmureanu, A., Zulfikar, C., and Parolai, S. (2016). State-of-the Art and Future of Earthquake Early Warning in the European Region. *Bull. Earthquake Eng.* 14, 2441–2458. doi:10.1007/s10518-016-9922-7

Colombelli, S., Zollo, A., Festa, G., and Picozzi, M. (2014). Evidence for a Difference in Rupture Initiation between Small and Large Earthquakes. *Nat. Commun.* 5, 3958. doi:10.1038/ncomms4958

Crowell, B. W., Schmidt, D. A., Bodin, P., Vidale, J. E., Gomberg, J., Renate Hartog, J., et al. (2016). Demonstration of the Cascadia G-FAST Geodetic Earthquake Early Warning System for the Nisqually, Washington, Earthquake. *Seismological Res. Lett.* 87, 930–943. doi:10.1785/0220150255

Cua, G., Fischer, M., Heaton, T., and Wiemer, S. (2009). Real-time Performance of the Virtual Seismologist Earthquake Early Warning Algorithm in Southern California. *Seismological Res. Lett.* 80, 740–747. doi:10.1785/gssrl.80.5.740

Cua, G., and Heaton, T. H. (2009). *Characterizing Average Properties of Southern California Ground Motion Amplitudes and Envelopes*.

Dahmen, N., Hohensinn, R., and Clinton, J. (2020). Comparison and Combination of GNSS and Strong-Motion Observations: A Case Study of the 2016 Mw 7.0 Kumamoto Earthquake. *Bull. Seismological Soc. America* 110, 2647–2660. doi:10.1785/0120200135

Denolle, M. A. (2019). Energetic Onset of Earthquakes. *Geophys. Res. Lett.* 46, 2458–2466. doi:10.1029/2018gl080687

Emore, G. L., Haase, J. S., Choi, K., Larson, K. M., and Yamagiwa, A. (2007). Recovering Seismic Displacements through Combined Use of 1-Hz GPS and strong-motion Accelerometers. *Bull. Seismological Soc. America* 97, 357–378. doi:10.1785/0120060153

Given, D. D., Allen, R. M., Baltay, A. S., Bodin, P., Cochran, E. S., Creager, K., et al. (2018). Revised Technical Implementation Plan for the ShakeAlert System–An Earthquake Early Warning System for the West Coast of the United States. *U.S. Geological Survey Open-File Report 2018–1155* [Supersedes USGS Open-File Report 2014–1097], 42. doi:10.3133/ofr20181155

Goldberg, D. E., Melgar, D., Bock, Y., and Allen, R. M. (2018). Geodetic Observations of Weak Determinism in Rupture Evolution of Large Earthquakes. *J. Geophys. Res. Solid Earth* 123, 9950–9962. doi:10.1029/2018jb015962

Hanks, T. C., and Kanamori, H. (1979). A Moment Magnitude Scale. *J. Geophys. Res.* 84, 2348–2350. doi:10.1029/jb084ib05p02348

Hodgkinson, K. M., Mencin, D. J., Feaux, K., Sievers, C., and Mattioli, G. S. (2020). Evaluation of Earthquake Magnitude Estimation and Event Detection

Thresholds for Real-Time GNSS Networks: Examples from Recent Events Captured by the Network of the Americas. *Seismological Res. Lett.* 91, 1628–1645. doi:10.1785/0220190269

Hudnut, K. W., Brooks, B. A., Scharer, K., Hernandez, J. L., Dawson, T. E., Oskin, M. E., et al. (2020). Airborne Lidar and Electro-Optical Imagery along Surface Ruptures of the 2019 Ridgecrest Earthquake Sequence, Southern California. *Seismological Res. Lett.* 91, 2096–2107. doi:10.1785/0220190338

Hutchison, A. A., Böse, M., and Manighetti, I. (2020). Improving Early Estimates of Large Earthquake's Final Fault Lengths and Magnitudes Leveraging Source Fault Structural Maturity Information. *Geophys. Res. Lett.* 47, e2020GL087539. doi:10.1029/2020gl087539

Kobayashi, H., Koketsu, K., and Miyake, H. (2017). Rupture Processes of the 2016 Kumamoto Earthquake Sequence: Causes for Extreme Ground Motions. *Geophys. Res. Lett.* 44, 6002–6010. doi:10.1002/2017gl073857

Kodera, Y., Saitou, J., Hayashimoto, N., Adachi, S., Morimoto, M., Nishimae, Y., et al. (2016). Earthquake Early Warning for the 2016 Kumamoto Earthquake: Performance Evaluation of the Current System and the Next-Generation Methods of the Japan Meteorological Agency. *Earth, Planets and Space* 68, 1–14. doi:10.1186/s40623-016-0567-1

Kodera, Y., Yamada, Y., Hirano, K., Tamaribuchi, K., Adachi, S., Hayashimoto, N., et al. (2018). The Propagation of Local Undamped Motion (PLUM) Method: A Simple and Robust Seismic Wavefield Estimation Approach for Earthquake Early Warning. *Bull. Seismological Soc. America* 108, 983–1003. doi:10.1785/0120170085

Leonard, M. (2014). Self-consistent Earthquake Fault-Scaling Relations: Update and Extension to Stable continental Strike-Slip Faults. *Bull. Seismological Soc. America* 104, 2953–2965. doi:10.1785/0120140087

Li, J., Böse, M., Wyss, M., Wald, D. J., Hutchison, A., Clinton, J. F., et al. (2020). Estimating Rupture Dimensions of Three Major Earthquakes in Sichuan, China, for Early Warning and Rapid Loss Estimates. *Bull. Seismological Soc. America* 110, 920–936. doi:10.1785/0120190117

Manighetti, I., Campillo, M., Bouley, S., and Cotton, F. (2007). Earthquake Scaling, Fault Segmentation, and Structural Maturity. *Earth Planet. Sci. Lett.* 253, 429–438. doi:10.1016/j.epsl.2006.11.004

Manighetti, I., Campillo, M., Sammis, C., Mai, P., and King, G. (2005). Evidence for Self-Similar, Triangular Slip Distributions on Earthquakes: Implications for Earthquake and Fault Mechanics. *J. Geophys. Res. Solid Earth* 110. doi:10.1029/2004jb003174

Manighetti, I., King, G. C. P., Gaudemer, Y., Scholz, C. H., and Doubre, C. (2001). Slip Accumulation and Lateral Propagation of Active normal Faults in Afar. *J. Geophys. Res.* 106, 13667–13696. doi:10.1029/2000jb900471

Mattioli, G. S., Phillips, D. A., Hodgkinson, K. M., Walls, C., Mencin, D. J., Bartel, B. A., et al. (2020). The GAGE Data and Field Response to the 2019 Ridgecrest Earthquake Sequence. *Seismological Res. Lett.* 91, 2075–2086. doi:10.1785/0220190283

Meier, M.-A., Ampuero, J. P., and Heaton, T. H. (2017). The Hidden Simplicity of Subduction Megathrust Earthquakes. *Science* 357, 1277–1281. doi:10.1126/science.aan5643

Melgar, D., Crowell, B. W., Geng, J., Allen, R. M., Bock, Y., Riquelme, S., et al. (2015). Earthquake Magnitude Calculation without Saturation from the Scaling of Peak Ground Displacement. *Geophys. Res. Lett.* 42, 5197–5205. doi:10.1002/2015gl064278

Melgar, D., and Hayes, G. P. (2019). Characterizing Large Earthquakes before Rupture Is Complete. *Sci. Adv.* 5, eaav2032. doi:10.1126/sciadv.aav2032

Milliner, C., Bürgmann, R., Inbal, A., Wang, T., and Liang, C. (2020). Resolving the Kinematics and Moment Release of Early Afterslip within the First Hours Following the 2016 M_W 7.1 Kumamoto Earthquake: Implications for the Shallow Slip Deficit and Frictional Behavior of Aseismic Creep. *J. Geophys. Res. Solid Earth* 125, e2019JB018928. doi:10.1029/2019jb018928

Milliner, C., and Donnellan, A. (2020). Using Daily Observations from Planet Labs Satellite Imagery to Separate the Surface Deformation between the 4 July Mw 6.4 Foreshock and 5 July Mw 7.1 Mainshock during the 2019 Ridgecrest Earthquake Sequence. *Seismological Res. Lett.* 91, 1986–1997. doi:10.1785/0220190271

Perrin, C., Manighetti, I., Ampuero, J.-P., Cappa, F., and Gaudemer, Y. (2016a). Location of Largest Earthquake Slip and Fast Rupture Controlled by Along-Strike Change in Fault Structural Maturity Due to Fault Growth. *J. Geophys. Res. Solid Earth* 121, 3666–3685. doi:10.1002/2015jb012671

Perrin, C., Manighetti, I., and Gaudemer, Y. (2016b). Off-fault Tip Splay Networks: A Genetic and Generic Property of Faults Indicative of Their Long-Term Propagation. *Comptes Rendus Geosci.* 348, 52–60. doi:10.1016/j.crte.2015.05.002

Radiguet, M., Cotton, F., Manighetti, I., Campillo, M., and Douglas, J. (2009). Dependency of Near-Field Ground Motions on the Structural Maturity of the Ruptured Faults. *Bull. Seismological Soc. America* 99, 2572–2581. doi:10.1785/0120080340

Ruhl, C. J., Melgar, D., Geng, J., Goldberg, D. E., Crowell, B. W., Allen, R. M., et al. (2019). A Global Database of Strong-Motion Displacement GNSS Recordings and an Example Application to PGD Scaling. *Seismological Res. Lett.* 90, 271–279. doi:10.1785/0220180177

Satriano, C., Elia, L., Martino, C., Lancieri, M., Zollo, A., and Iannaccone, G. (2011). PRESTo, the Earthquake Early Warning System for Southern Italy: Concepts, Capabilities and Future Perspectives. *Soil Dyn. Earthquake Eng.* 31, 137–153. doi:10.1016/j.soildyn.2010.06.008

Scholz, C. H. (2019). *The Mechanics of Earthquakes and Faulting*. Cambridge University Press.

Scott, C. P., Arrowsmith, J. R., Nissen, E., Lajoie, L., Maruyama, T., and Chiba, T. (2018). The M 7 2016 Kumamoto, Japan, Earthquake: 3-D Deformation along the Fault and within the Damage Zone Constrained from Differential Lidar Topography. *J. Geophys. Res. Solid Earth* 123, 6138–6155. doi:10.1029/2018jb015581

Shen, Z.-K., Sun, J., Zhang, P., Wan, Y., Wang, M., Bürgmann, R., et al. (2009). Slip Maxima at Fault Junctions and Rupturing of Barriers during the 2008 Wenchuan Earthquake. *Nat. Geosci* 2, 718–724. doi:10.1038/ngeo636

Shirahama, Y., Yoshimi, M., Awata, Y., Maruyama, T., Azuma, T., Miyashita, Y., et al. (2016). Characteristics of the Surface Ruptures Associated with the 2016 Kumamoto Earthquake Sequence, central Kyushu, Japan. *Earth, Planets and Space* 68, 1–12. doi:10.1186/s40623-016-0559-1

Somei, K., Miyakoshi, K., Yoshida, K., Kurahashi, S., and Irikura, K. (2020). Near-Source Strong Pulses During Two Large MJMA 6.5 and MJMA 7.3 Events in the 2016 Kumamoto, Japan, Earthquakes. *Pure Appl. Geophys.*, 177. doi:10.1007/s00024-019-02095-6

Stubailo, I., Alvarez, M., Biasi, G., Bhadha, R., and Hauksson, E. (2021). Latency of Waveform Data Delivery from the Southern California Seismic Network during the 2019 Ridgecrest Earthquake Sequence and its Effect on ShakeAlert. *Seismological Soc. America* 92, 170–186. doi:10.1785/0220200211

Uchide, T., Horikawa, H., Nakai, M., Matsushita, R., Shigematsu, N., Ando, R., et al. (2016). The 2016 Kumamoto–Oita Earthquake Sequence: Aftershock Seismicity gap and Dynamic Triggering in Volcanic Areas. *Earth, Planets and Space* 68, 1–10. doi:10.1186/s40623-016-0556-4

Wang, K., and Bürgmann, R. (2020). Co- and Early Postseismic Deformation Due to the 2019 Ridgecrest Earthquake Sequence Constrained by Sentinel-1 and COSMO-SkyMed SAR Data. *Seismological Res. Lett.* 91, 1998–2009. doi:10.1785/0220190299

Wells, D. L., and Coppersmith, K. J. (1994). New Empirical Relationships Among Magnitude, Rupture Length, Rupture Width, Rupture Area, and Surface Displacement. *Bull. seismological Soc. America* 84, 974–1002.

Wesnousky, S. G. (1988). Seismological and Structural Evolution of Strike-Slip Faults. *Nature* 335, 340–343. doi:10.1038/335340a0

Wu, Y.-M., Yen, H.-Y., Zhao, L., Huang, B.-S., and Liang, W.-T. (2006). Magnitude Determination Using Initial P Waves: A Single-Station Approach. *Geophys. Res. Lett.* 33. doi:10.1029/2005gl025395

Yamada, M. (2007). *Early Warning for Earthquakes with Large Rupture Dimension*.

Yoshida, S. (2016). Earthquakes in Oita Triggered by the 2016 M 7.3 Kumamoto Earthquake. *Earth, Planets and Space* 68, 1–13. doi:10.1186/s40623-016-0552-8

Conflict of Interest: The authors declare that the research was conducted in the absence of any commercial or financial relationships that could be construed as a potential conflict of interest.

Publisher's Note: All claims expressed in this article are solely those of the authors and do not necessarily represent those of their affiliated organizations, or those of the publisher, the editors and the reviewers. Any product that may be evaluated in this article, or claim that may be made by its manufacturer, is not guaranteed or endorsed by the publisher.

frontiers in Earth Science

ORIGINAL RESEARCH
published: 16 August 2021
doi: 10.3389/feart.2021.685153

Between Necessity and Legal Responsibility: The Development of EEWS in Italy and its International Framework

Cecilia Valbonesi[1,2]*

[1]Dipartimento di Scienze Giuridiche, University of Florence, Florence, Italy, [2]Istituto Nazionale di Geofisica e Vulcanologia, Rome, Italy

Earthquake Early Warning Systems (EEWSs) represent a technical-scientific challenge aimed at improving the chance of the population exposed to the earthquake shaking of surviving or being less affected. The ability of an EEWS to affect the risk and, in particular, vulnerability and exposure, may determine serious legal responsibilities for people involved in the system, as scientists and experts. The main question concerns, in fact, the relationship between EEWSs and the predictability and avoidability of earthquake effects-i.e., the ground shaking affecting citizens and infrastructures - and the possibility for people to adopt self-protective behavior and/or for industrial infrastructures to be secured. In Italy, natural disasters, such as the 2009 L'Aquila earthquake, teach us that the relationship between science and law is really difficult. So, before EEW's become operational in Italy, it is necessary to: 1) examine the legislative and technical solutions adopted by some of the international legal systems in countries where this service is offered to citizens; 2) reconstruct the international and European regulatory framework that promotes the introduction of EW systems as life-saving tools for the protection of the right to life and understand whether and how these regulatory texts can impose an obligation on the Italian legal system to develop EEWS; 3) understand what responsibilities could be ascribed to the scientists and technicians responsible for managing EEWS in Italy, analyzing the different impact of vulnerability and exposure on the predictability and avoidability of the harmful event; 4) reflect on the lessons that our legal system will have to learn from other Countries when implementing EEW systems. In order to find appropriate solutions, it is essential to reflect on the opportunity to provide shared and well-structured protocols and creating detailed disclaimers clearly defining the limits of the service. A central role must be recognized to education, because people should not only expect to receive a correct alarm but must be able to understand the uncertainties involved in rapid estimates, be prepared to face the risk, and react in the right way.

Keywords: earthquake, early warning, criminal liability, negligence, risk

OPEN ACCESS

Edited by:
Simona Colombelli, University of Naples Federico II, Italy

Reviewed by:
Andrea Cerase, Sapienza Università di Roma, Italy
Vincenzo Mongillo, Università degli Studi di Roma La Sapienza, Italy

***Correspondence:**
Cecilia Valbonesi
cecilia.valbonesi@unifi.it

Specialty section:
This article was submitted to Geohazards and Georisks, a section of the journal Frontiers in Earth Science

Received: *24 March 2021*
Accepted: *07 July 2021*
Published: *16 August 2021*

Citation:
Valbonesi C (2021) Between Necessity and Legal Responsibility: The Development of EEWS in Italy and its International Framework. Front. Earth Sci. 9:685153. doi: 10.3389/feart.2021.685153

INTRODUCTION

Italy is one of the Countries characterized by the highest seismic hazard and risk worldwide.

Besides seismic hazard due to active geological process, the main reason for the high seismic risk lies in the vulnerability of buildings (Wang, 2011; Gómez-Novell et al., 2020; Sun et al., 2020).

Most damaging and deadly earthquakes in Italy are not huge (magnitude 5.8–6.5), with areas of destruction limited to a few tens of kilometers from the epicenter. This is probably the main reason why EEWS in Italy have not been developed and become operational yet. However, the Italian historical catalogue includes some larger events (M~7) that produced widespread damage and destruction. The most recent among these is the 1980 (M6.9) earthquake that hit Campania and Basilicata, producing strong damage in a broad area of southern Italy, including the metropolitan area of Naples, about 80 km from the epicenter.

For this reason, the EEW system PRESTo was developed like a rare and praiseworthy exception. PRESTo is "currently operative in the Campania-Lucania Apennine region to rapidly detect and characterize the small to moderate earthquakes occurring in the area. PRESTo (PRobabilistic and Evolutionary early warning SysTem) is a software platform for EEW that integrates algorithms for real-time earthquake location, magnitude estimation and damage assessment into a highly configurable and easily portable package" (Colombelli et al., 2012; Colombelli et al., 2014; Zollo et al., 2014a; Zollo et al., 2014b; Picozzi et al., 2015; Emolo et al., 2016; Colombelli et al., 2020).

Similar systems are under test in a few other regions of Italy and will probably increase in the near future (Zollo et al., 2014a).

However, such a major scientific challenge has to contend with a legislative and judicial system that is unprepared to accept and understand properly the exact expectations related to scientific progress (Foddai, 2017). The problem of the relationship between science and law origins from a profound cultural change that now characterizes our risk society: scientists and technicians are responsible for every "event of nature" and, above all, for its consequences (Luhmann, 1996; Beck, 2000; Perini, 2002).

The paradox is truly disturbing. On the one hand, we witness sophisticated possibility of dealing with natural and man-made risks, and, at the same time, science is offering us ever more precise, timely and accurate explanations of the phenomena occurring around us.

But on the other hand, the evolution of mankind, through the scientific development, creates a dangerous illusion: scientists are supposed to be able to dominate all the natural events. The power of uncertainty is completely renegaded and the impossibility to manage the consequences of natural disasters is called "negligence" (Pulitanò, 2006).

In the post - modern era uncertainty can no longer exists.

Most people blindly believe that nature can be man-made and controlled. So, when we face the harmful consequences of a natural phenomenon, we are only able to ask: "who's fault?" (Savona, 2010).

The undeniable anthropization of risks, related to the technical-scientific progress, takes on a peculiar aspect in the field of natural disasters. In that context, the overlapping of the concepts of risk and threat determines the tendency to identify the culprit in whom took the decision leading to the adverse event (Perini, 2010; Gargani, 2011; Perini, 2012; Gargani, 2016; Gargani, 2017; Gargani, 2019; Giunta, 2019).

Considering man responsible for every event "of nature" causes an indiscriminate expansion of the legal duty to prevent the harmful event. But this duty is based on a double fallacious assumption. First, the existence of a real capacity to take responsibility of protecting a legal asset (which, together with legal obligation, founds the duty of care). Secondly, the existence of valid precautionary rules, suitable to prevent a foreseeable and avoidable event. The violation of the duty of care and the incompliance with the precautionary rules determine the basis of the criminal culpable reproach (Mantovani, 2020).

In recent years, Italian criminal law made us familiar with extremely severe rulings, which can only be mentioned here.

The leading case must be found in the words of the Italian Supreme Court, which in 2010 ruled on the disaster that had struck the town of Sarno. The Court annulled the acquittal of the mayor, who was accused of the manslaughter of the citizens who had been swept away by the mudslide.

The Court stated that "if the fundamental characteristics of a natural phenomenon are not known - in particular its causes, the possibility of its development, its possible effects - the caution which must be exercised in dealing with it, in order to eliminate or reduce its consequences, must be the greatest, precisely because the most destructive effects cannot be excluded by an *ex ante* assessment based on reliable scientific knowledge" (see: Cass. Pen. Sez. IV, May 30, 2010, n. 16761, in DeJure).

From here on, everything thus becomes predictable and avoidable, including phenomena that have never happened before.

This principle reverberates in the judgment of the so - called Grandi Rischi trial, following the earthquake in L'Aquila (Notaro, 2013; Notaro, 2014; Simoncini, 2014; Amato and Galadini, 2015; Cerase, 2015; Fornasari and Insolera, 2015) and again, recently, in the rule of the Supreme Court which convicted two mayors for the death of two students who were swept away by a falling rock. In confirming the liability for manslaughter, the Court stated that "... the assessment of foreseeability, having predictive characteristics, while inevitably inspired from what has happened in the past, must necessarily be carried out by imagining that in the future a given natural phenomenon may manifest itself with characteristics of greater gravity, unless the characteristics of what happened in the past are sufficient to exclude the risk of more serious events" (see: Cass. Pen. Sez. IV, March 29, 2018, n. 14550, in DeJure).

This process of criminalizing natural risk management relegates the culpable reproach to a mere instrument of social composition. Courts, facing the harms outcoming from natural events, impose mild penalties, often suspended but able to guarantee compensation for victims.

Not only that, but the obstinate search for the culprit among those charged with Civil Protection duties deprives the population of the responsibility for observing self-protective behavior which, as the social sciences teach us, is a

fundamental element in preventing the harmful consequences of risk (Becker et al., 2020a; Becker et al., 2020b).

Such a drift is unacceptable and must be countered through an investigation on national and international legal instruments that offer concrete tools to ensure scientists and technicians a bit more tranquility in developing essential scientific and technological challenges such as the introduction of EEWS in Italy and Europe.

DIFFERENCES BETWEEN EEWS AND TSUNAMI EARLY WARNING SYSTEMS IN TERMS OF EVENT PREDICTABILITY AND AVOIDABILITY

The importance of the EEWS challenge can be better understood if we reflect, albeit briefly, on the differential and identity aspects of another fundamental sector of EW development in Italy and Europe, such as tsunamis EWS (TEWS) (Amato et al., 2021; Basili et al., 2021). We refer here to the TEWS coordinated by UNESCO-IOC worldwide, in which the target are tsunamis induced by large marine or coastal earthquakes (Amato, 2020).

When reflecting on the nature of this risk, its peculiarities become clear: unlike seismic risk, tsunami risk is characterized by an exquisitely predictive nature. Scientists manage technical-scientific data, resulting from a complex elaboration, which are potential precursors of the possible occurrence of a natural event that could threaten lives and infrastructures.

While EEWS predict an expected shaking, that could potentially cause damage, TEWS directly predict and try to avoid or minimize the occurrence of potential harms related to a tsunami on the coast.

Therefore, as we will try to explain later, the different object of predictability also implies a different asset of responsibilities.

Another essential topic involves the regulatory framework in which the TEWS operate. Italy is, in fact, part of the UNESCO-IOC ICG/NEAM that regulates and coordinates the Tsunami Warning Centers in the Mediterranean Sea and the North East Atlantic, offering them a copious, though not always well-ordered, production of guidelines to which the TWS of each Country must comply with (see: http://www.unesco.org/new/en/natural-sciences/ioc-oceans/sections-andprogrammes/tsunami/) (March 23, 2021).

The regulatory and institutional framework offers a valuable paradigm of comparison for the service performance which is useful for protecting operators from possible objections regarding the erroneous nature of some choices they might make. These rules are, in fact, the result of a cohesive international scientific community and they have, for this reason, an intrinsic validity.

This institutional and regulatory paradigm is absent for EEWS. So, scientists and civil protection operators develop and implement these systems without an internationally shared frame of reference (especially clear and shared guidelines) (Montagni, 2007). Consequently, they are more exposed to a possible criminal reproach for the possible harmful effects of the choices made.

THE FOCUS OF THE STUDY

For this reason, before EEW systems start their operational training in Italy, it will be important to: 1) first of all, look at the legislative and technical solutions adopted by some of the international legal systems that have been offering this service to citizens for a long time; 2) to reconstruct the international and European regulatory framework that promotes the introduction of EW systems as life-saving instruments for the protection of the right to life, and to understand whether and how these regulatory texts can impose an obligation for Italian legal system to develop EEWS; 3) to understand what responsibilities could be ascribed to scientists and technicians responsible for developing and managing EEWS in Italy; 4) to reflect on the lessons that our legal system will have to learn from other countries when implementing EEW systems.

AN INTERESTED LOOK AT THE TECHNICAL AND LEGISLATIVE EXPERIENCES OF OTHER COUNTRIES

As we have seen, the problems related to the implementation of TEWS are on the one hand, diminished and on the other hand, strongly stressed in EEWS.

The application of EEWS in Italy is conditioned by the morphological characteristics of the peninsula. Unlike the great earthquakes which take place in other Countries, such as Japan or Mexico, where response times could reach few tens of seconds, in Italy these response times are significantly reduced. This certainly affects the range of self-protective instruments that can be implemented. However, this peculiarity will certainly not discourage potential recourse to criminal justice which, among other things, will not even encounter the limits that might come from a behavioral paradigm positivized in precautionary rules.

Therefore, the need that operational steps of EEWS in Italy must be preceded by an appropriate regulatory framework, induce to examine the legislation of some of the Countries that have been offering an EEW service for many years, such as Mexico, Japan and the United States, with particular reference to the Californian experience.

Here it is possible to observe only some of the most interesting regulatory aspects. The research was carried out on the basis of the most significant scientific literature available, with constant reference to the evolution of legislation on the specific topics.

Mexico

Moving from Mexico, we can underline that the most important EEWS, which has been in operation for more than two decades, is the Mexican Seismic Alert System- SASMEX. The public warning system, operational since 1993, issues an alert when two or more seismic stations detect events with a magnitude higher than 5.5 (Suarez, 2018; Santos-Reyes, 2019).

As highlighted, "warnings are broadcast through TV channels, radio stations, and loudspeakers, together with a dedicated radio channel, SASPER, used to alert authorities, universities, schools,

emergency responders, and civil protection" (Beltramone and Carrilho Gomes, 2021). The SASMEX system has recently been complemented and regulated by the "TECHNICAL STANDARD - 2019 SEISMIC ALERT RECEIPTING EQUIPMENT 2019" published in the Official Gazette of Mexico City in August 2019 (see: https://www.consejeria.cdmx.gob.mx/gaceta-oficial) (Accessed February 23, 2021).

This Technical Standard contributes to the achievement of the goal of the Mexican National Civil Protection System, which is to safeguard life and protect society in the event of a disaster caused by natural agents, "...through actions that reduce or eliminate the loss of human life, the damage to a productive facility, the destruction of material assets, the damage to nature and the interruption of functions essential to society. The technical standards also aim to restore the population and its environment to the living conditions they had before the disaster".

Risk management and related responsibilities can be included in the framework of LEY GENERAL DE PROTECCIÓN CIVIL, Nueva Ley published in the Diario Oficial de la Federación el 6 de junio de 2012. Last amendment was published in DOF 19-01-2018 and in the REGLAMENTO de la Ley General de Protección Civil, DOF: May 13, 2014. (see: https://www.gob.mx/indesol/documentos/ley-general-de-proteccion-civil-60762) (Accessed February 23, 2021).

Japan

Even more interesting is the Japanese experience (Dando, 1960; Cleary, 2006; White Paper Disaster Management in Japan, 2019).

EEWS were initially developed in 1992 for slowing and stopping high-speed trains (called Shinkansen) prior to strong shaking. The success of that experiment, in addition to the devastating effects of the 1995 Kobe earthquake, convinced Government and scientists to build a national earthquake early warning system. On October 1, 2007, JMA launched the Earthquake Early Warning service (Kamigaichi et al., 2009; Mattsui, 2019; Johnson et al., 2020).

Japanese EEWS is an alert system based on seismic wave data recorded by seismometer stations. Today, earthquake early warnings are transmitted *via* J-ALERT and EAM (Emergency Alert Mail).

The procedure is very interesting: "J-ALERT disseminates urgent warnings (for tsunamis, earthquakes, and ballistic missile attacks) *via* municipal disaster prevention radio receivers, broadcast media, and mobile phones. The mobile phone notifications are delivered *via* EAM, which sends disaster and evacuation information to mobile phones in warning areas. EEWS and J-ALERT are operated by Japan's national government; EAM is provided as a free service by mobile phone carriers and was developed with their assistance" (see: https://reliefweb.int/sites/reliefweb.int/files/resources/Information-and-Communication-Technology-for-Disaster-Risk-Management-in-Japan.pdf) (Access December 12, 2020).

The legislative framework is also very interesting and can be examinated only partially. We can move from the Disaster Countermeasures Basic Act, 1961 (Act No. 223 of 1961) which establishes, at art. 52. that "1) The kind, nature, pattern or method of signal employed in the issuance and transmission of an alarm, warning, recommendations or orders for evacuation, shall be determined by the Office of the Prime Minister except where specified by Act. 2) No person shall be permitted to employ a signal provided under the preceding paragraph or similar signals for other than legitimate purposes" (see: https://www.adrc.asia/documents/law/DisasterCountermeasuresBasicAct.pdf).

The government's expertise on this regulation is confirmed by a valuable document available in English and Japanese, issued by the Cabinet Office, Government of Japan, in 2014, entitled Disaster Management in Japan, which provides an overview of the technical and legislative developments following each earthquake in Japan (see: http://www.bousai.go.jp/en/documentation/reports/index.html).

California

A more specific analysis should have been devoted to California systems and regulatory framework (Goltz, 2002; Allen and Kanamori, 2003; Farber and Chen, 2006; Wu et al., 2007; Wurman et al., 2007; Wahlstrom, 2009; Farber, 2011; Fick, 2017; Melgar and Hayes, 2019; Allen et al., 2020).

In this context we can only highlight that on October 17, 2019, the U.S.G.S. and the State of California kicked off the first public statewide test of the EEWS, which is powered by EEW alerts provided by the USGS, Shake Alert, 2021 (USGS, 2017; 2018. See: www.usgs.gov) (Accessed April 23, 2020).

Alerts are provided by two independent methods, the first through the federal Wireless Emergency Alert (WEA) system and the second through the University of California Berkeley's MyShake smartphone application.

ShakeAlerts are sent through WEA to those who could potentially suffer damage from quakes of magnitude 5 or higher (Allen and Melgar, 2019. See: https://www.usgs.gov/natural-hazards/earthquake-hazards/shakealert) (Accessed February 16, 2021).

Recently, a smartphone APP, called QuakeAlertUSA, was introduced in order to allow Californian users to countdown before the quakes arrive and to set the APP even for weak tremors.

The Californian authorities have also started issuing SMS alerts through Amber Alert-style Wireless Emergency System. (see: https://www.latimes.com/california/story/2020-02-12/californias-new-early-warning-earthquake-app-features-a-shaking-countdown).

The development and implementation of EEWS systems is part of the federal and state legislative framework, one of the main references to which is the California Emergency Service Act (see: https://www.caloes.ca.gov/LegalAffairsSite/Documents/Cal%20OES%20Yellow%20Book.pdf) which, in chapter § 8587.8. (Comprehensive statewide earthquake early warning system; features; compliance review; funding) states that all scientific partners "and other stakeholders, shall develop a comprehensive statewide earthquake early warning system in California through a public-private partnership, which shall include, but not be limited to, the following features (...) Establishment of warning notification distribution paths to the public;

Integration of earthquake early warning education with general earthquake preparedness efforts (...)".

In the federal legislation EEWS are regulated by Robert T. Stafford Disaster Relief and Emergency Assistance Act (see: https://www.fema.gov/sites/default/files/2020-03/stafford-act_2019.pdf) which, in Sec. 404. Hazard Mitigation, Use Of Assistance For Earthquake Hazards states that "Recipients of hazard mitigation assistance, provided under this section and section 203, may use the assistance to conduct activities 1) to help reduce the risk of future damage, hardship, loss, or suffering in any area affected by earthquake hazards, including improvements to regional seismic networks in support of building a capability for earthquake early warning; 2) improvements to geodetic networks in support of building a capability for earthquake early warning; and 3) improvements to seismometers, Global Positioning System receivers, and associated infrastructure in support of building a capability for earthquake early warning".

Recently, the FEMA Fact sheet Disaster Recovery Reform Act and Earthquake Early Warning Systems (see: https://www.fema.gov/sites/default/files/2020-09/fema_drra-earthquake-early-warning-systems_fact-sheet_September-2020.pdf) issued in September 2020, remembers that "Specifically, DRRA Section 1233 revised the Stafford Act by adding a new Section 404(g) to allow recipients of hazard mitigation assistance to leverage such funding to support building capability for earthquake early warning (EEW) systems".

The awareness of this regulatory framework shows how it is therefore necessary, at this point, to go into the deep of international and European sources of EEWS and understand how they could operate in the Italian legal system in terms of duties and responsibilities (Zschau et al., 2008; Clinton et al., 2016).

THE ROLE OF INTERNATIONAL AND EUROPEAN LEGAL SOURCES ON THE POSSIBLE CONFIGURABILITY OF A DUTY TO PROTECT THE POPULATION THROUGH THE IMPLEMENTATION OF EEW SYSTEMS

The absence of both EEW systems and the related national framework, aimed to regulate the introduction and development of these systems, do not prevent us from answering to some important questions arising from the fact that Italian law could be deeply influenced by European and International law.

The latter can, in fact, play a fundamental role in identifying obligations and responsibilities, especially since, as we shall later explain in more detail, many international "treaties" consider EEWS necessary for protecting human rights. More generally, the adoption of instruments aimed at offering safety solutions protect the rights to health of populations. Among these, an absolutely prominent role is reserved to EWs. Hence, we need to answer to a number of central questions concerning: 1) Whether there are and which ones of these international agreements highlight the need to transpose, at the national level, the EEWS as a fundamental tool for reducing the harmful impact of earthquakes; 2) Whether, in accordance with the duty to protect human rights, there are obligations for States to transpose these systems in legal frameworks; 3) Even in the absence of any official transposition of EEWS in national alert system, does the rank of these international sources, provide a legal duty, for engineers and scientists, to develop such systems and can the failure to implement this system results in legal consequences if an earthquake causes damage to property or casualties?

International Agreements Prescribing the Adoption of Early Warning Systems to Protect the Population

Our investigation will focus now on the importance that the developing of EWs (and, consequently, EEWS) have reached in the international institutional debate (**Table 1**). The first and most important stage in this process is the Hyogo Framework for Action (see: https://www.unisdr.org/2005/wcdr/intergover/official-doc/L-docs/Hyogo-framework-for-action-english.pdf) (Accessed March 1, 2021). This document represents one of the first and fundamental moments of the international awareness concerning the need to offer people effective protection from the consequences of natural disasters. The goal appears even more effective because of the direct involvement of individual governments. In the context of the Hyogo Framework for Action, EWS even emerges as the second priority for action: "2. identify, assess and monitor disaster risk and improve early warning".

Although it is not possible here to report on all the concrete development of the Hyogo second priority, it is nevertheless worth emphasizing how it has fostered shared policies, aimed at saving population from the effects of natural disasters.

In the same year, (2005), the Secretary General, Kofi Annan, requested the UN to draw up a report (Global Survey of Early Warning Systems), which provides a global assessment of the capacities, the existing gaps and the opportunities related to EWS. The Report aims to establish a "worldwide early warning system for natural hazards building on existing national and regional capacity" (see: https://www.undrr.org/publication/global-survey-early-warning-systems).

But the central role of EW systems has found its most compelling expression in the Sendai Framework for Disaster Risk Reduction 2015-2030, which recognize a decisive role to multi hazard early warning systems (see: https://www.undrr.org/publication/sendai-framework-disaster-risk-reduction-2015-2030) (Accessed March 1, 2021).

Sendai Framework includes seven goals and the seventh is: "Substantially increase public availability of and access to multi-hazard early warning systems, information and risk assessments by 2030".

So, in Sendai Framework, EWS and, consequently EEWS, appear to be a central tool to ensure a strong protection for the largest number of Countries involved and they will play a decisive role in the current and future challenge of disaster

risk reduction. In a global and international frame, they help in developing "policies and practices for disaster risk management (that) must be based on an understanding of risks in all their dimensions of vulnerability, capacity, and exposure of people and goods". Even more, EEWS implement the active and self-protective role played by individual stakeholders and community.

Great interest also shows the language used in Sendai Framework. The words chosen show a strong will to create, for the adherent Countries, specific duties of care. In defining the "guiding principles", it is clear that "every State has the primary responsibility to prevent and reduce the risk of disasters, including through international, supranational, interregional, cross-border and bilateral cooperation". The target is "to protect people and their property, health, livelihoods and productive, cultural and environmental resources, while promoting and protecting all human rights, including the right to development".

Consistent with a fundamental *bottom up* risk management strategy is the need to "empower local authorities and communities to reduce disaster risk appropriately, including through resources, incentives and decision-making responsibilities".

The purpose to ensure greater development of these goals necessarily involves the role of UNESCO, especially through UNESCO'S INTERNATIONAL PLATFORM ON EARTHQUAKE EARLY WARNING SYSTEMS (IP-EEWS) (see: https://en.unesco.org/news/launch-unesco-s-international-platform-earthquake-early-warning-systems) (Accessed March 1, 2021).

UNESCO stressed the importance of EEWS not only for human safety but also for the environment, so, "in December 2015, launched the International Platform on Earthquake Early Warning Systems". The project involves Italy through the participation of the University of Naples Federico II.

While the international framework appears to be aware of the importance of EEWS, the same cannot be said for the European Union policies, which have only partially acknowledged the need to implement the protection expressed by the Sendai Framework for Disaster Risk Reduction.

Two documents must be analyzed. First of all, we have the COMMISSION STAFF WORKING DOCUMENT Action Plan on the Sendai Framework for Disaster Risk Reduction 2015-2030-A disaster risk-informed approach for all EU policies (see: https://ec.europa.eu/transparency/regdoc/rep/10102/2016/EN/10102-2016-205-EN-F1-1.PDF) (Accessed March 2, 2021).

The European Commission, considering the central role played by the EU in determining the Sendai Framework, affirms that it "is the basis for a disaster risk-informed approach to policy-making, offering a coherent agenda across different EU policies to strengthen resilience to risks and shocks and supporting the EU priorities of investment, competitiveness, research and innovation".

The Document, in setting out Action Plan Implementation Priorities notes that "while several policy initiatives are already contributing to implement the Sendai Framework in a fragmented way, a more systematic risk-informed approach for all EU policies in order to reach the Sendai objectives does not exist".

So, the Action Plan wants to ensure the application of Sendai Priority 1: Understanding disaster risk, the development of global multi-risk in which EWS are essential for assuring a correct Assessment of risks and the Sendai Priority 3: Investing in disaster risk reduction for resilience, in which EWS take a leading role among the Key policies and practices.

Even more, European Commission wants to guarantee the greatest role recognized to multi hazard EWSs in Sendai Priority 4: Enhancing disaster preparedness for effective response and to "Build Back Better" in recovery, rehabilitation and reconstruction.

In reinforcing the determinations of the "Commission Staff Working Document: Action Plan on the Sendai Framework for Disaster Risk Reduction 2015-2030", the European Committee of the Regions (see: https://eur-lex.europa.eu/legal-content/EN/TXT/PDF/?uri=CELEX:52016AR5035&from=IT) (Accessed March 3, 2021), expressed, in 2017, an Official Opinion.

In *Considerando* 21, the European Committee of the Regions noted the importance of "promoting the use of IT communication technologies, ICT and automatic early warning networks, based on early detection, instant communication and proactive intervention protocols". While in *Considerando* 25 underlined "support for early warning systems, measures to improve redundant technologies used for communicating between civil protection systems and public warnings as well as a "build back better" approach following disasters".

This brief and certainly not exhaustive picture of the international and European regulatory framework that prescribe the use of EW for risk reduction purposes and for protecting the life and safety of the population and infrastructures, leads us to ask the second of the questions set out above. It is necessary to understand, on the one hand, whether these targets impose a legal duty, for Italy, to protect citizens through the introduction and development of EEW systems. On the other hand, we must establish whether this discipline can affect the legal asset and especially the responsibilities of scientists and engineers/technicians charged of civil protection functions (during an earthquake) (Dovere, 2017; Gargani, 2011; Gargani, 2016; Gargani, 2019).

TABLE 1 | International documents concerning EEWS.

- Hyogo Framework for Action, 2005
- Global Survey of Early Warning Systems, UNDRR, 2005
- Sendai Framework for Disaster Risk Reduction 2015-2030
- Unesco's International Platform on Earthquake Early Warning Systems (Ip-Eews), 2015
- Commission Staff Working Document - Action Plan on the Sendai Framework for Disaster Risk Reduction 2015-2030-A disaster risk-informed approach for all EU policies, European Commission, 2015
- Opinion of the European Committee of the Regions — Action Plan on the Sendai Framework for Disaster Risk Reduction 2015-2030 — A disaster risk-informed approach for all EU policies

Are There any Obligations for Countries to Transpose in Their Civil Protection Systems the EEWS in Accordance With Their Duty to Protect Human Rights?

The answer to this question implies consciousness of two crucial aspects.

On the first side, the development of EEWS represents, as we have seen also in the light of the documents examined so far, a functional measure to safeguard human rights and in particular to protect life and safety of the individuals and the community facing natural disasters.

Academics stated that "While the Convention on the Rights of People with Disabilities is the only human rights Treaty which explicit references to disasters, the applicability of human rights law to disasters is receiving greater attention from both the scholarly community and intergovernmental bodies at the regional and international levels" (Ferris, 2014; Crawford, 2019).

There are some different ways in which international human rights law is being used to strengthen efforts at prevention, response and recovery from disasters.

The most important are "The use of legal remedies as a way of holding governments accountable when they fail to prevent or reduce the risk of disasters" and "The use of primarily "soft" international law as reflected in the Guiding Principles on Internal Displacement, as a way of upholding the rights of those displaced by disasters" (Ferris, 2014; Conforti, 2019).

The main question concern if prevention could be a governmental responsibility. In order to answer we must note that the International Human Rights Conventions include the right to life and the related obligation of the State to protect life.

In these cases, "States have a responsibility to reduce the risks of disasters and to protect those at imminent risk of disasters through timely warnings and evacuations and when they fail to do so, they face domestic and international criticism and potential legal action" (Ferris, 2014).

The protection of life, to which the adoption of EEWS is expected to be instrumental, is a key element of one of the international conventions with the greatest potential for application. We are referring to the European Convention on Human Rights. The Article 2 establishes the right to life as a "core right" (Manes and Caianiello, 2020).

The doctrine reminds us that the absolute importance of life has allowed a progressively broader interpretation of Article 2, the operability of which has been recognized even when life has only been exposed to danger or the person involved in risk has ultimately been saved (Paliero and Viganò, 2013; Manes and Caianiello, 2020).

The breadth of this duty implies that national authorities not only must avoid to intentionally kill someone but also and above, are responsible for a positive obligation to protect life and safety of their citizens.

These positive obligations convey a State's duties to provide "measures to prevent a violation of the rights . . . whether it arises from the exercise of public power or from the action of a private individuals" (Manes, 2010; Manes and Caianiello, 2020).

In this regard, the principle of effectiveness requires to recognize "that a violation of the Convention committed by a private individual may be indirectly attributed to the State if this one has made it possible or probable". So, "in order not to incur in a violation, the State itself must provide the legislative, administrative and judicial framework capable of guaranteeing rights also in relations between individuals" (Zorzi Giustiniani, 2018; Manes and Caianiello, 2020).

The guarantee of the positive duty of protection and, in particular, of the protection of life imposed on Governments also means "protecting the life and safety of individuals who have entrusted themselves to the public apparatus, as in the case of schools, hospitals or nursing. This responsibility of States also occurs in the hypothesis of inadequate functioning of the health system or in cases where - in the face of emergency circumstances - assistance has been denied by the public administration" (Manes and Caianiello, 2020). This duty implies that Governments must activate instruments for ascertaining and compensating victims for damage. In Lopez de Sousa Fernandes v. Portugal, December 19, 2017, the European Court of Human Rights (ECHR), Grand Chamber, found that Portugal had not properly fulfilled its procedural duties. It failed to provide adequate means to find the truth about the unfortunate event discussed in Court.

At this point, answering the question posed above appears to be urgent. Can a State be held responsible for not having adopted appropriate systems to deal with the harmful consequences of an expected natural risk?

The answer to this question is provided by two judgments of the European Court of Human Rights which, however, do not concern seismic risk.

The first is the famous judgment Budayeva and Others v. Russia (European Court of Human Rights, Budayeva and others v. Russia, Applications nos. 15339/02, 21166/02, 20058/02, 11673/02 and 15343/02, judgment of March 20, 2008. (See: http://hudoc.echr.coe.int/sites/eng-press/pages/search.aspx?i=003-2294127-2474035) (Accessed December 3, 2020).

The case concerned a series of mudslides that struck the town of Tyrnauz in southern Russia in 2000, causing numerous victims.

The Strasbourg Court set out for the first time the criteria that must be analyzed in order to assess whether the conduct of the state authorities complied or not with the positive obligations to protect human rights arising from the European Convention on Human Rights. First, the Court assessed whether the risk of the event occurred was foreseeable by the authorities of the State ("foreseeability of the risk"). The analysis was carried out on the basis of a number of factual indices, such as the origin of the threat, the imminence of the risk and the recurrence of the disaster over time. The analysis showed that not only was the town of Tyrnauz notoriously prone to landslides, but the Russian Government had also been warned of the imminence of a possible event that would occur. From these assumptions, the Court concluded that the Russian Government could have reasonably foreseen the occurrence of the adverse event. After having established the foreseeability of the risk and the extent of the resulting event, the Court assessed whether the Russian authorities had done everything they could to protect the

rights of the people under their jurisdiction (the so-called "best efforts requirement"). The Court established that Russia government neither allocated resources to prevent the harms not even repaired the damage caused by previous events.

Even more relevant is the part in which the Court ruled that the Russian authorities had failed to adequately inform citizens about the risk and to promptly evacuate them from the affected area. All these circumstances led the Court to recognize the existence of a violation of the right to life under Article 2 of the Convention, because Russia failed to implement essential measures to protect people under its jurisdiction.

Not dissimilar conclusions were reached, 4 years later, in Kolyadenko and Others v. Russia (European Court of Human Rights, Öneryildiz v. Turkey, Application 48939/99, judgment of November 30, 2004. (See: http://hudoc.echr.coe.int/sites/fra/pages/search.aspx?i=003-1204313-1251361) (Accessed December 1, 2020), which concerned the flooding of the city of Vladivostok due to the exceptional discharge of water from the Pionerskoye reservoir adjacent to the city, caused by heavy rainfall into the Pionerskoye river.

The Court affirmed that the Russian authorities could and should have made an early assessment of the risk and taken the necessary measures to save the victims. Great interest must be posed in the confirmation of the Court's statutes in Budayeva and Others v. Russia. In both cases, the Court ruled that the duty for States to protect human rights does exist not only in the imminence of a catastrophe, but also in advance, since the moment when it is even abstractly foreseeable, by the authorities, that certain events could occur in the future. The authorities would have a duty to conduct risk assessment.

In this case too, the Court recognized a violation of the right to life (Article 2 of the Convention): Russia failed to secure the area by cleaning the Pionerskoye River and this was causally related to the disaster.

These judicial cases are very interesting for many reasons. The first, of course, relates to the possibility of arguing that Article 2 of the European Convention on Human Rights is a suitable instrument to establish the responsibility of the State for the harmful consequences arising from the failure to adopt risk management tools such as, among others, a proper warning of the population.

Moreover, the rules of Budayeva and Others v. Russia seems to open the way also for a preventive protection of the legal assets involved. In other words, the judgment tells us that the right to life must be safeguarded by Government not only because of the positive obligations of protection established by the European Convention on Human Rights but also, more in general, because the occurrence of certain disasters and their impact on the fundamental rights cannot always be unforeseeable by the authorities. So, a Government particularly exposed to certain types of disasters must plan in advance the essential measures to adapt to those consequences.

In this case, the possibility of appealing the Court before the event occurred is possible, however, by invoking the violation of Article 8 of the Convention. As jurisprudence on environmental disasters shows, private and family life would be profoundly affected if the event occurred and, in this case, the Government authority is responsible if it did not the necessary to avoid harms and causalities.

These encouraging prospects, however, cannot blur the difficulties of a fully applying EEWS in Italy. The first concerns, as is well known, the geological conformation of Italy, which in some cases would not allow potential victims the time to assume effectively protective behavior. But even if these precautionary measures were potentially feasible, maybe they could be effective, as we will see, only when applied to surgery operating rooms, trains and industrial processes. Only in these cases, when EEWS can stop the activity, they could have a real saving effectiveness. If the EEWS are used, even not directly, to save people from the collapse of structures, the paradigm changes. In this case, in fact, it would be more consistent to establish a Government's responsibility for not having made compulsory, for citizens, the structural adaptation of buildings to anti-seismic standards, rather than for failing to introduce warning instruments that, in certain areas, could not really save anyone.

Even if it is not yet Mandatory to Adopt EEWS, Does the Legal and Scientific Rank of International Documents Imposes to Technicians and Scientists the Development of These Life-Saving Systems? And Could the Failure to Comply With This Requirement Result in Legal Consequences if an Earthquake Causes Damage to Property or Persons?

It is clear from the picture outlined so far that it is difficult to enforce Governments in transposition and implementation of EEWS as essential tool for protecting and safeguarding the lives of their citizens. The complexity of these systems and the timing of their realization, among others, impose then a reflection on the possibility that the legal instruments, developed in the international scenario, find direct or indirect application in the Italian legal system. The investigation will focus on the possible influence of this legal framework in determining possible criminal liability linked to the harmful consequences produced by earthquakes on the life and on the public and private safety of citizens.

In order to answer this question, we must first try to establish the status and rank of the legal texts examined and, consequently, the scope of their application.

It is immediately necessary to clarify how these considerations are a small part of the broader debate on the influence of European Union law on the boundary of legality and the related duties that arise for a national system like the Italian one (Donini, 2011).

As pointed out by Doctrine (Bernardi, 2011; Bernardi, 2015), a process of transformation of legality is now taking place in Italy and more generally in the EU zone. This process, on the one hand, moves from the centrality acknowledged to the European Union law, whose primacy imposes direct effects on the national judicial system. On the other hand, it starts from the increasing role of

technology which affects the duty to criminalize a specific kind of behaviors (Bernardi, 2011). In fact, the Author pointed out that "in fields such as medical or entrepreneurial liability, it is not uncommon for the Government to abdicate its function of formulating rules, in particular precautionary rules (e.g., rules of safe conduct that impose a particular behavior in order to prevent the occurrence of harmful events) (Giunta 1999; Mantovani 2020). It benefits real epistemic communities considered scientifically more suitable for risk assessment and results in formulation and identification of scientific laws, and their accreditation protocols and organizational models (...)" (Palazzo, 2016).

Thus, the primacy of effectiveness over the authoritativeness of the rule and the penetrating role of the European Union's criminal jurisdiction, albeit indirectly (Article 83 TFEU), deploys the paradigm of legality (Giunta, 2020) and opens the door to European Union regulation which can integrate the criminal reproach, also and above all, in the field of negligence, traditionally based on precautionary rules, which are naturally osmotic to technical heteronymous rules.

The absence of European regulations and directives that can exert their indirect criminal cogency in our legal system, rises another fundamental question. Should the sources regulating EEWS systems be transposed into Italian civil protection system and how they might affect the structure of negligent criminal liability that can be recognized as consequences of an earthquake event?

The dual European and international nature of the regulations examined means that the answer should not be limited to the influence of European rules alone but should be broadened by giving it a general perspective.

This hermeneutical operation supposes establishing, at least, whether the Sendai Framework of Action, the Commission Staff Working Document: Action Plan on the Sendai Framework for Disaster Risk Reduction 2015-2030 and the Opinion expressed in 2017 by the European Committee of the Regions, cited above, due to their characteristics, have or not the status of soft law.

As correctly underlined, "Soft law refers to instruments such as declarations, recommendations, codes of conduct, action plans, expert opinions, and handbooks. Soft law is produced by state actors, international organizations, civil society organizations, multinationals, trade associations, and legal experts" (Bergtora Sandvik, 2018). No doubts that "Soft law can harden over time through state action, for example, as treaties or as customary law. In the context of the continued proliferation of lawmaking procedures and sites, soft law is many things to many actors: political and legal actors see soft law as a pragmatic instrument for governance; the business sector relies on soft law to facilitate private enterprise; and civil society uses soft law as a vehicle for social change" (Bergtora Sandvik, 2018).

However, soft law rules have no direct binding force. They "influence and restrict the will and freedom of their addressees", but "do not establish a real obligation or provide a specific sanction. If one does not consider the sanction to be a necessary attribute of the rule, he can either recognize these rules as sources of law, or (...) atypical sources" (Chiarelli, 2019).

The overcoming of the Kelsenian paradigm, due to a more technocratic reality, susceptible to continuous change, leaves room for a non-hierarchical system, where "horizontal logics (...) or at least communicative and dialogical logics prevail, aimed at promoting forms of negotiation, compromise (...)" (Bernardi, 2013).

This framework shows that both the Sendai Framework for Disaster Risk Reduction and the Commission Staff Working Document: Action Plan on the Sendai Framework for Disaster Risk Reduction 2015-2030, as well as the Official Opinion of the European Committee of the Regions, can be included in the genus of soft law regulations. (see: https://eur-lex.europa.eu/legal-content/EN/TXT/PDF/?uri=CELEX:52016AR5035&from=IT).

This affirmation is not denied even if compared with the further indicators provided by Academics that consider soft law those sources created by Organizations, not necessarily direct expression of state or territorial Authorities (especially the Sendai Framework), whose rules are formulated with general programmatic content. These rules are mandatory for the group from which they were created, or which adheres to them (we must think about the voluntary progressive adhesion to the Sendai Framework or to the recommendations stated by the European Commission), and they are also often effective at international level (Bernardi, 2011).

The force of these rules, independent, as we said, of a criminal punishment for non-compliance, depends on the membership of the national Government to the international Organization that produces them.

Thus, "not applying a rule laid down by an international organization in which one has freely decided to participate entails consequences in terms of international relations" (Persio, 2015). Academics underline that "soft law is suitable to replace the traditional international hard law because, although it is not submitted to the fundamental principle of *pacta sunt servanda*, typical of treaty law, they express the principle *inadimplenti non est adimplendum* and therefore can be considered *ius cogens*. The juridical nature of the rule of soft law, therefore, must be found in its effectiveness, that is, in the capacity of the rule to be shared and applied by its addressees" (Persio, 2015).

But the idea of rank and force of soft law is not always universally shared. However, it is undeniable that soft law is now widely applied in many areas of law.

Despite this, as correctly pointed out, the main role that can be recognized to European and international soft law sources, is certainly the impact they have on the judicial interpretation of law, assured by judges.

It has been stressed that "interpretation in conformity with EU law is linked to certain fundamental principles which regulate the relationship between national and EU law, such as, first and foremost, (...) the primacy of the European over the Italian law and the principle of loyal cooperation between both legal frameworks (Art. 4.3. TEU)" (Bernardi, 2011).

This conformity must be applied "to all internal rules, regardless when they were enacted and despite their hierarchical ranking, and must be applied to all rules, including criminal law". Such a wide-ranging conformity obligation affects "all EU law: to immediately applicable law

and not immediately applicable law, to primary and secondary law (...) to hard and even soft law. In short, it imposes itself on the entire system of the Treaties (Bernardi, 2011).

Of course, not all European legislative or non-legislative acts can be sources of soft law, but the openings of the European Court of Justice appear very significant indeed. The judges, analyzing the nature of recommendations, state that such acts, although not binding, "cannot therefore be considered as devoid of any legal effect. Indeed, national Courts must consider recommendations when they decide on criminal cases, in particular when they interpret national rules adopted in order to ensure their implementation or aim to increase the compulsory of UE rules" [Judgment December 13, 1989, case 322/88 (Grimaldi), par. 18. More recently, judgment of September 11, 2003, case C-207/01 (Altair Chimica)].

As pointed out, "in particular case it is mandatory, for national court, to take into account soft law in interpreting national law (including criminal law). This is the case, for example, of recommendations and opinions issued by the EU Council and Commission pursuant to Article 288 of the Treaty on the Functioning of the European Union (formerly Article 249 of the EC Treaty)" (Bernardi, 2013).

Both the Commission Staff Working Document: Action Plan on the Sendai Framework for Disaster Risk Reduction 2015-2030, and the Official Opinion issued by the European Committee of the Regions, contain programs and rules, expressed by UE Authorities and aimed to implement international goals that must be achieved also in the EU zone.

If we consider, as we consider, these documents as soft law, their prescription must influence and affect the Italian criminal law.

The same must be said for the Sendai Framework of Disaster Risk Reduction.

As underlined "If we accept a concept of interpretation in such a broad sense as to embrace the whole application of criminal rules or, if preferred, the so-called "law in action", it becomes even more evident that soft law can often have a significant influence on the decision of the criminal judge. For example, they may contribute to determine the standards of diligence that exclude negligence, since - according to the dominant thesis - the concept of "discipline" (art. 43 c.p.) must include the rules issued by private authorities. Moreover, it can be underlined that also the possible deference of the minority thesis, according to which soft law must be excluded from the concept of "discipline", does not imply at all its irrelevance in the evaluation of criminal negligence. It simply shifts its relevance from the area of specific negligence to the general one, because the standard of diligence, expressed by soft law, could help in evaluating a negligence and/or imprudence criminally relevant" (Bernardi, 2015).

This influence of soft law in Italian criminal law requires one more (linked) aspect to be clarified. Even if we do agree on the idea of the influence of soft law in the evaluation of criminal negligence, we must consider the specific nature of the rules expressed by Sendai Framework and the European Commission, above all. Their generic and programmatic character prevent them from integrating the evaluation of negligence because these rules cannot express the regulatory framework that the scientist or technician should have observed in the specific case. At most, their generic and programmatic nature could represent a hermeneutical standard in order to evaluate *in bonam partem* the criminal liability in case of harms and losses. Let's try to explain why.

The failure to comply with the international or UE rules that prescribes the introduction of EEWS in our legislation not only tells that there is still no suitable instrument for warning the population about seismic risk, but also that such instruments are not easy to develop. The improvement of these systems depends on politicians or civil protection top executives, who have decision-making powers to fund technical instruments, such as seismic networks, designed to reduce or neutralize the risks arising from earthquakes. Scientists, researchers or technicians do not have the power, the scientific and economic capacity to take similar decisions. So, not only they must not be accused of causing the death of citizens because of the failure to develop and disseminate early warning systems, but also their criminal responsibility can be absolutely denied when it is clear that the only safety measure which could have prevented people to die would have been an EEWS.

Finally, we think that a brief comment on Directive (Eu), 2018/1972 of the European Parliament and of the Council of December 11, 2018 (https://eur-lex.europa.eu/legal-content/EN/TXT/?uri=uriserv%3AOJ.L_.2018.321.01.0036.01.ENG) (Accessed December 3, 2021) establishing the European Electronic Communications Code could be useful. The Directive (*Considerando* 5) "establishes a regulatory framework to ensure the freedom to provide electronic communications networks and services" and, in particular, dictates "measures relating to public policy, public security and public health, consistent with Article 52(1) of the Charter of Fundamental Rights of the European Union".

Recalling that communication plays a central role in emergency management, *Considerando* 293 notes that "divergent national regulations have been developed regarding the transmission of public alerts by electronic communications services in the event of imminent or developing major emergencies and disasters". It is therefore necessary to approximate the necessary provisions and systems, the adoption of which remains discretional for States.

Furthermore, *Considerando* 294 states that "Where the effective reach of all end-users concerned, regardless of their place or Member State of residence, is ensured and respects the highest level of data security, Member States should be able to make provision for the transmission of public alerts by means of publicly available electronic communications services other than number-based mobile interpersonal communications services and broadcasting services used for broadcasting, or by means of mobile applications transmitted using Internet access services".

In other words, the Directive imposes uniform communication standards for the Member States especially when these instruments have civil protection functions but, despite the duty to introduce the single European emergency number (112), the Directive leaves the Member States free to implement the alert and alarm services they deem most appropriate for the protection of their citizens.

So, in order to guarantee an effective protection of their citizens, it would be desirable that the European institutions will soon coordinate the mandatory nature of these quality standards with equally compulsory indication of the type of warning system that can comply with the Commission Staff Working Document, prescription and targets.

The merging of procedural and modal requirements would give rise to a discipline, hopefully mandatory for Member States which could be obliged to adopt early warning systems also in the seismic field, thus conforming to international protection standards.

RISK DECLINATIONS AND THE FUTURISTIC CRIMINAL LIABILITY FOR IMPLEMENTING EEWS

The problems in defining the effectiveness of international and UE rules, which consider the adoption of EEWS a safe measure for the population and infrastructures, do not prevent us from an evaluation about the characteristics that criminal liability could assume once these systems will become operative in Italy.

The considerations that we will articulate here will start from the structure of criminal liability in Italy and will try to highlight the most important profiles of culpable responsibility.

It is not difficult to hypothesize that, in the event of a damage arising from an erroneous transmission of the early warning message, scientists and civil protection officers could be indicted for manslaughter, negligent injury or disaster (Castronovo, 2002; Piergallini, 2005; Accinni, 2006; Giunta 2012; Marinucci, 2012).

Such an inauspicious forecast, as we have seen, arises from the indiscriminate and confused role of risk in criminal reproach and is confirmed by some Italian judicial cases (Militello, 1988; Civello, 2013; Gargani, 2017; Iagnemma, 2021). These ones especially show how difficult could be, for a judge, understanding that risk is not a unitary concept (Alemanno, 2017; see Cass. pen. Sez. Un., April 24, 2014, n. 38343, DeJure). Risk, and in particular natural risk, has rather different declinations whose examination is important also for a more correct allocation of responsibility.

A criminal responsibility (for negligence) arises when someone (e.g., scientist or civil protection officers) foresees or can foresee the risk and its concrete development (event) and is able to avoid such consequences through the adoption of safety procedures and behaviors, related to precautionary rules.

Therefore, in order to understand concretely, each time, which event could be avoided and how it could be prevented, it is necessary to take note that natural risk is not a unique concept but represents the product of three different elements: hazard, vulnerability and exposure.

Even if jurisprudence is slowly approaching the awareness of the multiformity of the risk (Blaiotta 2007, 2010) and in some judicial cases the analysis of the different elements enters through the contribution of experts and technical consultants (Manna, 2009), nevertheless there is still a basic preconceived approach that does not allow the judge to correctly identify the area of competence, powers and therefore responsibility of each person who causally affect the production of the event (Micheletti, 2015).

The problem must be addressed in the light of the two key concepts that characterize culpable reproach: predictability and avoidability of the event (Giunta, 1993; Massaro, 2009; Brusco, 2010a; Brusco, 2010b; Verrico, 2011; Manna, 2013).

In order to understand criminal liability, we must first ask what aspect of the risk is predictable, or rather, what consequence of it can be predicted and avoided (or limited).

In the context of the criminal offences under our interest (harms, manslaughter, injury, disaster), it should be noted that it is not the risk itself that is relevant, but the possibility of foreseeing and avoiding the event that is harmful or dangerous to life, public safety or the infrastructures integrity.

Or, rather, the possibility of foreseeing and avoiding the harmful or dangerous consequences of an event that represents the materialization of a specific risk that also determines a precise competence of people involved.

What is important for criminal law is whether a concrete event, related to the individual risk declination (hazard, vulnerability and exposure), can be foreseen and avoided and in what concrete field of application this occurs.

In this regard, we have EEWSs developed to protect people against the effects of building collapse and infrastructure, as well as EEWSs designed to interrupt the movement of a train or the functionality of a surgery operating room, or even the work process on a building site or production in an industry.

In these two different cases, responsibility could change, even if, it should be clear, all EEWS share the same scientific background. The content of an EW message (which is based on estimates of location, magnitude and intensity and finally shaking at a specific site) has, in fact, the same level of uncertainty in all its applications.

Vulnerability and Exposure in Relation to the Foreseeability of the Event

First of all, this distinction is relevant in order to highlight the specific object of predictability which, in our case, determines a specific declination of criminal responsibility. Let's try to explain the reason.

EEWS are a precautionary tool: they allow us to know in advance the time of arrival and the expected level of shaking at each point, once the earthquake has occurred. And this is possible thanks to a rapid calculation of its characteristics, even if, as we will see in paragraph 6.4, the strong component of uncertainty that characterizes these data cannot be ignored.

This expected shaking is the naturalistic event which is not easily and univocally related to, or better, it does not always coincide with the event of final damage, punished by the criminal law.

The arrival of the shaking is, in fact, an intermediate event that may turn out differently from the final event of death, injury or disaster.

Sometimes, the causal chain registers a hiatus between the shaking and the final event that the criminal punishment wishes to prevent through the precautionary rule.

This is usually the case when EEWSs messages are conveyed as a tool to predict and avert (the risk declination of) vulnerability. In this case, the life and physical integrity of the message recipients are affected by the vulnerability of the structures that surround them. The chance to be safe depends as much on the stability of the structure as on the effectiveness of the population's self-protection behavior. In fact, in these cases, citizens are expected to adopt safety measures which can protect them from harms.

But we must underline that EEWS do not protect public safety with a direct impact on the vulnerability of buildings (Minson et al., 2018; Minson et al., 2019; Wald, 2020). In other words, they cannot foresee the vulnerability of the building. The scientific literature still underlines that is impossible to translate accurately and in real time the shaking of a building into a calculation of the damage it will suffer. The vulnerability of each building could be known exclusively referring to the single structure and to the related shaking effects. Only this parameter would make it possible to say that, through the EEWS, we can also predict the damaging effects on the people in the buildings who might be harmed by their collapse.

But this aspect, as mentioned, is still under development (Gasparini et al., 2007; Iervolino et al., 2007).

The predictability of the harmful event takes on a different aspect when the anticipation of the shaking, transmitted by EEWS, coincides directly with the automatic suspension of a service designed for safeguarding the life and health of citizens or the integrity of structures. In this case, the foreseeability of the risk is mainly (though not exclusively) determined by the specific element of risk, such as the exposure of the population to the harmful consequences of the shaking.

In this case, EEWS makes it possible to anticipate the effects that are intrinsically and specifically realized when the shaking occurs.

Here, the intermediate event (shaking) and the final event (death or injury) coincide in time and, consequently, also in terms of foreseeability.

An example can be the train slowing down, procedure that occurs automatically, saving passenger's lives.

Vulnerability and Exposure in Relation to the Avoidability of the Event

The dichotomy between vulnerability and exposure effects becomes even more evident when focus is placed on the avoidance of the event. The EEWS are precautionary instruments designed to avoid death, injury or other dangerous events by predicting and subsequently assessing the time of arrival and the level of shaking.

Not all EEWS are intended to avoid a harmful event in the same way.

This depends on the concrete object of the risk and on how it behaves. Again, when the EEWS is intended to prevent death and injury that would occur because of the vulnerability of a building, the content of the caution will have a peculiar face.

In particular, EEWSs will be designed to warn the population as soon as possible so that they can adopt self-protective behaviors that, in any case, depend on their willingness and preparation. When, on the other hand, the EEWS acts on the risk factor that concerns the population's exposure, the system fully and directly prevents the consequences that could directly result from the shaking.

This different phenomenology gives rise to a different precautionary standard of the rule.

In the first case, when the EEWS is intended to avert the consequences of the vulnerability of a building following shaking, it must be considered as a unilateral information message, addressed to the population. This message may not always have a precautionary nature. It enables the recipients to adopt specific behavior, which must, however, be contained in the message or, more often, are (un)known to a population previously prepared to manage the risk.

On the other hand, when the EEWS is intended to reduce or avoid the exposure of individuals to risk, it will constitute a precautionary rule that will automatically act on the structures and systems designed to receive it. In this case, the recipients of the precautionary rule are not the potential final victims of the shaking, but the persons responsible for the safety of the structures involved.

It is true that these rules could also be addressed even to users, but they may have small impact to the final event because they act at a later stage of it (e.g., train users, even if frightened, must not open the doors. But EEWS must have already stopped the train).

Criminal Responsibilities

Consequently, the framework of responsibilities changes significantly.

When the EEWS affects a risk related to the vulnerability of the structure, the responsible for its correct assessment and distribution could be the scientists who improve the scientific programs, the engineers/technicians who have developed them and/or the public or private office which disseminate the warning messages. In the event of a catastrophe linked to an erroneous EEW or lack of it, these subjects cannot (always) be held responsible for the events that may occur. And this for several reasons. First of all because, as we have seen, the communication rule has not always a genuine precautionary value. The cautionary information, if not correlated by a set of information indicating the ways to prevent the harmful event (*rectius*, self-protective information), will not be able to activate a culpable reproach in terms of criminal negligence. An empty information, lacking real safety indications, is not a real precautionary rule and does not determine any liability in the event of its eventual (incorrect) use (Grotto, 2015; Giunta, 2016).

The circumstance seems to be validated by a further consideration. The mitigating or impeding effect of the event is closely linked to the implementation of safe behavior adopted by the potential victims (Cerase, 2017). If this does not happen, the responsibility of the adverse event must be attributed to those who did not protect themselves and/or to the authorities which did not adequately educate the population.

Again, an apparently complementary but profoundly related responsibility lies those were required to build in accordance with the legal rules. If one person dies because of a building collapse due to a construction deficiency, consequent responsibility must be ascribed exclusively (or at most concurrently) to the builder or to

TABLE 2 | Solution suggested.

- The need to provide shared and well-structured protocols describing the service offered in its various forms
- The presence of detailed disclaimers clearly defining the limits of the service and identifying, with equal clarity, the responsible for each segment of the service
- The enhancement of the role that must be acknowledged to the population as the main owner of the adoption of self-protective measures
- A general reconsideration of the mandatory duties burdening on building owner who should be required to respect the parameters of anti-seismic construction

the administrative authorities who had granted the building permission.

For these reasons, EEWS and the linked responsibilities can also represent a means for persuading people to adopt mitigating risk policies in each territory.

A different picture must be drawn when the EEWS affects (at least primarily) the exposure of victims to specific risk such as those linked to transport systems, certain types of work or risky processes e.g., the ones taking place in operating rooms or in the chemical industry. In these cases, the rules to be adopted have a specific and detailed content and are therefore genuinely precautionary. The responsible for processing and transmitting scientific data are fully responsible for the consequences of their mistakes (unless there are aspects that invalidate the reproach, such as the existence of force majeure).

This happens, even more, when the harmful event occurs because of the negligence (in adopting precautionary measures) of people with a duty of care such as, for example, employers, managers of hospitals etc.

The Importance of Limits

This articulation of responsibilities is however conditioned by two further determining factors. The first relates to the concrete possibility of releasing an EEW with a real mitigating or preventing effect on the adverse event. In the epicentral areas, there is always a "blind zone" where the spatial and temporal conditions could prevent the possibility to convey a useful message.

The second is the coefficient of scientific uncertainty that characterizes the development of EEWS (Kuyuk et al., 2015).

This uncertainty, physiologic in this phase of EEWS development, is the consequence of a very rich debate that constitutes one of the greatest values of the entire scientific and technical challenge.

However, as is well known, it is difficult for the law, and especially for criminal law, to understand not only the mechanisms underlying science but, above all, the uncertainty which is its essence.

It is true that this mechanism and the related uncertainty should be explained during the trial by technical consultants and experts. Furthermore, it is true that, in criminal law, there is a rule of judgement whereby, when the public prosecutor is unable to prove guilt, the judge must acquit the defendant because the threshold of 'beyond all reasonable doubt's has not been crossed. But, unfortunately, it is even more true that, very often, the dynamics underlying science and its challenges are not well understood, and defendants are condemned almost on the basis of an objective liability, i.e., exclusively on the basis of the duty of care, without correctly assessing the culpability (Stella, 2002).

As well known, considering only the duty of care relevance violates, above all, the principle of personal responsibility (Donini, 2018).

CONCLUSION AND FUTURE DIRECTIONS

In spite of this effort to systematize the application of criminal reproach, it is easy to predict that the operation of the EEWS will require a very close dialogue between scientists and jurisprudence.

This dialogue can certainly be facilitated by the proper adoption of certain regulatory framework and solutions suggested by international experiences. We refer, in particular, to four fundamental aspects (**Table 2**): 1) the need to provide shared and well-structured protocols describing the service offered in its various forms; 2) the presence of detailed disclaimers clearly defining the limits of the service and identifying, with equal clarity, the responsible for each segment of the service; 3) the enhancement of the role that must be acknowledged to the population as the main owner of the adoption of self-protective measures; 4) a general reconsideration of the mandatory duties burdening on building owner who should be required to respect the parameters of anti-seismic construction.

About the first aspect, it can be said that the predetermination of a set of procedural rules, will ensure not only better functioning of the service but also greater tranquility for scientists and technicians.

As we have seen, the criminal reproach for negligence is based on the violation of a precautionary rule aimed at correctly predicting and preventing the harmful event, as far as possible.

The presence of a written rule fulfils a dual function: it is a guide for the technician and the scientist in the implementation of procedures and, equally, a paradigm for the judge who can decide, on the basis of the same set of rules, whether or not the defendant is responsible for the event. The defendant and the judge operate on the same set of rules and this makes it possible to limit the distorting practice that sees the creation of precautionary rules ex post, according to the well-known (wrong) principle of post hoc ergo propter hoc (Giunta, 2016).

An equally important role must be given to creation of an appropriate disclaimers accompanying the EEW service, especially when it is used through APPs.

The main role (even not exclusive and sufficient) that disclaimers probably have to play is to make the user aware of technical limitations of the operation of the service offered and to acquire their awareness and consent.

In this regard, there is much discussion on the real effect on limiting liability, especially criminal liability, that a disclaimer can guarantee. Even if, in the writer's opinion, its nature appears to be very close to the informed consent experimented in health services (such as the acceptance of the known negative consequences that fall within the area of permitted risk, linked to the use of the service), we must nevertheless be very frank.

The disclaimer cannot relieve the operators and developers from responsibility for errors or malfunctions which are attributable to their fault and which cause damage (incorrect

initial scientific data, poor maintenance, lack of supervision of the detection equipment).

These cannot be included, just as a medical error would not be included, in the area of permitted risk, negotiable with stakeholders. The protection of private and public life belongs to a public rank and it is not available to the parties' freedom of negotiation.

Rather, as is well known, the goal on which we must put all our efforts is not only training the population to deal with seismic risk but also rethinking the duties relating to the compliance of buildings with anti-seismic parameters.

About the first aspect, it must be mandatory organizing a widespread training and information campaign on seismic risk aimed at making citizens aware of what has to be done in the event of a quake (e.g., drop, cover and hold on) (Becker et al., 2020a; Arcieri, 2020; Catino, 2020). And fully aware citizens are allowed or even supposed to demand safe structures in which living and working.

No reason, not even of public finance, can further justify the political inertia in introducing a legal duty to adapt buildings to the anti-seismic parameters.

Italy should take inspiration from the provisions of other Countries such as California, Mexico, Japan and Turkey. Turkish government, in fact, after the 1999 Izmit earthquake, launched a building and urban renewal plan with Law 6306 of 2012. This is still the largest building and urban planning project in the world and envisages the anti-seismic adaptation or reconstruction of almost 6.5 million vulnerable buildings. The total investment for Turkey is of almost 410 billion euro over 15 years (see https://www.ingv.it/it/stampa-e-urp/stampa/news/2129-all-ingv-un-seminario-sui-disastri-naturali-e-sul-piano-di-edilizia-antisismica-della-turchia).

The undoubted complexity of the project should not exempt our legislator from abandoning a project like this which could overcome the Italian ancient habit to entrusting the solution of problems to a benevolent and unavoidable fate.

When the next earthquake comes and there will be casualties, nobody could deny, at least, a social and human responsibility both of the Italian society and its political class, which have not been able respectively to demand and to impose the dutiful respect of basic safety rules.

DATA AVAILABILITY STATEMENT

The original contributions presented in the study are included in the article/supplementary material, further inquiries can be directed to the corresponding author.

AUTHOR CONTRIBUTIONS

The author confirms being the sole contributor of this work and has approved it for publication.

FUNDING

This work has been carried out within the Project ART-IT (Allerta Rapida Terremoti in Italia), funded by the Italian Ministry of University and Research (Progetto Premiale 2015, DM. 850/2017).

ACKNOWLEDGMENTS

The author wants to thank Alessandro Amato for introducing her into the world of earthquakes (and for continuous discussion and suggestions), and Simona Colombelli for inspiring the scientific aspects of the research. The author is grateful to Fausto Giunta for his guidance in the research. The author acknowledges the Dipartimento di Scienze Giuridiche dell'Università degli Studi di Firenze and Istituto Nazionale di Geofisica e Vulcanologia for the support during the research. The ideas and opinions expressed in this paper must be attributed only to the author.

REFERENCES

Accinni, G. P. (2006). Criteri di imputazione per colpa tra leggi scientifiche e accertamenti giudiziali. *Riv. It. Dir. Proc. Pen.* 930.

Alemanno, A. (2017). "Prefazione: per una comprensione pluralistica del rischio," in *Rischio e Comunicazione. Teorie, Modelli, Problemi* (Milan: Egea), 11.

Allen, R. M., and Kanamori, H. (2003). The Potential for Earthquake Early Warning in Southern California. *Science* 300, 786–789. doi:10.1126/science.1080912

Allen, R. M., Kong, Q., and Martin-Short, R. (2020). The MyShake Platform: A Global Vision for Earthquake Early Warning. *Pure Appl. Geophys.* 177, 1699–1712. doi:10.1007/s00024-019-02337-7

Allen, R. M., and Melgar, D. (2019). Earthquake Early Warning: Advances, Scientific Challenges, and Societal Needs. *Annu. Rev. Earth Planet. Sci.* 47, 361–388. doi:10.1146/annurev-earth-053018-060457

Amato, A., Avallone, A., Basili, R., Bernardi, F., Brizuela, B., Graziani, L., et al. (2021). From Seismic Monitoring to Tsunami Warning in the Mediterranean Sea. *Seismol. Res. Lett.* 92, 1796–1816. doi:10.1785/0220200437

Amato, A., and Galadini, F. (2015). "La scienza mal compresa: esempi e riflessioni dal processo "Grandi Rischi"," in *Terremoti, Comunicazione, Diritto. Riflessioni Sul Processo Alla "Commissioni Grandi Rischi"* (Rome: Franco Angeli), 43.

Amato, A. (2020). Some Reflections on Tsunami Early Warning Systems and Their Impact, with a Look at the NEAMTWS. *Boll. Geofis. Teor. Appl.* 61, 403. doi:10.4430/bgta0329

Arcieri, S. (2020). Percezione del rischio e attribuzione di responsabilità. Available at: www.dirittopenaleuomo.org (Accessed July 3, 2021).

Basili, R., Brizuela, B., Herrero, A., Iqbal, S., Lorito, S., Maesano, F. E., et al. (2021). The Making of the NEAM Tsunami Hazard Model 2018 (NEAMTHM18). *Front. Earth Sci.* 8, 1. doi:10.3389/feart.2020.616594

Beck, U. (2000). *Società del rischio*. Bari: Cacucci. doi:10.1037/e707102007-001

Becker, J. S., Potter, S. H., Prasanna, R., Tan, M. L., Payne, B. A., Holden, C., et al. (2020b). Scoping the Potential for Earthquake Early Warning in Aotearoa New Zealand: A Sectoral Analysis of Perceived Benefits and Challenges. *Int. J. Disaster Risk Reduction* 51, 101765. doi:10.1016/j.ijdrr.2020.101765

Becker, J. S., Potter, S. H., Vinnell, L. J., Nakayachi, K., McBride, S. K., and Johnston, D. M. (2020a). Earthquake Early Warning in Aotearoa New Zealand: A Survey of Public Perspectives to Guide Warning System Development. *Humanit Soc. Sci. Commun.* 7 (1), 138. doi:10.1057/s41599-020-00613-9

Beltramone, L., and Carrilho Gomes, R. (2021). Earthquake Early Warning Systems as an Asset Risk Management Tool. *Civil Eng.* 120. doi:10.3390/civileng2010007

Bergtora Sandvik, K. (2018). Soft Law. The International Encyclopedia of Anthropology. Available at: www.researchgate.com (Accessed March 23, 2021).

Bernardi, A. (2015). Il principio di legalità alla prova delle fonti sovranazionali e private: riflessi sul diritto penale alimentare. *Rivista di Diritto Alimentare*, 43.
Bernardi, A. (2013). Interpretazione conforme al diritto UE e costituzionalizzazione dell'Unione Europea. Brevi osservazioni di un penalista. *Forum di Quaderni Costituzionali*, 2013, 1.
Bernardi, A. (2011). Sui rapporti tra diritto penale e soft law. *Riv. It. Dir. Proc. Pen*, 536.
Blaiotta, R. (2010). Il sapere scientifico e l'inferenza causale. *Cass. Pen.* 1265.
Blaiotta, R. (2007). La causalità giuridica alla luce della teoria del rischio. *Cass. Pen.* 365.
Brusco, C. (2010a). "Brevi considerazioni sulla prevedibilità dell'evento nel reato colposo," in *Responsabilità penale e rischio nelle attività mediche e d'impresa* (Florence: FUP), 493.
Brusco, C. (2010b). Rischio e pericolo, rischio consentito e principio di precauzione flessibilizzazione delle categorie del reato. *Criminalia*, 383.
Castronovo, D. (2002). Le definizioni legali di reato colposo. *Riv. It. Dir. Proc. Pen.* 495.
Catino, M. (2020). Errori e disastri nei sistemi complessi. Available at www.dirittopenaleuomo.org (Accessed July 3, 2021).
Cerase, A. (2015). "Quale idea della comunicazione del rischio? Tra teoria pressi e assunti impliciti," in *Terremoti, Comunicazione, Diritto. Riflessioni Sul Processo Alla "Commissioni Grandi Rischi"* (Rome: Franco Angeli), 145.
Cerase, A. (2017). "Rischio e comunicazione," in *Teorie, modelli e problemi* (Milan: Egea).
Chiarelli, M. (2019). La soft regulation e il caso delle nuove linee guida ANAC. *Federalismi*. 1.
Civello, G. (2013). *La colpa eventuale nella società del rischio: epistemologia dell'incertezza e verità soggettiva della colpa*. Turin: Giappichelli.
Cleary, W. B. (2006). *The Law of Criminal Negligence*. Contemporary Japan, 81.
Clinton, J., Zollo, A., Marmureanu, A., Zulfikar, C., and Parolai, S. (2016). State-of-the Art and Future of Earthquake Early Warning in the European Region. *Bull. Earthquake Eng.* 2441. doi:10.1007/s10518-016-9922-7
Colombelli, S., Carotenuto, F., Elia, L., and Zollo, A. (2020). Design and Implementation of a mobile Device App for Network-Based Earthquake Early Warning Systems (EEWSs): Application to the PRESTo EEWS in Southern Italy. NHESS, 921.
Colombelli, S., Caruso, A., Zollo, A., Festa, G., and Kanamori, H. (2014). A P Wave-Based, On-Site Method for Earthquake Early Warning. *Geophys. Res. Lett.* 1390. doi:10.1002/2014GL063002
Colombelli, S., Zollo, A., Festa, G., and Kanamori, H. (2012). Early Magnitude and Potential Damage Zone Estimates for the Great Mw 9 Tohoku-Oki Earthquake. *Geophys. Res. Lett.* 1, L22306. doi:10.1029/2012GL053923
Conforti, B. (2019). *Diritto Internazionale*. Naples: Editoriale Scientifica.
Crawford, J. (2019). *Brownlie's Principles of International Criminal Law*. Oxford: Oxford. doi:10.1093/he/9780198737445.001.0001
Dando, S. (1960). Basic Problems in Criminal Theory and Japanese Criminal Law. *Indiana L. J.* 423.
Directive (Eu) (2018/1972). Directive (Eu) 2018/1972 of the European Parliament and of the Council of 11 December 2018 Establishing the European Electronic Communications Code (Recast). Available at: https://eur-lex.europa.eu/legal-content/EN/TXT/PDF/?uri=CELEX:02018L1972-20181217&from=IT (Accessed December 28, 2020).
Disaster Countermeasures Basic Act (1961). (Act No. 223, November 15, 1961). Available at: https://www.adrc.asia/documents/law/DisasterCountermeasuresBasicAct.pdf (Accessed March 18, 2021).
Donini, M. (2011). *Europeismo giudiziario e scienza penale*. Milan: Giuffrè.
Donini, M. (2018). La personalità della responsabilità penale tra tipicità e colpevolezza. *Riv. It. Dir. Proc. Pen.* 1577.
Dovere, S. (2017). Protezione civile, sanità ed aviazione civile: il rischio penale fra presente e futuro. *Riv. It. Med. Leg.* 81.
Emolo, A., Picozzi, M., Festa, G., Martino, C., Colombelli, S., Caruso, A., et al. (2016). Earthquake Early Warning Feasibility in the Campania Region (Southern Italy) and Demonstration System for Public School Buildings. *Bull. Earthquake Eng.* 14 (9), 2513–2529. doi:10.1007/s10518-016-9865-z
Farber, D. A., and Chen, J. (2006). *Disaster and the Law*. New York.
Farber, D. A. (2011). Navigating the Intersection of Environmental Law and Disaster Law. *BYU. L. Rev.* 1783 (6/1).
Ferris, E. (2014). "How Can International Human Rights Law Protect Us from Disasters?," in American Society of International Law, Annual Meeting, 10 April 2014, 1.
Fick, B. (2017). Chapter 32, Section 69-70: California Seismic Safety Capital Access Loan Program. *U. Pac. L. Rev.* 48, 689.
Foddai, M. A. (2017). Controversie scientifiche e controversie giuridiche: i limiti della decisione giudiziale. *Politeia* 60.
Fornasari, G., and Insolera, G. (2015). "Scienza, rischi naturali, comunicazione del rischio e responsabilità penale," in *Terremoti, Comunicazione, Diritto. Riflessioni Sul Processo Alla "Commissioni Grandi Rischi"* (Rome: Franco Angeli), 1.
Gargani, A. (2017). Il rischio nella dinamica dei reati contro l'incolumità pubblica nei reati di pericolo astratto. *Cass. Pen.* 3874.
Gargani, A. (2019). "La responsabilità omissiva dei titolari di funzioni di protezione civile tra passato e futuro, La Protezione civile nella società del rischio," in *Il sistema di protezione civile: profili organizzativi, poteri ed ipotesi di responsabilità penale degli operatori* (Pisa: ETS), 111.
Gargani, A. (2011). La "flessibillizzazione" giurisprudenziale delle categorie classiche del reato difronte alle esigenze di controllo penale delle nuove fenomenologie di rischio. *Legislazione penale*, 397.
Gargani, A. (2016). *"Profili di responsabilità penale degli operatori della Protezione civile: la problematica delimitazione della posizione di garanzia"*. Milan: Giuffrè, 207.
Gasparini, P., Manfredi, G., and Zschau, J. (2007). *Earthquake Early Warning Systems*. Springer.
Giunta, F. (2019). Culpa Culpae. Available at: www.disCrimen.it (Accessed June 4, 2019).
Giunta, F. (2020). Europa e diritto penale. Tra linee di sviluppo e nodi problematici. Available at: www.disCrimen.it (Accessed March 26, 2020).
Giunta, F. (1999). I tormentati rapporti fra colpa e regola cautelare. *Dir. Pen. Proc.* 1295.
Giunta, F. (2012). Il reato colposo nel sistema delle fonti. La giustizia penale, 577.
Giunta, F. (1993). *Illiceità e colpevolezza nella responsabilità colposa*. Padua: Cedam.
Giunta, F. (2016). Quale colpa per la Protezione Civile. La Giustizia Penale, 125.
Goltz, J. D. (2002). Introducing Earthquake Early Warning in California: A Summary of Social Science and Public Policy Issues, A Report to OES and the Operational Areas. California Governor's Office of Emergency Service. Available at: https://www.caloes.ca.gov (Accessed March 10, 2021).
Gómez-Novell, O., García-Mayordomo, J., Ortuño, M., Masana, E., and Chartier, T. (2020). Fault System-Based Probabilistic Seismic Hazard Assessment of a Moderate Seismicity Region: The Eastern Betics Shear Zone (SE Spain). *Front. Earth Sci.* 8, 1. doi:10.3389/feart.2020.579398
Grotto, M. (2015). Obbligo di informazione e formazione dei lavoratori, nesso di rischio e causalità della colpa. Available at: www.penalecontemporaneo.it (Accessed September 16, 2015).
Iagnemma, C. (2021). Il reato omissivo improprio nel quadro di un approccio sistemico all'evento offensivo. Available at: www.disCrimen.it (Accessed July 3, 2021).
Iervolino, I., Manfredi, G., and Cosenza, E. (2007). *Earthquake Early Warning and Engineering Application Prospects, Earthquake Early Warning Systems*. Springer, 239.
Johnson, D. T., Fukurai, H., and Hirayama, M. (2020). Reflections on the TEPCO Trial: Prosecution and Acquittal after Japan's Nuclear Meltdown, the Asia-Pacific Journal, Japan Focus. Available at: https://apjjf.org/-David-T–Johnson–Hiroshi-Fukurai–Mari-Hirayama/5336/article.pdf (Accessed February 7, 2021).
Kamigaichi, O., Saito, M., Doi, K., Matsumori, T., Tsukada, S., Takeda, K., et al. (2009). Earthquake Early Warning in Japan: Warning: The General Public and Future Prospects. *Seismological Res. Lett.* 716. doi:10.1785/gssrl.80.5.717
Kuyuk, H. S., Colombelli, S., Zollo, A., Allen, R. M., and Erdik, M. O. (2015). Automatic Earthquake Confirmation for Early Warning System. *Geophys. Res. Lett.* 42, 5266–5273. doi:10.1002/2015gl063881
Luhmann, N. (1996). *Sociologia del rischio*. Milan: Bruno Mondadori. doi:10.1007/978-3-663-01103-3
Manes, V. (2010). L'eterointegrazione della fattispecie penale mediante fonti subordinate, tra riserva "politica" e specificazione "tecnica". *Riv. It. Dir. Proc. Pen.* 84.
Manes, V., and Caianiello, M. (2020). *Introduzione al diritto penale europeo*. Turin: Giappichelli.
Manna, A. (2009). I rapporti fra sapere scientifico e sapere giudiziario. *Cass. Pen.* 3633.

Manna, A. (2013). Prevedibilità-evitabilità dell'evento o prevedibilità-evitabilità del rischio nei delitti colposi di danno? *Archivio penale*, 1085.
Mantovani, F. (2020). *Diritto Penale, Parte Generale* (Padua: Cedam).
Marinucci, G. (2012). La responsabilità colposa: teoria e prassi. *Riv. It. Dir. Proc. Pen.* 1.
Massaro, A. (2009). «Concretizzazione del rischio» e prevedibilità dell'evento nella prospettiva della doppia funzione della colpa. *Cass. Pen.* 4699.
Mattsui, S. (2019). *Law and Disaster, Earthquake, Tsunami and Nuclear Meltdown in Japan*. London: Routledge.
Melgar, D., and Hayes, G. P. (2019). Characterizing Large Earthquakes before Rupture Is Complete. *Sci. Adv.* 5, eaav2032. doi:10.1126/sciadv.aav2032
Micheletti, D. (2015). Il criterio della competenza sul fattore di rischio concretizzatosi nell'evento L'abbrivio dell'imputazione colposa. *Criminalia*, 509.
Militello, V. (1988). *Rischio e responsabilità penale*. Milan: Giuffrè.
Minson, S. E., Baltay, A. S., Cochran, E. S., Hanks, T. C., Morgan, T., Mcbride, S. K., et al. (2019). The Limits of Earthquake Early Warning Accuracy and Best Alerting Strategy. *Scientific. Rep.* 9, 2478. doi:10.1038/s41598-019-39384-yAvailable at: https://europepmc.org/article/pmc/pmc6385233
Minson, S. E., Meier, M. A., Baltay, A. S., Hanks, T. C., and Cochran, E. S. (2018). The Limits of Earthquake Early Warning: Timeliness of Ground Motion Estimates. *Sci. Adv.* 4, eaaq0504. doi:10.1126/sciadv.aaq0504
Montagni, A. (2007). *Protezione civile e diritto penale. La protezione civile, profili costituzionali amministrativi, riflessi penali*. Milan: Giuffrè, 200 ss.
Notaro, D. (2013). "A ciascuno il suo": il nesso di causalità e colpa in materia penale fra scienza, ragione ed emozione. *Corriere Merito*, 5.
Notaro, D. (2014). Scientists and Earthquake Risk Prediction: "Ordinary" Liability in an Extraordinary Case? *Eur. J. Risk Regul.* 5, 159–167. doi:10.1017/S1867299X00003573
Palazzo, F. C. (2016). Il principio di legalità tra costituzione e suggestioni sovranazionali. *Leg. Pen.* 1.
Paliero, C. E., and Viganò, F. (2013). *Europa e diritto penale*. Milan: Giuffrè.
Perini, C. (2010). *Il concetto di rischio nel diritto penale moderno*. Milan: Giuffrè.
Perini, C. (2012). La legislazione penale, tra "diritto penale dell'evento" e "diritto penale del rischio". *Leg. Pen.* 1104.
Perini, C. (2002). Rischio tecnologico e responsabilità penale. Una lettura criminologica del caso Seveso e del caso Marghera. Rassegna italiana di criminologia, 389.
Persio, P. T. (2015). Il valore condizionante delle raccomandazioni del GAFI tra soft law e vocazione prescrittiva. *Cass. Pen.* 2064B.
Picozzi, M., Emolo, A., Martino, C., Zollo, A., Miranda, N., and Verderame, G. (2015). Earthquake Early Warning System for Schools: A Feasibility Study in Southern Italy. *Seismological Res. Lett.* 86, 398. doi:10.1785/0220140194
Piergallini, C. (2005). Il paradigma della colpa nell'età del rischio, prova di resistenza del tipo. *Riv. It. Dir. Proc. Pen.* 1696.
Pulitanò, D. (2006). Il diritto penale fra vincoli di realtà e sapere scientifico. *Riv. It. Dir. Proc. Pen.* 795.
Santos-Reyes, J. (2019). How Useful Are Earthquake Early Warnings? the Case of the 2017 Earthquakes in Mexico City. *Int. J. Disaster Risk Reduction* 40, 101148. doi:10.1016/j.ijdrr.2019.101148
Savona, P. (2010). Dal Pericolo Al Rischio: L'anticipazione Dell'intervento Pubblico. *Dir. Amm* 2010, 355.
Shake Alert (2021). Shake Alert. Available at: https://www.usgs.gov/natural-hazards/earthquake-hazards/shakealert (Accessed February 16, 2021).
Simoncini, M. (2014). When Science Meets Responsibility. The Mayor Risks Commission and the L'Aquila Earthquake. *Eur. J. Risk Regul.* 156.
Stella, F. (2002). *Giustizia e modernità*. Milan: Giuffrè.
Suarez, G. (2018). A Dedicated Seismic Early Warning Network: The Mexican Seismic Alert System- (SASMEX). *Seismological Res. Lett.* 382. doi:10.1785/0220170184
Sun, Y.-S., Li, H.-C., Chang, L.-Y., Ye, Z.-K., and Chen, C.-C. (2020). Real-time Probabilistic Seismic hazard Assessment Based on Seismicity Anomaly. *Nat. Hazards Earth Syst. Sci.* 20, 743–753. doi:10.5194/nhess-20-743-2020
USGS (2018). Revised Technical Implementation Plan for the ShakeALert System – an Earthquake Early Warning System for the West Coast of the United States, Report. Available at: www.usgs.gov (Accessed March 1, 2021).
USGS (2017). ShakeAlert—An Earthquake Early Warning System for the United States West Coast. USGS Paper. Available at: www.usgs.gov (Accessed March 1, 2021).
Verrico, A. (2011). La prevedibilità e l'evitabilità dell'evento nel caso di calamità naturali. *Cass. Pen.* 110.
Wahlstrom, M. (2009). *Disaster Risk and its Reduction: Who Is Responsible*. Fletcher Forum of World Affairs, 153.
Wald, D. J. (2020). Practical Limitations of Earthquake Early Warning. *Earthquake Spectra* 36, 1412–1447. doi:10.1177/8755293020911388 Available at: www.journals.sagepub.com/home/eqs.
Wang, Z. (2011). Seismic Hazard Assessment: Issues and Alternatives. *Pure Appl. Geophys.* 168, 11–25. doi:10.1007/s00024-010-0148-3
White Paper Disaster Management in Japan (2019). *Cabinet Office*.
Wu, Y.-M., Kanamori, H., Allen, R. M., and Hauksson, E. (2007). Determination of Earthquake Early Warning Parameters, τcandPd, for Southern California. *Geophys. J. Int.* 170, 711–717. doi:10.1111/j.1365-246x.2007.03430.x
Wurman, G., Allen, R. M., and Lombard, P. (2007). Toward Earthquake Early Warning in Northern California. *J. Geophys. Res.* 112, 1. doi:10.1029/2006jb004830
Zollo, A., Colombelli, S., Elia, L., Emolo, A., Festa, G., Iannaccone, G., et al. (2014a). "Chapter 7 an Integrated Regional and On-Site Earthquake Early Warning System for Southern Italy: Concepts, Methodologies and Performances," in *Early Warning for Geological Disasters, Advanced Technologies in Earth Sciences* (Springer).
Zollo, A., Festa, G., Emolo, A., and Colombelli, S. (2014b). Source Characterization for Earthquake Early Warning. *Encyclopedia Earthquake Eng.*, 1–21. doi:10.1007/978-3-642-36197-5_244-1
Zorzi Giustiniani, F. (2018). Something Old, Something New: Disaster Risk Reduction in International Law. *QIL* 7.
Zschau, J., Gasparini, P., Papadopuolus, G., Zollo, A., Manfredi, G., Milkereit, C., et al. (2008). SAFER Seismic Early Warning for Europe. FINAL REPORT. Available at: http://www.amracenter.com/SAFER/doc/dissemination/SAFER_Final_Report.pdf.

Conflict of Interest: The author declares that the research was conducted in the absence of any commercial or financial relationships that could be construed as a potential conflict of interest.

frontiers in Earth Science

ORIGINAL RESEARCH
published: 20 August 2021
doi: 10.3389/feart.2021.672613

Application of the Modified PLUM Method to a Dense Seismic Intensity Network of a Local Government in Japan: A Case Study on Tottori Prefecture

Takao Kagawa *

Faculty of Engineering, Tottori University, Tottori, Japan

An application of the PLUM (Propagation of Local Undamped Motion) method to real-time seismic intensity distribution from a dense seismic intensity network maintained by a local government in Japan is demonstrated. The JMA (Japan Meteorological Agency) has employed the PLUM method from March 2018 as a supplement to the traditional EEW (Earthquake Early Warning) which requires hypocenter determination. A dense observation network is desirable for upgrading accuracy and immediateness of EEW including the PLUM method. Seismic intensity meters in Tottori Prefecture, Japan, are suitable for the purpose because they have been improved to broadcast packets with peak ground acceleration and JMA seismic intensity at every 1 s. Also, 34 seismic intensity meters are installed in the target area while only six observation sites are used for the EEW by the JMA. The packet data are received at Tottori University, and the modified PLUM method considers wave propagation with damping from not only the observation points but also all evaluating grid points at a 1 km mesh. Additionally, P-wave amplitudes in preliminary tremors are also introduced to estimate seismic intensities from an empirical relationship. Applying the methodology to past earthquake data, more detailed and rapid evaluations of seismic intensity distribution are achieved. We expect the system will be utilized for earthquake disaster mitigation measures of local governments.

Keywords: real-time monitoring, seismic intensity network, PLUM method, attenuation, Tottori Prefecture

OPEN ACCESS

Edited by:
Simona Colombelli,
University of Naples Federico II, Italy

Reviewed by:
Masanori Kameyama,
Ehime University, Japan
Yuki Kodera,
Japan Meteorological Agency, Japan

***Correspondence:**
Takao Kagawa
kagawa@tottori-u.ac.jp

Specialty section:
This article was submitted to Solid Earth Geophysics, a section of the journal Frontiers in Earth Science

Received: *26 February 2021*
Accepted: *28 July 2021*
Published: *20 August 2021*

Citation:
Kagawa T (2021) Application of the Modified PLUM Method to a Dense Seismic Intensity Network of a Local Government in Japan: A Case Study on Tottori Prefecture. Front. Earth Sci. 9:672613. doi: 10.3389/feart.2021.672613

INTRODUCTION

Real-time shake map estimation using seismic intensity meters maintained by local governments in Japan has been enhanced. To improving the accuracy and rapidness of the EEW (Earthquake Early Warning), a dense observation network is desirable. Seismic intensity meters installed in all Japanese municipalities are the most suitable equipment for this purpose, since the station installation interval is less than 5 km in some areas. The seismic intensity meters in Tottori Prefecture have been upgraded to broadcast UDP (User Datagram Protocol) packets with peak ground acceleration and JMA (Japan Meteorological Agency) seismic intensity every second. At present, the system maintained by the prefecture is the only one that broadcasts such a packet. **Figure 1** shows the location of Tottori Prefecture in Japan and the layout of the 34 seismic intensity meters maintained by the prefecture. The data are received at Tottori University, Japan,

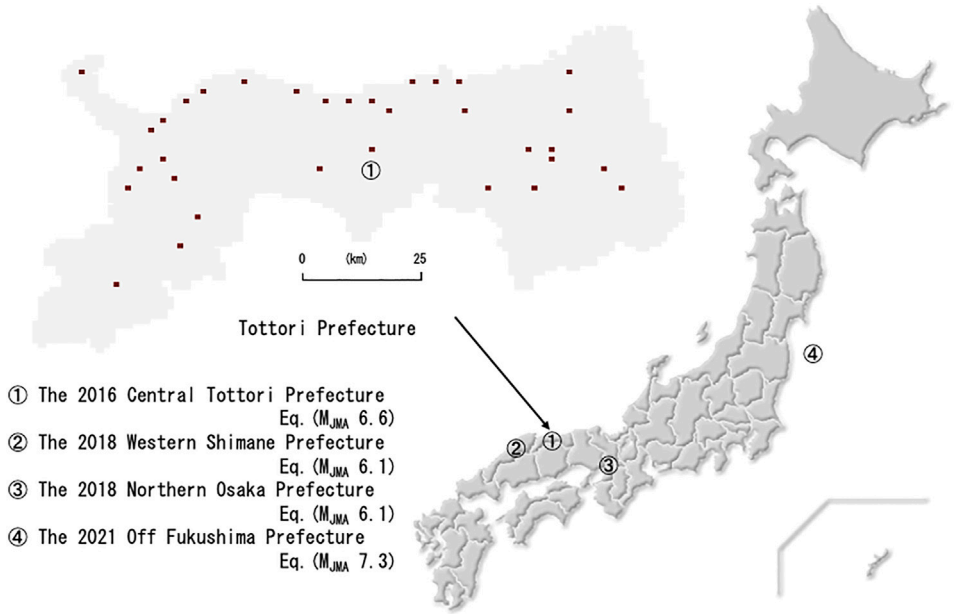

FIGURE 1 | Location map of Tottori Prefecture in Japan and epicenters of earthquakes handled in this study and the distribution map of 34 seismic intensity meters maintained by Tottori Prefecture.

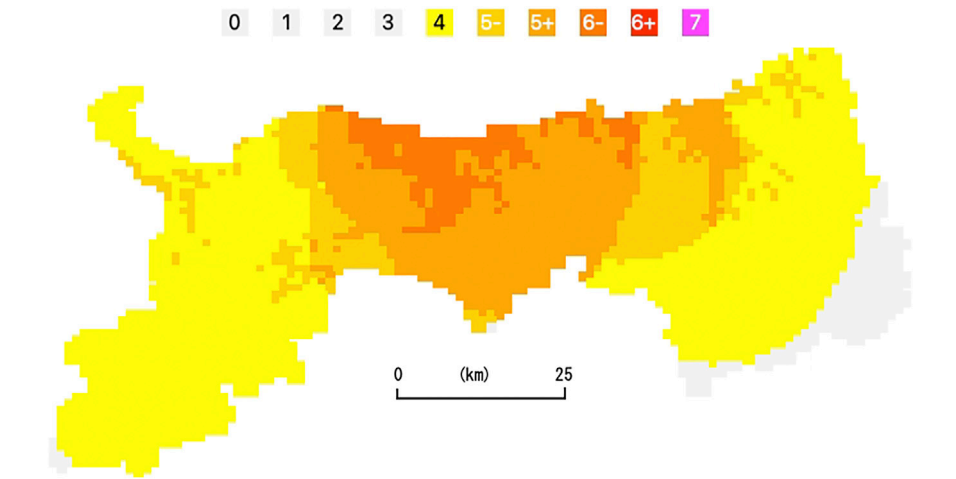

FIGURE 2 | Final seismic intensity distribution of the 2016 Central Tottori Prefecture Earthquake by the PLUM method with maximum values preserved.

and the PLUM (Propagation of Local Undamped Motion) method (Hoshiba, 2013) is applied to the data for estimating JMA seismic intensity distribution at 1 km grid points. However, in case of the 2016 Central Tottori Prefecture Earthquake, Japan, with M_{JMA} 6.6, the seismic intensities around the observation sites were overestimated to use as a reference for initial response to the disaster, since the seismic intensities are assumed to propagate without attenuation with emphasis on issuing earlier warning at the expense of accuracy.

In this study, three additional methodologies are introduced into the system to obtain more realistic seismic intensity distribution. One is the introduction of attenuation in seismic intensity propagation from observed sites, and the other is the assumption of every 1 km grid point for seismic intensity estimation as a secondary source point (Kagawa, 2019). The third is the usage of vertical P-wave amplitudes for seismic intensity estimation (Ueda et al., 2009). Using the methodologies, seismic intensity distributions with improved accuracy and rapidness are demonstrated. Although there are some issues such as underestimation due to the bias of the observation point arrangement, it is possible to provide generally good seismic intensity distribution in real time.

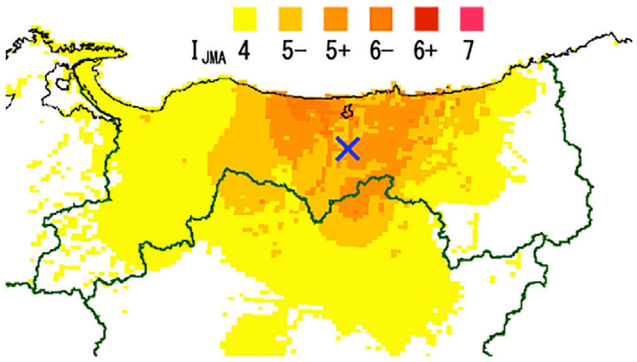

FIGURE 3 | Seismic intensity distribution of the 2016 Central Tottori Prefecture Earthquake interpolated by the JMA considering the site amplification factor (modified from the Japan Meteorological Agency, 2016b).

IMPROVEMENT OF SEISMIC INTENSITY METERS MAINTAINED BY TOTTORI PREFECTURE

We have improved the local seismic intensity meters in Tottori Prefecture so that they could send 1 s packets of peak ground acceleration and JMA seismic intensity. Since seismographs operated by local governments are used for disaster prevention purposes such as breaking news of seismic intensities immediately after an earthquake, improvements should not bother their operations. For this reason, we decided to transmit only real-time seismic intensity calculated on site and the maximum horizontal and vertical accelerations on the UDP. The seismic intensity is evaluated from 2 s data that start 1 s earlier. Data from 34 sites (**Figure 1**) are received at Tottori University *via* the Tottori Prefecture Information Highway, main line 10 Gbps and access point 1 Gbps, and when the vertical acceleration exceeds 1 cm/s^2, and output files with timestamp and site number are generated. There are far more seismographs available in Tottori Prefecture than the six points of JMA observation points for EEW purpose, so it is expected that the accuracy and rapidness will be improved.

In this study, the dataset due to the 2016 Central Tottori Prefecture Earthquake is used as a sample data. The epicenter location is indicated in **Figure 1**. All local seismic intensity meters have operated without problems while delivering 1 s packets mentioned above, have saved waveform records, and have stably transmitted many aftershock data. However, the system to receive the packets and to visualize the results was not completed at the time of the event, so 1 s packets used in this study were reproduced from the observed waveforms.

ESTIMATION OF REAL-TIME SEISMIC INTENSITIES

Application of the PLUM Method

First, we tried to apply the PLUM (Propagation of Local Undamped Motion) method (Hoshiba, 2013), which is employed in EEW operation by the JMA. Seismic intensity estimation by the PLUM method is shown in the following equation:

$$I(\mathbf{r}, t) \approx \max_i \left(F_{oi} + I\left(\mathbf{r}_i, t - \frac{|\mathbf{r} - \mathbf{r}_i|}{V_0} \right) \right), \text{where} |\mathbf{r} - \mathrm{r}_i| \le V_0 T.$$

Here, $I(\mathbf{r}, t)$ is the estimated seismic intensity at time t and point $\mathbf{r}$, $\mathbf{r}_i$ is the location of the ith seismic intensity meter, and F_{oi} is the site

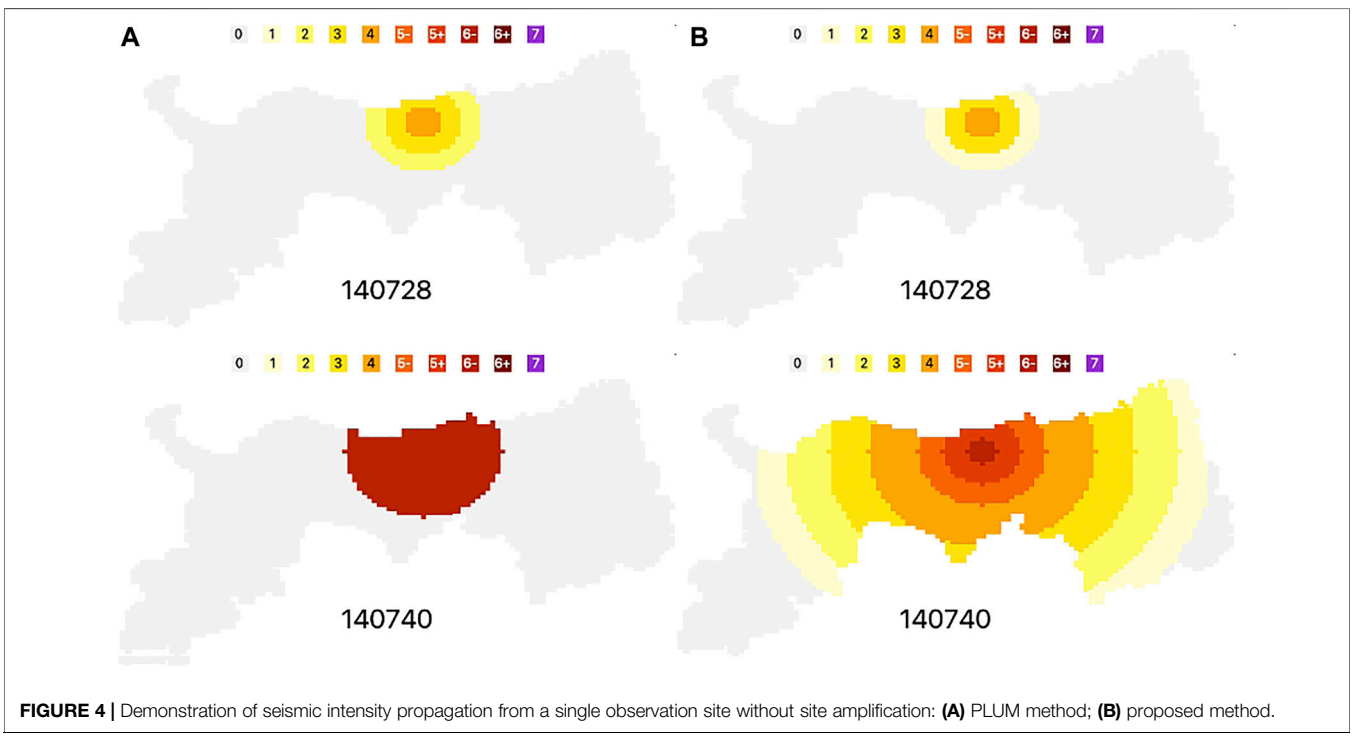

FIGURE 4 | Demonstration of seismic intensity propagation from a single observation site without site amplification: **(A)** PLUM method; **(B)** proposed method.

amplification estimated from AVS30 at the point (Midorikawa et al., 1994). Amplification at each estimating point in a 1 km grid is given from a dataset that was used for the earthquake damage estimation project of Tottori Prefecture (Tottori Prefecture, 2018), but the data are based on the national AVS30 distribution database provided by the J-SHIS map by the NIED (National Research Institute for Earth Science and Disaster Resilience, 2019). Assuming V_0 as the S-wave velocity and T as the lead time for estimation, i.e., how much the future is predicted from the present time, the maximum seismic intensity that can be propagated from the observation site within the distance range of V_0T is estimated considering time delay and site amplification. In this study, V_0 = 4.0 km/s is used as a standard upper crustal S-wave velocity in the area, and lead time T = 4 s is assumed to cover the delay due to data transmission and data analyses. As a result, the maximum applicable distance for seismic intensity propagation is 16 km that corresponds to an averaged spacing of seismic intensity meters.

Figure 2 shows a final seismic intensity distribution of the 2016 Central Tottori Prefecture Earthquake (M_{JMA} 6.6) with maximum values preserved. The maximum JMA seismic intensity observed was six lower, and the damage was spot limited. **Figure 3** shows the seismic intensity distribution interpolated by the JMA considering the site amplification factor at each estimating point. The points with JMA seismic intensity six lower are limited, and seismic intensity four does not cover almost the whole prefecture area. The distribution by the PLUM method is overestimated; however it is unavoidable since it treats wave propagation as undamped.

The PLUM method employs undamped propagation since it prioritizes quickness to broadcast EEW at the expense of some accuracy of seismic intensity distribution. Our purpose is to monitor the seismic intensity distribution more accurately and utilize it for the disaster mitigation response immediately after the earthquake, which is a little different from the concept of the PLUM method.

Introduction of Damping and Secondary Source Points

Attenuation (damping) is introduced into wave propagation to estimate more accurate seismic intensity distribution. In addition, all estimation points are considered as secondary sources that generate attenuating waves with the maximum value at the observation point. The following equation explains the methodology:

$$I(\mathbf{r}, t) \approx \max_k \left(F_{ok} + I\left(\mathbf{r}_k, t - \frac{|\mathbf{r} - \mathbf{r}_k|}{V_0} \right) - \alpha |\mathbf{r} - \mathbf{r}_k| \right), \text{where} |\mathbf{r} - \mathbf{r}_k| \le V_0 T.$$

Here, $\mathbf{r}_k$ is the location of the kth estimating point in 1 km grids and F_{ok} is the site amplification there. In the previous equation of the PLUM method, the maximum seismic intensity is selected from observation points $\mathbf{r}_i$ that satisfy the distance condition within V_0T. On the contrary, the proposed method searches the maximum value from all 1 km grid points $\mathbf{r}_k$ around the target point $\mathbf{r}$. If the kth grid point is the same as an observation point, estimation is updated with observed data like data assimilation of several-hour weather forecasting. The third term of the equation including a parameter α indicates attenuation. The damping parameter α is adjusted as 0.1 through trial and error. It means that JMA seismic intensity decreases 1.0 with distance 10 km. The result might be almost the same as the ground-motion–based EEW (i.e., Hoshiba and Aoki, 2015), but the methodology is simpler and values at the observation sites are assimilated every 1 s.

Figure 4 shows demonstrations of seismic intensity propagation from a single observation site without considering site amplification. The left column indicates the result by the PLUM method. At 14:07:28, three different observed values are propagated without attenuation, and it draws three circles with radius of 4, 8, and 12 km and is saturated with a seismic intensity of six lower as the maximum observed seismic intensity at the site

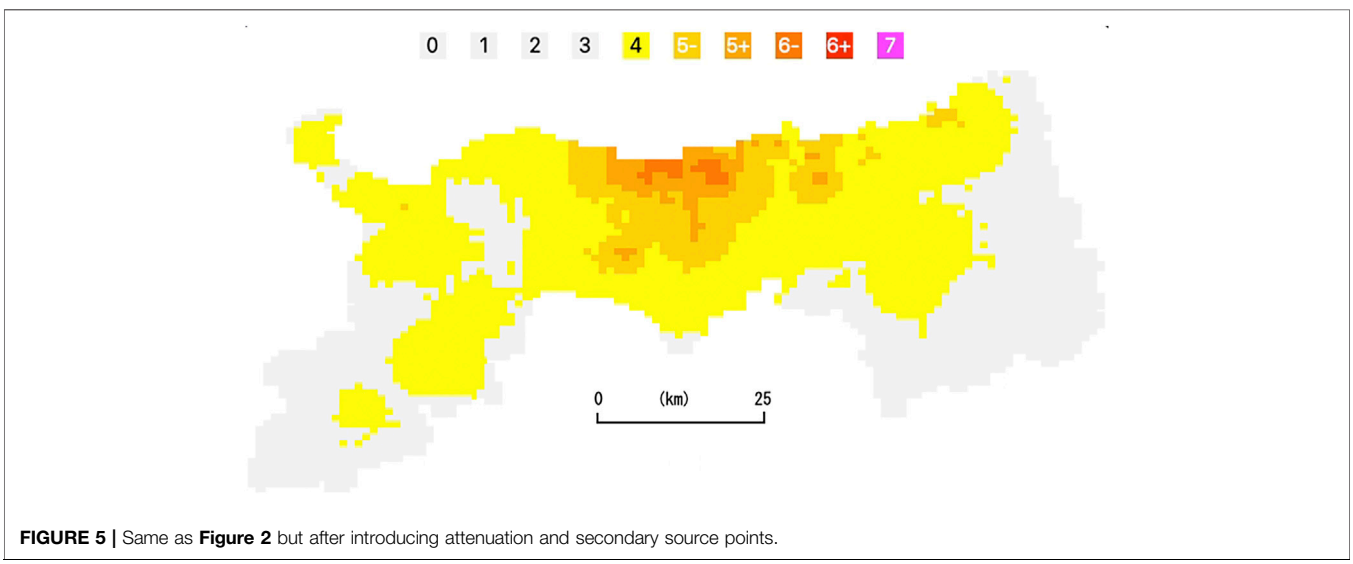

FIGURE 5 | Same as **Figure 2** but after introducing attenuation and secondary source points.

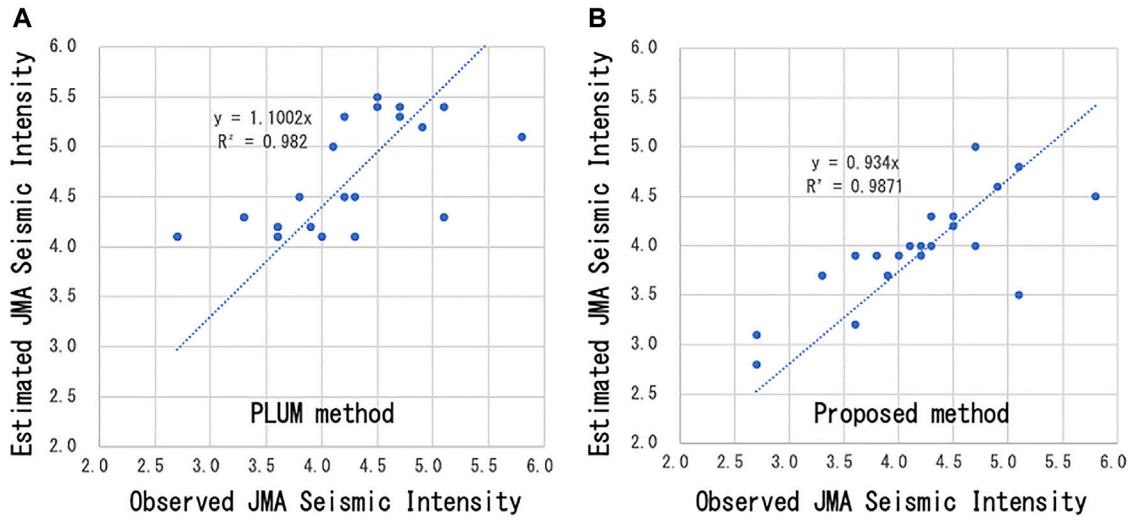

FIGURE 6 | Comparison between the observed and estimated JMA seismic intensities at the sites that are maintained by other organizations: **(A)** PLUM method; **(B)** proposed method.

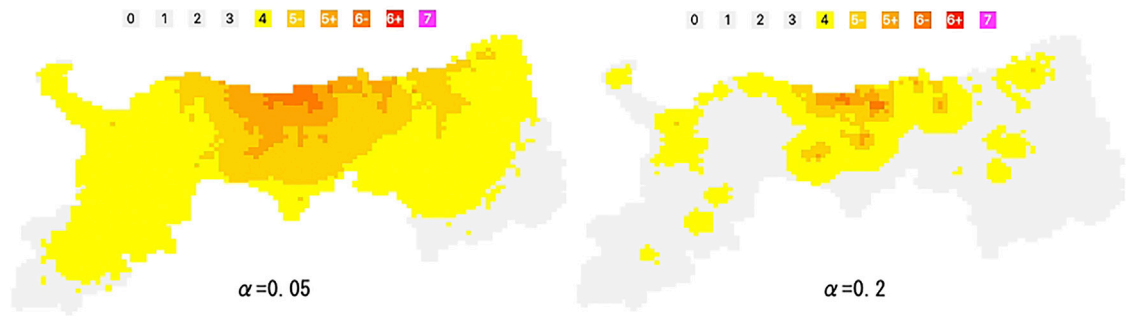

FIGURE 7 | Comparison of results with varying attenuation parameter α from the case of α = 0.1 in **Figure 5**.

in the bottom panel with a radius of 16 km (V_0T). The timestamp in the bottom panel indicates 40 s, but it was saturated at 14:07:33 in reality. The right column shows the result by the proposed method. The seismic intensity distribution at 14:07:28 is slightly attenuated, and it propagates with attenuation farther than that of the PLUM method. It is because every grid point works as a secondary source point. Different color scales comparing the previous figures are used here to see the distribution of small seismic intensity.

Figure 5 shows an application to the 2016 Central Tottori Prefecture Earthquake. The final distribution of JMA seismic intensity agrees well with the interpolated distribution by the JMA in **Figure 3**. The intensity six lower appears as spot limited in the coastal area, and the border of intensity four is almost the same as the JMA interpolation. However, intensity five lower is smaller than the JMA interpolation, especially in the southern and western part from the source area. It is because there are few observation points maintained by Tottori Prefecture (**Figure 1**). The seismic intensity meters are installed mainly at town halls in populated areas. They are not installed in mountain regions around prefecture borders. Moreover, JMA and NIED seismographs are used as substitutes for urban areas with large population to complement the seismic intensity distribution in Tottori Prefecture, but they are not included in the 34 sites used for this study.

In order to quantitatively evaluate the results of the PLUM method and the proposed method, we compared the estimated results at observation points other than the 34 points used in this study. They are six JMA, nine K-NET, and six KiK-net sites maintained by the NIED. The left and right panels in **Figure 6** show the results of the PLUM method and the proposed method, respectively. The horizontal axis indicates the observed JMA seismic intensities, and the vertical axis shows the estimated values. In the panels, approximate linear lines of intercept zero are shown with their inclination and correlation coefficients. It is clear that the PLUM method is overestimated but the proposed method is almost valid.

Figure 7 shows the examples of trial and error to obtain proper attenuation parameter α = 0.1. Comparing the results with the

case in **Figure 5**, it is found that smaller attenuation case (α = 0.05) results in slight overestimation, and larger attenuation (α = 0.2) shows underestimation. The operational parameter α = 0.1 was determined through these checks, although it has not been sufficiently quantitatively examined.

Introduction of P-Wave Amplitude

For the next approach, P-wave amplitudes are introduced for seismic intensity estimation. The 1 s packets from seismic intensity meters include maximum accelerations of horizontal and vertical components. In case that vertical acceleration is larger than the horizontal one, empirical estimation of JMA seismic intensity from P-wave amplitude (Ueda et al., 2009) is calculated, and the value is employed if it is larger than real-time seismic intensity observed at the time. The relationship is shown in **Figure 8** and the following equation (Ueda et al., 2009). They used 1,570 data at 124 sites due to 55 events including the main and aftershocks of the Mid Niigata Prefecture Earthquake in 2004 (M_{JMA} 6.8) and the Iwate-Miyagi Nairiku Earthquake in 2008 (M_{JMA} 7.2). The following equation is derived from least-squares approximation:

$$I_{JMA} = 2.18 \log(PGA_P) + 0.77$$

where I_{JMA} is the JMA seismic intensity and PGA_P is the peak ground acceleration of the vertical P wave. Both show a good correlation, but the number of data are not enough in large amplitude range. In this study, the maximum seismic intensity estimated from P-wave amplitude is set for 4.5 as shown in **Figure 8**.

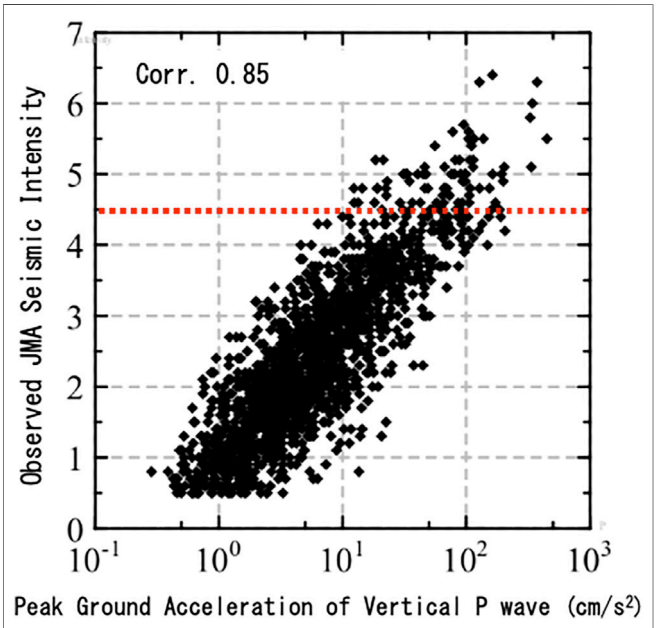

FIGURE 8 | Relationship between peak ground accelerations of the vertical P wave and observed seismic intensities (modified from Ueda et al., 2009).

The methodology mentioned above is applied for the 2016 Central Tottori Prefecture Earthquake. **Figure 9** shows the result under the same condition as in **Figures 2**, **5**. The results are almost same in their final seismic intensity distributions. The most expecting advantage for using P-wave amplitude is its rapidness of estimation. **Figure 10** shows the comparison of snapshots between estimation with the P wave in the right column and without the P wave in the left column. Time 14: 07:28 of the upper line panels is the timing when the first forecast-type EEW by the JMA (Japan Meteorological Agency, 2016a) was broadcasted, and warning-type EEW on the third forecast was broadcasted for general public at time 14:07:36 of the lower line panels. Both columns show the possibility that we can grasp realistic seismic intensity distribution as the same or faster than current EEW in case we use the data from a denser network.

Estimation with the P wave shows faster propagation of large seismic intensity area than that without the P wave. However, the final estimated distribution with P wave amplitude is almost the

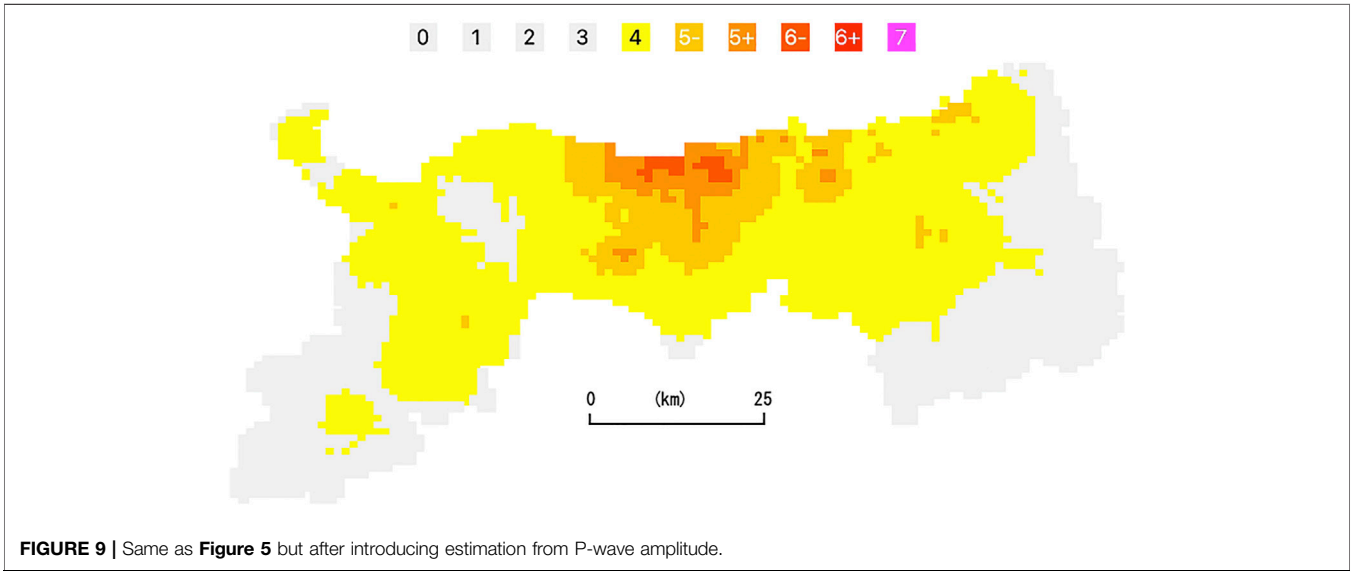

FIGURE 9 | Same as **Figure 5** but after introducing estimation from P-wave amplitude.

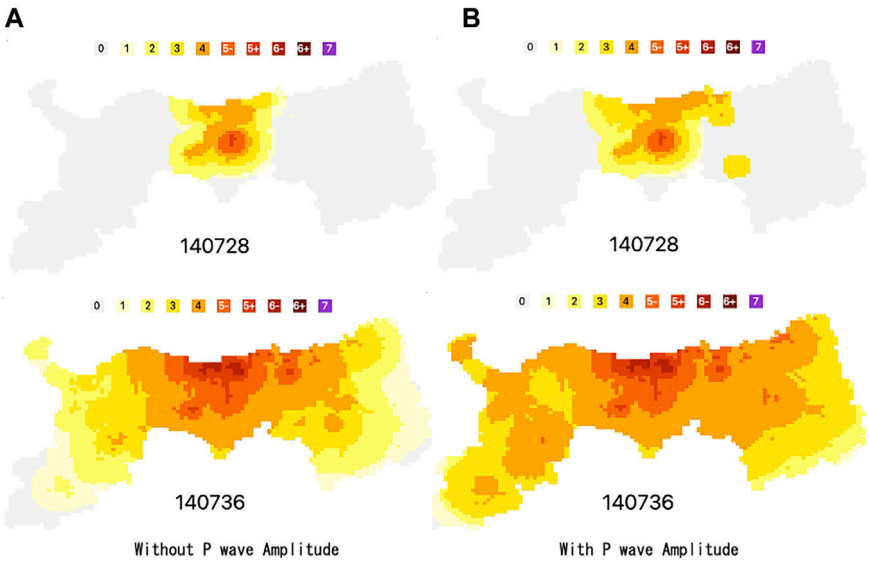

FIGURE 10 | Snapshots of real-time estimated seismic intensity distributions of the 2016 Central Tottori Prefecture Earthquake: estimation with the P wave **(A)** and without the P wave **(B)**.

same as that without the P wave, as compared between **Figures 5**, **9**. The right bottom panel of **Figure 10** corresponds to **Figure 9**. Note that the color scale is changed from the previous figures to grasp the situation of small seismic intensity. The scale is applied for the following figures.

DISCUSSION

Applications for other earthquakes are shown in this section, since the proposed methodology was found to be effective but only for a single near-field earthquake. The location of the additionally handled earthquakes is shown in **Figure 1**.

Figure 11 shows the estimated snapshot of JMA seismic intensity distribution due to the 2018 Western Shimane Prefecture Earthquake (M_{JMA} 6.1) on April 9 01:32. The shortest epicentral distance was about 50 km from the western prefecture border. Estimation with the P wave shows faster propagation of large seismic intensity area the same as the 2016 Central Tottori Prefecture case in **Figure 10**. **Figure 12** shows the seismic intensity distribution interpolated by the JMA,

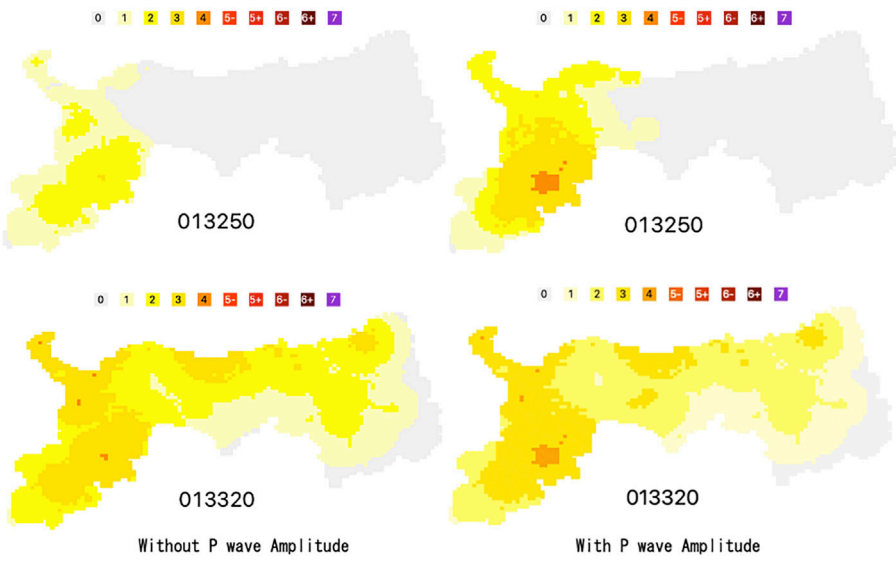

FIGURE 11 | Same as **Figure 10** but for the 2018 Western Shimane Prefecture Earthquake.

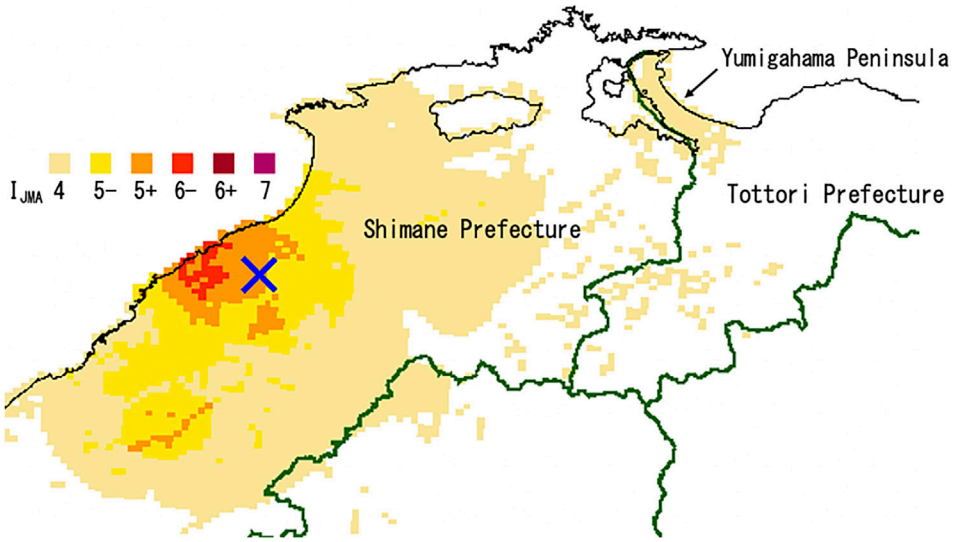

FIGURE 12 | Seismic intensity distribution of the 2018 Western Shimane Prefecture Earthquake interpolated by the JMA considering the site amplification factor (modified from the Japan Meteorological Agency, 2018).

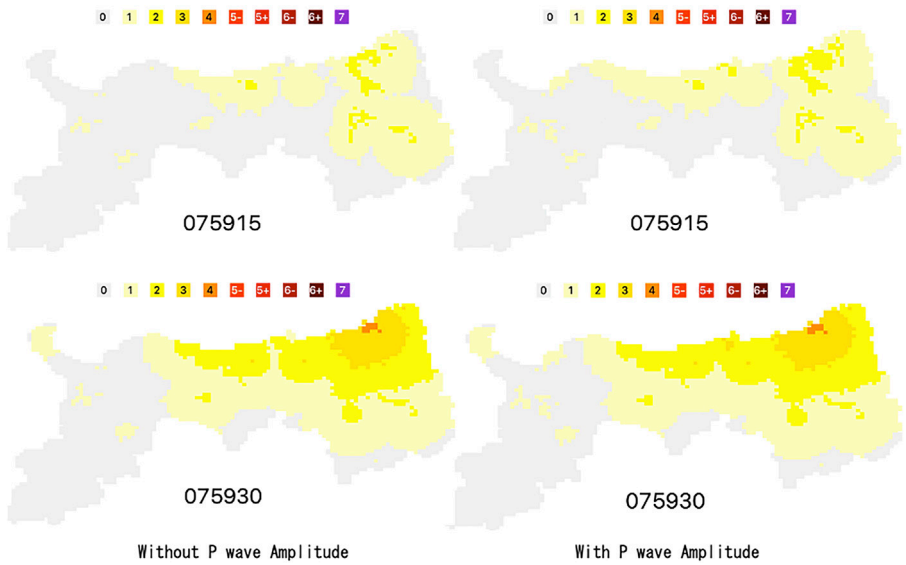

FIGURE 13 | Same as **Figure 10** but for the 2018 Northern Osaka Prefecture Earthquake.

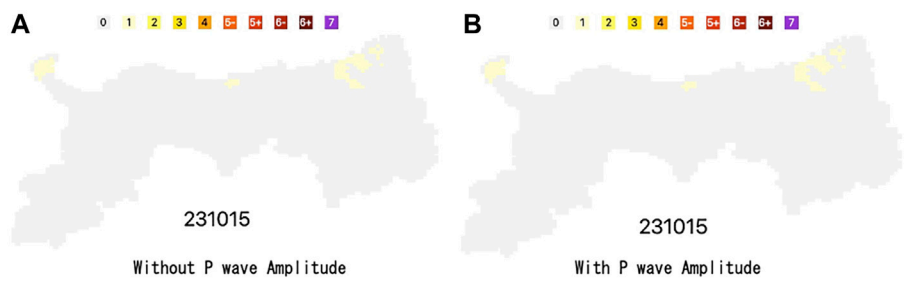

FIGURE 14 | Final seismic intensity distribution of the 2021 Off Fukushima Prefecture Earthquake estimation with the P wave **(A)** and without the P wave **(B)**.

but the color scale is slightly different from that of the previous figures. The largest JMA seismic intensity observed in the western part of the prefecture was 4 as estimated. Although a little overestimation is seen in large intensity area at southwest of the prefecture, the seismic intensity distribution is generally practical. A little underestimation is also noticed along the Yumigahama Peninsula indicated in **Figure 12**. The reason is considered to be the lack of observation points in the area, see **Figure 1**.

Figure 13 is the result of the 2018 Northern Osaka Prefecture Earthquake (M_{JMA} 6.1) on June 18 07:58. The shortest epicentral distance at the southeast prefecture border was about 150 km, and the largest JMA seismic intensity observed in the eastern part of the prefecture was 3, but 4 is estimated at the coastal area in eastern part in both cases. It is caused by large amplification around the site where intensity 3 was observed. The effects of P-wave amplitudes are noticed in limited areas along the coast in central part. It is because high-frequency amplitude in P-wave acceleration is not large for slightly long-distance earthquake. Unfortunately, the area is out of the range of seismic intensity distribution map published by the JMA because the target of the map is the range of JMA seismic intensity four or higher.

Finally, a case of long-distance earthquake is shown in **Figure 14**, but only for the final distributions. The source is the 2021 Off Fukushima Prefecture Earthquake (M_{JMA}7.3) on February 13 23: 07. The epicentral distance is about 750 km east, and the maximum observed JMA seismic intensity was 1. They were observed at a soft ground area in the eastern, central, and western part of the prefecture, as estimated in **Figure 14**. Estimation from P-wave amplitude does not work on this case, and the two panels are the same. It is also because of small acceleration due to the long-distance earthquake. The area is also out of the range of the seismic intensity distribution map by the JMA.

Four different types of earthquakes are treated in this study. The first is a near-field event that caused a disaster in Tottori Prefecture, the second is a disaster earthquake occurred in the neighboring prefecture, the third is a slightly long-distance event in the range of 150 km, and the fourth is a long-distance large earthquake with an epicentral distance of 750 km. Althrough they are limited cases, the proposed method seems to work well through the examinations so far.

It is being planned to install the methodology in a web-based display system, and its results will be provided for municipal crisis management for immediate response to earthquake disaster. We would like to make improvements any time as a problem arises.

CONCLUSION

Real-time seismic intensity estimation is established using seismic intensity meters maintained by local governments in Japan. The 34 seismic intensity meters of Tottori Prefecture were improved to broadcast 1 s packets with real-time peak ground acceleration and JMA seismic intensity. The modified PLUM method introduces wave attenuation from all estimation points in a 1 km grid as secondary sources. Vertical P-wave amplitude is also considered for intensity estimation. The methodologies were applied for four different types of earthquakes with epicentral distance 0–750 km and JMA magnitude range 6.1–7.3. The results were practical enough to estimate almost the same intensity distribution provided by the JMA after the earthquakes. Also, the estimations are expected to be faster than those of EEW by the JMA since denser seismograph network is employed for the proposed system. We hope that such real-time seismic intensity estimations would be widely constructed using next-generation seismic intensity meters.

DATA AVAILABILITY STATEMENT

The raw data supporting the conclusion of this article will be made available by the authors, without undue reservation.

AUTHOR CONTRIBUTIONS

The author confirms being the sole contributor of this work and has approved it for publication.

FUNDING

This study was supported by the Ministry of Education, Culture, Sports, Science, and Technology (MEXT) of Japan, under its Earthquake and Volcano Hazards Observation and Research Program.

ACKNOWLEDGMENTS

The author is genuinely grateful to the crisis management bureau, Tottori Prefecture, for the permission to improve their seismic intensity meters and to Takamizawa Cybernetics Co., Ltd. for the development of the 1 s packet transmission function.

REFERENCES

Hoshiba, M., and Aoki, S. (2015). Numerical Shake Prediction for Earthquake Early Warning: Data Assimilation, Real-Time Shake Mapping, and Simulation of Wave Propagation. *Bull. Seismological Soc. America* 105 (No. 3), 1324–1338. doi:10.1785/0120140280

Hoshiba, M. (2013). Real-Time Prediction of Ground Motion by Kirchhoff-Fresnel Boundary Integral Equation Method: Extended Front Detection Method for Earthquake Early Warning. *J. Geophys. Res. Solid Earth* 118, 1038–1050. doi:10.1002/jgrb.50119

Japan Meteorological Agency (2016b). Contents of Earthquake Early Warning of the 2016 Central Tottori Prefecture Earthquake. (in Japanese) Available at: https://www.data.jma.go.jp/svd/eew/data/nc/pub_hist/2016/10/20161021140724/content/content_out.html.

Japan Meteorological Agency (2016a). Estimated Seismic Intensity Distribution Map of the 2016 Central Tottori Prefecture Earthquake. (in Japanese). Available at: https://www.data.jma.go.jp/svd/eew/data/suikei/201610211407_562/201610211407_562_1.html.

Japan Meteorological Agency (2018). Estimated Seismic Intensity Distribution Map of the 2018 Western Shimane Prefecture Earthquake. (in Japanese). Available at: https://www.data.jma.go.jp/svd/eew/data/suikei/201804090132_571/201804090132_571_2.html.

Kagawa, T. (2019). An Approach for Monitoring Real Time Seismic Intensity Distribution Using Seismic Intensity Network Maintained by Local Government - Case Study on Tottori Prefecture -. *J. Jpn. Soc. Civil Eng. Ser. A1* 75 (No. 4), I_674–I_677. (in Japanese with English Abstract). doi:10.2208/jscejseee.75.i_674

Midorikawa, S., Matsuoka, M., and Sakugawa, K. (1994). Site Effects on Strong Motion Records Observed during the 1987 Chiba-Ken-Toho-Oki. 9th Japan Earthquake Engineering Symposium, Japan Earthquake.

National Research Institute for Earth Science and Disaster Resilience (2019). Data Download Page of Site Amplification Factor. Available at: https://www.j-shis.bosai.go.jp/map/JSHIS2/download.html?lang=en.

Tottori Prefecture (2018). Tottori Prefecture Earthquake Disaster Prevention Survey Research Report. (in Japanese).

Ueda, T., Kurahashi, S., Masaki, K., and Irikura, K. (2009). The New Method for Seismic Intensity Estimation by Using the P-Wave's Maximum Acceleration. *Bull. Aichi Inst. Technol.* 44, 131–138. (in Japanese with English Abstract).

Conflict of Interest: The author declares that the research was conducted in the absence of any commercial or financial relationships that could be construed as a potential conflict of interest.

frontiers in Earth Science

ORIGINAL RESEARCH
published: 20 August 2021
doi: 10.3389/feart.2021.685751

Feasibility Study of an Earthquake Early Warning System in Eastern Central Italy

Chiara Ladina[*1], *Simone Marzorati*[1], *Alessandro Amato*[2] *and Marco Cattaneo*[1]

[1]*Istituto Nazionale di Geofisica e Vulcanologia, Osservatorio Nazionale Terremoti, Ancona, Italy,* [2]*Istituto Nazionale di Geofisica e Vulcanologia, Osservatorio Nazionale Terremoti, Roma, Italy*

An earthquake early warning system (EEWS) is a monitoring infrastructure that allows alerting strategic points (targets) before the arrival of strong shaking waves during an earthquake. In a region like Central Italy, struck by recent and historical destructive earthquakes, the assessment of implementation of an EEWS is a significant challenge due to the proximity of seismic sources to many potential targets, such as historical towns, industrial plants, and hospitals. In order to understand the feasibility of an EEWS in such an area, we developed an original method of event declaration simulation (EDS), a tool for assessing the effectiveness of an EEWS for existing seismic networks, improving them with new stations, and designing new networks for EEW applications. Values of the time first alert (TFA), blind zone radius (BZ), and lead time (LT) have been estimated with respect to selected targets for different network configurations in the study region. Starting from virtual sources homogeneously arranged on regular mesh grids, the alert response was evaluated for actual and improved seismic networks operating in the area, taking into account the effects of the transmission and acquisition systems. In the procedure, the arrival times of the P wave picks, the association binder, the transmission latencies, and the computation times were used to simulate the configuration of PRESTo EEWS, simulating both real-time and playback elaborations of real earthquakes. The NLLOC software was used to estimate P and S arrival times, with a local velocity model also implemented in the PRESTo EEWS. Our results show that, although Italy's main seismic sources are located close to urban areas, the lead times calculated with the EDS procedure, applied to actual and to improved seismic networks, encourage the implementation of EEWS in the study area. Considering actual delays due to data transmission and computation time, lead times of 5–10 s were obtained simulating real historical events striking some important targets of the region. We conclude that EEWSs are useful tools that can contribute to protecting people from the harmful effects of earthquakes in Italy.

Keywords: earthquakes, early warning, seismic networks, seismic risk reduction, simulation

OPEN ACCESS

Edited by:
Simona Colombelli,
University of Naples Federico II, Italy

Reviewed by:
Ali Pinar,
Boğaziçi University, Turkey
Himanshu Mittal,
Ministry of Earth Sciences, India
Aldo Zollo,
University of Naples Federico II, Italy

***Correspondence:**
Chiara Ladina
chiara.ladina@ingv.it

Specialty section:
This article was submitted to Geohazards and Georisks, a section of the journal Frontiers in Earth Science

Received: *25 March 2021*
Accepted: *05 July 2021*
Published: *20 August 2021*

Citation:
Ladina C, Marzorati S, Amato A and Cattaneo M (2021) Feasibility Study of an Earthquake Early Warning System in Eastern Central Italy. Front. Earth Sci. 9:685751. doi: 10.3389/feart.2021.685751

1 INTRODUCTION

In the past twenty years, EEWSs have been implemented in different regions of the world and are considered a useful tool to reduce seismic risk (Satriano et al., 2011b). EEWSs were developed with different approaches, methodologies, and combining new experiences. At present, many countries have operational or prototype EEWSs. Allen et al. (2009b) described the status of EEW in the world

and the principal operating systems at that time. Other examples include EEWS in Japan (Odaka et al., 2003), Taiwan (Wu and Teng, 2002; Hsiao et al., 2009), Mexico (Suarez et al., 2009), Turkey (Erdik et al., 2003; Alcik et al., 2009), and Romania (Böse et al., 2007). The principal active systems are based on the software ElarmS (Allen and Kanamori, 2003; Allen et al., 2009a) and ShakeAlert (Kohler et al., 2020) in California, on Virtual Seismologist in California and Switzerland (Cua et al., 2009), in Europe (Clinton et al., 2016), and in particular PRESTo in Italy (Iannaccone et al., 2010; Satriano et al., 2011a).

Major developments have led to two main types of systems: a regional alert system and an on-site system (Satriano et al., 2011b; Zollo et al., 2014). The regional system, based on the use of a regional network that records seismic events, aims to detect, locate, and determine the magnitude of an event starting from the analysis of a few seconds of the first arrivals of the P waves recorded at the stations (Picozzi, 2012). The on-site system consists of a single sensor or more sensors near or inside the target structure to be alerted. In this system the P-wave recordings to the sensor are used to predict the peak ground motion at the site (Colombelli et al., 2015). This approach could be considered useful for sites located within the BZ of a regional EEW system, allowing for a useful warning before the arrival of strong shaking waves. Caruso et al. (2017) proposed a P-wave-based EEW approach called on-site alert level (SAVE). Many studies combined the two EEW approaches (Zollo et al., 2010; Colombelli et al., 2012a); these systems combine local parameters and predicted ground motions at a regional scale to provide reliable and rapid estimates of the seismic source and the expected damage zone (Colombelli et al., 2015).

The approaches for regional EEW can be classified as the "point-source" (simply the source as a concentrated volume) or "finite fault" (a more sophisticated and realistic characterization of the source, considering the entire fault area). Most studies have used the "point-source" demonstrating the reliability of this approach for the magnitude estimation of small to moderate events. However, it has been shown that this approach is not always accurate for strong earthquakes (magnitude> 6.5–7), due to the saturation of the P-wave parameters. Several authors (for example, Colombelli et al., 2012b) estimated the magnitude over time windows longer than the recorded P-wave and/or the S-wave signal to obtain more accurate final values. These magnitude calculations are reliable at the cost of requiring more data and time (Velazquez et al., 2020). In our study, the selected earthquakes have a moderate magnitude (≤ 6.5) and were considered as point sources.

Potentially, an EEWS can produce and transmit alert messages to different end-users to allow them to adopt several types of safety measures in a few seconds. The main benefits of an EEWS include public warning, first responder mobilization, and safety of health care and utility infrastructures, transit systems, and workplaces (Allen and Melgar, 2019). Whereas in most cases evacuation of buildings is unrealistic, due to the short time available to act; a portion of the affected population can receive the alert and take safety measures in certain types of structures and infrastructures (Iervolino et al., 2008).

Receiving an alert message increases personal situational awareness and yields a more rapid response, especially in well-trained people who can take precautionary and protective actions like "Drop-Cover-Hold on", suspending delicate medical procedures, or slowing down a train ride. In shaking areas, a time of 10 s allows people to protect themselves and prepare for evacuation (Fujinawa and Noda, 2013). A time interval of 5–7 s could be enough to trigger automatic mitigation actions (Cauzzi et al., 2016) at power plants, energy sector grids, and utilities infrastructures to prevent explosions, combustions, loss of water, flooding, fatal collisions, and elevator interruptions. Social studies have demonstrated that receiving alert messages even a few seconds before the shaking occurs help people to prepare and react in the proper way (Dunn et al., 2016; Becker et al., 2020a).

The elongated shape of the Italian peninsula, combined with the small damage area for moderate, but often destructing Apenninic earthquakes (M6-7), determine small distances between sources and potential EEW targets. For this reason, in many cases the time to start safety actions may be too short. Therefore, an evaluation of the feasibility of an EEW implementation is needed in this area. A first theoretical evaluation was performed by Olivieri et al. (2008) with RSN (National Seismic Network, IV, INGV Seismological Data Center, 2006) and by Picozzi et al. (2015) using the RAN seismic network (Italian strong motion network) managed by the National Civil Protection (Gorini et al., 2010), whose stations are mostly not connected in real-time.

Our study area extends for about 200 × 200 km in eastern central Italy and is characterized by the following two main seismic zones: 1) a NNW-SSE seismic zone elongated in the Appennines, where several moderate to strong earthquakes have occurred in the past and 2) a coastline-offshore seismic zone (**Figure 1a**), with less frequent and on average weaker seismicity. **Figure 1b** shows the target points chosen in the study compared to the individual and composite seismogenic sources from the DISS catalog (DISS Working Group, 2018). An individual seismogenic source (ISS) is a simplified, three-dimensional representation of a rectangular fault plane, whereas a composite seismogenic source (CSS) is a simplified, three-dimensional representation of a crustal fault containing an unspecified number of seismogenic sources that cannot be singled out. The area analyzed in our study is affected by different fault systems. We select as targets the cities with at least 40,000 inhabitants or with a significant cultural value. The selected cities are Ancona, Pesaro, Macerata, Ascoli Piceno, Fermo, Fabriano, Urbino, San Benedetto del Tronto, Civitanova Marche, Senigallia, Jesi, Perugia, Foligno, and Terni (**Table 1**).

In the study area, an EEWS based on PRESTo software has been operating since 2015. The system was based on permanent seismic networks managed by the INGV (National Institute of Geophysics and Vulcanology) composed by different sensors: velocimeters (short period and broad-band), high performance accelerometers, and MEMS. The seismic network in this area includes the RSN, a more dense local network (namely, the Alto Tiberina Near Fault Observatory—Taboo (Chiaraluce et al., 2014)), and some seismic stations installed for regional

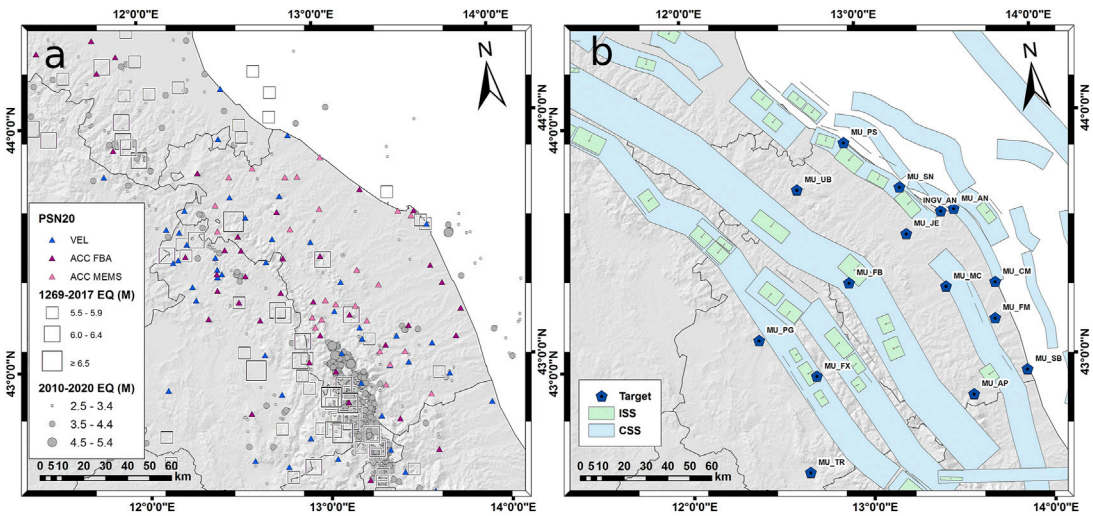

FIGURE 1 | Seismicity, seismic network, different fault zones, and selected targets of the study area. a) PSN20: Permanent Seismic Network in the year 2020. Blue triangles: velocimetric sensors. Purple triangles: FBA high performance accelerometer sensors. Pink triangles: MEMS accelerometer. Black squares: 1219–2019 EQ, moderate to strong earthquakes (M ≥ 5.5) extracted from CPTI15 database (Rovida et al., 2021). Grey circles: earthquakes recorded by the seismic network from 2010 to 2020 in the magnitude range 2.5 ≤ M ≤ 5.4. b) Pentagon: Targets. ISS: individual seismogenic source. CSS: composite seismogenic source (see text for explanation, DISS Working Group (2018)).

TABLE 1 | Target: city code. Place: extended name of cities.

Target	Place
MU_AP	Ascoli Piceno
MU_TR	Terni
MU_FX	Foligno
MU_SB	San Benedetto del Tronto
MU_FM	Fermo
MU_MC	Macerata
MU_FB	Fabriano
MU_CM	Civitanova Marche
MU_PG	Perugia
MU_JE	Jesi
INGV_AN	Ancona INGV headquarters
MU_AN	Ancona
MU_SN	Senigallia
MU_UB	Urbino
MU_PS	Pesaro

monitoring (Cattaneo et al., 2017). A first evaluation of the performance of the EEWS was made analyzing the seismic sequence of 2016–2017 (Festa et al., 2018). The system has been continuously operating over the years, without changing configuration, with some temporary interruptions.

In this work, the feasibility of a regional EEWS was evaluated by developing a procedure of event declaration simulation (EDS) for estimating the time useful to activate safety actions. The EDS procedure can be used for different applications: 1) to assess the feasibility of an EEWS in a specific area with an operating seismic network; 2) to plan the integration of new stations into an existing network; 3) to design a new network for an EEWS; and finally, 4) to assess the feasibility of an EEWS varying network density and trigger parameters. Regarding 3) and 4), the EDS can create virtual networks for the areas of interest and allow to plan investments and installations in advance.

The study was mainly based on the calculation of the time first alert (TFA)—the instant in which the event is declared starting from the coincidence of P phases at the stations, the blind zone radius (BZ)—the area in which no safety action can be carried out, and the lead time (LT)—the useful time to initiate safety actions on the targets. In the paper, we first propose a description of the method, of the parameters setting to obtain realistic simulations, and of the EDS validation with PRESTo EEWS. Then, an EDS application in eastern central Italy is showed, discussing the results of the TFA, BZ, and LT mapping in terms of feasibility and limits of the EEW implementation.

2 EVENT DECLARATION SIMULATION METHOD

The developed EDS is composed by a chain of subroutines including NonLinLoc modules (nonlinear location, or NLLoc; Lomax et al., 2009) in the preparatory phase and homemade python scripts in the core of the simulation that emulates some parameters similar to the PRESTo software. The NLLOC package is a well-known and widely used nonlinear inversion code, consisting of a set of programs and where it is possible to integrate an existing velocity model, travel-time calculation and probabilistic solution, for visualization of 3D volume data and location results (http://alomax.free.fr/nlloc/).

The procedure of event declaration simulation needs the following inputs: arrival times of the P phases to the seismic stations, arrival time of the S phases to the targets, a binding configuration and latencies of the real-time data transmission

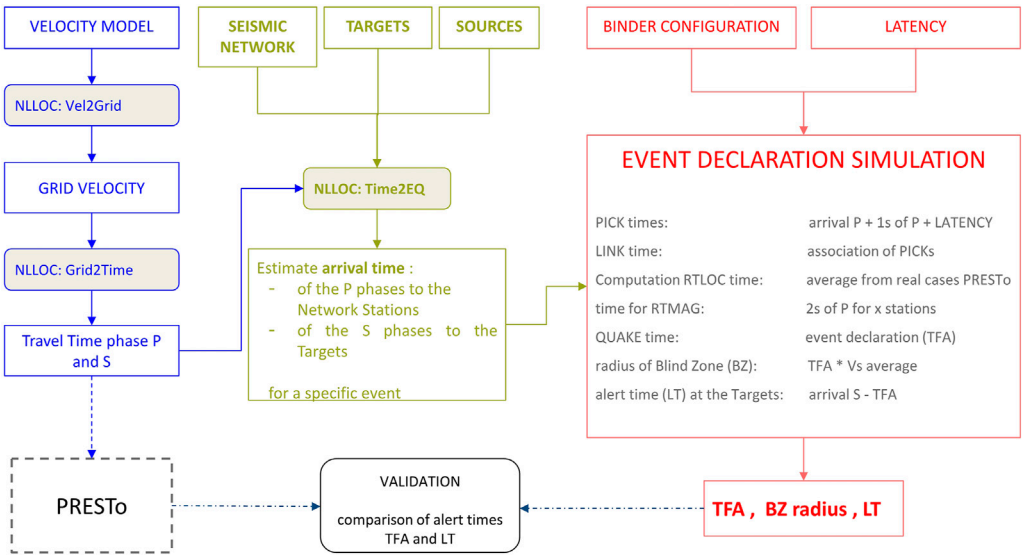

FIGURE 2 | Flow chart of the EDS method. **Left** (blue): P and S travel time calculation with NonLinLoc software modules (Lomax et al., 2009). **Middle** (green): P and S arrival time relative at seismic stations and targets respectively. **Right** (red): input parameters and elements of the EDS core. **Bottom**: terms of the validation.

vectors (**Figure 2**). To obtain the arrival time of P and S phases, a velocity model, a seismic network, a seismic source, and target locations are required.

Figure 2 shows the most important steps of the simulation procedure, exemplifying the main blocks of the procedure from the inputs to the three outputs: TFA, BZ, and LT.

Starting from a velocity model and using the NLLoc Vel2Grid module, it is possible to create a defined grid of velocities, covering the volume of the study area. Then, the NLLoc Grid2Time module calculates the travel times from node points of the 3D velocity grid to the location of the seismic stations. The so obtained travel times are the same in use in the PRESTo system to locate the real seismic events.

The procedure estimates the arrival times of the P phases to the seismic stations and arrival times of the S phases to the targets, taking advantage of the NLLoc Time2EQ module, given the locations of seismic stations, seismic source and targets.

In the core of the simulation, the expected TFA, BZ, and LT are calculated starting from P and S arrival times, binder configuration (coincidences), and data latencies (**Figure 2**).

The simulated parameters conceptually emulate some parameters of the PRESTo software.

"PICK time" is defined as the time of the P phase trigger at each seismic station, the sum of the estimated P phase arrival, the accumulation of 1 s of P waveform for the phase picker and the latency of the data packet. "LINK time" signs the moment when a certain number of PICKs are included in a relative small space and time interval and the binder declares an association. The simulation considers a "computation time" useful to locate the supposed event and the accumulation of 2 s of P waveform to compute the magnitude. The "computation time" and the time to compute the magnitude are inferred from real-time application of the PRESTo system implemented in the study area, collecting the log outputs relative to RTLOC and RTMAG modules (Zollo et al., 2010; Satriano et al., 2011b).

The integration of simulated parameters allows to calculate the "QUAKE time" (TFA) as the needed time to declare the event, summed to the "LINK time". The BZ is estimated multiplying the TFA times the average of the S velocity in the travelled volume. Finally, the useful time (LT) to initiate actions to secure the targets is obtained from the difference between the arrival time of S phase at the targets and the TFA.

3 EVENT DECLARATION SIMULATION CONFIGURATION

The aim of this work is to assess the feasibility of an EEWS in eastern central Italy where a dense seismic network operates, and the main characteristics of the seismicity are well-known (**Figure 1a, b**). The study area is inhabited by about 2.5 million people, distributed in some main cities with population ranging from tens of thousands up to one hundred thousand inhabitants, and in several small historical villages where few hundred people live. Moreover, in most of the target towns and villages, both along the coasts and in the inner Umbria and Marche regions, residents increase dramatically during the summer and other vacation periods.

One of the starting points of the analysis is the velocity model of the volume crossed by seismic waves. A grid of 300 km × 300 km, 67 km thick, starting from 3 km above sea level was created, that could include all the seismicity of the region. A step of 1 km divides nodes of the grid and the central origin geographic point is 43.25 N – 13.00 E. To make the simulation more reliable, we chose a modified version of a 1D velocity model calculated for the region from an instrumental earthquakes catalog (De Luca et al., 2009),

TABLE 2 | Configuration Parameters of the EDS binder.

Parameter	Value	Description
STA_CO (#)	6	Minimum number of triggered stations in the coincidence
SEC_CO (s)	3	Duration of the coincidence time window
SEC_AS (s)	10	Duration of the association window
AVEL_MIN (km/s)	3.85	Minimum apparent velocities of the coincidence picks
AVEL_MAX (km/s)	20	Maximum apparent velocities of the coincidence picks
VEL_SPA (km)	30	Distance to the first pick without apparent velocity checks
VEL_DIST (km)	120	Distance to the first pick beyond which picks are not associated

preserving the Vp/Vs ratio equal to 1.85 and inserting a gradient between velocity layers (**Supplementary Table 1**).

The configuration of the INGV seismic network has been evolving over the years. From 2015, when PRESTo software was installed for real-time monitoring and EEW testing, the number of stations has been increasing. Moreover, during the seismic sequence of the year 2016 (Chiaraluce et al., 2017) an emergency temporary seismic network was installed to densify the permanent network (Moretti et al., 2016; SISMIKO, 2020). Therefore, we set four seismic network configurations for EDS:

- PSN15: Permanent Seismic Network of the year 2015
- TSN16: Temporary Seismic Network of the 2016 seismic emergency (added to PSN15)
- PSN20: Permanent Seismic Network of the year 2020 (including PSN15)
- ASN20: Accelerometric Seismic Network of the year 2020.

The PSN15 is the same network configuration implemented in the real time PRESTo instance and contributed to validate EDS, to estimate data latencies and test performance of the PRESTo system in Festa et al. (2018). TSN16 was used to test the response of the network with a significant increase of the density of the PSN15 up to a station inter-distance of about 5 km in the epicentral area of the 2016–2017 seismic sequence. PSN20 contributed to augment dataset of the EDS validation comparing results with a playback instance of the PRESTo software. The ASN20 helped to estimate the network response if we consider only accelerometric components, corresponding to a reduction of the network density, balanced by the certainty of unclipped records. A list of the seismic stations belonging to each network is inserted in **Supplementary Table 2**.

The EDS is also able to manage arbitrary virtual networks, composed by scattered or equally spaced grid of stations to design network response in uncovered areas.

Also for the sources, we can input a single seismic source or a set of sources, scattered or equally spaced. The location of a single source, for example, is useful to reproduce the response of the seismic network in terms of TFA for an historical or a recent significant event. Furthermore, for the same event, the EDS returns LT relative to the main cities of the region. Extending the principle to a grid of equally spaced sources, the EDS can map the three output parameters (TFA, BZ, and LT) over the whole region. This approach allows classifying areas characterized by small or large TFA and BZ relative to the events' epicenters. In this work, for a first mapping of TFA and BZ, we choose a grid of sources 5 km spaced at depth of 10 km. The LT was estimated for all the selected cities (**Table 1**).

TABLE 3 | Transmission vector, mean and standard deviation of data latency, and number of stations used for each type.

Transmission vector	Latency (s)	Number of. Stations
TCP/IP internet from remote stations	1.86 ± 0.15	4
TCP/IP internet from other data centers	2.25 ± 0.73	15
GSM router	2.75 ± 0.32	5
UMTS router	2.83 ± 0.96	19
WiFi backbone	2.07 ± 0.33	34
LIBRA SATELLITE system	5.90 ± 0.12	2
Ka-sat SATELLITE system	2.64 ± 0.12	7

The number of triggered stations and the time interval for association are the main parameters for the set of the binder, the module that allows to declare an event. In the EDS, the binder configuration emulates the "Binder" of PRESTo software parameters (PRESTo, 2013). We adopt the setup used in the real-time PRESTo instance for choosing the values of binder parameters in the EDS (**Table 2**). The number of at least six stations in coincidence (STA_CO) inside a time window of 3 s (SEC_CO) is a good compromise between the heterogeneous density of the seismic network and the requirement of a rapid response of the system considered the distances of targets from the sources. The SEC_AS parameter is set to 10 s, a value that avoids the effect of the shift of a good location during grid search in the playback PRESTo instance with respect to the results of the real-time instance with SEC_AS = 15 s. The AVEL_MIN, AVEL_MAX, VEL_SPA, VEL_DIST parameters design a cone inside which the coincidence picks must fall.

A key factor to take into account for an EEWS is the data latency due to the communication protocol (Satriano et al., 2011a). The latency affects the alert times of the EEWS which can only be activated when a good part of the data is available in nearly true real-time. The seismic data of the stations in eastern central Italy are transmitted by different types of transmission vectors: TCP/IP, WiFi, GPRS/UMTS, and Satellite (SAT-LIBRA and KA-SAT). At the time of the analysis, LTE routers were not available. Starting from the PRESTo log files, the real latency data for 86 seismic stations for the period 2015–2019 were collected. The long time window of the analysis allowed in some cases to assess the improved performance of the stations after the change of the transmission protocol. An average value of the latency for each type of transmission vectors was calculated by the geometric mean to exclude outliers, that is, values significantly out of the

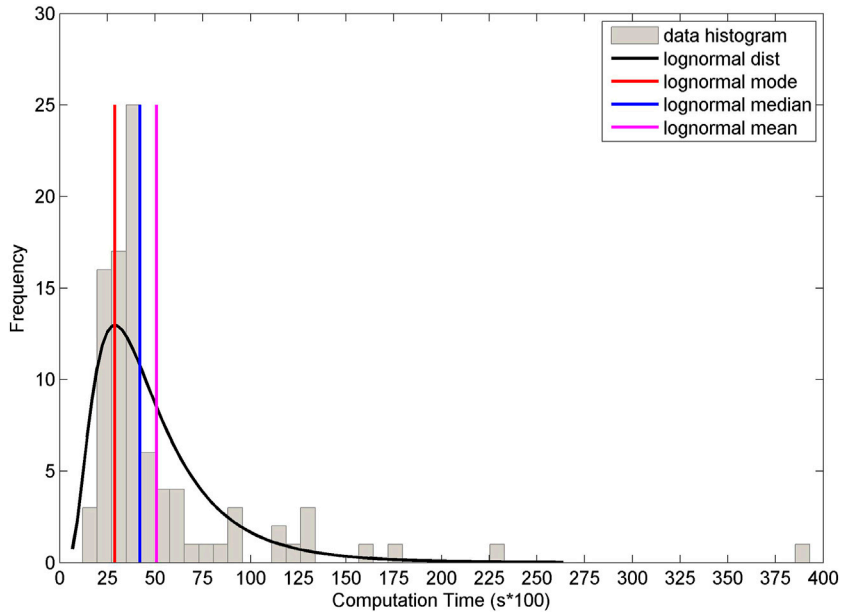

FIGURE 3 | Statistic of the computation time values.

trend, referred to a malfunction of the station. The results of the latency classification are listed in **Table 3** with the average values calculated and the number of stations used. Considering the main transmission vectors used in the network of this study, it is possible to make some considerations. As expected, the stations with a satellite time division multiple access carrier system (i.e., SAT-LIBRA) are those with the greatest latency and are not good for EEW application in small areas, but in our case few stations are equipped with this type of satellite transmission. Instead, another satellite system (i.e., KA-SAT) returns an average of 2.64 s, an acceptable value for EEW applications. The TCP/IP, WiFi, and GSM/UMTS latencies range between 1.86 and 2.83 s. The best value is for direct connection TCP/IP from remote stations. TCP/IP connections from other acquisition centers connected with a mixed copper-fiber line return a slight worsening. The transmission by WiFi backbone gives back a latency of 2.07 s, confirming suitable use for EEW systems. The WiFi system is not a public system, but a system dedicated to civil protection services, available thanks to the Regione Marche authority through an agreement with INGV. Each system used for data transmission (TCP/IP, WiFi, and GSM/UMTS, Satellite) could suffer temporary blackout of the communication lines. In case of a strong earthquake the redundancy of the transmission lines used in the network should reduce the risk of data blackout.

Besides transmission times, another important parameter for an efficient EEWS is the computing time, defined as the difference between the association time of the stations and the computed TFA.

During this time, in the real-time system, the location and magnitude are estimated and the event is declared. The EDS does not simulate the earthquake location process and the magnitude estimate. So, the computing times inserted in our simulation are extracted from a statistics of the real-time PRESTo instance. The time difference between "QUAKE time" and "LINK time" was calculated and compared on a dataset of 91 events (**Supplementary Table 3**) detected in real-time by the PRESTo system and re-simulated by EDS. The events, belonging to the INGV bulletin, were selected from August 2016 to May 2020, with magnitude $3.0 \leq Mw \leq 6.0$. These events were detected by the system in real-time for the same period in the study area. The calculation times, taken from the system files in real-time, were distributed according to a lognormal curve (**Figure 3**). The calculated values are mode equal to 0.29 s, median equal to 0.42 s, and average 0.51 s. Following these results, a value of 0.30 s was chosen as the average computation time for the simulation.

4 EVENT DECLARATION SIMULATION VALIDATION

The simulation procedure was validated comparing the first time of the alerts (TFA) of the EDS with first "QUAKE time" of the PRESTo instances. In the comparison with real time outputs of the PRESTo system, the values of mean latencies belonging to different transmission vectors are inserted in the EDS. Differently, for the comparison with PRESTo playback outputs, a zero latency was set in EDS. These two approaches help to increase the reliability of the validation, excluding that results are affected by a bad estimate of the latencies.

Figure 4 shows a detail of the processing of Mw 5.4 October 26, 2016 event and the comparison of arrival times relative to P phases of the triggered stations, the TFA and the arrival of S phases useful to calculate the LT at the target INGV_AN in the city of Ancona (epicentral distance 88 km). The black marks represent an operator review of the P phases at the triggered stations and the S phase at the target station (cT0). The black

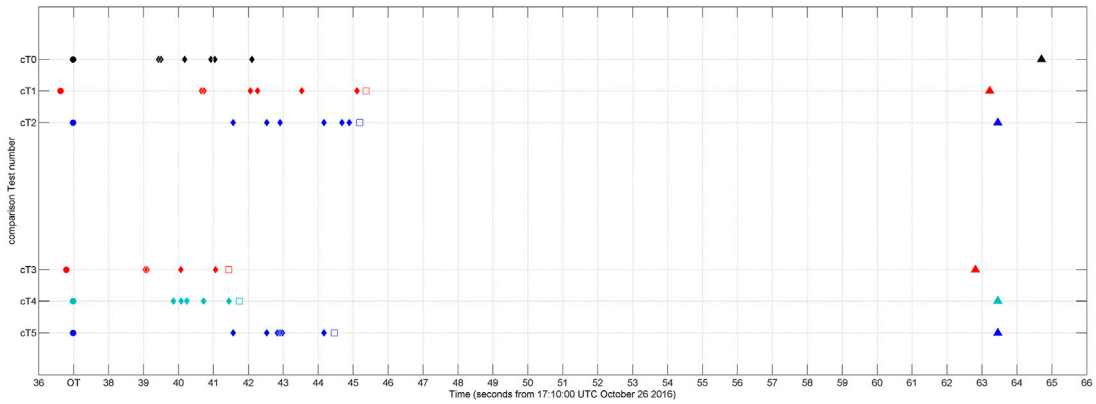

FIGURE 4 | Comparison of arrival times relative to Mw 5.4 October 26, 2016 earthquake. Circles: Origin Time. Diamonds: P phase arrival times of the triggered stations. Squares: TFA. Triangles: S phase arrival times at INGV_AN target in city of Ancona (88 km epicentral distance). cT0: arrival times of human event revision. cT1: PRESTo real time instance with PSN15. cT2: EDS with real latency and with PSN15. cT3: PRESTo playback instance with PSN15 and TSN16. cT4: EDS with zero latency and PSN15 + TSN16. cT5: EDS with real latency with PSN15 + TSN16.

point represents the origin time of the located event, taken into account for the EDS test. The red marks are relative to PRESTo instances (cT1, cT3), while the blue marks are relative to EDS (cT2, cT4, cT5).

The arrival times of operator reviewed P phases are lesser than the PRESTo and EDS real time tests where the data latencies are present. The reviewed arrival time is more similar for the tests in playback where zero latency is setting up but a 1 s of P waveform analysis remains.

The comparison of the TFA between PRESTo and EDS is very good for the two approaches, that is, real-time (cT1 vs cT2) and playback (cT3 vs cT4). The effect of the data latencies in the real time case imply a delay of about 3 s of the TFA with respect to the last P phase arrival time of the human reviewed case. This result is coherent with the values of the mean latencies calculated for the different transmission protocol ranging between 2 and 3 s inserted in the test, and 1 s needed to process the P waveform. The playback version of the test return a little early TFA respect to the last reviewed P phase, both for PRESTo and EDS, but the difference is small, 0.7 and 0.4 s respectively. Finally, the EDS allows to estimate a theoretical TFA adding emergency temporary seismic stations, active in epicentral area at the time of the earthquake, and stations data latencies (cT5). The effect on TFA is about 1 s of the advance respect the PRESTo real-time case (cT1), simply for the early achievement of the station coincidence determined by an augmented network density in the epicentral area. The values of S phase arrival times of PRESTo and EDS are coherent thanks to the same modeling of velocity volume used for travel time computation. From the good simulation of the TFA and S phase arrival at the target by EDS, a good estimate of the LT follows.

For a general validation of the TFA estimated with EDS, we selected 20 seismic events with $3.0 \leq Mw \leq 6.5$, all elaborated also by PRESTo playback instance and 16 events by real-time instance. The selected events are scattered over the study area and over time, with the aim to insert in these tests different and unfavorable states of the network in terms of station inter-distances. The events belong to a time window from August 24, 2016, to January 28, 2020, with the hypocentral depth between 6.8 and 33.3 km (**Supplementary Table 4**). The time window includes some major events of the 2016 Central Italy sequence, located in the southern sector of the region, while the other events were chosen in order to perform tests in the northern part of the region.

Table 4 summarizes the results of EDS estimates of TFA compared with real-time and playback PRESTo instances obtained by setting up the PSN15 configuration network. Moreover, the playback configuration (zero latency) was used to return a TFA mean difference, adding PSN16 emergency temporary station data relative to 2016–2017 events and the PSN20 network configuration for more recent events.

The TFA validation results return mean values lower than 1.0 s. The negative sign indicates an early TFA of the EDS, ascribable to non-simulation of the recursive recalculation of the location and magnitude that occurs in some real cases (PRESTo system) with the arrival of new data. The results of PSN15 real-time and playback cases (validation test 1 and 2) are similar, confirming a reliable simulation for both data latencies and station triggering, respectively. The last case (validation test 3) takes advantage of using 2016 temporary stations and latest installed stations, therefore the network density augmented in a part of analysis. The third test shows a better result, reducing the mean and the uncertainty of TFA difference.

The success of the EDS validation tests allows to perform simulations useful to quantify the EEW response of the actual seismic networks operating in eastern central Italy and to estimate the LT for the main cities in the region.

5 EVENT DECLARATION SIMULATION APPLICATIONS, RESULTS AND DISCUSSION

The EDS was developed to evaluate the EEW response of INGV seismic network in eastern central Italy in terms of TFA, BZ, and

TABLE 4 | Results of the TFA comparison relative to real time and in playback PRESTo instances.

Validation test	Network configuration	PRESTo instance	TFA diff (EDS-PRESTo)
1	PSN15	Real time	−0.80 ± 1.15 s
2	PSN15	Playback	−0.95 ± 1.43 s
3	PSN20 + TSN16	Playback	−0.42 ± 0.72 s

TABLE 5 | Results of tests with single source and different network configurations.

Single source test	Network configuration	Time first alert (s)	Blind zone radius (km)
SST1	PSN15	8.7	26.5
SST2	PSN15 + TSN16	6.3	18.3
SST3	ASN20	9.8	31.4
SST4	VIRT5KM	6.9	20.5

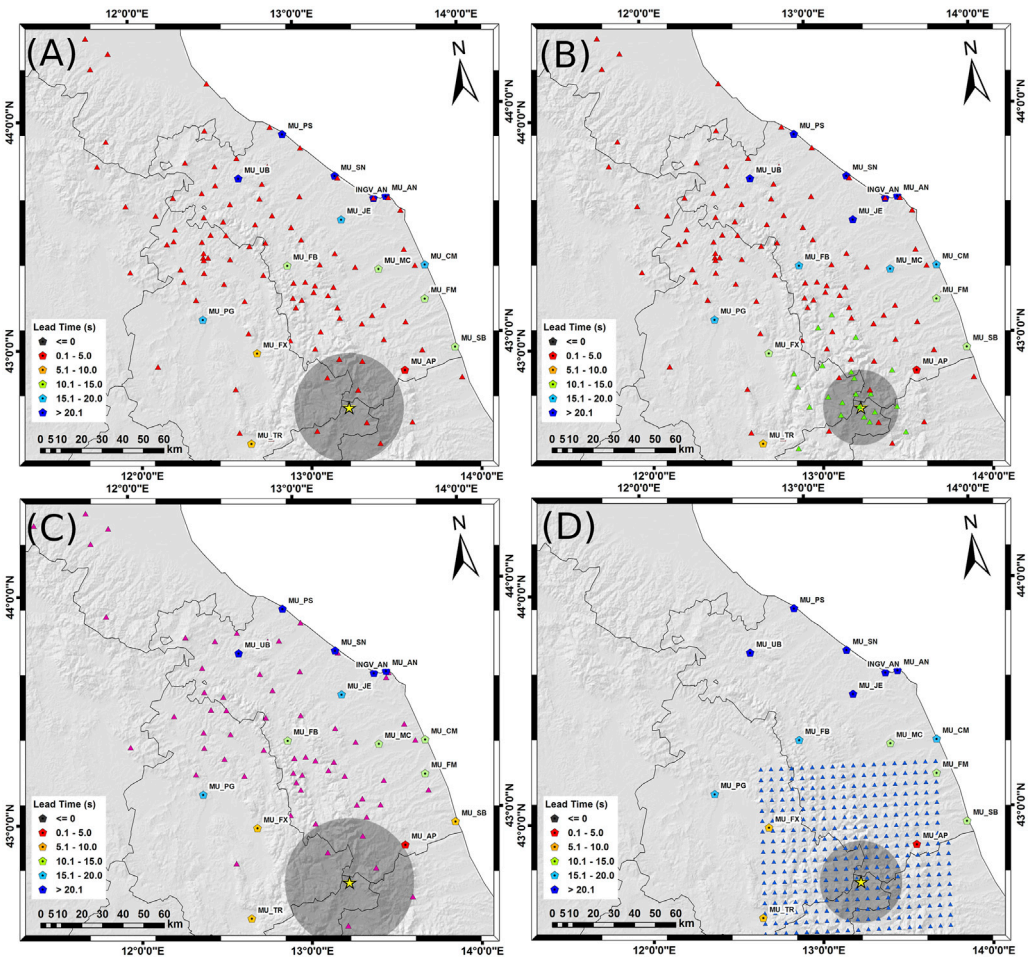

FIGURE 5 | EDS of the EEW response relative to a single source. Yellow star: location of the Mw 6.0 August 24, 2016 earthquake. Gray circle: Blind Zone. Pentagon: Targets. Legend: color map of the LT (s) linked to the targets. **(A)** SST1 test. Red triangles: PSN15 network. **(B)** SST2 test. Red triangles: PSN15 network; green triangles: TSN16. **(C)** SST3 test. Purple triangles: ASN20. **(D)** SST4 test. Blue triangles: 5 km inter-distance virtual network.

TABLE 6 | Results of LT for selected targets. Target: city code. Place: extended name of cities. LT: Values of LT in seconds referred to the test in **Table 4**.

Target	LT (s)			
	SST1	SST2	SST3	SST4
MU_AP	2.2	4.6	1.2	4.0
MU_TR	7.4	9.8	6.4	9.2
MU_FX	7.9	10.3	6.8	9.7
MU_SB	10.1	12.5	9.0	11.8
MU_FM	11.6	14.0	10.5	13.4
MU_MC	12.9	15.3	11.9	14.7
MU_FB	14.8	17.2	13.7	16.5
MU_CM	15.7	18.1	14.6	17.4
MU_PG	17.0	19.4	16.0	18.8
MU_JE	19.5	21.9	18.5	21.3
INGV_AN	22.7	25.1	21.6	24.5
MU_AN	23.3	25.7	22.2	25.0
MU_SN	25.6	28.0	24.6	27.4
MU_UB	29.0	31.4	27.9	30.7
MU_PS	32.6	35.0	31.5	34.4

LD, but it is useful also to reproduce and design the feasibility of the system in different or not yet monitored areas.

The first possible application allowed by EDS is the response of a seismic network relative to one single seismic event with the aim of assessing LT for a set of targets.

Considering the hypocentral location of the Mw 6.0 August 24, 2016, event, we have simulated the response of four network configurations (**Table 5**), assessing the LT for the main cities of the study area (**Figure 5**). During the analysis, the calculation of the BZ is performed by multiplying the TFA by the average Vs estimated at the last station useful for coincidence. The TFA value is calculated as the arrival time of the P wave at the last station, added to the latency value and the estimated computing time of the system. Vs is calculated as the product of mean Vp at the last station for coincidence by the ratio Vs/Vp (De Luca et al., 2009, reported in **Supplementary Table 1**). In the first test (SST1), we used the PSN15 seismic network, the existing network at the time of the event. The second test (SST2) was performed inserting all stations of the TSN16, simulating the presence of the whole emergency network. This temporary seismic network was installed after the earthquake of August 24, 2016. The third test (SST3) represents the unfavorable case of a network consisting of only the current accelerometric INGV stations (ASN20). The last test (SST4) is an example of the design of a virtual arbitrary seismic network with the station inter-distance of 5 km. The calculated mean latency was associated to the PSN15 stations used for the latency statistics, a 2.75 s GSM/UMTS mean latency was associated to the TSN16 stations, and the mean latency was associated at new stations not present in PSN15, depending on their transmission vector. The virtual network with the inter-distance of 5 km was designed like a GSM/UMTS network and a mean latency of 2.75 s was applied to all virtual stations.

The network response in terms of TFA varies in dependence of the seismic station distribution and of network density around the epicentral area (**Figure 5**). The addition of TSN16 to PSN15 around the seismic event causes a reduction of TFA from 8.7 to 6.3 s (gain of 2.4 s) and a reduction of the blind zone (BZ) radius from 26.5 to 18.3 km (**Table 5**). In the third case, the sparse distribution of the accelerometric stations around the epicentral area causes a worsening of the network response with respect to the other two tests and TFA and BZ jump to 9.8 s and 31.4 km respectively. In the SST3 test, the MU_AP target has not safely time for activate protection actions, being on the BZ border, and MU_SB, MU_FX, and MU_TR targets have less than 10 s of LT (**Figure 5C** and **Table 6**). The sample SST4 returns similar values of the SST2 test (**Table 5** and **Table 6**), strengthening the idea that the EDS can represent a tool for design an improvement of the EEWS starting from an existent seismic network or a new EEWS imaging an entirely new network in uncovered areas.

The EDS is also a tool to map the TFA, BZ, and LT over the territory. Indeed, it is possible to configure the procedure including a set of sources, every combined with a TFA and a BZ value. Moreover, it is possible to obtain LT linked to each epicentral location referred to a single target.

The example to explain the use of EDS to mapping EEW parameters is showed in **Figure 6**, where the PSN20 is applied. In the left column, a set of locations referred to the main historical seismic events of Mw ≥ 5.5 from 1269 to 2017 AD that hit the region is presented (**Figure 6A**), extracted from CPTI15 catalog (Rovida et al., 2021). In the right column, a grid of sources with inter-distance of 5 km, depth of 10 km and covering the whole region is depicted (**Figure 6B**). The example of historical events answers the question of which TFA and BZ would occur with the actual seismic network if seismic events repeat in the same locations. Each historical epicentral location is mapped in terms of TFA and BZ (**Figures 6C, E**). Smaller TFA (red points) are mapped where the network is denser in inland areas at the center of the network. For southern inland events and coastal events (yellow dots), the EEWS provides less protection which is significantly reduced for northern events (green dots) where TFA greater than 10 s results in BZ with a radius greater than 30 km.

The same principle can be extended to the whole territory, mapping TFA (**Figure 6D**), and BZ (**Figure 6F**) with the grid of sources. The map of the TFA depicts the edges of the areas within which, if a seismic event occurs, the EEWS responds with a TFA threshold. In particular, for the eastern part of central Italy, with the actual INGV network, an EEWS could produce TFA less than 7.5 s for a large inland area that includes part of the most active seismic zones. Around the Adriatic coast, the seismic network is less dense and an earthquake that occurs off-shore is out of the network. Therefore, the coastal and off-shore TFAs are shorter than those in the inland zones. Besides, the elongated distribution of the seismic stations next to the coast could cause bad locations and estimate of the magnitude by the EEWS, worsening even more the protection provided by the alarm. Also, the northern part of the region is lacking stations and the resulting TFA are similar to the off-shore values. For the largest part of the region, a BZ ranging between 20 and 30 km from the epicenter would not be protected by a warning. The BZ radius increases up to over 30–40 km for the off-shore locations and the EEW system could not produce a TFA for coastal cities. To overcome this problem, offshore seismometers would be extremely useful.

The EDS allows exporting results of the TFA values to map LT referred to a single target. The LT map helps to link places of

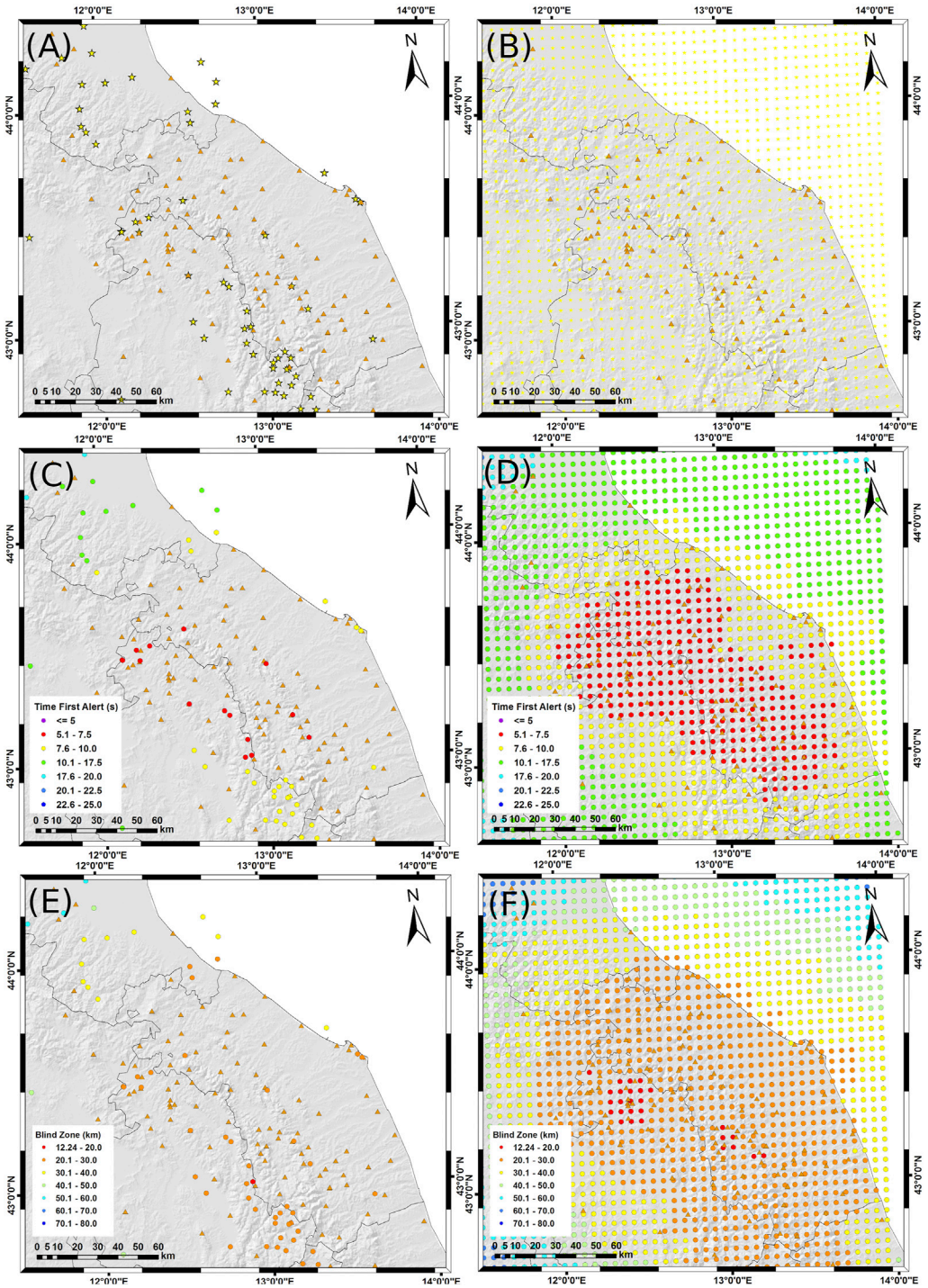

FIGURE 6 | TFA and BZ mapping. **(A)**: historical events from CPTI15 v3.0 Mw ≥ 5.5 from1269 to 2017 AD, depth 10 km before 1997. **(B)**: virtual grid of sources distant of 5 km and depth of 10 km. **(C)**: mapping of TFA with historical events. **(D)**: mapping of TFA with virtual grid. **(E)**: mapping of BZ with historical events. **(F)**: mapping of BZ with virtual grid.

hypothetical epicenters and the time available for safety actions at the target. For example, the map in **Figure 7** shows the LT available for the city of Fabriano (in particular for the location of the city Hall, MU_FB target). The color map shows the values of LT in equally spaced sources, located at 10 km depth. The black dots limit the epicenters for which the city of Fabriano falls in the BZ. Indeed, in this zone the LT is negative (≤0 s). The area marked with red dots corresponds to a 0 s < LT ≤ 5 s where an

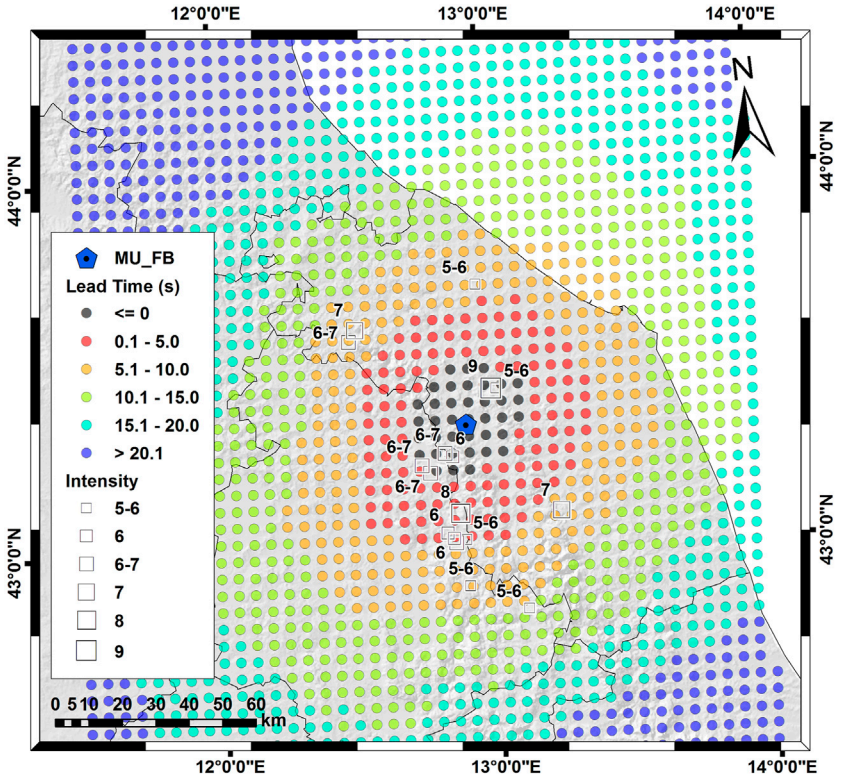

FIGURE 7 | LT mapping for city of Fabriano and historical destructive earthquake. Blue pentagon: place of city of Fabriano (MU_FB target). Colored circles: values of LT in seconds. Squares: CPTI15 v3.0 historical earthquakes and macroseismic intensity (DBMI15 v3.0, Locati et al., 2021) estimated for the city of Fabriano.

alarm could be provided but security actions are unlikely. In the orange area (5 s < LT ≤ 10 s) triggering automatic actions would be possible (Cauzzi et al., 2016). Besides the orange area (LT > 10 s), trained people can take precautionary and protective actions (Fujinawa and Noda, 2013) and the probability of a successful alert increases significantly (Becker et al., 2020b).

This argument makes sense in particular for those earthquakes that could damage the target. Therefore, the destructive earthquakes for the city of Fabriano, extracted from CPTI15 catalog (Rovida et al., 2021), overlap the LT map in **Figure 7**. Clearly, most of the events fall in black and red areas, since the MU_FB target is placed close to the inland active seismic zone (**Figure 1**) and the EEWS would be almost useless. However, some historical events that caused damages with a macroseismic intensity from five to six to 7, fall in the orange area where automatic actions are possible. For the southernmost event (Mw 6.5 on October 30, 2016), an EEWS could have provided an alert 10 s before the arrival of the first S seismic waves to the city of Fabriano, a good LT to take several safety actions.

6 CONCLUSION

The feasibility of an EEWS derives from the design of a seismic network with respect to the seismic sources located within or around it. EEWSs are today an effective contribution to the problem of seismic risk mitigation, but few countries have operational systems (Satriano et al., 2011b). Implementation of EEWSs in Italy is a challenge. Italy is an elongated peninsula, with its central part crossed by a mountain chain that is seismically active and runs very close to urbanized areas. Therefore, the simulations of seismic networks contribute in the field of territorial safety by identifying the time in which some types of protection actions could be activated.

In this work, we have developed a simulation procedure (EDS), useful to estimate the feasibility of an EEWS and showed some applications in eastern central Italy, where INGV manages a dense seismic network. A validation process was performed by comparing results of simulations with real-time and playback instances of the EEW PRESTo system implemented in the same region (Festa et al., 2018).

EDS is a tool to simulate different seismic network responses reproducing the physical contest of a specific historical or recent earthquake; moreover, EDS is a tool to map EEW parameters (TFA, BZ, and LT) to classify the whole territory in terms of areas where it is possible to activate safety actions. With EDS, it is possible to model real seismic networks inserting actual or theoretical data latencies due to different transmission vectors and to design new seismic networks in uncovered areas.

As expected, the results of the EDS application in eastern central Italy highlights short, but still useful, alert times for innermost land and coastal areas overlooking the active

seismic zones. However, we have shown that most of the currently used transmission vectors have latencies between 2 and 3 s, an acceptable value for seismic early warnings. The quantitative estimate of TFA, BZ, and LT supplies useful information to project an improvement of the EEWS with the aim to reduce as much as possible the TFA. Modern approaches include the use of low-cost sensors for a greater diffusion of the seismic monitoring throughout the territory, and the development of networks oriented toward smart cities using fast protocols and connectivity (Ladina et al., 2016; Pierleoni et al., 2018; D'Alessandro et al., 2019). In the area of the 2016 Central Italy sequence, we have estimated a gain of about 2.5 s of LT, adding the 2016 emergency temporary stations (station inter-distance about 5 km) over the permanent network, with a data latency similar to GPRS connections. The result was repeated setting a virtual network in a station grid with a constant inter-distance of 5 km and a mean data latency of 2.6 s to demonstrate the ability to project an EEWS in uncovered areas and to obtain realistic times of the first alert.

Although the Italian territory is mostly characterized by seismic sources next to urbanized areas, the lead times calculated with EDS procedure encourage the opportunity of implementing an EEWS for several interesting targets. Simulating historical events, a LT between 5 and 10 s was reproduced for some of these targets. We conclude that automatic safety actions, situational awareness and a more rapid response by well-trained people are a realistic goal in eastern central Italy.

We are aware that the study presented here has some limitations, first of all the system performance is evaluated analyzing mainly the rapidity of an EWS, whereas no evaluation assessment is made on the reliability of the earthquake impact prediction. This implies that the evaluation of the shaking could be inaccurate or even lead to false or missed alerts. However, the goal of our analysis was to determine whether an EWS could be a viable solution to reduce seismic exposure in certain regions of Italy, and in which conditions (network geometry, transmission times, etc.). Our results are encouraging provided that some technological issues are considered and that people's awareness of seismic risk is increased. Further studies will be dedicated to a more thorough assessment of EWS.

The development of a widespread monitoring infrastructure near the main seismic sources, the massive training of citizens, and the collaboration with civil protection authorities could improve the scenarios simulated in this work, making an EEWS really effective in protecting people from the harmful effects of earthquakes in Italy.

DATA AVAILABILITY STATEMENT

The raw data supporting the conclusions of this article will be made available by the authors, without undue reservation.

AUTHOR CONTRIBUTIONS

Conceptualization; methodology; validation; data analysis and curation: CL, SM; data analysis supervision: AA, MC; writing-original draft preparation; writing-review and editing: CL, SM, AA, MC. All authors contributed to manuscript, read and approved the submitted version.

FUNDING

This work has been carried out within the Project ART-IT (Allerta Rapida Terremoti in Italia), funded by the Italian Ministry of University and Research (Progetto Premiale 2015, DM. 850/2017), and supported also by the Agreement between Civil Protection Department of the Regione Marche and INGV.

ACKNOWLEDGMENTS

The authors thank Mario Locati for support with DBMI15 v2.0, Luca Elia for suggestion and explanations with PRESTo configuration, and Simona Colombelli for the suggestions about the details of the work.

SUPPLEMENTARY MATERIAL

The Supplementary Material for this article can be found online at: https://www.frontiersin.org/articles/10.3389/feart.2021.685751/full#supplementary-material

REFERENCES

Alcik, H., Ozel, O., Apaydin, N., and Erdik, M. (2009). A Study on Warning Algorithms for Istanbul Earthquake Early Warning System. *Geophys. Res. Lett.* 36, L00B05. doi:10.1029/2008GL036659

Allen, R. M., Brown, H., Hellweg, M., Khainovski, O., Lombard, P., and Neuhauser, D. (2009a). Real-time Earthquake Detection and hazard Assessment by ElarmS across California. *Geophys. Res. Lett.* 36, L00B08. doi:10.1029/2008GL036766

Allen, R. M., Gasparini, P., Kamigaichi, O., and Böse, M. (2009b). The Status of Earthquake Early Warning Around the World: An Introductory Overview. *Seismological Res. Lett.* 80 (5), 682–693. doi:10.1785/gssrl.80.5.682

Allen, R. M., and Kanamori, H. (2003). The Potential for Earthquake Early Warning in Southern California. *Science* 300, 786–789. doi:10.1126/science.1080912

Allen, R. M., and Melgar, D. (2019). Earthquake Early Warning: Advances, Scientific Challenges, and Societal Needs. *Annu. Rev. Earth Planet. Sci.* 47, 361–388. doi:10.1146/annurev-earth-053018-060457

Becker, J. S., Potter, S. H., Prasanna, R., Tan, M. L., Payne, B. A., Holden, C., et al. (2020b). Scoping the Potential for Earthquake Early Warning in Aotearoa New Zealand: A Sectoral Analysis of Perceived Benefits and Challenges. *Int. J. Disaster Risk Reduction* 51, 101765. doi:10.1016/j.ijdrr.2020.101765

Becker, J. S., Potter, S. H., Vinnell, L. J., Nakayachi, K., McBride, S. K., and Johnston, D. M. (2020a). Earthquake Early Warning in Aotearoa New Zealand: a Survey of Public Perspectives to Guide Warning System Development. *Humanit Soc. Sci. Commun.* 7. doi:10.1057/s41599-020-00613-9

Böse, M., Ionescu, C., and Wenzel, F. (2007). Earthquake Early Warning for Bucharest, Romania: Novel and Revised Scaling Relations. *Geophys. Res. Lett.* 34, L07302. doi:10.1029/2007GL029396

Caruso, A., Colombelli, S., Elia, L., Picozzi, M., and Zollo, A. (2017). An On-Site Alert Level Early Warning System for Italy. *J. Geophys. Res. Solid Earth* 122. doi:10.1002/2016JB013403

Cattaneo, M., Frapiccini, M., Ladina, C., Marzorati, S., and Monachesi, G. (2017). A Mixed Automatic-Manual Seismic Catalog for Central-Eastern Italy: Analysis of Homogeneity. *Ann. Geophys.* 60, 6. doi:10.4401/ag-7333

Cauzzi, C., Behr, Y., Le Guenan, T., Douglas, J., Auclair, S., Woessner, J., et al. (2016). Earthquake Early Warning and Operational Earthquake Forecasting as Real-Time hazard Information to Mitigate Seismic Risk at Nuclear Facilities. *Bull. Earthquake Eng.* 14, 2495–2512. doi:10.1007/s10518-016-9864-0

Chiaraluce, L., Amato, A., Carannante, S., Castelli, V., Cattaneo, M., Cocco, M., et al. (2014). The Alto Tiberina Near Fault Observatory (Northern Apennines, Italy). *Ann. Geophys.* 57, 3. doi:10.4401/ag-6426

Chiaraluce, L., Di Stefano, R., Tinti, E., Scognamiglio, L., Michele, M., Casarotti, E., et al. (2017). The 2016 Central Italy Seismic Sequence: A First Look at the Mainshocks, Aftershocks, and Source Models. *Seismological Res. Lett.* 88 (3), 757–771. doi:10.1785/0220160221

Clinton, J., Zollo, A., Marmureanu, A., Zulfikar, C., and Parolai, S. (2016). State-of-the Art and Future of Earthquake Early Warning in the European Region. *Bull. Earthquake Eng.* 14, 2441–2458. doi:10.1007/s10518-016-9922-7

Colombelli, S., Amoroso, O., Zollo, A., and Kanamori, H. (2012a). Test of a Threshold-Based Earthquake Early-Warning Method Using Japanese Data. *Bull. Seismological Soc. America* 102, 1266–1275. doi:10.1785/0120110149

Colombelli, S., Caruso, A., Zollo, A., Festa, G., and Kanamori, H. (2015). A P Wave-based, On-site Method for Earthquake Early Warning. *Geophys. Res. Lett.* 42, 1390–1398. doi:10.1002/2014GL063002

Colombelli, S., Zollo, A., Festa, G., and Kanamori, H. (2012b). Early Magnitude and Potential Damage Zone Estimates for the Great Mw 9 Tohoku-Oki Earthquake. *Geophys. Res. Lett.* 39, a–n. doi:10.1029/2012gl053923

Cua, G., Fischer, M., Heaton, T., and Wiemer, S. (2009). Real-time Performance of the Virtual Seismologist Earthquake Early Warning Algorithm in Southern California. *Seismological Res. Lett.* 80, 740–747. Number 5. doi:10.1785/gssrl.80.5.740

D'Alessandro, A., Costanzo, A., Ladina, C., Buongiorno, F., Cattaneo, M., Falcone, S., et al. (2019). Urban Seismic Networks, Structural Health and Cultural Heritage Monitoring: The National Earthquakes Observatory (INGV Ltaly) Experience. *Front. Built Environ.* doi:10.3389/fbuil.2019.00127

De Luca, G., Cattaneo, M., Monachesi, G., and Amato, A. (2009). Seismicity in Central and Northern Apennines Integrating the Italian National and Regional Networks. *Tectonophysics* 476, 121–135. doi:10.1016/j.tecto.2008.11.032

DISS Working Group (2018). Database of Individual Seismogenic Sources (DISS), Version 3.2.1: A Compilation of Potential Sources for Earthquakes Larger Than M 5.5 in Italy and Surrounding Areas. Istituto Nazionale di Geofisica e Vulcanologia. Available at: http://diss.rm.ingv.it/diss/. doi:10.6092/INGV.IT-DISS3.2.1

Dunn, P. T., Ahn, A. Y. E., Bostrom, A., and Vidale, J. E. (2016). Perceptions of Earthquake Early Warnings on the U.S. West Coast. *Int. J. Disaster Risk Reduction* 20, 112–122. doi:10.1016/j.ijdrr.2016.10.019

Erdik, M., Fahjan, Y., Ozel, O., Alcik, H., Mert, A., and Gul, M. (2003). Instabul Earthquake Rapid Response and the Early Warning System. *Bull. Earthquake Eng.* 1 (1), 157–163. doi:10.1023/A:1024813612271

Festa, G., Picozzi, M., Caruso, A., Colombelli, S., Cattaneo, M., Chiaraluce, L., et al. (2018). Performance of Earthquake Early Warning Systems during the 2016-2017 Mw 5-6.5 Central Italy Sequence. *Seismol. Res. Lett.* 89, 1–12. doi:10.1785/0220170150

Fujinawa, Y., and Noda, Y. (2013). Japan's Earthquake Early Warning System on 11 March 2011: Performance, Shortcomings, and Changes. *Earthquake Spectra* 29 (S1), S341–S368. doi:10.1193/1.4000127

Gorini, A., Nicoletti, M., Marsan, P., Bianconi, R., De Nardis, R., Filippi, L., et al. (2010). The Italian strong Motion Network. *Bull. Earthquake Eng.* 8, 1075–1090. doi:10.1007/s10518-009-9141-6

Hsiao, N.-C., Wu, Y.-M., Shin, T.-C., Zhao, L., and Teng, T.-L. (2009). Development of Earthquake Early Warning System in Taiwan. *Geophys. Res. Lett.* 36, L00B02. doi:10.1029/2008GL036596

Iannaccone, G., Zollo, A., Elia, L., Convertito, V., Satriano, C., Martino, C., et al. (2010). A Prototype System for Earthquake Early-Warning and Alert Management in Southern Italy. *Bull. Earthquake Eng.* 8, 1105–1129. doi:10.1007/s10518-009-9131-8

Iervolino, I., Galasso, C., and Manfredi, G. (2008). "Information-dependent lead-time Maps for Earthquake Early Warning in the Campania Region," in The 14th World Conference on Earthquake Engineering, Beijing, China, October 12-17, 2008.

INGV Seismological Data Centre (2006). *Rete Sismica Nazionale (RSN)*. Italy: Istituto Nazionale di Geofisica e Vulcanologia (INGV). doi:10.13127/sd/x0fxnh7qfy

Kohler, M. D., Smith, D. E., Andrews, J., Chung, A. I., Hartog, R., Henson, I., et al. (2020). Earthquake Early Warning ShakeAlert 2.0: Public Rollout. *Seismol. Res. Lett.* 91 (3), 1763–1775. doi:10.1785/0220190245

Ladina, C., Marzorati, S., Monachesi, G., Cattaneo, M., Frapiccini, M., and Castelli, V. (2016). Strong-motion Observations Recorded in Strategic Public Buildings during the 24 August 2016 Mw 6.0 Amatrice (central Italy) Earthquake. *Ann. Geophys.* 59. Fast Track 5 (2016): The Amatrice seismic sequence: preliminary data and results. doi:10.4401/ag-7194

Locati, M., Camassi, R., Rovida, A., Ercolani, E., Bernardini, F., Castelli, V., et al. (2021). *Database Macrosismico Italiano (DBMI15), versione 3.0*. Istituto Nazionale di Geofisica e Vulcanologia (INGV). doi:10.13127/DBMI/DBMI15.3

Lomax, A., Michelini, A., and Curtis, A. (2009). "Earthquake LocationEarthquake Location, Direct, Global-Search Methods," in *Encyclopedia of Complexity and System Science* (New York: Springer), 2449–2473. doi:10.1007/978-0-387-30440-3_150

Moretti, M., Pondrelli, S., Margheriti, L., Abruzzese, L., Anselmi, M., Arroucau, P., et al. (2016). SISMIKO: Emergency Network Deployment and Data Sharing for the 2016 central Italy Seismic Sequence. *Ann. Geophys.* 59. Fast Track 5. doi:10.4401/ag-7212

Odaka, T., Ashiya, K., Tsukada, S., Sato, S., Ohtake, K., and Nozaka, D. (2003). A New Method of Quickly Estimating Epicentral Distance and Magnitude from a Single Seismic Record. *Bull. Seismological Soc. America* 93 (1), 526–532. doi:10.1785/0120020008

Olivieri, M., Allen, R. M., and Wurman, G. (2008). The potential for earthquake early warning in Italy using ElarmS. *Bull. Seismol. Soc. Am.* 98 (1), 495–503. doi:10.1785/0120070054

Picozzi, M. (2012). An Attempt of Real-Time Structural Response Assessment by an Interferometric Approach: A Tailor-Made Earthquake Early Warning for Buildings. *Soil Dyn. Earthquake Eng.* 38, 109–118. doi:10.1016/j.soildyn.2012.02.003

Picozzi, M., Zollo, A., Brondi, P., Colombelli, S., Elia, L., and Martino, C. (2015). Exploring the Feasibility of a Nationwide Earthquake Early Warning System in Italy. *J. Geophys. Res. Solid Earth* 120, 2446–2465. doi:10.1002/2014JB011669

Pierleoni, P., Marzorati, S., Ladina, C., Raggiunto, S., Belli, A., Palma, L., et al. (2018). Perfarmance Evaluation of a Low-Cost Sensing Unit for Seismic Applications: Field Testing during Seismic Events of 2016-2017 in Central Ltaly. *IEEE Sensor Joumal* 18, 16. doi:10.11O9/JSEN.2018.285006510.1109/jsen.2018.2850065

PRESTo (2013). Probabilistic and Evolutionary Early Warning SysTem. Available at: http://www.prestoews.org (Accessed March 25, 2021).

Rovida, A., Locati, M., Camassi, R., Lolli, B., Gasperini, P., and Antonucci, A. (2021). *Catalogo Parametrico dei Terremoti Italiani (CPTI15), versione 3.0*. Istituto Nazionale di Geofisica e Vulcanologia (INGV). doi:10.13127/CPTI/CPTI15.3

Satriano, C., Elia, L., Martino, C., Lancieri, M., Zollo, A., and Iannaccone, G. (2011a). PRESTo, the Earthquake Early Warning System for Southern Italy: Concepts, Capabilities and Future Perspectives. *Soil Dyn. Earthquake Eng.* 31, 137–153. doi:10.1016/j.soildyn.2010.06.008

Satriano, C., Wu, Y.-M., Zollo, A., and Kanamori, H. (2011b). Earthquake Early Warning: Concepts, Methods and Physical Grounds. *Soil Dyn. Earthquake Eng.* 31, 106–118. doi:10.1016/j.soildyn.2010.07.007

SISMIKO (2020). Coordinamento Delle Reti Sismiche mobile in Emergenza. Available at: http://sismiko.ingv.it (Accessed March 25, 2021).

Suarez, G., Novelo, D., and Mansilla, E. (2009). Performance Evaluation of the Seismic Alert System (SAS) in Mexico City: A Seismological and a Social Perspective. *Seismological Res. Lett.* 80 (5), 707–716. doi:10.1785/gssrl.80.5.707

Velazquez, O., Pescaroli, G., Cremen, G., and Galasso, C. (2020). A Review of the Technical and Socio-Organizational Components of Earthquake Early Warning Systems. *Front. Earth Sci.* 8, 533498. doi:10.3389/feart.2020.533498

Wu, Y.-M., and Teng, T. L. (2002). A Virtual Subnetwork Approach to Earthquake Early Warning. *Bull. Seismological Soc. America* 92 (5), 2008–2018. doi:10.1785/0120010217

Zollo, A., Amoroso, O., Lancieri, M., Wu, Y.-M., and Kanamori, H. (2010). A Threshold-Based Earthquake Early Warning Using Dense Accelerometer Networks. *Geophys. J. Int.* 183, 963–974. doi:10.1111/j.1365-246X.2010.04765.x

Zollo, A., Colombelli, S., Elia, L., Emolo, A., Festa, G., Iannaccone, G., et al. (2014). "An Integrated Regional and On-Site Earthquake Early Warning System for Southern Italy: Concepts, Methodologies and Performances," in *Book: Early Warning for Geological Disasters, Advanced Technologies in Earth Sciences*, 117–137. doi:10.1007/978-3-642-12233-0_7

Conflict of Interest: The authors declare that the research was conducted in the absence of any commercial or financial relationships that could be construed as a potential conflict of interest.

frontiers in Earth Science

ORIGINAL RESEARCH
published: 26 August 2021
doi: 10.3389/feart.2021.696191

Four Years of Earthquake Early Warning in Southern Iberia: 2016–2019

Marta Carranza[1], *Maurizio Mattesini*[2,3], *Elisa Buforn*[2,3]*, *Aldo Zollo*[4] *and Irene Torrego*[2]

[1]Instituto Geográfico Nacional, Madrid, Spain, [2]Departamento de Física de la Tierra y Astrofísica, Universidad Complutense de Madrid, Madrid, Spain, [3]Instituto de Geociencias (UCM-CSIC), Facultad de Ciencias Físicas, Madrid, Spain, [4]Dipartimento di Fisica Ettore Pancini, Universitá Federico II, Naples, Italy

The performance of an earthquake early warning system (EEWS) for southern Iberia during the period of 2016–2019 is analyzed. The software PRESTo (PRobabilistic and Evolutionary early warning SysTem; the University of Naples Federico II, Italy) operating at the Universidad Complutense de Madrid has detected 728 events ($2 < M_w < 6.3$), with 680 earthquakes occurring in southern Iberia. Differences between the EEWS origin time and epicenter and those of the Instituto Geográfico Nacional (IGN) catalog are less than 2 s and 20 km, respectively, for 70% of the detected earthquakes. The main differences correspond to the EEWS magnitude that is underestimated for earthquakes that occurred at the west of the Gibraltar Strait (M_w differences larger than 0.3 for 70%). To solve this problem, several relationships have been tested, and a modification to those that currently use PRESTo is proposed. Other improvements, such as to densify the network or to use 3D Earth models, are proposed to decrease the time needed to issue the alert and avoid the false alerts (19 events over a total of 728 events). The EEWS has estimated the depth for 680 events and compared to those from the IGN (491 events). The performance of PRESTo during the 2020–2021 Granada swarm is analyzed. The hypocentral locations for the three largest earthquakes are close to those from the IGN (differences from 1 to 7 km for the epicenter and 0 s for the time origin), although there are some differences in their magnitude estimations that varies from 0.2 to 0.5. The PRESTo first times are 17, 25, and 41 s after the origin time. This study shows that the actual PRESTo EEWS configured for the southern Iberia may generate effective warnings despite the low seismicity rate in this region. To decrease the warning time, the geometry and density of the seismic network must be improved together with the use of 3D Earth models and on-site system approaches.

Keywords: EEWS, southern Iberia, magnitude, Granada 2020–21 swarm, PRESTo

OPEN ACCESS

Edited by:
Mitsuyuki Hoshiba,
Japan Meteorological Agency, Japan

Reviewed by:
Dayi Chen,
Central Weather Bureau, Taiwan

***Correspondence:**
Elisa Buforn
ebufornp@ucm.es

Specialty section:
This article was submitted to Geohazards and Georisks, a section of the journal Frontiers in Earth Science

Received: *16 April 2021*
Accepted: *06 July 2021*
Published: *26 August 2021*

Citation:
Carranza M, Mattesini M, Buforn E, Zollo A and Torrego I (2021) Four Years of Earthquake Early Warning in Southern Iberia: 2016–2019. Front. Earth Sci. 9:696191. doi: 10.3389/feart.2021.696191

INTRODUCTION

Many large earthquakes have occurred in southern Iberia, located at the plate boundary between Eurasia and Africa, some of which caused severe damage and generated devastating tsunamis [Lisbon 1755, I_{max} = X; Saint Vincent Cape (SVC), 1969 Mw = 7.8; Boumerdes 2003, Mw = 6.8; **Figure 1**]. The 20th century has not been very seismically active, with a deficit of large earthquakes (Buforn et al., 2015). During the period 2000–2020, three moderate earthquakes ($5.0 < Mw < 6.5$) have occurred in this region, resulting in serious damage: the 2004 Al Hoceima, Morocco (M_w = 6.4, Ait Brahim et al., 2004), and the 2011 Lorca, Spain (M_w = 5.1, Morales et al., 2014), or social alarm, such

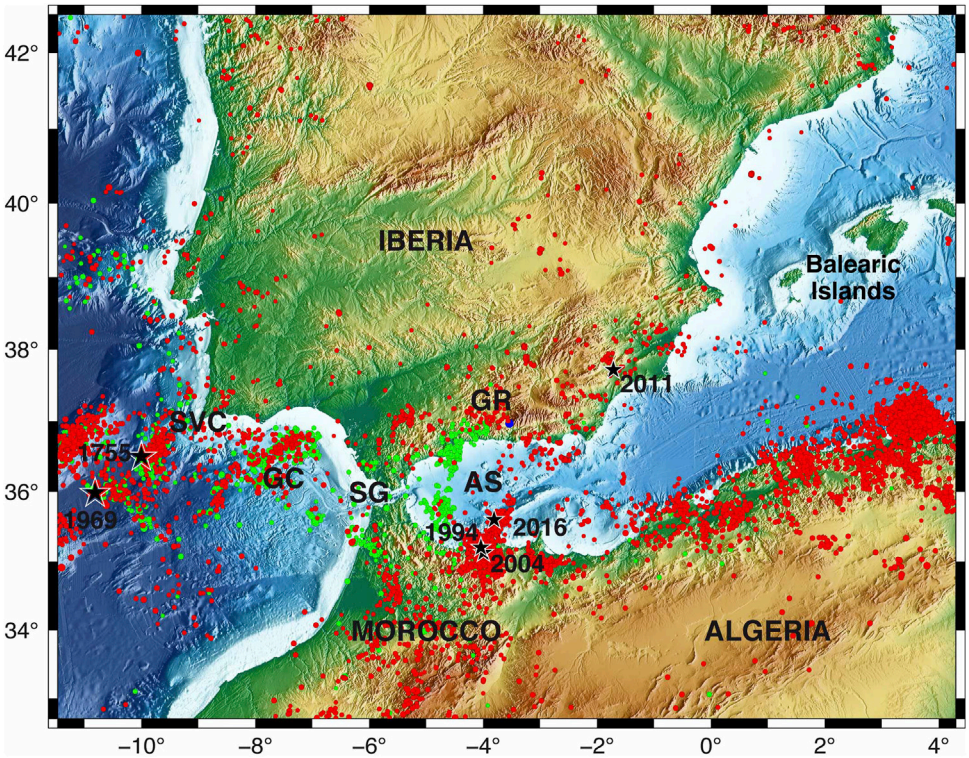

FIGURE 1 | Seismicity of the Ibero–Maghrebian Region for the period of 2000–2019 (M ≥ 3.0) taken from the IGN catalog (https://www.ign.es/web/ign/portal/sis-catalogo-terremotos). Red circles correspond to shallow earthquakes (h < 40 km), green to intermediate depths (40 < h < 150 km), and blue to deep events (h > 150 km). Stars show the epicenters of large or recent earthquakes. SG = Strait of Gibraltar, SVC = Saint Vincent Cape, GC = Gulf of Cadiz, AS = Alboran Sea, and GR = Granada.

as the one observed in the 2016 Alboran Sea (M_w = 6.4, Buforn et al., 2017; Stich et al., 2020). To mitigate the damage generated by earthquakes in the region, the Universidad Complutense de Madrid (UCM) has led two projects to study the feasibility of an earthquake early warning system (EEWS) in the region, namely, the ALERTES (2011–2013) and the ALERTES-RIM (2014–2016) projects, with the participation of the Real Instituto y Observatorio de la Armada, San Fernando (ROA), and the Institut Geologic de Catalunya (IGC, actually ICGC) (Buforn et al., 2016; Carranza et al., 2017).

The aim of an EEWS is to provide warnings within a few seconds after the occurrence of an earthquake prior to the arrival of the strong shaking, S-wave, at a target site. An EEWS uses data from a seismic network, together with the implementation of an algorithm capable of performing a real-time analysis of seismograms through telemetry, to determine the location, origin time, and magnitude. From the first few seconds of signal receipt, generally 3 s, the system ideally generates a warning before the arrival of the S wave motion at a target location (Wu and Kanamori, 2005; Zollo et al., 2010).

The elapsed time between the warning and the S-wave arrival, known as the lead time, is the time available to take actions designed to reduce the damage. However, there is a region known as the blind zone in which the S-wave arrives before the warning is issued (Satriano et al., 2011). The EEWS estimates the earthquake magnitude from several alert parameters obtained from the first seconds of the P-wave. The basic hypothesis is that these parameters provide enough information about the size of the earthquake (Wu and Kanamori, 2005; Zollo et al., 2006). Typically, EEWSs have two different configurations: a regional configuration, where the seismic network is located between the epicenter and the targets to trigger a warning, or an on-site configuration, in which the stations are located at the target site of the warning. These two configurations can be integrated into the same EEWS, which is especially useful in regions with more than one seismogenic zone, such as southern Iberia (Zollo et al., 2010).

Since 2011, the ALERTES and ALERTES-RIM projects have allowed us to study the feasibility of establishing an EEWS in the Ibero–Maghrebian region (IMR) that encloses southern Iberia and northern Morocco and Algeria. Carranza et al. (2013) obtained the relationships for the IMR that correlate the alert parameters P_d and τ_c with the magnitude and the peak ground velocity, respectively. Pazos et al. (2015) tested the performance of three different software platforms (Earthworm, SeisComP3, and PRESTo) during the simulation of four representative earthquakes that occurred in SW Iberia. In October 2015, an EEWS based on PRESTo software (Probabilistic and Evolutionary early warning SysTem, Satriano et al., 2011; Zollo et al., 2016) was installed at the Universidad Complutense of Madrid (Spain). Carranza et al. (2017) have

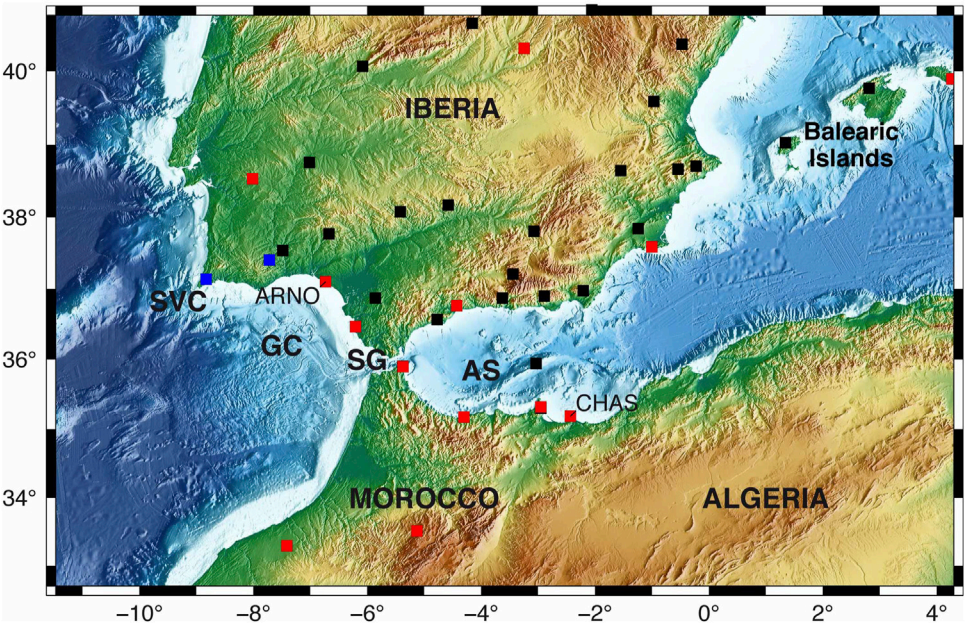

FIGURE 2 | PRESTo receiving stations. Black squares = IGN, red = WM, blue = IPMA stations. SVC = Saint Vincent Cape; GC = Gulf of Cadiz; SG = Strait of Gibraltar; and AS = Alboran Sea.

analyzed the first five months (October 2015–February 2016) of the system's real-time performance, discussing the hypocentral location and the magnitude obtained by the EEWS in comparison with the values provided by the Instituto Geográfico Nacional (IGN). These authors have included a detailed study of lead times provided by PRESTo for the 2016 Alboran Sea earthquakes and the 2016 southwest SVC (M_w 4.5) earthquakes.

In this article, we discuss the performance of PRESTo in the IMR for the period of 2016–2020. An important point of this study is to check the performance of an EEWS in a region of moderate magnitude earthquakes where large shocks are separated by long time intervals and where for the studied period, 2016–2019, only one shock has Mw = 6.4. To improve the PRESTo results, we tested different relationships to obtain the magnitude and possible modifications to the EEWS. In this study, we also discuss the PRESTo performance during the recent seismic sequence in Granada, where a swarm of earthquakes (more than 1900 small events, M < 3.0 and 31 earthquakes with 3.0 > M > 4.5) occurred from December 2020 to mid-February 2021.

THE EEWS AT THE IBERO–MAGHREBIAN REGION

The EEWS was configured for a part of the IMR boundary box 32.7°N to 40.75°N and 11.47°W to 4.3°E (**Figure 1**) using a 2-km × 2-km grid. The PRESTo platform (Satriano et al., 2011; www.prestoews.org) developed by the RISSC Lab (the Experimental and Computational Seismology Laboratory of the Physics Department at the University of Naples Federico II, Naples, Italy) was installed on a Linux machine at the Universidad Complutense of Madrid (Dept. Física de la Tierra y Astrofísica). This software uses a regional approach where the seismic stations are deployed around the source region and the targets to protect, and its configuration has been adapted to the characteristics of IMR (for further details, see Carranza, 2016; Carranza et al., 2013, Carranza et al., 2017). The SeisComP3 software package and the SeedLink communication protocol are used to continuously receive the real-time signal of the stations, 39 velocity broadband seismic stations installed in the IMR: 26 from the Instituto Geográfico Nacional (IGN, https://doi.org/10.7914/SN/ES), 13 from the Western Mediterranean network (WM, https://doi.org/10.14470/JZ581150), and 2 from the Instituto Português do Mar e da Atmosfera (IPMA, https://doi.org/10.7914/SN/PM) network (**Figure 2**).

The regional velocity grid model used for determining the hypocentral locations was generated from the NonLinLoc software package (Lomax et al., 2009). It is derived from the 1D velocity model used by the IGN catalog (Carreño et al., 2003). Our EEWS declares an event when a minimum of five stations are triggered. The maximum standby time, defined as the time which the EEWS is waiting for a fifth station detecting the earthquake since the first detection, is set to 45 s. All the arrivals detected within 3 min, after the first pick, are associated with the same event. Once the earthquake's hypocenter is located, PRESTo measures the de P_d parameter in the first 2 and 4 s of the P wave (previously integrated and filtered with a two-pole high-pass Butterworth filter with a corner frequency of 0.075 Hz). The magnitude is estimated from the empirical relationship proposed by Carranza et al. (2017) for the IMR and normalized to a reference distance of 10 km

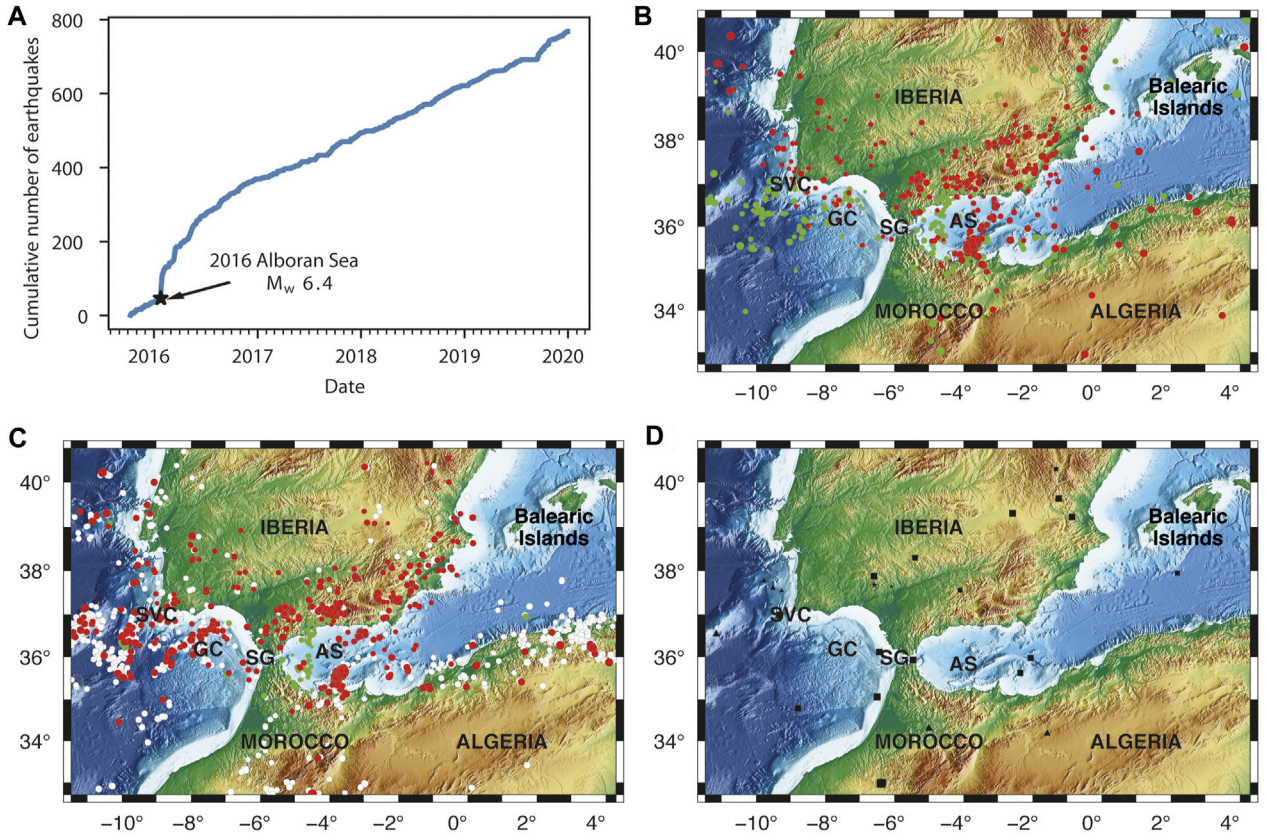

FIGURE 3 | (A) Cumulative number of earthquakes detected by PRESTo from October 2015 to December 2019. **(B)** Epicenters detected by PRESTO from 2016 to 2019. **(C)** Comparison between the epicenters detected by PRESTo and IGN (in red) and only by IGN (white). **(D)** PRESTo false detections (black squares), explosions in mines (stars), or lost earthquakes (triangles). Acronyms same as those in **Panel 1**.

$$M_w = \frac{\log P_d + 8.35 + 1.70\,log\,(R/10)}{1.02}. \quad (1)$$

Here, P_d (peak ground displacement) is in cm and R is the hypocentral distance in km. The parameters calculated by PRESTo are updated as more stations detect the earthquake, up to 40 s after the first assessment. An alert is given for magnitudes larger than 5, and then an email is sent to some selected users. We have fixed this M_w threshold because earthquakes with such a magnitude have produced economic losses and human victims (the 2011 Lorca M_w = 5.1 earthquake).

We have also studied the time needed to issue the first warning after the origin time. The alert time can be affected by delays in the data transmission between the seismic stations and the reception center. This time delay (Δt) is estimated as the difference between the theoretical fastest alert and the observed alert time. The theoretical fastest alert is obtained as the time at the fifth station detecting the earthquake plus a 3-s window for measuring P_d.

Data and Results

The PRESTo software installed at UCM began its operations on October 9, 2015, and 768 earthquakes were detected until December 31, 2019. In that study, we analyzed the results from January 1, 2016, to December 31, 2019. **Figure 3A** shows the cumulative number of events detected by the EEWS *versus* time. Nearly half were detected in 2016 due to an increase in the seismicity of the region caused by the Alboran Sea seismic sequence (main shock January 25, Mw = 6.4). Since 2017, the seismicity has decreased, and the number of detected events is similar to that before 2016.

For the period 2016–2019, PRESTo detected 728 events, of which 680 (93.4%) corresponded to earthquakes located inside the IMR (**Figure 3B** and 2.0 < M_w < 6.3). We carried out a comparison of our results with the hypocentral locations and magnitudes obtained by the IGN. Previously, we homogenized the magnitudes estimated by the IGN to M_w using different scales (Carranza et al., 2013; Cabañas et al., 2015).

In **Figure 3C**, the distribution of epicenters located by PRESTo is represented by red circles, while white circles are the epicenters located by the IGN and not detected by the EEWS. We observe that the most undetected earthquakes occurred in northern Algeria, where the EEWS is not configured due to the lack of seismic stations (**Figure 2**), northern Morocco, where only few stations are available, or in the SVC-GC region that is characterized by offshore

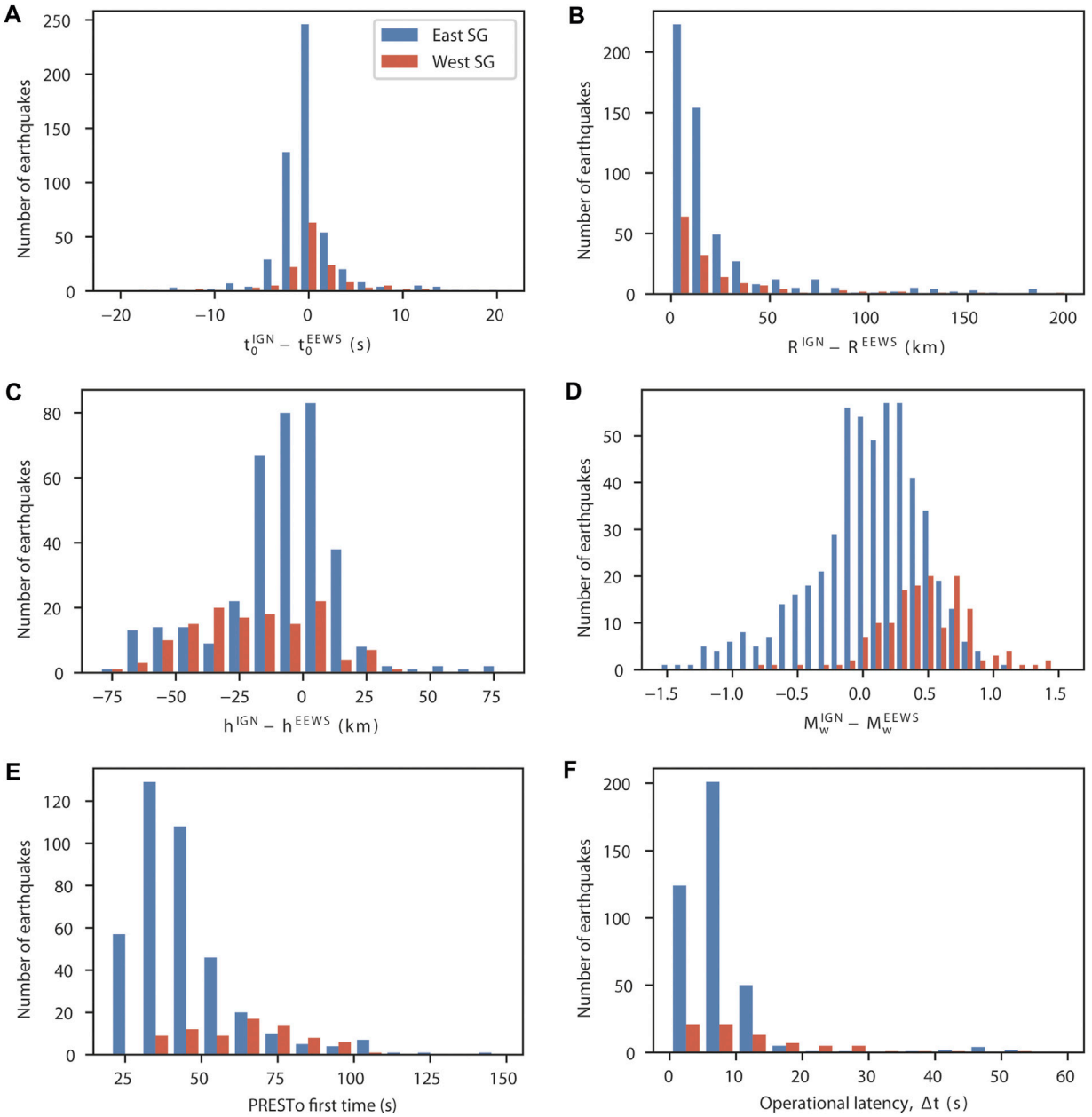

FIGURE 4 | Comparison between IGN and PRESTo final estimations: **(A)** difference on origin time, **(B)** epicenter, **(C)** on depth, **(D)** on M_w, **(E)** PRESTo first time estimation, and **(F)** the operational latency. Red bars correspond to earthquakes located in the western Strait of Gibraltar, and blue bars correspond to earthquakes located in the eastern Strait of Gibraltar (SG).

epicenters. For the detected earthquakes, the EEWS has obtained similar magnitudes and epicenters of the IGN (differences on a median are less than 0.3 and 12 km, respectively). When moving to the western side of the Gibraltar Strait, the number of earthquakes detected by the system is lower than the number of IGN locations, and in general, the PRESTo hypocenters are deeper. In northern Algeria, the number of earthquakes detected by EEWS is less (27%) than that of the IGN; however, we must remember that PRESTo has not been configured for Algeria.

The EEWS also detected seven events that correspond to mine explosions, and nineteen were false detections corresponding to teleseismic events with an M_w larger than 5.0. Six of these false detections are earthquakes that occurred outside the network and were located by PRESTo at the border region with an azimuth (that varies from 6° to 10°) roughly corresponding to the real azimuth. Seven false detections were large teleseismic earthquakes ($6.0 < M_w < 7.1$) that occurred at intermediate depths (50 km < h < 300 km) or very deep depths (h ≅ 500 km), such as those in Argentina or the Flores Sea. The percentage of false detections is

rather low, 2.6% (19 events over a total of 728), and the M_w estimated by PRESTo for the 19 false detections varies from 2.5 to 4.7, which is lower than the magnitude's threshold used to generate an alert (M = 5). Twenty-two earthquakes occurred in other zones of the Iberian Peninsula or in the Atlantic Ocean (**Figure 3D**). This means that 6.6% of the detected events correspond to false detections.

In **Figure 4**, we show the comparison of the PRESTo results and IGN locations plotting the difference between the IGN- and PRESTo-estimated parameters. We plotted the results for the region east of the Gibraltar Strait (EGS) earthquakes (536 events) in blue and those to the west of the Gibraltar Strait (WGE) earthquakes (144 events) in red.

The final PRESTo origin time estimation has a difference less than or equal to 2 s for 69% of the events, which increases up to 88% for differences lower than 5 s (**Figure 4A**). No significant difference was identified between the WGS and EGS earthquakes. For the WGS events, only one had a time difference larger than 20 s (33 s). For the EGS region, 17 earthquakes (less than 3%) had time differences larger than 20 s. Of them, 7 occurred in Algeria (3.8 < Mw < 4.6), 4 were part of a swarm that occurred in Jaen at the northern border of the EEWS region (M_w > 3.5), and PRESTo wrongly located earthquakes in the Balearic Islands. Finally, and six earthquakes occurred in Murcia or Alicante (eastern border of the EEWS region).

The difference in the modulus of the epicentral location (**Figure 4B**) is lower than 20 km for 70% of the EEWS-detected earthquakes, and there is no difference for WSG and ESG earthquakes. Five earthquakes have differences ranging from 600 to 880 km, which corresponds to earthquakes incorrectly located in the Balearic Islands and with time differences larger than 20 s. These differences in the location and, consequently, the magnitude may be due to the area coverage by the grid, which is relatively large.

The comparison of focal depth could only be carried out for 491 over a total of 680 earthquakes due to the lack of this parameter in the IGN estimations (**Figure 4C**). For some events with a focus offshore in the WGS region, the IGN either estimates the depth or it needs to use a fixed depth value. As a general tendency, PRESTo has obtained deeper foci than the IGN. While 75% of the EGS earthquakes have depth differences less than 20 km, this percentage suddenly decreases to 44% for the WGS events.

Differences in M_w estimated by PRESTo and IGN are shown in **Figure 4D**. There is a different behavior between WGS earthquakes, most of which have positive values and negative EGS values. For 55.0% of the EGS earthquakes, the M_w difference is less than or equal to 0.3, and the distribution has a larger dispersion moving toward negative values. For the WSG events, 70% have an M_w difference larger than 0.3, and the distribution is displaced to positive values and centered on 0.5 s. If we assume that the IGN magnitudes are correct (which is not necessarily true), then **Figure 4D** implies that PRESTo underestimates the magnitude of the WGS events.

The PRESTo first time (PET) and operational latency time are given in **Figures 4E,F**, respectively. Due to a problem with the system clock, only data from January 2016 to July 2018 are available. The PET for the EGS region varies from 20 to 50 s for most events, while for the WGS region, the PETs are somehow larger (from 30 to 100 s), with an average value of approximately 66 s. The operational latency is less than 10 s for most EGS events and slightly larger for the WGS region.

Performance of PRESTo for Period 2016–2019

From January 2016 to December 2019, PRESTo detected 680 earthquakes that occurred in the EEWS-defined region. The number of events with magnitudes $4 < M_w < 5$ detected by our EEWS is 59 *versus* the 95 shocks given by the IGN (https://www.ign.es/web/ign/portal/sis-catalogo-terremotos). The 36 earthquakes lost by PRESTo correspond to the 2016 Alboran aftershocks (8 events, Carranza et al., 2017), Algerian earthquakes (18 events), or Alboran intermediate depth events (3 shocks, h > 40 km), and 7 are earthquakes not detected by PRESTo. The 680 events detected by our EEWS have small differences with IGN determinations of the origin time, that is, less than 0.2 s for approximately 50% of earthquakes, and epicentral location, that is, less than 20 km for approximately 70% of events. The EEWS estimated the focal depth for the 680 earthquakes, while the IGN only estimated this parameter for 491 shocks, providing a clear indication of the good performance of PRESTo. Depth differences between the IGN and our EEWS are sometimes greater than 20 km. However, for offshore earthquakes, in particular, those for the Gulf of Cádiz and Saint Vincent Cape regions, depth is the worst estimated parameter by the IGN. For the 2007/02/12 SW Saint Vincent Cape earthquake (M_w = 5.9), the IGN estimated h = 65 km, while detailed studies for this earthquake estimated depths ranging from 30 to 40 km (Stich et al., 2007; Custodio et al., 2012; Pro et al., 2013). Additionally, for M_w = 5 (23–01–2016), PRESTo has estimated h = 76 km, and the IGN h = 55 ± 44 km (Carranza et al., 2017). Therefore, for EGS earthquakes, we can conclude that focal depth estimations are more accurate. For the Alboran 2016 (M_w = 6.4) earthquake, PRESTo estimated h = 18 *versus* 12 km from the IGN and 7 km from slip inversion (Buforn et al., 2017). A refined depth is important, for example, the Lorca earthquake produces a large damage because of its shallow depth (h = 7 km), but in southern Iberia (Durcal, southern of Granada city) deep earthquakes (h ≈ 650 km) also occur with moderate-to-large magnitude such as the 1954 (M_w = 7.8) and 2010 (M_w = 6.2) Granada earthquakes. The deep earthquakes do not produce damage, and consequently, the EEWS should not generate an alert for them.

The largest differences between PRESTo and IGN estimations are retained in the values of M_w, and this is the basic parameter needed to give an alert. First, we can consider that the final magnitude estimated by PRESTo is more reliable than the first estimation (using only five stations) because generally, it has been obtained using more stations. If we assume that the IGN magnitudes are correct, we conclude that for WGS events, PRESTo underestimates M_w (**Figure 4D**), which is the zone where the largest earthquakes have occurred (**Figure 1**).

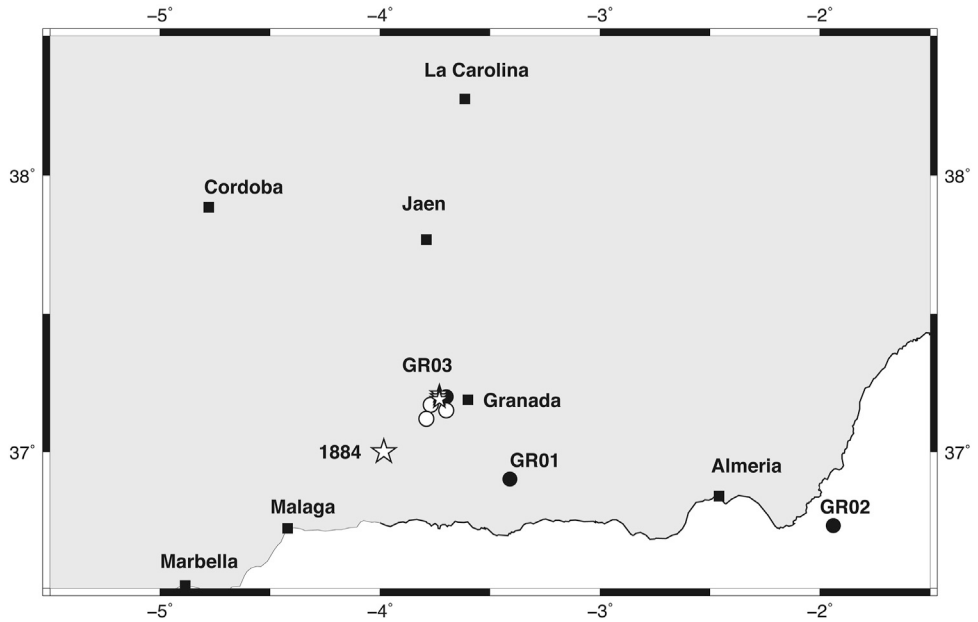

FIGURE 5 | The Granada 2020–21 swarm. Black circles show the first PRESTo estimation, white circles show the final estimation, and white stars represent the IGN-derived epicenters and the 1884 epicenter (I_{max} = IX-X).

TABLE 1 | Origin time, hypocentral location, and magnitude obtained by IGN and PRESTo (first alert and end time) for the Granada 2021 swarm.

Date	Parameters	IGN	PRESTo first alert	PRESTo end time
2021/01/26	t_0 (hh:mm:ss)	21:36:33	21:36:31	21:36:33
	Latitude (°)	37.21	36.90	37.15
	Longitude (°)	−3.73	−3.41	3.70
	Depth (km)	-–	49	14
	M_w	4.1	4.1	3.7
2021/01/26	t_0 (hh:mm:ss)	21:44:18	21:44:03	21:44:18
	Latitude (°)	37.20	36.73	37.17
	Longitude (°)	−3.73	−1.94	−3.77
	Depth (km)	–	4	1
	M_w	4.2	4.5	3.7
2021/01/26	t_0 (hh:mm:ss)	21:54:55	21:54:56	21:54:55
	Latitude (°)	37.19	37.20	37.12
	Longitude (°)	3.74	3.70	3.79
	Depth (km)	–	1	4
	M_w	4.4	4.4	4.2

IGN, Instituto Geográfico Nacional; PRESTo, PRobabilistic and Evolutionary early warning SysTem.

APPLICATION TO THE 2020–2021 GRANADA SEISMIC SWARM

In December of 2020, a seismic crisis began in Granada (**Figure 1**) as a swarm of earthquakes, which was still active as this paper was being written. It is worth noting that in this zone, on December 25th, 1884, the last great damaging earthquake occurred in Spain (I_{max} = IX–X, Udías and Muñoz, 1979, **Figure 5**). We present the performance of PRESTo for this swarm. The swarm began on December 1, 2020, and lasted until February 19, 2021, during which more than 1900 earthquakes occurred, five with $M_w > 4.0$ and two with I_{max} = V–VI (EMS–98). The earthquakes produced serious damage in the area located west of the city of Granada (https://www.ign.es/resources/sismologia/noticias/InformeIGN_SantaFe.pdf).

During the swarm, PRESTo detected 12 earthquakes, three of which corresponded to the largest shocks that occurred on January 26th at 21 h 36 m (GR01), 21 h 44 m (GR02), and 21 h 54 m (GR03). Two other large shocks (January 23rd and January 28th, both M_w = 4.4) occurred when the EEWS was not

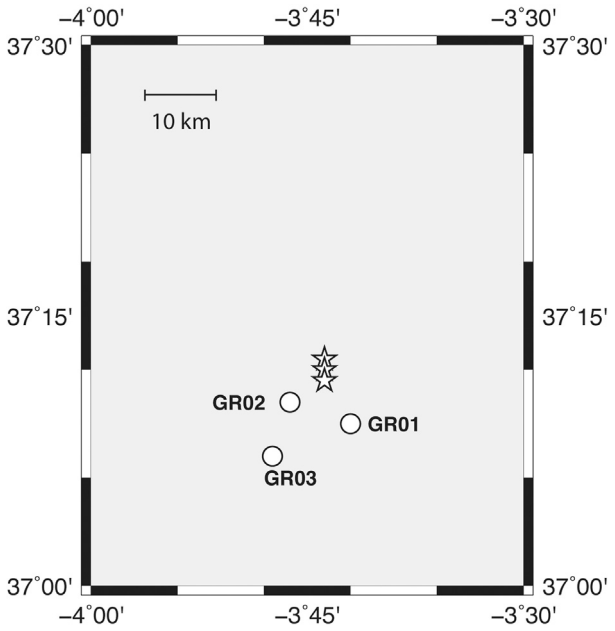

FIGURE 6 | PRESTo final epicenters (white circles) and IGN (white stars).

operating due to electric power supply problems. In **Table 1**, we present the origin time (t_0), hypocenter, and magnitude (Mw) estimated by PRESTo (first alert time and the end of the process, 40 s later) and the IGN estimations for GR01, GR02, and GR03 (**Figures 5**, **6**). The t_0 estimated at the PRESTo first detection is lower than that given by the IGN for GR01 and GR02 and equal for GR03. However, at the end of the process, the time origin is equal.

The minor difference on the epicentral location corresponds to the largest event GR03. One observes that the first epicentral location (black circle, **Figure 5**) is similar in latitude to that of the IGN, with the difference being approximately 1 km in latitude and 4 km in longitude. The final PRESTo epicentral location (white circle **Figures 5**, **6**) barely varies from the initial value (**Table 1**), with a difference in latitude with respect to the IGN location (white star **Figures 5**, **6**) increasing to 6 km and a similar enhancement along the longitudinal direction (5 km). For GR01, the first epicentral location of the epicenter is located SE of the IGN location, with a difference of 31 km in latitude that decreases to 4 km for the final PRESTo estimation and a difference in longitude of 32 km for the first estimation that is reduced to 3 km for the final PRESTo estimation.

The GR02 event has the worst results. The first PRESTo estimation locates the epicenter offshore at 200 km in the SSE direction to the IGN epicenter, with a 47-km difference in latitude and a 183-km difference in longitude (**Figure 6**). The final estimation reduces this difference to 1 km in latitude and 4 km in longitude (**Figure 6**). The low number of stations in the east direction (**Figure 2A**) may explain why a larger error is found in the longitude (Carranza et al., 2017).

Depth has been estimated by PRESTo (14 km for GR01 and 1 km for GR02 and Gr03 at the final estimation), while the IGN does not provide this parameter. PRESTo estimated Mw 4.1, 4.5, and 4.4 for GR01, GR02, and GR03, respectively, at the first alert and Mw 3.7, 3.7, and 4.2 at the end of the process (40 s later), implying an error of 0.3–0.4 with respect to the IGN M_w estimations. The first PRESTo estimation of 17, 25, and 41 s was given for GR01, GR02, and GR03, respectively, after the origin time and experienced a 3-s theoretical delay in the data transmission. This warning time could have been shorter if some new stations installed in the Granada region were included in the EEWS.

DISCUSSION

The comparison between the EEWS results and those of the IGN catalog shows that the major differences are on magnitude, with a different behavior for WGS and ESG earthquakes. An important

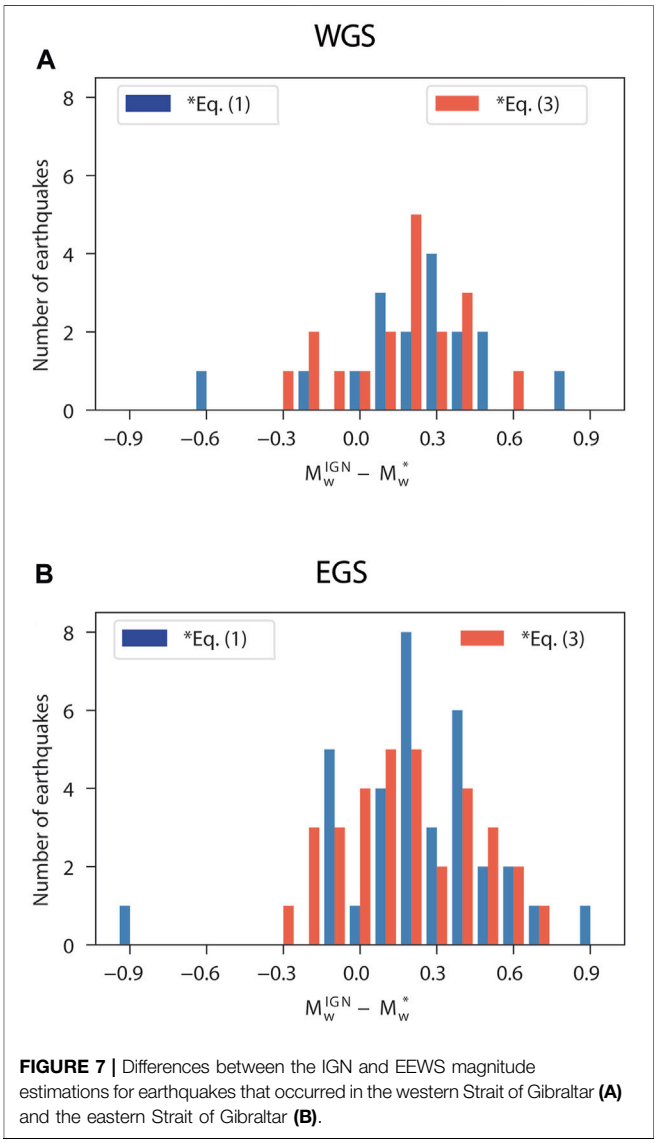

FIGURE 7 | Differences between the IGN and EEWS magnitude estimations for earthquakes that occurred in the western Strait of Gibraltar **(A)** and the eastern Strait of Gibraltar **(B)**.

point is that the IGN catalog uses three different magnitude scales. For earthquakes with offshore epicenter, such as the SVC-GC region (**Figure 1**), the scale is m_b, while for those that occurred in southern Spain or the Alboran Sea is m_{bLg} and for larger earthquakes is Mw (https://www.ign.es/web/resources/docs/IGNCnig/SIS-Tipo-Magnitud.pdf). Thus, we have homogenized the magnitudes estimated by the IGN to M_w by using the relationship proposed by Carranza et al. (2013) and Cabañas et al. (2015). The converted values are still found within an error of ±0.3 Mw, which is the median value for the difference between IGN and EEWS magnitudes (Carranza et al., 2017).

Carranza (2016) proposed two different relationships to estimate the M_w for WGS and EGS earthquakes in base of the observed differences (**Figure 4D**). Using these two equations in PRESTo instead of **Eq. (1)** for earthquakes in WGS and EGS during the period of 2016–2019, the results not only do improve but actually give higher differences. The same happens with another relationship for the whole IMR normalized to a reference distance of 200 km proposed by Carranza (2016), which does not give better results.

Finally, we consider the coefficient accuracy (Carranza et al., 2013), which is given as follows:

$$\log\left(P_d^{200}\right) = -8.3\,(\pm\,0.6) + 1.00\,(\pm\,0.13)M_w. \tag{2}$$

This correlation equation was computed with the mean value of the binned data ($\Delta M_w = 0.3$ bins) and weighted by the standard deviation of each mean value. From this expression, we observe that the independent term has the larger error (0.6), so we have checked different values for this term on **Eq. 1**. The best results have been obtained for the following relationship:

$$M_w = \frac{\log_{10}P_d + 8.30 + 1.70\log_{10}\left(\frac{R}{10}\right)}{1.02}. \tag{3}$$

In **Figures 7A,B**, we plotted the M_w difference between the IGN magnitudes and PRESTo magnitudes using **Eq. 1** (blue bars) or **Eq. 3** (red bars). For the WGS region, the M_w differences decrease from −0.3 to 0.6 vs. −0.6 to 0.8 and are more centered. For the EGS region, we observe a similar behavior; the difference decreases from −0.9 to 0.9 vs. −0.3 to 0.7. From **Figures 7A,B**, we observe that a simple static correction of 0.2 to the PRESTo-derived magnitude would provide an excellent fit of the IGN magnitude. Besides, the EEWS gives M_w estimations on a real time, while the IGN catalog is continuously revised. In fact, there are differences between the first IGN earthquake estimation and those of the catalog, where more stations were added with respect to the first estimation. For the largest and damaging earthquakes occurred in the period 2000–2020 [2004 Alhoceima, Morocco, M_w = 6.4; 2011 Lorca, Spain M_w = 5.1; 2016 Alboran Sea (M_w = 6.4) the EEWS results (simulation and real time) are very close to those from the IGN catalog (M_w = 6.6, 4.9 and 6.5, respectively) (Carranza et al., 2017)].

For the Granada 2020–2021 swarm, we observe a similar behavior for the EEWS estimated M_w values, with a difference of 0.3–0.4 with respect to those from the IGN.

A possible explanation for the differences in magnitude between the WGS and EGS regions is the low magnitude of the data (M_w < 5.0). In the studied period, only one earthquake (2016 Alboran shock M_w = 6.4) had a magnitude larger than 6.0, 11 had M_w > 5.0, but three of them occurred in Algeria, where the EEWS was not configured. Another issue is the poor azimuthal coverage of the stations used; most of them are located on the Iberian Peninsula (29 stations), with three on the Balearic Islands and only 7 in northern Africa (**Figure 2**), while many of the earthquakes have offshore focuses (**Figure 1**). This deficient azimuthal coverage may explain the large differences in the origin time, or epicenter, between the IGN and PRESTo estimations. This earthquake mislocation, in particular, due to an average 20–25 km depth differences (**Figure 4C**) can reasonably explain the magnitude discrepancy (ΔM) between PRESTo and IGN estimates. From **Eq. 3**

$$\Delta M = \left(\frac{1.7}{1.02}\right)log\frac{R}{R-25}. \tag{4}$$

Depending on R, (ΔM) can vary by 0.5 if R = 50 km to 0.2 if R = 100 km. For large earthquakes, several authors have shown that extended time windows are needed to obtain a proper M_w estimation (Colombelli, et al., 2014; Colombelli and Zollo, 2015; Carranza, 2016). We think that to extend the time window, we can improve the P_d estimation and M_w.

The three Granada largest swarm earthquakes were felt over a wide area, with maximum EMS-98 intensities of IV-V for GR01 and GR02 and V-VI for GR03. In **Table 2**, we list the lead times for the seven largest towns closest to the epicenter (11 < R < 127 km) for both the first detection and end times. Granada and Jaen (**Figure 6**) are located inside the blind zone for the first detection due to their proximity to the epicenter (11 and 63 km, respectively). However, for Malaga (87 km), there is a 2-s lead time, which increases to 11 s for La Carolina, Córdoba (119 km), and Almeria (121 km) or 13 s for Marbella. However, these seven towns are inside of the no-warning zone waiting until the end of the process.

The 2020–2021 Granada swarm shows that the EEWS has worked despite the low-moderate magnitude of the targeted earthquakes. Our EEWS is a regional system designed for large earthquakes and not probed for a situation similar to the Granada swarm. Nonetheless, we believe we can improve the efficiency of the Granada swarm.

TABLE 2 | Lead times at the seven cities closest to the epicenter for the largest Granada 2021 earthquakes.

City	Distance (km)	First alert lead time (s)	End-time lead time (s)
Granada	11	–13	–54
Jaen	63	–2	–51
Málaga	82	2	–47
La Carolina	119	11	–38
Córdoba	119	11	–38
Almería	121	11	–38
Marbella	127	13	–36

TABLE 3 | Radius of potential damage zone (PDZ) for different magnitudes (Carranza, 2016).

Magnitude M_w	R_{PDZ} (km) (Wald et al., 1999)	R_{PDZ} (km) (Faenza and Michelini, 2010)
8.0	79 ± 5	227 ± 8
7.0	21 ± 4	60 ± 5
6.0	6 ± 2	15 ± 3
5.0	2 ± 1	7 ± 2

For our regional EEWS, Carranza (2016) has estimated the potential damage zone (PDZ, alert zone), which is the area where the EEWS predicts a peak ground shaking level that could produce damage. In terms of intensity, this damage level corresponds to I=VII, strong perceiving shaking moderate damage that the USGS shake-maps associate with PGA = 21.5% g and PGV = 20 cm/s. Carranza (2016) has used two different relationships to estimate the PDZ for magnitudes 5 to 8 (**Table 3**): 1) the one of Wald et al. (1999) that was proposed for the United States and 2) the one of Faenza and Michelini (2010) introduced for Italy. For the 2011 Lorca earthquake (M_w = 5.1), the observed maximum intensity was VII (EMS-98) for a zone of 7 km around the epicenter, which is in agreement to the values shown in **Table 3**. For the 2016 Alboran earthquake (M_w = 6.4), with focus offshore, the observed maximum intensity was in Melilla (I=VI) located at 84 km from the epicenter. From **Table 3**, we conclude that for this M_w = 6.4, the radius of PDZ must be 12 km for the study by Wald et al. (1999) and 33 km for the study by Faenza and Michelini (2010). These values are in agreement to the observed intensity (VI) at 84 km. Unfortunately, we do not have other earthquakes with intensity equal to or larger than VII. However, we can safely conclude that in our regional EEWS, both the magnitude and the location of earthquakes used to map in real time the PDZ through an *a priori* GMPE are in agreement to the observed intensities.

The warning time is a critical value in an EEWS. The PRESTo end time of the detected earthquakes varies between 20 and 50 s for earthquakes in the EGS region and between 30 and 100 s in the WGS region. This difference is mainly due to the location of the epicenter with respect to the seismic network. To improve the EEWS results, we must increase the number of stations used. In the last years, the WM, IGN, and IPMA have installed new stations. We plan to add some of these stations to the EEWS, including, for instance, the TARIF station (WM) installed at the SG. Another solution is the use of a more detailed Earth model, including 3D models. The largest earthquakes in this region occur at SW of Saint Vincent Cape, such as the Lisbon 1755 (I_{max} = X) or the 1969 (Mw = 7.8) earthquakes (**Figure 1**), both with the marine focus and tsunami. It is a tectonically very complex region where the transition from oceanic to a continental crust starts. The use of 1D Earth models limits the accuracy on the hypocentral location and time origin. The present version of PRESTo estimates the hypocenter and the origin time by using a nonlinear algorithm (NonLinLoc software, Lomax 2009) and a 1D Earth model. However, the algorithm has already implemented the possibility to use a 3D Earth model. Recent studies for the hypocentral location in this region show that the use of 3D Earth models improves the estimation of focal parameters (Cabieces et al., 2020). It is understood that if we manage to improve the origin time and hypocenter, both the *R* parameter (**Eq. 3**) and the M_w will be also enhanced.

The use of an on-site method is another possible choice to improve the EEWS. A regional EEWS needs a minimum number of stations to declare an event (5 stations in our configuration), and the signal is transmitted from the stations to a "control" center where it is analyzed. As our network is sparse and disperse, and the largest and damaging earthquakes are located offshore (at 200 km from the coast), we expect that an on-site EEWS would reduce the time needed to issue a warning at a site as only one station is needed, and, furthermore, the latency time will decrease to 0.

Finally, the use of OBS telemetry would further help to reduce the lead time. This would be an optimal solution, but unfortunately not feasible at the moment due to the high cost of the equipment, maintenance, and data transmission.

CONCLUSION

The analysis of our EEWS performance between the periods of 2016 and 2019 shows that PRESTo detected 55 M_w > 4.0 earthquakes of 95 that occurred in southern Iberia, confirming the preliminary results shown by Carranza et al. (2017). The lost earthquakes are aftershocks of the Mw = 6.4 Alhoceima 2016, and earthquakes occurred in Algeria, where the EEWS is not configured or where the system was not operating. The origin time and the epicentral location are generally adequately determined, with low differences with respect to the IGN determinations (less than 0.2 s and 18 km, respectively, of the median values). The difference between the PRESTo estimated magnitudes and the IGN catalog lowers with the use of the modified relationship proposed in this study. Notably, we found a lower number of lost earthquakes or false detections.

One possible solution to the problems found could be deploying new stations in northern Africa. For the offshore foci west of Saint Vincent Cape, the use of a permanent real-time OBS would be an optimal solution.

The use of a more detailed 3D Earth model developed for the region could also improve the epicentral locations, depths, and origin times determined by the EEWS.

It is also necessary to improve the relationships for magnitude estimation. For this, we have modified and tested different relationships used on the EEWS, but more data and larger earthquakes are still needed to enhance the results.

The Granada 2020–21 swarm has demonstrated that an EEWS is useful and can provide alerts, even for moderate magnitude earthquakes. However, for this type of seismicity, it would be more efficient to use an on-site EEWS to reduce the number of lost aftershocks and the time needed to issue a warning. This could be achieved by using a shorter time window.

DATA AVAILABILITY STATEMENT

The raw data supporting the conclusions of this article will be made available by the authors, without undue reservation.

AUTHOR CONTRIBUTIONS

MC configured PRESTo, developed the relationships, and proposed its modifications. MM and EB have prepared the manuscript, tables, and part of figures. IT has prepared the data analysis and part of figures. All authors have contributed to the interpretation and discussion.

FUNDING

This work has been partially supported by the Spanish Ministerio de Economia, Industria y Competitividad, project CGL2017-86097-R, and the Comunidad de Madrid, project CT105/19/PEJD-2019-PRE/AMB-16483.

ACKNOWLEDGMENTS

The authors wish to thank the Real Insituto y Observatorio de la Armada (ROA), the Instituto Geográfico Nacional (IGN), and the IPMA for the real-time data reception. The authors thank the reviewer for their comments and suggestions.

REFERENCES

Ait Brahim, L., Nakhcha, C., Tadili, B., El Mabret, A., and Jabour, N. (2004). Structural Analysis and Interpretation of the Surface Deformations of the February 24th, 2004 Al Hoceima Earthquake. *CSEM-EMSC NewsLetter* 21, 10–12.

Buforn, E., Pazos, A., Roca, A., Carranza, M., Martín Dávila, J. M., Udías, A., et al. (2016). ALERTES: An Earthquake Early Warning System for the Ibero-Maghrebian Región. *Cahiers du Centre Européen de Géodynamique et de Séismologie* 31, 31–40.

Buforn, E., Pro, C., Sanz de Galdeano, C., Cantavella, J. V., Cesca, S., Caldeira, B., et al. (2017). The 2016 South Alboran Earthquake (Mw= 6.4): A Reactivation of the Ibero-Maghrebian Region? *Tectonophysics* 712-713, 704–715. doi:10.1016/j.tecto.2017.06.033

Buforn, E., Udías, A., and Pro, C. (2015). Large Earthquakes at the Ibero-Maghrebian Region: Basis for an EEWS. *Pure Appl. Geophys.* 172 (9), 2387–2396. doi:10.1007/s00024-014-0954-0

Cabañas, L., Rivas-Medina, A., Martínez-Solares, J. M., Gaspar-Escribano, J. M., Benito, B., Antón, R., et al. (2015). Relationships between M W and Other Earthquake Size Parameters in the Spanish IGN Seismic Catalog. *Pure Appl. Geophys.* 172 (9), 2397–2410. doi:10.1007/s00024-014-1025-2

Cabieces, R., Buforn, E., Buforn, E., Cesca, S., and Pazos, A. (2020). Focal Parameters of Earthquakes Offshore Cape St. Vincent Using an Amphibious Network. *Pure Appl. Geophys.* 177, 1761–1780. doi:10.1007/s00024-020-02475-3

Carranza, M., Buforn, E., Colombelli, S., and Zollo, A. (2013). Earthquake Early Warning for Southern Iberia: APwave Threshold-Based Approach. *Geophys. Res. Lett.* 40 (17), 4588–4593. doi:10.1002/grl.50903

Carranza, M., Buforn, E., and Zollo, A. (2017). Performance of a Network-Based Earthquake Early Warning System in the Ibero-Maghrebian Region. *Seismological Res. Lett.* 88 (6), 1499–1507. doi:10.1785/0220170081

Carranza, M. (2016). *Sistema de alerta sísmica temprana para el sur de la Península Ibérica: determinación de los parámetros de la alerta*. Ph. D. Thesis. Madrid: Universidad Complutense de Madrid.

Carreño, E., López, C., Bravo, B., Expósito, P., Gurria, E., and García, O. (2003). Sismicidad de la Península Ibérica en la época instrumental: 1985-2002. In *Física de la Tierra*. Madrid: Servicio de Publicaciones, Universidad Complutense, Vol. 15, 73–91. Available at: https://revistas.ucm.es/index.php/FITE/article/view/FITE0303110073A.

Colombelli, S., and Zollo, A. (2015). Fast Determination of Earthquake Magnitude and Fault Extent from Real-timeP-Wave Recordings. *Geophys. J. Int.* 202, 1158–1163. doi:10.1093/gji/ggv217

Colombelli, S., Zollo, A., Festa, G., and Picozzi, M. (2014). Evidence for a Difference in Rupture Initiation between Small and Large Earthquakes. *Nat. Commun.* 5, 3958. doi:10.1038/ncomms4958

Custodio, S., Cesca, S., and Heimann, S. (2012). Fast Kinematic Waveform Inversion and Robustness Analysis: Application to the 2007 Mw 5.9 Horseshoe Abyssal Plain Earthquake Offshore Southwest Iberia. *Bull. Seismological Soc. America* 102, 361–376. doi:10.1785/0120110125

Faenza, L., and Michelini, A. (2010). Regression Analysis of MCS Intensity and Ground Motion Parameters in Italy and its Application in ShakeMap. *Geophys. J. Int.* 180, 1138–1152. doi:10.1111/j.1365-246x.2009.04467.x

Lomax, A., Michelini, A., and Curtis, A. (2009). EarthquakeEarthquake LocationEarthquake Location , Direct, Global-SearchGlobal-Search Methods, in *Encyclopedia of Complexity and System Science*, 5, (Springer, New York), 2449–2473, doi:10.1007/978-0-387-30440-3_150

Morales, J., Cantavella, J. V., de Lis Mancilla, F., Lozano, L., Stich, D., Herraiz, E., et al. (2014). The 2011 Lorca Seismic Series: Temporal Evolution, Faulting Parameters and Hypocentral Relocation. *Bull. Earthquake Eng.* 12, 1871–1888. doi:10.1007/s10518-013-9476-x

Pazos, A., Romeu, N., Lozano, L., Colom, Y., López Mesa, M., Goula, X., et al. (2015). A Regional Approach for Earthquake Early Warning in South West Iberia: A Feasibility Study. *Bull. Seismological Soc. America* 105, 560–567. doi:10.1785/0120140101

Pro, C., Buforn, E., Bezzeghoud, M., and Udías, A. (2013). The Earthquakes of 29 July 2003, 12 February 2007, and 17 December 2009 in the Region of Cape Saint Vincent (SW Iberia) and Their Relation with the 1755 Lisbon Earthquake. *Tectonophysics* 583, 16–27. doi:10.1016/j.tecto.2012.10.010

Satriano, C., Elia, L., Martino, C., Lancieri, M., Zollo, A., and Iannaccone, G. (2011). PRESTo, the Earthquake Early Warning System for Southern Italy: Concepts, Capabilities and Future Perspectives. *Soil Dyn. Earthquake Eng.* 31 (2), 137–153. doi:10.1016/j.soildyn.2010.06.008

Stich, D., Mancilla, F., Pondrelli, S., and Morales, J. (2007). Source Analysis of the February 12th 2007, Mw 6.0 Horseshoe Earthquake: Implications for the 1755 Lisbon Earthquake. *Geophs. Res. Lett.* 34. doi:10.1029/2007GL0300127

Stich, D., Martín, R., Morales, J., López-Comino, J. A., and Mancilla, F. L. (2020). Slip Partitioning in the 2016 Alboran Sea Earthquake Sequence (Western Mediterranean). *Front. Earth. Sci.* 8, 587356. doi:10.3389/feart.20210.3389/feart.2020.587356

Udías, A., and Muñoz, D. (1979). The Andalusian Earthquake of 25 December 1884. *Tectonophysics* 53, 291–299. doi:10.1016/0040-1951(79)90074-x

Wald, D. J., Quitoriano, V., Heaton, T. H., and Kanamori, H. (1999). Relationships between Peak Ground Acceleration, Peak Ground Velocity, and Modified Mercalli Intensity in California. *Earthquake Spectra* 15, 557–564. doi:10.1193/1.1586058

Wu, Y.-M., and Kanamori, H. (2005). Rapid Assessment of Damage Potential of Earthquakes in Taiwan from the Beginning of P Waves. *Bull. Seismological Soc. America* 95, 1181–1185. doi:10.1785/0120040193

Zollo, A., Amoroso, O., Lancieri, M., Wu, Y.-M., and Kanamori, H. (2010). A Threshold-Based Earthquake Early Warning Using Dense Accelerometer Networks. *Geophys. J. Int.* 183, 963–974. doi:10.1111/j.1365-246x.2010.04765.x

Zollo, A., Emolo, A., Festa, G., Picozzi, M., Elia, L., Martino, C., et al. (2016). Concept, Implementation and Testing of PRESTo: Real-Time Experimentation in Southern Italy and Worldwide Applications," in *EGU General Assembly 2016*. (Vienna, Austria: Abstract) 17–22.

Zollo, A., Lancieri, M., and Nielsen, S. (2006). Earthquake Magnitude Estimation from Peak Amplitudes of Very Early Seismic Signals on strong Motion Records. *Geophys. Res. Lett.* 33 (23), 2–7. doi:10.1029/2006GL027795

Conflict of Interest: The authors declare that the research was conducted in the absence of any commercial or financial relationships that could be construed as a potential conflict of interest.

Publisher's Note: All claims expressed in this article are solely those of the authors and do not necessarily represent those of their affiliated organizations, or those of the publisher, the editors and the reviewers. Any product that may be evaluated in this article, or claim that may be made by its manufacturer, is not guaranteed or endorsed by the publisher.

frontiers in Earth Science

ORIGINAL RESEARCH
published: 09 September 2021
doi: 10.3389/feart.2021.707654

Status of Earthquake Early Warning in Switzerland

Frédérick Massin, John Clinton and Maren Böse*

Swiss Seismological Service, ETH Zürich, Zürich, Switzerland

The Swiss Seismological Service (SED) at ETH has been developing methods and open-source software for Earthquake Early Warning (EEW) for more than a decade and has been using SeisComP for earthquake monitoring since 2012. The SED has built a comprehensive set of SeisComP modules that can provide EEW solutions in a quick and transparent manner by any seismic service operating SeisComP. To date, implementations of the Virtual Seismologist (VS) and Finite-Fault Rupture Detector (FinDer) EEW algorithms are available. VS provides rapid EEW magnitudes building on existing SeisComP detection and location modules for point-source origins. FinDer matches growing patterns of observed high-frequency seismic acceleration amplitudes with modeled templates to identify rupture extent, and hence can infer on-going finite-fault rupture in real-time. Together these methods can provide EEW for all event dimensions from moderate to great, if a high quality, EEW-ready, seismic network is available. In this paper, we benchmark the performance of this SeisComP-based EEW system using recent seismicity in Switzerland. Both algorithms are observed to be similarly fast and can often produce first EEW alerts within 4–6 s of origin time. In real time performance, the median delay for the first VS alert is 8.7 s after origin time (56 earthquakes since 2014, from M2.7 to M4.6), and 7 s for FinDer (10 earthquakes since 2017, from M2.7 to M4.3). The median value for the travel time of the P waves from event origin to the fourth station accounts for 3.5 s of delay; with an additional 1.4 s for real-time data sample delays. We demonstrate that operating two independent algorithms provides redundancy and tolerance to failures of a single algorithm. This is documented with the case of a moderate M3.9 event that occured seconds after a quarry blast, where picks from both events produced a 4 s delay in the pick-based VS, while FinDer performed as expected. Operating on the Swiss Seismic Network, that is being continuously optimised for EEW, the SED-ETHZ SeisComP EEW system is achieving performance that is comparable to operational EEW systems around the world.

Keywords: Switzerland, Swiss Seismic Network, earthquake early warning, Virtual Seismologist, FinDer, finite-fault

OPEN ACCESS

Edited by:
Giovanni Martinelli,
National Institute of Geophysics and Volcanology, Italy

Reviewed by:
Ran Novitsky Nof,
Geological Survey of Israel, Israel
Ali Pinar,
Boğaziçi University, Turkey

****Correspondence:***
Frédérick Massin
fmassin@ethz.ch

Specialty section:
This article was submitted to Solid Earth Geophysics, a section of the journal Frontiers in Earth Science

Received: *10 May 2021*
Accepted: *16 August 2021*
Published: *09 September 2021*

Citation:
Massin F, Clinton J and Böse M (2021) Status of Earthquake Early Warning in Switzerland. Front. Earth Sci. 9:707654. doi: 10.3389/feart.2021.707654

INTRODUCTION

Earthquake Early Warning (EEW) aims to detect seismic events and quantify their impact as soon as possible after they occur, ideally allowing seconds of warning time in advance of the arrival of strong ground motion in affected areas. If appropriate protective actions are promptly taken, the impact of an earthquake can be reduced. EEW systems are used to deliver public warnings in Japan (Doi, 2011), Mexico (Cuéllar et al., 2014), South Korea (Sheen et al., 2017), Taiwan (Hsiao et al., 2009), and along

the west coast of the United States of America (Given et al., 2018). EEW systems and underlying algorithms are tested worldwide (e.g., Allen and Melgar, 2019), including Europe (Clinton et al., 2016) and Switzerland (Behr et al., 2015).

In Switzerland EEW has been in a demonstration phase for more than a decade. Over this period, the operational EEW algorithms have evolved, the background software has changed, and the network has been both densified and upgraded with a focus on low latency data flow. Together, these changes have significantly improved the existing EEW system in terms of speed and reliability. Speed has been chiefly addressed by network changes. Reliability has been improved by incorporating a second EEW algorithm that is independent of phase picking.

There are both scientific and technical challenges that need to be addressed when building an EEW system. Using the same single software framework that integrates EEW algorithms as well as other basic seismic monitoring services saves time and resources that would be required to develop and maintain independent systems, and improves the reliability of both EEW and standard network processes. In 2012, the Swiss Seismological Service (SED) at ETH Zurich migrated to the SeisComP framework (Hanka et al., 2010) for seismic data acquisition and management, and automatic and manual earthquake monitoring (Diehl et al., 2013). In the ensuing years, two complimentary EEW algorithms were added to SeisComP, first the Virtual Seismologist (VS, Cua, 2005; Cua and Heaton, 2007) was included in 2013 (Behr et al., 2016), followed by the Finite-Fault Rupture Detector (FinDer) algorithm (Böse et al., 2012; Böse et al., 2015; Böse et al., 2018a) in 2017. The development and testing of both algorithms, using datasets that include large events, are summarised in the Method section. Currently, these two algorithms are integrated in SeisComP via four modules developed by the SED and Gempa GmbH. We name our technical framework implemented in SeisComP the ETHZ-SED SeisComP EEW system (ESE). ESE is currently limited to the production of source parameters, and further work is required to translate these into alerting parameters.

In this paper, we summarise the EEW architecture in place in Switzerland and report on the performance of ESE during the 2020 earthquake sequence that included the M_{Lhc}4.3 Elm mainshock. We also review the real-time performance over the last decade, and demonstrate how the current ESE configuration would perform in real-time simulations (playbacks) of the major earthquakes recorded in Switzerland since 2009. Our study documents steadily decreasing EEW delays since 2009, with relatively small location and magnitude errors, as well as consistent performance during the vigorous Elm sequence. We show how an EEW system that includes multiple independent algorithms can perform in a robust manner, even during complicated seismicity patterns.

THE ETHZ-SED SEISCOMP EEW SYSTEM

ESE consists of two EEW algorithms embedded in SeisComP: 1) The Virtual Seismologist (VS) which provides fast network-based magnitude estimates for moderate-sized point-source earthquakes using conventional triggering and phases association techniques; and 2) the Finite-Fault Rupture Detector (FinDer), which matches the evolving patterns of high-frequency seismic ground motions to track ongoing rupture extent without requiring phase picks.

Virtual Seismologist

The Virtual Seismologist was developed as a Bayesian approach for estimating the earthquake magnitude, location, and peak ground motion distribution using P-wave arrival detection and ground motion amplitudes, predefined prior information (e.g., network topology, station health status, regional hazard maps, earthquake forecasts, Gutenberg-Richter magnitude-frequency relationship), and envelope attenuation relationships (Cua, 2005; Cua and Heaton, 2007; Cua et al., 2009). In operational systems, so far only the magnitude component has been used, with origins (nucleation time, hypocenter, and related quality metrics) derived from independent location algorithms. The first real-time VS prototype system was developed at SED-ETH Zurich in 2006–2012 using the location from Earthworm origins (Johnson et al., 1995) for input to the VS magnitude estimation. The current approach in SeisComP adopts this same strategy–a SeisComP VS magnitude module, *scvsmag*, provides rapid magnitude estimates based on independently determined rapid point-source pick-based origins, from SeisComP modules, such as *scautoloc* (Behr et al., 2015) or *scanloc* (Gempa GmbH, 2016; Grigoli et al., 2018). Hence, VS can be easily tested using existing SeisComP setups.

The Earthworm implementation of VS was one of the three EEW algorithms included in the original CISN ShakeAlert EEW system (Behr et al., 2015), and it was continuously real-time tested in California (from 2008 to 2016) and Switzerland (2010–2016). VS was integrated into SeisComP by SED-ETH Zurich and gempa GmbH in 2012–2013, with funding from the EU projects NERA (Network of European Research Infrastructures for Earthquake Risk Assessment and Mitigation) and REAKT (Strategies and Tools for Real-Time EArthquake RisK ReducTion). Both (Earthworm and SeisComP-based) VS implementations are based on a point-source hypothesis and focus on the processing of available pick and envelope data, without including prior information.

The VS magnitude estimation relationships consist of 1) a relationship between observed ground motion ratios (between vertical acceleration and vertical displacement) and magnitude, and 2) envelope attenuation relationships describing how various channels of envelope amplitudes vary as a function of magnitude and distance. These relationships were derived from a Southern California dataset with events in the 2.5 to 7.6 magnitude range and the Next Generation Attenuation (NGA) strong motion dataset (Cua, 2005). These relationships, as well as VS performance during large magnitude earthquakes, have been shown to work reasonably well in Northern California and Switzerland with a standard magnitude error of ±0.5 magnitude units (Behr et al., 2012; Behr et al., 2016). The VS magnitude evaluation procedure is used as defined in Cua (2005) and Cua and Heaton (2007), without taking into account

station-specific amplification corrections. The only change in the SeisComP implementation (since Behr et al., 2016) is the reduction in the length of the earliest ground motion envelope window from 3 to 1 s. Although SeisComP can produce origins for earthquakes at any depth, the VS magnitude estimation relationships are calibrated with earthquakes of an average depth of 3 km. For this reason, it is expected that VS magnitudes may systematically underestimate magnitudes for deep earthquakes.

Since EEW alerts from VS use traditional locators for early origins, all sensor types can be used in the location process–even from high gain broadband or short period sensors that subsequently clip. The VS magnitude module only uses on-scale data, and will use high-gain data as long as it does not saturate (saturation is identified as having been reached by a configurable ratio or 2^{23} counts, sufficient in Switzerland as all data is recorded from high dynamic range sensors on 24 bit digitisers).

Finite Fault Rupture Detector

While VS is a classical point-source algorithm, the second algorithm integrated into ESE, the Finite-Fault Rupture Detector (FinDer), determines line-source models, which are characterized by a length, strike and centroid position that describe the fault rupture (Böse et al., 2012; Böse et al., 2015; Böse et al., 2018a). These models can be determined for all earthquakes with M > 2.5, but they are most important in large events (M > 6) when the point-source approximation becomes invalid. This is because EEW usually predicts seismic ground-motions outside of the epicentral area and these motions are strongly controlled by the rupture-to-site distance rather than hypocentral distance that a point-source algorithm could provide.

In contrast to VS and many other point-source EEW algorithms, FinDer does not rely on phase picks, but interprets the spatially distributed peak ground motions. FinDer is a template matching approach which compares temporally and spatially evolving high-frequency seismic ground-motions to theoretical template maps. These templates are pre-calculated for different magnitudes and line-source models from empirical ground-motion models using a grid of 5 km × 5 km resolution. This means that all FinDer determined source locations (which are centroids rather than hypocenters) basically have an uncertainty of 2.5 km. The FinDer magnitude, M_{fd}, is estimated empirically from the length of the FinDer line-source.

FinDer has undergone extensive real-time and offline tests in California (Böse et al., 2018a), Central America (Porras et al., 2021, subm.), Chile (Carrasco and Böse, 2017), Italy (Böse et al., 2018b), Japan (Meier et al., 2020), and China (Li et al., 2020; Li et al., 2021 subm.) for small to large earthquakes using seismic data, and for large global earthquakes using felt-reports (Böse et al., 2021b). FinDer is one of two seismic algorithms adopted by the US West Coast ShakeAlert warning system (Given et al., 2018). The FinDer core code has been jointly developed by Caltech, USGS and SED-ETHZ.

For the Swiss installation, we use two FinDer template sets that account for different attenuation characteristics of PGA amplitudes in the Swiss foreland and alpine regions (Cauzzi et al., 2014). To trigger, FinDer requires PGA >2.0 cm/s/s at three neighboring stations. FinDer uses a cascade of increasing PGA thresholds in its binary template matching (2.0/4.6/10.5/23.2/48.6/90.7/148.8 cm/s^2). See Böse et al. (2018a) for details. The goal of this setting is to detect earthquakes with magnitude over 3.5, but as demonstrated in this manuscript, FinDer may detect events as small as M2.7, if they show abnormally strong high-frequency radiation and station geometry is favourable. The FinDer template sets and thresholds are the only configuration adjustments for operating FinDer in Switzerland. FinDer uses data from both strong motion and high gain broadband sensors (but, unlike VS, not from short period sensors), with high gain sensors initially preferred when sensors are co-located. Once the ground motion is observed to exceed the dynamic range of a high gain sensor, if there is no co-located strong motion sensor, the corresponding station is removed from processing.

Integration in SeisComP3

The SeisComP software (Hanka et al., 2010) is an open-source real-time platform for seismic monitoring widely adopted by the seismological community. It was originally developed for tsunami early warning. All of its components (acquisition and processing) are implemented in a real-time manner, involving delays only where methodologically required (e.g., STA/LTA is delayed by the duration of STA; Allen, 1982; or VS station magnitudes require 1s duration post-pick; Behr et al., 2015). The same software can be used for acquisition, data management, automatic and manual processing, from separate clients, while connected and informed from a central network management instance, thus allowing minimal maintenance. SeisComP includes all the components required for the implementation of new approaches: an extensive data model, an efficient messaging system, multiple input and output interfaces, an API for C++ and python.

Figure 1 summarises the overall architecture of how EEW, and in particular the VS and FinDer algorithms, are embedded with SeisComP. A generic pre-processing module, *sceewenv*, (that can alternatively be used directly as a library within the individual EEW modules) listens to incoming seismic data and provides real-time EEW parameters to the client EEW algorithms. For the VS module, *scvsmag*, these are 1 s ground motion displacement and acceleration envelopes. For the FinDer module, *scfinder*, these are 1 s ground motion acceleration envelopes. This module can also produce other EEW parameters that could be used in different EEW algorithms that may be added to SeisComP in future, such as ground motion displacement from high rate GNSS displacement time series for use in EEW methods based on real-time GNSS data, such as FinDerS or FinDerS+ (Böse et al., 2021a). The EEW modules provide locations and magnitudes, with uncertainties and other algorithm-specific output, to *sceewlog*, which collates solutions from the different algorithms, and disseminates low-latency messages to be used by end-user client applications, such as the open source client software EEW Display (Cauzzi et al., 2016) as well as providing summary reports to EEW operators e.g., *via* email. The method-agnostic processing and logging modules *sceewenv* and *sceewlog* have been released in 2021, replacing the original VS-specific

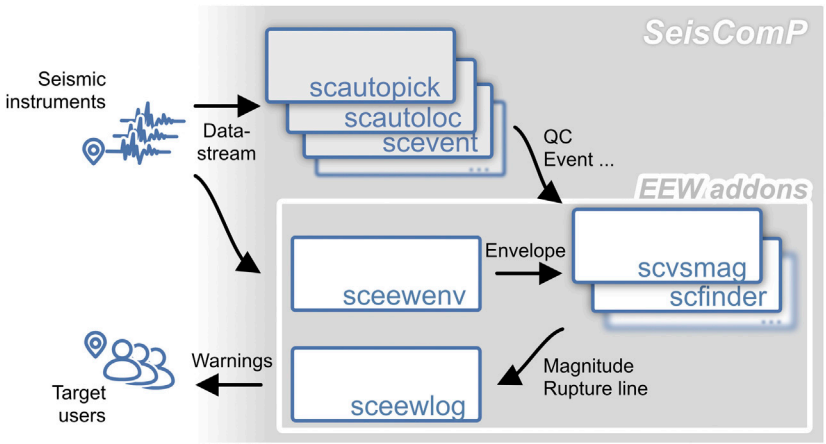

FIGURE 1 | Schematic workflow of the SED-ETHZ SeisComP EEW system (ESE). The main SeisComP framework includes automatic picking and location modules (*scautopick* and *scautoloc*) which can be tuned for event detection with P-wave arrival detection at four stations. The VS algorithm is implemented in the *scvsmag* module. FinDer is a stand-alone library that is integrated in the *scfinder* wrapper module. SeisComP event detections are fed into VS together with acceleration and displacement envelope amplitudes (provided by the *sceewenv* module), while FinDer only relies on envelopes for detecting intermediate events with co-seismic ground motion detection at three stations. Both can provide EEW to target users via the *sceewlog* module using multiple real-time dissemination interfaces. It allows the EEWD open-source client software to display end-user EEW information (Cauzzi et al., 2016).

scenvelope and *scvsmaglog* modules, as described in Behr et al. (2016), in order to support the integration of FinDer.

VS relies on the SeisComP picking and location modules. SeisComP can be tuned in order to allow event detection with four stations only. This can be done via the primary SeisComP location module (*scautoloc*) with conservative adjustments preventing origins to be located in regions without picks at closest stations, or using the *scanloc* location module (Grigoli et al., 2018; Scanloc Documentation, 2021). The VS module listens for these origins and creates fast magnitudes using the acceleration and displacement envelope amplitudes continuously made available by the *sceewenv* module. A first magnitude is available once 1 s of envelope data at a single station becomes available. VS magnitudes are updated every second for up to a maximum of 30 s. The original VS station magnitude relationships are generated using the entire waveforms of the training dataset, including surface waves. New stations that are included from picked stations when updated origins become preferred (new origins become available at least every 10 s, as long as new picks continue to be associated). Since mid-2017 in the online (real-time) system, *scautoloc* has been configured to provide first origins using four instead of six stations; since late 2018 a second location algorithm, *scanloc*, was added that is also capable of providing first origins from four station picks. We also use an automatic secondary picking that is triggered by the initial STA/LTA picks, using the method of Baer and Kradolfer (1987) that provides more precise picks, although with added latency.

FinDer has been implemented as a library (since FinDer version 2; Böse et al., 2018a) which is integrated within a SeisComP wrapper module (*scfinder*). This module also integrates the same envelope library as used in *sceewenv*. FinDer only uses envelopes from broadband high-gain seismographs and accelerographs, using the same logic as VS in case of velocimeter clipping. The *scfinder* module provides an amplitude-based, independent evaluation of the centroid location, length, azimuth, and magnitude of a finite-fault rupture assuming a line-source. We have started using FinDer in for online (real-time) testing in Switzerland in mid-2017.

In addition to being operated in real-time online, the ESE system can be operated in playback mode, replaying events as though they were occurring "in real-time." The playback ESE system presented in this paper has the same configuration as the current real-time system. This allows us to demonstrate the capabilities of the current ESE configuration for past earthquakes. In this paper, we use the playback system with the 100 largest earthquakes with magnitudes over 2.7 within Switzerland since 2009. We describe the outcome for the eight largest earthquakes with magnitudes from 3.9 to 4.6 in the result section, and present complete results for all 100 events in the **Supplementary Material**.

SEISMIC MONITORING AND SEISMICITY IN SWITZERLAND

Swiss Seismic Network

The current Swiss Seismic Network consists of over 200 permanent stations (CH network code; Swiss Seismological Service (SED) at ETH Zurich, 1983). The goal of this network is to monitor seismicity of the territory, support science and assess the seismic risk. In recent years, efforts have been made towards making this network ready for EEW. The majority of the stations (currently 171) include modern broadband EpiSensor strong motion accelerometers. All stations operate modern ultra-low latency digitisers–mainly Nanometrics Centaur, though there are significant numbers of Nanometrics Taurus and Kinemetrics Q330. A major densification of the strong motion network has

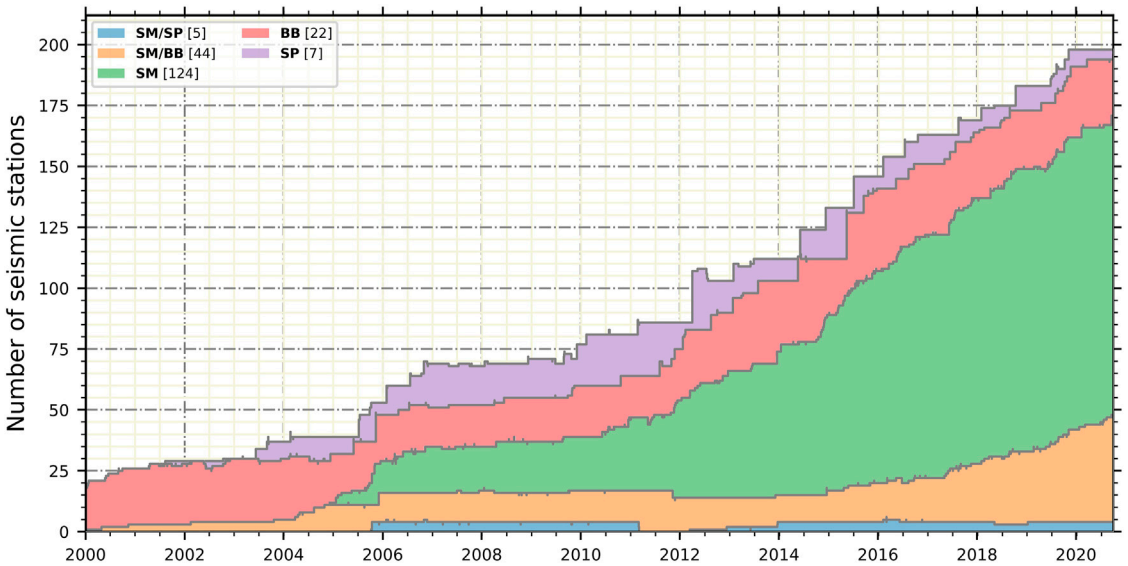

FIGURE 2 | Evolution of seismic instrumentation in the Swiss National Network (network code CH) since 2000. Only modern high quality, real-time instruments are shown (neglecting analog low gain short period and strong motion instruments). SM: strong motion accelerograph. BB: broadband seismograph. SP: short period seismograph. The numbers of stations deployed today in each category are indicated in the legend.

occurred in the framework of the SSMNet renewal project that started in 2009, and is nearing completion, with the addition of 100 new strong motion stations. In the last 7 years, the first generation broadband seismic network and many legacy short period stations, installed around the turn of the century, have been upgraded, with all existing sites being refurbished with replacement of digitisers and addition of strong motion sensors. Additionally, about 10 new stations with both broadband and strong motion sensors have been installed. The growth in stations and sensor types in the CH network, since 2000, is shown in **Figure 2**.

This modern network is augmented by a 1) varying number of temporary stations targeting scientific and engineering risk studies, monitoring aftershock sequences, and industrial activity, in particular geothermal projects–the majority of these also stream in real time with low latency similar to the national network, currently this numbers ~70 stations; as well as 2) about 50 stations from neighbouring agencies that are important to ensure high quality earthquake analysis–these stations have varying latency.

The Swiss Seismic Network uses the Seedlink protocol for all real time communications. Although this is not optimum for EEW since it has a fixed 512-byte packet size, the high sampling rates adopted at all Swiss stations (200 sps for stations that include high gain sensors; 250 sps for strong motion only stations) means the packet reception interval ranges between 1 and 2 s (**Supplementary Figure SA1a**). The data packet reception delay is under 0.5 s on average (**Supplementary Figure SA1a**). Together, this means the data sample delay–estimated as (transmission delay added to half of the packet reception interval) averages at 1.46 s with a standard deviation of +1.17 s/−0.30 s. **Figure 3A** presents the data sample delays for each of the 272 low-latency stations operated by the SED in April 2020.

Figures 3B,C present a map of the current network, showing the real-time stations monitored and operated by the SED, omitting stations operated by foreign agencies. All stations indicated in green include a strong motion sensor–either stand-alone or together with another high gain sensor. If there is no strong motion sensor, the colour indicates whether the available sensor is broadband or short period. In **Figure 3B**, the background colour indicates the distance to the fourth closest seismic station at any given point–this shows the network density, tailored for the VS algorithm, which requires four station picks to trigger a first location. The majority of the country lies within 20 km of the fourth station, and in many places where seismicity is high, as seen in **Figure 4**, for example in the Basel region or in the Canton of Valais in the SW, this distance is reduced to under 10 km. In **Figures 3A,C** map of theoretical EEW delay is shown, assuming shallow 5 km earthquake sources. For this figure, the travel times computed with the iasp91 velocity model from all sources to each station are combined with the observed latencies for the individual station (**Figure 3A**). Event processing and magnitude determination add very small additional delays (Behr et al., 2015), though any additional latency arising from sending alerts to the public is not included. A significant part of the country is expected to provide the first alert within 5 s of origin time, and the entire country lies within 10 s.

Seismic Activity in Switzerland

Switzerland is a country with moderate seismic hazard. On average, between 1,000 and 1,400 earthquakes are identified every year, of which 24 are equal to or above M2.5 (Diehl

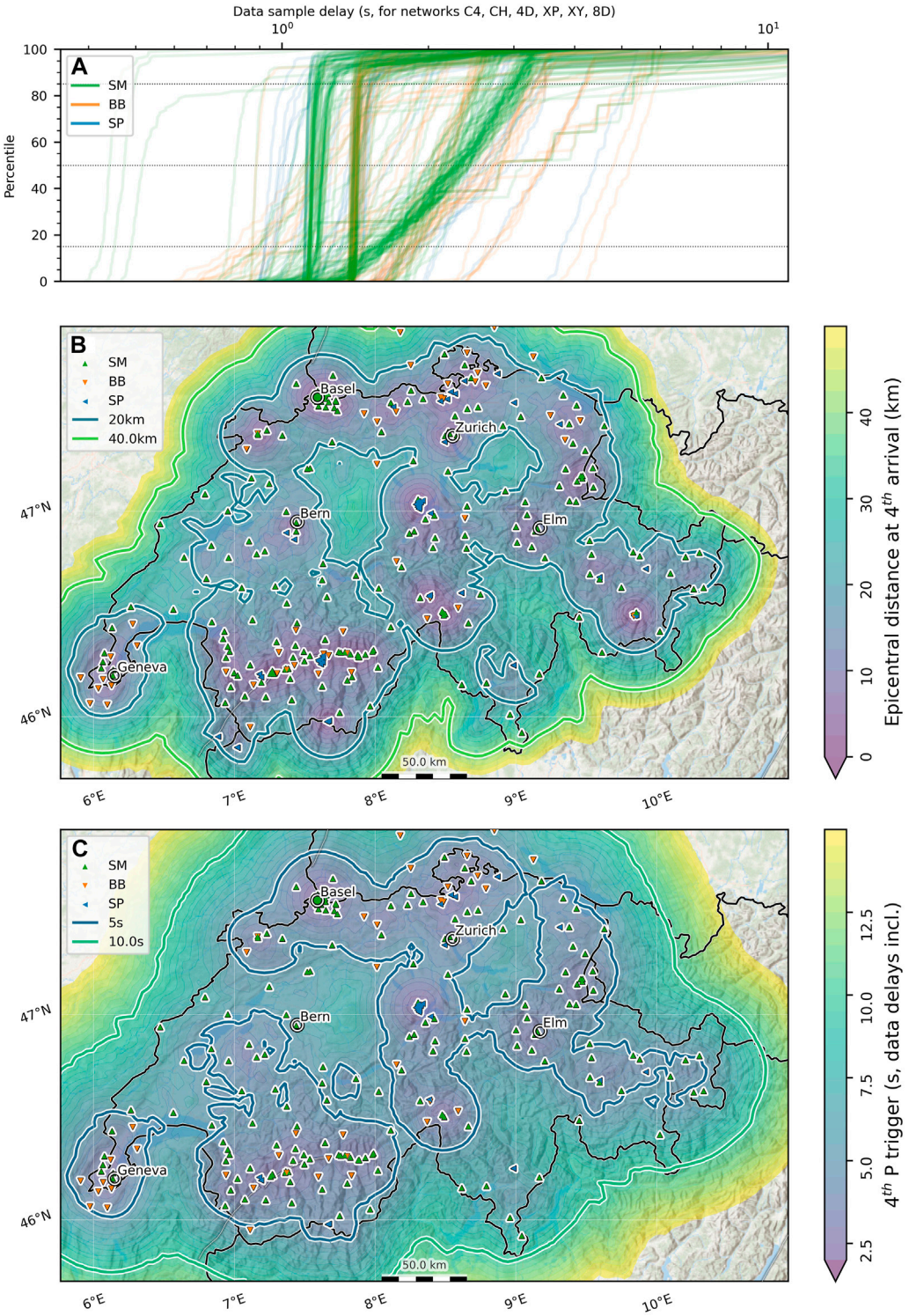

FIGURE 3 | Summary of Swiss seismic network performance for EEW. **(A)** shows data sample delay percentiles for each seismic sensor operated by SED. The majority of stations have very fast, reliable delays of either 1.1 or 1.3 s, depending on sampling rate. Stations operating older dataloggers exhibit larger delays with higher range. Data sample delays are defined as the sum of the packet reception delay from end-time to reception, and half of the inter-packet reception interval. **(B)** Station map with channel type distribution and map of the distance to the fourth closest station. **(C)** Station map with channel type distribution and P-wave delays for triggering four stations (for iasp91 velocity model, hypocenters at 5 km depth, and seismic data sample delays in **(A)**. The corresponding image considering only the closest station is provided in the **Supplementary Figure SA2**. The map shows all permanent and temporary stations operated by the SED across the Switzerland region in April 2021. Stations operated by foreign networks are not included. SM: strong motion accelerograph. BB: broadband seismograph. SP: short period seismograph. Indicated are the major cities, as well as the village of Elm close to the sequence discussed in this paper.

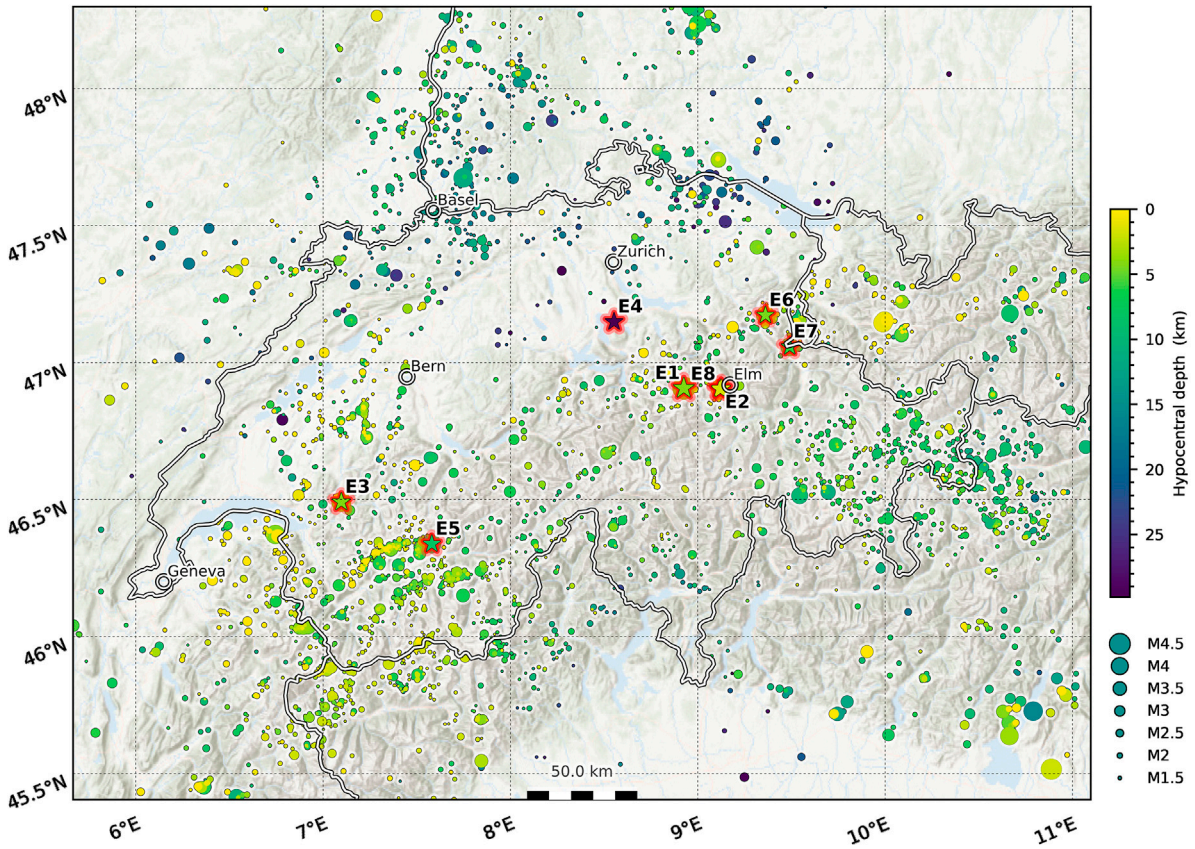

FIGURE 4 | Seismicity from the SED-ETHZ earthquake catalogue within and around Switzerland between January 2009 to April 2021. Circles: all earthquakes with magnitude over 1. The significant events listed in **Table 1** are indicated with stars: E1: M_{Lh}4.6 Linthal 2017; E2: M_{Lh}4.3 Elm 2020; E3: M_{Lh}4.3 Chateau-d'Oex 2017; E4: M_L4.2 Zug 2012; E5: M_{Lh}4.1 Leukerbad 2016; E6: M_L4.1 Buchs 2009; E7: M_{Lh}4.1 Sargans 2013; E8: M_{Lhc}3.9 Elm 2020.

TABLE 1 | Source parameters of the eight earthquakes to occur within Switzerland with magnitude 3.9 ≤ M_L ≤ 4.6 since 2009.

	Magnitude	Place name	Origin time	Origin location	Depth
E1	M_{Lh} 4.6	Urnerboden	2017-03-06T20:12:07.40	46.907°N, 8.925°E	4.2
E2	M_{Lh} 4.3	Elm	2020-10-25T19:35:43.38	46.905°N, 9.125°E	1.4
E3	M_{Lh} 4.3	Château-d'Oex	2017-07-01T08:10:34.07	46.491°N, 7.097°E	4.3
E4	M_L 4.2	Zug	2012-02-11T22:45:26.80	47.149°N, 8.553°E	32.4
E5	M_{Lh} 4.1	Leukerbad	2016-10-24T14:44:11.58	46.338°N, 7.580°E	8.2
E6	M_L 4.1	Buchs	2009-01-04T15:30:30.10	47.173°N, 9.361°E	4.5
E7	M_{Lh} 4.1	Sargans	2013-12-12T00:59:18.86	47.058°N, 9.491°E	5.9
E8*	M_{Lhc} 3.9	Elm	2020-11-10T12:53:23.11	46.903°N, 9.115°E	1.7

** The M_{Lhc}3.9 Elm 2020 earthquake is an aftershock. All times are in UTC. Depths are in km below sea level. Coordinates are given in WGS84.*

et al., 2021) and about 25 are felt by the population. There is a roughly 1% probability for a damaging earthquake with magnitude M6+ to occur in or near Switzerland each year (Wiemer et al., 2016).

The seismicity between 2009 to today (which covers the testing period of EEW in Switzerland) is presented in **Figure 4**. Highlighted in this map are all earthquakes with a local magnitude over 3.9 in Switzerland within the time window, that are also listed in **Table 1**. The largest earthquake occurred in 2017 in Central Switzerland, near the village of Urnerboden, with M_{Lh}4.6. A particular focus of this paper relates to events associated with the joint second largest earthquake to occur in the time window, the M_{Lh}4.3 earthquake near Elm that occurred in 2020.

All catalogue events described in this paper are provided with their local magnitude. The local magnitude scale has evolved over time at the SED in an effort to use all available data from the also evolving seismic network, although efforts have been made to remain calibrated to the original implementation of Kradolfer and Mayer-Rosa (1988), which

was based on a very limited amount of observations from a sparse network, with few near-field records and all stations located on hard rock sites. All local magnitudes prior to October 2012 are labelled M_L, even though the original implementation was modified in 2000 to be computed using horizontal components, now possible due to the newly installed three component seismometers. In 2012, as part of a migration to SeisComP, all local magnitudes were labelled as M_{Lh}, although the attenuation relation was not changed. In November 2020, the SED migrated to M_{Lhc} as the preferred magnitude scale. This scale is extended to take into account site amplification factors (allowing usage of the increasing number of stations deployed in soft sediments, in particular the new strong motion sites located in urban areas) as well as a new calibration for stations at close epicentral distances (Racine et al., 2020). For EEW magnitudes, we adopt the convention M_{VS} (VS) and M_{fd} (FinDer). The FinDer magnitude is sensitive to high-frequency motions and thus related to the energy magnitude (Böse et al., 2018a; Li et al., 2020).

REAL-TIME EEW PERFORMANCE DURING THE 2020 ELM SEQUENCE

The M_{Lh} 4.3 Elm earthquake on October 25, 2020 and its aftershock sequence occurred in the upper Sernftal in the Glarus Alps, a region with a moderate station density. Fortunately the network in this region had very recently been densified–a few months earlier, a foreshock on 26 May M_{Lh} 3.1, triggered the exercise of the ETHZ-SED aftershock pool, presently consisting of six streaming, autonomous stations with short period and strong motion sensors. Two stations (8D.ELM0 and 8D.ELM1) were installed within a few kilometers of the sequence. Hence, by the time of the mainshock, the region was well monitored with low latency strong motion instruments, with four stations within 10 km (**Figure 3**). Winter was drawing in, and the aftershock stations in the Sernftal, a deep alpine valley that receives little sunlight and can expect heavy snowfall, were at risk of losing power. Hence, a third aftershock station (8D.ELM3), on mains power, was immediately deployed even closer to the on-going cluster. The sequence was vigorous, with on the order of 300 events detected in the 2 months following the mainshock, extending over a roughly EW trend, with events being particularly shallow between 0 and 3 km. On November 10, 2020, the largest aftershock (M_{Lhc} 3.9) of the series so far occured.

Both the mainshock and the largest aftershock triggered both EEW algorithms. Strong motions observed by the aftershock stations for both events are remarkable. Despite the moderate event size, a peak ground acceleration (PGA) of 405 cm/s^2 and peak ground velocity (PGV) of 6.1 cm/s was observed at 8D.ELM0 (at 2.4 km epicentral distance) during the mainshock–this is the strongest ground motion in terms of both PGA and PGV ever recorded at a free-field station in Switzerland. In the aftershock, extreme motions were also observed at the closest station (PGA 103 cm/s^2 and PGV 1.3 cm/s at 8D.ELM3 at 1.6 km epicentral distance). The main M_{Lhc}3.9 aftershock was preceded by a small M_{Lhc} 1.0 quarry blast that occurred near Brugg, Canton Valais (**Figure 5**), 21 s before and at a distance 130 km, that had important effects on the ESE system.

Figure 6 summarises the network density, out to 35 km, and observed ground motions for the mainshock (top) and the aftershock (bottom). For each station, the temporal evolution of PGA is shown until the time when final PGA is reached. Expected P- and S-wave arrival times are also indicated. For the mainshock, there are four stations within 10 km, and the sixth closest station is at 16 km distance. The P-wave arrived at the fourth and sixth station after 2.5 and 3.5 s, respectively. For the aftershock, now also recorded at 8D.ELM0, the time to the fourth station is only marginally reduced, while the time to the sixth station is reduced by 1.5 s. As expected, in both events, the PGA at all stations is reached during, or shortly after, the S-wave arrival.

During the mainshock, at the closest station 8D.ELM0, the PGA of 405 cm/s^2 (equivalent to intensity VI, Faenza and Michelini, 2010), is reached shortly after the S-wave arrival, only 1.5 s after origin time and before the P-wave arrives at the fourth station. The first EEW alert from VS was produced 4.1 s after the origin time, roughly at the same time when the PGA (46 cm/s^2, intensity IV) was reached at the fourth station. The first FinDer solution was available 0.8 s later.

The M_{Lhc}3.9 aftershock was detected by FinDer with a similar delay as the mainshock (4.7 s after origin time), while the first VS alert was issued 8 s after origin time, almost 4 s later than observed in the mainshock. This delay was produced by erroneous mixing of picks from the closest stations to this event and those from the small quarry blast. As shown in **Figure 5**, the theoretical P-wave arrivals from this event almost coincide with the nucleation time at Elm, thus triggering association of the arrival times at stations close-by Elm to an incorrect origin location for the blast. In the next section we describe how we resolved this issue afterwards.

In order to model ground motions, the Swiss Seismic Network adopts Swiss-specific GMPE based on stochastic simulations (Cauzzi et al., 2015) and GMICE (Faenza and Michelini, 2010) that provide earthquake intensity in the EMS-98 scale, as adopted in SED shakemaps (Cauzzi et al., 2015) that are available for each event on the SED website (http://seismo.ethz.ch, last accessed August 2021). In this study the accurate prediction of ground motion is not a primary goal, rather we wish to compare the predicted peak motions and corresponding felt intensities for the evolving EEW solutions alongside the final catalogue parameters. Hence, for simplicity, we use the empirical intensity prediction equation from Allen et al. (2012) that provides intensity in Modified Mercalli Intensity, and use a simple iasp91 velocity model to estimate the distance of S-wave fronts at a given time. The maps in **Figure 7** show the estimated earthquake locations, predicted MMI intensity and available warning (or lead) times between the first alert (assuming alerts are available as soon as the first EEW solution is available, and there is no delay due to downstream alert dissemination to users) and the arrival of the peak ground motion (assumed to coincide with the S-wave arrival) for the two events. The 5 km resolution adopted by

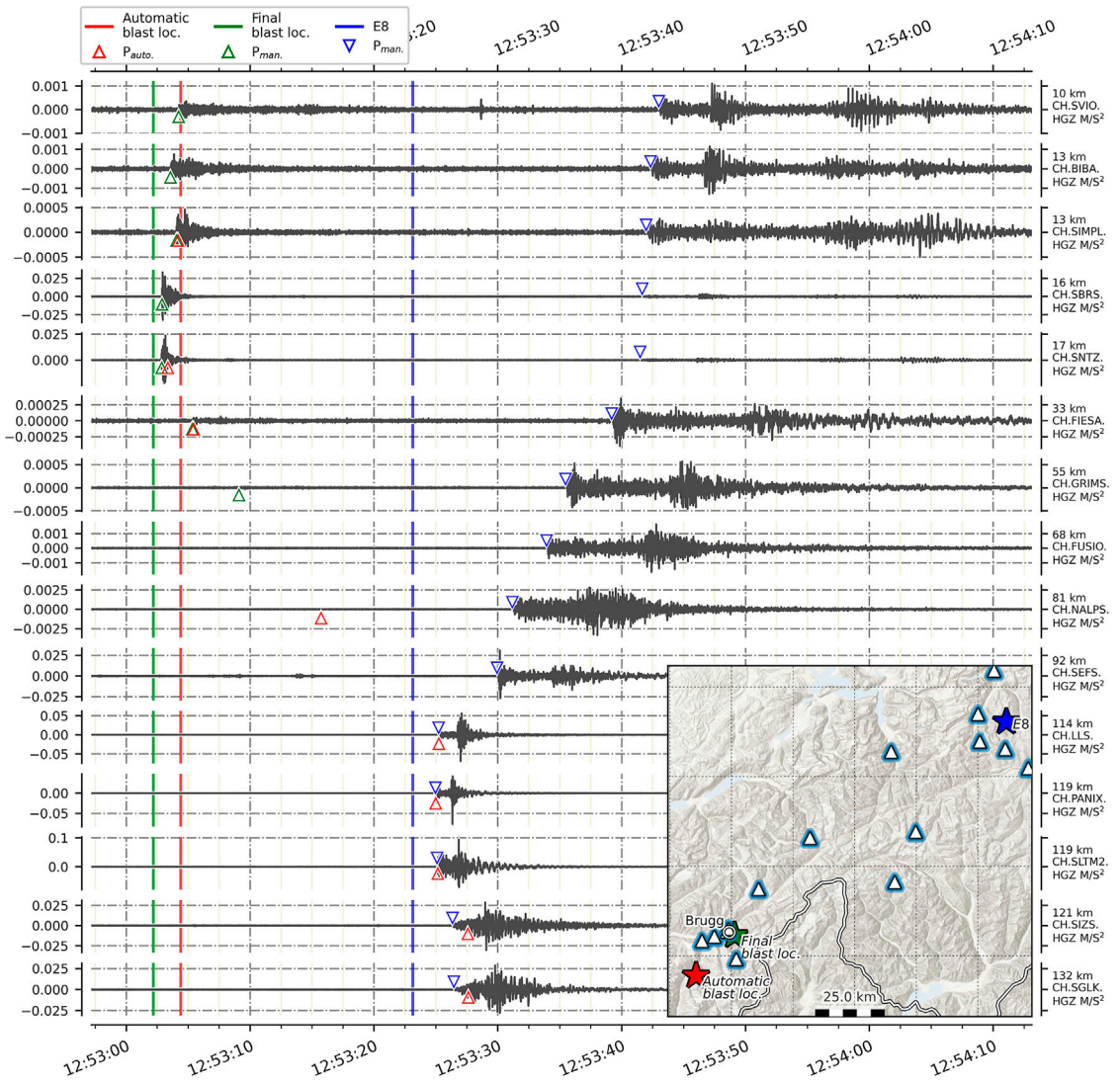

FIGURE 5 | Seismograms recorded during the M_{Lhc}3.9 Elm aftershock. The map inset shows the seismic stations (triangles) as well as the locations of the aftershock (E8, blue); the M_{Lhc}1.0 quarry blast that preceded the event (green), and the automatic blast location that included Elm aftershock phases (red). The seismograms are ordered and labelled by distance to the quarry blast. Vertical lines and stars mark origin times in the seismograms and event locations on the map, respectively. P-wave arrivals are marked by triangles on the seismograms. The final origins of the blast and E8 are associated with manually picked arrival times. The automatic blast location is based on automatic P-wave picks, and erroneously incorporates stations close to E8.

FinDer (see FinDer section) appears coarse compared to the expected rupture dimension of such a small earthquake, but is acceptable considering location uncertainties. While the main strength of FinDer is in the finite-source characterization of large earthquakes (M > 5.5), the algorithm can often provide reasonable estimates of fault rupture strike in smaller events if their spatial PGA distributions show effects of rupture directivity (Böse et al., 2018a). This, however, is not the case in the Elm events and the FinDer estimated strike does not match the strike predicted by the focal mechanism (**Figure 7**) and aftershock distribution.

The late alert zone (where the S-wave arrives before the alert) extends to 11 and 13 km from the mainshock and aftershock, respectively. For the M_{Lh} 4.3 Elm earthquake an EEW message provided without additional latency could have preceded the felt ground shaking within 11–15 km around the epicenter, where intensity exceeded III.

Figure 8 illustrates the temporal evolution of VS and FinDer results during the M_{Lh}4.3 Elm mainshock (top, A–D), and the M_{Lhc} 3.9 aftershock (bottom, E–H). In general, the performance of the two algorithms is similar during both events, though the VS solution for the aftershock was delayed due to the earlier described picking problem.

VS origins are derived from automatic picks, with a minimum of four and increasing in number as energy appears at later stations received at the processing hub. In contrast, in order to

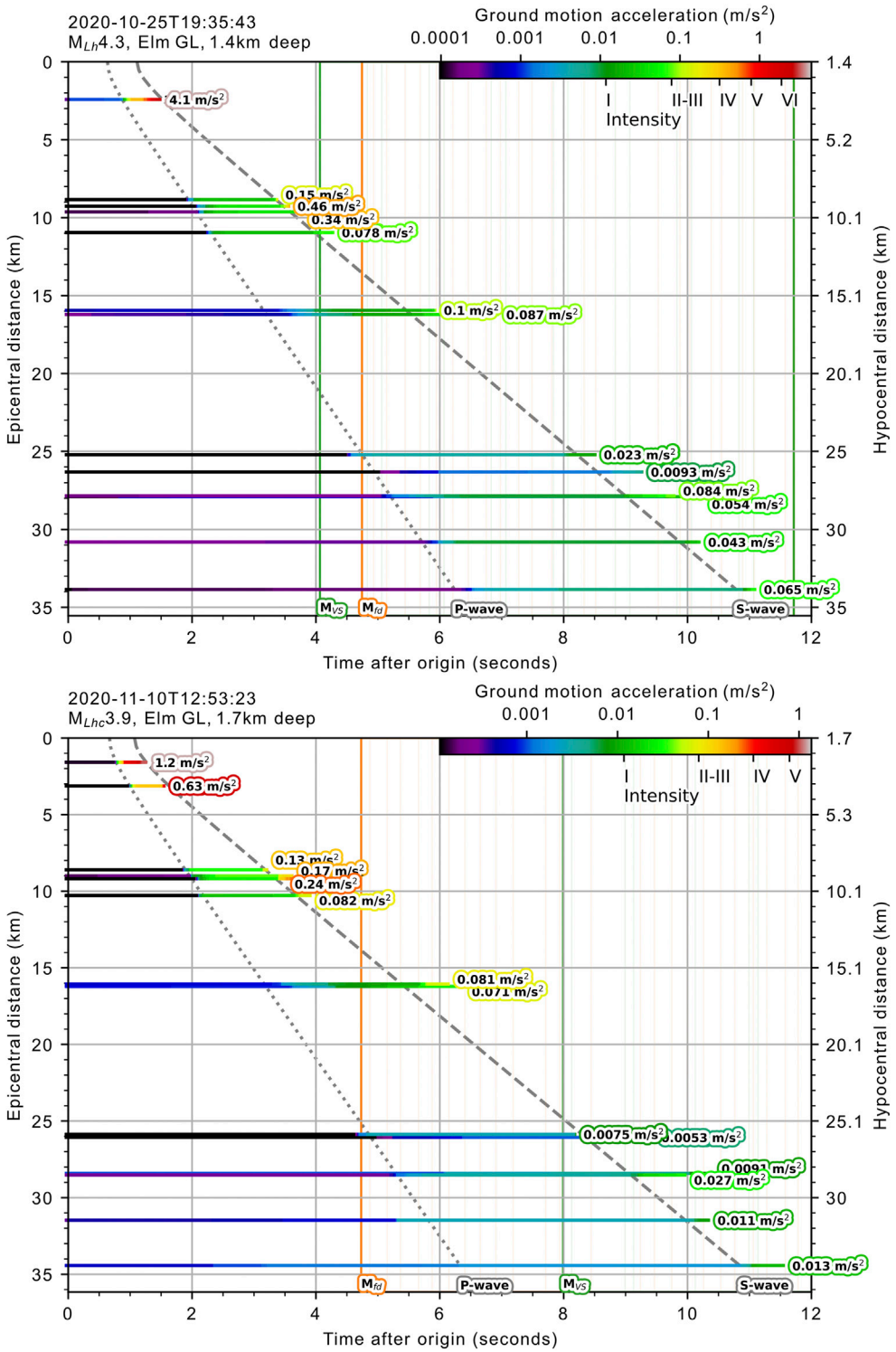

FIGURE 6 | Available seismic data for the M_{Lh} 4.3 Elm earthquake **(top)** and M_{Lhc} 3.9 aftershock **(bottom)** as a function of time and distance from origin. Each line shows the temporal evolution of horizontal peak ground acceleration (PGA) at a given station until its peak value is reached (labels left-sided on PGA time, with highest PGA plotted on top). Intensity equivalents are derived from Faenza and Michelini (2010). Vertical lines indicate the first magnitude estimates from VS (M_{VS}) and FinDer (M_{fd}). Dotted and dashed curves show the theoretical P- and S-wave arrivals computed with the iasp91 velocity model.

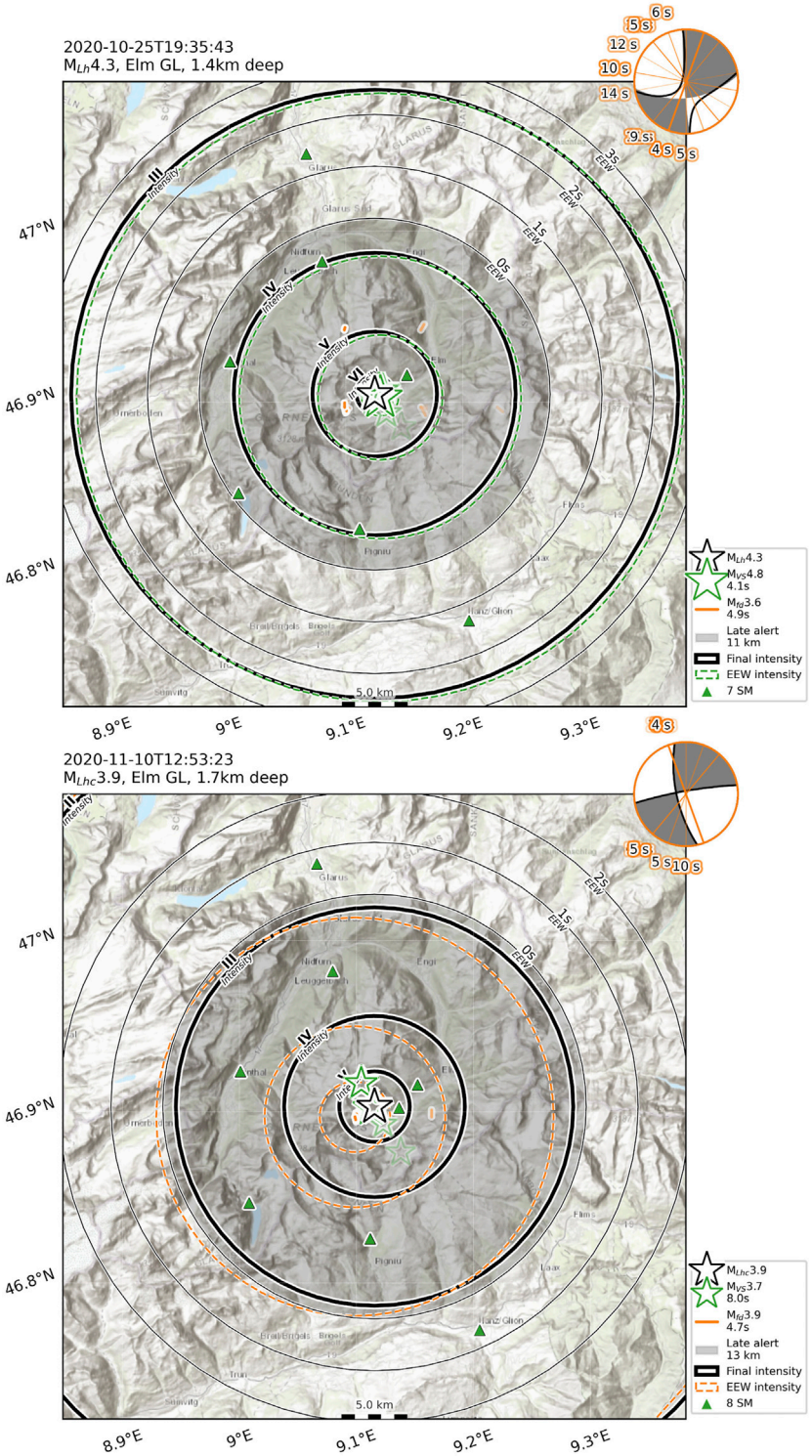

FIGURE 7 | Geographical comparison of VS (green), FinDer (orange) and catalogue (black) earthquake parameters estimates for the M_{Lh} 4.3 Elm earthquake **(top)** and M_{Lhc} 3.9 aftershock **(bottom)**. Origin locations are represented with stars or lines for rupture models from FinDer, the brightest symbols representing the earliest estimates (see first delay in legend). Intensity iso-lines from the catalogue origin (solid black) can be compared to the earliest EEW estimates (dashed lines), following a generic intensity prediction equation (Allen et al., 2012). The late alert area (grey circle) and available warning (lead) time from the EEW (thin black lines, modeled as the time difference between the S-wave arrivals, as predicted from the iasp91 velocity model, and the first EEW solution) are indicated. The polar plot in the upper right corner shows the evolution of the FinDer fault-line model azimuths (orange, labelled with delay after origin), and the catalogue focal mechanism (grey).

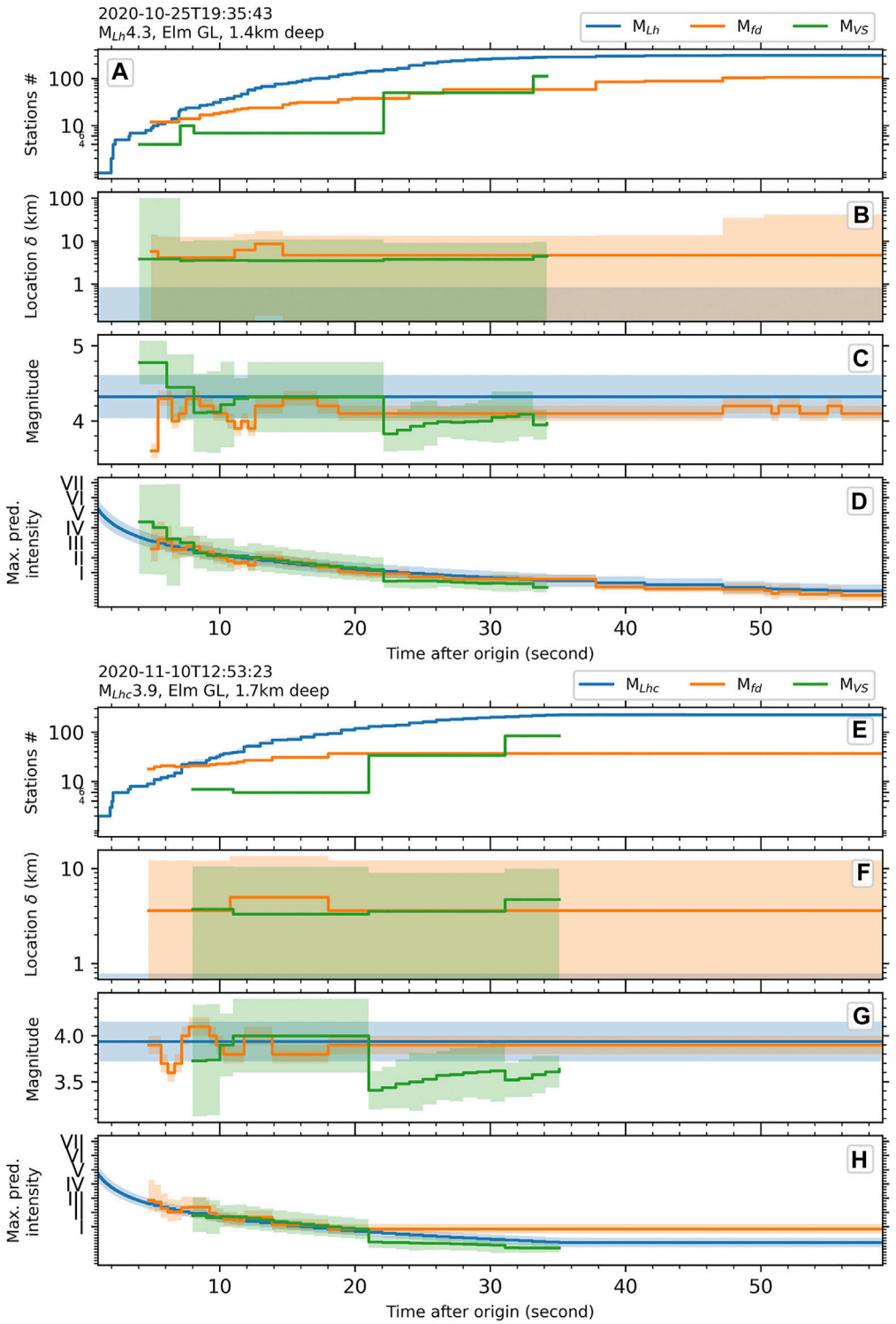

FIGURE 8 | Temporal evolution of VS (green) and FinDer (orange) earthquake parameter estimates for the M_{Lh} 4.3 Elm earthquake **(top)** and M_{Lhc} 3.9 aftershock **(bottom)**. Parameters from catalogue solution are indicated in blue. **(A,E)**: number of stations contributing to locations for each algorithm; blue line shows the cumulative number of stations where P-wave has reached. **(B,F)**: EEW centroid hypocentral location errors (lines, uncertainty indicated by shaded area). **(C,G)**: Magnitudes (lines, uncertainty indicated by shaded area). **(D,H)**: Maximum predicted intensity (see **Supplemental Material**, section Maximum predicted intensity) at the reference S-wave front edge considering final centroid location, using the reference final source parameters (blue line) and EEW parameters (green and orange lines) and related uncertainties (shaded areas).

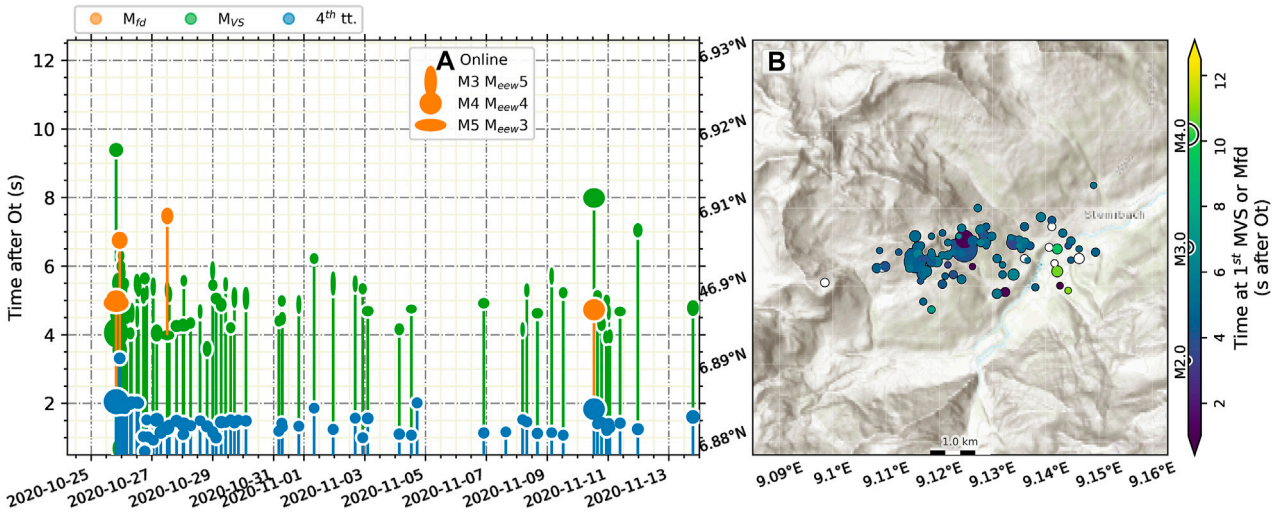

FIGURE 9 | Temporal **(A)** and geographical **(B)** overview of the VS (green, 83 earthquakes), and FinDer (orange, five earthquakes) performances for the first 3 weeks of the Elm earthquake sequence, showing events with magnitude over 1.2. **(A)** Delays for each event: the first VS and first FinDer origin times are indicted by the green and orange ellipses, respectively. For comparison, the delay to the P-wave arrival at the fourth active station, indicating the lower boundary for EEW (neglecting data delay), is shown in blue. The heights of the ellipses for VS and FinDer represent the first EEW magnitude estimates, and their widths represent the final magnitude (following magnitude scale in **B**). While first VS magnitudes for some of the smaller events tend to be overestimated, they converge towards correct solutions during subsequent updates. **(B)** The final locations are color-coded with delays of the first EEW (VS or FinDer) solution. Further details on errors are provided in **Figure 10**.

constrain the location, FinDer uses all stations streaming, including those that did not yet record the event. The FinDer station counts in **Figures 8A,E** show stations with PGA over 2 cm/s^2, so these numbers are not directly comparable to the pick counts for VS. Nevertheless, it is apparent that FinDer integrates new stations at a faster rate than VS, since in the current configuration, VS origins are only updated every 10 s and not on significant change in station number.

VS and FinDer origins/centroid locations are similar and relatively stable over time (**Figures 8B,F**). The magnitude estimates provided by the two algorithms show more significant fluctuation over time (**Figures 8C,G**). For VS, the magnitude is updated every 1 s, and at least 1 s of data after the P-wave pick is required at each station. Since initial magnitudes use very short waveform durations from a few stations, initially fluctuations can be expected. There also is a significant difference in the magnitude evolutions of FinDer and VS as they integrate new stations. FinDer magnitudes, which are updated irregularly in response to the changing ground-motion field, tend to stabilize over time, while VS magnitudes can jump as updated origins include additional stations for magnitude determination.

Figures 8D,H show the maximum intensity at any point on the evolving S-wave front edge (see **Supplementary Material** for explanation). The uncertainties in location and magnitude are taken into account in the uncertainty in the intensity prediction. For both the mainshock and aftershock, the maximum predicted intensity evaluated for VS and FinDer do not deviate from the reference prediction by more than their uncertainties, demonstrating the stability of both algorithms in this example.

The ESE system operated throughout the Elm sequence, with VS providing results for all earthquakes with magnitude over 1.2 and FinDer only providing results for five earthquakes with magnitudes above 2.0. Since FinDer requires a threshold in amplitude to be exceeded at three or more sensors across the network, it only produces solutions for the largest events in this sequence. VS builds on traditional STA/LTA picks, so it is sensitive to much smaller events.

Figure 9 shows the delays of the first M_{VS} and M_{fd} for the entire Elm sequence following the mainshock for magnitudes above M_L2. Also indicated is the delay to the fourth observed P-wave arrival time after origin time (neglecting data delay), providing an estimate of the best possible EEW delay considering the actual network geometry. Apparent is the effect of the installation of the last aftershock station in the days after the 25 October mainshock. In general, we observe delays of 1.5–2 s for travel times, and first EEW estimates, the majority from VS, became available within 4–6 s.

Figure 10 provides an overview for the errors in hypocentral location, timing and magnitude for all EEW estimates (with 83 earthquakes for VS, and five earthquakes for FinDer). The median location error of the first EEW estimates is about 5 km. Larger location errors are produced with the earliest VS origins from a handful of smaller earthquakes. These poor origins were produced by unrelated or false picks across the network, and subsequent origins quickly migrate to close to the catalogue solution when integrating additional data. Magnitude errors are centered at about +0.1 unit of magnitude, with stronger over-estimation when associated with origins with large location errors. The median magnitude error in FinDer is about zero, though there is a heavy tail with magnitude

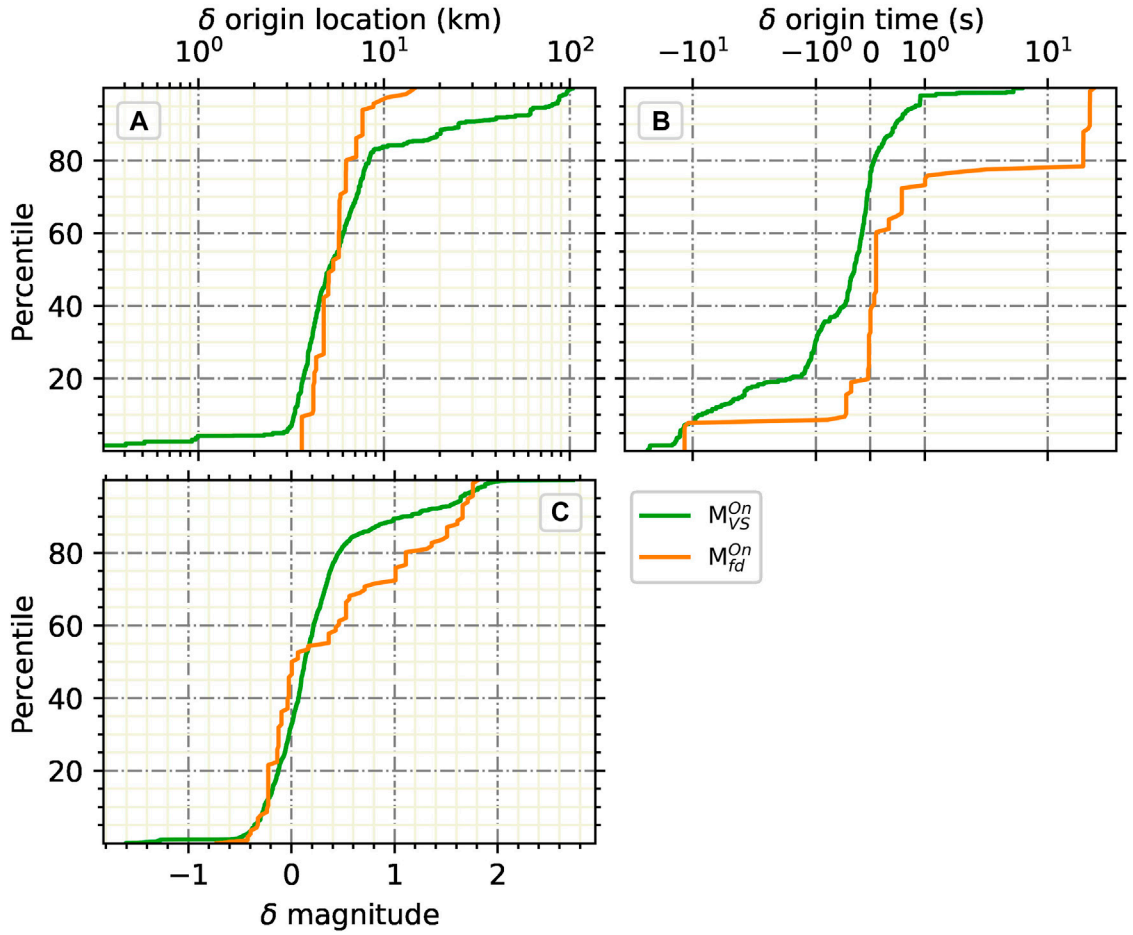

FIGURE 10 | Cumulated distributions of errors (δ) from VS (green, 83 earthquakes) and FinDer (orange, five earthquakes) from online operation during the Elm earthquake sequence for events with magnitude above 1.2. Errors are inferred as the difference between the attributes of the final and the EEW (VS or FinDer) solutions. **(A)** Errors in hypocentral location. **(B)** Errors in earthquake origin time. **(C)** Errors in magnitude.

overestimates of 0.5–1.6 over the 60th percentile–which is an outlier from a single event.

REAL-TIME AND PLAYBACK EEW PERFORMANCE DURING SIGNIFICANT EVENTS

The ESE supports real-time re-processing of all historic events associated with archived waveforms using the latest system and algorithm configurations (note that the system and algorithms underwent a number of changes during the testing period). These playbacks allow us to evaluate EEW performance for historical earthquakes, neglecting packet delay (with a 0.4 s median, **Supplementary Figure SA1a**), while still being subject to the original packet reception interval (with a median of 1.6 s, **Supplementary Figure SA1b**).

We run ESE playbacks for the 100 largest earthquakes with magnitudes over 2.7 within Switzerland (and Liechtenstein) since 2009. We also collect the corresponding EEW solutions provided in real-time for the same events beginning from late-2014 for VS and mid-2017 for FinDer. The VS primary location method has been configured to use four stations instead of six since mid-2017. The full overview of the playback results is provided in the **Supplementary Figure SA3** and **Supplementary Table SA1**. Here we focus on the performance for the eight largest playback earthquakes over magnitude 3.9, as presented in **Table 1**.

Figure 11 provides an overview of ESE real-time and playback performance for these eight events. Earthquakes E6, E4 and E7 (M_l4.1 Buchs 2009, M_l4.2 Zug 2012, and M_{Lh}4.1 Sargans 2013) occurred before 2015, without available real-time results. Although they have observed arrival time delays of 2–7 s (after reference origin time) to the fourth closest station, EEW times are slow. This is because a significant number of key near field strong motion stations were recorded on offline, low resolution (12 or 16 bit) accelerometers (that have subsequently been replaced)–thus in playback there are relatively long packet reception intervals, since we use a constant 512-byte

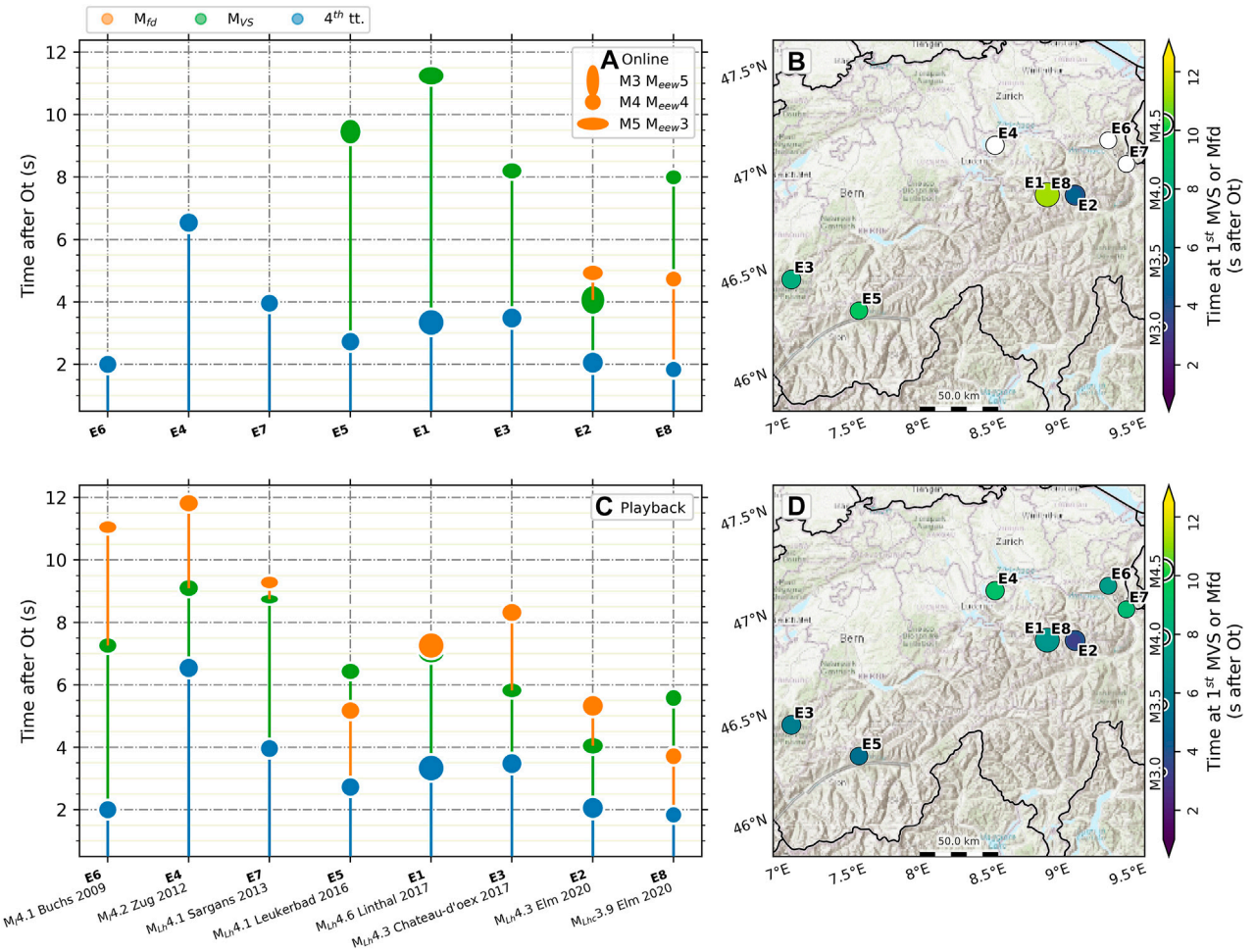

FIGURE 11 | Temporal **(A,C)** and geographical **(B,D)** overview of the VS (green), and FinDer (orange) performance for the eight largest earthquakes over magnitude 3.9 in Switzerland since 2009. The plotting conventions are the same as for **Figure 9**. **(A,B)** Online (real-time) results, provided by the real-time ESE system. The online ESE database includes VS results since late-2014, and FinDer results since mid-2017. The VS primary location method has been configured for using four stations since mid-2017. **(C,D)** Playback results, obtained with the ESE playback system. The EEW methods in the playback system are configured in a similar way to the post-2019 online system with the exception of one parameter in one of the VS location methods, adjusted for not aggregating triggers more than 7 s apart. Further details on errors are provided in **Figure 12**.

packet size. As a consequence for playbacks, first VS estimates are produced in 7–9 s while FinDer requires 9–12 s, a situation that would not be repeated today. This is confirmed in **Supplementary Figure SA3**, where the delay times to the fourth closest stations are observed to reduce over time, and are now generally stable and match that in the theoretical delays seen in **Figure 3**.

Earthquakes E5, E1, E3 (M_{Lh}4.1 Leukerbad 2016, M_{Lh}4.6 Linthal 2017, and M_{Lh}4.3 Chateau-d'Oex 2017) occurred before FinDer was included in ESE, and before the VS configuration was adjusted to provide a location with four stations. Thus, despite travel time delays of 3–4 s, online VS results came in 8–11 s, with incorrect first location for E5 and E1. These issues are corrected in playback, with VS in 6–7 s and similar FinDer performance.

Earthquakes E2 and E8 (M_{Lh}4.3 Elm 2020, and M_{Lhc}3.9 Elm 2020) both occurred when FinDer was online and VS configured for location with four stations. Their playback results are similar to those obtained online with the exception of improved VS performance for the M_{Lhc}3.9 Elm 2020 aftershock. This improvement was achieved by adjusting one parameter in the *scanloc* location method (Scanloc Documentation, 2021, Grigoli et al., 2018) avoiding aggregation of late triggers separated by an unrealistically large time difference to be related to the same event, considering that many stations are available in between but not triggered.

In general, the performance of the top 100 events in both real-time and playback matches these largest earthquakes, as seen in **Supplementary Figure SA3**. Since 2013, with the dense network and well configured algorithms, the large majority of events

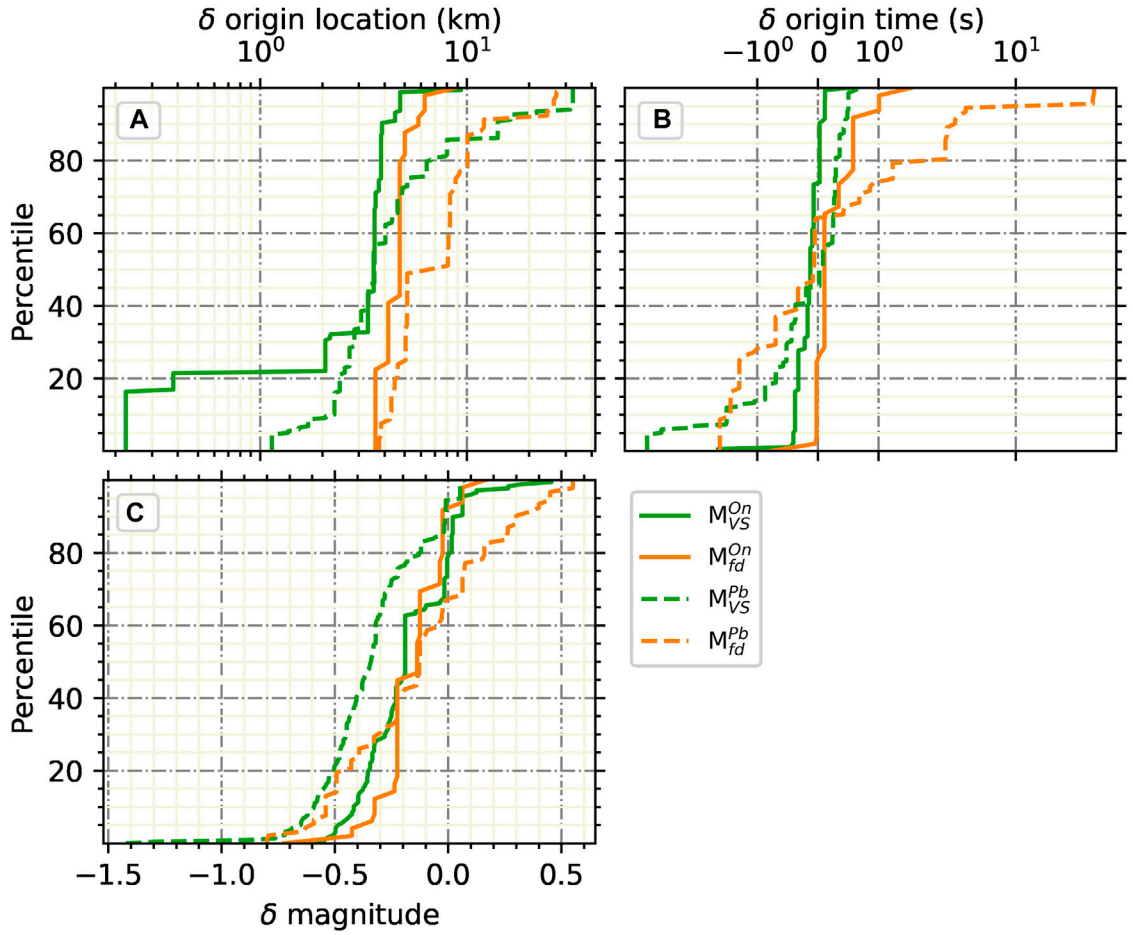

FIGURE 12 | Cumulated distributions of errors (δ) from VS (green) and FinDer (orange) for the eight largest earthquakes over magnitude 3.9 in Switzerland and Lichtenstein since 2009. We use the same plotting conventions as in **Figure 10**, adding playback results (*Pb*, dashed lines) to the online (real-time) results (*On*, solid lines).

would have been first characterised within 10 s, and many far faster.

A detailed error analysis of all EEW solutions for these eight largest earthquakes is shown in **Figure 12**. FinDer systematically has higher errors in location than VS, because it is using a coarser location grid and determining a centroid rather than hypocenter location (see FinDer section). Playback results are observed to be on average slightly worse for both algorithms, though this is explained since additional, older events, with a relatively sparse data coverage, are included in playback. For these largest events, in real-time both algorithms tend to underestimate magnitudes by 0.2 on average. In playback, VS performs worse with a 0.4 average underestimation. Since playback using the latest configuration allows solutions using fewer stations, playbacks result in faster earliest solutions but with slightly increased errors (faster solutions in playback are also facilitated by neglecting the packet reception delay). Nevertheless, in playback, both FinDer and VS provide rapid, blunder-free and complimentary EEW performance. Both algorithms perform well even for intermediate magnitude earthquakes in Switzerland. **Supplementary Figure SA4** presents the error analysis for all 100 largest events. A more reduced average magnitude underestimation by VS of about 0.15 magnitude units is apparent.

DISCUSSION

The Swiss Seismological Service (SED) operates a prototype EEW system for Switzerland, called ESE (SED-ETHZ SeisComP EEW system). The key recent change of ESE is the integration of the FinDer algorithm in mid-2017 alongside the existing VS algorithm. Having two independent algorithms adds robustness to the system as demonstrated here for the M_{Lhc}3.9 Elm earthquake. A small quarry blast that occurred in another part of Switzerland in the seconds before this event caused significant delays in the pick-based VS algorithm, while FinDer, based on the emerging spatial patterns of strong motion, was unaffected and provided timely alerts.

The EEW performance presented in this study is made possible by sustained efforts to develop and maintain an EEW-ready seismic monitoring infrastructure. The Swiss Seismic Network was not primarily developed for EEW.

However, since 2009, every opportunity to upgrade and extend the permanent network has been taken with EEW in mind. In particular, the number of strong motion stations has grown very rapidly (**Figure 2**) to the stage where today over 175 permanent stations are equipped with strong motion sensors (**Figure 3B**). Further, the majority of stations have dataloggers that support low latency streaming (**Figure 3A**). Finally, uptime for the majority of stations averages over 99% each year. With this observational capability, Switzerland provides an excellent opportunity for developing, testing and demonstrating EEW. Further, these high-quality waveform data are available in real-time and in open archives. Although seismicity in Switzerland is moderate, a number of events with magnitude over four have recently been recorded available to demonstrate performance.

These measures ensure event detection for significant seismic events is now routinely observed in under 10 s across the country (last 5 years in **Supplementary Figure SA3a**) resulting in a maximum late-warning area of 32 km radius (S-wave distance for 10 s in **Supplementary Figure SA5c**). Further, for large portions of the country, in particular regions with significant recent and historic seismicity (**Figure 3C**), alerts are available in the order of 5 s (late-warning area of 14 km radius, **Supplementary Figure SA5**). Our study does not address missed and false alerts because event playback does not allow us to look into false positive rates, and configuration changes do not allow us to go further back in time before 2018. Since 2018, 1.5% of the MVS exceeding 2.5 did not correspond to true seismic events. The rate of false positives from FinDer has been variable over time, but during the last 6 months no M_{VS} or M_{fd} solution exceeded 2.5 without a true seismic event.

ESE performance in Switzerland compares well with the US ShakeAlert system, the state-of-the art EEW system currently operating across the US West Coast. ShakeAlert and ESE in Switzerland are both operating on dense networks that have been optimised for low latency. Like ESE, ShakeAlert combines FinDer with a point source algorithm, EPIC (Kohler et al., 2020). The FinDer delays in both systems are similar, while VS in Switzerland is about 1 s slower than EPIC in ShakeAlert. The fastest alerts in ShakeAlert (both EPIC and FinDer) are about 3 s, 20% of alerts are faster than 5.5 s, the median alert delay after event nucleation throughout the US West Coast is 7.2 s, with 80% of first alerts faster than 10.5 s, and 90% of first alerts are faster than 13.5 s, varying with epicentral station density (and magnitude for marginal events; J. Andrews, written communication, May 2021).

We demonstrated in this paper, the current EEW performance of ESE in Switzerland using the observed seismicity occurring over the last 10 years, with a maximum magnitude of M_L 4.6. Of course events of this type are not the target for the EEW system–damage is not observed and shaking intensities are moderate and restricted to narrow regions around the epicenter. Nevertheless, the delays and the precision in location and magnitude presented here can be expected to be repeated during more significant events since VS and FinDer have been extensively tested as described in the method section. ESE also operates effectively in regions with larger events M6+ seismicity, the ESE framework is being continuously tested in Nicaragua, El Salvador, and Costa Rica (Massin et al., 2018, 2020, Porras et al., 2021). In addition, the performance of FinDer is continuously monitored and improved in the US West Coast ShakeAlert warning system (Given et al., 2018), which uses another, Earthworm-based wrapper but the same FinDer algorithm code.

This study also documents the impact of recent improvements in the configuration of VS as compared to Behr et al. (2015). In addition to the network densification, key VS configuration changes include the SeisComP location module migration from the six station configuration of *scautoloc* to the four station configuration of both *scautoloc* and *scanloc*; and implementation of 1 s magnitude windows instead of the original 3 s. In Behr et al. (2015), the observed real-time VS delays fell between 12 and 14 s for the 16th and 84th percentile for earthquakes within Switzerland, while we report real-time VS delays since 2014 from 6.5 to 12.5 s, respectively (with a 8.7 s median or a 27 km late alert zone radius, **Supplementary Figure SA5**). The median first magnitude delay in playback is about 7.3 s for VS and 5.8 s for FinDer, corresponding to the propagation of S-waves over 22 and 17 km, respectively (varying by about 4 km depending on the depth). Comparing VS and FinDer on the intersecting subsets of nine earthquakes since 2017 that have results for both algorithms shows real-time median delays of 8.5 and 7 s for VS and FinDer, both improving by about 1s in playback (**Supplementary Figure SA6**).

In ESE in Switzerland, the first VS magnitude is generally available 4–5 s after the P-wave arrives at the fourth station; for FinDer the performance is less predictable in the magnitude range considered here (FinDer requires PGA >2 cm/s/s at three neighboring stations). Playbacks with the current configuration are faster than real-time performance, though earliest playback solutions tend to have larger errors. FinDer can overestimate magnitudes of small earthquakes (**Supplementary Figure SA4**), but does not for earthquakes over M3.9 (**Figure 12**). VS, by contrast, allows continuous (configuration and metadata) quality control with background seismicity and computation stress testing with intense sequences of non-damaging events, but shows increased magnitude under-estimation errors on the largest earthquakes (by 0.7 and 0.4 units in median for playbacks and online, **Figure 12**) compared to smaller earthquakes (by 0.2 and 0.3 units in median for playbacks and online, **Supplementary Figure SA4**).

In general, comparing playback and online results in the current configuration of the ESE underlines the trade-off between detection speed and location errors. Although each processing stage of the ESE provides quality metrics, an independent and unified real-time quality evaluation procedure of EEW magnitudes is still missing for detecting potential errors in EEW. VS uses quality parameters of the origin location and magnitude to produce likelihood estimates of correct event detection (Behr et al., 2016). The VS likelihood is an example of an empirical approach for identifying incorrect event parameters, while FinDer uses cross-correlation coefficients and misfit values. With the introduction of FinDer as a major component of ESE, it is critical to develop a tool for quantitative decision-making in the EEW context. Minson et al. (2017), for example, demonstrate how an optimal EEW solution can be identified among multiple options, using available ground motion

observations. We intend to implement a similar methodology in ESE in future.

The current ESE configuration can still be improved. We demonstrate how an adjustment of the ESE configuration can improve EEW in presence of a simultaneous quarry blast during the M_{Lhc}3.9 Elm 2020 aftershock using the playback functionality of the ESE (developed by Behr et al., 2015; Behr et al., 2016). Future improvement towards a better VS location method configuration might tend toward more location updates. The current ESE configuration for VS limits the location update interval to 10 s, ignoring stations that become available for origin and subsequent magnitude evaluation. This arbitrary limitation aiming at controlling usage of computing resources will hopefully become unnecessary in the short term.

CONCLUSION

We document the latest status of ESE, the SED-ETHZ SeisComP EEW system, that includes the VS and FinDer algorithms. In general, both algorithms are observed to be similarly fast. The pick-based VS method provides fast locations and magnitudes for any event that triggers the national network. Since 2014, the median delay for the first VS alert is 8.7 s after origin time. FinDer relies on recognition of peak amplitudes exceeding a certain threshold (here 2 cm/s^2), so is only activated for larger events ($M > 3.5$), but events as small as M2.7 have been detected. Since 2017, the median delay for the first FinDer alert is 7 s. Playbacks of the largest 100 events, with $M \geq 2.7$, over the last 10 years using the current configuration indicate median delays of 7.3 and 5.8 s for VS and FinDer, respectively–though FinDer only provides a solution for 37 of these events. The median value for the travel time of the P waves from event origin to the fourth station accounts for 3.5 s of delay; with an additional 1.4 s for data sample delays in real-time testing.

Operating two independent algorithms provides redundancy and increase the tolerance to failures of a single algorithm. In this manuscript, we demonstrate this for the M_{Lhc}3.9 Elm earthquake, for which an independent quarry blast in the seconds before delays the pick-based VS by 4 s, while FinDer is not affected by the small amplitudes of quarry blast signals and performs as expected.

The Swiss Seismic Network continues to be optimised for EEW–today over 175 permanent stations include strong motion stations, and the majority of stations have been upgraded to include low-latency streaming. Station uptime is high. With the EEW methodologies integrated in SeisComP, and the quality of the monitoring infrastructure, the ESE system in Switzerland is achieving a performance in terms of speed that is similar to the US ShakeAlert EEW system.

DATA AVAILABILITY STATEMENT

The original contributions presented in the study are included in the article **Supplementary Material**, further inquiries can be directed to the corresponding author. We use waveform data from the permanent networks CH (Swiss Seismological Service (SED) at ETH Zurich, 1983) and C4 (CERN, 2016); as well as the temporary networks 4D (Swiss Seismological Service (SED) at ETH Zurich, 1985), 8D (Swiss Seismological Service (SED) at ETH Zurich, 2005), XY (Swiss Seismological Service (SED) at ETH Zurich, 2018) and XP (Swiss Seismological Service (SED) at ETH Zurich, 2012). The SED-ETHZ station inventory, waveform and event catalogue data are available at http://eida.ethz.ch via webservices following the International Federation of Digital Seismograph Networks (https://www.fdsn.org/webservices). The 100 largest earthquakes within Switzerland over magnitude 2.7 since 2009 can be extracted from querying the SED-ETHZ FDSN web-service with https://tinyurl.com/3f8wzdu3. The results provided in this study are produced within the SeisComP software (Helmholtz Centre Potsdam GFZ German Research Centre for Geosciences and gempa GmbH, 2008), analysed with Obspy (The ObsPy Development Team, 2019), all figures are made with Matplotlib (Hunter, 2007) and all maps with The Basemap toolkit (https://github.com/matplotlib/basemap) and the "World Ocean Base" map layer (Esri, GEBCO, NOAA, Garmin, HERE, and other contributors. "World_Ocean_Base" [basemap]. Scale Not Given. "World Ocean Base." February 24, 2014. https://www.arcgis.com/home/item.html?id=1e126e7520f9466c9ca28b8f28b5e500). The SeisComP playback utility that we use for real-time simulation is available at https://github.com/SED-EEW/sc3-playback. Licenses, documentations and source codes for VS and FinDer can be found on the SED-ETHZ website at http://seismo.ethz.ch/en/research-and-teaching/fields_of_research/earthquake-early-warning. All websites were last accessed in August 2021. Supplemental material contains one table, five figures and a detailed description of the ground-motion intensity prediction method.

AUTHOR CONTRIBUTIONS

FM: Co-responsible for EEW at SED-ETHZ. Contributed to the design of the work and technical information, provided analysis of data, figures, and draft. MB: Co-responsible for EEW at SED-ETHZ and for the development of FinDer. Contributed to the design of the work, technical information, interpretation, analysis of data, draft and critical revision. JC: Director of seismic networks at SED and the related activities. Contributed to the design of the work, technical information, interpretation, analysis of data, draft and critical revision.

ACKNOWLEDGMENTS

The ETHZ-SED seismic network receives real-time seismic waveforms from the Zentralanstalt für Meteorologie und Geodynamik in Vienna (ZAMG, network code OE, https://doi.org/10.7914/SN/OE), the Istituto Nazionale di Geofisica e Vulcanologia in Rome (INGV, network code IV, https://doi.org/10.13127/SD/X0FXNH7QFY), the Istituto di Geofisica, Università di Genova (network code GU, https://doi.org/10.7914/SN/GU), the Zivilschutz der Autonomen Provinz Bozen-Südtirol (network code SI), the Istituto Nazionale di Oceanografia e di Geofisica Sperimentale (OGS, network code OX, https://doi.org/10.7914/SN/OX) in Trieste, the Landeserdbebendienst

Baden-Württemberg in Freiburg (LED, network code LE), the Bundesanstalt für Geowissenschaften und Rohstoffe in Hannover (BGR, network code GR, https://doi.org/10.25928/mbx6-hr74), the Réseau Sismologique et Géodésique Français (RESIF, network code FR, http://dx.doi.org/10.15778/RESIF.FR and RA, https://doi.org/10.15778/RESIF.RA), and the AlpArray Seismic Network Team (AlpArray Seismic Network, network code Z3, https://doi.org/10.12686/alparray/z3_2015). The authors especially thank the SED Electronic Laboratory team, who build and maintain the seismic network, as well as Philipp Kästli, Stefan Heimers, Roman Racine and Luca Scarabello who maintain and develop the hardware and software infrastructure of the seismic network.

SUPPLEMENTARY MATERIAL

The Supplementary Material for this article can be found online at: https://www.frontiersin.org/articles/10.3389/feart.2021.707654/full#supplementary-material

REFERENCES

Allen, R. (1982). Automatic Phase Pickers: Their Present Use and Future Prospects. *Bull. Seismological Soc. America* 72, S225–S242. doi:10.1785/bssa07206b0225

Allen, R. M., and Melgar, D. (2019). Earthquake Early Warning: Advances, Scientific Challenges, and Societal Needs. *Annu. Rev. Earth Planet. Sci.* 47, 361–388. doi:10.1146/annurev-earth-053018-060457

Allen, T. I., Wald, D. J., and Worden, C. B. (2012). Intensity Attenuation for Active Crustal Regions. *J. Seismol* 16 (3), 409–433. doi:10.1007/s10950-012-9278-7

Baer, M., and Kradolfer, U. (1987). An Automatic Phase Picker for Local and Teleseismic Events. *Bull. Geol. Soc. America* 77 (4), 1437–1445. doi:10.1785/bssa0770041437

Behr, Y., Clinton, J. F., Cauzzi, C., Hauksson, E., Jónsdóttir, K., Marius, C. G., et al. (2016). The Virtual Seismologist in SeisComP3: A New Implementation Strategy for Earthquake Early Warning Algorithms. *Seismological Res. Lett.* 87, 363–373. doi:10.1785/0220150235

Behr, Y., Clinton, J., Kästli, P., Cauzzi, C., Racine, R., and Meier, M.-A. (2015). Anatomy of an Earthquake Early Warning (EEW) Alert: Predicting Time Delays for an End-To-End EEW System. *Seismological Res. Lett.* 86 (3), 830–840. doi:10.1785/0220140179

Behr, Y. D., Cua, G. B., Clinton, J. F., and Heaton, T. H. (2012). Evaluation of Real-Time Performance of the Virtual Seismologist Earthquake Early Warning Algorithm in Switzerland and California, 53. American Geophysical Union.

Böse, M., Clinton, J., Massin, F., Cauzzi, C., Smith, D., and Andrews, J. (2018b). Offline-Performance of FinDer v.2 during the 2016/17 Central Italy Earthquake Sequence. *EGU Gen. Assembly* 20, 4650. doi:10.13140/RG.2.2.14290.04808

Böse, M., Felizardo, C., and Heaton, T. H. (2015). Finite-Fault Rupture Detector (FinDer): Going Real-Time in Californian ShakeAlert Warning System. *Seismological Res. Lett.* 86, 1692–1704. doi:10.1785/0220150154

Böse, M., Heaton, T. H., and Hauksson, E. (2012). Real-time Finite Fault Rupture Detector (FinDer) for Large Earthquakes. *Geophys. J. Int.* 191, 803–812. doi:10.1111/j.1365-246X.2012.05657.x

Böse, M., Hutchison, A. A., Manighetti, I., Li, J., Massin, F., and Clinton, J. F. (2021a). "FinDerS(+): Real-Time Earthquake Slip Profiles and Magnitudes Estimated from Backprojected Slip with Consideration of Fault Source Maturity Gradient,". in press in *The New Frontiers of Earthquake Early Warning Systems*.

Böse, M., Julien-Laferrière, S., Bossu, R., and Massin, F. (2021b). Near Real-Time Earthquake Line-Source Models Derived from Felt Reports. *Seismol. Res. Lett.* 92 (3), 1961–1978. doi:10.1785/0220200244

Böse, M., Smith, D. E., Felizardo, C., Meier, M.-A., Heaton, T. H., and Clinton, J. F. (2018a). FinDer v.2: Improved Real-Time Ground-Motion Predictions for M2-M9 with Seismic Finite-Source Characterization. *Geophys. J. Int.* 212, 725–742. doi:10.1093/gji/ggx430

Carrasco, S., and Böse, M. (2017). "FinDer Performance Using CSN Network: a strong-motion Based Algorithm for Earthquake Early Warning," in *Third Colloquium of Geophysical Signatures of Earthquakes and Volcanoes, Chile*.

Cauzzi, C., Behr, Y., Clinton, J., Kästli, P., Elia, L., and Zollo, A. (2016). An Open-Source Earthquake Early Warning Display. *Seismological Res. Lett.* 87 (3), 737–742. doi:10.1785/0220150284

Cauzzi, C., Edwards, B., Fäh, D., Clinton, J., Wiemer, S., Kästli, P., et al. (2014). New Predictive Equations and Site Amplification Estimates for the Next-Generation Swiss ShakeMaps. *Geophys. J. Int.* 200 (1), 421–438. doi:10.1093/gji/ggu404

CERN (2016). *CERN Seismic Network*. Other/Seismic Network. ETH Zurich. doi:10.12686/sed/networks/c4

Clinton, J., Zollo, A., Marmureanu, A., Zulfikar, C., and Parolai, S. (2016). State-of-the Art and Future of Earthquake Early Warning in the European Region. *Bull. Earthquake Eng.* 14 (9), 2441–2458. doi:10.1007/s10518-016-9922-7

Cua, G. B. (2005). *Creating the Virtual Seismologist: Developments in Ground Motion Characterization and Seismic Early Warning*. California: California Institute of Technology Pasadena.

Cua, G., Fischer, M., Heaton, T., and Wiemer, S. (2009). Real-time Performance of the Virtual Seismologist Earthquake Early Warning Algorithm in Southern California. *Seismological Res. Lett.* 80 (5), 740–747. doi:10.1785/gssrl.80.5.740

Cua, G., and Heaton, T. (2007). "The Virtual Seismologist (VS) Method: a Bayesian Approach to Earthquake Early Warning," in *Earthquake Early Warning Systems* (Berlin, Heidelberg: Springer Berlin Heidelberg), 97–132. doi:10.1007/978-3-540-72241-0_7

Cuéllar, A., Espinosa-Aranda, J. M., Suárez, R., Ibarrola, G., Uribe, A., Rodríguez, F. H., et al. (2014). "The Mexican Seismic Alert System (SASMEX): Its Alert Signals, Broadcast Results and Performance During the M 7.4 Punta Maldonado Earthquake of March 20th, 2012," in *Early Warning for Geological Disasters. Advanced Technologies in Earth Sciences*. Editors F. Wenzel and J. Zschau (Berlin, Heidelberg: Springer). doi:10.1007/978-3-642-12233-0_4

Diehl, T., Clinton, J., Cauzzi, C., Kraft, T., Kästli, P., Deichmann, N., et al. (2021). Earthquakes in Switzerland and Surrounding Regions during 2017 and 2018. *Swiss J. Geosci.* 114 (1), 4–29. doi:10.1186/s00015-020-00382-2

Diehl, T., Deichmann, N., Clinton, J., Husen, S., Kraft, T., Plenkers, K., et al. (2013). Earthquakes in Switzerland and Surrounding Regions during 2012. *Swiss J. Geosci.* 106 (3), 543–558. doi:10.1007/s00015-013-0154-4

Doi, K. (2011). The Operation and Performance of Earthquake Early Warnings by the Japan Meteorological Agency. *Soil Dyn. Earthquake Eng.* 31 (2), 119–126. doi:10.1016/j.soildyn.2010.06.009

Faenza, L., and Michelini, A. (2010). Regression Analysis of MCS Intensity and Ground Motion Parameters in Italy and its Application in ShakeMap. *Geophys. J. Int.* 180 (3), 1138–1152. doi:10.1111/j.1365-246x.2009.04467.x

Given, D., Allen, R. M., Baltay, A. S., Bodin, P., Cochran, E. S., Creager, K., et al. (2018). *Implementation Plan for the ShakeAlert System-An Earthquake Early Warning System for the West Coast of the United States*. Reston, Virginia: US Geological Survey–1155. Available at: https://pubs.usgs.gov/of/2018/1155/ofr20181155.pdf.

Grigoli, F., Scarabello, L., Böse, M., Weber, B., Wiemer, S., and Clinton, J. F. (2018). Pick- and Waveform-Based Techniques for Real-Time Detection of Induced Seismicity. *Geophys. J. Int.* 213 (2), 868–884. doi:10.1093/gji/ggy019

Hanka, W., Saul, J., Weber, B., Becker, J., and Harjadi, P.Fauzi, & GITEWS Seismology Group (2010). Real-time Earthquake Monitoring for Tsunami Warning in the Indian Ocean and beyond. *Nat. Hazards Earth Syst. Sci.* 10 (12), 2611–2622. doi:10.5194/nhess-10-2611-2010

Helmholtz Centre Potsdam GFZ German Research Centre for Geosciences and gempa GmbH (2008). *The SeisComP Seismological Software Package*. GFZ Data Services. doi:10.5880/GFZ.2.4.2020.003

Hsiao, N.-C., Wu, Y.-M., Shin, T.-C., Zhao, L., and Teng, T.-L. (2009). Development of Earthquake Early Warning System in Taiwan. *Geophys. Res. Lett.* 36, L00B02. doi:10.1029/2008GL036596

Hunter, J. D. (2007). Matplotlib: A 2D Graphics Environment. *Comput. Sci. Eng.* 9 (3), 90–95. doi:10.1109/mcse.2007.55

Johnson, C. E., Bittenbinder, A., Bogaert, B., Dietz, L., and Kohler, W. (1995). Earthworm: A Flexible Approach to Seismic Network Processing, n.D. Earthworm: A Flexible Approach to Seismic Network Processing. *IRIS Newsl.* 14(2), 1–4.

Kohler, M. D., Smith, D. E., Andrews, J., Chung, A. I., Hartog, R., Henson, I., et al. (2020). Earthquake Early Warning ShakeAlert 2.0: Public Rollout. *Seismological Res. Lett.* 91 (3), 1763–1775. doi:10.1785/0220190245

Kradolfer, U., and Mayer-Rosa, D. (1988). Attenuation of Seismic Waves in Switzerland, *Recent Seismological Investigations in Europe. Proceedings of the XIX General Assembly of the ESC*. Moscow, 481–488.

Li, J., Böse, M., Feng, Y., and Yang, C. (2021). "Real-time Characterization of Finite Rupture and its Implication for Earthquake Early Warning: Application of FinDer to Existing and Planned Stations in Southwest China,". subm. in *The New Frontiers of Earthquake Early Warning Systems*.

Li, J., Böse, M., Wyss, M., Wald, D. J., Hutchison, A., Clinton, J. F., et al. (2020). Estimating Rupture Dimensions of Three Major Earthquakes in Sichuan, China, for Early Warning and Rapid Loss Estimates. *Bull. Seismol. Soc. Am.* 110 (2), 920–936. doi:10.1785/0120190117

Massin, F., Clinton, J., Racine, R., Rossi, Y., Böse, M., Strauch, W., et al. (2020). 2020 Annual Meeting. *Seismological Res. Lett.* 91, 1095–1338. Number 2B. doi:10.1785/0220200043

Massin, F., Strauch, W., Clinton, J. F., Böse, M., and Ramirez, J. (2018). 2018 Seismology of the Americas Meeting Building Eew in Nicaragua: Performance and Perspectives. 2018 Seismology of the Americas Meeting. *Seismological Res. Lett.* 89, 717–966. Number 2B. doi:10.1785/0220180082

Meier, M.-A., Kodera, M., Böse, A., Chung, A., Hoshiba, M., Cochran, E., et al. (2020). How Often Can Earthquake Early Warning Systems Alert Sites with High-Intensity Ground Motion? *J. Geophys. Res. Solid Earth* 125 (2), e2019JB017718. doi:10.1029/2019jb017718

Minson, S. E., Wu, S., Beck, J. L., and Heaton, T. H. (2017). Combining Multiple Earthquake Models in Real Time for Earthquake Early Warning. *Bull. Seismological Soc. America* 107(4), 1868–1882. doi:10.1785/0120160331

Porras, J., Massin, F., Arroyo-Solórzano, M., Arroyo, I., Linkimer, L., Böse, M., et al. (2021). "Preliminary Results of an Earthquake Early Warning System in Costa Rica,". in *The New Frontiers of Earthquake Early Warning Systems*.

Racine, R., Cauzzi, C., Clinton, J., Fäh, D., Edwards, B., Diehl, T., et al. (2020). Updated Determination of Earthquake Magnitudes at the Swiss Seismological Service, Online. *EGU Gen. Assembly 2020*, EGU2020–8273. doi:10.5194/egusphere-egu2020-8273.2020

Scanloc Documentation (2021). Available at: https://docs.gempa.de/scanloc/current/(last accessed August, 2021).

Sheen, D. H., Park, J. H., Chi, H. C., Hwang, E. H., Lim, I. S., Seong, Y. J., et al. (2017). The First Stage of an Earthquake Early Warning System in South Korea. *Seismological Res. Lett.* 88 (6), 1491–1498. doi:10.1785/0220170062

Swiss Seismological Service (SED) At ETH Zurich (1983). *National Seismic Networks of Switzerland*. Other/Seismic Network. Zurich: ETH Zürich. doi:10.12686/sed/networks/ch

Swiss Seismological Service (SED) At ETH Zurich (2018). *Stations Deployed for Risk Model Switzerland*. Other/Seismic Network. Zurich: ETH Zurich. doi:10.12686/sed/networks/xy

Swiss Seismological Service (SED) At ETH Zurich (2005). *Temporary Deployments in Switzerland Associated with Aftershocks and Other Seismic Sequences*. Zurich: ETH Zurich. doi:10.12686/sed/networks/8d

Swiss Seismological Service (SED) At ETH Zurich (1985). *Temporary Deployments in Switzerland Associated with Glacier Monitoring*. Zurich: ETH Zurich. doi:10.12686/sed/networks/4d

Swiss Seismological Service (SED) At ETH Zurich (2012). *Temporary Deployments in Switzerland Associated with Landslides*. Other/Seismic Network. Zurich: ETH Zurich. doi:10.12686/2034sed/networks/xp

The ObsPy Development Team (2019). *ObsPy 1.1.1*. Version 1.1.1. Zenodo. doi:10.5281/zenodo.1040770

Wiemer, S., Danciu, L., Edwards, B., Marti, M., Fäh, D., Hiemer, S., et al. (2016). Seismic Hazard Model 2015 for Switzerland (SUIhaz2015). *Swiss Seismological Serv. (Sed) ETH Zurich*. doi:10.12686/a2

Conflict of Interest: The authors declare that the research was conducted in the absence of any commercial or financial relationships that could be construed as a potential conflict of interest.

Publisher's Note: All claims expressed in this article are solely those of the authors and do not necessarily represent those of their affiliated organizations, or those of the publisher, the editors and the reviewers. Any product that may be evaluated in this article, or claim that may be made by its manufacturer, is not guaranteed or endorsed by the publisher.

frontiers in Earth Science

ORIGINAL RESEARCH
published: 13 September 2021
doi: 10.3389/feart.2021.718216

Applicability of Accurate Ground Motion Estimation Using Initial P Wave for Earthquake Early Warning

Zijun Wang[1,2] *and Boming Zhao*[1,2]*

[1]*Key Laboratory of Urban Underground Engineering of Ministry of Education, Beijing Jiaotong University, Beijing, China,* [2]*School of Civil Engineering, Beijing Jiaotong University, Beijing, China*

The earthquake early warning (EEW) system is capable of mitigating seismic hazards and reducing deaths, injuries, and economic losses. Although EEW approaches have already been developed worldwide, improving the accuracy and applicability is still controversial. Aiming at the ground motion estimation using the initial P wave, we investigated eight representative characteristic parameters, i.e., the peak measurements and integral quantities, using the database of the 2008 Wenchuan earthquake, where the aftershocks with the criteria that 4.0 ≤ Ms ≤ 6.5 and epicentral distance less than 150 km are analyzed. We established the relationships between the eight characteristic parameters and four ground motion parameters, respectively, based on which the estimation accuracy and reliability and the extent to which the increasingly expanding time windows could affect the estimates are analyzed accordingly. We found that the integral quantities could also be a robust estimator for peak ground acceleration (PGA), peak ground velocity (PGV), and spectral intensity (SI), while the peak measurement is more useful in estimating peak ground displacement (PGD). In addition, for estimating the ground motion of events with magnitudes less than 6.5, a 2-s window could effectively improve the estimation accuracy by approximately 11.5–18.5% compared with using a 1-s window, as the window increases to 3 s, the accuracy would further improve while the growth rate will be reduced to around 3.0–8.0%.

Keywords: earthquake early warning, ground motion estimation, Wenchuan earthquake, initial P wave, characteristic parameters

OPEN ACCESS

Edited by:
Huseyin Serdar Kuyuk,
Harvard University, United States

Reviewed by:
Jia Cheng,
Ministry of Emergency Management, China
Ali Pinar,
Boğaziçi University, Turkey

***Correspondence:**
Boming Zhao
bmzhao@bjtu.edu.cn

Specialty section:
This article was submitted to Geohazards and Georisks, a section of the journal Frontiers in Earth Science

Received: *31 May 2021*
Accepted: *19 August 2021*
Published: *13 September 2021*

Citation:
Wang Z and Zhao B (2021) Applicability of Accurate Ground Motion Estimation Using Initial P Wave for Earthquake Early Warning. Front. Earth Sci. 9:718216. doi: 10.3389/feart.2021.718216

INTRODUCTION

The earthquake early warning (EEW) system is capable of mitigating seismic hazards and reducing deaths, injuries, and economic losses (Allen and Melgar, 2019; Zollo et al., 2016; Hoshiba, 2014). By regional and on-site algorithms, alerts could be sent ahead of the earthquake events induced ground shaking at target locations so that appropriate measures can be taken immediately against seismic hazards (Cremen and Galasso, 2020; Satriano et al., 2011), e.g., slowing the high-speed trains to reduce accidents and shutting down gas valves to prevent fires in a short term. The EEW systems are generally regarded as positive measures by relevant stakeholders that many earthquake-prone countries and regions are operating or testing their own systems.

The regional approach leverages the information from the seismic network deployed next to the epicenter to evaluate the relevant source parameters (event location and magnitude) and predict the regional seismic intensities using the traditional ground motion prediction equation (GMPE)

TABLE 1 | Seismic events studied in this paper.

No.	Origin time (UT)		Latitude	Longitude	Focal depth (km)	Ms	Number of records
1	2008.08.05	17:49:16	32.72	105.61	13	6.5	5
2	2008.05.25	16:21:47	32.55	105.48	14	6.4	6
3	2008.05.12	14:43:15	31.27	103.82	14	6.3	7
4	2008.05.12	19:11:01	31.26	103.67	14	6.3	15
5	2008.08.01	16:32:42	32.02	104.85	14	6.2	4
6	2008.05.13	15:07:08	30.95	103.42	14	6.1	12
7	2008.05.18	1:08:24	32.2	105.08	13	6.1	8
8	2008.07.24	15:09:28	32.76	105.61	10	6	3
9	2008.05.12	14:54:17	31.26	103.59	13	5.8	4
10	2008.05.12	15:34:42	31.29	103.77	13	5.8	7
11	2008.05.27	16:37:51	32.78	105.7	15	5.7	3
12	2008.07.24	3:54:43	32.72	105.63	10	5.7	2
13	2008.05.12	15:01:34	31.45	104.49	13	5.5	6
14	2008.05.12	16:10:57	31.14	103.6	10	5.5	3
15	2008.05.12	16:21:40	31.53	104.28	11	5.5	11
16	2008.05.13	7:46:18	31.34	103.58	13	5.4	13
17	2008.05.12	17:42:24	31.48	104.13	14	5.3	10
18	2008.05.27	16:03:22	32.76	105.65	15	5.3	5
19	2008.05.12	16:35:05	31.29	103.65	14	5.2	3
20	2008.05.12	17:06:59	31.16	103.69	10	5.2	4
21	2008.05.12	17:31:15	31.16	103.56	10	5.2	6
22	2008.05.12	16:26:12	31.4	104.12	12	5.1	7
23	2008.05.12	16:47:23	32.16	105.12	9	5.1	3
24	2008.05.12	22:46:06	32.72	105.64	10	5.1	8
25	2008.05.12	17:23:35	32.19	104.92	20	5	3
26	2008.05.12	18:23:39	30.97	103.48	9	5	8
27	2008.05.12	19:33:20	32.55	105.35	16	5	5
28	2008.05.13	1:29:06	31.21	103.68	24	4.9	12
29	2008.05.12	16:50:39	32.24	105.19	21	4.8	3
30	2008.05.13	2:26:17	31.47	104.1	11	4.8	4
31	2008.05.12	19:52:25	32.71	105.36	20	4.7	3
32	2008.05.12	20:29:58	31.4	104.07	11	4.6	4
33	2008.05.13	0:28:53	31.26	103.76	16	4.5	4
34	2008.05.13	13:36:29	32.47	105.23	11	4.4	3
35	2008.05.12	20:15:40	31.87	104.57	9	4.3	10
36	2008.05.12	20:11:59	31.32	104.24	15	4.2	7
37	2008.05.13	7:43:51	31.37	104.34	14	4	3

(Satriano et al., 2011). While on the other hand, the on-site system often consists of a limited set of seismic stations located at particular target sites of interest, which typically provide rapid ground motion estimates, using only information on the characteristics of P waves recorded at one seismic station, where an early warning is often most needed (Kanamori, 2005). A number of algorithms account for the uncertainties of ground motion estimation by considering a confidence interval on the estimate with width equivalent to two standard deviations of the empirical relationship used to derive ground shaking (Wu and Kanamori, 2005; Wu and Kanamori, 2008; Zollo et al., 2010; Zollo et al., 2016).

Western China is an earthquake-prone area with high intensity and frequency, which poses a great threat to the city and transportation system (Xu et al., 2009). For instance, most of the high-speed railways in China have no choice but to be constructed in the areas of moderate to high level of seismic fortification intensity, being prone to derail or overturn in case of dynamic actions and causing catastrophic hazards, even in small seismic events. Effective detection of these events is a necessary condition for disaster prevention and mitigation. However, since China is of a vast territory, it is not possible to set up dense strong ground motion station networks on a large scale at present, and for infrastructures such as high-speed railway which is linearly distributed, it is required to investigate the approach that can be used for single station, which is also expected to improve the reliability of an on-site system, where no information or constraint on the earthquake source is available in real-time.

In this paper, aiming at the ground motion estimation using the initial P wave and among the possible parameters measurable in real-time, i.e., the peak measurements and the integral quantities, we investigated eight representative parameters using the database of the 2008 Wenchuan earthquake (China Strong Motion Networks Centre, 2020). The estimation accuracy and reliability in the established relationships toward four different ground motion parameters are analyzed, respectively. To further investigate that to what an extent the initial signal window length could affect the estimates, we compared the variation tendency of standard deviation and determination coefficient between the leading parameters and the corresponding ground motion parameters of different time window. We found that the integral quantities could also be a robust estimator for PGA, PGV

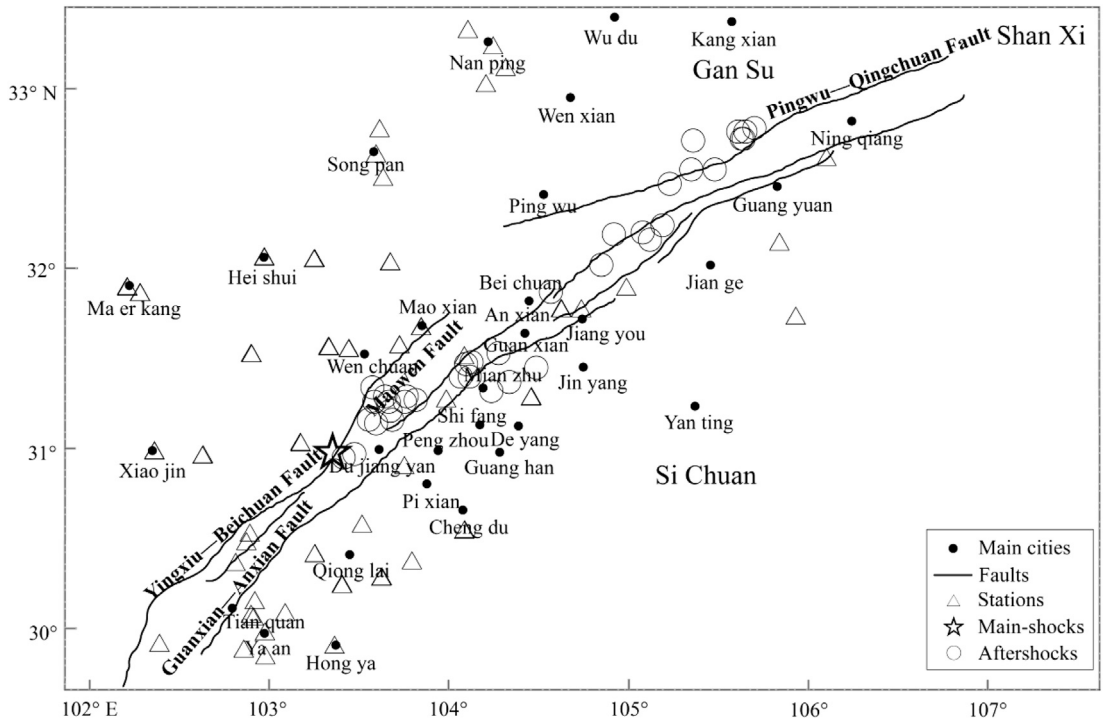

FIGURE 1 | Map of stations (triangles) and the main-shock (star) together with the aftershocks (circles) used in this study. A sketch indicating the surface rupture area.

TABLE 2 | Regression coefficients of the characteristic parameters and PGA.

(s)	PGA	P_a	P_v	P_d	IA2	IV2	ID2	CAV	si
1	A	0.730	0.771	0.557	0.372	0.384	0.238	0.748	0.743
	B	0.561	1.844	2.187	0.907	2.162	2.126	0.982	1.572
	stv	0.244	0.245	0.355	0.245	0.260	0.382	0.245	0.274
	R^2	0.723	0.719	0.410	0.719	0.683	0.317	0.720	0.684
2	A	0.786	0.791	0.564	0.413	0.397	0.250	0.831	0.760
	B	0.463	1.811	2.154	0.745	2.073	2.094	0.712	1.467
	stv	0.205	0.231	0.347	0.200	0.244	0.371	0.203	0.248
	R^2	0.803	0.751	0.436	0.813	0.722	0.357	0.808	0.703
3	A	0.814	0.786	0.535	0.429	0.400	0.246	0.867	0.776
	B	0.417	1.774	2.056	0.653	2.008	2.009	0.542	1.410
	stv	0.195	0.227	0.354	0.184	0.238	0.369	0.186	0.245
	R^2	0.823	0.760	0.414	0.843	0.735	0.362	0.841	0.731

Note: R^2 is the coefficient of determination.

and SI, while the peak measurement is more useful in estimating PGD. In addition, we show that for estimating the ground motion of events with magnitudes less than 6.5, a 1 s of P wave is not enough, while a 2-s window could effectively improve the estimation accuracy, as the window increases to 3 s, the accuracy would further improve while the growth rate is not that much.

DATA AND PRE-PROCESSING

The 2008 Ms 8.0 Wenchuan earthquake provided an opportunity to collect sound qualified data in a large scale that China Strong Motion Net Centre (CSMNC) recorded 383 aftershocks until September 30, 2008 (China Strong Motion Networks Centre, 2020). More than 600 cases with magnitudes above Ms 4.0 were acquired, among them 56 aftershocks were larger than Ms 5.0 and 8 aftershocks, larger than Ms 6.0. These events were over a rupture length of about 300 km with focal depths ranging from 2 to 20 km. Since the near-fault records of the destructive earthquakes are most important for the EEW system purposes (Nakamura et al., 2011; Satriano et al., 2011), we then selected 37 aftershocks with the criteria that Ms greater than 4.0 and epicentral distance less than 150 km. However, some traces were not recorded from the very beginning that the first P wave arrivals were lost, which were not satisfied with the aim of our study and these cases were discarded.

These records were obtained by the strong motion seismographs with a dynamic range of ±2 g mainly installed at free-field sites and the sampling rate was 200 Hz. We used the proposed three-step detection method to pick the P wave in real-time (Wang and Zhao, 2017) and double checked the arrival time by manual inspection for each waveform. In addition, each record has been checked that the signal noise ratio (SNR) above three is finally adopted (Küperkoch et al., 2010). With the detected P wave, the corresponding early-measured attributes could be calculated based on their formulas or physical meanings. The seismic events studied in this paper are listed in **Table 1** while the distributions of these events along the ruptures with the stations are shown in **Figure 1**.

TABLE 3 | Regression coefficients of the characteristic parameters and PGV.

(s)	PGV	P_a	P_v	P_d	IA2	IV2	ID2	CAV	si
1	A	0.613	0.770	0.721	0.310	0.398	0.325	0.626	0.740
	B	–0.947	0.289	1.029	–0.656	–0.655	1.043	–0.594	0.009
	stv	0.349	0.278	0.289	0.352	0.272	0.322	0.350	0.320
	R^2	0.472	0.665	0.639	0.464	0.680	0.552	0.468	0.556
2	A	0.690	0.818	0.727	0.362	0.426	0.336	0.730	0.814
	B	–1.044	0.289	0.977	–0.796	0.609	0.968	–0.825	–0.051
	stv	0.313	0.244	0.275	0.312	0.230	0.305	0.312	0.272
	R^2	0.574	0.743	0.672	0.579	0.771	0.598	0.577	0.682
3	A	0.728	0.822	0.736	0.385	0.434	0.331	0.779	0.864
	B	–1.091	0.263	0.887	–0.881	0.552	0.859	–0.980	–0.078
	stv	0.300	0.229	0.262	0.292	0.213	0.300	0.292	0.248
	R^2	0.609	0.772	0.702	0.631	0.803	0.610	0.630	0.742

TABLE 4 | Regression coefficients of the characteristic parameters and PGD.

(s)	PGD	P_a	P_v	P_d	IA2	IV2	ID2	CAV	si
1	A	0.439	0.712	0.928	0.211	0.376	0.445	0.431	0.542
	B	–1.749	–0.658	0.653	–1.543	–0.291	0.812	–1.499	–1.049
	stv	0.588	0.520	0.397	0.593	0.511	0.405	0.592	0.575
	R^2	0.139	0.326	0.607	0.123	0.349	0.592	0.127	0.176
2	A	0.578	0.831	0.976	0.300	0.446	0.472	0.604	0.713
	B	–1.859	–0.567	0.680	–1.652	–0.202	0.772	–1.676	–0.997
	stv	0.556	0.474	0.350	0.556	0.454	0.360	0.557	0.526
	R^2	0.231	0.441	0.696	0.229	0.486	0.678	0.227	0.311
3	A	0.640	0.842	0.980	0.344	0.465	0.473	0.695	0.797
	B	–1.916	–0.586	0.541	–1.733	–0.229	0.655	–1.822	–1.001
	stv	–0.541	0.464	0.338	0.535	0.434	0.339	0.535	0.494
	R^2	0.271	0.465	0.715	0.288	0.530	0.715	0.288	0.392

TABLE 5 | Regression coefficients of the characteristic parameters and SI.

(s)	SI	P_a	P_v	P_d	IA2	IV2	ID2	CAV	si
1	A	0.582	0.755	0.736	0.293	0.393	0.334	0.593	0.676
	B	–0.400	0.804	1.600	–0.124	1.173	1.623	–0.065	0.487
	stv	0.369	0.295	0.284	0.372	0.285	0.317	0.371	0.352
	R^2	0.418	0.629	0.655	0.408	0.653	0.571	0.413	0.470
2	A	0.662	0.806	0.746	0.347	0.423	0.346	0.700	0.754
	B	–0.495	0.810	1.555	–0.258	1.133	1.551	–0.286	0.443
	stv	0.335	0.260	0.267	0.334	0.243	0.297	0.335	0.298
	R^2	0.520	0.711	0.696	0.524	0.747	0.623	0.522	0.606
3	A	0.701	0.812	0.755	0.372	0.431	0.339	0.753	0.842
	B	–0.542	0.786	1.462	–0.340	1.080	1.430	–0.436	0.445
	stv	0.322	0.247	0.253	0.314	0.226	0.295	0.315	0.257
	R^2	0.557	0.741	0.727	0.579	0.782	0.629	0.578	0.712

After the baseline error correction for the acceleration records, the signals were integrated to velocity records, and velocity records to displacement records, since they were required in the characteristic parameter calculations. Then, we applied a causal two-pole Butterworth filter with a cut-off frequency of 0.075 Hz on the vertical component to remove the undesired long-period trends after numerical integration (Boore et al., 2002). Zollo et al. (2010) have shown that this cut-off frequency preserves a scaling of the EEW parameters with magnitude in a broad range.

EEW Parameters Versus Ground Motion Parameters

The strengths of critical ground motions can be defined by the shock wave, where its effects are practically represented by the peak

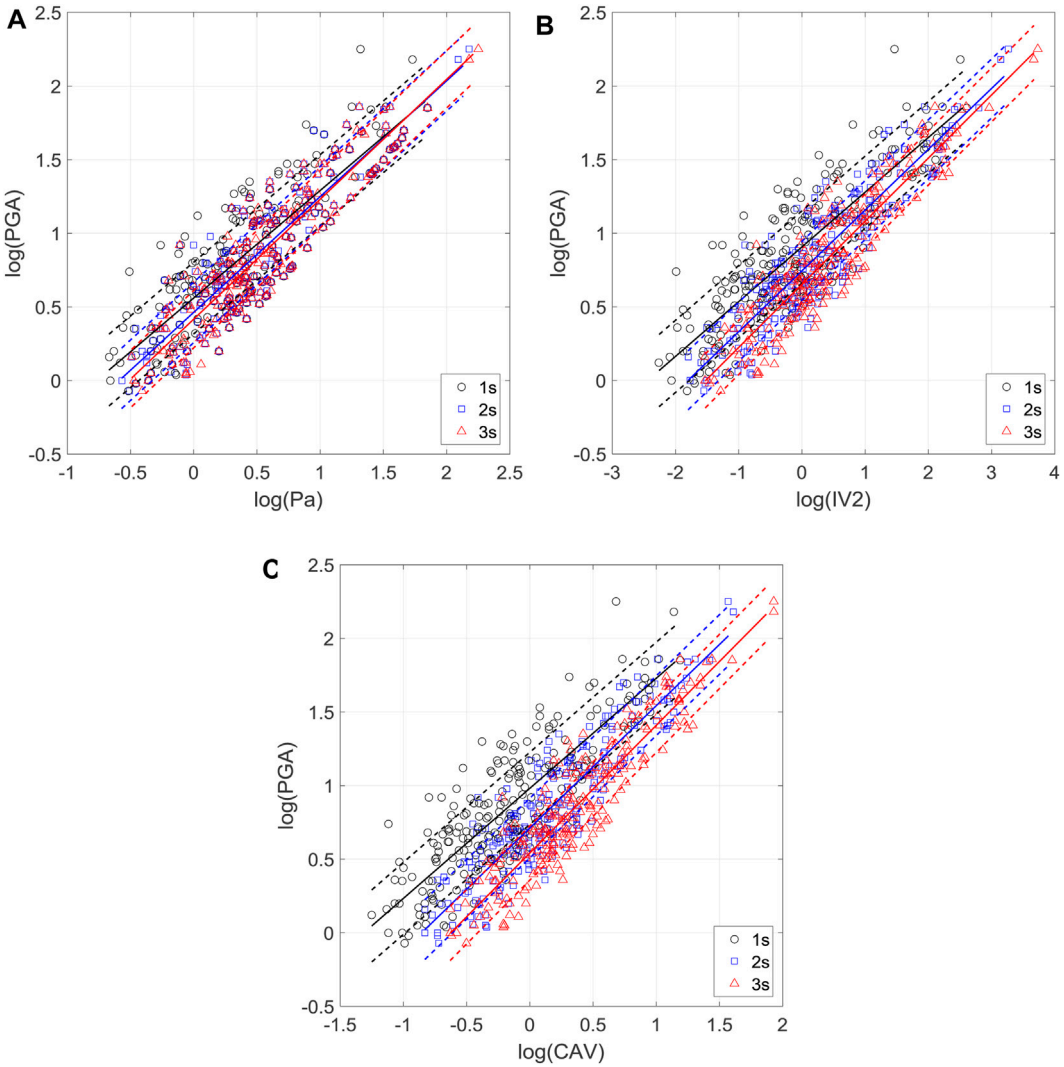

FIGURE 2 | (A–C) show P_a, IA2, and CAV calculated from the first 1 s (dark circles), 2 s (blue squares), and 3 s (red triangles) of P wave data, respectively. The PGA regression relationships determined by this study are shown as solid lines, and the standard deviations are shown as dashed lines.

ground acceleration (PGA), peak ground velocity (PGV), and peak ground displacement (PGD). In addition, the spectral intensity (SI) is defined as follows by Housner who regarded it as a seismic index reflecting the earthquake destructive power (Housner, 1952):

$$SI_\zeta = \int_{0.1}^{2.5} S_v(T,\zeta)dT, \quad (1)$$

where S_v is the relative velocity response spectrum of a single-degree-of-freedom system, T is the period, and ζ is the damping ratio which was set as 0.05 herein.

Therefore, for the EEW purposes, we used the PGA, PGV, PGD, and SI as parameters to assess the strengths of the ground motions during earthquake damage.

Normally a certain time window following the initial P wave arrival time t_i is used to determine the early-measured parameters, and among the possible parameters measurable in real-time, they could be categorized according to the signal type on which they are measured or their physical interpretation. The peak measurements, for example, the use of the peak displacement (P_d), peak velocity (P_v), or peak acceleration (P_a), of the first few seconds of the P wave have been shown to scale with ground motion (Colombelli et al., 2015; Bose et al., 2009). On the other hand, the integral quantities, for instance, the cumulative absolute velocity (CAV), are used in Istanbul EEW system (Erdik et al., 2003) as a rapid detector for strong ground shaking, which is computed from the integral of the acceleration a(t) as $CAV = \int_{t_i}^{t_{max}} |a(t)|dt$. The integral of the squared velocity (IV2), defined as $IV2 = \int_{t_i}^{t} v(t)^2 dt$, is related to the early-radiated energy (Festa et al., 2008). Wang and Zhao proposed to use the squared displacement integral (ID2), specified as $IV2 = \int_{t_i}^{t_i+\tau_o} u^2 dt$, to reflect the information of different periods from advancing rupture on fault plane (Wang and Zhao, 2018). However, there are several unresolved issues, for example, the

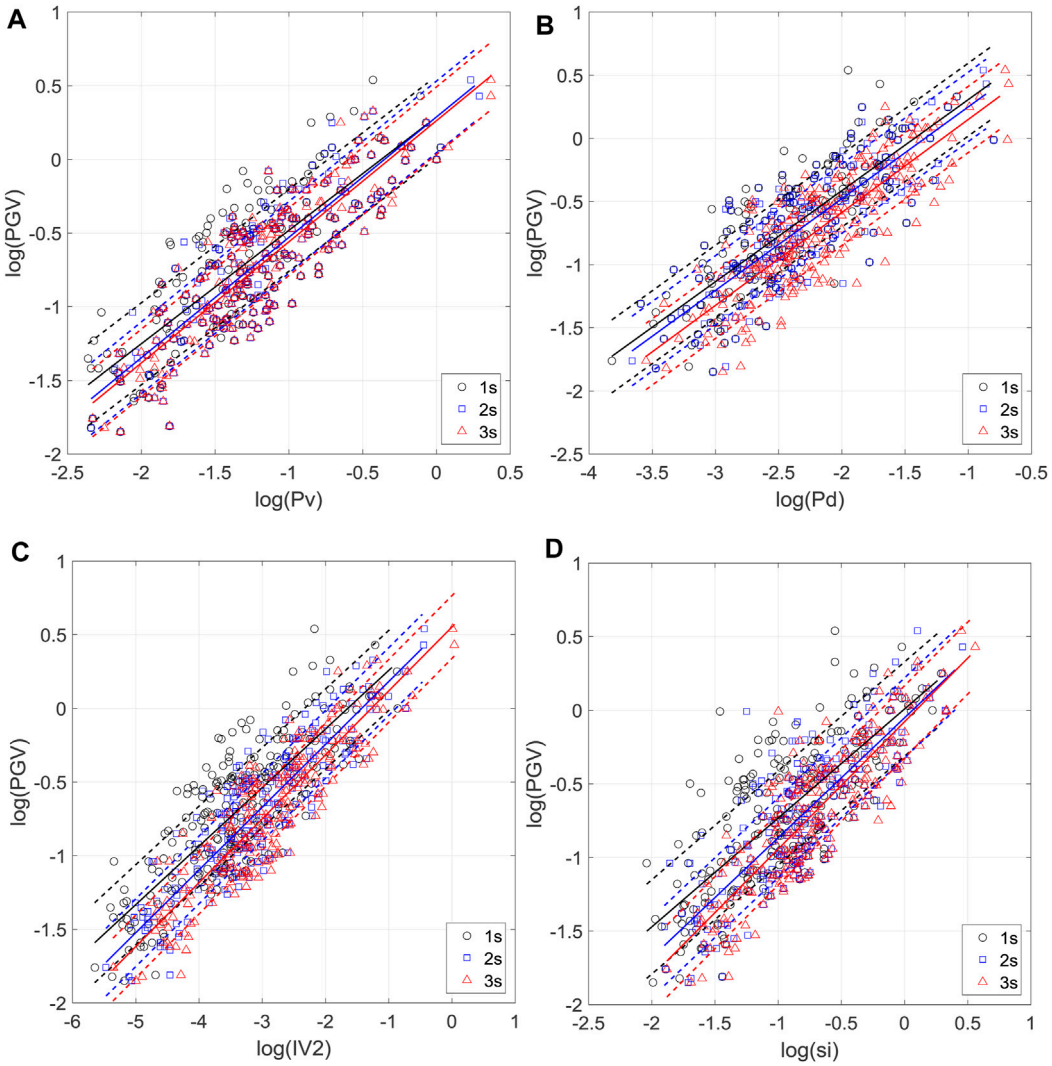

FIGURE 3 | (A–D) show P_v, P_d, IV2, and si calculated from the first 1 s (dark circles), 2 s (blue squares), and 3 s (red triangles) of P wave data, respectively. The PGV regression relationships determined by this study are shown as solid lines, and the standard deviations are shown as dashed lines.

estimation accuracy and reliability, in the empirical relationships toward different ground motion parameters and to what an extent that the length of the signal window could affect the estimates.

Therefore, on the basis of the initial P wave arrival time t_i, the early-measurable parameters were investigated and a linear regression model between the ground motion and the characteristic parameters is assumed as follows:

$$\log(P_{GM}) = A \times \log(P_{EEW}) + B \pm stv \quad (2)$$

where the P_{GM} stands for the ground motion parameters, i.e., PGA, PGV, PGD, and SI, P_{EEW} stands for the EEW characteristic parameters, i.e., P_a, P_v, P_d, IA2, IV2, ID2, CAV, and si, A and B are constants that are to be determined from the regression analysis, and stv is the standard deviation.

RESULTS

Since better estimates might be obtained by expanding the observation time window to update the characteristic parameters, the time windows of 1 s to 3 s are investigated, respectively. Under the current analytical form, the resulting best-fitting regression coefficients for the four ground motion parameters and the corresponding characteristic parameters are listed in **Tables 2**, **5**.

With the calculated standard deviation stv and the coefficient of determination R^2, the leading characteristic parameters for better estimating the ground motion parameters are selected. As for PGA, among the investigated parameters, P_a, IA2, and CAV could be good estimators that the corresponding stv reduce to 0.195, 0.184, and 0.186 while the R^2 rise to 0.823, 0.843, and 0.841 of a 3-s window, respectively. With regard to PGV, the

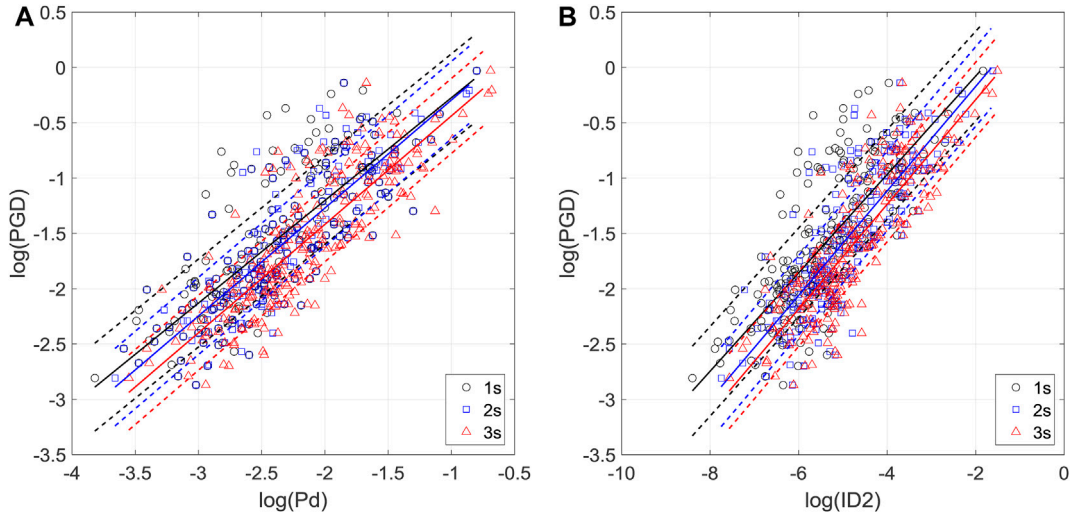

FIGURE 4 | (A–B) show P_d and ID2 calculated from the first 1 s (dark circles), 2 s (blue squares), and 3 s (red triangles) of P wave data, respectively. The PGD regression relationships determined by this study are shown as solid lines, and the standard deviations are shown as dashed lines.

characteristic parameters P_v, P_d, IV2, and si could give a better estimation that the stv are equal to 0.229, 0.262, 0.213, and 0.248 while the R^2 equal 0.772, 0.702, 0.803, and 0.742 of a 3-s window, respectively. In addition, the characteristic parameters correlate with displacement, i.e., P_d and ID2 are suitable for estimating PGD that the stv of the two correlations are 0.338 and 0.339 while both give a R^2 of 0.715 considering a 3-s window, respectively. In regard to SI, the characteristic parameters P_v, P_d, and IV2 could get good results that the stv are 0.247, 0.253, and 0.226 while the R^2 reach to 0.741, 0.727, and 0.782 of a 3-s window. Generally, the selected characteristic parameters used for estimating PGA demonstrate a highest correlation within the analyzed data, and the situations of PGV and SI are relatively on the same level, better than that of PGD.

With the corresponding leading parameters for estimating the four ground motion parameters, **Figures 2**, **5** illustrate the linear regressions curves aiming PGA, PGV, PGD, and SI, respectively. In each figure, the characteristic parameters calculated from the first 1 s, 2 s, and 3 s are shown with circles, squares, and triangles, respectively, where the solid line refers to the regression relationship while the dashed lines stand for the standard deviations. The regression curves show that the investigated characteristic parameters correlate well with the ground motion parameters, and the uncertainties of the ground motion determination for the events reduce along with the increases of the time windows, since most of the seismic accumulated energy could be released in a short time.

To further investigate that to what an extent the length of the initial signal window could affect the estimations, we compared the variation tendency of standard deviation and determination coefficient between the leading parameters and the corresponding ground motion parameters of different time window, which are shown in **Figure 6**. From the variation slope of each investigated parameter, both stv and R^2 could reflect the correlations with the increasing of the time window. For most cases, there is a significant stv reduction and R^2 increase while a gentle change for 1–2 s and 2–3 s, respectively. Specifically, we calculated the increase rates Δ of the standard deviation stv between each time window interval for each investigated correlations, which are listed in **Table 6**, **9**. For PGA, the reduction rates of stv among the three characteristic parameters are all above 15% over 1 to 2 s, where the IA2 has the highest rate of 18.37%, while those of the 2–3 s are reduced to 4.88–8.37%. With regard to PGV, the performance of P_v, IV2, and si demonstrated a similar trend as parameters for PGA, while which of P_d is slight small, giving a decrease rate of 4.84% for 1–2 s and 4.73% for 2–3 s, respectively. As for PGD and SI, except for P_d who performed similar as the case for PGV, the decrease rates of stv of other characteristic parameters are around 11.11–14.74% over 1–2 s and 3.43–7.0% over 2–3 s.

DISCUSSION AND CONCLUSION

In this paper, the proposed method is envisaged to be based on a single station and is expected to improve the reliability of an on-site system, where no information or constraint on the earthquake source is available in real-time. Aiming at the ground motion estimation using the initial P wave, we have investigated the continuous measurement of eight attributes for the fast prediction of the expected shaking at the same site, where the estimation accuracy and reliability toward different ground motion parameters and to what an extent that the length of the signal window could affect the estimates are proposed. Although the single station method is conceived, the methodology proposed here could be easily integrated in a network-based EEW platform.

The EEW characteristic parameters, i.e., P_a, P_v, P_d, IA2, IV2, ID2, CAV, and si values, for the selected aftershocks ($4.0 \leq Ms \leq 6.5$) of the 2008 Wenchuan earthquake were calculated,

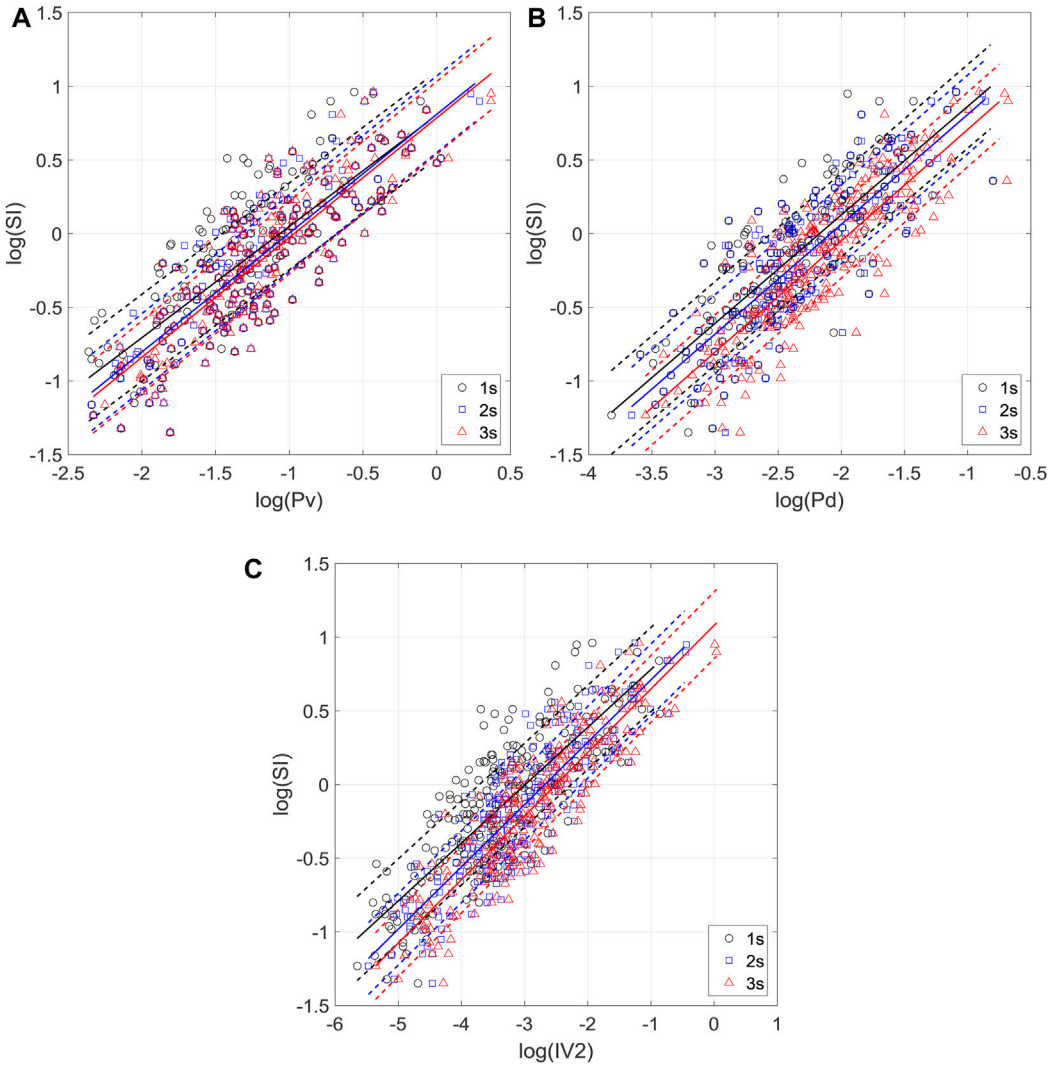

FIGURE 5 | (A–C) show P_v, P_d, and IV2 calculated from the first 1 s (dark circles), 2 s (blue squares), and 3 s (red triangles) of P wave data, respectively. The SI regression relationships determined by this study are shown as solid lines, and the standard deviations are shown as dashed lines.

and regression relationships between each of these parameters and ground motion parameters, i.e., PGA, PGV, PGD, and SI, were established, respectively. Our results show that for PGA, the characteristic parameters P_a, IA2, and CAV could be good estimators and for PGV, the P_v, P_d, IV2, and si could give a better estimation. The P_d and ID2 are suitable for estimating PGD while in regard to SI, the P_v, P_d, and IV2 could get good results. Therefore, for different ground motion parameters, using an appropriate parameter is necessary while it also could be suggested to combine two of the possible parameters together in the real EEW operations. In addition, the predicted peak ground shaking can be used to determine the expected intensity, through a regression relationship.

The integral quantities, i.e., IV2, ID2, and CAV, are directly correlated with the radiated energy E in the initial stages of seismic ruptures, which are often used to correlate the final earthquake size (Allen et al., 2009; Colombelli and Zollo, 2016). However, in this study, it is found these parameters could also link ground motion parameters. In addition, we also found that the frequency parameter si could correlate ground motion parameters (e.g., PGA and PGV that reflect the ground shaking intensity) well. Since the observation stations were mainly set on soil conditions, it is inferred that this frequency parameter can reflect information of site effects.

Since time is the key parameter of the early warning system, the longer the available time before the disaster phenomenon reaches the target, the more effective and comprehensive the countermeasures can be taken. In contrast of regional EEW systems, which yield more accurate estimates of the source parameters, the on-site EEW systems could provide faster warning times for near-source targets at the price of a lower accuracy on the estimation of earthquake parameters. There is always a trade-off between the early warning time and the reliability of earthquake information. From our results, a 2-s

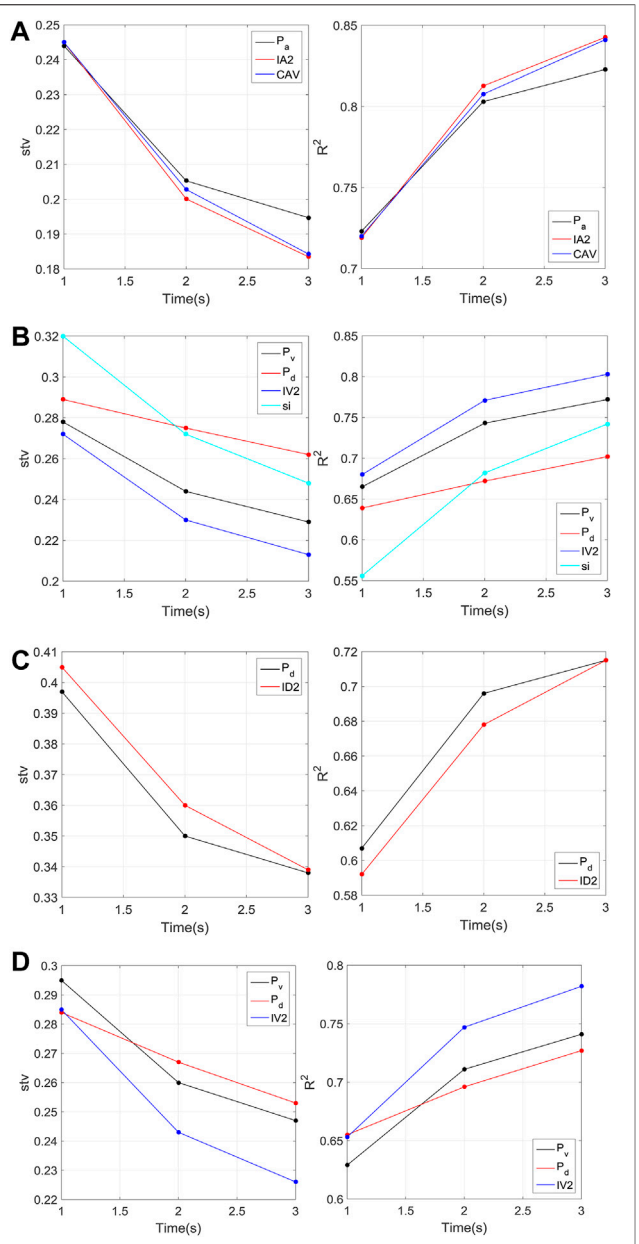

FIGURE 6 | Comparison of the standard deviation and coefficient of determination between the leading parameters for estimating **(A)** PGA, **(B)** PGV, **(C)** PGD, and **(D)** SI, respectively.

window could effectively improve the estimation accuracy by approximately 11.5–18.5% compared with using a 1-s window, as the window increases to 3 s, the accuracy would further improve while the growth rate will be reduced to around 3.0–8.0%. That is to say, for appropriate correlations between the characteristic parameters and ground motion parameters, a 2 s initial P wave might be enough for the first alert; meanwhile, the updating procedures should be considered certainly in real operations.

The 2008 Ms 8.0 Wenchuan earthquake occurred along the Longmenshan faults (Li et al., 2008), consisting of mountain-front fault, central fault, and mountain-back fault, which are

TABLE 6 | Comparison of the standard deviation stv between the leading 3 parameters for estimating PGA.

PGA	P_a		IA2		CAV	
	stv	Δ (%)	stv	Δ (%)	stv	Δ (%)
1	0.244	15.98	0.245	18.37	0.245	17.14
2	0.205	4.88	0.200	8.00	0.203	8.37
3	0.195		0.184		0.186	

TABLE 7 | Comparison of the standard deviation stv between the leading 4 parameters for estimating PGV.

PGV	P_v		P_d		IV2		si	
	stv	Δ (%)	stv	Δ (%)	stv	Δ (%)	stv	Δ (%)
1	0.278	12.23	0.289	4.84	0.272	15.44	0.320	15.00
2	0.244	6.15	0.275	4.73	0.230	7.39	0.272	8.82
3	0.229		0.262		0.213		0.248	

TABLE 8 | Comparison of the standard deviation stv between the leading 2 parameters for estimating PGD.

PGD	P_d		ID2	
	stv	Δ (%)	stv	Δ (%)
1	0.397	11.84	0.405	11.11
2	0.350	3.43	0.360	5.83
3	0.338		0.339	

TABLE 9 | Comparison of the standard deviation stv between the leading 3 parameters for estimating SI.

SI	P_v		P_d		IV2	
	stv	Δ (%)	stv	Δ (%)	stv	Δ (%)
1	0.295	11.86	0.284	5.99	0.285	14.74
2	0.260	5.00	0.267	5.24	0.243	7.00
3	0.247		0.253		0.226	

situated in the transitional area from the Tibetan Plateau to the South China Plate. This complicated geological and topographic environment caused complex focal mechanisms, propagation processes, and site effects, resulting in the ground motions to have the nature of complexity. Because aftershocks distribute on different secondary faults, their focal mechanisms present complex local tectonic stress field and even vary with time. Generally, for the southern segment, the thrust component is stronger than strike-slip component, while the northern segment corresponds to a section of mostly strike-slip mechanism; the middle segment may be related to the transition between the southern and northern segments (Zheng et al., 2010; Yi et al., 2012), since the used data cover the general magnitude gradients that are of concern for EEW systems, and multiple stations recorded the wave forms for each event within the specified range, providing important benefits for EEW studies. In addition, the earthquake rupture and the propagation process should be

investigated and studied to develop a better theoretical research of the phase nature.

The paper tested different attributes for the fast prediction of the expected shaking in real-time, while practical operations require consideration of other aspects. For example, the observation stations should be built with the ability to provide early warnings that the detection instruments are capable of improving the signal quality, especially for the vertical component. In addition, appropriate investigations of the observation locations with detailed surrounding seismic environments are also necessary. When calibrating the proposed method for a specific area, the possible impact of site effect, which may produce local, systematic amplification/attenuation of the perceived shaking, is required to have a detailed analysis.

DATA AVAILABILITY STATEMENT

The original contributions presented in the study are included in the article/Supplementary Material; further inquiries can be directed to the corresponding author.

AUTHOR CONTRIBUTIONS

ZW: conceptualization, methodology, data analysis, visualization, and writing the original draft. BZ: methodology, writing—review and editing, and supervision.

FUNDING

This research has been supported by the National Natural Science Foundation of China (Grant Nos. 51808045; 51778046; U1434210), the Research Grants from the National Institute of Natural Hazards, Ministry of Emergency Management of China (Grant No. ZDJ2020-14), and the Fundamental Research Funds for the Central Universities (2019RC047).

ACKNOWLEDGMENTS

We would like to thank the China Strong Motion Net Centre for the recorded data.

REFERENCES

Allen, R. M., and Melgar, D. (2019). Earthquake Early Warning: Advances, Scientific Challenges, and Societal Needs. *Annu. Rev. Earth Planet. Sci.* 47, 361–388. doi:10.1146/annurev-earth-053018-060457

Allen, R. M., Gasparini, P., Kamigaichi, O., and Böse, M. (2009). The Status of Earthquake Early Warning Around the World: An Introductory Overview. *Seismological Res. Lett.* 80, 682–693. doi:10.1785/gssrl.80.5.682

Boore, D. M., Stephens, C. D., and Joyner, W. B. (2002). Comments on Baseline Correction of Digital strong-motion Data: Examples from the 1999 Hector Mine, California, Earthquake. *Bull. Seismological Soc. America* 92, 1543–1560. doi:10.1785/0120000926

Bose, M., Hauksson, E., Solanki, K., Kanamori, H., Wu, Y.-M., and Heaton, T. H. (2009). A New Trigger Criterion for Improved Real-Time Performance of Onsite Earthquake Early Warning in Southern California. *Bull. Seismological Soc. America* 99 (2A), 897–905. doi:10.1785/0120080034

China Strong Motion Networks Centre (2020). China Strong Motion Networks Centre. Available at: www.cenc.ac.cn (Accessed November 05, 2020).

Colombelli, S., Caruso, A., Zollo, A., Festa, G., and Kanamori, H. (2015). A P Wave-based, On-site Method for Earthquake Early Warning. *Geophys. Res. Lett.* 42, 1390–1398. doi:10.1002/2014gl063002

Colombelli, S., and Zollo, A. (2016). Rapid and Reliable Seismic Source Characterization in Earthquake Early Warning Systems: Current Methodologies, Results, and New Perspectives. *J. Seismol.* 20 (4), 1–16. doi:10.1007/s10950-016-9570-z

Cremen, G., and Galasso, C. (2020). Earthquake Early Warning: Recent Advances and Perspectives. *Earth-Science Rev.* 205, 103184. doi:10.1016/j.earscirev.2020.103184

Erdik, M., Fahjan, Y., Ozel, O., Alcik, H., Mert, A., and Gul, M. (2003). Istanbul Earthquake Rapid Response and the Early Warning System. *Bull. Earthquake. Eng.* 1, 157–163. doi:10.1023/a:1024813612271

Festa, G., Zollo, A., and Lancieri, M. (2008). Earthquake Magnitude Estimation from Early Radiated Energy. *Geophys. Res. Lett.* 35, L22307. doi:10.1029/2008gl035576

Hoshiba, M. (2014). Review of the Nationwide Earthquake Early Warning in Japan during its First Five Years. *Earthquake Hazard. Risk Disasters* 2014, 509–529. doi:10.1016/b978-0-12-394848-9.00019-5

Housner, G. W. (1952). *Intensity of Ground Motion during Strong Earthquakes*. California: California Institute of Technology.

Kanamori, H. (2005). Real-Time Seismology and Earthquake Damage Mitigation. *Annu. Rev. Earth Planet. Sci.* 33, 195–214. doi:10.1146/annurev.earth.33.092203.122626

Küperkoch, L., Meier, T., Lee, J., and Friederich, W.EGELADOS Working Group (2010). Automated Determination of P-phase Arrival Times at Regional and Local Distances Using Higher Order Statistics. *Geophys. J. Int.* 181, 1159–1170. doi:10.1111/j.1365-246x.2010.04570.x

Li, Z. Q., Yuan, Y. F., Li, X. L., and Zeng, J. (2008). Preliminary Research on the Characteristics of the Ms 8.0 Wenchuan Earthquake hazard. *Seismol. Geol.* 30 (4), 855–876.

Nakamura, Y., Saita, J., and Sato, T. (2011). On an Earthquake Early Warning System (EEW) and its Applications. *Soil Dyn. Earthquake Eng.* 31, 127–136. doi:10.1016/j.soildyn.2010.04.012

Satriano, C., Wu, Y.-M., Zollo, A., and Kanamori, H. (2011). Earthquake Early Warning: Concepts, Methods and Physical Grounds. *Soil Dyn. Earthquake Eng.* 31, 106–118. doi:10.1016/j.soildyn.2010.07.007

Wang, Z., and Zhao, B. (2017). Automatic Event Detection and Picking of P, S Seismic Phases for Earthquake Early Warning and Application for the 2008 Wenchuan Earthquake. *Soil Dyn. Earthquake Eng.* 97, 172–181. doi:10.1016/j.soildyn.2017.03.017

Wang, Z., and Zhao, B. (2018). Method of Accurate-Fast Magnitude Estimation for Earthquake Early Warning -----Trial and Application for the 2008 Wenchuan Earthquake. *Soil Dyn. Earthquake Eng.* 109, 227–234. doi:10.1016/j.soildyn.2018.03.006

Wu, Y.-M., and Kanamori, H. (2008). Development of an Earthquake Early Warning System Using Real-Time strong Motion Signals. *Sensors* 8 (1), 1–9. doi:10.3390/s8010001

Wu, Y.-M., and Kanamori, H. (2005). Rapid Assessment of Damage Potential of Earthquakes in Taiwan from the Beginning of P Waves. *Bull. Seismological Soc. America* 95 (3), 1181–1185. doi:10.1785/0120040193

Xu, X., Wen, X., Yu, G., Chen, G., Klinger, Y., Hubbard, J., et al. (2009). Coseismic Reverse- and Oblique-Slip Surface Faulting Generated by the 2008 Mw 7.9 Wenchuan Earthquake, China. *Geology* 37, 515–518. doi:10.1130/g25462a.1

Yi, G. X., Long, F., and Zhang, Z. W. (2012). Spatial and Temporal Variation of Focal Mechanisms for Aftershocks of the 2008 Ms8.0 Wenchuan Earthquake. *Chin. J. Geophys.* 55 (4), 1213–1227.

Zheng, Y., Ni, S., Xie, Z., Lv, J., Ma, H., and Sommerville, P. (2010). Strong Aftershocks in the Northern Segment of the Wenchuan Earthquake Rupture Zone and Their Seismotectonic Implications. *Earth Planet. Sp* 62 (11), 881–886. doi:10.5047/eps.2009.06.001

Zollo, A., Amoroso, O., Lancieri, M., Wu, Y.-M., and Kanamori, H. (2010). A Threshold-Based Earthquake Early Warning Using Dense Accelerometer Networks. *Geophys. J. Int.* 183, 963–974. doi:10.1111/j.1365-246x.2010.04765.x

Zollo, A., Colombelli, S., and Emolo, A. (2016). An Integrated Regional and On-Site Earthquake Early Warning System for Southern Italy: Concepts, Methodologies and Performances. *Early Warning Geol. Disasters, chapter 7*, 117–137. doi:10.1007/978-3-642-12233-0_7

Conflict of Interest: The authors declare that the research was conducted in the absence of any commercial or financial relationships that could be construed as a potential conflict of interest.

Publisher's Note: All claims expressed in this article are solely those of the authors and do not necessarily represent those of their affiliated organizations, or those of the publisher, the editors, and the reviewers. Any product that may be evaluated in this article, or claim that may be made by its manufacturer, is not guaranteed or endorsed by the publisher.

frontiers in Earth Science

REVIEW
published: 22 September 2021
doi: 10.3389/feart.2021.722784

Real-Time Prediction of Impending Ground Shaking: Review of Wavefield-Based (Ground-Motion-Based) Method for Earthquake Early Warning

Mitsuyuki Hoshiba *

Meteorological Research Institute, Japan Meteorological Agency, Tsukuba, Japan

Earthquake early warning (EEW) systems aim to provide advance warning of impending ground shaking, and the technique used for real-time prediction of shaking is a crucial element of EEW systems. Many EEW systems are designed to predict the strength of seismic ground motions (peak ground acceleration, peak ground velocity, or seismic intensity) based on rapidly estimated source parameters (the source-based method), such as hypocentral location, origin time, magnitude, and extent of fault rupture. Recently, however, the wavefield-based (or ground-motion-based) method has been developed to predict future ground motions based directly on the current wavefield, i.e., ground motions monitored in real-time at neighboring sites, skipping the process of estimation of the source parameters. The wavefield-based method works well even for large earthquakes with long duration and huge rupture extents, highly energetic earthquakes that deviate from standard empirical relations, and multiple simultaneous earthquakes, for which the conventional source-based method sometimes performs inadequately. The wavefield-based method also enables prediction of the ongoing seismic waveform itself using the physics of wave propagation, thus providing information on the duration, in addition to the strength of strong ground motion for various frequency bands. In this paper, I review recent developments of the wavefield-based method, from simple applications using relatively sparse observation networks to sophisticated data assimilation techniques exploiting dense networks.

Keywords: earthquake early warning, real-time prediction, seismic ground motion, wavefield, data assimilation, site amplification

OPEN ACCESS

Edited by:
Mourad Bezzeghoud, Universidade de Évora, Portugal

Reviewed by:
Aldo Zollo, University of Naples Federico II, Italy
Maurizio Mattesini, Complutense University of Madrid, Spain

***Correspondence:**
Mitsuyuki Hoshiba
mhoshiba@mri-jma.go.jp

Specialty section:
This article was submitted to Solid Earth Geophysics, a section of the journal Frontiers in Earth Science

Received: *09 June 2021*
Accepted: *06 September 2021*
Published: *22 September 2021*

Citation:
Hoshiba M (2021) Real-Time Prediction of Impending Ground Shaking: Review of Wavefield-Based (Ground-Motion-Based) Method for Earthquake Early Warning. Front. Earth Sci. 9:722784. doi: 10.3389/feart.2021.722784

INTRODUCTION

Earthquake early warning (EEW) aims to prevent/mitigate earthquake disasters by providing people with enough time to take appropriate safety measures in advance of impending strong ground motion. EEW systems have been researched and developed in Japan, Mexico, Taiwan, the United States, European countries, China, Turkey, south Korea, and many other regions (e.g., Hoshiba et al., 2008; Cuellar et al., 2014; Chen et al., 2015; Cochran et al., 2018). The prediction of

strong ground motions is an important element of EEW, and many methods have been proposed; the basic algorithms are classified into three prediction concepts:

1): Predicting seismic wave propagation;
2): Predicting the amplitude of *S*-waves from those of preceding *P*-wave; and
3): Predicting an entire rupture based on the initial rupture.

EEW algorithms are constructed based on one or combination of these concepts. For example, the operational EEW system of the Japan Methodological Agency (JMA) combines Concepts 1) and 2) but does not adopt Concept 3) (Hoshiba, 2014).

Concept 1) is based on the fact that modern communication speeds (~10^5 km/s) are much faster than seismic wave velocity (~10^0–10^1 km/s); information about seismic waves detected near a hypocenter can be relayed to distant locations much faster than the seismic waves propagate. This concept assumes that observation sites are closer to the hypocenter than the prediction (target) site; the seismic observation network thus plays an important role.

Concept 2) is based on the fact that amplitudes of early *P*-wave arrivals are usually smaller than those of late arriving *S*-waves. The *S*-wave/*P*-wave amplitude ratio has been estimated theoretically or empirically, and many authors take a value of ~5. Because communication is not necessarily required, this concept can be used for even a single isolated site. However, this concept cannot be used in cases when the earthquake rupture duration is longer than *S*-*P* time (the time between *P* and *S* wave arrives), because *P* waves from later large ruptures may be contaminated by *S* waves from earlier small ruptures. This situation usually occurs at sites near the hypocenter (that is, short *S*-*P* time) of large (that is, long rupture duration) earthquakes. Discrimination of *P* waves in *S* wave train is required.

Concept 3) is based on the hypothesis that initial parts of small and large earthquake ruptures differ. Some authors have claimed that the final moment magnitude (Mw) can be estimated from the first several seconds of *P*-wave portion even for large events of long rupture duration (typical durations are ~10 and 30 s for Mw7 and 8 earthquakes, respectively), and that it may be possible to rapidly estimate the final Mw while the rupture is still ongoing (e.g., Olson and Allen, 2005; Zollo et al., 2006; Noda and Ellsworth, 2016; Melgar and Hayes, 2019). However, many authors have challenged this deterministic view of ruptures claiming that they are nondeterministic and statistically common rupture growth (e.g., Rydelek and Horiuchi, 2006; Meier et al., 2016; Okuda and Ide, 2018; Trugman et al., 2019). The debate over the deterministic nature of earthquake rupture has continued for more than 2 decades in research on EEW and the physics of earthquake rupture dynamics. Although some EEW algorithms are based on this concept, but many others are not.

In this review paper, I focus on Concept (1). When the characteristics of wave propagation are expressed simply and the source location and strength are estimated quickly, it is possible to easily predict waves strength at a given location.

TABLE 1 | Summary of wavefield-based (ground-motion-based) methods for real-time prediction of ground motion.

Basic theory (and name of method)	**Finite difference**	**Boundary integral equation**		**Radiative transfer theory (Numerical Shake Prediction)**
		PLUM (Propagation of Local Undamped Motion): Simplified approach of boundary Integral equation		
Equation	$\frac{1}{c(\boldsymbol{x})^2}\ddot{u}(\boldsymbol{x},t) = \nabla^2 u(\boldsymbol{x},t)$	$u(\boldsymbol{x}_p,t) = \int_{-\infty}^{\infty} d\tau \int \left(u(\boldsymbol{x}_1,t) \frac{\partial G(\boldsymbol{x}_p,t-\tau;\boldsymbol{x}_1,0)}{\partial \tau} - G(\boldsymbol{x}_p,t-\tau;\boldsymbol{x}_1,0) \frac{\partial u(\boldsymbol{x}_1,\tau)}{\partial \tau} \right) dS$	Assumption of plane wave propagation: $\lvert u(\boldsymbol{x}_p,t)\rvert_{\max t} \le \mathrm{Max}_i \lvert u(\boldsymbol{x}_i,t)\rvert_{\max t}$	$\dot{f}(\boldsymbol{x},t;\boldsymbol{q}) + c(\boldsymbol{x})\boldsymbol{q}\cdot\nabla f(\boldsymbol{x},t;\boldsymbol{q})$ $= -(g_s(\boldsymbol{x}) + h_s(\boldsymbol{x}))\cdot c(\boldsymbol{x})\cdot f(\boldsymbol{x},t;\boldsymbol{q}) + \frac{c(\boldsymbol{x})}{4\pi} \int g_s(\boldsymbol{x}) f(\boldsymbol{x},t;\boldsymbol{q}')d\boldsymbol{q}'$
Data assimilation	Effective	Effective only for low frequency	-	Effective
Frequency	Low frequency	-	-	High frequency
References	Furumura et al. (2019) Oba et al. (2020)	Hoshiba, (2013a)	Kodera et al. (2018) Cochran et al. (2019) Minson et al. (2020) Kilb et al. (2021)	Hoshiba and Aoki (2015) Ogiso et al. (2018) Wang et al. (2017a), (b)

Many authors have thus proposed methods to rapidly estimate origin time, hypocentral location, and earthquake magnitude for EEW purposes (the point-source algorithm). Moreover, the rapid estimation of source extent has also been investigated (the finite fault algorithm) (Yamada, 2014; Böse et al., 2018). In these "source-based methods," the strength of ground motion (e.g., peak ground acceleration, PGA; peak ground velocity, PGV; and/or seismic intensity) is usually evaluated based on Mw and distance (e.g., hypocentral distance, epicentral distance, or fault distance) using a ground motion prediction equation (GMPE). Nonetheless, the source-based methods have vulnerabilities, including underpredicting ground motion for extended ruptures in point-source algorithms, and incorrectly identifying multiple simultaneous earthquakes. Even when the hypocenter and magnitude are estimated precisely, the precision of predicted ground-motion strengths are controlled by the uncertainty in the GMPE. Recent theoretical works have suggested that the source-based methods are inherently limited in terms of the timeliness and accuracy of its prediction (Minson et al., 2018, 2019; Hoshiba, 2020).

As an alternative to source-based methods, another algorithm that has been intensively investigated over recent decade does not necessarily require source parameters to predict the strength of ground motion. Instead, future ground motions are predicted directly from observed ground motion, skipping the process of source estimation. The "wavefield-based method" or "ground-motion-based method" (hereinafter "wavefield-based method" for simplicity) first estimates the current wavefield, then predicts future wavefield based on the physics of wave propagation. Because source parameters are not estimated, this method avoids the vulnerabilities of the source-based method (rupture extent, and simultaneous multiple earthquakes).

This paper reviews recent developments, the current situation, and future prospects of the wavefield-based method by comparison with the source-based method.

THEORETICAL BACKGROUND

Prediction of seismic wave propagation is a key element of Concept (1). Because seismic wave is controlled by the physics of wave propagation, future wavefield can be predicted by wave propagation theory. In this section, I explain the theoretical background based on three independent approaches (summarized in **Table 1**): the finite difference method, the boundary integral equation method, and radiative transfer theory (RTT). In the following subsections, scalar wave expression is used for simplicity although seismic waves are vector waves.

Finite Difference Method

Wave propagation is expressed by the wave equation:

$$\frac{1}{c(x)^2}\ddot{u}(\mathbf{x},t) = \nabla^2 u(\mathbf{x},t), \tag{1}$$

where $u(\boldsymbol{x}, t)$ is the wave amplitude at location $\boldsymbol{x}$ and at time t, c is phase velocity, ∇^2 is the Laplacian, and $\ddot{u}$ is the second order differential of u with respect to t (i.e., $\partial^2 u/\partial t^2$). This equation implies that the time-evolution of a wave's amplitude, $\ddot{u}$, is determined by its spatial distribution ($\nabla^2 u$). Therefore, future wavefields can be predicted from the spatial distribution of a known wavefield when the velocity structure, $c(\boldsymbol{x})$, is known (**Figure 1**). **Eq. 1** is approximated as

$$u(\boldsymbol{x}, t+\Delta t) \approx 2u(\boldsymbol{x}, t) - u(\boldsymbol{x}, t-\Delta t) + \Delta t^2 \cdot c(\boldsymbol{x})^2 \cdot \nabla^2 u(\boldsymbol{x}, t). \tag{2}$$

The wavefield one time step Δt in the future, $u(\boldsymbol{x}, t+\Delta t)$, can be estimated from the current wavefield, $u(\boldsymbol{x}, t)$, and that one time step prior, $u(\boldsymbol{x}, t-\Delta t)$. Then, $u(\boldsymbol{x}, t+2\Delta t)$ is computed from $u(\boldsymbol{x}, t+\Delta t)$ and $u(\boldsymbol{x}, t)$ as,

$$u(\boldsymbol{x}, t+2\Delta t) \approx 2u(\boldsymbol{x}, t+\Delta t) - u(\boldsymbol{x}, t) + \Delta t^2 \cdot c(\boldsymbol{x})^2 \cdot \nabla^2 u(\boldsymbol{x}, t+\Delta t). \tag{3}$$

Thus, the wavefield at any future time can be obtained by repeating this procedure as needed. Note that this assumes that no new waves are radiated in the future, i.e., that no new earthquakes occur over the prediction period.

In this approach, precise monitoring of the spatial distribution of $u(\boldsymbol{x}, t)$ and $u(\boldsymbol{x}, t-\Delta t)$ is important for precise predictions. Once the detailed distribution of $u(\boldsymbol{x}, t)$ and $u(\boldsymbol{x}, t-\Delta t)$ are obtained, source parameters (radiation location and the strength of radiated waves, i.e., hypocenter location and magnitude) are not needed to predict the future wavefield. For precise estimation of the current wavefield, data assimilation is a powerful tool, which will be explained in a later section.

Furumura et al. (2019) and Oba et al. (2020) applied the finite difference approach to predict long-period ground motions (>3–10 s). Because they used a three-dimensional (3-D) velocity structure, they were able to predict not only the waveforms of direct *P*- and *S*-waves, but also those of reflected, refracted and surface (Rayleigh and Love) waves. At present, however, the finite difference method is not useful for computing short-period ground motions (<1 s) because the very fine mesh size required exceeds modern computing capabilities and the very precise velocity structure required to simulate wave propagation is not easily obtained by current survey techniques.

Boundary Integral Equation Method

Whereas the finite differential method represents wave propagation using differential form of the wave equation (**Eq. (1)**), boundary integral equation takes its integral form;

$$u(\boldsymbol{x}_p, t) = \int_{-\infty}^{\infty} d\tau \int \left(u(\boldsymbol{x}_1, \tau) \frac{\partial G(\boldsymbol{x}_p, t-\tau; \boldsymbol{x}_1, 0)}{\partial n} - G(\boldsymbol{x}_p, t-\tau; \boldsymbol{x}_1, 0) \frac{\partial u(\boldsymbol{x}_1, \tau)}{\partial n} \right) dS, \tag{4}$$

in 3-D space, where S is the surface enclosing the target site, $\boldsymbol{x}_p$, $\boldsymbol{x}_1$ is a location on S, $\partial/\partial n$ is the derivative with respect to the normal vector to S at $\boldsymbol{x}_1$, and G is the Green's function. S can be taken arbitrarily (**Figure 2A**). Here, the integrations are performed with respect to $\boldsymbol{x}_1$

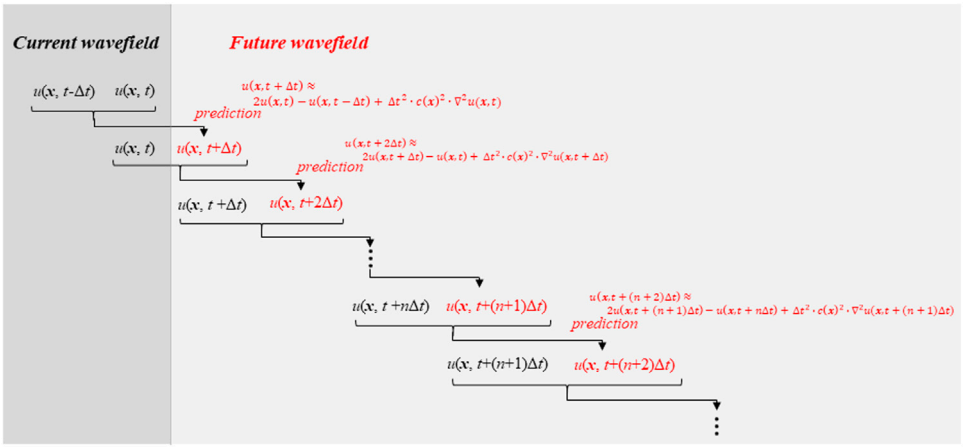

FIGURE 1 | The process for predicting future wavefield using the finite difference method. From the current wavefield, u ($\boldsymbol{x}$, t-Δt) and u ($\boldsymbol{x}$, t), the future wavefield, u ($\boldsymbol{x}$, t+Δt), is predicted, and then, from u ($\boldsymbol{x}$, t) and u ($\boldsymbol{x}$, t+Δt), u ($\boldsymbol{x}$, t+2Δt) is forecast. Repeating this process makes it possible to obtain the wavefields at any time in the future.

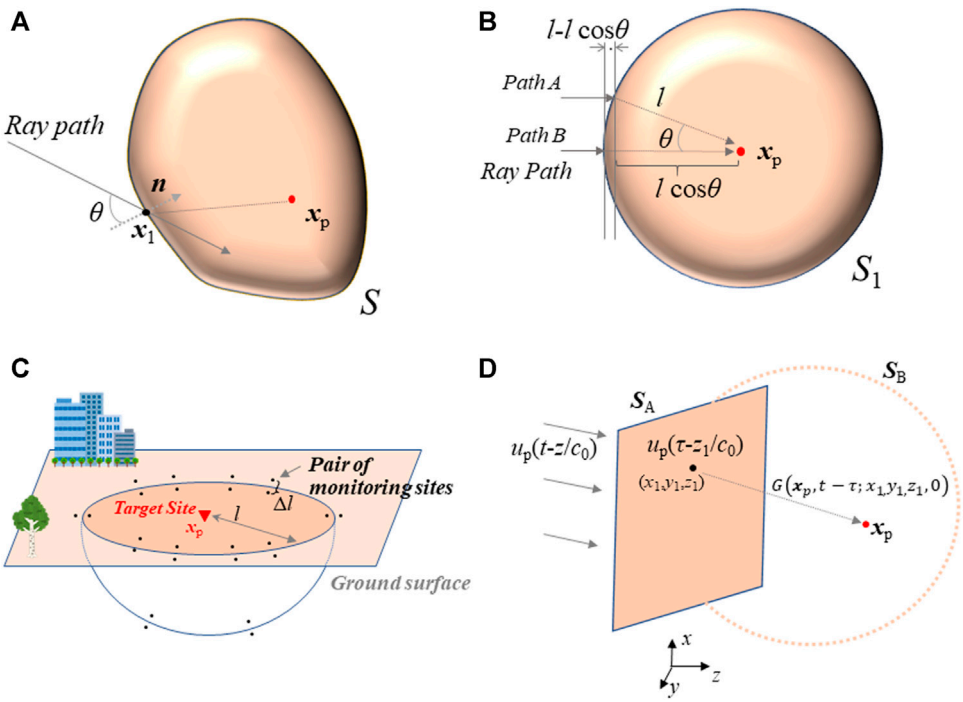

FIGURE 2 | Schematic illustration of the boundary integral equation method (After Hoshiba, 2013a). The surface S can be taken arbitrarily around the target site $\boldsymbol{x}_p$, and $\boldsymbol{x}_1$ is a location on S, and $\boldsymbol{n}$ is the normal vector to S at $\boldsymbol{x}_1$. Here θ is the angle of incoming ray paths from the surface normal. **(B)** Surface S_1 is taken around $\boldsymbol{x}_p$ as a sphere of radius l. When an incident plane wave is assumed, travel distance of path A is larger than B by l-l cos θ. **(C)** An example of deploying pairs of monitoring sites to predict ground motion at target site $\boldsymbol{x}_p$. The seismometer pairs are located at radius l on the ground surface and underground. Each seismometer in each pair is spaced by Δl. **(D)** An example of plane wave propagation. The surface S is divided into S_A and S_B. S_A is an infinite plane normal to the z axis, and S_B is a half space of infinite radius. Incident plane wave normal to S_A is assumed.

on S (i.e., the 2D integral), and with respect to the convolution integral τ. **Eq. 4** is valid when there are no radiations (i.e., no sources) inside S. **Eq. 4** is known as the Kirchhoff-Fresnel integral in wave propagation theory. Huygens' principle is its preliminary qualitative description, in which points on wavefront are virtual sources of secondary waves aligned along the wavefront.

As an example, let us take S_1 as a sphere of radius of l and centered on $\boldsymbol{x}_p$ in a homogenous velocity structure, c_0, such

that $|\boldsymbol{x}_p\text{-}\boldsymbol{x}_1| = l$ (**Figure 2B**). Because $G(\boldsymbol{x}_p, t; \boldsymbol{x}_1, 0) = 0$ when $t < l/c_0$, and taking travel-time into consideration, $G(\boldsymbol{x}_p, t + l/c_0\text{-}\tau\,; \boldsymbol{x}_1, 0) = 0$ when $t + l/c_0\text{-}\tau < l/c_0$, i.e., when $\tau > t$, so that

$$u\left(\boldsymbol{x}_p, t + l/c_0\right) = \int_{-\infty}^{t} d\tau \int \left(u(\boldsymbol{x}_1, \tau) \frac{\partial G\left(\boldsymbol{x}_p, t + l/c_0 - \tau;\ \boldsymbol{x}_1,\ 0\right)}{\partial n} - G\left(\boldsymbol{x}_p, t + l/c_0 - \tau; \boldsymbol{x}_1,\ 0\right) \frac{\partial u(\boldsymbol{x}_1, \tau)}{\partial n} \right) dS_1. \quad (5)$$

This means that the waveform at the target site at time l/c_0 in the future is predicted based on $u(\boldsymbol{x}_1, \tau)$ between the past (time -∞) and present (time t).

Green's function in a homogeneous 3-D structure is expressed as,

$$G\left(\boldsymbol{x}_p, t - \tau, \boldsymbol{x}_1,\ 0\right) = \frac{1}{4\pi\left|\boldsymbol{x}_p - \boldsymbol{x}_1\right|} \delta\left(t - \tau - \left|\boldsymbol{x}_p - \boldsymbol{x}_1\right|/c_0\right) = \frac{1}{4\pi l} \delta\left(t - \tau - l/c_0\right). \quad (6)$$

When the wavelength is much smaller than the spatial fluctuation of the absolute amplitudes of $u(\boldsymbol{x}_p, t)$ and $G(\boldsymbol{x}_p, t\text{-}\tau\,; \boldsymbol{x}_1, 0)$, the high frequency approximation is valid, and **Eq. 5** is approximated as

$$u\left(\boldsymbol{x}_p, t + l/c_0\right) \approx \int \frac{1}{4\pi c_0 l} (\cos\theta + 1)\, \dot{u}(\boldsymbol{x}_1,\ t)\, dS_1, \quad (7)$$

where θ ($=\theta(\boldsymbol{x}_1, t)$) is the angle of incoming ray paths from the surface normal (Shearer 1999; Hoshiba 2013a). The waveform at time $t + l/c_0$ is the weighted sum of the time differential of waveforms at $\boldsymbol{x}_1$ and t. This means that when $\dot{\boldsymbol{u}}(\boldsymbol{x}_1,\ t)$ and $\theta(\boldsymbol{x}_1, t)$ are obtained on surface S_1, we can predict the wave motion at $\boldsymbol{x}_p$ with a lead time of l/c_0. Here, source information (hypocentral location and magnitude) is not required. For near future predictions small values of l (i.e., small S_1) are used, and for predictions of more distant future larger values of l (larger S_1) are accordingly required. When the angle of waves approaching $\boldsymbol{x}_p$ is 0°, cos θ = 1 and cos θ +1 = 2, indicating their large contribution to constitute waveforms at $\boldsymbol{x}_p$. When the angle of waves travelling away from $\boldsymbol{x}_p$ is 180°, cos θ = -1 and cos θ +1 = 0, indicating no contribution. Thus, waves approaching $\boldsymbol{x}_p$ are important for predicting waveforms at $\boldsymbol{x}_p$, and those traveling away from $\boldsymbol{x}_p$ are negligible. At θ = 90° (as for large-angle refractions), cos θ +1 = 1; such waves are weighted half as strongly as those of θ = 0°. However, taking wavelength into consideration, the contribution is more concentrated around θ = 0. Based on Fresnel theory, the area that mainly affects the wave motion at $\boldsymbol{x}_p$ is approximately given by the relation of "(half wavelength) ≥(Path A)-(Path B)" in **Figure 2B**,

$$\lambda/2 \geq l - l\cos\theta \approx l \cdot \theta^2/2. \quad (8)$$

where an incident plane wave is assumed. This area is large for low-frequency waves, and small for high-frequency waves. For example, in a homogeneous velocity structure (c_0 = 3 km/s) and with l = 30 km, θ ≤0.32 rad (18°) for a 1 Hz wave, and θ ≤0.14 rad (8°) for a 5 Hz wave. Because contributions from outside this area are small, large angle refractions do not affect high-frequency waves, and the ray theory approach is valid.

Nagashima et al. (2008) and Kuyuk and Motosaka (2009) proposed a front-detection method. They tried to predict ground motion using waveforms of halfway applying empirical transfer function, which corresponds to empirically estimated Green's function. Iervolino et al. (2007) and Iervolino (2014) proposed to deploy some observation sites on a circle whose center location is the target site, which is similar to **Eqs 5**, **7**; this idea is essentially the basis of the boundary integral equation method. Hoshiba (2013a) explicitly introduced the boundary integral equation method for predicting future ground motion. Although it is relatively easier to take high-frequency waves in the boundary integral equation method than in the finite difference method, information on the time-dependent propagation direction (θ) is required. An array technique is useful to estimate θ. When pairs of seismometers are deployed as shown in **Figure 2C** and **Eq. 5** is approximated as

$$\left(\boldsymbol{x}_p, t + l/c_0\right) \approx \int_{-\infty}^{t} d\tau \int \left(u(\boldsymbol{x}_1, \tau) \frac{G\left(\boldsymbol{x}_p, t + \frac{l}{c_0} - \tau;\ \boldsymbol{x}_1 + \boldsymbol{n}_1\Delta l,\ 0\right) - G\left(\boldsymbol{x}_p, t + \frac{l}{c_0} - \tau;\ \boldsymbol{x}_1,\ 0\right)}{\Delta l} - G\left(\boldsymbol{x}_p, t + \frac{l}{c_0} - \tau; \boldsymbol{x}_1,\ 0\right) \frac{u(\boldsymbol{x}_1 + \boldsymbol{n}_1\Delta l, \tau) - u(\boldsymbol{x}_1, \tau)}{\Delta l} \right) dS_1 \quad (9)$$

where $\boldsymbol{n}_1$ is the inward-facing normal vector to S_1 at $\boldsymbol{x}_1$, and Δl is the distance between the seismometers in each pair. Each pair simply takes the place of an array.

At this point I wish to return to **Eq. 4** to review a relation between the boundary integral equation method and the source-based method. A point source at $\boldsymbol{x}_0$ instantaneously radiating at $t = t_0$ of amplitude A_0 is expressed by the source $A_0\delta(\boldsymbol{x}\text{-}\boldsymbol{x}_0)\,\delta(t\text{-}t_0)$. Waveforms at $\boldsymbol{x}_1$ on the surface S are given as $A_0\,G(\boldsymbol{x}_1, t; \boldsymbol{x}_0, t_0)$. When the source has volume V_0 and an arbitrary duration, and the source function is expressed as $A(\boldsymbol{x}_0, t_0)$, the waveforms at $\boldsymbol{x}_1$ are described as:

$$u(\boldsymbol{x}_1, t) = \int_{-\infty}^{\infty} dt_0 \int G(\boldsymbol{x}_1, t; \boldsymbol{x}_0,\ t_0) A(\boldsymbol{x}_0\,, t_0)\, dV_0. \quad (10)$$

In the source-based method, $A(\boldsymbol{x}_0, t_0)$ is first estimated from waveforms $u(\boldsymbol{x}_1, t)$ observed at multiple $\boldsymbol{x}_1$ locations, and then the waveform at $\boldsymbol{x}_p$ is predicted as:

$$u\left(\boldsymbol{x}_p, t\right) = \int_{-\infty}^{\infty} dt_0 \int G\left(\boldsymbol{x}_p, t; \boldsymbol{x}_0,\ t_0\right) A(\boldsymbol{x}_0\,, t_0)\, dV_0\,. \quad (11)$$

In the boundary integral equation method, the surface S is taken such that all $\boldsymbol{x}_1$ are located on S, but the source volume V_0 is outside S. Note that surface S can be of arbitrary shape. Using **Eqs. 4**, **10**,

$$\begin{aligned} u\left(\boldsymbol{x}_p, t\right) &= \int_{-\infty}^{\infty} d\tau \int \left[\left(\int_{-\infty}^{\infty} dt_0 \int G(\boldsymbol{x}_1, \tau; \boldsymbol{x}_0,\ t_0) A(\boldsymbol{x}_0\,, t_0)\, dV_0 \right) \frac{\partial G\left(\boldsymbol{x}_p, t - \tau;\ \boldsymbol{x}_1,\ 0\right)}{\partial n} - G\left(\boldsymbol{x}_p, t - \tau; \boldsymbol{x}_1, 0\right) \frac{\partial}{\partial n} \left(\int_{-\infty}^{\infty} dt_0 \int G(\boldsymbol{x}_1, \tau; \boldsymbol{x}_0,\ t_0) A(\boldsymbol{x}_0\,, t_0)\, dV_0 \right) \right] dS, \\ &= \int_{-\infty}^{\infty} dt_0 \int_{-\infty}^{\infty} d\tau \int \left[\int \left(G(\boldsymbol{x}_1, \tau; \boldsymbol{x}_0,\ t_0) \frac{\partial G\left(\boldsymbol{x}_p, t - \tau;\ \boldsymbol{x}_1,\ 0\right)}{\partial n} - G\left(\boldsymbol{x}_p, t - \tau; \boldsymbol{x}_1, 0\right) \frac{\partial G(\boldsymbol{x}_1, \tau; \boldsymbol{x}_0,\ t_0)}{\partial n} \right) dS \right] A(\boldsymbol{x}_0\,, t_0)\, dV_0, \\ &= \int_{-\infty}^{\infty} dt_0 \int G\left(\boldsymbol{x}_p, t; \boldsymbol{x}_0,\ t_0\right) A(\boldsymbol{x}_0\,, t_0)\, dV_0. \end{aligned} \quad (12)$$

where

$$\int_{-\infty}^{\infty} d\tau \int \left(G(\boldsymbol{x}_1, \tau;\ \boldsymbol{x}_0,\ t_0) \frac{\partial G(\boldsymbol{x}_p, t-\tau;\ \boldsymbol{x}_1,\ 0)}{\partial n} - G(\boldsymbol{x}_p, t-\tau; \boldsymbol{x}_1,\ 0) \frac{\partial G(\boldsymbol{x}_1, \tau; \boldsymbol{x}_0,\ t_0)}{\partial n} \right) dS = G(\boldsymbol{x}_p, t; \boldsymbol{x}_0,\ t_0) \tag{13}$$

is used, because $G(\boldsymbol{x}_1, t; \boldsymbol{x}_0, t_0)$ satisfies **Eq. 4**, **Eq. 12** means that the boundary integral equation method bypasses the process of estimating source function, $A(\boldsymbol{x}_0, t_0)$, to predict the waveform at $\boldsymbol{x}_p$ by using observations at many $\boldsymbol{x}_1$ locations. In the source-based method, the hypocentral distance is required to evaluate geometrical spreading attenuation (for example, the inverse of hypocentral distance for body waves). However, wave propagation physics suggests that geometrical spreading attenuation is determined by the local curvature of the wavefront: large curvatures give strong attenuation, small curvatures weak attenuation, and no curvature (e.g., plane wave) no attenuation. When the wavefield is estimated precisely and the curvature of wavefront is obtained, it is not necessary to estimate hypocentral distance to evaluate geometrical spreading attenuation.

Radiative Transfer Theory (RTT)

When the ray theory approach is valid, radiative transfer theory (RTT) is a powerful tool for representing high frequency wave propagation; scattering, attenuation and reflection are easily treated, although it is not easy to include refraction. In RTT, the propagation of energy is calculated instead of propagation of the wave itself. Many authors obtain the time history of energy, $F(\boldsymbol{x}, t)$, from the running average of the squared amplitude of the band-pass filtered waveform, $u(\boldsymbol{x}, t)$, at location $\boldsymbol{x}$ and time t (e.g., Hoshiba, 1995; Sato et al., 2012; Ogiso et al., 2018). RTT has been widely used to represent the envelope shape of high-frequency (≳1 Hz) seismic waveforms (Sato et al., 2012).

Hoshiba and Aoki (2015) applied RTT to EEW, but they considered in 2-D space. Here, I explain RTT in 3-D space. Following Hoshiba and Aoki (2015), when isotropic scattering is assumed, RTT is expressed as:

$$\dot{f}(\boldsymbol{x}, t: \boldsymbol{q}) + c(\boldsymbol{x})\, \boldsymbol{q} \nabla f(\boldsymbol{x}, t: \boldsymbol{q}) = -\left(g_s(\boldsymbol{x}) + h_s(\boldsymbol{x})\right) \cdot c(\boldsymbol{x}) \cdot f(\boldsymbol{x}, t: \boldsymbol{q}) + \frac{c(\boldsymbol{x})}{4\pi} \int g_s(\boldsymbol{x}) f(\boldsymbol{x}, t: q') dq', \tag{14}$$

where f is the energy density at location $\boldsymbol{x}$ and time t traveling in direction $\boldsymbol{q}$ (here $\boldsymbol{q}$ is the unit vector), $c(\boldsymbol{x})$ is the velocity of seismic wave at $\boldsymbol{x}$, and $g_s(\boldsymbol{x})$ and $h_s(\boldsymbol{x})$ are the strength of scattering and intrinsic absorption at $\boldsymbol{x}$, respectively (Sato et al., 2012). Here it is assumed that scattering does not cause wave conversion (i.e., $P \rightarrow S$ or $S \rightarrow P$). The time history of energy, $F(\boldsymbol{x}, t)$, is the sum of $f(\boldsymbol{x}, t: \boldsymbol{q})$ in all directions:

$$F(\boldsymbol{x}, t) = \int f(\boldsymbol{x}, t: \boldsymbol{q}) d\boldsymbol{q}. \tag{15}$$

Here, for simplicity, I assume that both the velocity and attenuation structures are homogeneous; thus, velocity, scattering strength, and intrinsic absorption are independent of $\boldsymbol{x}$: $c(\boldsymbol{x}) = c_0$, $g_s(\boldsymbol{x}) = g_0$ and $h_s(\boldsymbol{x}) = h_0$. Then **Eq. 14** is expressed as,

$$\dot{f}(\boldsymbol{x}, t: \boldsymbol{q}) + c_0 q \nabla f(\boldsymbol{x}, t: \boldsymbol{q}) = -(g_0 + h_0) c_0 f(\boldsymbol{x}, t: \boldsymbol{q}) + \frac{c_0}{4\pi} \int g_0 f(\boldsymbol{x}, t: q') dq'. \tag{16}$$

The left-hand side of **Eq. 16** represents advection, the first term on the right-hand side means attenuation, and the second term represents scattering from direction $\boldsymbol{q}'$ to $\boldsymbol{q}$. Because the first term on the left-hand side is the differential of f with respect to time, **Eq. 16** means that it is possible to predict future f provided that the current spatial and directional distributions of f are known. **Eq. 16** is approximated as:

$$f(\boldsymbol{x}, t + \Delta t: \boldsymbol{q}) \approx f(\boldsymbol{x}, t: \boldsymbol{q}) + \Delta t \left\{ -c_0 \boldsymbol{q} \nabla f(\boldsymbol{x}, t: q) - (g_0 + h_0) v_0 f(\boldsymbol{x}, t: \boldsymbol{q}) + \frac{c_0}{4\pi} \int g_0 f(\boldsymbol{x}, t: \boldsymbol{q}') d\boldsymbol{q}' \right\}. \tag{17}$$

Repeating this process makes it possible to predict f at any future time. Note that information about the earthquake hypocenter and magnitude is not required for this prediction.

To efficiently calculate RTT simulation, a particle method based on the Monte-Carlo technique has been widely used in recent decades (e.g., Gusev and Abubakirov, 1987; Hoshiba, 1991, 1995, 1997; Yoshimoto, 2000). In this method, the propagation of wave energy is simulated by the movement of a very large number of particles. Instead of the Eulerian representation expressed in **Eq. 16**, I use the Lagrangian representation,

$$\frac{Df(\boldsymbol{x}, t: q)}{Dt} = -(g_0 + h_0) c_0 f(\boldsymbol{x}, t: q) + \frac{c_0}{4\pi} \int g_0 f(\boldsymbol{x}, t: q') dq' = -g_0 c_0 f(\boldsymbol{x}, t: q) + \frac{c_0}{4\pi} \int g_0 f(\boldsymbol{x}, t: q') dq' - h_0 c_0 f(\boldsymbol{x}, t: q). \tag{18}$$

First, let us consider the case of $h_0 = 0$, which means no attenuation due to absorption. The first term on the right-hand side means that the energy propagating in direction $\boldsymbol{q}$ is attenuated by scattering in proportion to f. The energy density, f, decreases exponentially as travel distance increases. The second term is the contribution of energy changing direction from $\boldsymbol{q}'$ to $\boldsymbol{q}$. As shown in **Figure 3**, this physical process is simulated by many particles through a probabilistic process (Hoshiba and Aoki, 2015). The probability that energy travels without scattering during the time interval Δt is exp $(-g_0 c_0 \Delta t)$, which is approximated as $1-g_0 c_0 \Delta t$ when $g_0 c_0 \Delta t \ll 1$. The probability that scattering occurs during this time interval is given by 1- exp $(-g_0 c_0 \Delta t) \approx g_0 c_0 \Delta t$. When scattering occurs, the

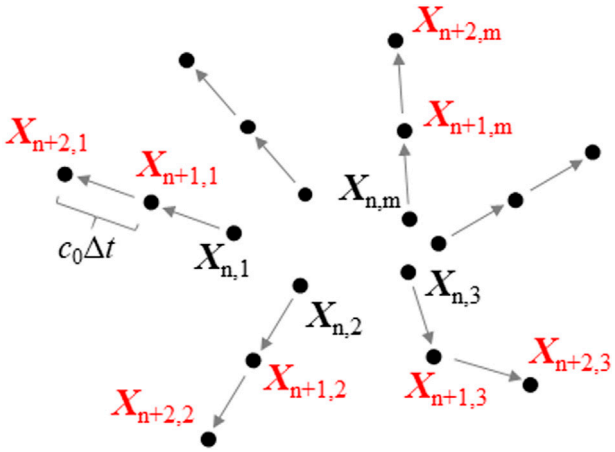

FIGURE 3 | Schematic illustration of radiative transfer theory, simulated using a very large number of particles. When the propagation direction, $\boldsymbol{q}_m$, is known, the future locations of the mth particle ($\boldsymbol{X}_{n+1,m}$, $\boldsymbol{X}_{n+2,m}$, ...) are easily predicted from its current location $\boldsymbol{X}_{n,m}$, that is $\boldsymbol{X}_{n+1,m} = \boldsymbol{X}_{n,m} + c_0\Delta t\, \boldsymbol{q}_m$ and $\boldsymbol{X}_{n+2,m} = \boldsymbol{X}_{n,m} + 2c_0\Delta t\, \boldsymbol{q}_m$, if scattering does not occur. If scattering occurs, the propagation direction is newly given by the probability density as shown for $\boldsymbol{X}_{n+1,3}$.

probability density of scattering from $\boldsymbol{q}'$ toward $\boldsymbol{q}$ is $1/(4\pi)$ because scattering is assumed to be isotropic. These processes are simulated by using a very large number of particles.

Let the number of particles be M, and let $\boldsymbol{X}_{n,m}$ be the location of the mth particle at time, n. When traveling in direction $\boldsymbol{q}_m$, the particle is expected to move by $v_0\Delta t\, \boldsymbol{q}_m$ over the time interval Δt, if scattering does not occur. In contrast, if scattering occurs, the particle changes direction. Let R_1, R_2 and R_3 be independent uniform random variables between 0 and 1. When $R_1 \geq g_0 v_0 \Delta t$ (i.e., no scattering), the particle moves to $\boldsymbol{X}_{n,m} = \boldsymbol{X}_{n-1,m} + c_0\Delta t\, \boldsymbol{q}_m$ in the next time step. When $R_1 < g_0 c_0 \Delta t$ (i.e., with scattering), the particle's new direction is determined as $\boldsymbol{q}_N = (2\pi\ R_2,\ \cos^{-1}(1-2R_3))$ and the particle is located at $\boldsymbol{X}_{n,m} = \boldsymbol{X}_{n-1,m} + c_0\Delta t\, \boldsymbol{q}_N$ after Δt. At the next time step, $\boldsymbol{q}_m = \mathrm{q}_N$ is used as the propagation direction.

The third term on the right-hand side of **Eq. 18** represents attenuation due to absorption. When the mth particle has energy $q_{n-1,m}$ at time n-1, the energy is attenuated as:

$$q_{n,m} = q_{n-1,m} \cdot \exp(-h_0 c_0 \Delta t) \approx q_{n-1,m}(1 - h_0 c_0 \Delta t) \tag{19}$$

with increasing n, where $h_0 v_0 \Delta t << 1$ is assumed. The energy of the particle is attenuated as the elapsed time increases regardless of scattering. In this paper, because h_0 is assumed to be homogeneous (i.e., independent of $\boldsymbol{x}$), amount of attenuation of each particle is assumed to be the same for all m.

Hoshiba and Aoki (2015) and Ogiso et al. (2018) applied RTT to real-time predictions of the strength of seismic ground motion for EEW. They called the method "Numerical Shake Prediction," because of its analogy to numerical weather prediction in meteorology, in which physical processes are simulated from a precise estimate of the present conditions. Because they focused on predicting seismic intensity, which is mainly determined by relatively high frequency component of waveforms, ray theory is a good approximation and RTT is applicable. They succeeded in predicting the time trace of future seismic intensities. Whereas the finite difference method is a good approach for predicting low-frequency waveforms but not high frequency waveforms, RTT is valid for high-frequency but does not necessarily hold for low-frequency because RTT is based on ray theory.

Propagation of Local Undamped Motion (PLUM) Method

For real-world application of the boundary integral equation method, a precise estimation of the wavefield distribution is required. Because quite dense observation networks are not yet available at present except few cases, it is not easy to directly apply the boundary integral equation method. Some approximations have been introduced, and the propagation of local undamped motion (PLUM) method is one of them (Kodera et al., 2018).

For plane wave propagation, let us assume the surface enclosing $\boldsymbol{x}_p$ to be an infinite plane, S_A, and half sphere of infinite radius, S_B, as shown in **Figure 2D**. Because S_B is located infinitely far from $\boldsymbol{x}_p$, contribution from S_B is negligible. Plane waves propagating in the $+z$ direction are expressed as $u(\boldsymbol{x}, t) = u(x, y, z, t) = u_p(t\text{-}z/c_0)$. Then, as $\partial/\partial n = \partial/\partial z$, $\partial u/\partial n = \partial u/\partial z$. The contribution from S_A is

$$\begin{aligned} u(\boldsymbol{x}_p, t) = \int_{-\infty}^{\infty} d\tau \iint_{-\infty}^{\infty} \Bigg(u_p\left(\tau - \frac{z_1}{c_0}\right) \frac{\partial G(\boldsymbol{x}_p, t-\tau;\ x_1,\ y_1,\ z=z_1,\ 0)}{\partial z} \\ - G(\boldsymbol{x}_p, t-\tau; x_1,\ y_1,\ z_1,\ 0) \frac{\partial u(\tau - z_1/c_0)}{\partial z} \Bigg) dx_1 dy_1 \\ = \boldsymbol{u}_p\left(t - \frac{|z_p - z_1|}{c_0} - \frac{z_1}{c_0}\right) = u\left(\boldsymbol{x}_1, t - \frac{|z_p - z_1|}{c_0}\right). \end{aligned} \tag{20}$$

Here

$$\begin{aligned} \iint_{-\infty}^{\infty} G(0,\ 0,\ z_p, t-\tau;\ x_1,\ y_1,\ z_1,\ 0) dx_1 dy_1 \\ = \frac{c_0}{2} H\left(t - \tau - \frac{|z_p - z_1|}{c_0}\right) \end{aligned} \tag{21}$$

is used, where G is given by **Eq. 6** and H is the step function. This is the Green's function in 1-D space. **Eq. 20** means that plane wave propagates without attenuation:

$$|u(\boldsymbol{x}_p,\ t)|_{max\ t} = |u(\boldsymbol{x}_1,\ t)|_{max\ t}, \tag{22}$$

where $|\cdot|_{max t}$ indicates the maximum amplitude, such as PGA for accelerograms or PGV for velocity waveforms. Because plane waves form when a hypocenter is located infinitely far away, some attenuation is expected for hypocenters at finite distances,

$$|u(\boldsymbol{x}_p,\ t)|_{max\ t} \leq |u(\boldsymbol{x}_1,\ t)|_{max\ t}, \tag{23}$$

for waves arriving at $\boldsymbol{x}_p$ later than $\boldsymbol{x}_1$, where PGA (or PGV) is expected to occur at $\boldsymbol{x}_p$ later than $\boldsymbol{x}_1$. Plane waves correspond to

the prediction for the most severe scenario. When several stations are available for monitoring the wavefield around the target site, the simple relation,

$$\left|u\left(\boldsymbol{x}_{\mathrm{p}},\ t\right)\right|_{\max\ \mathrm{t}} \leq \mathrm{Max_i}\left|\ u\left(\boldsymbol{x}_{\mathrm{i}},\ t\right)\ \right|_{\max\ \mathrm{t}}, \tag{24}$$

may be valid, where i is the index of the monitoring site. Strictly speaking, this relation does not hold well for multiple simultaneous sources (i.e., multiple waves propagating towards $\boldsymbol{x}_{\mathrm{p}}$); nonetheless, it is an indicator of the possible strength of ground motions. **Eq. 24** is the basis of the PLUM method, in which $\mathrm{Max}_i\left|u\left(\boldsymbol{x}_i, t < t_c\right)\right|_{\max\ t}$ is the predicted strength of ground motions accounting for the site amplification (see later section for site amplification correction) and t_c is the current time. Because it assumes plane wave propagation and thus the most severe scenario, PLUM tends to overpredict ground motions. However, because the prediction is based on actual observations of ground motions, PLUM acts to reduce underpredictions and missed alarms.

Because PLUM assumes plane waves propagation, the distance between the monitoring and target sites must be much smaller than the hypocentral distance. The use of sites far from $\boldsymbol{x}_{\mathrm{p}}$ as monitoring sites gives a long lead time, but is prone to overprediction. For this reason, long lead time predictions are not given by the PLUM method. In contrast, when monitoring sites around $\boldsymbol{x}_{\mathrm{p}}$ are sparse, few sites are available for use in the PLUM method. Kodera et al. (2016) applied PLUM to the 2016 Kumamoto, Japan, earthquakes sequence (Mw6.2 and 7.1) and its foreshocks and aftershocks, and Kodera et al. (2018) tested PLUM using data from the 2011 Tohoku earthquake (Mw9.0) and its aftershocks, in which they used sites within 30 km of the target site, $\boldsymbol{x}_{\mathrm{p}}$, as monitoring sites, taking the stations interval within the observation network into account. Minson et al. (2020) reported a real-time application of PLUM to the 2019 Ridgecrest, California, earthquakes (Mw6.4 and 7.1). Cochran et al. (2019) and Kilb et al. (2021) applied PLUM to earthquakes in southern California and the west coast of USA, respectively. Meier et al. (2020) compared the performance of PLUM, point source algorithm and finite fault algorithm. Otake et al. (2020) investigated an approach similar to PLUM, but using machine-learning instead of the physics of wave propagation.

The PLUM method was implemented into the JMA's operational EEW system in 2018, in addition to the point-source algorithms. Since then, PLUM has prevented underprediction caused by uncertainties in the GMPE, and sometimes issued earlier warnings than the point-source algorithm. Kodera et al. (2020) summarized its performance. For example, during the 2018 Eastern Iburi, Hokkaido, Japan, earthquake (Mw6.6, focal depth: 37 km), PLUM issued a public warning 13.35 s after the origin time, 3.1 s earlier than the point-source algorithms. For this earthquake, the GMPE significantly underpredicted PGA and PGV at near-source sites (Dhakal et al., 2019), meaning that the point-source algorithm underpredicted ground motions even when source parameters (hypocentral location and magnitude) were precisely estimated. In contrast, PLUM predicted them appropriately, reflecting the strong ground motion observed at neighboring sites.

DATA ASSIMILATION

The first step in obtaining a precise prediction using the wavefield-based method is to estimate the current wavefield. Data assimilation is a powerful technique for estimating current conditions that is widely used in numerical weather prediction, oceanography and rocket control (Kalnay, 2003; Awaji et al., 2009). **Figure 4** illustrates the data assimilation procedure: the spatial distribution of the wavefield is estimated from not only actual observations but also the simulation of wave propagation based on wave propagation physics, leading to a precise estimation of the current wavefield. Therefore, data assimilation incorporates actual observations into the simulation of wave propagation. In this section, I will explain data assimilation technique, following Hoshiba and Aoki (2015).

Let $\boldsymbol{u}_{\mathrm{n}}$ indicate the wavefield in the model space at time $t_{\mathrm{n}} = n\Delta t$, in which $\boldsymbol{u}_{\mathrm{n}} = [u\ (\boldsymbol{x},\ n\Delta t),\ u\ (\boldsymbol{x}\ (n\text{-}1)\Delta t)\ ]$ in the finite difference method, or $\boldsymbol{u}_{\mathrm{n}} = [f\ (\boldsymbol{x},\ n\Delta t\text{: }\boldsymbol{q})\ ]$ in RTT. When the 3-D space is discretized as 0 to $L_{\mathrm{x}}\Delta x$, 0 to $L_{\mathrm{y}}\Delta y$ and 0 to $L_{\mathrm{z}}\Delta z$, the number of elements of $\boldsymbol{u}_{\mathrm{n}}$ is $I = 2{\cdot}L_{\mathrm{x}}L_{\mathrm{y}}{\cdot}L_{\mathrm{z}}$ in the finite difference method, and when the azimuth is discretized as 0 to $L_{\mathrm{q}}\Delta q$, the number is $I = L_{\mathrm{x}}L_{\mathrm{y}}{\cdot}L_{\mathrm{z}}L_{\mathrm{q}}$ in RTT. When $\boldsymbol{u}_{\mathrm{n\text{-}1}}$ is given, we can predict $\boldsymbol{u}_{\mathrm{n}}$ by simulating the propagation of the wave; this prediction one time-step-ahead is expressed as $\boldsymbol{u}_{\mathrm{n}} = P\ (\boldsymbol{u}_{\mathrm{n\text{-}1}})$, where P is the operation of **Eq. 2** or **Eq. 17**. To discriminate between $\boldsymbol{u}_{\mathrm{n}}$ before and after being combined with the actual observations, the wavefields before and after are denoted $\boldsymbol{u}_{\mathrm{n}}^{b}$ and $\boldsymbol{u}_{\mathrm{n}}^{a}$. P is applied to the wavefield after the combination at one time step before, i.e., $t_{\mathrm{n\text{-}1}}$; thus, the one step-ahead prediction is expressed as:

$$\boldsymbol{u}_{n}^{b} = P\left(\boldsymbol{u}^{a}{}_{n-1}\right). \tag{25}$$

Let $\boldsymbol{v}_{\mathrm{n}} = (v_{\mathrm{n1}}, v_{\mathrm{n2}}, v_{\mathrm{n3}}, \ldots v_{\mathrm{nj}}, \ldots v_{\mathrm{nJ}})^{T}$ be the actual observation in observational space at time t_{n}, in which v_{nj} means the observed data at the jth element. Let the total number of observation elements be J. Usually I (the number of grids in model space) is much larger than J (number of observation elements). Data assimilation is expresses as

$$\boldsymbol{u}^{a}{}_{n} = \boldsymbol{u}^{b}{}_{n} + \boldsymbol{W}\left(\boldsymbol{v}_{n} - \boldsymbol{H}\boldsymbol{u}^{b}{}_{n}\right) \tag{26}$$

Here $\boldsymbol{H}$ is the $J{\times}I$ matrix called the observation matrix and it means the interpolation of grid points onto the location of the observation point, and then $(\boldsymbol{v}_{\mathrm{n}} - \boldsymbol{H}\boldsymbol{u}_{\mathrm{n}}^{b})$ is the difference between the one-step-ahead prediction and the actual observation at time t_{n}. $\boldsymbol{W}$ is the $I{\times}J$ matrix called weight matrix, and $\boldsymbol{W}\ (\boldsymbol{v}_{\mathrm{n}} - \boldsymbol{H}\boldsymbol{u}_{\mathrm{n}}^{b})$ indicates the correction of the one-step-ahead prediction in the simulation of wave propagation. From $\boldsymbol{u}_{\mathrm{n}}{}^{\mathrm{a}}$, $\boldsymbol{u}_{\mathrm{n+1}}{}^{\mathrm{b}}$ is obtained from **Eq. 25**. Iterative application of **Eqs 25**, **26** produces time-evolutional estimation of wavefield. The process of the left side in **Figure 4** indicates repeated application of one-step-ahead prediction, that is, the simulation of wave propagation. In the data assimilation technique, actual observations are included in the simulation to correct the wavefield at each time step; that is, actual data are assimilated in the simulation process.

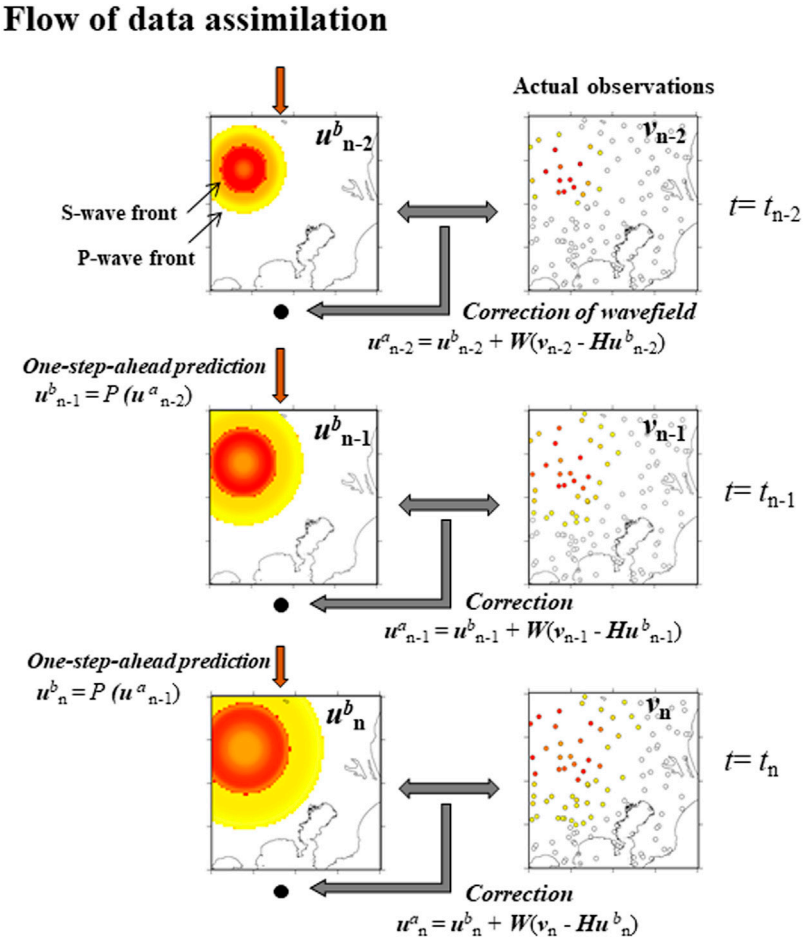

FIGURE 4 | The flow of the data assimilation process. One-step-ahead prediction, $\boldsymbol{u}_n^b = P(\boldsymbol{u}_{n-1}^a)$, is combined with actual observations, $\boldsymbol{v}_n$, to correct the estimation of the current wavefield (after Hoshiba and Aoki, 2015). By repeating this process, the current wavefield, $\boldsymbol{u}_n^a$, is estimated by using not only the current observation ($\boldsymbol{v}_n$), but also all past observations ($\boldsymbol{v}_{n-1}$, $\boldsymbol{v}_{n-2}$, $\boldsymbol{v}_{n-3}$, . . .).

The parameter setting of $\boldsymbol{W}$ is important in data assimilation, and several techniques have been proposed. The simplest is the optimal interpolation method, in which $\boldsymbol{W}$ is constant irrespective of time n, though in the Kalman filter method it changes with increasing n. In the optimal interpolation method, Matrix $\boldsymbol{W}$ is expressed in relation to the errors in the one-step-ahead prediction (background error, σ_b), and in the observations (observational error, σ_o). When the correlation distance of the background error and the ratio σ_o/σ_b are assumed, matrix $\boldsymbol{W}$ is obtained (for detail, see Awaji et al., 2009; Kalnay, 2003; Hoshiba and Aoki, 2015).

When the correlation distance is large, the $\boldsymbol{W}(\boldsymbol{v}_n - \boldsymbol{H}\boldsymbol{u}_n^b)$ correction is applied to a wide area around each observation point, and when the distance is small, the correction is restricted to a small area around each observation point. The density of observation network, therefore, may influence the parameter setting of the correlation distance: large distance for sparse network and small distance for dense network. For sparse network, observation of each site needs to represent wavefield of wide area around the site, but small area for dense network. In general, dense network can reconstruct the complicated wavefield in data assimilation better than sparse network. When too large correlation distance is used, seismic wave propagates artificially faster than actual velocity in the process of $\boldsymbol{W}(\boldsymbol{v}_n - \boldsymbol{H}\boldsymbol{u}_n^b)$ correction, which reduces the accuracy of arrival time of strong shaking. The correlation distance at each observation point can be varied according to the network distribution: for example, small correlation distances where station interval is small around the site, and large correlation distances where station interval is large.

When the observational errors are assumed to be much larger than the background errors, $\sigma_o/\sigma_b >> 1$, $\boldsymbol{W} \approx 0$ and then $\boldsymbol{u}_n^a \approx \boldsymbol{u}_n^b$. Iterative application of **Eqs 25**, **26**, therefore, results in just the simulation of wave propagation, because the observation have no effect. In contrast, $\sigma_o/\sigma_b \approx 0$ corresponds to the case where the contours of the actual observations are drawn independently at each time step, because the one-step-ahead prediction has little effect in **Eq. 26**. The ratio, σ_o/σ_b, at each observation point also can be varied according to quality condition. For example, large

σ_o/σ_b for noisy stations in urban areas and small σ_o/σ_b for quiet stations in mountain areas.

Although the wavefield is observable at the ground surface when stations are densely deployed at the surface (i.e., 2-D space), the underground wavefield at depths of more than a few kilometers cannot be observed because many borehole observations deeper than a few kilometers are not realistic. Because actual seismic wavefields are expressed in 3-D space, assumptions are required to apply data assimilation to estimate the 3-D wavefield. Handling the difference between the 2- and 3-D spaces is an important subject for future advancement of the data assimilation technique.

PREDICTION

Once the present wavefield, $\boldsymbol{u}_{\mathrm{n}}{}^{\mathrm{a}}$, has been estimated precisely by the data assimilation technique, the future wavefield, $\boldsymbol{u}^{P}$, is predicted from the current wavefield, $\boldsymbol{u}^{\mathrm{a}}{}_{\mathrm{n}}$,

$$\boldsymbol{u}^{P}{}_{n+1} = P\left(\boldsymbol{u}^{a}{}_{n}\right) \tag{27}$$

and $\boldsymbol{u}^{\mathrm{P}}{}_{\mathrm{n}+2}$ is forecast from $\boldsymbol{u}^{\mathrm{P}}{}_{\mathrm{n}+1}$, that is $\boldsymbol{u}^{\mathrm{P}}{}_{\mathrm{n}+2} = P\left(\boldsymbol{u}^{\mathrm{P}}{}_{\mathrm{n}+1}\right) = P^2\left(\boldsymbol{u}^{a}{}_{\mathrm{n}}\right)$. Repeating this process

$$\boldsymbol{u}^{P}{}_{n+k} = P\left(\boldsymbol{u}^{P}{}_{n+k-1}\right) = P^2\left(\boldsymbol{u}^{P}{}_{n+k-2}\right) = \ldots = P^{k-1}\left(\boldsymbol{u}^{P}{}_{n+1}\right) = P^{k}\left(\boldsymbol{u}^{a}{}_{n}\right). \tag{28}$$

Future wavefield at any time can be predicted from the current wavefield.

REAL-TIME CORRECTION OF THE SITE AMPLIFICATION FACTOR

Site amplification is an important factor to determine seismic-wave amplitude in addition to source and propagation factors, and it depends on frequency. In application of the wavefield-based method, the frequency-dependent site amplification should be removed from the observed amplitude when simulating wave propagation described in the previous section, and then include it to evaluate waveforms at target sites, especially those characterized by large amplification factors. Many previous studies have investigated frequency-dependent site amplification in the frequency domain by assuming a model,

$$O_{kl}\left(f\right) = S_k\left(f\right) T_{kl}\left(f\right) A_l\left(f\right), \tag{29}$$

where $O_{kl}(f)$, $S_k(f)$, $T_{kl}(f)$, and $A_l(f)$ represent the observed seismic wave spectrum from event k at site l, the source spectrum characterizing event k, the propagation factor between event k and site l, and the site amplification factor at site l, respectively, and f is the frequency of the seismic waves. When borehole is available at the site, fine vertical structures of velocity and attenuation can be obtained, and $A_l(f)$ is estimated theoretically. However, borehole observation at all sites is not realistic at present. Instead of the theoretical approach, many empirical approaches have been proposed to obtain the relative site amplification factors, $\{A_2(f)/A_1(f)\}$: spectral ratio (e.g., Ikeura and Kato, 2011); spectrum inversion of source, propagation, and site factors (e.g., Iwata and Irikura, 1988; Kato et al., 1992); coda normalization method (e.g., Phillips and Aki, 1986), and others. These approaches usually neglect phase characteristics, focusing on amplitude characteristics, $|A_2(f)/A_1(f)|$. For example, in the spectral ratio method, when sites 1 and 2 are adjacent, compared to the hypocentral distance, $|T_{k2}(f)| \approx |T_{k1}(f)|$ is assumed, then

$$\left|\frac{O_{k2}\left(f\right)}{O_{k1}\left(f\right)}\right| = \left|\frac{S_k\left(f\right)}{S_k\left(f\right)}\right| \cdot \left|\frac{T_{k2}\left(f\right)}{T_{k1}\left(f\right)}\right| \cdot \left|\frac{A_2\left(f\right)}{A_1\left(f\right)}\right| \approx \left|\frac{A_2\left(f\right)}{A_1\left(f\right)}\right|. \tag{30}$$

The relative site amplification factor, $|A_2(f)/A_1(f)|$, can be estimated from spectral ratio of observed waveforms, $|O_{k2}(f)/O_{k1}(f)|$. When the site amplification factor at site 1 relative to site 1' (different location from site 1) is known, that is $|A_1(f)/A_{1'}(f)|$, it is easy to estimate the amplification factor at site 2 relative to site 1′ from $|A_2(f)/A_{1'}(f)| = |A_1(f)/A_{1'}(f)| \cdot |A_2(f)/A_1(f)|$. By repeating the process, it is possible to estimate relative site amplification factor even when the two sites are not adjacent. Here, $|A_2(f)/A_1(f)|$ (and $|A_2(f)/A_{1'}(f)|$) is used to correct the difference of site-amplification condition.

In EEW, it is preferable to correct the frequency-dependent site amplification factor in real time. As $|A_2(f)/A_1(f)|$ is expressed in the frequency domain, it may be possible to apply a fast Fourie transform (FFT) with a short time interval (i.e., every 1 s or less) to ongoing waveforms at site 1, multiply them by $|A_2(f)/A_1(f)|$, and then perform an inverse FFT to predict ongoing waveforms at site 2 (**Figure 5**). Instead of methods in the frequency domain, a method in the time domain was proposed (Hoshiba, 2013b; Pilz and Parolai, 2016), in which a causal recursive filter, which allows correction of site amplification factors in real time, is used. The time domain filter alleviates computational workload of the system, comparing with that of the frequency domain analysis, and makes it easy to estimate continuously site-corrected waveforms regardless of whether earthquakes are occurring or not. Trigger is not required in the continuous operation, which minimizes the fluctuation of the workload.

Hoshiba (2013b) proposed to model the frequency dependent site amplification using the form:

$$F\left(s\right) = G_0 \prod_{n=1}^{N}\left(\frac{\omega_{2n}}{\omega_{1n}}\right) \cdot \frac{s+\omega_{1n}}{s+\omega_{2n}} \cdot \prod_{m=1}^{M}\left(\frac{\omega_{2m}}{\omega_{1m}}\right)^2 \cdot \frac{s^2 + 2h_{1m}\omega_{1m}s + {\omega_{1m}}^2}{s^2 + 2h_{2m}\omega_{2m}s + {\omega_{2m}}^2}, \tag{31}$$

where N and M are the numbers of the first- and second-order filters, respectively, and $s = i\,(2\pi f)$. Here $\omega_{1\mathrm{n}}$, $\omega_{2\mathrm{n}}$, $\omega_{1\mathrm{m}}$,

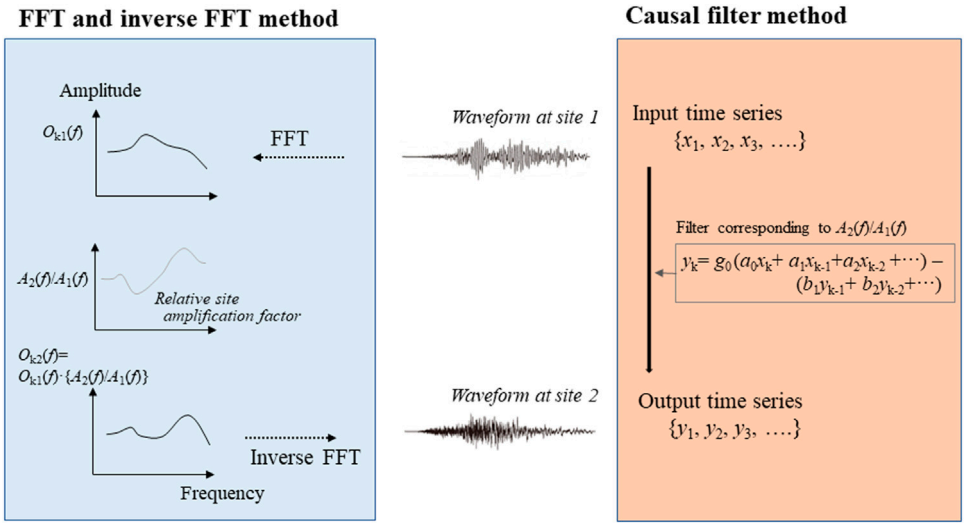

FIGURE 5 | Comparison of the causal filter method with the FFT (and inverse FFT) method. In the FFT method, the frequency-dependent site amplification factor is corrected in the frequency domain. In the causal filter method, it is done in the time domain.

and ω_{2m} are the angular frequencies and h_{1m} and h_{2m} are the damping factors that characterize the frequency dependence, respectively. Note that $s^2+2h\omega_m s+\omega_m{}^2$ represents a damping oscillation. Parameter ω_{1n}, ω_{2n}, ω_{1m}, ω_{2m}, h_{1m} and h_{2m} are positive numbers, and are estimated to satisfy $|A_2(f)/A_1(f)|\approx|F(s)|$.

The filter is modeled as **Eq. 31**, where $F(s)$ is represented by combination of first and second orders of s,

$$F_{1n}(s)=\left(\frac{\omega_{2n}}{\omega_{1n}}\right)\cdot\frac{s+\omega_{1n}}{s+\omega_{2n}},$$
$$F_{2m}(s)=\left(\frac{\omega_{2m}}{\omega_{1m}}\right)^2\cdot\frac{s^2+2h_1\omega_{1m}s+\omega_{1m}{}^2}{s^2+2h_2\omega_{2m}s+\omega_{2m}{}^2} \quad (32)$$

By a mapping procedure called the bilinear transform,

$$s=\frac{2}{\Delta T}\cdot\frac{1-z^{-1}}{1+z^{-1}}, \quad (33)$$

and pre-warping for ω_{1n}, ω_{2n}, ω_{1m}, and ω_{2m} of the digital filtering technique,

$$\omega\rightarrow\frac{2}{\Delta T}tan\left(\frac{\omega\Delta T}{2}\right), \quad (34)$$

the transfer function, $F(z)$, is obtained (Scherbaum, 1996) in a form of infinite impulse response (IIR) filter, where ΔT is the sampling interval of the digital waveforms and z = exp $(s\Delta T)$:

$$F_{1n}(z)=g_0\cdot\frac{a_0+a_1z^{-1}}{1+b_1z^{-1}},\ F_{2m}(z)=g_0\cdot\frac{a_0+a_1z^{-1}+a_2z^{-2}}{1+b_1z^{-1}+b_2z^{-2}}. \quad (35)$$

The recursive filters are given by $y_k = g_0\ (a_0x_k + a_1x_{k-1})$-$b_1y_{k-1}$ for $F_{1n}(z)$, and by $y_k = g_0\ (a_0x_k + a_1x_{k-1}+a_2x_{k-2})$ -$(b_1y_{k-1}+ b_2y_{k-2})$ for $F_{2m}(z)$, where x_k and y_k are the input and output of the time series of the digitized waveform, respectively.

Applying **Eqs 33**, **34**, g_0, a_0, a_1, and b_1 for $F_{1n}(z)$ are,

$$g_0=\frac{tan\left(\frac{\omega_{2n}\Delta T}{2}\right)}{tan\left(\frac{\omega_{1n}\Delta T}{2}\right)}\cdot\frac{1}{1+tan\left(\frac{\omega_2\Delta T}{2}\right)},\ a_0=1+tan\left(\frac{\omega_{1n}\Delta T}{2}\right),$$
$$a_1=tan\left(\frac{\omega_{1n}\Delta T}{2}\right)-1,\ b_1=\frac{tan\left(\frac{\omega_{2n}\Delta T}{2}\right)-1}{1+tan\left(\frac{\omega_{2n}\Delta T}{2}\right)} \quad (36)$$

and, g_0, a_0, a_1, a_2, b_1, and b_2 for $F_{2m}(z)$ are,

$$g_0=\left\{\frac{tan\left(\frac{\omega_{2m}\Delta T}{2}\right)}{tan\left(\frac{\omega_{1m}\Delta T}{2}\right)}\right\}^2\cdot\frac{1}{1+2h_2\ tan\left(\frac{\omega_{2m}\Delta T}{2}\right)+tan^2\left(\frac{\omega_{2m}\Delta T}{2}\right)},$$
$$a_0=1+2\,h_1\,tan\left(\frac{\omega_{1m}\Delta T}{2}\right)+tan^2\left(\frac{\omega_{1m}\Delta T}{2}\right),$$
$$a_1=2\,tan^2\left(\frac{\omega_{1m}\Delta T}{2}\right)-2,$$
$$a_2=1-2h_1\ tan\left(\frac{\omega_{1m}\Delta T}{2}\right)+tan^2\left(\frac{\omega_{1m}\Delta T}{2}\right),$$
$$b_1=\frac{2\,tan^2\left(\frac{\omega_{2m}\Delta T}{2}\right)-2}{1+2\,h_2\,tan\left(\frac{\omega_{2m}\Delta T}{2}\right)+tan^2\left(\frac{\omega_{2m}\Delta T}{2}\right)},$$
$$b_2=\frac{1-2h_2\ tan\left(\frac{\omega_{2m}\Delta T}{2}\right)+\tan^2\left(\frac{\omega_{2m}\Delta T}{2}\right)}{1+2h_2\ tan\left(\frac{\omega_{2m}\Delta T}{2}\right)+tan^2\left(\frac{\omega_{2m}\Delta T}{2}\right)}. \quad (37)$$

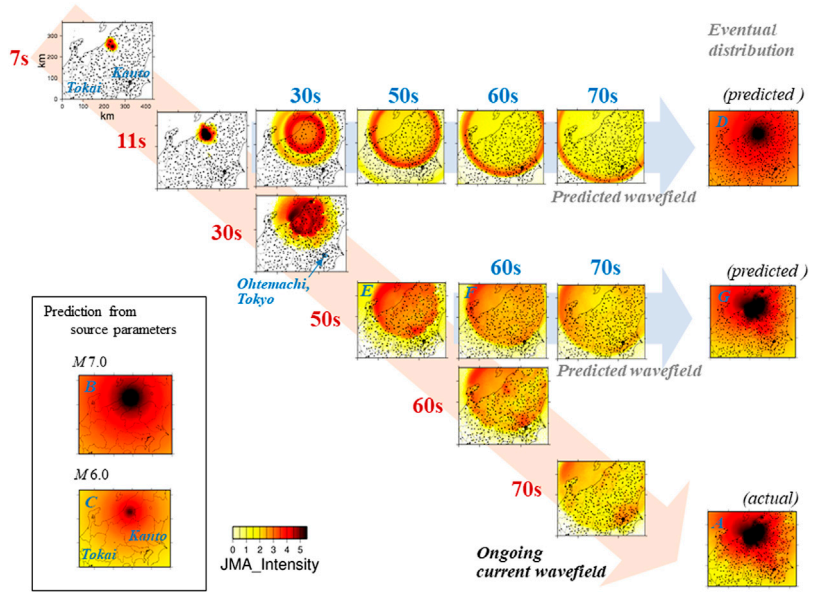

FIGURE 6 | An example application of the wavefield based method using a Mw6.4 earthquake (the largest aftershock of the Mw6.7 Chuetsu, Niigata, Japan earthquake; October 23, 2004). Data from K-NET and KiK-net of the National Research Institute for Earth Science and Disaster Prevention (NIED) were used. The locations of observation points are shown by small dots. The actual eventual distribution of ground motion was complicated **(A)** relatively strong ground motion was observed at Kanto, and weak one at Tokai. This complicated distribution is not reproduced by the source-based method, as shown in **(B,C)** using M7.0 and M6.0, respectively. In the wavefield-based method, the predicted eventual distribution from the observation at t = 11s **(D)** is similar to the prediction using a M7.0 event **(B)**. At t = 50s, strong ground motions were observed to be propagating toward Tokyo **(E)**, and the updated prediction indicates the arrival of the strong ground motions at Tokyo at t = 60s **(F)** The predicted eventual distribution from t = 50s **(G)** reproduces well the actual distribution **(A)**.

The causal filter, $F(z)$, makes it possible to correct the relative site amplification factor in real time in the time domain. Ogiso et al. (2016) evaluated the relative site amplification factors of more than 2,200 stations in Japan and obtained their IIR filters, and Xie et al. (2019) also applied this technique. Pilz and Parolai (2016) extended this method to include phase characteristics.

In many researches of site amplification factors to estimate $|A_2(f)/A_1(f)|$, hard rock site is chosen for site 1 as a reference site. However, site 1 is not necessarily hard rock site here, because the purpose of the site factor correction is to make virtually the site conditions common to isolate seismic wave propagation. For the boundary equation method, for example, $\boldsymbol{x}_1$ and $\boldsymbol{x}_\mathrm{p}$ corresponds to site 1 and site 2, respectively. Many locations are assumed for site 1 ($\boldsymbol{x}_1$), but site 2 ($\boldsymbol{x}_\mathrm{p}$) is single location. By applying $F(z)$ to waveforms obtained at site 1, the waveforms are virtually converted to those having the site amplification of site 2. The integrals in **Eqs 5**, **7**, **9** are carried out for waveforms of the common site amplification. In finite difference method and RTT, future wavefields are predicted by using the site-factor corrected waveforms. For prediction of amplitude at each location, it is necessary to convert inversely the waveforms to those having the site amplification factor at the individual location. For the inverse process, that is application of $|A_1(f)/A_2(f)|$, $F^{-1}(s)$ can be used. Because denominator and numerator are the same order of s (**Eq. 31**), and $h_{1\mathrm{m}}$ and $h_{2\mathrm{m}}$ are positive numbers, both forward, $F(s)$, and inverse, $F^{-1}(s)$, filters are stable, where all poles and all zeros are distributed in the left half space in the s-plane (Scherbaum, 1996).

For the PLUM method (**Eq. 24**), the IIR filter $F_{\mathrm{pi}}(z)$ can be applied, which represents site amplification at the target site p relative to site i. Applying $F_{\mathrm{pi}}(z)$ to u ($\boldsymbol{x}_i$, t) to obtain the corrected waveforms, u_c ($\boldsymbol{x}_i$, t), and then

$$\left|u\left(x_p,t\right)\right|_{\max t} \le \mathrm{Max_i}\left|u_c\left(x_i,t\right)\right|_{\max t}, \tag{38}$$

can be used instead of **Eq. 24**. For the boundary integral equation method,

$$\boldsymbol{u}\left(\boldsymbol{x}_p,t\right) = \int_{-\infty}^{\infty} d\tau \int \left(\boldsymbol{u}_c\left(\boldsymbol{x}_1,\tau\right) \frac{\partial G\left(\boldsymbol{x}_p,t-\tau;\,\boldsymbol{x}_1,\,0\right)}{\partial n} - G\left(\boldsymbol{x}_p,t-\tau;\boldsymbol{x}_1,\,0\right) \frac{\partial \boldsymbol{u}_c\left(\boldsymbol{x}_1,\tau\right)}{\partial n} \right) dS, \tag{39}$$

can be applied instead of **Eq. 4**.

EXAMPLE OF APPLICATION

Here, I provide an example of a real-time prediction by the wavefield-based approach.

Figure 6 shows the case of a Mw6.4 earthquake, the largest aftershock of the Mw6.7 Chuetsu, Niigata, Japan, earthquake (October 23, 2004) using radiative transfer theory. Small dots in the panels indicate the locations of observation points (many stations for site 1 in **Eq. 30**). Site amplification factors are corrected relative to that of the target site, Ohtemachi, Tokyo; i.e., Tokyo is the site 2. The distribution of observation of strong ground motions was complicated,

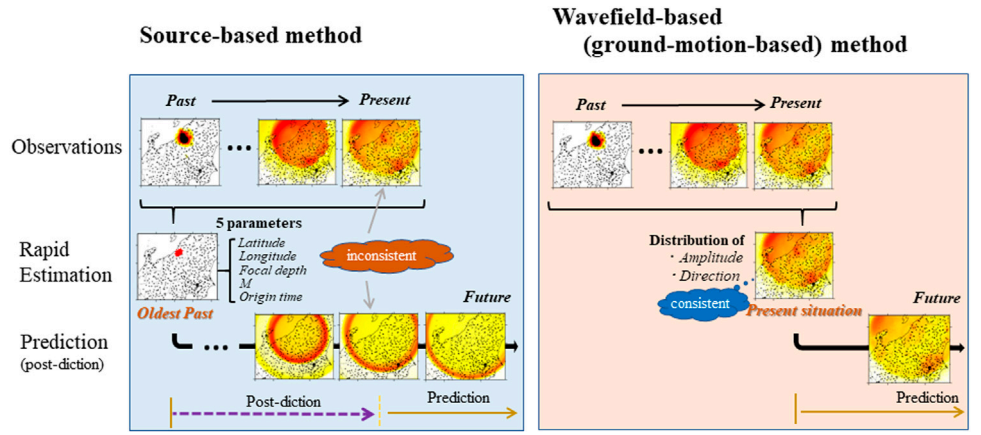

FIGURE 7 | Comparison of the wavefield-based (ground-motion-based) method and the source-based method. This figure and comparison of the two methods are presented in detail in the Summary. In the source-based method, we look back to the "oldest past situation" to represent it by five parameters, and then expand again to reconstruct the spatial distribution from the oldest past situation. In the wavefield-based method, all data up to the present are used to estimate "present situation," and then we predict future spatial distribution from the present situation.

differing from the concentric circles predicted by the source-based method. For example, relatively strong shaking was observed in Kanto, but weak shaking was observed in Tokai. Especially strong shaking was observed towards Tokyo. At t = 11s, strong ground motions were observed around the focal region, and the prediction from the observation indicates that the strong ground motion propagates like an expanding circle, with a final distribution similar to that predicted for a M7.0 event. At t = 50s, strong ground motions were observed toward Tokyo, and the prediction shows that the strong ground motion arrives at Tokyo 10 s later. The final eventual distribution is predicted to be the almost the same as the actual observation.

Prediction of distant future is normally less precise than that of near future. As shown in **Figure 6**, predicted wavefield at 70 s from 11 s does not forecast well the actual wavefield, but that from 50 s predicts it better. For improvement of distant-future prediction, introduction of velocity and attenuation structures is a key. Ogiso et al. (2018) introduced heterogeneous structures in the calculation of the radiative transfer theory. They estimated $g_s(\boldsymbol{x})$ and $h_s(\boldsymbol{x})$ at first, and then used **Eq. 14** instead of **Eq. 16** in the prediction. Estimation of detail velocity and attenuation structures contributes to the precise prediction, especially that of distant future.

Hoshiba and Aoki (2015) applied the technique to data of the 2011 Tohoku earthquake (Mw9.0) and the 2004 Chuetsu, Niigata, earthquake (mainshock, Mw6.7), and Ogiso et al. (2018) did it to data of the 2016 Kumamoto earthquake (Mw7.1) incorporating the heterogeneous attenuation structure. Wang et al. (2017a, b) also used the technique for real-time prediction of ground shaking. Furumura et al. (2019) and Oba et al. (2020) used the finite difference approach to predict long period ground motions (>3–10 s) for the 2007 Off Niigata earthquake (Mw6.6) and the 2004 Off Kii Peninsula earthquake (Mw7.4), respectively.

SUMMARY

One of important key elements of EEW is the real-time prediction of ground motion, as well as the rapid transmission of monitored data and the wide dissemination of warnings. Because seismic motion is a wave propagation phenomenon, the physics of wave propagation, which have been well studied in many research fields, is the basis of real-time prediction of ground motion. In history of EEW research, in the source-based method many authors have focused on rapidly estimating source parameters (e.g., source location, magnitude, source extent), from which peak ground motions (PGA, PGV or seismic intensity) are estimated using a GMPE. Although GMPEs usually indicates empirical relations between the peak ground motion and the source parameters, they do not express the physics of wave propagation in detail; notably, the causality of the occurrence of peak ground motions is not included in it. In the near fault region, PGA and PGV occur before rupture completion, that is, before estimation of eventual magnitude, which essentially leads to late EEWs (Hoshiba, 2020). GMPEs are mainly aimed at explaining the peak ground motion of anticipated future earthquakes (or of past events at locations where seismometers were not deployed). Thus, GMPEs are not necessarily constructed for the purpose of real-time prediction, such as EEW. Instead of borrowing GMPEs, new technique based on the physics of wave propagation for the purpose of the real-time prediction of ground motion is a key to more precise and timely warning. The wavefield-based method described in this review follows this strategy.

To conclude, I compare the wavefield-based (ground-motion-based) method with the conventional method based on source parameters (**Figure 7**) (Hoshiba and Aoki, 2015). In the source-based method, using monitored data from past to

present we look back to the "oldest past situation". Not only is the future situation predicted, the past situation is post-dicted from the "oldest past situation". The time needed for estimation of the source parameters can be regarded as blind time with respect to EEW. In contrast, all data up to the present are used in the wavefield-based method to estimate the "present situation" of wave propagation. Post-diction is not performed in the process.

In the source-based method, information about the very complicated space-time distribution of ground motion is first compressed in order to represent it with a limited number of parameters (such as latitude, longitude, focal depth, origin time, and M), and then it is expanded again to predict ground motion. It is difficult to completely reconstruct the spatial distribution of ground motion even for the present situation: inevitably there are discrepancies between the predicted present situation and the actual present observation. As a result, even if estimation of the source parameters is precise, the prediction of ground motion is not necessarily precise. In contrast, in the wavefield-based method the actual present observation is reflected as much as possible in the estimate of the present situation. Discrepancies are minimized between the estimated present situation and the actual present observation before proceeding to the prediction.

AUTHOR CONTRIBUTIONS

MH designed the study, performed analyses, and drafted the article.

FUNDING

This research was partially supported by the JSPS KAKENHI Grant Number 17H0264.

ACKNOWLEDGMENTS

I appreciate reviewers' careful reading of the article and constructive comments. Waveform data from K–NET and KiK-net (NIED) are used. I thank NIED for their efforts. Discussions with M. Ogiso, Y. Kodera, S. Aoki, N. and Hayashimoto were useful in this research. M. Kamachi, Y. Fujii, N. Usui, and T. Toyoda helped me to learn data assimilation technique. Figures are produced using Generic Mapping Tools (Wessel and Smith, 1995). Any opinions, findings and conclusions described in this paper are solely those of the author and do not necessarily reflect the view of JMA.

REFERENCES

Awaji, T., Kamachi, M., Ikeda, M., and Ishikawa, Y. (2009). *Data Assimilation: Innovation Combining Observation and Model (In Japanese)*, pp284. Kyoto: Kyoto University Press.

Böse, M., Smith, D. E., Felizardo, C., Meier, M.-A., Heaton, T. H., and Clinton, J. F. (2018). FinDer v.2: Improved Real-Time Ground-Motion Predictions for M2-M9 With Seismic Finite-Source Characterization. *Geophys. J. Int.* 212, 725–742. doi:10.1093/gji/ggx430

Chen, D. Y., Hsiao, N. C., and Wu, Y. M. (2015). The Earthworm Based Earthquake Alarm Reporting System in Taiwan. *Bull. Seismological Soc. America.* 105, 568–579. doi:10.1785/0120140147

Cochran, E. S., Bunn, J., Minson, S. E., Baltay, A. S., Kilb, D. L., Kodera, Y., et al. (2019). Event Detection Performance of the PLUM Earthquake Early Warning Algorithm in Southern California. *Bull. Seismol. Soc. Am.* 109, 1524–1541. doi:10.1785/0120180326

Cochran, E. S., Kohler, M. D., Given, D. D., Guiwits, S., Andrews, J., Meier, M. A., et al. (2018). Earthquake Early Warning ShakeAlert System: Testing and Certification Platform. *Seismol. Res. Lett.* 89, 108–117. doi:10.1785/0220170138

Cuéllar, A., Espinosa-Aranda, J. M., Suárez, R., Ibarrola, G., Uribe, A., Rodríguez, F. H., et al. (2014). *The Mexican Seismic Alert System (SASMEX): Its Alert Signals, Broadcast Results and Performance During the M 7.4 Punta Maldonado Earthquake of March 20th, 2012, 2012, in Early Warning for Geological Disasters*. Berlin, Germany: Springer, 71–87. doi:10.1007/978-3-642-12233-0_4

Dhakal, Y. P., Kunugi, T., Kimura, T., Suzuki, W., and Aoi, S. (2019). Peak Ground Motions and Characteristics of Nonlinear Site Response During the 2018 Mw 6.6 Hokkaido Eastern Iburi Earthquake. *Earth Planets Space.* 71, 56. doi:10.1186/s40623-019-1038-2

Furumura, T., Maeda, T., and Oba, A. (2019). Early Forecast of Long-Period Ground Motions via Data Assimilation of Observed Ground Motions and Wave Propagation Simulations. *Geophys. Res. Lett.* 46, 138–147. doi:10.1029/2018GL081163

Gusev, A. A., and Abubakirov, I. R. (1987). Monte-Carlo Simulation of Record Envelope of a Near Earthquake. *Phys. Earth Planet. Interiors.* 49, 30–36. doi:10.1016/0031-9201(87)90130-0

Hoshiba, M., and Aoki, S. (2015). Numerical Shake Prediction for Earthquake Early Warning: Data Assimilation, Real-Time Shake Mapping, and Simulation of Wave Propagation. *Bull. Seismological Soc. America.* 105, 1324–1338. doi:10.1785/0120140280

Hoshiba, M. (1995). Estimation of Nonisotropic Scattering in Western Japan Using Coda Wave Envelopes: Application of a Multiple Nonisotropic Scattering Model. *J. Geophys. Res.* 100, 645–657. doi:10.1029/94jb02064

Hoshiba, M., Kamigaichi, O., Saito, M., Tsukada, S. Y., and Hamada, N. (2008). Earthquake Early Warning Starts Nationwide in Japan. *Eos Trans. AGU.* 89, 73–74. doi:10.1029/2008EO080001

Hoshiba, M. (1997). Seismic Coda Wave Envelope in Depth-Dependent S Wave Velocity Structure. *Phys. Earth Planet. Interiors.* 104, 15–22. doi:10.1016/s0031-9201(97)00055-1

Hoshiba, M. (1991). Simulation of Multiple-Scattered Coda Wave Excitation Based on the Energy Conservation Law. *Phys. Earth Planet. Interiors.* 67, 123–136. doi:10.1016/0031-9201(91)90066-q

Hoshiba, M. (2013a). Real-Time Prediction of Ground Motion by Kirchhoff-Fresnel Boundary Integral Equation Method: Extended Front Detection Method for Earthquake Early Warning. *J. Geophys. Res. Solid Earth.* 118, 1038–1050. doi:10.1002/jgrb.50119

Hoshiba, M. (2013b). Real-Time Correction of Frequency-Dependent Site Amplification Factors for Application to Earthquake Early Warning. *Bull. Seismological Soc. America.* 103, 3179–3188. doi:10.1785/0120130060

Hoshiba, M. (2014). "Review of the Nationwide Earthquake Early Warning in Japan During its First Five Years," in *Earthquake Hazard, Risk, and Disasters*. Editor M. Wyss (Elsevier), 505–529. doi:10.1016/b978-0-12-394848-9.00019-5

Hoshiba, M. (2020). Too-Late Warnings by Estimating Mw: Earthquake Early Warning in the Near-Fault Region. *Bull. Seismol. Soc. Am.* 110, 1276–1288. doi:10.1785/0120190306

Iervolino, I. (2014). "Engineering Earthquake Early Warning via Regional Networks," in *Early Warning for Geological Disasters—Scientific Methods and Current Practice*. Editors J. Zschau and F. Wenzel (Berlin, Heidelberg, New York: Springer), 333–351. doi:10.1007/978-3-642-12233-0_17

Iervolino, I., Manfredi, G., and Cosenza, E. (2007). "Earthquake Early Warning and Engineering Application Prospects," in *Earthquake Early Warning Systems*. Editors P. Gasparini, G. Manfredi, and J. Zschau (Berlin, Heidelberg: Springer), 233–247. doi:10.1007/978-3-540-72241-0_12

Ikeura, T., and Kato, K. (2011). Evaluation of Relative Site Amplification Factors by Combining Average Spectral Ratios of Strong Ground Motions Simultaneously Observed at Adjacent Two Sites. *J. JAEE.* 11, 48–67. (in Japanese with English abstract). doi:10.5610/jaee.11.4_48

Iwata, T., and Irikura, K. (1988). Source Parameters of the 1983 Japan Sea Earthquake Sequence. *J,Phys,Earth.* 36, 155–184. doi:10.4294/jpe1952.36.155

Kalnay, E. (2003). *Atmospheric Modeling, Data Assimilation and Predictability*. New York, NY: Cambridge University Press, pp341.

Kato, K., Takemura, M., Ikeura, T., Urao, K., and Uetake, T. (1992). Preliminary Analysis for Evaluation of Local Site Effects From Strong Motion Spectra by an Inversion Method. *J,Phys,Earth.* 40, 175–191. doi:10.4294/jpe1952.40.175

Kilb, D., Bunn, J., Saunders, J., Cochran, E., Minson, S., Baltay, A., et al. (2021). The PLUM Earthquake Early Warning Algorithm: A Retrospective Case Study of West Coast, USA, Data. *J. Geophys. Res. Solid Earth.* 126. doi:10.1029/2020jb021053

Kodera, Y., Hayashimoto, N., Moriwaki, K., Noguchi, K., Saito, J., Akutagawa, J., et al. (2020). First-Year Performance of a Nationwide Earthquake Early Warning System Using a Wavefield-Based Ground-Motion Prediction Algorithm in Japan. *Seismol. Res. Lett.* 91, 826–834. doi:10.1785/0220190263

Kodera, Y., Saitou, J., Hayashimoto, N., Adachi, S., Saitou, J., Hayashimoto, N., et al. (2016). Earthquake Early Warning for the 2016 Kumamoto Earthquake: Performance Evaluation of the Current System and the Next-Generation Methods of the Japan Meteorological Agency. *Earth Planets Space.* 68, 202. doi:10.1186/s40623-016-0567-1

Kodera, Y., Yamada, Y., Hirano, K., Tamaribuchi, K., Adachi, S., Hayashimoto, N., et al. (2018). The Propagation of Local Undamped Motion (PLUM) Method: a Simple and Robust Seismic Wavefield Estimation Approach for Earthquake Early Warning. *Bull. Seismol. Soc. Am.* 108, 983–1003. doi:10.1785/0120170085

Kuyuk, H. S., and Motosaka, M. (2009). Real-Time Ground Motion Forecasting Using Front-Site Waveform Data Based on Artificial Neural Network. *J. Disaster Res.* 4, 260–266. doi:10.20965/jdr.2009.p0260

Meier, M.-A., Heaton, T., and Clinton, J. (2016). Evidence for Universal Earthquake Rupture Initiation Behavior. *Geophys. Res. Lett.* 43, 7991–7996. doi:10.1002/2016GL070081

Meier, M. A., Kodera, Y., Böse, M., Chung, A., Hoshiba, M., Cochran, E., et al. (2020). How Often Can Earthquake Early Warning Systems Alert Sites With High-Intensity Ground Motion? *J. Geophys. Res. Solid Earth.* 125, e2019JB017718. doi:10.1029/2019JB017718

Melgar, D., and Hayes, G. P. (2019). Characterizing Large Earthquakes Before Rupture Is Complete. *Sci. Adv.* 5, eaav2032. doi:10.1126/sciadv.aav2032

Minson, S. E., Baltay, A. S., Cochran, E. S., Hanks, T. C., Page, M. T., McBride, S. K., et al. (2019). The Limits of Earthquake Early Warning Accuracy and Best Alerting Strategy. *Sci. Rep.* 9, 2478. doi:10.1038/s41598-019-39384-y

Minson, S. E., Meier, M.-A., Baltay, A. S., Hanks, T. C., and Cochran, E. S. (2018). The Limits of Earthquake Early Warning: Timeliness of Ground Motion Estimates. *Sci. Adv.* 4, eaaq0504. doi:10.1126/sciadv.aaq0504

Minson, S. E., Saunders, J. K., Bunn, J. J., Cochran, E. S., Baltay, A. S., Kilb, D. L., et al. (2020). Real-Time Performance of the PLUM Earthquake Early Warning Method During the 2019 M 6.4 and 7.1 Ridgecrest, California, Earthquakes. *Bull. Seism. Soc. Amer.* 110, 1887–1903. doi:10.1785/0120200021

Nagashima, I., Yoshimura, C., Uchiyama, Y., Maseki, R., and Itoi, T. (2008). "Real-time Prediction of Earthquake Ground Motion Using Empirical Transfer Function," in Proceedings of 14th world conference on earthquake engineering, S02–S023.

Noda, S., and Ellsworth, W. L. (2016). Scaling Relation Between Earthquake Magnitude and the Departure Time From Pwave Similar Growth. *Geophys. Res. Lett.* 43, 9053–9060. doi:10.1002/2016GL070069

Oba, A., Furumura, T., and Maeda, T. (2020). Data Assimilation-Based Early Forecasting of Long-Period Ground Motions for Large Earthquakes along the Nankai Trough. *J. Geophys. Res. Solid Earth.* 125, e2019JB019047. doi:10.1029/2019JB019047

Ogiso, M., Aoki, S., and Hoshiba, M. (2016). Real-Time Seismic Intensity Prediction Using Frequency-Dependent Site Amplification Factors. *Earth Planet. Sp.* 68, 83. doi:10.1186/s40623-016-0467-4

Ogiso, M., Hoshiba, M., Shito, A., and Matsumoto, S. (2018). Numerical Shake Prediction for Earthquake Early Warning Incorporating Heterogeneous Attenuation Structure: The Case of the 2016 Kumamoto Earthquake. *Bull. Seismol. Soc. Am.* 108, 3457–3468. doi:10.1785/0120180063

Okuda, T., and Ide, S. (2018). Hierarchical Rupture Growth Evidenced by the Initial Seismic Waveforms. *Nat. Commun.* 9, 3714. doi:10.1038/s41467-018-06168-3

Olson, E. L., and Allen, R. M. (2005). The Deterministic Nature of Earthquake Rupture. *Nature.* 438, 212–215. doi:10.1038/nature04214

Otake, R., Kurima, J., Goto, H., and Sawada, S. (2020). Deep Learning Model for Spatial Interpolation of Real-Time Seismic Intensity. *Seismol. Res. Lett.* 91, 3433–3443. doi:10.1785/0220200006

Phillips, W. S., and Aki, K. (1986). Site Amplification of Coda Waves From Local Earthquakes in Central California. *Bull. Seism. Soc. Amer.* 76, 627–648. doi:10.1785/bssa0760030627

Pilz, M., and Parolai, S. (2016). Ground-Motion Forecasting Using a Reference Station and Complex Site-Response Functions Accounting for the Shallow Geology, *Bull. Seismological Soc. America.* 106, 1570–1583. doi:10.1785/0120150281

Rydelek, P., and Horiuchi, S. (2006). Is Earthquake Rupture Deterministic? *Nature* 442, E5. doi:10.1038/nature04963

Sato, H., Fehler, M. C., and Maeda, T. (2012). *Seismic Wave Propagation and Scattering in the Heterogeneous Earth*. 2nd edition. Berlin, Heidelberg: Springer, pp494. doi:10.1007/978-3-642-23029-5

Scherbaum, F. (1996). *Of Poles and Zeros: Fundamentals of Digital Seismology*. Dordrecht, Netherlands: Kluwer Academic Publishers, 156.

Shearer, P. M. (1999). *Introduction to Seismology*. Cambridge, United Kingdom: Cambridge University Press, pp260.

Trugman, D. T., Page, M. T., Minson, S. E., and Cochran, E. S. (2019). Peak Ground Displacement Saturates Exactly When Expected: Implications for Earthquake Early Warning. *J. Geophys. Res. Solid Earth.* 124, 4642–4653. doi:10.1029/2018JB017093

Wang, T., Jin, X., Wei, Y., and Huang, Y. (2017a). Real-Time Numerical Shake Prediction and Updating for Earthquake Early Warning. *Earthq. Sci.* 30, 251–267. doi:10.1007/s11589-017-0195-2

Wang, T., Jin, X., Huang, Y., and Wei, Y. (2017b). Real-time 3-D Space Numerical Shake Prediction for Earthquake Early Warning. *Earthq. Sci.* 30, 269–281. doi:10.1007/s11589-017-0196-1

Wessel, P., and Smith, W. H. F. (1995). New Version of the Generic Mapping Tools. *Eos Trans. AGU.* 76, 329. doi:10.1029/95eo00198

Xie, Q., Ma, Q., Zhang, J., and Yu, H. (2019). Study on Real-Time Correction of Site Amplification Factor. *Nat. Hazards Earth Syst. Sci.* 19, 2827–2839. doi:10.5194/nhess-19-2827-2019

Yamada, M. (2014). "Estimation of Fault Rupture Extent Using Near-Source Records for Earthquake Early Warning," in *Early Warning for Geological Disasters - Scientific Methods and Current Practice*. Editors J. Zschau and F. Wenzel (Berlin, Heidelberg, New York: Springer), 29–47. doi:10.1007/978-3-642-12233-0_2

Yoshimoto, K. (2000). Monte Carlo Simulation of Seismogram Envelopes in Scattering Media. *J. Geophys. Res.* 105, 6153–6161. doi:10.1029/1999JB900437

Zollo, A., Lancieri, M., and Nielsen, S. (2006). Earthquake Magnitude Estimation From Peak Amplitudes of Very Early Seismic Signals on Strong Motion Records. *Geophys. Res. Lett.* 33, L23312. doi:10.1029/2006GL027795

Conflict of Interest: The author declares that the research was conducted in the absence of any commercial or financial relationships that could be construed as a potential conflict of interest.

Publisher's Note: All claims expressed in this article are solely those of the authors and do not necessarily represent those of their affiliated organizations, or those of the publisher, the editors and the reviewers. Any product that may be evaluated in this article, or claim that may be made by its manufacturer, is not guaranteed or endorsed by the publisher.

frontiers in Earth Science

TECHNOLOGY AND CODE
published: 23 September 2021
doi: 10.3389/feart.2021.700843

Preliminary Results of an Earthquake Early Warning System in Costa Rica

Juan Porras[1], Frédérick Massin[2], Mario Arroyo-Solórzano[3], Ivonne Arroyo[3], Lepolt Linkimer[3], Maren Böse[2] and John Clinton[2]*

[1]Department of Earth Sciences, University of Pisa, Pisa, Italy, [2]Swiss Seismological Service, Swiss Federal Institute of Technology, Zürich, Switzerland, [3]Red Sismológica Nacional y Escuela Centroamericana de Geología, Universidad de Costa Rica, San Jose, Costa Rica

We analyze the performance of a prototype earthquake early warning system deployed at the National Seismological Network of Costa Rica in collaboration with the Swiss Seismological Service by presenting the real-time performance during six earthquakes (Mw 5.1-6.4) that took place during 2018 and 2019. We observe that, despite only limited efforts to optimize the existing network of 158 stations, for EEW purposes, the network density allows fast determination of source parameters using both the Virtual Seismologist and the Finite Fault Rupture Detector algorithms. Shallow earthquakes on or near-shore are routinely identified within 11–20 s of their occurrence. The warning times for the capital city of San Jose are of 43 s for epicenters located at 220 km, like for the Mw 6.4 Armuelles earthquake. On the other hand, during the time analyzed, the EEW system did not provide positive warning times for earthquakes at distances less than 40 km from San Jose. Even though large (Mw > 7) distant historical earthquakes have not caused heavy damage in San Jose, there is potential for developing an EEW system for Costa Rica, especially for the purposes of rapid earthquake notifications, disaster response management, and seismic risk mitigation.

Keywords: Virtual Seismologist, Finite Fault Rupture Detector, seismic network, open-source software, seismic risk mitigation

OPEN ACCESS

Edited by:
Mourad Bezzeghoud, Universidade de Évora, Portugal

Reviewed by:
Gerardo Suarez, National Autonomous University of Mexico, Mexico
Simone Cesca, German Research Centre for Geosciences, Germany

****Correspondence:***
Juan Porras
j.porrasloria@studenti.unipi.it

Specialty section:
This article was submitted to Solid Earth Geophysics, a section of the journal Frontiers in Earth Science

Received: *26 April 2021*
Accepted: *18 August 2021*
Published: *23 September 2021*

Citation:
Porras J, Massin F, Arroyo-Solórzano M, Arroyo I, Linkimer L, Böse M and Clinton J (2021) Preliminary Results of an Earthquake Early Warning System in Costa Rica. Front. Earth Sci. 9:700843. doi: 10.3389/feart.2021.700843

INTRODUCTION

Costa Rica is located at the boundary of three major tectonic plates and one microplate (**Figure 1**). There is a subduction zone in the Pacific side of the country, where the Cocos plate is subducting underneath the Caribbean plate and the Panama microplate at rates from 83 mm/yr in the Northern Pacific of the country to 89 mm/yr in Southeast Costa Rica (DeMets et al., 1994). Large (up to Mw 7.7) seismogenic zone earthquakes have occurred historically along this plate boundary. Intermediate-depth earthquakes (depths 40–200 km) also occur beneath most of Costa Rica (e.g., Lücke and Arroyo, 2015). In addition, shallow earthquakes are common along the central Costa Rica Deformed Belt (CCRDB) and the North Panama Deformed Belt (NPDB), which define the limit between the Caribbean plate and the Panama microplate (Montero, 2001), and along the Panama Fracture Zone (PFZ) which separates the Cocos and Nazca plates. This complex tectonic setting generates high-seismicity rates. Since 1821, the nation has faced 68 damaging earthquakes, with an average rate of one every three years (Montero, 1989; Peraldo and Montero, 1994; Linkimer and Alvarado, 2014).

The National Seismological Network of Costa Rica (RSN) is a research program at the University of Costa Rica (UCR) which includes a seismic network designed to monitor seismic and volcanic

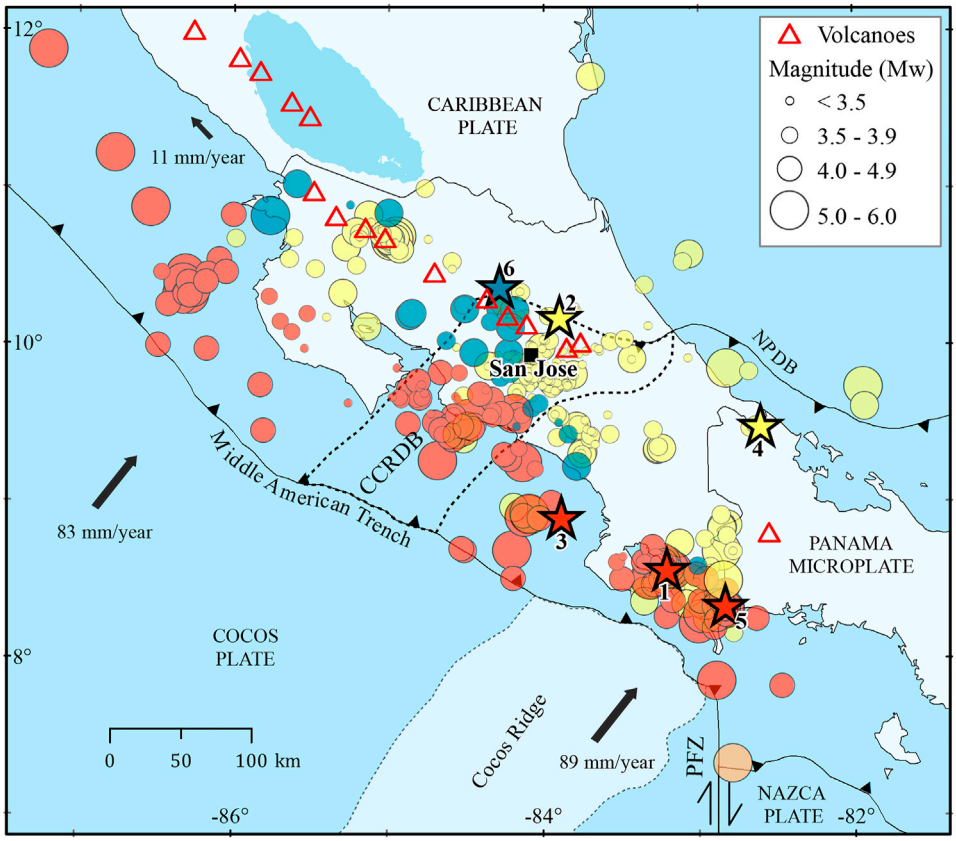

FIGURE 1 | Tectonic framework of Costa Rica and felt earthquakes during 2018 and 2019, as reported to RSN. The origin of the earthquakes is differentiated by color: red interplate subduction, orange Panama Fracture Zone, yellow shallow crustal earthquakes, and blue intraslab subduction earthquakes. The region contained within the dotted lines represents the central Costa Rica Deformed Belt (CCRDB). The dashed line represents the simplified northeast boundary of the Central American Forearc Block along the Volcanic Arc Faults (VAF). The numbered stars represent the earthquakes shown in **Table 1**. The largest events, 1 and 5, are examined in detail. Volcanos in the region are indicated by red triangles.

activity within the country (Linkimer et al., 2018). Recently, the RSN has focused on rapid dissemination of seismic information and within minutes after an earthquake, data are available in a website, social networks, a smartphone application, and intensity maps (e.g., Porras, 2017).

The aim of an earthquake early warning (EEW) system is to detect and quantify the effect of earthquakes as soon as possible after they have begun and, if necessary, to warn people that they are about to experience strong and potentially destructive shaking (Allen et al., 2009). Conventional EEW systems characterize the location and magnitude of an earthquake based on the rapid detection of the fastest seismic waves, the P-waves, that travel at ~6 km/s. With the knowledge of the source, an alert can be disseminated to end users through TV, cell phone applications, radio systems, or dedicated alerting devices. In addition to alerting the public, these alerts can be used to perform automated emergency responses, such as the shutdown of critical systems, slowing and stopping of trains to prevent derailment, shutting off gas or water mains, and stopping elevators to the nearest floor and opening its door, to just name a few applications.

EEW systems have been developed in many countries. They are operational in Mexico (Cuéllar et al., 2018), Taiwan (Hsiao et al., 2009), and Japan (Hoshiba and Ozaki, 2014; Kodera et al., 2016), which are regions located in subduction tectonic environments with different potential of generating destructive interplate earthquakes, and California (Given et al., 2018). Test systems continue to run, in particular in Europe (Clinton et al., 2016), for example, in Switzerland (Massin et al., 2021), Italy (Zollo et al., 2014), Romania (Böse et al., 2007), and Turkey (Wenzel et al., 2014).

The effectiveness of EEW systems depends on many factors that include the density of the seismic network, the quality and design of the acquisition, and telemetry infrastructure as well as the data processing resources (Behr et al., 2015). There are other aspects related to the earthquake characteristics which must also be considered, such as the epicentral location, tectonic environment, depth, and fault kinematics.

Over the last decades, SED-ETH has developed EEW methodologies such as the Virtual Seismologist (VS) (Cua and Heaton, 2007), a traditional pick-based point source algorithm, and the Finite Fault Rupture Detector (FinDer) (Böse et al., 2012), an approach that uses the spatial extent of peak ground motions

to infer the strike and length of the finite fault. As described in Massin et al. (2021), both these algorithms have been implemented as a set of modules that operate within the SeisComP3 system (Hanka et al., 2010). We call these modules ESE (the ETHZ-SED SeisComP EEW system). Utilizing two very different EEW approaches provide redundant and independent EEW results. VS is more suited for small and intermediate-magnitude earthquakes that are well-approximated by a point-source, while FinDer has been developed to resolve high magnitude earthquakes when source finiteness becomes significant. Their different methodologies provide different advantages and independent solutions to the same EEW system.

Since ESE is embedded within SeisComP, EEW can readily be tested in any SeisComP environment (Massin et al., 2021). SeisComP is widely used across Central America (Massin et al., 2018). In 2016, the Swiss Seismological Service (SED-ETH) and the Nicaraguan Institute of Territorial Studies (INETER) started a joint project named "Earthquake Early Warning in Nicaragua and Central America" (EWARNICA), funded by the Swiss Development Agency to assess the feasibility of EEW in the region, starting with Nicaragua.

In the first phase of the project (2016–2018), a prototype EEW system was implemented at INETER. In a second phase (2018–2021), this system was extended to El Salvador and Costa Rica, and the RSN was able to participate during 2018–2019. Currently, the RSN is not an active partner in this project because the lack of personnel does not allow it to cope with more projects in addition to the pre-existing ones in the UCR.

In this work, we report on the performance of ESE at the RSN. We use the solutions of two earthquakes in Costa Rica and Panama (Mw 6.1 and Mw 6.4) for which the EEW system has performed optimally. In addition, we present results from four smaller earthquakes (Mw 5.1-5.4) from different parts of the country that allows us to further analyze factors such as the earthquake magnitude and the station density. The main motivation to show these results is to document the potential for the development of an EEW system in Costa Rica.

DATA AND METHODOLOGY

Data

The data used in this study primarily comes from the RSN Seismic Network, whose code is TC in the FDSN, the International Federation of Digital Seismograph Network (Red Sismológica Nacional de Costa Rica, 2017). The RSN is composed of 37 broadband (BB) and 121 short period (SP) sensors from which 69 have strong motion (SM) sensors incorporated. These SM sensors are early generation Sixaolas, version 3, with low resolution microelectromechanical system (MEMS) accelerometers. This is problematic for small and moderate earthquakes (Mw < 6), which are poorly resolved even in the near field. This density and quality of strong motion sensors would need to be addressed if an EEW system is to be developed for this network. The median data delay of the TC network is 3.75 s (April 2020), defined as the delay between the signal being recorded at the sensor/datalogger in the field and the arrival of the corresponding digitized waveform at the processing hub (Behr et al., 2015). Though this delay is long, it is not unexpected as the TC network is setup for earthquake and volcano monitoring, but not for EEW systems.

In addition to their own seismic stations, the RSN incorporates real-time data from other seismic networks in Nicaragua (Code NU), Panama (PA), and from the OVSICORI-UNA in Costa Rica (OV), shared directly or via the Incorporated Research Institutions for Seismology (IRIS) (**Figure 2**). These stations have significantly longer delays. Earthquake locations in the RSN are performed both automatically and manually by using the open-source software SeisComP3 (Hanka et al., 2010) and SeisAn (Havskov et al., 2020), respectively.

Six significant earthquakes that occurred during 2018 and 2019 were selected to analyze the performance of the EEW system (**Table 1** and **Figure 1**). The first earthquake, which we call the Golfito earthquake, happened on August 17th, 2018, 23:22:24 UTC, with a magnitude of Mw 6.2 and a depth of 21 km. This event happened in the South Pacific of Costa Rica and is associated to the subduction of the Cocos plate beneath the Caribbean plate. The solution of the focal mechanism reported by the RSN shows a thrust fault with strike: 291°, dip: 52°, and rake: 90°. This earthquake generated intensities of up to VI in the epicentral area and of IV in San Jose at a distance of 180 km (Arroyo and Linkimer, 2021).

The second event, referred to as Armuelles earthquake, took place near the locality of Armuelles in Panama, few kilometers away from the border with Costa Rica. It is associated to a strike-slip fault (strike: 304°, dip: 76°, and rake: 4°) within the subducting Cocos plate. This earthquake occurred on June 26th, 2019, at 05: 23:48 UTC, with a magnitude of Mw 6.4 and a depth of 29 km. Intensities of VI-VII were reported in the localities of Golfito and Paso Canoas in Costa Rica and Armuelles and David in Panama, while in San Jose, the Central Pacific, and the South Caribbean of Costa Rica, it was felt with intensities of IV-V (Red Sismológica Nacional de Costa Rica, 2019). This event nucleated 50 km SE of the Golfito event.

The other four events analyzed are intermediate-magnitude earthquakes (Mw 5.1-5.4) located in different regions of Costa Rica (**Table 1** and **Figure 1**). One of them occurred on November 17th, 2018 (Mw 5.1), in the central part of the country, where the network density is high, with a depth of 8 km and is associated to a shallow crustal fault. The next earthquake took place on January 31st, 2019 (Mw 5.4), offshore the central Pacific of Costa Rica at a depth of 15 km and associated to the subduction process. A subsequent event took place on April 1st, 2019 (Mw 5.2), originated by a crustal fault in the southern Caribbean of Costa Rica at a depth of 10 km. The last earthquake nucleated on August 6th, 2019 (Mw 5.4), in the Wadati–Benioff zone beneath central Costa Rica, at 105 km depth.

Methodology

The deployment process of the EEW system at the RSN started with the setup of a Dell Workstation with 6 cores in the RSN laboratory; it was modified with a 500 GB solid state drive disk and 12 GB random access memory to work as a dedicated EEW

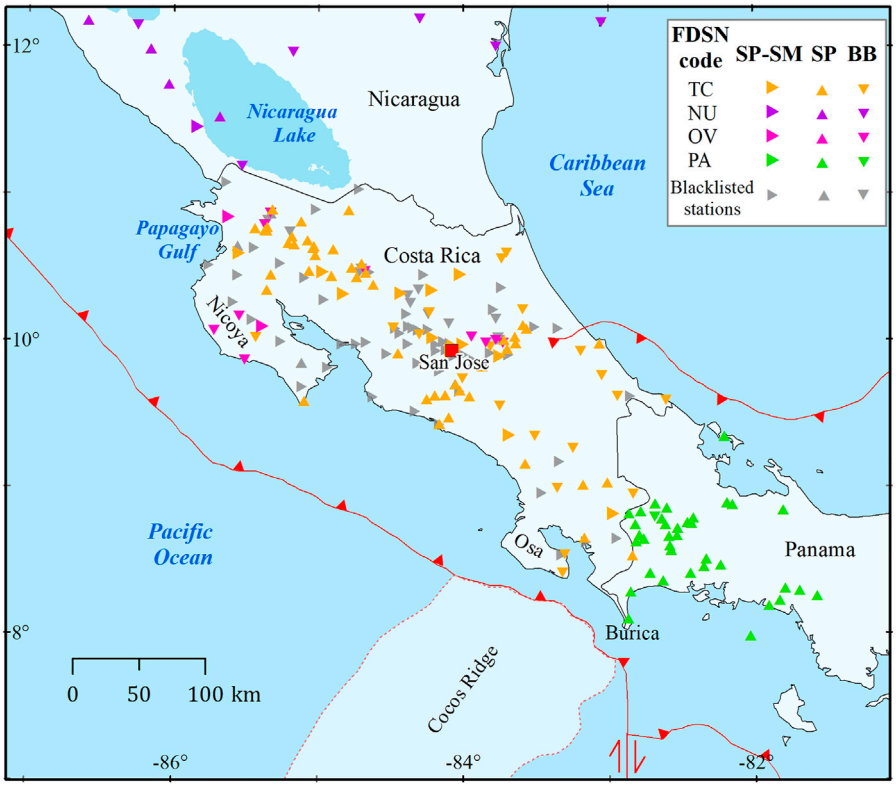

FIGURE 2 | Seismic stations used in this study. BB are broadband sensors, SP are short-period geophones, and SP-SM are short period and strong motion sensors. The stations are differentiated by FDSN (International Federation of Digital Seismograph Network) web services: TC, Red Sismológica Nacional de Costa Rica (light grey); NU, Nicaraguan Seismic Network (light blue); OV, Observatorio Vulcanológico y Sismológico de Costa Rica (light red); and PA, ChiriNet, Panama (orange). The blacklisted stations are represented in black color.

TABLE 1 | Seismic source parameters reported by the RSN for the six earthquakes used in this study. N=number, OT = origin time, Mw = moment magnitude, Lon = longitude, Lat = latitude, D. (km) = epicentral distance to San Jose, and T. (s) = time for S-wave to arrive at San Jose.

N	Date	OT (UTC)	Mw	Depth (km)	Lon	Lat	D. (km)	T. (s)
1	August 17th, 2018	23:22:24	6.1	21.0	−83.209	08.574	180	36
2	November 17th, 2018	14:12:53	5.1	7.9	−83.895	10.181	35	−1
3	January 31st, 2019	13:09:51	5.4	14.8	−83.863	08.868	120	12
4	April 1st, 2019	13:44:49	5.2	10.5	−82.655	09.486	160	21
5	June 26th, 2019	05:23:48	6.4	29.0	−82.833	08.336	220	43
6	August 6th, 2019	21:14:10	5.4	104.8	−84.283	10.370	50	4

server. Ubuntu server 16.04 LTS was chosen as the operating system and SeisComP3 was installed and configured to read real-time waveforms from the RSN main acquisition server via the Seedlink protocol.

For each earthquake analyzed, the waveforms were processed by using the VS and FinDer algorithms compiled within the SeisComP software in the EEW server. The VS method is a pick-based point-source approach for EEW. The location is determined using the standard SeisComP module scautoloc, requiring 6 triggered stations. The VS magnitude as implemented at the time required a minimum of 3 s of data following the P-wave arrival. This algorithm combines relationships between the final magnitude and the ratios between ground motion acceleration and displacement and specific ground motion prediction equations (GMPEs) for P- and S-waves (Cua and Heaton, 2007). Once a first solution is available, VS solutions are updated every second, each one consisting of values of magnitude, latitude, longitude, depth, and creation time.

The FinDer EEW algorithm (Böse et al., 2012; Böse et al., 2018) uses template matching to automatically provide estimates of the fault rupture extent in real-time (assuming a line-source) by estimating the current centroid position, length, and strike. Unlike VS, FinDer is not based on picks. Its approach compares

TABLE 2 | Solutions of the Virtual Seismologist (VS) and Finite Fault Rupture Detector (FinDer) for the Golfito and Armuelles earthquakes. Sol = solution, M = magnitude value (VS or FinDer), Lat = latitude, Lon = longitude, CT = creation time, Tdiff (s) = time difference in seconds between CT and OT, #st = number of stations used in the VS solution, L.E. (km) = location error, and M.E. = absolute value of magnitude error. The best solutions are chosen when the smallest location differences are obtained compared to the RSN solution.

—	Sol	M	Lat	Lon	Depth (km)	CT (UTC)	Tdiff (s)	#st	L.E. (km)	M.E.
A) Golfito earthquake (August 17th, 2018); RSN: Mw 6.1; depth = 21 km. 180 km to San Jose										
VS	First	5.8	8.609	–83.202	22.7	23:22:36.76	12.8	6	4	0.3
	Best	5.8	8.609	–83.202	22.7	23:22:36.76	12.8	6	4	0.3
	Last	5.8	8.663	–83.192	3.2	23:23:06.92	42.9	85	20	0.3
FinDer	First	5.5	9.132	–83.454	20.0	23:22:44.12	20.1	—	68	0.6
	Best	6.4	8.276	–83.180	20.0	23:23:16.70	52.7	—	33	0.3
	Last	6.6	8.186	–83.408	20.0	23:24:45.06	141.1	—	48	0.5
B) Armuelles earthquake (June 26th, 2019); RSN: Mw 6.4; depth = 29 km. 220 km to San Jose										
VS	First	6.1	8.318	–82.948	12.0	05:24:03.01	15.0	4	21	0.3
	Best	6.2	8.195	–82.859	19.9	05:24:07.01	19.0	7	18	0.2
	Last	6.5	8.306	–82.946	7.2	05:24:32.06	44.1	41	25	0.1
FinDer	First	5.8	8.373	–82.955	20.0	05:24:06.00	18.0	—	17	0.6
	Best	5.8	8.373	–82.955	20.0	05:24:06.00	18.0	—	17	0.6
	Last	6.8	8.688	–83.322	20.0	05:24:56.86	68.9	—	67	0.4

the observed spatial extent of ground motion with a set of pre-calculated fixed depth templates using a combined grid-search and divide-and-conquer approach. FinDer keeps track of the evolving dimensions of a rupture in progress until peak shaking is reached. In case of a major earthquake, where the finite fault is significant, the estimates of source geometries as provided by FinDer make predicted shaking intensities more accurate for EEW (Böse et al., 2018).

In contrast to VS, the FinDer solutions presented in this study are updated irregularly, only when a new solution differs from the previous one. It is important to highlight that VS uses any sensor type for detection, and for magnitude, it can use all on-scale data, whereas FinDer can only use unsaturated BB or SM data (current configuration within ESE is to identify a waveform as saturated once it reaches with a raw amplitude (in counts) above 80% of 2^{23}; this assumes all digitizers are 24 bit). This is problematic at the RSN as the SM sensors are noisy and the majority of the streamed real-time data come from SP sensors, not used by FinDer. FinDer is also more sensitive to gross errors in sensor metadata gains, timing errors, and late arriving data.

In our study, the warning times available for each earthquake assume the strong shaking arrives with the first arriving S-waves. The S-wave velocity is based on the P-wave velocity model for Costa Rica from Quintero and Kissling (2001) and a Vp/Vs ratio of 1.75, as used by the RSN. In this study, all warnings were calculated for the capital city San Jose as target, which is also the most populated region of Costa Rica (**Figure 2**).

The key parameters used to evaluate EEW solutions here are the location error—the difference in km between the final RSN hypocenter and each EEW hypocenter; the magnitude error—the difference between the final RSN magnitude and each EEW magnitude; and the time difference between the origin time of each earthquake which is based on the final RSN location and the creation time for each EEW solution.

The results presented in this paper span the one year testing period of 2018–2019. Following the larger earthquakes, the performance was reviewed, and the algorithms were tuned using event playback, which favored an improvement of the EEW system over time. During this step, we optimized the configuration of the P-wave arrival detection parameters and the hypocenter location grid, and we created and managed a blacklist of problematic stations (e.g., those with high latency or excessively noisy stations). Blacklists are maintained independently for each algorithm, as they are susceptible to different issues. Crucially, EEW algorithms are very

TABLE 3 | Solutions of VS and FinDer for the other four earthquakes in different regions of Costa Rica. Sol = solution, M = magnitude, Lat = latitude, Lon = longitude, CT = creation time, Tdiff (s) = time difference in seconds between CT and OT, #st = number of stations used in the VS solution, L.E. (km) = location error, and M.E. = absolute value of magnitude error. The best solutions are chosen when the smallest location differences are obtained compared to the RSN solution.

—	Sol	M	Lat	Lon	Depth (km)	CT (UTC)	Tdiff (s)	# st	L.E. (km)	M.E.
A) November 17th, 2018; Mw 5.1; central Costa Rica; depth: 7.9 km. 35 km to San Jose										
VS	First	4.8	9.767	–83.950	1.0	14:13:04.21	11.2	7	47	0.3
	Best	4.8	10.158	–83.893	6.6	14:13:27.41	34.4	85	3	0.3
	Last	4.8	10.165	–83.901	5.2	14:13:34.43	41.4	95	3	0.3
B) January 31st, 2019; Mw 5.4; Central Pacific of Costa Rica; depth: 14.8 km. 120 km to San Jose										
VS	First	4.6	8.938	–83.809	16.5	13:10:12.60	21.6	11	10	0.8
	Best	5.0	8.873	–83.841	10.0	13:10:23.72	32.7	67	5	0.4
	Last	5.3	8.904	–83.835	1.1	13:10:42.78	51.8	94	15	0.1
FinDer	First	4.2	8.997	–83.408	20.0	13:10:12.43	21.4	—	52	1.2
	Best	4.5	8.997	–83.454	20.0	13:10:14.52	23.5	—	47	0.9
	Last	6.2	8.952	–83.362	20.0	13:12:07.39	136.4	—	56	0.8
C) April 1st, 2019; Mw 5.2; South Caribbean of Costa Rica; depth: 10.5 km. 160 km to San Jose1										
VS	First	4.6	9.257	–82.911	10.0	13:45:12.41	23.4	7	38	0.6
	Best	4.9	9.430	–82.679	10.0	13:45:22.49	33.5	43	7	0.3
	Last	5.3	9.419	–82.657	10.0	13:45:39.54	50.5	78	8	0.1
FinDer	First	4.7	9.049	–82.793	10.0	13:45:09.97	21.0	—	51	0.5
	Best	5.6	9.094	–82.793	10.0	13:45:17.41	28.4	—	46	0.4
	Last	5.9	9.319	–83.068	10.0	13:45:29.29	40.3	—	49	0.7
D) August 6th, 2019; Mw 5.4; central Costa Rica; depth: 104.8 km. 50 km to San Jose										
VS	First	4.7	10.403	–84.300	233.4	21:14:30.57	20.6	17	129	0.7
	Best	4.7	10.299	–84.270	101.0	21:14:35.67	25.7	57	9	0.7
	Last	5.1	10.303	–84.280	84.8	21:14:57.85	47.9	129	22	0.3
FinDer	First	4.7	9.905	–84.241	85.0	21:14:47.11	37.1	—	56	0.7
	Best	4.7	9.905	–84.241	85.0	21:14:47.11	37.1	—	56	0.7
	Last	5.1	9.770	–84.241	85.0	21:15:47.75	97.8	—	70	0.3

susceptible to individual timing and metadata errors, in particular in terms of gain. We performed a detailed revision of the seismic network metadata and improved the telemetry configuration and delay by decreasing the number of retransmission nodes.

RESULTS

Tables 2 and **3** summarize the real-time performance of VS and FinDer with the first, last, and best solution, which was chosen as the solution with the smallest difference in location error when

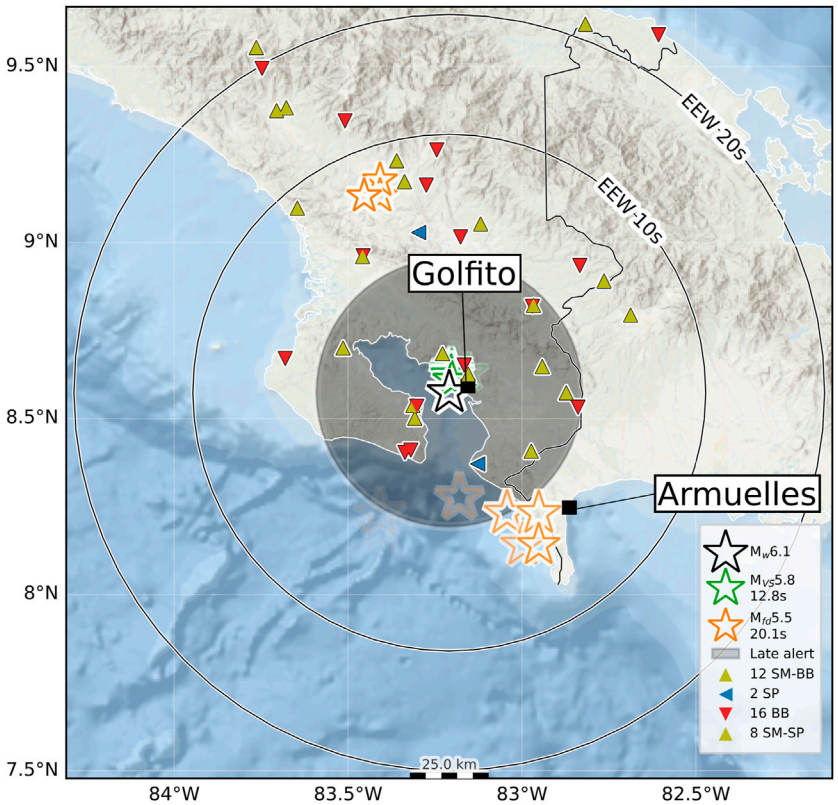

FIGURE 3 | Map of the 2018 Golfito earthquake (Mw 6.1). Solutions provided by VS and FinDer are shown as green and orange stars, respectively. The RSN location is represented as a black star (Arroyo and Linkimer, 2021). Triangles represent the seismic stations and are color coded (see inset) based on the sensor type, as short period (SP), broad band (BB), and strong motion (SM). SP stations are used by VS, but not by FinDer. The blind zone is the concentric shadow area around the RSN location and represents the late alert zone. The thin black circles represent the warning time at different distances from the epicenter.

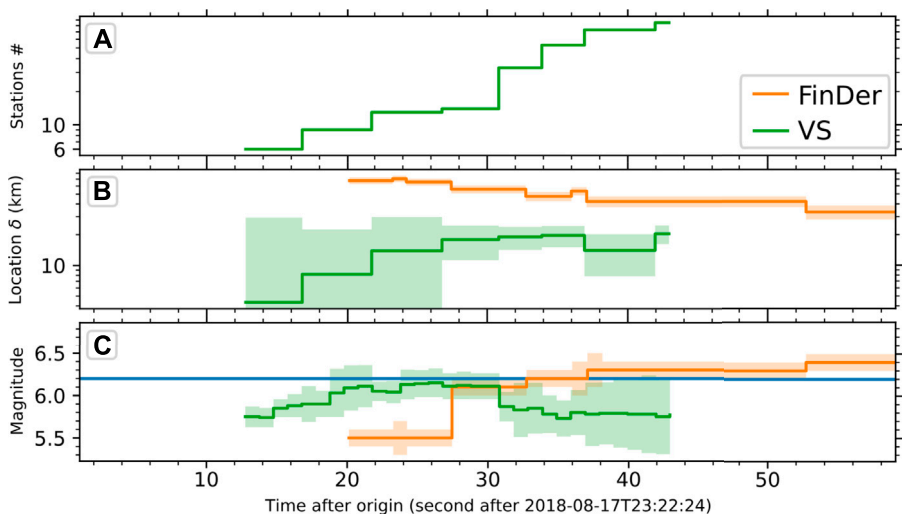

FIGURE 4 | Time evolution of the **(A)** number of stations contributing to the location, **(B)** the location error (km), and **(C)** EEW magnitude for the 2018 Golfito earthquake (Mw 6.1).

compared to the reference revised network solution (RSN). The complete list of the VS and FinDer solution updates for each earthquake is available in the supplementary material. In this analysis, we do not discuss the line-source component of the FinDer solutions (which actually is the most important output of FinDer); we treat FinDer as point-source algorithm reporting the FinDer centroid solution and the equivalent magnitude results.

Golfito Earthquake

The Mw 6.2 Golfito earthquake occurred on August 17, 2018. VS provided 31 and FinDer 20 updates in real time. The first VS and FinDer solutions were determined 12.8 and 20.1 s after the origin time (OT), with location errors of 4 and 68 km, respectively (**Table 2**). The blind zone of this earthquake covered a radius of ~40 km from the epicenter (**Figure 3**); all VS solutions were located within 20 km of the RSN epicenter, while the FinDer solutions had location errors between 33 and 70 km (**Figures 4A,B**). Considering that San Jose is 181 km from the hypocenter and a S-wave velocity of 3.7 km/s, the EEW system issued a warning time of 36 s before the S-wave arrived in San Jose, where an intensity of IV was experienced.

Though both algorithms correctly and immediately recognized the event to be significant, their initial magnitudes were underestimated, with errors up to 0.5 units for both VS and FinDer (**Figure 4C**). They approached the Mw 6.2 reference magnitude with the incorporation of more stations. The best VS and FinDer solutions were obtained 12.8 and 52.7 s after the OT, with location errors of 4 and 33 km, respectively (**Table 2**).

This event occurred shortly after the collaboration began, and since alerts were sounded at RSN using the open-source software Earthquake Early Warning Display (EEWD) (Cauzzi et al., 2016), many seconds before the ground motions were felt, it was very encouraging and provided a first real-time experience of the performance of the EEW system. It was the first big event after the deployment of the EEW system, and, despite no significant effort to optimize the network for EEW, the system performed very well with a first solution 12 s after the OT and location error of 4 km.

During the Golfito earthquake, all available stations were used by the EEW system, and, without being optimized, the main limitations on the algorithms were that the FinDer location error was always above 30 km, which is expected as this earthquake is located at the edge of the network. Furthermore, the two closest stations (TC.EDAD. and TC.EDS2) had huge delays during the Golfito earthquake, and a number of close-by stations (FITO, JIME, NELY, and PANO) had been blacklisted for FinDer, because of previous issues. Despite that, the FinDer magnitude was stable, and the line-source strike was estimated as 330°, which is close to the RSN moment tensor solution (286°) (Arroyo and Linkimer, 2021). In contrast, the VS location errors remained always below 20 km; however, the VS magnitude dropped significantly after 30 s when P-wave energy from the many stations in the central valley near San Jose began to be incorporated.

After this event, we identified several issues to improve. The PA stations in **Figure 2** were not incorporated into the RSN network, thus leaving a big gap towards Panama. Changes in the configuration of the EEW system needed to be made including the blacklisting of stations with recurrent false trigger, adjustment of the STA/LTA detection and AIC re-picker filters, incorporation of the UCR velocity model, and optimization of the location grid used by SeisComP.

Armuelles Earthquake

Nearly one year later, the largest event during the testing period, the Armuelles earthquake, occurred 50 km to the SE of the Golfito earthquake. At that time, the PA stations were already incorporated into the RSN network (though with higher latency) and the algorithms had been optimized as described before. At this stage, the blacklist includes 82 stations.

VS provided 30 and FinDer 14 solutions during this event. At that time, VS had been modified to produce a solution with only four stations instead of six, resulting in the first two solutions provided 15.0 and 16.0 s after the OT with location errors of 21 km, while the last VS solution was estimated with 41 readings 44.1 s after the OT. On the other hand, the first and last FinDer solutions were provided 18 and 68.9 s after the OT (**Table 2**). The blind zone of this event covers a radius of 50 km from the epicenter and considering its hypocenter at 222 km from San Jose (**Figure 5**) and an S-wave velocity of 3.9 km/s resulted in 43 s of warning time for the Armuelles earthquake.

The VS location errors ranged between 18 and 84 km with 7 and 5 stations, respectively, while for FinDer, the errors were between 17 and 67 km, respectively (**Figures 6A,B**). At 17.0 s after the OT, a false pick increased dramatically the VS location error by placing the solution 83 km south of the RSN location; however, two seconds later, the error decreased to 18 km after incorporating two more stations into the VS solution. The FinDer locations for the Armuelles earthquake were more stable than those provided by VS, with errors of less than 30 km during the first 31 s along an alignment marked by the solution updates, which might give insights into the evolution of the earthquake rupture during the updating process.

The magnitude variation for both algorithms is much more stable than the magnitude performance of the Golfito earthquake (**Figure 6C**), with errors of less than one unit. The fact that the earliest solution was available 15 s after the OT, that is, 3 s later than the first solution of the Golfito earthquake, can be explained by the increased depth of the event (7 km deeper) and the location further south and across the border, further away from the denser parts of the network. The additional stations in Panama, despite their higher latency and only available to VS, contributed positively to obtain stable magnitude and location results. At the time of the Armuelles earthquake, we had a more robust EEW system.

Intermediate-Magnitude Earthquakes

In addition to the two significant earthquakes described before, the EEW solutions for four intermediate-magnitude (Mw 5.1-5.4) seismic events in different regions of Costa Rica are reported to observe the effect of the seismic network density and the geographical variation of earthquakes in the EEW performance (**Figure 7**).

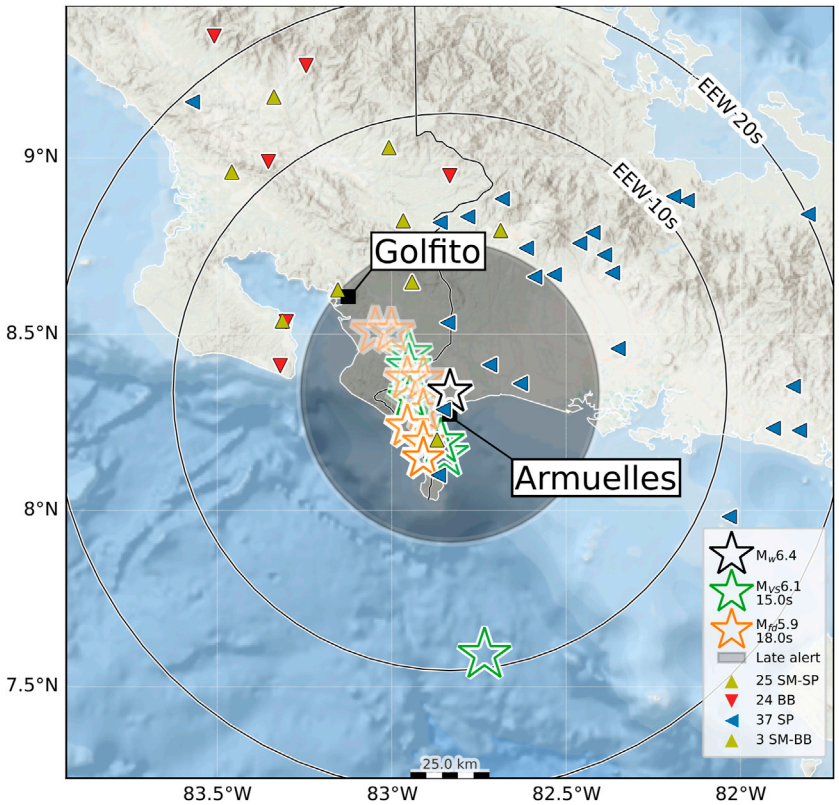

FIGURE 5 | Map of the 2019 Armuelles earthquake (Mw 6.4). Solutions provided by VS and FinDer are shown as green and orange stars, respectively. The RSN location is represented as a black star. Triangles represent the seismic stations and are color coded (see inset) based on the sensor type, as short period (SP), broad band (BB), and strong motion (SM). SP stations are used by VS, but not by FinDer. The blind zone is the concentric shadow area around the RSN location and represents the late alert zone. The thin black circles represent the warning time at different distances from the epicenter.

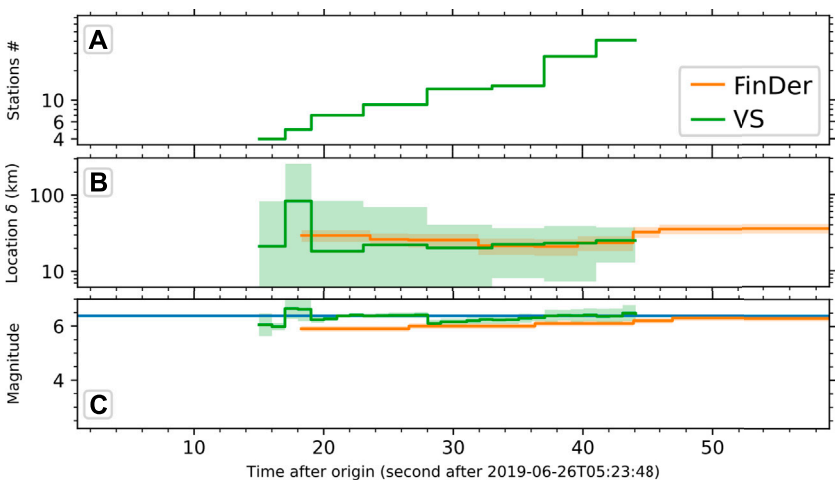

FIGURE 6 | Time evolution of the **(A)** number of stations contributing to the location, **(B)** the location error (km), and the **(C)** EEW magnitude for the 2019 Armuelles earthquake (Mw 6.4).

The event of November 17th, 2018 (Mw 5.1), in the central part of the country where the network density is high occurs within 35 km of San Jose and was the closest event to the capital from the earthquakes analyzed. The first VS solution was available just 11.2 s after the OT with seven stations and a location error of 47 km due to single false pick, which was

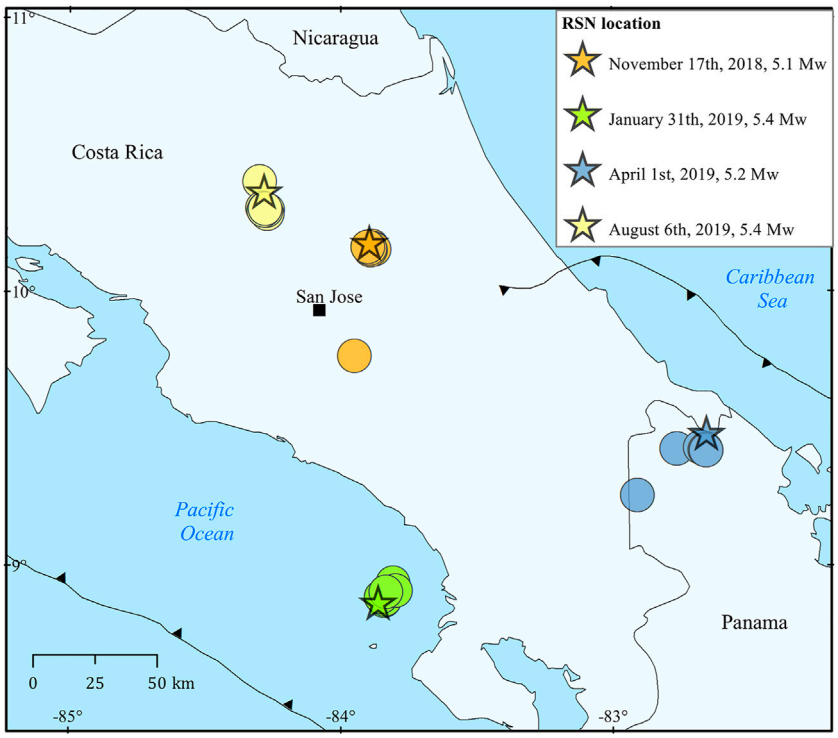

FIGURE 7 | Solutions for four events selected in different regions of Costa Rica (**Table 3**). The stars represent the RSN locations, and the circles represent the VS solutions. The colors correspond to the date of the earthquake, as shown in the inset.

corrected after two seconds, leading to a more reasonable error of 12 km that is dominated by an error in depth. The best solution was obtained with a location error of 3 km, 85 stations, and 34.4 s after the OT (**Table 3**). The magnitude estimation was very stable, varying between 4.7 and 4.8. FinDer was not running at that time. Regardless of its fast first solution 11 s after the OT, the alert arrived one second after the S-wave arrival in San Jose due to its vicinity to the target.

The first solution for the earthquake on January 31st, 2019, in the Central Pacific of Costa Rica (Mw 5.4) came from FinDer 21.4 s after the OT with a location error of 52 km. This event was outside of the network coverage, and we obtained a warning time of 12 s for San Jose. The high location error was corrected to 10 km with the first VS solution 0.2 s later with 11 stations. The VS location error decreased up to 5 km 32.7 s after the OT with 67 stations (**Table 3**).

For the event that took place on April 1st, 2019, in the South Caribbean of Costa Rica with Mw 5.2, the first solution came also from FinDer 21.0 s after the OT with a location error of 51 km and a magnitude of 4.7. The first VS solution was available two seconds later, with seven stations and a location error of 38 km. A first alert provided a warning of 21 s for San Jose. The VS location error decreased to 15 km 30 s after the OT with 23 stations and the best VS solution was obtained 33.5 s after the OT with 43 stations and a location error of 7 km (**Table 3**). Recalling that FinDer uses only data from BB and SM sensors to match ground motion templates, its performance for the middle-magnitude events in the Central Pacific and South Caribbean of Costa Rica was affected by the few (<4) BB triggered stations and the blacklisted low resolution MEMS SM sensors.

Another earthquake analyzed occurred on August 6th, 2019 (Mw 5.4), in the Wadati–Benioff zone beneath central Costa Rica, at 105 km depth. The significant depth of this event resulted in a first VS solution obtained 20.6 s after the OT, with a location error of 129 km by using 17 stations, which decreased rapidly to an error of 31 km just two seconds later with 37 stations and to 9 km after 3 s with 57 stations. The high density of stations in central Costa Rica contributed to rapidly improve the VS source parameters. On the contrary, FinDer was limited by the few BB and SM sensors EEW capable, obtaining the first solution 37.1 s after the OT with location error of 56 km (**Table 3**). Even though the epicenter was located in a high station density region, we obtained only 4 s of warning due to the significant depth of this event.

DISCUSSION

The RSN seismic network, composed mainly of SP sensors with low resolution SM MEMS and with a high median data delay of 3.75 s, is not designed for EEW systems since RSN is oriented towards earthquake and volcano monitoring using pick-based algorithms. With this in mind, the EEW system was deployed at RSN to assess its potential in Costa Rica with the existing infrastructure.

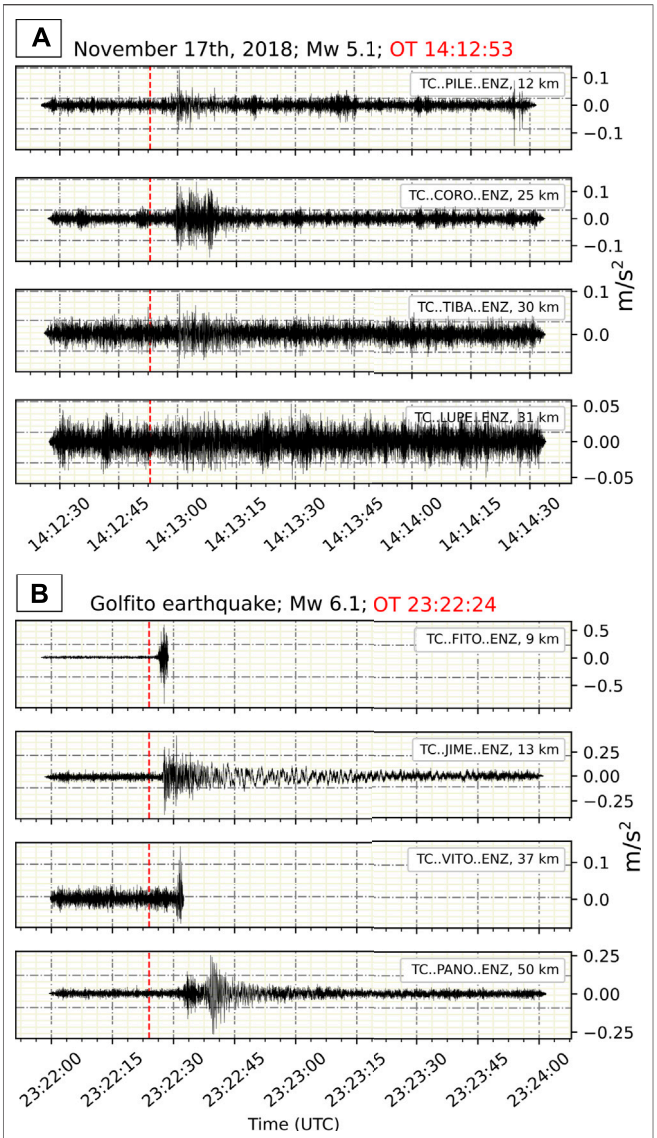

FIGURE 8 | Closest four vertical SM recordings of the **(A)** November 17th, 2018 (Mw 5.1), and **(B)** Golfito (Mw 6.1) earthquakes. The vertical red lines indicate the origin times. Left vertical axis is in counts and the corresponding acceleration value is indicated in the right vertical axis. The epicentral distance of each station is indicated in the labels after the station name. **(A)** The low resolution of the strong motion MEMS sensors and **(B)** the lost signals shortly after the P-wave arrival during the Golfito earthquake, most likely due to failure of communication or mains power.

Evaluating the EEW performance over time with different events becomes difficult, as the number of stations monitored by the seismic network, their EEW performance, and the configuration of the EEW system were not constant over the test period. Also, the performance of VS and FinDer are compared in terms of point-source characteristics, even though FinDer is also capable of tracking the current rupture size (which is actually the main output of FinDer).

The first EEW solutions for the Golfito (12.8 s) and Armuelles (15 s) earthquakes are similarly fast considering differences in event depth, but subsequent EEW updates for the Armuelles earthquake are more stable. This is attributed to the optimization of the EEW system, for which the main changes included the incorporation of 25 SP stations from the PA network after the Golfito earthquake (which help improving the VS estimates), the blacklisting of 82 stations which are not EEW operational (due to low resolution data, poor timing, or high latency) and other changes in configuration, such as the STA/LTA detector, re-picker filters, and the customization of the location grid. It is noted that once the network has been optimized, FinDer approaches and at times exceeds the speeds of the VS alerts.

The aforementioned customization of the EEW system provided a much more robust FinDer performance during the Armuelles earthquake, with a much lower FinDer location error than the one for the Golfito earthquake and a low magnitude fluctuation for both algorithms. These results show that the EEW system at RSN already operated satisfactorily without any customization for VS, and with relatively minor efforts, we were able to improve the FinDer speed and stability. A number of critical issues to FinDer, such as the handling of latent data and faster magnitude convergence, have been addressed in the latest FinDer release in 2021.

The results of the intermediate-magnitude earthquakes indicate that VS performs better than FinDer in the RSN network since it is composed mainly of SP sensors and the VS system can use these for location and also for magnitude, when on-scale. The VS magnitudes are generally robust even using few stations. Thus, VS has an advantage especially in the regions of higher station density including different sensor types, such as central Costa Rica.

Limitations related to the seismic network have been revealed. These include the high median data delay of 3.75 s that would need to be reduced for EEW. Other station issues observed are GPS timing problems and low resolution of the strong motion MEMS sensors (**Figure 8A**); these problems led to a large proportion of the network, 82 stations, being blacklisted, significantly reducing the number of operational EEW stations at RSN. A final challenge observed was the lack of network resilience during strong motions. At numerous near-field stations, the signal was lost shortly after the P-wave arrival, most likely due to failure of communication or mains power (**Figure 8B**). Redundancy here should be considered. The efforts for network optimization outlined here have to be taken if EEW is to become a product at RSN (Massin et al., 2020).

As with all EEW systems, we can expect alerts to arrive only after the onset of strong shaking for earthquakes close to the target. With the examples presented here, where alerts have been provided within 11 s of event initiation, we can expect late alerts for all shallow crustal events within 40 km of the capital. Unfortunately, if the present network delivers EEW, this would mean late alerts for repeats of some historically destructive events near San Jose, such as the Cartago earthquake (M 6.4) in 1910 (Montero and Miyamura, 1981) and the Cinchona earthquake (Mw 6.1) in 2009 (Linkimer and Alvarado, 2014), which were originated by local faults with epicenters at 20 and 30 km of the city, respectively.

The alert time is modest (<5 s) for seismic events close to San Jose originated in the subduction zone, such as the 1990 Cobano (Mw 7.0) and 1999 Quepos (Mw 6.9) earthquakes, and at intermediate depth in the subducting slab, like the 1992 Naranjo earthquake (Mw 6.5). Nevertheless, warnings could be sent for the public in coordination with local authorities. Like in other nations, automated procedures for heavily-exposed industrial partners can also be considered, including actions mentioned before. It is also worth noting that even if alerts are late, EEW can provide earthquake parameters and shaking information concurrent with the arrival of ground motions, which can be effectively used to inform geoscientists, civil authorities, and the wider public before the onset of cascading failures of communications and power infrastructures that may occur.

In summary, it is clear that even with the performance presented here, the EEW can be useful for providing rapid earthquake notification for San Jose. During the testing period, a small crustal earthquake (May 9th, 2019, Mw 3.3) near San Jose was detected by VS after only 5.8 s. As the event was small and only very locally felt, it was not detailed in this study. If results like this could be replicated by using an improved seismic network, the epicentral region that receives late alerts may be reduced significantly.

CONCLUSIONS

With the existing RSN network, which has not been optimized for EEW systems, and using the SED-developed ESE EEW system for selected earthquake of 2018–2019, we observe warning times for San Jose of 36–43 s for distant (180–220 km) earthquakes. Epicenters at less than 40 km do not allow positive warning times for the metropolitan area of San Jose. FinDer has performed well for the M > 6 earthquakes; however, it is limited for the intermediate-magnitude (Mw 5.1–5.4) events since the majority of stations in the RSN network include SP sensors not used by FinDer. Additionally, VS, trigger-based and capable of using any seismic sensor, has proved to be successful for the six earthquakes studied here.

We have identified limitations in the EEW system related to noisy or high-latency stations which reduced the number of operational EEW stations. Despite that, the current RSN network has the potential to provide alerts for large (M > 6) earthquakes occurring at distances larger than 40 km by using FinDer and VS. This could be further improved by increasing the density of operational EEW stations in the country and reducing data delays. We also demonstrated the feasibility of rapid earthquake notification from the current RSN network in all studied cases, potentially providing alerts for disaster response management and seismic risk mitigation.

DATA AVAILABILITY STATEMENT

The original contributions presented in the study are included in the article/**Supplementary Material**; further inquiries can be directed to the corresponding author.

AUTHOR CONTRIBUTIONS

JP: former researcher at the RSN; contributed to the implementation and testing of the EEW system and analysis and interpretation of data, writing, and some of the figures. FM: responsible for the implementation of the EEW system; trainer of the staff of the seismic networks in Central America in EEW related topics; contributed to the design of the work, technical information, analysis of data, critical revision, and some of the figures. MA-S: researcher at the RSN; contributed to monitor the EEW system during the testing period; provided substantial contributions to the interpretation and analysis of data, technical information, and critical revision and prepared some of the figures. IA: current coordinator of the RSN; contributed to the data interpretation and writing. LL: coordinated the RSN during a portion of the EEW testing period and contributed to the data interpretation and writing. MB: researcher at the SED; responsible for the development of FinDer; provided substantial contributions to the design of the work, technical information, interpretation and analysis of data, and critical revision. JC: director of seismic networks at SED; responsible for the EWARNICA project; provided substantial contributions to the design of the work, technical information, interpretation and analysis of data, and critical revision.

FUNDING

This work was mainly supported by the Swiss Development Agency and partially by the projects 113-B5-704 and 113-B9-911 of the University of Costa Rica.

ACKNOWLEDGMENTS

The authors thank the Swiss Development Agency for providing financial support to the EWARNICA project, which serves as framework for this study, and for supporting the training in the SeisComP software for technical staff of the RSN and other seismic networks in Central America. The authors also thank the Nicaraguan Seismic Network (NU, doi: 10.7914/SN/NU), the Observatorio Vulcanológico y Sismológico de Costa Rica (OV, doi: 10.7914/SN/OV), and the ChiriNet Panama seismic network (PA, doi: 10.7914/SN/PA) for sharing some of their stations in real-time with the RSN and reinforcing the seismic network coverage in Costa Rica.

SUPPLEMENTARY MATERIAL

The Supplementary Material for this article can be found online at: https://www.frontiersin.org/articles/10.3389/feart.2021.700843/full#supplementary-material

REFERENCES

Allen, R. M., Gasparini, P., Kamigaichi, O., and Böse, M. (2009). The Status of Earthquake Early Warning Around the World: An Introductory Overview. *Seismol. Res. Lett.* 80 (5), 682–693. doi:10.1785/gssrl.80.5.682

Arroyo, I. G., and Linkimer, L. (2021). Geometría de la zona sismogénica interplacas en el Sureste de Costa Rica a la luz de la secuencia de Golfito del 2018. *GeofInt* 60 (1), 51–75. doi:10.22201/igeof.00167169p.2021.60.1.2026

Behr, Y., Clinton, J., Kästli, P., Cauzzi, C., Racine, R., and Meier, M.-A. (2015). Anatomy of an Earthquake Early Warning (EEW) Alert: Predicting Time Delays for an End-To-End EEW System. *Seismol. Res. Lett.* 86 (3), 830–840. doi:10.1785/0220140179

Böse, M., Ionescu, C., and Wenzel, F. (2007). Earthquake Early Warning for Bucharest, Romania: Novel and Revised Scaling Relations. *Geophys. Res. Lett.* 34 (7), 1–6. doi:10.1029/2007GL029396

Böse, M., Heaton, T. H., and Hauksson, E. (2012). Real-time Finite Fault Rupture Detector (FinDer) for Large Earthquakes. *Geophys. Jour. Int.* 191 (2), 803–812. doi:10.1111/j.1365-246X.2012.05657.x

Böse, M., Smith, D. E., Felizardo, C., Meier, M.-A., Heaton, T. H., and Clinton, J. F. (2018). FinDer v.2: Improved Real-Time Ground-Motion Predictions for M2-M9 with Seismic Finite-Source Characterization. *Geophys. J. Int.* 212, 725–742. doi:10.1093/gji/ggx430

Cauzzi, C., Behr, Y., Clinton, J., Kästli, P., Elia, L., and Zollo, A. (2016). An Open-Source Earthquake Early Warning Display. *Seism. Res. Lett. Online* 87 (3), 737–742. doi:10.1785/0220150284

Clinton, J., Zollo, A., Marmureanu, A., Zulfikar, C., and Parolai, S. (2016). State-of-the Art and Future of Earthquake Early Warning in the European Region. *Bull. Earthquake Eng.* 14, 2441–2458. doi:10.1007/s10518-016-9922-7

Cua, G., and Heaton, T. (2007). "The Virtual Seismologist (VS) Method: A Bayesian Approach to Earthquake Early Warning," in *Earthquake Early Warning Systems* (Berlin, Heidelberg: Springer), 97–132.

Cuéllar, A., Suárez, G., and Espinosa-Aranda, J. M. (2018). A Fast Earthquake Early Warning Algorithm Based on the First 3 S of the P-Wave Coda. *Bull. Seismol. Soc. Am.* 108 (4), 2068–2079. doi:10.1785/0120180079

DeMets, C., Gordon, R. G., Argus, D. F., and Stein, S. (1994). Effect of Recent Revisions to the Geomagnetic Reversal Time Scale on Estimates of Current Plate Motions. *Geophys. Res. Lett.* 21 (20), 2191–2194. doi:10.1029/94gl02118

Given, D., Allen, R. M., Baltay, A. S., Bodin, P., Cochran, E. S., Creager, K., et al. (2018). *Implementation Plan for the ShakeAlert System-An Earthquake Early Warning System for the West Coast of the United States*. Pasadena, CA: US Geological Survey (USGS) Open-File Report, 1155. Available at: https://pubs.usgs.gov/of/2018/1155/ofr20181155.pdf.

Hanka, W., Saul, J., Weber, B., Becker, J., and Harjadi, P. (2010). Real-time Earthquake Monitoring for Tsunami Warning in the Indian Ocean and beyond. *Nat. Hazards Earth Syst. Sci.* 10 (12), 2611–2622. doi:10.5194/nhess-10-2611-2010

Havskov, J., Voss, P. H., and Ottemöller, L. (2020). Seismological Observatory Software: 30 Yr of SEISAN. *Seismol. Res. Lett.* 91 (3), 1846–1852. doi:10.1785/0220190313

Hoshiba, M., and Ozaki, T. (2014). "Earthquake Early Warning and Tsunami Warning of the Japan Meteorological Agency, and Their Performance in the 2011 off the Pacific Coast of Tohoku Earthquake (M_w 9.0)," in *Early Warning for Geological Disasters* (Berlin, Heidelberg: Springer), 1–28. doi:10.1007/978-3-642-12233-0_1

Hsiao, N.-C., Wu, Y.-M., Shin, T.-C., Zhao, L., and Teng, T.-L. (2009). Development of Earthquake Early Warning System in Taiwan. *Geophys. Res. Lett.* 36 (5), 3–7. doi:10.1029/2008GL036596

Kodera, Y., Saitou, J., Hayashimoto, N., Adachi, S., Morimoto, M., Nishimae, Y., et al. (2016). Earthquake Early Warning for the 2016 Kumamoto Earthquake: Performance Evaluation of the Current System and the Next-Generation Methods of the Japan Meteorological Agency. *Earth Planets Space* 68 (1), 202. doi:10.1186/s40623-016-0567-1

Linkimer, L., and Alvarado, G. E. (2014). Distribución espacio-temporal de la sismicidad sentida en Costa Rica (1976-2013) en el marco histórico del 30 aniversario (1982-2012) de la Red Sismológica Nacional (RSN: UCR-ICE). *Rev. Geol. Amér. Cent.* 30, 45–71. doi:10.15517/rgac.v0i0.16569

Linkimer, L., Arroyo, I. G., Alvarado, G. E., Arroyo, M., and Bakkar, H. (2018). The National Seismological Network of Costa Rica (RSN): An Overview and Recent Developments. *Seismol. Res. Lett.* 89 (2A), 392–398. doi:10.1785/0220170166

Lücke, O. H., and Arroyo, I. G. (2015). Density Structure and Geometry of the Costa Rican Subduction Zone from 3-D Gravity Modeling and Local Earthquake Data. *Solid Earth* 6, 1169–1183. doi:10.5194/se-6-1169-2015

Massin, F., Strauch, W., Andrews, C. J., Böse, M., and Ramirez, J. (2018). Building EEW in Nicaragua: Performance and Perspectives. *Seismol. Res. Lett.* 89 (2B), 717–966. doi:10.1785/0220180082

Massin, F., Clinton, J., Racine, R., Böse, M., Rossi, Y., Marroquin, G., et al. (2020). "The Future strong Motion National Seismic Networks in Central America Designed for Earthquake Early Warning," in EGU General Assembly Conference Abstracts, Vienna, Austria, 19437. doi:10.1785/0220200043

Massin, F., Clinton, J. F., and Böse, M. (2021). Status of Earthquake Early Warning in Switzerland. Lausanne, Switzerland. *Front. Earth Sci.* 9, 707654. doi:10.3389/feart.2021.707654

Montero, W., and Miyamura, S. (1981). Distribución de intensidades y estimación de los parámetros focales de los terremotos de Cartago de 1910, Costa Rica, América Central. *Rev. Inst. Geogr. Nacional. Julio-diciembre* 2, 9–34.

Montero Pohly, W. (1989). Sismicidad Histórica De Costa Rica. *GeofInt* 28 (3), 531–559. doi:10.22201/igeof.00167169p.1989.28.3.623

Montero, W. (2001). Neotectónica de la región central de Costa Rica: frontera oeste de la microplaca de Panamá. *Rev. Geol. Amér. Cent.* 24, 29–56.

Peraldo, G., and Montero, W. (1994). Los temblores del periodo colonial de Costa Rica. San Jose, Costa Rica: Edit. Tecnol. Costa Rica.

Porras, J. L. (2017). *Atenuación sísmica en Costa Rica a partir de intensidades y Coda Q. [license's thesis]*. San Jose, Costa Rica: University of Costa Rica.

Quintero, R., and Kissling, E. (2001). An Improved P-Wave Velocity Reference Model for Costa Rica. *GeofInt* 40 (1), 3–19. doi:10.22201/igeof.00167169p.2001.40.1.416

Red Sismológica Nacional de Costa Rica (2017), Información de la Red Sismológica Nacional de Costa Rica," in *The Costa Rica National Seismological Network Catalog during 1975-2017*. Universidad de Costa Rica. doi:10.15517/TC

Red Sismológica Nacional de Costa Rica (2019). *Informe preliminar sobre el sismo de Armuelles, 25 de junio de 2019*. Available at: https://rsn.ucr.ac.cr/actividad-sismica/reportes-sismicos/12963-informe-preliminar-sobre-el-sismo-de-armuelles-25-de-junio-de-2019 (Accessed October 15, 2020).

Wenzel, F., Erdik, M., Köhler, N., Zschau, J., Milkereit, C., Picozzi, M., et al. (2014). "EDIM: Earthquake Disaster Information System for the Marmara Region, Turkey," in *Early Warning for Geological Disasters: Scientific Methods and Current Practice* (Heidelberg: Springer-Verlag), 103–116. doi:10.1007/978-3-642-12233-0_6

Zollo, A., Colombelli, S., Elia, L., Emolo, A., Festa, G., Iannaccone, G., et al. (2014). "An Integrated Regional and On-Site Earthquake Early Warning System for Southern Italy: Concepts, Methodologies and Performances," in *Early Warning for Geological Disasters: Scientific Methods and Current Practice* (Heidelberg: Springer-Verlag), 117–137. doi:10.1007/978-3-642-12233-0_7

Conflict of Interest: The authors declare that the research was conducted in the absence of any commercial or financial relationships that could be construed as a potential conflict of interest.

frontiers in Earth Science

ORIGINAL RESEARCH
published: 29 September 2021
doi: 10.3389/feart.2021.667160

Design, Implementation and Testing of a Network-Based Earthquake Early Warning System in Greece

M. Bracale[1], *S. Colombelli*[1]*, *L. Elia*[1], *V. Karakostas*[2] *and A. Zollo*[1]

[1]*Department of Physics, University of Naples Federico II, Naples, Italy,* [2]*Department of Geophysics, Aristotle University of Thessaloniki, Thessaloniki, Greece*

In this study we implemented and tested the Earthquake Early Warning system PRESTo (PRobabilistic and Evolutionary early warning System, Satriano et al., 2011) on the Greek Ionian islands of Lefkada, Zakynthos and Kefalonia. PRESTo is a free and open source platform for regional Earthquake Early Warning developed at the University of Naples Federico II, which is currently under experimentation in Southern Italy, in the area covered by the Irpinia Seismic Network. The three Ionian islands selected for this study are located on the North-Western part of the Hellenic trench. Here the seismicity rate and the seismic hazard, coupled with the vulnerability of existing critical infrastructures, make this region among the highest seismic risk areas in Europe, where the application of Earthquake Early Warning systems may become a useful strategy to mitigate the potential damage caused by earthquakes. Here we studied the feasibility of implementing an Earthquake Early Warning system on an existing seismic network, which was not specifically made for earthquake early warning purposes, and evaluated the performance of the system, using a data set of real-earthquake recordings. We first describe the technical details of the implementation of PRESTo in the area of interest, including the preliminary parameter configuration and the empirical scaling relationship calibration. Then we evaluated the performance of the system through the off-line analysis of a database of real earthquake records belonging to the most recent M > 4.0 earthquakes occurred in the area. We evaluated the performance in terms of source parameter estimation (location, magnitude), accuracy of ground shaking prediction and lead-time analysis. Finally, we show the preliminary results of the real-time application of PRESTo, performed during the period 01–31 July 2019.

Keywords: earthquake early warning (EEW), ionian islands, real-time seismology, seismic risk, real-time source parameters

OPEN ACCESS

Edited by:
Carmine Galasso,
University College London,
United Kingdom

Reviewed by:
Elisa Zuccolo,
Fondazione Eucentre, Italy
Raffaele De Risi,
University of Bristol, United Kingdom

***Correspondence:**
S. Colombelli
simona.colombelli@unina.it

Specialty section:
This article was submitted to Geohazards and Georisks, a section of the journal Frontiers in Earth Science

Received: *12 February 2021*
Accepted: *13 September 2021*
Published: *29 September 2021*

Citation:
Bracale M, Colombelli S, Elia L, Karakostas V and Zollo A (2021) Design, Implementation and Testing of a Network-Based Earthquake Early Warning System in Greece. Front. Earth Sci. 9:667160. doi: 10.3389/feart.2021.667160

INTRODUCTION

Every year devastating earthquakes cause enormous damage in terms of lives and serious threats for human activities in the active seismic regions of the world. During the last 20 years the development of Earthquake Early Warning Systems (EEWS) has allowed to reduce the potential damage directly related to the strong shaking caused by earthquakes or indirectly produced by fires, explosions, tsunamis and other phenomena triggered by the seismic event. Recent examples of successful applications of EEWS are the two earthquakes that occurred in Mexico in September 2017 (Suárez

et al., 2018). During the Mw 8.2, September, 7 Tehuantepec earthquake, the Mexican alert system SASMEX gave almost 2 min of warning to Mexico city, prior to the arrival of the strong-motion seismic waves. The second example is the Mw 7.1 Morelos earthquake occurred on September 19, 2017, for which the short epicentral distance to Mexico City allowed for a few seconds of warning prior to the arrival of the *S* waves. In both cases, the warning was used to start public measures for reducing human losses in the city, including prompt evacuation of schools and buildings. Another relevant example of successful application of EEW alerts is the case of the Mw 9.0 Tohoku-oki (Japan) earthquake. At the time of that earthquake and tsunami, several million people near the epicenter received the EEW about 15–20 s before the most severe shaking occurred, and many more people in surrounding districts had greater lead time before less severe shaking started. About 90% of these people were able to take advance actions to save their own lives and those of family members or to take other actions according to prior planning (Fujinawa and Noda, 2013).

An EEWS is a complex, monitoring infrastructure able to quickly detect an ongoing earthquake, estimate its potential damage and provide an alert message to the target sites, before the arrival of the destructive waves. This is possible thanks to the different velocity of propagation between the P-waves and the S-waves and to the different velocity of propagation between seismic waves (travelling at the speed of ~3.5–6.5 km/s in the upper crust) and electromagnetic signals (i.e., the alarm signal, travelling at the speed of light). In case of a potentially damaging earthquake, a notification is sent to the target site where the time available from the moment of the alert release to the arrival of the strongest shaking can be used to activate emergency procedures and automatic mechanisms to mitigate the collateral damage, such as to stop elevators, machinery, high speed trains or to stop gas supplies to building (Allen et al., 2009).

Most of the existing EEWSs are based on regional (network-based) or on-site (single-station) configurations, depending on the geometry of the network and of its relative position with respect to the source area (Satriano et al., 2011). The regional configuration consists of a network of stations deployed in the source area, while target sites to be protected are situated far away from it. In this configuration, the near-source, early P-wave signals collected at the stations are used to detect the occurrence of the earthquake, determine its location and magnitude and estimate its shaking potential to nearby and distant sites through the use of empirical attenuation relationships. The alert notification can reach the site to protect within a variable time from the earthquake origin, which typically range from a few seconds (at very short distances from the source), to several tens of seconds (at hundreds kilometers from the source).

Occasionally, the near-source S-wave signals are also used jointly to the P-waves, to better constrain the real-time magnitude estimate (Lancieri and Zollo, 2008), although accurate, automatic, estimation of the first S-wave arrival is a difficult task, due to the high noise contamination related to the presence of large amplitude P-wave coda.

On-site or stand-alone early warning systems are individual or small-aperture array of sensors deployed in proximity of the target site to protect. In this case, the initial P-wave signals are analysed and used as proxies of the late arriving, strongest shaking waves at the same site, with no or poor available information on the earthquake source parameters (such as location and magnitude) (Wu et al., 2005; Caruso et al., 2017). Finally, hybrid approaches are based on the joint use of both regional and on-site configurations, as proposed by Zollo et al. (2021) and Colombelli et al. (2012).

During the last decade the implementation of EEWS is increasing all over the world. Operative systems are currently running in, Japan (Hoshiba, 2014), Mexico (Cuéllar et al., 2014), California (Kohler et al., 2017), Taiwan (Wu et al., 2014) and Romania (Böse et al., 2007), while EEWS development and testing are ongoing in several other active seismic regions of the world, such as Turkey, Switzerland, North Korea, China, Ibero-Maghrebian region (Allen et al., 2009; Clinton et al., 2016). In Italy, currently, the system PRESTo (Satriano et al., 2011) is running in Southern Italy, having the Irpinia Seismic Network (ISNet) as core seismic monitoring infrastructure.

Greece is the most active seismic region of Europe, with more than 60% of the European earthquakes occurring in this region (Papazachos and Papazachou 2003). The geodynamic processes that produce high seismic activity are related to the convergence of the Eurasian and the Eastern Mediterranean lithospheric plates, forming the long Hellenic trench, the dextral strike slip motion along the North Anatolian fault and North Aegean Trough and the fast movement of the Aegean to the south-southwest (Meier et al., 2004; Papadimitriou et al., 2016).

The Ionian islands are located north of the northwest termination of the Hellenic Trench. In this area (**Figure 1**) the NNE-SSW trending Kefalonia Transform Zone (KTFZ) is prevailing. Here the seismicity rate is the highest in Greece being characterized by a huge number of small magnitude earthquakes, frequently occurring moderate and strong earthquakes with magnitude up to about 7.0. Over the last decade, on average, an earthquake with magnitude between 4 and 4.9 occurs every 10 days, events in the range M 5–M 5.9 occur once every 4–5 months and M > 6 events every 6 years (Karakostas et al., 2010; Karakostas and Papadimitriou, 2010, 2015; Papadimitriou et al., 2013, 2017, Gospondinov et al., 2015, Kostoglou et al., 2020; Karakostas et al., 2020, among others).

Within the framework of past European projects (SAFER (https://cordis.europa.eu/project/id/36935), REAKT (https://cordis.europa.eu/project/id/282862), 2006–2014), several feasibility studies were carried on in order to build the infrastructure for an EEWS in Greece. Test-site applications (touristic harbours and hospitals) in the city of Patras were chosen to provide the opportunity to implement and test scientific products and results achieved in the project (Cauzzi et al., 2016). Specifically, Sokos et al. (2016) discuss the limits and potential of a network-based EEW system for the city of Patras (Greece), which is the third largest city in Greece and represents an ideal candidate for earthquake early warning due to its high seismic hazard and to the presence of critical structures such as the Rion-Antirion bridge. Within the project, the Virtual Seismologist (VS, Cua 2005; Cua and Heaton 2007; Cua et al., 2009) EEW software was installed at the Seismological Laboratory of the University of

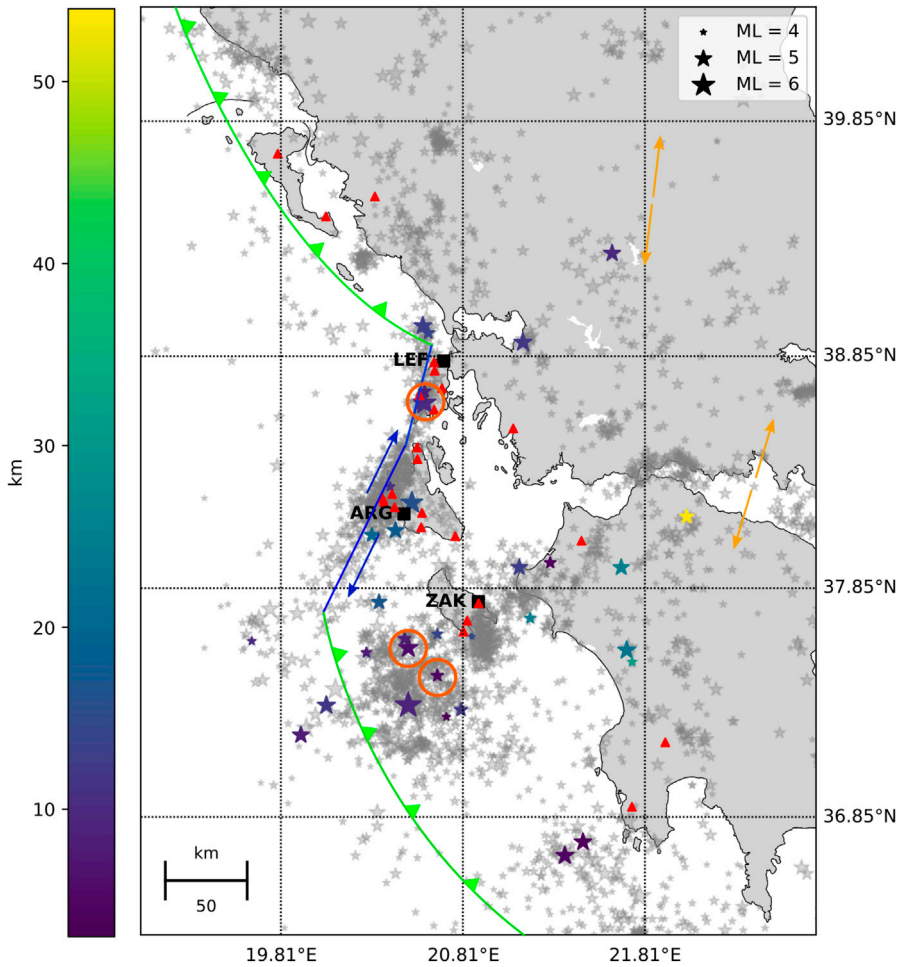

FIGURE 1 | Event and Station distribution. The map shows the epicentral position of the events (colored stars), the stations used in this work (triangles), and the three considered targets (squares). The size of the stars is proportional to the earthquake magnitude, while the depth is shown through the color scale. The three events selected for the scenario analysis are indicated with an orange circle. Grey stars show all the events with magnitude M > 3.5 occurred since 2000 and the colored lines show the major faults of the area. Orange arrows show the approximate direction of relative plate motion. Blue line represents the dextral Kefalonia Transform Faut Zone. The green line to the north represents the collision between the Apulia microplate and the Greek mainland, while the green line to the south depicts the subduction of the eastern Mediterranean oceanic plate beneath the Aegean.

Patras (UPAT). Given the available station density and network telemetry, the performance of the system was evaluated through synthetic tests and simulations, assuming a fully operational seismic network and the absence of delays in data transmission/processing. The analysis showed that the average time needed for the first magnitude estimate from VS was rather large (tens of seconds) and not satisfactory for routine operational use of EEW, indicating that the seismic networks in Greece need enhancements for regional EEW, either by adding stations or by upgrading the hardware to reduce delays.

Following the route traced by Sokos et al., (2016), here we studied the feasibility of implementing an EEWS on the existing nationwide seismic network, which was not specifically designed for earthquake early warning purposes, and evaluated the performance of the system, using a data set of real earthquake recordings. In the present study we implemented and tested the regional EEWS PRESTo (PRobabilistic and Evolutionary early warning SysTem), developed by RISSC-Lab research group at the University of Naples Federico II, on three Greek Ionian islands of Zakynthos, Lefkada and Kefalonia, which are located on the North-Western part of the Hellenic trench. Here the high seismicity rate and the seismic hazard could make the implementation of an EEWS relevant to reduce the potential damage caused by earthquakes. At the same time, the geography of the area and the station geographical distribution make the implementation of an EEWS really challenging.

MATERIALS AND METHODS

Dataset Description

The area of interest of this study is embedded in a rectangle of 350 km x 200 km (**Figure 1**). Within this area, we used the 3-component, velocimetric stations of the Hellenic Unified Seismic

Network (HUSN) maintained by the National Observatory of Athens, the Aristotle University of Thessaloniki, the National and Kapodostrian University of Athens and the University of Patras (HUSN, doi:10.7914/SN/HL). The network started being deployed in 1964 and was updated gradually in the following years, resulting in a heterogenous deployment, in terms of sensor typology and geographical distribution. The seismological network has almost its present geometry since 2014, by the installation of nine seismological stations with online connection maintained by the Department of Geophysics of the Aristotle University of Thessaloniki in cooperation with the union of the municipalities of the Ionian islands (PED-IN).

Among the available stations, we selected 23 stations for which it was possible to have real time data, including stations located on the islands (16) and on the mainland (7). With this selection, the geographical distribution of the network becomes heavily heterogeneous, with an inter-station distance varying from few kilometres for stations located on the same island to tens of kilometres considering also the other stations. Moreover, for offshore events in the South-West area, the network configuration makes the number and azimuthal coverage of recording data rather poor.

The collected earthquake dataset is composed by 31 (in **Supplementary Table S1**) earthquakes (**Figure 1**), occurred between 2010 and 2019, with local magnitude (ML) ranging from 4.0–6.6. The complete list of selected events is reported in **Supplementary Table S1** of Supplementary Material. Among the largest events the database includes the 2018, ML 6.6 Zakynthos earthquake, the 2015 ML 6.0 Lefkada earthquake and the 2014 ML 5.8, Kefalonia earthquake. Most of the events have shallow depths (5–15 km), with the deepest earthquakes located in the South West area, along the subduction fault area of the Hellenic Trench. We used a total number of 254 records, and the histogram distribution of these records as a function of distance is available in **Supplementary Figure S1** of the Supplementary Material.

Review of PRESTo Methodology

PRESTo (Satriano et al., 2011) is a free and open-source software platform for Earthquake Early Warning which integrates algorithms for real-time data collection, event detection, rapid earthquake location, magnitude estimation and damage assessment. It uses a regional, network-based approach, processing the real-time ground motion recorded by the stations of a seismic network and providing a prediction of the ground motion at the target. In PRESTo, the Filter-Picker algorithm (Lomax et al., 2012) first identifies the arrival time of the P-wave at each station, based on the real-time evaluation of a specific characteristic function, accounting for both the signal amplitude and its frequency content, in a short and long signal time window. An earthquake is declared when the triggering condition is satisfied by a small (<4) number of stations satisfying spatial and temporal coincidence criteria. As soon as an earthquake is detected, the real-time location is obtained through the RTLoc algorithm (Satriano et al., 2008), which can provide probabilistic estimates of hypocenter coordinates and origin time based on the use of both triggered and non-triggered stations, and on the recorded P-wave arrival times at pairs of stations. The event magnitude is estimated with a Bayesian, probabilistic approach (RTMag, Lancieri and Zollo, 2008) from the analysis of the early peak displacement amplitude in short time windows (2–4 s), on both P and S-waves, and through the use of an empirical scaling relationship relating the early peak ground displacement amplitude to the final event magnitude and hypocentral distance, at any recording station.

At any time t, after the first event detection the conditional probability density function (PDF) of magnitude given the observed data vector is expressed, through the Bayes' theorem, as the product between the conditional PDF of data, given the magnitude, and a priori PDF based on the prior information available before the time t. In the proposed methodology the a priori distribution is derived by the Gutenberg-Richter occurrence law (see Lancieri and Zollo, 2008 for details of the methodology). Both location and magnitude estimation algorithms (RTMag and RTLoc), provide as output a Probability Density Function (PDF), at each time step after the event origin. Then, the predicted outcome (magnitude or hypocentral location) corresponds to the maximum of PDF.

Once location and magnitude of the ongoing event are known, the peak ground motion is predicted through a regional ground motion prediction equation (GMPE), specifically calibrated for the considered area.

Configuration of PRESTo for the Selected Area

For the current experimentation, we installed PRESTo on a dedicated machine at the seismological station of Thessaloniki, that was configured to receive and process in real-time data from the HUSN stations. As previously mentioned, the software PRESTo is based on a sequence of algorithms for real-time data collection, event detection and location, magnitude estimation and shaking prediction. Each of these algorithms is based on several configuration parameters that require a proper calibration to be adapted to a given network and seismic area. A robust analysis of a massive earthquake catalogue, covering large magnitude and distance ranges, would be needed to correctly calibrate the parameters. Due to the unavailability of such a massive catalogue for the considered area, for the purpose of the present work, we mostly verified whether the default configuration parameters of PRESTo could be adapted to the Greek seismicity. In a few cases, we introduced correction coefficients or performed a trial-and-error analysis to find more suitable parameter. The specific calibration of each module is discussed below.

The phase picking and earthquake detection algorithm (Filter Picker, Lomax et al., 2012) requires the calibration of several parameters, (including, among others, the length of short and long-time windows for average signal computation, the minimum number of triggering stations for the event declaration, the amplitude threshold for event declaration). The proper calibration of each parameter requires a dedicated analysis of a massive number of recorded waveforms and this goes well beyond the purpose of the present work (see Vassallo

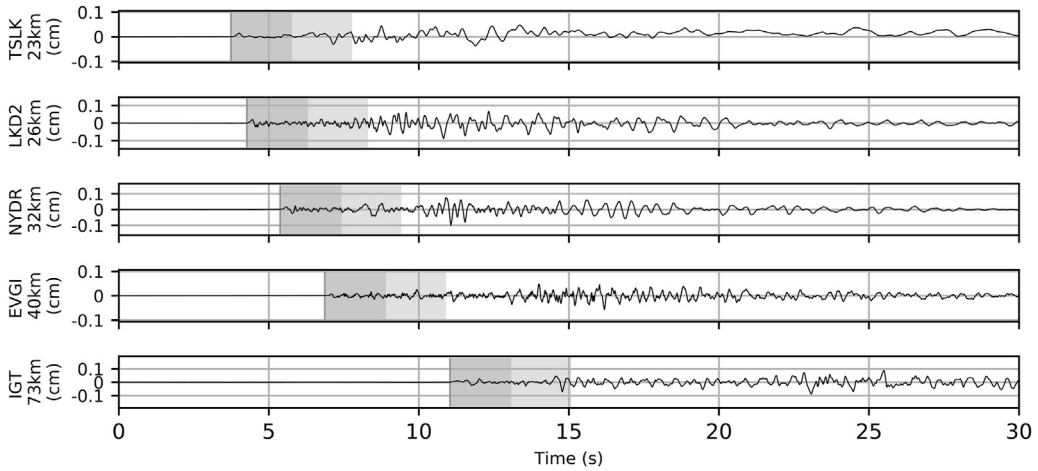

FIGURE 2 | Data. Example of displacement waveforms used for the analysis. The figure shows the waveforms recorded during the 2019-01-15 event (ID XXVIII). From top to bottom, the waveforms are sorted by source-to-receiver (hypocentral) distance. The P-wave arrival time is shown with a vertical grey solid line, corresponding to the beginning of the first, dark gey box, while the 2P and 4P time windows are shown with the dark and light grey bars.

et al., 2012. Here, we used 7 records (of 12 min length, acquired by different stations and including noise and seismic events) which are representative for the recorded signals in different conditions (i.e., different background noise level and seismic events). Starting from the default Filter Picker configuration parameters, we slightly changed the configuration parameters around their standard values and evaluated the response of the algorithm. We choose the optimal parameters as those that maximise the correct detection of seismic events and minimize both missed and false event declaration. Specifically, we choose 0.5 and 5 s as a short and long-time window respectively, for the characteristic function evaluation and set to 9 the threshold value of this characteristic function for the event declaration. Finally, an event is declared when the triggering condition is satisfied by multiple stations within a pre-determined space-time window, depending on the network geometry, density and distribution. Given the characteristics of the Greek network, we required 3 stations to be triggered within 90 km and 16 s.

As for the location algorithm, here we used the RTLoc method (Satriano et al., 2008) as it is, and adapted it to the area by including the velocity model of Papadimitriou et al. (2017), that was specifically made for the Lefkada and Kefalonia area. On average, for depths between 0 and 40 km, the P-to-S velocity ratio, is 1.83 ± 0.01.

The empirical scaling relationship used for the magnitude computation has the form (Zollo et al., 2006):

$$log(P_d) = A + BM + Clog(R) \quad (1)$$

$$log(P_{d_{10}}) = log(P_d) - Clog(R/10) = A' + B'M \quad (2)$$

where P_d is the initial Peak Displacement (Lancieri and Zollo, 2008), M is the earthquake magnitude, R is the true hypocentral distance (with respect to the real hypocentral location, as provided by NOA reference catalogue available at http://www.gein.noa.gr/en/seismicity/earthquake-catalogs) and A, B, C, A', B' are empirical coefficients to be calibrated from data for a 2 s and a 4 s P-wave time window, separately. As for the distance, for the calibration phase and the computation of empirical scaling relationships, we forced the earthquake location to the true value by temporarily deactivating in PRESTo the location module, which was then reactivated during the remaining performance analysis. The initial peak displacement (P_d) is defined as the absolute maximum amplitude on displacement waveforms, measured in a short time window (2 s, 4 s) after the P-wave arrival. The peak displacement is measured on integrated velocimetric waveforms, band-pass filtered in the range 0.075–3 Hz, to remove the noise and low frequency drift introduces by the integration operation. Examples of displacement waveforms with the portion of P-wave signals used are shown in **Figure 2**. In **Eq. 2**, P_{d10} is the P_d value once it has been corrected by the geometrical spreading effect. The coefficients have been specifically calibrated for each time window, using the available data in this study through a standard regression analysis and are reported in **Table 1** for 2P and 4P time windows, respectively, while the beta value of the Gutenberg Richter for the prior distribution to be used in RTMag algorithm was set b = 0.9 (Papadopoulos, 2014). As for the use of two equations, since it may occur that the P-wave peak amplitude

TABLE 1 | Coefficients for magnitude scaling relationship. The table shows the coefficients of the scaling relationship defined by **Eq. 1** and **Eq. 2** for 2P and 4P time windows. The standard deviation of each coefficient is also provided (but not used for predictions).

Coefficient	2s time window		4s time window	
	Value	Stand. Dev	Value	Stand. Dev
A	−6.01	0.33	−6.4	0.3
B	1.01	0.06	1.13	0.05
C	−1.90	0.11	−1.89	0.10
A′	−8.8	0.05	−8.0	0.5
B′	1.15	0.12	1.07	0.10

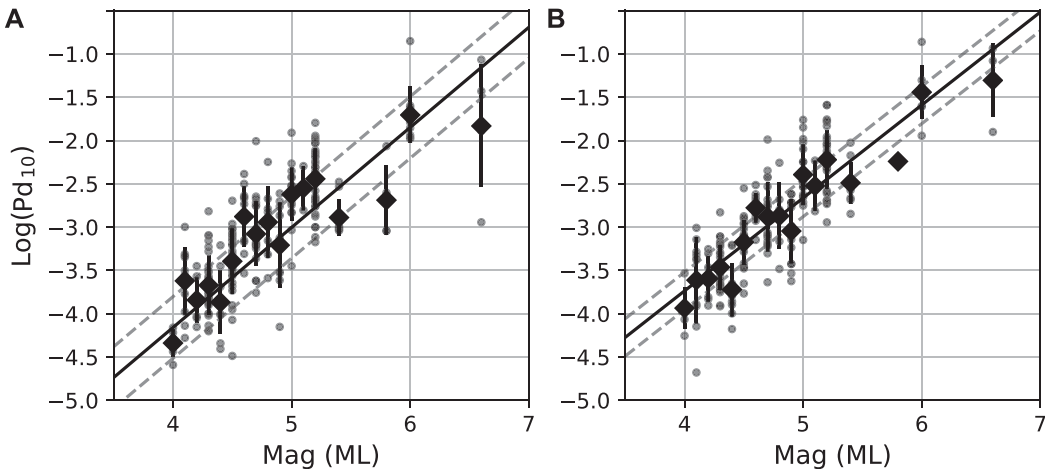

FIGURE 3 | Calibration laws for magnitude prediction. The figure shows the logarithm of measured P_d as a function the event magnitude for 2P**(A)** and 4P**(B)** time windows. The figure shows the observed data (grey dots), the average P_d value for each magnitude (dark diamonds). The linear regression obtained using the average values is shown through a solid black line, while dashed lines represent the standard error bounds (one standard deviation), as obtained from the fitting procedure. In both panels, the observed P_d is referred to a distance of 10 km, as obtained by **Eq. 2**.

increases with time within the P-wave time window especially for M > 6 events (Colombelli et al., 2012), the use of a larger time window with specifically calibrated coefficients is more appropriate. **Figure 3** shows the scaling between P_d and Magnitude for the two selected time windows, while **Supplementary Figure S2** in Supplementary Material shows the distribution of residuals after the calibration. The residuals are normally distributed on zero (mean value 0.05), with a standard deviation of 0.26.

Due to the sparse station distribution of the used Greek network we decided to exclude the use of S-waves for EEW given the low level of accuracy in bracketing with automatic algorithms the S-phase on seismic records. Indeed, as proved in previous works (Satriano et al., 2011), the use of the S-waves for a regional EEWS is critical, since it grounds on the reliable estimation of the S-arrival time, which in turn depends on a precise earthquake location obtained in real-time from the P-wave readings.

The Ground Motion Prediction Equation (GMPE) is used to predict the median Peak Ground Motion value (PGA or PGV) once the earthquake location and magnitude are known. Due to the unavailability of a massive catalogue for the considered area, we evaluated the prediction error for both PGA and PGV, using the standard GMPE calibrated by Akkar and Bommer (2007) for the European large earthquake dataset and already implemented in PRESTo. With respect to the original GMPE, we discarded site and fault coefficients. The functional form of the ground motion prediction equation used in this work to predict either PGA and PGV (denoted as PGX in the equation) is given by (Akkar and Bommer, 2007):

$$log(PGX) = b_1 + b_2 M + b_3 M^2 + (b_4 + b_5 M) log\left(\sqrt{R_{JB}^2 + b_6^2}\right) \quad (3)$$

TABLE 2 | Coefficients for ground shaking prediction relationship. The table shows the coefficients of the ground motion prediction equation of Akkar and Bommer (2007) for PGV and PGA (from b2 to b6), while the additional correction coefficients is included in parameter b1.

Parameter	PGV	PGA
b1	−1.451	1.411
b2	1.063	0.767
b3	0.079	−0.074
b4	−2.948	−3.162
b5	0.306	0.321
b6	5.547	7.682

Where M is the earthquake magnitude, R_{JB}^2 here is assumed to be the hypocentral distance and coefficients b_1 to b_6 are reported in **Table 2**.

For both quantities (PGA and PGV), while no apparent trend with distance is observed, we found that the mean value of residuals (computed as observed minus predicted value) is not centred at zero, suggesting the possibility of introducing a constant correction coefficient to account for the observed bias. **Figures 4A,B** shows the logarithm of observed PGA and PGV values, as a function of distance with respect to the theoretical scaling laws of Akkar and Bommer (2007) for three magnitude classes. The comparison shows that, after correcting the theoretical laws with a constant coefficient, the observed data are in good agreement with the theoretical laws. **Figures 4C,D** shows the distribution of prediction errors (for PGA and PGV) as a function of distance, with different colors for the same magnitude classes, once the constant bias has been corrected, while the coefficients of Akkar and Bommer (2007) scaling relationships and the constant correction coefficient (included in the b1 value) are reported in **Table 2**.

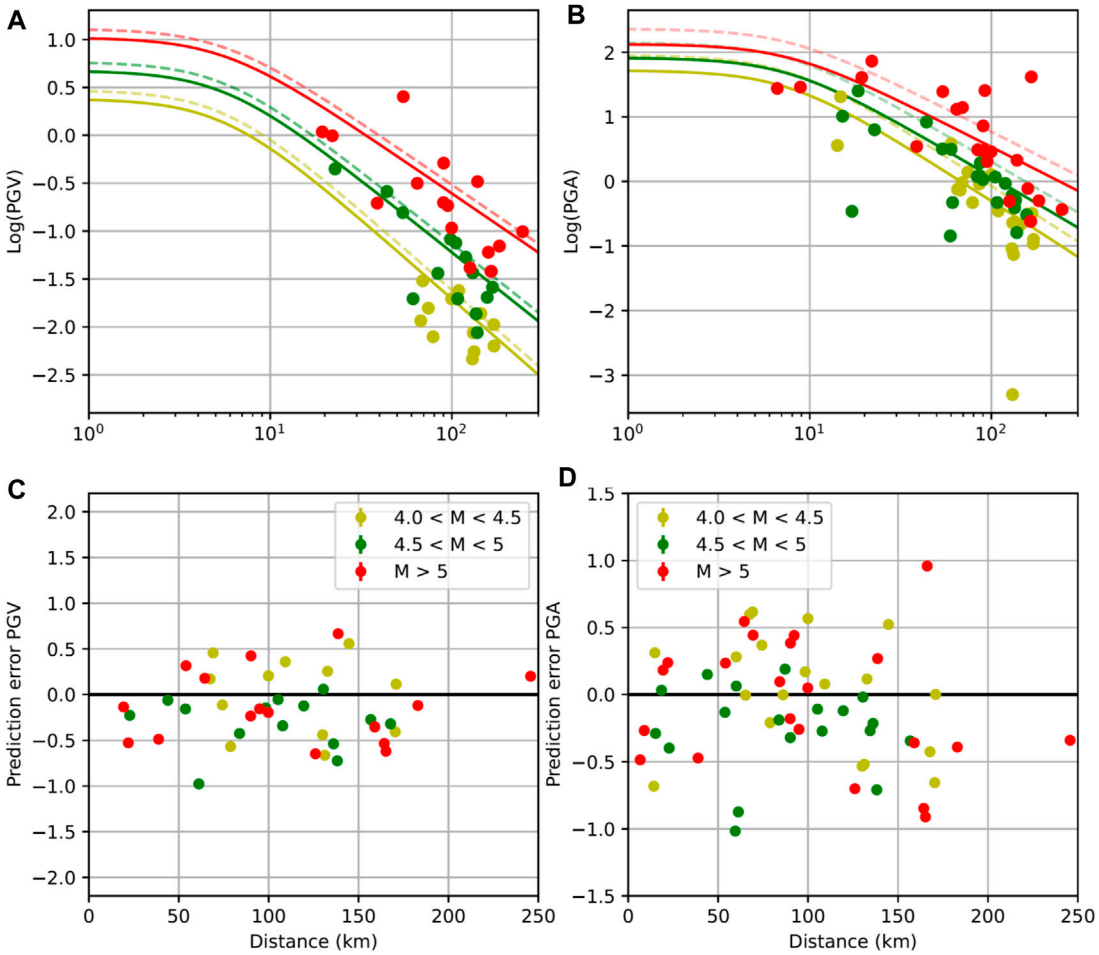

FIGURE 4 | Calibration of GMPE and prediction error. **(A)** and **(B)** show the logarithm of observed PGA and PGV as a function of the hypocentral distance in logarithmic scale, where units are cm/s^2 for PGA and cm/s for PGV. Circles represent the observed data while the theoretical scaling laws obtained by correction of Akkar and Bommer (2007) are shown with dashed lines (corresponding to the central magnitude value of each interval **(C)** and **(D)** show the prediction error on PGV **(A)** and PGA **(B)** for all the records available in the dataset. The average value has been corrected using the Akkar and Bommer (2007) GMPE. Solid lines show the corrected curves, including the coefficients, while dashed lines are those uncorrected. In all panels, the events have been grouped in three ranges of magnitudes, shown with different colors.

RESULTS

The performance analysis is crucial to understand whether and how the available network is suitable for earthquake early warning applications and how the existing network can be improved to optimize the performance. We first choose a subset of 3 earthquakes, among those available in the dataset, to perform a specific scenario-analysis, which are the M4.7 2013-5-23 earthquake, the M5.4 2018-10-30 earthquake and the M6.0 2015-11-17 earthquake. Then we evaluate the overall performance of the system in terms of first-alert times and in terms of accuracy of the estimates of source parameters (location and magnitude) on the whole dataset. Since the performance of an EEWS is strongly dependent on the network geometry, number and coverage of stations, we selected events with magnitude greater than 4 that were occurred in two different areas of the country and have been recorded by a sufficient number of stations. The selected earthquakes are indicated in **Figure 1** with circles.

Scenario Analysis

For the 3 selected events, we looked at the detailed time evolution of earthquake source parameters (epicentral coordinates, depth and magnitude), prediction error on PGA and number of available data, starting from the first available estimate and stopping when the latest station has recorded the P-wave signal. **Figure 5** show the time evolution of real-time estimates for the M4.7 2013-5-23 earthquake (Panels A, D, G, J, M), the M5.4 2018-10-30 earthquake (Panels B, E, H, K, N) and the M6.0 2015-11-17 earthquake (Panels C, F, I, L, O).

Overall, after a few seconds from the first estimate, for the three events the estimates of location and magnitude converge to the real value, as it can be seen from the timelines of **Figure 5**. As for the earthquake location, we separately analysed the time

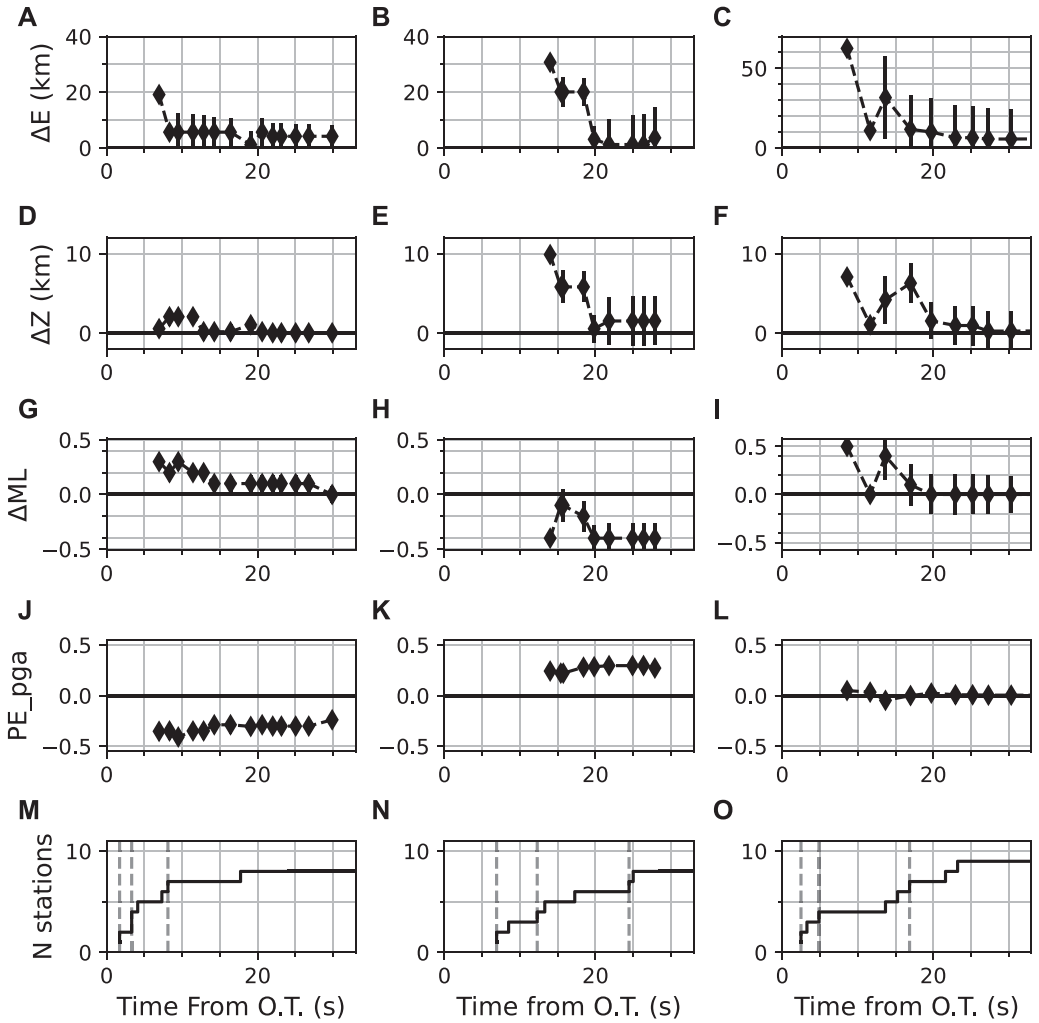

FIGURE 5 | Scenario analyses for the three selected earthquakes. The figure shows the time evolution of the estimated source parameters, for the three scenario earthquakes: magnitude M4.7 **(A, D, G, J, M)**, magnitude M5.4 **(B, E, H, K, N)**, magnitude M6.0 **(C, F, I, L, O)**. From top to bottom the figure shows the residuals on: epicentral coordinate estimation, depth estimation, local magnitude, peak ground shaking prediction and number of triggering stations as a function of time. The time axis is given with respect to the origin time (O. T.) of the event. For each quantity, the average value and the standard error bars (standard deviation) are represented with filled diamonds and black line, respectively. As for the location, we first computed the location error from the probability density function defined in Satriano et al., 2008. We then estimated the distance between the pick of the pdf (which is the observed value) and its boundary, defined by cutting the pdf at 68%. This error is finally propagated in the magnitude scaling law and in the GMPE. Vertical dashed lines in **(M–O)** indicate the use of 1, 3 and 6 stations, respectively.

evolution of epicentral and depth estimates, with the relative uncertainties. For the three events, as soon as a consistent (>6) number of stations is used, the estimates of both epicentral position and source depth converge to the real value, with a relative uncertainty (error bound) of about ±10 km for the epicentral position and ±2 km for the depth. Differently from what is expected, the uncertainties on the source depth turn out to be overall smaller than those on the epicentral position. This is likely due to the fact that most the events in the dataset have similar, shallow depths and the initial, a-priori solution for the source depth (set to 15 km) is very close to the real value in most of the cases. Thus, the real-time location estimates soon converge and stabilize to the true solutions. As for the magnitude, the real-time estimates show nearly stable residuals, distributed around zero shortly after the very first estimates, with a final average uncertainty of about 0.25 units, except for the M 5.4 event (**Figure 5H**), for which we found a systematic underestimation of magnitude of about 0.3 units (despite of a good location estimate). This could be probably due to the poor number of stations and azimuthal coverage, or to source effects (such as finite fault, fault orientation, directivity) which are not considered in the prediction model of **Eq. 1**, or propagation/site effects that produce lower observed amplitudes. Finally, for the three events, the prediction error on PGA (panels J, K, L), (computed as the difference in logarithm between observed and predicted PGA value) is not centred on zero (due to errors in location and

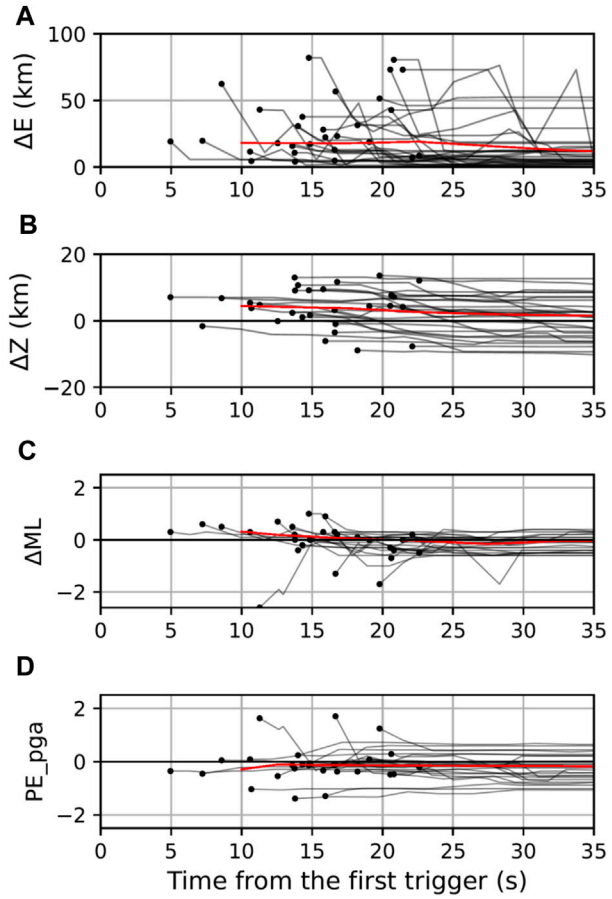

FIGURE 6 | Time evolution of location and magnitude residuals for all the events. The figure shows the evolution of location, and magnitude residuals and the prediction error on PGA for all the considered events. For each line, the black point identifies the time of the first triggered station. From top to bottom, the figure shows epicentral residuals **(A)**, depth residuals **(B)** and magnitude residuals **(C)**, prediction error on PGA **(D)**. The thin, red line is the average value of residuals as a function of time.

magnitude) although it is nearly stable with time around ±0.3–0.4, and is consistent with the typical standard deviation on PGA prediction (Akkar and Bommer, 2007; Bindi et al., 2011).

Overall Performance Analysis

The time of the first alert (alert time) is the shortest time needed for the system to provide a warning and it depends on the number of triggered stations required for the event declaration and on the spatial distribution of these stations. We evaluated the detection time when the triggering condition is satisfied by 1 and 3 stations, respectively, as the difference between the event declaration time and the earthquake origin time. When a single or 3 stations are required, the detection times range between 3 and 24 s and follow a non-gaussian, unimodal distribution, having a median value of 1.9 and 9.8 s, respectively. The detailed results for the detection times are reported in **Supplementary Table S2** of the Supplementary Material, in terms of minimum, maximum and median value for the selected events.

We also analysed the performance of the EW system for the whole dataset, by looking at the time evolution of residuals for magnitude and location estimates (**Figure 6**) and for PGA prediction error. As expected, both for the location and magnitude, the residuals generally decrease with time, as more stations contribute to the estimates. Specifically, for the earthquake location (**Figures 6A,B**), we observed that depth residuals are rather small since the initial estimates and converge to an average value about 7 km. Epicentral location residuals are larger (as also observed in the scenario analysis) and slowly decrease, reaching a nearly constant average value of about 20 km, after 17 s from the first P-wave trigger. We believe that the large final average value is likely due to the presence of a few (5) events in the data-set, located outside the network, in the South-West area, for which location residuals are very large (>50 km), because of the high level of noise contaminating data, the low number of triggering stations, and the poor azimuthal coverage. As for the magnitude estimates, the average residuals (represented by the red line in **Figure 6C**) are nearly stable around zero since the very first estimates and range between ± 0.5 points. For a few events, the residuals are rather large (±1) at the beginning but converge to zero, with a certain delay from the first P-wave trigger, depending on the availability and quality of recorded waveforms. As for the prediction error on PGA, we found that this is nearly stable around zero, with a maximum variation within the ±1 interval.

Lead-Time Analysis

The "lead-time" is one relevant parameter for an earthquake early warning system, and it corresponds to the time available at the target for taking emergency measures to mitigate the earthquake impact in real-time. We computed the lead-time for the three main towns of the islands which are Lefkada (Lefkada Island), Zakynthos (Zakynthos Island) and Argostoli (Kefalonia Island), denoted ad "LEF", "ZAK" and "ARG", respectively in **Figure 1**. The lead-time is computed as the difference between the theoretical S-waves arrival time at the target and the first-alert at the network (i.e., the alert time provided by PRESTo). Because of the sparse network density and coverage in the South-West area, we excluded 5 events located in this area for the computation of the lead-times. **Figures 7A–C** shows the lead-time as a function of distance, for the three selected targets. For the considered network and set of events, negative lead-times (e.g. S waves arrive before the first-alert issuing) are found at distances smaller than 20–25 km, as it is shown with vertical lines. At larger distances, lead times are of the order of 10 s for 70–75 km, and are about 20 s for distances larger than 100–120 km.

In order to account for the very sparse network distribution, we also estimated the lead-time by simulating a single-station, on-site EWS. Specifically, for this simulation, we assume each single station of the network to behave as an on-site EW system, i.e., as if each station would coincide with a target site. As for the regional system, instead, for the lead-time computation, we considered 2 seconds of computational time after the time of the first triggered station. In **Figures 7A–C** we compared the lead-times between the regional and on-site configurations. The figure shows that, at short distances, the lead-times are larger

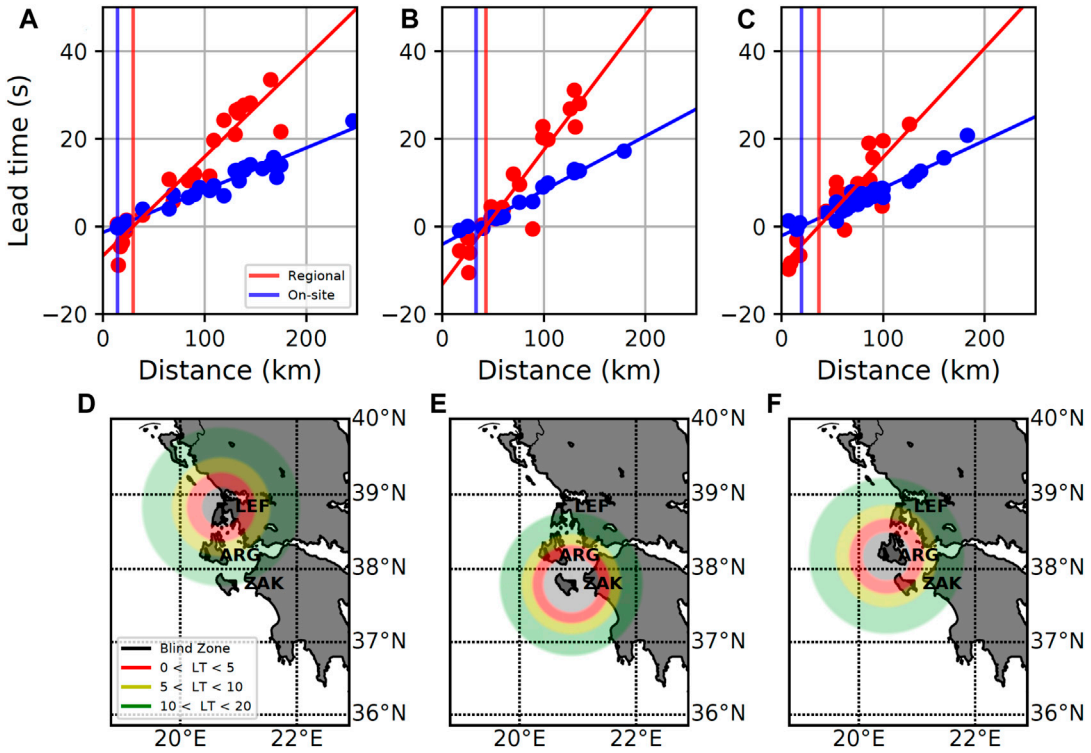

FIGURE 7 | Lead Times. Panels **(A)**, **(B)**, **(C)** show the distribution of lead-time as a function of distance for the three targets. In red the lead time for a regional EEWS with detection for trigger of three stations, in blue the lead time for an on-site single station EEWS. The vertical lines represent the blind zone radius relative to the target where the two EEWSs are applied. The analysis has been repeated for the three targets **(A)** Lefkada, **(B)** Zakynthos, **(C)** Argostoli. Panels **(D–F)** show the lead-time map for each target **(D)**, Lefkada, **(E)**, Zakynthos, **(F)**, Argostoli), for all the available events. The map shows the epicentral positions that would provide a given lead-time to the considered target. Specifically, the red circle represents the epicentral locations that would provide less than 5 s to the target. The yellow circle represents the epicentral locations that would provide 5–10 s to the target and green circle those that would give 10–20 s of lead time. The grey area represents the blind zone, where no alert can be provided to the target.

for the on-site than for the regional approaches, while at larger distances, the regional configuration provides larger lead-times, as expected (Satriano et al., 2011). In the figure, red lines correspond to the regional configuration, with three stations needed for the event declaration, while the blue lines define the lead-time for the on-site configuration. Both for regional and on-site configurations, the fit has been obtained through a linear regression analysis, considering the lead time for each event as a function of the relative target to source distance. It is worth to mention that the lead-times estimated in our work are also affected by the sparse station distribution, which is reflected into large P-wave arrival times at the network, as it can be seen from the histogram of **Figure 8** showing the P-wave travel times at the three selected targets, while **Supplementary Table S3** of the Supplementary Material shows the fit parameters of lead-time as a function of distance.

Finally, a useful scheme to assess the performance of PRESTo EWS for earthquakes in Ionian islands is provided in the form of a map in **Figures 7D–F** for the three selected targets, assuming that the target is at the centre of the map. In the maps, the grey area shows the blind zone, where no warning time is available. Red, yellow and green circles represent the areas with 0–5 s, 5–10 s and 10–20 s of warning time, respectively.

DISCUSSION

The aim of this study was to design, implement, validate and test the regional EEWS PRESTo on the three Ionian Islands of Lefkada, Kefalonia and Zakynthos, which are in an extremely high seismic hazard region of Europe. Here we focus on PRESTo EW software and did not explore the application of other algorithms for EEW such as Virtual Seismologist (Cua and Heaton, 2007), E-larms (Allen, 2007), PLUM (Kodera et al., 2018). The comparison of performances of different algorithms is beyond the purpose of the present study. We applied the Early Warning System PRESTo through the off-line analysis of 31 earthquakes with local magnitude greater then 4, occurred between 2011 and 2019. We studied the performance of the alert system in terms of rapidity of the first alert release, accuracy of source parameter estimates (magnitude, location) and ground motion prediction and in terms of available lead-time.

When considering only the events occurring close to the islands and inland, the application showed that, on average, about 20 s after the earthquake origin time the event is fully described, with an accuracy of 20 km on the epicentral position, 7 km on the depth, and 0.1 on the local magnitude. In terms of

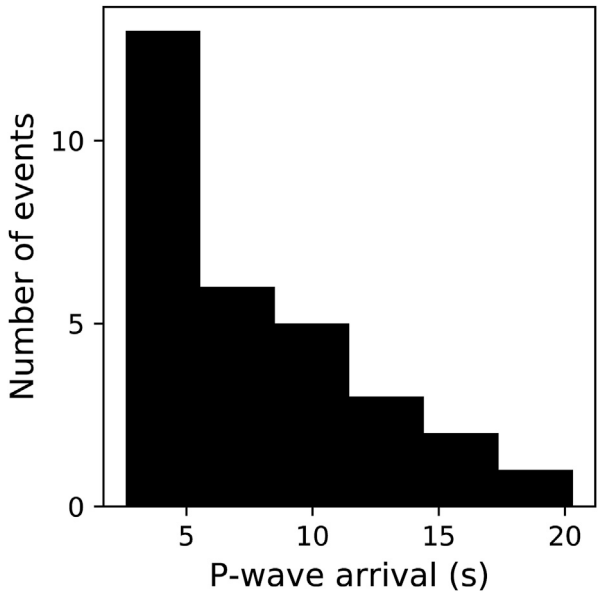

FIGURE 8 | Histograms of P-wave travel times. The figure shows the histogram of P-wave arrival times observed at the network.

lead-time, the system shows highly variable timing, depending on the earthquake location, and varying in the range from a few to tens of seconds. The blind zone radius depends on the source-to-receiver distance and for this reason, it changes from target to target. The average value between the three targets is 36 km. This value appears to be rather large and many of the strongest events could occur within the blind zone. However, both lead-times and blind zones here are computed through the theoretical arrival of the S-wave, while in most of the cases, the peak value of ground shaking occurs at a later time (either on the S-wave or on surface waves), thus providing additional warning time.

The GMPE shown in **Figure 4** can be used to evaluate the significance of the expected ground shaking at different distances. For example, for analyzed events with magnitude in the range M4 – M6, recorded at distances between 20 and 50 km, we expect a PGV in the range between 0.3–3 cm/s, which corresponds to a perceived shaking from weak to moderate, and an expected damage from none to light, assuming the PGV-IMM conversion table (Worden et al., 2012). These levels of shaking apparently do not justify the implementation of an Early Warning system in this area. However, we point out that from the historical catalogue of Greek earthquakes, large events with magnitude greater that 6.5, producing strong-to-severe shaking at the same distance range, may occur, and these are the shocks the Early Warning system is addressed to. Moreover, the experience of large populated areas (such as Italy), shows that even moderate events (shallow, M around 4 events) can be perceived by the population and produce panic and social consequences, which civil protection and authorities need to account and manage, making the effectiveness of Early Warning Systems very relevant even for small magnitude events.We also evaluated the lead-time by including the events in the South-West area (see **Supplementary Table S3** of the Supplementary Material). When the South-Western events are excluded, the slope of the lead-time regression line vs distance increases for all the targets, confirming that the performance of the regional approach improves. Similarly, the radius of the blind zone reduces when excluding stations in the South-Western area, as shown by **Supplementary Table S3**.

Our analysis shows that when the event occurs close to the target islands or in the South-West region, the on-site approach offers better performances in terms of lead-times. The regional approach becomes more performing when the target is located in a different island than the one where the earthquake occurs.

EEWS using a regional approach, are generally made with dense distribution of sensors surrounding the fault area. In the case of Greece, the density, coverage and number of stations on the three islands is rather large, while a non-uniform station distribution (in terms of number and distance) is available inland. Most of the seismicity occurs between the islands and the sea, several kilometres away from the coast, or in the South West area, where the station coverage is rather poor. For most of the events, the network configuration makes the azimuthal coverage rather poor, with consequent large errors on the estimation of location, magnitude and, consequently, on the ground motion prediction. Additional observables could be included to better constrain the hypocentre position in real-time. Among them, for example, the joint use of time, amplitude ratio and back-azimuth estimates, as proposed by Zollo et al., (2021), could represent a valid strategy to avoid wrong location estimates for off-network events.

In view of a future implementation of an integrated onsite and regional EEWS in this region of Greece, two main critical issues should be considered and solved. The first one is the seismic network density and areal coverage. This would obviously require the installation of new stations, mainly at the sea bottom, which represents a difficult and expensive operation. The problem may be partially solved by using a hybrid EEW approach, in which each seismic station can operate as a stand-alone, onsite EEW system and within the regional configurations. In this view, a single station (or small arrays of stations) deployed at the islands, could be used for the P-wave based early earthquake detection, while the network of stations could confirm or possibly cancel the alert issued by the single sensor. This would increase the available lead-time for earthquakes occurring at the sea, keeping at the same time the accuracy and reliability of source parameter estimates, provided by the network-based approach.

The second main issue is the performance of data communication and transmission system, which was not originally designed for running EEW applications. The current Greek network has a station-server transmission time of about 5–7 s on average, but it may reach extreme values up to 10–15 s. The solution to this problem demands a new technological improvement, requiring the development and installation of more advanced communication systems and digital, dedicated data transmission lines, which should be designed in all its components to have fixed and certified deadline for data release of less than one second, which is now quite a standard for modern communication technologies.

From July 2nd –July 10th, 2019, the software PRESTo has been operative, to start the evaluation of a potential real-time application.

Although a reliable estimation of real-time performances would require several months of experimentation with the occurrence of moderate-to-strong events in different areas of the country, here we can rapidly comment the preliminary results of this test, to discuss the most critical issues that were observed.

During the period, PRESTo detected a total of 35 small events, with magnitude larger than 1, and 6 of them having magnitude larger than 3. Two main issues raised during the real-time operation mode. The first problem is related to a few external events (for example occurring on the island of Creta) that were located as internal. In these cases, indeed, the location algorithm often tends to look for and force the solution within the area covered by network. Ad-hoc solutions in terms of space and time coincidence criteria or apparent wave velocity could be included to avoid the detection of such external events. Alternatively, constraints on the location probability distributions could be adopted to distinguish the case of an external event from that of an internal earthquake.

The second problem is related to the missed detection, i.e., the occurrence of multiple events that are detected as if they were a single earthquake. This issue reflects a peculiarity of the seismicity of this area, for which different magnitude earthquakes often occur in a really short time window (5–10 s). The detection algorithm is not able to recognize the individual earthquakes and the results is that a wrong event is detected, by considering waves from both events. This is the case of one of the detected events, that was preceded few seconds before by another earthquake, belonging to the same faults system. In this case, the system was not able to detect both events separately, resulting in a wrong detection. The occurrence of multiple events is a critical issue of all network-based EEWS and more adapted strategies should be considered, as for instance, those proposed by Liu and Yamada (2014) and Wu et al. (2015) who applied a Bayesian, EEW probabilistic scheme to identify multiple concurrent earthquakes through the scan of a posterior probability density function which jointly uses wave time and displacement amplitude information from triggered and not-triggered stations.

The last critical issue to consider is the maintenance of the network, that must be continuously operative in real-time, with no interruption of data recording and communications.

In conclusion, the results achieved in this study represents a first attempt and provide preliminary guidelines to build an integrated regional/onsite earthquake early warning system for Greece and could be useful for further nationwide applications in the region, to optimize the software and for studying its strengths and weaknesses.

DATA AVAILABILITY STATEMENT

The raw data supporting the conclusions of this article will be made available by the authors, without undue reservation.

AUTHOR CONTRIBUTIONS

MB implemented and applied the methodology, analysed the results and prepared the related figures. SC and MB wrote the text. All authors contributed to the methodological development, the interpretation of the results and the manuscript redaction.

ACKNOWLEDGMENTS

The work has been made in collaboration with the Aristotle University of Thessaloniki which provided knowledge, data, and stations availability and took place for 5 months in Thessaloniki and 5 months at the University of Naples Federico II. This research used the algorithm NonLinLoc by Lomax (http://alomax.free.fr/nlloc/) and the PRESTo software (http://www.prestoews.org/). The seismograms used in this study and their relative the information have been downloaded from the European Integrated Data Archives (EIDA) knot, maintained by the Institute of Geodynamics, National Observatory of Athens (http://www.gein.noa.gr/en/seismicity/earthquake-catalogs, http://eida.gein.noa.gr/waveform/, http://www.gein.noa.gr/en/networks/husn). The authors wish to thank Prof. E. Papadimitriou for inviting MB to the Aristotle University of Thessaloniki in the framework of Erasmus project and for the continuous cooperation during his stay, A. Kostoglou for his technical assistance and fruitful discussions, and the union of municipalities of the Ionian Islands (PED-IN) for its continuous support in the operation of the seismological network. The authors wish to thank the Editor CG, the two Reviewers EZ and RDR, and an Reviewer for the significant comments, which really improved the original version of the manuscript.

SUPPLEMENTARY MATERIAL

The Supplementary Material for this article can be found online at: https://www.frontiersin.org/articles/10.3389/feart.2021.667160/full#supplementary-material

REFERENCES

Akkar, S., and Bommer, J. J. (2007). Prediction of Elastic Displacement Response Spectra in Europe and the Middle East. *Earthquake Engng Struct. Dyn.* 36 (10), 1275–1301. doi:10.1002/eqe.679

Allen, R. M., Gasparini, P., Kamigaichi, O., and Böse, M. (2009). The Status of Earthquake Early Warning Around the World: An Introductory Overview. *Seismol. Res. Lett.* 80 (5), 682–693. doi:10.1785/gssrl.80.5.682

Allen, R. M. (2007). "The ElarmS Earthquake Early Warning Methodology and Application across California," in *Earthquake Early Warning Systems*. Editors P. Gasparini, G. Manfredi, and J. Zschau (Berlin, Heidelberg: Springer). doi:10.1007/978-3-540-72241-0_3

Bindi, D., Pacor, F., Luzi, L., Puglia, R., Massa, M., Ameri, G., et al. (2011). Ground Motion Prediction Equations Derived From the Italian Strong Motion Database. *Bull. Earthquake Eng.* 9, 1899–1920. doi:10.1007/s10518-011-9313-z

Böse, M., Ionescu, C., and Wenzel, F. (2007). Earthquake Early Warning for Bucharest, Romania: Novel and Revised Scaling Relations. *Geophys. Res. Lett.* 34, L07302. doi:10.1029/2007GL029396

Caruso, A., Colombelli, S., Elia, L., Picozzi, M., and Zollo, A. (2017). An On-Site Alert Level Early Warning System for Italy. *J. Geophys. Res. Solid Earth.* 122, 2106–2118. doi:10.1002/2016JB013403

Cauzzi, C., Gasparini, P., and Wiemer, S. (2016). Preface to the Special Issue "Strategic Applications of Real-Time Risk Mitigation Strategies and Tools: Case Studies and Lessons Learned in REAKT. *Bull. Earthquake Eng.* 14, 2437–2439. doi:10.1007/s10518-016-9966-8

Clinton, J., Zollo, A., Marmureanu, A., Zulfikar, C., and Parolai, S. (2016). State-of-the Art and Future of Earthquake Early Warning in the European Region. *Bull. Earthquake Eng.* 14 (9), 2441–2458. doi:10.1007/s10518-016-9922-7

Colombelli, S., Amoroso, O., Zollo, A., and Kanamori, H. (2012). Test of a Threshold-Based Earthquake Early-Warning Method Using Japanese Data. *Bull. Seismological Soc. America.* 102, 1266–1275. doi:10.1785/0120110149

Cua, G., and Heaton, T. (2007). "The Virtual Seismologist (VS) Method: a Bayesian Approach to Earthquake Early Warning," in *Earthquake Early Warning Systems*. Editors P. Gasparini, G. Manfredi, and J. Zschau (Berlin, Heidelberg: Springer), 97–132. doi:10.1007/978-3-540-72241-0_7

Cua, G., Fischer, M., Heaton, T., Wiemer, S., and Giardini, D. (2009), Real-Time Performance of the Virtual Seismologist Earthquake Early Warning Algorithm in Southern California, *Seismological Research Letters.* 80 (5), 740–747. doi:10.1785/gssrl.80.5.740

Cuéllar, A., Espinosa-Aranda, J. M., Suarez, R., Ibarrola, G., and Uribe, A. (2014). "The Mexican Seismic Alert System (SASMEX): its Alert Signals, Broadcast Results and Performance During the M 7.4 Punta Maldonado Earthquake of March 20th, 2012," in *Early Warning for Geological Disasters*. Editors F. Wenzel and Z. Zschau (Berlin: Springer-Verlag), 71–87. doi:10.1785/gssrl.80.5.740

Fujinawa, Y., and Noda, Y. (2013). Japan's Earthquake Early Warning System on 11 March 2011: Performance, Shortcomings, and Changes. *Earthquake Spectra.* 29 (1_Suppl. l), 341–368. doi:10.1193/1.4000127

Gospodinov, D., Karakostas, V., and Papadimitriou, E. (2015). Seismicity Rate Modeling for Prospective Stochastic Forecasting: the Case of 2014 Kefalonia, Greece, Seismic Excitation. *Nat. Hazards.* 79, 1039–1058. doi:10.1007/s11069–015–1890–8

Hoshiba, M. (2014). "Review of the Nationwide Earthquake Early Warning in Japan During its First Five Years," in *Earthquake Hazard, Risk, and Disasters*. Editor J. F. Shroder (Waltham, MA: Academic), 505–529.

Karakostas, V. G., and Papadimitriou, E. E. (2010). Fault Complexity Associated With the 14 August 2003 Mw6.2 Lefkada, Greece, Aftershock Sequence. *Acta Geophysica.* 58, 838–854. doi:10.2478/s11600-010-0009-6

Karakostas, V. G., Papadimitriou, E. E., Karamanos, C. K., and Kemenztetzidou, D. A. (2010). Microseismicity and Seismotectonic Properties of the Lefkada – Kefalonia Seismic Zone. *Bull. Geol. Soc. Greece.* 43, 2053–2063. doi:10.12681/bgsg.11395

Karakostas, V., Kostoglou, A., Chorozoglou, D., and Papadimitriou, E. (2020). Relocation of the 2018 Zakynthos, Greece, Aftershock Sequence: Spatiotemporal Analysis Deciphering Mechanism Diversity and Aftershock Statistics. *Acta Geophys.* 68, 1263–1294. doi:10.1007/s11600-020-00483-4

Karakostas, V., Papadimitriou, E., Mesimeri, M., Gkarlaouni, Ch., and Paradisopoulou, P. (2015). The 2014 Kefalonia Doublet (Mw6.1 and Mw6.0) Central Ionian Islands, Greece: Seismotectonic Implications Along the Kefalonia Transform Fault Zone. *Acta Geophysica.* 63, 1. doi:10.2478/s11600-014-0227-4

Kodera, Y., Yamada, Y., Hirano, K., Tamaribuchi, K., Adachi, S., Hayashimoto, N., et al. (2018). The Propagation of Local Undamped Motion (PLUM) Method: A Simple and Robust Seismic Wavefield Estimation Approach for Earthquake Early Warning. *Bull. Seismol. Soc. Am* 108 (2), 983–1003. doi:10.1785/0120170085

Kohler, M. D., Cochran, E. S., Given, D., Guiwits, S., Neuhauser, D., Henson, I., et al. (2017). Earthquake Early Warning ShakeAlert System: West Coast Wide Production Prototype. *Seismol. Res. Lett.* 89 (1), 99–107. doi:10.1785/0220170140

Kostoglou, A., Karakostas, V., Bountzis, P., and Papadimitriou, E. (2020). The February-March 2019 Seismic Swarm Offshore North Lefkada Island, Greece: Microseismicity Analysis and Geodynamic Implications. *Appl. Sci.* 10, 4491. doi:10.3390/app10134491

Lancieri, M., and Zollo, A. (2008). A Bayesian Approach to the Real-Time Estimation of Magnitude From the EarlyPandSwave Displacement Peaks. *J. Geophys. Res.* 113, B12302. doi:10.1029/2007JB005386

Liu, A., and Yamada, M. (2014). Bayesian Approach for Identification of Multiple Events in an Early Warning System. *Bull. Seismological Soc. America.* 104 (3), 1111–1121. doi:10.1785/0120130208

Lomax, A., Satriano, C., and Vassallo, M. (2012). Automatic Picker Developments and Optimization: FilterPicker-Aa Robust, Broadband Picker for Real-Time Seismic Monitoring and Earthquake Early Warning. *Seismological Res. Lett.* 83, 531–540. doi:10.1785/gssrl.83.3.531

Meier, T., Rische, M., Endrun, B., Vafidis, A., and Harjes, H.-P. (2004). Seismicity Of The Hellenic Subduction Zone In The Area Of Western And Central Crete Observed By Temporary Local Seismic Networks. *Tectonophy.* 383 (3–4), 149–169. doi:10.1016/j.tecto.2004.02.004

Papadimitriou, E., Gospodinov, D., Karakostas, V., and Astiopoulos, A. (2013). Evolution of the Vigorous 2006 Swarm in Zakynthos (Greece) and Probabilities for Strong Aftershocks Occurrence. *J. Seismol.* 17, 735–752. doi:10.1007/s10950-012-9350-3

Papadimitriou, E., Karakostas, V., Mesimeri, M., and Vallianatos, F. (2016). The Mw6.7 12 October 2013 Western Hellenic Arc Main Shock And Its Aftershock Sequence: Implications Of The Slab Properties. *Inter. J. Earth Sci.* 105, 2149–2160. doi:10.1007/s00531-016-1294-3

Papadimitriou, E., Karakostas, V., Mesimeri, M., Chouliaras, G., and Kourouklas, C. (2017). The Mw6.5 17 November 2015 Lefkada (Greece) Earthquake: Structural Interpretation by Means of the Aftershock Analysis. *Pure Appl. Geophys.* 174 (10), 3869–3888. doi:10.1007/s00024-017-1601-3

Papazachos, B. C., and Papazachou, C. (2003). *The Earthquakes of Greece*. Thessaloniki: Ziti Publication, 317.

Popandopoulos, G. A. (2014). Gutenberg-Richter Law Parameters Analysis Using the Hellenic Unified Seismic Network Data Through FastBee Technique. *Earth.* 3 (No. 5), 122–131. doi:10.11648/j.earth.20140305.12

Satriano, C., Elia, L., Martino, C., Lancieri, M., Zollo, A., and Iannaccone, G. (2011). PRESTo, the Earthquake Early Warning System for Southern Italy: Concepts, Capabilities and Future Perspectives. *Soil Dyn. Earthquake Eng.* 31 (2), 137–153. doi:10.1016/j.soildyn.2010.06.008

Satriano, C., Lomax, A., and Zollo, A. (2008). Real-Time Evolutionary Earthquake Location for Seismic Early Warning. *Bull. Seismological Soc. America.* 98 (3), 1482–1494. doi:10.1785/0120060159

Sokos, E., Tselentis, G.-A., Paraskevopoulos, P., Serpetsidaki, A., Stathopoulos-Vlamis, A., and Panagis, A. (2016). Towards Earthquake Early Warning for the Rion-Antirion Bridge, Greece. *Bull. Earthquake Eng.* 14, 2531–2542. doi:10.1007/s10518-016-9893-8

Suárez, G., Espinosa-Aranda, J. M., Cuéllar, A., Ibarrola, G., García, A., Zavala, M., et al. (2018). A Dedicated Seismic Early Warning Network: The Mexican Seismic Alert System (SASMEX). *Seismological Res. Lett.* 89 (2A), 382–391. doi:10.1785/0220170184

Vassallo, M., Satriano, C., and Lomax, A. (2012). Automatic Picker Developments and Optimization: A Strategy for Improving the Performances of Automatic Phase Pickers. *Seismological Res. Lett.* 83 (3), 541–554. doi:10.1785/gssrl.83.3.541

Worden, C. B., Gerstenberger, M. C., Rhoades, D. A., and Wald, D. J. (2012). Probabilistic Relationships between Ground–Motion Parameters and Modified Mercalli Intensity in California. *Bull. Seismol. Soc. Am* 102 (1), 204–221. doi:10.1785/0120110156

Wu, S., Yamada, M., Tamaribuchi, K., and Beck, J. L. (2015). Multi-events Earthquake Early Warning Algorithm Using a Bayesian Approach. *Geophys. J. Int.* 200, 791–808. doi:10.1093/gji/ggu437

Wu, Y.-M., and Hiroo, K. (2005). Rapid Assessment of Damage Potential of Earthquakes in Taiwan from the Beginning of P Waves. *Bull. Seismological Soc. America.* 95 (3), 1181–1185. doi:10.1785/0120040193

Wu, Y.-M., Hsiao, N-C., Chin, T-L., Chen, D-Y., Chan, Y-T., and Wang, K-S. (2014). "Earthquake Early Warning System in Taiwan," in *Encyclopedia of Earthquake Engineering*. Editors M. Beer, I. A. Kougioumtzoglou, E. Patelli, and S. K. Au (Berlin: Springer). doi:10.1007/978-3-642-36197-5_99-1

Zollo, A., Caruso, A., de Landro, G., Colombelli, S., and Elia, L. (2021). A Bayesian Method for Real-Time Earthquake Location Using Multiparameter Data. *J. Geophys. Res. Solid Earth.* 126, e2020JB020359. doi:10.1029/2020JB020359

Zollo, A., Lancieri, M., and Nielsen, S. (2006). Earthquake Magnitude Estimation From Peak Amplitudes of Very Early Seismic Signals on Strong Motion Records. *Geophys. Res. Lett.* 33, L23312. doi:10.1029/2006GL027795

Conflict of Interest: The authors declare that the research was conducted in the absence of any commercial or financial relationships that could be construed as a potential conflict of interest.

Publisher's Note: All claims expressed in this article are solely those of the authors and do not necessarily represent those of their affiliated organizations, or those of the publisher, the editors and the reviewers. Any product that may be evaluated in this article, or claim that may be made by its manufacturer, is not guaranteed or endorsed by the publisher.

frontiers in Earth Science

ORIGINAL RESEARCH
published: 04 October 2021
doi: 10.3389/feart.2021.726045

Developments of the Nationwide Earthquake Early Warning System in Japan After the 2011 M_w9.0 Tohoku-Oki Earthquake

Yuki Kodera[1], Naoki Hayashimoto[2], Koji Tamaribuchi[1], Keishi Noguchi[2], Ken Moriwaki[2], Ryo Takahashi[2], Masahiko Morimoto[2], Kuninori Okamoto[2] and Mitsuyuki Hoshiba[1]*

[1]Meteorological Research Institute, Japan Meteorological Agency, Tsukuba, Japan, [2]Seismology and Volcanology Department, Japan Meteorological Agency, Tokyo, Japan

OPEN ACCESS

Edited by:
Katsuichiro Goda,
Western University , Canada

Reviewed by:
Jindong Song,
Institute of Engineering Mechanics, China Earthquake Administration, China
Gemma Cremen,
University College London, United Kingdom

***Correspondence:**
Yuki Kodera
y_kodera@mri-jma.go.jp

Specialty section:
This article was submitted to Solid Earth Geophysics, a section of the journal Frontiers in Earth Science

Received: 16 June 2021
Accepted: 17 September 2021
Published: 04 October 2021

Citation:
Kodera Y, Hayashimoto N, Tamaribuchi K, Noguchi K, Moriwaki K, Takahashi R, Morimoto M, Okamoto K and Hoshiba M (2021) Developments of the Nationwide Earthquake Early Warning System in Japan After the 2011 M_w9.0 Tohoku-Oki Earthquake. Front. Earth Sci. 9:726045. doi: 10.3389/feart.2021.726045

In Japan, the nationwide earthquake early warning (EEW) system has been being operated by the Japan Meteorological Agency (JMA) since 2007, disseminating information on imminent strong ground motion to the general public and advanced technical users. In the beginning of the operation, the system ran based mainly on standard source-based algorithms with a point-source location estimate and ground motion prediction equation. The point-source algorithms successfully provided ground motion predictions with high accuracy during the initial operation; however, the 2011 M_w9.0 Tohoku-Oki earthquake and the subsequent intense aftershock and triggered earthquake activities underscored the weaknesses of the source-based approach. In this paper, we summarize major system developments after the Tohoku-Oki event to overcome the limits of the standard point-source algorithms and to enhance the EEW performance further. In addition, we evaluate how the system performance was influenced by the updates. One of significant improvements in the JMA EEW system was the implementation of two new ground motion prediction methods: the integrated particle filter (IPF) and propagation of local undamped motion (PLUM) algorithms. IPF is a robust point-source algorithm based on the Bayesian inference, and PLUM is a wavefield-based algorithm that predicts ground motions directly from observed shakings. Another notable update was the incorporation of new observation facilities including S-net, a large-scale ocean bottom seismometer network deployed along the Japan and Kuril trenches. The prediction accuracy and warning issuance performance analysis for the updated JMA EEW system showed that IPF improved the source-based ground motion prediction accuracy and reduced the risk of issuing overpredicted warnings. PLUM made the system less likely to underpredict strong ground motions and improved the warning issuance timeliness. The detection time analysis for the S-net incorporation suggested that S-net enabled the system to issue the first EEW report earlier than before the S-net incorporation for earthquakes around the Japan and Kuril trenches. Those findings indicate that the JMA EEW system has made substantial progress both on software and hardware aspects over the 10 years after the Tohoku-Oki earthquake.

Keywords: earthquake early warning, ground motion prediction, real-time analysis, hypocenter determination, ocean bottom seismometer, 2011 Tohoku-Oki earthquake

INTRODUCTION

It has been 10 years since the 2011 off the Pacific coast of Tohoku earthquake (Tohoku-Oki earthquake), a M_w9.0 megathrust event in the Japan Trench, occurred on March 11, 2011. The resulting strong ground shaking and large tsunami caused severe damage in a large part of eastern Japan. The Tohoku-Oki earthquake and subsequent intense seismic activity also had shed light on technical limitations of the Japanese nationwide earthquake early warning (EEW) system, which afterwards led to further developments of the system.

To mitigate earthquake damage, EEW systems have been developed and/or operated in many earthquake-prone regions around the world such as Japan (e.g., Nakamura, 1988; Hoshiba et al., 2008), Mexico (Espinosa-Aranda et al., 2009), the west coast of the United States (Böse et al., 2013; Kilb et al., 2021), Taiwan (Chen et al., 2015), Europe (Clinton et al., 2016), China (Zhang et al., 2016), Korea (Sheen et al., 2017), and Israel (Nof and Kurzon, 2021). In Japan, the Japan Meteorological Agency (JMA) has been operating the nationwide EEW system since 2007 to disseminate information on imminent strong ground motion to the general public and advanced technical users (Hoshiba et al., 2008).

In the beginning of the operation, the system ran based mainly on standard source-based algorithms that used a point-source model (PSM) estimate and ground motion prediction equation (GMPE) (Kamigaichi, 2004). The PSM algorithms successfully provided ground motion predictions with high accuracy during the initial operation (Doi, 2011; JMA, 2014). However, the prediction performance was poor for the Tohoku-Oki event and subsequent intense earthquake sequences in 2011 (Hoshiba et al., 2011; Kodera et al., 2018). For the mainshock, the system successfully issued a public warning for the Tohoku region (the nearest region from the epicenter) before the S-wave hit; on the other hand, the system underpredicted ground motions for the Kanto region, ~300 km to the southwest of the epicenter, due to the fault finiteness (i.e., the PSM algorithms were unable to capture the spatial extent of the fault rupture). Just after the mainshock, the system missed several large aftershocks; the P-wave picking algorithm did not work because the P-wave onsets overlapped with large coda waves of the mainshock or previous aftershocks. In addition, the system overpredicted ground motions for multiple simultaneous earthquakes, failing to associate P-wave travel times and mislocating the hypocenters.

Over the past 10 years, JMA has taken various measures to overcome those technical limitations and to enhance the system performance further. One of significant updates of the JMA EEW system was the implementation of two novel approaches: the integrated particle filter (IPF) and propagation of local undamped motion (PLUM) algorithms (Tamaribuchi et al., 2014; Kodera et al., 2018). Another notable development was the incorporation of new observation facilities. In this article, we report the system improvements on prediction algorithms and seismic networks from 2011 to 2020 and investigate how those updates influenced the system performance using actual EEW reports issued from April 2016 to December 2020.

The Initial Japan Meteorological Agency Earthquake Early Warning System

JMA launched EEW service for the general public in October 2007 (Hoshiba et al., 2008). The initial EEW system was operated by incorporating two different seismic networks (Kamigaichi et al., 2009; Doi, 2011), versatile seismometers of JMA (Harada, 2007; ~220 accelerometers) and Hi-net of the National Research Institute for Earth Science and Disaster Resilience (NIED; Okada et al., 2004; Aoi et al., 2020; ~800 high-sensitivity velocity meters) (**Figure 1A**). Versatile means that the seismometers can calculate and transmit various observation quantities related to EEW such as P-wave arrival, displacement amplitude, and epicentral distance given by the B-Δ algorithm (Odaka et al., 2003; Tsukada et al., 2004; Harada, 2007). The system provided ground motion predictions based on the PSM estimation. Source parameter estimates were given by several algorithms running in parallel. The B-Δ, territory, and grid-search algorithms (Kamigaichi, 2004) were employed as the main source estimation methods. Real-time data from the JMA versatile seismometers were fed into these algorithms. The not-yet-arrived-data (NYAD) algorithm (Horiuchi et al., 2005), which provided source parameters from the Hi-net stations, was also implemented as an independent subsystem. In addition, the system was receiving source estimates from an external subsystem based on a classical hypocenter determination approach using automatic P- and S-wave picks at the JMA and Hi-net stations (we refer to this algorithm as Hypoon). The system received hypocenter estimates from NYAD and Hypoon only if the location errors were smaller than rejection thresholds. Source estimates given by different algorithms were combined into a single event in the event identification process if the source parameters were similar to each other. After that, ground motion predictions were calculated from the estimated source parameters and GMPE. The GMPE employed in the JMA EEW system was one proposed by Si and Midorikawa (1999), which determines a peak ground velocity (PGV) from a point-source location, magnitude, and hypocentral distance. The PGV was converted into a JMA seismic intensity (JMA, 1996) with the empirical equation proposed by Matsuoka and Midorikawa (1994). Finally, the system issued EEW reports including predicted JMA intensities and estimated source parameters.

In the JMA EEW system, JMA seismic intensity is used as the ground motion metric. The JMA intensity is represented in two different ways: the 10-degree discrete representation I_{JMA} (i.e., I_{JMA} = 0, 1, 2, 3, 4, five lower (5L), five upper (5U), 6L, 6U, 7) and the continuous representation I_{inst} (e.g., I_{inst} = 2.5, 4.8). I_{inst} can be converted into I_{JMA} by rounding off I_{inst} to the nearest I_{JMA} value (e.g., $2.5 \leq I_{inst} < 3.5$ corresponds to $I_{JMA} = 3$, and $4.5 \leq I_{inst} < 5.0$ is equivalent to I_{JMA} = 5L). The JMA EEW system issues a public warning if the maximum predicted intensity is 5L or more on I_{JMA} (4.5 or more on I_{inst}; Hoshiba et al., 2008). I_{JMA} = 5L corresponds to the intensity threshold at or above which severe earthquake damage is likely to occur.

JMA evaluated the system prediction accuracy by calculating a prediction score, defined as the ratio of sub-prefectural areas

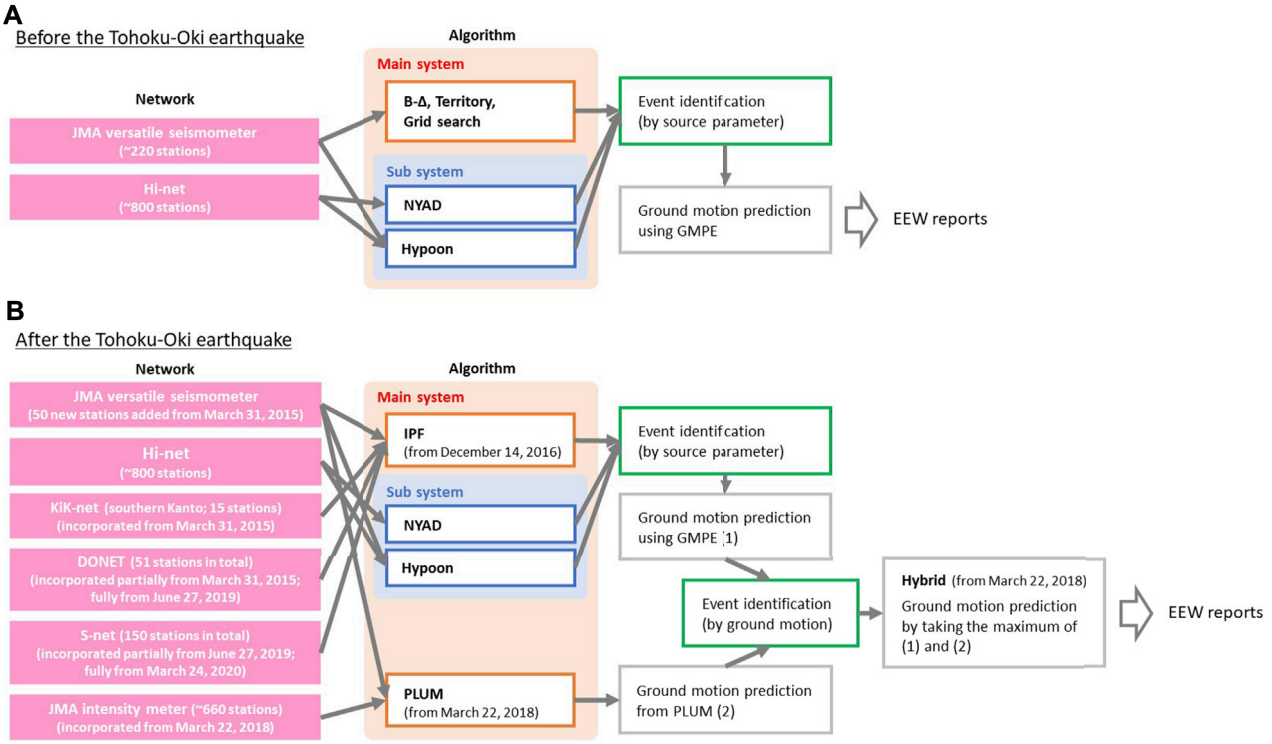

FIGURE 1 | Data flow diagrams with seismic networks and ground motion prediction algorithms of the JMA EEW system **(A)** before and **(B)** after the Tohoku-Oki earthquake.

whose intensity prediction error is within one unit on I_{JMA} among all areas with predicted or observed $I_{JMA} \geq 4$ (Doi, 2011). From October 2007 to March 2010, the system successfully provided accurate ground motion predictions, and the prediction score was as high as ~80%. However, the prediction score decreased to 28% in Japanese fiscal year 2010 (from April 2010 to March 2011) due to the occurrence of the Tohoku-Oki earthquake (JMA, 2014).

The Japan Meteorological Agency Earthquake Early Warning System After the 2011 Tohoku-Oki Earthquake

Over the 10 years after the Tohoku-Oki earthquake, JMA has upgraded the EEW system by introducing new ground motion prediction algorithms and seismic observation facilities (**Figure 1B**).

New Ground Motion Prediction Algorithms

The Integrated Particle Filter Algorithm

IPF (Tamaribuchi et al., 2014) is a PSM algorithm that has been employed in the JMA EEW system since December 14, 2016 (JMA, 2016) to reduce the risk of overprediction due to the misassociation of P-wave picks for multiple simultaneous earthquakes. IPF estimates source parameters based on the Bayesian inference (Liu and Yamada, 2014; Wu et al., 2015); hypocenter locations are determined using not only P-wave travel times but also various observed quantities such as velocity amplitude, untriggered station distribution, and epicentral distance estimated from B-Δ. For the association of P-wave picking data, IPF also takes into account velocity amplitudes in addition to travel time differences, to discriminate the occurrence of multiple simultaneous earthquakes from a single large event. Retrospective simulations with the intense earthquake sequences caused by the 2011 Tohoku-Oki and 2016 Kumamoto earthquakes showed that IPF could reduce the substantial number of overpredicted warnings compared to the PSM algorithms in the initial JMA EEW system (Tamaribuchi et al., 2014; Kodera et al., 2016).

In the updated EEW system, IPF is implemented as the main PSM algorithm, replacing the B-Δ, territory, and grid-search algorithms. The NYAD and Hypoon algorithms are still working in the updated system; JMA has decided to leave the two algorithms because the two algorithms use denser seismic networks than IPF (the difference comes from whether Hi-net is incorporated or not) and therefore could sometimes provide source parameter estimates timelier than IPF.

IPF is being operated with JMA versatile seismometers. Additionally, IPF uses three seismic networks maintained by NIED: DONET, S-net, and a part of KiK-net (Kaneda et al., 2015; Kawaguchi et al., 2015; Kanazawa et al., 2016; Uehira et al., 2016; Mochizuki et al., 2016; Okada et al., 2004; Aoi et al., 2020; **Figures 1B**, **2A**,**B**; as of December 2020).

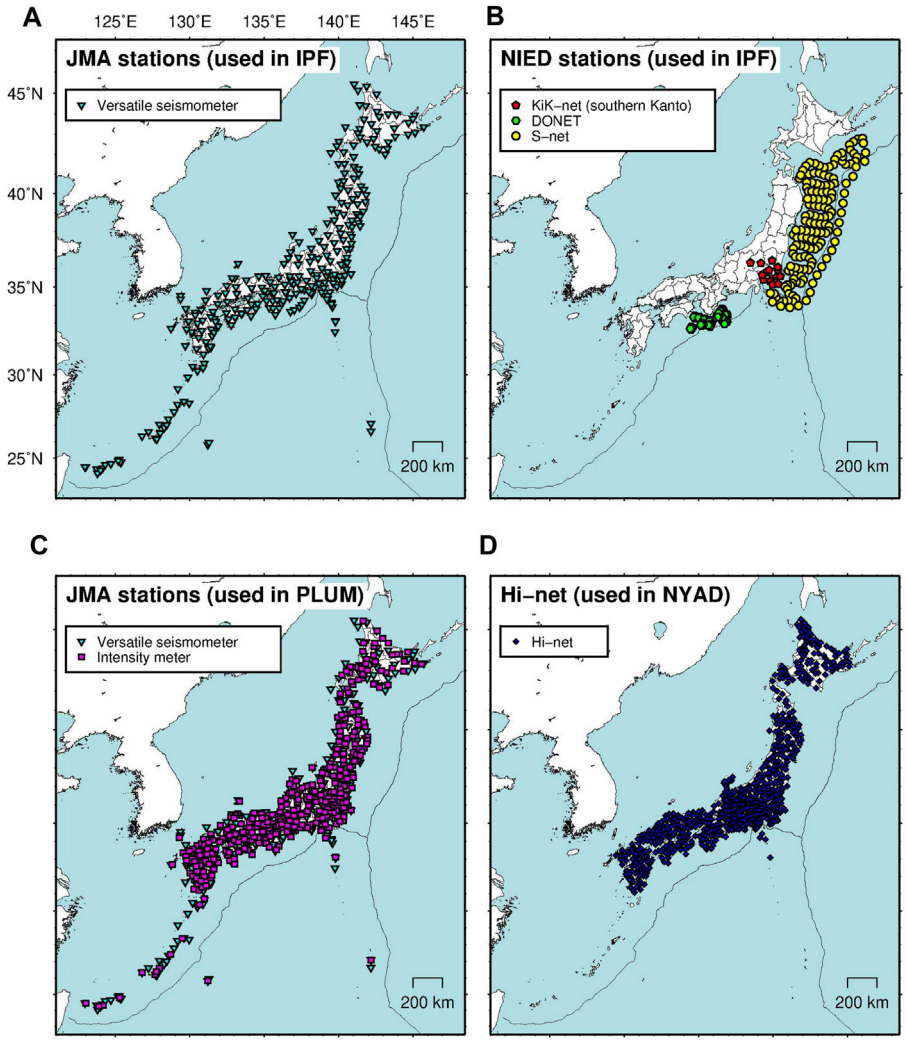

FIGURE 2 | Locations of **(A)** JMA stations used in IPF, **(B)** NIED stations used in IPF, **(C)** JMA stations used in PLUM, and **(D)** Hi-net stations used in NYAD.

The Propagation of Local Undamped Motion Algorithm

PLUM (Kodera et al., 2018) is a wavefield-based algorithm (Hoshiba, 2013; Hoshiba and Aoki, 2015) that has been implemented since March 22, 2018 (JMA, 2018) to provide accurate ground motions for large earthquakes with nonnegligible finite faults and for intense earthquake sequences for which PSM algorithms could fail to estimate correct source parameters. PLUM provides ground motion predictions without assuming specific source models; instead, PLUM predicts future ground motions directly from ground shakings observed near the target sites, assuming unattenuated plane wave incident. In the JMA EEW system, a predicted intensity at target site k is given by $I_{pred}^{(k)} = \max\{Ir_{obs}^{(1)} - F_0^{(1)}, \cdots, Ir_{obs}^{(N)} - F_0^{(N)}\} + F_0^{(k)}$, where $Ir_{obs}^{(i)}$ $(i = 1, \cdots, N)$ are observed real-time seismic intensities (Kunugi et al., 2013) at seismometers located within 30 km from target site k. $F_0^{(i)}$ and $F_0^{(k)}$ are scalar site amplification factors at individual sites (Iwakiri et al., 2011) converted into equivalent seismic intensity differences. Kodera et al. (2018) showed that the JMA EEW system could predict ground motions without underprediction for the Tohoku-Oki mainshock if PLUM was implemented. In addition, other offline simulations indicated that PLUM reduced the number of missed earthquakes for intense earthquake sequences during the 2011 Tohoku-Oki and 2016 Kumamoto events (Kodera et al., 2016; 2018). In the first year after the PLUM implementation, the JMA EEW system issued warnings with a better detection rate, especially for earthquakes whose observed ground motions were near the warning threshold (Kodera et al., 2020).

As of December 2020, PLUM is being operated with two JMA seismic networks, versatile seismometers and intensity meters (**Figure 2C**).

The Hybrid Algorithm

In the updated EEW system, two different ground motion predictions are given by the PSM and PLUM algorithms. The

two ground motion predictions are combined in the ground-motion-based event identification process to obtain the final ground motion prediction result (**Figure 1B**). The event identification process assumes that the two ground motion predictions are from the same event if there are one or more overlapped sub-prefectural areas with predicted intensities of 3 or more. The final ground motion predictions are given by taking the maximum of predicted intensities for each area. We refer to this procedure as the hybrid algorithm (Kodera et al., 2018).

New Seismic Observation Facilities

After the Tohoku-Oki earthquake, in addition to the introduction of the new ground motion prediction algorithms, JMA has incorporated new inland and offshore seismic observation facilities for more robust and timelier EEW issuances (**Figure 2**).

Inland Networks

The initial JMA EEW system was being operated with ~220 JMA versatile seismometers and ~800 Hi-net stations (**Figure 1A**). On March 31, 2015, JMA installed 50 new versatile seismometers mainly on the Pacific side to enhance the detection capability (JMA, 2015; **Figure 1B**). Deep borehole seismometers of KiK-net (15 stations in the southern Kanto region) were also added for the main PSM algorithms to obtain additional lead times for earthquakes in the Kanto region (JMA, 2015; **Figures 1B**, **2B**). On March 22, 2018, the start date for the PLUM operation, the system incorporated JMA intensity meters (seismometers that can transmit seismic intensities only) to perform the PLUM algorithm with a denser seismic network (Kodera et al., 2018). As of December 2020, real-time seismic intensities from ~660 JMA intensity meters are fed into PLUM (**Figures 1B**, **2C**). The Hi-net high-sensitivity velocity meters (**Figure 2D**) are used only for the NYAD and Hypoon algorithms.

Offshore Networks

To enhance the detection capability for offshore earthquakes, JMA also incorporated two ocean-bottom seismometer (OBS) networks maintained by NIED (**Figures 1B**, **2B**). One of the OBS networks is DONET (Kaneda et al., 2015; Kawaguchi et al., 2015; Aoi et al., 2020), which consists of 22 OBSs across the Kumano-Nada (DONET1) and 29 OBSs off the Kii channel (DONET2). JMA incorporated the DONET stations partially on March 31, 2015 (JMA, 2015) and fully on June 27, 2019 (JMA, 2019b; **Figure 1B**). The other network is S-net (Kanazawa et al., 2016; Mochizuki et al., 2016; Uehira et al., 2016; Aoi et al., 2020), 150 OBSs deployed along the Japan and Kuril trenches. 125 and 25 OBSs of S-net were introduced in the system on June 27, 2019 (JMA, 2019b) and on March 24, 2020 (JMA, 2020a), respectively (**Figure 1B**).

For robust magnitude estimates with OBSs, a new magnitude estimation algorithm specialized for OBSs was developed and introduced (Hayashimoto et al., 2019; Hayashimoto et al., 2021; submitted to Quarterly Journal of Seismology). For inland seismometers, the JMA EEW system calculates magnitudes from the vector sum of three-component displacements. However, for OBSs, three-component displacements could overestimate magnitudes because of horizontal site amplification caused by thick sedimentary layers (Hayashimoto and Hoshiba, 2013; Nakamura et al., 2014) and acceleration offset signal contamination by device orientation changes when strong motions hit (Hayashimoto et al., 2016; Nakamura and Hayashimoto, 2019; Takagi et al., 2019). Hayashimoto et al. (2019) found that those overestimation effects could be mitigated by using vertical-component instead of three-component displacements. JMA therefore implemented a new magnitude estimation equation based solely on vertical-component displacements for OBSs. In addition, to eliminate possible amplitude anomalies at OBSs near hypocenters, the new magnitude estimation algorithm requires three or more OBSs to calculate magnitudes (i.e., magnitude estimates are unavailable until the system has received displacement amplitudes from three or more OBSs; Hayashimoto et al., 2021, submitted).

Performance Evaluation for the Updated Japan Meteorological Agency Earthquake Early Warning System

To evaluate the performance of the updated JMA EEW system, we assessed how the IPF and PLUM implementation influenced the prediction accuracy and warning issuance performance. Also, we analyzed how the S-net incorporation contributed to the detection timeliness for earthquakes around the Japan and Kuril trenches. A part of the prediction accuracy and warning issuance performance analysis in this study is the same as what Kodera et al. (2020) conducted but with an extended analysis period.

Prediction Accuracy Changes With the Integrated Particle Filter and Propagation of Local Undamped Motion Implementation

We investigated how the prediction accuracy of the JMA EEW system changed with the IPF and PLUM implementation, using the maximum and final ground motion prediction results. We focused on the maximum ground motion predictions for the accuracy evaluation because the system issues warnings once predicted ground motions exceed the warning threshold. The final ground motion predictions were also used because their prediction errors would indicate the upper limit of prediction accuracy for target algorithms. For PLUM, the final ground motion predictions are the same as the maximum ground motion predictions. In this analysis, the prediction accuracy was evaluated for three different periods: 1) April 1, 2016 to December 14, 2016, 2) December 14, 2016 to March 22, 2018, and 3) March 22, 2018 to December 31, 2020. December 14, 2016 and March 22, 2018 are the start dates for the IPF and PLUM operation, respectively. To evaluate the system performance before the IPF and PLUM implementation, we took the analysis period from April 1, 2016. We focused only on recent EEW reports for the evaluation of the previous PSM algorithms to exclude the possible performance change due to different software versions. The analysis period was relatively short compared to the entire operation period of the previous PSM algorithms but was enough long to capture the algorithms' characteristics because during the period the system processed

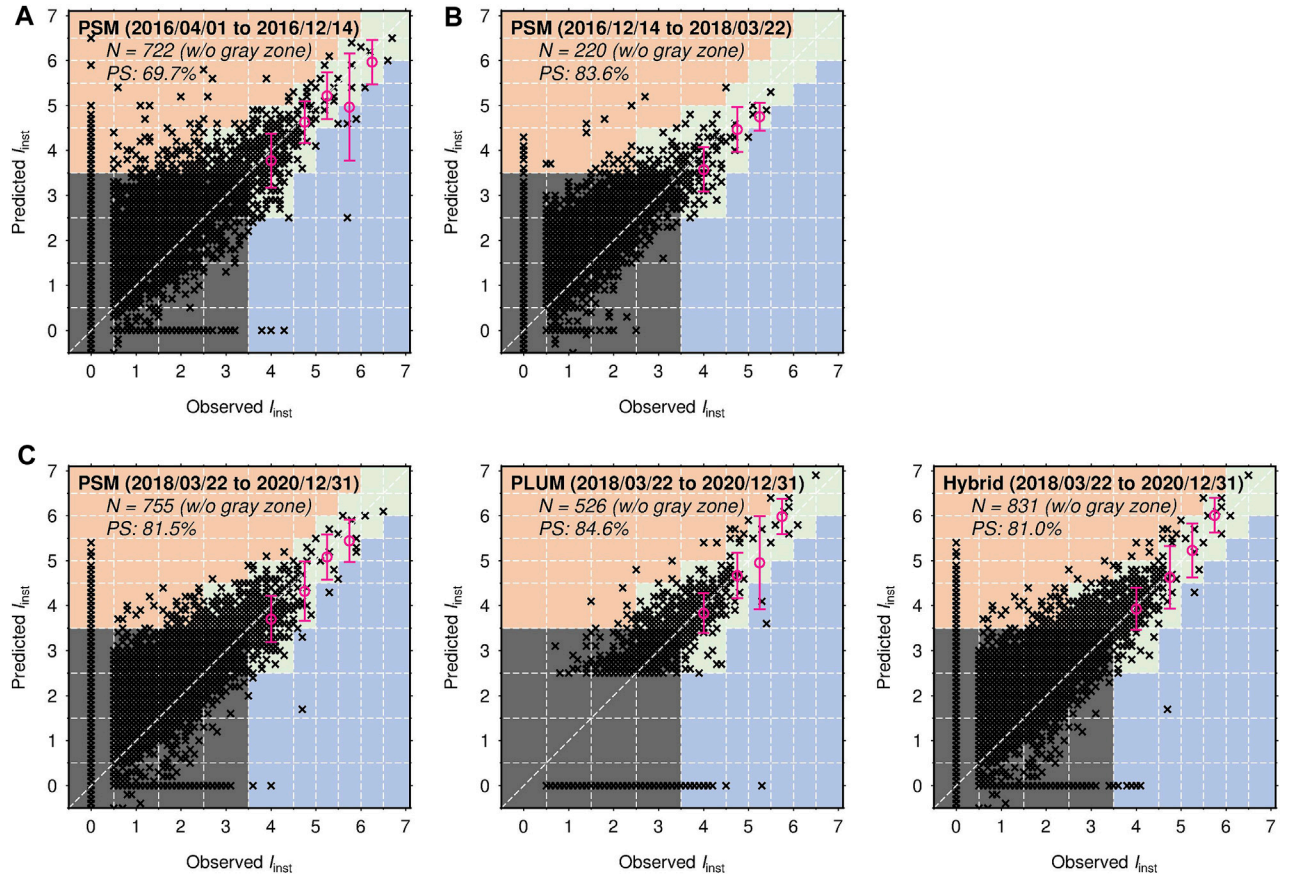

FIGURE 3 | Comparisons of observed and predicted intensities using the maximum ground motion prediction results for the three periods: **(A)** April 1, 2016 to December 14, 2016 (the start date for the IPF operation), **(B)** December 14, 2016 to March 22, 2018 (the start date for the PLUM operation), and **(C)** March 22, 2018 to December 31, 2020. Intensities were plotted on an area-by-area basis; that is, each intensity was obtained by taking the maximum among those at all sites in a sub-prefectural area. Circles and bars in magenta indicate the mean and standard deviation of predicted intensities for each observed I_{JMA} (data points with a predicted intensity equal to 0 were eliminated for the calculation). Green zone is one in which prediction errors were within one I_{JMA} unit (we assumed that those errors were acceptable). Orange and blue zones are ones in which ground motions were overpredicted and underpredicted with intensity errors of two or more units, respectively. Data points with predicted and observed $I_{JMA} \leq 3$ (i.e., $I_{inst} < 3.5$) are in the gray zone. The prediction score (PS) was calculated, defined as the ratio of areas whose intensity prediction error was within one I_{JMA} unit among areas with an observed or predicted intensity of four or more (data points in the gray zone were eliminated for the calculation). For **(C)**, comparison plots for the PLUM and hybrid algorithms are shown in addition to that for PSM because the period was after the PLUM operation.

many earthquakes including the 2016 Kumamoto earthquake sequence.

For each period, we calculated the prediction score. For the score calculation, predicted intensities were compared to observed intensities on an area-by-area basis (i.e., each intensity was obtained by taking the maximum of predicted or observed intensities in a sub-prefectural area; for the definition of the sub-prefectural areas, see **Figure 1C** in Kodera et al. (2020)). The prediction score was defined as the ratio of areas in which the difference between predicted and observed I_{JMA} was equal to or less than one I_{JMA} unit among areas with predicted or observed $I_{JMA} \geq 4$ (Doi, 2011). A predicted/observed I_{inst} was set to 0.0 if there was no available predicted/observed intensity for a target area. Intensities predicted by the PSM algorithms were obtained from hypocenter estimates using two or more stations. Intensities predicted by PLUM were what satisfied the EEW issuance condition of PLUM (i.e., predicted $I_{inst} \geq$ 2.5; Kodera et al., 2020). The prediction accuracy analysis in this study was done with earthquakes for which the JMA EEW system issued EEW reports.

During the first period, which is before the IPF and PLUM operation, the prediction score was 69.7% with the maximum ground motion predictions (**Figure 3A**) and 86.1% with the final predictions (**Figure 4A**). The prediction score with the maximum predictions was low mainly due to overprediction for events of the 2016 Kumamoto earthquake sequence (Kodera et al., 2016). The system still had difficulty in distinguishing multiple simultaneous events from a large earthquake because IPF had not been implemented yet. The system overpredicted ground motions for several concurrent aftershocks, mislocating the hypocenters. The prediction score with the final predictions was higher than that with the maximum predictions, although the prediction accuracy was still affected by the overprediction for the Kumamoto earthquake sequence. The underprediction case

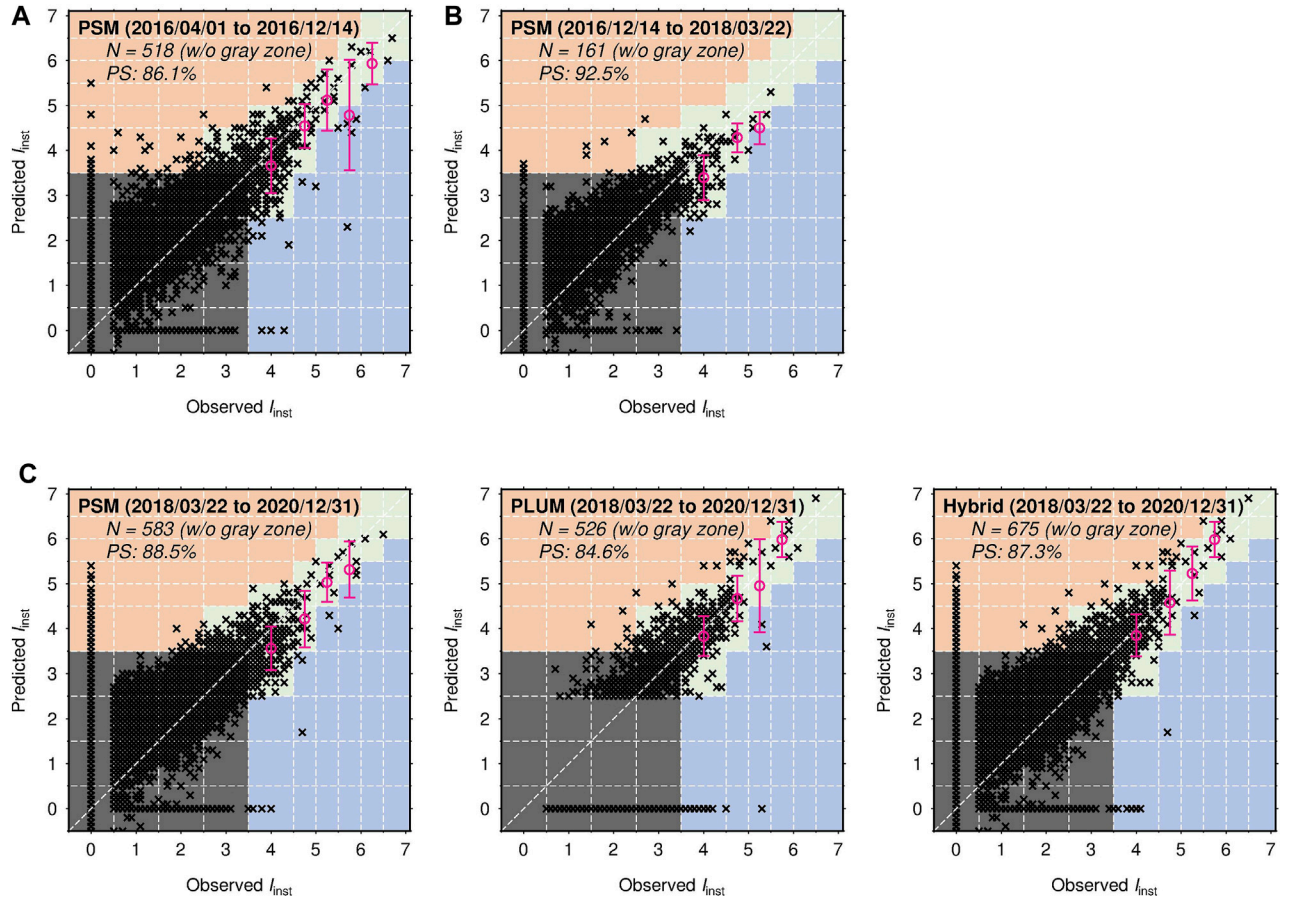

FIGURE 4 | The same figure as **Figure 3** but using the final ground motion prediction results.

with predicted $I_{JMA} = 2$ and observed $I_{JMA} = 6L$ in **Figure 4A** was due to duplicated event declarations; the system declared two events, one of which had a poor source location estimate because the location was determined only with seismometers far from the actual epicenter.

For the second period, just after the IPF implementation, the prediction score was 83.6% with the maximum ground motion predictions and 92.5% with the final predictions, higher than those during the first period (**Figures 3B**, **4B**). IPF did not provide mislocated hypocenters for multiple simultaneous events, and therefore the prediction accuracy was improved compared to that before the IPF implementation. However, there was still an overprediction case in which ground motions were overpredicted with errors of ≥ 2 I_{JMA} units. The overprediction was caused by M4.5 and M4.0 earthquakes in January 2018 that occurred simultaneously, ~400 km away from each other (JMA, 2019a). The magnitude of the M4.5 earthquake was overestimated because the system calculated the magnitude with displacement amplitudes of the M4.0 earthquake. Although the IPF and NYAD algorithms provided correct hypocenter location estimates for the two events, the subsequent event identification process associated the two earthquakes incorrectly. In 2019, JMA updated the event identification and magnitude calculation criteria to address the overprediction issue (JMA, 2019a). Without ground motion predictions for the M4.5 and M4.0 earthquakes, the prediction score would have been 89.8% with the maximum predictions and 97.4% with the final predictions (**Supplementary Figures S1B, S2B**).

During the third period, after the PLUM implementation, the prediction score of PSM was 81.5 and 88.5% with the maximum and final ground motion predictions, respectively (**Figures 3C**, **4C**). As during the second period, IPF provided accurate source parameter estimates without hypocenter mislocation for multiple simultaneous earthquakes. However, an overprediction issue occurred again on July 30, 2020 (JMA, 2020b). For a M6.0 earthquake that occurred near the Torishima island (the epicenter was ~500 km southward of the Japan mainland), the system issued an overpredicted warning, estimating a M7.3 earthquake whose location was ~440 km northward of the actual epicenter. The overprediction was significant because no felt ground shaking was observed although EEW users received the warning. The Hypoon algorithm provided a mislocated hypocenter estimate, and the system used the source estimate because the location estimation errors (calculated by Hypoon) were lower than the rejection criteria. The magnitude was calculated with a displacement amplitude observed at a

seismometer in the Hahajima island, ~800 km southward of the estimated source location. After the overprediction issue, as a tentative measure, JMA modified the magnitude calculation logic, imposing the condition that seismometers used for the magnitude estimation must be located within 700 km from the estimated epicenter. Without the M6.0 near-Torishima event, the prediction score of the PSM algorithms would have been 85.5 and 94.3% with the maximum and final ground motion predictions, respectively (**Supplementary Figures S1C, S2C**). For the maximum ground motion predictions, there were several overprediction cases in which I_{JMA} = 4 was predicted but $I_{JMA} \leq$ 2 was observed. Those overpredictions occurred mainly because of magnitude overestimation in an early stage with a small number of seismometers and unstable hypocenter location estimates using seismometers at the network boundary.

During the second and third periods, the PSM algorithms tended to underpredict ground motions especially for strong shakings of $I_{JMA} \geq$ 5L in the final EEW reports, with prediction errors of one to three I_{JMA} units (**Figures 4B,C**). Most of those strong shakings were caused by large inland earthquakes and were observed near the epicenters. The PSM algorithms underpredicted the strong ground motions because of GMPE errors and/or minor magnitude underestimation, although accurate source locations were estimated. The underprediction case with predicted I_{JMA} = 2 and observed I_{JMA} = 5L during the third period was due to a hypocenter estimate with a large location error caused by duplicated event declarations (two events were declared for this earthquake, and the PSM algorithms provided an accurate source location estimate in the other declared event; therefore, EEW users also received more accurate EEW reports for this earthquake).

During the third period, the PLUM prediction score was 84.6% (**Figures 3C**, **4C**; the maximum and final ground motion predictions are the same for PLUM). The prediction score for PLUM was influenced by prediction errors for inland earthquakes. The assumption of unattenuated wave incidence did not hold for sites near epicenters of shallow inland earthquakes; PLUM therefore overpredicted ground motions for several inland events. In addition, PLUM missed ground motions for three inland earthquakes with observed $I_{JMA} \geq$ 5L. This was because the strong motions were so localized that seismometers used for PLUM did not observe $I_{JMA} \geq$ 3, the EEW issuance threshold of PLUM. On the other hand, PLUM did not cause significant overpredictions, compared to PSM; the maximum overprediction error of PLUM was 3 on the I_{JMA} units (i.e., predicted I_{JMA} = 5U but observed I_{JMA} = 3; the intensity difference between 5L and 5U is counted as one I_{JMA} unit although the interval is 0.5 I_{inst}) while that of PSM was 6 (predicted I_{JMA} = 5U but observed I_{JMA} = 0) with the final ground motion predictions during the third period (**Figure 4C**). In addition, PLUM predicted strong shakings caused by large inland earthquakes with smaller underprediction errors than PSM.

The prediction score for the hybrid algorithm was 81.0 and 87.3% with the maximum and final predictions, respectively (**Figures 3C**, **4C**). Without the M6.0 near-Torishima earthquake, the score would be 84.7 and 92.2% (**Supplementary Figures S1C, S2C**). The prediction score for the hybrid algorithm was similar to but slightly smaller than that for PSM, influenced by PLUM ground motion predictions. This indicates that the hybrid algorithm inherited the characteristics of both PSM and PLUM.

Warning Issuance Performance Changes With the Integrated Particle Filter and Propagation of Local Undamped Motion Implementation

We also evaluated how the warning issuance performance was changed by the IPF and PLUM implementation. We investigated which earthquakes with $I_{JMA} \geq 1$ ($I_{inst} \geq 0.5$; felt earthquakes) were warned/missed by the JMA EEW system, taking the same analysis period as in *Prediction Accuracy Changes With the Integrated Particle Filter and Propagation of Local Undamped Motion Implementation*. In addition, the warning timeliness was assessed by calculating warning issuance time differences between PSM and PLUM. From April 2016 to December 2020, there was no overprediction case in which the system issued a warning for an earthquake with observed I_{JMA} = 0, except for the M6.0 near-Torishima earthquake in July 2020.

During the first period, the JMA EEW system issued warnings for large earthquakes with a high detection rate (**Figure 5A**). Especially, warnings were issued for all earthquakes with observed $I_{JMA} \geq$ 5U, except for two inland earthquakes of the 2016 Kumamoto earthquake sequence. However, the system issued overpredicted warnings for M2–3-class (i.e., 2.0 ≤ M < 4.0) earthquakes of the Kumamoto earthquake sequence with observed $I_{JMA} \leq$ 3, providing mislocated hypocenter estimates.

During the second period, the system issued warnings with a similar detection rate to that during the first period for earthquakes with observed $I_{JMA} \geq$ 5L (**Figure 5B**). An overpredicted warning was issued for the simultaneous occurrence of the M4.5 and M4.0 earthquakes in January 2018, which was not due to hypocenter mislocation but due to incorrect event association in the event identification process (in **Figure 5B**; only the M4.5 earthquake is plotted). IPF did not cause overpredicted warnings for earthquakes with observed $I_{JMA} \leq$ 3.

During the third period, PSM and PLUM detected warning events with a low missing rate for observed $I_{JMA} \geq$ 5U (**Figure 5C**). For earthquakes with 4.5 ≤ I_{inst} < 5.0 (earthquakes near the warning threshold), PLUM had a higher detection rate than PSM. This was because PLUM was less likely to underpredict strong motions for inland earthquakes than PSM (see *Prediction Accuracy Changes With the Integrated Particle Filter and Propagation of Local Undamped Motion Implementation*). There were two earthquakes with observed I_{JMA} = 3 for which the system issued overpredicted warnings, owing to source parameter estimates by IPF. Those were due to magnitude overestimation in an early stage and unstable hypocenter location estimates at the seismometer network boundary. Although the system also issued overpredicted warnings after the IPF implementation, the overpredicted earthquakes with observed $I_{JMA} \leq$ 3 had larger magnitudes (M5–6-class; 5.0 ≤ M < 7.0) than those during the first period (M2–3-class).

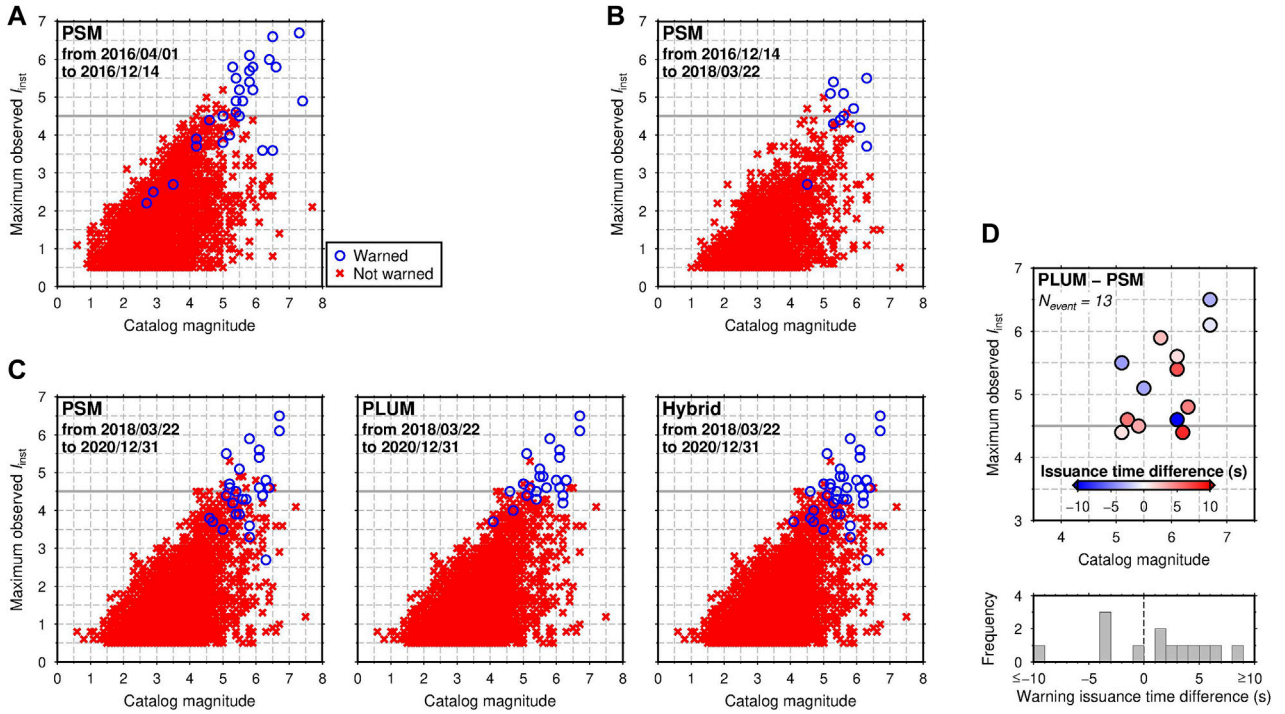

FIGURE 5 | (A–C) Earthquakes with a warning issued by the PSM, PLUM, and hybrid algorithms (blue circle) and earthquakes without a warning issued (red cross). In this analysis, earthquakes with $I_{JMA} \geq 1$ ($I_{inst} \geq 0.5$; felt earthquakes) were used. The analysis periods were the same as in **Figure 3**. Each earthquake was plotted with the peak observed intensity and catalog magnitude. For multiple simultaneous earthquakes, only one of the earthquakes was plotted. The horizontal gray line along I_{inst} = 4.5 indicates the warning threshold. **(D)** Warning issuance time differences between the PSM and PLUM algorithms with earthquakes for which both of the PSM and PLUM algorithms satisfied the warning condition during the third period (upper panel) and the histogram of the warning issuance time differences (lower panel). Circles in blue (red) correspond to earthquakes for which PLUM (PSM) satisfied the warning condition earlier than PSM (PLUM).

To assess the warning timeliness, we evaluated warning issuance time differences between PSM and PLUM, using the 13 earthquakes warned by both of PSM and PLUM during the third period (**Figure 5D**). For five out of the 13 earthquakes, the warning issuance times of PLUM were earlier than those of PSM. The median time difference was ~3.4 s. The warning timeliness was improved for those events because PLUM was less likely to underpredict strong ground motions than PSM, and PLUM used the denser JMA seismic network than IPF.

Detection Capability Changes With the S-Net Incorporation

Focusing on the S-net incorporation, we investigated how the new observation facilities changed the detection capability of the JMA EEW system. The timeliness of the first EEW report was evaluated for earthquakes around the Japan and Kuril trenches, where S-net has been deployed. Here, we use the term "detection time" as the time when the system issued the first EEW report.

The target area for the detection time analysis is shown in **Figure 6A**. For earthquakes inside the area, we calculated the cumulative distribution functions (CDFs) of detection times before and after June 27, 2019, the start date for the S-net incorporation (**Figure 6B**). The CDF after the S-net incorporation took smaller values for all detection times than the CDF before the incorporation, indicating that S-net successfully improved the detection timeliness for earthquakes around the Japan and Kuril trenches. Especially, after the S-net incorporation, the system issued the first EEW report within 21.78 and 30.14 s from the origin time for 50 and 75% of earthquakes inside the area, respectively, which were 3.90 and 8.83 s earlier than before the incorporation.

In addition, we also calculated the CDFs for earthquakes outside the target area (**Figure 6C**). The CDF values did not change drastically before and after the S-net introduction. The detection time difference was less than ~2.0 s, implying that the detection time variability due to temporal seismicity change was within ~2.0 s. The detection time reduction for earthquakes inside the area was larger than ~2.0 s; therefore, the timeliness improvement by S-net was significant.

DISCUSSION

IPF has been implemented to overcome the overprediction issue caused by the mislocation of multiple simultaneous earthquakes. Before the IPF operation, the prediction score for the PSM

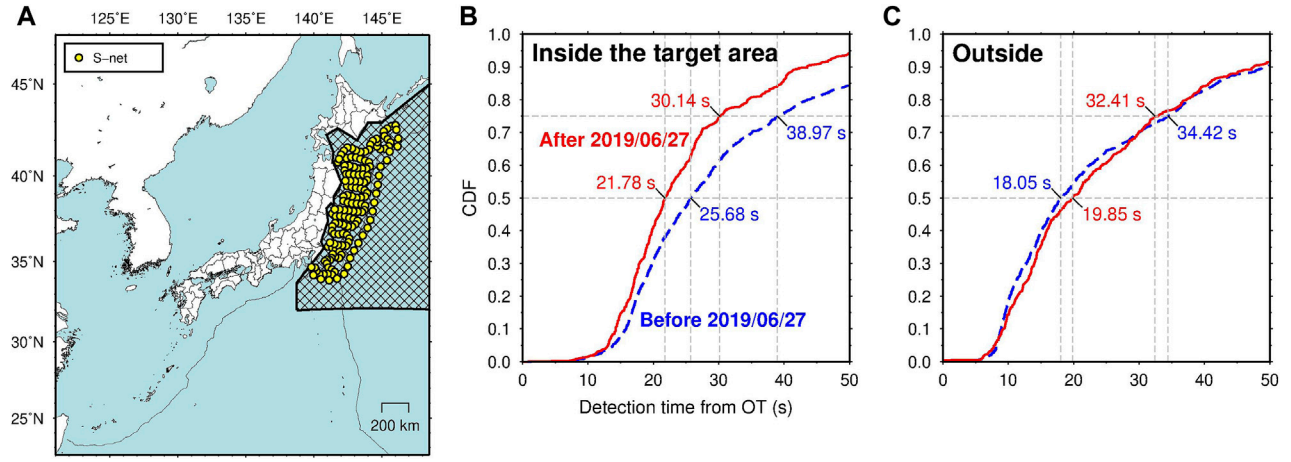

FIGURE 6 | (A) The target area for the detection time analysis for S-net (shaded area) and the locations of S-net stations. **(B)** the CDFs of detection times for earthquakes inside the target area before and after June 27, 2019, the start date for the S-net incorporation (that is, from April 1, 2016 to June 27, 2019 and from June 27, 2019 to December 31, 2020; blue broken and red solid lines, respectively). The detection time means the time when the JMA EEW system issued the first EEW report. The detection times for CDF values of 0.50 and 0.75 are shown. OT, origin time. **(C)** The same figure as **(B)** but for earthquakes outside the target area.

algorithms was 69.7% with the maximum ground motion predictions; after the IPF implementation, the prediction score increased to more than 80% (83.6% from December 14, 2016 to March 22, 2018 and 81.6% from March 22, 2018 to December 31, 2020). After the IPF operation, the PSM algorithms caused significant ground motion overpredictions for the M4.5 and M4.0 earthquakes in January 2018 and for the M6.0 near-Torishima earthquake in July 2020, which were not due to IPF but due to the event identification process and the Hypoon algorithm. Without the two overprediction cases, the prediction score would have been 89.8% from December 14, 2016 to March 22, 2018 and 85.5% from March 22, 2018 to December 31, 2020. Those results indicate that IPF provided source parameter estimates with a higher accuracy than the previous PSM algorithms. The warning performance analysis showed that, before the IPF implementation, the system issued overpredicted warnings for M2–3-class earthquakes because of mislocated source estimates provided by the previous PSM algorithms. On the other hand, IPF did not cause overpredicted warnings for earthquakes with observed $I_{JMA} \leq 3$, except for two M5–6-class events. There were several earthquakes with observed $I_{JMA} = 4$ for which IPF satisfied the warning condition; however, their magnitudes were M4-class or more. These imply that IPF reduced the risk of issuing overpredicted warnings with small (M2–3-class) earthquakes.

The prediction score for PSM using the final EEW reports was ~90% after the IPF operation; however, even with the final ground motion predictions, the PSM algorithms were likely to underpredict strong shakings caused by large inland earthquakes, because of GMPE errors and/or minor magnitude underestimation. Especially, the underprediction due to GMPE errors underscored the prediction accuracy limitation of the source-based approach; that is, correct hypocenter location and magnitude estimates do not always provide accurate ground motions because of GMPE errors (Hoshiba et al., 2010).

After the IPF operation, significant ground motion overpredictions occurred for the M4.5 and M4.0 earthquakes in January 2018 and for the M6.0 near-Torishima earthquake in July 2020. The first case was due to incorrect event association in the event identification process. The other case was because of a mislocated hypocenter estimate from the Hypoon algorithm. Those overprediction cases indicate that there are still technical challenges that need to be addressed to attain more robust source-based ground motion predictions. A possible solution for the technical issues is to skip the event identification process by integrating the different PSM algorithms into a single algorithm. The integration may be possible by feeding all available seismic data into IPF, although the current IPF algorithm does not incorporate Hi-net high-sensitivity velocity meters. Several previous studies suggested that the Hi-net velocity sensors could be used for a PSM algorithm in combination with accelerometers if the instrumental response was corrected (Yamada et al., 2014; Noguchi et al., 2020; Yamada et al., 2021).

PLUM has been introduced to provide robust ground motion predictions for complex earthquake scenarios such as a large earthquake with a finite fault and an intense earthquake sequence. The prediction score for PLUM was 84.6%, which was affected by prediction errors for shallow inland earthquakes. On the other hand, PLUM predicted strong ground motions caused by large inland earthquakes with smaller underprediction errors than PSM. The warning performance analysis showed that, for earthquakes near the warning threshold (i.e., the peak observed intensity was $4.5 \leq I_{inst} < 5.0$), PLUM detected the strong motions and satisfied the warning condition with a lower missing rate than PSM. In addition, there were five events for which the warning issuance time of PLUM was earlier than that of

PSM. Those results indicate that PLUM attains the robustness and timeliness of the ground motion prediction for strong shakings, at the expense of the prediction accuracy for shallow inland events (robustness here means that the capability of predicting ground motions without missing or underprediction). The PLUM's characteristics discussed here were already mentioned in Kodera et al. (2020) but were validated with a longer analysis period in this study. Reducing prediction errors for inland earthquakes is one of technical issues for PLUM. A more complicated wave propagation model may be required to improve the PLUM prediction performance for inland earthquakes. Another technical challenge for PLUM is that lead times given by PLUM are limited because ground motions are predicted based on direct observations at nearby seismometers. Introducing P-wave information and/or an attenuating wave propagation model may lengthen available lead times (Kodera, 2018; 2019).

Owing to the PLUM implementation, the JMA EEW system attained robust and timely ground motion predictions for earthquakes with high observed intensities. At the same time, the system had a higher possibility of overprediction for shallow inland earthquakes than before. Although the PLUM implementation caused an adverse effect on the system prediction accuracy, the prediction accuracy analysis for the hybrid algorithm indicates that the adverse impact was not very large. The prediction score for the hybrid algorithm was 81.0% with the maximum ground motion predictions and 87.3% with the final predictions. Those percentages were lower than those for PSM; however, the differences were limited to within ~1%, implying that the prediction errors due to PLUM were acceptable.

Two large-scale OBS networks, DONET and S-net, have been incorporated into the JMA EEW system to improve the detection capability for offshore earthquakes. The detection capability analysis for S-net showed that S-net shortened detection times for earthquakes around the Japan and Kuril trenches substantially. This indicates that the current JMA EEW system would issue public warnings with longer lead times than the system in 2011 if large earthquakes occur again around the Japan trench. In the western region of the Nankai trough, along which a M9-class megathrust earthquake is anticipated, NIED is planning to construct a new large-scale OBS network, N-net (Aoi et al., 2020). The N-net observation data will be transmitted to the JMA EEW system in real time. N-net would improve the detection timeliness for earthquakes around the network as well as S-net.

CONCLUSION

The 2011 M_w9.0 Tohoku-Oki earthquake and subsequent intense earthquake sequence underscored technical limitations of the source-based algorithms employed in the initial JMA EEW system. To overcome the technical issues and to enhance the system performance further, JMA has implemented the IPF and PLUM algorithms and incorporated new observation facilities including S-net.

To evaluate the prediction accuracy changes with the IPF and PLUM implementation, we calculated a prediction score, defined as the ratio of sub-prefectural areas for which ground motions are predicted within intensity errors of one I_{JMA} unit among all areas with predicted or observed $I_{JMA} \geq 4$. Before the IPF implementation, the prediction score based on the maximum prediction results was as low as 69.7% because of mislocated hypocenter estimates provided by the previous PSM algorithms for multiple simultaneous earthquakes. IPF increased the prediction score to more than 80%, providing accurate source parameter estimates based on the Bayesian inference. In addition, IPF reduced the number of overpredicted warnings for earthquakes with a small magnitude (M2–3-class) and low peak intensity ($I_{JMA} \leq 3$).

The PLUM implementation made the system less likely to underpredict strong ground motions caused by large inland earthquakes, which was due to PLUM's ground motion prediction approach using direct observation of ongoing ground shakings. PLUM also enabled the system to issue warnings with a low missing rate for earthquakes whose observed intensities were just above the warning threshold. The warning timeliness was improved by PLUM for five out of the 13 earthquakes warned by both of PSM and PLUM. The median of the improved warning times was ~3.4 s.

The detection time analysis for S-net showed that the incorporation of S-net shortened 50th and 75th percentile detection times (times required to issue the first EEW report) by 3.90 and 8.83 s, respectively, for offshore earthquakes around the Japan and Kuril trenches.

Those findings indicate that, over the 10 years after the Tohoku-Oki earthquake, the JMA EEW system has made substantial progress both on software and hardware aspects. At the same time, there is still room for further improvements of the system on the ground motion prediction algorithms and observation facilities. The JMA EEW system in the next 10 years will achieve more accurate, timely, and robust EEW issuance for possible future large earthquakes.

DATA AVAILABILITY STATEMENT

EEW reports issued by the JMA EEW system were obtained from an internal database of JMA. Earthquake locations and observed JMA intensities can be obtained from the JMA website at https://www.data.jma.go.jp/svd/eqev/data/bulletin/index_e.html (last accessed June 2021).

AUTHOR CONTRIBUTIONS

YK designed the study, performed the analyses, and drafted the article. NH, KN, KM, RT, MM, and KO maintained the JMA EEW system and made the database of EEW reports. KT developed the IPF algorithm. YK and MH proposed the PLUM algorithm. NH, KN, and MH developed the algorithms

to process OBS data. All authors read and approved the final article.

ACKNOWLEDGMENTS

The authors would like to thank the handling editor and two reviewers for their useful comments and suggestions that improved the article. The JMA EEW system has been developed based on joint research of JMA and the Railway Technical Research Institute, technological achievements by NIED, and research led by Kyoto University that was supported by funding for Next Generation World-Leading Researchers from the Cabinet Office of Japan. The JMA EEW system uses seismic data obtained from observational facilities of NIED, in addition to those of JMA (as of December 2020). Figures were drawn using Generic Mapping Tools (Wessel and Smith, 1998).

SUPPLEMENTARY MATERIAL

The Supplementary Material for this article can be found online at: https://www.frontiersin.org/articles/10.3389/feart.2021.726045/full#supplementary-material

REFERENCES

Aoi, S., Asano, Y., Kunugi, T., Kimura, T., Uehira, K., Takahashi, N., et al. (2020). MOWLAS: NIED Observation Network for Earthquake, Tsunami and Volcano. *Earth Planets Space* 72, 126. doi:10.1186/s40623-020-01250-x

Böse, M., Allen, R., Brown, H., Gua, G., Fischer, M., Hauksson, E., et al. (2014). "CISN ShakeAlert: An Earthquake Early Warning Demonstration System for California," in *Early Warning for Geological Disasters—Scientific Methods and Current Practice*. Editors J. Zschau and F. Wenzel (Berlin, Germany: Springer), 49–69. doi:10.1007/978-3-642-12233-0_3

Chen, D. Y., Hsiao, N. C., and Wu, Y. M. (2015). The Earthworm Based Earthquake Alarm Reporting System in Taiwan. *Bull. Seismological Soc. America* 105 (2A), 568–579. doi:10.1785/0120140147

Clinton, J., Zollo, A., Marmureanu, A., Zulfikar, C., and Parolai, S. (2016). State-of-the Art and Future of Earthquake Early Warning in the European Region. *Bull. Earthquake Eng.* 14 (9), 2441–2458. doi:10.1007/s10518-016-9922-7

Doi, K. (2011). The Operation and Performance of Earthquake Early Warnings by the Japan Meteorological Agency. *Soil Dyn. Earthquake Eng.* 31 (2), 119–126. doi:10.1016/j.soildyn.2010.06.009

Espinosa-Aranda, J. M., Cuellar, A., Garcia, A., Ibarrola, G., Islas, R., Maldonado, S., et al. (2009). Evolution of the Mexican Seismic Alert System (SASMEX). *Seismological Res. Lett.* 80 (5), 694–706. doi:10.1785/gssrl.80.5.694

Harada, S. (2007). Earthquake Versatile Observation System. *Q. J. Seismology* 70, 73–81.

Hayashimoto, N., and Hoshiba, M. (2013). Examination of Travel Time Correction and Magnitude Correction of Tonankai Ocean Bottom Seismographs for Earthquake Early Warning. *Q. J. Seismology* 76, 69–81.

Hayashimoto, N., Nakamura, T., and Hoshiba, M. (2019). A Technique for Estimating the UD-Component Displacement Magnitude for Earthquake Early Warnings that Can Be Applied to Various Seismic Networks Including Ocean Bottom Seismographs. *Q. J. Seismology* 83, 1.

Hayashimoto, N., Nakamura, T., and Hoshiba, M. (2016). Stability of Ocean Bottom Seismograph Data Exposed to strong Shaking: Efforts for Utilizing OBS for Earthquake Early Warning. *ECGS ESC/EAEE Jt. Workshop Proc.* 31, 41–49.

Horiuchi, S., Negishi, H., Abe, K., Kamimura, A., and Fujinawa, Y. (2005). An Automatic Processing System for Broadcasting Earthquake Alarms. *Bull. Seismological Soc. America* 95 (2), 708–718. doi:10.1785/0120030133

Hoshiba, M., and Aoki, S. (2015). Numerical Shake Prediction for Earthquake Early Warning: Data Assimilation, Real-Time Shake Mapping, and Simulation of Wave Propagation. *Bull. Seismological Soc. America* 105 (3), 1324–1338. doi:10.1785/0120140280

Hoshiba, M., Iwakiri, K., Hayashimoto, N., Shimoyama, T., Hirano, K., Yamada, Y., et al. (2011). Outline of the 2011 off the Pacific Coast of Tohoku Earthquake (M W 9.0) -Earthquake Early Warning and Observed Seismic Intensity-. *Earth Planet. Sp* 63, 547–551. doi:10.5047/eps.2011.05.031

Hoshiba, M., Kamigaichi, O., Saito, M., Tsukada, S. y., and Hamada, N. (2008). Earthquake Early Warning Starts Nationwide in Japan. *Eos Trans. AGU* 89, 73–74. doi:10.1029/2008EO080001

Hoshiba, M., Ohtake, K., Iwakiri, K., Aketagawa, T., Nakamura, H., and Yamamoto, S. (2010). How Precisely Can We Anticipate Seismic Intensities? A Study of Uncertainty of Anticipated Seismic Intensities for the Earthquake Early Warning Method in Japan. *Earth Planet. Sp* 62 (8), 611–620. doi:10.5047/eps.2010.07.013

Hoshiba, M. (2013). Real-time Prediction of Ground Motion by Kirchhoff-Fresnel Boundary Integral Equation Method: Extended Front Detection Method for Earthquake Early Warning. *J. Geophys. Res. Solid Earth* 118, 1038–1050. doi:10.1002/jgrb.50119

Iwakiri, K., Hoshiba, M., Nakamura, K., and Morikawa, N. (2011). Improvement in the Accuracy of Expected Seismic Intensities for Earthquake Early Warning in Japan Using Empirically Estimated Site Amplification Factors. *Earth Planet. Sp* 63 (2), 57–69. doi:10.5047/eps.2010.12.002

Japan Meteorological Agency JMA (2020b). Press release: On the implementation of an urgent improvement of earthquake early warning. Retrieved from: https://www.jma.go.jp/jma/press/2008/07a/kaizen_20200807.pdf (last accessed June, , 2021).

Japan Meteorological Agency JMA (2014). Document No. 1: On the Dissemination History and Accuracy Evaluation of Recent Earthquake Early Waning reportsThe Fifth Meeting of the Committee of Evaluation and Improvement of Earthquake Early Warning. Retrieved from: https://www.data.jma.go.jp/svd/eqev/data/study-panel/eew-hyoka/05/shiryou1.pdf (last accessed June, 2021).

Japan Meteorological Agency JMA (2019a). Document No. 2: Document of the Ninth Meeting of the Technical Panel of the Committee of Evaluation and Improvement of Earthquake Early Warning. The Ninth Meeting of the Technical Panel of the Committee of Evaluation and Improvement of Earthquake Early Warning. Retrieved from: http://www.data.jma.go.jp/svd/eqev/data/study-panel/eew-hyoka/t09/20190305_siryou2.pdf (last accessed June, 2021).

Japan Meteorological Agency JMA (2016). Press Release: On a Technical Improvement of Earthquake Early Warning (The IPF Algorithm) and Measure for the False Earthquake Early Warning Report on August 1, 2016. Retrieved from: https://www.jma.go.jp/jma/press/1612/13a/EEW_kaizen_201612.pdf (last accessed June, 2021).

Japan Meteorological Agency JMA (2018). Press Release: On an Improvement of Earthquake Early Warning—The Prediction Accuracy of Seismic Intensity when Large Earthquakes Occur Is Improved. Retrieved from: https://www.jma.go.jp/jma/press/1803/08c/EEW_kaizen_201803.pdf (last accessed June, 2021).

Japan Meteorological Agency JMA (2020a). Press Release: On the Additional Use of New Ocean Bottom Seismometers for Earthquake Early Warning. Retrieved from: https://www.jma.go.jp/jma/press/2003/19a/20200319_eewkatsuyouS6.pdf (last accessed June, 2021).

Japan Meteorological Agency JMA (2015). Press Release: On the Start Date for Using New Observation Data for Earthquake Early Warning. Retrieved from: https://www.jma.go.jp/jma/press/1503/24a/eewkatsuyou20150324.pdf (last accessed June, 2021).

Japan Meteorological Agency JMA (2019b). Press Release: On the Use of New Ocean-Bottom Seismic Observation Data for Earthquake Early Warning. Retrieved from: https://www.jma.go.jp/jma/press/1906/21a/eewkatsuyou20190621.pdf (last accessed June 2021).

Japan Meteorological Agency JMA (1996). *Seismic Intensity*. (Tokyo, Japan: Gyosei).

Kamigaichi, O. (2004). JMA Earthquake Early Warning. *J. JAEE* 4 (3), 134–137. doi:10.5610/jaee.4.3_134

Kamigaichi, O., Saito, M., Doi, K., Matsumori, T., Tsukada, S., Takeda, K., et al. (2009). Earthquake Early Warning in Japan: Warning the General Public and Future Prospects. *Seismological Res. Lett.* 80 (5), 717–726. doi:10.1785/gssrl.80.5.717

Kanazawa, T., Uehira, K., Mochizuki, M., Shinbo, T., Fujimoto, H., Noguchi, S., et al. (2016). S-net Project, Cabled Observation Network for Earthquakes and Tsunamis. *SubOptic*. WE2B–3.

Kaneda, Y., Kawaguchi, K., Araki, E., Matsumoto, H., Nakamura, T., Kamiya, S., et al. (2015). "Development and Application of an Advanced Ocean Floor Network System for Megathrust Earthquakes and Tsunamis," in *Seafloor Observatories*. (Berlin, Germany: Springer), 643–662. doi:10.1007/978-3-642-11374-1_25

Kawaguchi, K., Kaneko, S., Nishida, T., and Komine, T. (2015). "Construction of the DONET Real-Time Seafloor Observatory for Earthquakes and Tsunami Monitoring," in *Seafloor Observatories*. (Berlin, Germany: Springer), 211–228. doi:10.1007/978-3-642-11374-1_10

Kilb, D., Bunn, J. J., Saunders, J. K., Cochran, E. S., Minson, S. E., Baltay, A., et al. (2021). The PLUM Earthquake Early Warning Algorithm: A Retrospective Case Study of West Coast, USA, Data. *J. Geophys. Res. Solid Earth* 126, e2020JB021053. doi:10.1029/2020JB021053

Kodera, Y. (2019). An Earthquake Early Warning Method Based on Huygens Principle: Robust Ground Motion Prediction Using Various Localized Distance-Attenuation Models. *J. Geophys. Res. Solid Earth* 124 (12), 12981–12996. doi:10.1029/2019JB017862

Kodera, Y., Hayashimoto, N., Moriwaki, K., Noguchi, K., Saito, J., Akutagawa, J., et al. (2020). First-year Performance of a Nationwide Earthquake Early Warning System Using a Wavefield-Based Ground-Motion Prediction Algorithm in Japan. *Seismological Res. Lett.* 91 (2A), 826–834. doi:10.1785/0220190263

Kodera, Y. (2018). Real-time Detection of Rupture Development: Earthquake Early Warning Using P Waves from Growing Ruptures. *Geophys. Res. Lett.* 45, 156–165. doi:10.1002/2017GL076118

Kodera, Y., Saitou, J., Hayashimoto, N., Adachi, S., Morimoto, M., Nishimae, Y., et al. (2016). Earthquake Early Warning for the 2016 Kumamoto Earthquake: Performance Evaluation of the Current System and the Next-Generation Methods of the Japan Meteorological Agency. *Earth Planets Space* 68 (1), 202. doi:10.1186/s40623-016-0567-1

Kodera, Y., Yamada, Y., Hirano, K., Tamaribuchi, K., Adachi, S., Hayashimoto, N., et al. (2018). The Propagation of Local Undamped Motion (PLUM) Method: A Simple and Robust Seismic Wavefield Estimation Approach for Earthquake Early Warning. *Bull. Seismological Soc. America* 108 (2), 983–1003. doi:10.1785/0120170085

Kunugi, T., Aoi, S., Nakamura, H., Suzuki, W., Morikawa, N., and Fujiwara, H. (2013). An Improved Approximating Filter for Real-Time Calculation of Seismic Intensity. *Jssj* 65 (3), 223–230. doi:10.4294/zisin.65.223

Liu, A., and Yamada, M. (2014). Bayesian Approach for Identification of Multiple Events in an Early Warning System. *Bull. Seismological Soc. America* 104 (3), 1111–1121. doi:10.1785/0120130208

Matsuoka, M., and Midorikawa, S. (1994). The Digital National Land Information and Seismic Microzoning. in Proceeding of the 22nd Symposium of Earthquake Ground Motion, AIJ, Tokyo, Japan, 23–34.

Mochizuki, M., Kanazawa, T., Uehira, K., Shimbo, T., Shiomi, K., Kunugi, T., et al. (2016). *S-net Project: Construction of Large Scale Seafloor Observatory Network for Tsunamis and Earthquakes in Japan*. AGU Fall Meeting, San Francisco, United States. NH43B–1840.

Nakamura, T., and Hayashimoto, N. (2019). Rotation Motions of Cabled Ocean-Bottom Seismic Stations during the 2011 Tohoku Earthquake and Their Effects on Magnitude Estimation for Early Warnings. *Geophys. J. Int.* 216 (2), 1413–1427. doi:10.1093/gji/ggy502

Nakamura, T., Nakano, M., Hayashimoto, N., Takahashi, N., Takenaka, H., Okamoto, T., et al. (2014). Anomalously Large Seismic Amplifications in the Seafloor Area off the Kii peninsula. *Mar. Geophys. Res.* 35, 255–270. doi:10.1007/s11001-014-9211-2

Nakamura, Y. (1988). On the Urgent Earthquake Detection and Alarm System (UrEDAS). in Proceedings of Ninth World Conference on Earthquake Engineering, Tokyo and Kyoto, Japan, August 2–9, 1988, 7, 673–678.

Nof, R. N., and Kurzon, I. (2021). TRUAA-earthquake Early Warning System for Israel: Implementation and Current Status. *Seismological Res. Lett.* 92 (1), 325–341. doi:10.1785/0220200176

Noguchi, K., Hayashimoto, N., Tamaribuchi, K., and Kodera, Y. (2020). Improvement of IPF Method with Utilization of Hi-Net. *SSJ Fall Meet.* 2020, S15–S06.

Odaka, T., Ashiya, K., Tsukada, S., Sato, S., Ohtake, K., and Nozaka, D. (2003). A New Method of Quickly Estimating Epicentral Distance and Magnitude from a Single Seismic Record. *Bull. Seismological Soc. America* 93 (1), 526–532. doi:10.1785/0120020008

Okada, Y., Kasahara, K., Hori, S., Obara, K., Sekiguchi, S., Fujiwara, H., et al. (2004). Recent Progress of Seismic Observation Networks in Japan -Hi-Net, F-Net, K-NET and KiK-Net-. *Earth Planet. Sp* 56, xv–xxviii. doi:10.1186/BF03353076

Sheen, D. H., Park, J. H., Chi, H. C., Hwang, E. H., Lim, I. S., Seong, Y. J., et al. (2017). The First Stage of an Earthquake Early Warning System in South Korea. *Seismological Res. Lett.* 88 (6), 1491–1498. doi:10.1785/0220170062

Si, H., and Midorikawa, S. (1999). New Attenuation Relationships for Peak Ground Acceleration and Velocity Considering Effects of Fault Type and Site Condition. *Nihon Kenchiku Gakkai Kozokei Ronbunshu* 64 (523), 63–70. doi:10.3130/aijs.64.63_2

Takagi, R., Uchida, N., Nakayama, T., Azuma, R., Ishigami, A., Okada, T., et al. (2019). Estimation of the Orientations of the S-net Cabled Ocean-Bottom Sensors. *Seismological Res. Lett.* 90 (6), 2175–2187. doi:10.1785/0220190093

Tamaribuchi, K., Yamada, M., and Wu, S. (2014). A New Approach to Identify Multiple Concurrent Events for Improvement of Earthquake Early Warning. *Jssj* 67 (67), 41–55. doi:10.4294/zisin.67.41

Tsukada, S., Odaka, T., Ashiya, K., Ohtake, K., and Nozaka, D. (2004). Analysis of the Envelope Waveform of the Initial Part of P-Waves and its Application to Quickly Estimating the Epicentral Distance and Magnitude. *Jssj* 56 (56), 351–361. doi:10.4294/zisin1948.56.4_351

Uehira, K., Kanazawa, T., Mochizuki, M., Fujimoto, H., Noguchi, S., Shinbo, T., et al. (2016). *Outline of Seafloor Observation Network for Earthquakes and Tsunamis along the Japan Trench (S-Net)*. EGU General Assembly 2016, Vienna, Austria, EGU2016–13832.

Wessel, P., and Smith, W. H. F. (1998). New, Improved Version of Generic Mapping Tools Released. *Eos Trans. AGU* 79 (47), 579. doi:10.1029/98EO00426

Wu, S., Yamada, M., Tamaribuchi, K., and Beck, J. L. (2015). Multi-events Earthquake Early Warning Algorithm Using a Bayesian Approach. *Geophys. J. Int.* 200 (2), 791–808. doi:10.1093/gji/ggu437

Yamada, M., Tamaribuchi, K., and Wu, S. (2014). Faster and More Accurate Earthquake Early Warning System. *J. JAEE* 14 (4), 21–24. doi:10.5610/jaee.14.4_21

Yamada, M., Tamaribuchi, K., and Wu, S. (2021). The Extended Integrated Particle Filter Method (IPFx) as a High-Performance Earthquake Early Warning System. *Bull. Seismological Soc. America* 111 (3), 1263–1272. doi:10.1785/0120210008

Zhang, H., Jin, X., Wei, Y., Li, J., Kang, L., Wang, S., et al. (2016). An Earthquake Early Warning System in Fujian, China. *Bull. Seismological Soc. America* 106 (2), 755–765. doi:10.1785/0120150143

Conflict of Interest: The authors declare that the research was conducted in the absence of any commercial or financial relationships that could be construed as a potential conflict of interest.

frontiers in Earth Science

ORIGINAL RESEARCH
published: 09 November 2021
doi: 10.3389/feart.2021.681199

Applicability of On-Site P-Wave Earthquake Early Warning to Seismic Data Observed During the 2011 Off the Pacific Coast of Tohoku Earthquake, Japan

Seiji Tsuno *

Seismic Data Analysis Laboratory, Center for Railway Earthquake Engineering Research, Railway Technical Research Institute, Tokyo, Japan

In this study, the on-site P-wave earthquake early warning (EEW) based on the site-specific spectral ratio of S-wave to P-wave to efficiently incorporate the site characteristics, which can potentially issue the earthquake warning by the time of T*s-p*, was developed. The spectral ratio of S-wave to P-wave that are related to the source effects, the path effects, and the site effects are significantly affected by the site effects contrast to the source effects and the path effects in practical. At first, the on-site P-wave EEW method which multiplies a site-specific spectral ratio of S-wave to P-wave prepared in advance by P-wave observed in the real-time at seismic stations is applied to seismic data for moderate-sized earthquakes with a magnitude (*Mj*) of 5.0–6.0, occurred in the eastern Japan, observed at both the sedimentary basin site and the rock site. As a result, this method predicted well the observed S-wave in the single indicator of SI within the logarithmic standard deviation of 0.25 as well as in the frequency of more than 0.5 Hz. It is, also, confirmed that the site-specific spectral ratio of S-wave to P-wave at a seismic station was stably retrieved from 20 data samples at least. To investigate the applicability of this method to earthquake ground motions induced by a large-scaled earthquake, finally, this method is applied to seismic data during the 2011 off the Pacific coast of Tohoku earthquake, Japan (*Mw* 9.0). The prediction of S-wave using a time-window of 10 s after P-wave arrived, could not reproduce the observation with the underestimation; however, the prediction of S-wave using a time-window of more than 20 s containing P-wave propagated from an area generating strong motions in the fault, could reproduce the observation. Even in the case of the large-scaled earthquake, the on-site P-wave EEW method based on the site-specific spectral ratio of S-wave to P-wave at a seismic station availably works by using the gradually increasing time-windows after P-wave arrived in the single indicator of SI as well as in the frequency content, avoiding the mixture of S-wave into a part of P-wave.

Keywords: on-site EEW, P-wave, site-specific ratio, prediction of S-wave, real-time, the 2011 off the Pacific coast of Tohoku earthquake, Tohoku region

OPEN ACCESS

Edited by:
Simona Colombelli,
University of Naples Federico II, Italy

Reviewed by:
Masato Motosaka,
Tohoku University, Japan
José Borges,
University of Evora, Portugal

***Correspondence:**
Seiji Tsuno
tsuno.seiji.75@rtri.or.jp

Specialty section:
This article was submitted to Solid Earth Geophysics, a section of the journal Frontiers in Earth Science

Received: *16 March 2021*
Accepted: *22 October 2021*
Published: *09 November 2021*

Citation:
Tsuno S (2021) Applicability of On-Site P-Wave Earthquake Early Warning to Seismic Data Observed During the 2011 Off the Pacific Coast of Tohoku Earthquake, Japan. Front. Earth Sci. 9:681199. doi: 10.3389/feart.2021.681199

INTRODUCTION

Earthquake Early Warning (EEW) systems are installed to many fields in the world based on their own concepts to provide warning prior to the strength of ground shaking (e.g., Allen et al., 2009). The on-site EEW methods, which estimate the strength of ground shaking at the same location by generally using a begging part immediately after the arrival of P-wave, have been developed (e.g., Nakamura, 1988; Allen and Kanamori, 2003; Odaka et al., 2003; Wu and Kanamori, 2005; Wu et al., 2007). On-site EEW methods, which can be operated by a single station and/or a seismic network, are based on the empirical relationships between an amplitude of P-wave and a strength of ground shaking (Wu and Kanamori, 2005), or based on the estimation of an earthquake magnitude (Nakamura, 1988; Allen and Kanamori, 2003; Wu et al., 2007) and an epicentral distance (Odaka et al., 2003) to rapidly predict the strength of ground shaking. Recently, the real-time ground motion prediction using the observed data at front stations in the direction of incoming seismic waves have been developed (e.g., Hoshiba, 2013; Hoshiba and Aoki, 2015; Yang and Motosaka, 2015). However, especially for the on-site EEW method operated by a single station, data recorded in the real-time by a dense seismic network is quite useful, and it is desirable that site characteristics are efficiently incorporated to the method to reflect the difference of the strength of ground shaking in the sites.

In the field of railway, Japan, on-site EEW using P-wave (Nakamura, 1988; Odaka et al., 2003) has been developed to stop the train quickly during the occurrence of earthquakes. At the same time, the own dense seismic network has been installed with the interval distance of 5–40 km and about 100 km along railway lines and coast lines respectively, especially in the eastern Japan (Nakamura, 1988; Nakamura, 1996; Miyakoshi et al., 2019). Recently, after the 2011 off the Pacific coast of Tohoku earthquake (*Mw* 9.0) occurred at the plate boundary of the Pacific plate subducting beneath Tohoku-Japan, seismic stations were installed with the interval distance of 50 km inland in the eastern Japan (Yamamoto and Tomori, 2013).

Miyakoshi and Tsuno (2015) illustrated the relationships between P-wave at the basement and S-wave at the ground surface with the empirical estimations for the physical parameters, using seismic data of KiK-net observed in the Kanto basin, Japan. Tsuno and Miyakoshi (2019) developed the relationships between P-wave at the ground surface and S-wave at the ground surface by interpreting the deconvolution of the transfer function of the P-wave and the convolution of the transfer function of the S-wave with the seismic data observed in the Kanto Region. In this study, the availability of an on-site P-wave EEW based on the site-specific spectral ratio of S-wave to P-wave at a seismic station, which directly predicts S-wave from P-wave (e.g. Miyakoshi and Tsuno, 2015; Tsuno and Miyakoshi, 2019; Zhao and Zhao, 2019) without any estimation of an earthquake magnitude and an epicentral distance was quantitatively examined by applying to seismic data in the Tohoku Region for moderate-sized earthquakes with a magnitude (*Mj*) of 5.0–6.0, occurred in the eastern Japan. Finally, the applicability of this method to seismic data for the large-scaled earthquake of the 2011 off the Pacific coast of Tohoku earthquake (Mw 9.0), Japan was investigated.

DATA

Seismic data recorded at KS and SS stations respectively installed in the rock site and in the sedimentary basin site in the Tohoku Region, Japan by JR East, were used. As for geophysical information around the seismic stations, AVS30 (Aaverage Velocity of S-wave up to a depth of 30 m) at KS station located in Ayukawa, Miyagi Pref. is about 470 m/s and that at SS station located in Shin-Nagamachi, Miyagi Pref. is about 290 m/s, as shown by J-SHIS (Japan Seismic Hazard Information Station). Seismic data of moderate-sized earthquakes with a magnitude (*Mj*) of 5.0–6.0, occurred in the eastern Japan for a period from November/2007 to August/2018 and the mainshock of the 2011 off the Pacific coast of Tohoku earthquake (*Mw* 9.0) were analyzed in this study. As for moderate earthquakes, 58 and 95 earthquakes with high signal-to-noise ratio at KS and SS stations respectively were selected. Location of epicenters and seismic stations used in this study are shown in **Figure 1**. Information of PGAs, PGVs, and the peak frequency in the seismic data of the moderate-sized earthquakes with a magnitude (*Mj*) of 5.0–6.0 at KS and SS stations are shown with those of the 2011 off the Pacific coast of Tohoku earthquake (*Mw* 9.0) in **Figure 2**. As an example, waveforms of acceleration for 3 components during an earthquake (*Mj* 5.9) occurred on 11th/April 2011 are shown in **Figure 3**.

ON-SITE P-WAVE EARTHQUAKE EARLY WARNING

Method

Assuming an earthquake ground motion observed in a far field induced by a double couple point source, the earthquake ground motions of P-wave and S-wave at the basement in the frequency domain are expressed, as follows (e.g. Iwata and Irikura, 1986; Aki and Richard, 2002).

$$O_{\mathrm{b}}^{P}(\omega) = \frac{R_{\theta\phi}^{P}}{4\pi\rho {V_{\mathrm{P}}}^{3}} \frac{1}{r} \Omega(\omega) \cdot \exp\left(-\frac{\omega}{2Q_{\mathrm{P}}} \frac{r}{{V'}_{\mathrm{P}}} \right) \quad (1)$$

$$O_{\mathrm{b}}^{S}(\omega) = \frac{R_{\theta\phi}^{S}}{4\pi\rho {V_{\mathrm{S}}}^{3}} \frac{1}{r} \Omega(\omega) \cdot \exp\left(-\frac{\omega}{2Q_{\mathrm{S}}} \frac{r}{{V'}_{\mathrm{S}}} \right) \quad (2)$$

Here, ω is an angular frequency, ρ and V is a density and a velocity of body waves in and around an earthquake source region, r is distance from an earthquake source, $R_{\theta\phi}$ is a radiation coefficient, Ω (ω) is an earthquake source spectrum and Q is an internal attenuation in the crust. V' is the average velocity of body waves in the crust. The subscripts of P and S represent P-wave and S-wave, respectively. The subscript of b, also, represents the basement.

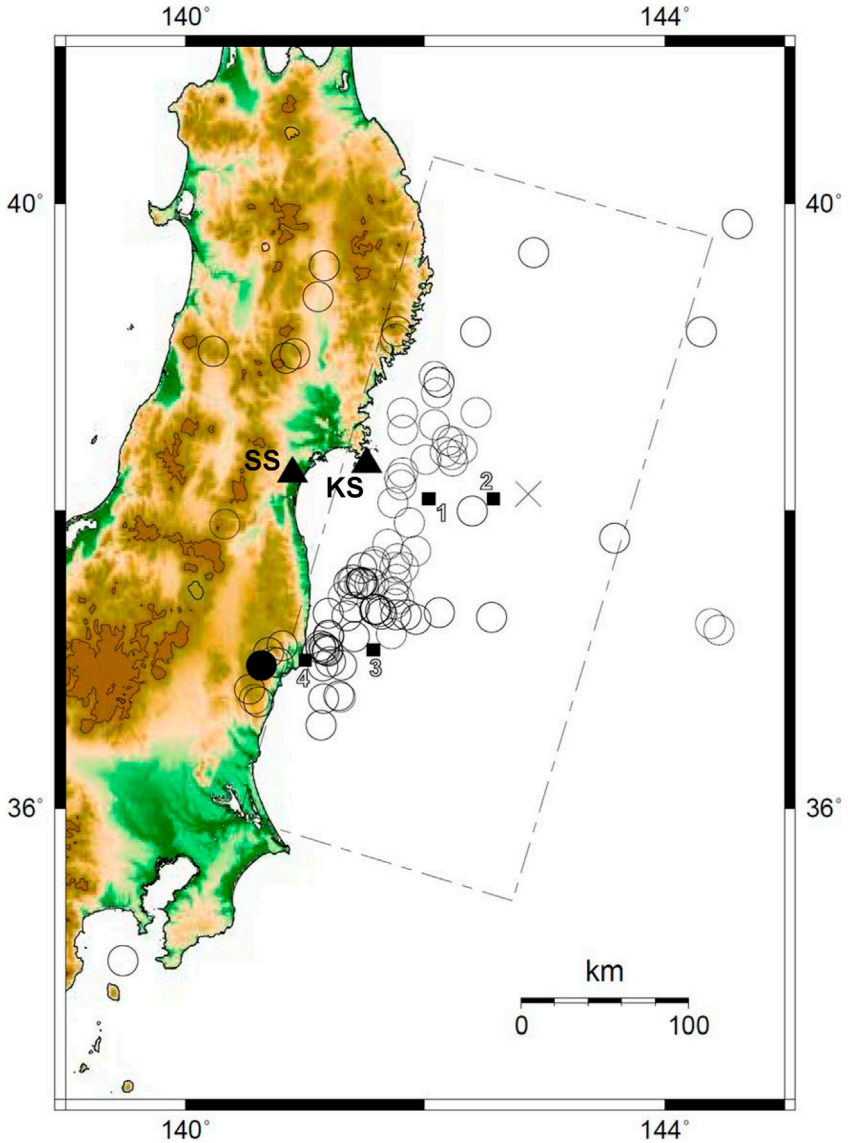

FIGURE 1 | Location of epicenters for moderate-sized earthquakes and seismic stations used in this study. Open circles show the location of epicenters for the moderate-sized earthquakes with a magnitude (*Mj*) of 5.0–6.0 for a period from November/2007 to August/2018 and, closed triangles show the location of seismic stations. A closed circle shows location of epicenter for an earthquake (*Mj* 5.9) occurred on 11th/April 2011. The earthquake source fault plane of the 2011 off the Pacific coast of Tohoku earthquake (*Mw* 9.0) occurred on 11th/March 2011 by Suzuki et al. (2011) and the hypocenter by JMA is also shown with a broken rectangle and a diagonal cross, respectively. Closed rectangles show location of epicenters for the strong motion generation areas (SMGAs of *M*7-class events) estimated by Asano and Iwata (2012).

In the logarithmic ratio of **Eqs. 1**, **2**, the relationships between the S-wave at the basement and the P-wave at the basement is expressed by the following equations.

$$\log O_{\mathrm{b}}^{S}(\omega) = \log O_{\mathrm{b}}^{P}(\omega) + a_1(\omega) \tag{3}$$

$$a_1(\omega) = \log \frac{{V_{\mathrm{P}}}^3}{{V_{\mathrm{S}}}^3} + \log \frac{R_{\theta\phi}^{S}}{R_{\theta\phi}^{P}} + \log e^{\frac{r\omega}{2}\left(-\frac{1}{Q_{\mathrm{S}}V'_{\mathrm{S}}} + \frac{1}{Q_{\mathrm{P}}V'_{P}}\right)} \tag{4}$$

$a_1(\omega)$ includes the influence of the source effect and the path effect, which are V_P/V_S around an earthquake source region, the ratio of the S-wave radiation coefficient to that of the P-wave, and the internal attenuation of the P-wave and S-wave propagating in the crust.

The relationships between the P-wave at the basement and P-wave at the ground surface, and between the S-wave at the basement and S-wave at the ground surface are expressed using the transfer functions $G^P(\omega)$ and $G^S(\omega)$ based on the P-wave and S-wave subsurface structures from the basement to the ground surface, as follows.

$$O_{\mathrm{s}}^{P}(\omega) = O_{\mathrm{b}}^{P}(\omega) \cdot G^{P}(\omega) \tag{5}$$

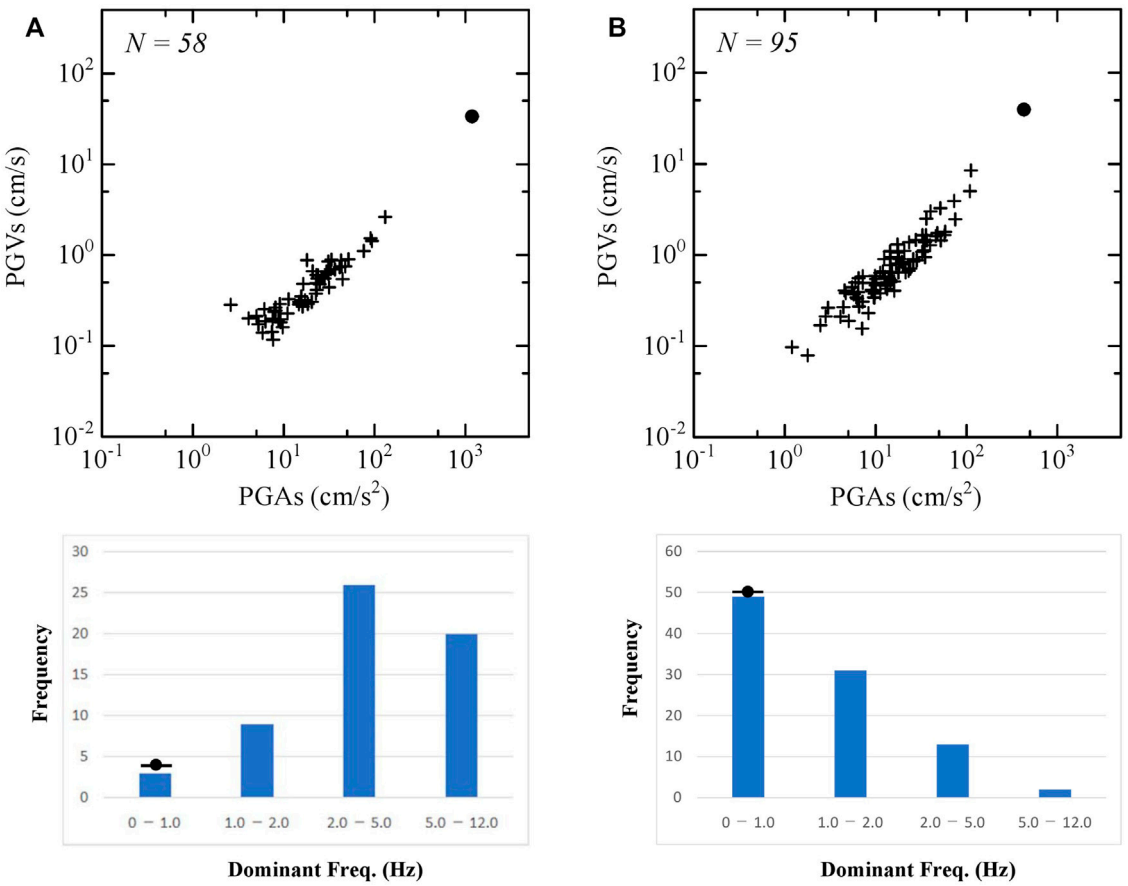

FIGURE 2 | Information of PGAs, PGVs, and the peak frequency in the seismic data used in this study. *N* in the figures indicates the number of earthquakes used. Crosses and a circle in the figure of PGAs and PGVs at KS and SS stations show data of the moderate-sized earthquakes with a magnitude (*Mj*) of 5.0–6.0 and data of the 2011 off the Pacific coast of Tohoku earthquake (*Mw* 9.0), respectively. Histograms of the dominant frequency (Hz) for data of the moderate-sized earthquakes observed at KS and SS stations are shown with that of the 2011 off the Pacific coast of Tohoku earthquake (*Mw* 9.0) by a circle in the figure. **(A)** KS station **(B)** SS station.

$$O_s^S(\omega) = O_b^S(\omega) \cdot G^S(\omega) \tag{6}$$

The subscript of s represents the ground surface.

In the logarithm of **Eqs. 5**, **6**, $a_2(\omega)$ and $a_3(\omega)$ which includes the influence of the site effect related to the P-wave and the S-wave subsurface structures respectively, are expressed by the following equations.

$$\log O_s^P(\omega) = \log O_b^P(\omega) + a_2(\omega) \tag{7}$$

$$\log O_s^S(\omega) = \log O_b^S(\omega) + a_3(\omega) \tag{8}$$

$$a_2(\omega) = \log G^P(\omega) \tag{9}$$

$$a_3(\omega) = \log G^S(\omega) \tag{10}$$

Finally, the relationships between the P-wave at the surface and the S-wave at the surface from **Eqs. 3**, **7**, **8** is expressed by the following equations.

$$\log O_s^S(\omega) = \log O_s^P(\omega) + b(\omega) \tag{11}$$

$$b(\omega) = a_1(\omega) - a_2(\omega) + a_3(\omega) \tag{12}$$

$b(\omega)$ includes the influence of the source effect, the path effect, and the site effect (Tsuno and Miyakoshi, 2019). In practically, $b(\omega)$ is estimated from a spectral ratio of S-wave to P-wave using seismic data observed at the ground surface at a seismic station. Miyakoshi and Tsuno (2015) investigated the relationships between P-wave at the basement and S-wave at the ground surface, by the theoretical technique, the empirical formulas, and observation data. As a result, Miyakoshi and Tsuno (2015) concluded that the spectral ratio of S-wave at the ground surface to P-wave at the basement was significantly affected by the site effects contrast to the source effects and the path effects.

The method of on-site P-wave EEW directly predicts S-wave by multiplying a site-specific spectral ratio of S-wave to P-wave prepared in advance by P-wave observed in the real-time at a seismic station, as expressed by the **Eq. 11** in the frequency domain with a logarithm (Tsuno and Miyakoshi, 2019; Zhao and Zhao, 2019). Therefore, this method using P-wave can significantly reduce the time of T*s-p* to issue the warning than

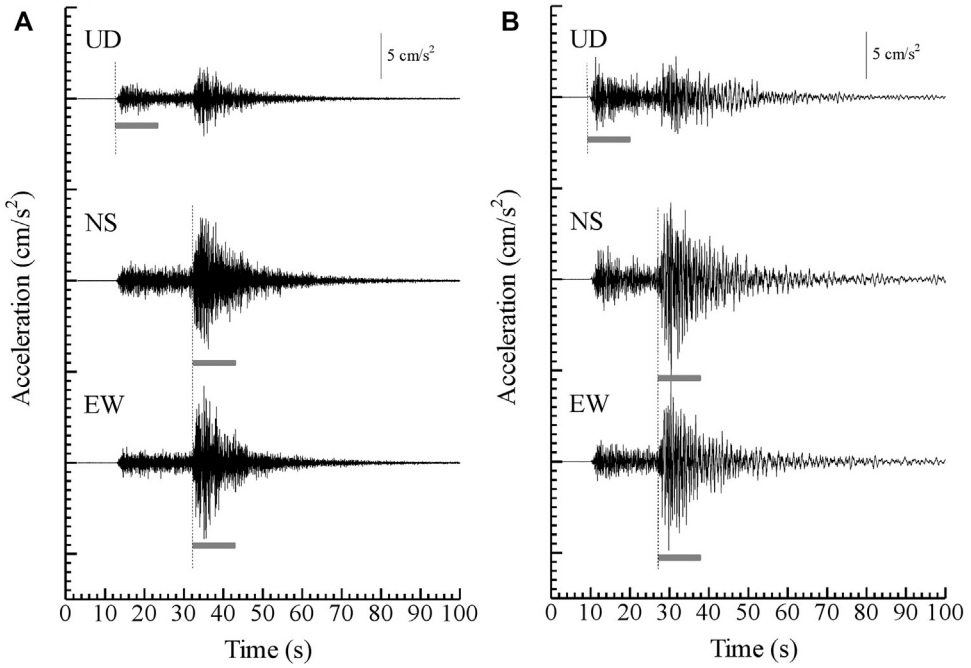

FIGURE 3 | Waveforms of acceleration for 3 components during an earthquake (*Mj* 5.9) occurred on 11th/April 2011 observed at KS and SS stations. Broken lines show an onset of P-wave for UD component and onsets of S-wave for NS and EW components. Under lines show a time-window of 10.24 s for each component, to estimate a spectral ratio of S-wave to P-wave. **(A)** KS station **(B)** SS station.

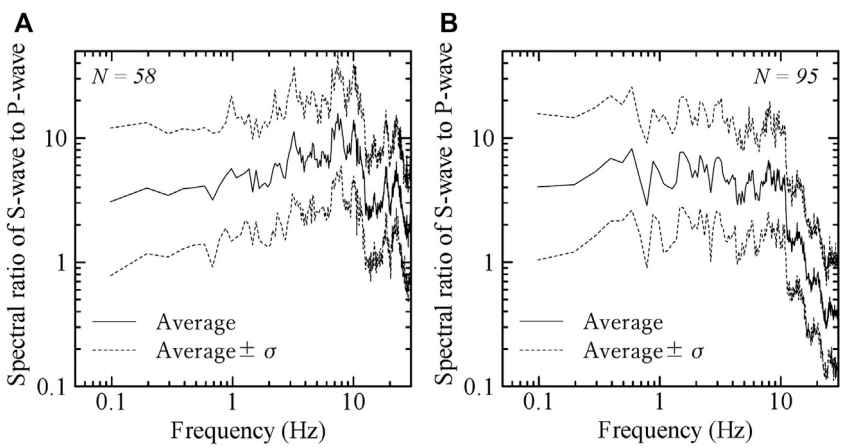

FIGURE 4 | Estimated site-specific spectral ratios of S-wave to P-wave for a time-window of 10.24 s at KS and SS stations. *N* in the figures indicates the number of earthquakes used. **(A)** KS station **(B)** SS station.

the previous method mainly using S-wave. Specifically, S-wave was predicted in the frequency domain, by using P-wave as shown in **Figure 3** with an underline for UD component.

Site-specific Ratio of S-Wave to P-Wave Observed

A site-specific spectral ratio of S-wave to P-wave for Fourier spectrum and pseudo-velocity response spectrum (a damping coefficient of 20%), and a site-specific ratio of S-wave to P-wave for SI (Spectral Intensity; Housner, 1965) using seismic data of moderate-sized earthquakes at KS and SS stations as shown in **Figure 1** were estimated. SI is calculated by averaging velocity response with a damping coefficient of 20% from a period of 0.1–2.5 s. At first, onsets of P-wave and S-wave for all the data were visually read as shown in **Figure 3**. Fourier spectrum and pseudo-velocity response spectrum of S-wave in horizontal components and P-wave in a vertical component without a

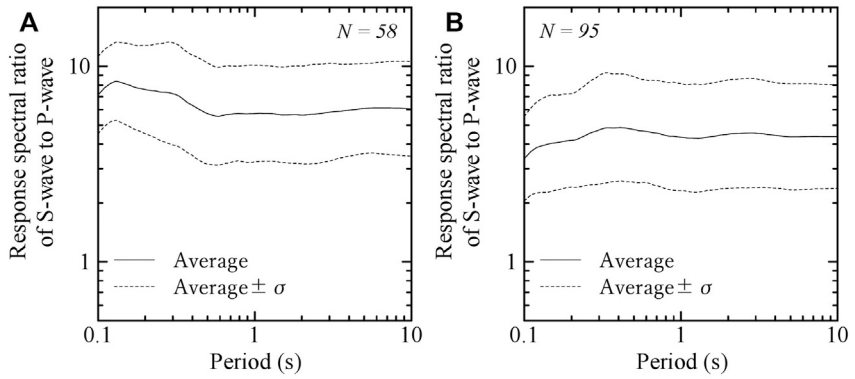

FIGURE 5 | Estimated site-specific response spectral ratios of S-wave to P-wave for a time-window of 10.24 s at KS and SS stations. *N* in the figures indicates the number of earthquakes used. **(A)** KS station **(B)** SS station.

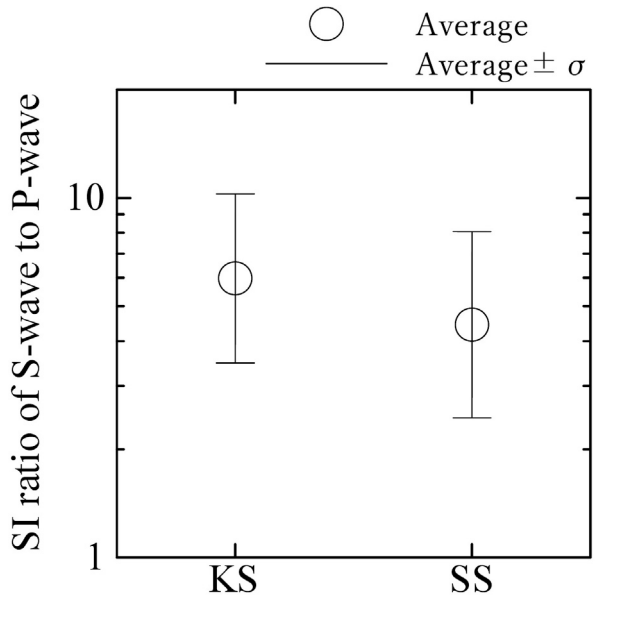

FIGURE 6 | Estimated site-specific SI ratios of S-wave to P-wave for a time-window of 10.24 s at KS and SS stations.

smoothing process were calculated using time-windows of 10.24 s after the onsets. The time of T*s-p* in the seismic data used was sufficiently secured to avoid mixing S-wave into a part of P-wave, which means the time of T*s-p* is longer than 10.24 s in this study. Spectral ratios of S-wave to P-wave were calculated by dividing the Fourier spectrum and pseudo-velocity response spectrum of S-wave which is the arithmetic mean for the NS component and the EW component, by those of P-wave for the UD component. Finally, the spectral ratios of S-wave to P-wave and SI ratio of S-wave to P-wave were averaged by those for all the seismic data at each seismic station.

Estimated site-specific spectral ratios, response spectral ratios, and SI ratios of S-wave to P-wave for a time-window of 10.24 s at KS and SS stations are shown in **Figures 4–6** with a plus and a minus of one standard deviation, respectively. The spectral ratio of S-wave to P-wave at the ground surface was significantly affected by the subsurface velocity structure and therefore, the spectral ratio of S-wave to P-wave at SS station in the sedimentary basin site had a large amplification in a wide frequency range of 0.3–10 Hz. On the other hand, the spectral ratio of S-wave to P-wave at KS station in the rock site had a large amplification in a frequency range of 3–10 Hz, especially it had the peak at the high frequency of around 10 Hz. The negative value for the spectral ratio of S-wave to P-wave in the frequency indicates that site amplification of P-wave is larger than that of S-wave as shown in the **Eq. 12**. Site-specific response spectral ratios have a more smoothed tendency than site-specific spectral ratios in the frequency/period domain without the negative value. Site-specific SI ratios of S-wave to P-wave are 6 and 4.5 at KS and SS stations, respectively.

A stability of site-specific spectral ratio of S-wave to P-wave, using seismic data with the different number of datasets was examined. RMS (Root Mean Square) between the spectral ratio of S-wave to P-wave using seismic data to the full datasets, for KS and SS stations is shown in **Figure 7**. The number of full datasets is 58 and 95 for KS and SS stations, respectively. In general, as the number of datasets increases, the spectral ratio becomes stable. In this study, RMS becomes stable enough by 40 and 20 data samples for KS and SS stations, respectively.

Prediction of S-Wave From P-Wave in the Real-Time

S-wave was predicted by multiplying the site-specific spectral ratio of S-wave to P-wave prepared in advance by P-wave observed in the real-time at each seismic station, using the **Eq. 11**. As an example, Fourier spectra of S-wave for the earthquake of *Mj* 5.9, occurred on 11th/April 2011 at KS and SS stations whose accelerations are shown in **Figure 3**, predicted

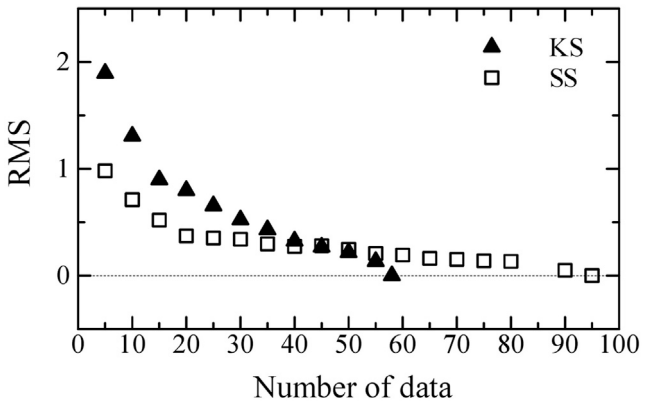

FIGURE 7 | RMS between the spectral ratio of S-wave to P-wave using seismic data to the full datasets, for KS and SS stations. The number of full datasets is 58 and 95 for KS and SS stations, respectively.

by this method were shown in **Figure 8**. Predicted Fourier spectrum of S-wave was in good agreement to the observed with the dominant frequency of about 10 Hz for the earthquake at KS station. On the other hand, predicted Fourier spectrum of S-wave was in good agreement to the observed with the dominant frequency of 1–2 Hz for the earthquake at SS station. The on-site P-wave EEW method could well explain Fourier spectrum of the S-wave in the frequency of more than 0.5 Hz at both KS and SS stations in which the site conditions are different. However, this method could not well explain Fourier spectrum of the S-wave in the frequency of less than 0.5 Hz. Miyakoshi and Tsuno (2015) pointed out that the spectral ratio of S-wave to P-wave at the basement is relatively affected by both the source effects and the path effects in the low frequency and in the high frequency, respectively. Even at the ground surface, therefore, the difference between the observation and the prediction in the low frequency are caused by the influence of the radiation coefficient in $a_1(\omega)$ of the **Eq. 4**. Pseudo-velocity response spectra (a damping coefficient of 20%) of S-wave for the earthquake of *Mj* 5.9, occurred on 11th/April 2011 at KS and SS stations whose accelerations are shown in **Figure 3**, predicted by this method were shown in **Figure 9**, with the average ± the standard deviation. The predicted response spectra of S-wave were in good agreement to those observed in periods of 0.1–10 s at both KS and SS stations, indicating the observations mostly within the average ± one standard deviation of the predictions. Predicted SIs of S-wave for all the earthquakes at KS and SS stations against those observed are shown in **Figure 10**. The predictions of SI of S-waves were in good agreements with the observations within the logarithmic standard deviation of 0.25.

It was indicated that the on-site P-wave EEW method, based on the site-specific spectral ratio of S-wave to P-wave can predict the observed S-wave in the single indicator of SI as well as in the frequency/period content for the moderate-sized earthquakes.

APPLICATION OF THE ON-SITE P-WAVE EEW METHOD TO THE 2011 OFF THE PACIFIC COAST OF TOHOKU EARTHQUAKE

The applicability of the on-site P-wave EEW method to seismic data observed at KS and SS stations, during the 2011 off the Pacific coast of Tohoku earthquake (Mw 9.0), Japan was investigated. Waveforms of acceleration for 3 components during the 2011 off the Pacific coast of Tohoku earthquake (*Mw* 9.0) occurred on 11th/March 2011 observed at KS and SS stations are shown **Figure 11**.

In the real-time, S-waves were predicted by multiplying the site-specific spectral ratio of S-wave to P-wave prepared in advance (See **Figure 4**) by the different time-windows of 10, 20, and 25 s after P-wave arrived. Predicted Fourier spectra of

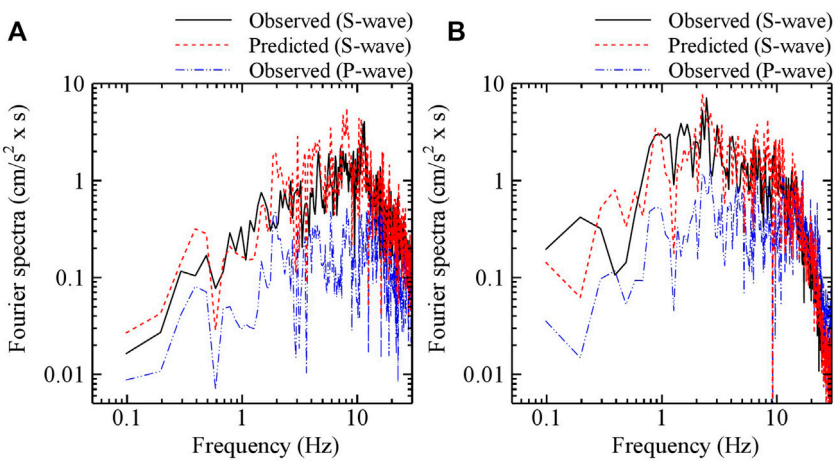

FIGURE 8 | Predicted Fourier spectra of S-wave for the earthquake of *Mj* 5.9 on 11th/April 2011 at KS and SS stations whose accelerations are shown in **Figure 3**. Observed Fourier spectra of P-wave for the earthquake are also shown. **(A)** KS station **(B)** SS station.

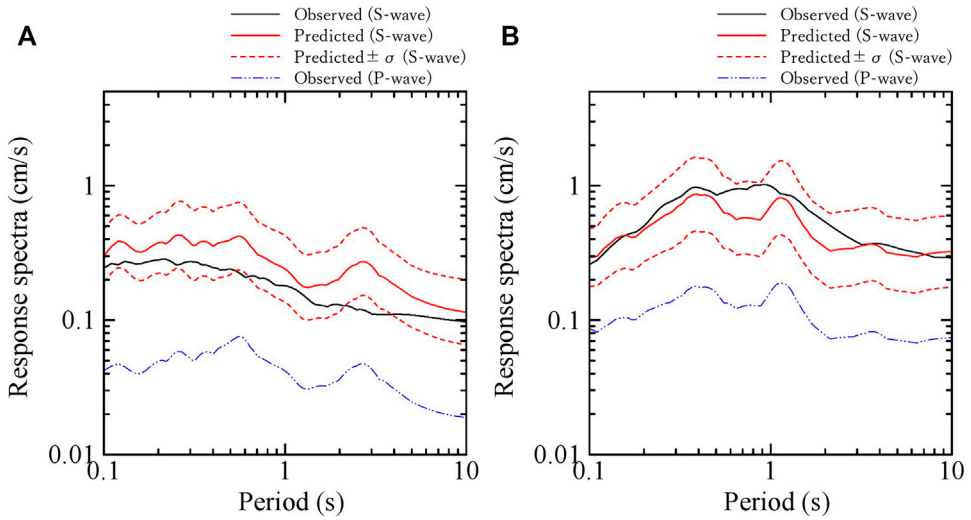

FIGURE 9 | Predicted pseudo-velocity response spectra (a damping coefficient of 20%) of S-wave for the earthquake of *Mj* 5.9 on 11th/April 2011 at KS and SS stations whose accelerations are shown in **Figure 3**, with the average ± the standard deviation. Observed pseudo-velocity response spectra of P-wave for the earthquake are also shown. **(A)** KS station **(B)** SS station.

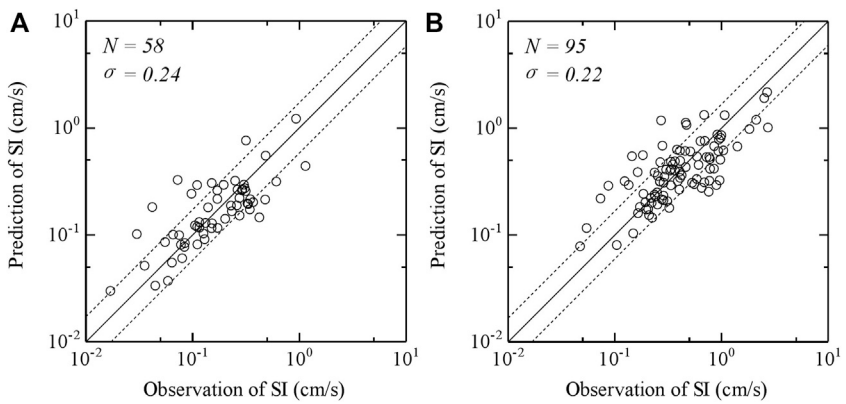

FIGURE 10 | Predicted SIs of S-wave for all the earthquakes at KS and SS stations against those observed. *N* and σ in the figures indicate the number of earthquakes and one logarithmic standard deviation, respectively. **(A)** KS station **(B)** SS station.

S-wave for time-windows of 10, 20, and 25 s at KS and SS stations were shown in **Figures 12**, **13**, respectively. As a result, the S-wave predicted for the 2011 off the Pacific coast of Tohoku earthquake, using the time-window of 10 s in P-wave after P-wave arrived, could not reproduce the S-wave observed with the underestimation at both KS and SS stations. On the other hand, the S-wave predicted using the time-windows of 20 and 25 s in P-wave could reproduce the S-wave observed at both KS and SS stations. It was point out that an area generating strong motions in the earthquake source fault differed from an area which the fault rupture started in the large-scaled earthquake event. To directly predict S-wave from P-wave observed in the real-time, therefore, a time-window containing P-wave induced by an area generating strong motions in the fault is necessary to be analyzed. As for strong motion generation areas (SMGAs) for the 2011 off the Pacific coast of Tohoku earthquake as shown in **Figure 1**, (Asano and Iwata, 2012) reported that two strong motion generation areas (SMGA1 and SMGA2) are identified in the Miyagi-oki region west of the hypocenter and another two strong motion generation areas (SMGA3 and SMGA4) are in the Fukushima-oki region southwest of the hypocenter. Also, they indicated that the strong ground motions in the frequency range 0.1–10 Hz along the Pacific coast are mainly controlled by these SMGAs of *M*7-class events existing in the deeper portion of the source fault plane. In their results, the strong ground motions observed in Miyagi Pref. where the KS and SS stations are located, are significantly affected by SMGA1 (Length: 36 km, width: 36 km, rise time: 6.9 s, and rupture velocity: 4 km/s) and

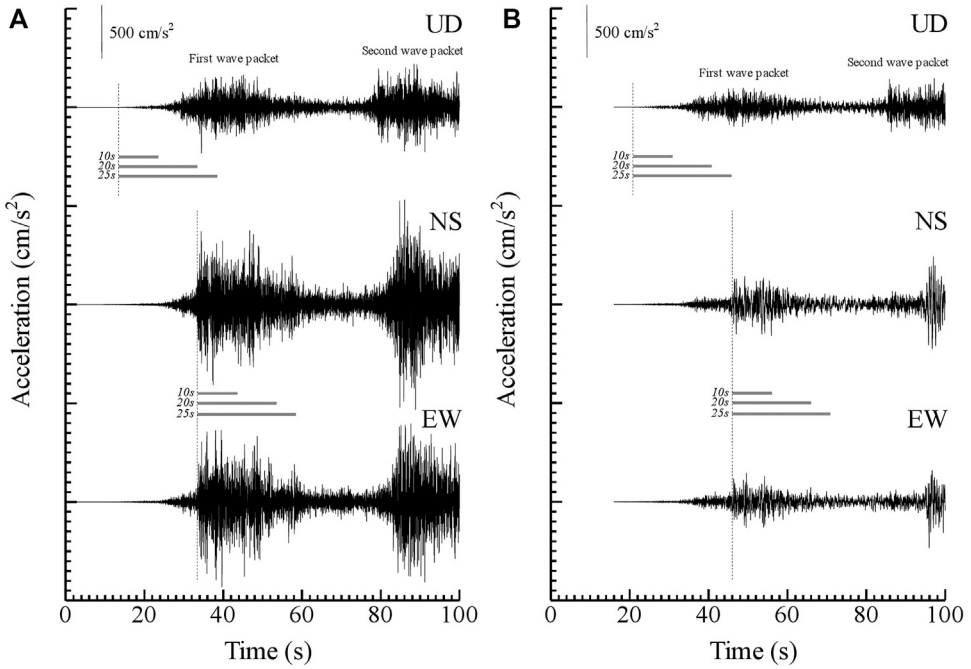

FIGURE 11 | Waveforms of acceleration for 3 components during the 2011 off the Pacific coast of Tohoku earthquake (*Mw* 9.0) occurred on 11th/March 2011 observed at KS and SS stations. Broken lines show onsets of P-wave for UD component and S-wave for NS and EW components. Under lines show time-windows of 10, 20, and 25 s for each component. The first and second wave packet are generated by different the strong motion generation areas (SMGAs) estimated by Asano and Iwata (2012). **(A)** KS station **(B)** SS station.

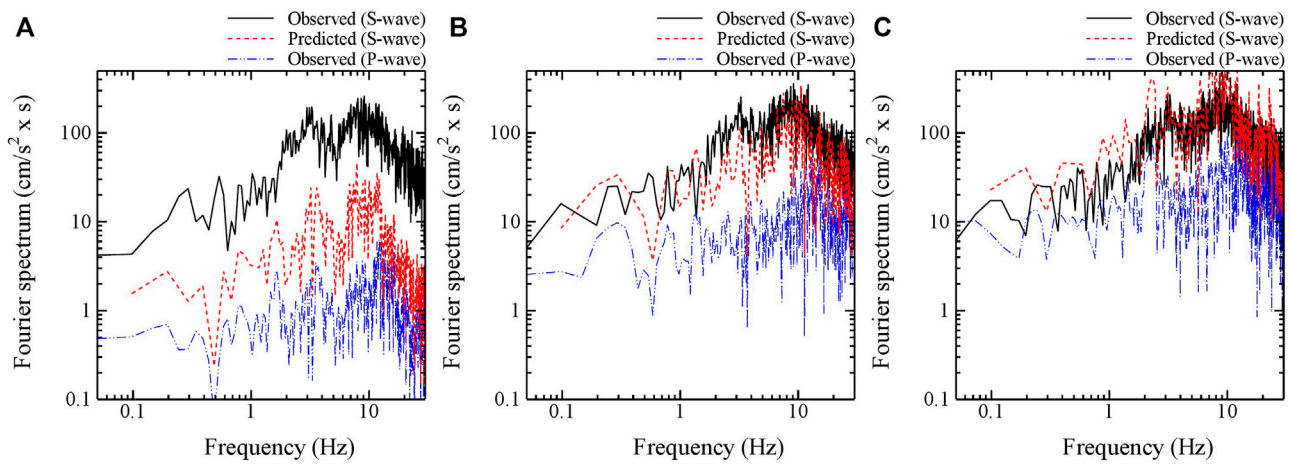

FIGURE 12 | Predicted Fourier spectra of S-wave for time-windows of 10, 20, and 25 s during the 2011 off the Pacific coast of Tohoku earthquake (*Mw* 9.0) at KS station. **(A)** Time-window of 10 s **(B)** Time-window of 20 s **(C)** Time-window of 25 s.

SMGA2 (Length: 36 km, width: 36 km, rise time: 6.9 s, and rupture velocity: 4 km/s). Specially, the first and the second wave packets of strong ground motions observed at the KS and SS stations as shown in **Figure 11** are generated by SMGA1 and SMGA2, respectively (Asano and Iwata, 2012). To accurately predict the amplitude of S-wave by P-wave observed in the real-time during the 2011 off the Pacific coast of Tohoku earthquake, it is necessary that strong ground motions generated by SMGA1 is contained in the observed P-wave. In this study, the time-window of 20 s in a UD component after P-wave arrived at KS and SS stations includes strong ground motions generated by SMGA1 at least. Therefore, the S-wave predicted using the time-windows of 20 and 25 s in P-wave could reproduce the S-wave observed at both KS and SS stations.

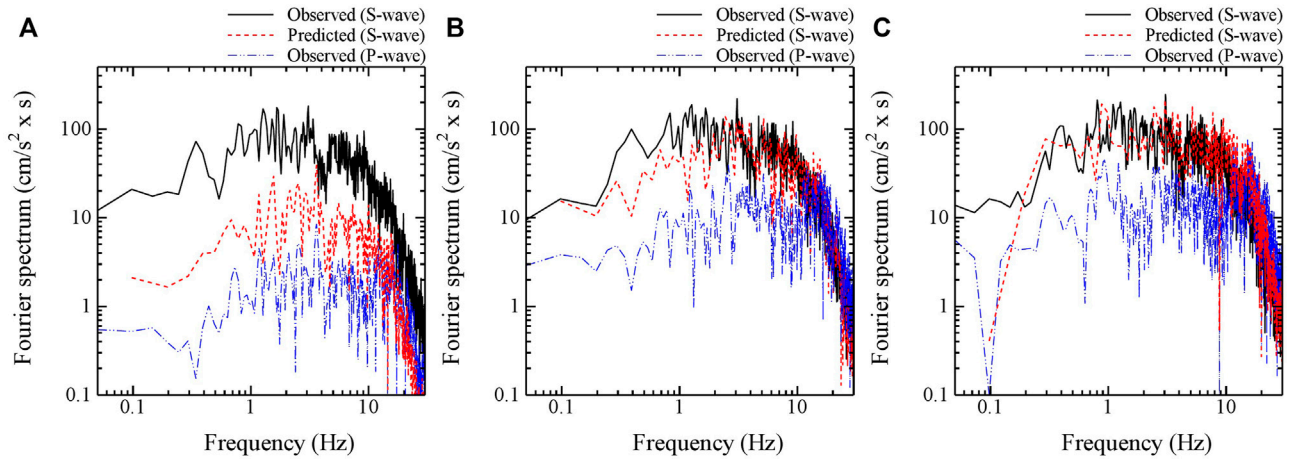

FIGURE 13 | Predicted Fourier spectra of S-wave for time-windows of 10, 20, and 25 s during the 2011 off the Pacific coast of Tohoku earthquake (*Mw* 9.0) at SS station. **(A)** Time-window of 10 s **(B)** Time-window of 20 s **(C)** Time-window of 25 s.

On the other hand, the discrepancy between the S-wave observed and the S-wave predicted even using the appropriate time-windows in P-wave at KS and SS stations is larger in the low frequency than in the high frequency caused by the source effects, as shown in **Figures 12B**, **13C**. It might be caused by that the prediction of S-wave for this large-scaled earthquake (Mw 9.0) which significantly affected the ground motions in the low frequency, was performed by the site-specific spectral ratio of S-wave to P-wave using seismic data of moderate-sized earthquakes with a magnitude (*Mj*) of 5.0–6.0.

DISCUSSION

In the real-time, SI of S-wave by multiplying the site-specific spectral ratio of SI prepared in advance (See **Figure 6**) by SI of P-wave observed were predicted. The predicted SI of S-wave and the observed SI of S-wave with the time interval of one second until the time that S-wave arrived at each KS and SS stations during the 2011 off the Pacific coast of Tohoku earthquake is shown in **Figure 14**. The predicted SI of S-wave is gradually increasing until S-wave for the first wave packet arrives at each KS and SS stations. The values of the predicted SI immediately before S-wave for the first wave packet arrives reproduce well the maximum values of S-wave observed at both KS and SS stations. On the other hand, the lead time from the last prediction to the arrival of S-wave is not sufficient at KS station, because SMGA1 generating the strong ground motions for the first wave packet which is in the Miyagi-oki region west of the hypocenter, is close to KS station. At SS station which is located to more inland than KS station, however, the lead time of 10 s could be earned by this on-site P-wave EEW method.

Even in the case of the large-scaled earthquake, the on-site P-wave EEW method availably works by using the gradually increasing time-windows after P-wave arrived in the single indicator of SI as well as in the frequency content. Note that in principle, this method can be applied to P-wave observed in the real-time until S-wave arrives. In case of mixing S-wave into a part of P-wave, the prediction overestimated the observation, as the predicted Fourier spectra of S-wave for the time-windows of 25 s after P-wave arrived at KS station shown in **Figure 12C**.

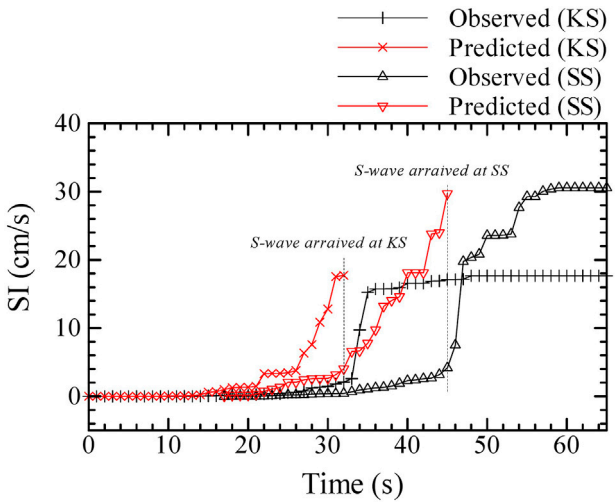

FIGURE 14 | Predicted SI of S-wave and observed SI of S-wave with the time interval of one second during the 2011 off the Pacific coast of Tohoku earthquake (*Mw* 9.0) at KS and SS stations. Predicted SI of S-wave by using P-wave in the real-time, is shown until the time that S-wave arrived at each KS and SS station.

CONCLUSIONS

In this study, at first, the on-site P-wave EEW method which multiplies a site-specific spectral ratio of S-wave to P-wave prepared in advance by P-wave observed in the real-time at seismic stations is applied to seismic data for moderate-sized

earthquakes with a magnitude (*Mj*) of 5.0–6.0, occurred in the eastern Japan, observed at both the sedimentary basin site and the rock site. As a result, this method predicted well the observed S-wave in the single indicator of SI within the logarithmic standard deviation of 0.25 as well as in the frequency of more than 0.5 Hz. It is, also, confirmed that the site-specific spectral ratio of S-wave to P-wave at a seismic station was stably retrieved from 20 data samples at least. To investigate the applicability of this method to earthquake ground motions induced by a large-scaled earthquake, finally, this method is applied to seismic data during the 2011 off the Pacific coast of Tohoku earthquake, Japan (*Mw* 9.0). The prediction of S-wave using a time-window of 10 s after P-wave arrived, could not reproduce the observation with the underestimation; however, the prediction of S-wave using a time-window of more than 20 s containing P-wave propagated from an area generating strong motions in the fault, could reproduce the observation. Even in the case of the large-scaled earthquake, the on-site P-wave EEW method based on the site-specific spectral ratio of S-wave to P-wave at a seismic station availably works by using the gradually increasing time-windows after P-wave arrived in the single indicator of SI as well as in the frequency content, avoiding the mixture of S-wave into a part of P-wave.

Practically, this on-site P-wave EEW will be installed with the regional EEW (Odaka et al., 2003) in the field of railway, Japan, to further improve the safety from earthquakes. The threshold levels for the single indicators to issue earthquake early warning is empirically set on around less than 10 cm/s in SI and/or less than 100 cm/s^2 in PGA and therefore, the nonlinearity of the soft soil at the surface layers is not necessary to be considered from a practical point of view. As the future work, however, the influence of nonlinearity of the soft soil at the surface layers should be investigated to accurately predict earthquake ground motions in the case of strong ground motions. Also, the effects of 2-D and 3-D irregularity of the sedimentary basin should be investigated as well as the nonlinearity of the soft soil at the surface layers.

DATA AVAILABILITY STATEMENT

The data analyzed in this study is subject to the following licenses/restrictions: Original data is provided by JR-East. ST has the results processed in this study. Requests to access these datasets should be directed to Seiji Tsuno, tsuno.seiji.75@rtri.or.jp.

AUTHOR CONTRIBUTIONS

ST analyzed the seismic data. ST drafted the manuscript.

ACKNOWLEDGMENTS

Seismic data recorded at two seismic stations maintained by JR-East were used. The geophysical information of a site condition in J-SHIS by NIED (National Research Institute for Earth Science and Disaster Resilience) at seismic stations were used. Location of hypocenters for the moderate-sized earthquakes with a magnitude (*Mj*) of 5.0–6.0 and the 2011 off the Pacific coast of Tohoku earthquake estimated by JMA (Japan Meteorological Agency) were used. We also thank two reviewers for their comments and suggestions, which significantly contributed to improving the quality of this paper.

REFERENCES

Aki, K., and Richard, P. G. (2002). *Quantitative Seismology*. 2nd Edition. Sausalito, CA: University Science Books.

Allen, R. M., Gasparini, P., Kamigaichi, O., and Böse, M. (2009). The Status of Earthquake Early Warning Around the World: An Introductory Overview. *Seismological Res. Lett.* 80, 682–693. doi:10.1785/gssrl.80.5.682

Allen, R. M., and Kanamori, H. (2003). The Potential for Earthquake Early Warning in Southern California. *Science* 300, 786–789. doi:10.1126/science.1080912

Asano, K., and Iwata, T. (2012). Source Model for strong Ground Motion Generation in the Frequency Range 0.1-10 Hz during the 2011 Tohoku Earthquake. *Earth Planet. Sp* 64, 1111–1123. doi:10.5047/eps.2012.05.003

Hoshiba, M., and Aoki, S. (2015). Numerical Shake Prediction for Earthquake Early Warning: Data Assimilation, Real-Time Shake Mapping, and Simulation of Wave Propagation. *Bull. Seismological Soc. America* 105 (3), 1324–1338. doi:10.1785/0120140280

Hoshiba, M. (2013). Real-time Prediction of Ground Motion by Kirchhoff-Fresnel Boundary Integral Equation Method: Extended Front Detection Method for Earthquake Early Warning. *J. Geophys. Res. Solid Earth* 118, 1038–1050. doi:10.1002/jgrb.50119

Housner, G. W. (1965). "Intensity of Earthquake Ground Shaking Near the Causative Fault," in Proceeding of the 3rd World Conf. Earthq. Eng., New Zealand, January 1, 1965, 94–115.

Iwata, T., and Irikura, K. (1986). Separation of Source, Propagation and Site Effects from Observed S-Waves. *Jssj* 239, 579–593. doi:10.4294/zisin1948.39.4_579

Miyakoshi, H., Tsuno, S., Chimoto, K., and Yamanaka, H. (2019). Spatial Variation of S-Wave Site Amplification Factors Estimated Using Observed Ground Motion Data in the Tokyo Metropolitan Area. *J. Seismology* 23 (I-34), 1–18. doi:10.1190/segj2018-130.1

Miyakoshi, H., and Tsuno, S. (2015). Influence of the Source, Path, and Site Effects on the Relationship between P-Waves at the Seismic Bedrock and S-Waves on the Ground Surface. *Jssj* 68, 91–105. doi:10.4294/zisin.68.91

Nakamura, Y. (1988). "On the Urgent Earthquake Detection and Alarm System (UrEDAS)," in Proc. of 9th World Conference on Earthquake Engineering, Tokyo-Kyoto, Japan, Aug 2-9, 1988, 673–678.

Nakamura, Y. (1996). Research and Development of Intelligent Earthquake Disaster Prevention Systems UrEDAS and HERAS. *Doboku Gakkai Ronbunshu* 1996, 1–33. doi:10.2208/jscej.1996.531_1

Odaka, T., Ashiya, K., Sato, S., Ohtake, K., and Nozaka, D. (2003). A New Method of Quickly Estimating Epicentral Distance and Magnitude from a Single Seismic Record. *Bull. Seismological Soc. America* 93, 526–532. doi:10.1785/0120020008

Suzuki, W., Aoi, S., Sekiguchi, H., and Kunugi, T. (2011). Rupture Process of the 2011 Tohoku-Oki Mega-Thrust Earthquake (M9.0) Inverted from strong-motion Data. *Geophys. Res. Lett.* 38, a–n. doi:10.1029/2011GL049136

Tsuno, S., and Miyakoshi, H. (2019). Investigation of Earthquake Warning for the Threshold of P-Wave, Using an Amplitude Ratio of S-Wave to P-Wave. *J. JAEE* 19 (6), 105–106. doi:10.5610/jaee.19.6_105

Wu, Y.-M., Kanamori, H., Allen, R. M., and Hauksson, E. (2007). Determination of Earthquake Early Warning Parameters, τc and Pd,

for Southern California. *Geophys. J. Int.* 170, 711–717. doi:10.1111/j.1365-246x.2007.03430.x

Wu, Y.-M., and Kanamori, H. (2005). Rapid Assessment of Damage Potential of Earthquakes in Taiwan from the Beginning of P Waves. *Bull. Seismological Soc. America* 95, 1181–1185. doi:10.1785/0120040193

Yamamoto, S., and Tomori, M. (2013). Earthquake Early Warning System for Railways and its Performance. *J. JSCE* 1, 322–328. doi:10.2208/journalofjsce.1.1_322

Yang, Y., and Motosaka, M. (2015). Ground Motion Estimation Using Front Site Wave Form Data Based on RVM for Earthquake Early Warning. *J. Disaster Res.* 10 (4), 667–677. doi:10.20965/jdr.2015.p0667

Zhao, C., and Zhao, J. X. (2019). S- and P-Wave Spectral Ratios for On-Site Earthquake Early Warning in Japan. *Bull. Seismol. Soc. Am.* 109 (1), 395–412. doi:10.1785/0120180116

Conflict of Interest: The author declares that the research was conducted in the absence of any commercial or financial relationships that could be construed as a potential conflict of interest.

Advantages of publishing in Frontiers

OPEN ACCESS
Articles are free to read for greatest visibility and readership

FAST PUBLICATION
Around 90 days from submission to decision

HIGH QUALITY PEER-REVIEW
Rigorous, collaborative, and constructive peer-review

TRANSPARENT PEER-REVIEW
Editors and reviewers acknowledged by name on published articles

Frontiers
Avenue du Tribunal-Fédéral 34
1005 Lausanne | Switzerland

Visit us: www.frontiersin.org
Contact us: frontiersin.org/about/contact

REPRODUCIBILITY OF RESEARCH
Support open data and methods to enhance research reproducibility

DIGITAL PUBLISHING
Articles designed for optimal readership across devices

FOLLOW US
@frontiersin

IMPACT METRICS
Advanced article metrics track visibility across digital media

EXTENSIVE PROMOTION
Marketing and promotion of impactful research

LOOP RESEARCH NETWORK
Our network increases your article's readership